NASA Contractor Report 201633

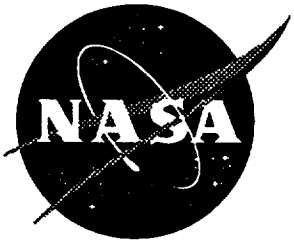

Experimental and Computational Aerothermodynamics of a Mars Entry Vehicle

Brian R. Hollis
North Carolina State University, Raleigh, North Carolina

Grants NAG1-1663 and NAGW-1331

December 1996

National Aeronautics and
Space Administration
Langley Research Center
Hampton, Virginia 23681-0001

EXPERIMENTAL AND COMPUTATIONAL AEROTHERMODYNAMICS OF A MARS ENTRY VEHICLE

by

BRIAN R. HOLLIS

A dissertation submitted to the Graduate Faculty of North Carolina State University in partial fulfillment of the requirements for the Degree of Doctor of Philosophy

Aerospace Engineering
Hypersonic Aerothermodynamics

Raleigh, North Carolina
1996

ABSTRACT

HOLLIS, BRIAN, R. Experimental and Computational Aerothermodynamics of a Mars Entry Vehicle (under the direction of Dr. John N. Perkins).

An aerothermodynamic database has been generated through both experimental testing and computational fluid dynamics simulations for a 70 deg sphere-cone configuration based on the NASA Mars-Pathfinder entry vehicle. The aerothermodynamics of several related parametric configurations were also investigated. Experimental heat-transfer data were obtained at hypersonic test conditions in both a perfect-gas air wind tunnel and in a hypervelocity, high-enthalpy expansion tube in which both air and carbon dioxide were employed as test gases. In these facilities, measurements were made with thin-film temperature-resistance gages on both the entry vehicle models and on the support stings of the models. Computational results for freestream conditions equivalent to those of the test facilities were generated using an axisymmetric/2D laminar Navier-Stokes solver with both perfect-gas and nonequilibrium thermochemical models. Forebody computational and experimental heating distributions agreed to within the experimental uncertainty for both the perfect-gas and high-enthalpy test conditions. In the wake, quantitative differences between experimental and computational heating distributions for the perfect-gas conditions indicated transition of the free shear layer near the reattachment point on the sting. For the high-enthalpy cases, agreement to within, or slightly greater than, the experimental uncertainty was achieved in the wake except within the recirculation region, where further grid resolution appeared to be required. Comparisons between the perfect-gas and high-enthalpy results indicated that the wake remained laminar at the high-enthalpy test conditions, for which the Reynolds number was significantly lower than that of the perfect-gas conditions.

EXPERIMENTAL AND COMPUTATIONAL AEROTHERMODYNAMICS OF A MARS ENTRY VEHICLE

by

BRIAN R. HOLLIS

A dissertation submitted to the Graduate Faculty of North Carolina State University in partial fulfillment of the requirements for the Degree of Doctor of Philosophy

Aerospace Engineering
Hypersonic Aerothermodynamics

Raleigh, North Carolina
1996

Approved by:

Dr. John N. Perkins, Chairman	Dr. Fred R. DeJarnette, Co-Chairman
Dr. Ndaona Chokani	Dr. J. M. Anthony Danby
Dr. Gerald D. Walberg	

To my parents, who have always supported my work.

BIOGRAPHY

The author was born on May 5, 1967 in DuBois (which is NOT pronounced 'doo-bwa'), Pennsylvania. He graduated from the DuBois High School in May of 1985, and entered the University of Virginia in August of 1985. He completed his thesis, "Design of a Hybrid Airship", and graduated with a Bachelor of Science Degree in Aerospace Engineering in May of 1989. He entered the Department of Mechanical and Aerospace Engineering at North Carolina State University in August of 1989. After conducting research at the Naval Surface Warfare Center, he completed his thesis, "A Fine-Wire Thermocouple Stagnation Temperature Probe for Use in Hypersonic Flows of Nitrogen", and graduated with a Master of Science degree in Aerospace Engineering in May of 1991. He then entered the Doctoral program at North Carolina State University. He pursued his doctoral research at the NASA Langley Research Center in the Experimental Hypersonics and the Aerothermodynamics Branches. He completed his dissertation, "Experimental and Computational Aerothermodynamics of a Mars Entry Vehicle", and received a Doctor of Philosophy Degree in Aerospace Engineering in December of 1996.

ACKNOWLEDGMENTS

I am grateful for the aid which has been provided to me during the course of this research program, and I want to take this opportunity to acknowledge those who have helped me along the way.

I would first like to thank the faculty of the Department of Mechanical and Aerospace Engineering at North Carolina State University for creating the educational environment in which I learned the skills required to complete this research. More specifically, I owe thanks to my committee members, Dr.'s John Perkins, Fred DeJarnette, Ndaona Chokani, Gerald Walberg and Anthony Danby for supporting my work. Thanks also go to Dr.'s Graham Candler, Robert Gould and Hassan Hassan who provided numerous intellectual challenges during my education. Additional thanks to Graham Candler (now at the University of Minnesota) for the use of his NEQ2D code in this work.

This dissertation research was carried out during a four-year stay at the NASA Langley Research Center, and could not have been undertaken without the support of numerous people there. Thanks go first to Charles Miller, Experimental Hypersonics Branch Head and later Aerothermodynamic Branch Head. This work would not have been possible without the support from the EHB and AB in the form of funding, computational resources, access to Langley shops and labs, and wind tunnel test time.

Conducting this research at Langley was an excellent learning experience, and along the way, many of the members of the EHB and AB Branches have helped me in one way or another. On the experimental side of this work, Scott Berry, Mike DiFulvio, Dr. Scott Holland, Tom Horvath, and (soon-to-be) Dr. Ron Merski were great sources of information on heat-transfer measurement techniques, model construction and instrumentation, data reduction, and impulse-facility testing. On the computational side of this work, thanks to Steve Alter, Dr. Peter Gnoffo, Dr. Robert Mitchletree, and Dr. Jim Moss for many discussions on Mars-Pathfinder flow field solutions, wake flow behavior, grid generation, and grid adaptation. Additional thanks to Steve Alter for the use of the VGM code in this research, and to Richard Wheless for

graphics assistance.

The experimental phase of this research was made possible through the hard work of the personal of Langley's shops and labs who machined, instrumented and assembled the wind tunnel models which I tested. In the order in which the models were put together, I owe thanks to: Eugene Robbins and Dave Farringer in the Fabrication Division, who helped me design the models and who fabricated their components; Harry Walthall in the Glass Lab, who drilled and polished the models; and Ed Self, Steve Parrish and Greg Draughon in the Microelectronics Lab who instrumented the models. They built more than 40 test models, which in total were instrumented with several thousand thin film gages, and put in the overtime hours to finish them all before the test scheduling deadlines.

Thanks also go to those who operated the facilities in which these models were tested: Sheila Wright, Bert Senter, and all of the technicians at the Langley 31-Inch Mach 10 Tunnel; and at GASL, to John Calleja, the HYPULSE facility engineer, for many discussions on the operational aspects of HYPULSE, and to Ed Poole, the HYPULSE facility technician, for all his hard work installing and wiring the gage connections for the numerous models tested in HYPULSE.

And finally, thanks to my parents, who have waited patiently through these many years of schooling.

Funding for this research was provided by NASA Grants NAG-1-1663 and NAGW-1331 to North Carolina State University.

TABLE OF CONTENTS

LIST OF TABLES

LIST OF FIGURES

LIST OF SYMBOLS

a	speed of sound (m/sec)
B	bias error of a measurement
C_H	Stanton number, $q/\left[\rho_\infty U_\infty \left(h_{0,2}-h_w\right)\right]$
c_p	isobaric specific heat (J/kg-K)
c_v	isochoric specific heat (J/kg-K)
D_s	diffusion coefficient of species s (m^2/sec)
D_{sr}	binary diffusion coefficient for species s and r (m^2/sec)
d	molecular diameter (m)
E	voltage (V)
E	total internal energy (J/kg)
e	internal energy (J/kg)
e_v	vibrational energy (J/kg)
$e_{v,s}$	vibrational energy of species s (J/kg)
$e^*_{v,s}$	vibrational energy of species s evaluated at temperature T (J/kg)
H	total enthalpy (J/kg)
h	enthalpy (J/kg)
h_v	vibrational enthalpy of species s (J/kg)
k	thermal conductivity (W/m-K)
J	transformation Jacobian
$k_{b,r}$	backward reaction rate coefficient
$k_{f,r}$	forward reaction rate coefficient
k_v	thermal conductivity of vibrational energy (W/m-K)
Kn	Knudsen number, $\lambda_{mfp}\lvert\vec{\rho}\rvert/\rho$
L	length (m)
M	Mach number, U/a
N	number density (#/m^3)
P	pressure (Pa)
P	precision error of a measurement
Pr	Prandtl number, $\mu c_p/k$

Q	heat energy (J/m^2)
$Q_{T\text{-}V}$	translation-vibration energy exchange rate (W/m^3)
q	heat transfer rate (W/m^2)
q_v	vibrational heat transfer rate (W/m^2)
R	radius (m)
R	gage resistance (Ω)
R	gas constant (kJ/kg-mol-K)
$R_{b,r}$	backward reaction rate
Re	Reynolds number, $\rho u x / \mu$
$R_{f,r}$	forward reaction rate
R_u	universal gas constant (kJ/kg-K)
S	surface distance (m)
s	standard deviation
T	temperature (K)
T_v	vibrational temperature (K)
t	time (sec)
t_{95}	95th percentile point of two-tailed Student distribution
u,v,w	Cartesian velocity vector components (m/sec)
U	velocity magnitude (m/sec)
U	uncertainty of a measurement
W_s	molar weight of species s (g/g-mol)
$\dot{w}_s$	rate of production of species s (kg/m^3-sec)
X_s	mass fraction of species s
x,y,z	Cartesian coordinates (m)
x^*	dimensionless penetration depth, $x/[2(\alpha t)^{1/2}]$
Y_s	mole fraction of species s

GREEK SYMBOLS

α	angle-of-attack (deg)
α	thermal diffusivity, $k/(\rho c_p)$ (m^2/sec)

α_R	coefficient of resistance (1/°R)
β	thermal product, $(\rho c_p k)^{1/2}$ (W-sec$^{1/2}$/m^2- K)
δ_{ij}	Kronecker delta
Γ_s	molar concentration of species s (g-mol/g)
γ	ratio of specific heats
ϕ	roll angle (deg)
λ	heat transfer correction factor (1/K)
λ_{mfp}	mean free path, $1/(\sqrt{2}\,\pi d^2 n)$ (m)
μ	translational viscosity (kg/m-sec)
μ_v	vibrational viscosity (kg/m-sec)
θ_v	characteristic vibrational temperature (K)
ρ	density (kg/m^3)
ρ	density of species s (kg/m^3)
σ	heat-transfer residual, $\Delta q/q$
$\hat{\sigma}$	residual RMS, $(\sigma_1^2 + \sigma_2^2 + .. + \sigma_n^2)^{1/2}$
τ_{ij}	viscous shear stress tensor
$<\tau_s>$	translation-vibrational energy relaxation time for species s (sec)
τ_{sr}	translation-vibrational energy relaxation time for species s due to collisions with species s (sec)
ξ,η,ζ	transformed coordinates
Ψ	free shear layer turning layer (deg)

SUBSCRIPTS AND SUPERSCRIPTS

0	stagnation
0,2	post-normal-shock stagnation conditions
2	post-normal-shock static conditions
∞	freestream conditions
298	condition at 298 K temperature
300	condition at 300 K temperature
b	model forebody radius
c	corner radius
D	diameter

f	frustrum radius
FR	Fay-Riddell
s	sting radius
s	species s
r	species r
ref	reference
v	vibrational mode
w	wall conditions

CHAPTER 1
INTRODUCTION

Section 1.1 Overview

The research presented herein deals with the aerothermodynamics of an atmospheric entry vehicle. The purpose of an entry vehicle is to deliver a payload (scientific, military or human) into the atmosphere or to the surface of a planet. As such a vehicle travels through the atmosphere of a planet, it is exposed to aerothermodynamic (and aerodynamic) loads, the magnitude of which depend on the entry flight path and the geometry of the craft. These loads must be accurately predicted by the designers of the vehicle in order to ensure the completion of its mission.

The entry-vehicle geometry of interest in this work is a blunt sphere-cone configuration, which is based on a Mars probe currently being built by NASA that will utilize aerobraking in the atmosphere of Mars instead of propulsion for deceleration from interplanetary velocities. The use of aerobraking permits the design of a vehicle of much less total mass in comparison to an entry vehicle with an on-board propulsion system. However, the fact that an aerobraking vehicle will enter the atmosphere at high speed and then be decelerated by the aerodynamic drag produced by passage through the atmosphere means that greater aerothermodynamic loads will be produced on the vehicle.

Because of the severe environment to which an aerobraking entry vehicle will be exposed, there is little room for error in the design of the craft. The performance of the vehicle must be accurately predicted in order to ensure that its construction is sufficiently durable to withstand the atmospheric entry loads. In order to make these predictions, mission planners and vehicle designers must rely on a database of experimental test results and computational fluid dynamics simulations.

This work details the creation of an entry vehicle aerothermodynamic database through

experimental heat-transfer testing and computational fluid dynamics (CFD) simulations. The primary subject of this database is a spherically-blunted, large-angle cone configuration based on NASA's Mars-Pathfinder probe. This database is supplemented by data on several additional parametric configurations. The experimental data were gathered in a series of perfect-gas wind tunnel tests and high-enthalpy impulse facility tests. Computational data were generated through the use of a computational fluid dynamics code to produce solutions of the Navier-Stokes equations for perfect-gas and nonequilibrium flows with freestream conditions equivalent to the experimental test conditions. These data and the details of the experimental and computational research carried out to produce this database are presented in this report.

Section 1.2 Aerobraking and Aeroassisted Orbit Transfer

The entry vehicle configuration on which this work is based was designed to make use of aerobraking during entry into the atmosphere of Mars. Aerobraking is a type of orbital maneuver of the class known as Aeroassisted Orbit Transfer. Aeroassisted Orbit Transfer is defined (Walberg, 1985) as the method by which changes in a vehicle's orbit are produced through the use of aerodynamic forces or a combination of aerodynamic forces and propulsion systems, as opposed to only the use of a vehicle's propulsion system. The use of aeroassisted orbit transfer in both orbital and interplanetary missions has been the subject of much study (Walberg, 1985, Walberg, 1988), as vehicles designed to make use of aeroassisted maneuvers can benefit from a greatly reduced propellant mass requirement, which results in a lower total vehicle mass. Such a vehicle is commonly referred to as an Aeroassisted Orbit Transfer Vehicle, or AOTV. AOTV missions can be divided into three general categories: 1) synergetic plane change, 2) orbital transfer applications, and 3) interplanetary mission applications (which includes aerobraking). Synergetic plane change is defined as the use of aerodynamic and propulsive forces to effect a change in a vehicle's orbital inclination. Orbital transfer applications involve the use of aeroassist to produce a decrease

in a vehicle's orbital attitude (and possibly a change in orbital inclination). In interplanetary applications, aerodynamic forces (and also in some cases propulsive forces) are employed to convert the initial hyperbolic approach trajectory of an interplanetary vehicle to a circular or elliptical orbit about the target planet, or to decelerate the vehicle to a safe atmospheric entry velocity. In interplanetary applications, aerodynamic drag is used to produce a decrement in velocity, as opposed to synergetic plane change or orbital transfer, in which both aerodynamic lift and drag can be employed to produce both a velocity decrement and a change in orbital inclination. For this reason, the term aerobraking is often applied to the use of aeroassisted orbit transfer in interplanetary mission applications.

Section 1.3 Aerobraking and Mars Exploration Missions

Manned and unmanned exploration of Mars has long been one of the main interplanetary exploration aims of NASA. While manned missions to Mars are goals for the 21st century or beyond, exploration of Mars through unmanned probes has been in progress for decades and will continue into the next century. Because of the associated mass savings, aerobraking will be a key element in future Mars missions (Braun, Powell, and Hartung, 1990, Walberg, 1991).

The first NASA spacecraft to enter the Martian atmosphere and land on the surface of the planet were the two Mars Viking probes in the 1970's. The Viking configuration (Figure 1.3.1) was an axisymmetric, hemispherically-blunted 70 deg cone with rounded corners and an afterbody with two conical frustrums. Although the Viking spacecraft did not utilize aerobraking, the general configuration of the Viking entry vehicle aeroshell is being used in the design of current and future Mars probes which will utilize aerobraking.

The Viking aeroshell geometry was incorporated into the design of the Mars-Pathfinder (formerly known as MESUR - Mars Environmental Survey) probe (Bourke, Golombek, Spears and Sturms, 1992;

Tauber, Henline, Chargin, Papadopoulos, Chen, Yang and Hamm, 1992) which is scheduled for launch on December 5, 1996, and for arrival on the auspicious date of July 4, 1997. Mars-Pathfinder is intended to be the first in a series of Mars orbiters and landers (hence the name Pathfinder) which will be sent to Mars over the next decade through the Mars Surveyor program. The Mars-Pathfinder probe consists of a forebody aeroshell heat shield and a payload packaged in the afterbody of the craft. The aeroshell is a 3.5 m diameter, 70 deg half-angle sphere-cone (Figure 1.3.2) with a nose-to-base radius ratio of 0.5 and a 0.05 corner-to-base radius. The afterbody is a 49.6 deg conical frustrum shape with a 0.53 frustrum-to-base radius ratio. The aeroshell is designed to be ejected once the craft has decelerated to parachute deployment speed, from which point the payload will descend to the surface via the parachute.

It should be noted that although the geometries of the Viking and Pathfinder probes are similar, their atmospheric entry trajectories are much different. The Viking probe was propulsion-decelerated for an entry from orbit at the relatively modest speed of 4.4 km/sec, whereas the Pathfinder probe was designed for a direct (no orbital insertion) high-speed entry into the Martian atmosphere at 7 km/sec. Deceleration to parachute deployment speed will be accomplished entirely by aerobraking within the atmosphere of Mars. This high entry velocity will lead to much greater heating loads on the Pathfinder aeroshell, which shields the scientific payload in the afterbody of the vehicle from the direct effects of entry heating. Consequentially, the accurate characterization of the flow field around the vehicle is of great importance in the design of aerobraking vehicles such as Mars-Pathfinder.

Section 1.4 Blunt-Body Aerobrake Wake Flow

One of the critical aspects in the design of Pathfinder and other planetary probes is the structure of the flow in the wake of the forebody aeroshell because this is where the payload will be located. The behavior of the wake flow must be fully understood in order to ensure that the payload structural design and

thermal protection shielding are sufficient to withstand the aerodynamic and aerothermodynamic loads produced in the wake. While forebody flow fields have been the subject of much research, less is known about the behavior of wake flows. A NASA program which would have provided flight data on wake flows, the Aeroassist Flight Experiment (AFE), was unfortunately canceled. Spacecraft designers thus must rely on the relatively limited database from computational fluid dynamics and ground-based experimentation.

The general character of the flow in the near-wake of a blunt-body is illustrated in Figure 1.4.1. The near wake flow field is characterized by a large region of separated, recirculating flow behind the base of body. This region is produced when the forebody boundary layer separates from the body at its corner to form a free shear layer. The angle of this shear layer with respect to the freestream, Ψ, is termed the free shear layer turning angle. Downstream of the base, the free shear layer is turned back toward the freestream direction through a series of compression waves which coalesce into a recompression shock. Within the viscous recirculation region, the flow velocity is generally much lower than in the outer inviscid flow region, but may still reach supersonic speeds, which would lead to the formation of a shock structure as the reversed flow approached the base of the body. The surface heat-transfer and pressure loads on the surface of the body within this separated flow region are generally at least an order of magnitude lower than on the forebody of the vehicle.

In Figure 1.3.1 the structure of the wake behind a blunt body in the absence of an afterbody or payload was illustrated. Now consider Figure 1.4.2, in which a vehicle with a large afterbody, the AFE, is shown. A recirculation zone will still be produced as the shear layer separates at the trailing corner of the aeroshell. However, depending on the free shear layer turning angle, the payload may not necessarily be contained entirely within the protective zone of the separation region. Impingement of the free shear layer on a portion of the payload would lead to much higher heating and pressure loads in that region. Thus, it can be seen that the shear layer must be characterized accurately so that the payload may either be sized to fit within the separation region, or be of durable enough construction to withstand the loads produced by the high-speed flow outside of the separation region. For this reason, special emphasis was placed on the

measurement of afterbody and wake heating rates in this research.

Section 1.5 Description of Research

As flight testing of planetary entry vehicles is generally prohibitively expensive, mission planners must rely on experimental ground testing and computational fluid dynamics simulations in their design. Both techniques have their advantages and disadvantages, and thus a combination of the two provides the best approach to the design of a planetary probe. Experimentation can provide direct measurements of aerodynamic loads and detailed surface temperature and heating distributions. However, even high-enthalpy impulse facilities are not able to duplicate the entire range of hypersonic flight conditions which such a vehicle may encounter. Furthermore, physical design limitations (i.e. the presence of a sting to support a model) may make it difficult to build models which accurately represent the actual vehicle geometry under consideration. CFD can, in theory, be used to simulate complete vehicle flow fields in any flight regime of interest. However, the reliability of the physical and thermochemical models, solution techniques and grid generation methods employed in CFD codes cannot be adequately assessed without an experimental database with which to compare results. It is thus desirable when designing a new entry vehicle or planning for the use of an existing design at different flight conditions to rely on both experimental data and computational predictions of vehicle performance.

The purpose of this research was to generate an experimental surface heating database for a blunt-body atmospheric entry vehicle configuration, and to demonstrate the capability to predict the flow field around such a vehicle through computational fluid dynamics. Because of its relevance to NASA's ongoing Mars exploration initiative, the configuration chosen for this study was that of the Mars-Pathfinder probe. Special attention was given to obtaining detailed surface heating data on the afterbody and in the wake of the vehicle on the model's sting because of the lack of available data in this region and its importance in

planetary probe design. Furthermore, testing was carried out in a CO_2 environment (as well as in air) because of the lack of data for conditions representative of the Martian atmosphere, which is 97% CO_2.

The experimental database was generated through hypersonic aerothermodynamic testing in the NASA Langley 31-Inch Mach 10 Air Tunnel and in the NASA HYPULSE Expansion Tube. CFD solutions were generated through the use of the non-equilibrium Navier-Stokes solver NEQ2D. Aerothermodynamic tests were first conducted in the 31-Inch Mach 10 Air Tunnel. Perfect-gas data from these tests were used for preliminary, baseline assessment of code performance, as well as of the experimental test techniques. Tests were then conducted in the HYPULSE Expansion Tube in both air and CO_2 test gases. These tests provided data for comparison of code performance in predicting flows with chemical and vibrational non-equilibrium.

The results of this experimental and computational research are detailed in this work. Chapter 2 presents a brief review of existing experimental and computational literature relevant to this study. The choice of vehicle geometries, and the design and construction of the test models is discussed in Chapter 3. Chapter 4 provides descriptions of the 31-Inch Mach 10 Air Tunnel and the HYPULSE Expansion Tube, their operating characteristics, and the methods for determining freestream flow properties in these facilities. The facilities' data acquisition systems and the techniques employed to reduce and analyze the experimental heat-transfer data are detailed in Chapter 5. The experimental results from the tests in these facilities are presented and discussed in Chapter 6. The Navier-Stokes solver which was employed in this work, NEQ2D, as well as the techniques used to generate and adapt grids for use with this code is discussed in Chapter 7. Computational results from NEQ2D for perfect-gas air, non-equilibrium air, and non-equilibrium CO_2 cases are presented in Chapter 8, and comparisons are made with the experimental data. A summary and discussion of the conclusions drawn from this research are presented in Chapter 9. References consulted in this research are listed in Chapter 10. The experimental databases from the 31–Inch Mach 10 Air Tunnel tests and the HYPULSE Expansion Tube tests are presented in detail in tabular and graphical form in Appendices A and B, respectively. The results of wind-tunnel-model material thermal properties

calibration tests, which were conducted in order to increase the accuracy of the experimental heat-transfer measurement techniques, are presented in Appendix C. Results from a series of hemisphere tests in the HYPULSE facility are also presented in Appendix C.

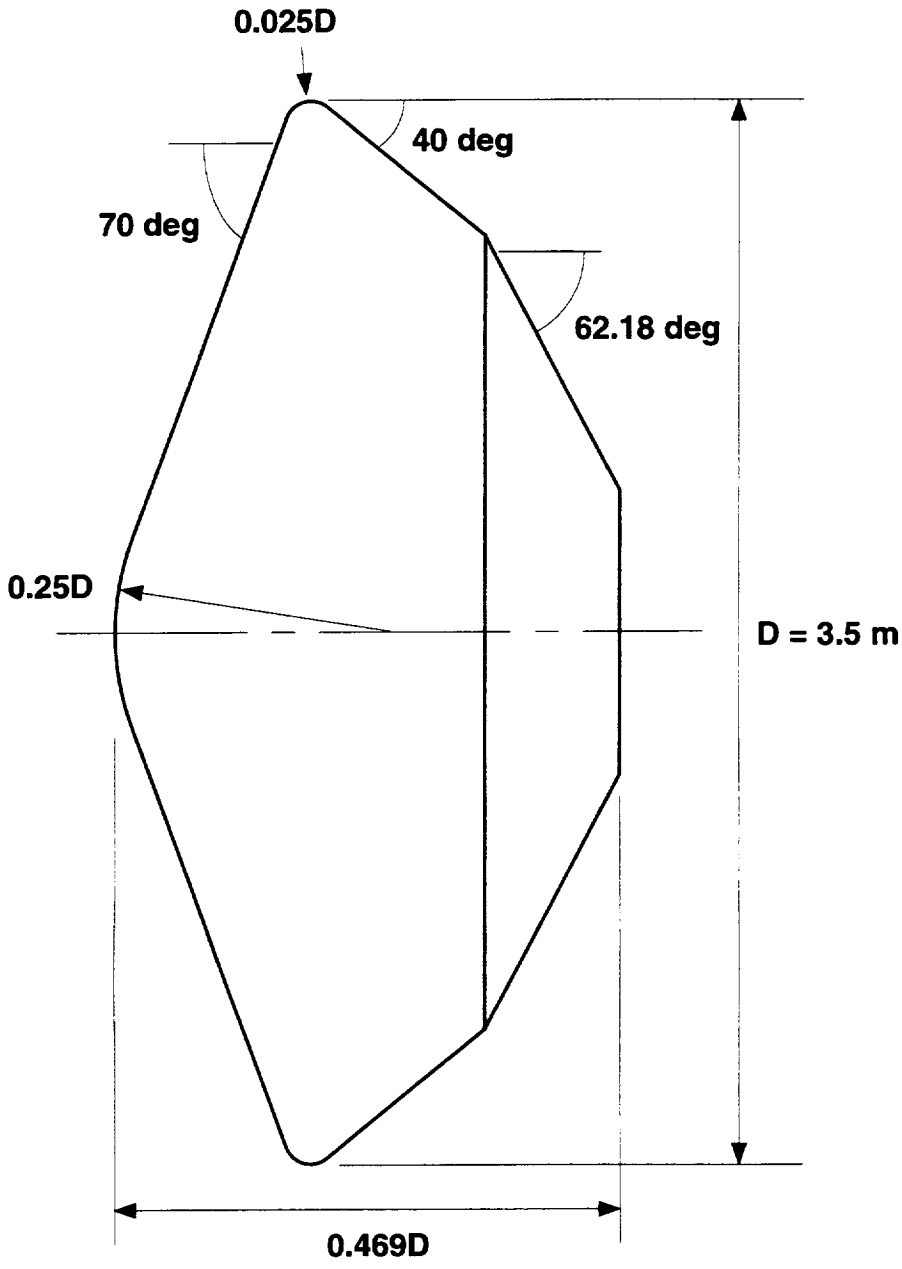

FIGURE 1.3.1 Mars Viking Geometry

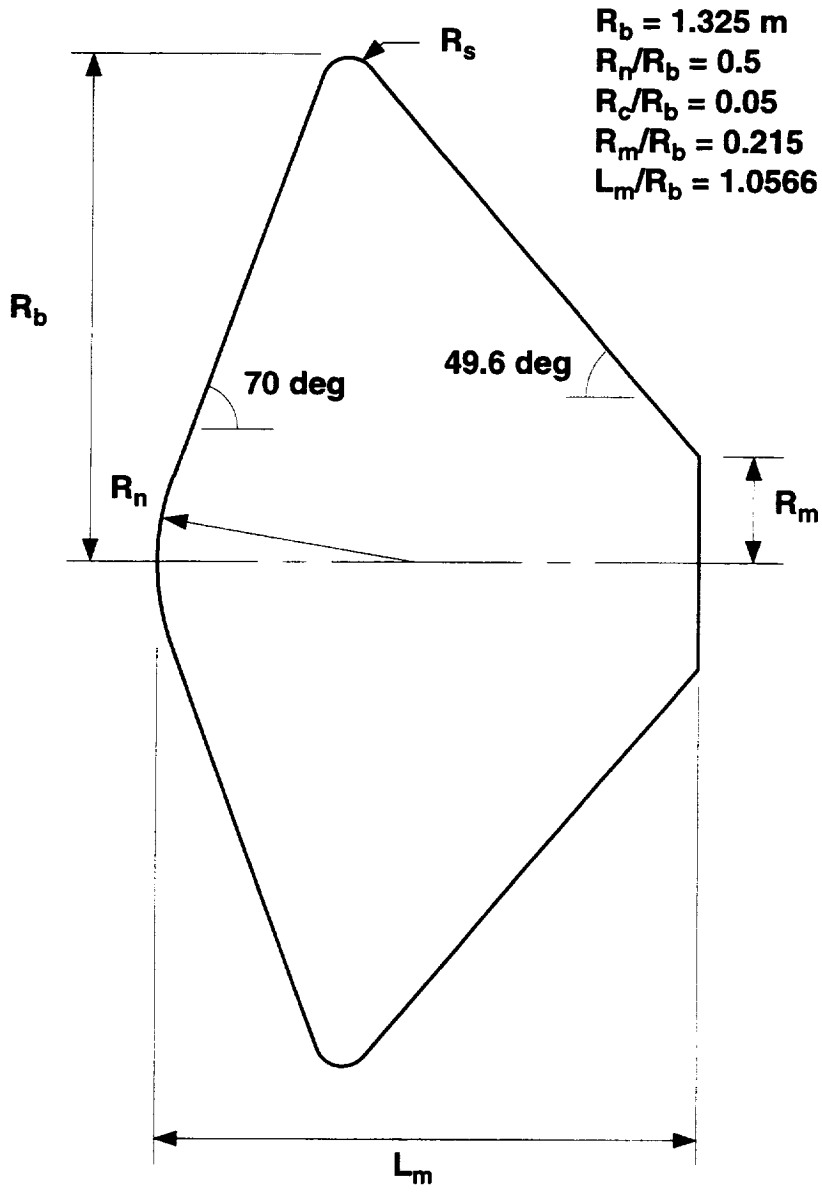

Figure1.3.2 Mars Pathfinder Geometry

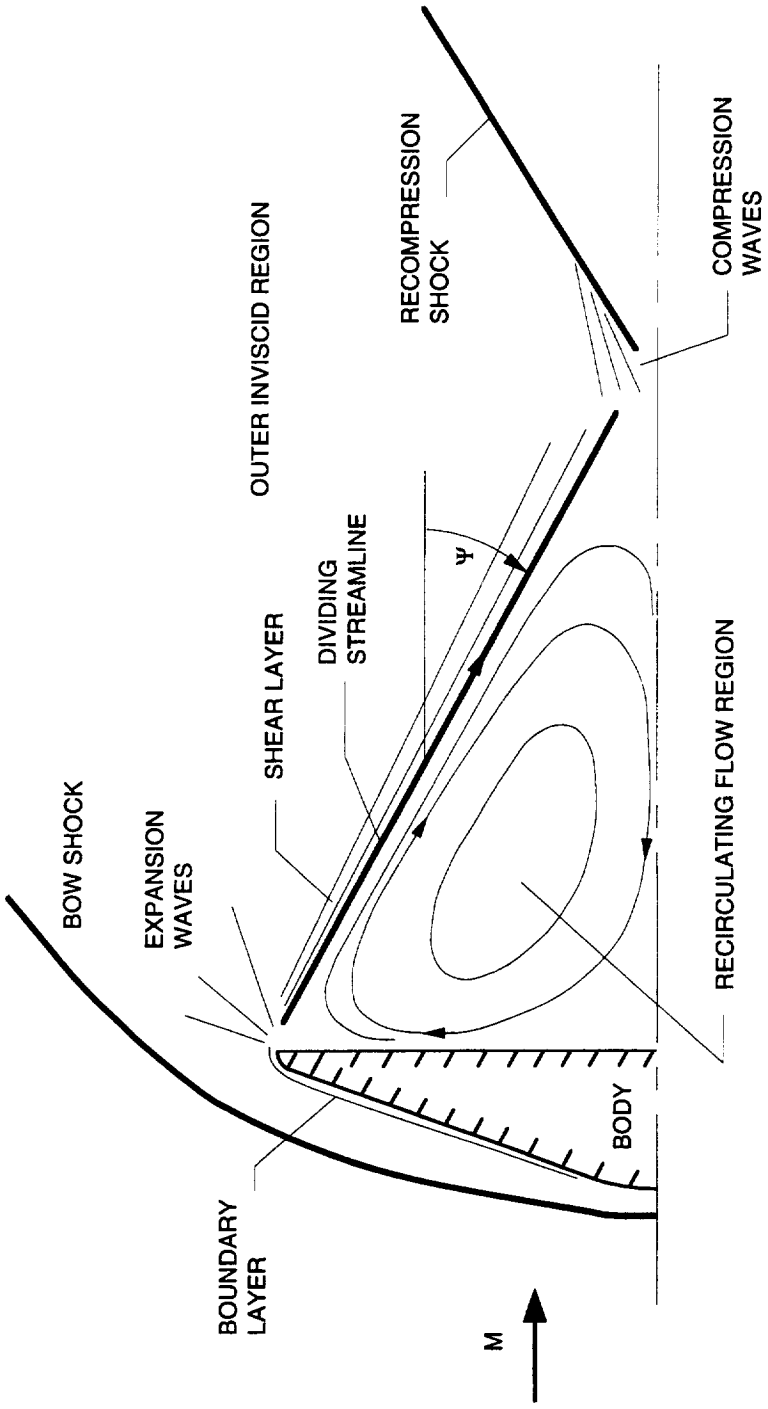

Figure 1.4.1 Blunt-Body Wake Flow Structure

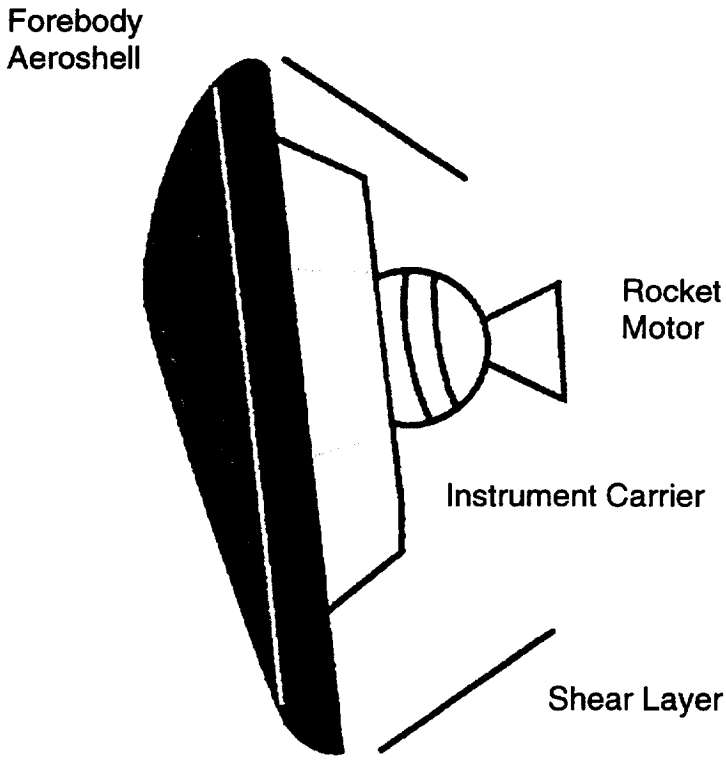

Figure 1.4.2 Aeroassist Flight Experiment (AFE) Vehicle

CHAPTER 2
LITERATURE REVIEW

This research deals with hypersonic flow around a blunt body entry vehicle. The general category of blunt bodies can be defined, in contrast to that of slender bodies, as dealing with vehicles which have a frontal surface with a very large radius of curvature in relation to the length of the vehicle. Hypersonic flows around blunt bodies are characterized by large angle, detached shock waves, behind which extremely high temperatures and pressures are generated. Examples include the Apollo command module, the Mars Viking, Venus Pioneer, and Jupiter Galileo probes, and the Space Shuttle. Blunt body hypersonics thus can be seen to be very important to the design of both manned and unmanned spacecraft, and has been the subject of a great deal of research.

Within the broad category of blunt body hypersonics, it is the narrower field of aerodynamic heating of planetary entry vehicles that is the subject of this work. In this field, the focus of most research has been on the forebody of the entry vehicle, as opposed to the afterbody or wake. This is partly due to the fact that, in the past, entry vehicles such as Apollo or the Mars-Viking probe were equipped with large, well-insulated heat shields behind which a small, modestly shielded payload could be safely sheltered, and thus the nature of the afterbody and wake flow was of less concern. More recently, new entry vehicles (e.g. AFE or Mars-Pathfinder) have featured large payloads which may not be completely shielded by the forebody of the craft, and thus the study of the wake flow has become of greater interest.

The subject of this research is a geometry closely resembling the Mars-Pathfinder entry vehicle, which is a 70 deg half-angle spherically-blunted cone. In the past ten years, a great deal of work has been carried out on such large-angle conical entry bodies. Owing to the wide-spread availability of high-speed computing resources and the dearth of hypersonic test facilities, the bulk of this work has been computational, rather than experimental, and in both fields the research has focussed primarily on the

forebody of the vehicle. Many of these studies have focussed on geometries similar to the Mars-Viking probe built by NASA in the 1970's, a 70 deg half-angle cone with a spherically-blunted nose, to which the Mars-Pathfinder is essentially identical in geometry if not in size.

It should be mentioned that at the time of the preparation of this report, there is an ongoing international investigation of blunt body wake heating in high-enthalpy and low density flows, which is under the auspices of AGARD (NATO's Advisory Group for Aerospace Research and Development). Several of the studies discussed in this chapter are a result of this project, which is known as the AGARD 18 Working Group, (anon., AGARD Advisory Report No. 319). Researchers involved with this project will likely be presenting additional experimental and computational data at or around the time of publication of this work.

Section 2.1 Experimental studies

In the 1950's and 1960's, the Cold War focussed most hypersonic research on the study of small-angle sphere-cone shapes in order to support the development of intercontinental ballistic missiles. The space race shifted the emphasis somewhat toward blunter geometries, as these are more efficient for decelerating a vehicle from planetary entry speeds. Experimental studies of blunt body hypersonics began with the Mercury and Apollo programs and have continued to the present with the AFE and Mars-Pathfinder projects. These and other projects have led to numerous blunt body aerothermodynamic studies in both conventional wind tunnels and high-enthalpy impulse facilities, with instrumentation ranging from phase change paint to fast-response thin-film gauges.

Some of the earliest documented heat-transfer data on large-angle conical bodies is from Stewart and Marvin (1969). They tested sphere-cone models with half-angles of 50 deg to 70 deg in the NASA Ames 42-Inch Shock Tunnel in air at Mach 15 at angles-of-attack from 0 deg to 30 deg. The models were

instrumented with back-face thermocouples, and the data were reduced using the thin-skin equations (e.g. Schultz and Jones, 1973). Non-dimensionalized zero degree angle-of-attack results agreed fairly well with simple analytical solutions using Lees theory, while no predictions were made for angle-of-attack cases. Stewart and Chen (1993) later tested a family of 70 deg sphere-cones with different corner radii in the same facility in air, CO_2, and CO_2-Ar environments. Models were tested at angles-of-attack of 0 deg, 10 deg, and 20 deg. The models were again instrumented with back-face thermocouples and the data were reduced by the thin-skin technique. Navier-Stokes solutions were computed for the 0 deg case using a modified version of Candler's NEQ2D code (Chen, Henline, Stewart and Candler, 1993). Although qualitative agreement between non-dimensionalized experimental data and computations was observed, the magnitudes of the heating rates differed by from 5% to 45% between experiment and computation.

Several researchers have carried out heat-transfer tests on large-angle cones in conventional low-enthalpy wind tunnels at the NASA Langley Research Center (LaRC). Shih and Gay (1984) tested a family of low L/D (lift-to-drag ratio) AOTV configurations and measured heat-transfer rates via the phase-change paint technique. Heating data were reported for both the forebody and the model sting at angles-of-attack from 0 deg to 30 deg. In tests at a freestream Reynolds number of 0.4×10^{-6} ft^{-1}, peak sting heating rates were found to be from 10% to 25% of the stagnation point heating rate depending on model angle-attack, while the peak heating location was from 0.6 to 1.8 body radii down the sting from the base of the model.

Shimshi (1992) tested 50 deg, 60 deg and 70 deg sphere-cone models in the NASA LaRC 15-Inch Mach 10 Air Tunnel at Reynolds numbers of 1.0 to 4.0×10^{6} ft^{-1} at 0 deg to 20 deg angles-of-attack. Heating data were obtained from thermocouple-instrumented models using the thin-skin technique, and from phosphor-coated ceramic models using the two-color thermographic phosphor technique (Buck, 1991, Merski, 1991). Shimshi also analyzed previously unpublished thin-skin heating technique data from Reddy and Miller (1986) tests in the NASA LaRC 20-Inch Mach 6 Air Tunnel. Shimshi's tests showed the theoretically expected decrease in stagnation point heating and increase in corner heating with increasing cone angle. These effects are due to the effective increase with cone-angle in the nose radius of the model,

which lowers the stagnation point heating, and the movement of the sonic line toward the corner, which leads to increased heating there. Shimshi also carried out heating computations using an inviscid (Weilmuenster and Hamilton, 1983) code to provide edge conditions for boundary layer computations (Hamilton, Weilmuenster and DeJarnette, 1985, Hamilton, Millman and Greendyke, 1993). Agreement was fairly good with the exceptions of small discontinuities in the predictions around the stagnation region and general over-prediction of the leeside heating values.

Dye (1993) tested an Aeroassisted Space Transportation Vehicle (ASTV) configuration in the NASA LaRC 31-Inch Mach 10 Air Tunnel. The ASTV concept was a 70 deg sphere-cone with a nose radius to body radius of 1.0, as compared to that of 0.5 for Mars-Pathfinder. Forebody, base and sting heating rates were measured with thin-film gages on Macor substrates at $\alpha = 0$ deg at a Reynolds number of 0.5×10^{-6} ft^{-1}. Surface pressure measurements were also made. Navier-Stokes computations were performed with the TUFF code (Molvick, 1989). Good agreement was observed for surface pressure distributions in the wake, but the heating rates differed considerably, possibly due to grid resolution or to the presence of a backward facing step near the shear layer reattachment point on the sting of the model. On the forebody, the measured and computed heating distributions were qualitatively similar, but the measured values were consistently higher than the computations by approximately 20%. Pressure distributions were again in good agreement. In light of the discussion on Macor material properties in Appendix C, it would seem that the forebody agreement would probably be very good if the Macor values presented in this report were used to re-reduce these data.

Wells (1988, 1990) has generated a large experimental database on the AFE vehicle from tests in the NASA LaRC 31-Inch Mach 10 Air and 20-Inch Mach 6 CF_4 Tunnels. Although the AFE is geometrically quite different from Mars-Pathfinder, analogies can be made between the wake flow structure of the two vehicles. Wells measured surface heating rates on the forebody and on the sting of an AFE model with thin-film gages on Macor substrates, and also took detailed flow field schlieren pictures and surface oil flow photographs. Wells measured the wake shear layer impingement location on the sting as a

function of angle-of-attack, and noted that the location of peak sting heating on the sting appeared to be slightly different from that of the flow stagnation point at shear layer reattachment. Computations made using the Navier-Stokes code LAURA (Gnoffo, 1990) produced sting heating rates very close to the measured values. Wells' work is notable as being one of the first detailed studies of wake heating with accurate, modern, fast-response, instrumentation (i.e. thin-film gages) and for its use in the code-calibration of LAURA for the AFE program (Gnoffo, 1989).

As part of the AGARD 18 Working Group project, Holden, Kolly, and Chadwick (1995) tested a 70 deg sphere-cone model in the LENS (Large Energy National Shock Tunnel) facility. Surface pressure and heating measurements were made on the forebody and sting of the model. The forebody heat-transfer measurements were made using coaxial surface thermocouples, while the sting measurements were made with thin-film gages. Tests were conducted in air at both continuum and low-density conditions. Good agreement was observed between DSMC computations (Moss, Price, Dogra, and Hash, 1995) and the experimental data at the low density test point, while Navier-Stokes computations and experimental data at the continuum test point differed significantly. The LENS study is notable for the work done on quantifying the wake flow establishment process. Based on sting pressure measurements, it was concluded that the recirculating base flow region established in ~50-60 flow lengths, where a flow length is defined as the unit of time required for the freestream flow to travel a representative distance, in this case the base radius of the model.

Allgre and Bisch (1994, 1995) conducted heat-transfer tests on a 70 deg sphere-cone model in the French SR3 low density facility as part of the AGARD 18 Working Group. Heating measurements were made using the thin-skin technique on a steel model with back-face chromel-alumel thermocouples. Experimental data were compared to Navier-Stokes and DSMC computations (Moss, Price, Dogra, and Hash, 1995). DSMC results were in good agreement with experimental data. Navier-Stokes heat-transfer computations differed significantly from the experimental data when conventional no-slip boundary conditions were employed; however, it was found that the inclusion of a slip boundary condition led to

better agreement between experimental and computational results.

The 70 deg sphere-cone configuration was also tested in the German VG2 vacuum wind tunnel (Legge, 1994) and the VG3 free-jet facility at Göttingen (Legge, 1993) as part of the AGARD 18 project. The focus of these test was primarily on wake flow field density measurements, although a limited amount of forebody heating data was gathered. Further AGARD tests were conducted on the 70 deg sphere-cone configuration in the High Enthalpy Reflected Shock Tunnel at Göttingen (HEG) of the German DLR (Kastell, Horvath and Eitelberg 1994, Kastell, Hannemann Eitelberg, Horvath, 1995). The test model had surface coaxial thermocouple instrumentation on the forebody and thin-film gages on the model support sting. The model was tested at a variety of high-enthalpy conditions, and it was found that the peak wake-heating rates varied between 10% and 25% of the forebody stagnation point rate.

This same model was tested in the NASA LaRC 15-Inch Mach 6 Air Tunnel by Horvath, McGinnley and Hannemann (1996). In addition to the data obtained from the model sensors, flow field data were gathered through schlieren photography, pitot probe surveys and hot-wire anemometer surveys. Freestream Reynolds numbers for these tests ranged between 1.0×10^6 ft^{-1} to 8.0×10^6 ft^{-1}. The main purpose of these tests was to determine whether the wake shear layer was behaving in a laminar, transitional or turbulent manner. Based on the flow field data and on comparisons with laminar Navier-Stokes computations, it was concluded that the wake flow field for this model was either transitional or turbulent across the entire range of test Reynolds numbers.

Finally, the experiments of Reddy (1980), and Miller, Micol and Gnoffo (1985) in the HYPULSE Expansion Tube (at that time the NASA Expansion Tube) must be mentioned. Although they tested significantly different types of geometries than considered here (30 deg and 40 deg sphere-cones for Reddy, biconics for Miller et al) their work pioneered the use of thin-film gages for heating measurements in the HYPULSE Expansion Tube.

Section 2.2 Computational studies

Interest in planetary exploration missions has produced a large volume of computational work on hypersonic, blunt body flow fields. In the 1960's and 1970's, boundary layer analyses and Euler solvers were used to model flows around vehicles such as Apollo and the Space Shuttle. By the late 1970's, viscous shock layer codes had been developed that were used in the design of the Galileo probe. Full Navier-Stokes computations became possible in the 1980's and could be employed in the AFE program. In the 1990's, the Mars-Pathfinder program has produced numerous chemically reacting, nonequilibrium, Navier-Stokes CFD studies. This section will, for the most part, deal with CFD research relating to the Mars-Pathfinder probe.

Li (1989) developed a three-dimensional Navier-Stokes code which employed an implicit ADI formulation. Li compared forebody heat-transfer results from his code to experimental data on different entry vehicle configurations from various sources. Of interest are the comparisons to the previously mentioned data of Wells (1990) and Reddy and Miller (1986). Li cited significant differences between measured and computed results, but was unable to resolve the discrepancies.

Papadopoulos, Tauber and Chang (1990) used an explicit finite-difference code to model the effects of dust impact on the Mars-Viking type probe during atmospheric entry. Their analysis included an equilibrium Mars atmospheric chemistry model.

Weilmuenster and Hamilton (1990) employed an inviscid Euler code coupled to an axisymmetric analogue boundary layer code to compute solutions for a 70 deg sphere-cone at 0 deg and 20 deg angles-of-attack in a perfect gas environment. Coupling of Euler solutions and boundary layer computations was also employed by Rochelle, Bousolog, and Ting (1990) who examined several Mars and Earth atmosphere entry vehicle configurations. Their work included nonequilibrium chemistry and radiation effects.

Gupta and Lee (1993) carried out a viscous shock layer analysis of the flow field around the Mars-Pathfinder forebody at several points along the vehicle's trajectory. They modeled cases with and without

surface ablation and with finite-rate and equilibrium chemistry models, and estimated the effects of surface radiation. Non-equilibrium chemistry effects were not found to be significant on the forebody of the vehicle, nor was radiative heat transfer. Surface ablation was found to cause a small decrease in heating at the stagnation point, and a much larger decrease at the shoulder of the vehicle.

Mitchletree (1994, 1995), Mitchletree and Gnoffo (1994), and Nettlehorst and Mitchletree (1994) have employed the LAURA code in the design and development of the Mars-Pathfinder probe. LAURA was used to generate aerodynamic and aerothermodynamic data at various points along the Mars-Pathfinder entry trajectory. Their analyses included the afterbody and near wake, and it was found that afterbody heating rates were at least an order of magnitude lower than on the forebody, and had a local maximum on the afterbody base corner. A large, separated recirculation region was identified in the wake, and smaller counter-rotating vortices were observed on the afterbody of the vehicle.

Haas and Venkatapathy (1995) have employed the GASP code (McGrory, Slack, Applebaum, and Walters, 1993) to compute forebody and wake solutions for the Mars-Pathfinder probe at several points along its entry trajectory. Their computations employed third-order, upwind TVD-limited inviscid flux formulations and a finite-rate Martian atmospheric chemistry model. Their forebody heating results were in good agreement with those of Mitchletree (1994). Wake flow field results identified the extreme sensitivity of the recirculation zone at the base of the vehicle to the grid resolution. Computations on a coarse grid showed a single large vortex in this region, while computations on a finer grid resolved the single vortex into one large vortex and two smaller counter-rotating vortices. Afterbody heating rates changed noticeably with grid resolution, but remained within the Mars-Pathfinder design limits. They also observed fluctuations in the wake structure, which they attributed to physically unsteady wake flow behavior.

There are several studies in which Candler's NEQ2D code (which is employed in this research) or variants of it were used for computation of entry vehicle flow fields. This code is detailed in Candler and MacCormack (1991). Modifications for computation of Martian atmospheric entry flows are presented in Candler (1990). In these two works, the NEQ2D code was used to compute non-equilibrium flow over a 60

deg sphere-cone configuration in both an ionizing air atmosphere for Earth entry and a CO_2 atmosphere for Mars entry.

Resseler, Shivananda, Zabrensky and Cruz (1992) employed Candler's code in a parametric study of drag and heat transfer on various configurations proposed for the MESUR probe. Chen, Henline, Stewart and Candler (1993) employed the NEQ2D code to simulate the flow field around the Mars-Pathfinder configuration during Mars entry. They employed two different chemical kinetic models in this work, and found that they produced quite different results for surface heating with non-catalytic wall boundary conditions.

Gochberg, Allen, Gallis and Deiwert (1996) used a modified version of the NEQ2D code as well as a Direct Simulation Monte Carlo code (Gallis and Harvey, 1995) to perform computations for the 70 deg sphere-cone tests in the LENS (Holden, Kolly and Chadwick, 1995) and HEG (Kastell, Horvath and Eitelberg, 1994) facilities. Large differences in surface heating rates were observed between the computations and the experimental data. Gochberg et al identified impulse facility flow establishment, wake rarefaction and shear layer transition as possible causes of these discrepancies.

Although outside the scope of the present work, a great deal of analysis has been done recently on Mars-Pathfinder flow fields at low density conditions using the Direct Simulation Monte Carlo (DSMC) method. Much of this research has been part of the AGARD 18 Working Group, and has involved comparison of DMSC results with low density wind tunnel data. Some of this research is presented in the works of Moss, Dogra, and Wilmoth (1993a), Harvey and Gallis (1995), Gallis and Harvey (1995), Moss, Price, Dogra, and Hash (1995), and Wilmoth, Mitchletree, Moss, and Dogra (1993). Comparisons of DMSC and Navier-Stokes computations at low density conditions are presented in Dogra, Moss, Wilmoth, Taylor and Hassan (1994a), Moss, Mitchletree, Wilmoth, and Dogra (1993b), and Dogra, Moss, Wilmoth, Taylor and Hassan (1994b).

CHAPTER 3
MODEL DESIGN AND INSTRUMENTATION

Section 3.1 Model Configurations

The purpose of the experimental portion of this research was to generate an aerothermodynamic data base for a blunt body aerobrake type vehicle. Because of its relevance to both ongoing and future NASA missions, as discussed in Chapter 1, a hemispherically-blunted 70 deg cone configuration based on the Mars-Pathfinder spacecraft was selected as the baseline geometry for this research. This geometry, which will be identified as MP-1 (from Mars-Pathfinder), is shown in Figure 3.1.1. In addition to the baseline MP-1 geometry, a limited number of tests were conducted on three parametric geometries and two smaller scale versions of MP-1. The parametric geometries are identified as MP-2, MP-3, and MP-4, and the scaled geometries are identified as MP-1 (88%) and MP-1 (75%).

By comparing the geometry of MP-1 shown in Figure 3.1.1 to that of the Mars-Pathfinder vehicle shown in Figure 1.2.2, it can be seen that the forebody geometries (though not scales) are identical, while the afterbody frustrum radius (relative to the forebody base radius) and cone angle of the MP-1 geometry are slightly larger than that of Mars-Pathfinder. These configuration changes were made in order to fit to the test models a sting (Figure 3.1.2) of large enough diameter to safely withstand the aerodynamic loads imposed on the model during testing, as well as of sufficient internal volume to contain the electrical leads for the thin film gages with which the models were instrumented. As the presence of the sting would have significant effects on the wake flow field and would thus have to be accounted for in comparisons to CFD results in any respect, these alterations to the afterbody from the Mars-Pathfinder geometry were considered to be acceptable for the purposes of this study. The sting was, in fact, an integral part of this study, and was fully instrumented in order to permit measurements in the wake of the test model.

The overall size of the MP-1 models was dictated by the requirement that the models fit within the inviscid test core of the HYPULSE Expansion Tube. Calibration studies in the HYPULSE facility (Calleja et al, 1990) have shown that the inviscid test core pitot pressure variation immediately downstream of the mouth of the expansion tube is less than ±6% across a diameter of approximately 3-in. Based on this information, it was estimated that a model forebody base diameter of 2.0-in. would be the maximum for which reflections of the forebody bow shock from the wall boundary layer would not interfere with the wake flow region until well downstream of the area in which measurements were to be made. The forebody base radii of the parametric configurations were also fixed at 2.0-in.

The parametric geometries tested in this study, MP-2, MP-3 and MP-4, are shown along with the MP-1 geometry in Figure 3.1.3. The model stings and sting adapters for tests in the 31-Inch Mach 10 Air Tunnel and the HYPULSE Expansion Tube are also shown in this figure. The sting/adapter junctions were located sufficiently far downstream of the models that shock-induced boundary layer separation near the adapter would not influence the near-wake region behind the model in which measurements were taken.

While the afterbody geometries of the MP-1 through MP-4 configurations are identical, the forebody geometries are each different. The MP-2 forebody geometry (Figure 3.1.4) is a hyperboloid with the same forebody base radius and the same radius of curvature at the geometric center of the nose as the MP-1 geometry. Away from the centerline, the radius of curvature of the hyperboloid geometry gradually increases, and towards the outer radius of the configuration the MP-2 geometry asymptotically approaches that of the 70 deg sphere-cone MP-1. The MP-2 configuration was included in this study because of results from the AFE program (Jansen, 1987, Micol, 1992) which suggested that the discontinuity in surface curvature at a sphere-cone junction (or ellipsoid-cone junction in the case of the AFE vehicle) could produce unfavorable pitching moment characteristics. It was suggested by Jansen that a geometrically-matched hyperboloid geometry would produce aerodynamic forces (lift and drag) similar to that of a sphere-cone or ellipsoid-cone configuration, but would not exhibit the unfavorable pitching moment characteristics. Furthermore, the blunter nose region of the hyperboloid geometry would lead to lower heating rates than

that of a similar sphere-cone geometry. This configuration then, could be of interest to future planetary mission planners.

The MP–3 and MP–4 geometries are 70 deg sphere-cone configurations like the MP–1 geometry. MP–3 and MP–4 differ from MP–1 in that their corner radii are, respectively, two times and four times that of the MP–1 corner radius. These configurations were included in this study in order to assess the effects of the corner radius on the wake flow field. Interest in wake flow behavior also led to the inclusion of the MP–1 (88%) and MP–1 (75%) configurations, which are smaller versions (88% scale and 75% scale) of MP–1, in this study. These two scaled configurations were tested in the HYPULSE Expansion Tube in order to examine the effects of model size on wake flow establishment times.

Section 3.2 Model Construction

Heat-transfer test models for this study were fabricated from Macor, a glass-ceramic material which is a trademark of the Corning Glass Works. Glass or ceramic materials such as Macor, or quartz or pyrex, are commonly used in the construction of heat-transfer models because of their relatively low thermal conductivity and thermal diffusivity. Because of these characteristics, the thermal penetration depth of an aerodynamic heating load into the substrate of a model built from one of these materials is small. This produces a larger and more easily measured surface temperature rise than would occur in higher conductivity materials such as metals. Also, because of the small thermal penetration depth, the substrate of the model effectively can be treated as being of infinite thickness with respect to the penetration depth (Schultz and Jones, 1973). This "semi-infinite" substrate assumption is a requirement in commonly-used heat-transfer data reduction techniques. These techniques are discussed in Chapter 5. Of these materials, Macor was chosen because it is more easily machined than quartz, while its thermal properties vary less with temperature than those of pyrex. The thermal properties of Macor were thoroughly investigated as part of

this study, as detailed in Appendix C. Based on this investigation, the following curve fits for the thermal properties of Macor were used in this research:

$$\rho = 2543.84 \quad (\mathrm{kg/m^3}) \tag{3.2.1}$$

$$k = 0.33889 + 7.4682 \cdot 10^{-3} \cdot T - 1.6118 \cdot 10^{-5} \cdot T^2 + 1.2376 \cdot 10^{-8} \cdot T^3 \quad (\mathrm{W/m-K}) \tag{3.2.2}$$

$$\alpha = 1.3003 \cdot 10^{-6} - 2.2523 \cdot 10^{-9} \cdot T + 1.8571 \cdot 10^{-12} \cdot T^2 \quad (\mathrm{m^2/sec}) \tag{3.2.3}$$

Heat-transfer test models for each of the MP-1 through MP-4 entry vehicle configurations were fabricated from Macor. The MP–1 (88%) and MP–1 (75%) models were not instrumented (see Section 3.3), and were thus fabricated from stainless steel (Figure 3.1.5), as were several extra uninstrumented MP–1 and MP-2 models, which were denoted as MP-1 (SS) and MP-2 (SS). A total of 26 Macor entry vehicle models (10 MP–1, 10 MP-2, 3 MP-3 and 3 MP-4) models and 11 stainless steel entry vehicle models were built (4 MP–1 (SS), 3 MP–1 (88%), 3 MP–1 (75%) and 1 MP-2 (SS)) for use in this study. Model stings were fabricated from stainless steel and were slotted to accept an instrumented, contoured Macor insert. A total of 6 model stings were built. Additionally, an uninstrumented MP-1 model and sting were fabricated from aluminum for use in surface oil-flow tests in the 31-Inch Mach 10 Air Tunnel.

In order to ensure that the semi-infinite substrate assumption was valid for the Macor models, the model skin had to be thick enough that the heat transfer and temperature rise at the back face of the substrate (the interior of the model) would be negligible with respect to that at the surface of the model. The relevant non-dimensional parameter for substrate thermal penetration depth is:

$$x^* = \frac{x}{2\sqrt{\alpha t}} \tag{3.2.4}$$

Approximate expressions (i.e. assuming temperature-independent thermal properties and a constant heat-transfer rate) for the back face temperature and heat transfer in terms of this parameter have been derived in Schultz and Jones (1973):

$$\frac{T_x}{T_s} = e^{(-x^*)^2} - \left(x^* \sqrt{\pi}\right) erfc(x^*) \tag{3.2.5}$$

$$\frac{q_x}{q_s} = erfc(x^*) \tag{3.2.6}$$

For a specified temperature or heating ratio at the back-face of the substrate at a given test time, the required thickness can be estimated from Figure 3.2.1. Ideally, the heat transfer or temperature rise at the back face should be zero, but more realistic values of 5% to 10% of that at the surface are generally considered acceptable.

The entry vehicle models tested in this study were designed with a minimum 0.1-in. wall thickness. The thickness of the Macor sting inserts is equal to this minimum value, as is that of a small region in the middle of the conical flank of the entry vehicle models. Elsewhere on the models, the thickness is 0.25-in. or greater. Referring to Figure 3.2.1, it can be seen that for a nominal room temperature value for Macor diffusivity of 7.9×10^{-7} m^2/sec, the back-face heat transfer will be no more than 5% of that on the surface for up to 1 sec from the time when heating begins. However, this analysis is conservative because the thermal diffusivity of Macor decreases with temperature, which has the effect of increasing the semi-infinite test time. The same analysis for the 0.25-in. thickness extends the 5% back-face heating time to 6.25 sec. HYPULSE test times are on the order of 200-300 μsec, while 31-Inch Mach 10 Air test times are on the order of 2-3 sec. With the 0.1-in. minimum model wall thickness, satisfaction

of the semi-infinite assumption in HYPULSE tests presents no difficulty. For Mach 10 Tunnel tests, the data averaging period can be shortened slightly to avoid violating this assumption.

In addition to the entry vehicle models, several hemisphere models of various radii were included in this study for evaluation and calibration purposes. A hemispherical geometry was suitable for these purpose because simple engineering theory can be used to compute the stagnation point heating rate (e.g. Fay and Riddell, 1958) and the shape of the surface heat-transfer distribution (e.g. Lees, 1956). Hemispheres of 1-in. radius were tested in the 31-Inch Mach 10 Air Tunnel in an investigation of material thermal properties, while 1/4-in., 3/8-in. and 1/2-in. radius hemisphere models were tested in the HYPULSE Expansion Tube in order to assess the quality of heating data from that facility. The 1/4-in., 3/8-in. and 1/2-in. radius hemispheres tested in HYPULSE were all made from Macor. For the material properties tests in the 31-Inch Mach 10 Air Tunnel, 1-in. radius hemispheres were fabricated from both quartz and Macor. For these tests, 3 Macor hemispheres of each of the smaller radii and 2 each of the Macor and quartz 1-in. radius hemispheres were fabricated. Curve fits used in this research for quartz thermal properties (see Appendix C) are:

$$\rho = 2192.5 \ \ (\mathrm{kg/m^3}) \tag{3.2.4}$$

$$k = 0.96157 + 9.5491 \cdot 10^{-4} \cdot T + 5.5465 \cdot 10^{-7} \cdot T^2 \ \ (\mathrm{W/m-K}) \tag{3.2.5}$$

$$\alpha = 1.5191 \cdot 10^{-6} - 4.136 \cdot 10^{-9} \cdot T + 7.2707 \cdot 10^{-12} \cdot T^2 - 4.4242 \cdot 10^{-15} \cdot T^3 \ (\mathrm{m^2/sec}) \tag{3.2.6}$$

Section 3.3 Model Instrumentation

Surface heating data were gathered through the use of thin-film resistance gages. A thin-film gage

consists of a small metallic sensing element of ~1000 Å thickness through which a constant electrical current is conducted. The electrical resistance of the gage is a function of temperature, and thus an increase in gage temperature due to aerodynamic heating of a model's surface produces a voltage increase across the sensor. A measured voltage time-history can be converted to a temperature time-history using pre-test sensor calibrations, and heat-transfer rates can then be computed through one of the techniques which will be discussed in Chapter 5.

Thin-film gages were chosen for use in this research because of the advantages they offer over other types of sensors, such as thin-skin calorimeters or coaxial surface thermocouples. Thin-film gage response is very rapid (< 1 μsec), which allows for the recording of detailed time-history data. Furthermore, they are much more sensitive than other types of gages, which means that accurate measurements can be made even in regions of very low heating, such as in the wake of a blunt body. Additionally, the small size of thin-film sensors permits detailed resolution of heating distributions even on small-size models such as those in this research. In fact, given the model size limitations for testing in HYPULSE, it would have been practically impossible to use any other type of sensor in this work.

Thin-film gages were applied to the surfaces of the models either by a metal deposition process or by hand-painting. Metal deposition was used to apply all of the gages except for a few gages in regions of extreme surface curvature where deposition was impractical, such as the corners of the entry vehicle models and the smaller radii (1/4-in., 3/8-in. and 1/2-in.) hemispheres, which were hand-painted. Palladium was used for the deposited gages, while platinum was used for the hand-painted gages. Gages were applied in a simple bar pattern of 0.1 in. length between thick-film silver electrical leads (Figure 3.2.1). The leads connected to gold pads around holes drilled in the surface for the gage wiring. A thin (~5000 Å) over-layer of Al_2O_3 was applied to the surfaces of the gages and leads (SiO_2 was used on the quartz models) in order to electrically insulate them from the atmosphere. This was necessary because at the high temperatures produced in the HYPULSE Expansion Tube, a small amount of oxygen ionization, which causes gage shorting, may be produced in the acceleration gas during tests in air.

Each Macor entry vehicle model carried a total of 37 thin-film gages, while each Macor sting insert had an additional 33 gages. The model and sting gages were positioned at ~0.1 in. intervals along a single ray emanating from the geometric center of the model (Figure 3.3.2). This gage arrangement provided coverage on the forebody, afterbody, base, and model sting. Thin-film gages on the hemispheres were positioned in a single ray through the geometric center of the model. The 1-in. radius models had 23 thin-film gages (Figure 3.3.3), the 1/2-in. models had 17 gages, the 3/8-in. models had 9 gages and the 1/4-in. models had a single gage (Figure 3.3.4).

Further details on the construction and use of thin-film heat-transfer gages can be found in Miller (1981), in which the development of the thin-film technique for heat-transfer testing in NASA Langley wind tunnels is detailed. Although thin-film gages are now commonly used in conventional wind tunnels, their initial development (e.g. Vidal, 1956, Hartunian and Varwig, 1962) was motivated by the need for fast-response sensors for use in short-duration impulse facilities such as HYPULSE. The use of the thin-film gages in HYPULSE (which was then the Langley 6-Inch Expansion Tube) is discussed by Miller, Micol and Gnoffo (1985) and Reddy (1980).

While thin-film gages have many desirable performance qualities, their fragility (the sensing element is only on the order of 1000 Å thick) presented some difficulties because of the harsh post-test environment of the HYPULSE Expansion Tube. As is common in impulse facilities, thin-film gages exposed directly to the flow in the HYPULSE facility are usually destroyed by the extremely high temperature and pressure loads created by the post-test arrival of the driver gas and/or the post-test impact of debris from the primary steel diaphragm or secondary Mylar diaphragm. Even gages not exposed directly to the flow (i.e. gages on the model sting, which were shielded by the model itself) can experience some degradation, and therefore have a limited lifetime in terms of number of test runs for which their performance is acceptable. In addition to gage degradation, it was anticipated the surfaces of the Macor ceramic models would also be damaged by the post-test environment.

Because of this harsh post-test environment, it was expected that while each instrumented sting

could be used for a number of runs, the Macor models would need to replaced after each run due to damage to the thin-film gages and degradation of the model surface. Therefore, in order to maximize the amount of wake heating data which could be obtained, additional uninstrumented stainless steel models were machined for use with the instrumented stings. These models, which were relatively inexpensive and easy to produce, were fabricated from 17-4 PH hardened steel and thus could be expected to withstand several HYPULSE runs before their surfaces became too damaged for further use. Because it was anticipated that the forebody data would be relatively well-behaved, and thus fewer repeat runs would be required to amass a credible forebody heating data base, the use of uninstrumented models with instrumented stings was seen as an economical means to maximize the amount of wake data that could be obtained. For the HYPULSE test series, in addition to the instrumented Macor ceramic entry vehicle models, uninstrumented stainless steel models of the MP-1, MP-2, MP–1 (88%) and MP–1 (75%) configurations were fabricated and tested.

Section 3.4 Gage Calibration

Each thin-film heat-transfer gage was calibrated prior to testing through immersion in a hot oil bath. A constant 1 mA current was passed through the gage to produce an output gage voltage which was dependent on the oil-bath temperature. Voltage data were taken at 25 °F intervals from 75 °F to 225 °F (297 K to 381 K). Within this range, the voltage-temperature relationship for a thin-film gage is linear (Figure 3.4.1) and can be expressed by:

$$R = R_0[1 + \alpha_R(T - T_0)] \tag{3.4.1}$$

where:

$$\alpha_R = \frac{1}{R_0}\frac{\Delta R}{\Delta T} \tag{3.4.2}$$

α_R is referred to as the temperature coefficient of resistance, and subscript 0 refers to conditions at the base calibration temperature of 75 °F (297.22 K). Note that at higher temperatures, the T-V relationship for a thin-film gage may be non-linear; however, in this research, the highest model surface temperatures (at the stagnation point) remained below 450 K throughout the data acquisition window during tests in both the 31-Inch Mach 10 and HYPULSE facilities, and so non-linear gage response was not a cause for concern.

Through Ohm's law, the surface temperature can be related to the gage voltage (at a constant gage current) by:

$$T-T_1 = \frac{(E-E_1)}{\alpha_R R_0}\frac{R_1}{E_1} \tag{3.4.3}$$

where subscript 1 refers to ambient pre-test conditions. By substitution of equation (3.4.1), this can be expressed in terms of pre-test gage voltage as:

$$T-T_1 = \frac{(E-E_1)}{E_1\alpha_R}\left[1 + \alpha_R(T_1-T_0)\right] \tag{3.4.4}$$

In order to ensure that gage wear from repeated testing did not affect the gage resistances, and thus alter the voltage-temperature calibrations, models tested in the 31-Inch Mach 10 Tunnel were recalibrated after the test series. The thin-film gages were found to have endured the repeated testing in the Mach 10 facility very well. Most gages tested had a change in α_R of less than ±1% after an average of six runs per model. In the HYPULSE Expansion Tube, the entry vehicle models were replaced after each run, so gage wear was not an issue on the models themselves. However, the model stings had to be replaced after an

average of 5 runs, by which time the majority of the gages had been damaged. Between sting replacements, the ambient resistance of each gage was checked after each run, and data were ignored from gages which showed a significant resistance change.

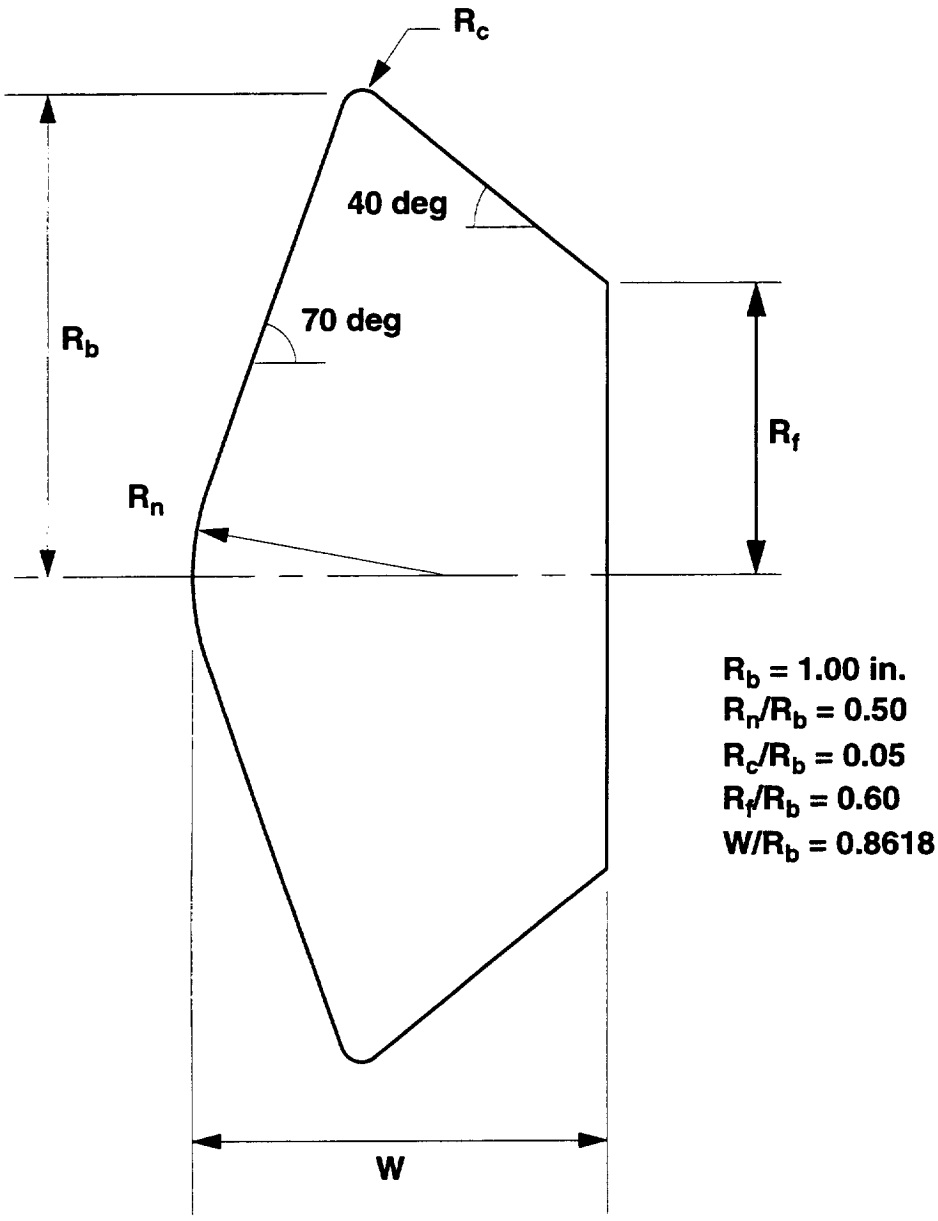

Figure 3.1.1 MP-1 Geometry

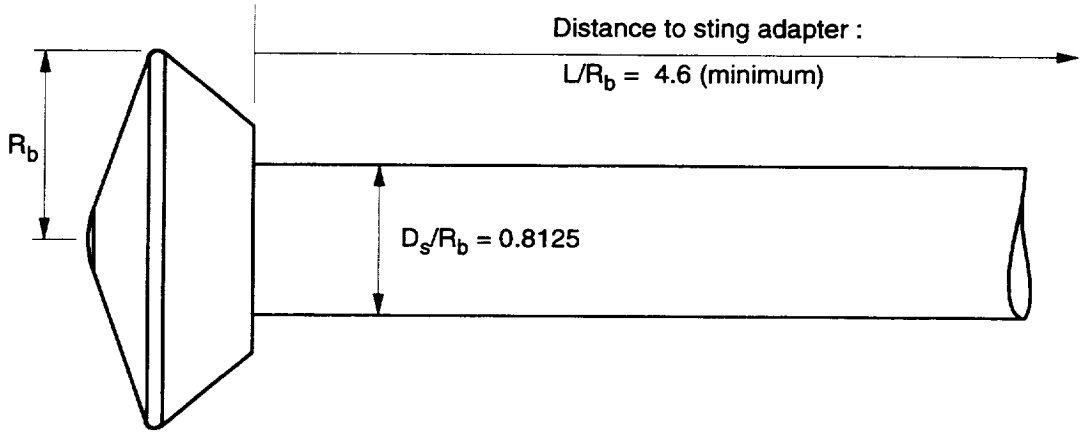

Figure 3.1.2 MP–1 Model and Sting

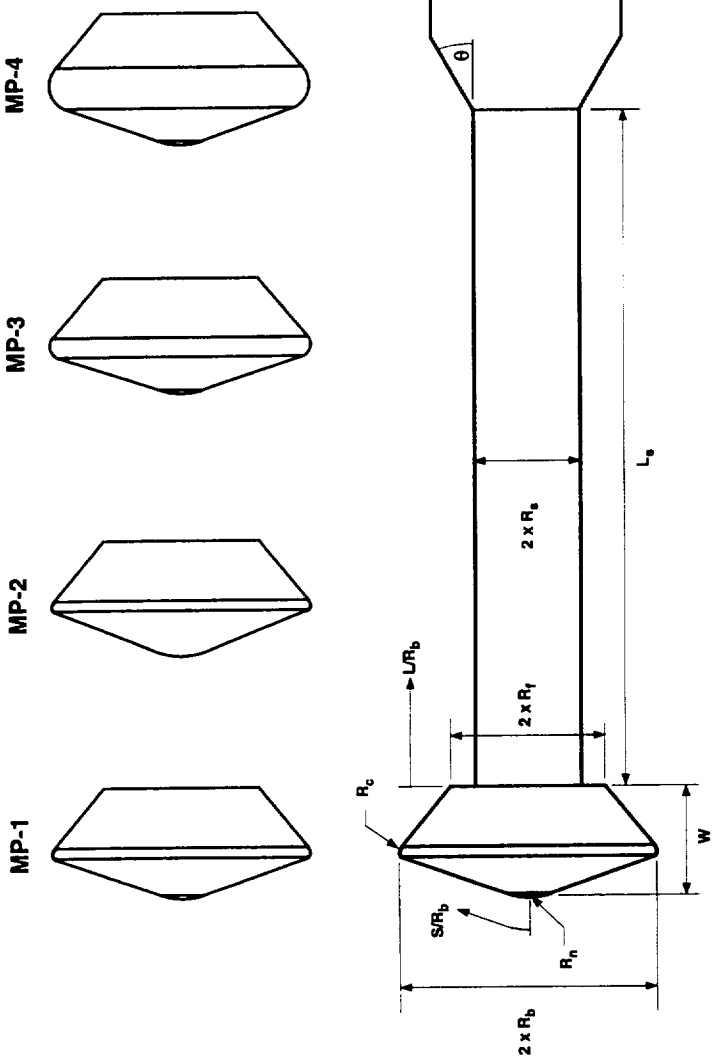

MODEL	CONFIGURATION	31-Inch Mach 10								HYPULSE		
		R_b	R_n/R_b	R_f/R_b	R_c/R_b	W/R_b	R_s/R_b	L_s/R_b	R_x/R_b	θ(deg)	L_s/R_b	R_x/R_b	θ(deg)
MP-1	70 deg Sphere-Cone	1.0 in.	0.5	0.6	0.05	0.862	0.406	5.250	0.406	30	4.625	1.00	45
MP-2	70 deg Asymptote Hyperboloid	1.0 in.	"	0.6	0.05	0.834	0.406	5.250	0.406	30	4.625	1.00	45
MP-3	70 deg Sphere-Cone	1.0 in.	0.5	0.6	0.10	0.915	0.406	5.200	0.406	30	4.620	1.00	45
MP-4	70 deg Sphere-Cone	1.0 in.	0.5	0.6	0.20	1.021	0.406	5.200	0.406	30	4.620	1.00	45

Figure 3.1.3 Parametric Entry Vehicle Configurations

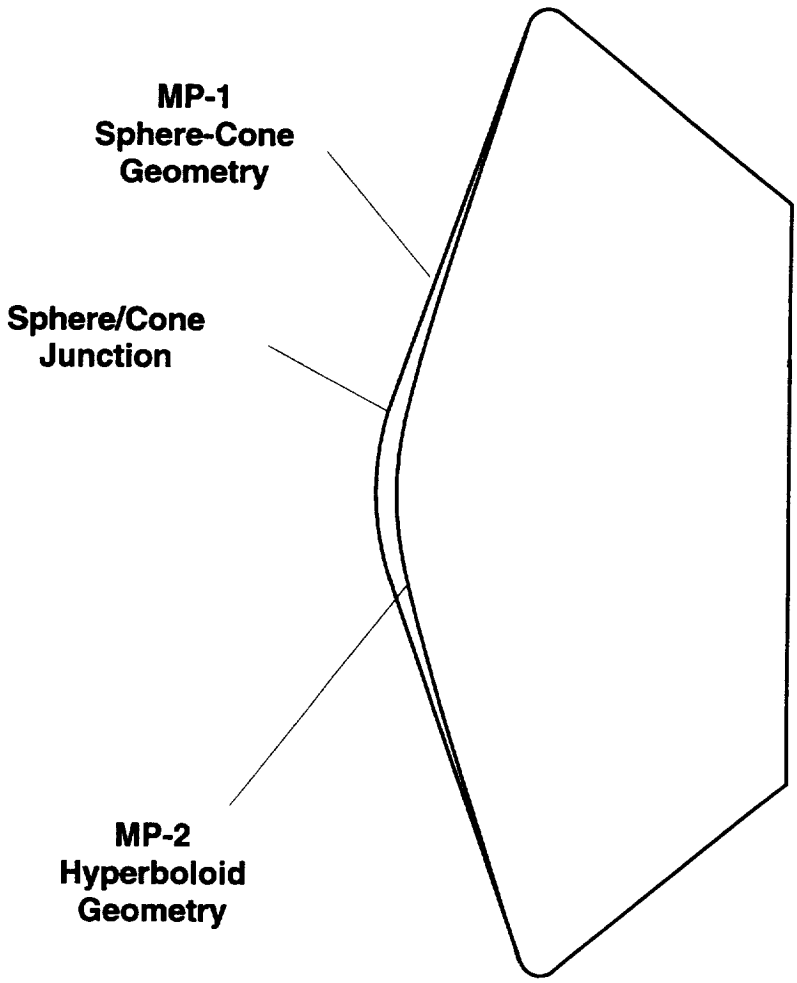

Figure 3.1.4 MP–1 and MP-2 Configurations

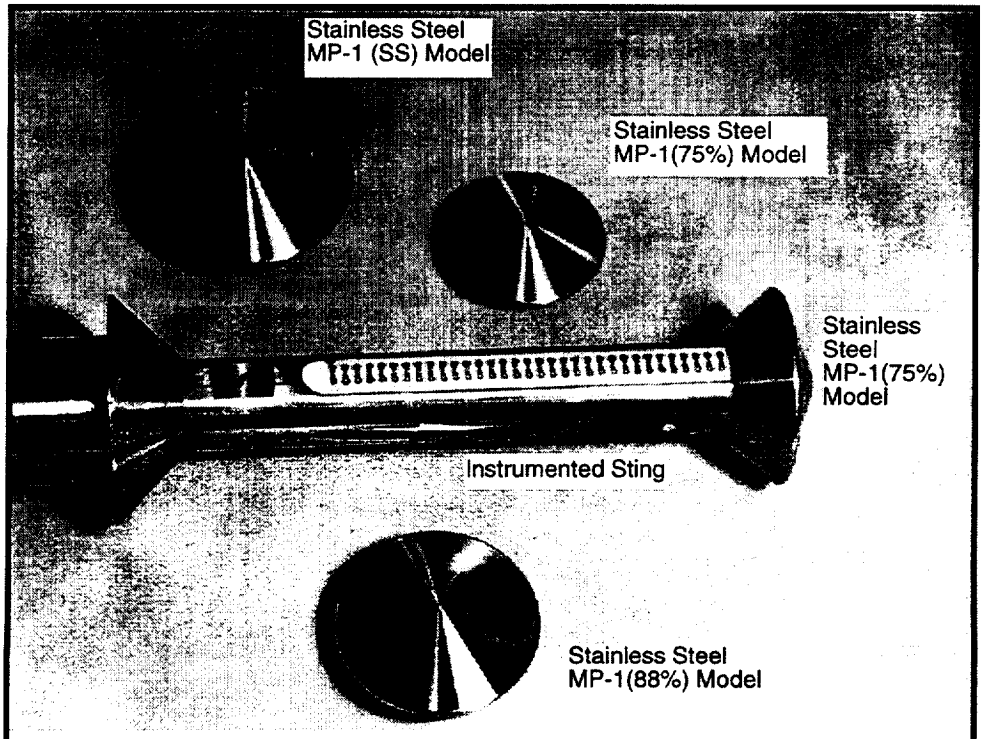

Figure 3.1.5 Scaled Stainless-Steel MP-1 Models

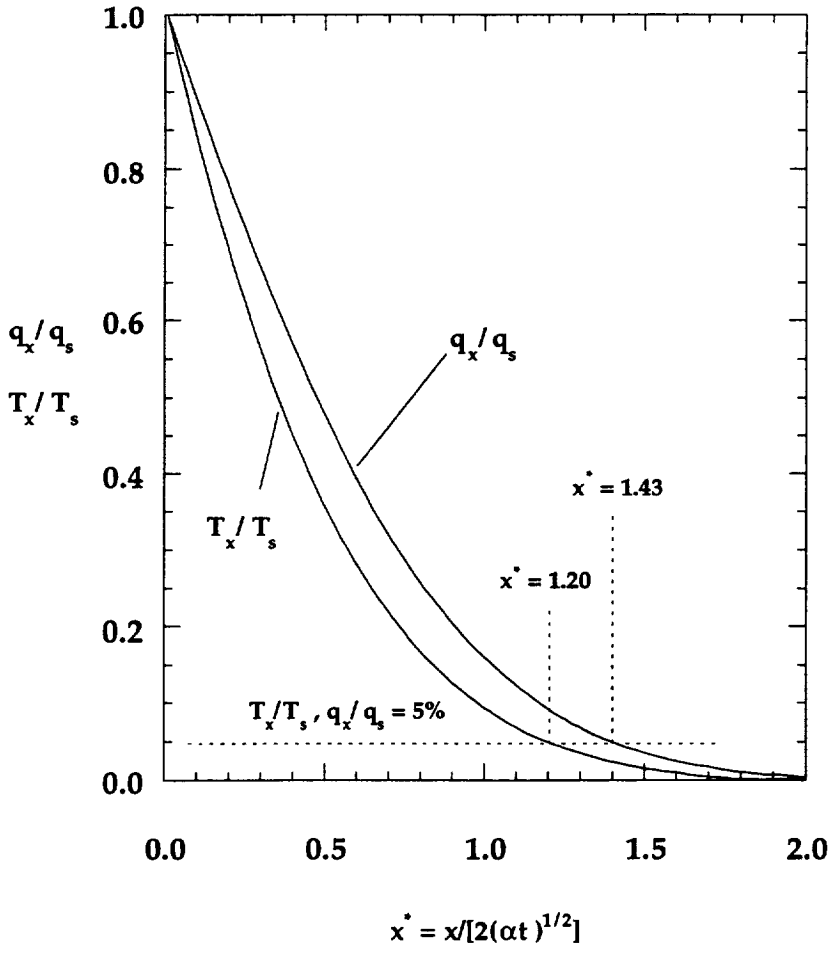

Figure 3.2.1 Semi-Infinite Test Time vs. Substrate Thickness

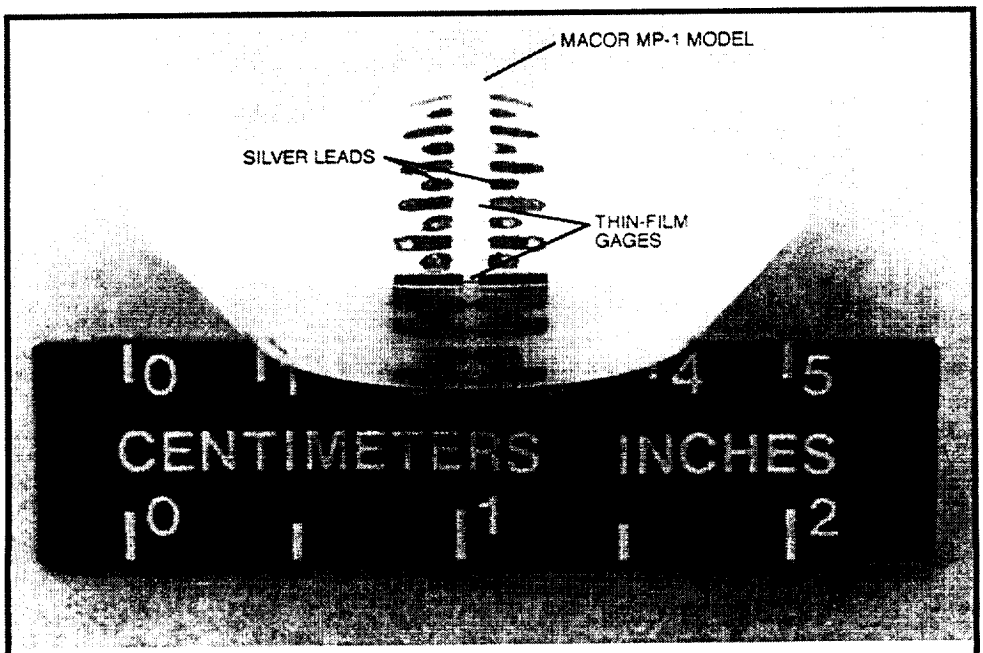

Figure 3.3.1 Thin-Film Gage Details

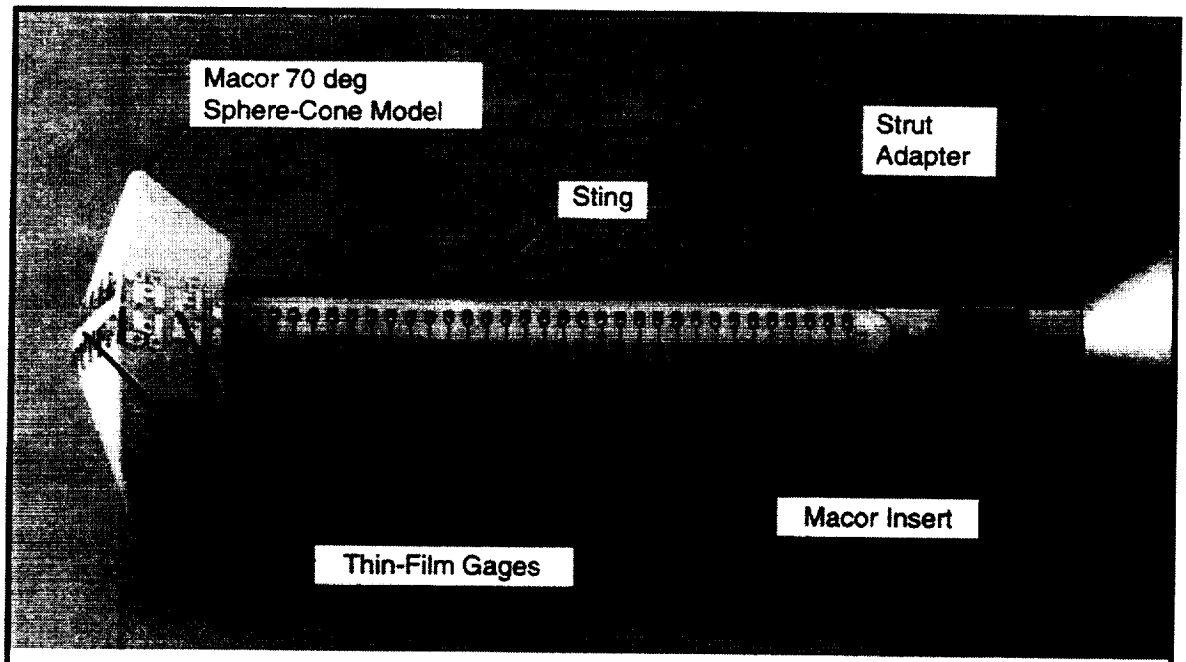

Figure 3.3.2 Thin-Film Gage Layout on MP-1 Model

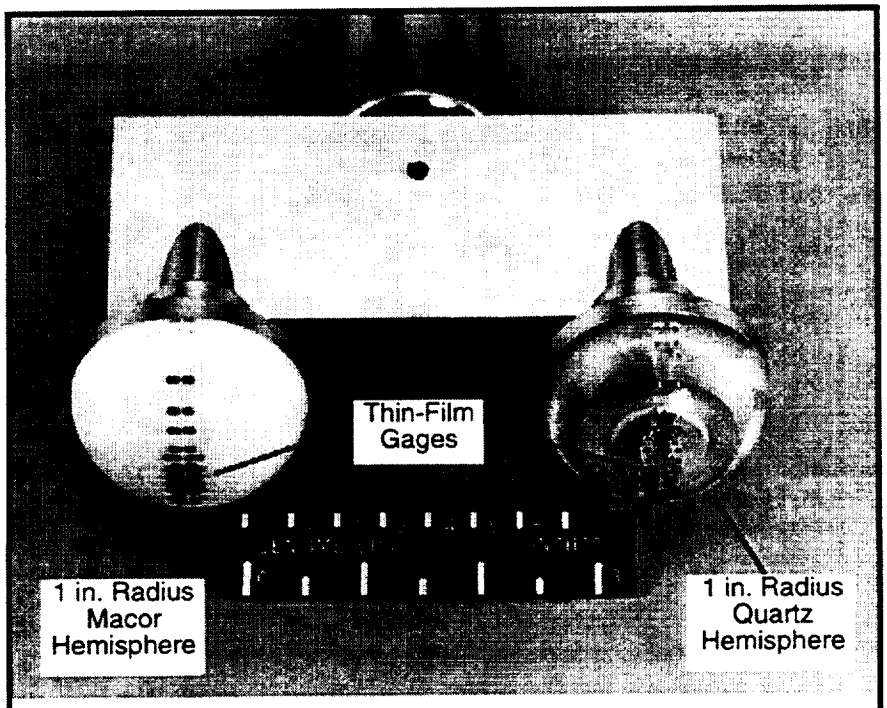

Figure 3.3.3 Thin-Film Gage Layout
on 1-in. Radius Hemispheres

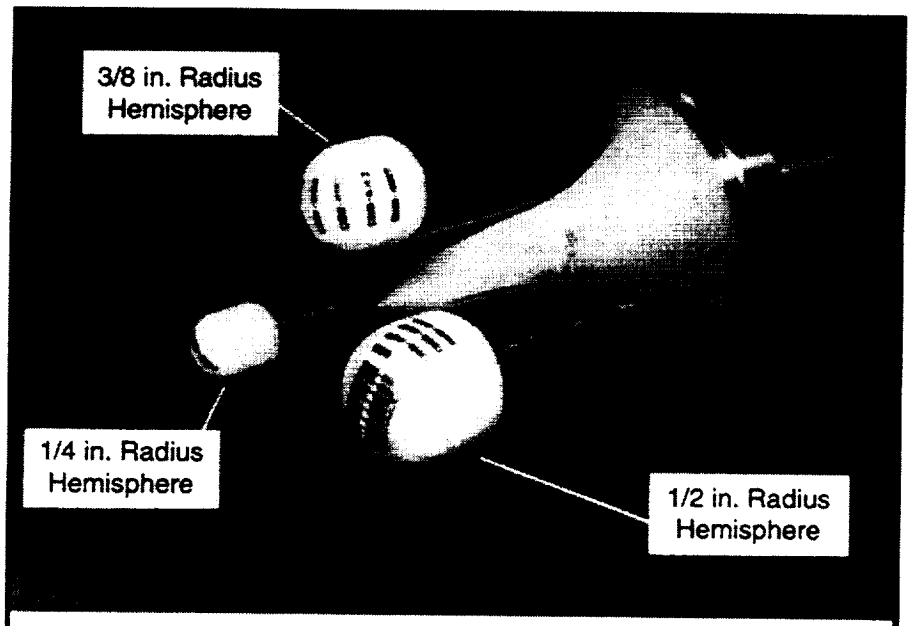

Figure 3.3.4 Thin-Film Gage Layout on 1/4-in., 3/8-in. and 1/2-in. Rad. Hemispheres

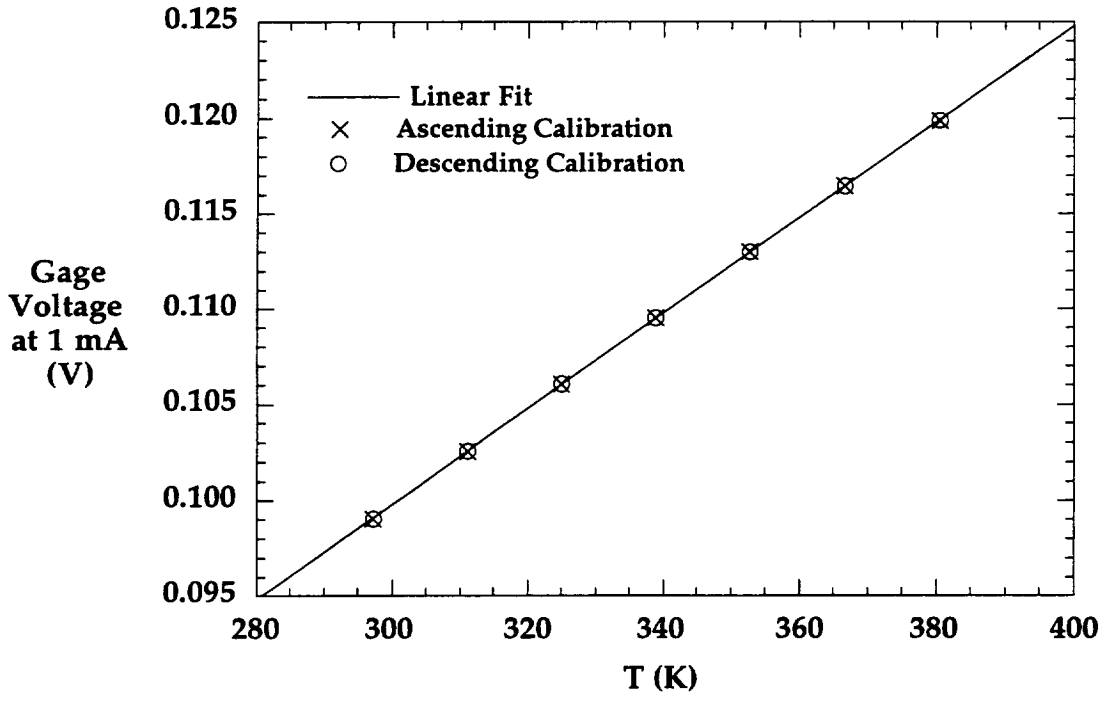

Figure 3.4.1 Typical Thin-Film Gage Voltage-Temperature Calibration

CHAPTER 4
EXPERIMENTAL FACILITIES

Section 4.1 Overview

Aerodynamic heating tests were conducted in two hypersonic facilities: a conventional wind tunnel, the NASA Langley 31-Inch Mach 10 Air Tunnel (Figure 4.1.1); and an impulse facility, the NASA HYPULSE Expansion Tube (Figure 4.1.2). The 31-Inch Mach 10 Air Tunnel provided a high flow quality, perfect-gas test environment in which very repeatable heat-transfer data suitable for CFD code calibration studies could be obtained. Furthermore, its inexpensive operating costs (relative to an impulse facility) and short test turn-around time made it possible to generate a large database covering a range of flow conditions, angles-of-attack, and model configurations. The HYPULSE Expansion Tube provided a high-enthalpy, hypervelocity flow environment in which chemical and thermal nonequilibrium phenomena were produced. Valuable information was gained by testing in HYPULSE both because the test conditions approximate those of actual planetary entry, and because the data can be used for comparison with state-of-the-art non-equilibrium Navier-Stokes CFD codes.

Section 4.2 NASA Langley 31-Inch Mach 10 Air Tunnel

4.2.1 Facility Description

The 31-Inch Mach 10 Air Tunnel was originally known as the Langley Continuous-Flow Hypersonic Tunnel, and was designed to operate as a blowdown start, continuous running tunnel. However,

the facility has only operated in the blowdown mode since the 1970's due to energy conservation measures. Operational characteristics of this wind tunnel are discussed in detail in Miller (1990) and Micol (1995), of which the following is a summary. The facility (Figure 4.2.1) consists of a high pressure air storage system, a 12.5 MW electrical resistance heater in a vertical pressure vessel, a settling chamber, nozzle, test section, adjustable second minimum, subsonic diffuser, aftercooler, vacuum spheres and vacuum pumps. The air storage system has a 865 ft^3 capacity with a 4400 psia maximum pressure. The settling chamber, test section, second minimum and diffuser are all water-cooled. 5-micron filters are located upstream of the settling chamber, which is faired into the three-dimensional contoured nozzle leading to the 31-in. by 31-in. square test section.

Models are inserted into the test section by a sidewall-mounted hydraulically-operated injection system. The injection system housing is isolated from the test section by a pneumatically-sealed sliding door, which permits model changes without a facility shutdown when operating in the continuous mode. This system is capable of injecting a model to the tunnel centerline in under 0.6 seconds. Angle-of-attack can be varied ±90 deg (limited by model size) at 5 deg/sec, and the sideslip angle can be varied by ±5 deg at 2 deg/sec. For aerothermodynamic testing, tunnel run times are typically limited to 3-5 seconds in order to satisfy the semi-infinite thickness assumption and to minimize lateral conduction effects. Much longer test times are possible for aerodynamic testing.

Pitot pressure surveys (from Micol, 1995) across the center 7 in. of the test core are shown in Figure (4.2.2). Flow quality is excellent, with a pitot pressure variation of less than ±1% across the test core. This is due in part to the three-dimensional contoured design of the nozzle (Beckwith and Miller, 1990), which eliminates the centerline disturbances typically observed in axisymmetric contoured nozzles. Because of the high flow quality in this facility and because of its high temperature driver (1000 K reservoir temperature), which leads to higher, and thus more easily measured heating rates, the 31-Inch Mach 10 Air Tunnel is an ideal facility for aerothermodynamic research and is considered to be Langley's premier facility for CFD code calibration studies (Micol 1995).

4.2.2 Flow Conditions

The 31-Inch Mach 10 Air Tunnel has been calibrated for operation at reservoir pressures from 125 psia to 1450 psia (862 kPa to 1000 kPa) with a reservoir temperature of 1800 °R (1000 K), which produces freestream unit Reynolds numbers of 0.25 to 2.1×10^6 ft^{-1}. Nominal flow conditions at the operating points for this study are given in Table 4.2.1. For each actual run, the flow conditions were computed using the GASPROPS code (Hollis, 1996). These flow properties are given in Appendix A. Note that although metric units are generally used throughout this work, 31-Inch Mach 10 Air Tunnel operating points are commonly identified by the *per foot* freestream Reynolds number, and that practice is followed herein.

In the GASPROPS code, the flow is modeled as that of a real (virial) gas at all points in the tunnel. A real gas model (Sychev, Vasserman, Kozlov, Spiridonov, and Tsymarny, 1987) is necessary because the density in the tunnel reservoir is high enough that intermolecular forces, which can be neglected in most applications, have a noticeable affect on the properties of the test gas. Because of the intermolecular forces, the perfect gas equation of state is not applicable, and the specific heats are functions of both temperature and density instead of only temperature.

The measured reservoir pressure, reservoir temperature and pitot pressure are required as inputs to GASPROPS. Due the presence of the test model, the pitot pressure usually cannot be measured directly during a run and thus instead is obtained from facility calibration data. The total enthalpy and entropy of the gas are first computed from the measured reservoir stagnation pressure and temperature. The flow is then assumed to expanded isentropically from the reservoir through the nozzle to an assumed Mach number in the test section. Freestream conditions are determined by iteration on the density and temperature of the gas to fulfill the conservation of total enthalpy and entropy at the assumed Mach number. Next, pitot conditions are computed by iteration on density and temperature to satisfy the conservation of total momentum and enthalpy across a normal shock. The computed pitot pressure and the actual measured (or

calibration) pitot pressure are then compared, and a new Mach number is computed through Newtonian iteration. This process continues until convergence is reached. Generalized equations for these computations are presented in Hollis (1996).

The run-to-run repeatability of 31-Inch Mach 10 Air Tunnel conditions was assessed through a statistical analysis of the flow conditions for all of the runs conducted in this research. Standard deviations were computed for each of the flow properties from the data presented in Appendix A. In accordance with the standards suggested by the AIAA Ground Test Standards Subcommittee (Anon., AIAA S-071, 1995), uncertainty bounds of (±) two standard-deviations, which corresponds to a 95% confidence level, were assigned to each of the individual values. These uncertainty bounds are given in Table 4.2.1 as percentages of the individual properties. None of the properties were found to have an uncertainty greater than ±2%.

Section 4.3 NASA HYPULSE Expansion Tube

4.3.1 Facility Description

The NASA HYPULSE Expansion Tube was originally known as the Langley 6-Inch Expansion Tube, and was operated at the NASA Langley Research Center in the 1970's. Budget constraints led to the facility being mothballed in 1982 as interest in hypersonic research declined. However, the National Aero-Space Plane (NASP) program and the Strategic Defense Initiative (SDI) generated renewed interest in hypersonics in the late 1980's. As a result, the 6-Inch Expansion Tube was put back into commission by the General Applied Sciences Laboratories (GASL) in 1989. The facility was renamed the HYPULSE (from hypervelocity impulse) Expansion Tube and is currently operated by GASL at their Ronkonkoma, New York location, although it remains under NASA ownership. The original operating characteristics of HYPULSE as the Langley Expansion Tube are described by Moore (1975) and Miller and Jones (1983);

GASL's updates to the facility are detailed by Tamagno, Bakos, Pulsonetti and Erdos (1990).

The HYPULSE Expansion Tube (Figure 4.3.1) consists of a stainless steel driver vessel, a diaphragm section, a stainless steel cylindrical tube divided by a secondary Mylar diaphragm into an driven (intermediate) section and an acceleration section, a test section/dump tank, and a vacuum pumping system. The driver vessel is designed to hold the high pressure driver gas and is rated at 138 MPa maximum pressure. It has an internal diameter of 16.5 cm and is 2.44 m long. The driver section is designed to accommodate an internal electrical resistance heater or a parallel-rail electric arc heater to heat the driver gas, although neither are currently employed. GASL has modified the driver vessel by inserting a removable plug section, which by reducing the total driver volume reduces the recoil impulse and post-test aerodynamic loads on the model but does not affect the flow quality or test time. The driver section and the driven section are separated by the diaphragm section. This section can accept either a single diaphragm or a 15.24 cm spacing double diaphragm, which is the current mode of operation. The double diaphragms are scored cross-wise to insure that they rupture into four triangular petals. Brass damper pads are installed on the walls of the diaphragm section downstream from the diaphragms to absorb the impact of the petals when the diaphragms bursts and prevent damage to the wall. The driven and acceleration sections are comprised of sections of 15.2 cm internal diameter stainless steel tube rated at 34.5 MPa. The lengths of these sections are determined by the number of sections of tubing and the placement of the secondary Mylar diaphragm. For this research, HYPULSE was configured with a 7.44 m driven section and a 14.14 m acceleration section. The acceleration section exits into the test section/dump tank, which is a 10.5 m long stainless steel vessel with an internal diameter of 120 cm and a 1 MPa pressure rating. GASL has added linear motion rollers to the test section/dump tank and driver section to permit them to recoil from the impulsive loads produced during operation. The vacuum pumping system consists of a 250-scfm roughing pump and two 50 cm diameter diffusion pumps.

In the HYPULSE operating sequence, the roughing pump is used to initially evacuate the driven and acceleration sections and the test section, and then the acceleration and test sections are drawn down to a

10^{-5} mm Hg vacuum with the diffusion pumps while the driver section is filled with high pressure helium. The driven and acceleration sections are then filled with the desired test gas. The driver section is then pressurized with helium to the burst point of the double diaphragms. In the first stage of operation after the the double diaphragms are burst, HYPULSE acts a shock tube with the interaction of the high pressure driver gas and the lower pressure driven gas producing an incident shock wave and a trailing expansion fan which is washed downstream with the driver gas. The secondary Mylar diaphragm, which is typically of 0.0025-in. or 0.005-in. thickness, is ruptured by the arrival of the incident shock wave. This initiates the expansion tube phase of the sequence as the incident shock increases in Mach number on entering the lower pressure expansion section and a second downstream-travelling expansion fan is produced. The wave structure in HYPULSE is illustrated by the distance-time (X-T) diagram in Figure 4.3.2. The test flow core is region 5, which is delimited by the acceleration gas/driven gas interface and the arrival of a disrupting wave from upstream. As discussed by Tamagno et al (1990), the disrupting wave can be either the tail of the second unsteady expansion fan, a reflected expansion from the interaction of the second expansion fan and the driver gas/driven gas interface, or the reflection of the primary expansion off the upstream end of the driver. In practice, the third effect is rarely seen, and the test period is usually terminated by the arrival of the expansion fan. The choice of driver gas, driver, driven, and intermediate section pressures and the lengths of the driven and acceleration sections will determine the actual wave structure and test period duration. Nominal test periods in HYPULSE are on the order of 200-300 μsec. Well-behaved forebody heating data were gathered over time intervals approaching these nominal values. However, due to the extremely low magnitude of the heating in the wake, the measured afterbody and sting surface heating rates were found to be quite sensitive to noise and to fluctuations in the freestream conditions. For this reason, the test time window was generally held to a more conservative range of 100-150 μsec, as is discussed in more detail in Section 4.3.2.

It must be noted that the expansion tube method of operation of HYPULSE provides a unique high-enthalpy, hypervelocity testing capability. Equivalent or even greater velocities and enthalpies can be

produced in reflected shock tunnels such as the University of Queensland T4 facility (Porter, Mee, and Paull, 1993), the GALCIT (Graduate Aeronautical Laboratories at California Institute of Technology) T5 facility (Germain, Cummings and Hornung, 1993) or the LENS (Large Energy National Shock Tunnel) facility at the Calspan-University at Buffalo Research Center (Holden, Kolly, and Chadwick, 1995). However, this is accomplished through stagnation of the flow by the reflected shock, which can produce dissociated freestream flow. In HYPULSE, the high velocity is produced by flow expansion into the lower-pressure acceleration section, and thus there is generally no freestream dissociation, although a small amount of dissociation can be produced in the acceleration gas by the non-instantaneous rupture of the Mylar diaphragm. The use of expansion tubes is also being pursued in Australia at the University of Queensland. However, their TQ (Neely, 1991) and X1 (Neely and Morgan, 1993) facilities are too small for practical applications (38mm diameter), while the larger X3 facility (Doolan and Morgan, 1994) is still under development.

4.3.2 Flow Conditions and Test Times

In this research, only CO_2 and air were employed as test gases during the Mars entry vehicle model testing, while a limited number of He tests were also carried out as part of the calibration hemisphere study. However, HYPULSE can be operated with air, CO_2, N_2, O_2, or He as test gases. The full range of HYPULSE operating conditions is detailed by Erdos, Calleja, and Tamagno (1994). The test conditions for this research are commonly referred to as "The Langley Conditions" as they were derived from the conditions at which the facility was originally operated when it was at NASA Langley. The calibration of HYPULSE for air, CO_2 and He gases at these conditions is discussed in Calleja, Tamagno, and Erdos (1990). Nominal flow properties at these operating conditions are given in Table 4.3.1

For the Langley Conditions, nominal steady test flow times have been determined by researchers at GASL (Tamagno et al, 1990) through examination of pitot and expansion tube wall pressure data to be on

the order of 250-300 μsec for each of the test gases. However, because the goal of this work was to produce an experimental database suitable for comparison with computational results, these test flow times were carefully re-examined. This was done in order to reduce the uncertainty in freestream flow conditions, and to ensure that time-averaging windows selected for the heating data did not extend into periods of unsteady flow. To this end, wall pressure traces from each run (the test model left no room for a pitot pressure probe) were inspected in order to accurately determine the steady flow duration.

A typical wall pressure time-history for a HYPULSE run, which is similar to data from previous studies (Miller, 1977, Calleja et al, 1990), is shown in Figure 4.3.3. The wall pressure data typically show a broad initial peak of ~50 μsec duration which is caused by the arrival of the incident shock and acceleration gas/test gas interface. Over the next 50-100 μsec, the wall pressure decreases until a point is reached where the pressure trace "flattens out". The pressure remains approximately constant for a period of 100-200 μsec, and then begins to gradually "ramp" back up. The behavior may continue for 50-100 μsec, after which the arrival of the unsteady expansion wave system can be identified clearly by a rapid increase in pressure. The steady test flow can be associated with the "trough" centered ~150 μsec from the incident shock arrival. However, the boundaries of this trough are subject to interpretation, which can make it difficult to clearly identify the test time. Therefore, for the sake of consistency, a criterion for determining the length of the steady test flow period was established, as follows: For each run, the wall pressure was first averaged over a 100 μsec interval centered at a fixed time from the incident shock arrival. This fixed time was ~150 μsec for CO_2 tests and ~175 μsec for air tests (Figures 4.3.4 and 4.3.5); these values correspond to the center of the trough as determined by the average of all of the tests conducted in this study. The window of steady test flow was then defined as the time interval over which the wall pressure deviated by no more than ±5% from the average value. Based on all the CO_2 and air tests conducted, the average steady test flow window was found to be 146 μsec for CO_2 and 122 μsec for air. For He, the window was ~100 μsec; however, due to the limited number of He runs made, this cannot be considered a statistically valid average.

It was observed that the start of the test-time window, as determined from the ±5% pressure variation criterion, corresponded closely with the point at which measured heating rates on the test models reached constant levels. However, it was often observed that the heating rates remained constant for ~30-60 μsec past the end of this window. That suggests that these times represent fairly conservative performance estimates for HYPULSE, as the steady flow durations defined in this research are only approximately half of the nominal values stated for HYPULSE at the Langley conditions. Nevertheless, it was felt that a conservative estimate would serve better when experimental data were compared with CFD predictions. The test time windows as determined in this manner were thus used to define the interval over which heating data were averaged, and the average wall pressure over this period was used in the computation of freestream conditions.

For each HYPULSE run, freestream flow conditions were computed using the ERGAS (from Equilibrium Reacting Gas) code developed by Miller (1972); GASL employs a similar in-house code, EQSTATE (Calleja et al, 1990). An idealized, one-dimensional equilibrium chemistry model for the flow field is used in ERGAS in the computation of freestream properties. Upstream shock-tube properties are not used in the solution, rather the freestream is determined by modeling it as the flow behind a moving shock wave (i.e. the incident shock wave). The freestream can thus be computed from the measured pitot pressure and freestream static pressure in the test section and the freestream velocity. In practice, the parameters generally cannot all be measured during a test, so some assumptions must be made. The freestream static pressure is assumed to be equal to the wall pressure measured at the last station immediately before the end of the acceleration section of the tube. The pitot pressures are computed from calibrations of wall to pitot pressure measurements (DiFulvio, 1993). The freestream velocity is assumed to be equal to the incident shock speed, which is determined from upstream wall pressure transducer data. The shock speed is computed from the time required for the pressure disturbance caused by the incident shock to travel between stations, which is approximately constant by the end of the expansion tube.

Nominal flow properties at the Langley conditions as computed using ERGAS are given in Table

4.3.1. Actual values for each HYPULSE run in this research are given in Appendix B. A run-to-run repeatability analysis like that for the 31-Inch Mach 10 Air Tunnel conditions was performed for the HYPULSE test conditions. These uncertainty estimates are given in Table 4.3.1 as percentages of the individual values. Uncertainties in the various freestream parameters were found to vary from ±1% to ±10%. The freestream velocity and density are the parameters which have the most influence on the surface heat transfer rate:

$$q \approx \rho_\infty^{0.5} U_\infty^3 \tag{4.3.1}$$

and their uncertainties were only between ±1% and ±4%.

Table 4.2.1 Flow Conditions for the NASA Langley 31-Inch Mach 10 Air Tunnel

	$Re_\infty = 0.5\text{x}10^6$ ft^{-1}	$Re_\infty = 1.0\text{x}10^6$ ft^{-1}	$Re_\infty = 2.0\text{x}10^6$ ft^{-1}
P_∞ (Pa)	69 ± 1.1%	130.6 ± 0.5%	242 ± 0.5%
T_∞ (K)	53.31 ± 0.4%	52.45 ± 0.8%	51.48 ± 0.8%
ρ_∞ (kg/m^3)	$4.510\text{x}10^{-3}$ ± 1.4%	$8.680\text{x}10^{-3}$ ± 0.7%	$1.646\text{x}10^{-2}$ ± 0.7%
U_∞ (m/s)	1416 ± 0.2%	1422 ± 0.3%	1425 ± 0.2%
M_∞	9.675 ± 0.1%	9.795 ± 0.1%	9.928 ± 0.1%
Re_∞ (1/m)	$1.621\text{x}10^6$ ± 1.7%	$3.187\text{x}10^6$ ± 1.1%	$6.198\text{x}10^6$ ± 0.9%
$P_{0,2}$ (Pa)	8383 ± 1.2%	16280 ± 0.5%	31000 ± 0.5%
$T_{0,2}$ (K)	1008 ±0.3%	1015 ± 0.6%	1017 ± 0.3%
$H_{0,2} - H_{298}$ (MJ/kg)	0.756 ± 0.5%	0.764 ± 1.0%	0.767 ± 0.5%
ρ_2/ρ_∞	5.967 ± 0.1%	5.979 ± 0.1%	5.989 ± 0.1%

Table 4.3.1 Flow Conditions for the NASA HYPULSE Expansion Tube

	Air	CO_2	He*
P_∞ (Pa)	1824 ± 9.9%	1191 ± 10.8%	1511
T_∞ (K)	1113 ± 9.3%	1088 ± 8.7%	302
ρ_∞ (kg/m^3)	5.712×10^{-3} ± 1.8%	5.789×10^{-3} ± 3.1%	2.416×10^{-3}
U_∞ (m/s)	5162 ± 0.9%	4772 ± 1.1%	6170
M_∞	7.93 ± 4.1%	9.71 ± 4.1%	6.04
Re_∞ (1/m)	0.668×10^6 ± 3.9%	0.660×10^6 ± 4.9%	0.70×10^6
$P_{0,2}$ (kPa)	147.2 ± 1.3%	129.6 ± 1.8%	81.7
$T_{0,2}$ (K)	6028 ±0.8%	3703 ± 0.9%	3968
$H_{0,2} - H_{298}$ (MJ/kg)	14.18 ± 1.4%	12.25 ± 2.1%	19.0
ρ_2/ρ_∞	18.98 ± 1.0%	10.98 ± 0.7%	3.70

* No statistics computed for He as only two runs were made

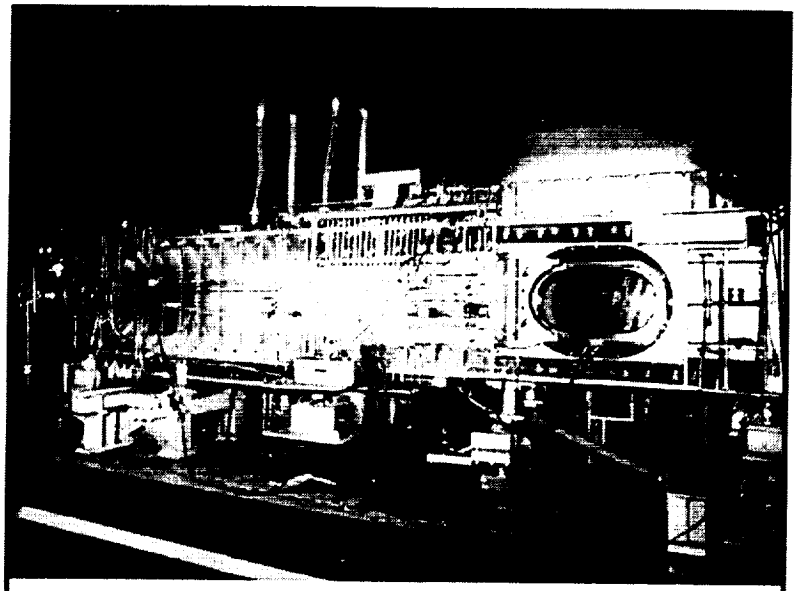

Figure 4.1.1 NASA Langley 31-Inch Mach 10 Air Tunnel

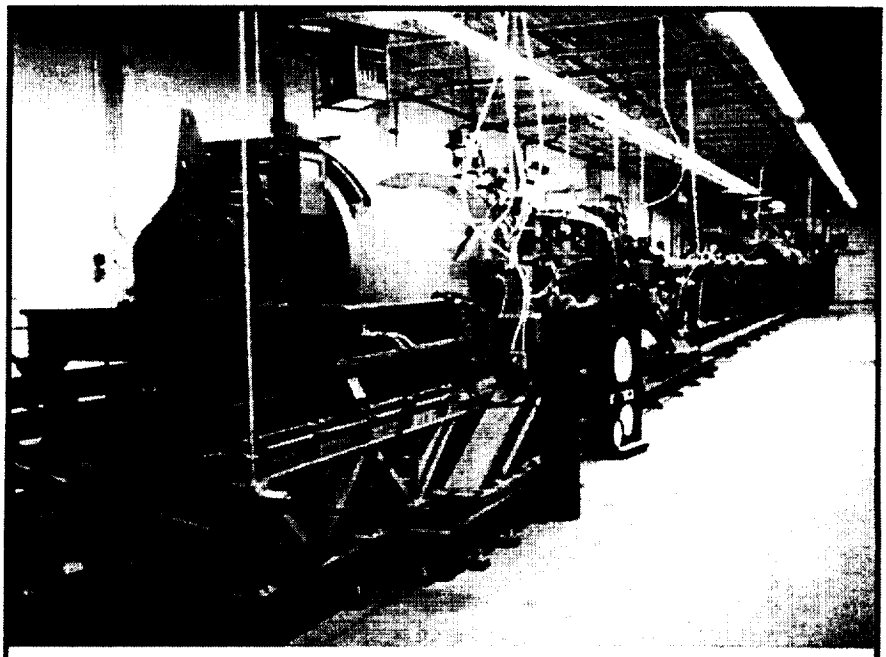

Figure 4.1.2 NASA HYPULSE Expansion Tube

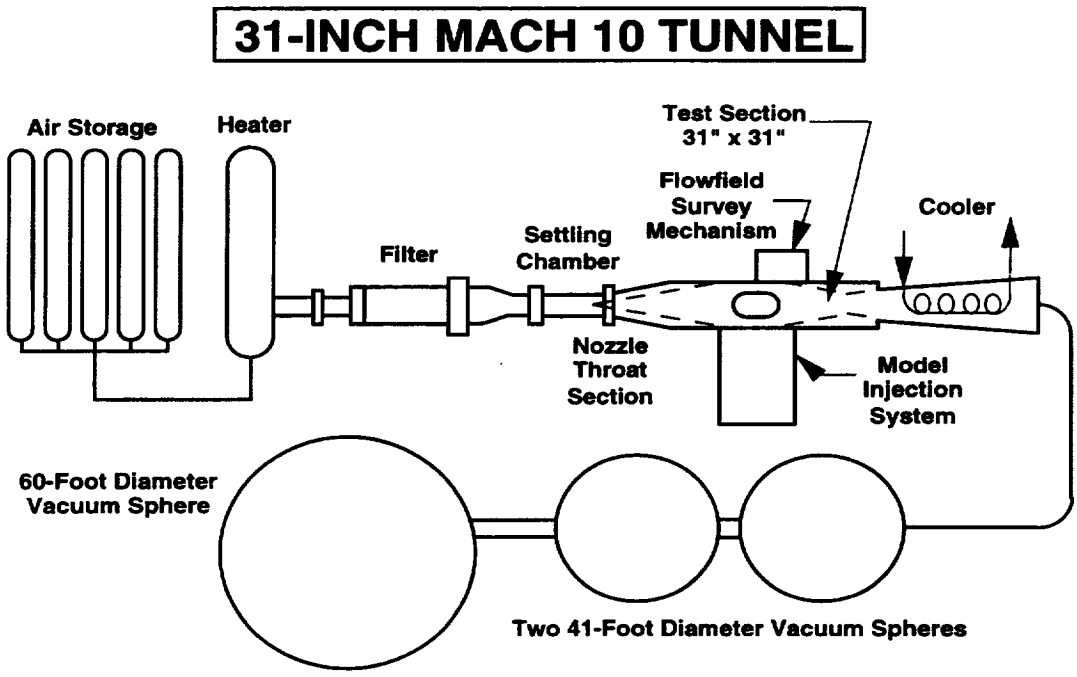

Figure 4.2.1 Schematic of NASA Langley 31-Inch Mach 10 Air Tunnel

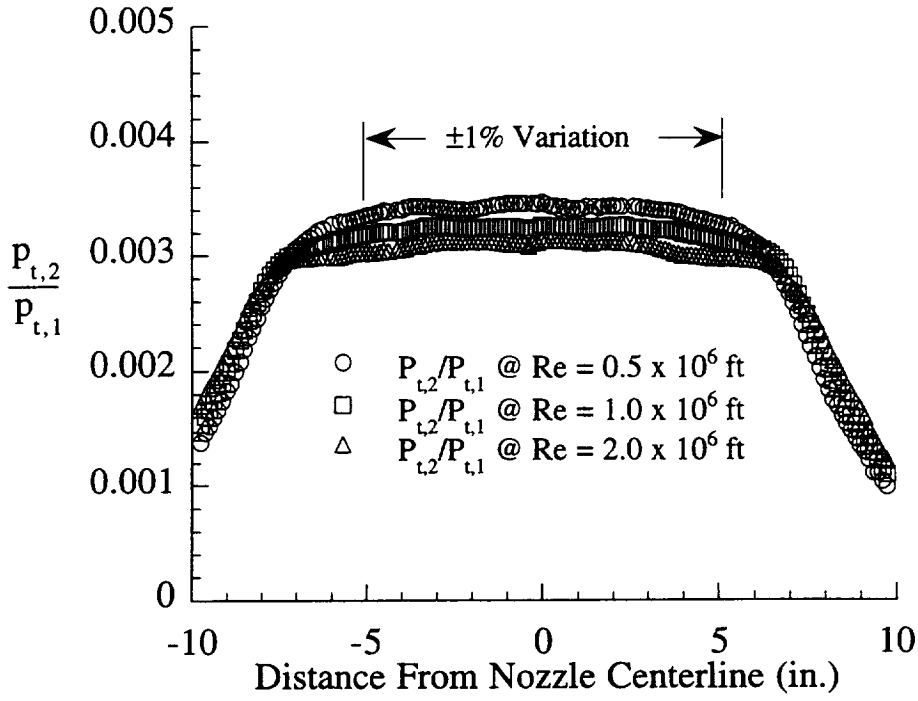

Figure 4.2.2 NASA Langley 31-Inch Mach 10 Air Tunnel Pitot Calibration (from Micol, 1995)

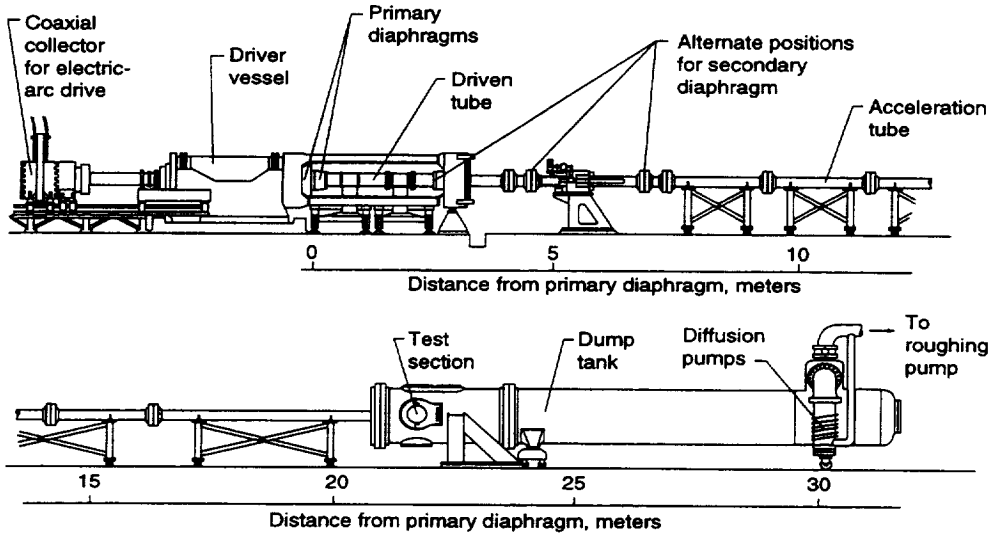

Figure 4.3.1 Schematic of NASA HYPULSE Expansion Tube

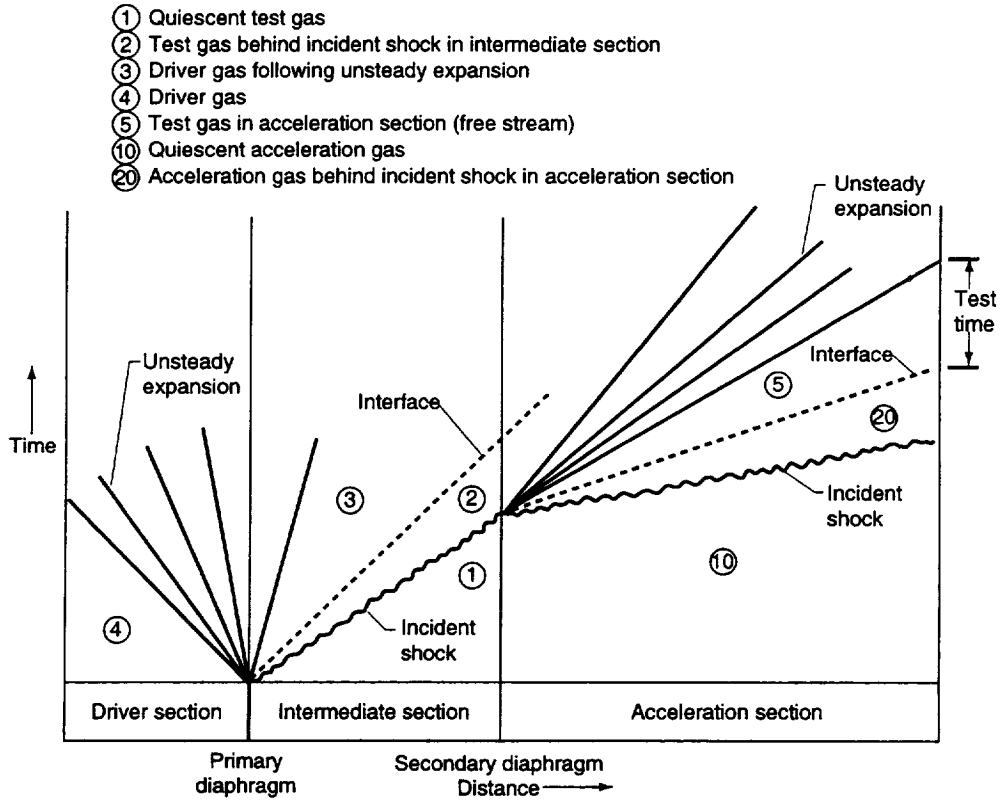

Figure 4.3.2 X-T Diagram for NASA HYPULSE Expansion Tube

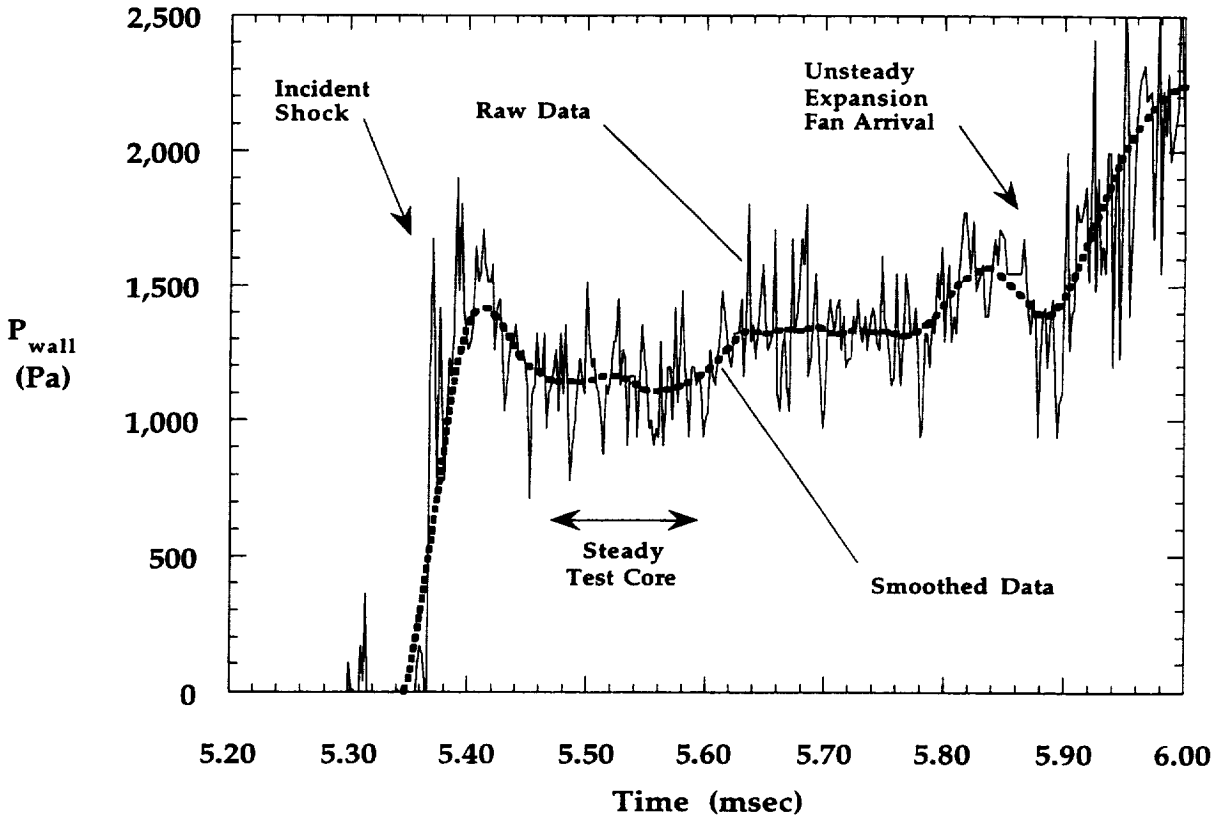

Figure 4.3.3 Typical HYPULSE Wall Pressure Time History

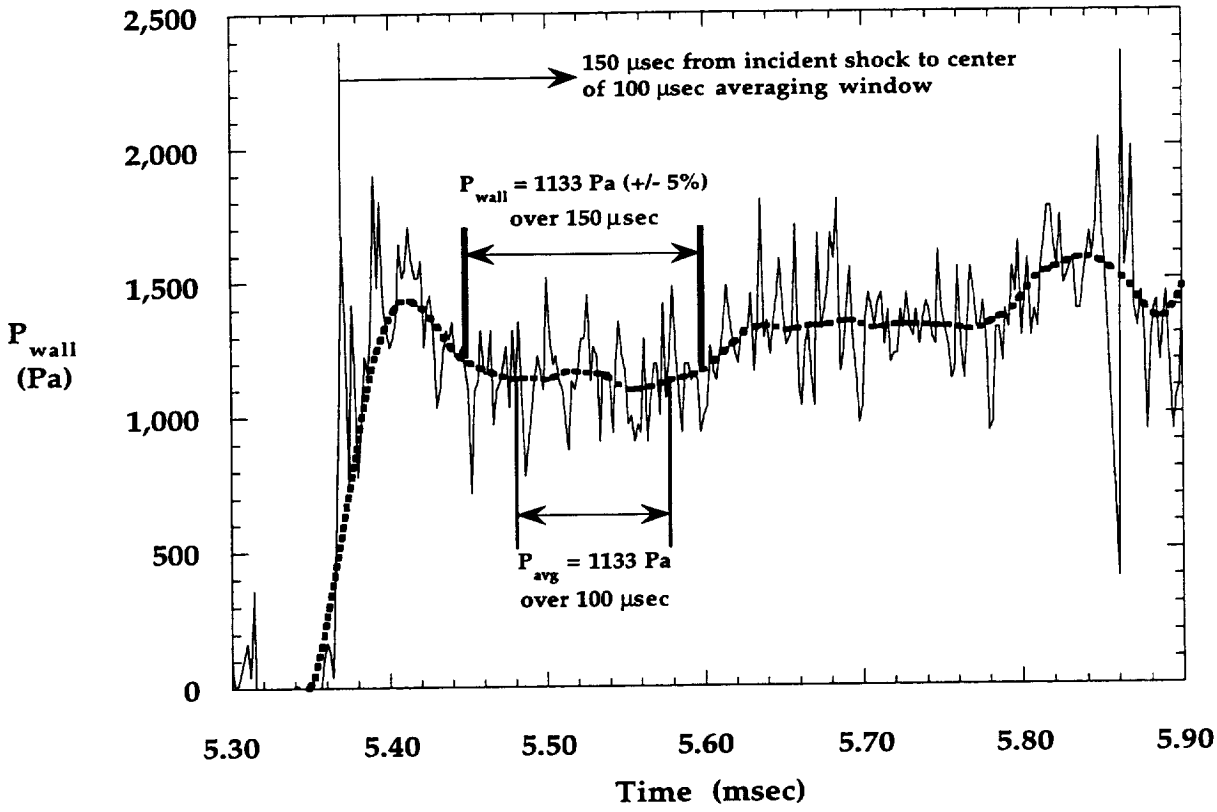

Figure 4.3.4 Typical CO_2 Test Window

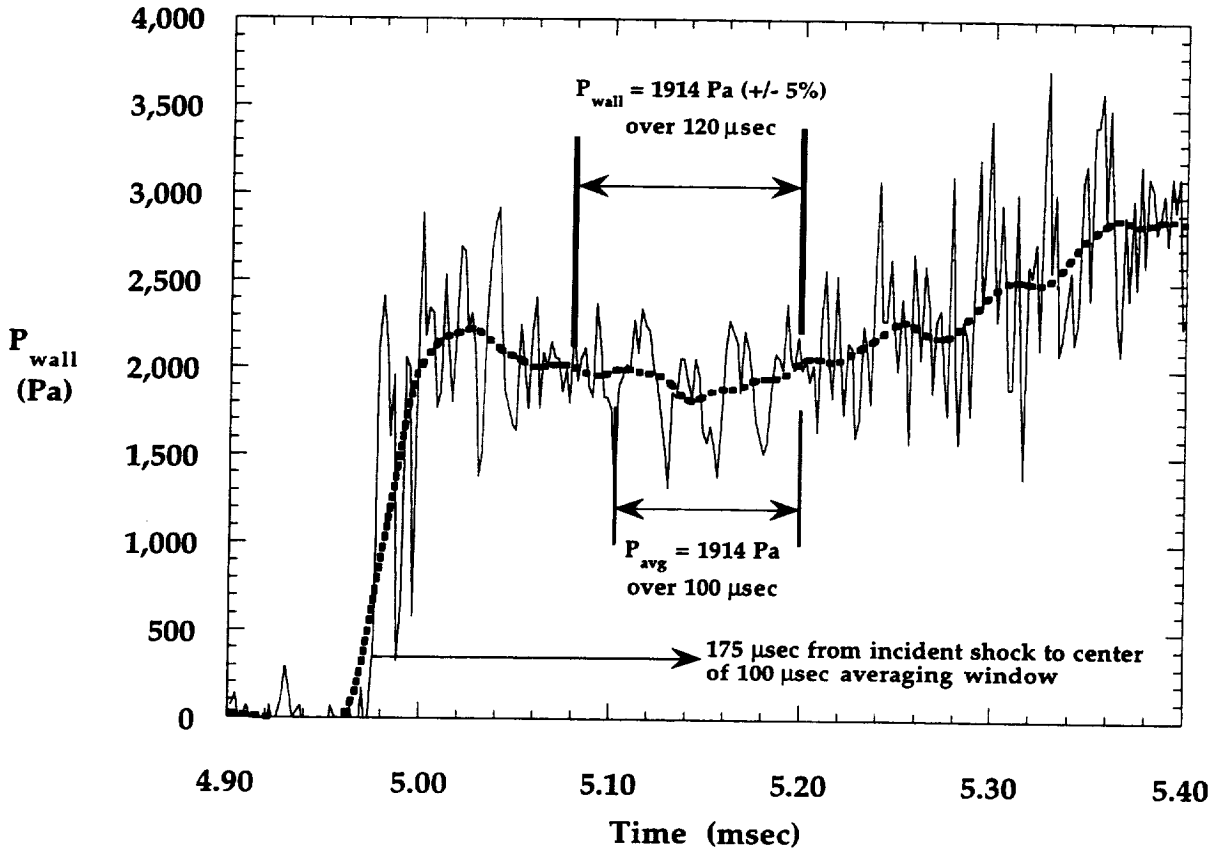

Figure 4.3.5 Typical Air Test Window

CHAPTER 5
DATA ACQUISITION AND REDUCTION

Section 5.1 Data Acquisition Systems

The data acquisition system in the 31-Inch Mach 10 Tunnel is a NEFF Instrumentation Corporation 50 kHz or 100 kHz throughput rate, amplifier per channel, analog-to-digital unit. The NEFF system has a 256 channel capability. The data sampling rate and channel gains and filter settings are programmable. For thin-film heat transfer tests such as those discussed in this work, the filter setting is generally 100 Hz and the data sampling rate is 50 Hz.

In the HYPULSE facility, data acquisition is handled with a LeCroy Model 6810 Waveform Digitizer. The LeCroy system is capable of processing 152 channels of data (80 channels at the time this research was conducted), of which 10 are reserved for facility use. For heat transfer testing, thin film gage current is supplied by a LAMBDA™ type LQ411 low-noise linear power supply through GASL manufactured, 20-channel, floating ground-point gage control units. The data sampling rate for the present work was 500 kHz.

Section 5.2 1DHEAT Data Reduction Code

All thin-film gage heat transfer data from the 31-Inch Mach 10 Air Tunnel and the HYPULSE Expansion Tube were reduced using the 1DHEAT data reduction code (Hollis, 1995). The 1DHEAT (One-Dimensional Hypersonic Experimental Aero-Thermodynamic) code incorporates both analytical and numerical techniques for the computation of heat-transfer rates from measured surface temperature time-

history data. 1DHEAT can be employed to reduce both thin-film gage and coaxial surface thermocouple data from gages on substrates of Macor, quartz, pyrex, Upilex, chromel, or constantan. Additionally, the numerical technique can be used to reduce data from gages with multiple-layer substrates comprised of layers of different materials, for instance, thin-film gages on a thin Macor insert layer in a metal model. In this research, only models with thin-film gages on single-layer Macor or quartz substrates were tested.

5.2.1 Analytical Techniques

1DHEAT incorporates two analytical heat-transfer techniques, the direct semi-infinite technique (Schultz and Jones, 1973, Cook, 1970b), and the indirect semi-infinite technique (Kendall, Dixon, and Schulte, 1967). Both schemes are based on the assumption of one-dimensional heat transfer into a solid of semi-infinite thickness (see Section 3.2) with respect to thermal penetration depth. It is also assumed that the thickness of the gage is much less than the thermal penetration depth into the solid, and thus the gage has negligible effect on the heat transfer to the substrate. A generic gage and substrate for which these assumptions are satisfied is illustrated in Figure 5.2.1. With these assumptions, the temperature distribution within the substrate can be given by the partial differential equation:

$$\frac{\partial}{\partial x}\left(k\frac{dT}{dx}\right) = \rho c_p \frac{\partial T}{\partial t} \tag{5.2.1}$$

for which the boundary conditions are:

$$T\left(x, t=t_0\right) = T_0 \tag{5.2.2a}$$

$$T(x=0,\ t) = T_{surf}(t) \tag{5.2.2b}$$

$$q(x=\infty,t) = -k\frac{\partial T}{\partial x}(x=\infty,t) = 0 \tag{5.2.2c}$$

In general, the thermal conductivity, specific heat, and density are all functions of temperature, however, in order to obtain a solution to equation (5.2.1), it is commonly assumed that the thermal properties are all constant. For this case, equation (5.2.1) simplifies to:

$$\frac{\partial^2 T}{\partial x^2} = \frac{1}{\alpha_0}\frac{\partial T}{\partial t} \tag{5.2.3}$$

where:

$$\alpha_0 = \frac{k}{\rho c_p} = \text{constant} \tag{5.2.4}$$

With the simplifying assumption of constant substrate thermal properties, a solution for the surface heat-transfer rate can, through somewhat lengthy manipulation (e.g. Schultz and Jones, 1973, Hollis, 1995), be obtained. The surface heat-transfer rate is then given as a function of the temperature-time history measured with the gages as:

$$q(t_n) \equiv q_n = \frac{2\beta_0}{\sqrt{\pi}}\sum_{i=1}^{i=n}\frac{T_i - T_{i-1}}{\sqrt{t_n - t_i} + \sqrt{t_n - t_{i-1}}} \tag{5.2.5}$$

where the thermal product of the substrate is:

$$\beta_0 = \sqrt{\rho c_p k} \tag{5.2.6}$$

As an alternative to equation (5.2.5), which is referred as the *direct method*, the total heat energy added to the substrate can first be computed as detailed by Kendall et al (1967):

$$Q_n = \frac{\beta_0}{\sqrt{\pi}} \sum_{i=1}^{i=n} \frac{(T_i - T_1) + (T_{i-1} - T_1)}{\sqrt{t_n - t_i} + \sqrt{t_n - t_{i-1}}} \tag{5.2.7a}$$

The *indirect method* heating rate can then be computed through a finite-difference approximation to the time derivative of equation (5.2.7a) as in Hedlund, Hill, Ragsdale and Voisinet (1980).

$$q(t_n) \equiv q_n = \frac{dQ_n}{dt} \cong \frac{-2Q_{n-8} - Q_{n-4} + Q_{n+4} + 2Q_{n+8}}{40\Delta t} \tag{5.2.7b}$$

Over a given time interval, the two schemes represented by equations (5.2.5) and (5.2.7) will yield approximately identical time-averaged heat transfer values. However, the instantaneous heating rates are not, in general, identical. This is because the temperature difference term in the numerator of equation (5.2.5) tends to accentuate fluctuations in the heat transfer rate, whereas the temperature sum term in the numerator of equation (5.2.7a) and the wide numerical differencing stencil in equation (5.2.7b) tend to smooth fluctuations in the heating rate. This is illustrated with sample data from the 31-Inch Mach 10 Tunnel in Figure (5.2.2). As a result of this difference, the indirect method is preferable in situations where

there is a relatively high noise level in the data, or if only time-averaged values are of interest. The direct method would be preferred in a situation where the transient behavior of the heat transfer was of interest, such as in turbulent flows.

The heat-transfer data reduction techniques of equations (5.2.5) and (5.2.7) are generally not adequate for use with hypersonic heat-transfer data. This is because of the assumption that the material properties of the substrate remain constant with temperature. For most materials, these properties are functions of temperature, and models tested in hypersonic facilities usually experience relatively large temperature increases over a test period. An empirical method of correcting for the effects of variable thermal properties is to multiply the computed heat-transfer rate from equation (5.2.5) or (5.2.7) by a correction factor:

$$q_{\beta(T)} = q_{\beta_0}\left(1 + \lambda\, \Delta T_s\right) \tag{5.2.8a}$$

where λ is a correction factor which accounts for the variation of thermal properties with temperature, ΔT_s is the surface temperature rise, and $q_{\beta,0}$ is the computed constant-thermal-properties heat transfer rate. Correction factors for various substrates have been determined by Hartunian and Varwig (1962), Cook (1970a), Cook and Felderman (1966), and Miller (1981). For this work, new correction factors (Hollis, 1995) were derived for the substrates of interest, Macor and quartz, through comparisons with solution computed using the finite-volume technique described in the next section. The derivation of these correction factors is presented in Appendix C. While these correction factors do lead to accurate results, their derivation is strictly empirical. Therefore, it is suggested that they only be used for quick initial analysis of data, and that a numerical technique like that presented in the next section be used for final data analysis.

As shown in equation (5.2.5) or (5.2.7a), the material thermal properties have a direct linear effect on the computed heat-transfer rate. This is an important and often overlooked point which is emphasized

here because in the course of this research it was found that there is very little consistent data available on the thermal properties of materials commonly used in the construction of heat transfer test models. As part of this research project, a investigation into the properties of Macor and quartz, the two materials used in this study, was conducted. The results of this investigation are presented in Appendix C.

5.2.2 Numerical Techniques

The analytical techniques presented in section (5.2.1) are classical methods that have been in use for decades and are still of utility for reduction of experimental data. These can easily be encoded into a data reduction scheme and can be used for rapid real-time analysis of heat-transfer data. However, now that high-speed computing resources are commonly available, it is routinely possible to compute a numerical solution to equation (5.2.1). A numerical method has the advantage of directly incorporating the variation of material properties into the solution instead of using an empirical correction factor as in equation (5.2.8).

1DHEAT incorporates an implicit, one-dimensional, finite-volume numerical scheme for computation of surface heating rates. In this scheme, temperature distributions within the substrate are determined from a control-volume energy balance (Figure 5.2.3):

$$q_{in} - q_{out} = q_{stored} \tag{5.2.9}$$

which is discretized as:

$$\left[-k_{i-\frac{1}{2}}\frac{\left(T_i^n - T_{i-1}^n\right)}{\left(x_i - x_{i-1}\right)}\right] - \left[-k_{i+\frac{1}{2}}\frac{\left(T_{i+1}^n - T_i^n\right)}{\left(x_{i+1} - x_i\right)}\right] = \left[\left(\rho c_p\right)_i\frac{\left(T_i^n - T_i^{n-1}\right)}{\Delta t}\right]\Delta x_i \tag{5.2.10}$$

Rearrangement of equation (5.2.10) leads to:

$$T_{i-1}^{n}\left[k_{i-1/2}\right] + T_{i}^{n}\left[-k_{i-1/2} - k_{i+1/2}\frac{(x_i - x_{i-1})}{(x_{i+1} - x_i)} - (\rho c_p)_i (x_i - x_{i-1})\frac{\Delta x_i}{\Delta t}\right]$$
$$+ T_{i+1}^{n}\left[k_{i+1/2}\frac{(x_i - x_{i-1})}{(x_{i+1} - x_i)}\right] = \left[(\rho c_p)_i (x_i - x_{i-1})\frac{\Delta x_i}{\Delta t}\right] T_i^{n-1} \qquad (5.2.11)$$

which is a tridiagonal system of equations that can be solved using the Thomas algorithm (Thomas, 1949). The boundary conditions for equation (5.2.11) are the measured gage temperature at the exterior of the substrate, and at the back face of the substrate (the interior of the test model), either a measured temperature, a constant temperature, or an adiabatic boundary. A measured interior temperature is the most physically accurate boundary condition, but as this is usually not easily measured, the adiabatic interior boundary condition is generally used. The rationale for the condition is that over the short duration of the test period, the heat pulse generally does not penetrate deeply into the substrate, and thus there is negligible heat transfer at the interior boundary.

The finite-volume model has the advantage of being applicable to a multiple-layer substrate, where each of the layers is a different material with different thermal properties. One such example of this is the reduction of data using the 1DHEAT code by Berry and Nowak (1996) from thin-film gages deposited on a layer of Upilex which was then applied to the surface of a Macor model. One important note for a multiple-layer substrate is that the cell wall thermal conductivity, $k_{i-1/2}$, is not a linear average of the cell center values on either side, but is based instead on the electrical resistor analogy (White, 1988):

$$k_{i-\frac{1}{2}} = \frac{1}{\frac{1-F_i}{k_{i-1}} + \frac{F_i}{k_i}} \tag{5.2.12a}$$

where

$$F_i = \frac{(\Delta x_i)/2}{x_i - x_{i-1}} \tag{5.2.12b}$$

In this work, the indirect, semi-infinite method was used for rapid, preliminary analysis of the data. The validity of this analysis was later verified by comparison with finite-volume method results for selected data sets. In all cases, the indirect method analysis results were found to agree with the finite-volume results to within less than ±1% during the time period for which the semi-infinite assumption was considered valid. This can be seen in Figure 5.2.4, in which the Stanton number distribution on a 2-in. diameter hemisphere in the 31-Inch Mach 10 Tunnel at the $Re_\infty = 1 \times 10^6$ ft^{-1} condition is shown. Stanton numbers computed from the indirect and direct methods and the finite-volume method can all be seen to be in close agreement. In order to illustrate the need to account to take into account the variation of model substrate thermal properties, the distribution computed with the assumption of constant thermal properties is also shown. The surface temperature rise during this test was only on the order of 100 K and yet the computed constant properties stagnation point Stanton number is in error by 6%.

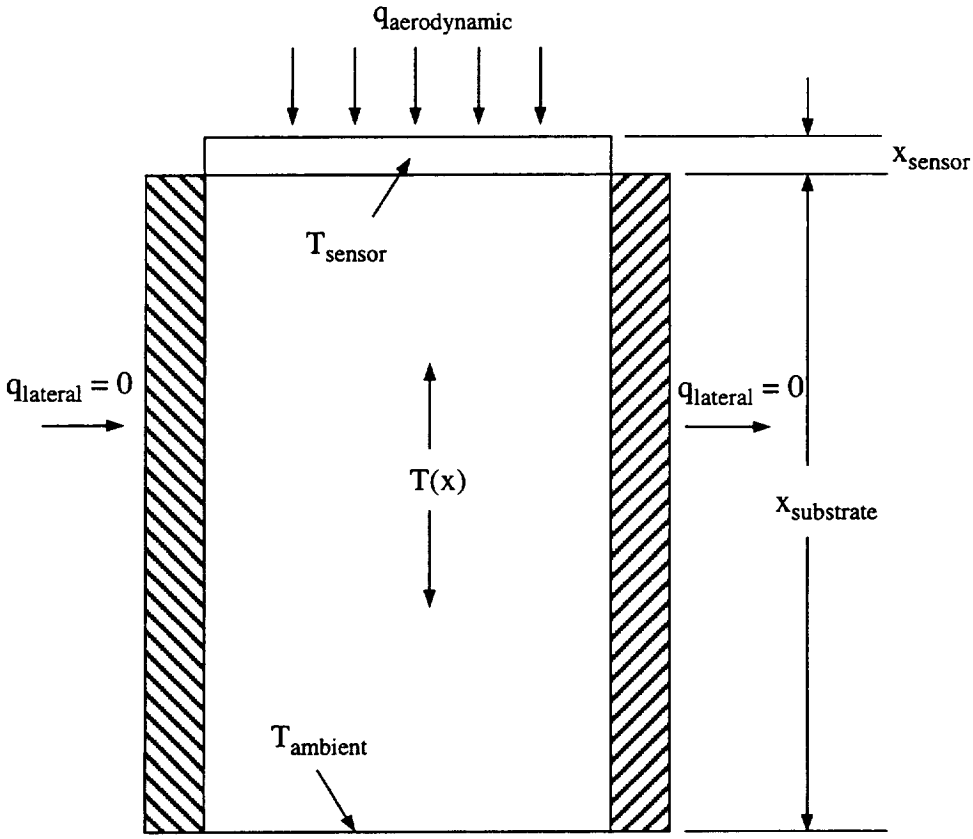

Figure 5.2.1 Sensor and One-Dimensional Semi-Infinite Substrate

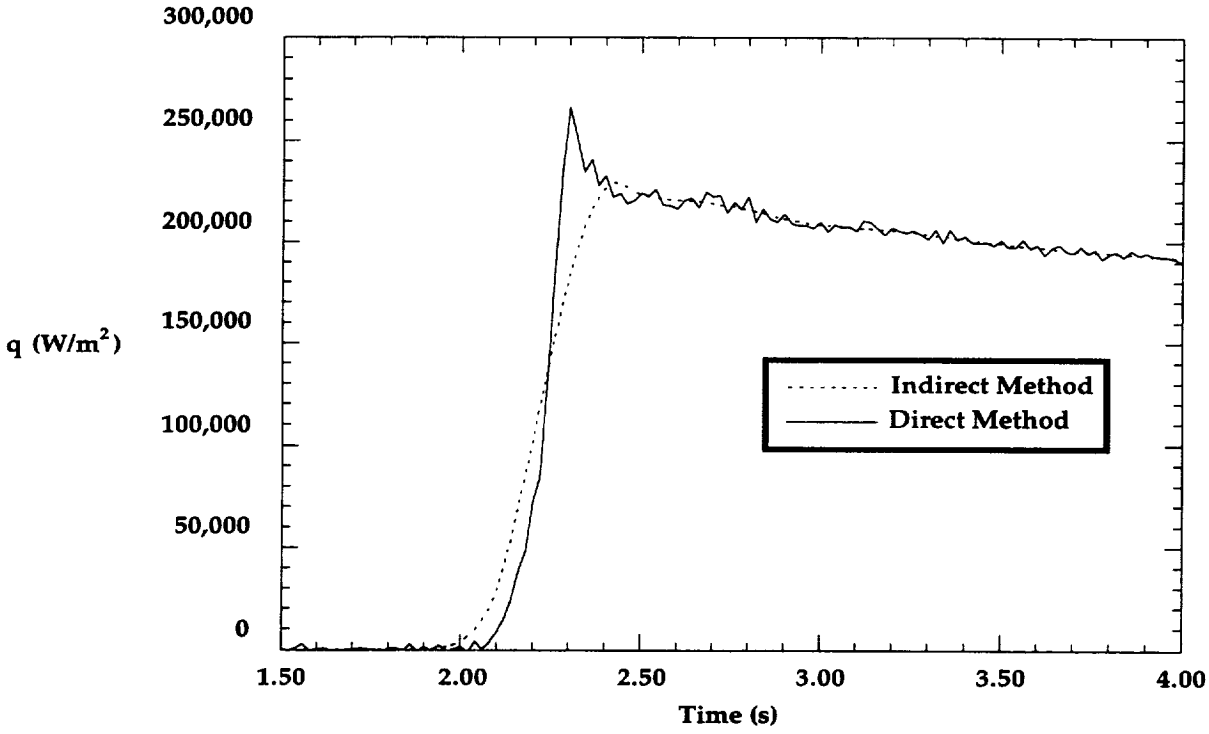

Figure 5.2.2 Sample 31-Inch Mach 10 Heating Data, Direct and Indirect Heating Method Computations

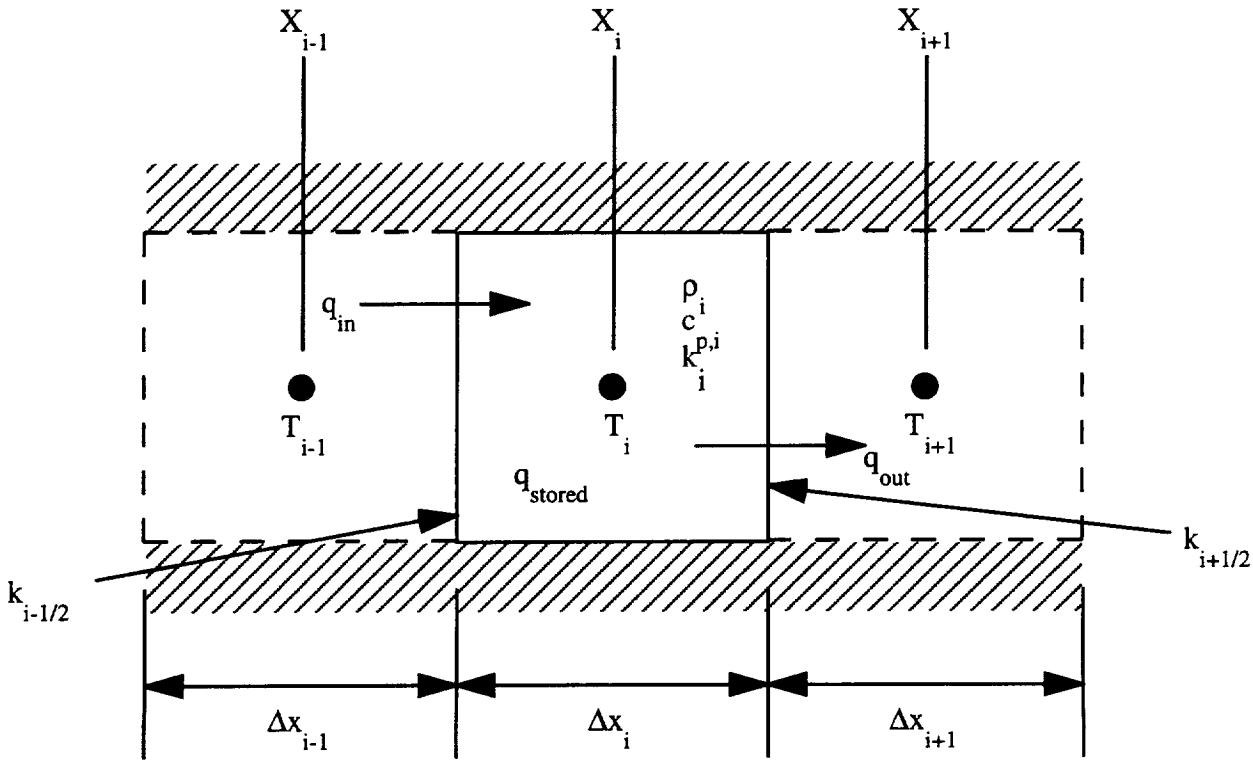

Figure 5.2.3 Finite-Volume Energy Balance and Nomenclature

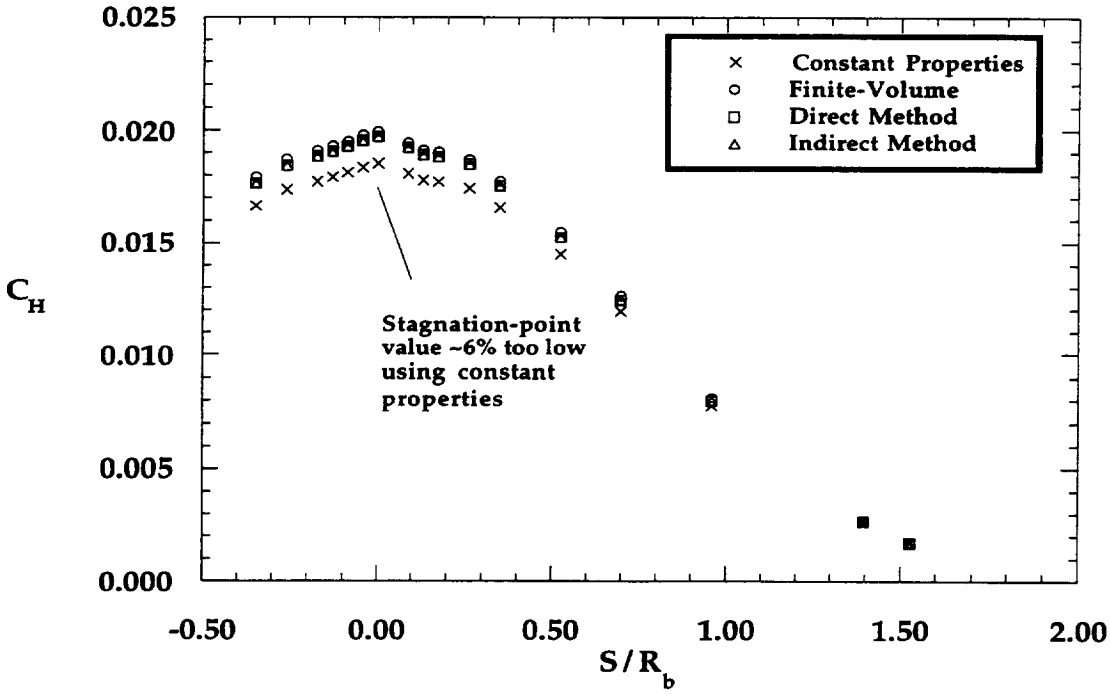

Figure 5.2.4 Comparison of Heat Transfer Data Reduction Techniques: C_H Distribution on Hemisphere in LaRC 31-Inch Mach 10 Air Tunnel

CHAPTER 6
EXPERIMENTAL RESULTS

Aerothermodynamic data from the tests conducted in the 31-Inch Mach 10 Air Tunnel and the HYPULSE Expansion Tube will be presented in this chapter in the form of the Stanton number as defined by:

$$C_H = \frac{q}{\rho_\infty U_\infty (h_0 - h_w)} \tag{6.0.1}$$

For the data from both facilities, the reported Stanton numbers have been time-averaged over the steady flow test period in order to minimize measurement precision error due to random fluctuations in freestream flow properties or system noise. At the data acquisition system sampling rates in each facility, approximately 50 to 75 data points were acquired during the time-averaging window of each test.

The aerothermodynamic data are reported in terms of the Stanton number rather than a dimensional heat-transfer rate because, owing to the short duration of heat-transfer tests in the Mach 10 Tunnel, model surface temperatures do not have sufficient time to reach thermal equilibrium, and thus the measured surface heat-transfer rates decrease with time as the wall temperature increases. This transient behavior of the surface temperature is accounted for in the definition of the Stanton number through the enthalpy difference term in the denominator of equation (6.0.1). As long as the heat conduction within the model surface remains approximately one-dimensional, the enthalpy difference term in equation (6.0.1) will decrease at the same rate as the heat-transfer rate decreases, and thus the Stanton number will remain a constant.

The one-dimensional heat conduction assumption is valid as long as there are no large streamwise or transverse temperature gradients along the surface of the model. This assumption could be invalid in the case of a region of large surface curvature, or in the neighborhood of a shock-interaction on the model. In

the Mach 10 tests, the Stanton number appeared to exhibit a small departure from one-dimensional behavior in the immediate region of the junction of the afterbody and the forebody corner, which caused C_H to vary with time. This was due to the large temperature gradient which occurred between the forebody, which was exposed to flow elevated to high temperature by passage through the bow shock, and the afterbody, which was exposed to low temperature recirculating flow. However, 31-Inch Mach 10 Air Tunnel test times were sufficiently limited that the temperature gradient at the corner remained small, and so the C_H values in this area varied by no more than 5% over the data acquisition period.

In the HYPULSE Expansion Tube, model surface temperatures are essentially "frozen" with respect to the high freestream total temperature of the flow because of the extremely short duration (100-300 μsec) of a test. Thus, changes in the convective heating at the wall due to the change in surface temperature or to lateral and transverse conduction are negligible, and so the surface heat-transfer rates can be considered to be constants. However, the aerothermodynamic data from HYPULSE also will be presented in terms of C_H in order to be consistent with the 31-Inch Mach 10 data.

The Stanton number data will be plotted vs. gage surface positions given in terms of S/R_b, the normalized distance from the symmetry axis, or in terms of L/R_b, the normalized distance from the model base/sting junction. The numerical S/R_b or L/R_b values can be related to model surface features using Figure 6.0.1, in which the surface (and cartesian) coordinates of various control points along the model and sting for each of the configurations are given. In order to emphasize the details of both the forebody and wake heating distributions, which differ by one to two orders of magnitude, the Stanton number distributions will in some cases be plotted on both linear and logarithmic scales. In other cases, the forebody and wake data will be plotted on separate linear scales.

An example of the aerothermodynamic environment of the MP-1 entry vehicle configuration is shown in Figures 6.0.2 and 6.0.3. This distribution is taken from 31-Inch Mach 10 Air Tunnel Test 293, Run 010. For this α = 0 deg case, the highest C_H is measured at the stagnation point (point A). C_H decreases with S/R_b along the cone-portion of the forebody (point B to point C) until the forebody corner is

reached. As the flow accelerates around this corner, the boundary layer grows thinner, which leads to a local heating maximum at the corner. The boundary layer separates from the body to form a free shear layer after it turns this corner (after point D), and a recirculating flow region is formed behind the model. Stanton numbers along the afterbody and base within this recirculation region (points D through G) are much lower than on the forebody. Stanton numbers remain low along the sting, but rise gradually toward a local maximum in the region after the free-shear-layer impingement point on the sting (approximately midway between points G and H). The Stanton number distribution on the sting and afterbody can be seen more clearly in the log scale plot (Figure 6.0.3). The maximum C_H value on the sting is an order of magnitude less than at the forebody stagnation point, while the minimum value is at least two orders of magnitude lower. One feature not apparent on the linear scale plot, but which can be seen on the log scale plot, is a small local maximum near the afterbody corner (point F). This maximum is caused by thinning of the boundary layer as the recirculating flow accelerates around this corner. Stanton number distributions in HYPULSE are similar to the Mach 10 distributions, however, the heat-transfer rates are much greater owing to the higher total enthalpy in HYPULSE.

Section 6.1 31-Inch Mach 10 Air Tunnel Data

Two separate aerothermodynamic test series, identified as LaRC 31-Inch Mach 10 Air Tunnel Tests 293 and 307, were conducted in the 31-Inch Mach 10 Air Tunnel. In the first series, Test 293, each of the four parametric entry vehicle configurations, MP-1, MP-2, MP-3, and MP-4, was tested at nominal freestream Reynolds numbers of 0.5, 1.0, and 2.0×10^6 ft^{-1}. Measurements were also made with each of the models at angles-of-attack of from 0 deg to -20 deg at the 1.0×10^6 ft^{-1} Reynolds number condition. Additionally, the MP-1 configuration was tested further at angle-of-attack with the model rolled to position the thin-film gages at angles of from 0 deg to 180 deg from the vertical axis. In the second series, Test

307, transition grit was applied to the surface of a stainless steel (full-scale) MP-1 model (designated MP-1 SS) in order to determine if the forebody boundary layer could be tripped into turbulent behavior in order to produce a turbulent wake. The thermal properties tests with the 2-in. diameter hemispheres were also part of Test 307, but discussion of those results will be deferred until Appendix C.

A total of 39 heat-transfer runs were made in Test 293, and in the entry-vehicle phase of Test 307, 16 heat-transfer runs were made. The analysis and interpretation of the data are presented in this chapter, while the complete data for each of the runs as well as the run flow conditions and the test matrix are given in Appendix A.

6.1.1 Reynolds Number Effects

Each of the four parametric entry vehicle configurations was tested at each of the 31-Inch Mach 10 Air Tunnel operating points of 0.5, 1.0, and 2.0×10^6 ft^{-1} freestream Reynolds number. Stanton number distributions for these runs are presented in Figures 6.1.1-6.1.4. In these figures, the distributions are normalized by the measured stagnation point Stanton number for each run, which is listed in the data tables in Appendix A.

Normalized forebody distributions showed no Reynolds number effects for any of the configurations. However, the sting distributions changed noticeably with Reynolds number. As shown in Figure 6.1.1 for the MP-1 configuration, as Re_∞ was increased, the peak sting value increased from 8% of the forebody stagnation point at a Reynolds number of 0.5×10^6 ft^{-1}, to 11% at 1.0×10^6 ft^{-1}, and to 15% at 2.0×10^6 ft^{-1}. The location of the peak also moved slightly upstream toward the model from an S/R_b value of approximately 4.5 at the lowest Reynolds number to approximately 4.25 at the highest Reynolds number. As shown in Figures 6.1.2-6.1.4, the influence of the Reynolds number on the sting distributions for the other configurations was similar to that observed with the MP-1 configuration.

The upstream movement of the peak heating point with increasing Reynolds number suggests a

decrease in the size of the wake vortex; however, as shown by Wells (1990), the free shear layer reattachment point on the sting (which defines the end of the wake vortex) is near to, but not coincident with, the peak heating point. Therefore, oil flow runs were conducted with an uninstrumented aluminum MP-1 model and sting in order to visualize surface streamline patterns and to identify the actual location of shear layer reattachment. The location of the shear layer reattachment was identified in photographs (Figures 6.1.5-6.1.7) of surface oil flow patterns at each of the three Reynolds numbers. From these photographs, it appears that the reattachment point also moved slightly upstream toward the base with increasing Reynolds number just as the peak heating point did. Also of interest in these photographs is the location of the boundary layer separation on the afterbody of the model. At the lowest Reynolds number, separation appeared to take place after the model corner on the cone frustrum part of the afterbody. At the other two Reynolds numbers, separation appeared to occur right at the junction of the corner and afterbody.

The influence of the Reynolds number on the peak sting heating location is shown more clearly in Figure 6.1.8, where the L/R_b location of the peak is plotted vs. the Reynolds number for each of the four configurations. The reattachment location on the MP-1 configuration from the oil flow tests is also plotted in Figure 6.1.8. As shown in this figure, the effect of the Reynolds number on the location of the peak heating point and reattachment point was to cause a slight, but measurable, upstream (toward the model base) movement with increasing Reynolds number for all configurations. However, according to laminar theory (Berger, 1971), the size of the recirculation region increases with Reynolds number. While oil flow patterns alone should not be considered as conclusive proof, the experimentally observed behavior of the wake does suggest that the wake may be transitional or turbulent in the Mach 10 tests. The subject will be addressed in more depth later in this chapter in the discussion of the Test 307 transition grit data, in the comparisons with the HYPULSE data, and in Chapter 8 in the presentation of comparisons between the experimental data and computational results.

6.1.2 Angle-of-Attack Effects

Stanton number distributions on the MP-1 configuration at angles-of-attack of 0 deg, –4 deg, –12 deg, and –20 deg are shown in Figure 6.1.9. On the forebody, the geometric stagnation point Stanton number (that is, at point A) remained nearly constant, although the actual maximum forebody heating point moved slightly windward of the stagnation point. The forebody peak value was approximately equal to the stagnation point value at α = -4 deg, and increased to 5% higher than the stagnation point value at α = -20 deg. Forebody corner C_H values exhibited greater dependence on α. At the windward corner, C_H increased by nearly 50% between α = 0 deg and α = -20 deg, while over the same range the leeward corner value decreased by nearly 50%. Over this range of α, the sting peak heating point moved upstream toward the model from an S/R_b location of ~4.5 to ~2.5, while the magnitude of the peak increased from 10% of the stagnation point at 0 deg to 38% at -20 deg.

Three-dimensional C_H distributions for each angle-of-attack were obtained for the MP-1 configuration by varying the model roll angle, ϕ, between 0 deg and 180 deg (relative to ϕ = 0 deg when the thin-film gages are on the vertical axis) at angles-of-attack of -4 deg, -12 deg and -20 deg. These distributions are presented in Figures 6.1.10 through 6.1.12. At angle-of-attack, shear layer reattachment on the leeward side of the sting occurred much further downstream on the sting and produced a much smaller heating peak than on the windward side. For example, at α = -20 deg, the peak windward side sting heating was 2.7 times the peak leeward side heating.

Stanton number distributions on the MP-2, MP-3, and MP-4 configurations at angles-of-attack of 0 deg, –4 deg, and –20 deg are shown in Figures 6.1.13-6.1.15. The behavior of the C_H distributions on these configurations was nearly identical to that of the distributions on MP–1. The effects of model configuration and angle-of-attack on the sting peak heating are shown in Figure 6.1.16, where the location of the peak windward side sting C_H is plotted against L/R_b, the distance from the model base. The model configuration had a negligible effect on the peak location, however, the peak location varied with α from

L/R_b = 0.5 at α = -20 deg to L/R_b = 3.5 at α = +4 deg (model at α = -4 deg with ϕ = 180 deg).

6.1.3 Configuration Effects

As discussed in Chapter 3, the parametric configuration MP-2 was a hyperboloid which was geometrically matched to the MP–1 configuration, while the MP-3 and MP-4 configurations were 70 deg sphere-cones configurations with corner radii two or four times, respectively, that of MP-1. C_H distributions on these three configurations are compared to that on MP-1 at α = 0 deg for each of the three Reynolds number test points in Figures 6.1.17 through 6.1.19. C_H distributions on all four configurations at angles-of-attack of -4 deg and -20 deg are shown in Figures 6.1.20 and 6.1.21. In order to emphasize the features both on the forebody and on the sting, each distribution in Figures 6.17 through 6.1.21 is split into two plots. The first plot shows the forebody distribution, while the second plot shows the afterbody and sting distribution.

C_H values on the MP-2 hyperboloid geometry were ~8% lower at the stagnation point than the values measured on the other three sphere-cone configurations. Although the hyperboloid and sphere-cone models have the same stagnation-point radius-of-curvature, the radius-of-curvature of the hyperboloid asymptotically increases along the body to an effectively infinite value, whereas that of the sphere-cone models remains constant on the hemispherical cap. This gives the hyperboloid a larger effective nose radius-of-curvature, and thus the stagnation region Stanton number distribution is lower on a hyperboloid than on a sphere-cone. Because of the asymptotical convergence of the hyperboloid geometry to that of the MP-1 sphere-cone, the MP-2 C_H distributions approached those of the MP-1 sphere-cone away from the stagnation region.

The larger corner radii of the MP-3 and MP-4 configurations had no effect on the forebody distributions upstream of the corners. As will be shown in the computational solutions presented in Chapter 8 (as well as by Zoby and Sullivan, 1964), the sonic-line position on the forebody of a 70 deg

sphere-cone occurs at the cone-corner junction. Thus, the effect on the flow field cannot propagate upstream along the cone segment of the body, and so the sphere-cone distributions (MP-1, MP-3, and MP–4) can be expected to be identical along the forebody up to the corner. The corner radius does affect the flow field in the corner region; however, owing to the practical difficulty of fitting the thin-film gage leads into the small volume available at the corner of a model, the gage spacing was not sufficient to completely resolve the corner heating distributions. The forebody distributions shown in Figures 6.1.17 through 6.1.19 are somewhat deceptive in that the C_H distribution on the largest corner-radii model, MP-4, appears to have a larger corner heating peak than on the other models. However, this was only an artifact of the gage placement, which was such that one of the corner gages on the MP-4 model was closer to the corner heating peak than were those on the other models. In the same manner, one of the MP-3 gages was closer to the peak at the α = –20 deg case (Figure 6.1.21) and so this geometry appeared to have the highest corner heating, when, in fact, the model with the smallest corner-radius, MP-1, would be excepted to have the highest heating.

Corner radius had little apparent effect on the wake flow field. It appears from the data plotted in Figures 6.1.17-6.1.21 that the peak sting C_H location was not affected by the corner radius. The magnitude of the peak did decrease with increasing corner radius, although the total change between the largest and smallest corner radii model distributions was only on the order of 2%. However, these effects are nearly within the repeatability of the data, as evidenced by the anomalous behavior of the MP-4 distribution in Figure 6.1.19. Note also that owing to the similarity between the MP-2 and MP-1 geometries downstream of the forebody stagnation point, the wake distributions on these models were essentially identical.

6.1.4 Transition Grit Effects

Since the state of the wake flow must be defined in order to properly interpret the wake data and to employ it in comparisons to other data sets or to computational solutions, one of the areas of concern in

this study was whether or not the free shear layer and reattached boundary layer on the sting remained laminar or entered into a transitional or turbulent state. Because optical access limitations prevented the use of schlieren photography in the Mach 10 Tunnel, the only information available on the wake was the surface heating data obtained using the thin-film heat-transfer gages.

With the aim of gathering more information on the location and effects of transition on the wake flow behavior, aluminum oxide grit was applied to the surface of a stainless steel MP-1 forebody model in order to promote transition of the forebody boundary layer. Grit size was approximately 0.015-in. diam., and was fixed to the model surface using commercially available spray adhesive. Wake heating data were gathered with an instrumented sting, but an uninstrumented stainless steel forebody model was used in these tests in order to avoid damaging the delicate thin-film gages of one of the instrumented Macor forebody models.

Sting Stanton number distributions from each of the three Reynolds number operating points are plotted in Figures 6.1.22a - 6.1.22c in terms of L/R_b, the nondimensional distance along the sting from the base of the model. Distributions from the earlier (Test 293) runs with the instrumented Macor forebody models are also shown for comparison. At each of the operating points, sting distributions with the instrumented Macor models and the uninstrumented stainless steel model without transition grit were identical, which demonstrated that the roughness of the model material did not affect the shear layer behavior.

The transition grit appeared to have no effect on the wake heating in the low Reynolds number runs (Figure 6.1.22a). The transition grit was not observed to have any effect in the first runs at the intermediate and high Reynolds numbers; therefore, an extremely high concentration of transition grit was then applied to the models, which produced the distributions shown for runs 14, 18, and 19 in Figure 6.1.22b and runs 17 and 20 in Figure 6.1.22c. While this large amount of grit produced some small changes in the sting distributions, these changes were attributed to alteration of the actual surface geometry of the model by the thickness of the grit rather than to any change in the state of the shear layer.

The ineffectiveness of the transition grit can be attributed to one or both of two factors: either the local Reynolds number on the forebody was simply too low for transition to take place even with transition grit; or, transition did occur on the forebody, but the boundary layer relaminarized as it went around the forebody corner. These effects have both been shown in previous research. Forebody heating data from tests on a similar 70-deg sphere-cone geometry by Horvath et al (1996) showed that transition grit could produce a turbulent forebody boundary layer at freestream Reynolds numbers based on diameter of $2x10^6$ and $4x10^6$, but not at $0.5x10^6$. Based on these results, it is thus doubtful that transition could be produced in the current tests in which $Re_{\infty,D}$ corresponded to values of $8.3x10^4$, $1.67x10^5$, and $3.33x10^5$. Furthermore, even if transition could occur on the forebody, the favorable pressure gradient produced at the forebody corner would tend to dissipate the turbulence, as shown by Pirri (1971).

It can be concluded from the transition grit test data that the boundary layer was laminar at separation and that the freestream Reynolds numbers of these tests were too low even for forebody transition to be promoted by artificial means. However, these results do not help to establish the state of the free shear layer or reattached boundary layer on the sting. Conclusions regarding the state of the wake thus must be drawn by comparisons with laminar CFD solutions. Therefore, further discussion of this topic will be deferred until the presentation of the computational results in Chapter 8.

6.1.5 Repeatability

The repeatability of the 31-Inch Mach 10 data was investigated by performing multiple runs at selected test points. The $Re_\infty = 1.0x10^6$ ft^{-1}, $\alpha = 0$, $\phi = 0$ test point was repeated for each of the four entry vehicle configurations. The data from these tests is plotted in Figures 6.1.23 through 6.1.26. Stanton number distributions were repeatable to within approximately ±1%. This excellent measurement repeatability is due mainly to high flow quality of the facility and the repeatability of the freestream flow conditions, which were discussed in Section 4.2.

Section 6.2 HYPULSE Expansion Tube Data

High-enthalpy, hypervelocity aerothermodynamic data were obtained from a test series conducted in the NASA HYPULSE Expansion Tube. In this test series, each of the four parametric entry vehicle configurations, MP-1, MP-2, MP-3, and MP-4, was tested at a nominal freestream Reynolds number of 0.2×10^6 ft^{-1} in CO_2 at zero angle-of-attack. The MP-1 and MP-2 configurations also were tested in air at a Reynolds number of 0.2×10^6 ft^{-1} at zero angle-of-attack. Also, a limited number of runs were made in both test gases with MP-1 and MP-2 models at a -4 deg angle-of-attack (owing to the small diameter of the HYPULSE Expansion Tube, testing at higher angles-of-attack was not practical). Runs were also made in both air and CO_2 with the small-scale MP-1 (88%) and MP-1 (75%) models in order to investigate the effects of model size on flow establishment time.

A total of 38 heat-transfer runs were made in the HYPULSE test series. The analysis and interpretation of the data are presented in this chapter, while the complete data for each of the runs as well as run flow conditions and the test matrix are given in Appendix B.

6.2.1 Wake Flow Establishment

Before presentation of the HYPULSE data, the subject of wake flow establishment first must be addressed. Wake flow establishment is an important issue because in a short-duration impulse facility such as HYPULSE, the time required for the vortex structure in the wake of a blunt body to be formed and to reach a steady-state can require a significant fraction of the total available test time. This is in contrast to a conventional wind tunnel, in which the flow establishment process represents an extremely small fraction

of the total test time.

Experimental data from a HYPULSE run are time-averaged in order to minimize precision error due to electrical noise and freestream fluctuations. When this is done, the period of transient behavior due to the establishment process must be excluded from the data-averaging window, or the resulting average will be biased by the establishment process. In order to correctly define this data-averaging window, a criterion for determining when the flow has established is required.

The flow establishment time is commonly defined in terms of the non-dimensional establishment parameter:

$$\tau = \frac{U_\infty \Delta t_{est}}{y_{ref}} \tag{6.2.1}$$

In equation (6.2.1), Δt_{est} is defined as the time from the arrival of the incident shock, U_∞ is the freestream velocity and y_{ref} is a reference length, which in this work was taken to be the difference between the radii of the model forebody and the sting. The τ parameter represents the number of volumes of freestream flow of length y_{ref} which must pass over the test model before the flow becomes established. Past research (Holden, 1971) has shown that the establishment of an attached forebody flow typically requires less than 5 flow lengths, while separated wake flow (such as the wake of a blunt body) requires on the order of 50 to 70 flow lengths.

The flow establishment time is often determined by examination of pressure or heating time-history plots of individual wake gages (Holden, Kolly and Chadwick, 1995). The flow is considered to be established when the mean values reach a specified percentage (e.g. 98%) of their final mean values. However, because the final mean values are not known exactly until the data-averaging window is specified, this approach can be subject to interpretation. Furthermore, the time-histories of gages at different wake locations may reach their mean established values at different times, which complicates this method of

analysis. For these reasons, it was decided that a global process for determining when the flow establishes throughout the wake was required.

The first step in defining a global establishment criterion was to generate for each HYPULSE run plots of heat-transfer rate vs. gage location at each discrete time during the data acquisition period. A computer slide show "movie" of these distributions was then made for each run using commercially available software. These motion pictures provided a dynamic, graphical illustration of the establishment process in which the effects of the wave structure in the facility could be seen, and in which the point at which the flow established could usually be identified clearly.

A static analog of one such heating distribution movie (from HYPULSE Run 749) is presented in Figures 6.2.1a through 6.2.1f, in which several sequential distributions are overlaid on each individual plot. The wall pressure time-history for this same run is plotted in Figure 6.2.2. In this sequence of figures, the arrival of the incident shock wave can be identified in Figure 6.2.1a by an initial large jump in heating from a zero baseline. Heating rates then fluctuate rapidly as the outer inviscid region of the wake establishes (Figures 6.2.1b). The heating distributions then begin to converge to a steady-state as the viscous recirculation region behind the body forms (Figure 6.2.1c). The data-averaging window is defined as the period during which the entire distribution remains approximately constant (Figure 6.2.1d). The duration of the period of established flow is bounded (Figure 6.2.1e) by the end of the steady flow test window as determined by the wall pressure (see Section 4.3.2), although in fact, there often appears to be little change in the distribution for a considerable time after the end of the test window. Finally, the arrival of the unsteady expansion fan after the end of the test period produces a noticeable perturbation in the distribution, as shown in Figure 6.2.1f.

Although this motion picture approach is a useful analytical tool, it still does not provide a numerical criterion for determining when the flow has established, and thus it is still somewhat arbitrary. Also, as illustrated by Figures 6.2.1a-6.2.1f, the presentation of the motion picture in a static, hard copy format is somewhat difficult. Furthermore, the generation of a motion picture for each run is also a time-

consuming process.

For these reasons, a criterion with a more numerical basis was derived through the use of a normalized heat-transfer residual defined by:

$$\sigma(t) = \frac{\Delta q(t)}{q(t)} \tag{6.2.2}$$

where the numerator is a numerical evaluation of:

$$\Delta q = \frac{\partial q}{\partial t}\Delta t \tag{6.2.3}$$

In theory, the time-history of this residual will approach zero as the heat-transfer rate approaches a constant, established value. In practice, the residual will approach some small value of a magnitude determined by the signal-to-noise ratio of the experimental data. In order to characterize the entire wake region with a single variable, a root-mean-square time-history is computed from the individual gage time-histories by:

$$\hat{\sigma}(t) = \sqrt{\frac{1}{n}\left(\sigma_1^2 + \sigma_2^2 + \ldots + \sigma_n^2\right)} \tag{6.2.4}$$

The residual-RMS time-history is plotted in Figure 6.2.3 for the same run for which the heating distribution movie was presented. The features of the establishment process seen in the wall pressure time-history and the motion picture can also be identified in this figure. The arrival of the incident shock wave and acceleration gas/test gas interface initially produces an extremely high residual-RMS. $\hat{\sigma}$ then drops rapidly as the forebody flow field and outer inviscid region of the wake establish. The residual-RMS then gradually approaches a minimum value which corresponds to the period of established flow. Experimental noise causes $\hat{\sigma}$ to fluctuate about this minimum until the end of the steady flow test period as determined

from the wall pressure. The arrival of the unsteady expansion fan after the end of the test window can be identified by an abrupt increase in $\hat{\sigma}$.

In regard to the use of this wake flow establishment criteria, experience has shown that gages which have "gone bad" (i.e. gages that produce an extremely noisy signal due to bad electrical connections or gage damage) should not be included in the RMS computation of equation (6.2.3) or they will bias the results. Also, in order to mask high-frequency signals caused by turbulence or electrical noise, a wide differencing stencil such as that in Eq. (5.2.7b) should be used to compute the derivative in equation (6.2.3).

Through examination of the heating distribution movies and residual-RMS time-histories from several runs, it was determined that over the time-interval during which the distributions appeared to experience a minimal magnitude of fluctuation, the residual-RMS value was roughly 0.02 or lower. This RMS value was thus selected as the criterion for determining when the wake flow became established. The wake flow data for all of the HYPULSE runs then were averaged over the period of each run during which $\hat{\sigma}$ was less than or equal to 0.02, provided that this period did not extend past the end of the test window as defined from the wall pressure. The forebody data were time-averaged across the entire test period, as the wake establishment process had no effect on the forebody flow.

In terms of the previously defined non-dimensional establishment parameter, τ, wake flow establishment using the RMS criterion was found to require between 40 and 70 flow lengths in CO_2 at α = 0 deg, with an average value of 51. In air at $\alpha = 0$ deg, τ varied from 50 to 90 and had an average value of 65. The dimensional establishment times computed from the τ values in this study represent about 75% of the total available test time for either gas in HYPULSE. These establishment parameter values are consistent with recent work by Holden, Kolly and Chadwick (1995), in which an establishment parameter value of 50 was measured in tests with a 70 deg sphere-cone model in an impulse facility.

Model configuration had no apparent effect on τ, but model angle-of-attack produced a moderate decrease in the establishment parameter due to the fact that a smaller volume of fluid is shielded by the model at angle-of-attack. At α = -4 deg, the average values for τ were 40 in CO_2 and 55 in air. Although

the smaller-scale MP-1 (75%) and MP-1 (88%) models were expected to produce shorter dimensional establishment times than the full-scale models, the scatter of the data was great enough that no effect could be observed.

6.2.2 Repeatability and Averaged Heating Distributions

Due to the highly dynamic nature of impulse facility operation, the repeatability of data obtained in an impulse facility is generally not as good as in a conventional facility. Run flow properties are dependent on the diaphragm burst process, which is usually not the instantaneous event assumed in idealized models of impulse facility operation (such as in Section 4.3). Because of this, there is a greater run-to-run variation of the flow properties, and thus of the heating data, than in a conventional facility, as can be seen in Tables 4.2.1 and 4.3.1. Furthermore, the initial impulsive loads imposed on the test model by the arrival of the incident shock wave can sometimes damage or even destroy the delicate thin-film gages. Thus, while the run-to-run repeatability of aerothermodynamic data from a conventional facility generally can be taken for granted, as was demonstrated in Section 6.1.5, the repeatability of data from an impulse facility must be investigated just as carefully as the wake flow establishment process.

In order to ensure that spurious data from individual bad gages, or from an entire bad run, was not included in this database, each test condition (model configuration, test gas, and angle-of-attack) in HYPULSE was repeated at least once. In the case of the MP-1 configuration, which is the main subject of the work, the zero degree angle-of-attack case was repeated three times at the CO_2 test condition and four times at the air test condition. For each run, the quality of data obtained from each thin-film gage was evaluated by computing the standard deviation of the Stanton number over the data-averaging window (the normalized standard deviations, s/C_H, for each gage during a run are included in the data in Appendix B). The data from individual gages with relatively high standard deviations was excluded from this database, and in a few cases, all the data from a run was excluded due to poor gage performance or unsteadiness in the

freestream conditions. For each test case, the time-averaged C_H values from all the runs at that case were averaged in order to obtain the most accurate values for the reported C_H distributions. These averaged distributions are used in this section in the analysis of the experimental data, and will be employed in Chapter 8 in the comparisons with computational results. The averaged C_H distributions for each test case are given in Tables 6.2.1 through 6.2.9. Uncertainty estimates for the average values, which are discussed in Section 6.3, are also included in these tables.

The individual run Stanton number distributions and the averaged Stanton number distributions on the MP-1 configuration at $\alpha = 0$ deg and $\alpha = -4$ deg in CO_2 are plotted in Figures 6.2.4 and 6.2.5. These data are plotted on both linear and logarithmic scales in order to emphasize the details of both the forebody and wake distributions. Data for the MP-1 configuration at $\alpha = 0$ deg and $\alpha = -4$ deg in air are presented in Figures 6.2.6 and 6.2.7. C_H distributions for MP-2 at $\alpha = 0$ deg and $\alpha = -4$ deg in CO_2 and $\alpha = 0$ deg in air are plotted in Figures 6.2.8 through 6.2.10. Finally, the C_H distributions for the MP-3 and MP-4 configurations in CO_2 are presented in Figures 6.2.11 and 6.2.12.

6.2.3 Angle-of-Attack Effects

The investigation of angle-of-attack effects in HYPULSE was limited to the MP-1 and MP-2 configurations. Because of the small size of the test core, the models could only be tested at small values of α. The support stand in this facility is set in 4 deg increments, therefore, all angle-of-attack runs were made at $\alpha = -4$ deg with the exception of a single $\alpha = -8$ deg run with the MP-1 configuration.

Angle-of-attack effects are shown in Figures 6.2.13 and 6.2.14 for the MP-1 configuration in CO_2 and in air, respectively, and in Figure 6.2.15 for the MP-2 configuration in CO_2. In all three cases, the effect of α on the forebody distribution was small. Stagnation point C_H values were essentially unaffected. The windward and leeside distributions showed, respectively, a small increase and a small decrease. Measured windward and leeside corner values changed by less than 10% between 0 and -4 deg, although due

to model size limitations as noted in Section 6.1.3, the gage spacing at the corners may not have been small enough to fully resolve the corner heating peaks. Model angle-of-attack had a greater effect on the wake C_H distributions. For both the MP-1 and MP-2 configurations in CO_2, the location of the peak sting heating point moved approximately 0.75 body radii upstream toward the model for the α = -4 deg case, and the magnitude of the peak increased by approximately 30%. In air, the peak moved upstream 0.5 body radii and increased by approximately 25%.

6.2.4 Configuration Effects

Configuration effects on the Stanton number distributions are shown for the α = 0 deg case in CO_2 and air in Figures 6.2.16 and 6.2.17, respectively, and for the α = -4 deg case in CO_2 in Figure 6.1.18. As in Section 6.1.3, the forebody and wake distributions are presented in terms of S/R_b in separate plots in order to highlight the details in each region.

Each of the four entry vehicle configurations was tested in CO_2 at α = 0 (Figure 6.2.16). Stagnation point C_H values for the three sphere-cone configurations were nearly identical, while the value for the MP-2 hyperboloid was approximately 25% lower than that of the sphere-cones due to its greater effective radius-of-curvature at the nose. Away from the stagnation point, the distributions of the MP–1 and MP–2 configurations were nearly identical owing to the similarity of these two geometries; however, the MP-3 and MP-4 C_H distributions along the cone portion of the forebodies were approximately 20% higher than those for the MP-1 configuration. This is in contrast to both theory and experimental data from the Mach 10 tests. Zoby and Sullivan, (1964) have shown that for body radii greater than one-half of the nose radii, (which is true for the present configurations) the corner will not have any effect on the upstream distribution because the sonic point will be located at or before the sphere-corner junction. Furthermore, the heating data (Figures 6.1.17 through 6.1.19) on the different configurations in the 31-Inch Mach 10 Air Tunnel showed no upstream effects of corner radius. The most likely explanation for the differences in the

sphere-cone C_H distributions is that because the freestream velocities and total enthalpy levels for the MP-1 runs 747, 749 and 903 (Table B.2 in Appendix B) were among the lowest values of the whole test series, the Stanton numbers computed for the nominal freestream conditions from the dimensional heating rates may have been biased slightly downward. This illustrates the danger of drawing conclusions about subtle configuration effects from a limited database in an impulse facility. In fact, the configuration effects on the C_H forebody distributions were only slightly greater than the estimated uncertainties for the HYPULSE tests, which will be presented in Section 6.3. If the MP-3 and MP-4 distributions are accepted as being more accurate than the MP-1 distribution, then the differences between the hyperboloid and sphere-cone distributions are much more pronounced. The effectively blunter nose radius of the MP-2 distribution produced C_H values lower than those of the MP-3 and MP-4 sphere-cones along the entire forebody right up to the forebody corner region.

As shown in Figure 6.2.17, any configuration effects on the sting distributions at $\alpha = 0$ in CO_2 were within the scatter of the data. However, if the above hypothesis that the MP-1 data are biased slightly low is accepted, than an adjustment for this would raise the Stanton number distribution for this configuration. The HYPULSE data would then be consistent with the 31-Inch Mach 10 data, in which a very slight decrease in wake Stanton numbers with corner radius was observed.

The MP–1 and MP–2 configurations were both tested in air at α = 0 (Figure 6.2.17). No configuration effects could be observed on the forebody except within the stagnation point region, where stagnation point C_H values for the MP-2 hyperboloid were approximately 10% lower than on the MP-1 configuration. As the two geometries are essentially identical away from the stagnation point, no configuration effects were expected in the wake, nor could any be observed in these tests.

The MP–1 and MP–2 configurations were also both tested in CO_2 at α = -4 (Figure (6.2.18)). Once again, no configuration effects were observed in the wake. However, on the forebody, the larger effective nose radius-of-curvature of the MP-2 configuration produced lower Stanton numbers over almost the entire forebody. C_H values on the windward side and at the stagnation point were about 25% lower on

the MP-2 models. The difference in leeward side Stanton numbers decreased with distance from the stagnation point and approached zero at the leeward corner. The large difference between the sphere-cone and hyperboloid heating distributions across the entire forebody is consistent with the differences at $\alpha = 0$ between the MP-3 and MP-4 sphere-cone distributions and the MP-2 hyperboloid distribution, which lends more weight to the hypothesis that the MP-1 distribution at $\alpha = 0$ is biased slightly low.

6.2.5 Test Gas Effects and Comparison with Perfect Gas Data

Comparisons between the aerothermodynamic data from the HYPULSE tests and those from the 31-Inch Mach 10 tests are presented in the form of normalized Stanton number distributions $C_H/C_{H,0}$. Normalized forebody and wake distributions for each of the four configurations are shown in Figures 6.2.19 through 6.2.22.

As discussed in Section 6.1.1, no influence of Reynolds number was observed on the normalized forebody distributions in the Mach 10 tests. The normalized forebody data for the MP-1 and MP-2 configurations from the HYPULSE air tests agreed closely with these Mach 10 results. The normalized forebody data from the HYPULSE CO_2 tests was slightly lower than the Mach 10 data for the MP-1 configuration, slightly higher for MP-4, and in close agreement for MP-2 and MP-3. In general, the CO_2 distributions were also all slightly flatter on the cone portion of the forebody due to the higher shock density ratio in the CO_2 tests.

While test gas/Reynolds number effects were small on the forebodies of the models, large effects were observed in the wake. As was discussed in Section 6.1.1, the size of the wake vortex was observed to decrease with increasing Reynolds number in the Mach 10 tests, which is suggestive of non-laminar wake flow. However, as shown by the data from the HYPULSE tests, which were characterized by freestream Reynolds numbers of 0.2×10^6 ft^{-1}, the peak heating point for all configurations in both CO_2 and air was much closer to the body than that of the lowest Reynolds number (0.5×10^6 ft^{-1}) Mach 10 data. This

suggests that the reattachment point has moved closer to the base, which is the behavior predicted by laminar theory. While vibrational or chemical non-equilibrium may have some influence on the wake structure, the relatively closely agreement between the data from the two different thermochemical environments of the HYPULSE air and CO_2 test conditions suggests that this influence is not large. Thus, the comparison between the Mach 10 and HYPULSE wake heating distributions provides further evidence that the wake flow may be transitional or turbulent in the Mach 10 tests. In contrast, the wake appears to remain laminar in the HYPULSE tests.

Section 6.3 Uncertainty Analysis

The accuracy of the 31-Inch Mach 10 Air Tunnel data and HYPULSE Expansion Tube data was assessed by consideration of the sources of precision error and bias error for tests in these facilities. Uncertainty estimates for the Stanton numbers were computed following the procedure outlined by the AIAA Standards Committee (anon., AIAA publication S-071,1995). In this methodology, the simplest form for the uncertainty estimate for a quantity is given by:

$$U = t_{95}\sqrt{B^2 + P^2} \tag{6.3.1}$$

In Eq. (6.3.1), t_{95} represents the 95th percentile point of the two-tailed Student's "t" distribution. The accepted standard choice of the 95th percentile indicates that the measured quantity is expected to fall within the estimated uncertainty range 95 times out of 100. The value of t_{95} depends on the number of measurements made of a quantity, and approaches 2 in the limit of an infinite number of data points. However, according to the AIAA standard, $t_{95} = 2$ is an acceptable standard regardless of the number of data points. The variables B and P represent the experimental bias and the experimental precision, respectively.

The bias, B, represents the difference between the actual and measured value of a quantity due to systemic errors, while the precision, P, represents the difference between the actual and measured values due to random errors. In the context of the present work, bias can include errors due to gage calibration, material thermal properties and the data reduction technique, while precision can include errors due to fluctuations in the freestream flow, electrical noise in the data acquisition system, and poor gage performance due to wear or damage.

In the estimation of uncertainty limits for the Stanton number, the precision limit for each gage was taken to be equal to the standard deviation, s, of the time-averaged values of C_H computed from the data from all of the runs at each test point. For points at which no repeat runs were made, the precision limit was taken to be the average value of P computed at similar conditions. For instance, the gage precision limits for the $Re_\infty = 1.0\text{x}10^6$ ft^{-1}, $\alpha = -4$ deg test point in the 31-Inch Mach 10 Air Tunnel, at which only a single run was made, were taken to be equal to the precision limits from the $Re_\infty = 1.0\text{x}10^6$ ft^{-1}, $\alpha = 0$ deg case, for which several repeat runs were made. As will be shown in this section, the precision error for tests in the 31-Inch Mach 10 facility is small in comparison to the total uncertainty, and so this approximation does not have a significant effect on the overall error analysis. For tests in HYPULSE, the total uncertainty is due almost entirely to the precision error. Therefore, multiple runs were made at most of the HYPULSE test points in order to better evaluate the precision error.

As noted by Hedlund and Kammeyer (1996), there exists no means of applying an exact specified convective heat load to a model in a wind tunnel, and thus it is not possible to directly determine the bias limit of a heat transfer gage. In this work, an estimate for the bias limit was made through the use of the hemisphere calibration data which is presented in Appendix C. Stagnation point Stanton numbers computed for each of the hemisphere test points (six runs at three different freestream Reynolds numbers) using the Fay-Riddell method were taken to be the "exact" values for C_H at those conditions. The normalized overall uncertainty for the stagnation point measurement was then computed as:

$$\frac{U}{C_H} = 2\left|1 - \overline{\left(\frac{C_{H,\,measured}}{C_{H,\,Fay\text{-}Riddell}}\right)}\right| \tag{6.3.2}$$

The average value of the ratio of measured C_H to Fay-Riddell C_H for these runs was 0.966, which produced a normalized overall uncertainty of 0.068. The bias error was then estimated by:

$$\left(\frac{B}{C_H}\right)^2 = \left(\frac{U}{2\,C_H}\right)^2 - \left(\frac{P}{C_H}\right)^2 \tag{6.3.3}$$

The precision error was taken to be equal to the standard deviation of the normalized stagnation point Stanton number data for the hemisphere tests, which was 0.0154. The estimated bias error was then computed to be equal to 3.03% of the Stanton number. It is assumed that this bias error is due almost entirely to uncertainty in the macor thermal properties values, which are discussed in Appendix C. Because of the lack of material properties data, this 3.03% value most probably is not a conservative estimate for the bias error; however, the purpose of this work is a comparison of experimental and computational methods, not the actual design of a vehicle, for which a conservative estimate would be more appropriate.

Using the results of the above computations, an estimate of the normalized overall uncertainty in the computed Stanton number for any gage can be made by:

$$\frac{U}{C_H} = 2\sqrt{\left(\frac{S}{C_H}\right)^2 + 0.0303^2} \tag{6.3.4}$$

It is recognized that this formulation is not strictly valid as the bias computation was performed for a model different than those that were tested. Furthermore, the use of the 31-Inch Mach 10 Air Tunnel bias estimation with HYPULSE Expansion Tube data ignores facility-specific sources of bias in the

HYPULSE Expansion Tube. However, as no true standard exists for the computation of convective heating bias error, it is felt that Equation (6.3.4) provides an adequate approximation of the experimental uncertainty for heat-transfer testing. Furthermore, the bias error represents a small fraction of the total uncertainty in HYPULSE tests, so the effect of this approximation on the error analysis will be small.

Sample error band estimates are plotted in Figures 6.3.1 through 6.3.3 for three test points: the MP-1 configuration at 0 deg in the Mach 10 tunnel at the 1.0×10^6 ft^{-1} freestream Reynolds number; in HYPULSE in CO_2; and in HYPULSE in air. Uncertainty estimates for the Mach 10 tests were much smaller than for HYPULSE, and were due almost entirely to bias error in the Macor thermal properties data. The HYPULSE uncertainty values were due almost entirely to the precision error of run-to-run repeatability. For the 31-Inch Mach 10 Air Tunnel data, the average uncertainty was ±7% of C_H on the forebody and ±8% in the wake. For the HYPULSE CO_2 data, the average uncertainty was ±11% of C_H on the forebody and ±17% in the wake, and for the HYPULSE air data, the average uncertainty was ±12% of C_H on the forebody and ±22% in the wake. In both facilities the greater uncertainty for the wake Stanton number is due to the fact that the wake heating is one to two orders of magnitude lower than the forebody heating, and thus a greater precision error is produced by the higher signal-to-noise ratio of the wake data.

Uncertainty band estimates for each of the HYPULSE test points are included in the data in Tables 6.2.1 through 6.2.9. Separate uncertainty estimates are not given for the 31-Inch Mach 10 data. The uncertainty for these tests was due almost entirely to the bias error, which is taken to be constant, and so the uncertainty band estimates for all the 31-Inch Mach 10 data were essentially identical to those for the sample condition presented in Figure 6.3.1.

Table 6.2.1: MP-1 Configuration, CO_2 Test Gas, $\alpha = 0$ deg

GAGE ID	S/R_b	L/R_b	$C_{H,avg}$	q_{300K} (W/cm^2)	U_{tot}/C_H
TF1	-1.872	-	1.204e-04	4.075	0.209
TF2	-1.772	-	1.873e-04	6.339	0.209
TF3	-1.678	-	1.303e-04	4.410	0.209
TF4	-1.554	-	*	*	*
TF5	-1.429	-	*	*	*
TF6	-1.305	-	*	*	*
TF7	-1.180	-	*	*	*
TF8	-1.083	-	1.022e-03	34.579	0.180
TF9	-1.000	-	1.218e-02	412.421	0.140
TF10	-0.900	-	1.170e-02	396.174	0.167
TF11	-0.800	-	1.211e-02	409.882	0.096
TF12	-0.700	-	1.120e-02	379.082	0.126
TF13	-0.600	-	1.296e-02	438.652	0.101
TF14	-0.500	-	1.362e-02	460.991	0.200
TF15	-0.400	-	1.429e-02	483.668	0.126
TF16	-0.300	-	1.515e-02	512.776	0.111
TF17	-0.200	-	1.696e-02	574.208	0.096
TF18	-0.100	-	2.203e-02	745.641	0.117
TF19	0.000	-	2.421e-02	819.426	0.126
TF20	0.100	-	2.142e-02	725.163	0.238
TF21	0.200	-	1.719e-02	581.654	0.082
TF22	0.300	-	1.551e-02	524.792	0.084
TF23	0.400	-	1.436e-02	486.206	0.102
TF24	0.500	-	1.330e-02	449.991	0.144
TF25	0.600	-	1.302e-02	440.514	0.125
TF26	0.700	-	1.191e-02	403.113	0.168
TF27	0.800	-	1.192e-02	403.452	0.093
TF28	0.900	-	1.154e-02	390.590	0.107
TF29	1.000	-	1.173e-02	397.021	0.177
TF30	1.083	-	8.584e-04	29.054	1.364
TF31	1.180	-	*	*	*
TF32	1.305	-	*	*	*
TF33	1.429	-	*	*	*
TF34	1.554	-	1.709e-04	5.784	0.209
TF35	1.678	-	8.483e-05	2.871	0.209
TF36	1.772	-	1.190e-04	4.028	0.209
TF37	1.872	-	6.565e-05	2.222	0.209
TF38	1.931	0.015	4.340e-05	1.469	2.422
TF39	2.036	0.121	7.161e-05	2.424	1.629
TF40	2.141	0.226	9.741e-05	3.297	1.614
TF41	2.246	0.331	1.250e-04	4.232	0.144
TF42	2.351	0.436	1.300e-04	4.401	0.745
TF43	2.456	0.541	1.236e-04	4.185	0.105
TF44	2.561	0.646	2.408e-04	8.151	0.308
TF45	2.666	0.750	2.432e-04	8.230	0.176
TF46	2.771	0.855	3.470e-04	11.746	0.479
TF47	2.876	0.960	4.330e-04	14.654	0.316
TF48	2.981	1.065	5.808e-04	19.657	0.396
TF49	3.086	1.170	7.704e-04	26.074	0.109
TF50	3.191	1.275	8.393e-04	28.407	0.209
TF51	3.296	1.380	9.272e-04	31.383	0.225
TF52	3.401	1.485	9.432e-04	31.925	0.286
TF53	3.506	1.590	9.508e-04	32.182	0.229
TF54	3.611	1.696	9.813e-04	33.214	0.170
TF55	3.716	1.801	9.789e-04	33.134	0.201
TF56	3.821	1.906	9.220e-04	31.207	0.076
TF57	3.926	2.011	8.585e-04	29.057	0.102
TF58	4.031	2.116	8.997e-04	30.451	0.223
TF59	4.136	2.221	8.671e-04	29.347	0.227
TF60	4.241	2.326	8.558e-04	28.966	0.083
TF61	4.346	2.431	8.105e-04	27.434	0.109
TF62	4.451	2.536	7.718e-04	26.122	0.062
TF63	4.556	2.641	8.267e-04	27.981	0.209
TF64	4.661	2.745	7.222e-04	24.444	0.169
TF65	4.766	2.850	6.785e-04	22.965	0.209
TF66	4.871	2.955	6.599e-04	22.337	0.328
TF67	4.976	3.060	6.520e-04	22.067	0.101
TF68	5.081	3.165	6.030e-04	20.411	0.128
TF69	5.186	3.270	6.686e-04	22.631	0.198
TF70	5.291	3.375	6.444e-04	21.810	0.073

Table 6.2.2: MP-1 Configuration, CO_2 Test Gas, α = -4 deg

GAGE ID	S/R_b	L/R_b	$C_{H,avg}$	q_{300K} (W/cm^2)	U_{tot}/C_H
TF1	-1.872	-	2.748e-04	9.301	0.543
TF2	-1.772	-	3.028e-04	10.248	1.470
TF3	-1.678	-	3.525e-04	11.929	
TF4	-1.554	-	*	*	*
TF5	-1.429	-	*	*	*
TF6	-1.305	-	*	*	*
TF7	-1.180	-	*	*	*
TF8	-1.083	-	5.588e-03	189.142	1.772
TF9	-1.000	-	1.283e-02	434.218	0.296
TF10	-0.900	-	1.002e-02	339.008	0.296
TF11	-0.800	-	1.329e-02	449.821	0.296
TF12	-0.700	-	1.231e-02	416.516	0.296
TF13	-0.600	-	1.233e-02	417.329	0.296
TF14	-0.500	-	1.293e-02	437.501	0.296
TF15	-0.400	-	1.573e-02	532.339	0.281
TF16	-0.300	-	1.789e-02	605.617	0.296
TF17	-0.200	-	2.252e-02	762.327	0.296
TF18	-0.100	-	*	*	*
TF19	0.000	-	2.469e-02	835.842	0.296
TF20	0.100	-	2.337e-02	790.944	0.316
TF21	0.200	-	1.994e-02	675.003	0.381
TF22	0.300	-	1.493e-02	505.465	0.296
TF23	0.400	-	*	*	*
TF24	0.500	-	1.491e-02	504.721	0.296
TF25	0.600	-	1.583e-02	535.707	0.256
TF26	0.700	-	*	*	*
TF27	0.800	-	1.657e-02	561.007	0.296
TF28	0.900	-	1.408e-02	476.628	0.296
TF29	1.000	-	1.346e-02	455.575	0.260
TF30	1.083	-	1.489e-03	50.391	0.296
TF31	1.180	-	2.803e-04	9.486	0.296
TF32	1.305	-	4.009e-04	13.570	0.296
TF33	1.429	-	3.129e-04	10.590	0.296
TF34	1.554	-	2.853e-04	9.656	0.296
TF35	1.678	-	1.318e-04	4.461	0.291
TF36	1.772	-	1.538e-04	5.205	0.296
TF37	1.872	-	1.045e-04	3.538	0.296
TF38	1.931	0.015	6.225e-05	2.107	0.296
TF39	2.036	0.120	6.788e-04	22.974	2.431
TF40	2.141	0.225	4.967e-04	16.810	2.482
TF41	2.246	0.330	2.299e-04	7.781	0.378
TF42	2.351	0.435	3.885e-04	13.148	0.296
TF43	2.456	0.540	6.324e-04	21.404	0.748
TF44	2.561	0.645	1.063e-03	35.974	0.111
TF45	2.666	0.750	1.230e-03	41.619	0.068
TF46	2.771	0.855	1.170e-03	39.616	0.171
TF47	2.876	0.960	1.261e-03	42.679	0.202
TF48	2.981	1.065	1.176e-03	39.793	0.251
TF49	3.086	1.170	1.173e-03	39.692	0.242
TF50	3.191	1.275	1.123e-03	38.020	0.189
TF51	3.296	1.380	1.089e-03	36.860	0.196
TF52	3.401	1.485	9.858e-04	33.367	0.126
TF53	3.506	1.590	1.084e-03	36.683	0.102
TF54	3.611	1.695	1.067e-03	36.102	0.118
TF55	3.716	1.800	1.058e-03	35.806	0.139
TF56	3.821	1.905	1.052e-03	35.608	0.107
TF57	3.926	2.010	1.142e-03	38.660	0.126
TF58	4.031	2.115	1.029e-03	34.826	0.209
TF59	4.136	2.220	1.049e-03	35.495	0.126
TF60	4.241	2.326	*	*	*
TF61	4.346	2.430	9.674e-04	32.742	0.126
TF62	4.451	2.535	9.739e-04	32.965	0.102
TF63	4.556	2.640	9.769e-04	33.063	0.126
TF64	4.661	2.745	9.603e-04	32.502	0.061
TF65	4.766	2.850	9.382e-04	31.755	0.071
TF66	4.871	2.955	9.887e-04	33.462	0.071
TF67	4.976	3.060	9.326e-04	31.566	0.077
TF68	5.081	3.165	9.641e-04	32.631	0.126
TF69	5.186	3.270	9.519e-04	32.218	0.100
TF70	5.291	3.375	9.655e-04	32.680	0.063

Table 6.2.3: MP-1 Configuration, Air Test Gas, α = 0 deg

GAGE ID	S/R_b	L/R_b	$C_{H,avg}$	q_{300K} (W/cm^2)	U_{tot}/C_H
TF1	-1.872	-	2.698e-04	11.276	0.228
TF2	-1.772	-	2.746e-04	11.477	0.228
TF3	-1.678	-	1.500e-04	6.269	0.228
TF4	-1.554	-	*	*	*
TF5	-1.429	-	8.517e-04	35.597	0.228
TF6	-1.305	-	1.286e-04	5.375	0.228
TF7	-1.180	-	*	*	*
TF8	-1.083	-	2.672e-03	111.699	1.098
TF9	-1.000	-	1.774e-02	741.454	0.134
TF10	-0.900	-	2.171e-02	907.591	0.094
TF11	-0.800	-	1.777e-02	742.916	0.072
TF12	-0.700	-	1.869e-02	781.159	0.126
TF13	-0.600	-	1.574e-02	657.862	0.134
TF14	-0.500	-	1.697e-02	709.271	0.134
TF15	-0.400	-	1.925e-02	804.774	0.268
TF16	-0.300	-	1.938e-02	809.998	0.134
TF17	-0.200	-	2.107e-02	880.633	0.134
TF18	-0.100	-	2.734e-02	1142.900	0.110
TF19	0.000	-	2.958e-02	1236.188	0.128
TF20	0.100	-	2.592e-02	1083.446	0.124
TF21	0.200	-	1.946e-02	813.342	0.134
TF22	0.300	-	1.928e-02	805.819	0.134
TF23	0.400	-	1.757e-02	734.348	0.062
TF24	0.500	-	1.805e-02	754.410	0.134
TF25	0.600	-	1.547e-02	646.578	0.191
TF26	0.700	-	1.520e-02	635.293	0.134
TF27	0.800	-	1.536e-02	641.980	0.189
TF28	0.900	-	1.800e-02	752.320	0.134
TF29	1.000	-	1.977e-02	826.299	0.181
TF30	1.083	-	1.503e-03	62.819	0.228
TF31	1.180	-	*	*	*
TF32	1.305	-	*	*	*
TF33	1.429	-	1.579e-04	6.600	0.228
TF34	1.554	-	4.467e-04	18.670	0.228
TF35	1.678	-	*	*	*
TF36	1.772	-	5.347e-04	22.348	0.228
TF37	1.872	-	4.165e-04	17.408	0.228
TF38	1.931	0.015	5.076e-05	2.122	0.501
TF39	2.036	0.121	8.766e-05	3.664	0.068
TF40	2.141	0.226	1.517e-04	6.340	0.799
TF41	2.246	0.331	1.851e-04	7.735	0.253
TF42	2.351	0.436	2.185e-04	9.134	0.611
TF43	2.456	0.541	2.330e-04	9.738	0.636
TF44	2.561	0.646	3.467e-04	14.492	0.430
TF45	2.666	0.750	3.784e-04	15.814	0.361
TF46	2.771	0.855	3.948e-04	16.501	0.591
TF47	2.876	0.960	6.211e-04	25.959	0.292
TF48	2.981	1.065	7.525e-04	31.452	0.451
TF49	3.086	1.170	9.457e-04	39.525	0.453
TF50	3.191	1.275	1.066e-03	44.539	0.378
TF51	3.296	1.380	1.290e-03	53.916	0.304
TF52	3.401	1.485	1.331e-03	55.644	0.386
TF53	3.506	1.590	1.423e-03	59.486	0.248
TF54	3.611	1.696	1.520e-03	63.519	0.275
TF55	3.716	1.801	1.542e-03	64.438	0.230
TF56	3.821	1.906	1.531e-03	64.003	0.243
TF57	3.926	2.011	1.505e-03	62.902	0.080
TF58	4.031	2.116	1.486e-03	62.122	0.185
TF59	4.136	2.221	1.528e-03	63.850	0.155
TF60	4.241	2.326	1.421e-03	59.392	0.285
TF61	4.346	2.431	1.506e-03	62.965	0.130
TF62	4.451	2.536	1.307e-03	54.627	0.237
TF63	4.556	2.641	1.191e-03	49.779	0.228
TF64	4.661	2.745	1.278e-03	53.404	0.243
TF65	4.766	2.850	1.067e-03	44.596	0.185
TF66	4.871	2.955	1.185e-03	49.507	0.310
TF67	4.976	3.060	1.071e-03	44.763	0.077
TF68	5.081	3.165	1.023e-03	42.740	0.127
TF69	5.186	3.270	1.046e-03	43.736	0.288
TF70	5.291	3.375	9.185e-04	38.389	0.204

Table 6.2.4: MP-1 Configuration, Air Test Gas, α = -4 deg

GAGE ID	S/R_b	L/R_b	$C_{H,avg}$	q_{300K} (W/cm^2)	U_{tot}/C_H
TF1	-1.872	-	3.593e-04	15.022	0.143
TF2	-1.772	-	3.965e-04	16.577	0.143
TF3	-1.678	-	2.638e-04	11.030	0.143
TF4	-1.554	-	5.380e-04	22.492	0.143
TF5	-1.429	-	7.069e-04	29.555	0.143
TF6	-1.305	-	9.835e-04	41.121	0.143
TF7	-1.180	-	8.808e-04	36.825	0.143
TF8	-1.083	-	2.811e-03	117.541	0.143
TF9	-1.000	-	1.554e-02	649.607	0.143
TF10	-0.900	-	1.631e-02	682.052	0.143
TF11	-0.800	-	1.659e-02	693.591	0.143
TF12	-0.700	-	1.681e-02	702.622	0.143
TF13	-0.600	-	*	*	*
TF14	-0.500	-	1.751e-02	731.973	0.143
TF15	-0.400	-	1.843e-02	770.355	0.143
TF16	-0.300	-	1.950e-02	815.218	0.143
TF17	-0.200	-	2.077e-02	868.358	0.143
TF18	-0.100	-	2.562e-02	1071.013	0.143
TF19	0.000	-	*	*	*
TF20	0.100	-	*	*	*
TF21	0.200	-	2.340e-02	978.320	0.143
TF22	0.300	-	2.036e-02	851.174	0.143
TF23	0.400	-	1.928e-02	805.936	0.143
TF24	0.500	-	*	*	*
TF25	0.600	-	1.909e-02	798.368	0.143
TF26	0.700	-	*	*	*
TF27	0.800	-	1.760e-02	735.778	0.143
TF28	0.900	-	1.945e-02	813.169	0.143
TF29	1.000	-	2.167e-02	906.155	0.143
TF30	1.083	-	3.192e-03	133.479	0.143
TF31	1.180	-	2.953e-04	12.344	0.143
TF32	1.305	-	4.792e-04	20.036	0.143
TF33	1.429	-	1.157e-03	48.375	0.143
TF34	1.554	-	1.199e-03	50.118	0.143
TF35	1.678	-	2.757e-04	11.526	0.143
TF36	1.772	-	4.557e-04	19.052	0.143
TF37	1.872	-	3.756e-04	15.704	0.143
TF38	1.931	0.015	*	*	*
TF39	2.036	0.121	*	*	*
TF40	2.141	0.226	3.115e-04	13.024	0.143
TF41	2.246	0.331	3.875e-04	16.200	0.143
TF42	2.351	0.436	4.649e-04	19.438	0.143
TF43	2.456	0.541	6.218e-04	25.999	0.143
TF44	2.561	0.646	8.313e-04	34.757	0.143
TF45	2.666	0.750	1.087e-03	45.448	0.143
TF46	2.771	0.855	1.438e-03	60.107	0.143
TF47	2.876	0.960	1.755e-03	73.369	0.143
TF48	2.981	1.065	1.766e-03	73.837	0.234
TF49	3.086	1.170	1.932e-03	80.792	0.157
TF50	3.191	1.275	1.957e-03	81.840	0.097
TF51	3.296	1.380	2.031e-03	84.908	0.095
TF52	3.401	1.485	1.974e-03	82.534	0.143
TF53	3.506	1.590	2.020e-03	84.448	0.068
TF54	3.611	1.696	2.027e-03	84.737	0.143
TF55	3.716	1.800	1.926e-03	80.508	0.132
TF56	3.821	1.905	1.942e-03	81.183	0.084
TF57	3.926	2.010	1.802e-03	75.363	0.143
TF58	4.031	2.115	1.824e-03	76.262	0.176
TF59	4.136	2.221	1.865e-03	77.985	0.143
TF60	4.241	2.325	1.744e-03	72.903	0.076
TF61	4.346	2.431	1.809e-03	75.618	0.143
TF62	4.451	2.535	1.679e-03	70.193	0.106
TF63	4.556	2.640	1.629e-03	68.096	0.143
TF64	4.661	2.745	1.612e-03	67.409	0.129
TF65	4.766	2.850	1.547e-03	64.695	0.115
TF66	4.871	2.955	1.686e-03	70.501	0.143
TF67	4.976	3.060	1.631e-03	68.188	0.143
TF68	5.081	3.165	1.245e-03	52.066	0.143
TF69	5.186	3.270	1.466e-03	61.279	0.253
TF70	5.291	3.375	1.402e-03	58.633	0.344

Table 6.2.5: MP-2 Configuration, CO_2 Test Gas, α = 0 deg

GAGE ID	S/R_b	L/R_b	$C_{H,avg}$	q_{300K} (W/cm^2)	U_{tot}/C_H
TF1	-1.864	-	2.041e-05	0.691	0.180
TF2	-1.764	-	7.084e-05	2.398	0.180
TF3	-1.670	-	4.416e-05	1.495	0.387
TF4	-1.545	-	3.277e-05	1.109	1.656
TF5	-1.421	-	*	*	*
TF6	-1.296	-	4.021e-05	1.361	1.911
TF7	-1.172	-	5.926e-05	2.006	0.180
TF8	-1.075	-	1.541e-03	52.175	0.315
TF9	-1.000	-	1.163e-02	393.636	0.255
TF10	-0.900	-	1.242e-02	420.375	0.143
TF11	-0.800	-	1.213e-02	410.559	0.117
TF12	-0.700	-	1.221e-02	413.098	0.161
TF13	-0.600	-	1.271e-02	430.190	0.141
TF14	-0.500	-	1.386e-02	469.114	0.109
TF15	-0.400	-	1.338e-02	453.037	0.088
TF16	-0.300	-	1.491e-02	504.653	0.109
TF17	-0.200	-	1.607e-02	543.915	0.109
TF18	-0.100	-	*	*	*
TF19	0.000	-	1.822e-02	616.685	0.148
TF20	0.100	-	1.795e-02	607.716	0.065
TF21	0.200	-	1.562e-02	528.853	0.074
TF22	0.300	-	1.385e-02	468.775	0.070
TF23	0.400	-	1.339e-02	453.206	0.062
TF24	0.500	-	1.335e-02	452.021	0.098
TF25	0.600	-	1.224e-02	414.282	0.081
TF26	0.700	-	1.195e-02	404.467	0.109
TF27	0.800	-	1.188e-02	402.098	0.095
TF28	0.900	-	1.213e-02	410.559	0.161
TF29	1.000	-	1.159e-02	392.451	0.061
TF30	1.075	-	1.459e-03	49.382	0.165
TF31	1.172	-	3.852e-05	1.304	0.822
TF32	1.296	-	3.514e-05	1.189	0.180
TF33	1.421	-	*	*	*
TF34	1.545	-	*	*	*
TF35	1.670	-	5.491e-05	1.859	0.326
TF36	1.764	-	5.030e-05	1.702	0.352
TF37	1.864	-	3.090e-05	1.046	0.180
TF38	1.923	0.015	7.565e-05	2.560	0.180
TF39	2.027	0.119	7.958e-05	2.694	0.449
TF40	2.132	0.224	8.945e-05	3.028	0.382
TF41	2.237	0.329	9.496e-05	3.214	0.245
TF42	2.343	0.435	2.246e-04	7.602	0.793
TF43	2.447	0.539	1.466e-04	4.963	0.656
TF44	2.553	0.645	3.340e-04	11.305	0.465
TF45	2.658	0.750	3.088e-04	10.452	0.180
TF46	2.763	0.855	*	*	*
TF47	2.868	0.961	5.662e-04	19.164	0.684
TF48	2.973	1.066	6.450e-04	21.832	0.507
TF49	3.078	1.171	7.451e-04	25.219	0.241
TF50	3.182	1.274	7.577e-04	25.646	0.066
TF51	3.288	1.381	7.579e-04	25.652	0.180
TF52	3.392	1.484	8.740e-04	29.582	0.088
TF53	3.497	1.589	8.437e-04	28.558	0.086
TF54	3.602	1.694	8.515e-04	28.822	0.194
TF55	3.707	1.799	8.926e-04	30.211	0.180
TF56	3.813	1.905	8.513e-04	28.814	0.158
TF57	3.918	2.010	7.533e-04	25.497	0.180
TF58	4.023	2.115	8.125e-04	27.500	0.252
TF59	4.128	2.220	8.030e-04	27.179	0.180
TF60	4.233	2.325	7.795e-04	26.382	0.101
TF61	4.338	2.430	7.528e-04	25.480	0.180
TF62	4.443	2.535	7.082e-04	23.970	0.134
TF63	4.548	2.640	7.022e-04	23.767	0.133
TF64	4.653	2.745	6.781e-04	22.953	0.134
TF65	4.758	2.850	6.650e-04	22.509	0.075
TF66	4.863	2.955	6.738e-04	22.805	0.122
TF67	4.968	3.060	6.135e-04	20.766	0.209
TF68	5.073	3.165	5.701e-04	19.298	0.061
TF69	5.177	3.270	6.198e-04	20.979	0.178
TF70	5.282	3.375	6.210e-04	21.019	0.187

Table 6.2.6: MP-2 Configuration, CO_2 Test Gas, α = -4 deg

GAGE ID	S/R_b	L/R_b	$C_{H,avg}$	q_{300K} (W/cm^2)	U_{tot}/C_H
TF1	-1.864	-	1.538e-04	5.205	1.508
TF2	-1.764	-	2.064e-04	6.985	0.144
TF3	-1.670	-	1.311e-04	4.438	0.809
TF4	-1.545	-	1.419e-04	4.804	0.153
TF5	-1.421	-	1.585e-04	5.365	0.153
TF6	-1.296	-	5.454e-05	1.846	0.153
TF7	-1.172	-	1.121e-04	3.796	1.043
TF8	-1.075	-	2.737e-03	92.652	0.072
TF9	-1.000	-	1.113e-02	376.628	0.104
TF10	-0.900	-	1.075e-02	363.885	0.092
TF11	-0.800	-	1.098e-02	371.534	0.148
TF12	-0.700	-	1.089e-02	368.441	0.265
TF13	-0.600	-	1.122e-02	379.708	0.244
TF14	-0.500	-	1.128e-02	381.959	0.134
TF15	-0.400	-	1.196e-02	404.941	0.165
TF16	-0.300	-	1.328e-02	449.398	0.180
TF17	-0.200	-	1.407e-02	476.103	0.192
TF18	-0.100	-	1.667e-02	564.341	0.078
TF19	0.000	-	1.686e-02	570.518	0.079
TF20	0.100	-	1.790e-02	605.956	0.134
TF21	0.200	-	1.501e-02	508.105	0.112
TF22	0.300	-	1.312e-02	443.932	0.134
TF23	0.400	-	1.372e-02	464.477	0.171
TF24	0.500	-	1.323e-02	447.892	0.176
TF25	0.600	-	1.320e-02	446.674	0.119
TF26	0.700	-	1.344e-02	454.831	0.134
TF27	0.800	-	1.272e-02	430.563	0.134
TF28	0.900	-	1.313e-02	444.423	0.148
TF29	1.000	-	1.299e-02	439.786	0.089
TF30	1.075	-	1.702e-03	57.592	0.556
TF31	1.172	-	1.729e-04	5.851	0.661
TF32	1.296	-	2.683e-04	9.081	0.811
TF33	1.421	-	2.212e-04	7.486	0.464
TF34	1.545	-	1.165e-04	3.943	0.153
TF35	1.670	-	6.963e-05	2.357	0.454
TF36	1.764	-	1.240e-04	4.196	1.428
TF37	1.864	-	7.020e-05	2.376	0.191
TF38	1.923	0.015	*	*	*
TF39	2.028	0.121	*	*	*
TF40	2.133	0.225	1.372e-04	4.644	0.578
TF41	2.238	0.330	2.122e-04	7.183	0.540
TF42	2.343	0.435	3.678e-04	12.448	0.153
TF43	2.448	0.540	5.260e-04	17.802	0.869
TF44	2.553	0.645	1.017e-03	34.408	0.153
TF45	2.658	0.750	1.066e-03	36.067	0.416
TF46	2.763	0.855	1.271e-03	43.029	0.153
TF47	2.868	0.961	1.295e-03	43.837	0.145
TF48	2.973	1.066	1.205e-03	40.793	0.183
TF49	3.078	1.171	1.161e-03	39.286	0.123
TF50	3.183	1.381	1.097e-03	37.140	0.153
TF51	3.288	1.485	1.055e-03	35.701	0.153
TF52	3.393	1.484	*	*	*
TF53	3.498	1.589	1.033e-03	34.953	0.078
TF54	3.603	1.694	9.879e-04	33.438	0.153
TF55	3.707	1.799	1.042e-03	35.283	0.135
TF56	3.813	1.905	9.599e-04	32.489	0.153
TF57	3.918	2.010	1.152e-03	39.005	0.153
TF58	4.023	2.115	9.618e-04	32.553	0.196
TF59	4.128	2.220	1.087e-03	36.788	0.153
TF60	4.233	2.325	9.839e-04	33.302	0.062
TF61	4.338	2.430	9.863e-04	33.384	0.150
TF62	4.443	2.535	9.846e-04	33.325	0.145
TF63	4.548	2.640	1.058e-03	35.822	0.094
TF64	4.653	2.745	9.742e-04	32.973	0.288
TF65	4.758	2.850	9.573e-04	32.401	0.161
TF66	4.863	2.955	9.783e-04	33.112	0.198
TF67	4.968	3.060	9.790e-04	33.135	0.174
TF68	5.073	3.165	1.065e-03	36.043	0.153
TF69	5.178	3.270	9.775e-04	33.084	0.209
TF70	5.283	3.375	9.829e-04	33.269	0.203

Table 6.2.7: MP-2 Configuration, Air Test Gas, $\alpha = 0$ deg

GAGE ID	S/R_b	L/R_b	$C_{H,avg}$	q_{300K} (W/cm^2)	U_{tot}/C_H
TF1	-1.864	-	1.720e-04	7.189	1.005
TF2	-1.764	-	*	*	*
TF3	-1.670	-	2.454e-04	10.257	0.073
TF4	-1.545	-	8.623e-04	36.040	0.162
TF5	-1.421	-	7.156e-04	29.909	0.164
TF6	-1.296	-	1.076e-03	44.960	0.431
TF7	-1.172	-	8.360e-04	34.943	0.246
TF8	-1.075	-	3.574e-03	149.377	0.143
TF9	-1.000	-	*	*	*
TF10	-0.900	-	2.045e-02	854.720	0.100
TF11	-0.800	-	1.918e-02	801.430	0.088
TF12	-0.700	-	1.795e-02	750.231	0.100
TF13	-0.600	-	1.803e-02	753.574	0.061
TF14	-0.500	-	1.864e-02	779.070	0.170
TF15	-0.400	-	1.882e-02	786.593	0.127
TF16	-0.300	-	1.999e-02	835.703	0.375
TF17	-0.200	-	2.167e-02	905.710	0.061
TF18	-0.100	-	2.552e-02	1109.673	0.125
TF19	0.000	-	2.557e-02	1068.713	0.100
TF20	0.100	-	2.600e-02	1128.272	0.121
TF21	0.200	-	2.259e-02	944.371	0.088
TF22	0.300	-	1.970e-02	823.373	0.102
TF23	0.400	-	1.685e-02	704.255	0.068
TF24	0.500	-	1.646e-02	687.746	0.104
TF25	0.600	-	*	*	*
TF26	0.700	-	1.616e-02	675.417	0.129
TF27	0.800	-	1.610e-02	672.909	0.068
TF28	0.900	-	1.742e-02	727.870	0.061
TF29	1.000	-	1.784e-02	745.633	0.072
TF30	1.075	-	2.840e-03	118.679	0.210
TF31	1.172	-	3.897e-04	16.290	0.647
TF32	1.296	-	4.075e-04	17.032	0.872
TF33	1.421	-	3.535e-04	14.773	1.759
TF34	1.545	-	4.648e-04	19.427	0.584
TF35	1.670	-	3.329e-04	13.914	0.779
TF36	1.764	-	5.585e-04	23.343	0.162
TF37	1.864	-	4.362e-04	18.231	0.162
TF38	1.923	0.015	*	*	*
TF39	2.028	0.121	*	*	*
TF40	2.133	0.225	*	*	*
TF41	2.238	0.330	*	*	*
TF42	2.343	0.435	*	*	*
TF43	2.448	0.540	*	*	*
TF44	2.553	0.645	*	*	*
TF45	2.658	0.750	*	*	*
TF46	2.763	0.855	*	*	*
TF47	2.868	0.961	5.863e-04	24.505	0.933
TF48	2.973	1.066	7.071e-04	29.554	0.850
TF49	3.078	1.171	8.371e-04	34.987	0.202
TF50	3.288	1.381	9.414e-04	39.346	0.162
TF51	3.393	1.485	8.050e-04	33.645	0.162
TF52	3.392	1.484	1.119e-03	46.753	0.468
TF53	3.497	1.589	1.352e-03	56.508	0.125
TF54	3.602	1.694	1.347e-03	56.278	0.096
TF55	3.707	1.799	1.419e-03	59.329	0.074
TF56	3.813	1.905	*	*	*
TF57	3.918	2.010	1.477e-03	61.732	0.162
TF58	4.023	2.115	*	*	*
TF59	4.128	2.220	1.430e-03	59.768	0.162
TF60	4.233	2.325	1.229e-03	51.367	0.162
TF61	4.338	2.430	1.395e-03	58.305	0.075
TF62	4.443	2.535	1.457e-03	60.896	0.162
TF63	4.548	2.640	1.323e-03	55.296	0.162
TF64	4.653	2.745	1.292e-03	54.000	0.162
TF65	4.758	2.850	*	*	*
TF66	4.863	2.955	7.068e-04	29.541	0.162
TF67	4.968	3.060	*	*	*
TF68	5.073	3.165	*	*	*
TF69	5.178	3.270	7.555e-04	31.577	0.162
TF70	5.283	3.375	6.367e-04	26.611	0.162

Table 6.2.8: MP-3 Configuration, CO_2 Test Gas, $\alpha = 0$ deg

GAGE ID	S/R_b	L/R_b	$C_{H,avg}$	q_{300K} (W/cm^2)	U_{tot}/C_H
TF1	-1.914	-	1.298e-04	4.392	0.199
TF2	-1.814	-	1.851e-04	6.264	0.748
TF3	-1.720	-	1.315e-04	4.452	0.526
TF4	-1.596	-	5.063e-05	1.714	0.199
TF5	-1.472	-	1.284e-04	4.345	0.199
TF6	-1.347	-	8.826e-05	2.987	0.199
TF7	-1.222	-	1.422e-04	4.814	0.199
TF8	-1.109	-	1.668e-03	56.466	0.427
TF9	-1.000	-	1.318e-02	446.234	0.117
TF10	-0.900	-	1.434e-02	485.242	0.061
TF11	-0.800	-	1.439e-02	487.120	0.161
TF12	-0.700	-	1.468e-02	496.902	0.101
TF13	-0.600	-	1.568e-02	530.630	0.092
TF14	-0.500	-	1.607e-02	543.763	0.159
TF15	-0.400	-	1.663e-02	562.954	0.069
TF16	-0.300	-	1.706e-02	577.592	0.127
TF17	-0.200	-	1.859e-02	629.225	0.077
TF18	-0.100	-	2.301e-02	778.861	0.203
TF19	0.000	-	2.377e-02	804.398	0.147
TF20	0.100	-	2.203e-02	745.624	0.070
TF21	0.200	-	1.845e-02	624.368	0.061
TF22	0.300	-	1.672e-02	566.000	0.109
TF23	0.400	-	1.581e-02	535.098	0.091
TF24	0.500	-	1.554e-02	526.010	0.084
TF25	0.600	-	1.517e-02	513.470	0.071
TF26	0.700	-	1.501e-02	507.919	0.061
TF27	0.800	-	1.424e-02	481.874	0.061
TF28	0.900	-	1.422e-02	481.180	0.089
TF29	1.000	-	1.281e-02	433.592	0.090
TF30	1.109	-	1.644e-03	55.642	0.097
TF31	1.222	-	5.451e-07	0.018	0.199
TF32	1.347	-	*	*	*
TF33	1.472	-	2.484e-07	0.008	0.199
TF34	1.596	-	6.048e-05	2.047	0.199
TF35	1.720	-	1.522e-04	5.153	0.119
TF36	1.814	-	1.731e-04	5.859	0.389
TF37	1.914	-	1.231e-04	4.167	0.199
TF38	-	-	-	-	-
TF39	2.028	0.070	*	*	*
TF40	2.133	0.175	*	*	*
TF41	2.238	0.280	*	*	*
TF42	2.343	0.385	*	*	*
TF43	2.448	0.490	*	*	*
TF44	2.553	0.595	*	*	*
TF45	2.658	0.700	*	*	*
TF46	2.763	0.805	*	*	*
TF47	2.868	0.910	5.982e-04	20.247	0.199
TF48	2.973	1.015	6.275e-04	21.237	0.253
TF49	3.078	1.120	7.373e-04	24.956	0.216
TF50	3.183	1.225	7.905e-04	26.756	0.183
TF51	3.288	1.330	9.028e-04	30.556	0.172
TF52	3.393	1.435	*	*	*
TF53	3.498	1.540	9.963e-04	33.721	0.199
TF54	3.603	1.645	9.940e-04	33.644	0.199
TF55	3.708	1.750	8.628e-04	29.203	0.144
TF56	3.813	1.855	9.090e-04	30.766	0.166
TF57	3.918	1.960	8.658e-04	29.304	0.204
TF58	4.023	2.065	8.260e-04	27.958	0.230
TF59	4.128	2.170	*	*	*
TF60	4.233	2.275	8.453e-04	28.611	0.134
TF61	4.338	2.380	8.816e-04	29.839	0.199
TF62	4.443	2.485	8.122e-04	27.491	0.186
TF63	4.548	2.590	7.654e-04	25.907	0.105
TF64	4.653	2.695	7.406e-04	25.066	0.206
TF65	4.758	2.800	6.934e-04	23.469	0.277
TF66	4.863	2.905	7.448e-04	25.209	0.199
TF67	4.968	3.010	7.174e-04	24.282	0.199
TF68	5.073	3.115	5.890e-04	19.936	0.199
TF69	5.178	3.220	6.287e-04	21.281	0.191
TF70	5.283	3.325	6.256e-04	21.173	0.264

Table 6.2.9: MP-4 Configuration, CO_2 Test Gas, $\alpha = 0$ deg

GAGE ID	S/R_b	L/R_b	$C_{H,avg}$	q_{300K} (W/cm^2)	U_{tot}/C_H
TF1	-2.000	-	8.676e-05	2.937	0.209
TF2	-1.900	-	1.018e-04	3.446	0.209
TF3	-1.806	-	1.448e-04	4.901	0.209
TF4	-1.682	-	1.126e-04	3.811	0.209
TF5	-1.557	-	1.130e-04	3.825	0.209
TF6	-1.433	-	1.206e-04	4.082	0.209
TF7	-1.308	-	1.996e-04	6.754	0.416
TF8	-1.161	-	1.028e-03	34.799	0.223
TF9	-1.000	-	6.887e-03	233.085	0.289
TF10	-0.900	-	1.568e-02	530.546	0.065
TF11	-0.800	-	1.489e-02	504.145	0.102
TF12	-0.700	-	1.605e-02	543.238	0.061
TF13	-0.600	-	1.664e-02	563.377	0.068
TF14	-0.500	-	1.771e-02	599.423	0.098
TF15	-0.400	-	1.767e-02	598.239	0.088
TF16	-0.300	-	1.800e-02	609.239	0.067
TF17	-0.200	-	1.909e-02	646.301	0.087
TF18	-0.100	-	2.292e-02	775.764	0.128
TF19	0.000	-	2.458e-02	831.950	0.061
TF20	0.100	-	2.249e-02	761.210	0.061
TF21	0.200	-	1.877e-02	635.301	0.093
TF22	0.300	-	1.788e-02	605.346	0.117
TF23	0.400	-	1.704e-02	576.746	0.061
TF24	0.500	-	1.776e-02	601.116	0.170
TF25	0.600	-	1.636e-02	553.730	0.101
TF26	0.700	-	1.639e-02	554.577	0.113
TF27	0.800	-	1.534e-02	519.207	0.094
TF28	0.900	-	1.544e-02	522.592	0.068
TF29	1.000	-	7.059e-03	238.923	0.093
TF30	1.161	-	8.249e-04	27.920	0.223
TF31	1.308	-	8.960e-05	3.033	2.295
TF32	1.433	-	*	*	*
TF33	1.557	-	5.382e-05	1.822	0.209
TF34	1.682	-	*	*	*
TF35	1.806	-	2.158e-04	7.304	0.209
TF36	1.900	-	1.801e-04	6.096	0.209
TF37	2.000	-	1.203e-04	4.072	0.209
TF38	-	-	-	-	-
TF39	2.114	0.070	*	*	*
TF40	2.219	0.175	*	*	*
TF41	2.324	0.280	*	*	*
TF42	2.429	0.385	*	*	*
TF43	2.534	0.490	*	*	*
TF44	2.639	0.595	*	*	*
TF45	2.744	0.700	*	*	*
TF46	2.849	0.805	*	*	*
TF47	2.954	0.910	*	*	*
TF48	3.059	1.015	7.520e-04	25.453	0.209
TF49	3.164	1.120	8.372e-04	28.336	0.209
TF50	3.269	1.225	8.332e-04	28.201	0.209
TF51	3.374	1.330	8.887e-04	30.079	0.209
TF52	3.479	1.435	*	*	*
TF53	3.584	1.540	8.885e-04	30.073	0.209
TF54	3.689	1.645	*	*	*
TF55	3.794	1.750	7.875e-04	26.654	0.209
TF56	3.899	1.855	8.432e-04	28.539	0.209
TF57	4.004	1.960	7.826e-04	26.488	0.209
TF58	4.109	2.065	7.759e-04	26.262	0.209
TF59	4.214	2.170	*	*	*
TF60	4.319	2.275	7.195e-04	24.353	0.209
TF61	4.424	2.380	*	*	*
TF62	4.529	2.485	6.742e-04	22.819	0.209
TF63	4.634	2.590	6.547e-04	22.159	0.209
TF64	4.739	2.695	6.337e-04	21.449	0.209
TF65	4.844	2.800	6.224e-04	21.066	0.209
TF66	4.949	2.905	*	*	*
TF67	5.054	3.010	*	*	*
TF68	5.159	3.115	*	*	*
TF69	5.264	3.220	5.884e-04	19.915	0.209
TF70	5.283	3.239	*	*	*

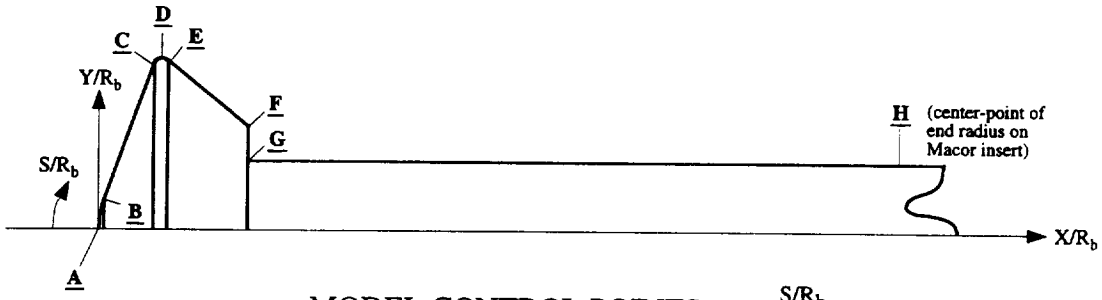

MODEL CONTROL POINTS S/R_b $(X/R_b, Y/R_b)$

Point	MP-1	MP-2	MP-3	MP-4	MP-1 (88%)	MP-1 (75%)
A	0.0000 (0.0000, 0.0000)	0.0000 (0.0000, 0.0000)	0.0000 (0.0000, 0.0000)	0.0000 (0.0000, 0.0000)	0.0000 (0.0000, 0.0000)	0.0000 (0.0000, 0.0000)
B	0.1745 (0.0302, 0.1710)	N/A (N/A, N/A)	0.1745 (0.0302, 0.1710)	0.1745 (0.0302, 0.1710)	0.1527 (0.0264, 0.1496)	0.1309 (0.0226, 0.1283)
C	1.0217 (0.3199, 0.9671)	1.0137 (0.2921, 0.9675)	0.9867 (0.3079, 0.9342)	0.9167 (0.2840, 0.8684)	0.8940 (0.2799, 0.8462)	0.7663 (0.2399, 0.7253)
D	1.0828 (0.3669, 1.000)	1.0748 (0.3391, 1.0000)	1.1089 (0.4019, 1.0000)	1.1610 (0.4719, 1.0000)	0.9475 (0.3210, 0.8750)	0.8121 (0.2752, 0.7500)
E	1.1177 (0.3990, 0.9883)	1.1097 (0.3712, 0.9883)	1.1787 (0.4662, 0.9766)	1.3007 (0.6005, 0.9532)	0.9780 (0.3492, 0.8648)	0.8383 (0.2993, 0.7412)
F	1.7218 (0.8618, 0.6000)	1.7138 (0.8340, 0.6000)	1.7646 (0.9150, 0.6000)	1.8502 (1.0214, 0.6000)	1.5066 (0.7541, 0.5250)	1.2913 (0.6463, 0.4500)
G	1.9155 (0.8618, 0.4063)	1.9075 (0.8340, 0.4063)	1.9583 (0.9150, 0.4063)	2.0439 (1.0214, 0.4063)	1.6253 (0.7541, 0.4063)	1.3350 (0.6463, 0.4063)
H	5.3655 (4.3118, 0.4063)	5.3575 (4.2840, 0.4063)	5.3583 (4.3150, 0.4063)	5.4439 (4.4214, 0.4063)	5.1734 (4.3041, 0.4063)	4.9328 (4.2462, 0.4063)

Figure 6.0.1 Surface Control Points on Entry Vehicle Models

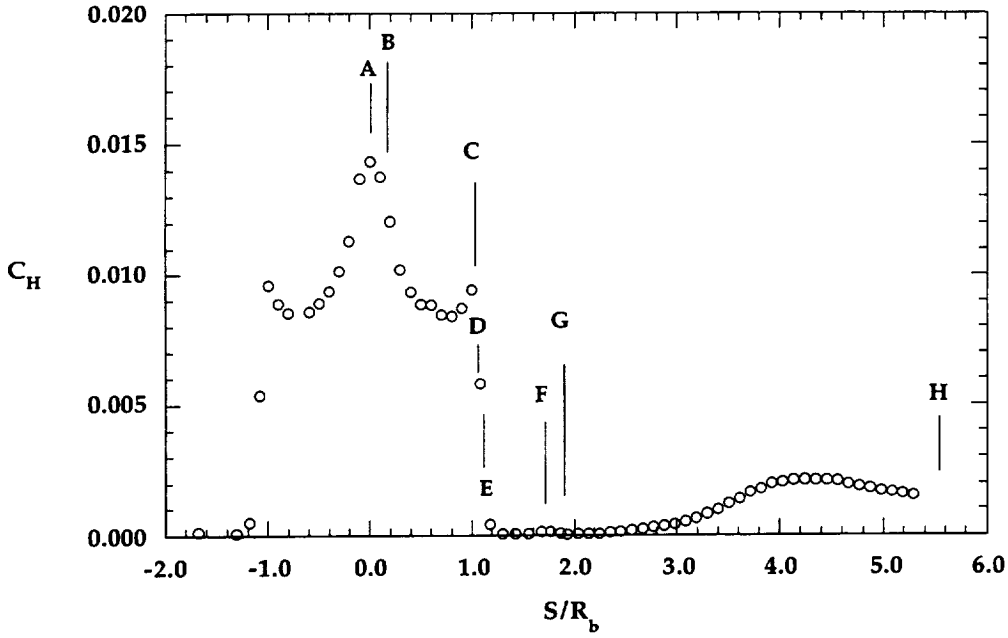

Figure 6.0.2 Typical Entry Vehicle C_H Data (linear scale)

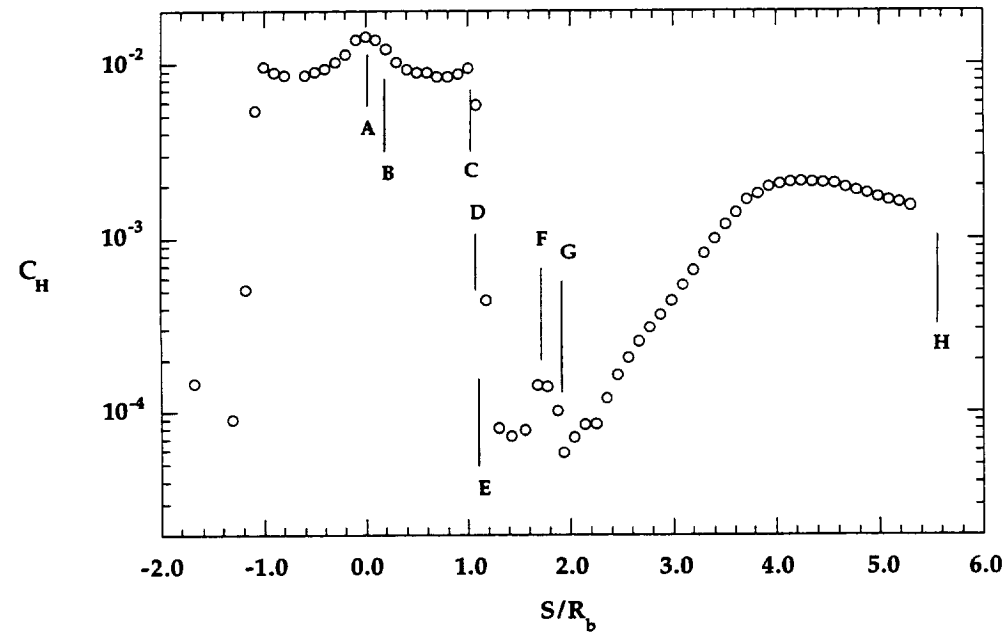

Figure 6.0.3 Typical Entry Vehicle C_H Data (log scale)

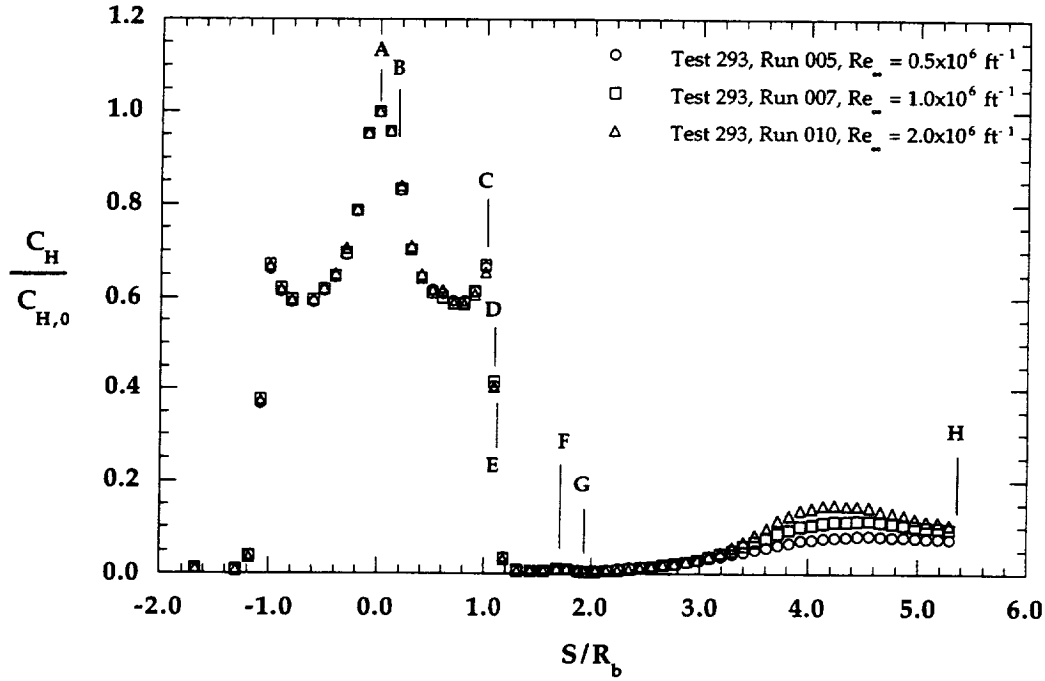

Figure 6.1.1a Reynolds Number Effects on MP-1 Configuration (linear scale)

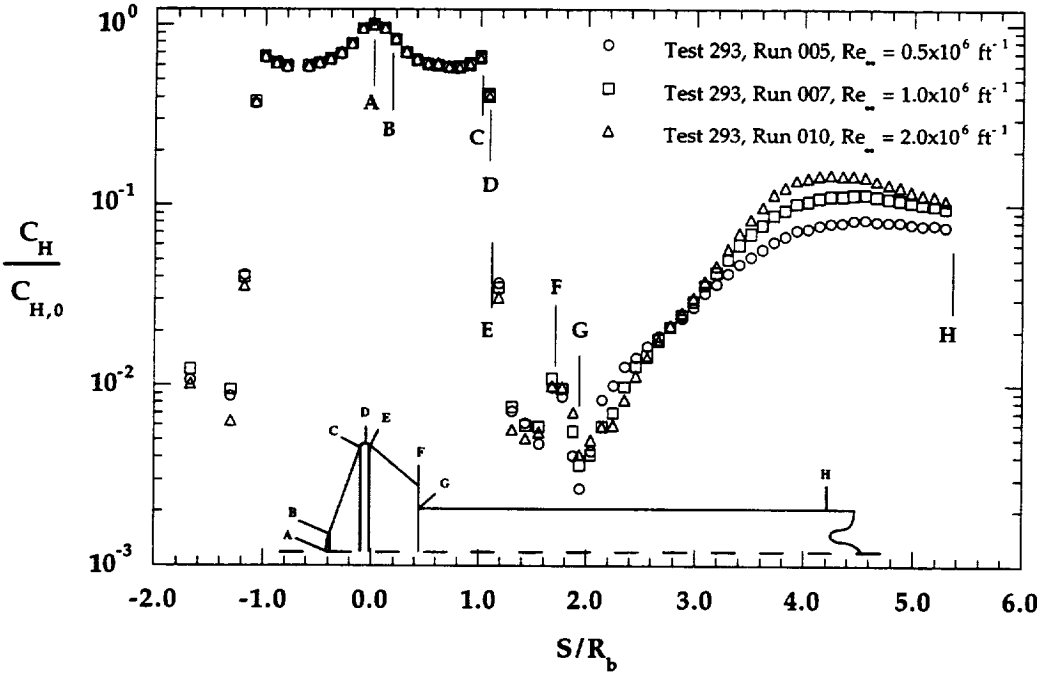

Figure 6.1.1b Reynolds Number Effects on MP-1 Configuration (log scale)

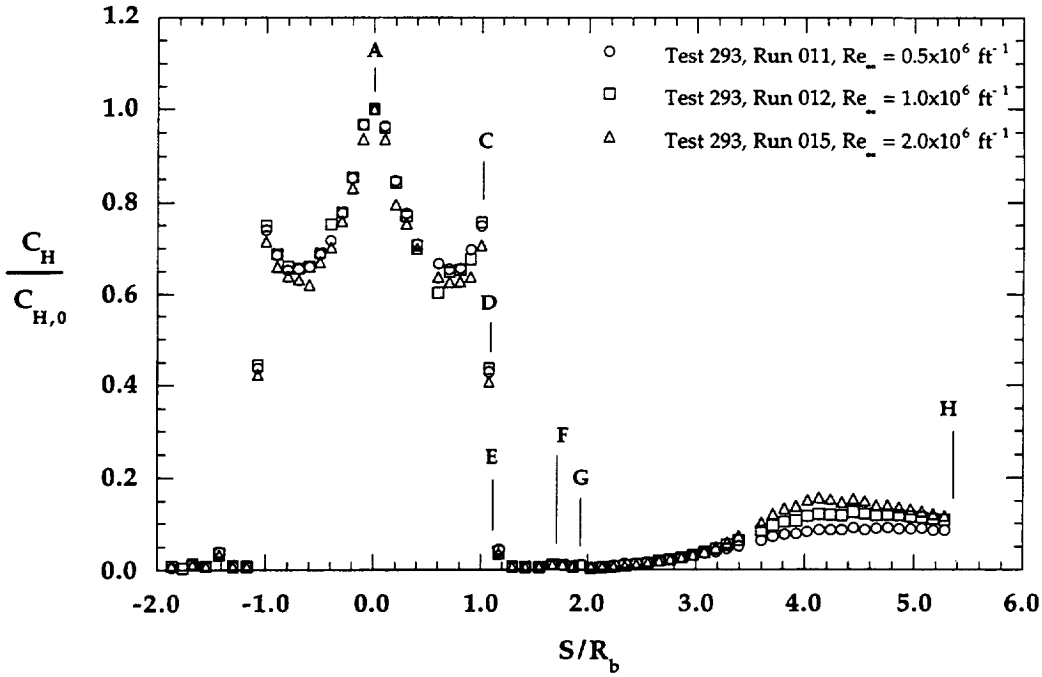

Figure 6.1.2a Reynolds Number Effects on MP-2 Configuration (linear scale)

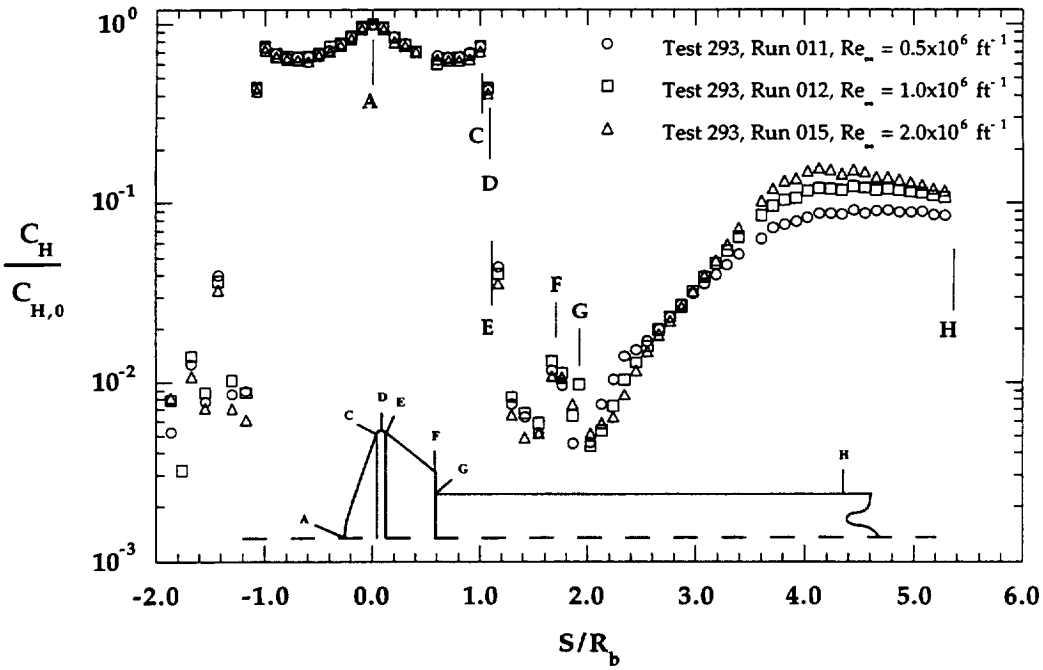

Figure 6.1.2b Reynolds Number Effects on MP-2 Configuration (log scale)

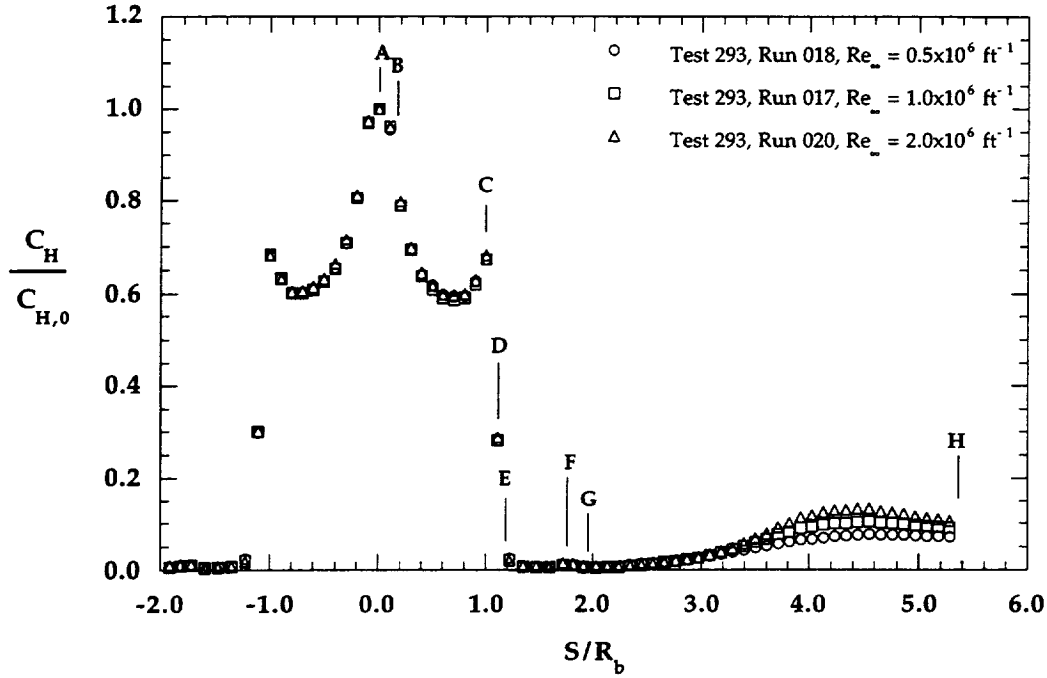

Figure 6.1.3a Reynolds Number Effects on MP-3 Configuration (linear scale)

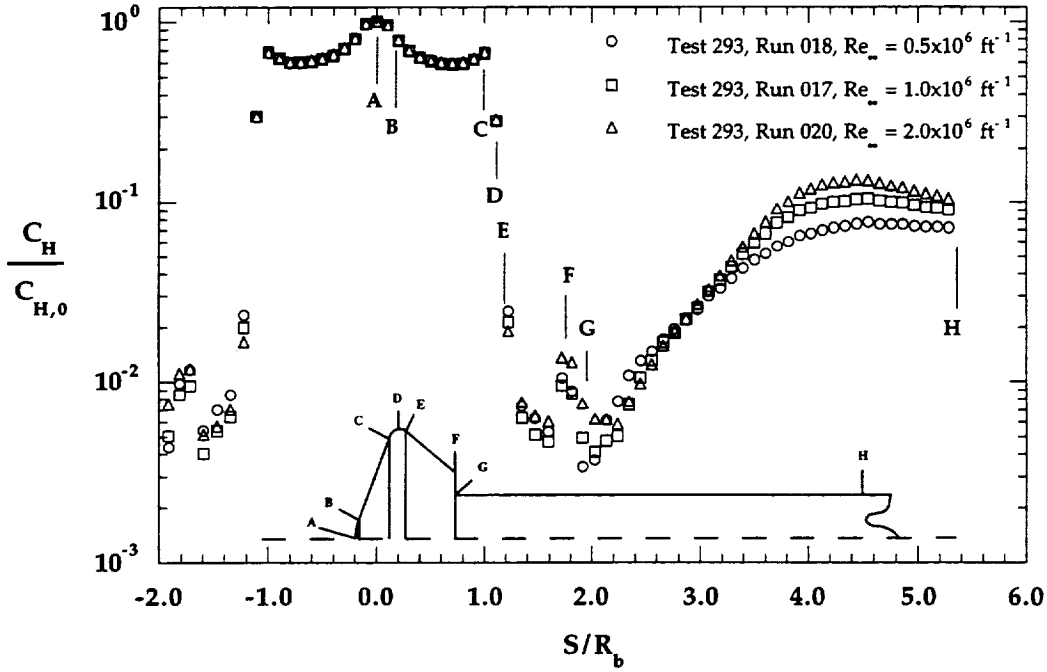

Figure 6.1.3b Reynolds Number Effects on MP-3 Configuration (log scale)

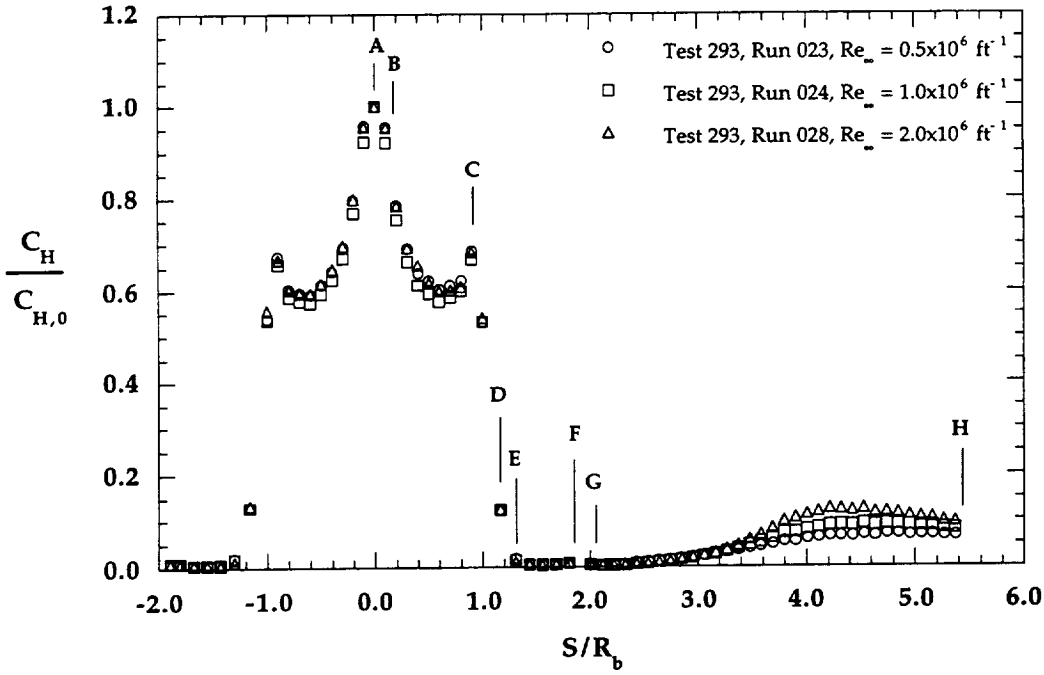

Figure 6.1.4a Reynolds Number Effects on MP-4 Configuration (linear scale)

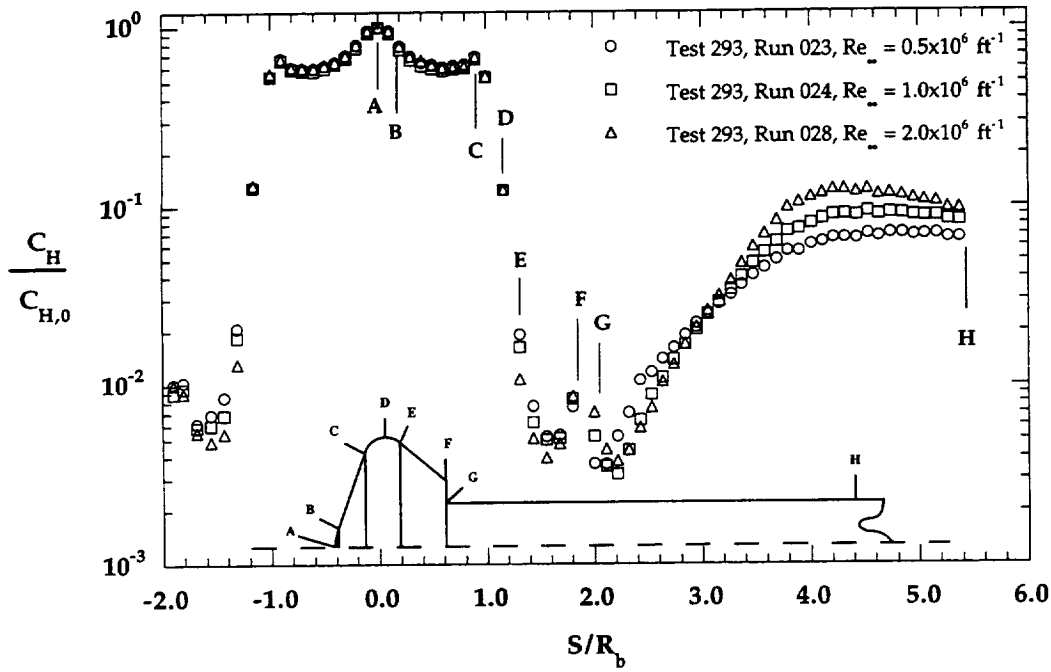

Figure 6.1.4b Reynolds Number Effects on MP-4 Configuration (log scale)

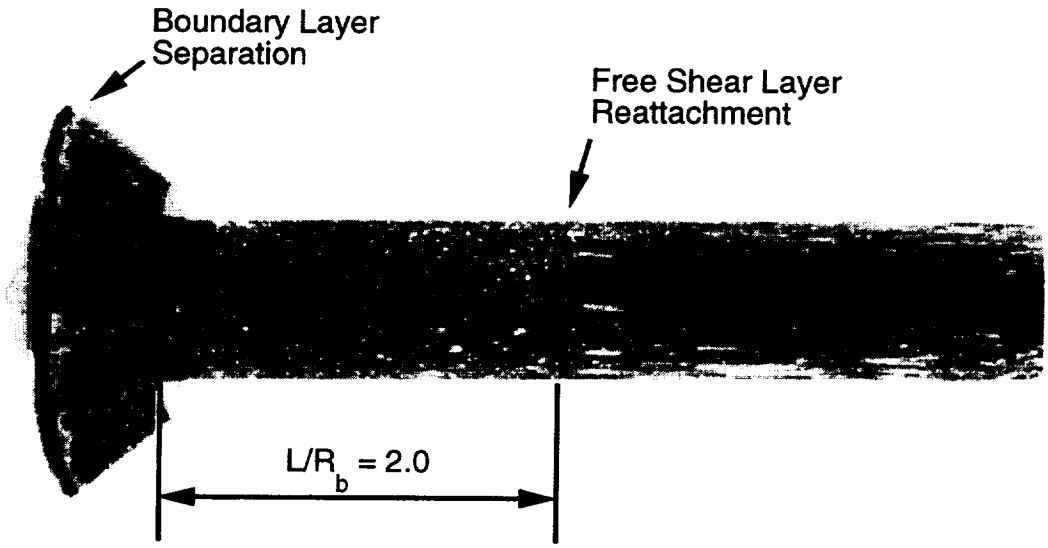

Figure 6.1.5 Oil Flow Patterns on MP-1 Configuration, $Re_\infty = 0.5x10^6$ ft^{-1}

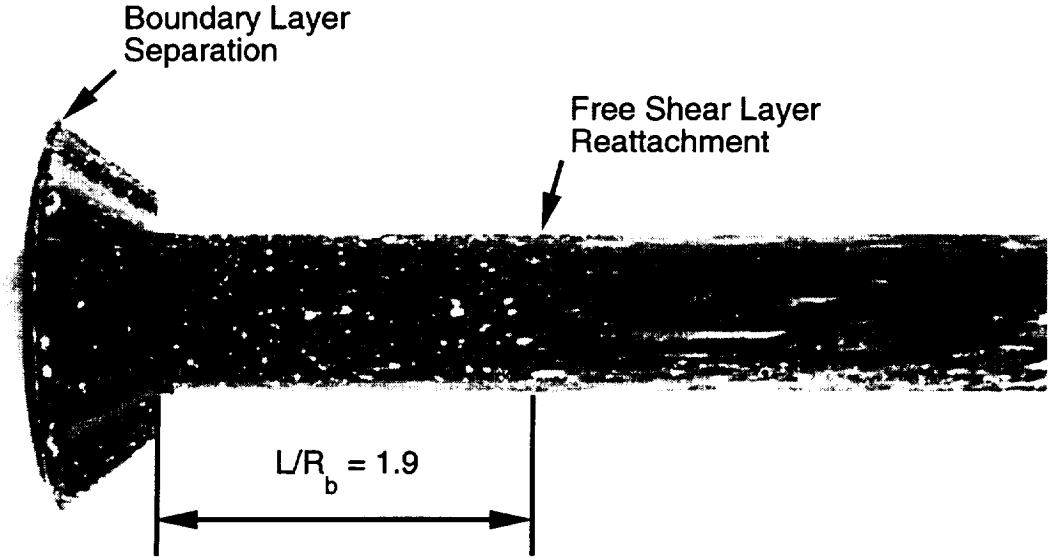

Figure 6.1.6 Oil Flow Patterns on MP-1 Configuration, $Re_\infty = 1.0x10^6$ ft^{-1}

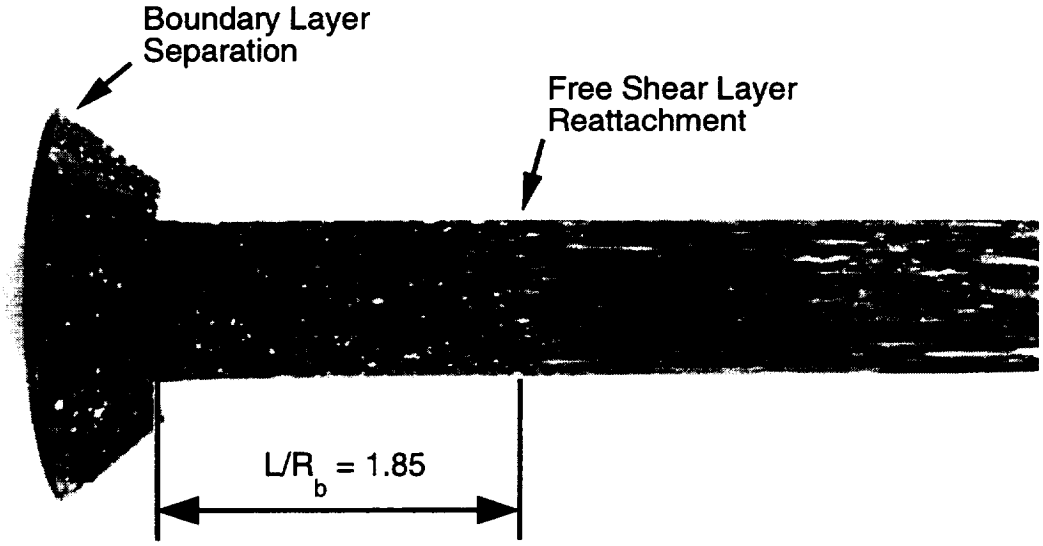

Figure 6.1.7 Oil Flow Patterns on MP-1 Configuration, $Re_\infty = 2.0x10^6$ ft^{-1}

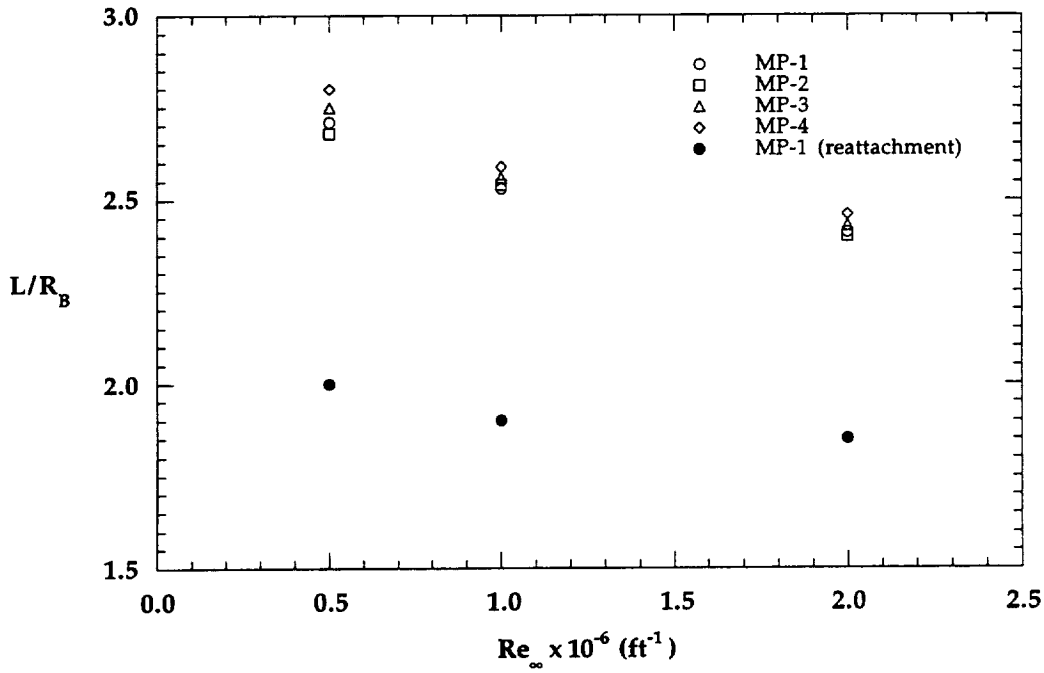

Figure 6.1.8 Reynolds Number Effects on Sting Peak C_H Location

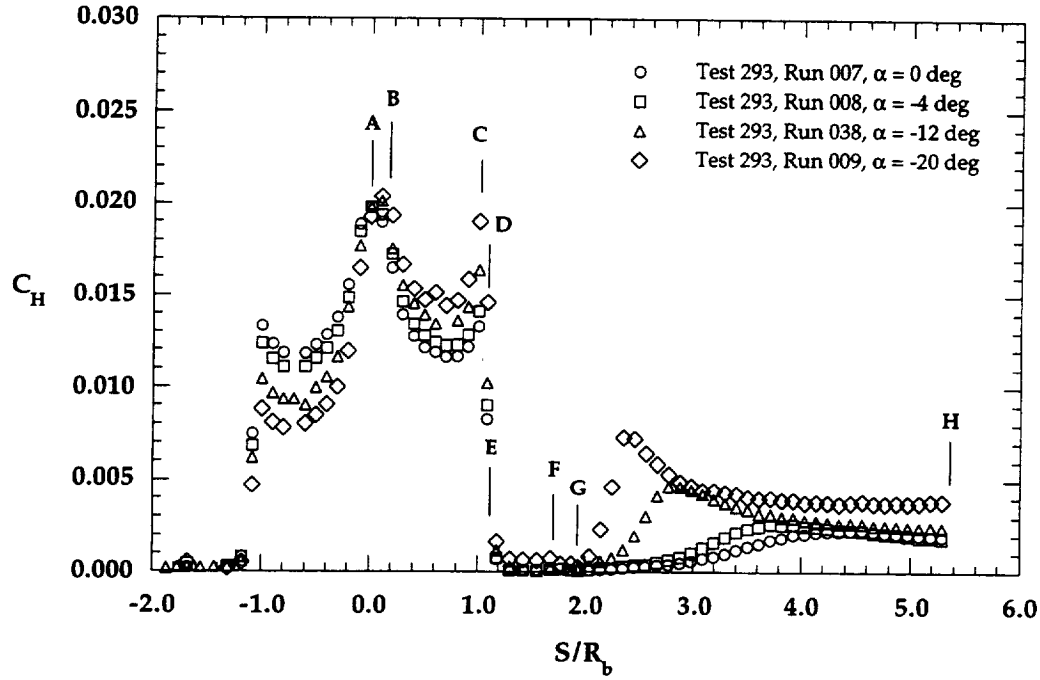

Figure 6.1.9a α Effects on MP-1 Configuration, Re_∞=1.0x10^6 ft^{-1} (linear scale)

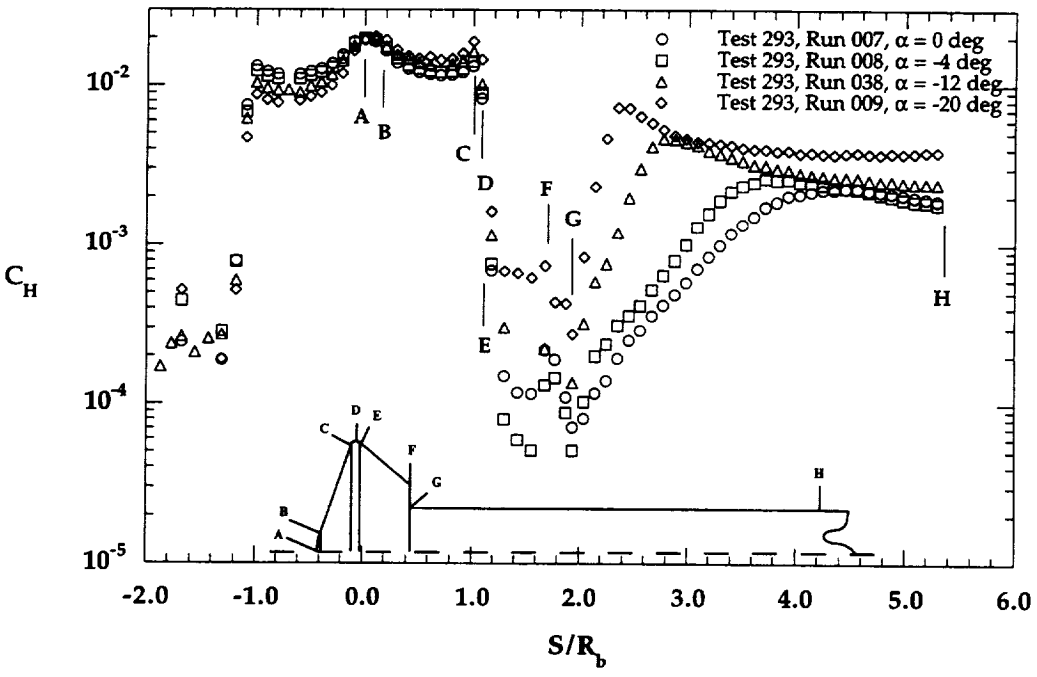

Figure 6.1.9b α Effects on MP-1 Configuration, Re_∞=1.0x10^6 ft^{-1} (log scale)

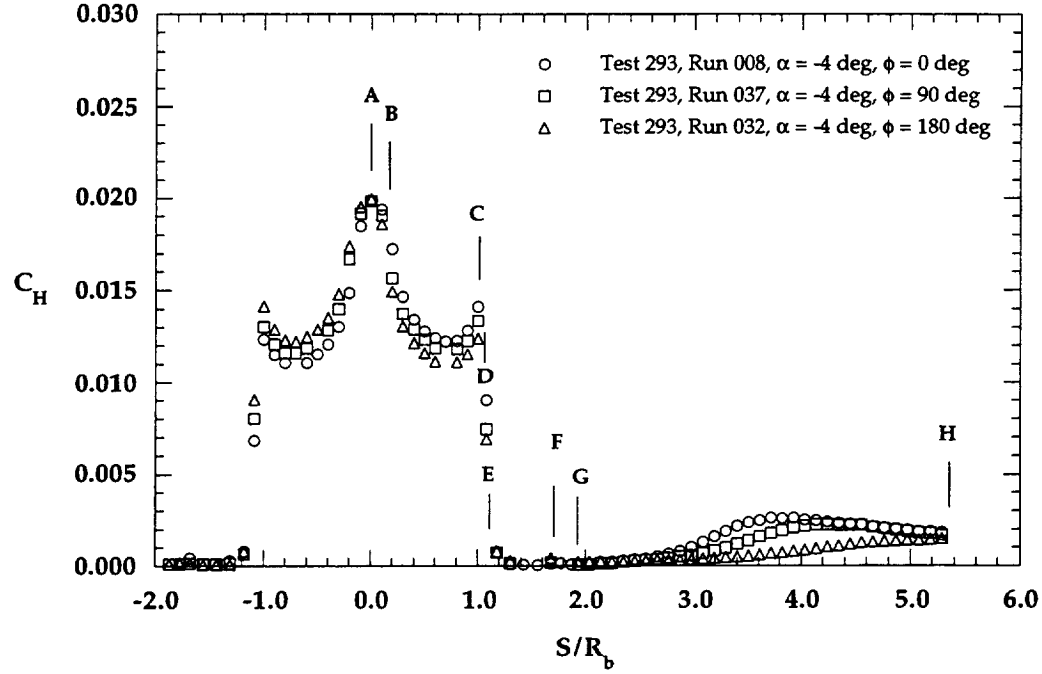

Figure 6.1.10a MP-1 C_H Distributions, α = -4 deg, Re_∞=1.0x10^6 ft^{-1} (linear scale)

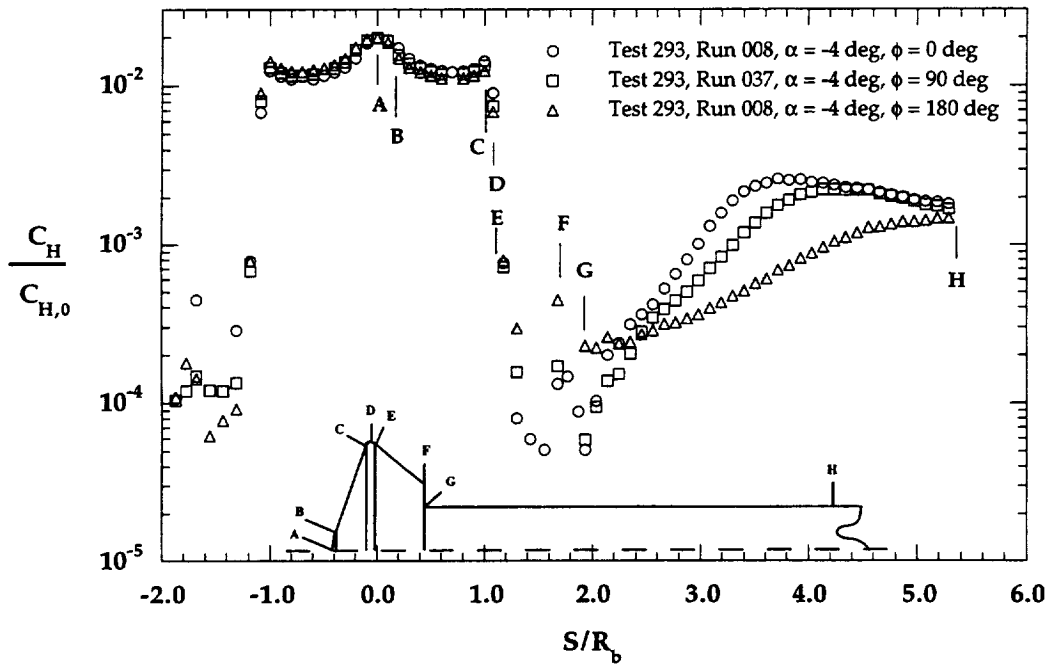

Figure 6.1.10b MP-1 C_H Distributions, α = -4 deg, Re_∞=1.0x10^6 ft^{-1} (log scale)

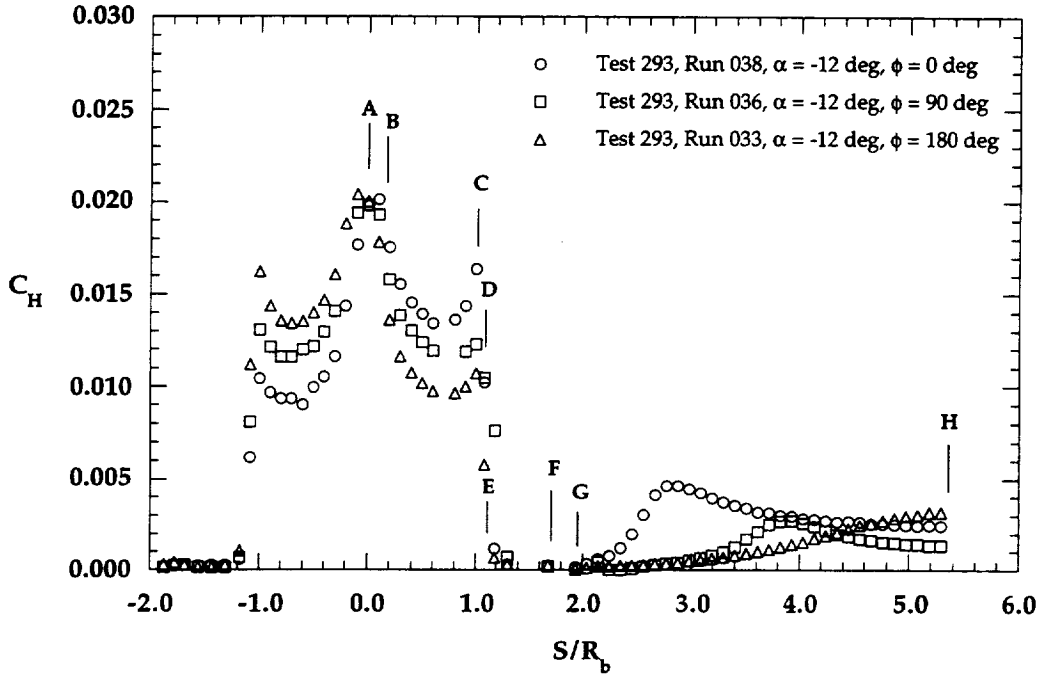

Figure 6.1.11a MP-1 C_H Distributions, α = -12 deg, Re_∞=1.0x10^6 ft^{-1} (linear scale)

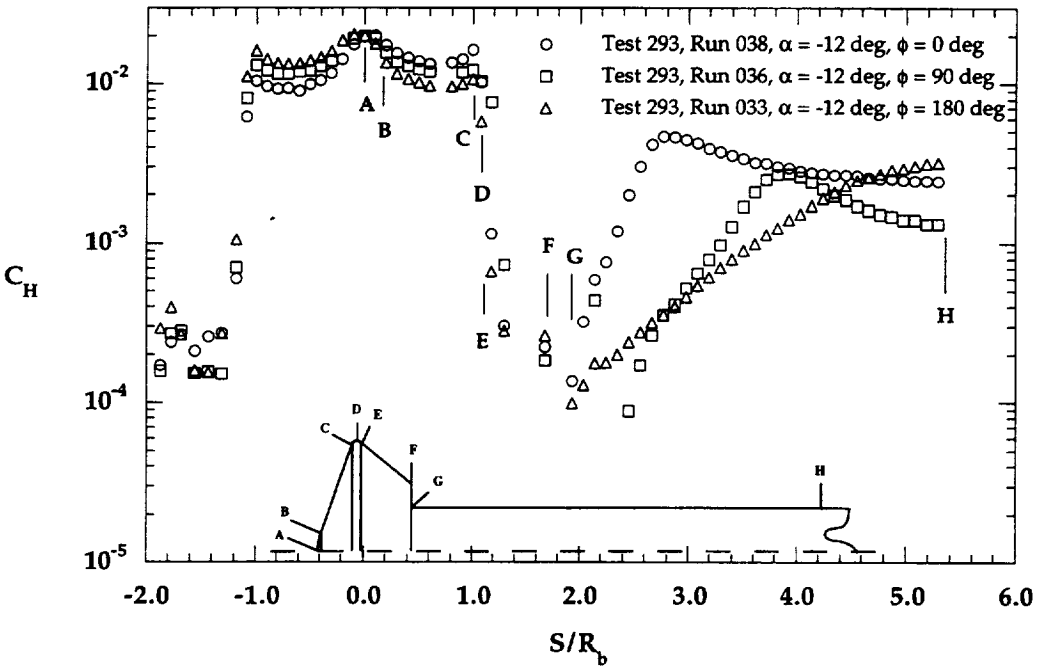

Figure 6.1.11b MP-1 C_H Distributions, α = -12 deg, Re_∞=1.0x10^6 ft^{-1} (log scale)

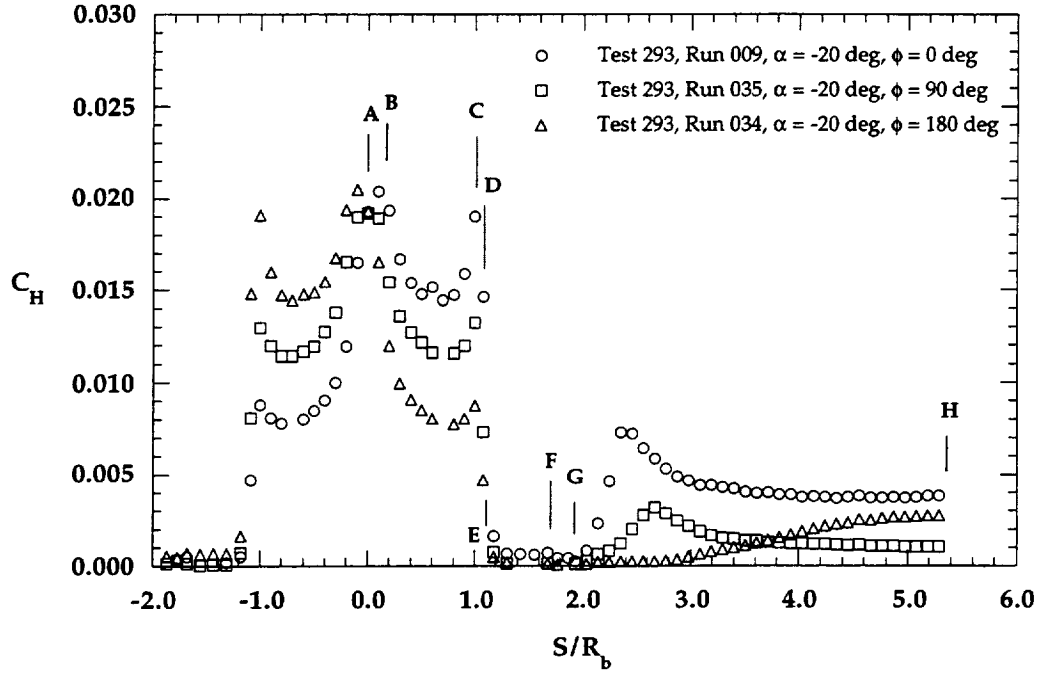

Figure 6.1.12a MP-1 C_H Distributions, α = -20 deg, Re_∞=1.0x10^6 ft^{-1} (linear scale)

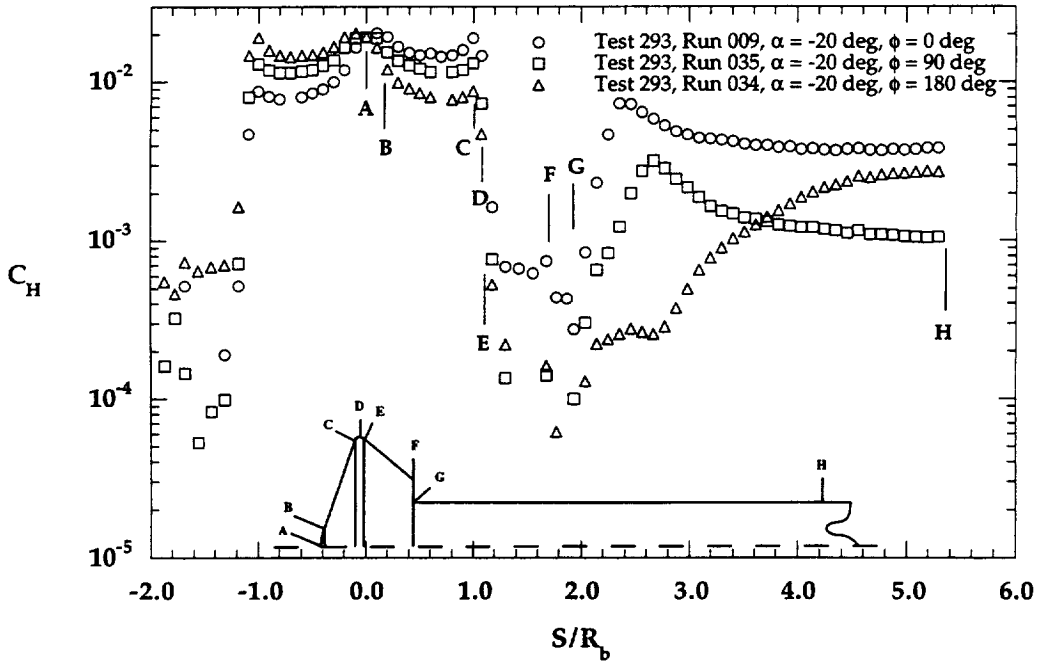

Figure 6.1.12b MP-1 C_H Distributions, α = -20 deg, Re_∞=1.0x10^6 ft^{-1} (log scale)

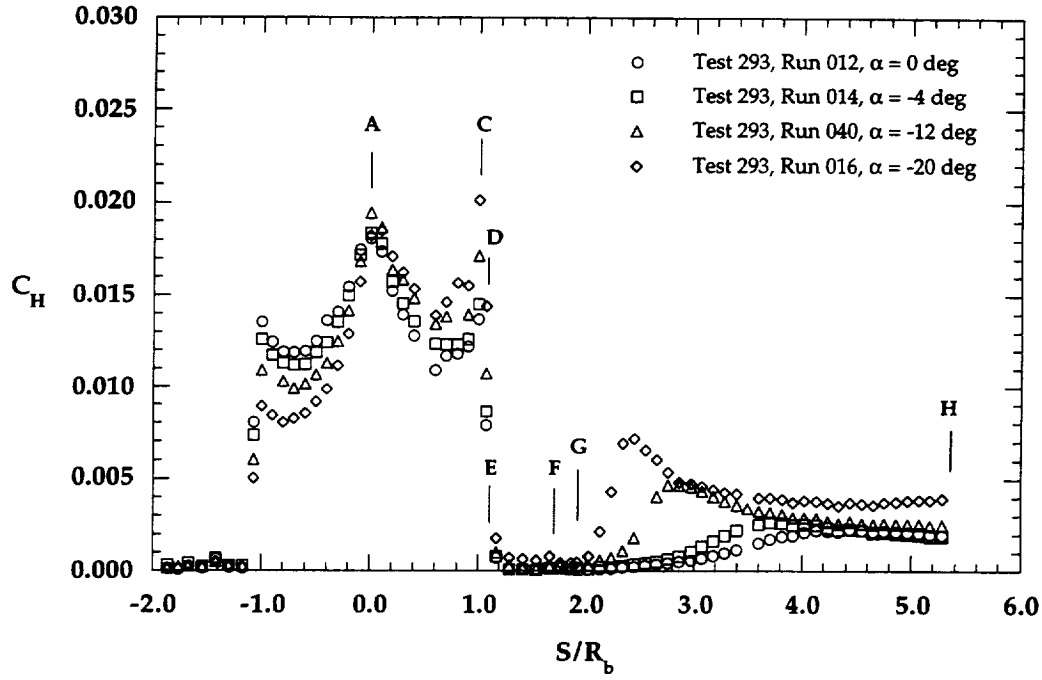

Figure 6.1.13a α Effects on MP-2 Configuration, Re_∞=1.0x10^6 ft^{-1} (linear scale)

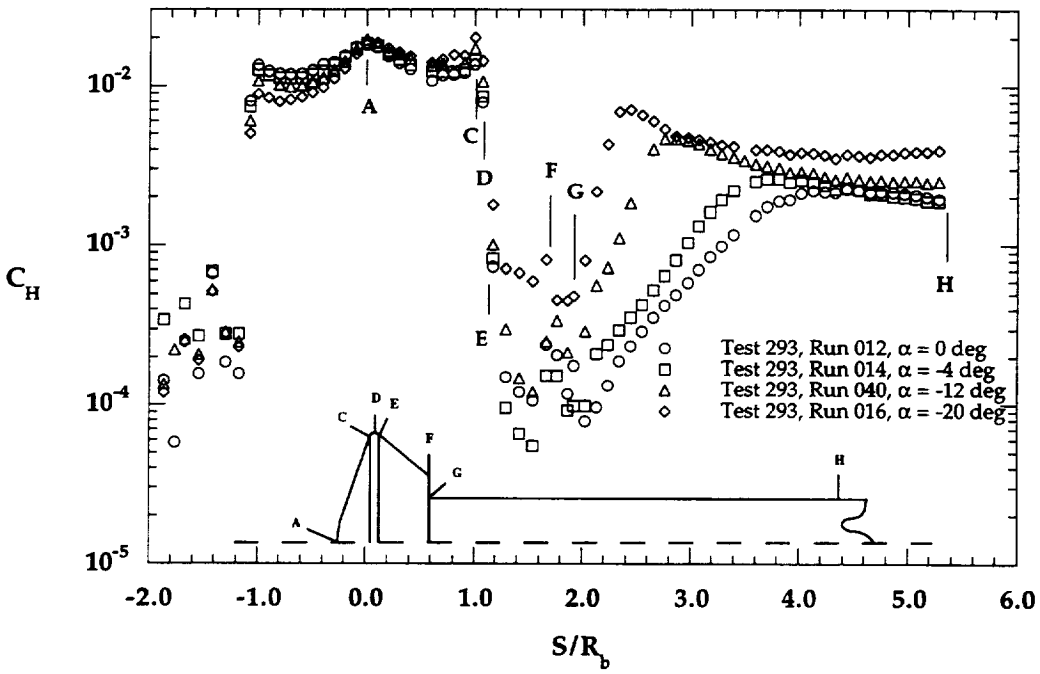

Figure 6.1.13b α Effects on MP-2 Configuration, Re_∞=1.0x10^6 ft^{-1} (log scale)

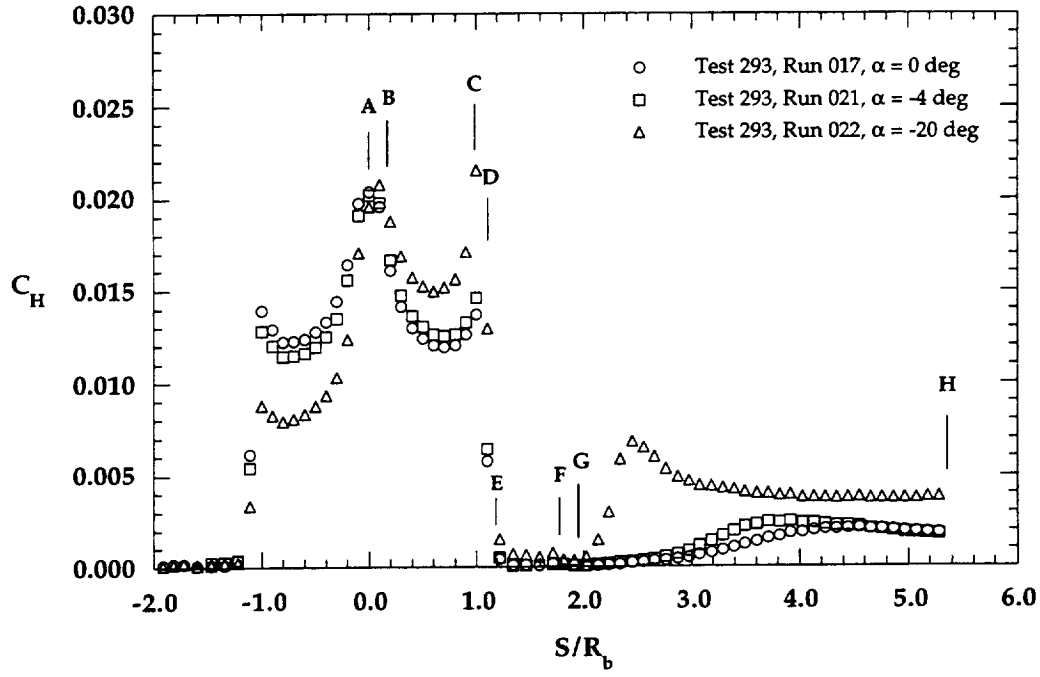

Figure 6.1.14a α Effects on MP-3 Configuration, $Re_\infty = 1.0x10^6$ ft^{-1} (linear scale)

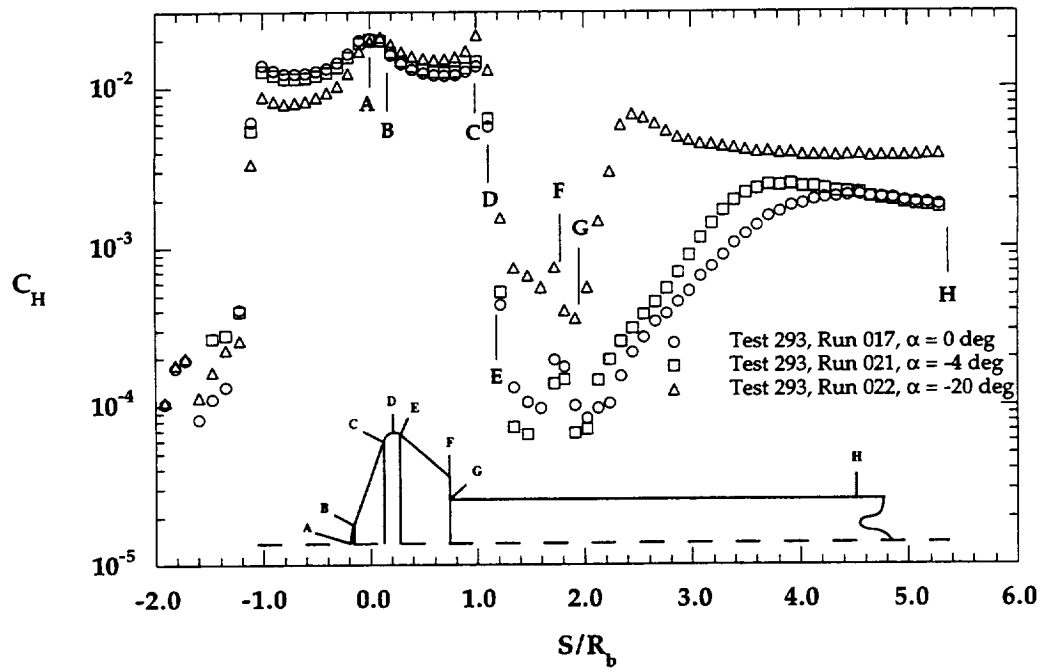

Figure 6.1.14b α Effects on MP-3 Configuration, $Re_\infty = 1.0x10^6$ ft^{-1} (log scale)

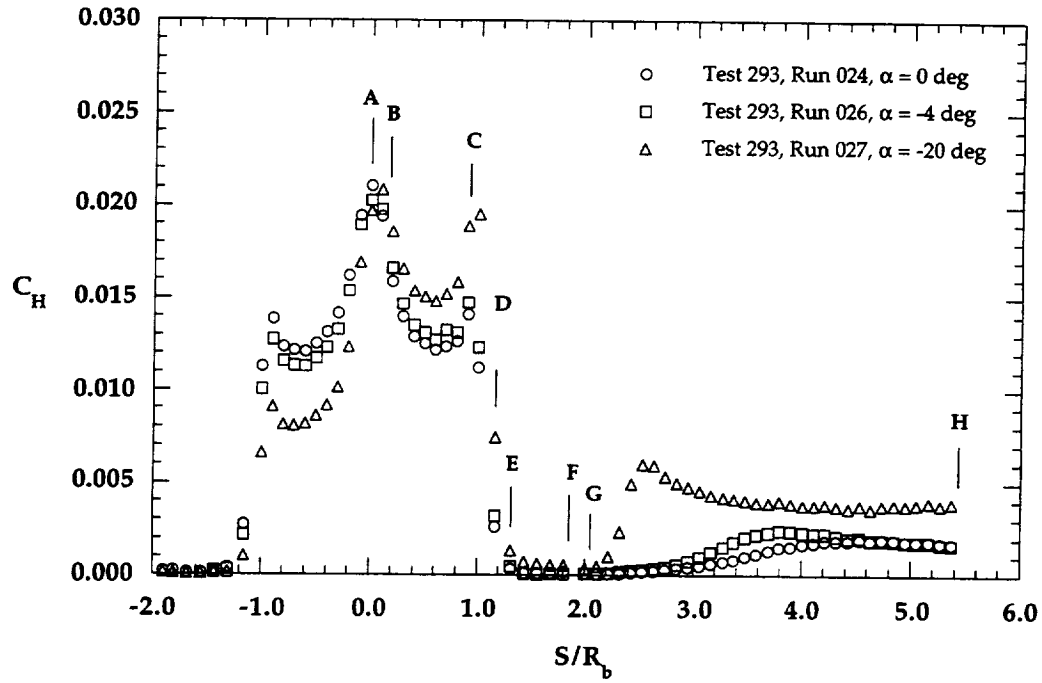

Figure 6.1.15a α Effects on MP-4 Configuration, $Re_\infty = 1.0x10^6$ ft^{-1} (linear scale)

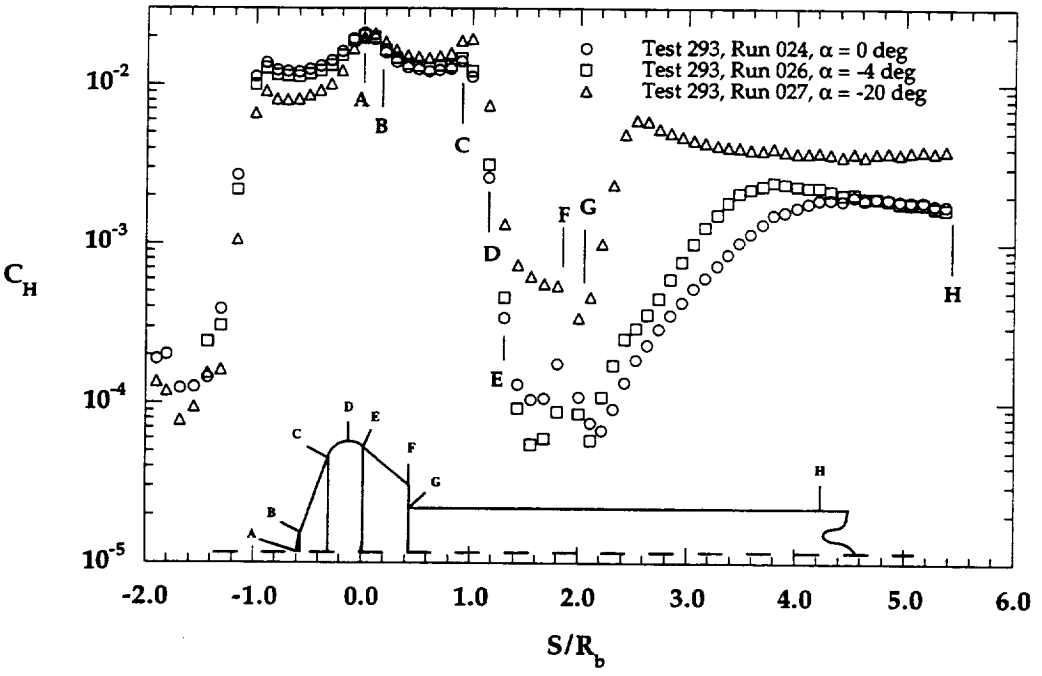

Figure 6.1.15b α Effects on MP-4 Configuration, $Re_\infty = 1.0x10^6$ ft^{-1} (log scale)

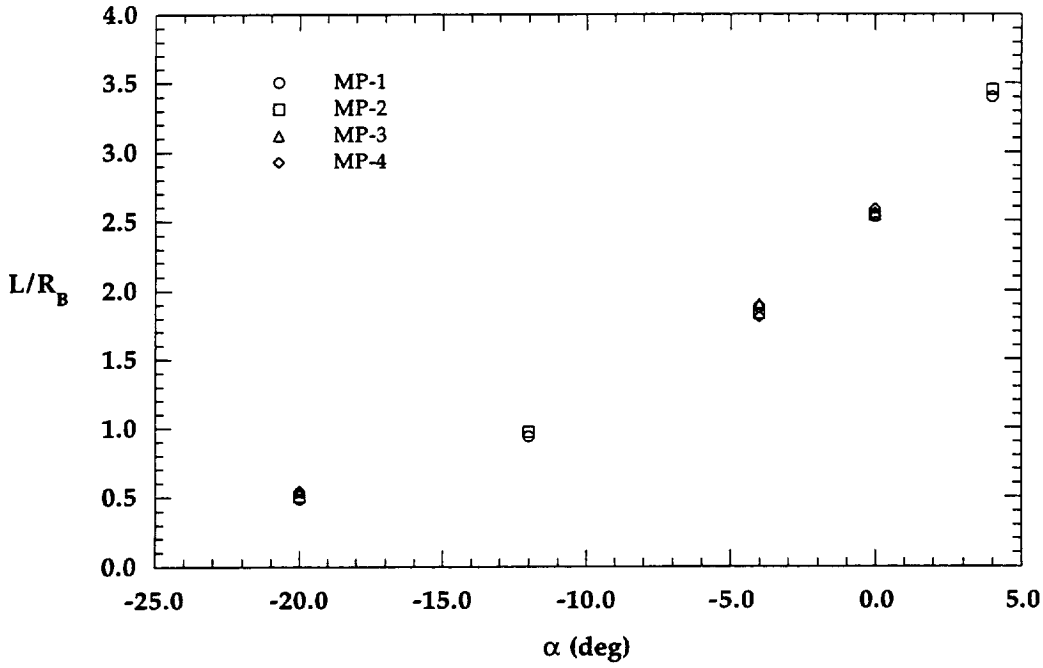

Figure 6.1.16 α Effects on Sting Peak C_H Location

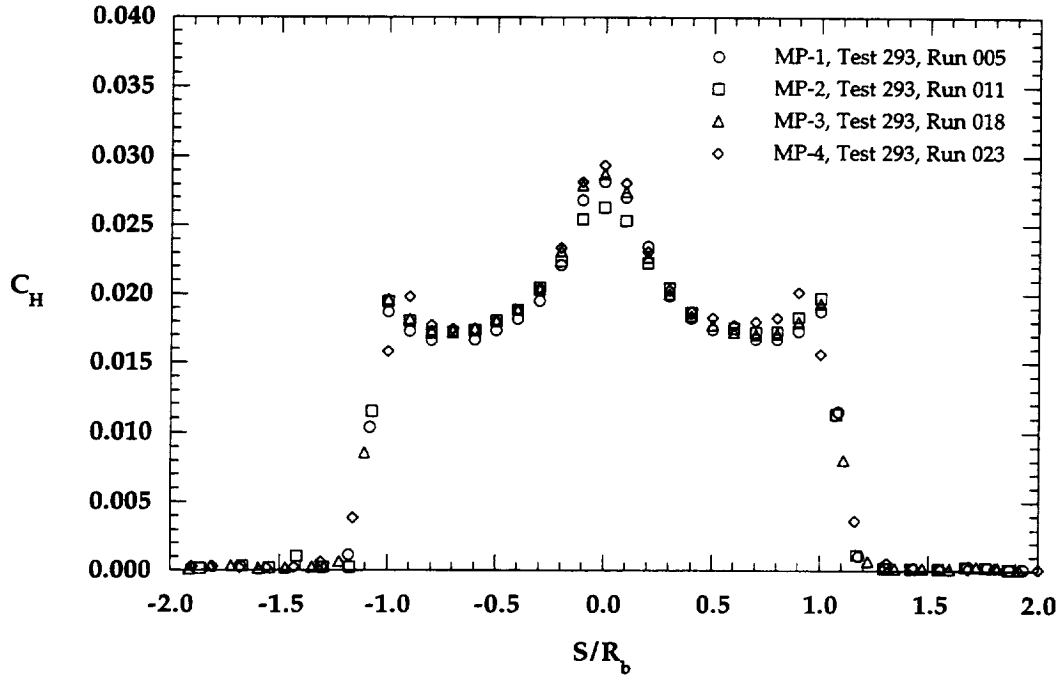

Figure 6.1.17a Configuration Effects on Forebody, α = 0 deg, $Re_\infty = 0.5 \times 10^6$ ft^{-1}

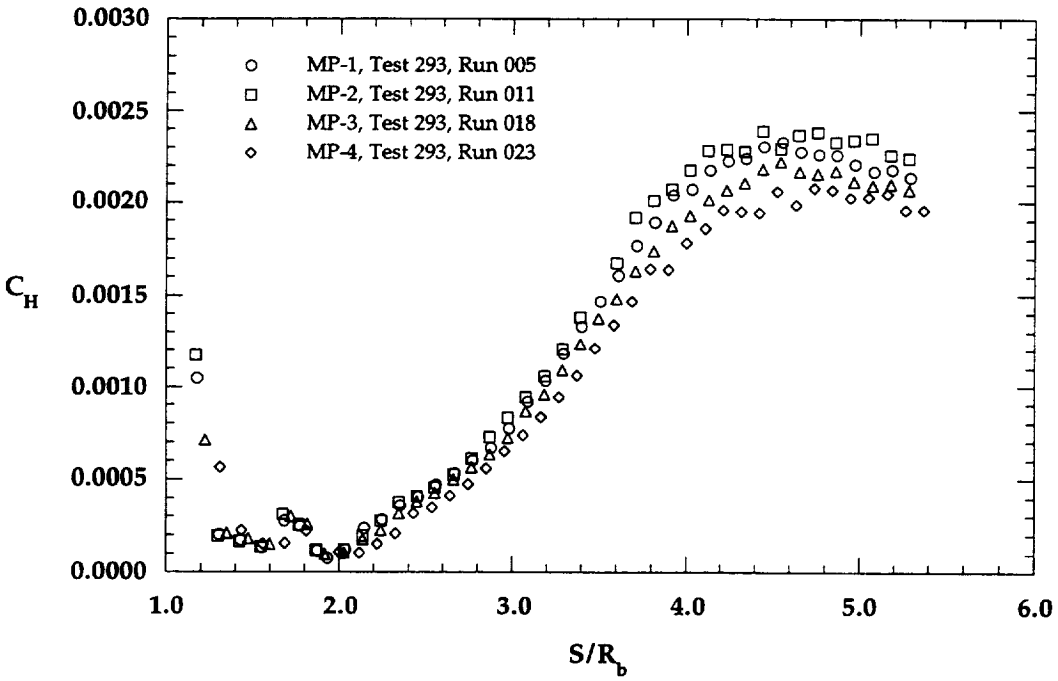

Figure 6.1.17b Configuration Effects on Wake, α = 0 deg, $Re_\infty = 0.5 \times 10^6$ ft^{-1}

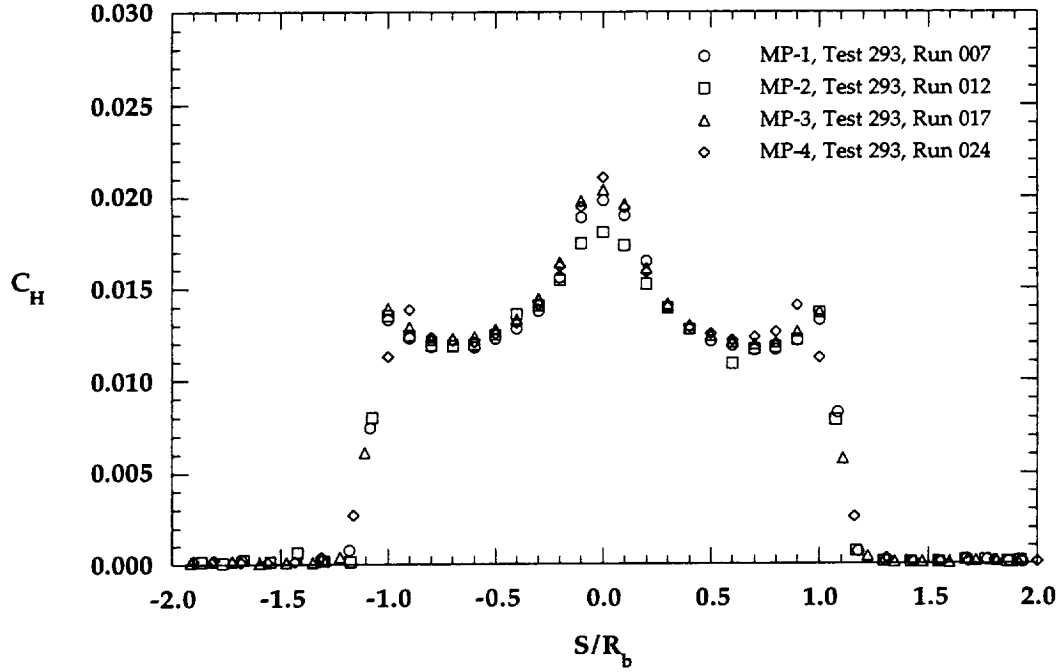

Figure 6.1.18a Configuration Effects on Forebody, $\alpha = 0$ deg, $Re_\infty = 1.0x10^6$ ft^{-1}

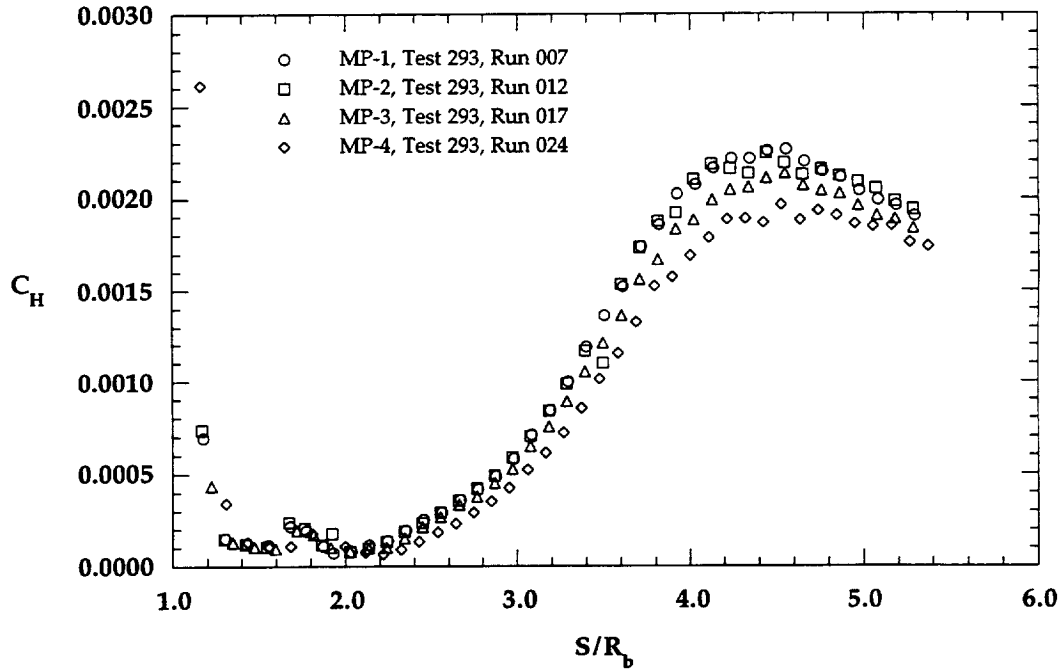

Figure 6.1.18b Configuration Effects on Wake, $\alpha = 0$ deg, $Re_\infty = 1.0x10^6$ ft^{-1}

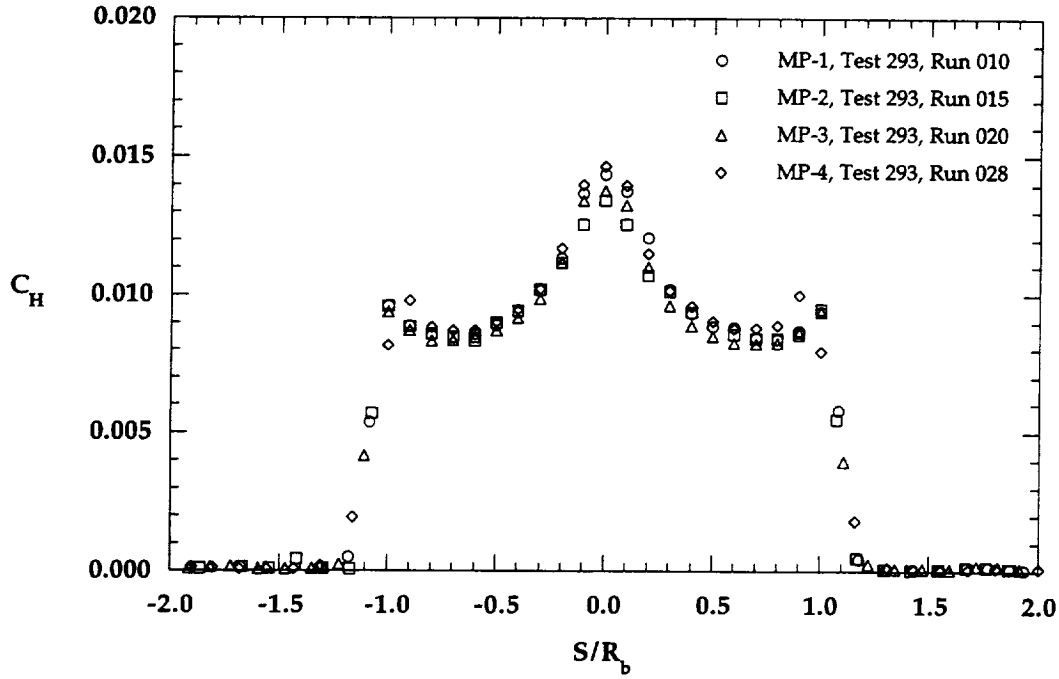

Figure 6.1.19a Configuration Effects on Forebody, $\alpha = 0$ deg, $Re_\infty = 2.0x10^6$ ft^{-1}

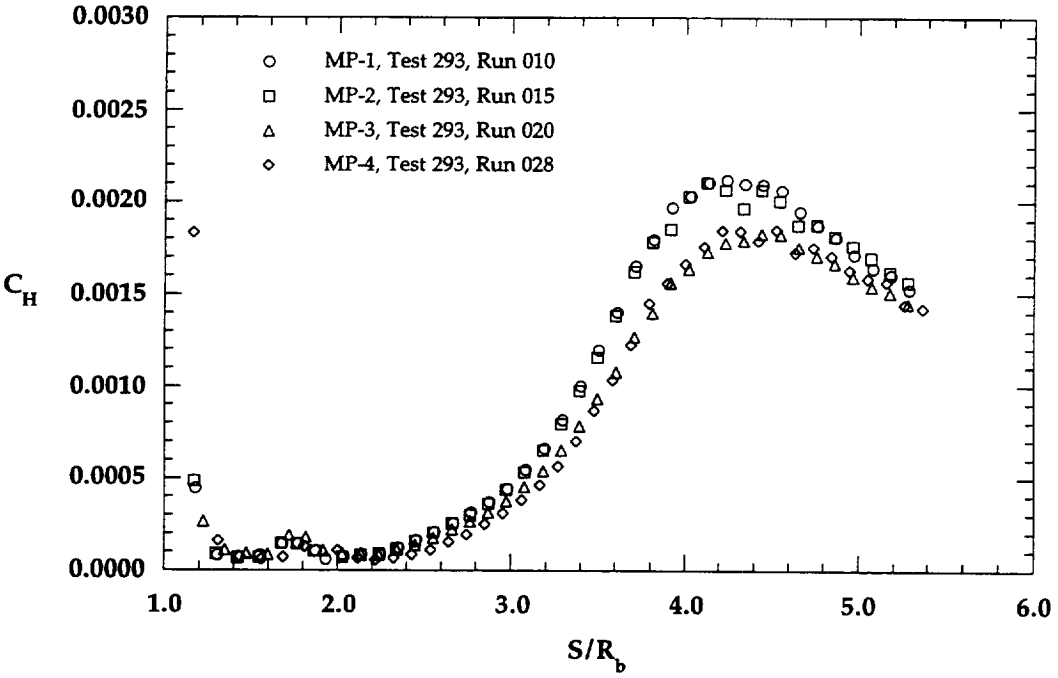

Figure 6.1.19b Configuration Effects on Wake, $\alpha = 0$ deg, $Re_\infty = 2.0x10^6$ ft^{-1}

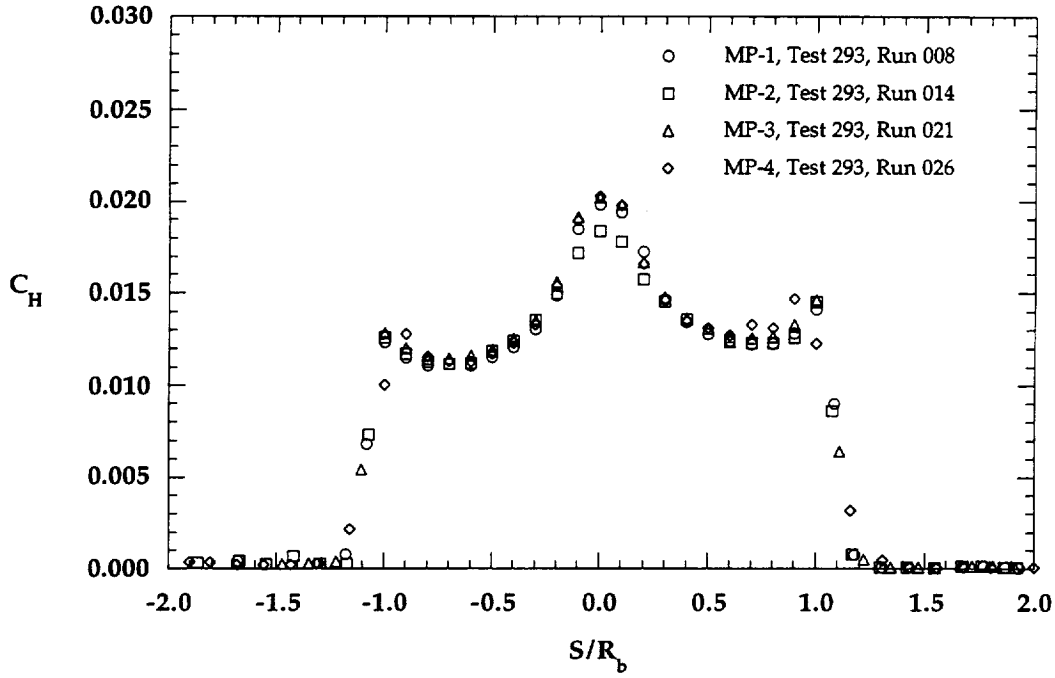

Figure 6.1.20a Configuration Effects on Forebody, α = -4 deg, Re_∞ = 1.0x10^6 ft^{-1}

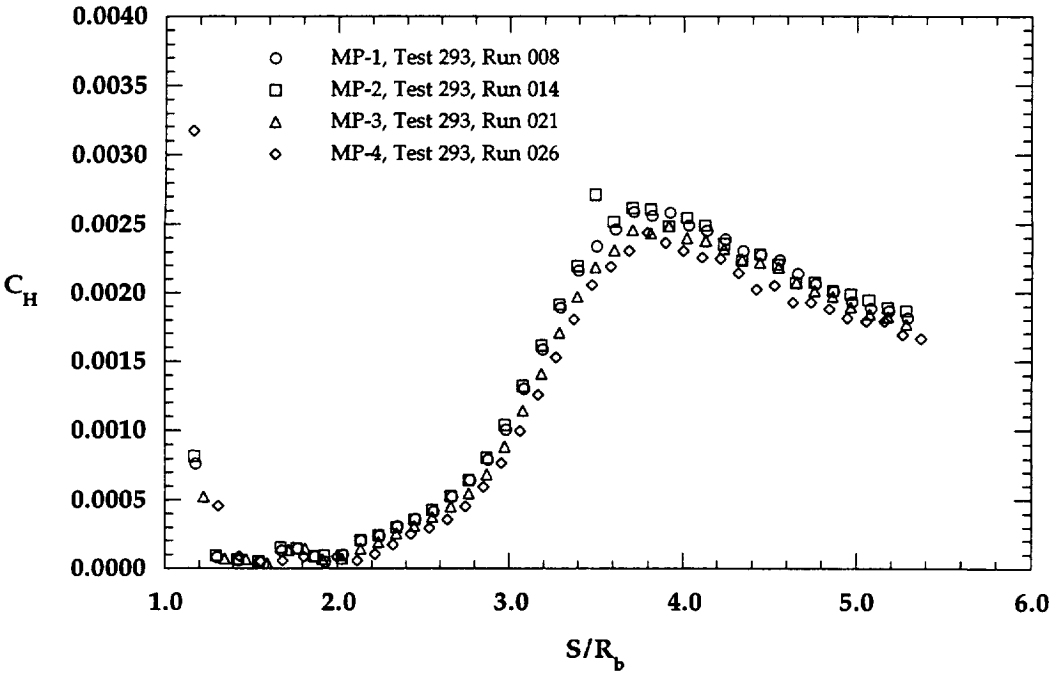

Figure 6.1.20a Configuration Effects on Wake, α = -4 deg, Re_∞ = 1.0x10^6 ft^{-1}

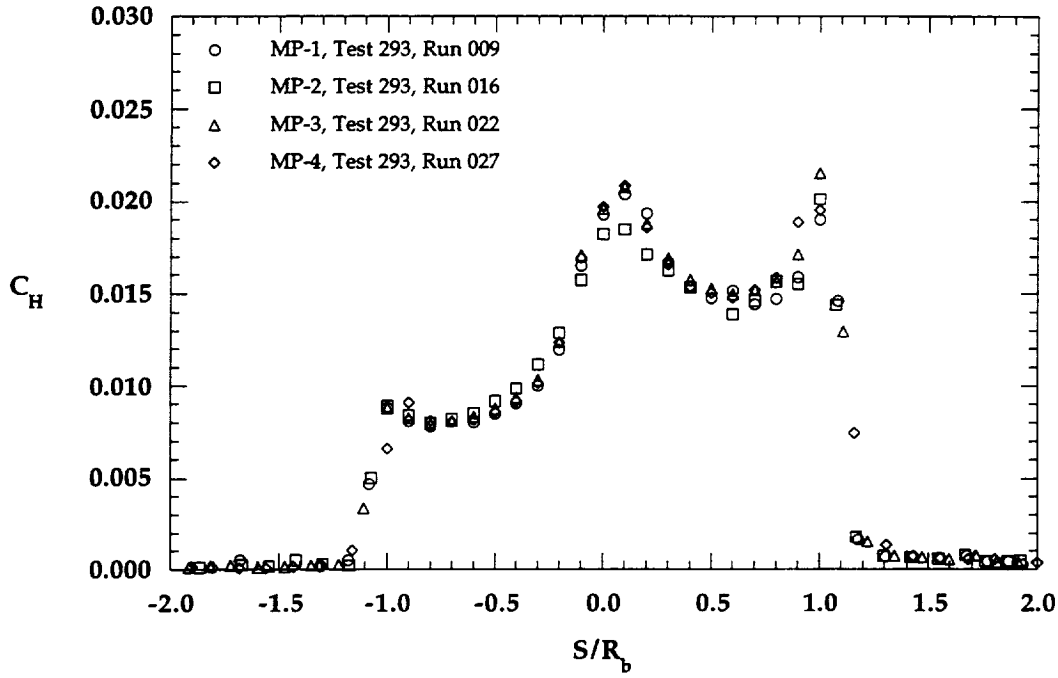

Figure 6.1.21a Configuration Effects on Forebody, α = -20 deg, Re_∞ = 1.0x10^6 ft^{-1}

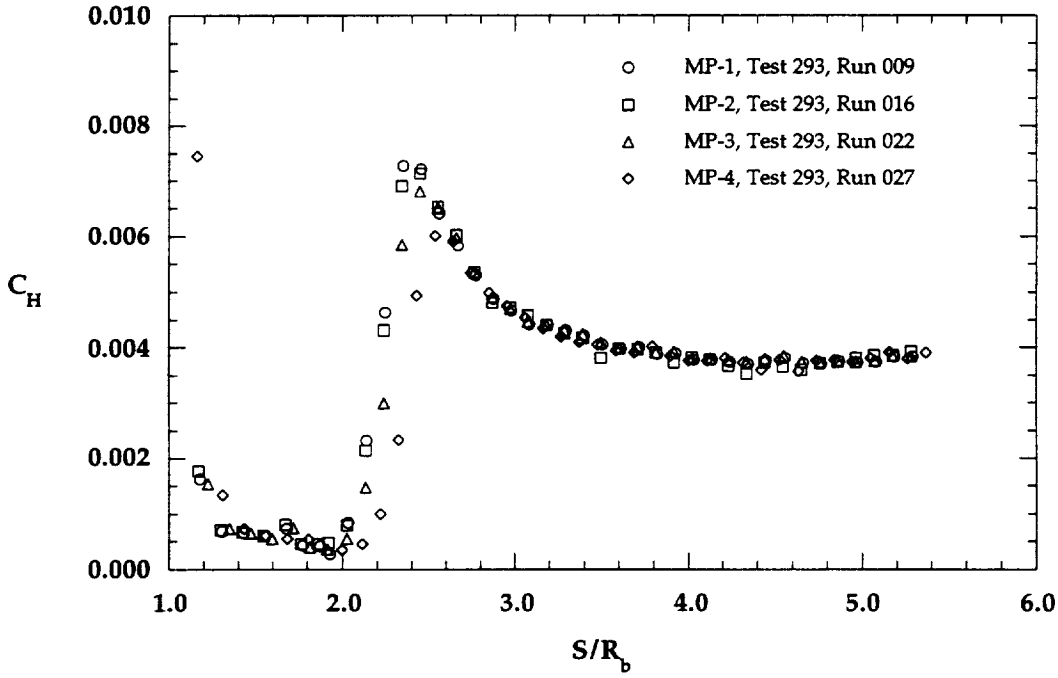

Figure 6.1.21b Configuration Effects on Wake, α = -20 deg, Re_∞ = 1.0x10^6 ft^{-1}

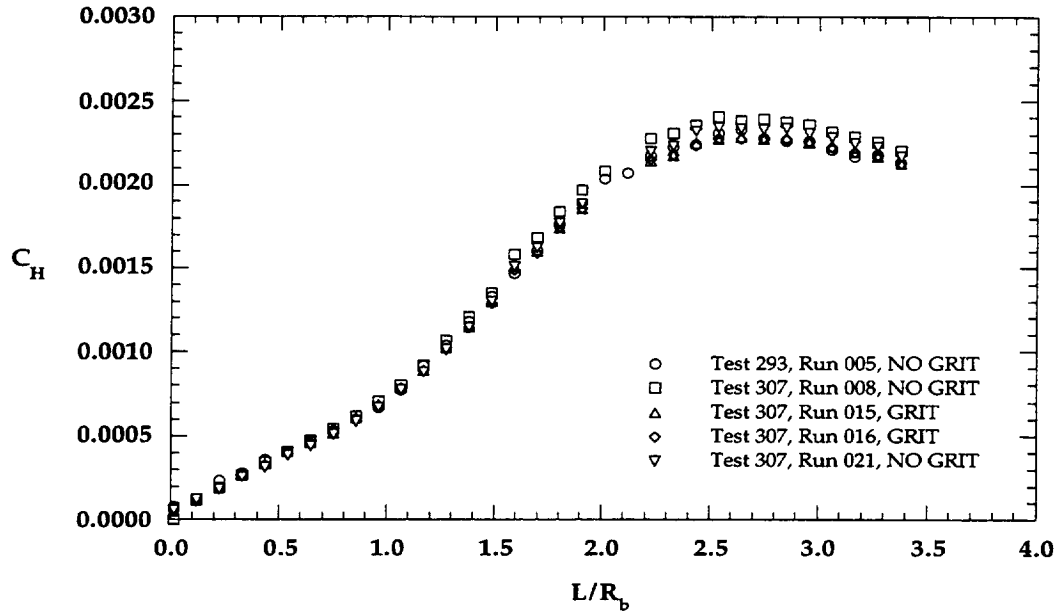

Figure 6.1.22a Transition Grit Effects, MP-1 Configuration, $Re_\infty = 0.5x10^6$ ft^{-1}

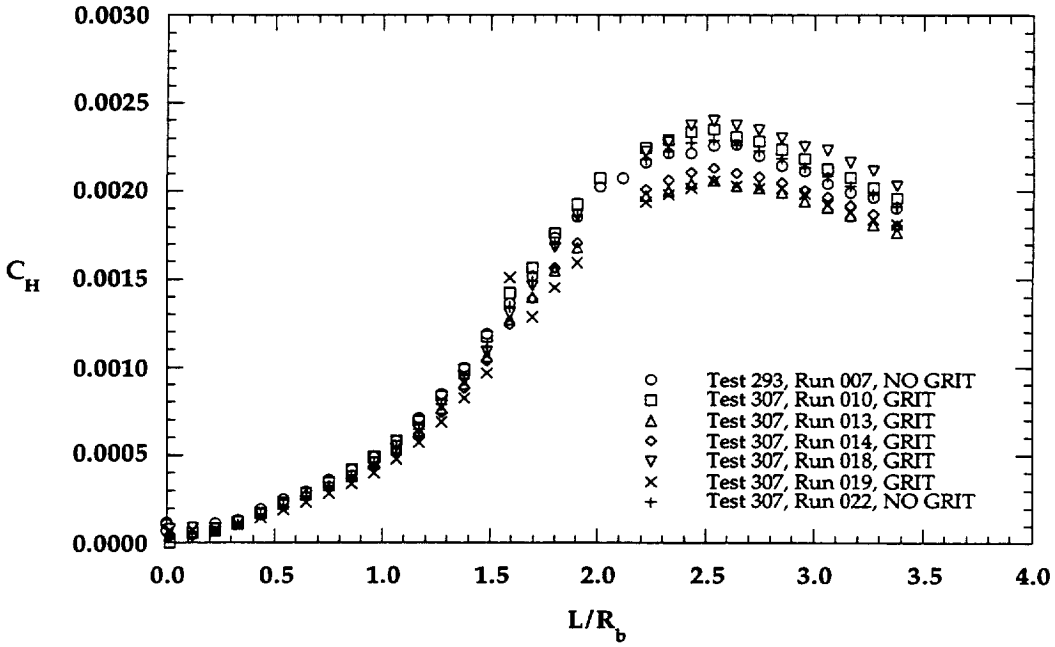

Figure 6.1.22b Transition Grit Effects, MP-1 Configuration, $Re_\infty = 1.0x10^6$ ft^{-1}

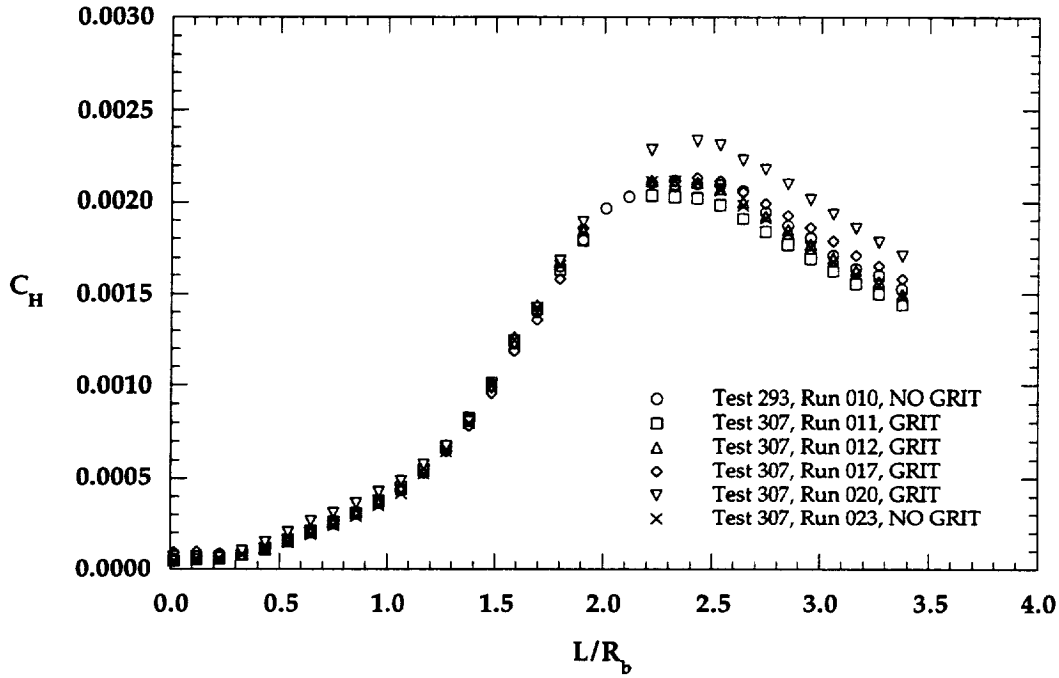

Figure 6.1.22c Transition Grit Effects, MP-1 Configuration, $Re_\infty = 2.0x10^6$ ft^{-1}

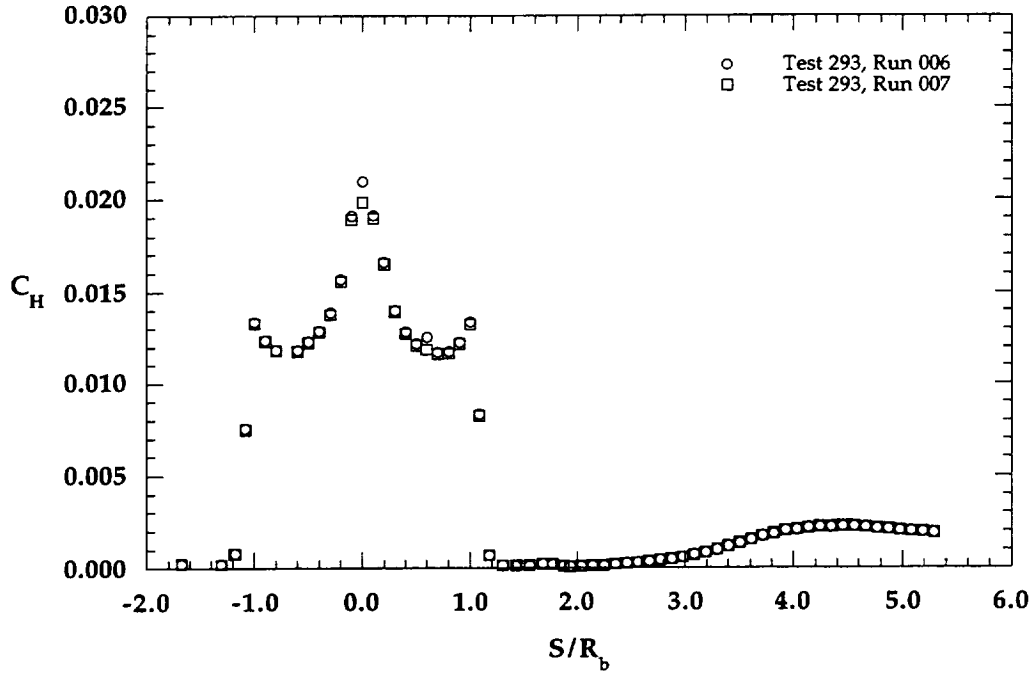

Figure 6.1.23a Repeatability, MP-1 Configuration, $Re_\infty = 1.0x10^6$ ft^{-1} (linear scale)

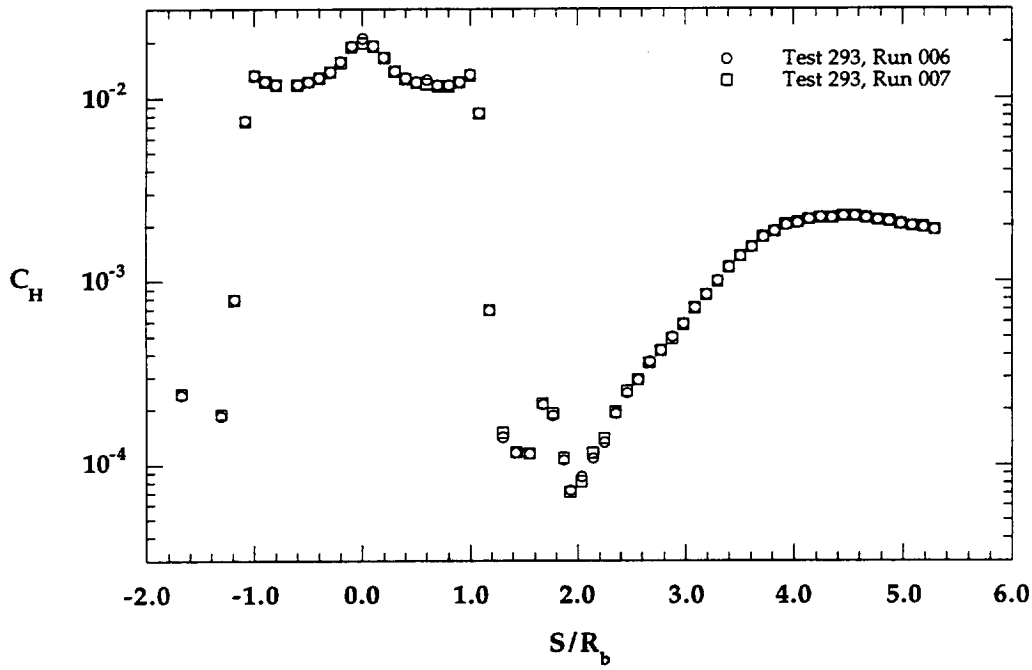

Figure 6.1.23b Repeatability, MP-1 Configuration, $Re_\infty = 1.0x10^6$ ft^{-1} (log scale)

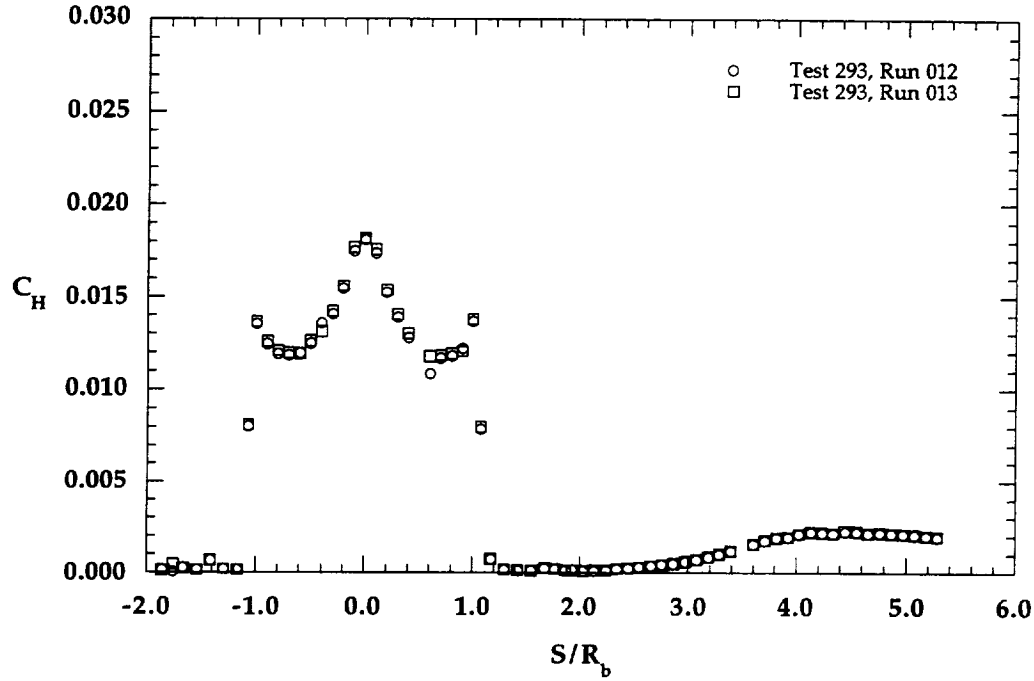

Figure 6.1.24a Repeatability, MP-2 Configuration, $Re_\infty = 1.0x10^6$ ft^{-1} (linear scale)

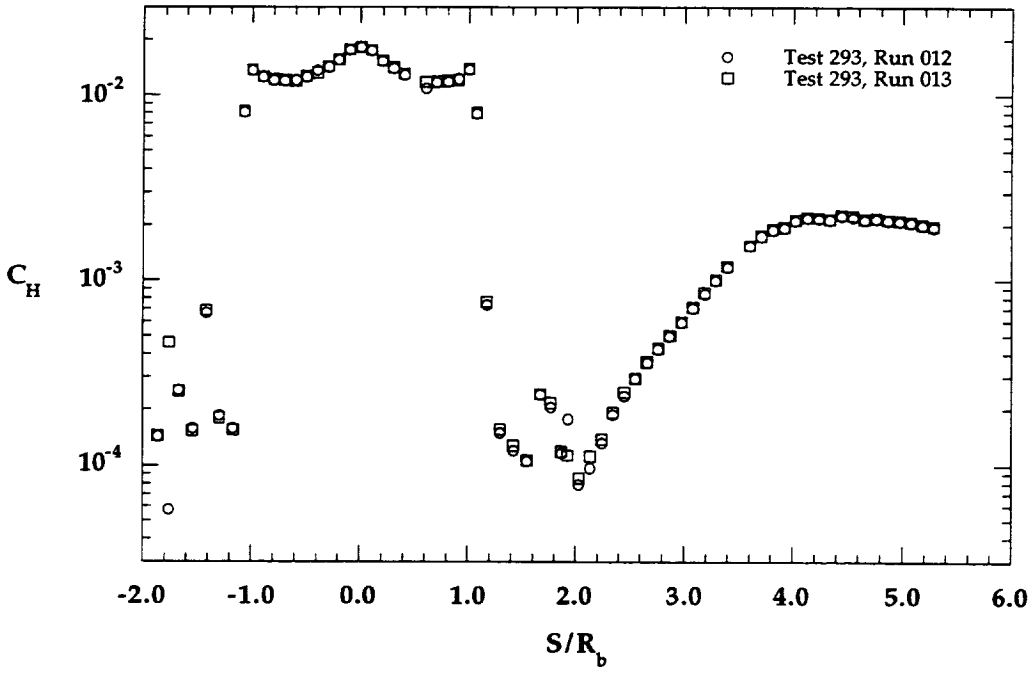

Figure 6.1.24b Repeatability, MP-2 Configuration, $Re_\infty = 1.0x10^6$ ft^{-1} (log scale)

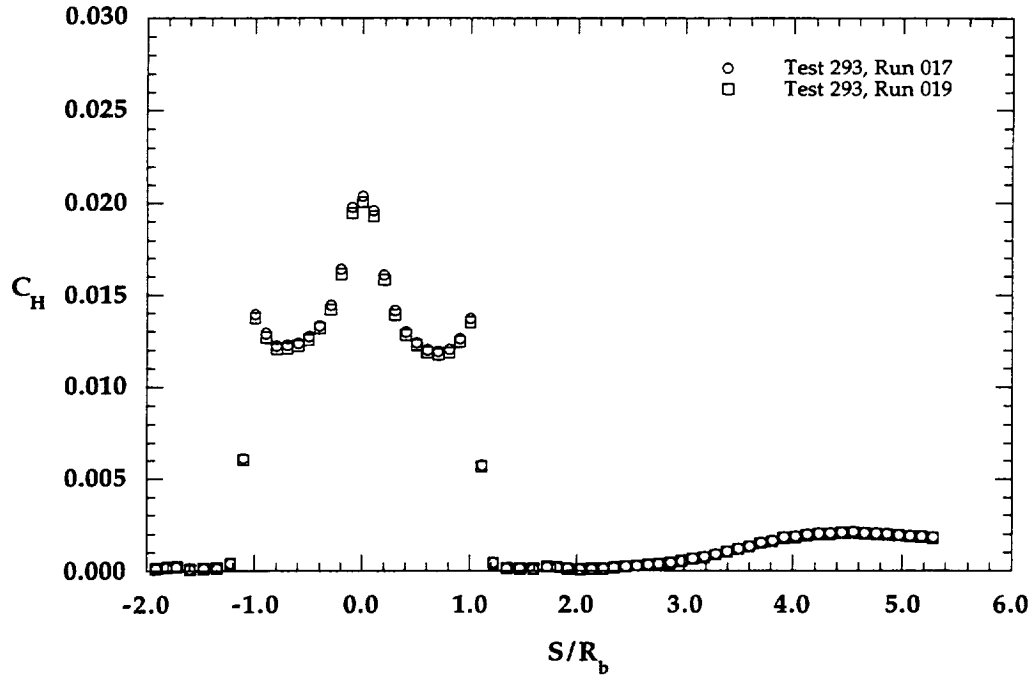

Figure 6.1.25a Repeatability, MP-3 Configuration, $Re_\infty = 1.0x10^6$ ft^{-1} (linear scale)

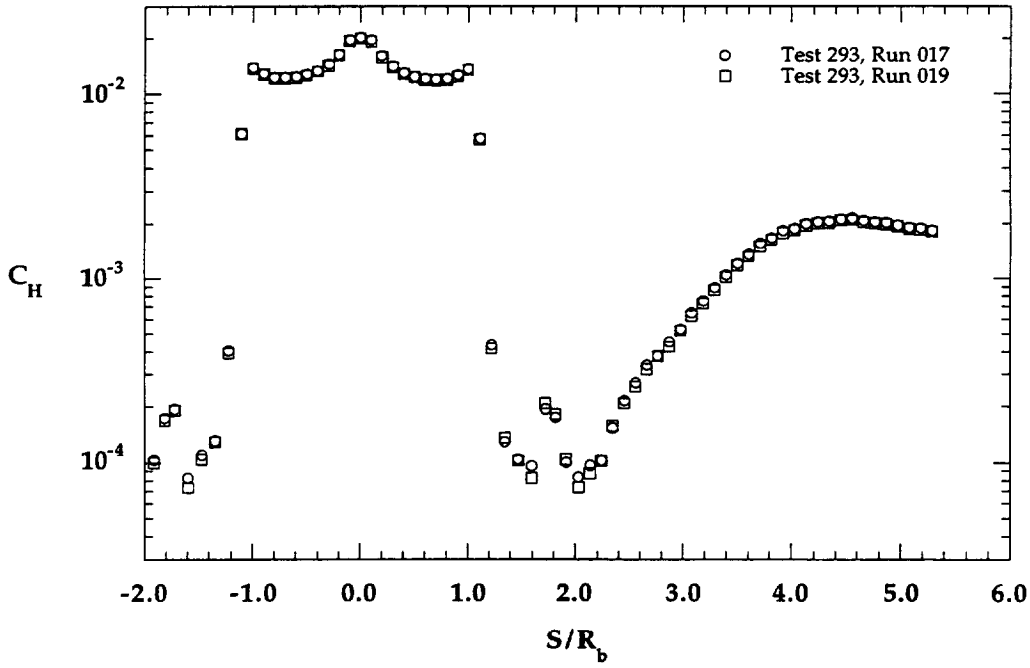

Figure 6.1.25b Repeatability, MP-3 Configuration, $Re_\infty = 1.0x10^6$ ft^{-1} (linear scale)

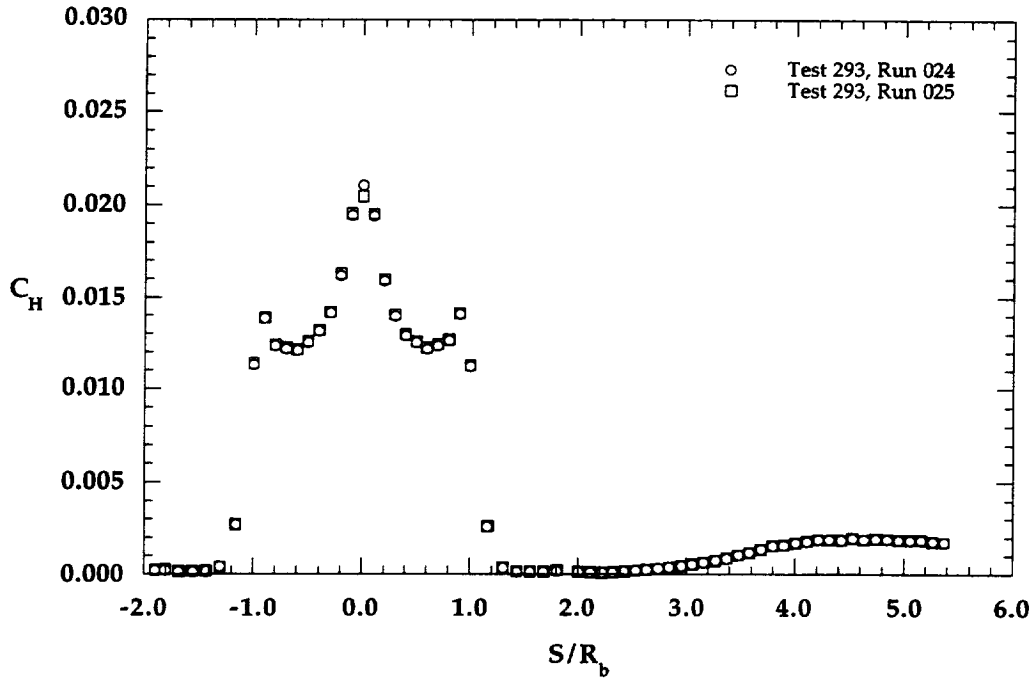

Figure 6.1.26a Repeatability, MP-4 Configuration, $Re_\infty = 1.0x10^6$ ft^{-1} (linear scale)

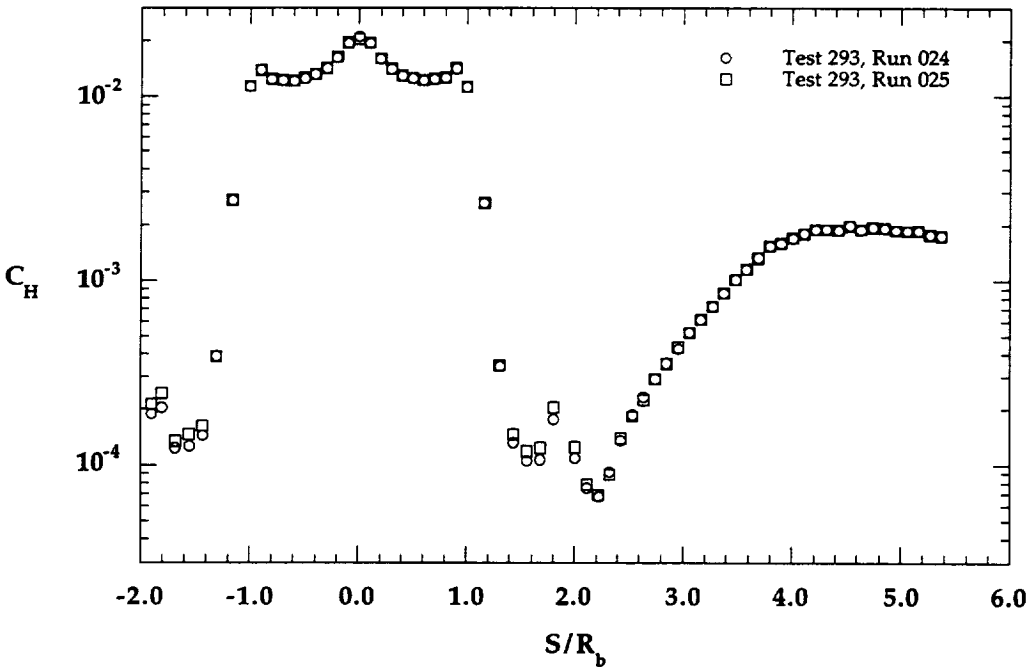

Figure 6.1.26b Repeatability, MP-4 Configuration, $Re_\infty = 1.0x10^6$ ft^{-1} (linear scale)

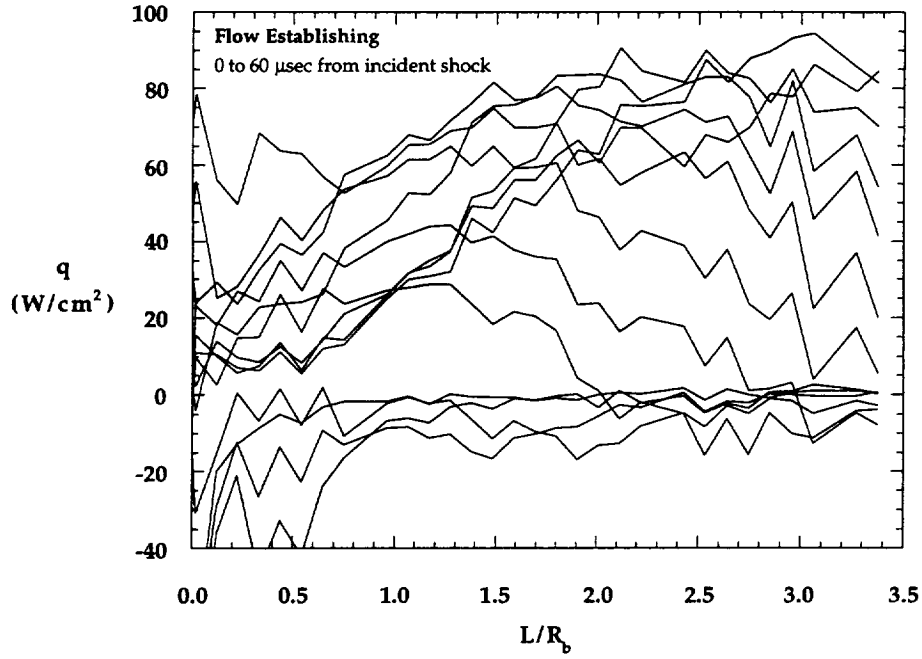

Figure 6.2.1a Wake Flow Establishment Movie, Run 749: 0 to 60 μsec

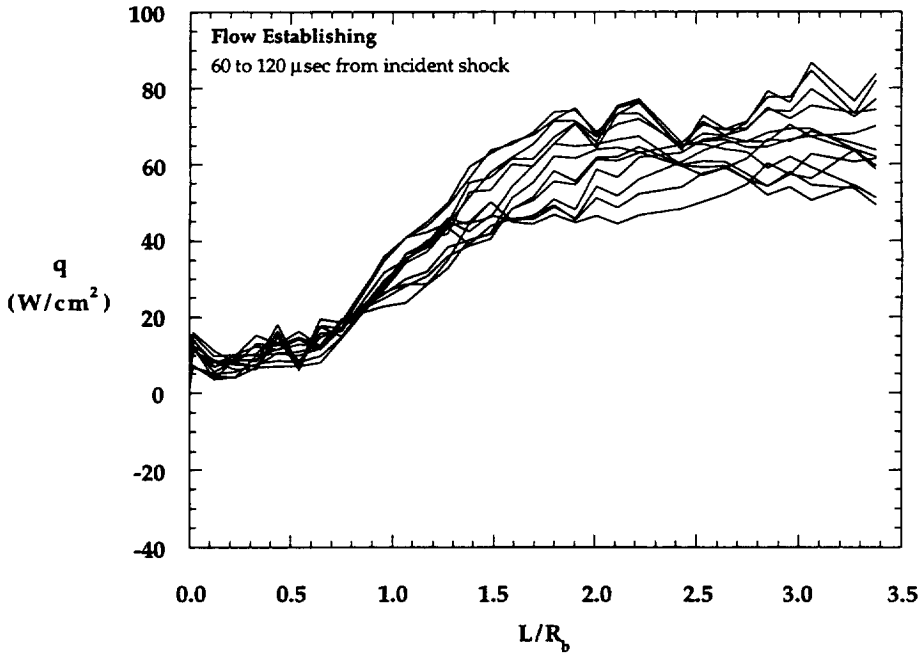

Figure 6.2.1b Wake Flow Establishment Movie, Run 749: 60 to 120 μsec

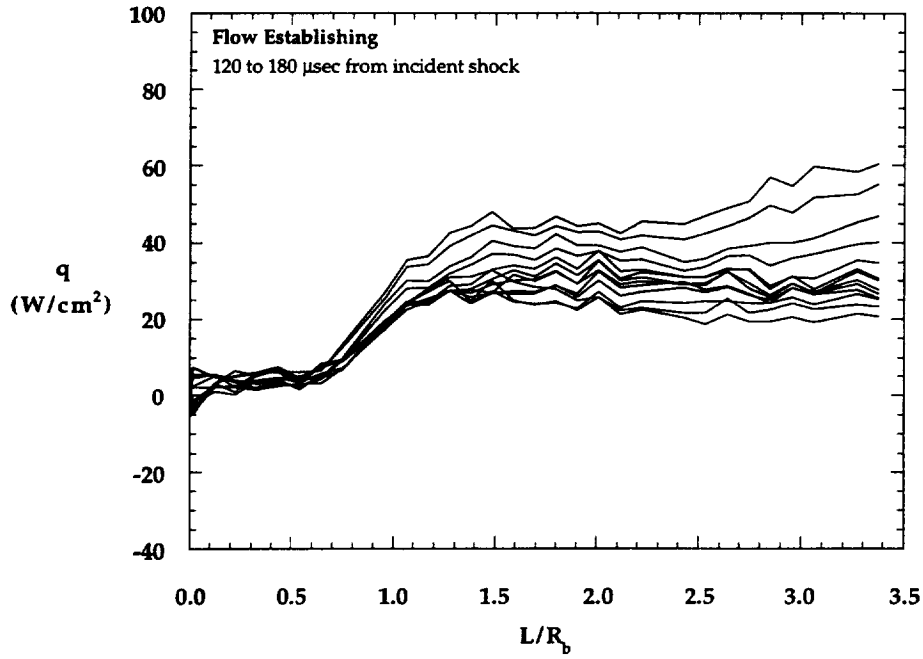

Figure 6.2.1c Wake Flow Establishment Movie, Run 749: 120 to 180 μsec

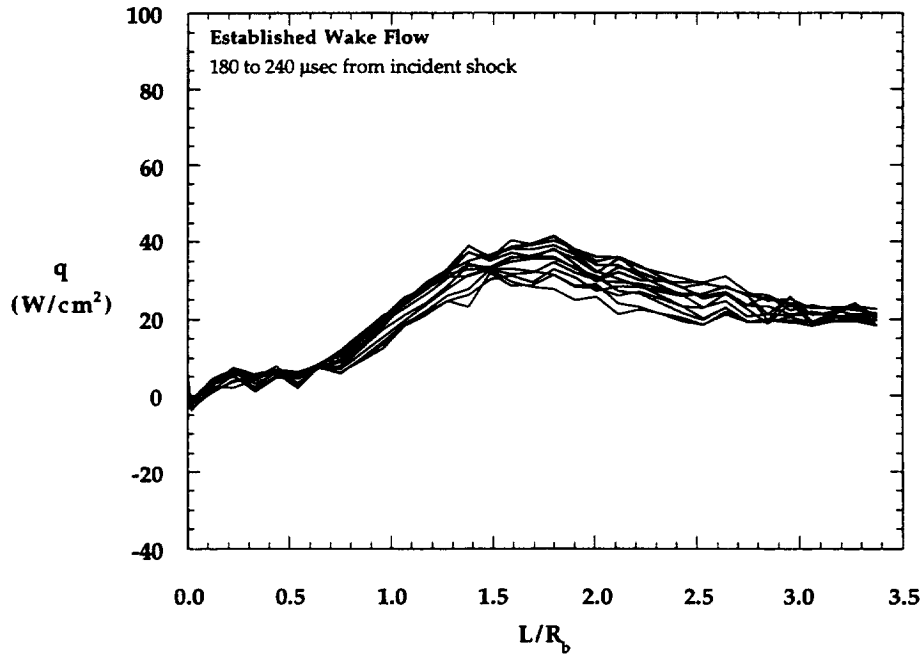

Figure 6.2.1d Wake Flow Establishment Movie, Run 749: 180 to 240 μsec

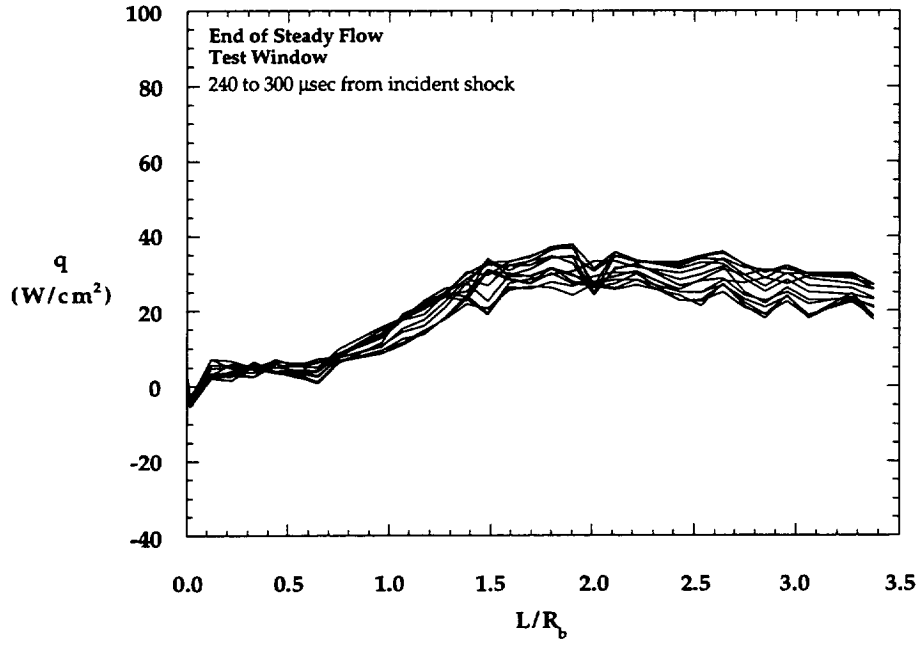

Figure 6.2.1e Wake Flow Establishment Movie, Run 749: 240 to 300 μsec

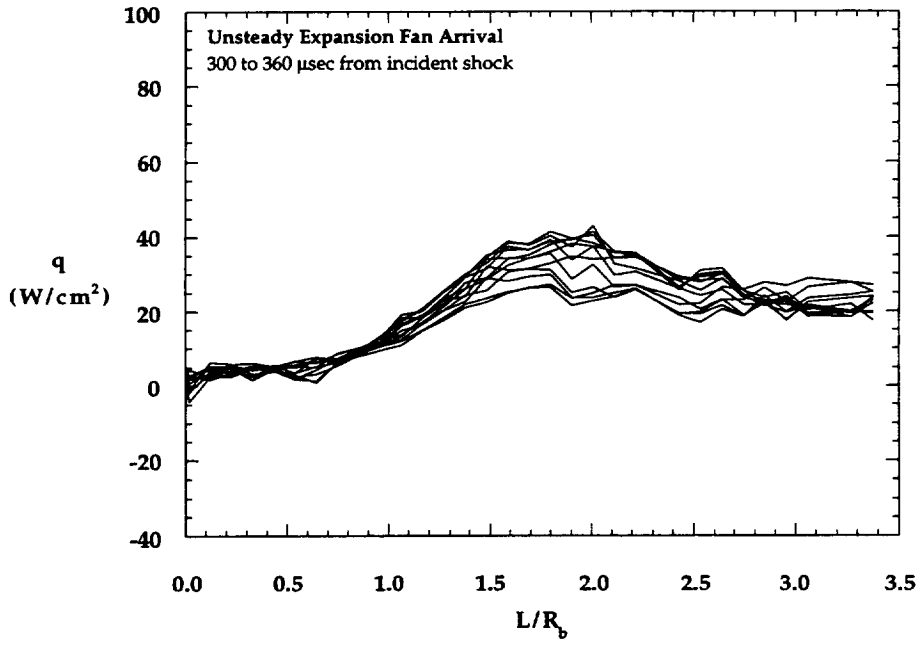

Figure 6.2.1f Wake Flow Establishment Movie, Run 749: 300 to 360 μsec

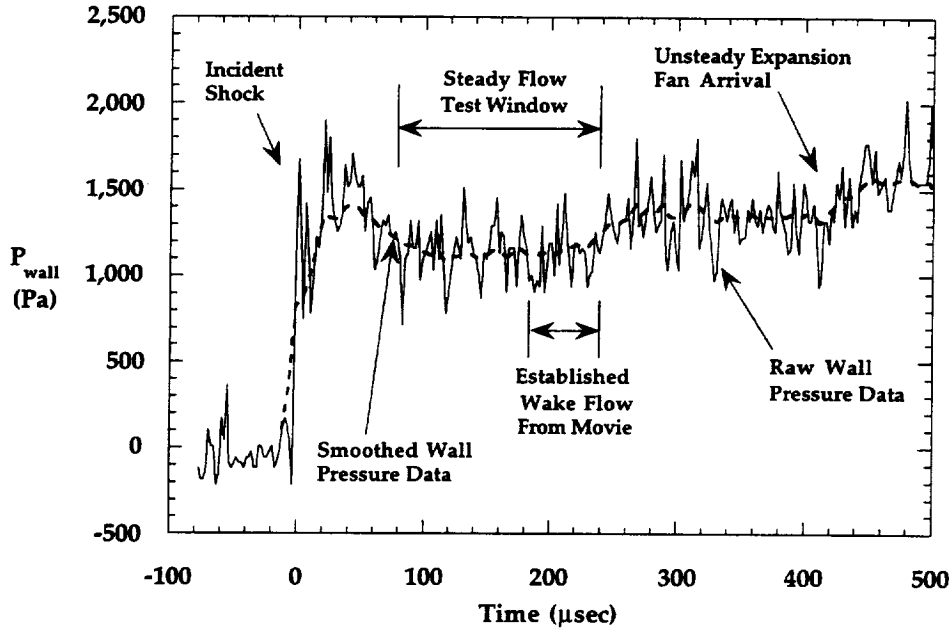

Figure 6.2.2 Wall Pressure Time-History, Run 749

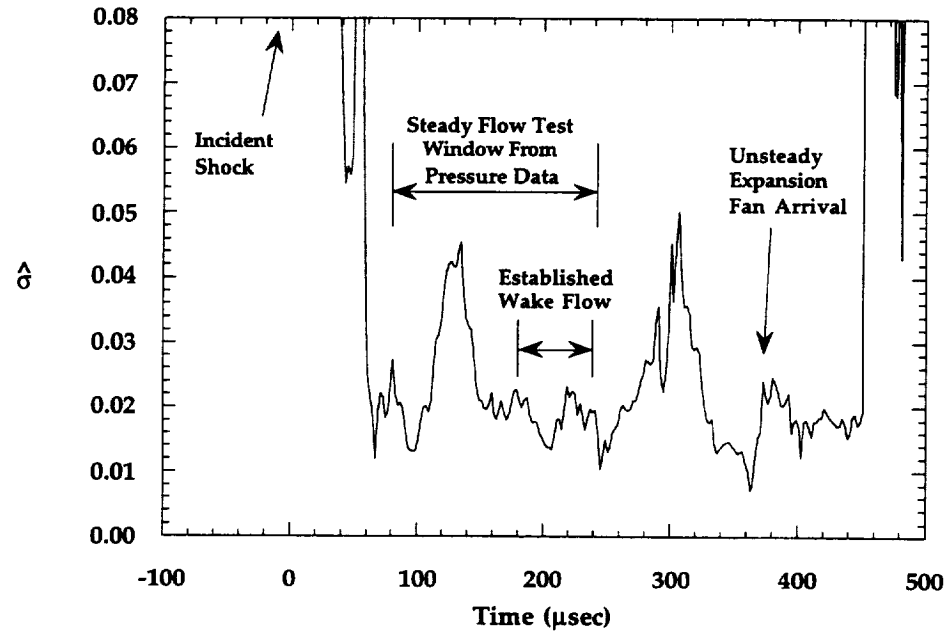

Figure 6.2.3 Wake RMS Time-History, Run 749

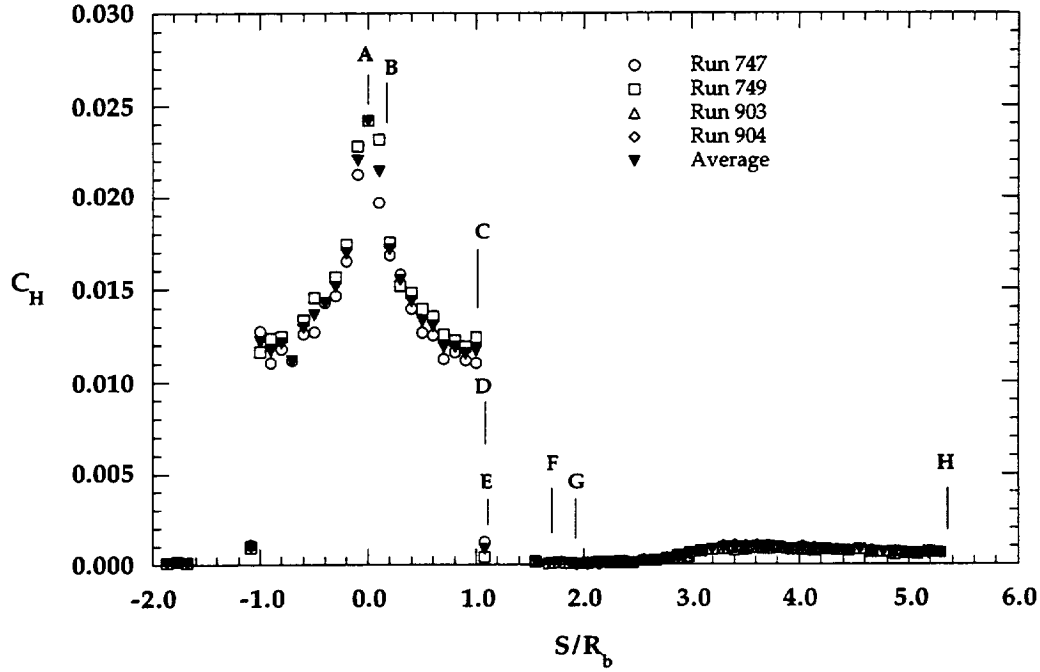

Figure 6.2.4a MP-1 Configuration, $\alpha = 0$ deg, CO_2 in HYPULSE (linear scale)

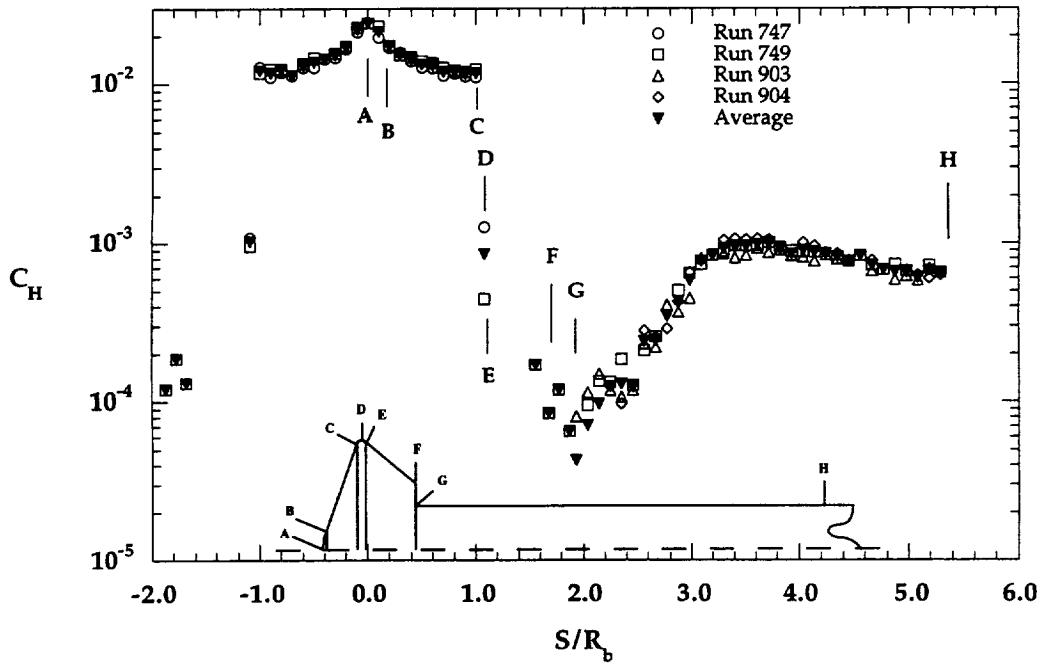

Figure 6.2.4b MP-1 Configuration, $\alpha = 0$ deg, CO_2 in HYPULSE (log scale)

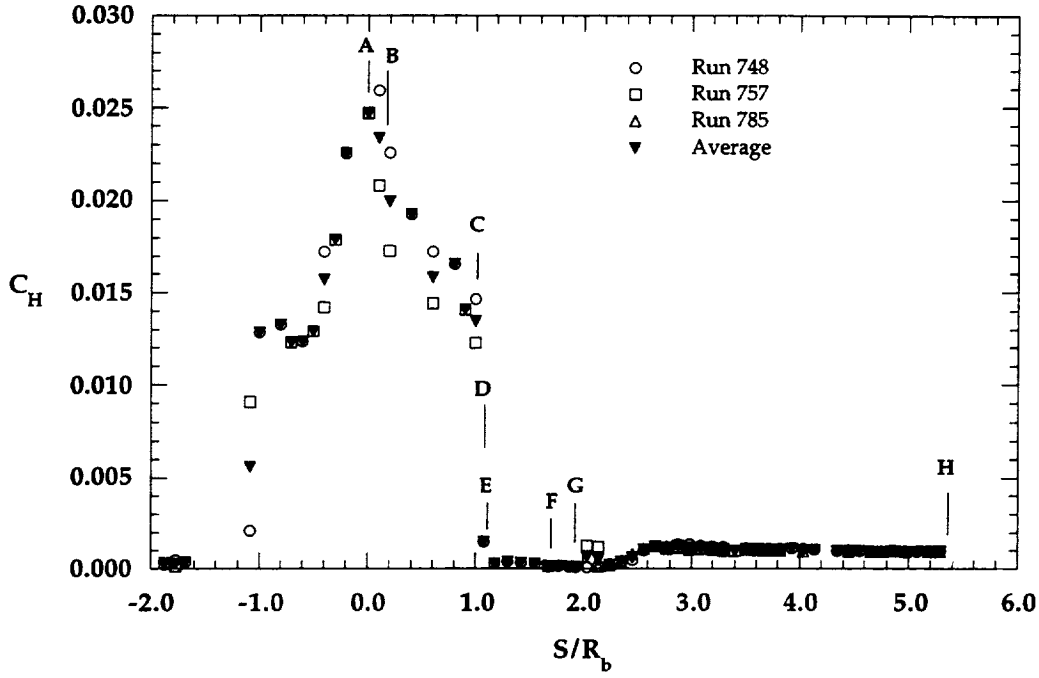

Figure 6.2.5a MP-1 Configuration, α = -4 deg, CO_2 in HYPULSE (linear scale)

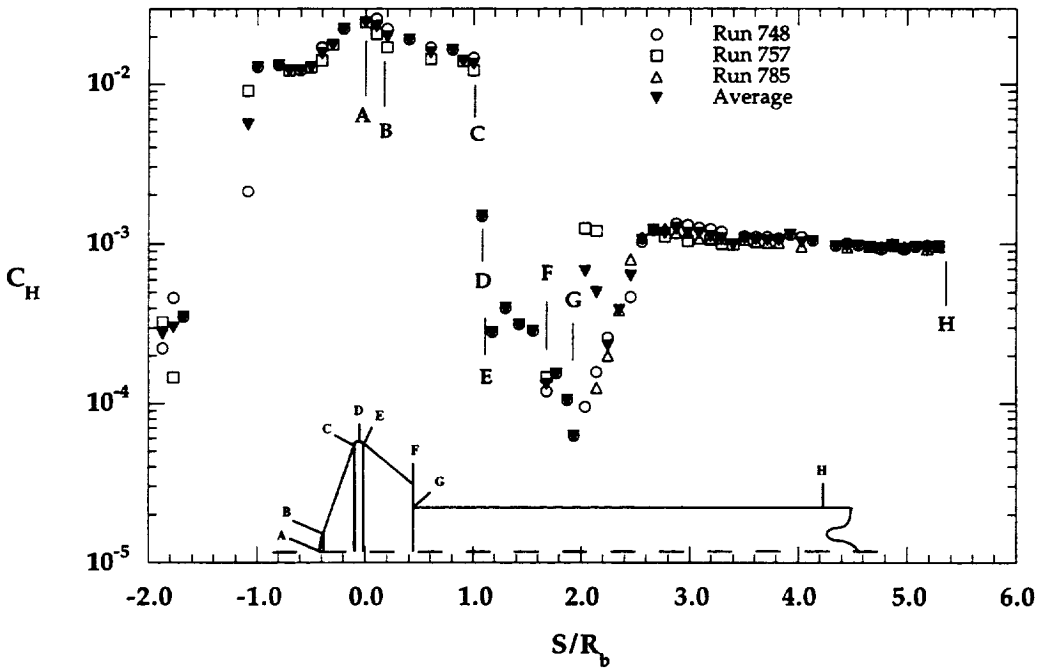

Figure 6.2.5b MP-1 Configuration, α = -4 deg, CO_2 in HYPULSE (log scale)

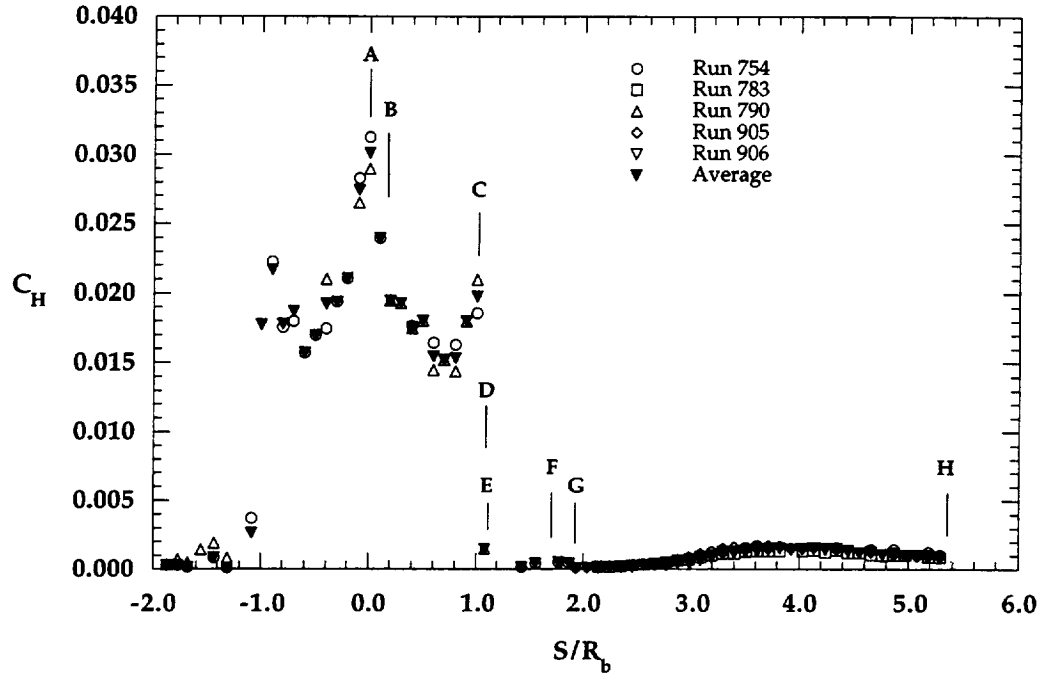

Figure 6.2.6a MP-1 Configuration, $\alpha = 0$ deg, Air in HYPULSE (linear scale)

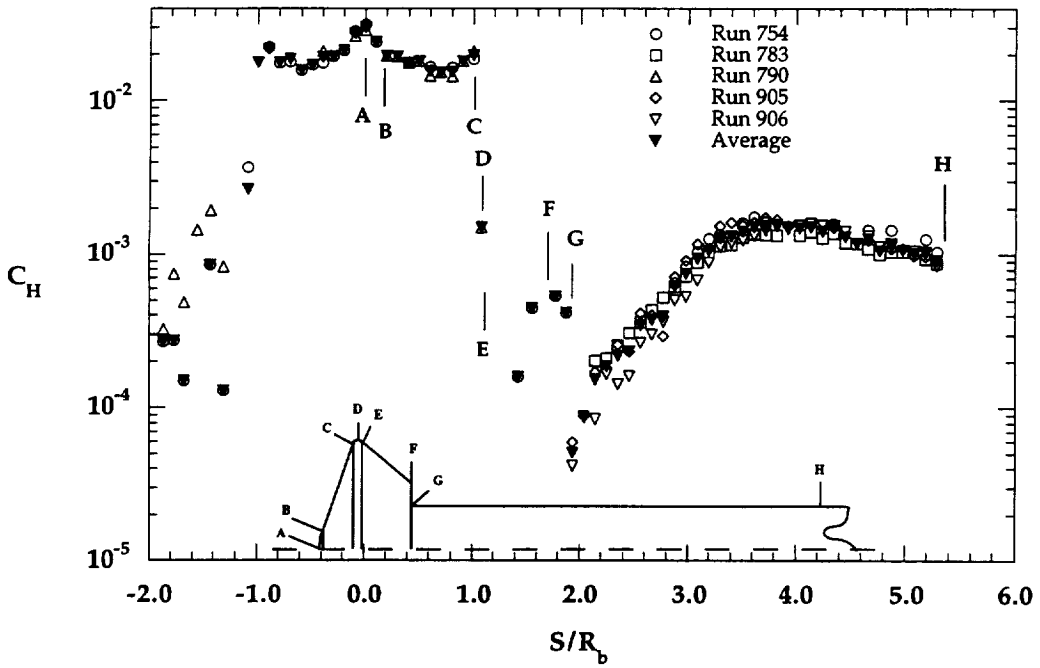

Figure 6.2.6b MP-1 Configuration, $\alpha = 0$ deg, Air in HYPULSE (log scale)

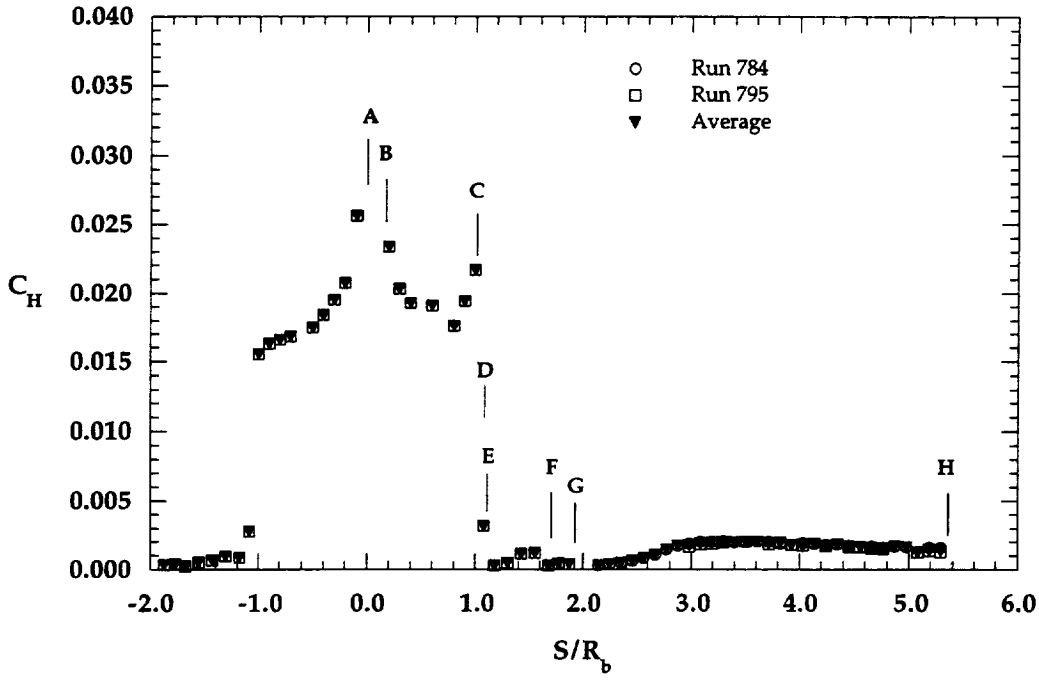

Figure 6.2.7a MP-1 Configuration, α = -4 deg, Air in HYPULSE (linear scale)

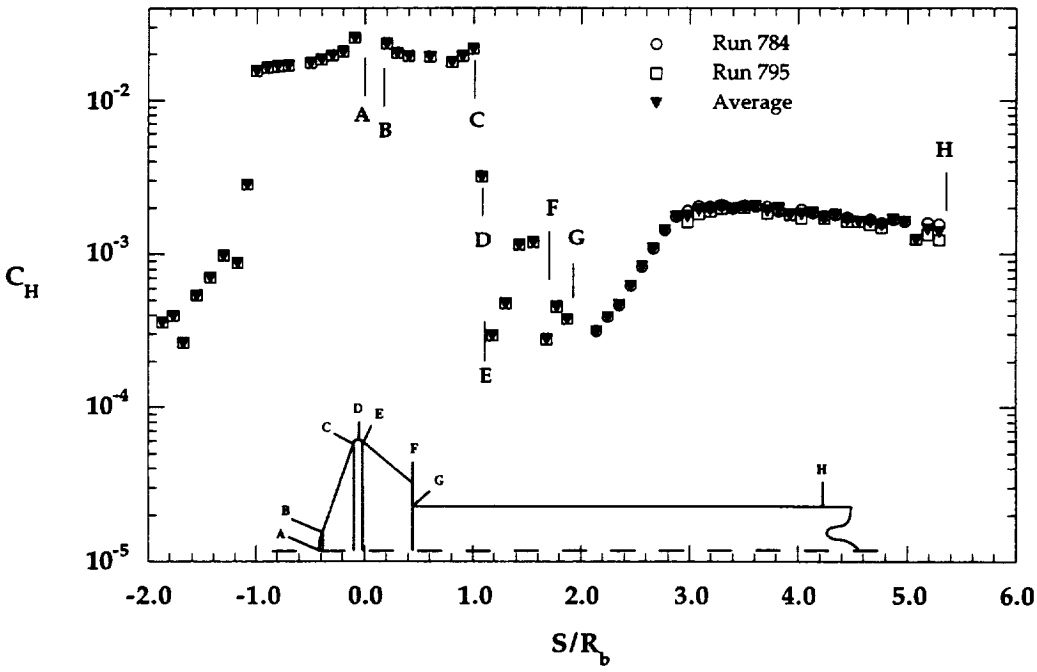

Figure 6.2.7b MP-1 Configuration, α = -4 deg, Air in HYPULSE (log scale)

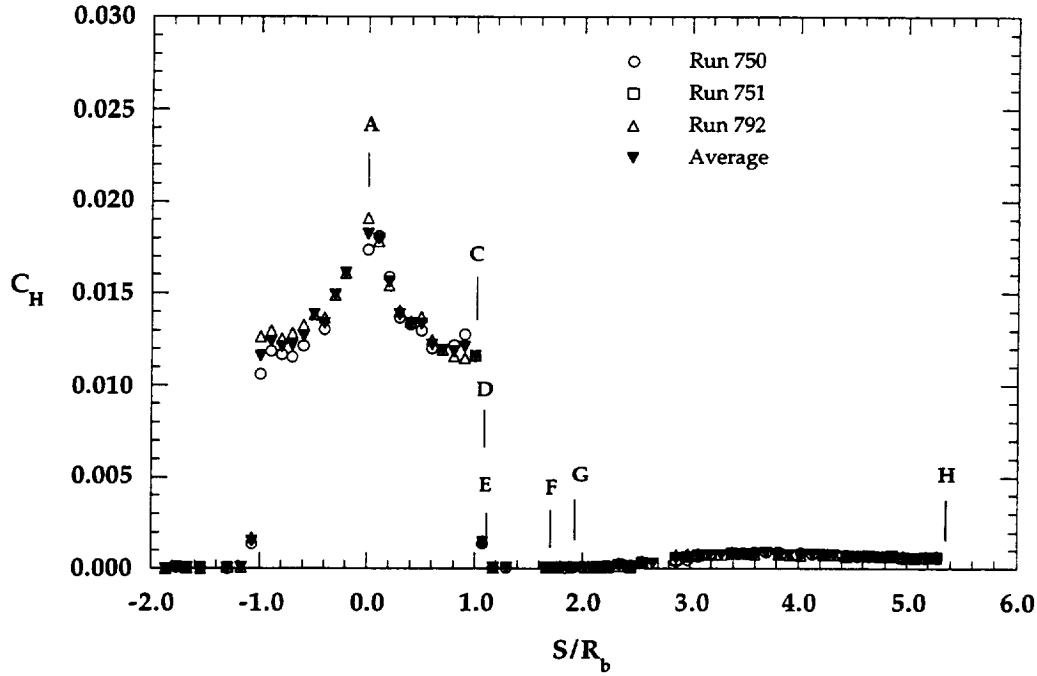

Figure 6.2.8a MP-2 Configuration, $\alpha = 0$ deg, CO_2 in HYPULSE (linear scale)

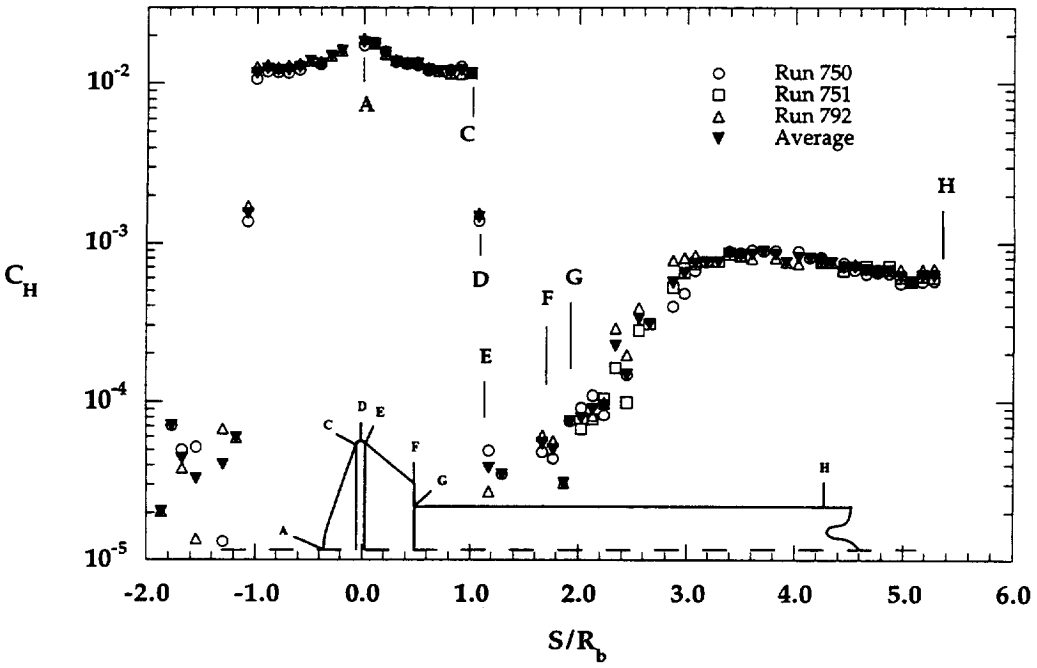

Figure 6.2.8b MP-2 Configuration, $\alpha = 0$ deg, CO_2 in HYPULSE (log scale)

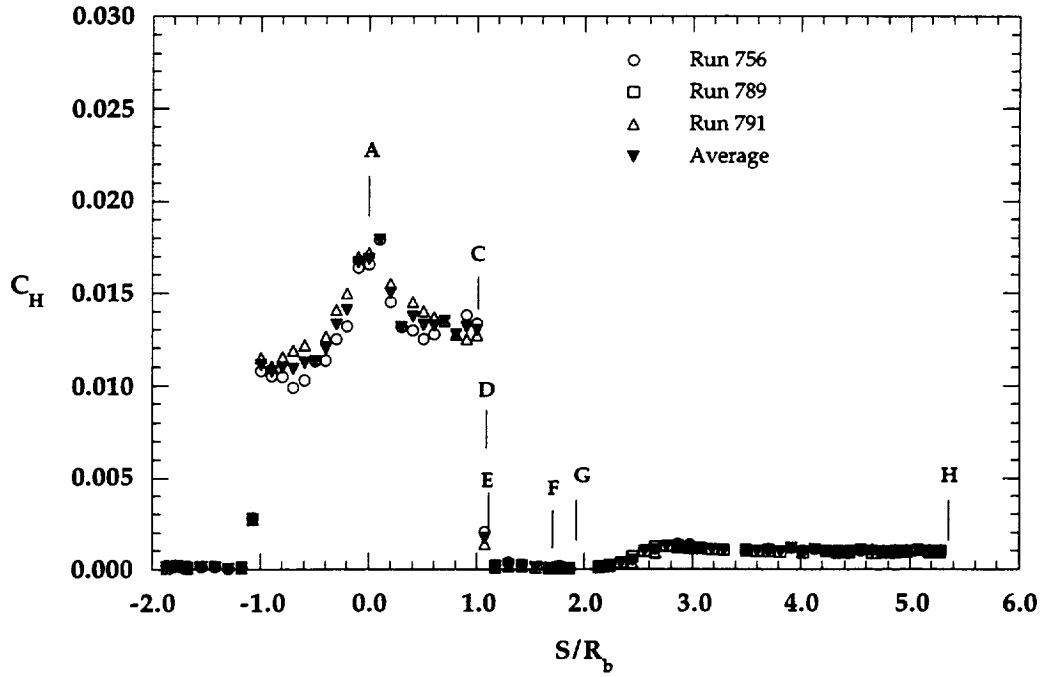

Figure 6.2.9a MP-2 Configuration, α = -4 deg, CO_2 in HYPULSE (linear scale)

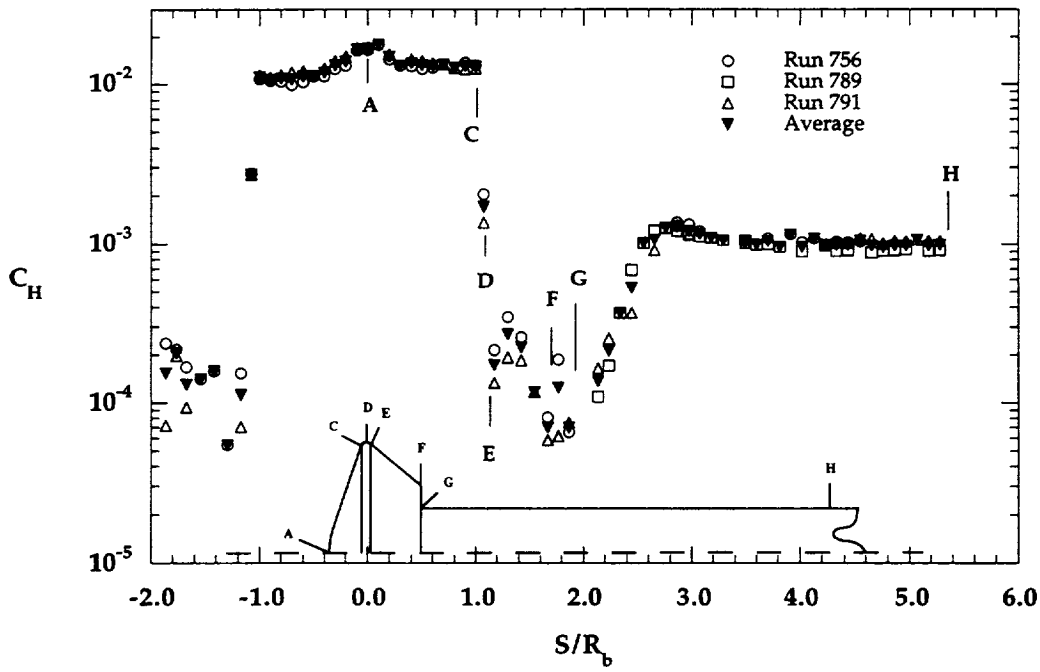

Figure 6.2.9b MP-2 Configuration, α = -4 deg, CO_2 in HYPULSE (log scale)

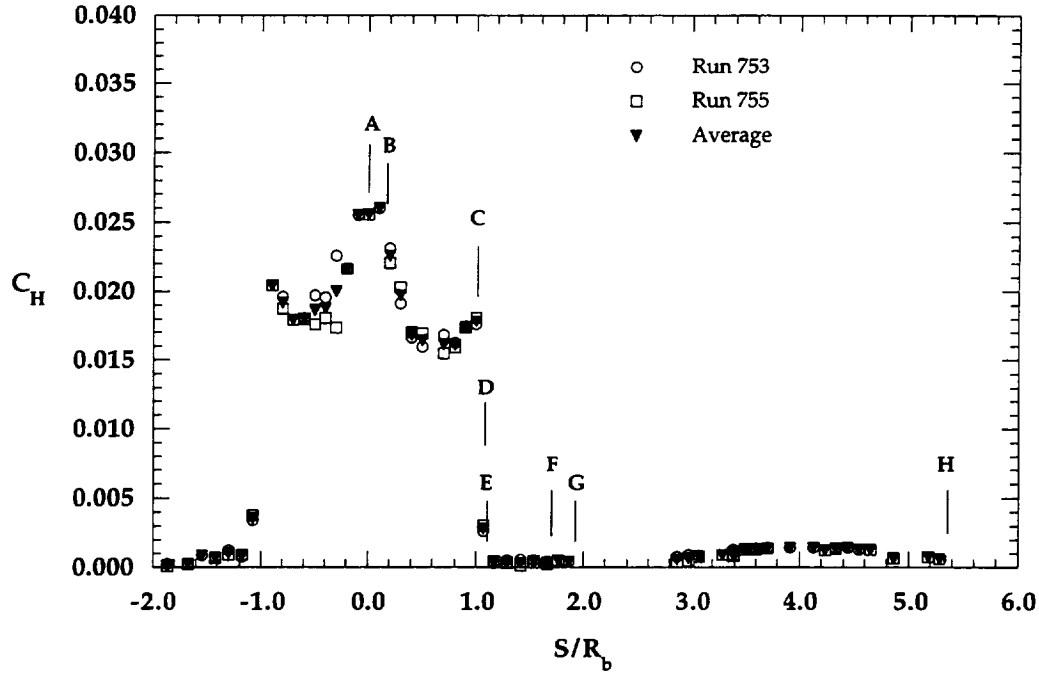

Figure 6.2.10a MP-2 Configuration, $\alpha = 0$ deg, Air in HYPULSE (linear scale)

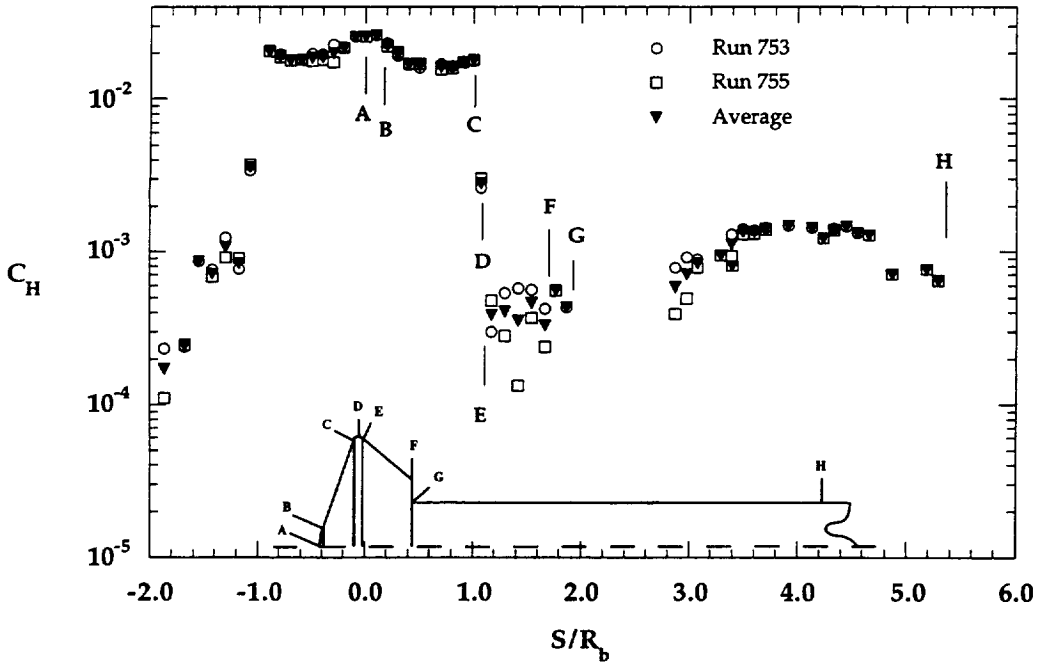

Figure 6.2.10b MP-2 Configuration, $\alpha = 0$ deg, Air in HYPULSE (log scale)

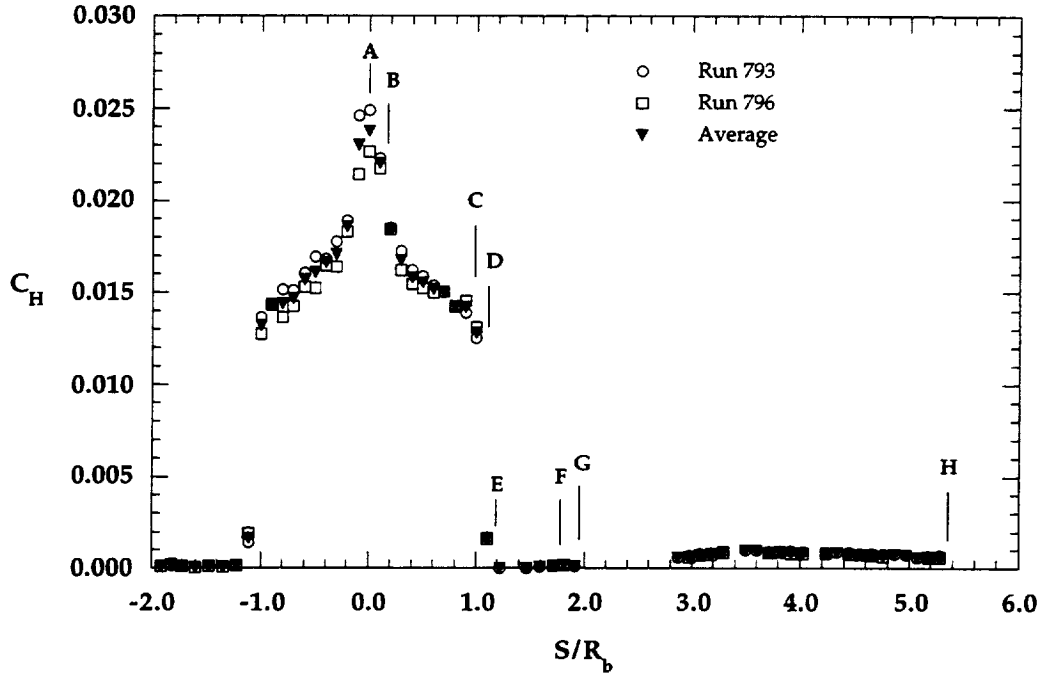

Figure 6.2.11a MP-3 Configuration, $\alpha = 0$ deg, CO_2 in HYPULSE (linear scale)

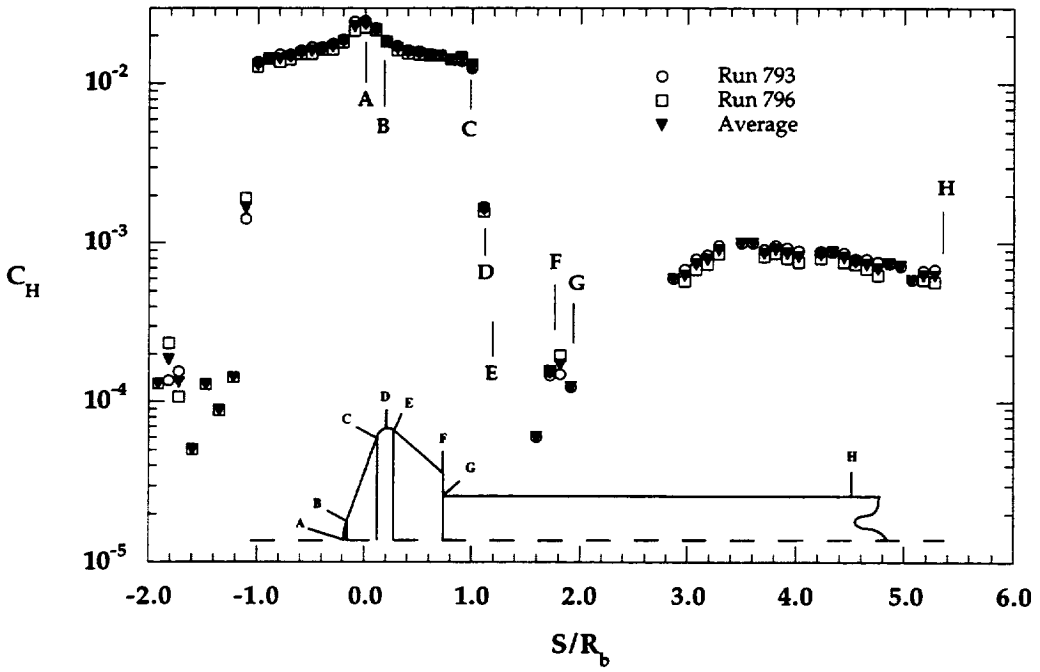

Figure 6.2.11b MP-3 Configuration, $\alpha = 0$ deg, CO_2 in HYPULSE (log scale)

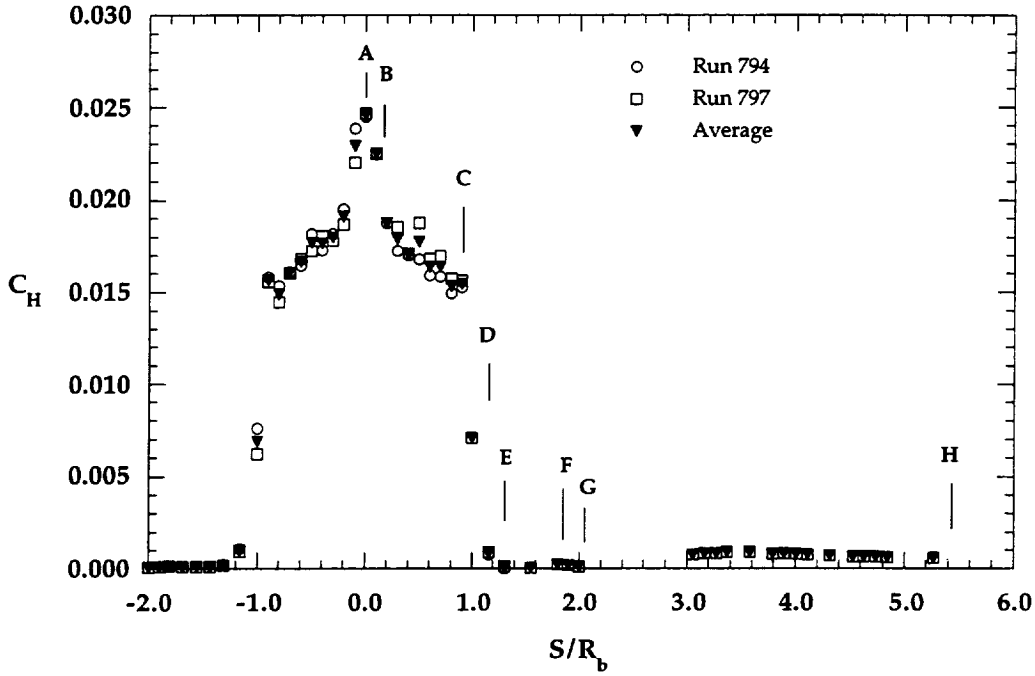

Figure 6.2.12a MP-4 Configuration, $\alpha = 0$ deg, CO_2 in HYPULSE (linear scale)

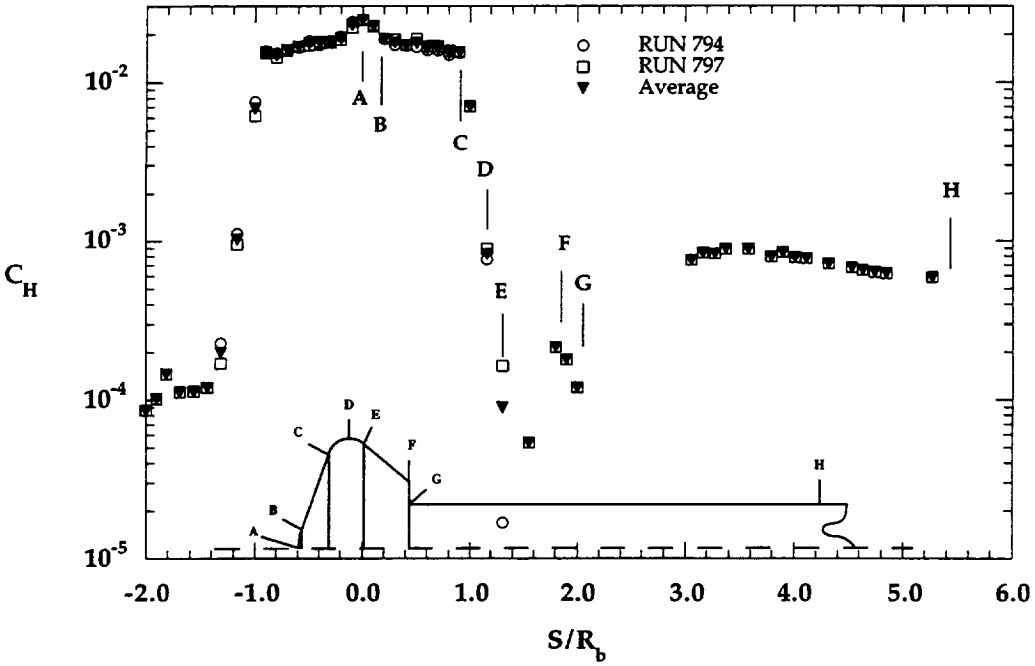

Figure 6.2.12b MP-4 Configuration, $\alpha = 0$ deg, CO_2 in HYPULSE (log scale)

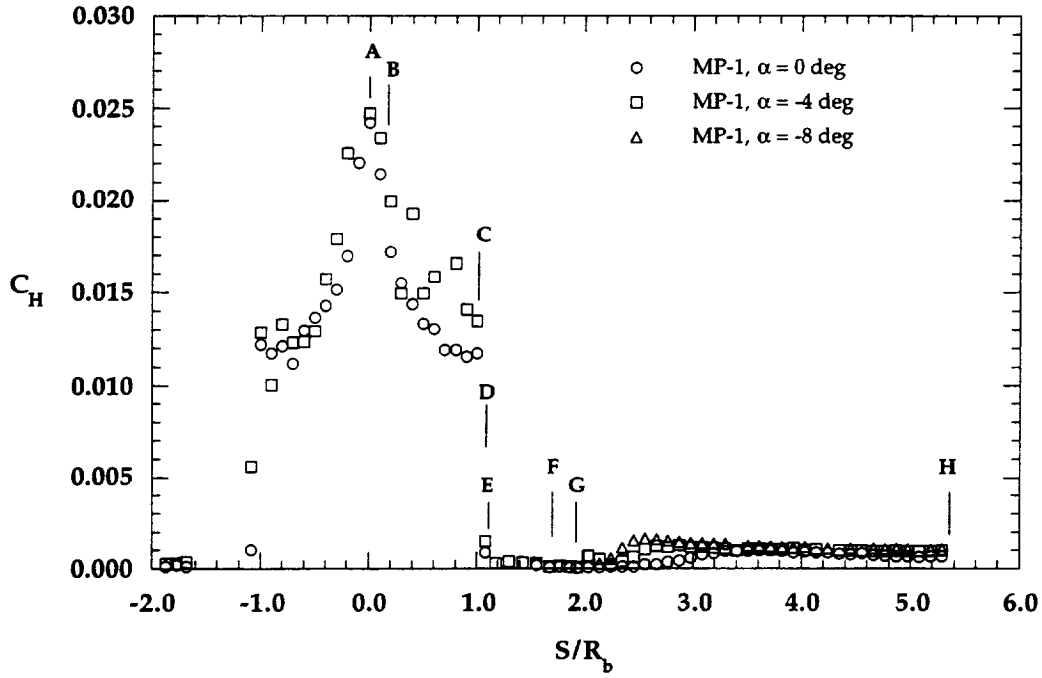

Figure 6.2.13a α Effects on MP-1 Configuration, CO_2 in HYPULSE (linear scale)

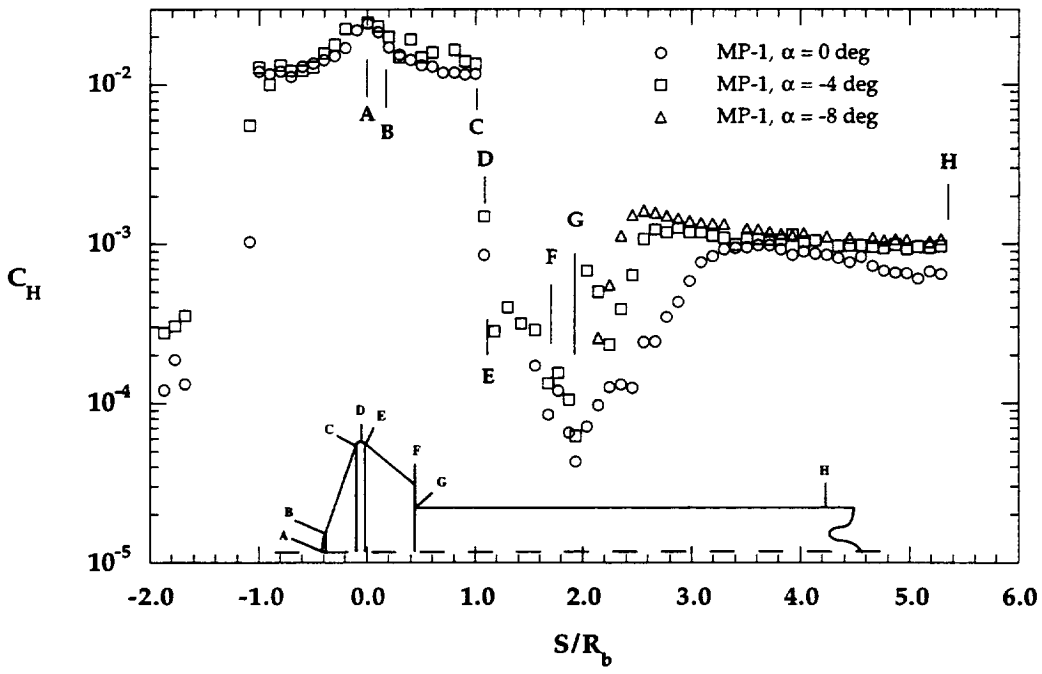

Figure 6.2.13b α Effects on MP-1 Configuration, CO_2 in HYPULSE (log scale)

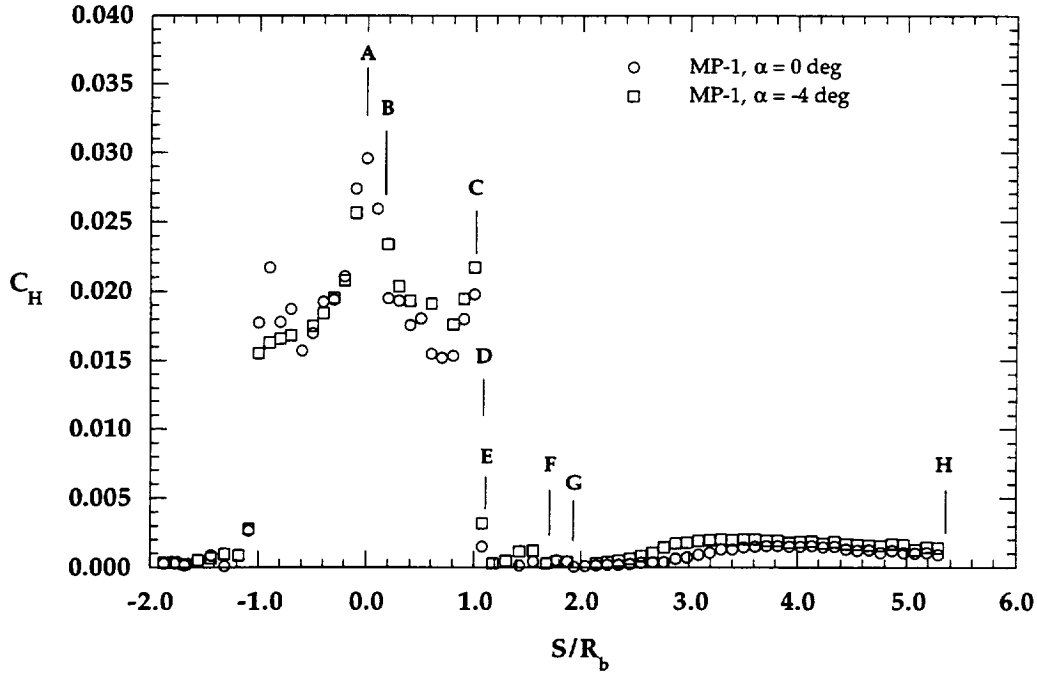

Figure 6.2.14a α Effects on MP-1 Configuration, Air in HYPULSE (linear scale)

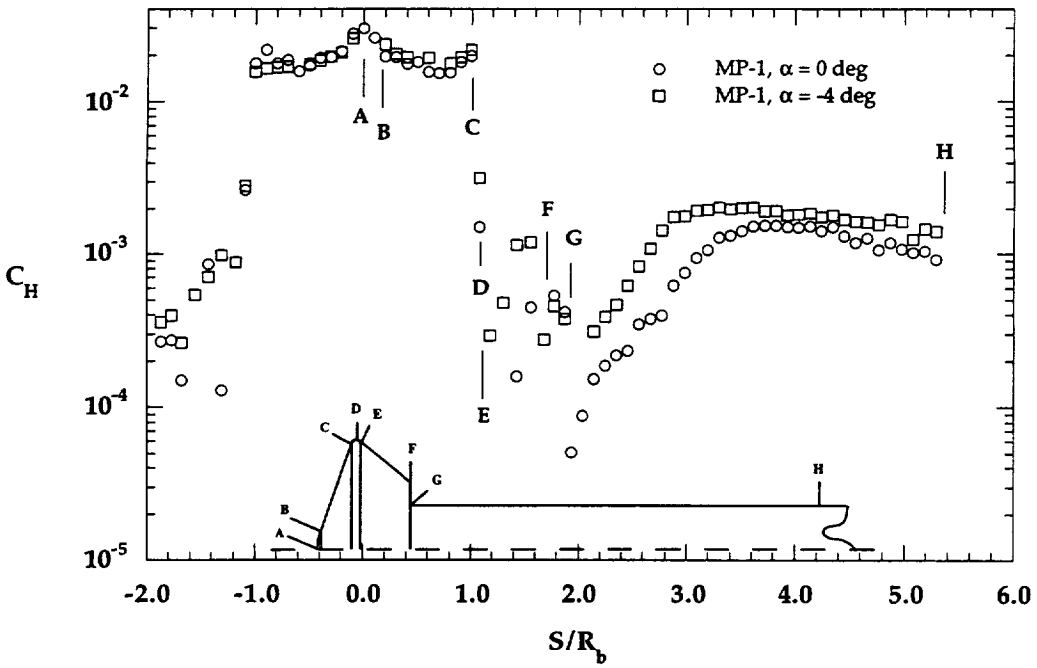

Figure 6.2.14b α Effects on MP-1 Configuration, Air in HYPULSE (log scale)

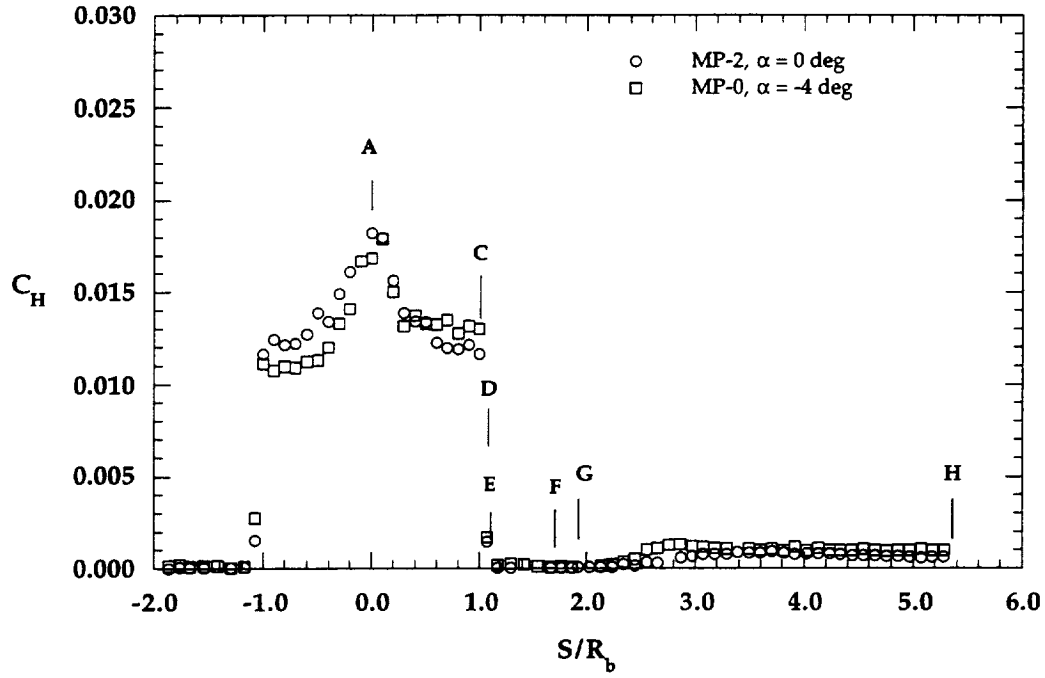

Figure 6.2.15a α Effects on MP-2 Configuration, CO_2 in HYPULSE (linear scale)

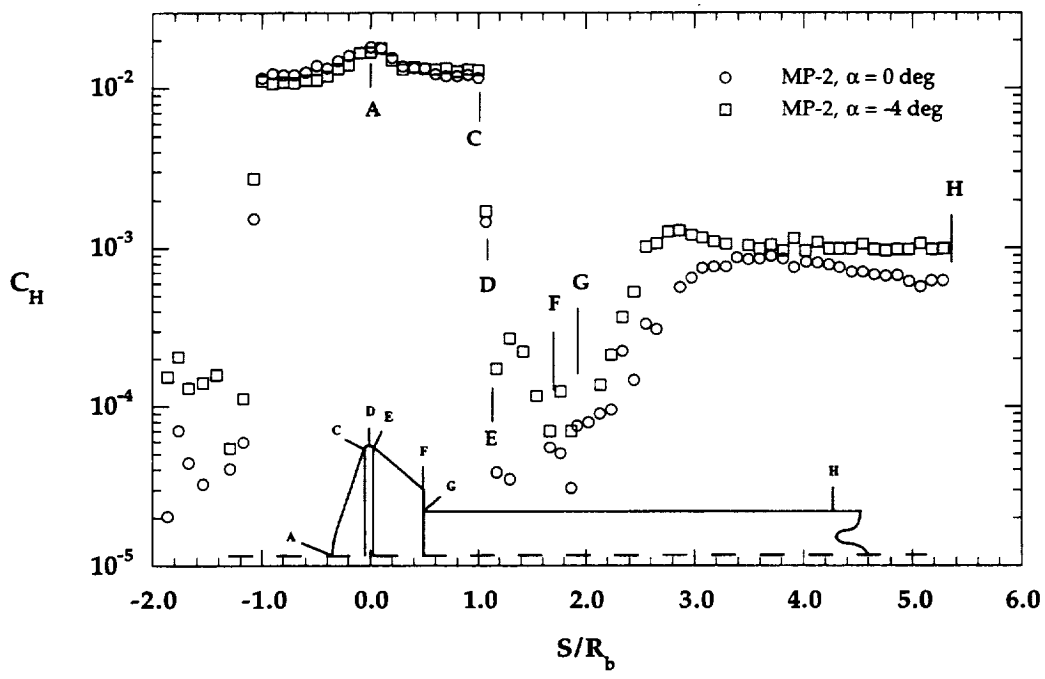

Figure 6.2.15b α Effects on MP-2 Configuration, CO_2 in HYPULSE (log scale)

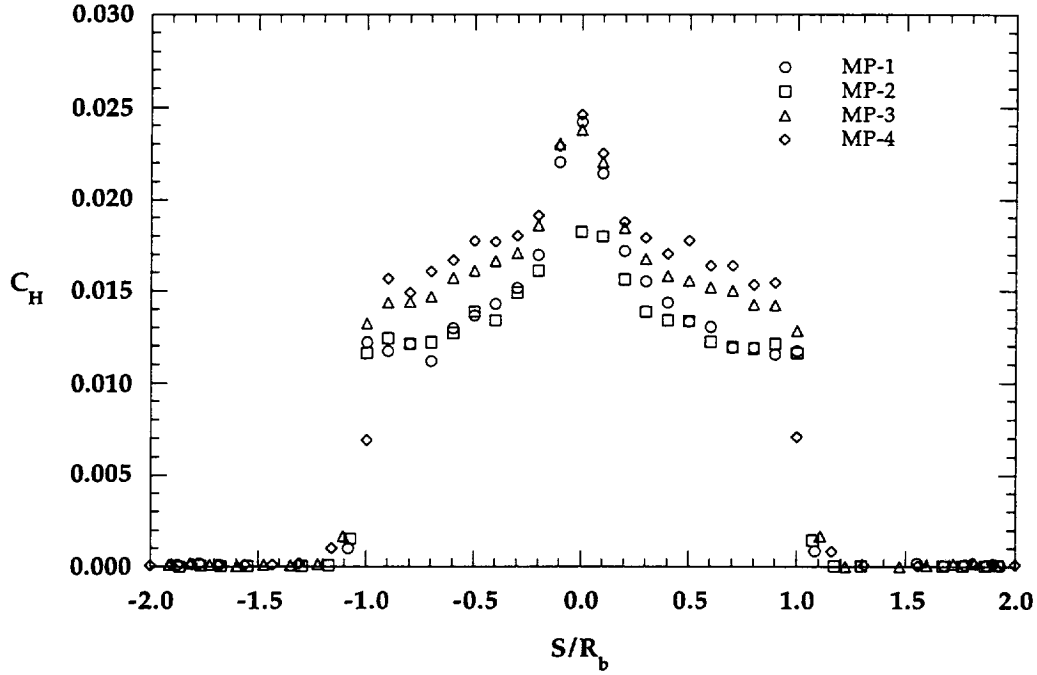

Figure 6.2.16a Configuration Effects on Forebody, $\alpha = 0$ deg, CO_2 in HYPULSE

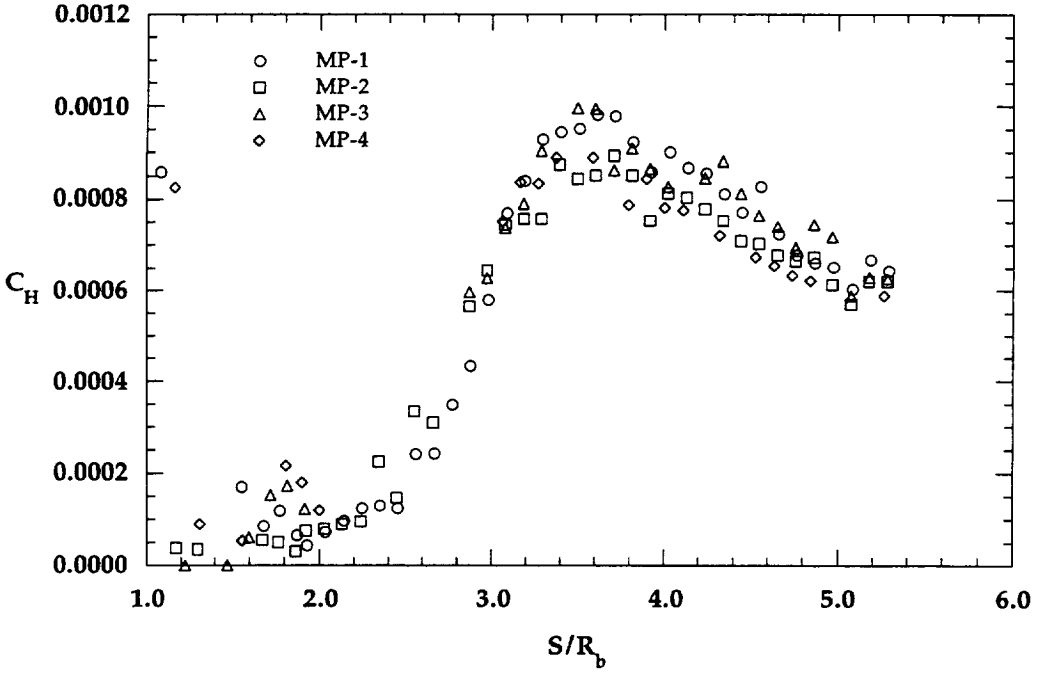

Figure 6.2.16b Configuration Effects on Wake, $\alpha = 0$ deg, CO_2 in HYPULSE

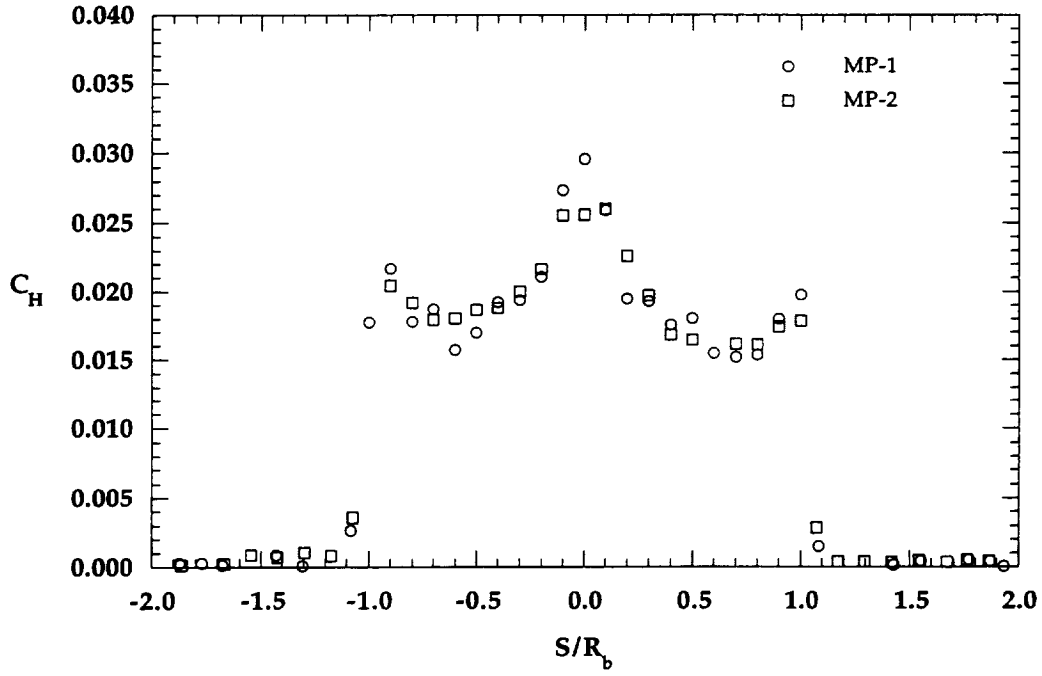

Figure 6.2.17a Configuration Effects on Forebody, $\alpha = 0$ deg, Air in HYPULSE

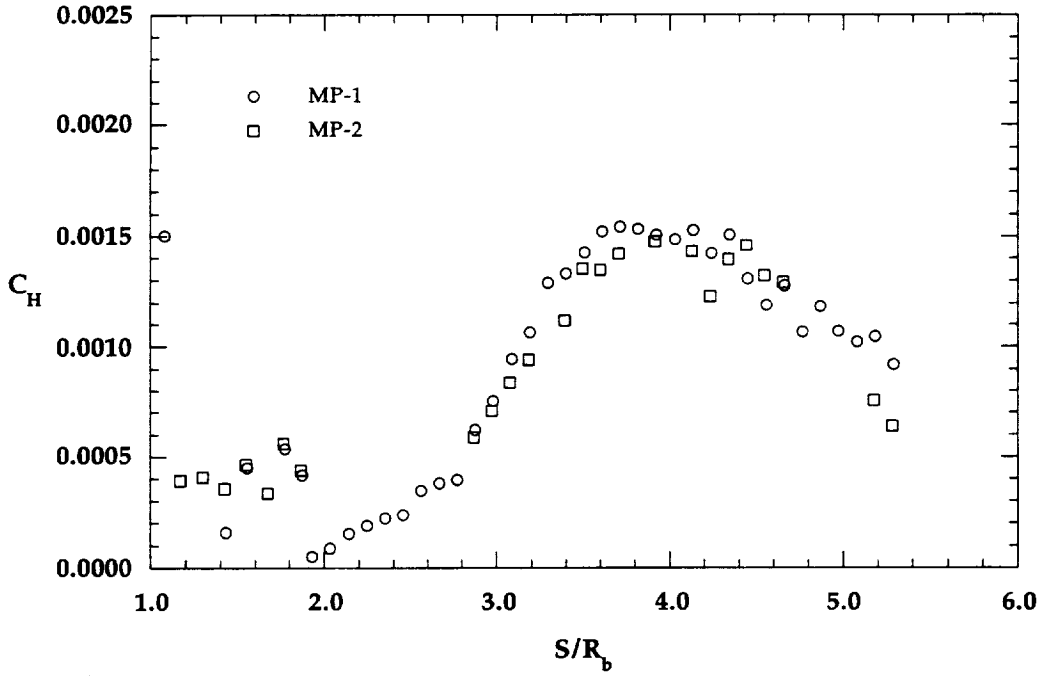

Figure 6.2.17b Configuration Effects on Wake, $\alpha = 0$ deg, Air in HYPULSE

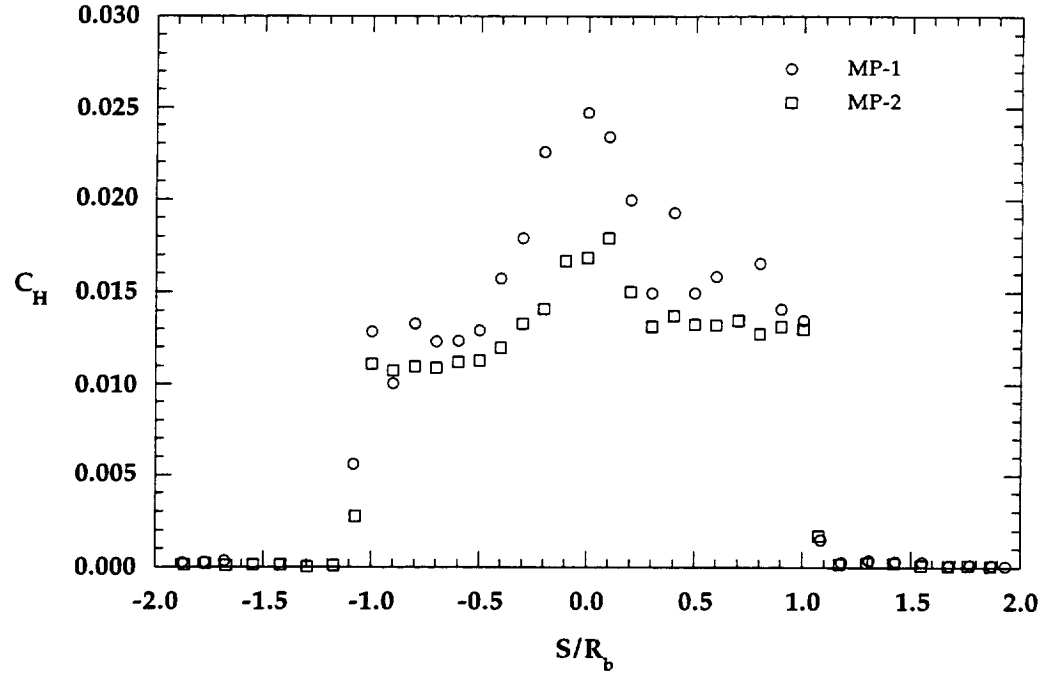

Figure 6.2.18a Configuration Effects on Forebody, α = -4 deg, CO_2 in HYPULSE

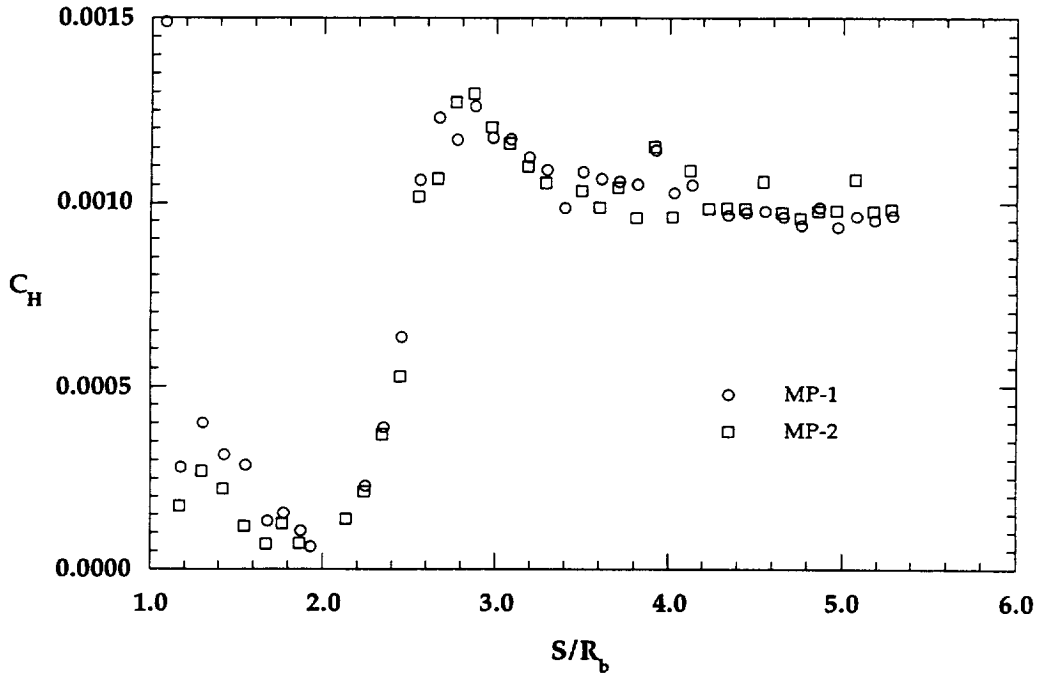

Figure 6.2.18b Configuration Effects on Wake, α = -4 deg, CO_2 in HYPULSE

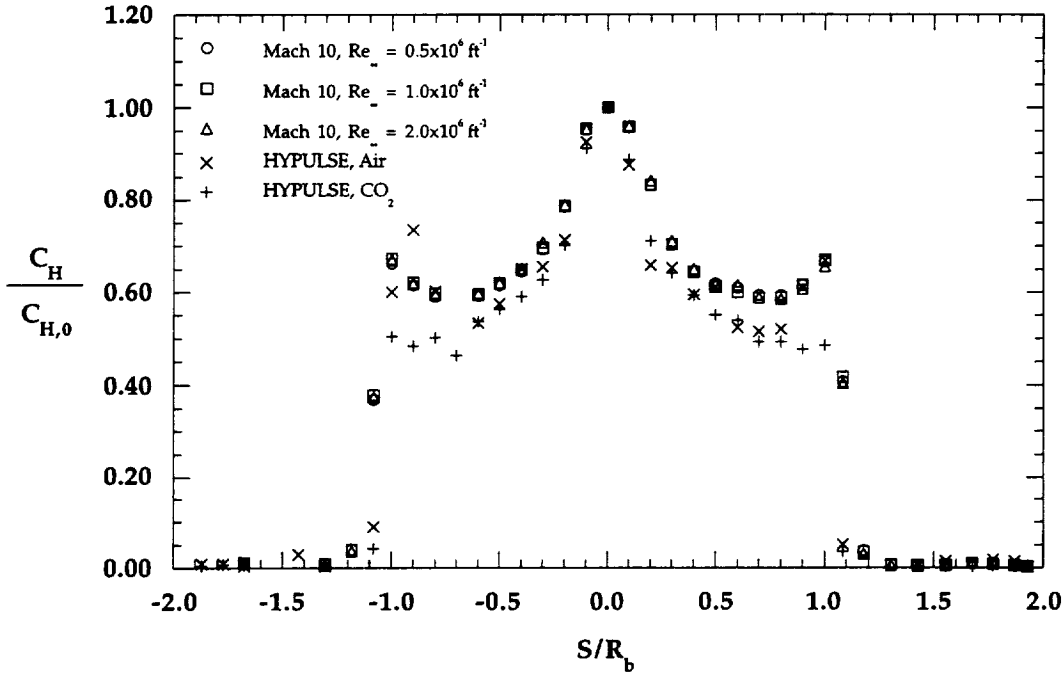

Figure 6.2.19a Comparison of Mach 10 and HYPULSE Data, MP-1 Forebody

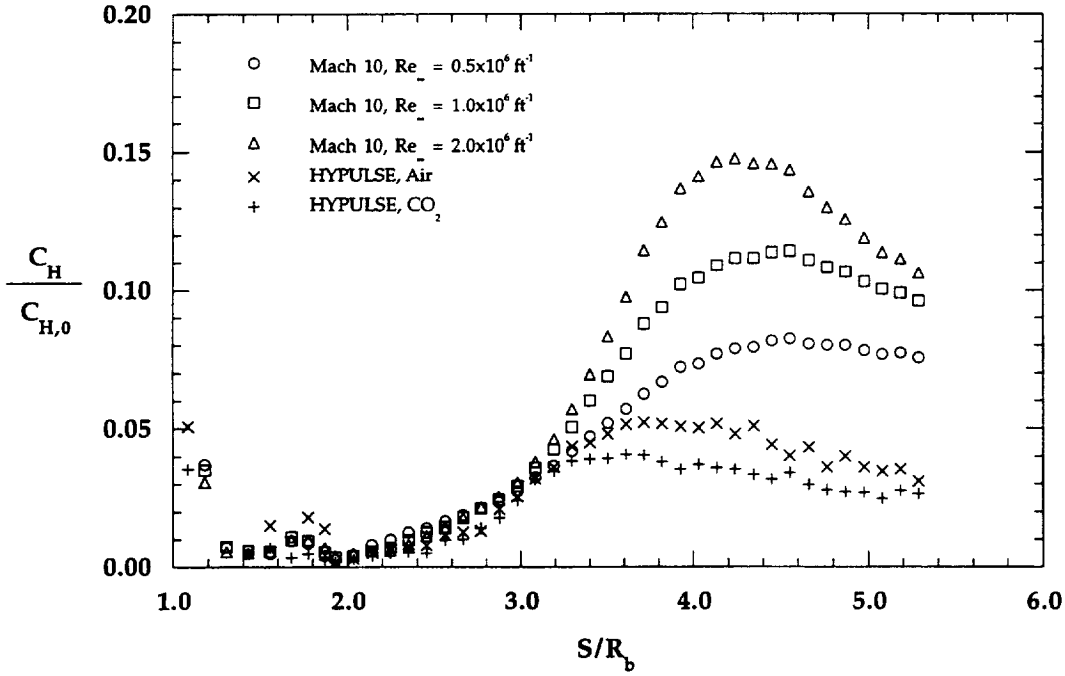

Figure 6.2.19b Comparison of Mach 10 and HYPULSE Data, MP-1 Wake

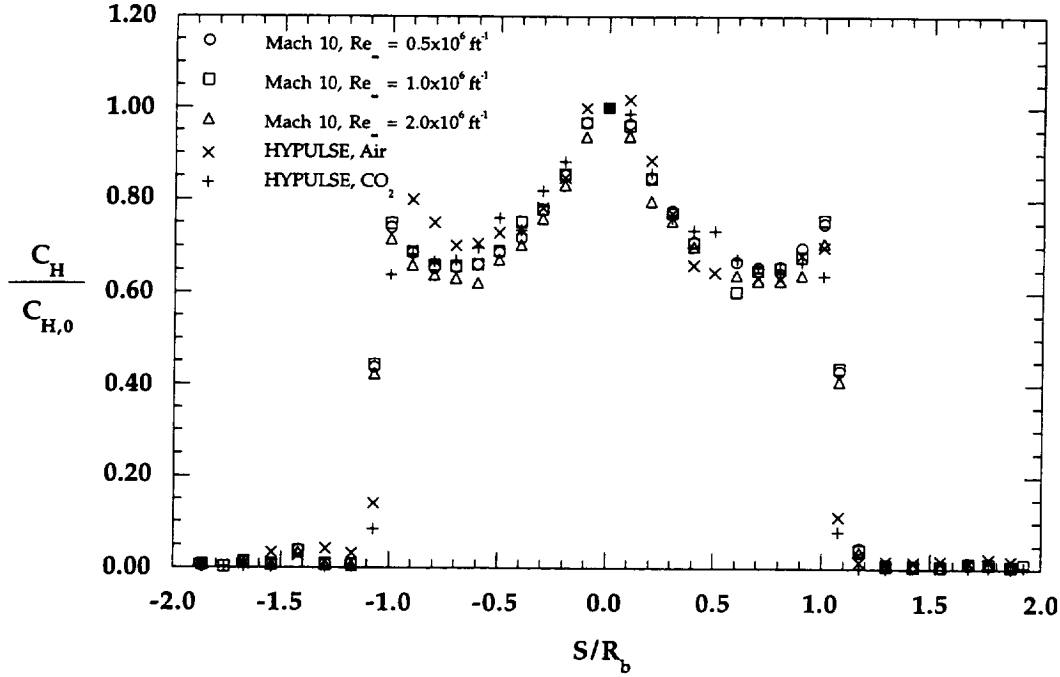

Figure 6.2.20a Comparison of Mach 10 and HYPULSE Data, MP-2 Forebody

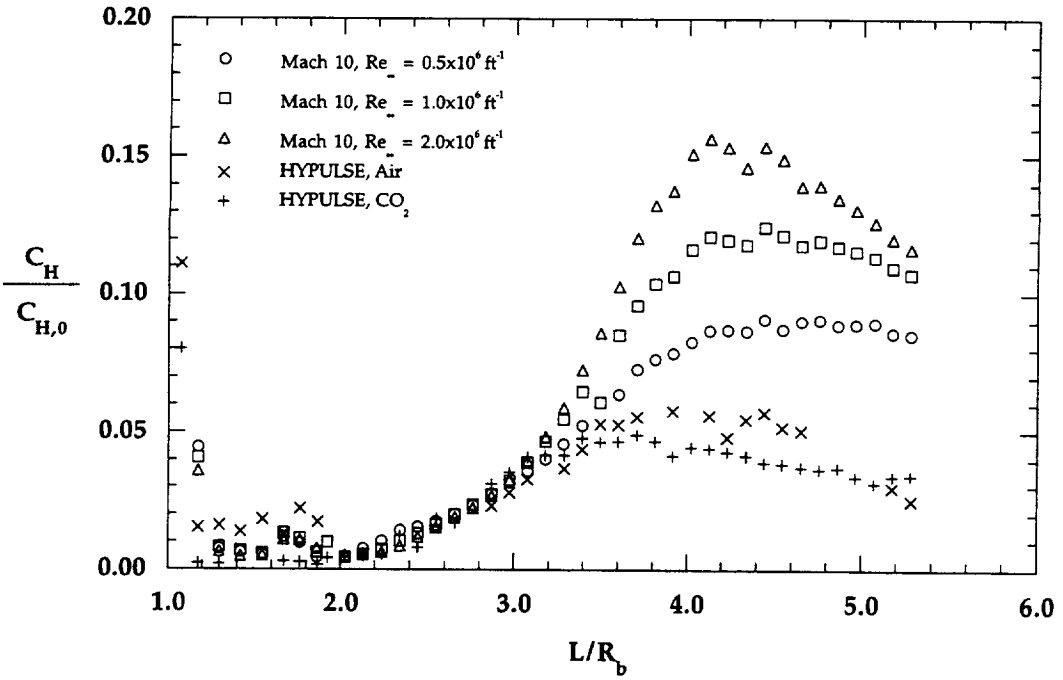

Figure 6.2.20b Comparison of Mach 10 and HYPULSE Data, MP-2 Wake

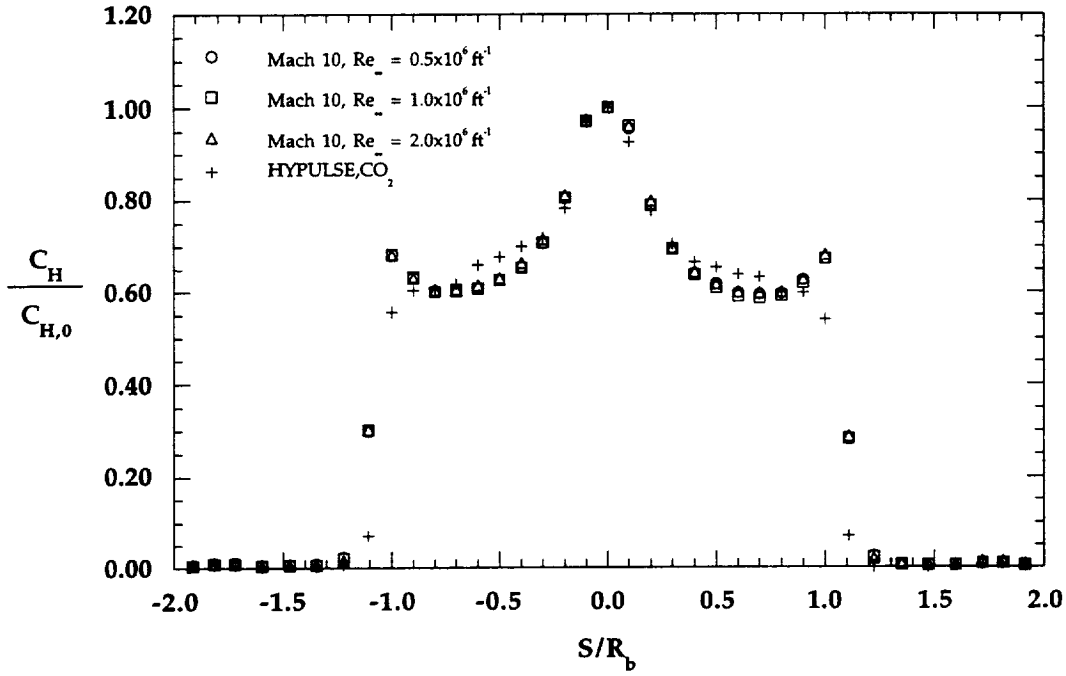

Figure 6.2.21a Comparison of Mach 10 and HYPULSE Data, MP-3 Forebody

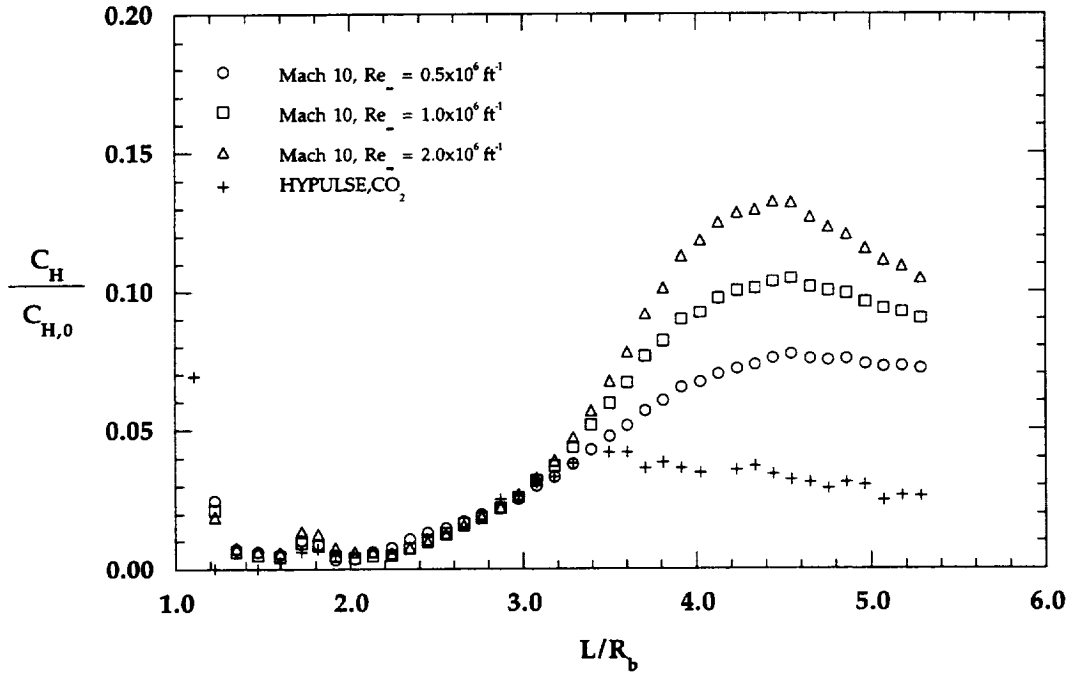

Figure 6.2.21b Comparison of Mach 10 and HYPULSE Data, MP-3 Wake

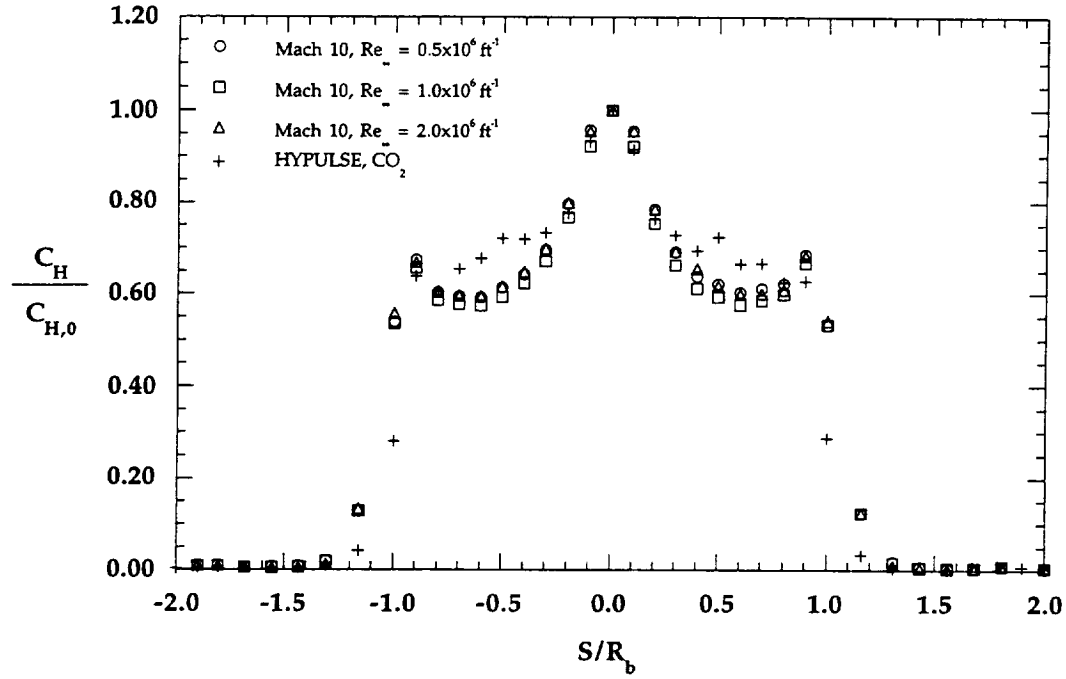

Figure 6.2.22a Comparison of Mach 10 and HYPULSE Data, MP-4 Forebody

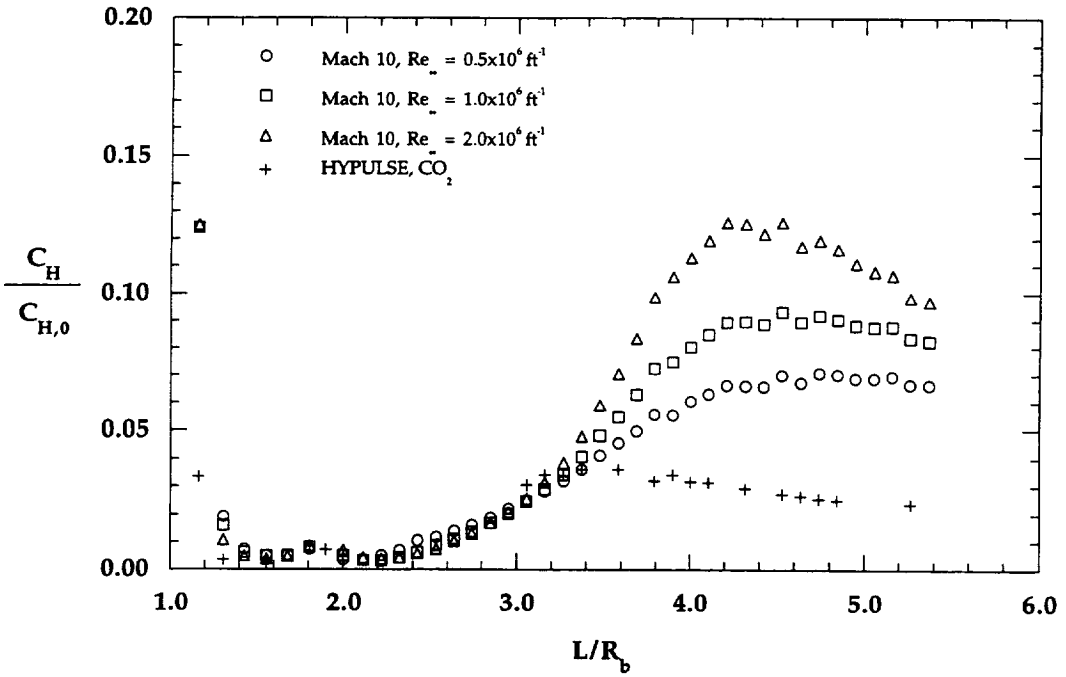

Figure 6.2.22b Comparison of Mach 10 and HYPULSE Data, MP-4 Wake

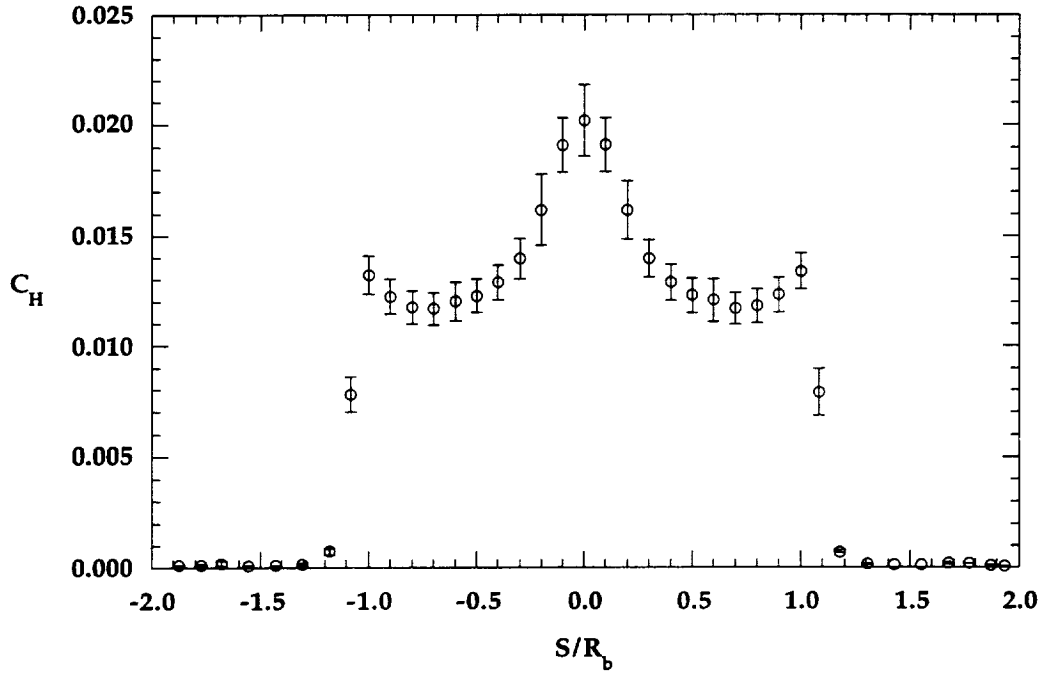

Figure 6.3.1a MP-1 Forebody Uncertainty Estimates, Re=1.0x10^6 ft^{-1} in Mach 10

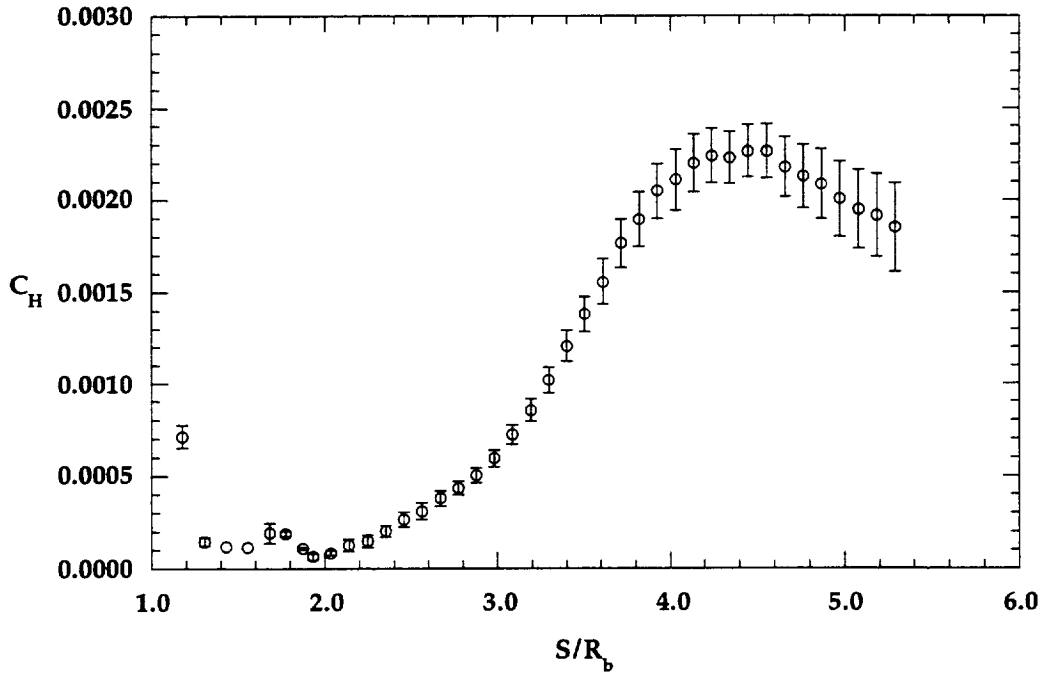

Figure 6.3.1b MP-1 Wake Uncertainty Estimates, Re=1.0x10^6 ft^{-1} in Mach 10

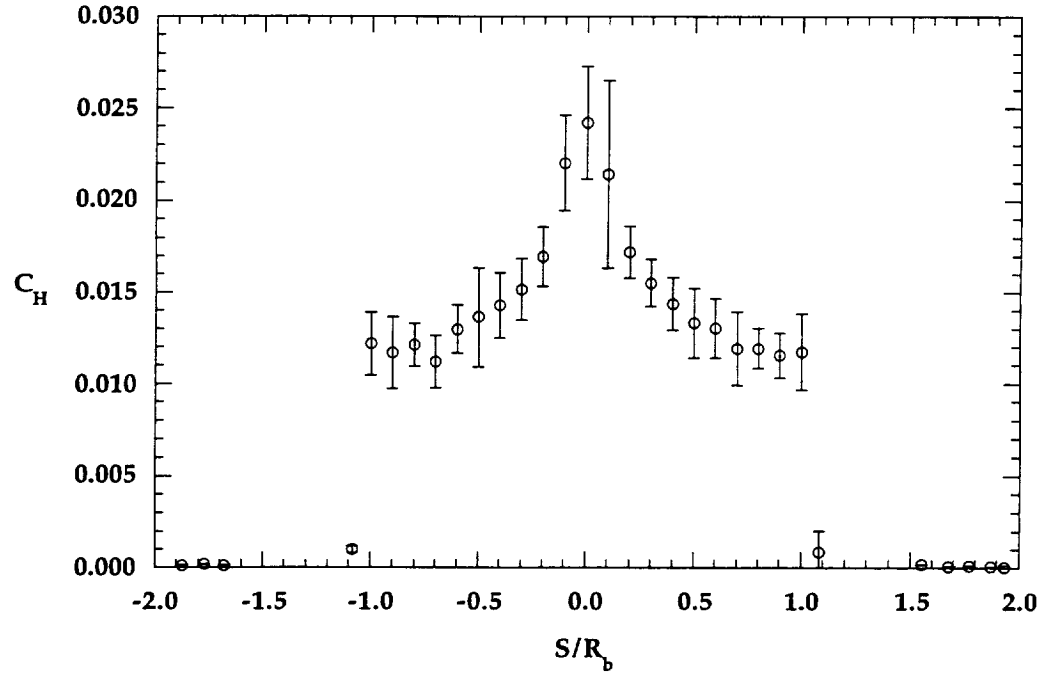

Figure 6.3.2a MP-1 Forebody Uncertainty Estimates, CO_2 in HYPULSE

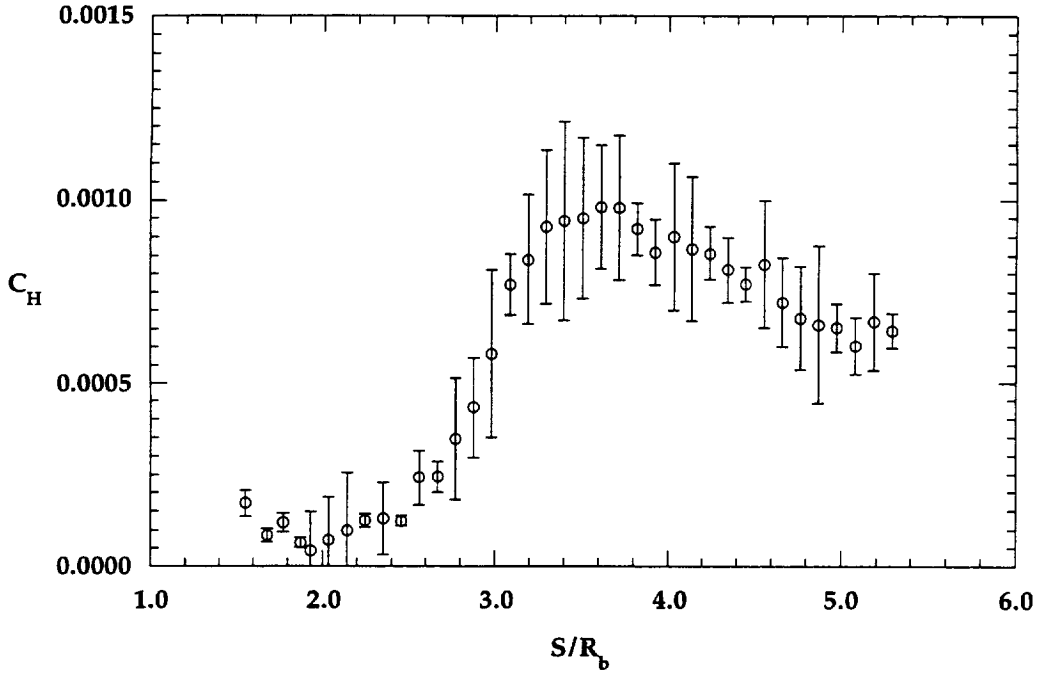

Figure 6.3.2b MP-1 Wake Uncertainty Estimates, CO_2 in HYPULSE

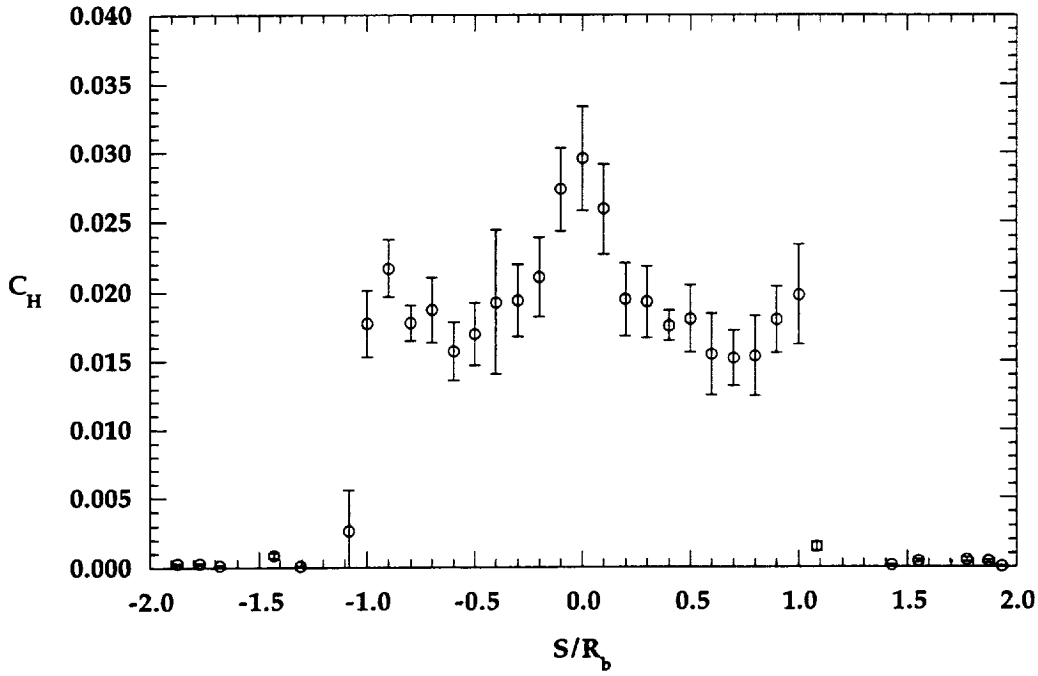

Figure 6.3.3a MP-1 Forebody Uncertainty Estimates, Air in HYPULSE

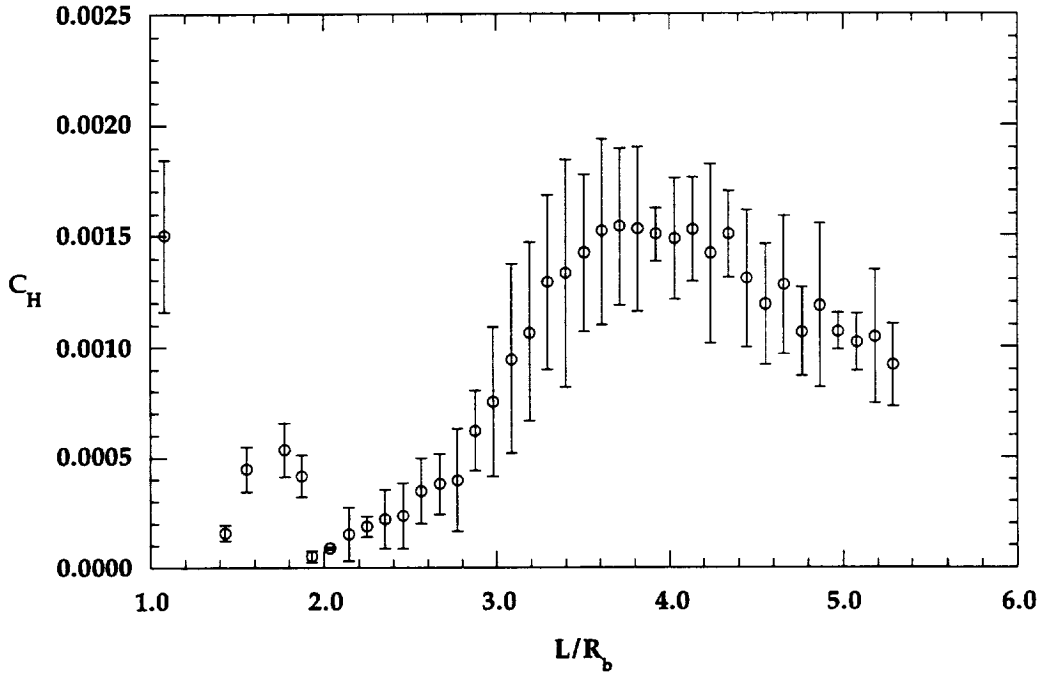

Figure 6.3.3b MP-1 Wake Uncertainty Estimates, Air in HYPULSE

CHAPTER 7
COMPUTATIONAL TECHNIQUES

Section 7.1 Governing Equations

7.1.1 Formulation of Governing Equations

The governing conservation equations for the hypersonic flow of a multi-species, ionizing gas in chemical and vibration nonequilibrium have been developed by Lee (1985). For the present work, the equations are simplified to the case of a non-ionizing gas with a single vibrational temperature for all molecules. The governing equations can be expressed in vector form for 2D/3D/axisymmetric flows as:

$$\frac{\partial U}{\partial t} + \frac{\partial E}{\partial x} + \frac{\partial F}{\partial y} + \sigma_2\left(\frac{F}{y}\right) + \sigma_3\frac{\partial G}{\partial z} = \frac{\partial E_v}{\partial x} + \frac{\partial F_v}{\partial y} + \sigma_2\left(\frac{F_v}{y}\right) + \sigma_3\frac{\partial G_v}{\partial z} + W \quad (7.1.1)$$

where:

$$U = \left[\rho_s,\ \rho u,\ \rho v,\ \sigma_3\rho w,\ \rho e_v,\ \rho E\right]^T \quad (7.1.2)$$

$$E = \left[\rho_s u,\ \left(\rho u^2 + p\right),\ \rho uv,\ \sigma_3\rho uw,\ \rho e_v u,\ \rho Hu\right]^T \quad (7.1.3a)$$

$$F = \left[\rho_s v,\ \rho uv,\ \left(\rho v^2 + p\right),\ \sigma_3\rho vw,\ \rho e_v v,\ \rho Hv\right]^T \quad (7.1.3b)$$

$$G = \left[\rho_s w,\ \rho uw,\ \rho vw,\ \sigma_3\left(\rho w^2 + p\right),\ \rho e_v w,\ \rho Hw\right]^T \quad (7.1.3c)$$

$$E_v = \begin{bmatrix} \rho D_s \dfrac{\partial Y_s}{\partial x} \\ \tau_{xx} \\ \tau_{xy} \\ \sigma_3 \tau_{xz} \\ -q_{v,x} + \dfrac{\partial}{\partial x}\left(\rho \sum_{s=1}^{n} h_{v,s} \dfrac{\partial Y_s}{\partial x}\right) \\ u\tau_{xx} + v\tau_{xy} + \sigma_3 w \tau_{xz} - q_{v,x} - q_x \end{bmatrix} \tag{7.1.4a}$$

$$F_v = \begin{bmatrix} \rho D_s \dfrac{\partial Y_s}{\partial y} \\ \tau_{xy} \\ \tau_{yy} \\ \sigma_3 \tau_{yz} \\ -q_{v,y} + \dfrac{\partial}{\partial y}\left(\rho \sum_{s=1}^{n} h_{v,s} \dfrac{\partial Y_s}{\partial y}\right) \\ u\tau_{xy} + v\tau_{yy} + \sigma_3 w \tau_{yz} - q_{v,y} - q_y \end{bmatrix} \tag{7.1.4b}$$

$$G_v = \begin{bmatrix} \rho D_s \dfrac{\partial Y_s}{\partial z} \\ \tau_{xz} \\ \tau_{yz} \\ \sigma_3 \tau_{zz} \\ -q_{v,z} + \dfrac{\partial}{\partial z}\left(\rho \sum_{s=1}^{n} h_{v,s} \dfrac{\partial Y_s}{\partial z}\right) \\ u\tau_{xz} + v\tau_{yz} + \sigma_3 w \tau_{zz} - q_{v,z} - q_z \end{bmatrix} \tag{7.1.4c}$$

$$W = \left[\dot{w}_s,\ 0,\ \sigma_2\left(p - \tau_{zz}\right)/y,\ 0,\ Q_{V-T},\ 0\right]^T \tag{7.1.5}$$

and where:

$$\sigma_2 = \begin{cases} 0, \text{ 2D system} \\ 1, \text{ axisymmetric system} \end{cases} \tag{7.1.6a}$$

$$\sigma_3 = \begin{cases} 0, \text{ 2D system} \\ 1, \text{ 3D system} \end{cases} \tag{7.1.6b}$$

The following definitions apply to equations (7.1.2 - 7.1.5):

Equation of state:

$$p = \sum_{s=1}^{n} p_s = R_u T \sum_{s=1}^{n} \frac{\rho_s}{W_s} \tag{7.1.7}$$

where n is the number of species.

Total internal energy:

$$E = \frac{u^j u^j}{2} + \sum_{s=1}^{n} X_s e_s \tag{7.1.8}$$

Species mass fraction:

$$X_s = \frac{\rho_s}{\rho} \tag{7.1.9}$$

Total enthalpy:

$$H = E + \frac{p}{\rho} \tag{7.1.10}$$

Viscous shear stress tensor:

$$\tau_{ij} = \mu\left(\frac{\partial u^i}{\partial x^j} + \frac{\partial u^j}{\partial x^i}\right) - \frac{2}{3}\mu\frac{\partial u^k}{\partial x^k}\delta_{ij} \tag{7.1.11}$$

Translational and vibrational heat-flux vectors:

$$q^j = -\mu\frac{\partial T}{\partial x^j} \tag{7.1.12a}$$

$$q_v^j = -\mu_v\frac{\partial T_v}{\partial x^j} \tag{7.1.12b}$$

Landau-Teller relation (Vincenti and Krueger, 1965) for translation-vibration energy exchange:

$$Q_{T-V} = \rho_s\frac{e_{v,s}^* - e_{v,s}}{<\tau_s>} \tag{7.1.13}$$

where $e_{v,s}^*$ is the species equilibrium vibrational energy at the translation temperature T. The mixture relaxation time is given by:

$$<\tau_s> = \frac{\sum_r N_r}{\sum_r N_r/\tau_{sr}} \tag{7.1.14}$$

where N_r is the species number density and τ_{sr} is the relaxation rate of species s due to collisions with species r.

Species production rate:

$$\dot{w}_s = W_s \sum_{r=1}^{n_r} \left(\beta_{s,r} - \alpha_{s,r}\right)\left(R_{f,r} - R_{b,r}\right) \tag{7.1.15}$$

where n_r is the number of chemical reactions, $\alpha_{s,r}$ and $\beta_{s,r}$ are the stoichiometric coefficients of the reactants and products for each reaction, and $R_{f,r}$ and $R_{b,r}$ are the forward and reverse reactions rates for each reaction.

Reaction rates:

$$R_{f,r} = k_{f,r} \prod_{s=1}^{n_r} \left(\frac{\rho_s}{W_s}\right)^{\alpha_{s,r}} \tag{7.1.16a}$$

$$R_{b,r} = k_{b,r} \prod_{s=1}^{n_r} \left(\frac{\rho_s}{W_s}\right)^{\beta_{s,r}} \tag{7.1.16b}$$

7.1.2 Transformation of Governing Equations

The governing equations are transformed between the physical (x,y,z,t) domain and the computational (ξ,η,ζ,τ) domain via the transformations:

$$\begin{aligned} \xi &= \xi(x,y,z) \\ \eta &= \eta(x,y,z) \\ \varsigma &= \varsigma(x,y,z) \\ \tau &= t \end{aligned} \tag{7.1.17a}$$

and

$$\begin{aligned} x &= x(\xi,\eta,\varsigma) \\ y &= y(\xi,\eta,\varsigma) \\ z &= z(\xi,\eta,\varsigma) \\ t &= \tau \end{aligned} \tag{7.1.17b}$$

The Jacobian of the transformation is given by:

$$J = \frac{\partial(\tau,\xi,\eta,\varsigma)}{\partial(t,x,y,z)} = \begin{vmatrix} 1 & 0 & 0 & 0 \\ \xi_t & \xi_x & \xi_y & \sigma_3\xi_z \\ \eta_t & \eta_x & \eta_y & \sigma_3\eta_z \\ \sigma_3\varsigma_t & \sigma_3\varsigma_x & \sigma_3\varsigma_y & \sigma_3\varsigma_z \end{vmatrix} = 1/\begin{vmatrix} 1 & 0 & 0 & 0 \\ x_\tau & x_\xi & x_\eta & \sigma_3 x_\varsigma \\ y_\tau & y_\xi & y_\eta & \sigma_3 y_\varsigma \\ \sigma_3 z_\tau & \sigma_3 z_\xi & \sigma_3 z_\eta & \sigma_3 z_\varsigma \end{vmatrix} \tag{7.1.18}$$

or

$$J = \frac{1}{\left[x_\xi\left(y_\eta(z_\varsigma)^{\sigma_3} - \sigma_3 y_\varsigma z_\eta\right) - x_\eta\left(y_\xi(z_\varsigma)^{\sigma_3} - \sigma_3 y_\varsigma z_\xi\right) + \sigma_3 x_\varsigma(y_\xi z_\eta - y_\eta z_\xi)\right]} \tag{7.1.19}$$

The metric terms are functions of the computational grid, and are computed from the (x,y,z) distributions in (ξ,η,ζ) space of the grid points.

The transformed set of governing equations is given by (Hoffman and Chang, 1993):

$$\frac{\partial \overline{U}}{\partial\tau} + \frac{\partial \overline{E}}{\partial\xi} + \frac{\partial \overline{F}}{\partial\eta} + \sigma_3\frac{\partial \overline{G}}{\partial\varsigma} + \sigma_2\overline{H} = \frac{\partial \overline{E}_v}{\partial\xi} + \frac{\partial \overline{F}_v}{\partial\eta} + \sigma_3\frac{\partial \overline{G}_v}{\partial\varsigma} + \sigma_2\overline{H}_v + \overline{W} \tag{7.1.20}$$

where:

$$\overline{U} = \frac{U}{J} \tag{7.1.21}$$

$$\overline{E} = \frac{1}{J}\left(\xi_t U + \xi_x E + \xi_y F + \sigma_3 \xi_z G\right) \tag{7.1.22a}$$

$$\overline{F} = \frac{1}{J}\left(\eta_t U + \eta_x E + \eta_y F + \sigma_3 \eta_z G\right) \tag{7.1.22b}$$

$$\overline{G} = \frac{1}{J}\left(\varsigma_t U + \varsigma_x E + \varsigma_y F + \sigma_3 \varsigma_z G\right) \tag{7.1.22c}$$

$$\overline{H} = \frac{1}{J}\left(\frac{F}{y}\right) \tag{7.1.23}$$

$$\overline{E_v} = \frac{1}{J}\left(\xi_x E_v + \xi_y F_v + \sigma_3 \xi_z G_v\right) \tag{7.1.24a}$$

$$\overline{F_v} = \frac{1}{J}\left(\eta_x E_v + \eta_y F_v + \sigma_3 \eta_z G_v\right) \tag{7.1.24b}$$

$$\overline{G_v} = \frac{1}{J}\left(\varsigma_x E_v + \varsigma_y F_v + \sigma_3 \varsigma_z G_v\right) \tag{7.1.24c}$$

$$\overline{H}_v = \frac{1}{J}\left(\frac{F_v}{y}\right) \tag{7.1.25}$$

$$\overline{W} = \frac{1}{J}(W) \tag{7.1.26}$$

Section 7.2 NEQ2D Navier-Stokes Solver

Solutions of the governing equation set for entry vehicle flow fields at the 31-Inch Mach 10 Air Tunnel and HYPULSE Expansion Tube test conditions were computed using NEQ2D, a 2D/axisymmetric nonequilibrium solver. NEQ2D was developed by Candler (1988), and has been used to compute solutions for perfect gas (Candler and MacCormack, 1987), ionizing, chemically reacting Earth atmosphere (Candler and MacCormack, 1991), and chemically reacting Martian atmosphere (Candler, 1990) flows.

The governing equations in 2D/axisymmetric form are solved through the Gauss-Seidel line relaxation method (MacCormack, 1985) after a first-order in time and second-order in space discretization (Beam and Warming, 1976) is applied:

$$\begin{aligned}\overline{U}_{i,j,k}^{(n+1)} = \overline{U}_{i,j,k}^{(n)} &- \Delta t\left[\left(\overline{E}^{(n+1)} - \overline{E}_v^{(n+1)}\right)_{(i+\frac{1}{2}),j,k} + \left(\overline{F}^{(n+1)} - \overline{F}_v^{(n+1)}\right)_{i,(j+\frac{1}{2}),k}\right] \\ &+ \Delta t\left[\left(\overline{E}^{(n+1)} - \overline{E}_v^{(n+1)}\right)_{(i-\frac{1}{2}),j,k} + \left(\overline{F}^{(n+1)} - \overline{F}_v^{(n+1)}\right)_{i,(j+\frac{1}{2}),k}\right] \\ &- \Delta t\sigma_2\left[\overline{H}^{(n+1)} - \overline{H}_v^{(n+1)}\right]_{i,j,k} + \Delta t\left(\overline{W}_{i,j,k}\right)^{(n+1)}\end{aligned} \tag{7.2.1}$$

where it is understood that $\Delta\xi = \Delta\eta = 1$ and that quantities with (±) one-half indices are evaluated midway between (i,j,k) nodes. The fluxes and source terms are linearized by Taylor series expansion as:

$$\left(\overline{E}^{(n+1)} - \overline{E}_v^{(n+1)}\right)_{(i+\frac{1}{2}),j,k} = \left(\overline{E}^{(n)} - \overline{E}_v^{(n)}\right)_{(i+\frac{1}{2}),j,k} + \left(\overline{A}^{(n)} - \overline{A}_v^{(n)}\right)_{(i+\frac{1}{2}),j,k}\Delta\overline{U}^{(n)} \tag{7.2.2a}$$

$$\left(\overline{F}^{(n+1)} - \overline{F}_v^{(n+1)}\right)_{i,(j+\frac{1}{2}),k} = \left(\overline{F}^{(n)} - \overline{F}_v^{(n)}\right)_{i,(j+\frac{1}{2}),k} + \left(\overline{B}^{(n)} - \overline{B}_v^{(n)}\right)_{i,(j+\frac{1}{2}),k}\Delta\overline{U}^{(n)} \tag{7.2.2b}$$

$$\left(\overline{H}^{(n+1)} - \overline{H}_v^{(n+1)}\right)_{i,j,k} = \left(\overline{H}^{(n)} - \overline{H}_v^{(n)}\right)_{i,j,k} + \left(\overline{M}^{(n)} - \overline{M}_v^{(n)}\right)_{i,j,k} \Delta \overline{U}^{(n)} \tag{7.2.3}$$

$$\left(\overline{W}^{(n+1)}\right)_{i,j,k} = \left(\overline{W}^{(n)}\right)_{i,j,k} + \left(\overline{N}^{(n)}\right)_{i,j,k} \Delta \overline{U}^{(n)} \tag{7.2.4}$$

where:

$$\overline{A}^{(n)}_{(i+\frac{1}{2}),j,k} = \left(\frac{\partial \overline{E}}{\partial \overline{U}}\right)^{(n)}_{(i+\frac{1}{2}),j,k}, \quad \overline{B}^{(n)}_{i,(j+\frac{1}{2}),k} = \left(\frac{\partial \overline{F}}{\partial \overline{U}}\right)^{(n)}_{i,(j+\frac{1}{2}),k}$$

(7.2.5a-7.2.5b)

$$\left(\overline{A}^{(n)}_{(i+\frac{1}{2}),j,k}\right)_v = \left(\frac{\partial \overline{E}_v}{\partial \overline{U}}\right)^{(n)}_{(i+\frac{1}{2}),j,k}, \quad \left(\overline{B}^{(n)}_{i,(j+\frac{1}{2}),k}\right)_v = \left(\frac{\partial \overline{F}_v}{\partial \overline{U}}\right)^{(n)}_{i,(j+\frac{1}{2}),k}$$

(7.2.6a-7.2.6b)

$$\overline{M}^{(n)}_{i,j,k} = \left(\frac{\partial \overline{H}}{\partial \overline{U}}\right)^{(n)}_{i,j,k}, \quad \overline{N}^{(n)}_{i,j,k} = \left(\frac{\partial \overline{W}}{\partial \overline{U}}\right)^{(n)}_{i,j,k} \tag{7.2.7-7.2.8}$$

The elements of the flux Jacobian matrices of equations (7.2.5 - 7.2.8) can be found in Hoffman and Chang (1993) or Gnoffo (1990). Viscous terms in equation (7.2.1) are evaluated with central differences. The inviscid fluxes are evaluated through the upwind Steger-Warming (1981) flux vector splitting method which has the form:

$$E = E_+ + E_- \tag{7.2.9}$$

where

$$E_{\pm} = A_{\pm}U = R\Lambda_{\pm}R^{-1}U \tag{7.2.10}$$

The matrices $\Lambda_{\pm}$ are diagonal matrices containing either the positive or negative eigenvalues of the matrix A, while the matrices R and R^{-1} contain the left and right eigenvectors of A (e.g. Gnoffo, 1990).

The flux can now be written as:

$$E_{i+\frac{1}{2},j} = (A_+)_{i,j}U_{i,j} + (A_-)_{i+1,j}U_{i+1,j} \tag{7.2.11}$$

where the Jacobian matrices are evaluated at i or $(i+1)$ depending on the signs of the eigenvalues.

MacCormack and Candler (1989) have shown that this flux splitting is highly dissipative in viscous regions, and have developed a modified splitting of the form:

$$E_{i+\frac{1}{2},j} = (A_+)_{(i+\frac{1}{2}),j}U_{i,j} + (A_-)_{i+\frac{1}{2},j}U_{i+1,j} \tag{7.2.12}$$

In this modified Steger Warming splitting, the Jacobian matrices are evaluated midway between points (i) and $(i+1)$. The flow variables required for this evaluation can be averaged between the two points or extrapolated in a MUSCL type approach (van Leer, 1979). The NEQ2D code incorporates both the original and modified Steger-Warming splittings. The code automatically switches (Gaitonde and Shang, 1992) between the original form around shocks in order to insure stability and the modified form in viscous regions in order to minimize dissipation.

In this study, 5 species Earth atmosphere (N_2, O_2, NO, N, O), 8 species Martian atmosphere (CO_2, CO, N_2, O_2, NO, C, N, O) and perfect-gas air models were employed to simulate test conditions in

the 31-Inch Mach 10 Air Tunnel and the HYPULSE Expansion Tube.

In the Earth atmosphere model, the reactions considered are:

$$N_2 + M \rightleftharpoons 2N + M$$
$$O_2 + M \rightleftharpoons 2O + M$$
$$NO + M \rightleftharpoons N + O + M$$
$$NO + O \rightleftharpoons O_2 + N$$
$$N_2 + O \rightleftharpoons NO + N$$

In the Martian atmosphere model, the following additional reactions are also considered:

$$CO_2 + M \rightleftharpoons CO + O + M$$
$$CO + M \rightleftharpoons C + O$$
$$CO + O \rightleftharpoons O_2 + C$$
$$CO_2 + O \rightleftharpoons O_2 + CO$$

Species reaction rate coefficients in NEQ2D take the form:

$$k_f = C_f T_q^{\eta_f} \exp\left(\theta_f / T_q\right) \tag{7.2.13}$$

$$k_b = C_b T_q^{\eta_b} \exp\left(\theta_b / T_q\right) \tag{7.2.14}$$

where T_q is the translation temperature, T, for exchange reactions and the geometric average:

$$T_{T\text{-}V} = \sqrt{T T_v} \tag{7.2.15}$$

for dissociation reactions (Park, 1987). The reaction rate coefficients, C_f, C_b, η_f, η_b, θ_f and θ_b are taken

from Park (1985) for the Earth atmosphere model and from Evans, Schexnayder and Grose (1974) for the Mars atmosphere model.

Species viscosities are determined from kinetic theory using the Lennard-Jones (6-12) potential (Hirschfelder, Curtiss and Bird, 1954) and mixture viscosities are evaluated through Wilke's (1950) mixing rule. Mixture translational and vibrational thermal conductivities are computed using an Eucken relation (Vincenti and Krueger, 1965). Species diffusion coefficients are evaluated as detailed by Lee (1985).

The vibrational energy of diatomic molecules (CO, N_2, NO and O_2) is determined from a simple harmonic oscillator model:

$$e_{v,s} = \frac{R_u}{W_s} \frac{\theta_{v,s}}{exp(\theta_{v,s}/T_v) - 1} \tag{7.2.16}$$

where $\theta_{v,s}$ is the characteristic vibrational temperature of the species. The polyatomic molecule CO_2 has three vibrational modes, and its vibrational energy is given by (Candler, 1990):

$$e_{v,CO_2} = e^1_{v,CO_2} + e^2_{v,CO_2} + e^3_{v,CO_2} \tag{7.2.17}$$

where

$$e^n_{v,CO_2} = g_n \frac{R_u}{W_{CO_2}} \frac{\theta^n_{v,CO_2}}{exp(\theta^n_{v,CO_2}/T_v) - 1} \tag{7.2.18}$$

and g_n is the degeneracy of the mode. Species vibrational relaxation times are determined from the Milikan and White (1963) formulation.

Section 7.3 Grid Generation and Adaptation

Flow field solutions were found to be highly dependent on grid resolution and grid quality, and therefore the grid generation and adaptation processes will be discussed in detail. The techniques employed to generate and adapt the grids will be covered in this section, while the effects of grid resolution and grid adaptation on the computed flow fields will be discussed in Chapter 8.

The process of constructing a computational grid for one of the different vehicle geometries and adapting this grid to the features of the vehicle flow field consisted of three steps: construction of an initial grid; adaptation of the grid to the bow shock and wall boundary layer; and adaptation of the grid to the wake flow. Baseline grids for each configuration had 125 streamwise points by 90 normal points. Grids with one-half (125 x 45), two times (125 x 179), and four times (125 x 357) the number of normal points were created from the final adapted (125 x 90 point) grids in order to study the effects of grid resolution on the flow field solutions.

Initial grids were generated for each configuration using an elliptical grid generation algorithm. The governing equation for construction of an elliptical grid is Poisson's equation (Thompson, Thames, and Mastin, 1974):

$$\xi_{xx} + \xi_{yy} = P(\xi, \eta) \tag{7.3.1}$$

$$\eta_{xx} + \eta_{yy} = Q(\xi, \eta) \tag{7.3.2}$$

The (x,y) location of grid points is determined by transforming Poisson's equation and solving the resulting set of elliptical partial differential equations:

$$a x_{\xi\xi} - 2b x_{\xi\eta} + c x_{\eta\eta} = -J^2 \left(P x_{\xi} + Q x_{\eta} \right) \tag{7.3.3}$$

$$ay_{\xi\xi} - 2by_{\xi\eta} + cy_{\eta\eta} = -J^2\left(Py_{\xi} + Qy_{\eta}\right) \tag{7.3.4}$$

where:

$$a = x_{\eta}^2 + y_{\eta}^2 \tag{7.3.5}$$

$$b = x_{\xi}x_{\eta} + y_{\xi}y_{\eta} \tag{7.3.6}$$

$$c = x_{\xi}^2 + y_{\xi}^2 \tag{7.3.7}$$

$$J = x_{\xi}y_{\eta} - x_{\eta}y_{\xi} \tag{7.3.8}$$

Grid clustering on the boundaries and within the domain is controlled through the source terms P and Q. Different forms for these source terms have been developed by Thomas and Middlecoff (1979), Hilgenstock (1988), and Steger and Sorenson (1979). In this work, the form developed by Steger and Sorenson, which provides for control of orthogonality and grid point clustering near the wall boundary, was employed. The Steger-Sorenson source terms are given by:

$$P(\xi,\eta_1) = P_1\exp\left[-a_1(\eta - \eta_1)\right] \tag{7.3.9}$$

$$Q(\xi,\eta_1) = Q_1\exp\left[-b_1(\eta - \eta_1)\right] \tag{7.3.10}$$

a_1 and b_1 are arbitrary constants, and P_1 and Q_1 evaluated at the wall boundary (η=η_1) by:

$$P_1 = J^{-1}\left(y_\eta R_1 - x_\eta R_2\right)\Big|_{\eta=\eta_1} \tag{7.3.11}$$

$$Q_1 = J^{-1}\left(-y_\xi R_1 + x_\xi R_2\right)\Big|_{\eta=\eta_1} \tag{7.3.12}$$

where:

$$R_1 = -J^{-2}\left(ax_{\xi\xi} - 2bx_{\xi\eta} + cx_{\eta\eta}\right)\Big|_{\eta=\eta_1} \tag{7.3.13}$$

$$R_2 = -J^{-2}\left(ay_{\xi\xi} - 2by_{\xi\eta} + cy_{\eta\eta}\right)\Big|_{\eta=\eta_1} \tag{7.3.14}$$

Orthogonality and normal grid spacing near the wall boundary are controlled by:

$$\nabla\xi\cdot\nabla\eta = |\nabla\xi||\nabla\eta|\cos\theta \tag{7.3.15}$$

and

$$ds = \left[\left(x_\xi d\xi + x_\eta d\eta\right)^2 + \left(y_\xi d\xi + y_\eta d\eta\right)^2\right]^{1/2} \tag{7.3.16}$$

By specifying orthogonality ($\theta = 90$ deg) and taking:

$$s_\eta = \left.\frac{ds}{d\eta}\right|_{\xi=\text{const}} = \frac{\Delta s}{\Delta\eta} \tag{7.3.17}$$

equations (7.3.15) and (7.3.16) can be solved for x_η and y_η:

$$x_\eta = -y_\xi s_\eta / \left(x_\xi^2 + y_\xi^2\right)^{1/2} \tag{7.3.18}$$

$$y_\eta = x_\xi s_\eta / \left(x_\xi^2 + y_\xi^2\right)^{1/2} \tag{7.3.19}$$

The elliptical PDE system of equations (7.3.3) and (7.3.4) is solved iteratively by successive over-relaxation (SOR) and the source terms P and Q are updated after each iteration. Starting from initial estimates for the grid (x,y) values and the source terms, the solution procedure is as follows:

1) Compute x_ξ, y_ξ, $x_{\xi\xi}$, and $y_{\xi\xi}$ from the (x,y) values at $\eta=\eta_1$

2) Compute x_η and y_η at $\eta=\eta_1$ from equations (7.3.18) and (7.3.19)

3) Compute $x_{\eta\eta}$ and $y_{\eta\eta}$ at $\eta=\eta_1$ via 2nd order forward differences:

$$x_{\eta\eta} = \left(-7x_{i1} + 8x_{i2} - x_{i3}\right)/\left(2\Delta\eta^2\right) - \left(3\ x_\eta\big|_{i1}\right)/\Delta\eta \tag{7.3.20}$$

$$y_{\eta\eta} = \left(-7y_{i1} + 8y_{i2} - y_{i3}\right)/\left(2\Delta\eta^2\right) - \left(3\ y_\eta\big|_{i1}\right)/\Delta\eta \tag{7.3.21}$$

4) Compute R_1 and R_2 from equations (7.3.13) and (7.3.14)

5) Update P_1 and Q_1 via:

$$P_1^{(n+1)} = P_1^{(n)} + \omega_P\left[J^{-1}\left(y_\eta R_1 - x_\eta R_2\right)^{(n+1)} - P_1^{(n)}\right] \tag{7.3.22}$$

$$Q_1^{(n+1)} = Q_1^{(n)} + \omega_Q\left[J^{-1}\left(-y_\xi R_1 + x_\xi R_2\right)^{(n+1)} - Q_1^{(n)}\right] \tag{7.3.23}$$

6) Perform an SOR sweep through the domain and update the grid (x,y) values

In order to ensure stability, the first derivatives x_ξ, y_ξ, x_η, and y_η are computed with either forward or backward differencing depending on the signs of P_1 and Q_1. The ξ-derivatives are computed with forward differencing if P_1 is positive and backward differencing if P_1 is negative. The η–derivatives are computed with forward differencing if Q_1 is positive and backward differencing if Q_1 is negative. Also, small values (on the order of 10^{-2}) are required for ω_P and ω_Q to keep the magnitude of the corrections in equations (7.3.22) and (7.3.23) from growing too large.

Initial wall cell spacings on the order of 10^{-5} m were typically specified. The spacings were somewhat greater than the desired values (10^{-6} to 10^{-7} m) as it is difficult to maintain grid orthogonality at the wall when extremely small spacings (relative to the physical domain size) are specified in an elliptical system. Clustering of points near the wall to achieve the desired spacing was left for the next step in the adaptation process.

After construction of an initial elliptical grid, a solution for the flow field was iteratively computed using the NEQ2D code. During the iteration, streamwise grid lines were aligned with the bow shock and the normal grid spacing near the wall was adjusted to the desired value using an algebraic adaptation algorithm described in Gnoffo, Hartung and Greendyke (1993). This method involves algebraic manipulation of cell spacings along normal (ξ = constant) grid lines.

The algebraic adaptation process is as follows. First, the height, Δs, of the first cell at the wall is set to a desired value. In the original algorithm, the cell Reynolds number:

$$Re_{cell} = \frac{\rho a \Delta s}{\mu} \tag{7.2.24}$$

is specified. However, owing to the large difference between the density of the attached forebody flow and that within the wake recirculation vortex of the entry vehicle geometry considered in the present work, it was found that specification of a uniform cell wall Reynolds number led to unreasonable cell height growth on the afterbody of the vehicle. Therefore, constant cell heights were instead specified. Test computations

were performed with wall cell heights of between 10^{-5} and 10^{-7} m. It was found that surface heat transfer rates were nearly invariant for wall cell heights of less than 10^{-5} m This spacing produced wall cell Reynolds numbers of 10 or below.

Next, the normal spacing of cells within the boundary layer is adjusted so that a specified fraction (typically 50-60%) of the total number of cells are clustered near the wall. Finally, the outer boundary of the grid is adjusted so that the bow shock is at a specified fraction (typically 70-90%) of the total distance along a ξ = constant coordinate line from the body. An additional step in the original algorithm in which grid lines are clustered at the shock was not employed in this work.

In order to accomplish these manipulations, the height of the wall cell is first nondimensionalized by:

$$\Delta\hat{s}(1) = \frac{\Delta s(1)}{s^*(K)} \tag{7.2.25}$$

where $\Delta s(1)$ is the specified wall cell height, $s^*(K)$ is the total distance along the ξ = constant grid line, K is the total number of points, and superscript * refers to the original grid. The arc-length distance, s, is nondimensionalized as:

$$\hat{s}(\mathrm{k}) = \frac{s(\mathrm{k})}{s^*(\mathrm{K})} \tag{7.2.26}$$

The nondimensional height of the next *kstr* cells (where *kstr* is the number of cells to be clustered near the wall) is set according to the stretching function:

$$\Delta\hat{s}(k) = \min \begin{cases} \left[1 + C\sin\left(\dfrac{(k-1)\pi}{kstr - 1}\right)\right]\Delta\hat{s}(k-1) & \\ & k = 2, kstr \\ \dfrac{1 - \hat{s}(k-\frac{1}{2})}{K + 1 - k} & \end{cases} \tag{7.2.27}$$

where $k-\frac{1}{2}$ is the cell face value, and C is defined by:

$$C = \left(\frac{kstr/K}{\Delta\hat{s}(1)} \right)^{1/kstr} - 1 \tag{7.2.28}$$

The remaining cells outside the boundary layer are equally spaced at:

$$\Delta\hat{s}(\mathrm{k}) = \Delta\hat{s}(\mathrm{k}-1), \quad k > kstr \tag{7.2.29}$$

Nondimensional arc lengths are obtained from:

$$\hat{s}(k+\tfrac{1}{2}) = \sum_{j=1}^{k} \Delta\hat{s}(j) \tag{7.2.30}$$

and the dimensional distribution is given by

$$s(\mathrm{k}) = \frac{s^{*}_{shock}\hat{s}(\mathrm{k})}{f_{shock}} \tag{7.2.31}$$

where s^{*}_{shock} is the shock position on the original grid, and f_{shock} is the specified fraction of the total arc length, s, at which the shock is to be positioned.

During computation of a flow field solution, this shock alignment algorithm was first employed after the computational residual had dropped by several orders of magnitude. Successive adaptations were then performed after the residual had again dropped by several orders of magnitude, and this process

continued until the movement of grid points became negligible. Typically, three to six adaptations were required to produce a converged grid. Examples of an original elliptical grid and a shock-aligned grid are shown in Figures 7.3.1 for the MP-1 configuration at the $Re_\infty = 0.5 \times 10^6$ ft^{-1} Mach 10 condition.

The solution of Poisson's equation with Steger-Sorenson source functions followed by algebraic adaptation to fit the shock and cluster points near the wall is a robust procedure which produces grids that are well-suited for computation of attached forebody flows such as that over the 70 deg sphere-cone geometry. However, computation of the wake flow field presents additional complications. As discussed in Chapter 1, the wake of a blunt body is typically characterized by a free shear layer and a recirculating flow region between the free shear layer and base of the body. The free shear layer and vortex structure are viscous-dominated regions in which grid spacing comparable to that in a wall boundary layer is required in order to properly resolve the flow field. Grid alignment with the flow direction is also a concern. In a hypersonic flow, the bow shock lies close to the body, and so alignment of the grid with the bow shock also serves to align the grid with the direction of the flow between the shock and body. However, this is not the case in the wake, and the shock-adapted grid lines can be highly skewed with respect to the flow streamlines. The lack of resolution within the free shear layer and recirculation region and skewness of the grid lines with respect to the flow direction introduce artificial viscosity into the computations and degrade the accuracy of the solution. As will be shown in the next chapter, this has a large effect on the size and shape of the recirculation zone and on the surface heating on the afterbody and sting.

In order to minimize grid resolution and skewness effects, grids were adapted to the wake flow structure using the Volume Grid Manipulator (VGM) code (Alter, 1996, 1997). The VGM code incorporates a variety of algebraic techniques for redistributing and clustering grid points and smoothing grid lines. In this work, VGM was used to smooth the outer boundary of the grid after the shock alignment process, cluster normal grid points within the wake recirculation region, and align streamwise wake grid lines with the free shear layer.

Examples of shock-aligned grids before and after adaptation to the wake flow features using VGM

are shown in Figure 7.3.2. As can be seen, the effects of this adaptation was to increase the normal grid point density in the region immediately behind the vehicle and to change the streamwise grid alignment within this region. In Figure 7.3.3, Mach number contours from computations on the grid before and after adaptation with VGM are shown. VGM adaptation was limited to the wake region, and thus no changes were produced in the computed forebody solutions. However, the computed structure of the wake recirculation zone was significantly altered. The free shear layer separation point moved upstream toward the corner, while the free shear layer reattachment point on the sting moved further downstream. The adaptation to the wake structure is illustrated better in Figure 7.3.4, in which the computed streamlines are superimposed on the two grids. As can be seen, the streamwise grid lines follow the free shear layer much more closely in the VGM-adapted grid. The growth of the recirculation zone produced by clustering of points within the viscous flow region and elimination of grid line skewness with respect to the shear layer is consistent with a reduction of grid-produced artificial viscosity. The changes in computed surface pressure and heating distributions produced by this reduction will be presented in greater detail in the next chapter.

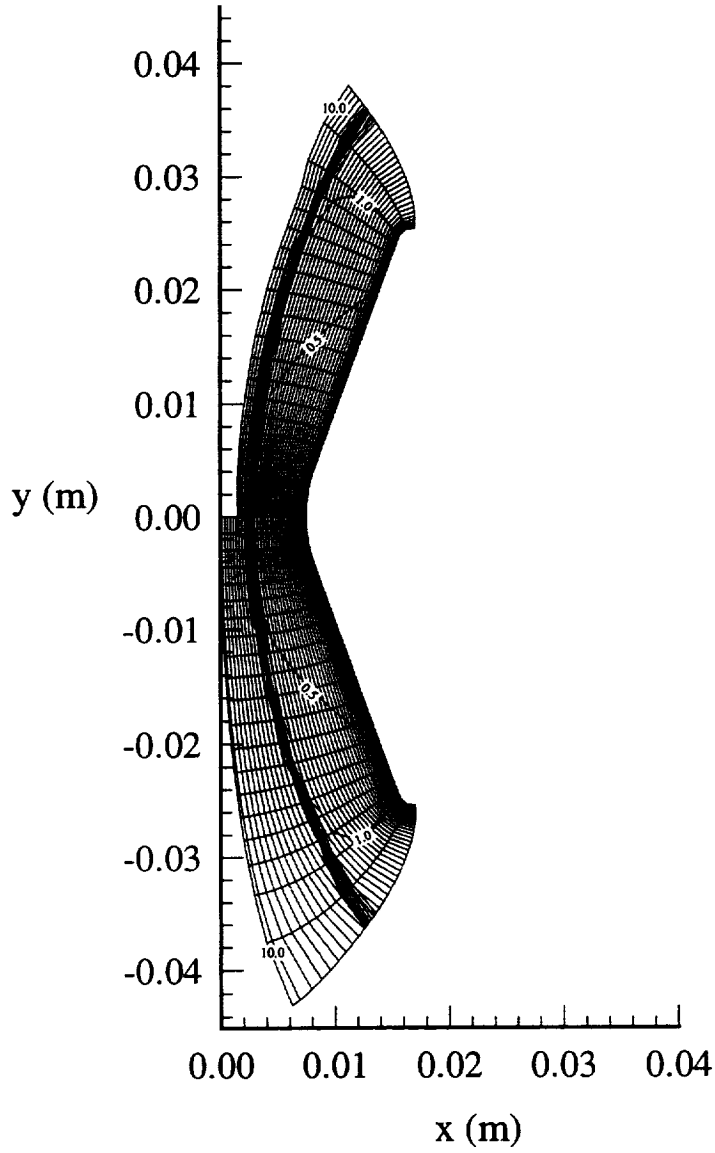

Figure 7.3.1 Mach Contours Superimposed on Original (bottom half) and Shock-Aligned (top half) Grids for MP-1 Configuration in 31–Inch Mach 10 Air Tunnel

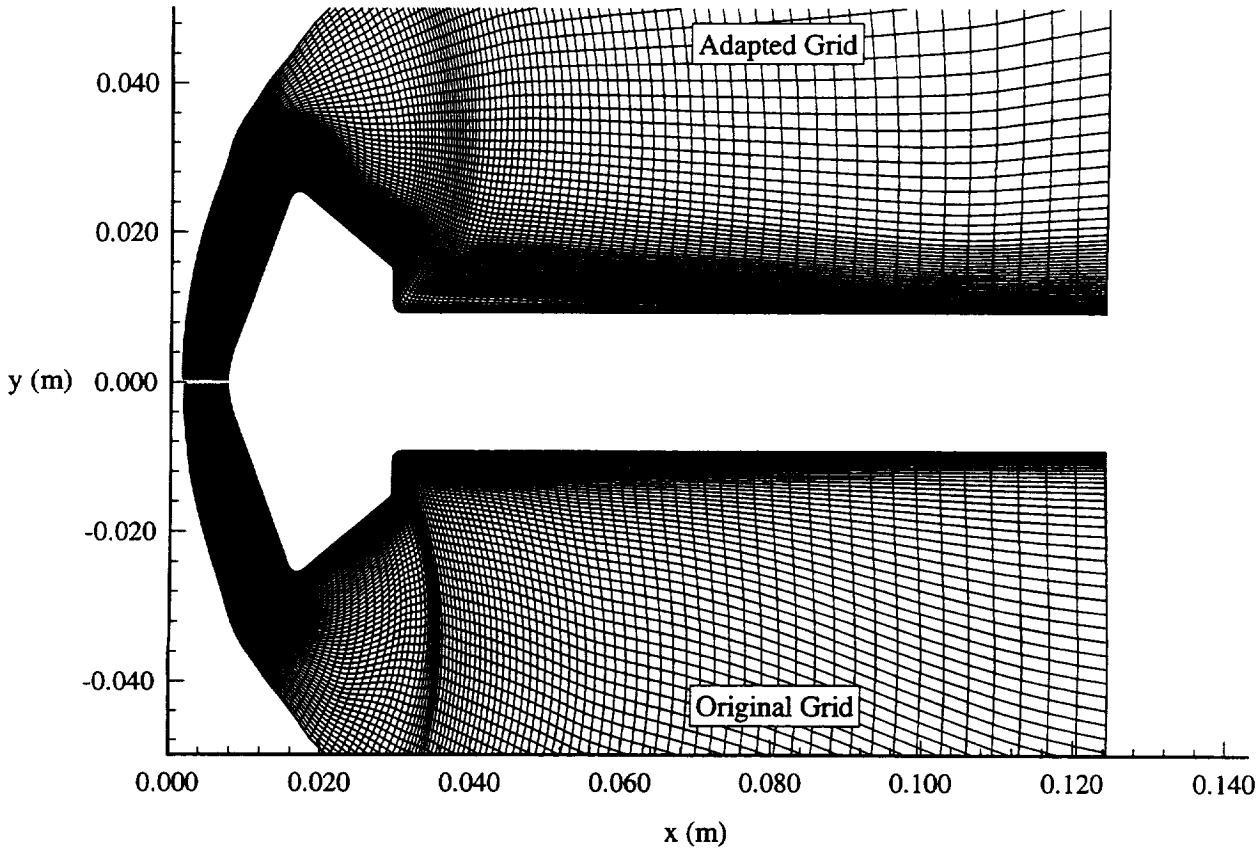

Figure 7.3.2 Shock-Aligned (125x90) Point Grids Before and After Shear Layer Adaptation for MP-1 Configuration in 31-Inch Mach 10 Air Tunnel

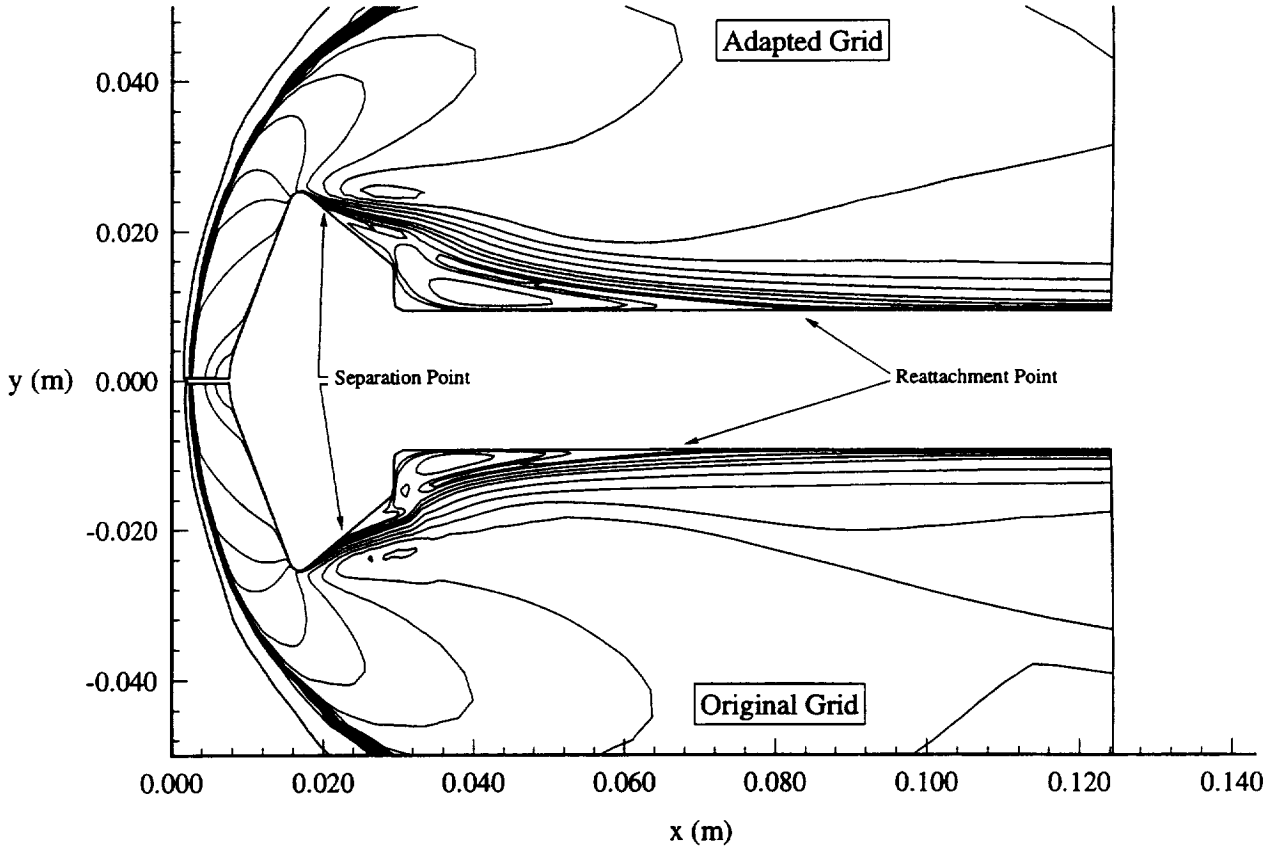

Figure 7.3.3 Mach Contours from Solutions on Original and Shear-Layer Adapted Grids for MP-1 Configuration in 31-Inch Mach 10 Air Tunnel

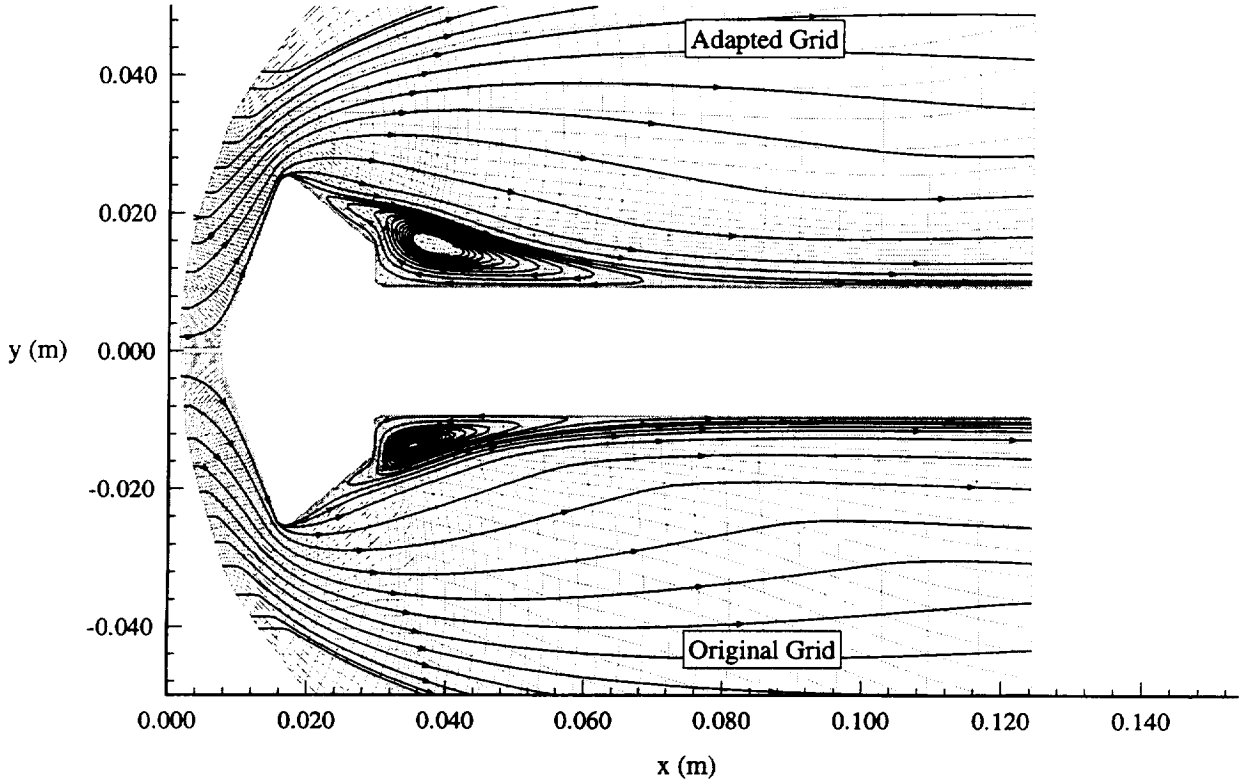

Figure 7.3.4 Streamlines from Solutions on Original and Shear-Layer Adapted Grids for MP-1 Configuration in 31-Inch Mach 10 Air Tunnel

CHAPTER 8
COMPUTATIONAL RESULTS AND COMPARISONS WITH EXPERIMENTAL DATA

Flow field solutions were computed for each of the four parametric geometries using the NEQ2D code at freestream conditions equivalent to the test conditions of the 31-Inch Mach 10 Air Tunnel and the HYPULSE Expansion Tube. The grid adaptation techniques discussed in Chapter 7 were used to improve the quality of the solutions, and grid resolution studies were conducted for each of the test conditions.

Freestream conditions for the computations were taken from the facility operating conditions listed in Tables 4.2.1 and 4.3.1. As discussed in Chapter 6, the surface temperature rise on the test models was small in comparison to freestream total temperatures, and therefore surface temperatures were fixed at a uniform value of 300 K for all computations. For the chemically reacting HYPULSE Expansion Tube cases, a non-catalytic surface boundary condition was imposed owing to the low surface temperature and the use of Macor, a glass-ceramic material, for fabrication of the test models.

Section 8.1 31-Inch Mach 10 Air Tunnel Test Conditions

8.1.1 Grid Resolution

Grid resolution effects on surface pressure and heating distributions were investigated for the MP-1 configuration at each of the three 31-Inch Mach 10 Air Tunnel operating points. The baseline grid resolution was 125 streamwise by 90 normal points for each case. The original baseline grid was aligned to the bow shock and adapted to the wake flow features as described in Chapter 7. Streamwise grid point

resolution was not found to have a significant effect on the surface distributions, and so the number of streamwise grid points was fixed at 125. However, surface distributions were extremely sensitive to the number of normal grid points, and therefore grids with 45, 125, 179, and 357 normal points were constructed in order to quantify the effects of normal grid point resolution. The computational grid for the MP-1 configuration is shown in Figure 8.1.1, and a close-up view of the forebody and near wake portion of the grid is shown in Figure 8.1.2

The effects of the normal grid point resolution on the surface pressure and heating distributions for the MP-1 configuration at each of the three Reynolds numbers test points are shown in Figures 8.1.3-8.1.8. For comparison, the wake distributions from the original grid before shear layer adaptation using VGM are also shown for the $Re_\infty = 0.5 \times 10^{-6}$ ft^{-1} case.

For the attached flow on the forebody, pressure distributions were insensitive to normal grid point resolution (Figures 8.1.3a, 8.1.5a, 8.1.7a), and only small effects were observed on the heating distributions (Figures 8.1.4a, 8.1.6a, 8.1.8a). The greatest sensitivity of the heating rates was observed at the nose around the stagnation point and at the corner. Heating rates in these areas decreased by ~3% between the 45 normal point grid and the 90 point grid, by ~1% between the 90 point grid and the 179 point grid and by less than 1% between the 179 and 357 point grids. It can thus be concluded that 90 normal points is sufficient to resolve the heating distributions on the forebody for perfect-gas conditions.

In contrast to the forebody distributions, both the pressure and heating distributions in the wake were found to be extremely sensitive to grid resolution and grid alignment. As discussed in Chapter 1, the wake of a blunt body is characterized by a free shear layer and recirculating flow region, as well as a recompression shock where the free shear layer reattaches to the sting. The free shear layer and the recirculation region are both dominated by viscous forces. Therefore, it is not appropriate to perform computations on grids which have large cell sizes in these regions such as are typically employed for flow fields away from a body. Instead, the grid resolution within these regions must be close to that employed in wall boundary layers. Furthermore, as was shown in Chapter 7, the grid must also be aligned with the

shear layer in order to avoid introducing numerical dissipation into the computations.

It is obvious that heating distributions on the afterbody and sting will be sensitive to the proper resolution of the viscous gradients within the shear layer and recirculation zone. However, the pressure distributions will also be affected to a lesser but still significant extent because both the free shear layer separation and reattachment points will be affected by the quality of the grid. Movement in the locations of the points alters the entire structure of the wake flow, and thus affects the surface pressure distributions. In general, the effects of increases in grid resolution on the surface pressure distributions were to increase the pressure on the afterbody, decrease the pressure between the base of the afterbody and shear layer reattachment on the sting, and to increase the pressure on the sting downstream of reattachment.

As seen in Figures 8.1.3b, 8.1.5b and 8.1.7b, the greatest sensitivity in the wake pressure distributions occurred within the recirculating flow region (S/R_b ~2.0 to ~ 4.0). Computations on the 45 normal point grids produced large errors in the both the shape and magnitude of the distributions within the recirculation region as well as in the location of the maximum sting pressure. Between the 90 and 179 point grids, pressures dropped by ~5 to 10%, while the changes between the 179 and 357 point grids were on the order of 5%. For comparison, the pressure distributions on a 90 normal point grid before shear layer grid adaptation are also shown in Figure 8.1.3b. This distribution does not compare well even to the coarsest adapted grid. Grid resolution increases produced changes of about the same order of magnitude on the afterbody (S/R_b ~1.0 to ~ 2.0) as were observed on the sting, while the distributions downstream of shear layer reattachment were slightly less sensitive to grid resolution. From these results, it would appear that the grid must be properly adapted to the shear layer and that at least 179 normal points are required in order to compute accurately the wake pressure distributions at these test conditions.

As shown in Figures 8.1.4b, 8.1.6b and 8.1.8b, the wake heating distributions were even more sensitive than pressure distributions to grid resolution and grid adaptation. The effect of increasing the grid resolution was to lower the heating throughout the wake. A downstream movement of the peak sting heating was also produced. As with the pressure distributions, the greatest sensitivity was again observed

on the sting between the base and shear layer reattachment. Heating rates within this area dropped by more than 20% between the 45 and 90 normal point grids, by 15 to 20% between the 90 and 179 point grids and by ~10% between the 179 and 357 point grids. Heating rates on the afterbody and on the sting downstream of reattachment were less sensitive, and the decrease in heating between the 179 and 357 point grids was only ~5%. Also, as shown in Figure 8.1.4b, heating rates on the non-adapted 90 normal point grid were much higher even than those on the coarsest adapted grid, and the shear layer reattachment point was further upstream.

From these heating results, it can be concluded that at least 179 normal points are required to compute accurately the heating rates on the afterbody and on the sting downstream of reattachment; furthermore, the grid must be properly aligned with the free shear layer and the majority of the points must be distributed within the free shear layer and recirculation region. However, even computations on an adapted 357 normal point grid still appear to produce errors in the sting heating rates within the recirculation region of 5 to 10%, although at least these errors are conservative in that the computations over-predict the heating rates. This was considered to be an acceptable magnitude of error as further increases in grid resolution were not considered practical in terms of computational requirements, especially in consideration of the fact that only 90 normal points were required for accurate forebody computations.

As result of this grid resolution study, it was decided that shear-layer adapted (125 x 357) point grids would be employed for the perfect gas test cases. This same resolution was also employed for the MP-2, MP-3 and MP-4 geometries, and the wake adaptation process detailed in Chapter 7 was followed in the construction of grids for these configuration. All results presented in the remainder of the section will be from computations on these (125 x 357) point grids.

8.1.2 Computed Flow Fields and Surface Distributions

Computed streamlines, wake flow structure details, Mach contours, pressure ratio, temperature, and

density ratio contours, and Knudsen number contours for the MP-1 geometry are shown in Figures 8.1.9-8.1.15 for the $Re_\infty = 0.5\text{x}10^6$ ft^{-1} condition, Figures 8.1.16-8.1.22 for the $Re_\infty = 1.0\text{x}10^6$ ft^{-1} condition, and Figures 8.1.23-8.1.29 for the $Re_\infty = 2.0\text{x}10^6$ ft^{-1} condition. Flow field details for the other configurations were qualitatively similar and will not be shown.

The structure of the wake is illustrated by the streamline plots in Figures 8.1.9, 8.1.16 and 8.1.23. As seen in these plots, the size of the main wake vortex increased a small amount with each increase in Reynolds number, as predicted by laminar theory (Berger, 1971). The boundary layer separation point is also seen to have moved further down the afterbody as the Reynolds number was decreased, from which it can be inferred that below some limiting Reynolds number, the boundary layer would remain attached to the afterbody. Such attached wake flow was observed on a similar geometry by Kuehn and Monson (1967) at $Re_{\infty,D} = 3200$, while separated flow was observed at $Re_{\infty,D} = 29{,}200$ (the lowest diameter-based Reynolds numbers for these tests was $Re_{\infty,D} = 83{,}300$). In addition to the main vortex, smaller counter-rotating vortices were also predicted to occur at the junction of the model and sting, and on the afterbody of the model. These small vortices were well defined at the highest Reynolds number, and decreased in size as Re_∞ was decreased; at the lowest Reynolds number, the afterbody vortex was not predicted to form.

The near-wake structure is presented in more detail in Figures 8.1.10, 8.1.17 and 8.1.24, in which streamlines are overlaid on contour plots of the v-component of velocity. The bow shock is well defined in these figures, and the series of compression waves near the shear layer reattachment which coalesce into the recompression shock can be seen clearly. Subtler details of the near-wake structure can also be identified in these plots. The size of the counter-rotating vortices and the location of shear layer separation and reattachment can be seen. Additionally, an expansion fan produced by the turning of the shear layer after it passes the base of the vehicle can be identified. There is also what appears to be a very weak shock which is produced by the curvature of the shear layer due to the influence of the upward flow in the afterbody vortex from the base of the model.

Computed Mach number contours are shown in Figures 8.1.11, 8.1.18 and 8.1.25. As expected,

the sonic line on the forebody can be seen to be located right at the start of the forebody corner, after which the Mach number increases rapidly. The recompression shock on the sting can be identified by its effects on the Mach contours. The flow within the wake vortex was predicted to remain subsonic except for within a very small region close to the sting at the highest Reynolds number.

As shown in the pressure ratio contours in Figures 8.1.12, 8.1.19 and 8.1.26, expansion of the forebody flow around the corner leads to low pressures in the wake; the recirculation vortex pressures are only slightly higher than the freestream pressure. The recompression shock is weak and does not produce a large increase in pressure. Computed wake flow field temperatures (Figures 8.1.13, 8.1.20 and 8.1.27) were also low, but remained much higher than the freestream temperature. A thin region of higher temperatures can be seen in the region of shear layer reattachment, which causes the higher heating rates along the sting near reattachment.

Expansion of the forebody flow around the corner produces a very low density wake (Figures 8.1.14, 8.1.21 and 8.1.27). Predicted densities within the wake vortex were less than 25% of the freestream density. This rapid expansion around the corner and the low wake densities suggested that non-continuum behavior could be a concern, and therefore local Knudsen numbers were computed throughout the flow field.

The local Knudsen number is given by (Bird, 1994):

$$Kn = \frac{\lambda_{mfp}}{\rho} |\nabla \rho| \tag{8.1.1}$$

where the mean free path is:

$$\lambda_{mfp} = \frac{1}{\sqrt{2}\,\pi d^2 N} \tag{8.1.2}$$

and where d is the molecular diameter and N is the number density of the flow.

According to Bird, the continuum assumption begins to break down for local Knudsen numbers above 0.1, and for Knudsen numbers above 0.2 the Navier-Stokes equations cannot be used to adequately represent the flow field. As shown in Figures 8.1.15, 8.1.22 and 8.1.29, the only region of concern in the flow fields was on the afterbody just past the corner. At the highest Reynolds number, the local Knudsen number exceeded 0.1 only in a very small area of about the height of the boundary layer. The $Kn = 0.1$ contour was predicted to expand as the Reynolds number decreased, and at the lowest Reynolds number the local Knudsen number exceeded 0.2 in a small region before the separation point. Because the free shear layer and recirculation region are dependent on the location of separation, the high local Knudsen numbers near the separation point at the lowest Reynolds number might be a cause for concern. However, as shown in Figure 8.1.30, when the computed streamlines from Figures 8.1.9 and 8.1.10 are compared to the surface oil flow patterns from Figure 6.1.5, it can be seen that the computed separation and reattachment locations agree well with those from the oil flow tests. It was therefore concluded that the continuum assumption is valid for these conditions and that the Navier-Stokes equations can be used to model the flow fields.

Computed surface pressure and heating distributions are shown for each test point for the MP-1 configuration in Figures 8.1.31-8.1.36, for MP-2 in Figures 8.1.37-8.1.42, for MP-3 in Figures 8.1.43-8.1.48 and for MP-4 in Figures 8.1.49-8.1.54. Axes with both the dimensional distributions and the distributions non-dimensionalized by the measured stagnation point values are shown in these plots.

Computed pressure distributions are characterized by nearly constant values on the forebody up to the corner, after which the pressure rapidly drops as the flow expands around the corner. A minimum pressure at least two orders of magnitude lower than that at the stagnation point is reached on the afterbody at the shear layer separation point. The pressure then increases sharply within the recirculation region and remains at a nearly constant value along the afterbody. A very small increase occurs at the afterbody corner after which it remains nearly constant on the base. Pressure decreases slightly on the sting in the direction away from the base within the region of the small secondary base vortex. Going along the sting, the pressure then begins to rise and it reaches a maximum in the region of the shear layer reattachment on the

sting.

Computed forebody heating distributions have a maximum at the stagnation point followed by a gradual decrease as the flow goes around the nose and along the cone. A narrow peak occurs right at the corner where the flow begins to accelerate and goes supersonic. Heating rates then drop rapidly as the flow expands around the corner and then separates on the afterbody. Heating distributions for the intermediate and high Reynolds number conditions have a local maximum on the afterbody in the region of the secondary afterbody vortex. The presence of this vortex is not predicted at the low Reynolds number and so no local afterbody heating maximum is produced. A second narrow peak occurs at the afterbody where the flow in the main vortex coming from the base is accelerated around the afterbody frustrum corner. Heating rates on the base are the lowest in the wake. Heating rates on the sting are highest around the free shear layer reattachment point. Heating rates along the sting decrease slowly in the downstream direction and decrease more rapidly in the upstream direction within the main wake vortex.

8.1.3 Reynolds Number Effects

Reynolds number effects on the normalized heating distributions for each of the four configurations are shown in Figures 8.1.55-8.1.58. Some small variations (less than 4%) occurred in the normalized forebody heating distributions for a few of the cases. However, these differences are attributed either to differences in the convergence level of the computations, or to the fact that the same grid was used at each Reynolds number test condition, which produced slight differences in the wall cell Reynolds numbers. Therefore, the computations are taken to show that the normalized forebody heating distributions are unaffected by Reynolds numbers.

Normalized heating distributions on the afterbody and sting were found to be dependent on Reynolds number. In general, the effect of an increase in freestream Reynolds number was an increase in the normalized peak sting heating and a movement of the peak upstream toward the base of the model. The

normalized peak heating at the afterbody corner also increased with Reynolds number, and a small local maximum was produced on the afterbody at the intermediate and high Reynolds number conditions. This local maximum is due to the formation of the second afterbody vortex, which was noted in the previous section.

For the MP-1 geometry (Figure 8.1.55b) the normalized peak sting heating increased from 6% of the stagnation point heating at the lowest Reynolds number to 8% at the highest Reynolds number. The movement of the peak was from 4.3 forebody radii from the base at the lowest Reynolds number to 4.0 forebody radii at the highest Reynolds number. However, as was experimentally shown by Wells (1988, 1990), the location of the peak is not coincident with the free shear layer reattachment location. As can be seen in the streamline plots discussed in the previous section, the reattachment point actually moved a small distance further away from the base as the Reynolds number was increased. The locations of the peak heating and reattachment points are plotted in Figure 8.1.59. These results show that the size of the wake vortex increases and the peak sting heating point moves upstream toward the reattachment point as the Reynolds number is increased.

8.1.4 Configuration Effects

Configuration effects on the forebody and wake heating distributions are shown for each of the three Reynolds numbers in Figures 8.1.60-8.1.62. On the forebody (Figures 8.1.60a, 8.1.61a and 8.1.62a), the increase in corner radius between the MP-1 and the MP-3 and MP-4 configurations resulted in corner heating peaks that were broader and of lesser magnitude. The decrease in the corner peak was on the order of 12% from the smallest corner radius geometry to the largest. Some inconsistencies were noted at the nose, but these were attributed to the typical phenomena of convergence problems at an axisymmetric stagnation point. Otherwise, the forebody distributions for the three sphere-cone geometries (MP-1, MP-3 and MP-4) were identical. The MP-2 hyperboloid heating rates were 5 - 7% lower than the sphere-cone heating rates in

the nose region due to the effectively larger nose radius of the hyperboloid. Away from the nose, the hyperboloid heating distributions approached those of the sphere-cones just as its geometry approaches that of the sphere-cones.

Configuration effects on the wake distributions (Figures 8.1.60b, 8.1.61b and 8.1.62b) were small and were harder to assess accurately because of the demonstrated sensitivity of the wake solutions to the structure of the computational grid. It appeared that the effect of increasing the corner radius was to cause a small decrease (on the order of 5 to 7% for the MP-4 geometry) in the peak sting heating rate but not to cause any significant movement of the peak in terms of distance from the base of the model. The hyperboloid wake heating distribution was very similar to that of the MP-1 sphere-cone, as would be expected due to the similarity of the two geometries.

8.1.5 Comparison with Experimental Data

Comparisons between the computed heating distributions and the experimental data are presented in this section. Heat-transfer rates from the numerical computations are all based on the uniform 300 K wall temperature for which solutions were computed. As was discussed in Chapter 6, experimental data were taken over time intervals for which the Stanton numbers remained independent of wall temperature. Experimental heat-transfer rates for a uniform 300 K wall temperature were thus determined from the reported C_H values by:

$$q_{300K} = C_H\left[\rho_\infty U_\infty \left(h_0 - h_{300K}\right)\right] \tag{8.2.1}$$

Comparisons for the forebody and wake heating distributions for each of the three Reynolds

numbers are presented in Figures 8.1.63-8.1.65 for the MP-1 configuration, Figures 8.1.66-8.1.68 for MP–2, Figures 8.1.69-8.1.71 for MP-3 and Figures 8.1.72-8.1.74 for MP-4. Error bars on the experimental data are based on the uncertainty analysis presented in Section 6.3 of Chapter 6. According to that analysis, the estimated uncertainties were on the order of 7 - 8% for tests in the 31-Inch Mach 10 Air Tunnel. Uncertainties in the computed heating rates can be estimated from the grid resolution study discussed in Section 8.1.1.

Very good agreement between the computational and experimental forebody heating rates was obtained for all configurations at all Reynolds numbers. For all comparisons but one (MP-3 at $Re_\infty = 2.0x10^6$ ft^{-1}), the computed heat-transfer rates at the stagnation point and around the nose were within the experimental uncertainty. The computations also resolved the corner heating peaks better than the experimental data due to gage spacing limitations in the construction of the test models. However, there was a definite bias with Reynolds number noted in the comparisons. At the lowest Reynolds number, computed heating rates were slightly higher than the experimental heating rates, but were well within the experimental uncertainty bounds; at the intermediate Reynolds number, the computed heat-transfer rates were again higher, and were just at the edge of the uncertainty bounds; at the highest Reynolds number, computed heating rates fell above the uncertainty bounds. This bias could be due to a facility-dependent calibration problem, to the use of the same grid at each Reynolds number, or to the uncertainty in Macor thermal properties used in the data reduction being greater than estimated.

The comparisons revealed very large differences in the form and magnitude of the experimental and computational heating distributions on the afterbody and sting. In general, the distributions were in reasonably good agreement on the afterbody frustrum and base, and on the sting near the base. However, the experimental heating rates around the shear layer reattachment point and further down the sting after the flow has reattached were much higher than the computed values. The differences between the two distributions increased rapidly with Reynolds number. For example, for the MP-1 configuration at the lowest Reynolds number, the computational and experimental peak sting heating rates were, respectively,

6% and 8% of the stagnation point heating; at the intermediate Reynolds number, the values were 7% and 11%; and at the highest Reynolds number the peak values were 8% and 15% of the stagnation point heating rate.

In previous sections, several different sources of error or uncertainty in either the experiments or computations have been investigated. These include: facility run condition repeatability (Section 4.2.2); temperature-dependence of Macor thermal properties (Section 5.2.2); run-to-run repeatability of heating data (Section 6.1.5); Macor thermal properties uncertainty (Section 6.3); grid adaptation to the shear layer (Section 7.3); grid resolution (Section 8.1.1); and non-continuum wake flow (Section 8.1.2). These different factors have all been determined either to not have any significant influence on the results, or their influences have been quantified, and the resulting uncertainties produced in the results have been estimated. None of these uncertainties are of large enough magnitude to produce the discrepancies between the experimental and computational wake heating results; furthermore, the close comparisons presented for the forebody demonstrate the soundness of both the experimental and computational techniques.

As the factors listed above have been eliminated as reasons for the differences between the experimental and computational results, the most likely explanation for these differences is then that they were a result of comparisons between laminar CFD solutions and transitional/turbulent experimental wake data. This explanation is suggested by the fact the differences between the experimental and computational results increase with Reynolds number, and by the fact that the size of the wake vortex predicted by laminar computations increases with Reynolds number, whereas the size determined from oil flow patterns decreases.

The following model (Figure 8.1.75) is proposed for transition to turbulence in the wake for these experiments: the forebody boundary layer is laminar, and remains laminar after separation until the shear layer reattachment region (the neck of the wake); in this area, the increasing pressure gradient produced by the series of compression waves that begin to turn the shear layer parallel to the sting causes the free shear layer to begin to transition to turbulent flow; however, because transition does not occur until close to

reattachment, the actual size of the wake vortex is fairly close to that predicted by laminar computations. Some of the turbulent disturbances within the free shear layer are ingested into the wake vortex, but the decreasing pressure gradient produced as the flow expands from rest at the reattachment stagnation point dissipates these disturbances. Thus, the experimental and computational results for the recirculation region agree fairly well. In the opposite direction, the transition to fully turbulent behavior of the reattached shear layer continues with distance along the sting. This produces the growing difference between the experimental and computational results in the direction downstream of reattachment.

This proposed model for transition is based primarily on the work of Lees (1964), as well as that of Demetriades (1964) and Zeiberg (1964). Lees correlated a large body of flight and ground test data and found that transition point first occurs in the far wake 40 to 50 body diameters from the vehicle, and then the transition point moves upstream toward the vehicle as the Reynolds number is increased. The far wake transition Reynolds number (based on local conditions) was found to remain constant at 5.6×10^4. When the transition point reaches the neck of the wake (the reattachment point on the sting in this case) it remains fixed there until the local Reynolds number in the free shear layer exceeds the free shear layer transition value, which is on the order of 1×10^5. Transition then proceeds further upstream in the free shear layer as the Reynolds number increases.

There exists a large range of scatter in the data examined by Lees, and these critical transition numbers are considered very approximate. The use of these exact values indicates that the transition point is stuck in the neck at the highest Reynolds number test condition, occurs about one body radii downstream of the neck at the intermediate Reynolds number, and is well past the end of the sting at the lowest Reynolds number. However, in addition to the scatter in the data examined by Lees, the data were taken on slender cones or hemispheres tested in either in flight or in ballistic ranges. Thus, the influence of the much greater cone angle and of the model sting in the present work is not accounted for in Lees' correlation. Therefore, these correlations are taken only as a very rough guide to the wake behavior.

Based on the analysis of the current experimental and computational results, it seems that the

reattached flow on the sting is transitional or turbulent. However, because the experimental and computational heating rates within the recirculation region agree fairly well, and because the reattachment locations from the oil flow patterns and from the computed streamlines do not differ too greatly, it would seem that transition cannot be occurring too far upstream of the neck. Furthermore, local Reynolds numbers for the free shear layer are lower than the critical transitional value of $1x10^5$. It is therefore concluded that the transition point is fixed in the neck near the reattachment point for all the test Reynolds numbers.

Section 8.2 HYPULSE Expansion Tube Test Conditions

8.2.1 Grid Resolution

Grid resolution effects on surface pressure and heating distributions were investigated for the MP-1 configuration for both the CO_2 and air test points. As with the Mach 10 tests, the baseline grid resolution was 125 streamwise by 90 normal points for each case, and the original baseline grid was aligned to the bow shock and adapted to the wake free shear layer as described in Chapter 7. Because of the additional computational requirements of the non-equilibrium thermochemical models used for these cases, the normal grid point resolution study was limited to grids with 45, 125, and 179 normal points. The computational grid for the CO_2 case is shown in Figure 8.2.1, and a close-up view of the forebody and near wake portion of the grid is shown in Figure 8.2.2; the overall grid and close-up view for the air case are shown in Figures 8.2.3 and 8.2.4

The effects of the normal grid point resolution on the surface pressure and heating distributions for the MP-1 configuration at the CO_2 and air test points are shown in Figures 8.2.5-8.2.8. For the attached flow on the forebody, pressure distributions were insensitive to normal grid point resolution (Figures 8.2.5a

and 8.2.7a). For the forebody heating distributions (Figures 8.2.6a and 8.2.8a) large differences were observed between the 45 and 90 point grids around the stagnation point for both cases and also at the nose/cone junction for the CO_2 case. For CO_2, the heating in these areas dropped by ~7%, and for air the heating dropped by ~10%. Between the 90 and 179 point grids, the heating rates dropped by only 2-3% for both cases. The 179 normal point grid was thus considered to be acceptable for the forebody flow.

As with the Mach 10 computations, wake surface pressure and heating distribution were much more sensitive to grid resolution and grid alignment. The greatest sensitivity was again on the sting between the base and the shear layer reattachment, while the values on the afterbody and on the sting downstream from reattachment were less sensitive. Between the 90 and 179 point grids, the maximum changes in pressure were ~8% for air and ~5% for CO_2, while the maximum changes in heating were ~15% for CO_2 and ~10% for air.

Based on the results, shear-layer adapted grids of 125 x 179 points were used for both the air and CO_2 test cases. The same grid resolution was also employed for the other configurations. However, it was recognized that the surface heating rates within the recirculation region would probably be over-predicted by up to 10%.

8.2.2 Computed Flow Fields and Surface Distributions

Computed streamlines, wake flow structure details, Mach contours, pressure ratio, temperature, translation to vibrational temperature ratio and density ratio contours, Knudsen number contours, and species mass concentrations for the MP-1 geometry are shown in Figures 8.2.9-8.2.19 for the CO_2 condition and in Figures 8.2.21-8.2.31 for the air condition. Flow field details for the other configurations were qualitatively similar and will not be shown.

The structure of the wake is illustrated by the streamline plots in Figures 8.2.9 and 8.2.10 for CO_2 and in Figures 8.2.21 and 8.2.22 for air. The wake vortices for these two conditions are similar to those for

the Mach 10 cases, although they are smaller as would be expected by the fact the HYPULSE Reynolds numbers were much lower than those in the Mach 10 tests. The two small, counter-rotating vortices can again be seen, as can the recompression shock and the expansion following the afterbody corner. The weak shock seen in the Mach 10 computations which was caused by the influence of the secondary afterbody vortex is not visible in these plots.

Computed Mach number contours are shown in Figures 8.2.11 and 8.2.23. The sonic line on the forebody can again be seen to be located right at the start of the forebody corner, after which the Mach number increases rapidly as the flow expands into the wake. The recompression shock on the sting can be identified by its effects on the Mach contours. The flow within the wake vortex was predicted to remain subsonic in both tests cases.

Expansion of the forebody flow around the corner leads to low pressures in the wake as shown in Figures 8.2.12 and 8.2.24. Recirculation vortex pressures were approximately equal to the freestream pressure. On the forebody, an overexpansion and recompression at the nose/cone junction can be seen for the CO_2 case.

The high total enthalpy of the HYPULSE test conditions produces extremely high temperatures behind the bow shock (Figures 8.2.13 and 8.2.25); however, vibrational non-equilibrium is limited to the region immediately behind the bow shock (Figures 8.2.14 and 8.2.26). Away from the shock, the forebody flow quickly reaches vibrational equilibrium. In the wake, the rapid expansion of the flow around the forebody corner produces a vibrationally frozen flow. In the outer, inviscid portion of the wake, vibrational temperatures remain frozen well above the translational temperatures, but the temperatures within the recirculation region and reattached shear layer begin to approach equilibrium.

Computed wake densities (Figures 8.2.15 and 8.2.27) were, at the lowest, on the order of 40% of the freestream density. This was much higher than in the perfect gas cases, and local Knudsen number computations (Figures 8.2.16 and 8.2.28) showed that the Knudsen numbers exceeded the 0.1 level in only a very tiny portion of the boundary layer just prior to separation, and never exceeded 0.2. The continuum

assumption can thus be considered as valid for the HYPULSE tests.

Species mass fractions are shown for the CO_2 test condition in Figures 8.2.17-8.2.20. Passage through the bow shock produces a high level of CO_2 dissociation and subsequent formation of CO, O_2 and O. For the air case (Figures 8.2.29-8.2.32) only a small amount of N_2 dissociation occurs behind the bow shock on the forebody. O_2 dissociation is nearly complete, leading to the formation of O and a small amount of NO. For both test conditions, chemical reactions in the wake were completely frozen by expansion around the forebody corner.

Computed surface pressure and heating distributions are shown for the MP-1 configuration in CO_2 and in air in Figures 8.2.33-8.2.36, and for the MP-2, MP-3 and MP-4 configurations in Figures 8.2.37-8.2.38, Figures 8.2.39-8.2.40, and Figures 8.2.41-8.2.42, respectively. Axes for both the dimensional distributions and the distributions non-dimensionalized by the measured stagnation point values are shown in these plots.

Pressure distributions are characterized by nearly constant values on the forebody up to the corner for the air case, and for the CO_2 case by an initial over-expansion and recompression at the nose/cone junction and then by constant levels up to the corner. For both test conditions, the pressure rapidly drops going around the corner and reaches a minimum on the afterbody at the shear layer separation point. The pressures are nearly constant on the afterbody and base except for a slight increase in the base pressure above the level of that on the afterbody. The maximum pressure on the sting occurs around the reattachment point and the pressure decreases gradually in both directions along the sting away from the reattachment point.

Forebody heating distributions for both cases have their maximum values at the stagnation point, after which the heating rates slowly decrease until the corner is reached. A narrow local maximum occurs at the forebody corner where the flow begins to accelerate. Heating rates then drop rapidly as the flow expands around the corner and the boundary layer separates from the afterbody. A small local maximum due to the secondary afterbody vortex is predicted for the CO_2 tests case, while that for the air case is larger. A large

peak is predicted at the frustrum corner for both test conditions, and another very small maximum is predicted for the secondary vortex at the base/sting junction. Heating rates on the sting are highest around the free shear layer reattachment point. Heating rates along the sting decrease slowly in the direction away from the base and more rapidly in the direction upstream toward the base.

8.2.3 Test Gas and Configuration Effects

Test gas effects in HYPULSE on the forebody and wake heating distributions for the MP-1 configuration are shown in Figure 8.2.43. On the forebody, the overexpansion and recompression of the flow off the hemispherical nose can be seen for the CO_2 case. Heating on the cone portion of the forebody was predicted to decrease nearly linearly for the CO_2 case, while the distribution for the air case was predicted to behave more like that seen in the perfect-gas computations. Computed heating distributions on the afterbody were similar for both cases, although the heating minimum at the separation point was lower in air. On the sting, the peak heating point was predicted to occur further downstream for the air case and to be ~3% higher relative to the stagnation point heating than in the CO_2 case.

Configuration effects for the CO_2 test case are illustrated in Figure 8.2.44. On the forebody, the computed heating rates were nearly identical for the three sphere-cone geometries except at the corner, where the greater radii of the MP-3 and MP-4 configurations produced broader and lower heating peaks. Unlike in the perfect-gas computations, the MP-2 hyperboloid heating was predicted to be much less (15 to 20% less) than that of the sphere-cones not only at the nose, but across the whole forebody right up to the corner. In the wake, the predicted MP-1 and MP-2 distributions agreed closely, while the peak heating rates of the MP-3 and MP-4 configurations were 5-6% less than those of MP-1 and MP-2.

8.2.4 Comparison with Perfect-Gas Computations

Comparisons between the normalized Mach 10 and HYPULSE heating distributions for each of the four configurations are presented in Figures 8.2.45 - 8.2.48. For all configurations, the normalized forebody distributions for the Mach 10 conditions and the HYPULSE air condition were in close agreement except at the corner, where the heating peak for the HYPULSE air condition was lower. The CO_2 distributions were slightly higher around the nose region, dropped below the other distributions at the nose/cone junction, and then decreased nearly linearly along the cone portion. The reason the HYPULSE CO_2 distributions were different was the higher normal-shock density ratio for the CO_2 condition: 19 for CO_2 as compared to 11 for HYPULSE air conditions and 6 for Mach 10 conditions (Tables 4.2.1 and 4.3.1). Because of this, the bow shock standoff distances were much smaller in CO_2 (see Figures 8.1.11, 8.2.11 and 8.2.21) and thus the forebody pressure distributions were much closer to what would be predicted by Newtonian theory (Figure 8.2.49).

Afterbody and base heating distributions were fairly similar for all cases, but the sting distributions for the HYPULSE conditions had heating peaks much smaller relative to the stagnation point heating than those in the Mach 10 tests, and the peaks were much closer to the base. This suggests that at the lower Reynolds numbers of the HYPULSE conditions the wake flow remains laminar, whereas it has been concluded that for the Mach 10 conditions the wake flow is transitional or turbulent.

8.2.5 Comparison with Experimental Data

Comparisons between computed heating distributions and experimentally-determined heating distributions are presented in Figures 8.2.50-8.2.54 for each of the four configurations. As with the perfect-gas comparisons, the heat-transfer rates are based on a uniform 300 K wall temperature. Error bars on the experimental data are taken from the analysis in Section 6.3.

Good agreement was observed on the forebody between the computed heating rates and the experimental data for all tests cases. For the MP-1 configuration in both CO_2 and air (Figures 8.2.50a and 8.2.50b) the computations were within the estimated experimental uncertainties (11-12%) except around the stagnation point for the air case. The MP-2 computations (Figure 8.2.52) were within the experimental uncertainty, as were the MP-3 computations except near the corners. Agreement was poorest for the MP-4 geometry, where the computations and the experimental data differed by ~15%.

As discussed in Section 6.3, the experimental uncertainties for the wake data were much higher (17% for CO_2 and 22% for air) than for the forebody. Also, as with the perfect gas computations, the wake demonstrated much more sensitivity to grid resolution and grid adaptation. Nevertheless, the computations and experimental data were in relatively good agreement for all cases.

For the CO_2 cases, the computed wake heating rates for the MP-1 and MP-2 geometries (Figures 8.2.50b and 8.2.52b) were within the average estimated experimental uncertainty for the portion of the sting downstream of reattachment, while within the recirculation region the computed values differed from the experimental data by more than the experimental uncertainty. The greater differences within the recirculation zone can be explained by the results of the grid resolution study (Section 8.2.1), in which it was estimated that the recirculation region heating would be over-predicted by at least 10%.

For the MP-1 air case (Figure 8.2.51b), the computations fell within the experimental uncertainty except in the region of the shear layer reattachment. For the MP-3 and MP-4 cases (Figures 8.2.53b and 8.2.54b), no data were available for comparison within the recirculation region, while downstream of reattachment the computed heating rates were 5 to 10% higher than the experimental uncertainty bounds.

In all cases, it was observed that the computed heating rates downstream of reattachment were lower than the experimental data. This is not taken as evidence of non-laminar flow. In the Mach 10 cases, the experimental and computational results increasingly diverge with distance down the sting from reattachment, which suggests the growth of turbulence in the reattached shear layer. In the HYPULSE cases, the differences between the two data sets do not grow with distance down the sting, which suggests

an overall bias in the comparison, not turbulence. This bias could be due to grid resolution, the thermochemical models employed in the NEQ2D code, or to the HYPULSE flow conditions differing from their assumed calibration values. Corrections are presented for this bias in Figures 8.2.5-8.2.59, in which the experimental and computational distributions are normalized by the respective stagnation point heating rates. These normalized distribution compare very well on both the forebody and in the wake, and therefore it is concluded that the wake remains laminar in the HYPULSE tests.

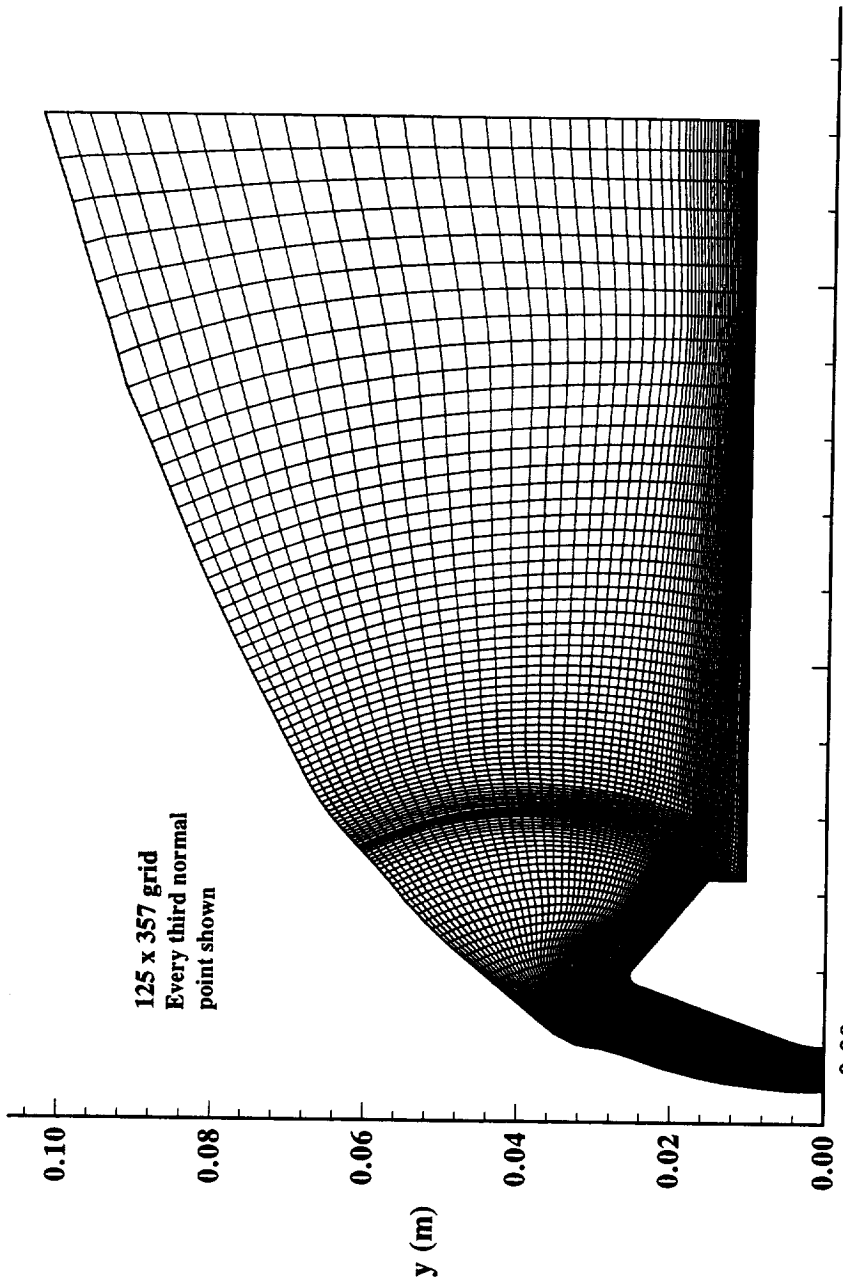

Figure 8.1.1 Computational Grid, MP-1 Configuration, 31-Inch Mach 10 Air Tunnel Tests

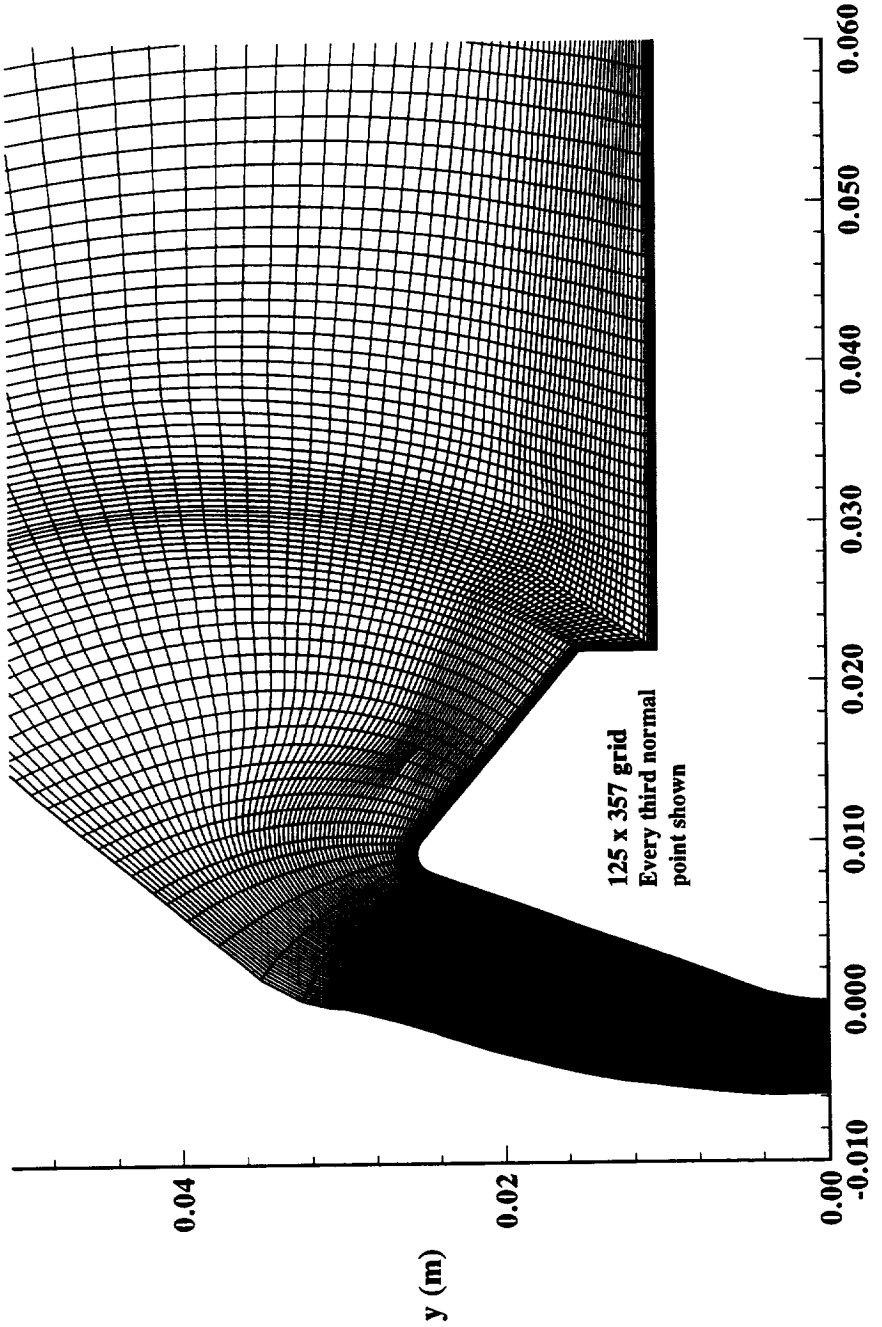

Figure 8.1.2 Computational Grid, MP-1 Configuration, Forebody and Near Wake Details, 31-Inch Mach 10 Air Tunnel Tests

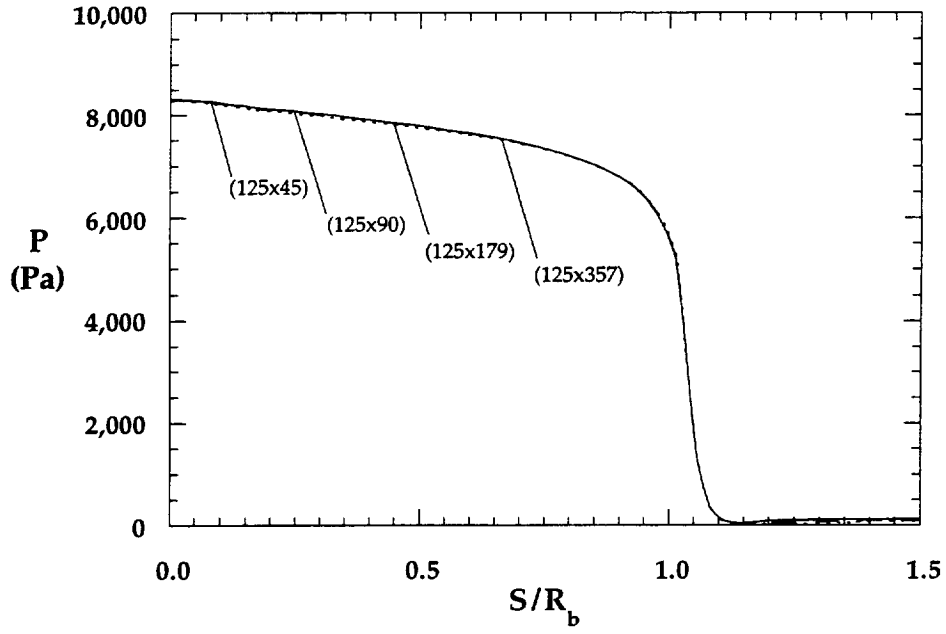

Figure 8.1.3a Grid Resolution Effects on Forebody Pressure, MP-1 Configuration, 31-Inch Mach 10, $Re_\infty = 0.5x10^{-6}$ ft^{-1}

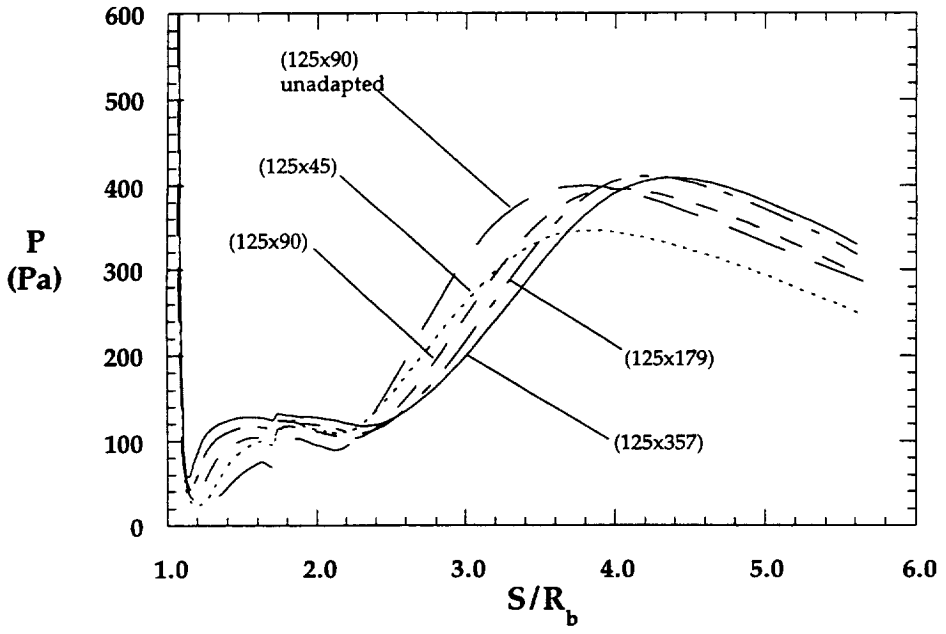

Figure 8.1.3a Grid Resolution Effects on Wake Pressure, MP-1 Configuration, 31-Inch Mach 10, $Re_\infty = 0.5x10^{-6}$ ft^{-1}

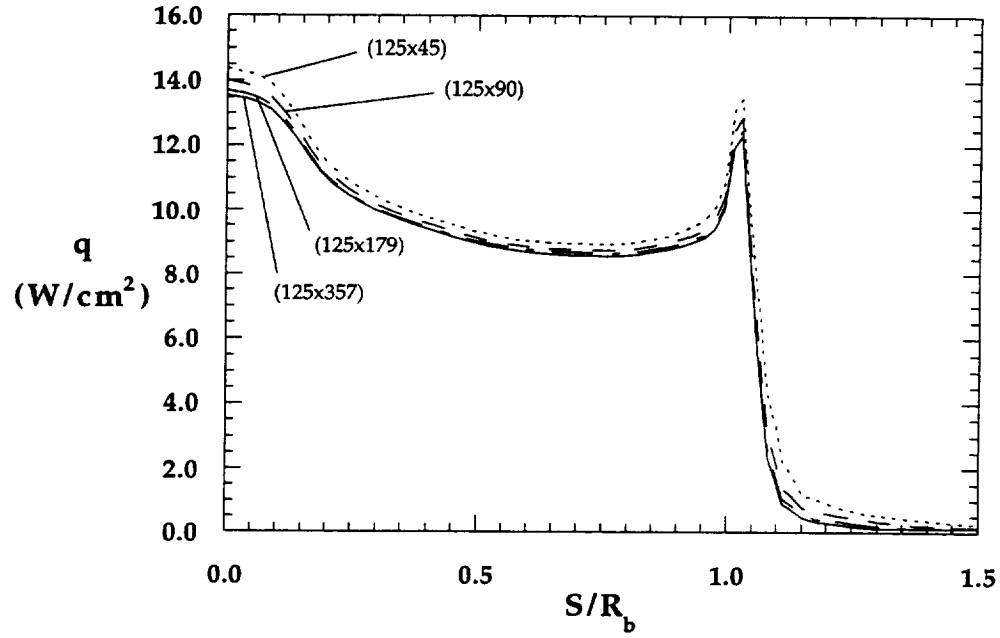

Figure 8.1.4a Grid Resolution Effects on Forebody Heating, MP-1 Configuration, 31-Inch Mach 10, $Re_\infty = 0.5x10^{-6}$ ft^{-1}

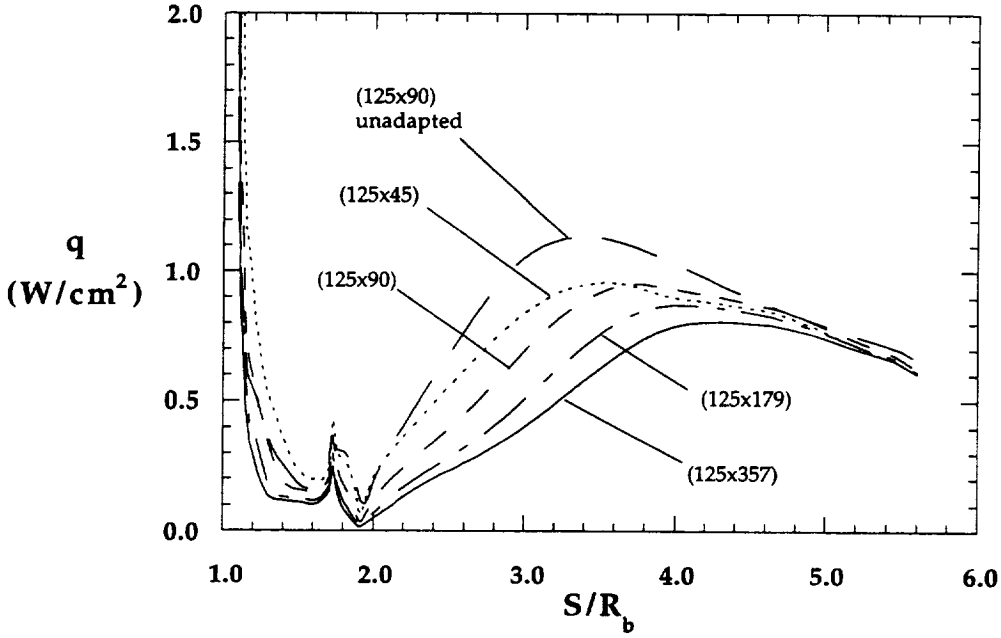

Figure 8.1.4b Grid Resolution Effects on Wake Heating, MP-1 Configuration, 31-Inch Mach 10, $Re_\infty = 0.5x10^{-6}$ ft^{-1}

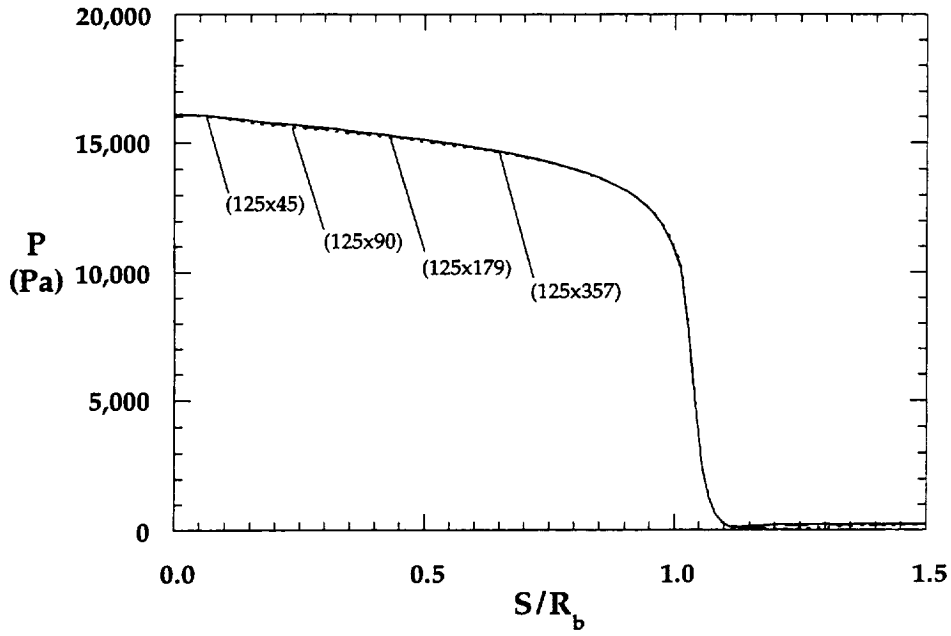

Figure 8.1.5a Grid Resolution Effects on Forebody Pressure, MP-1 Configuration, 31-Inch Mach 10, $Re_\infty = 1.0x10^{-6}$ ft^{-1}

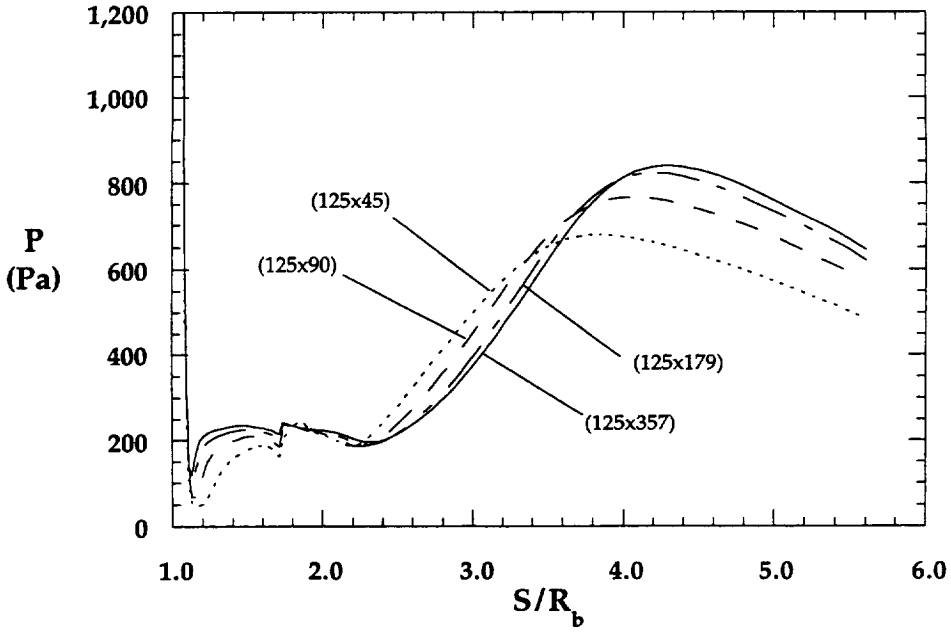

Figure 8.1.5b Grid Resolution Effects on Wake Pressure, MP-1 Configuration, 31-Inch Mach 10, $Re_\infty = 1.0x10^{-6}$ ft^{-1}

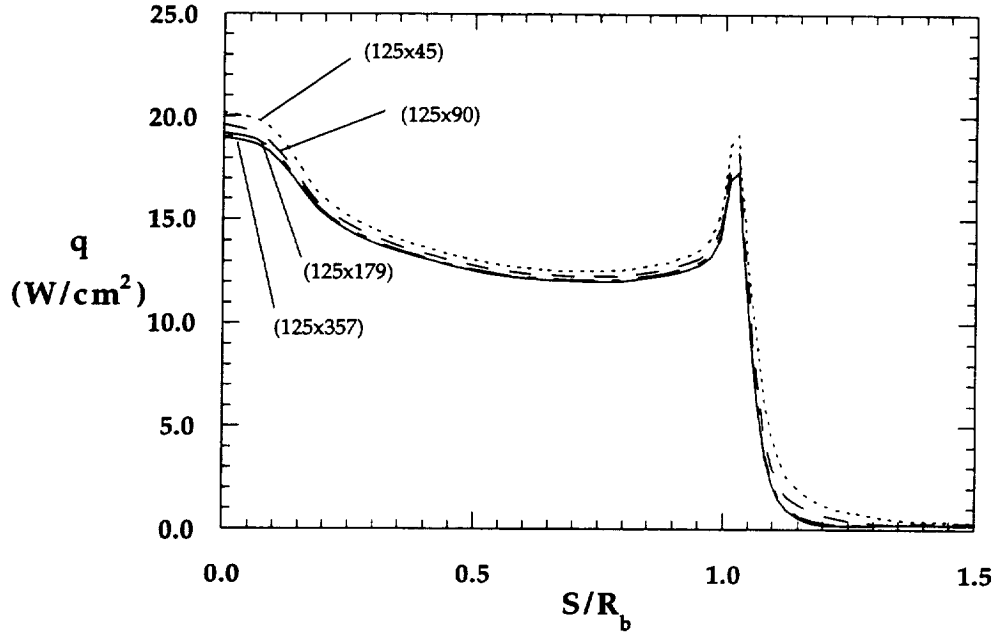

Figure 8.1.6a Grid Resolution Effects on Forebody Heating, MP-1 Configuration, 31-Inch Mach 10, $Re_\infty = 1.0x10^{-6}$ ft^{-1}

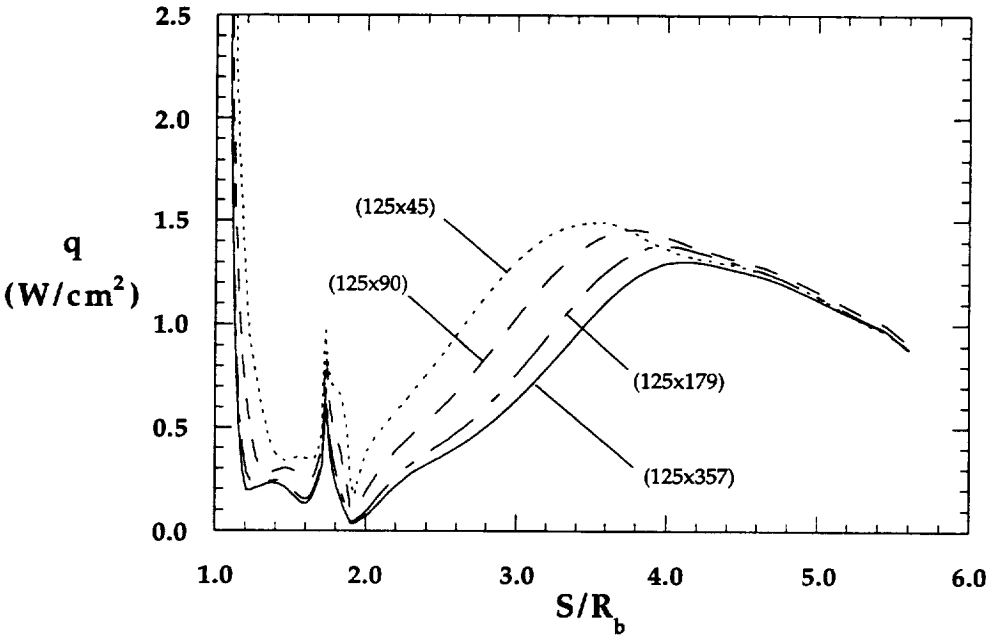

Figure 8.16b Grid Resolution Effects on Wake Heating, MP-1 Configuration, 31-Inch Mach 10, $Re_\infty = 1.0x10^{-6}$ ft^{-1}

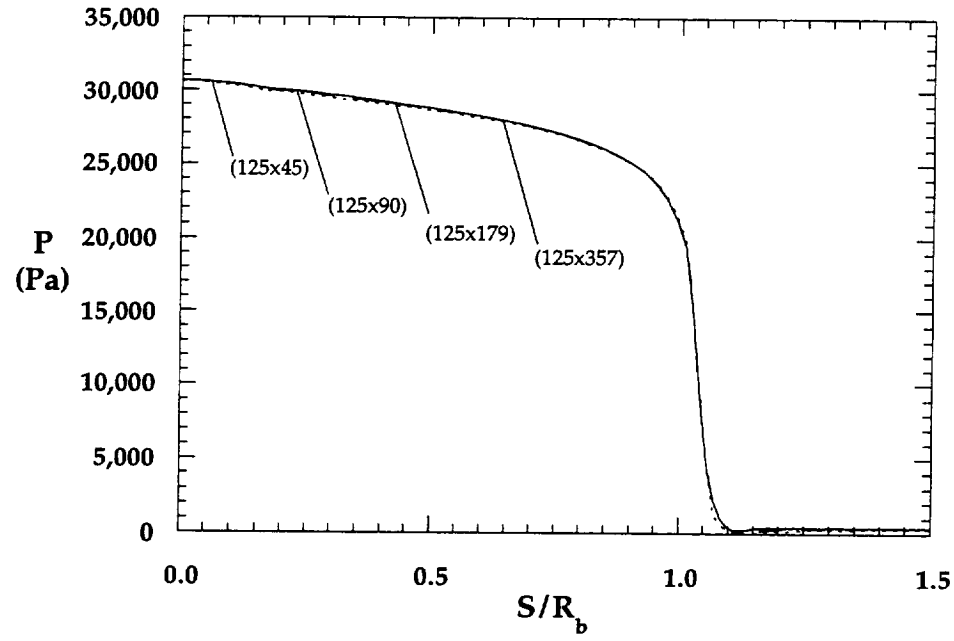

Figure 8.1.7a Grid Resolution Effects on Forebody Pressure, MP-1 Configuration, 31-Inch Mach 10, $Re_\infty = 2.0x10^{-6}$ ft^{-1}

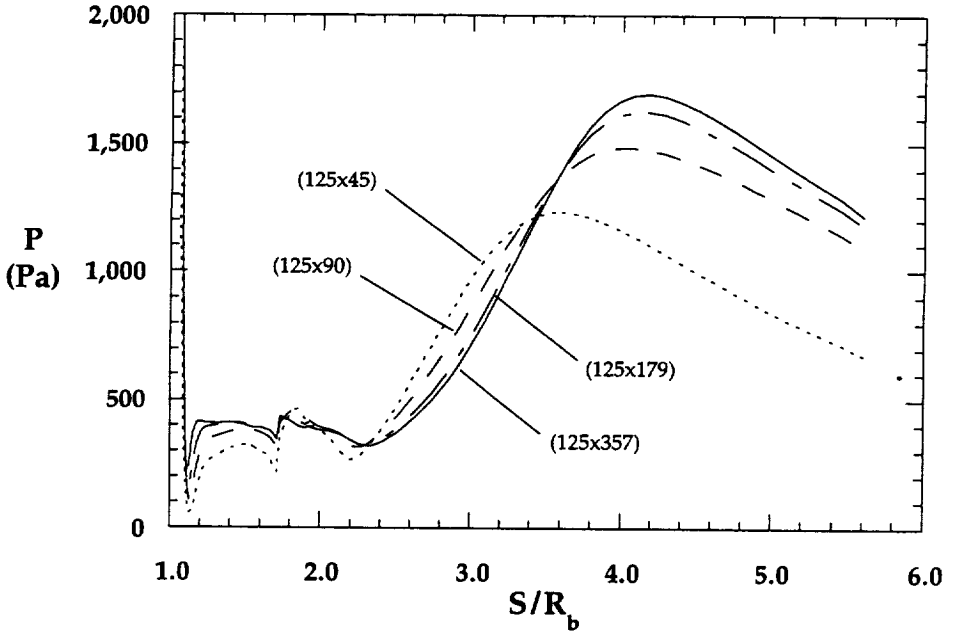

Figure 8.1.7b Grid Resolution Effects on Wake Pressure, MP-1 Configuration, 31-Inch Mach 10, $Re_\infty = 2.0x10^{-6}$ ft^{-1}

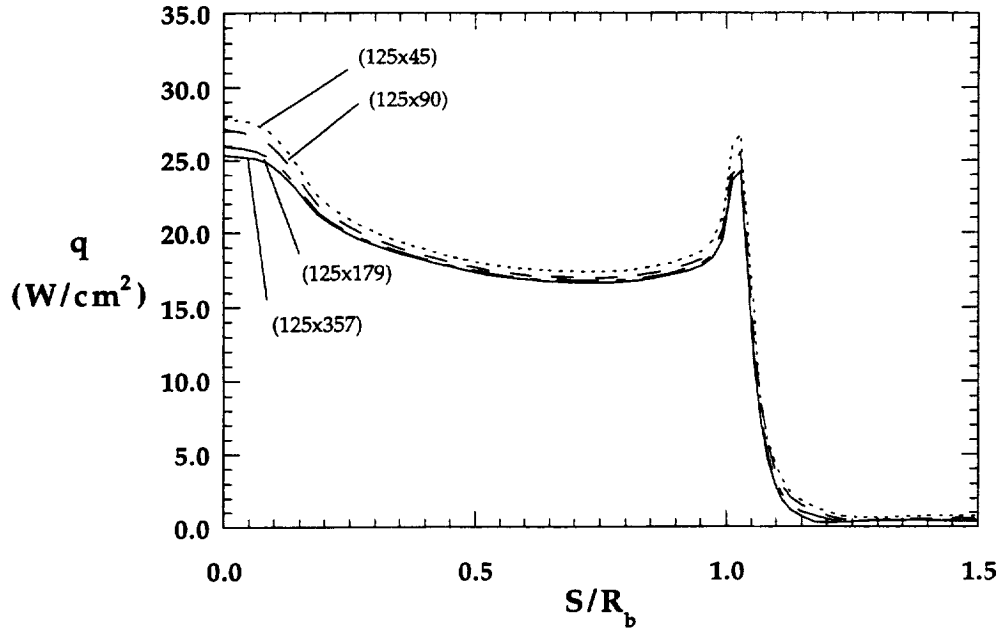

Figure 8.1.8a Grid Resolution Effects on Forebody Heating, MP-1 Configuration, 31-Inch Mach 10, $Re_\infty = 2.0x10^{-6}$ ft^{-1}

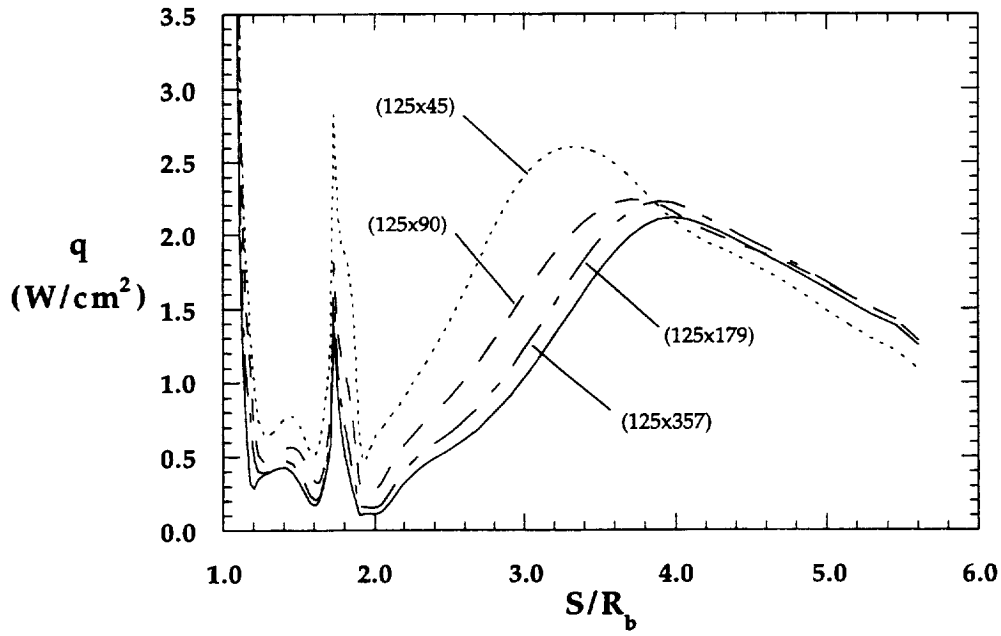

Figure 8.1.8b Grid Resolution Effects on Wake Heating, MP-1 Configuration, 31-Inch Mach 10, $Re_\infty = 2.0x10^{-6}$ ft^{-1}

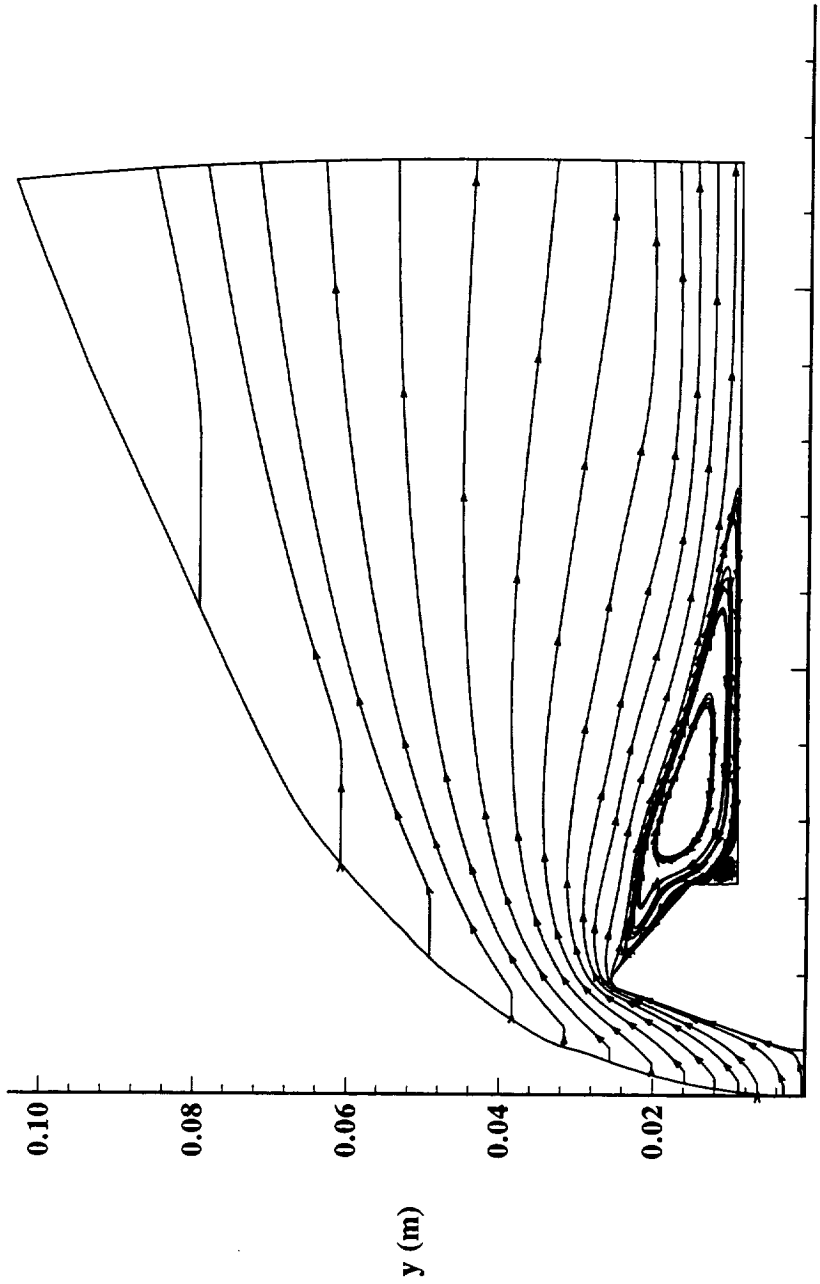

Figure 8.1.9 Computed Streamlines,
MP-1 Configuration, 31-Inch Mach 10, Re_∞ = 0.5x10E6 1/ft

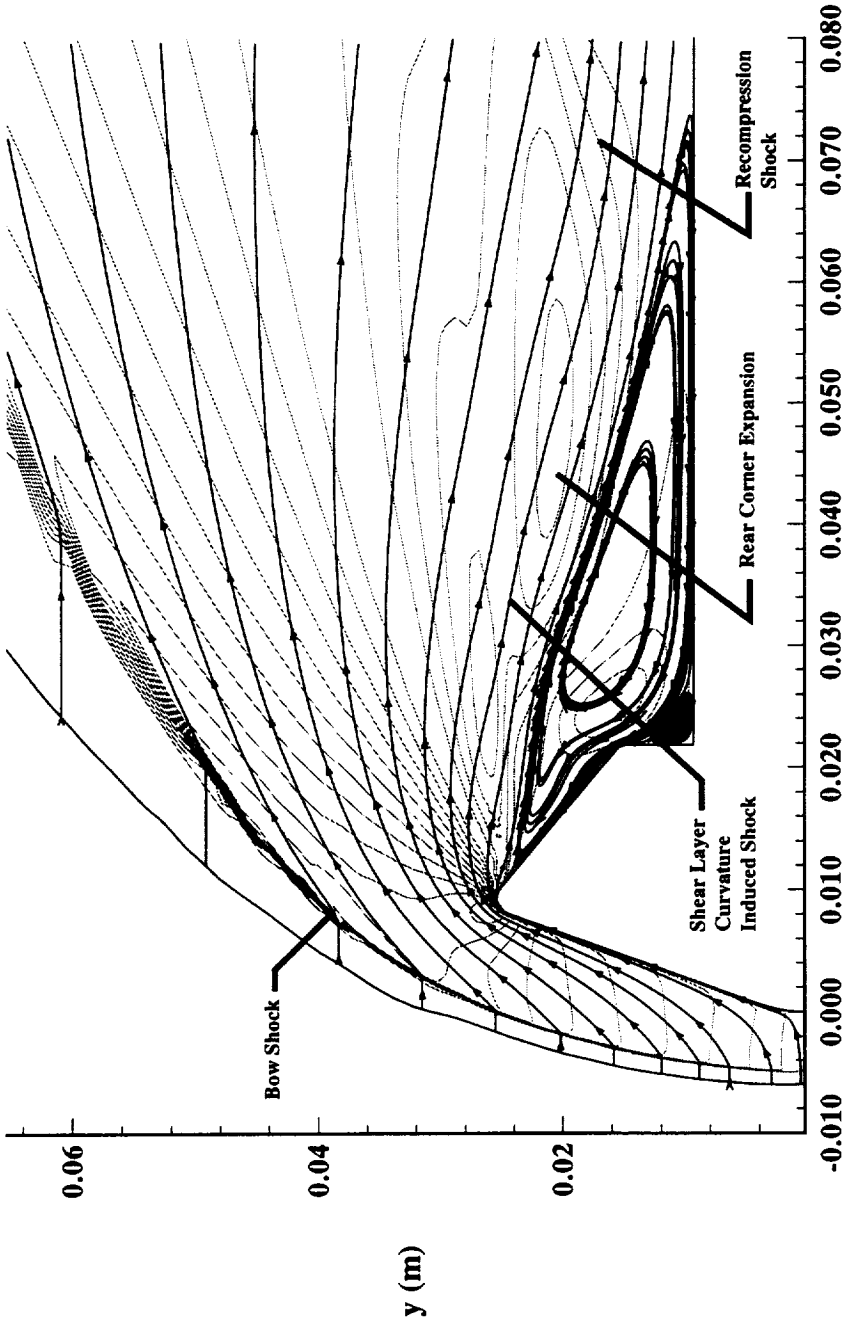

Figure 8.1.10 Computed Streamlines Superimposed on v-Velocity Contours, MP-1 Configuration, 31-Inch Mach 10, Re_∞ = 0.5x10E6 /1ft

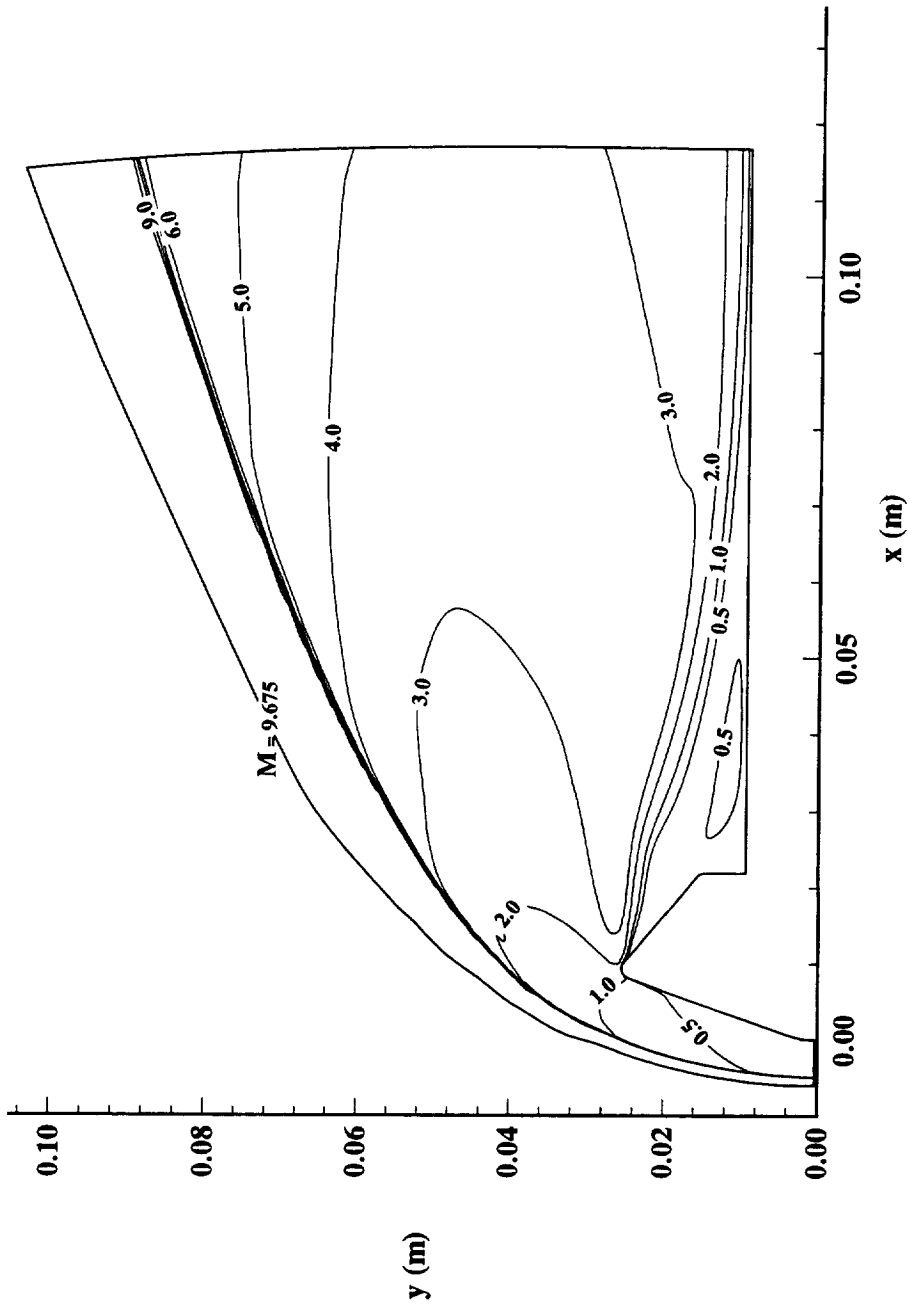

Figure 8.1.11 Computed Mach Contours,
MP-1 Configuration, 31-Inch Mach 10, Re_∞ = 0.5x10E6 1/ft

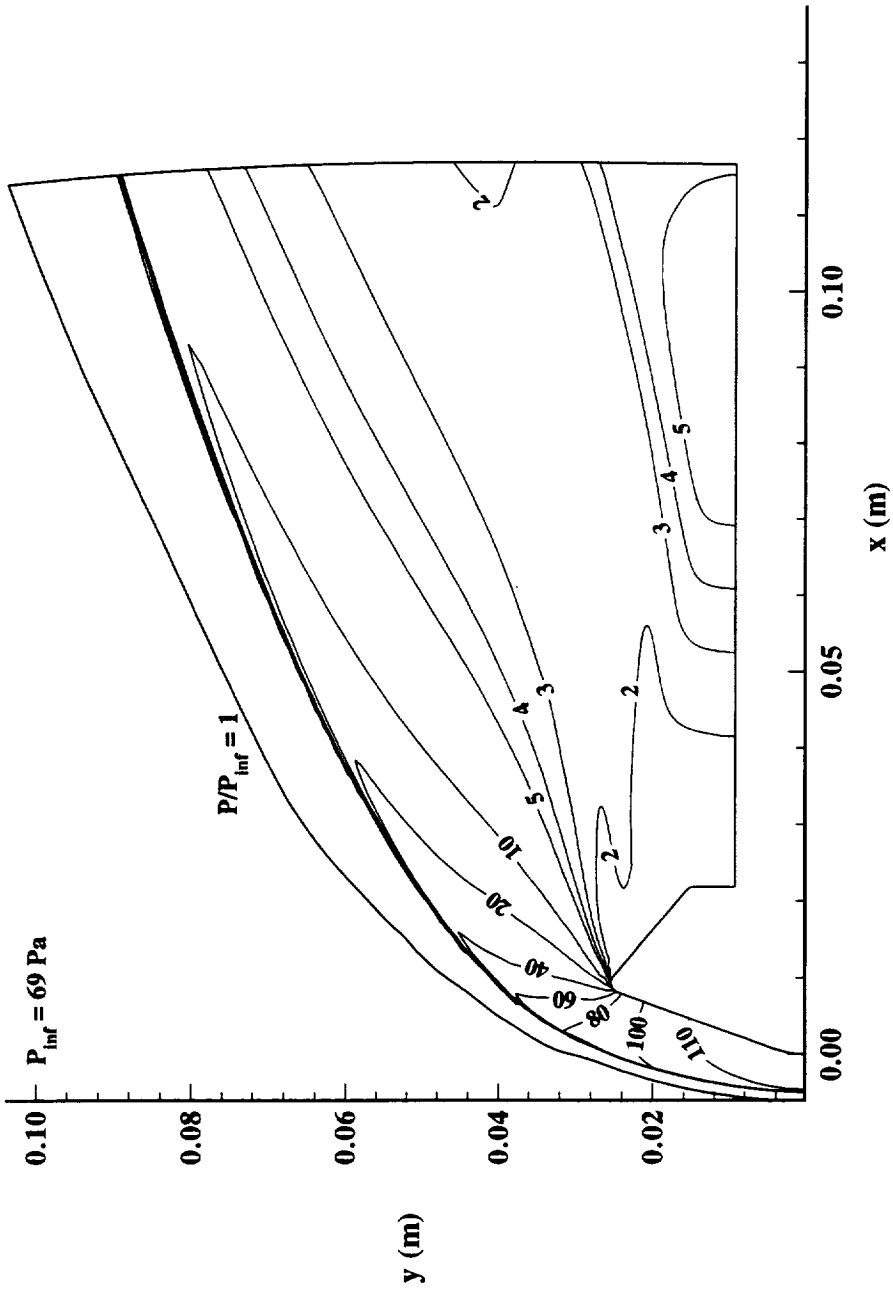

Figure 8.1.12 Computed Pressure Ratio Contours, MP-1 Configuration, 31-Inch Mach 10, Re_∞ = 0.5x10E6 1/ft

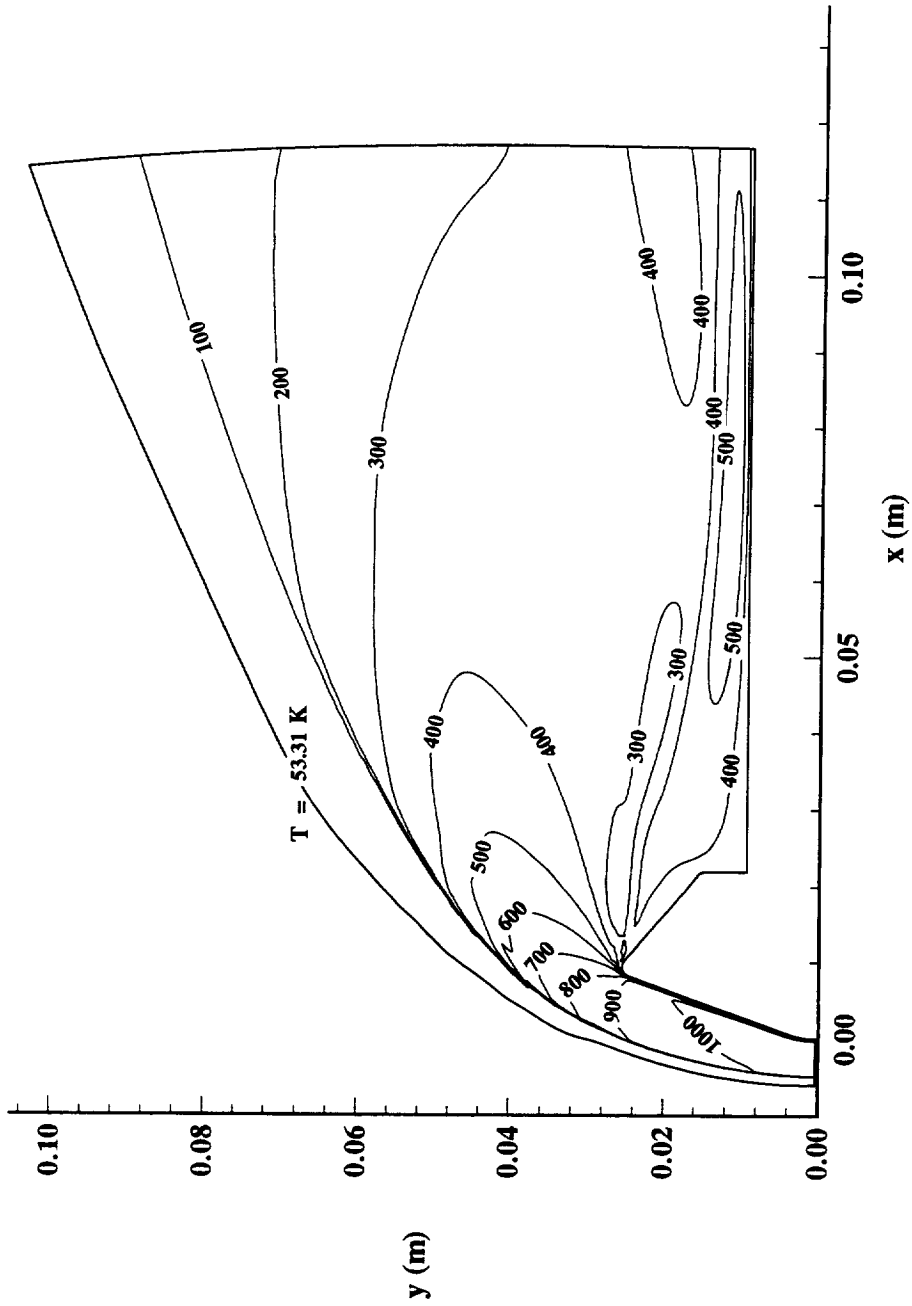

Figure 8.1.13 Computed Temperature Contours, MP-1 Configuration, 31-Inch Mach 10, $Re_\infty = 0.5x10E6$ 1/ft

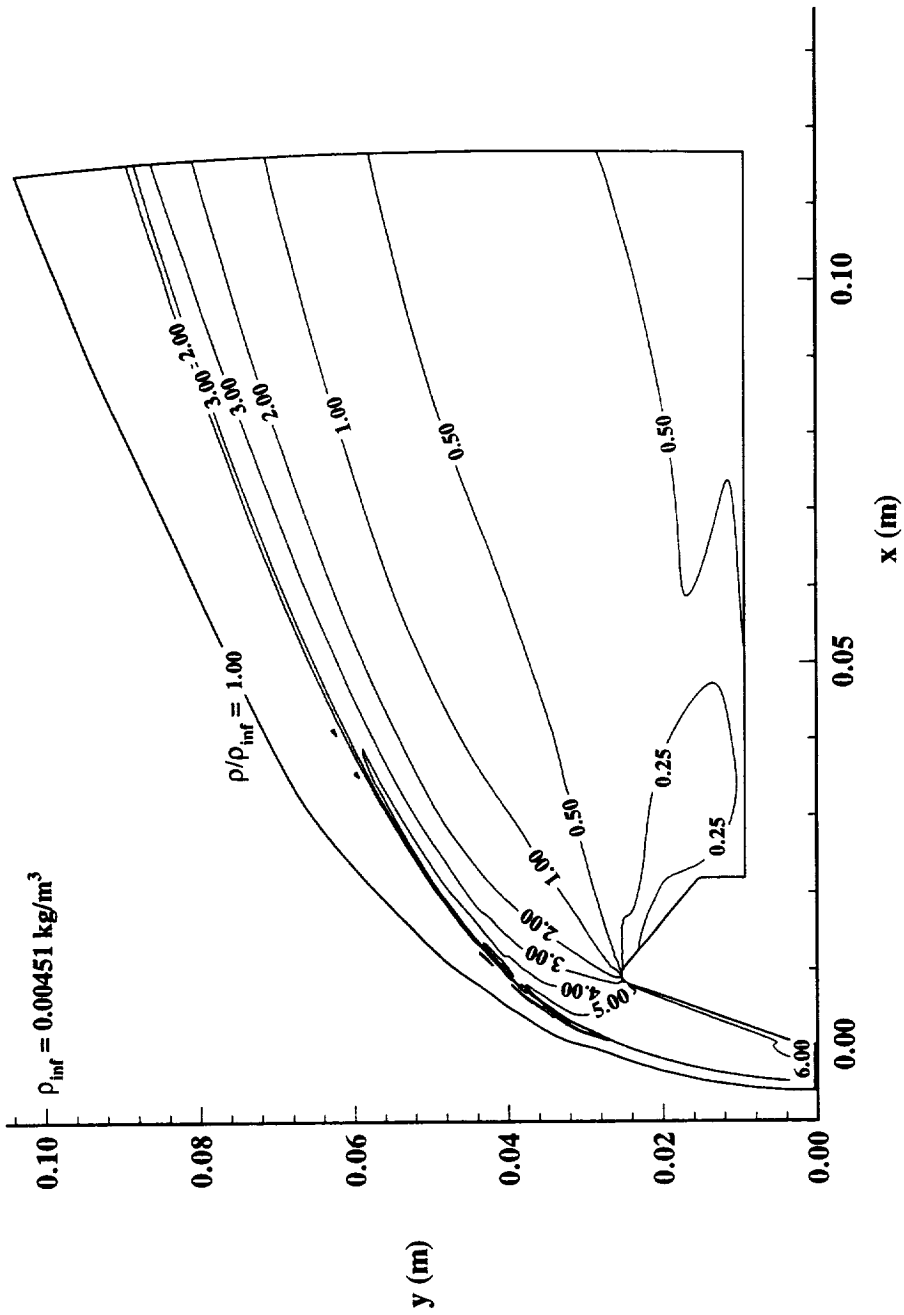

Figure 8.1.14 Computed Density Ratio Contours, MP-1 Configuration, 31-Inch Mach 10, Re_∞ = 0.5x10E6 1/ft

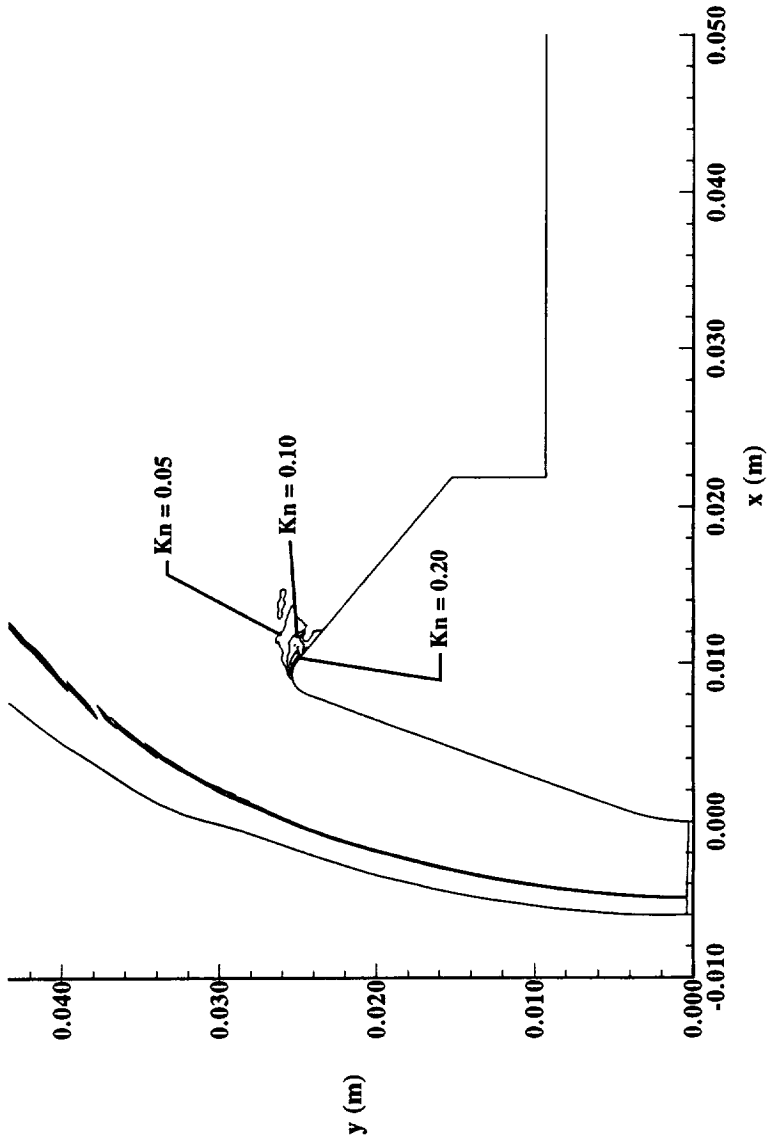

Figure 8.1.15 Computed Local Knudsen Number Contours, MP-1 Configuration, 31-Inch Mach 10, $Re_\infty = 0.5x10E6$ 1/ft

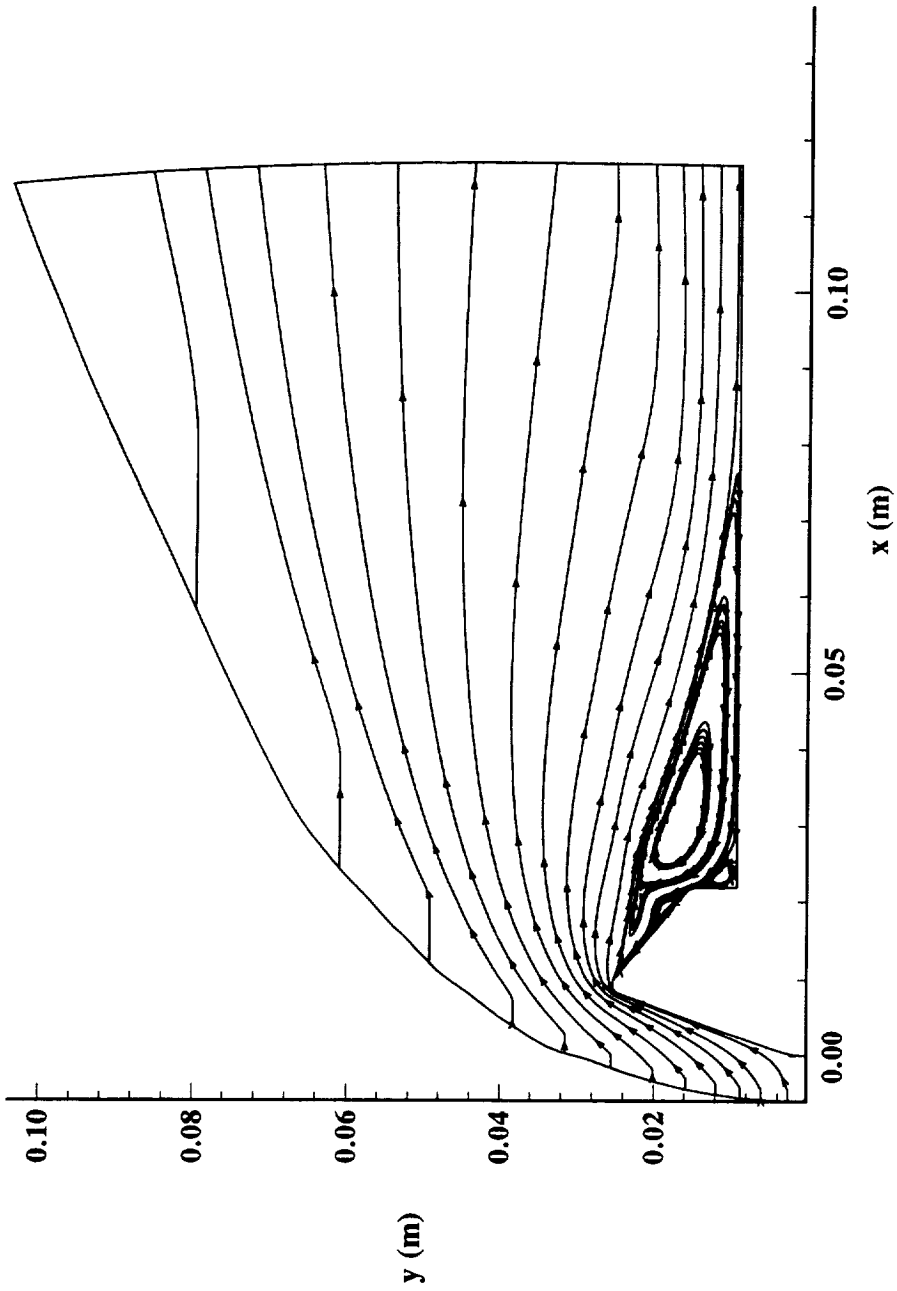

Figure 8.1.16 Computed Streamlines,
MP-1 Configuration, 31-Inch Mach 10, Re_∞ = 1.0x10E6 1/ft

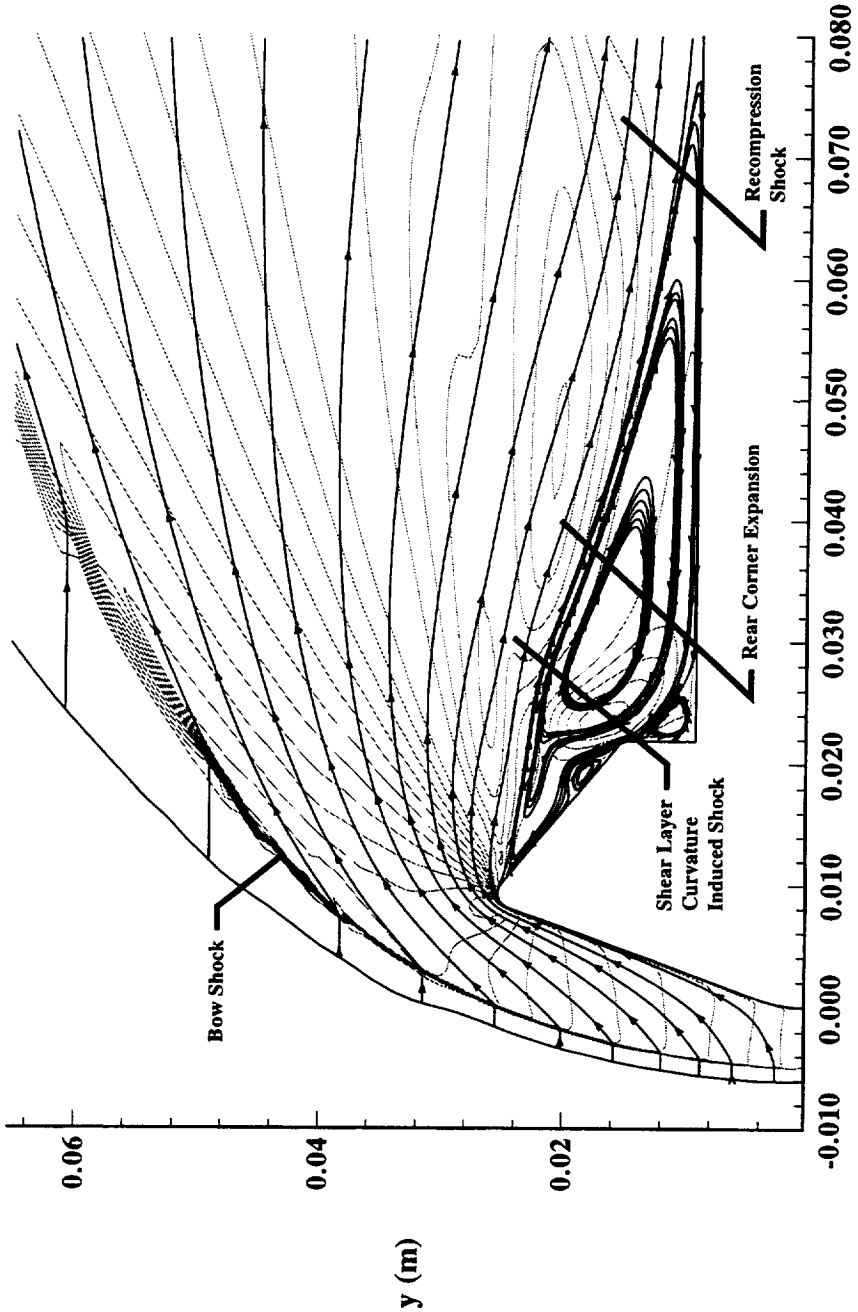

Figure 8.1.17 Computed Streamlines Superimposed on v-Velocity Contours, MP-1 Configuration, 31-Inch Mach 10, Re_∞ = 1.0x10E6 1/ft

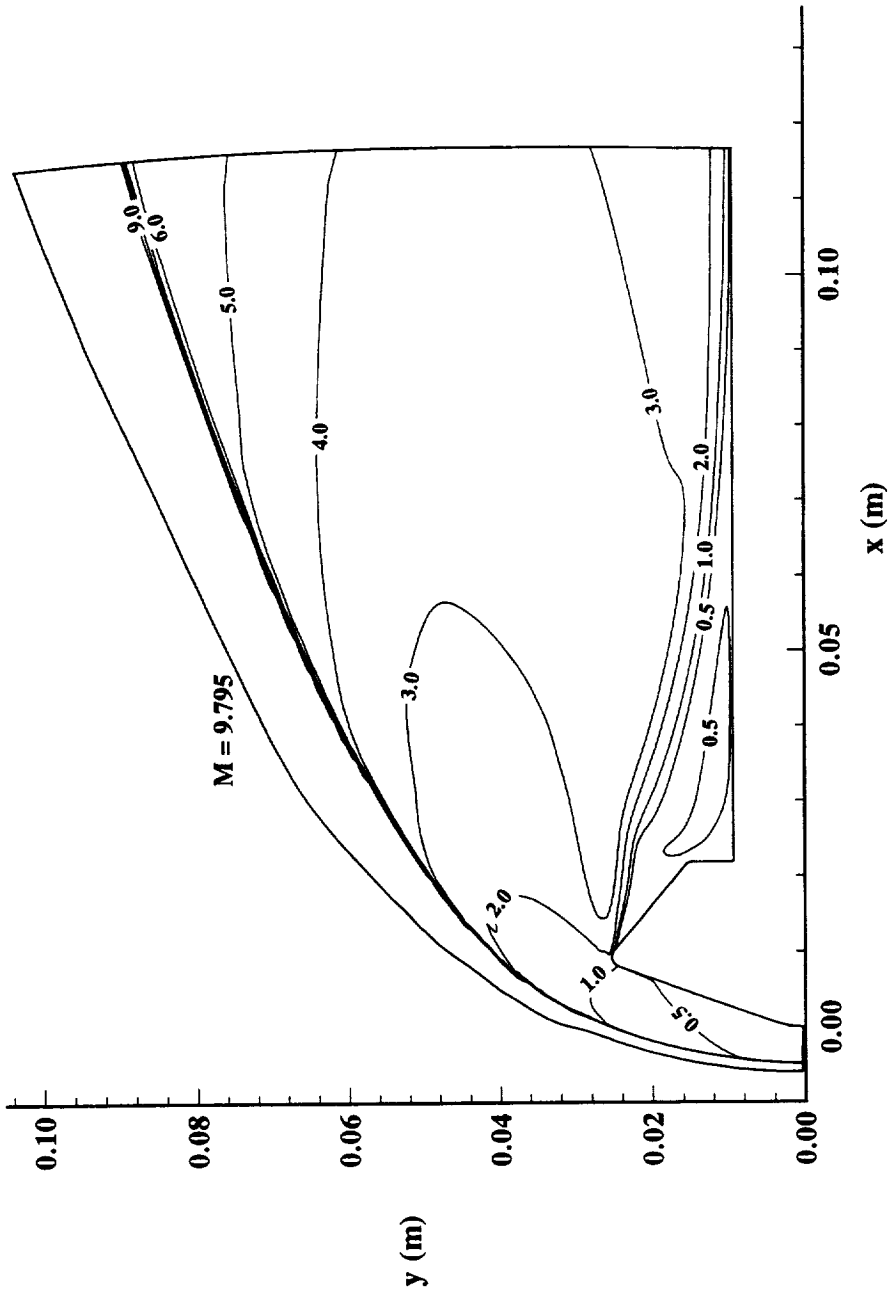

Figure 8.1.18 Computed Mach Contours, MP-1 Configuration, 31-Inch Mach 10, Re_∞ = 1.0x10E6 1/ft

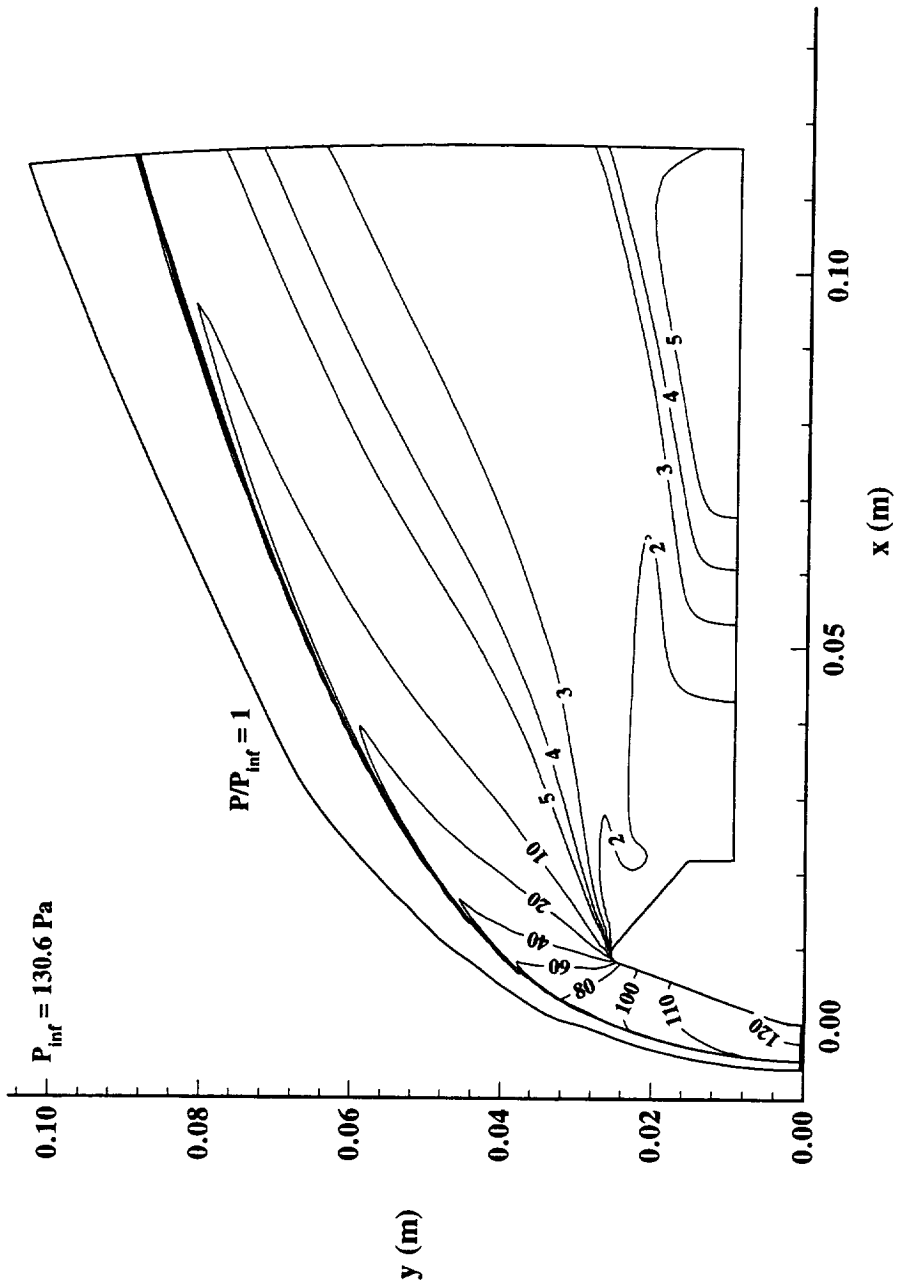

Figure 8.1.19 Computed Pressure Ratio Contours, MP-1 Configuration, 31-Inch Mach 10, Re_∞ = 1.0x10E6 1/ft

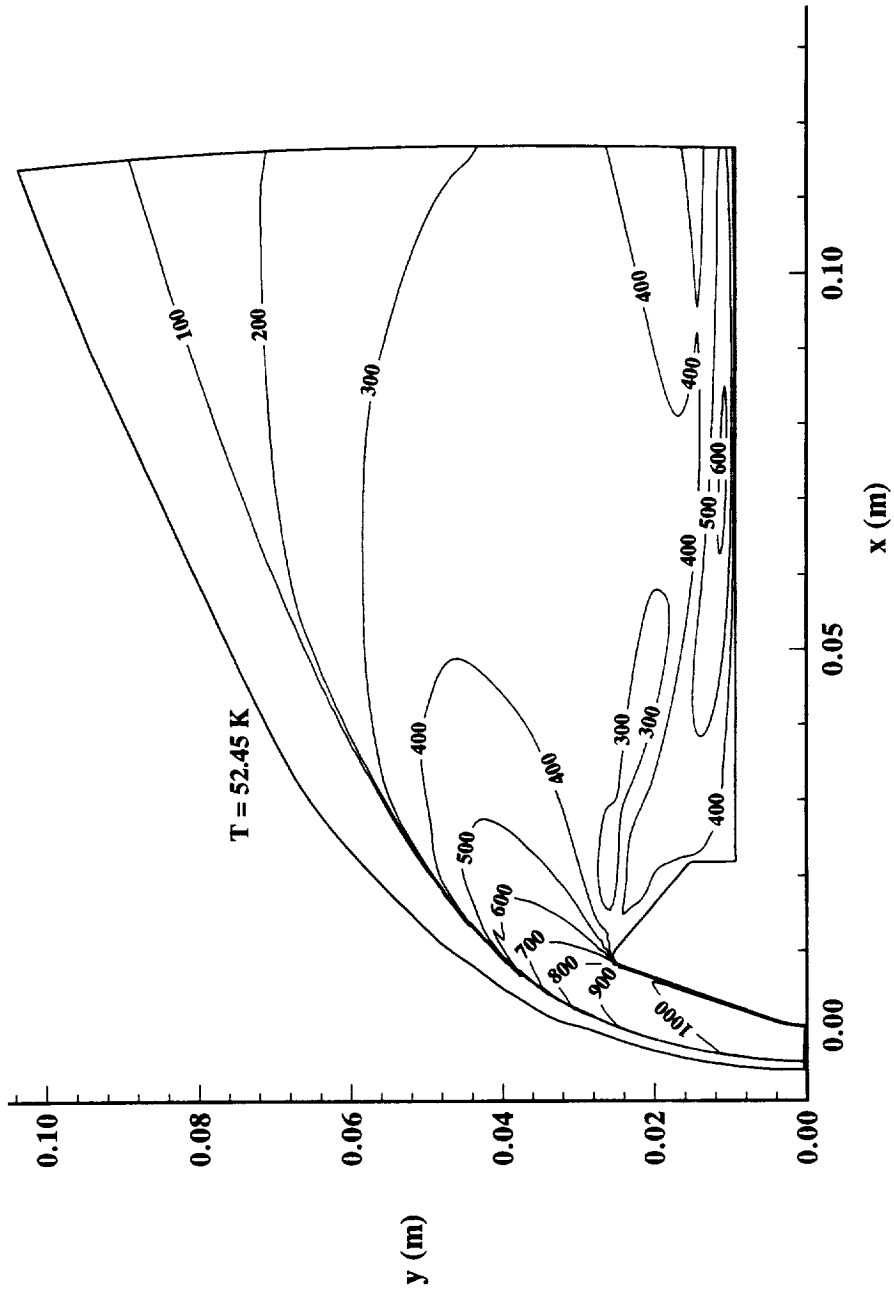

Figure 8.1.20 Computed Temperature Contours, MP-1 Configuration, 31-Inch Mach 10, Re_∞ = 1.0x10E6 1/ft

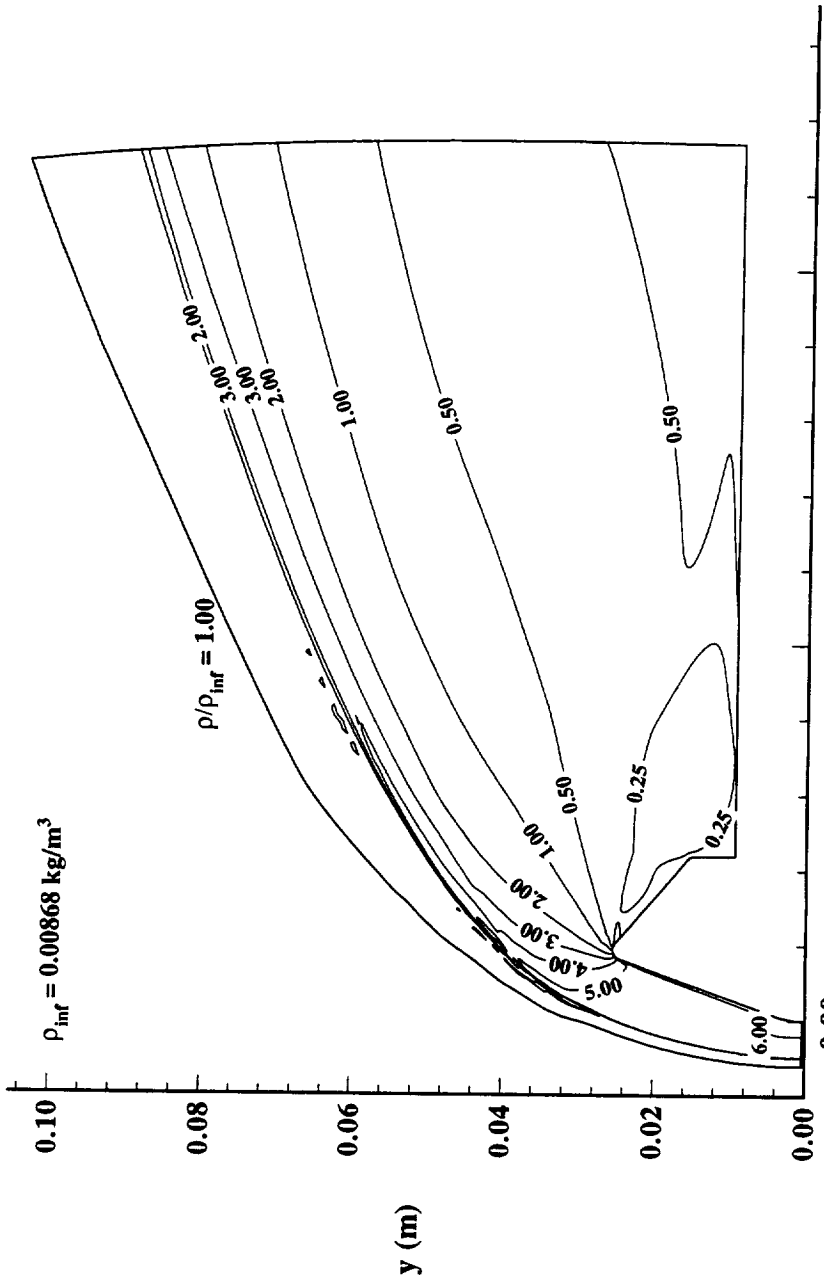

Figure 8.1.21 Computed Density Ratio Contours, MP-1 Configuration, 31-Inch Mach 10, Re_∞ = 1.0x10E6 1/ft

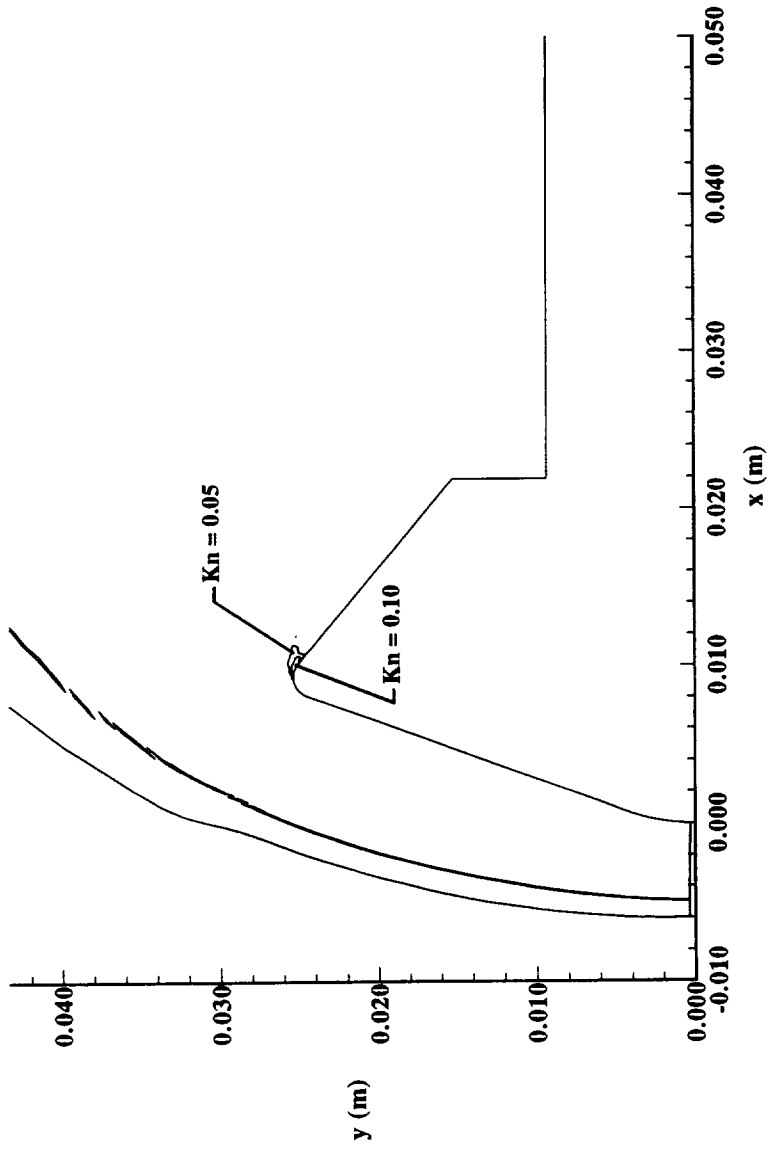

Figure 8.1.22 Computed Local Knudsen Number Contours, MP-1 Configuration, 31-Inch Mach 10, Re_∞ = 1.0x10E6 1/ft

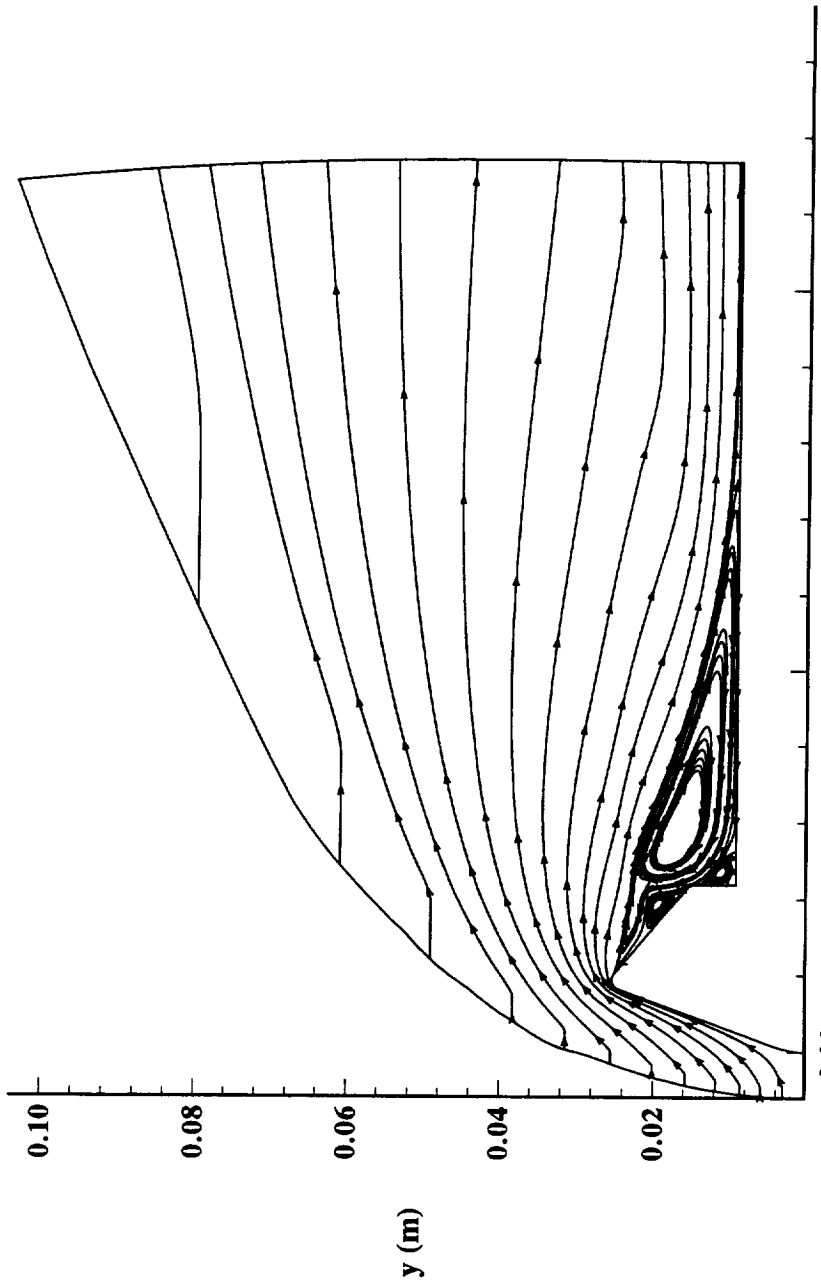

Figure 8.1.23 Computed Streamlines, MP-1 Configuration, 31-Inch Mach 10, Re_∞ = 2.0x10E6 1/ft

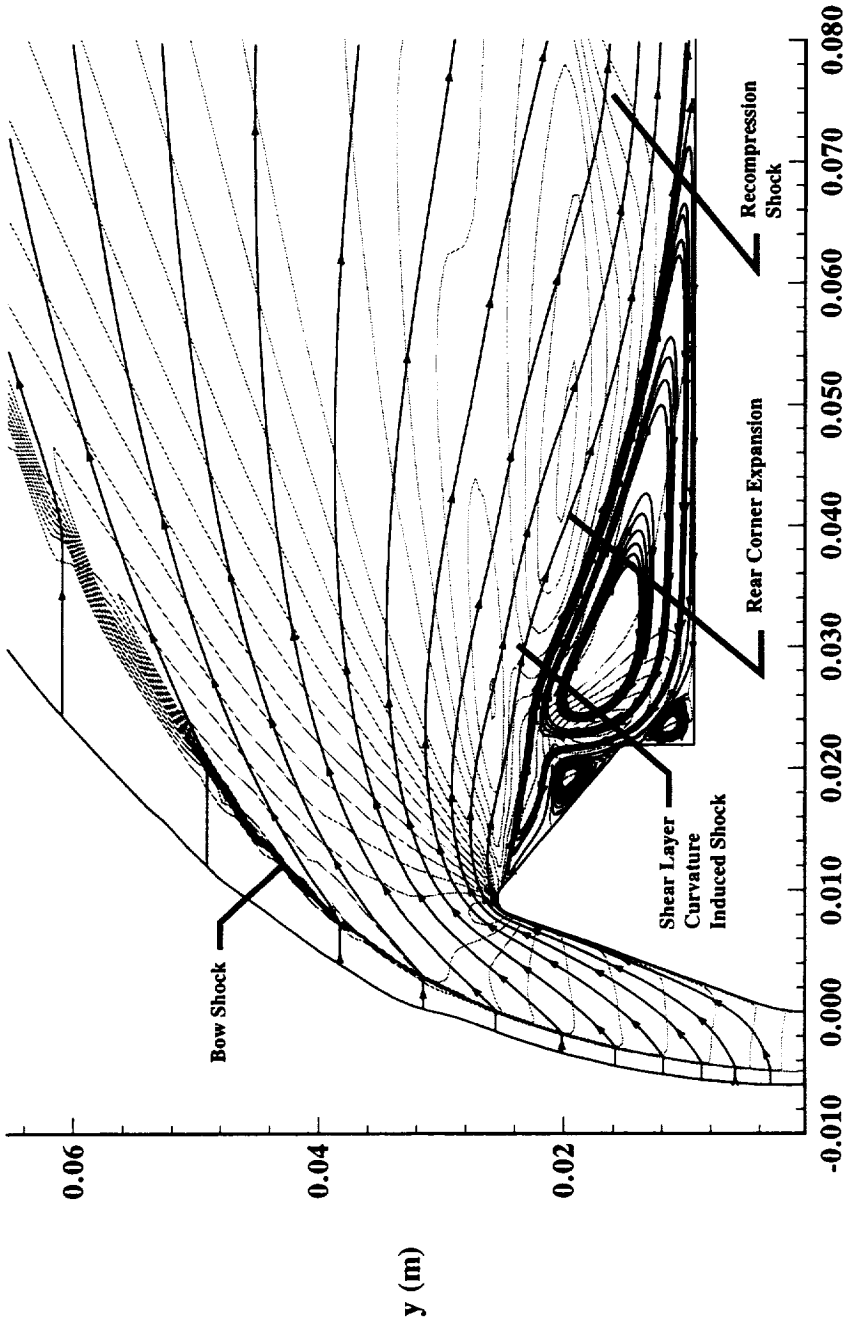

Figure 8.1.24 Computed Streamlines Superimposed on v-Velocity Contours, MP-1 Configuration, 31-Inch Mach 10, Re_∞ = 2.0x10E6 1/ft

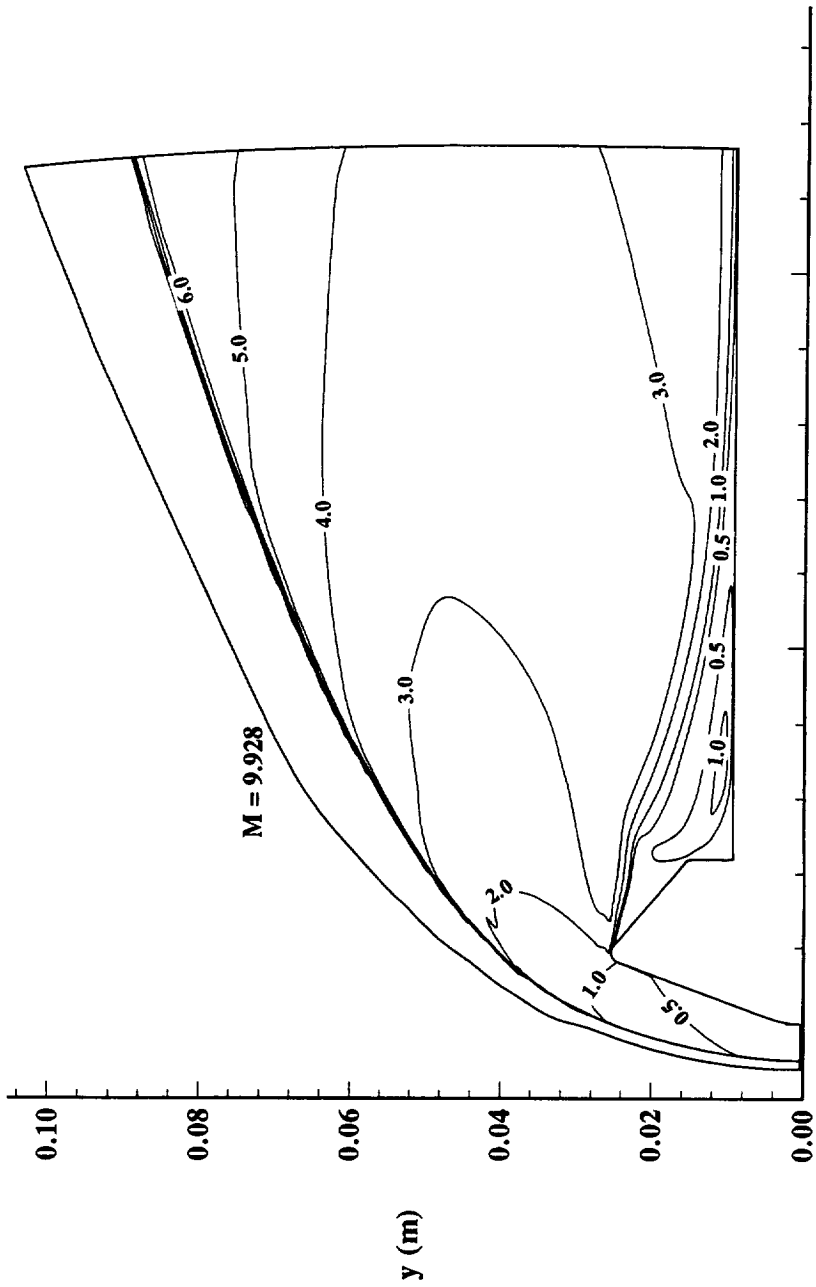

Figure 8.1.25 Computed Mach Contours, MP-1 Configuration, 31-Inch Mach 10, Re_∞ = 2.0x10E6 1/ft

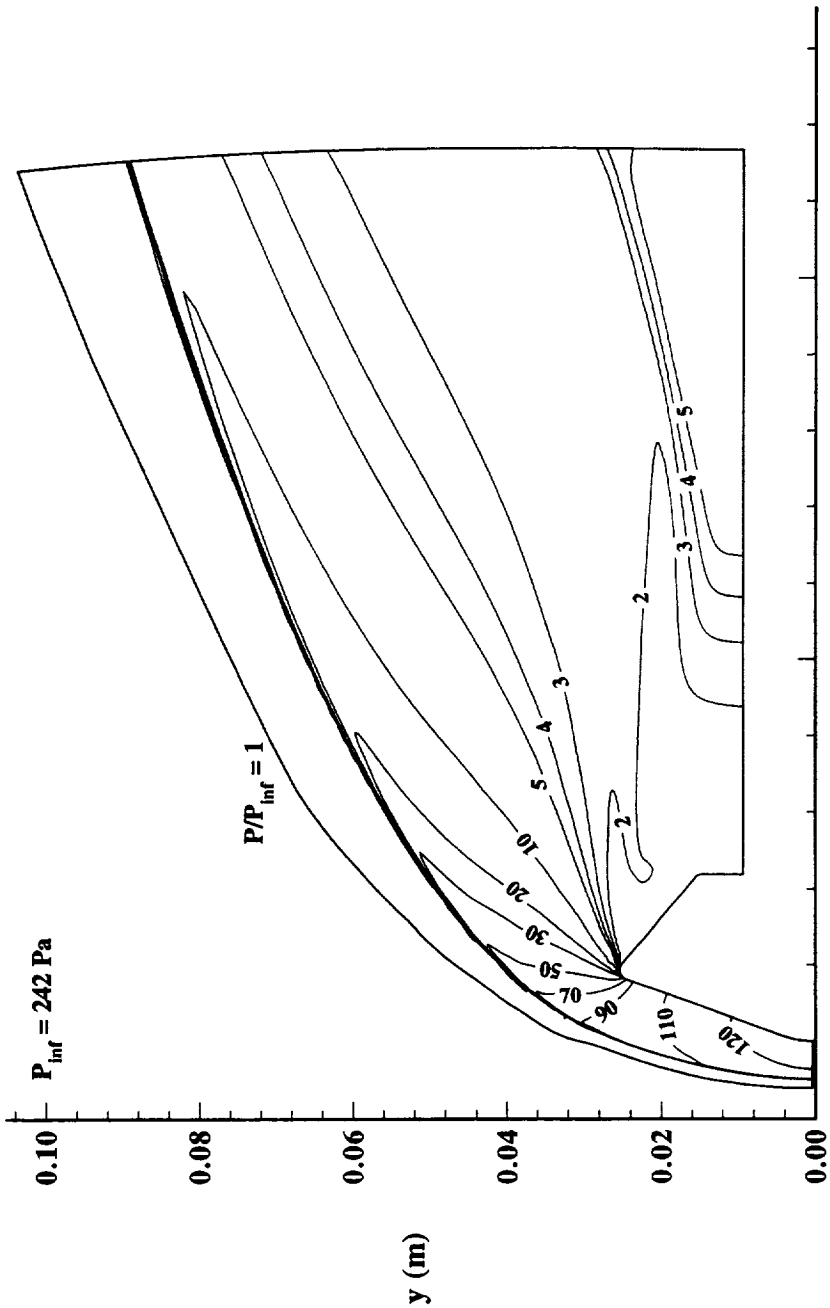

Figure 8.1.26 Computed Pressure Ratio Contours, MP-1 Configuration, 31-Inch Mach 10, Re_∞ = 2.0x10E6 1/ft

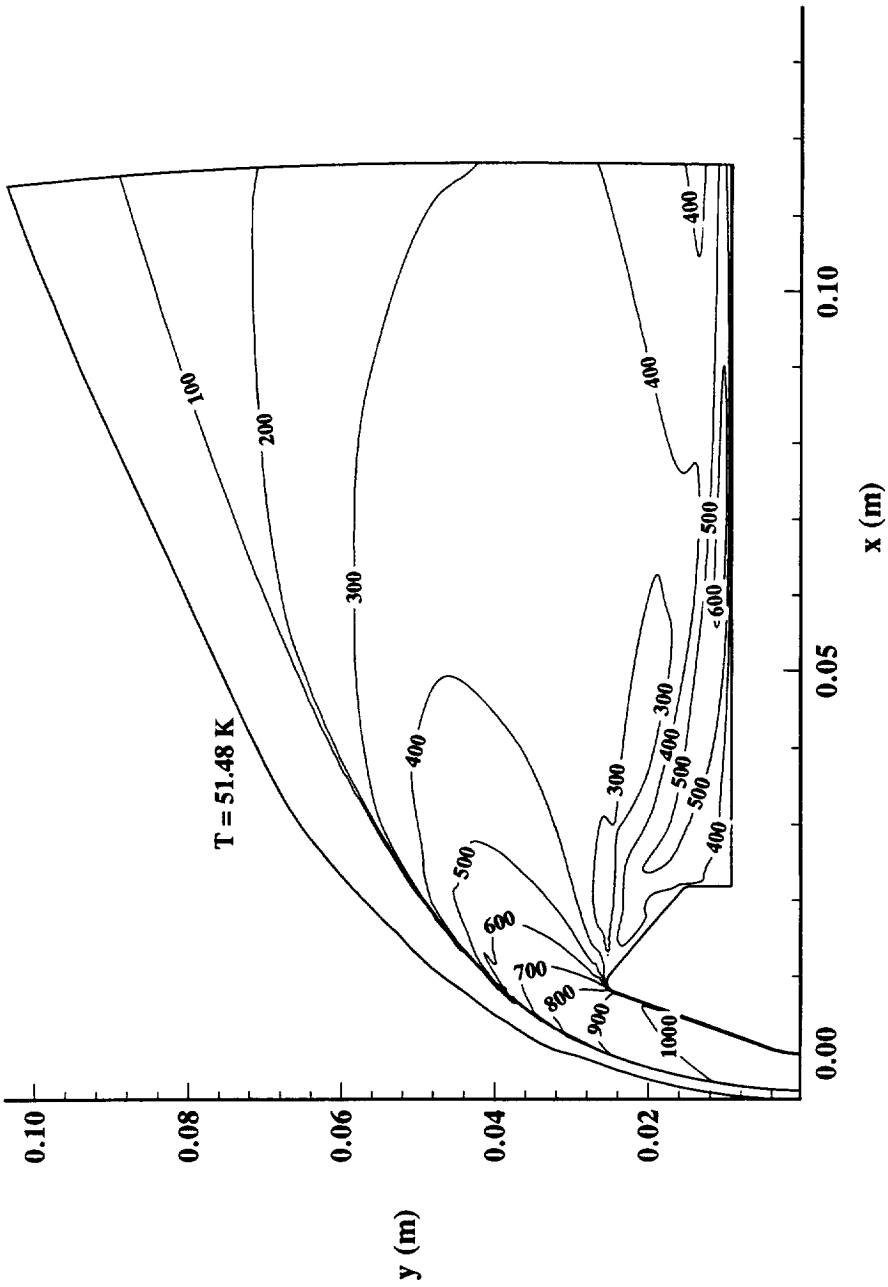

Figure 8.1.27 Computed Temperature Contours, MP-1 Configuration, 31-Inch Mach 10, Re_∞ = 2.0x10E6 1/ft

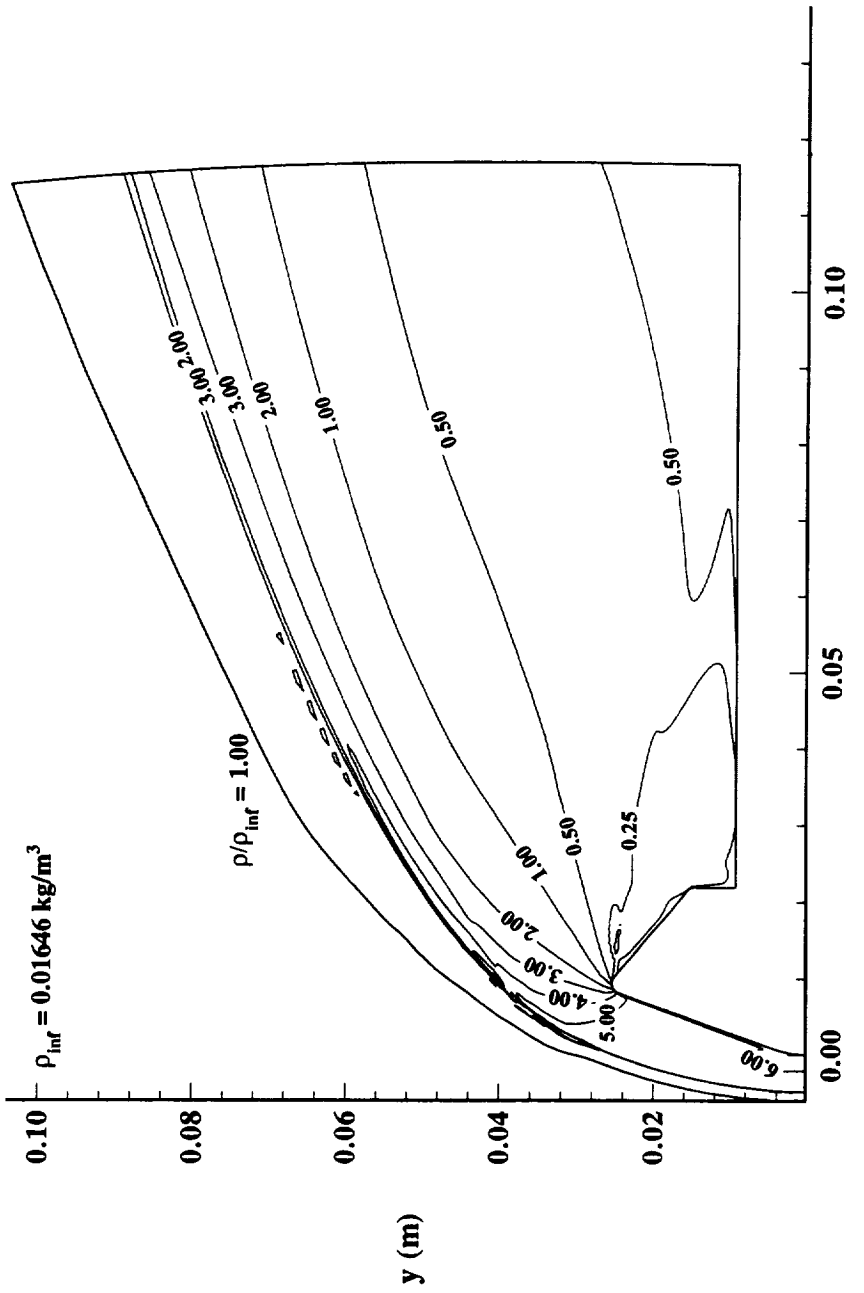

Figure 8.1.28 Computed Density Ratio Contours, MP-1 Configuration, 31-Inch Mach 10, Re_∞ = 2.0x10E6 1/ft

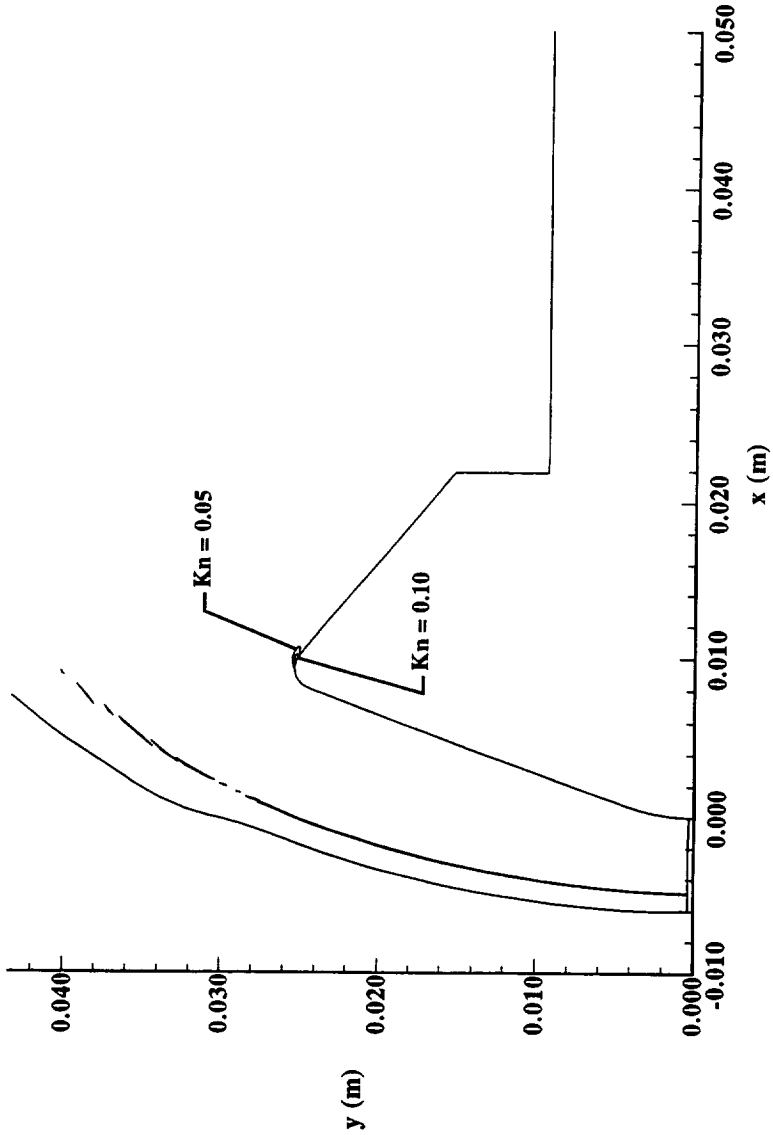

Figure 8.1.29 Computed Local Knudsen Number Contours, MP-1 Configuration, 31-Inch Mach 10, Re_∞ = 2.0x10E6 1/ft

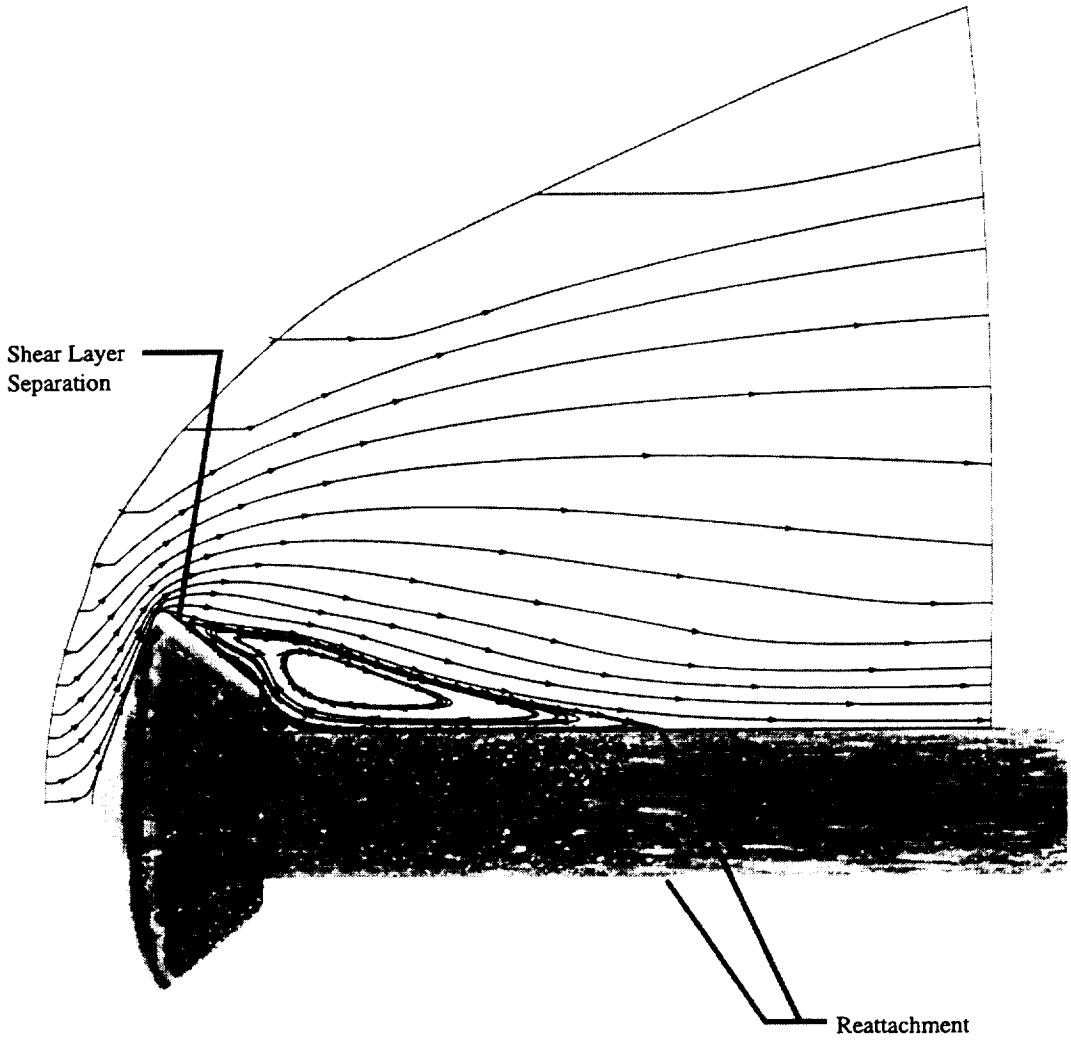

Figure 8.1.30 Comparison of Computed Streamline with Surface Oil Flow Patterns, 31-Inch Mach 10, Re_∞ = 0.5x10E6 1/ft

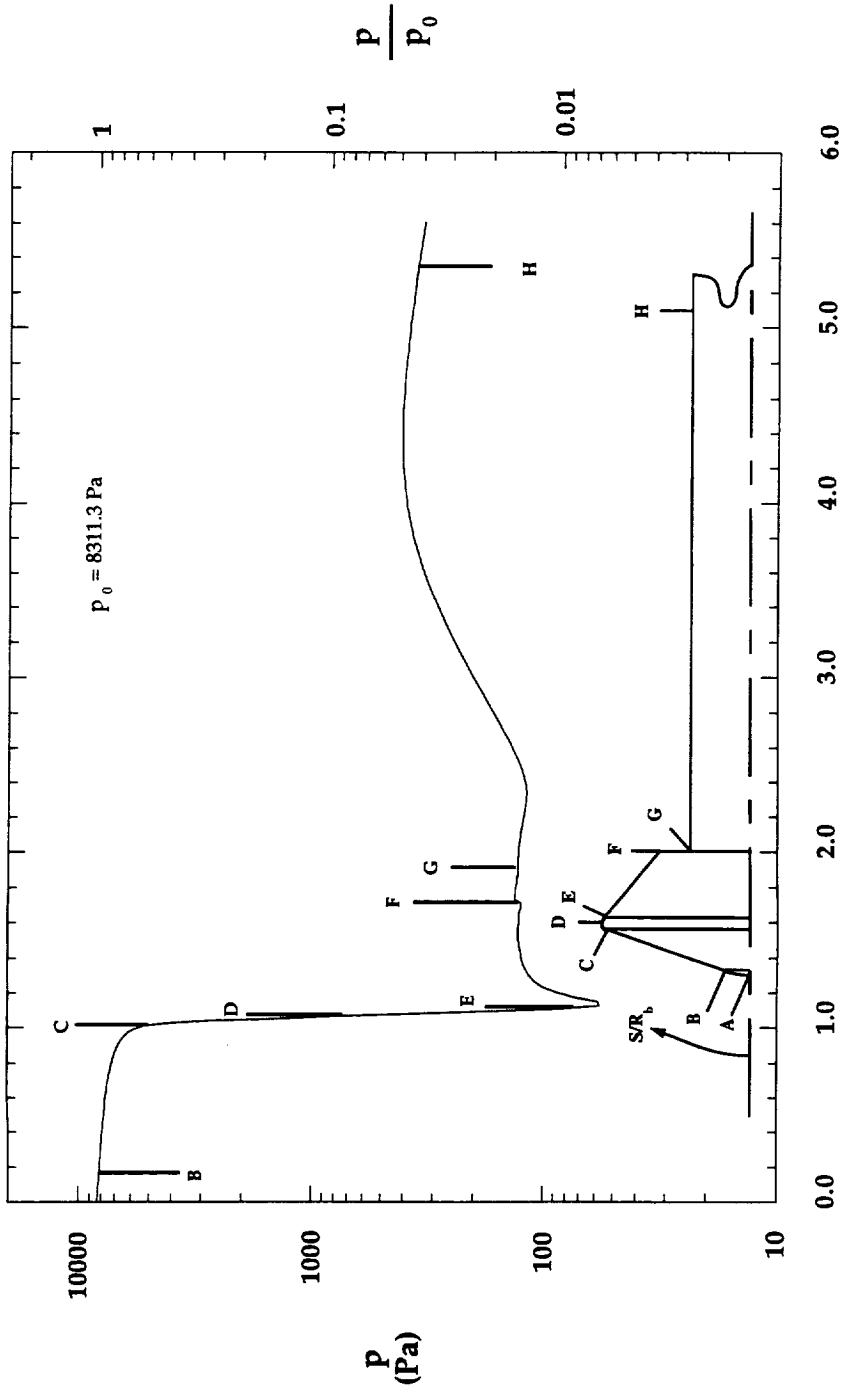

Figure 8.1.31 Computed Surface Pressure Distribution, MP-1 Configuration, 31-Inch Mach 10, $Re_\infty = 0.5x10E6$

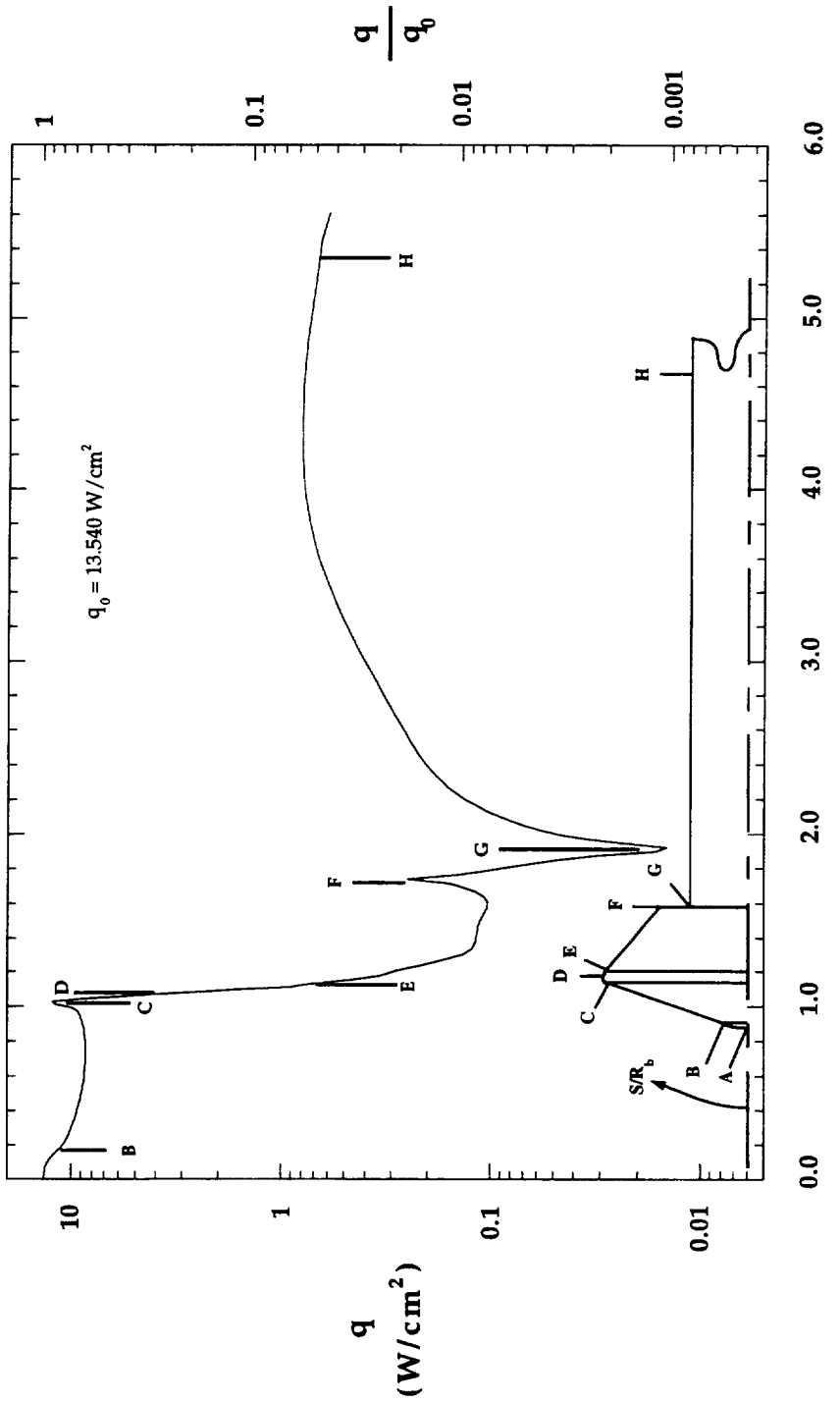

Figure 8.1.32 Computed Surface Heating Distribution, MP-1 Configuration, 31-Inch Mach 10, $Re_\infty = 0.5x10E6$

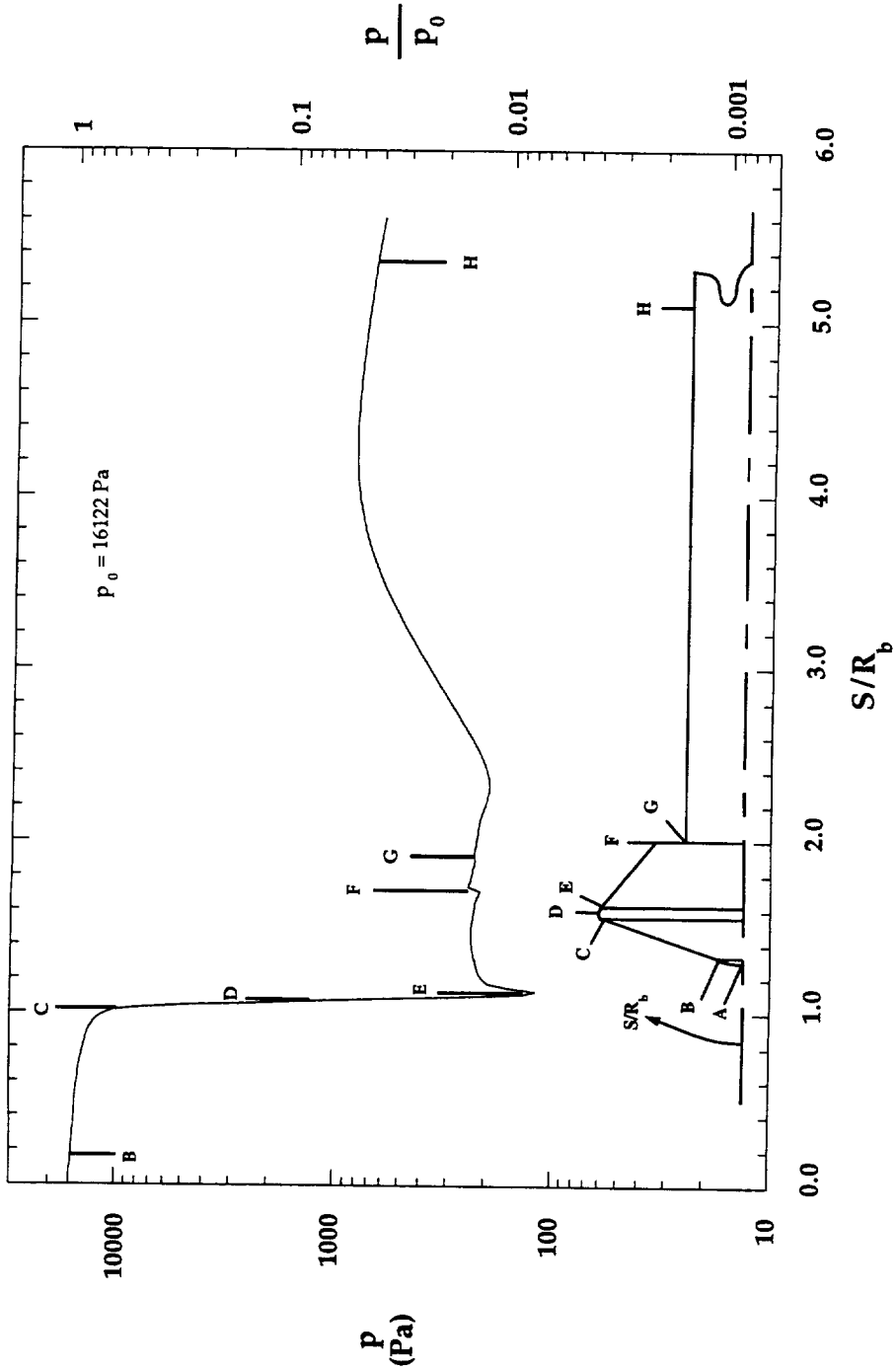

Figure 8.1.33 Computed Surface Pressure Distribution, MP-1 Configuration, 31-Inch Mach 10, $Re_\infty = 1.0x10E6$

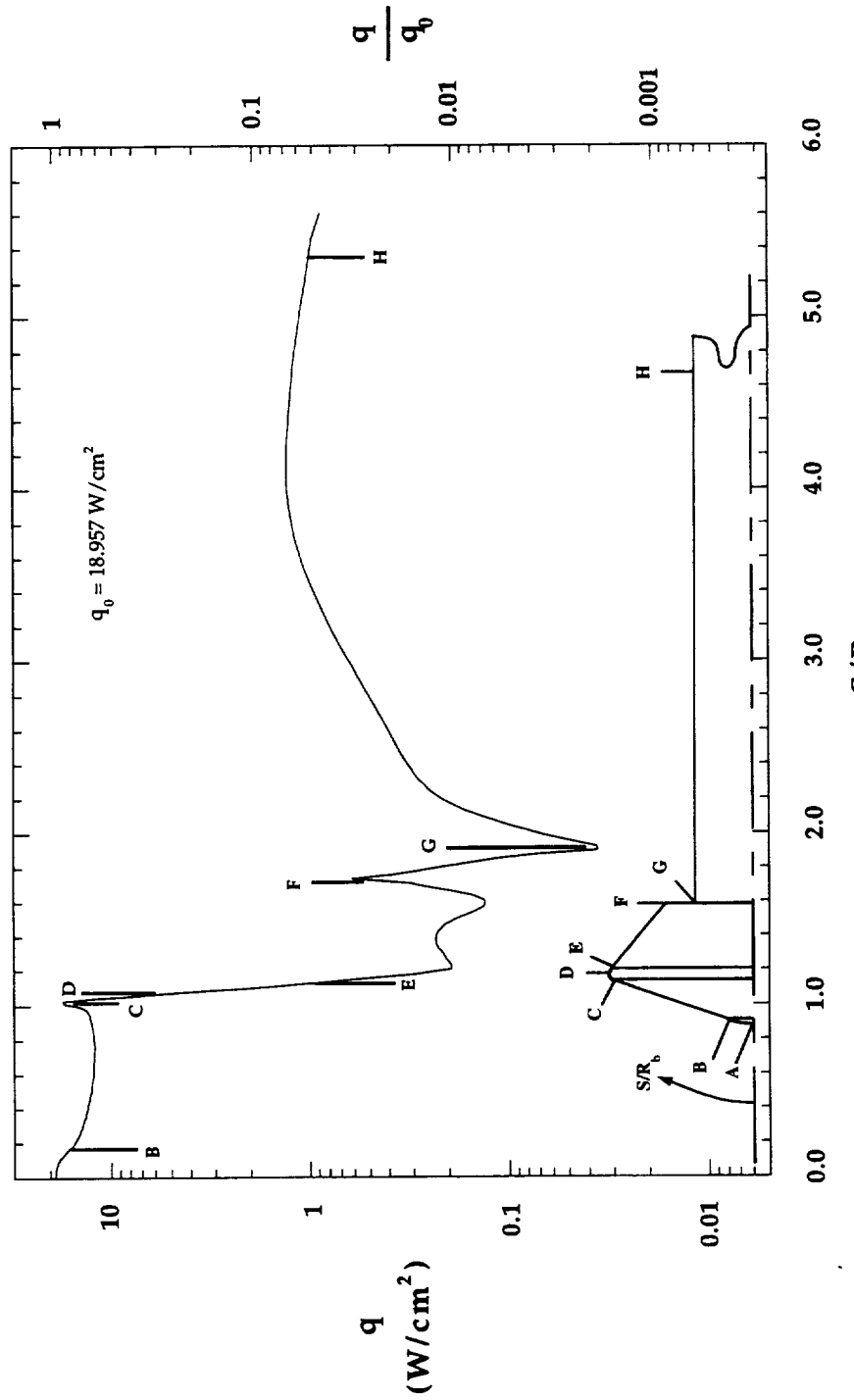

Figure 8.1.34 Computed Surface Heating Distribution, MP-1 Configuration, 31-Inch Mach 10, $Re_\infty = 1.0x10E6$

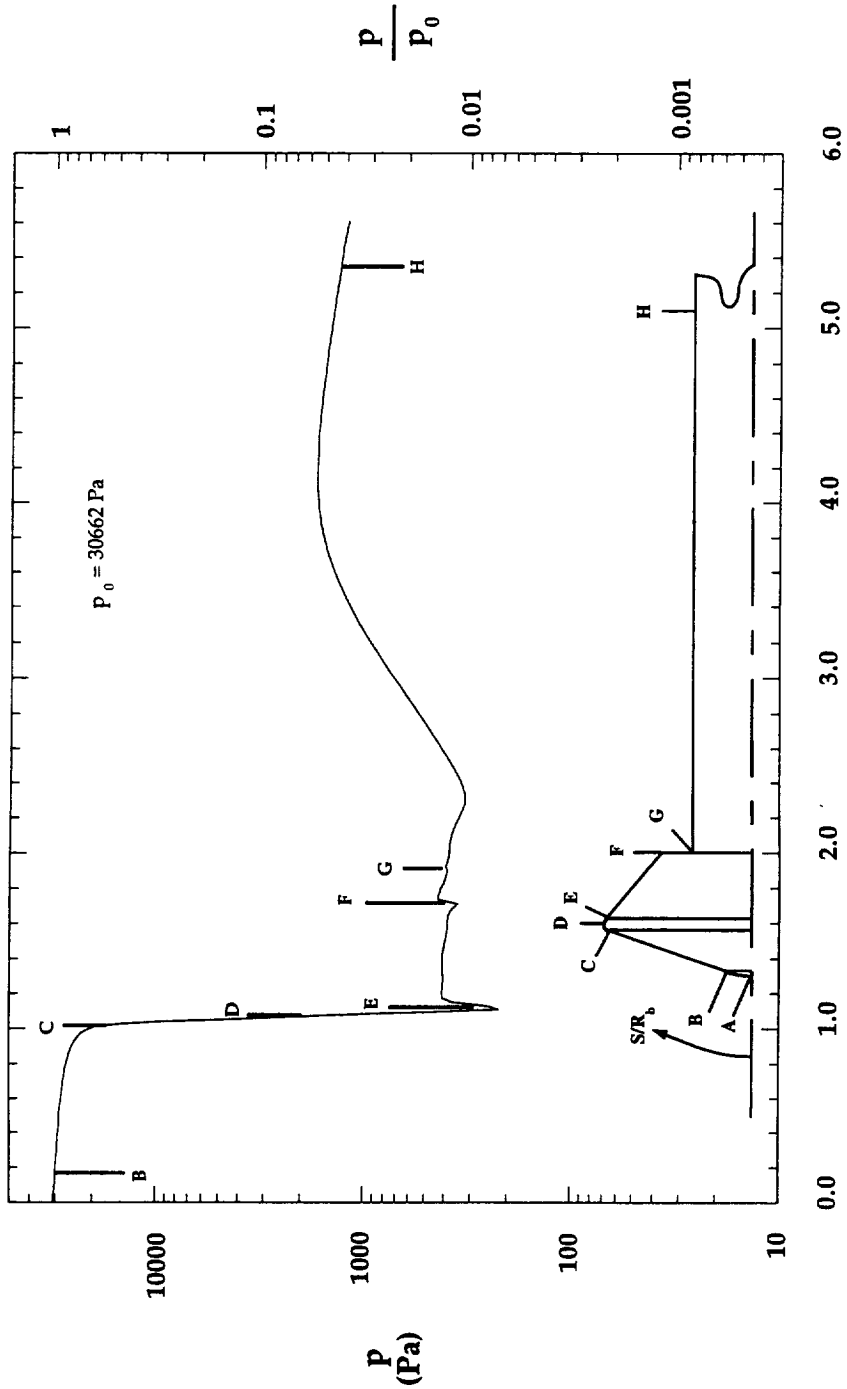

Figure 8.1.35 Computed Surface Pressure Distribution, MP-1 Configuration, 31-Inch Mach 10, $Re_\infty = 2.0x10E6$

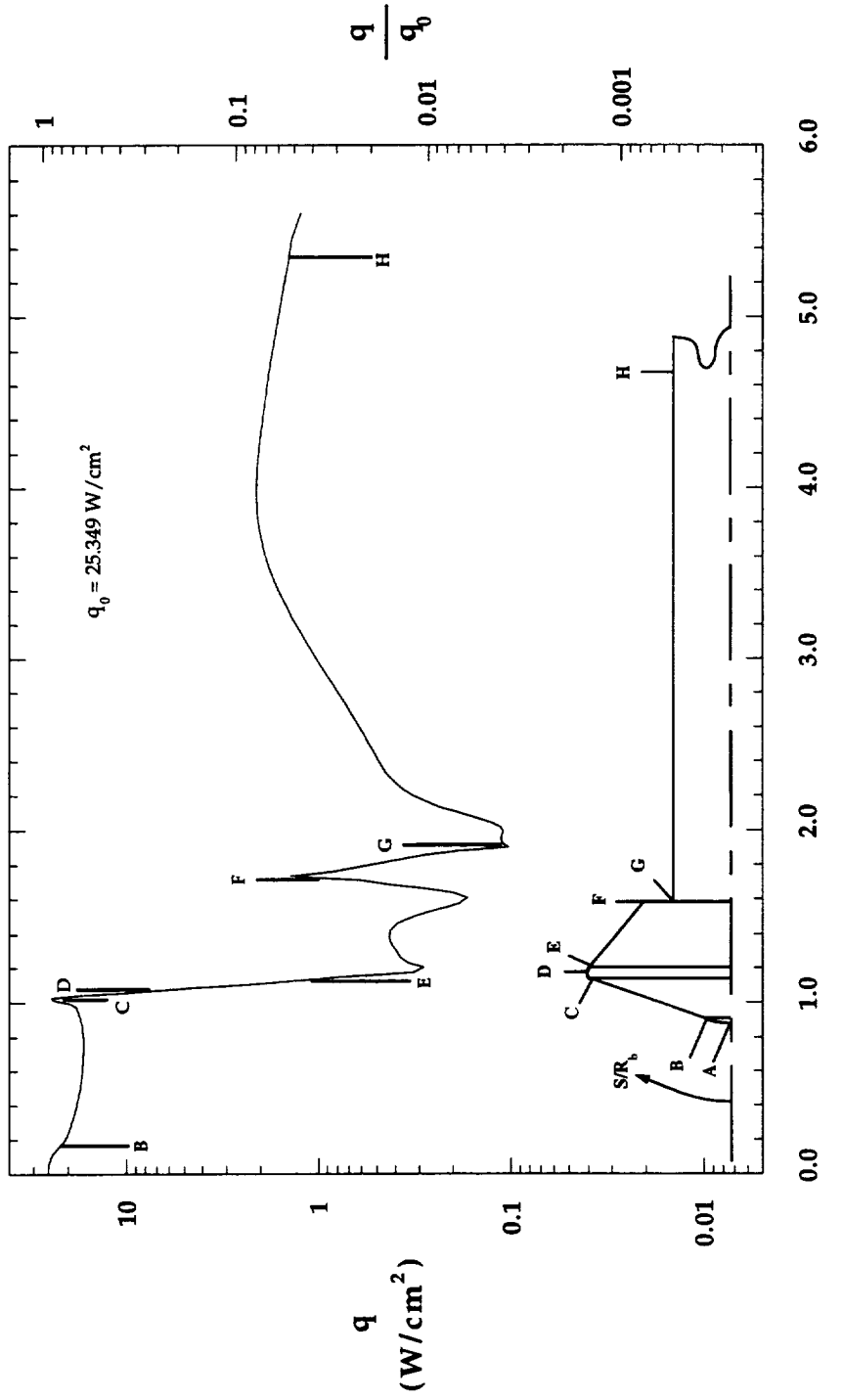

Figure 8.1.36 Computed Surface Heating Distribution, MP-1 Configuration, 31-Inch Mach 10, Re_∞ = 2.0x10E6

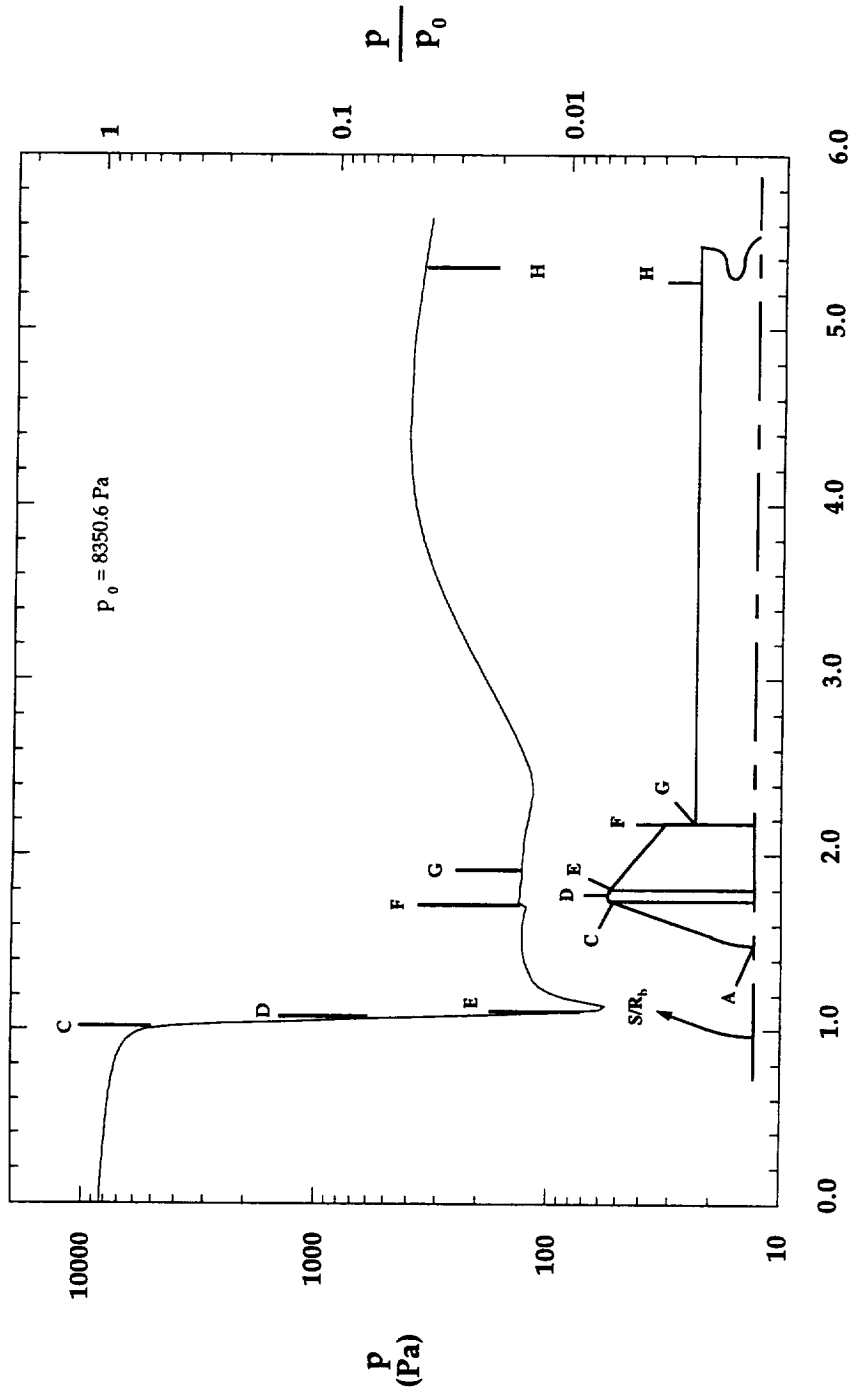

Figure 8.1.37 Computed Surface Pressure Distribution, MP-2 Configuration, 31-Inch Mach 10, $Re_\infty = 0.5x10E6$

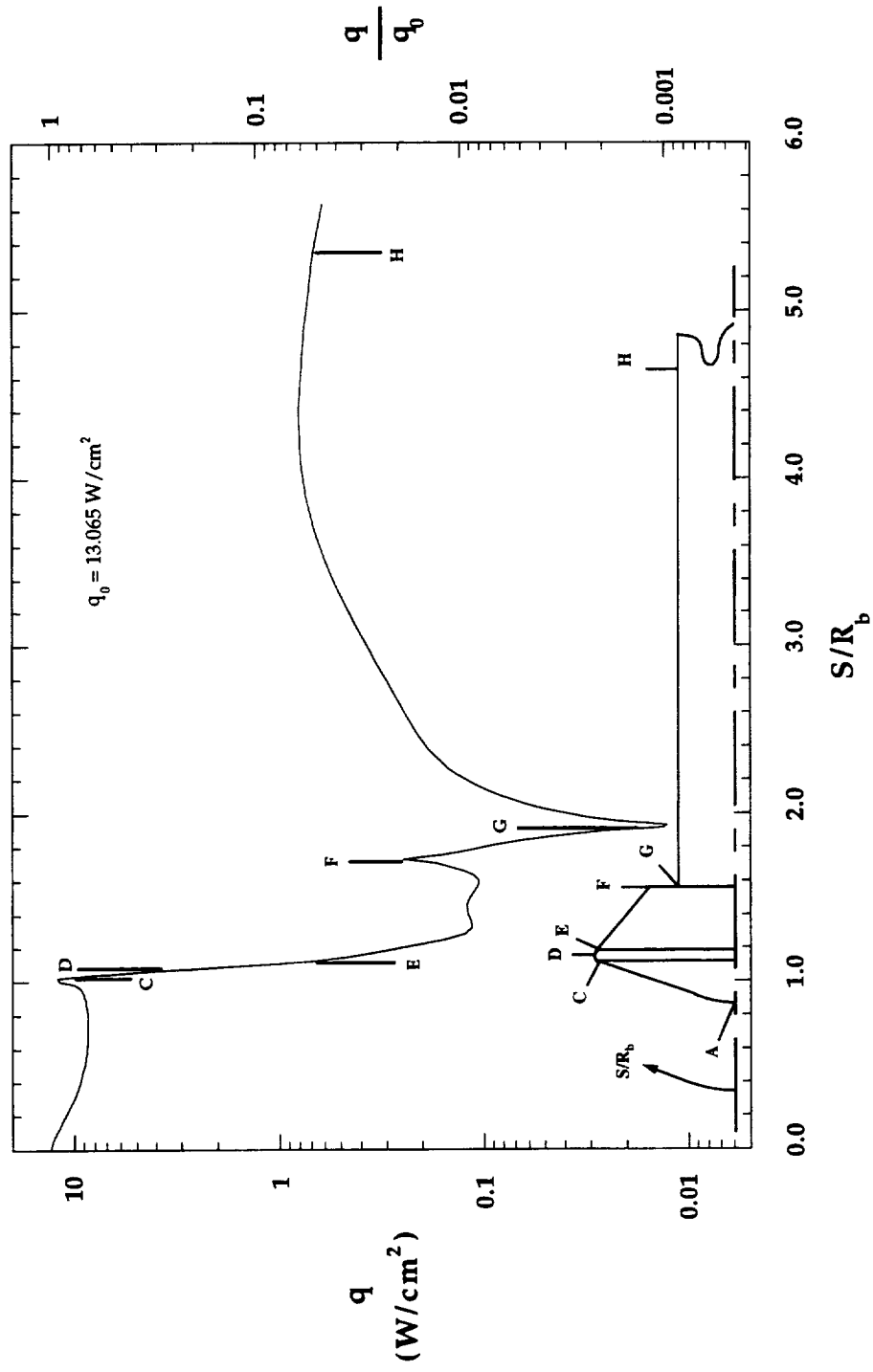

Figure 8.1.38 Computed Surface Heating Distribution, MP-2 Configuration, 31-Inch Mach 10, Re_∞ = 0.5x10E6

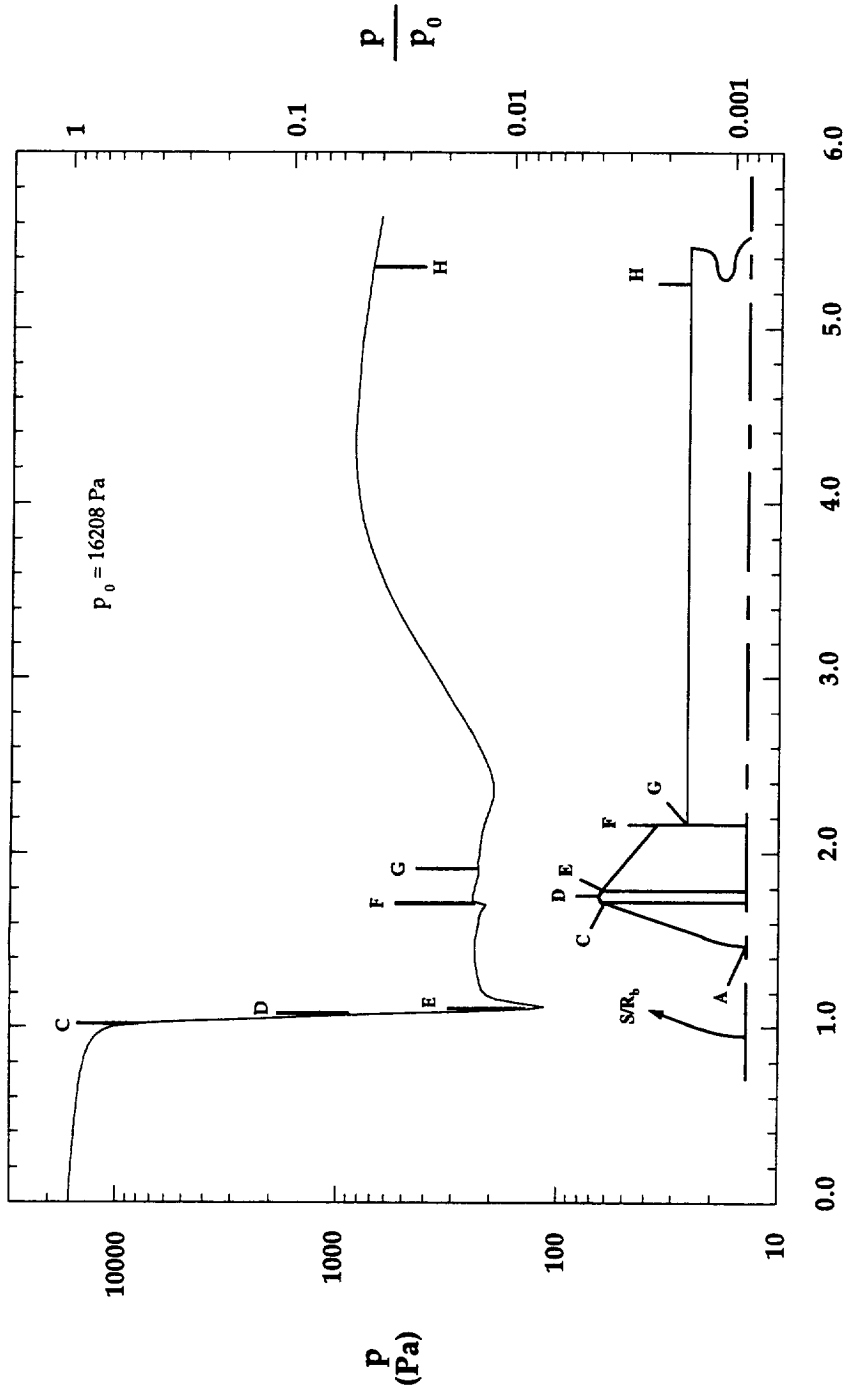

Figure 8.1.39 Computed Surface Pressure Distribution, MP-2 Configuration, 31-Inch Mach 10, Re_∞ = 1.0x10E6

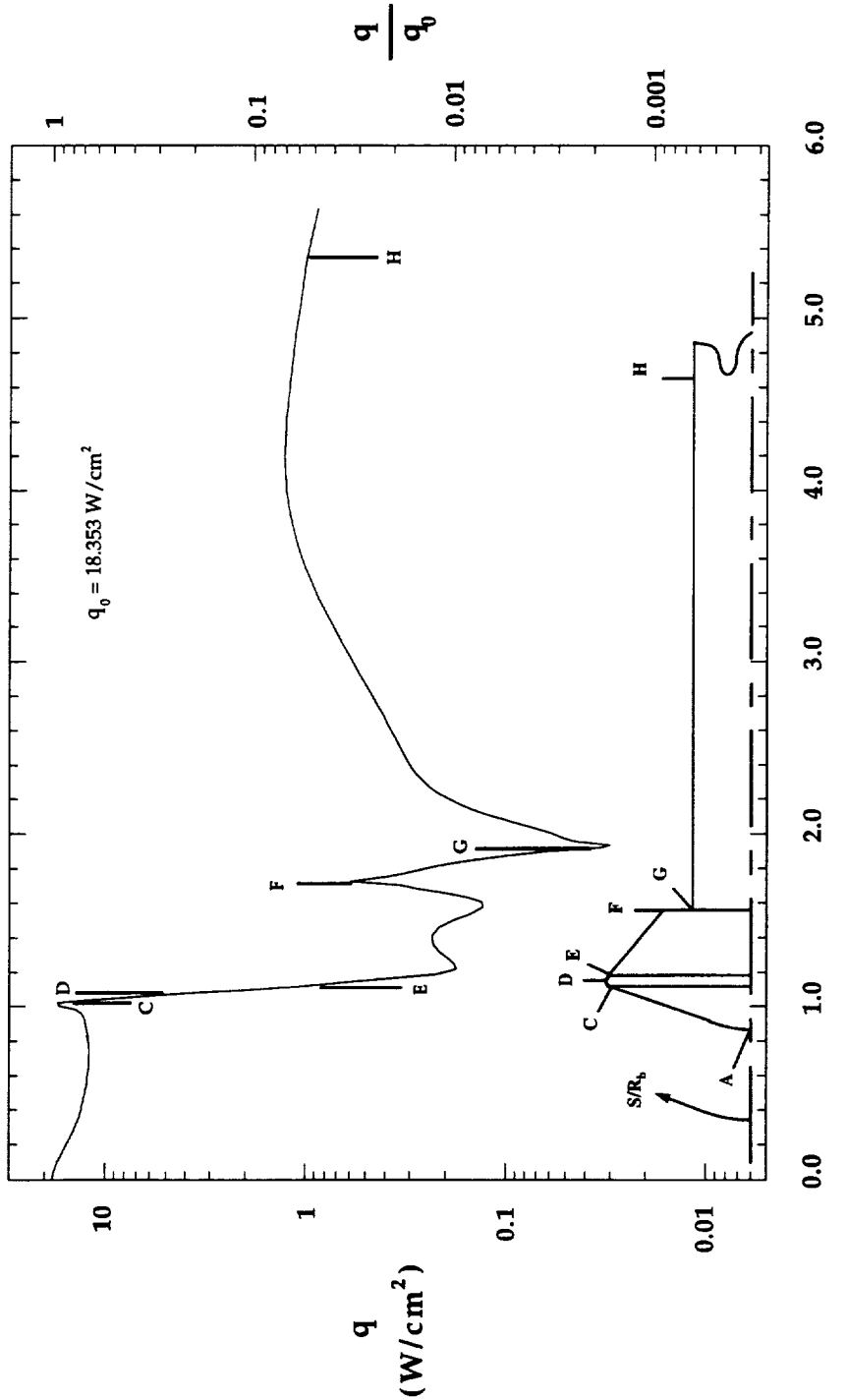

Figure 8.1.40 Computed Surface Heating Distribution, MP-2 Configuration, 31-Inch Mach 10, Re_∞ = 1.0x10E6

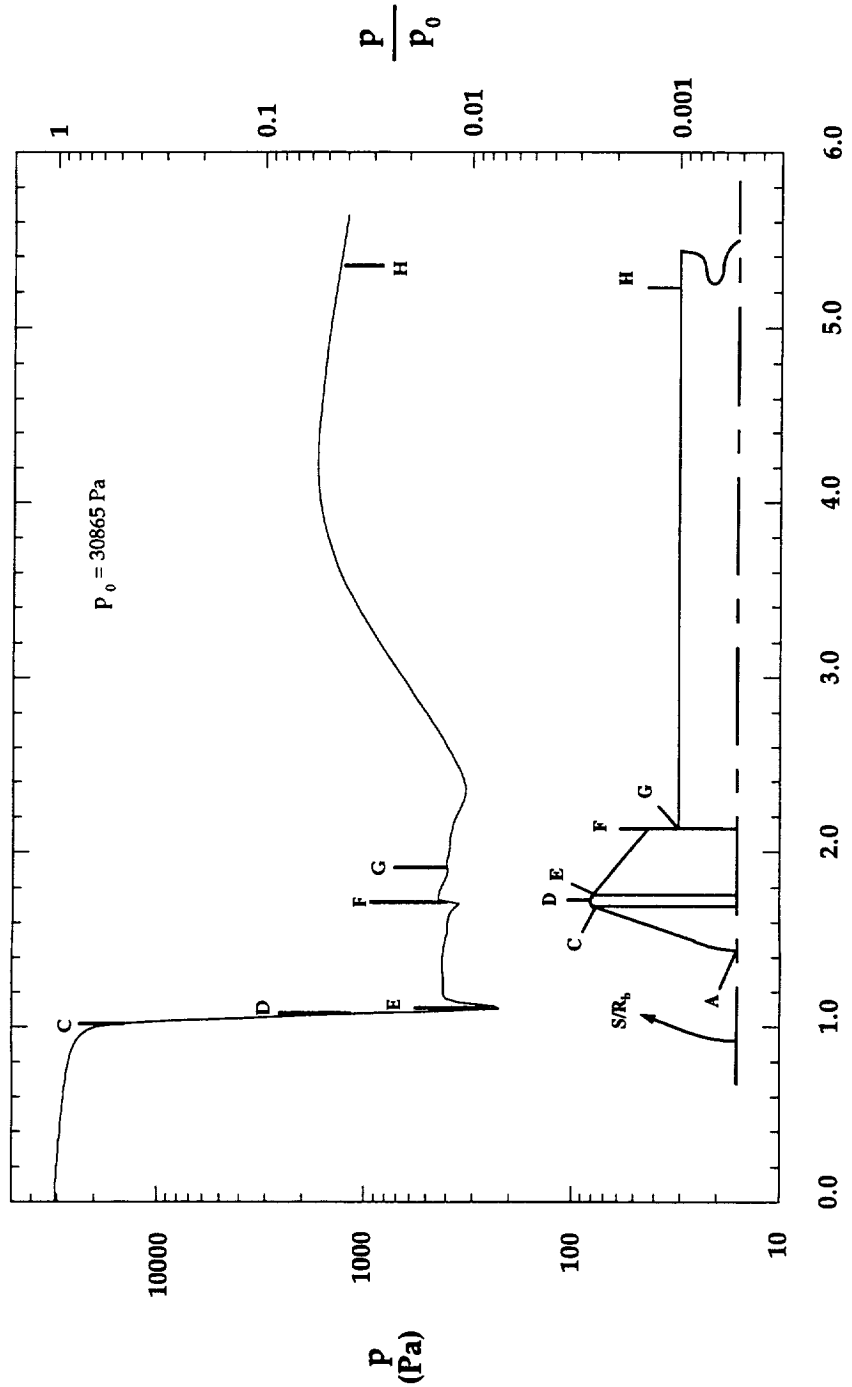

Figure 8.1.41 Computed Surface Pressure Distribution, MP-2 Configuration, 31-Inch Mach 10, $Re_\infty = 2.0x10E6$

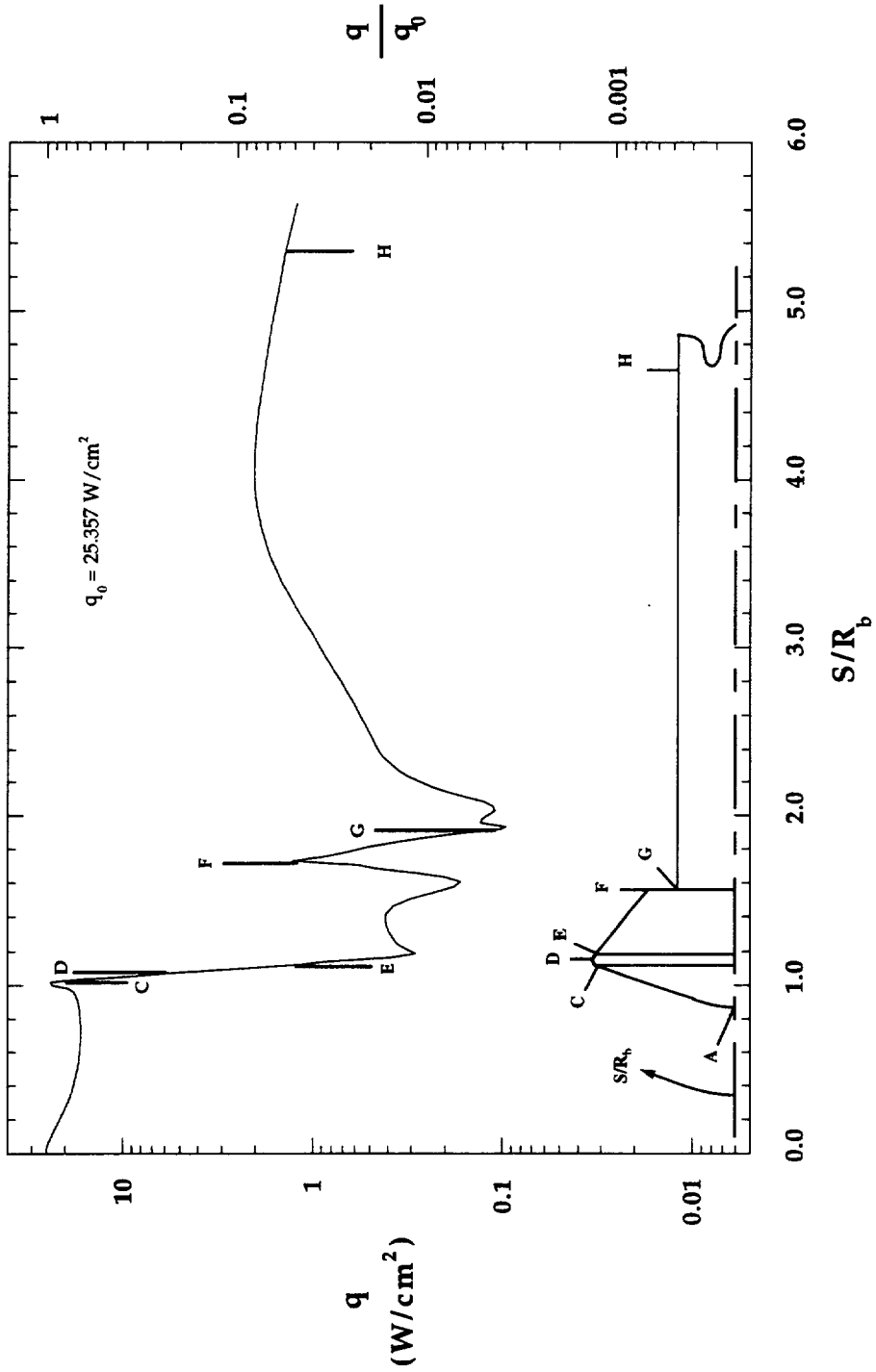

Figure 8.1.42 Computed Surface Heating Distribution, MP-2 Configuration, 31-Inch Mach 10, $Re_\infty = 2.0x10E6$

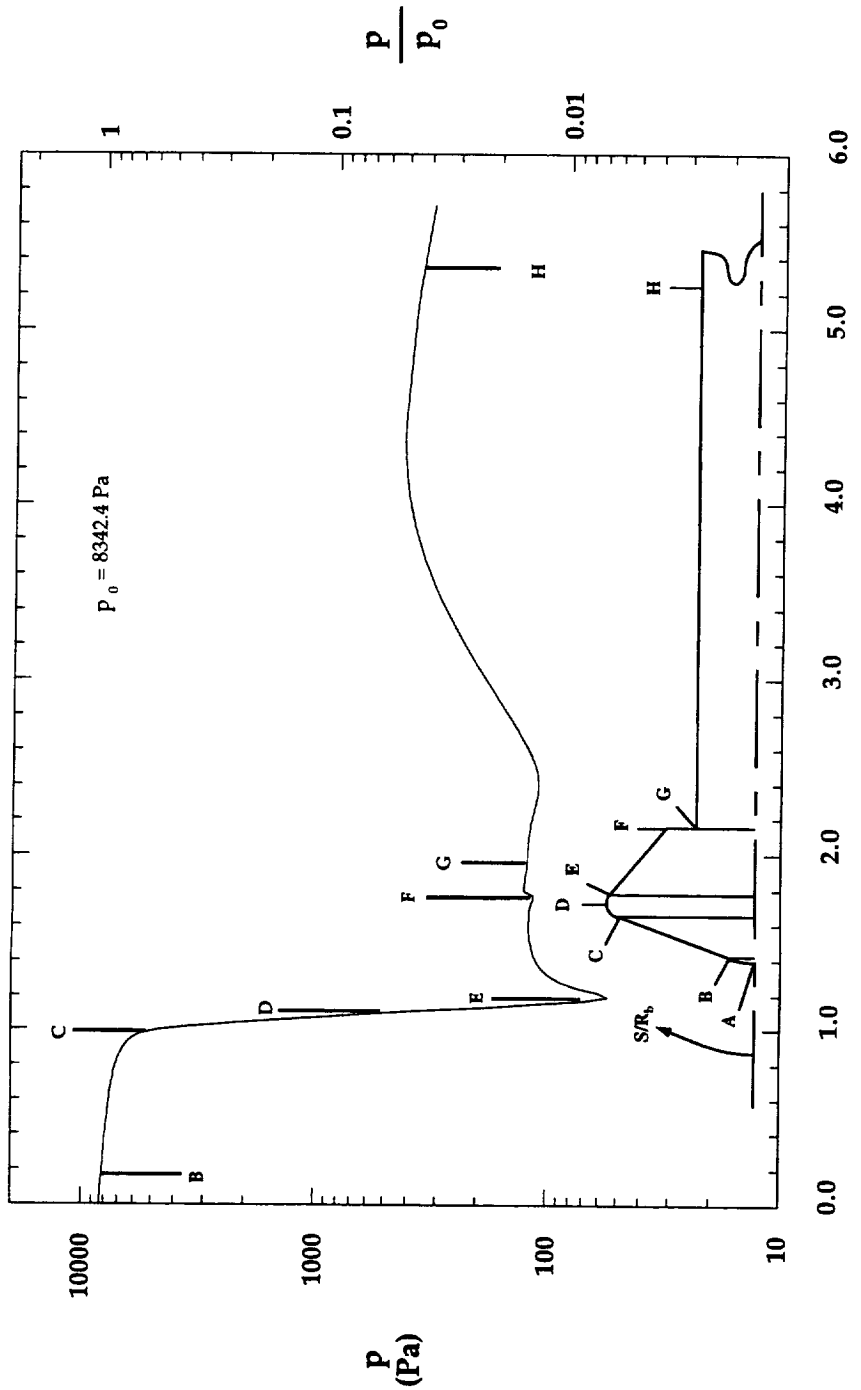

Figure 8.1.43 Computed Surface Pressure Distribution, MP-3 Configuration, 31-Inch Mach 10, $Re_\infty = 0.5x10E6$

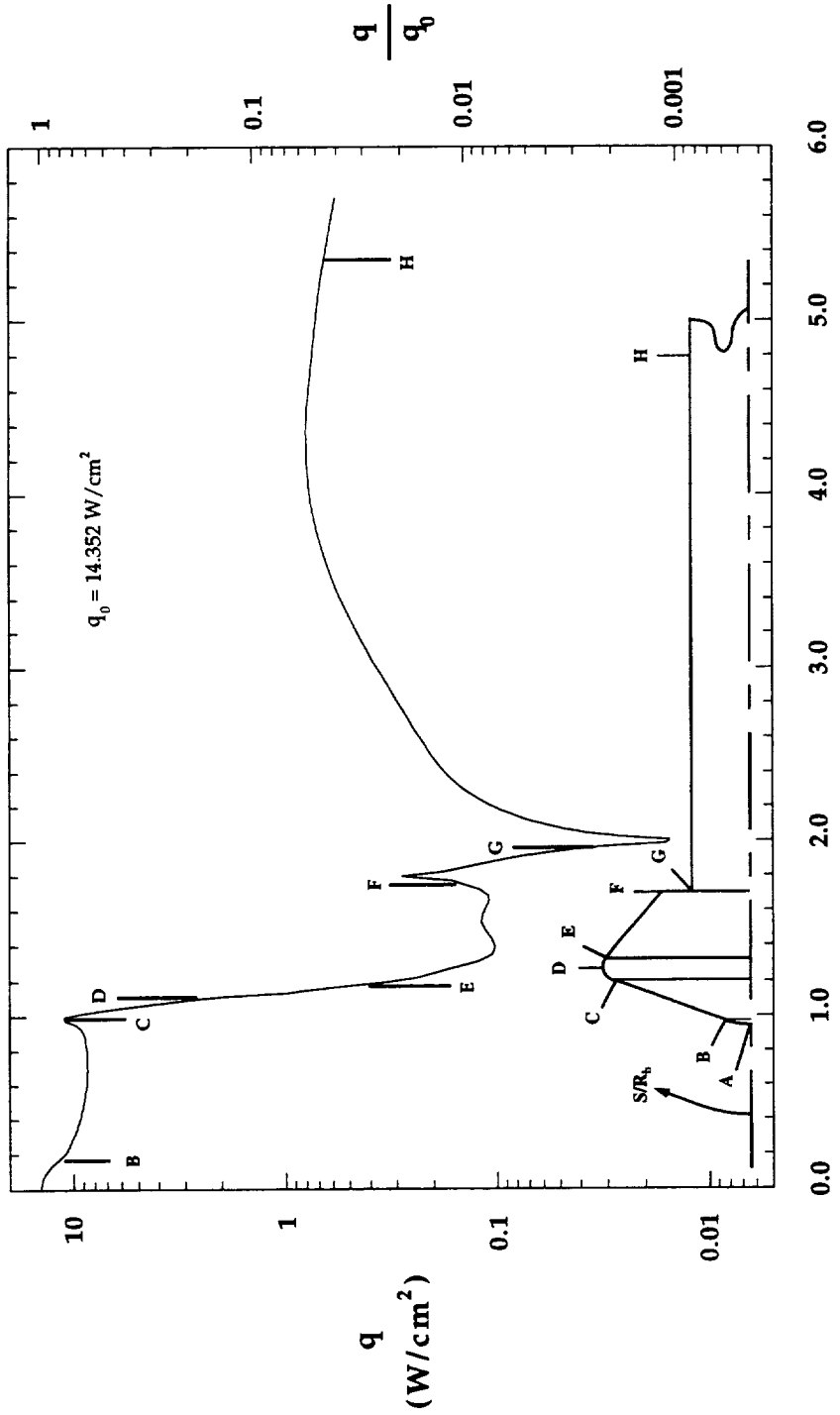

Figure 8.1.44 Computed Surface Heating Distribution, MP-3 Configuration, 31-Inch Mach 10, $Re_\infty = 0.5x10E6$

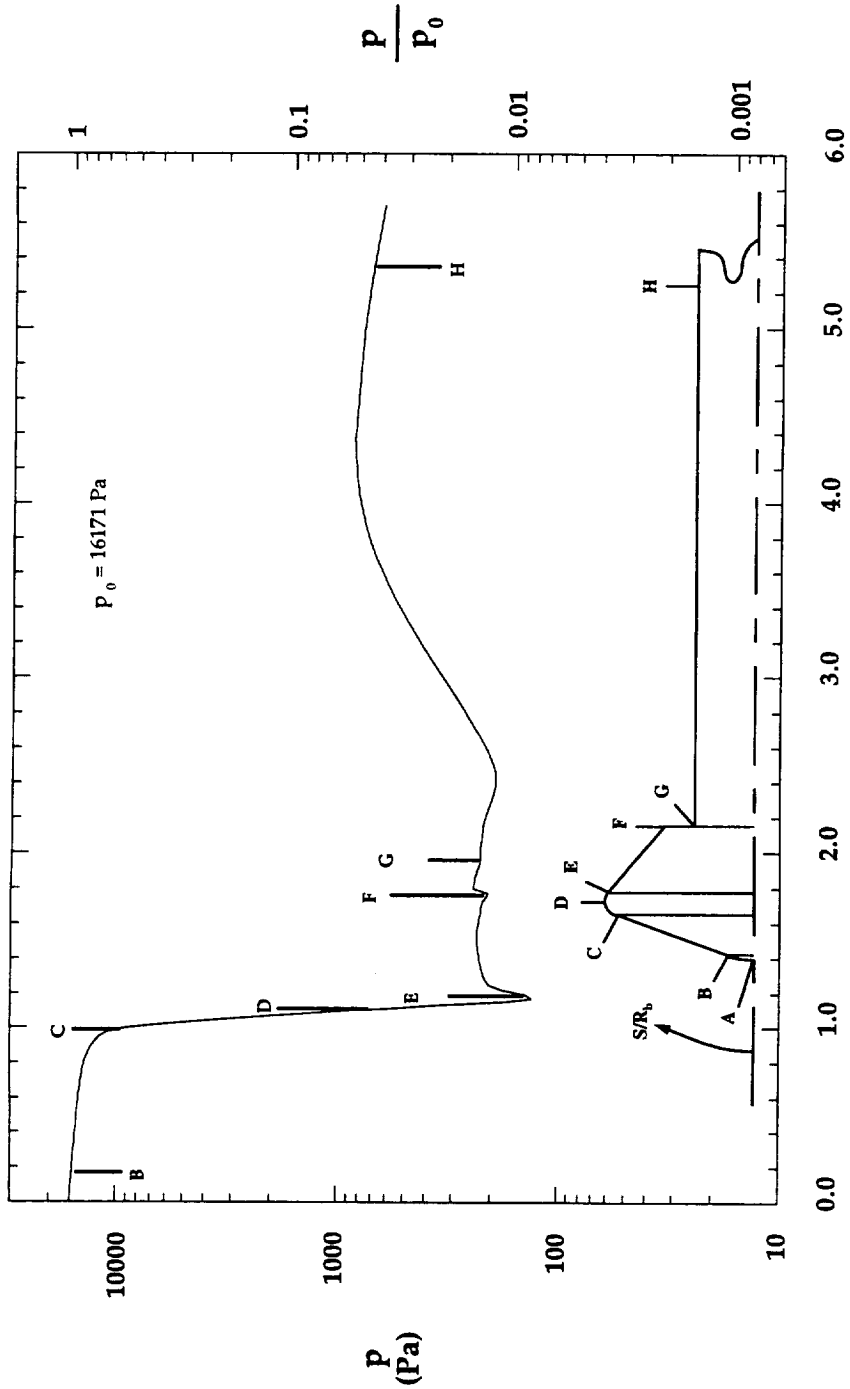

Figure 8.1.45 Computed Surface Pressure Distribution, MP-3 Configuration, 31-Inch Mach 10, $Re_\infty = 1.0x10E6$

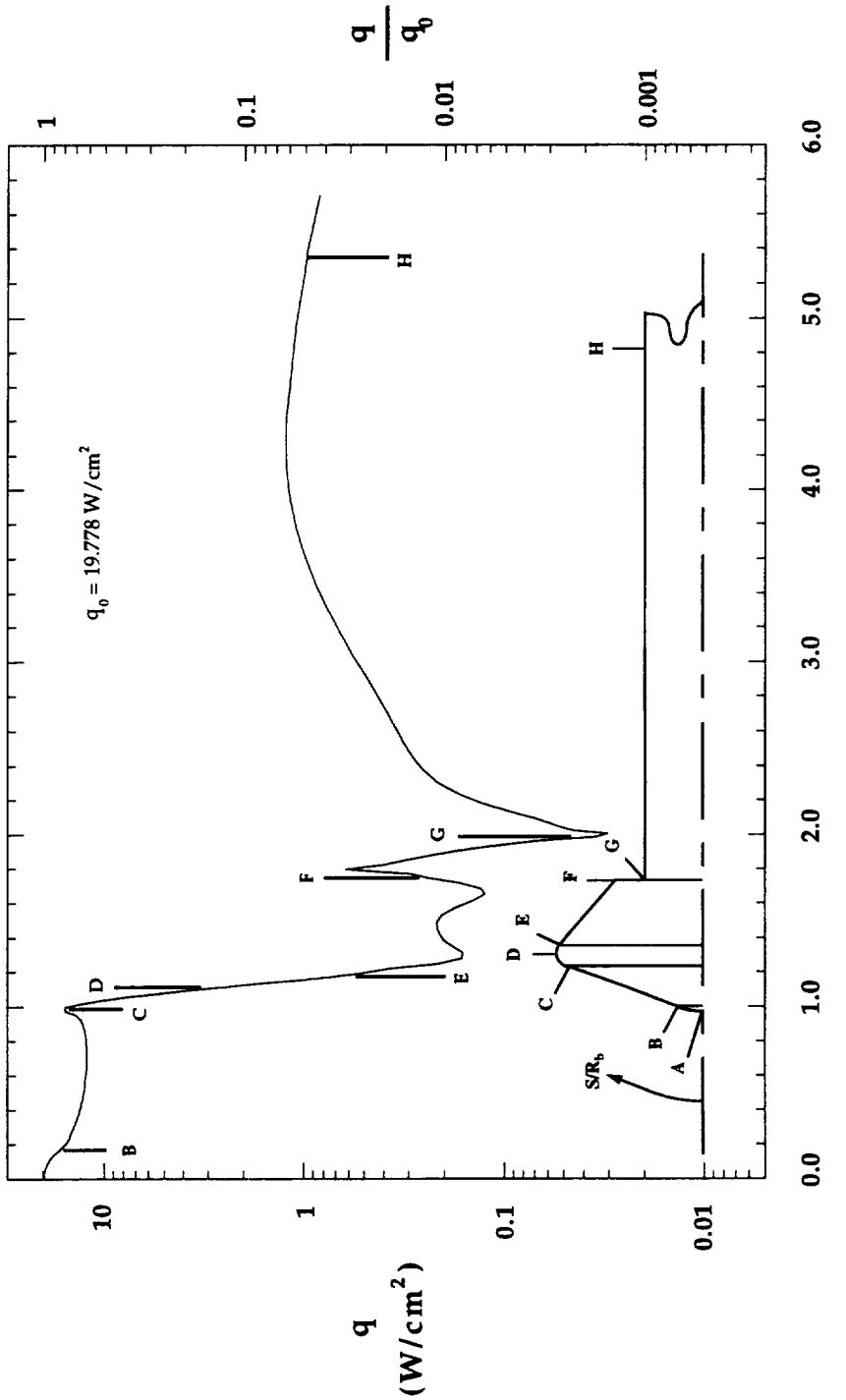

Figure 8.1.46 Computed Surface Heating Distribution, MP-3 Configuration, 31-Inch Mach 10, $Re_\infty = 1.0x10E6$

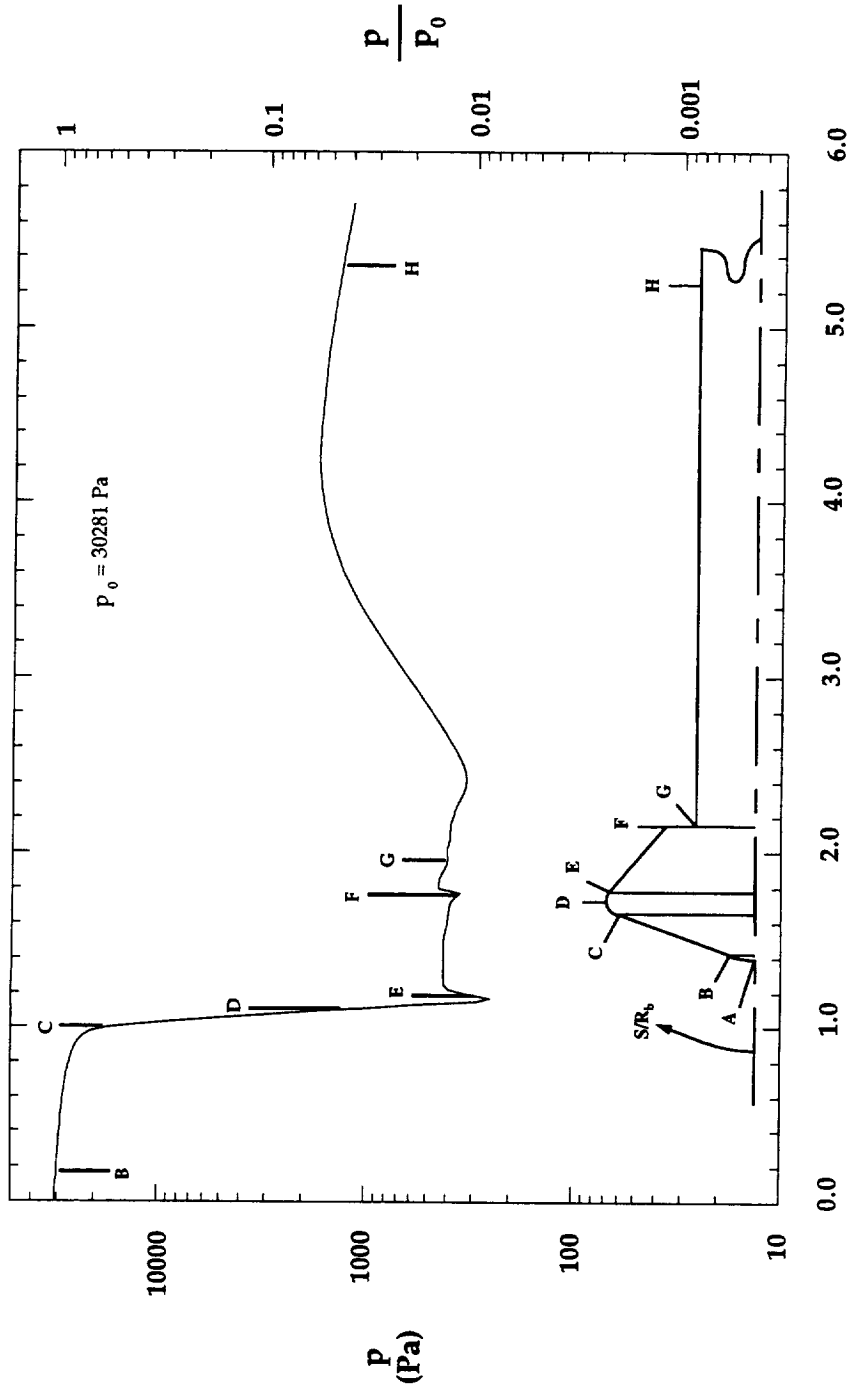

Figure 8.1.47 Computed Surface Pressure Distribution, MP-3 Configuration, 31-Inch Mach 10, $Re_\infty = 2.0x10E6$

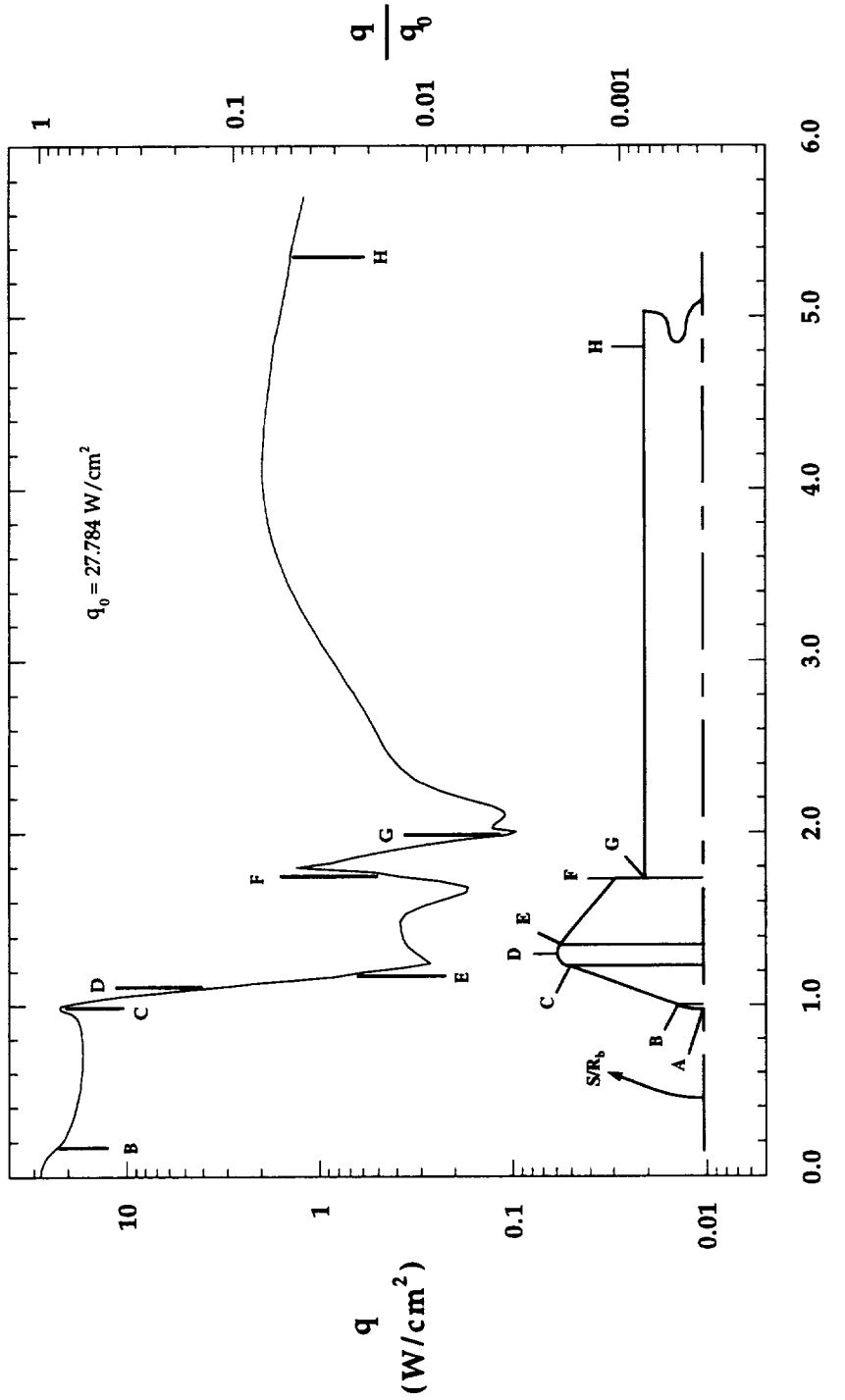

Figure 8.1.48 Computed Surface Heating Distribution, MP-3 Configuration, 31-Inch Mach 10, $Re_\infty = 2.0x10E6$

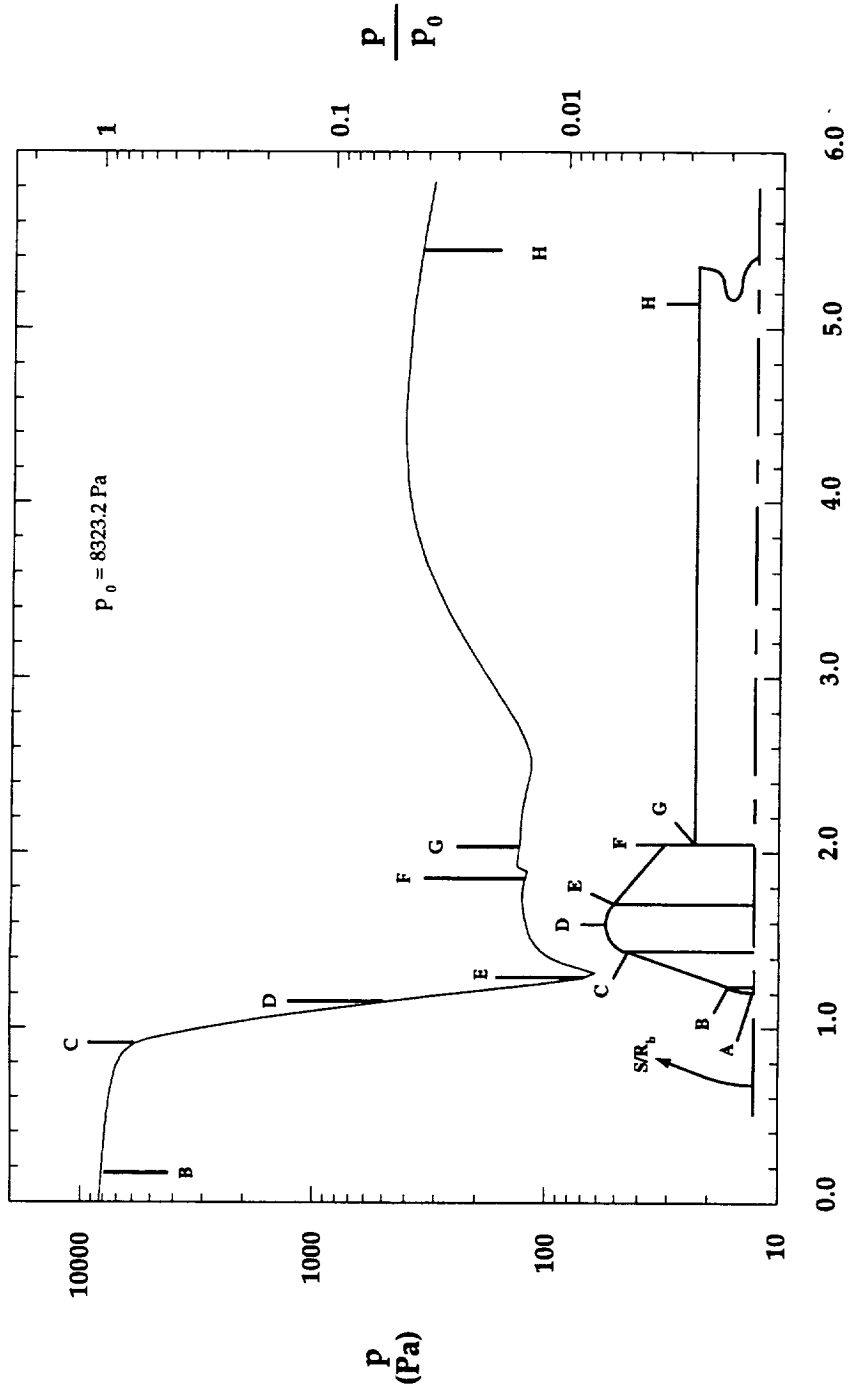

Figure 8.1.49 Computed Surface Pressure Distribution, MP-4 Configuration, 31-Inch Mach 10, $Re_\infty = 0.5x10E6$

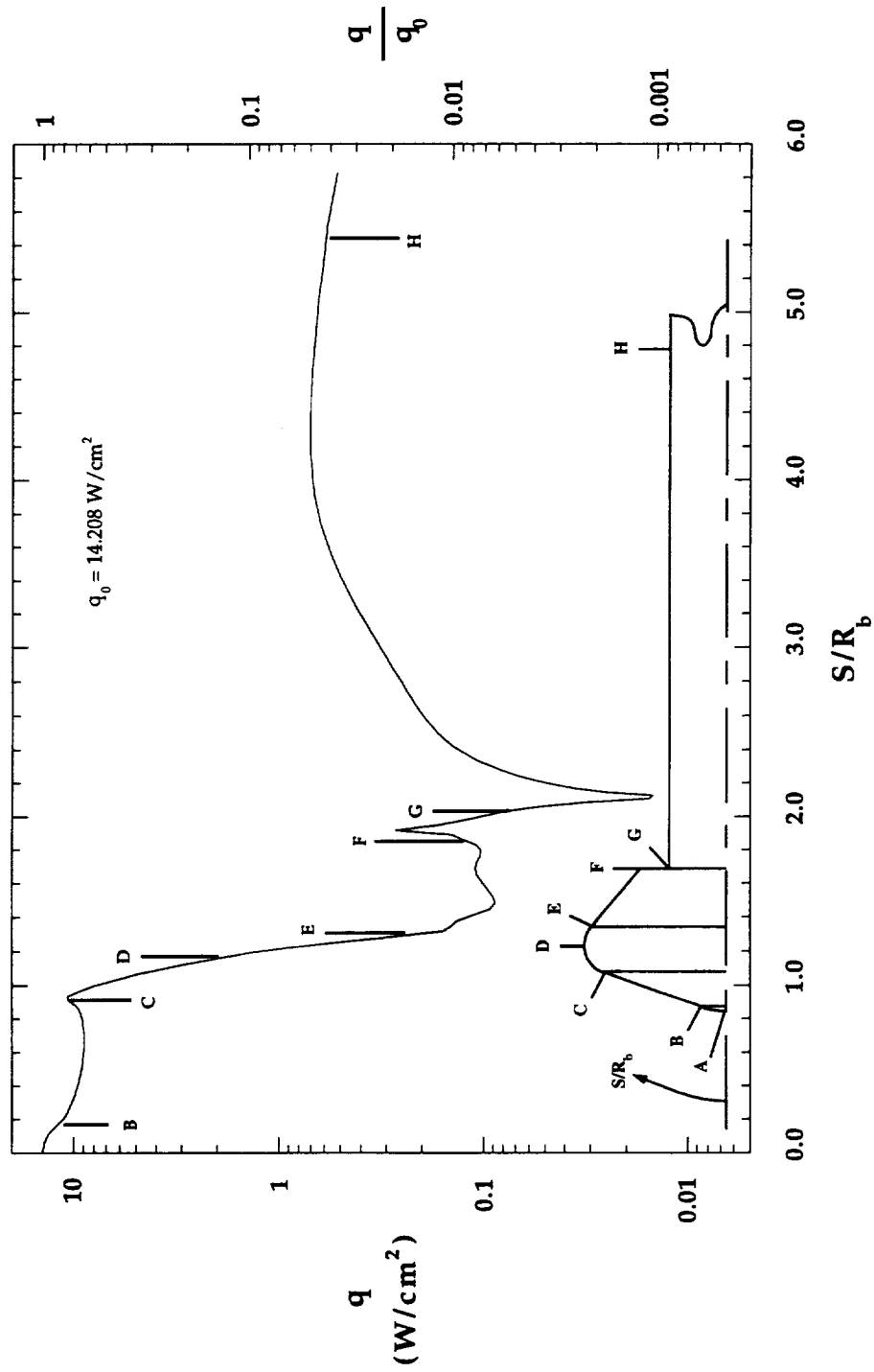

Figure 8.1.50 Computed Surface Heating Distribution, MP-4 Configuration, 31-Inch Mach 10, $Re_\infty = 0.5x10E6$

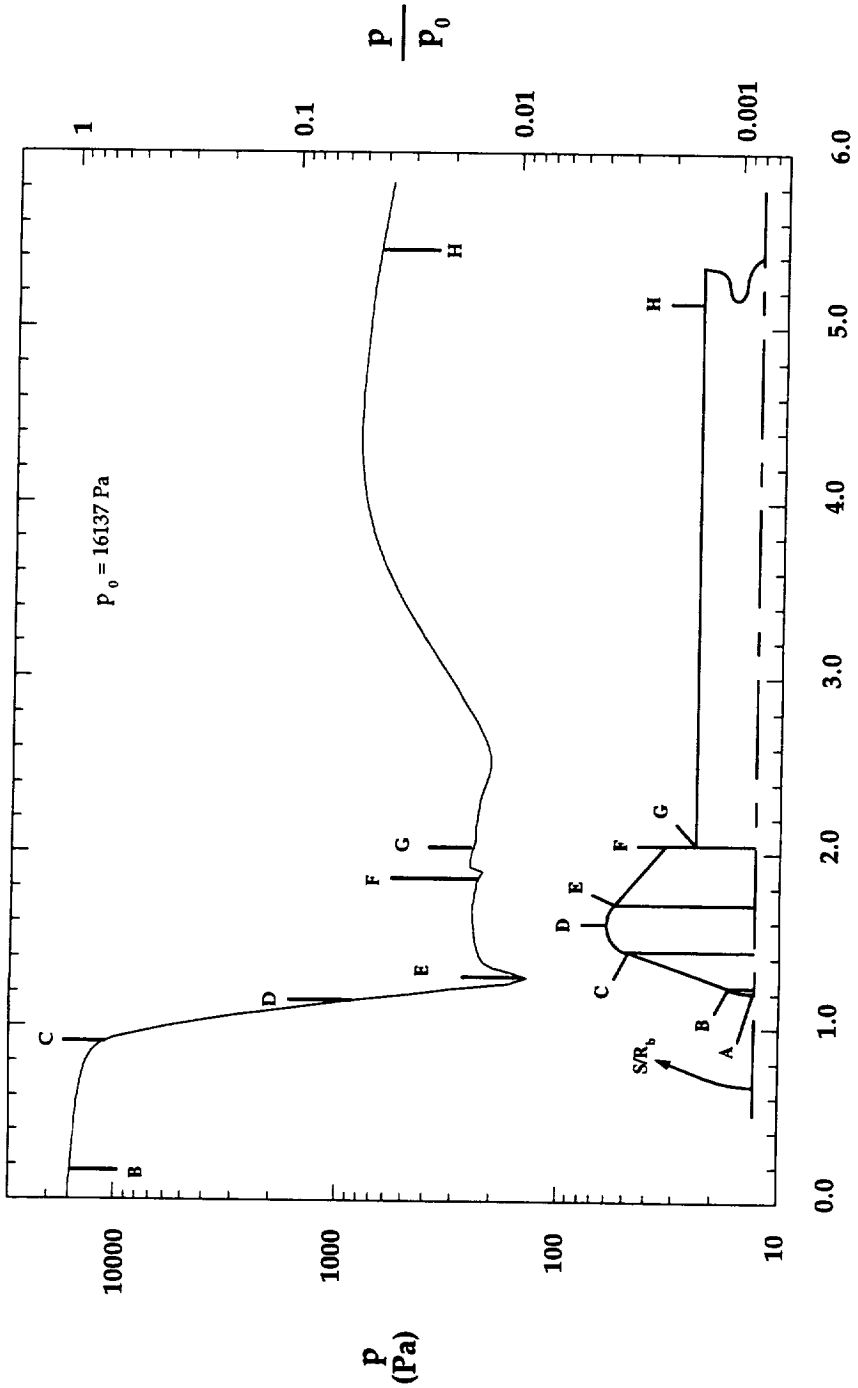

Figure 8.1.51 Computed Surface Pressure Distribution, MP-4 Configuration, 31-Inch Mach 10, $Re_\infty = 1.0x10E6$

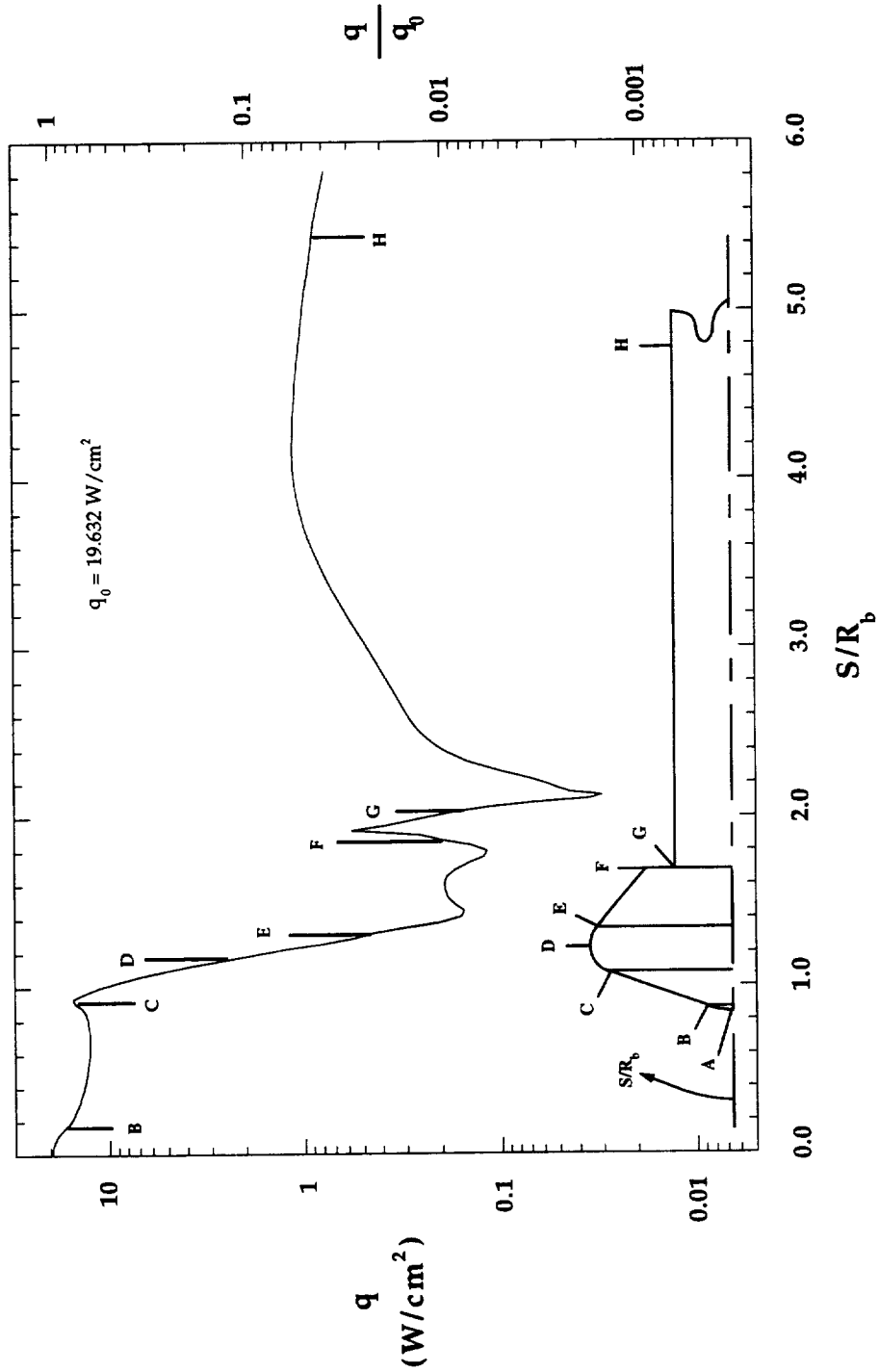

Figure 8.1.52 Computed Surface Heating Distribution, MP-4 Configuration, 31-Inch Mach 10, $Re_\infty = 1.0x10E6$

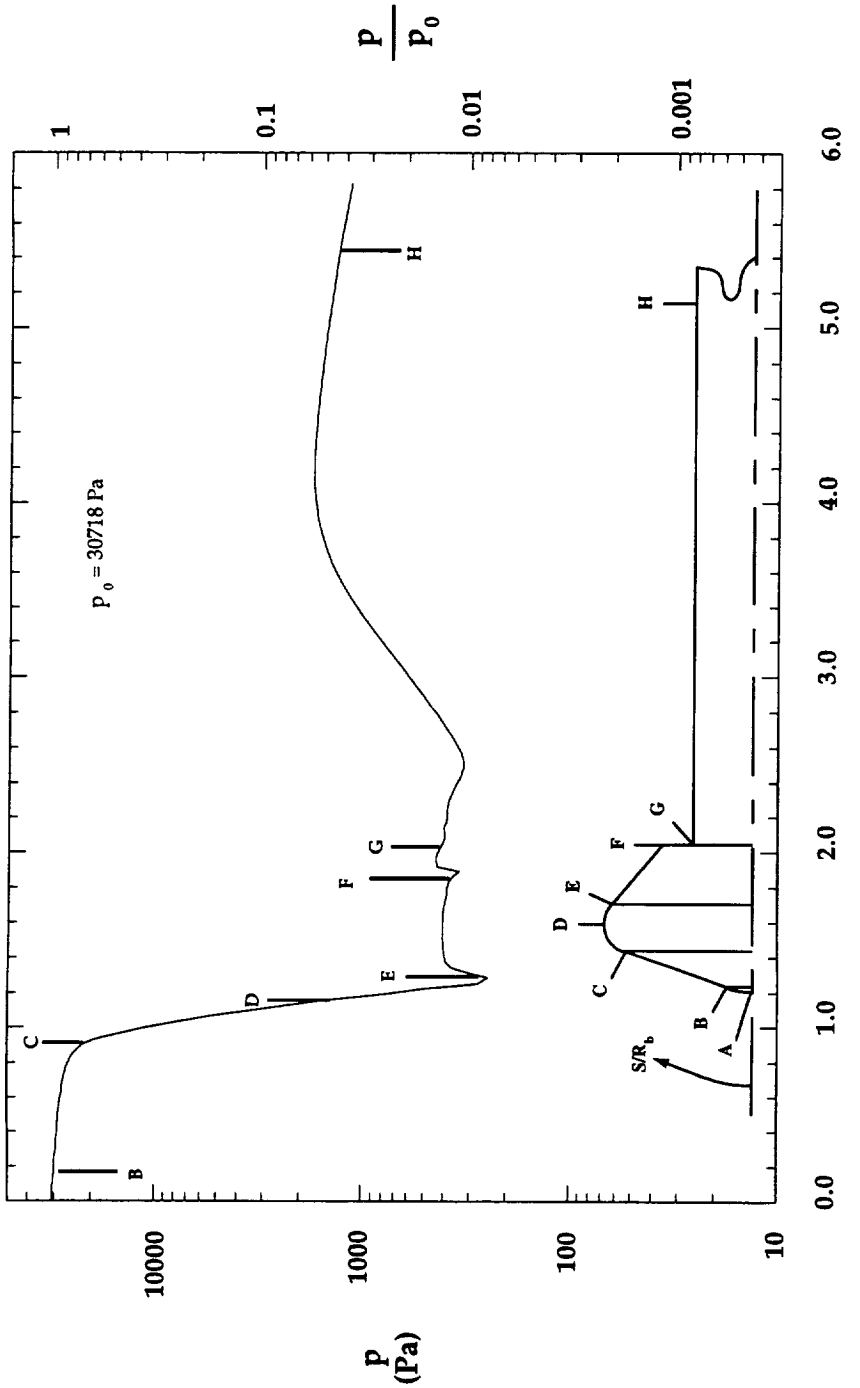

Figure 8.1.53 Computed Surface Pressure Distribution, MP-4 Configuration, 31-Inch Mach 10, $Re_\infty = 2.0x10E6$

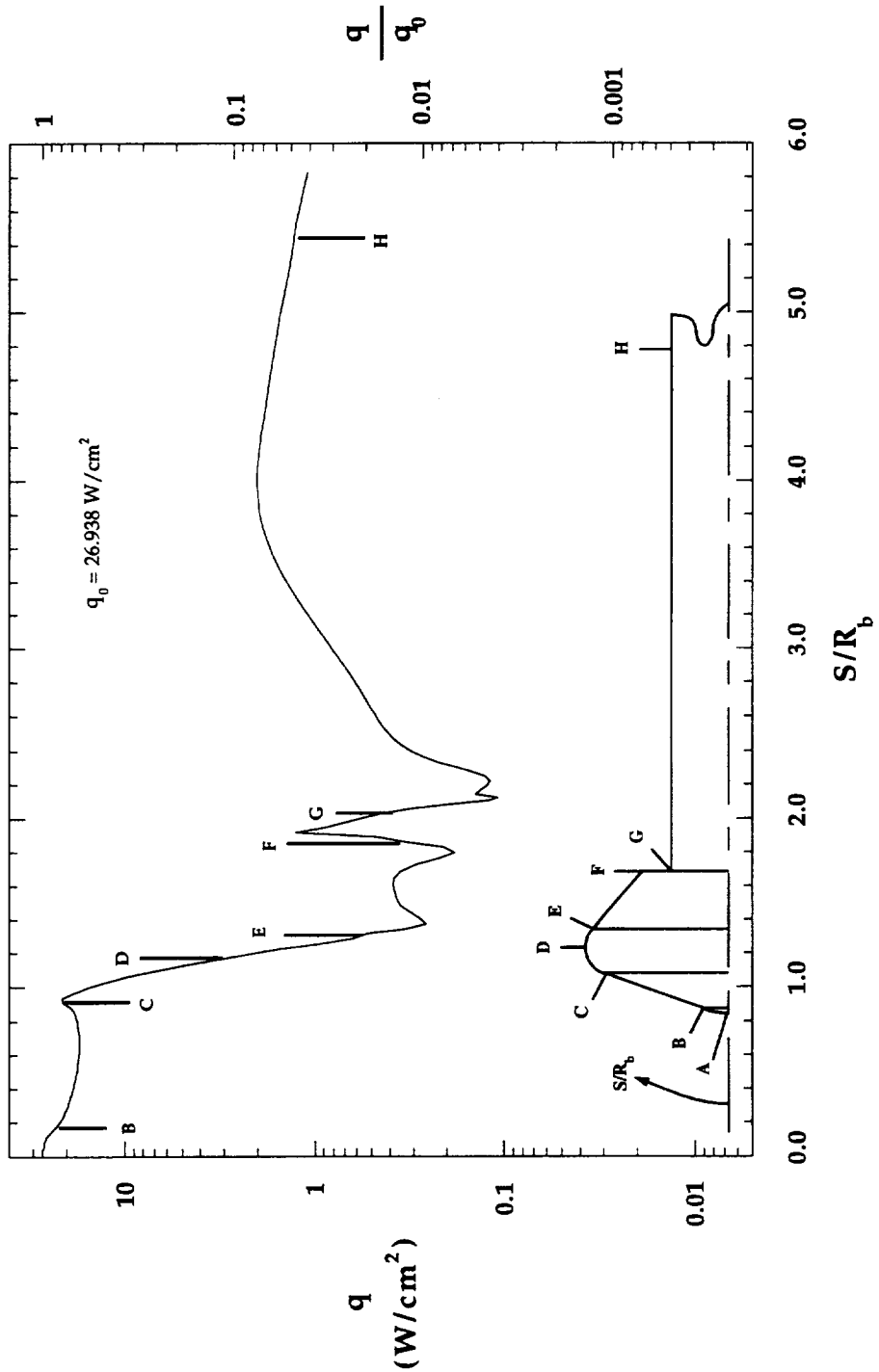

Figure 8.1.54 Computed Surface Heating Distribution, MP-4 Configuration, 31-Inch Mach 10, $Re_\infty = 2.0x10E6$

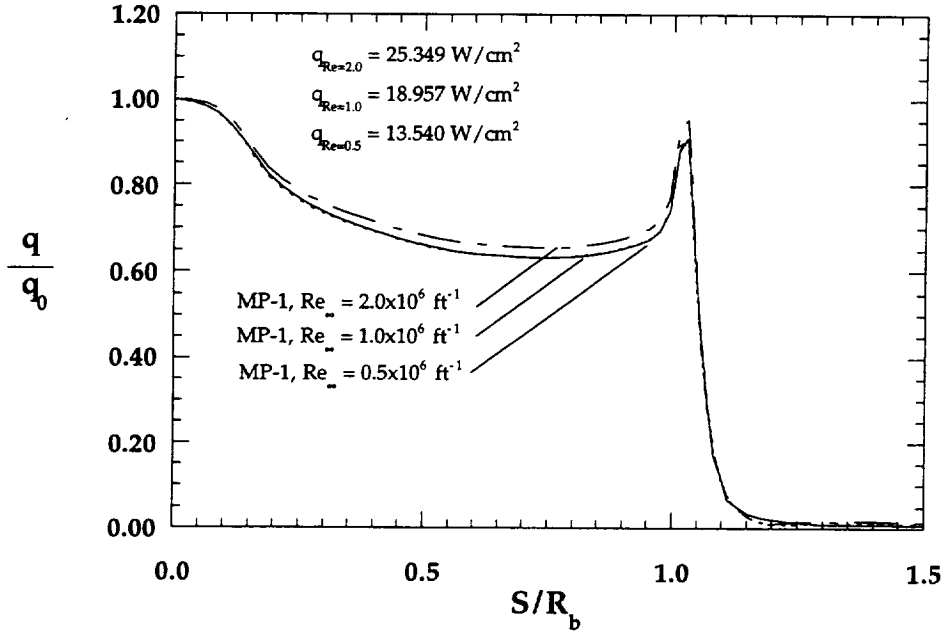

Figure 8.1.55a Reynolds Number Effects on Forebody Heating, MP-1 Configuration, 31-Inch Mach 10

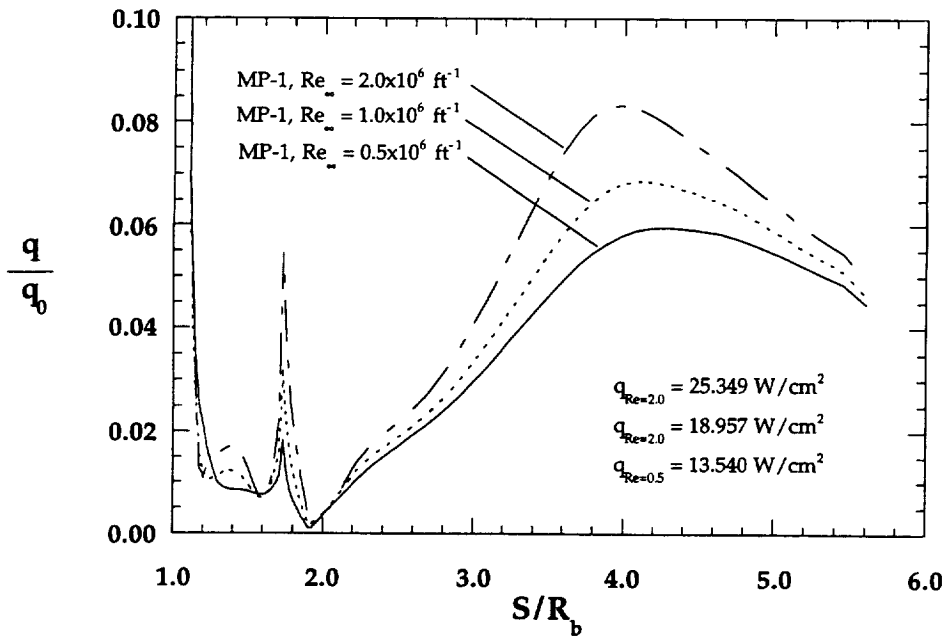

Figure 8.1.55b Reynolds Number Effects on Wake Heating, MP-1 Configuration, 31-Inch Mach 10

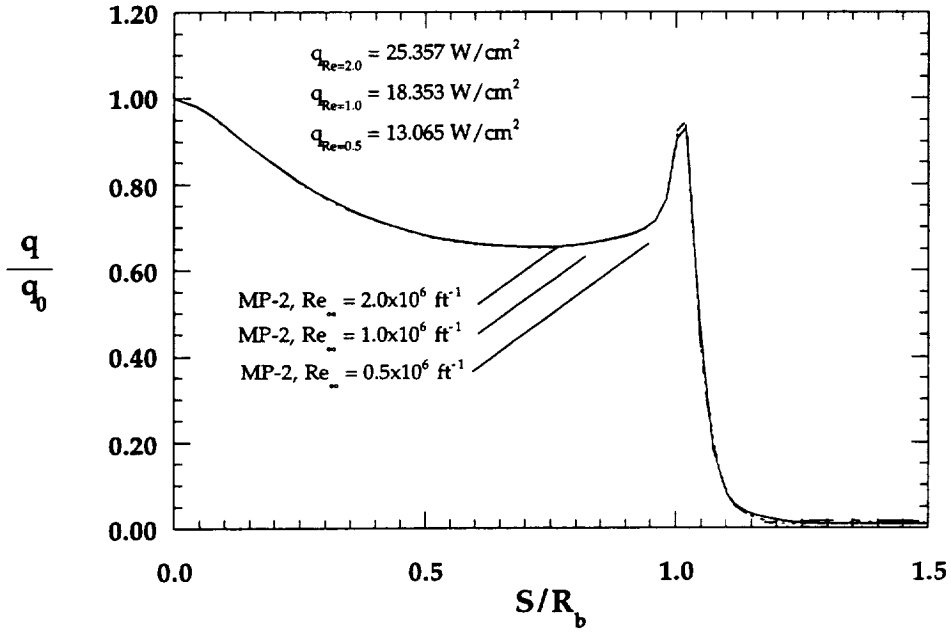

Figure 8.1.56a Reynolds Number Effects on Forebody Heating, MP-2 Configuration, 31-Inch Mach 10

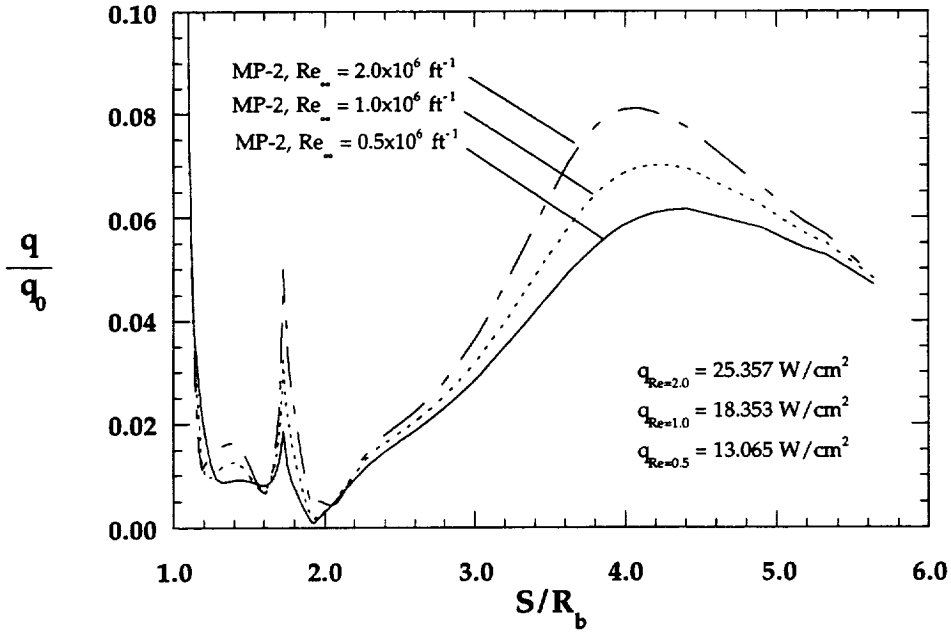

Figure 8.1.56b Reynolds Number Effects on Wake Heating, MP-2 Configuration, 31-Inch Mach 10

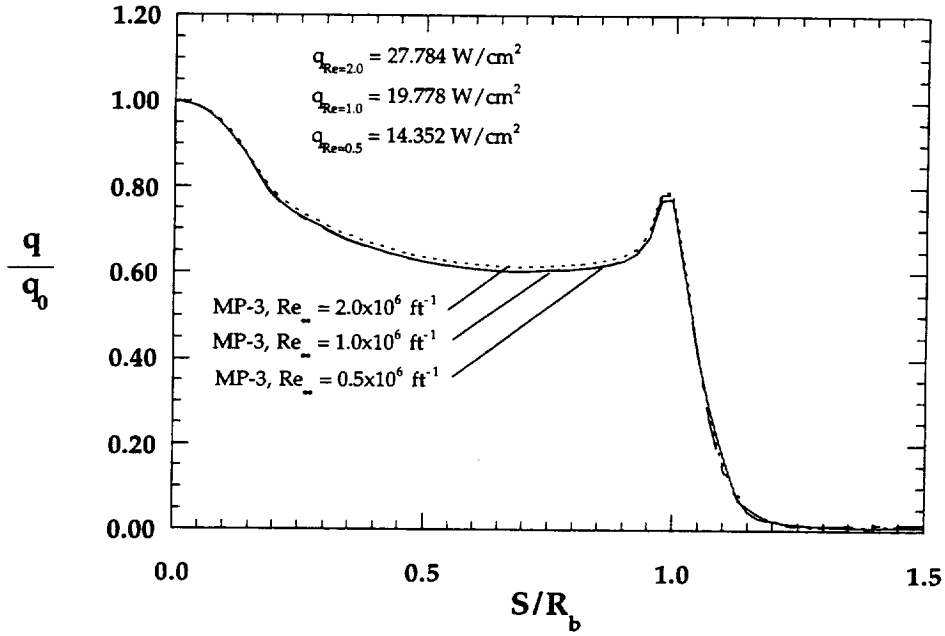

Figure 8.1.57a Reynolds Number Effects on Forebody Heating, MP-3 Configuration, 31-Inch Mach 10

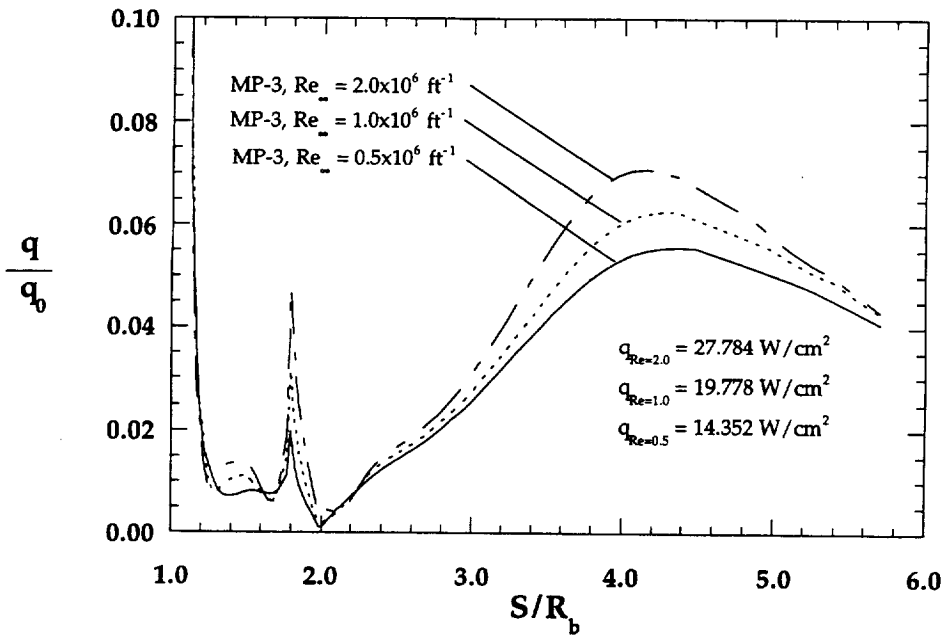

Figure 8.1.57b Reynolds Number Effects on Wake Heating, MP-3 Configuration, 31-Inch Mach 10

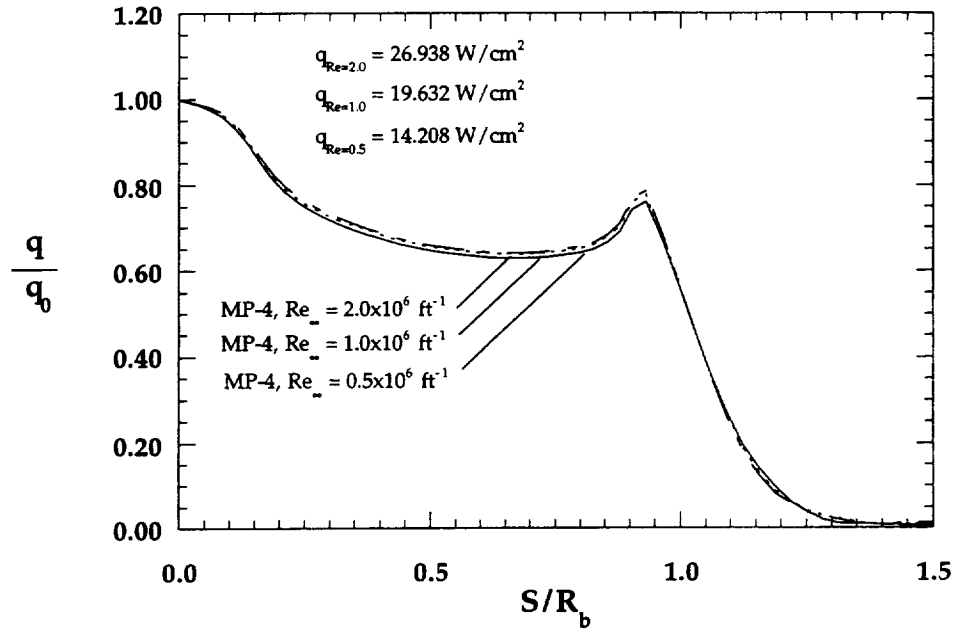

Figure 8.1.58a Reynolds Number Effects on Forebody Heating, MP-4 Configuration, 31-Inch Mach 10

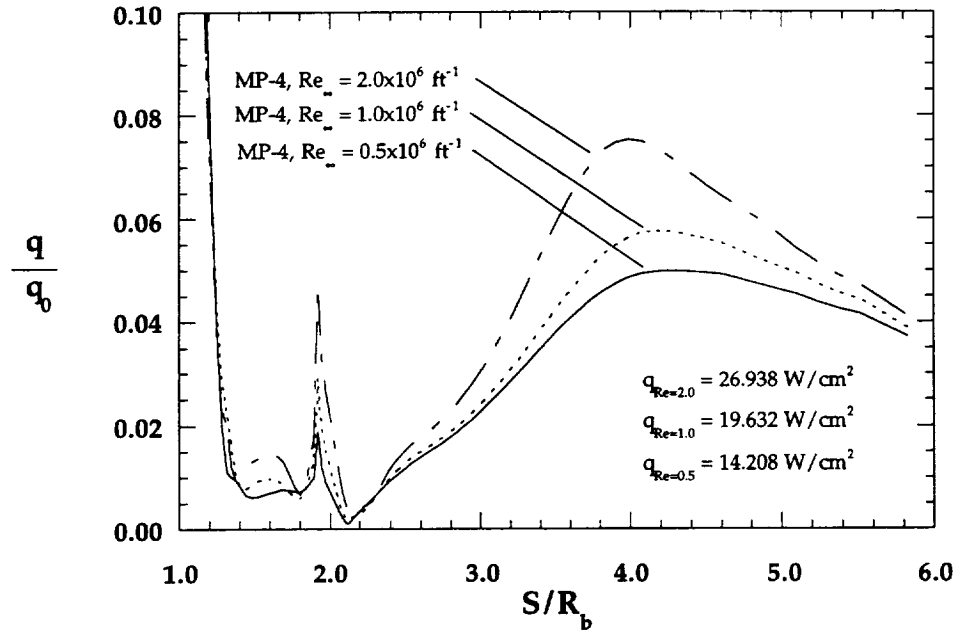

Figure 8.1.58b Reynolds Number Effects on Wake Heating, MP-4 Configuration, 31-Inch Mach 10

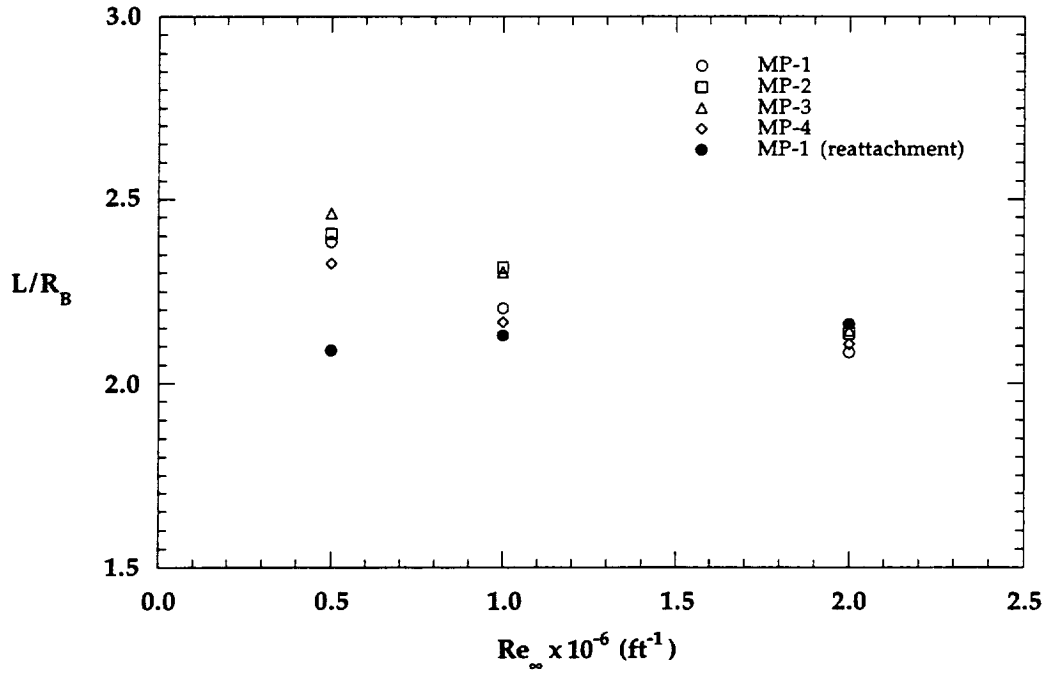

Figure 8.1.59 Reynolds Number Effects on Sting Peak Heating Location

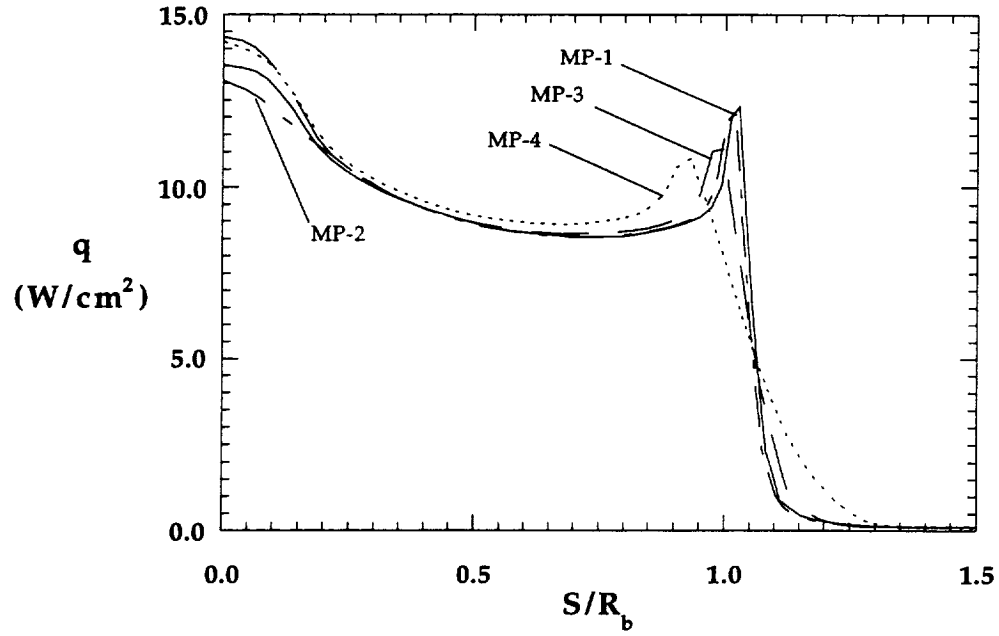

,Figure 8.1.60a Configuration Effects on Forebody Heating, 31-Inch Mach 10, $Re_\infty = 0.5x10^6$ ft^{-1}

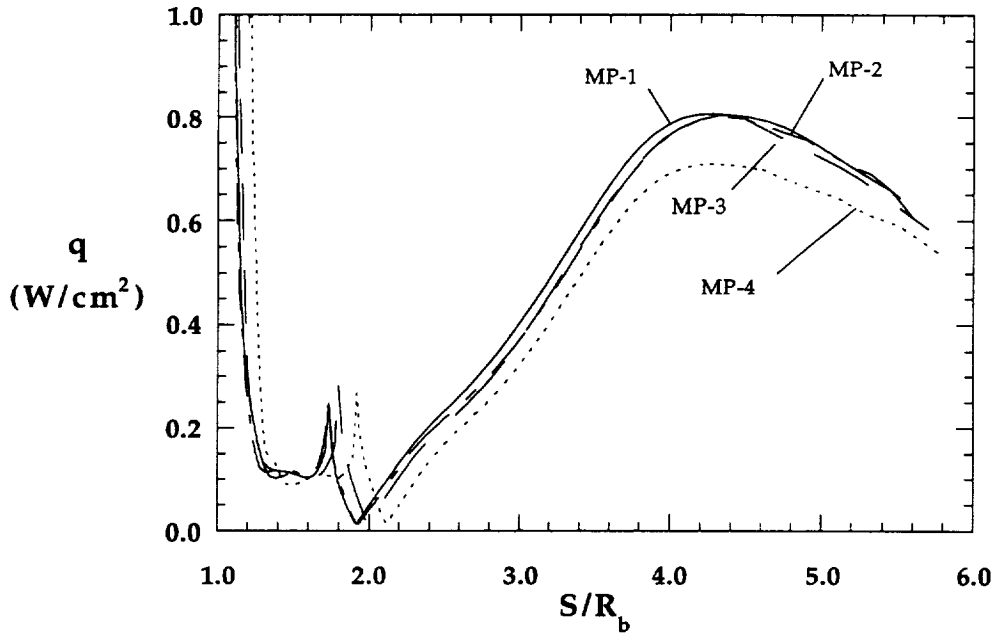

Figure 8.1.60b Configuration Effects on Wake Heating, 31-Inch Mach 10, $Re_\infty = 0.5x10^6$ ft^{-1}

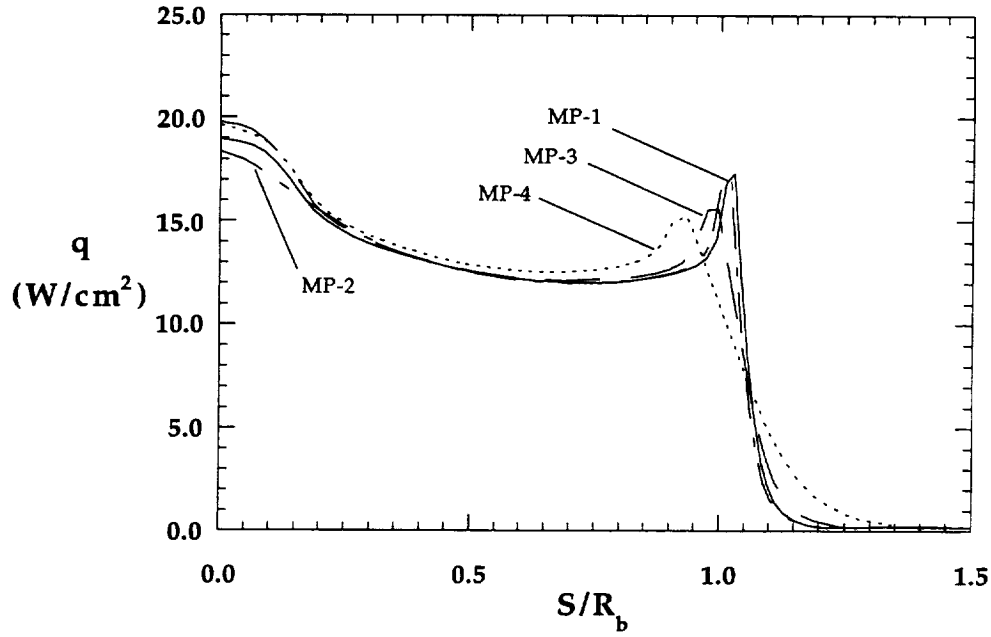

Figure 8.1.61a Configuration Effects on Forebody Heating, 31-Inch Mach 10, $Re_\infty = 1.0x10^6$ ft^{-1}

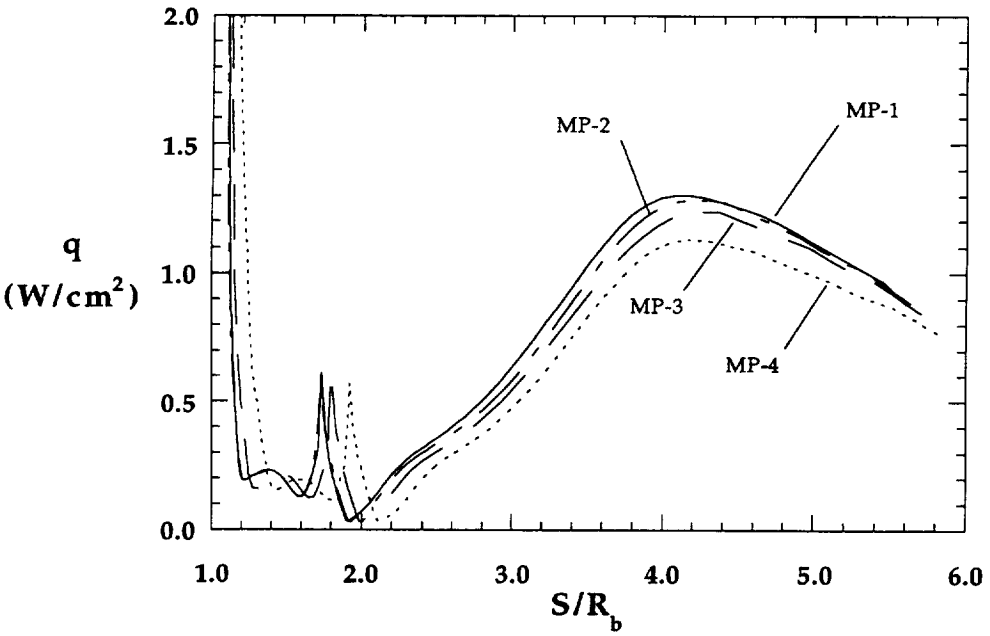

Figure 8.1.61b Configuration Effects on Wake Heating, 31-Inch Mach 10, $Re_\infty = 1.0x10^6$ ft^{-1}

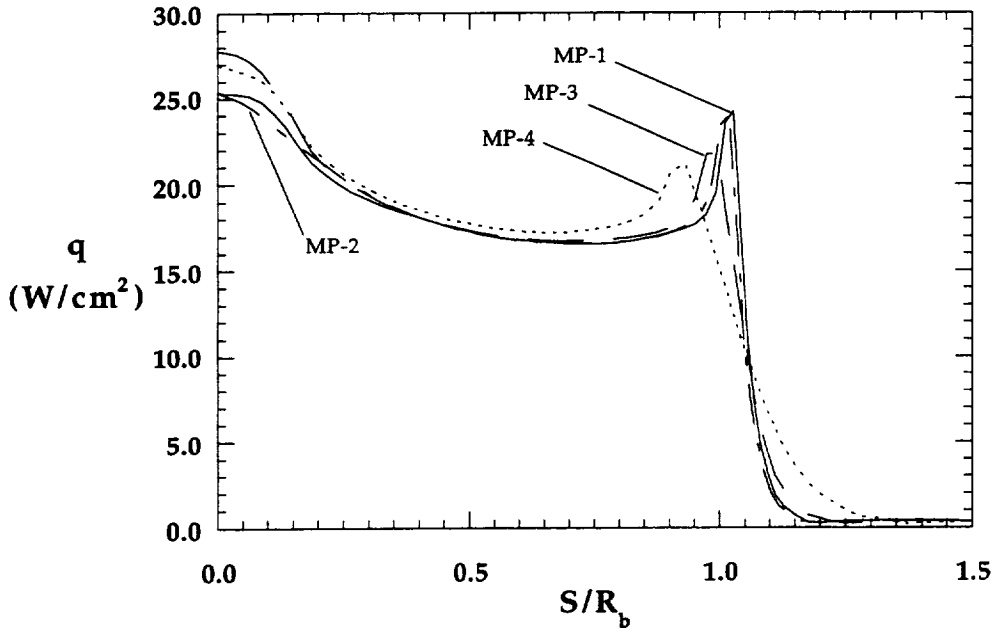

Figure 8.1.62a Configuration Effects on Forebody Heating, 31-Inch Mach 10, $Re_\infty = 2.0x10^6$ ft^{-1}

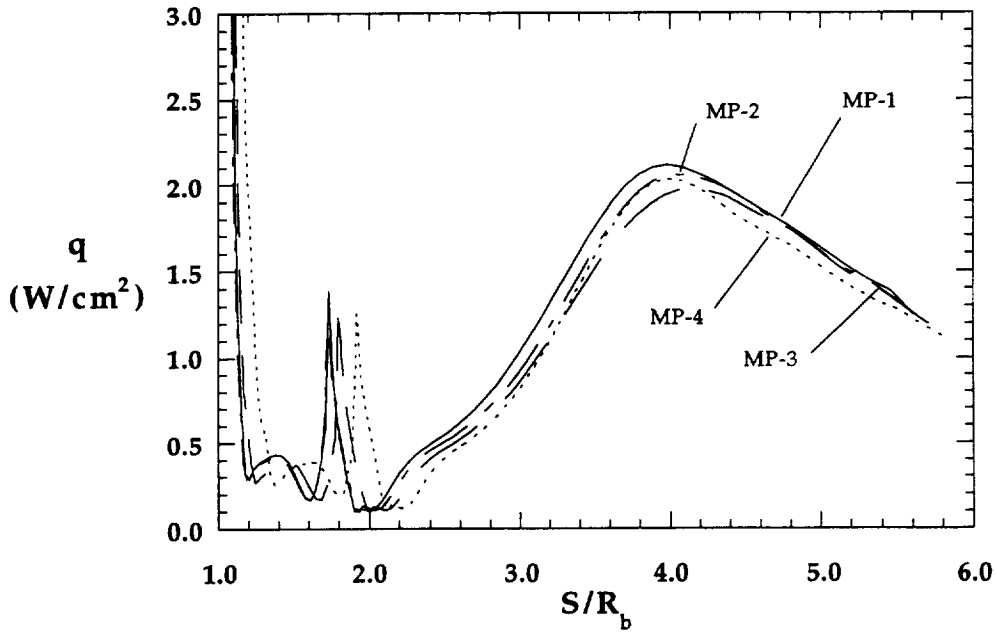

Figure 8.1.62b Configuration Effects on Wake Heating, 31-Inch Mach 10, $Re_\infty = 2.0x10^6$ ft^{-1}

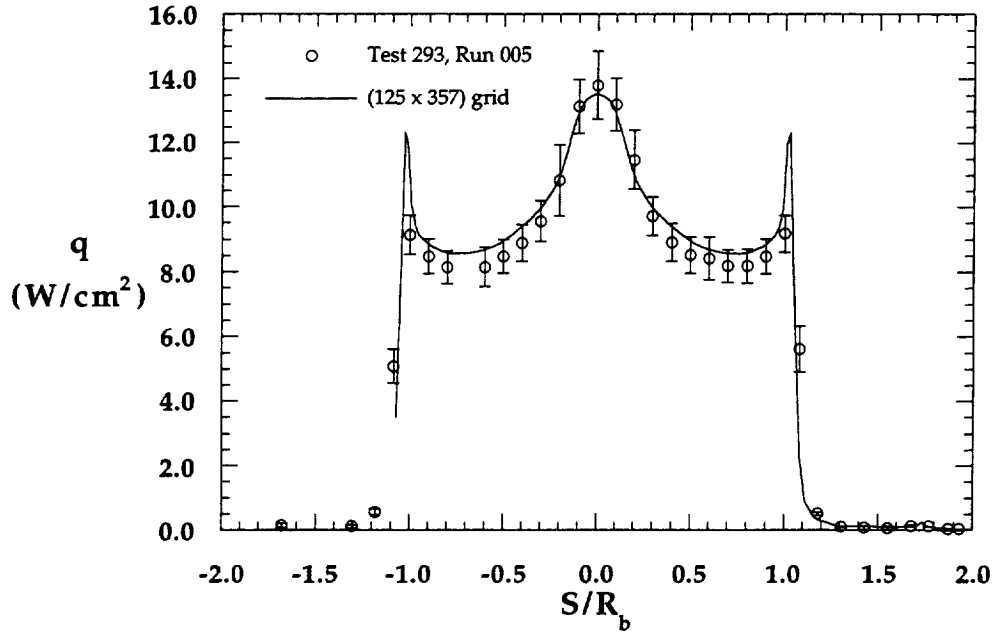

Figure 8.1.63a Comparison with Experimental Forebody Heating Distribution, MP-1 Configuration, 31-Inch Mach 10, $Re_\infty = 0.5x10^6$ ft^{-1}

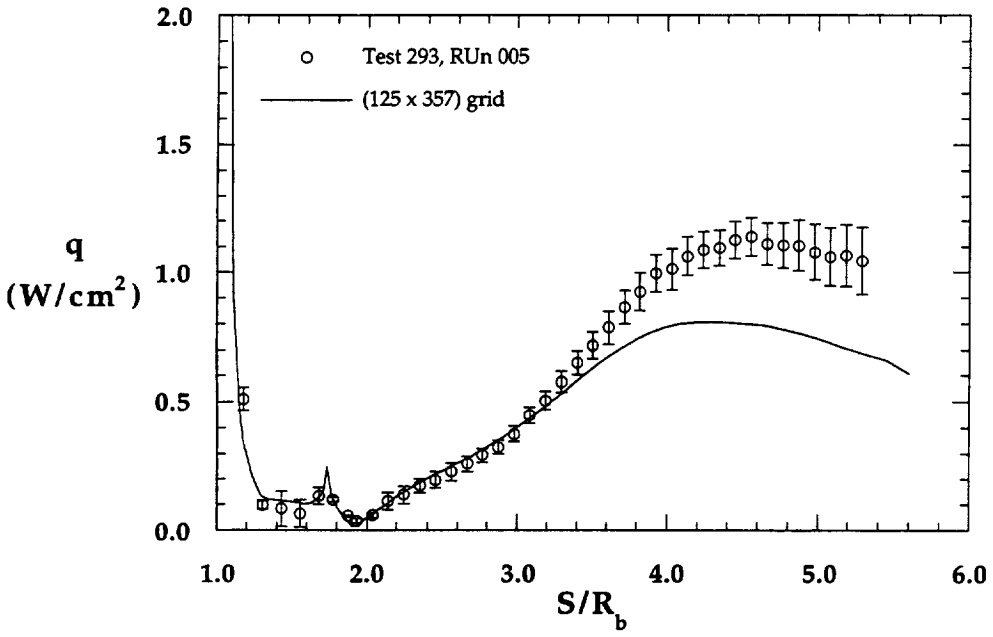

Figure 8.1.63b Comparison with Experimental Wake Heating Distribution, MP-1 Configuration, 31-Inch Mach 10, $Re_\infty = 0.5x10^6$ ft^{-1}

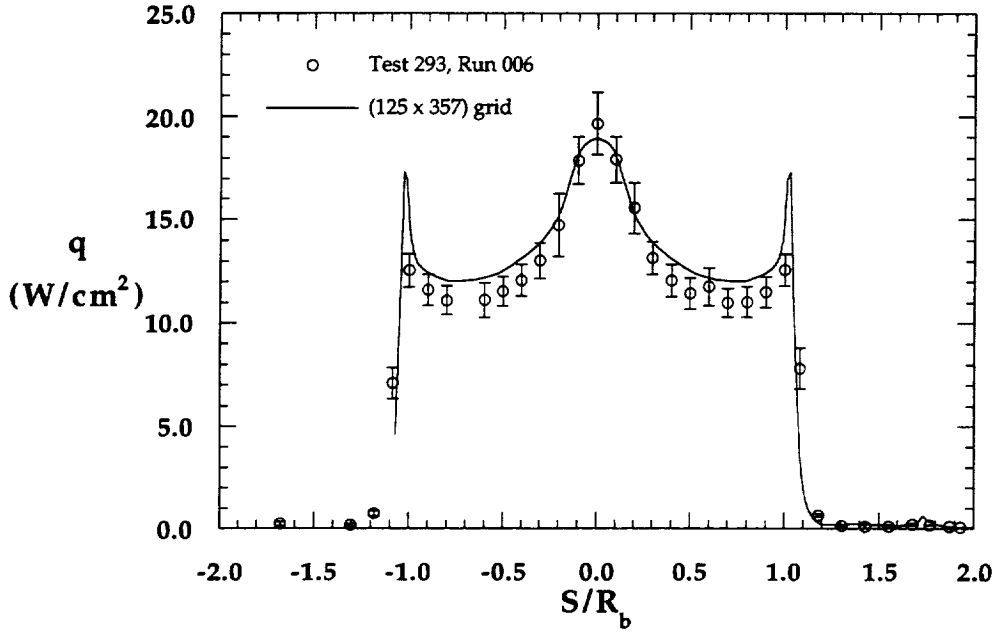

Figure 8.1.64a Comparison with Experimental Forebody Heating Distribution, MP-1 Configuration, 31-Inch Mach 10, $Re_\infty = 1.0x10^6$ ft^{-1}

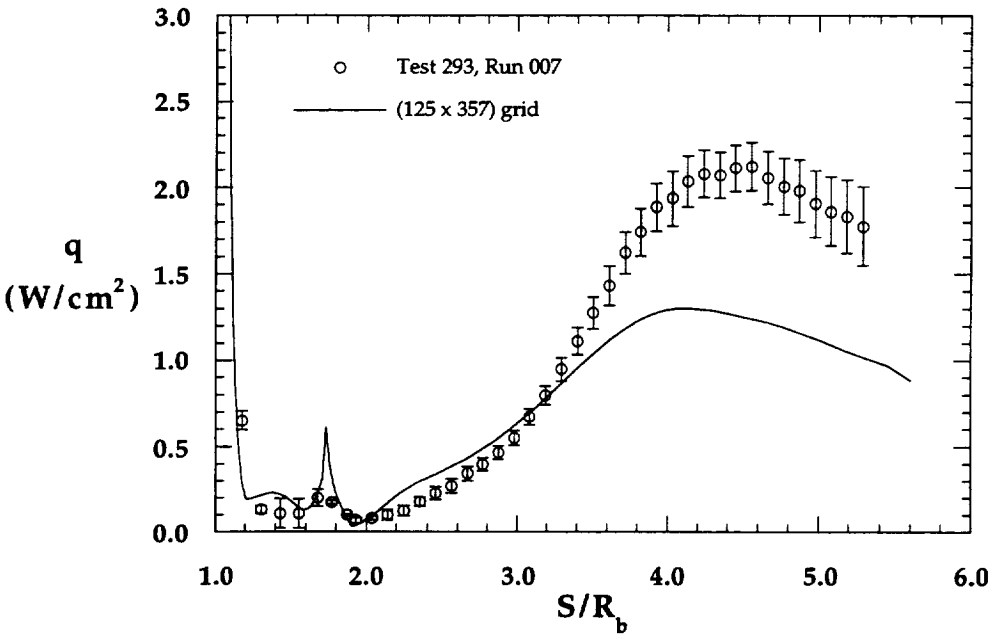

Figure 8.1.64b Comparison with Experimental Wake Heating Distribution, MP-1 Configuration, 31-Inch Mach 10, $Re_\infty = 1.0x10^6$ ft^{-1}

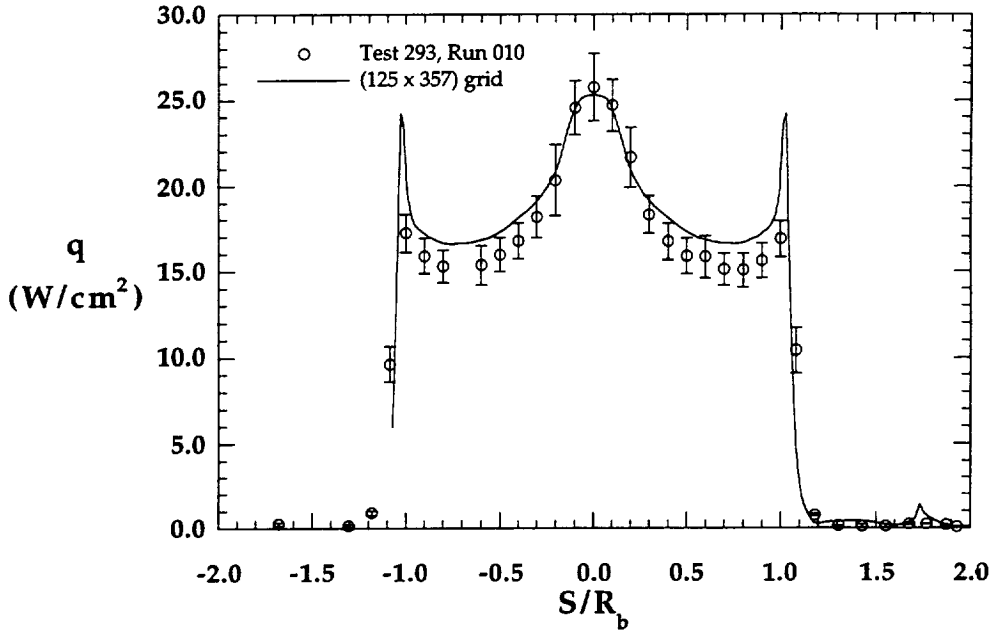

Figure 8.1.65a Comparison with Experimental Forebody Heating Distribution, MP-1 Configuration, 31-Inch Mach 10, $Re_\infty = 2.0x10^6$ ft^{-1}

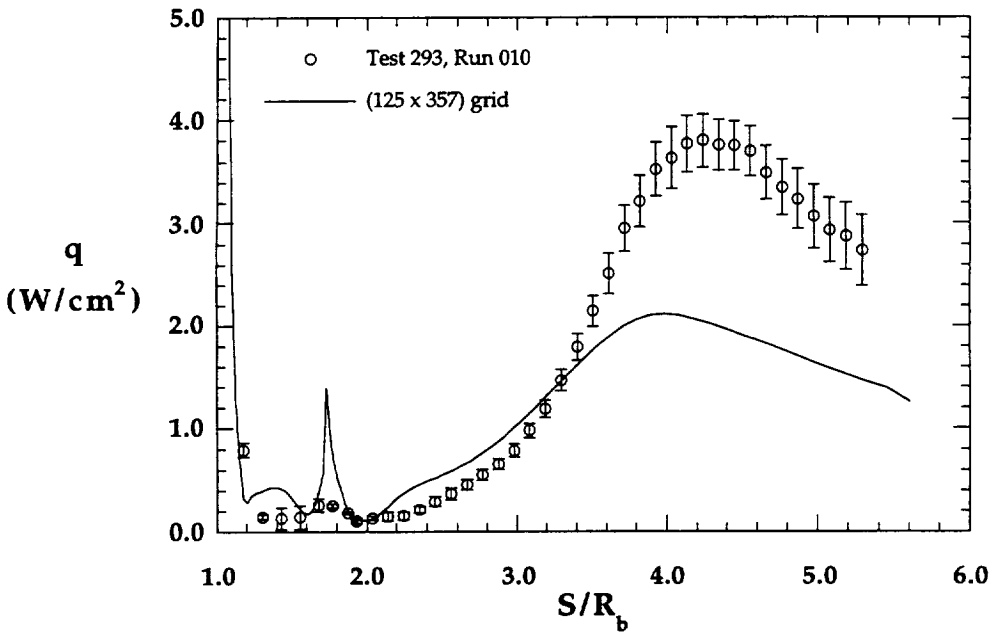

Figure 8.1.65b Comparison with Experimental Wake Heating Distribution, MP-1 Configuration, 31-Inch Mach 10, $Re_\infty = 2.0x10^6$ ft^{-1}

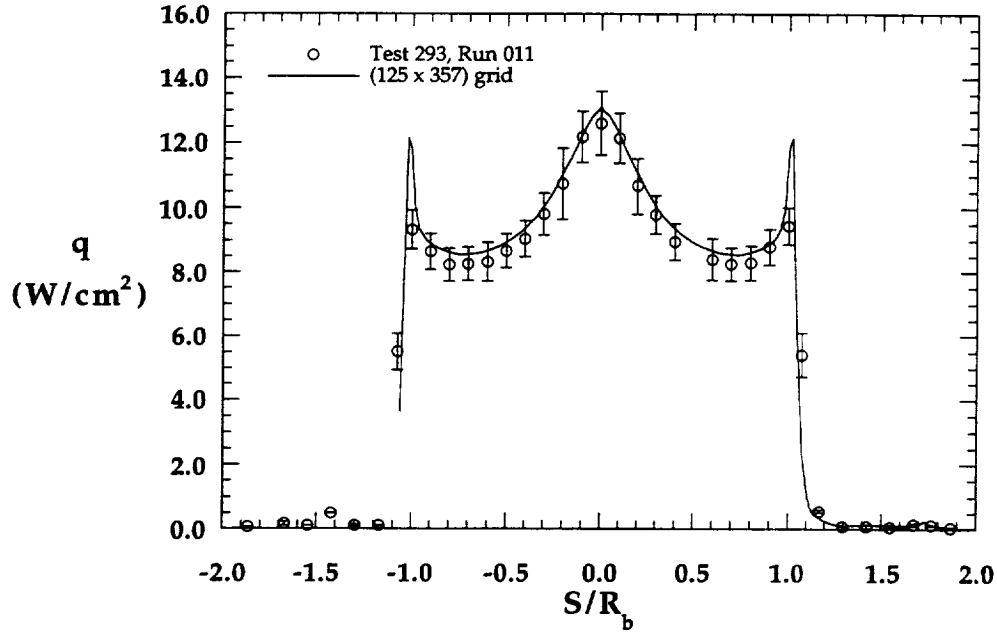

Figure 8.1.66a Comparison with Experimental Forebody Heating Distribution, MP-2 Configuration, 31-Inch Mach 10, $Re_\infty = 0.5x10^6$ ft^{-1}

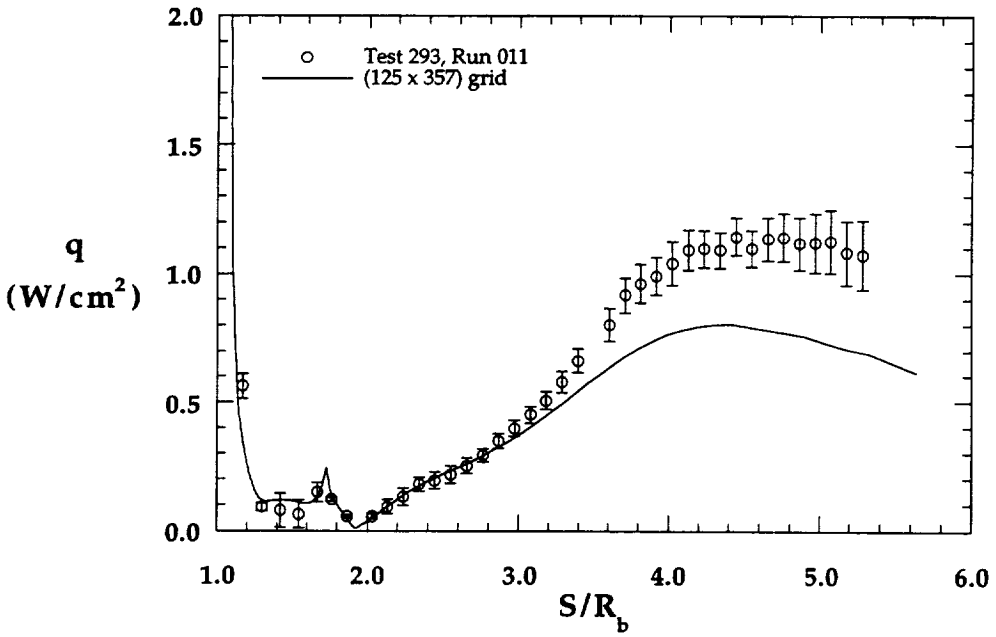

Figure 8.1.66b Comparison with Experimental Wake Heating Distribution, MP-2 Configuration, 31-Inch Mach 10, $Re_\infty = 0.5x10^6$ ft^{-1}

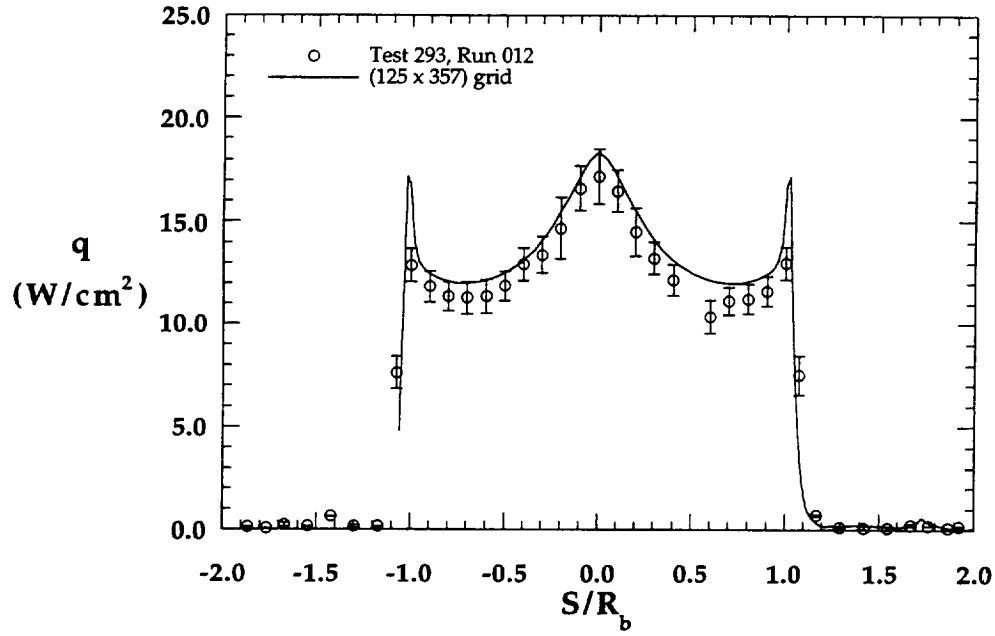

Figure 8.1.67a Comparison with Experimental Forebody Heating Distribution, MP-2 Configuration, 31-Inch Mach 10, $Re_\infty = 1.0x10^6$ ft^{-1}

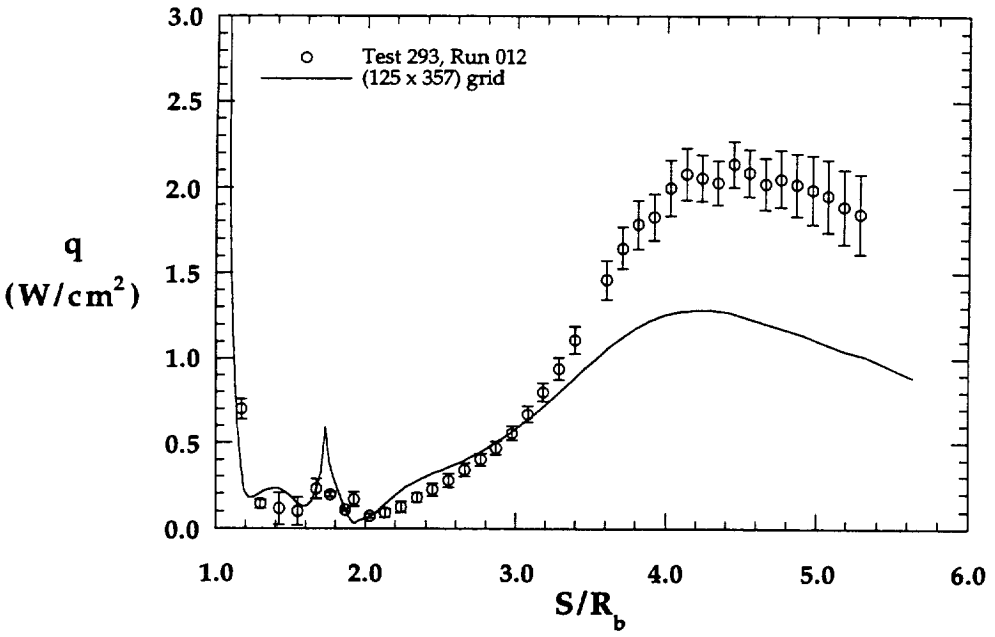

Figure 8.1.67b Comparison with Experimental Wake Heating Distribution, MP-2 Configuration, 31-Inch Mach 10, $Re_\infty = 1.0x10^6$ ft^{-1}

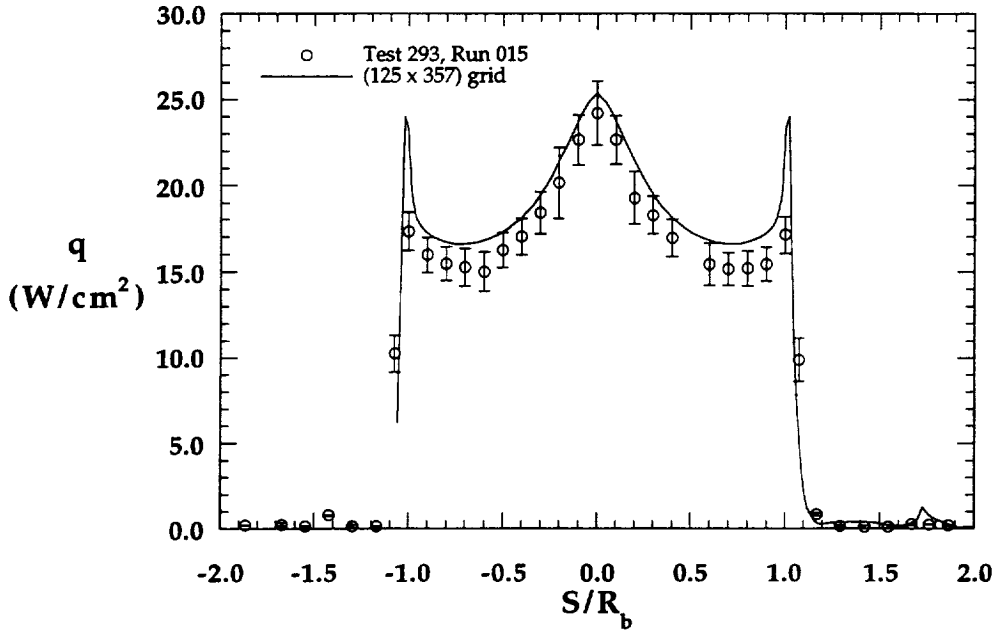

Figure 8.1.68a Comparison with Experimental Forebody Heating Distribution, MP-2 Configuration, 31-Inch Mach 10, $Re_\infty = 2.0x10^6$ ft^{-1}

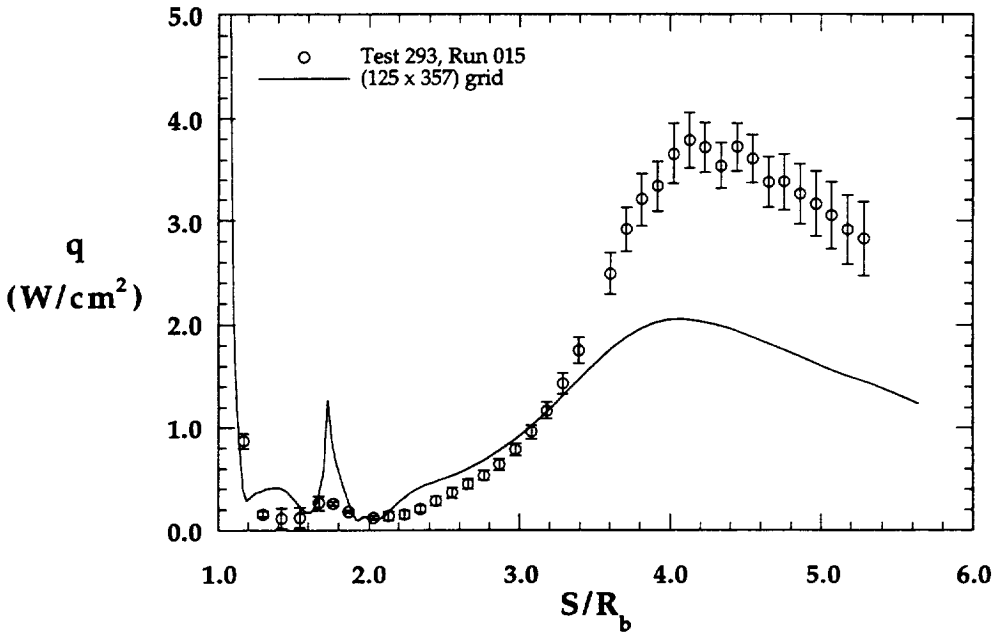

Figure 8.1.68b Comparison with Experimental Wake Heating Distribution, MP-2 Configuration, 31-Inch Mach 10, $Re_\infty = 2.0x10^6$ ft^{-1}

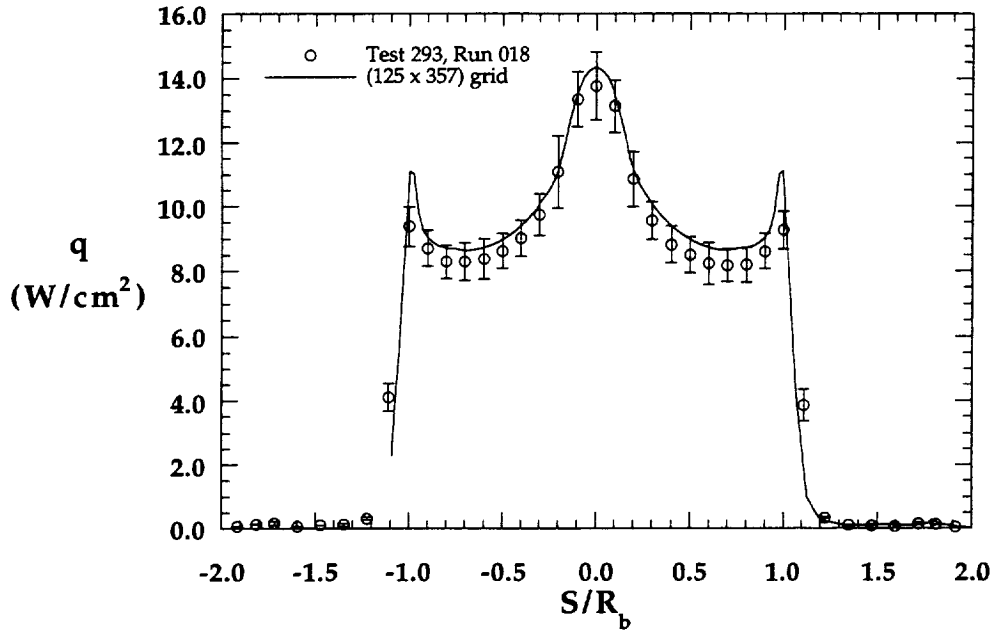

Figure 8.1.69a Comparison with Experimental Forebody Heating Distribution, MP-3 Configuration, 31-Inch Mach 10, $Re_\infty = 0.5x10^6$ ft^{-1}

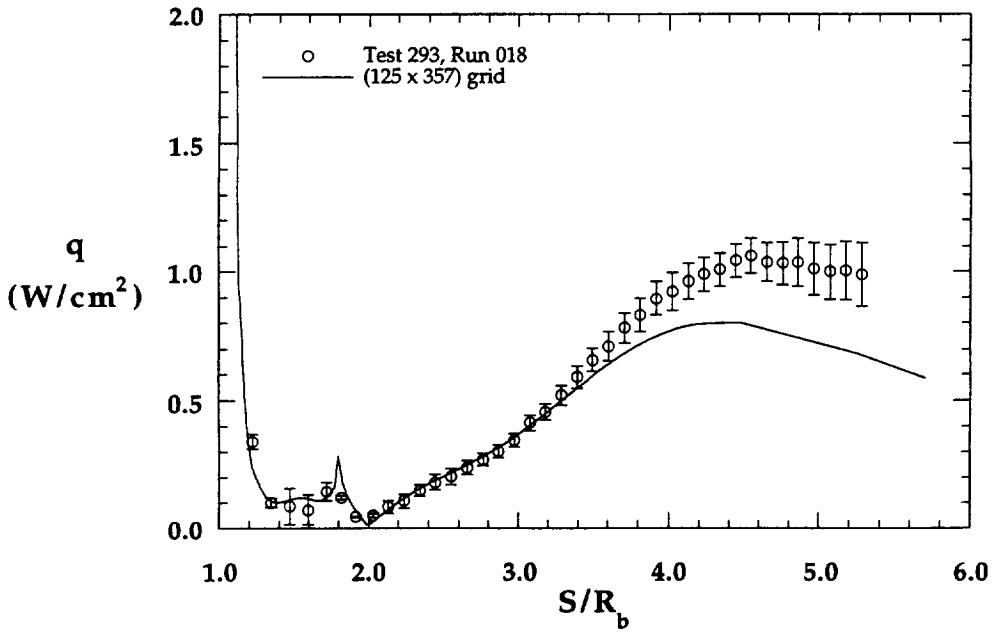

Figure 8.1.69b Comparison with Experimental Wake Heating Distribution, MP-3 Configuration, 31-Inch Mach 10, $Re_\infty = 0.5x10^6$ ft^{-1}

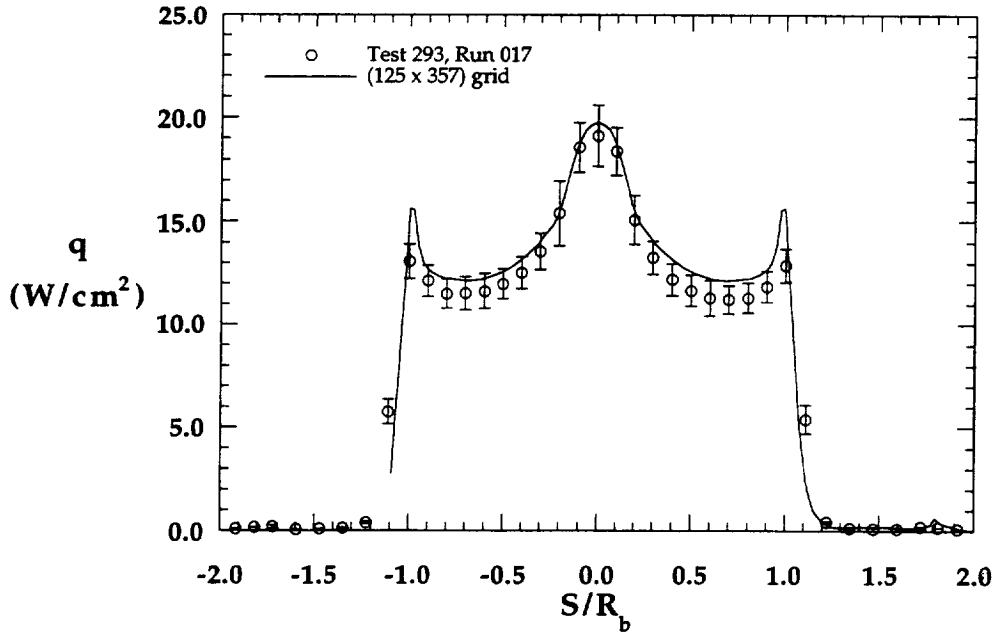

Figure 8.1.70a Comparison with Experimental Forebody Heating Distribution, MP-3 Configuration, 31-Inch Mach 10, $Re_\infty = 1.0x10^6$ ft^{-1}

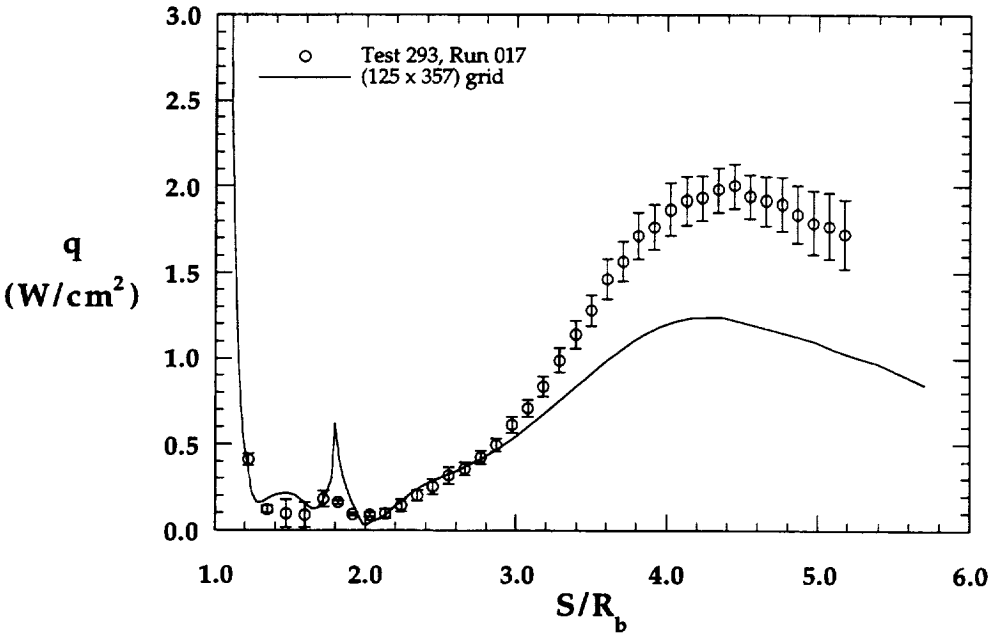

Figure 8.1.70b Comparison with Experimental Wake Heating Distribution, MP-3 Configuration, 31-Inch Mach 10, $Re_\infty = 1.0x10^6$ ft^{-1}

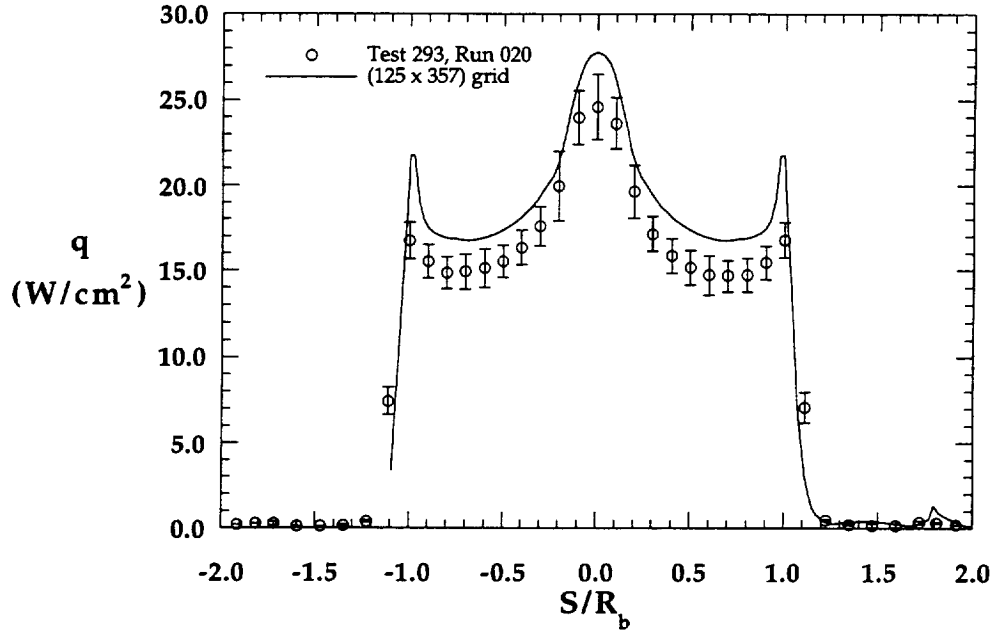

Figure 8.1.71a Comparison with Experimental Forebody Heating Distribution, MP-3 Configuration, 31-Inch Mach 10, $Re_\infty = 2.0x10^6$ ft^{-1}

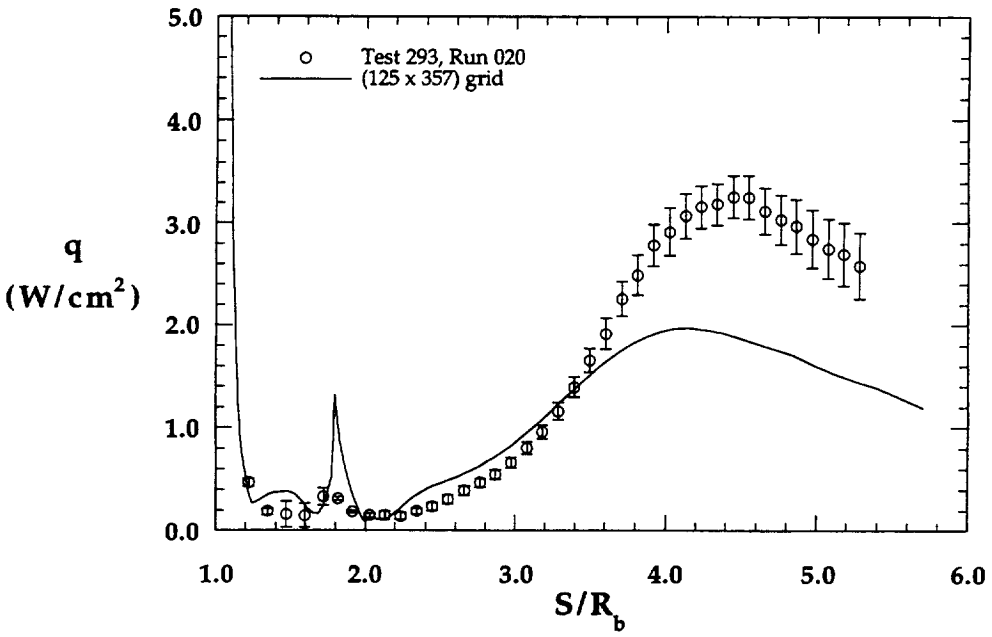

Figure 8.1.71b Comparison with Experimental Wake Heating Distribution, MP-3 Configuration, 31-Inch Mach 10, $Re_\infty = 2.0x10^6$ ft^{-1}

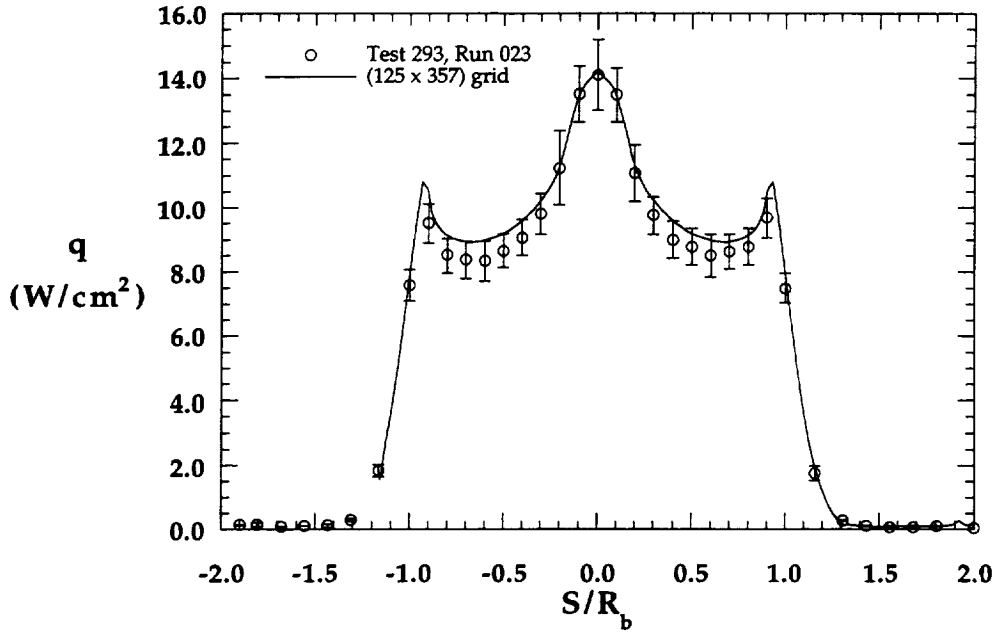

Figure 8.1.72a Comparison with Experimental Forebody Heating Distribution, MP-4 Configuration, 31-Inch Mach 10, $Re_\infty = 0.5x10^6$ ft^{-1}

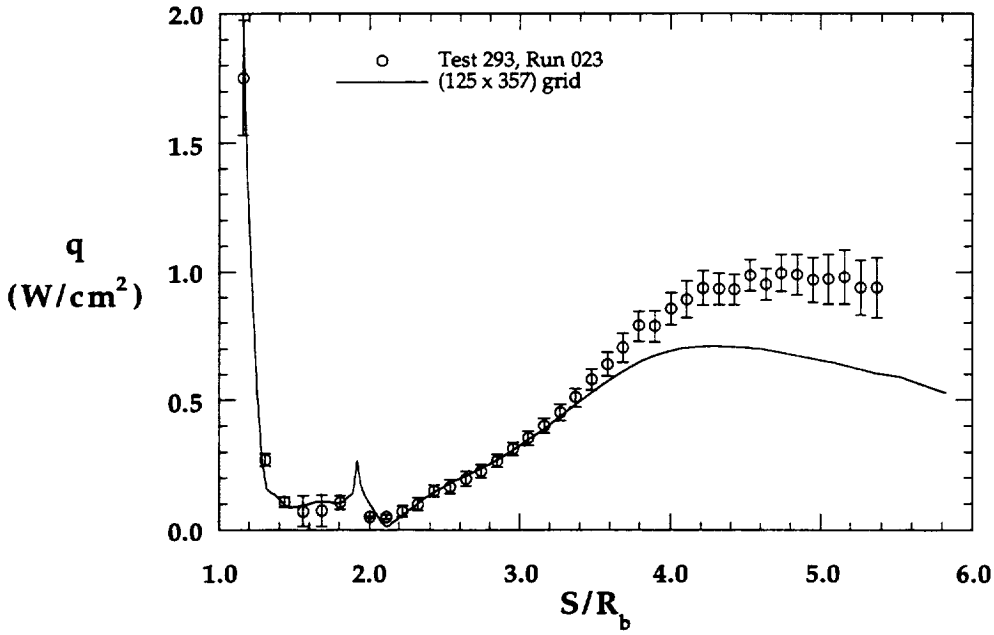

Figure 8.1.72b Comparison with Experimental Wake Heating Distribution, MP-4 Configuration, 31-Inch Mach 10, $Re_\infty = 0.5x10^6$ ft^{-1}

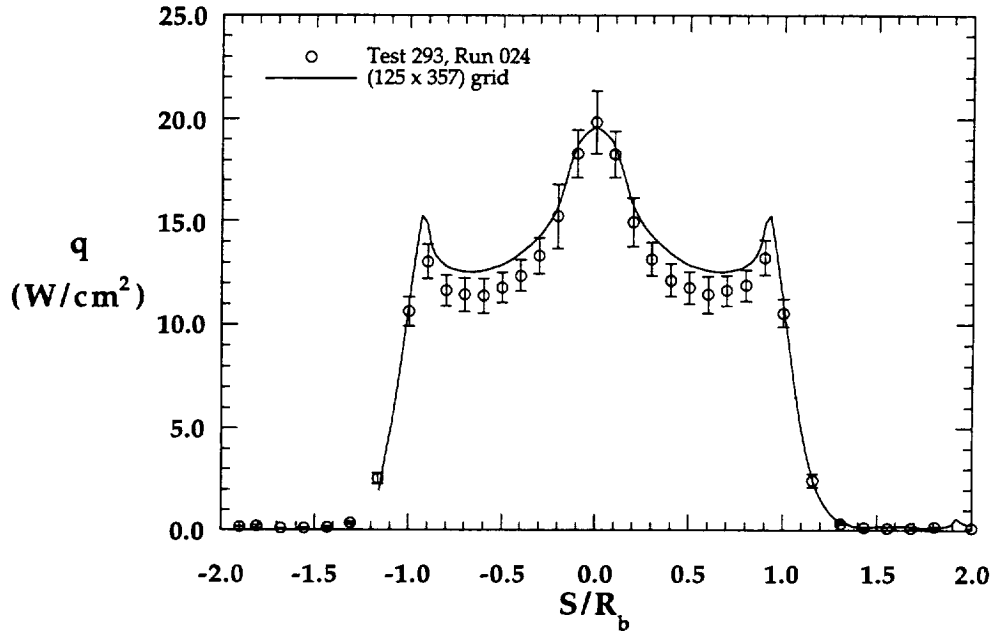

Figure 8.1.73a Comparison with Experimental Forebody Heating Distribution, MP-4 Configuration, 31-Inch Mach 10, $Re_\infty = 1.0x10^6$ ft^{-1}

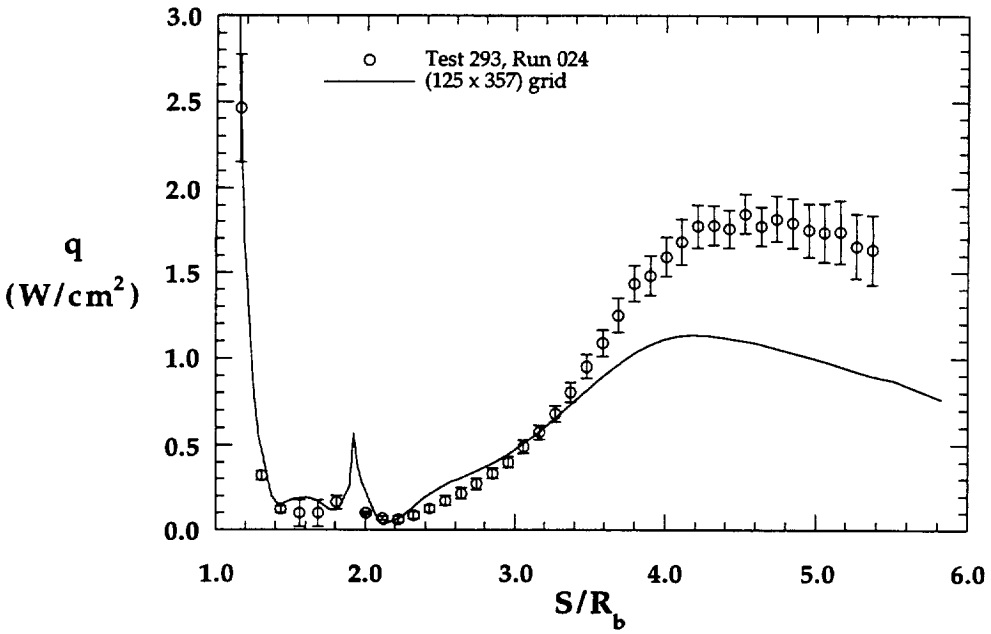

Figure 8.1.73b Comparison with Experimental Wake Heating Distribution, MP-4 Configuration, 31-Inch Mach 10, $Re_\infty = 1.0x10^6$ ft^{-1}

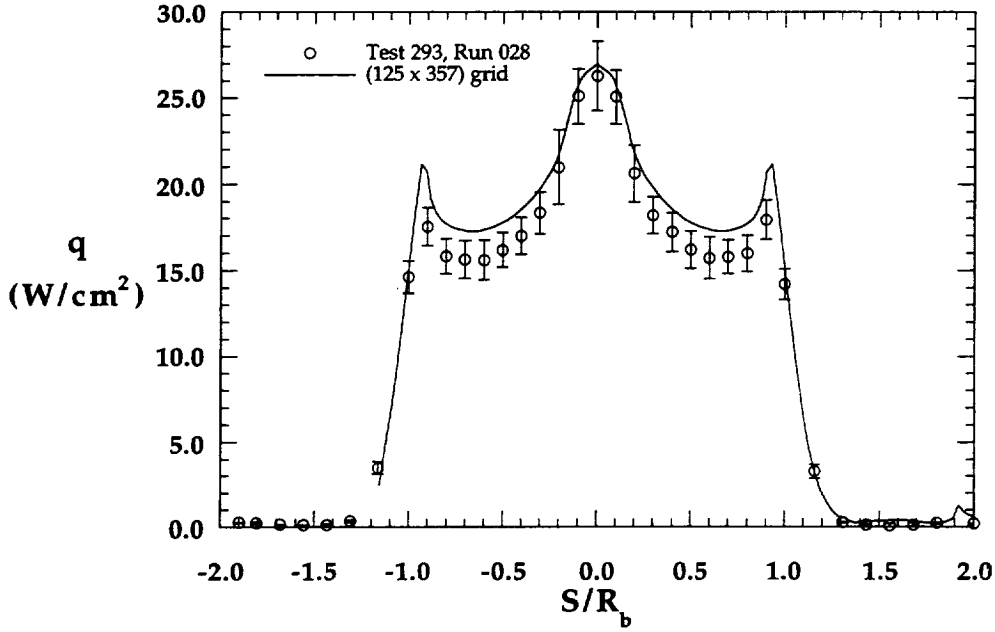

Figure 8.1.74a Comparison with Experimental Forebody Heating Distribution, MP-4 Configuration, 31-Inch Mach 10, $Re_\infty = 2.0x10^6$ ft^{-1}

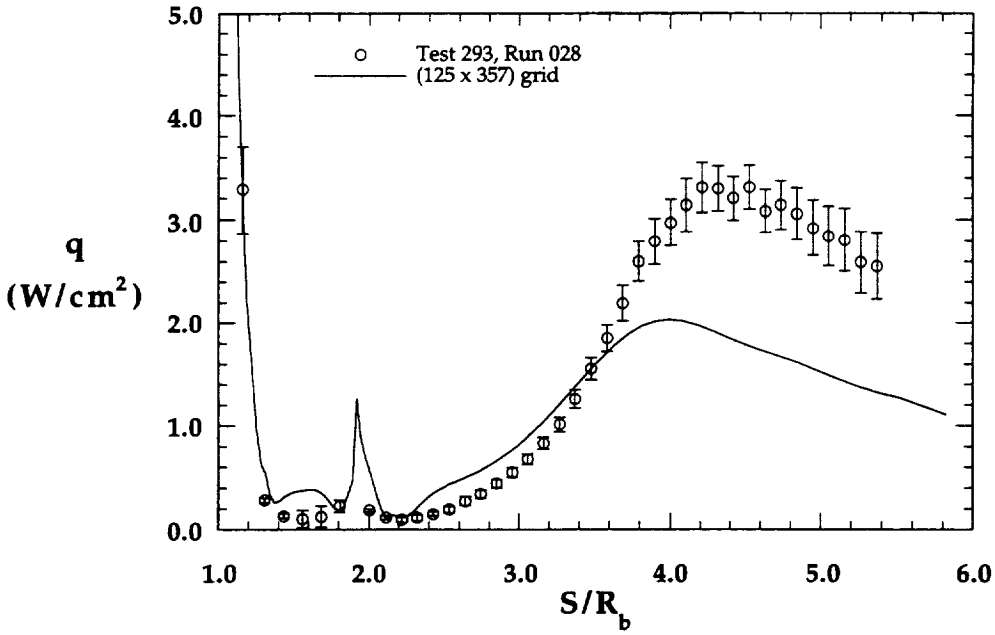

Figure 8.1.74b Comparison with Experimental Wake Heating Distribution, MP-4 Configuration, 31-Inch Mach 10, $Re_\infty = 2.0x10^6$ ft^{-1}

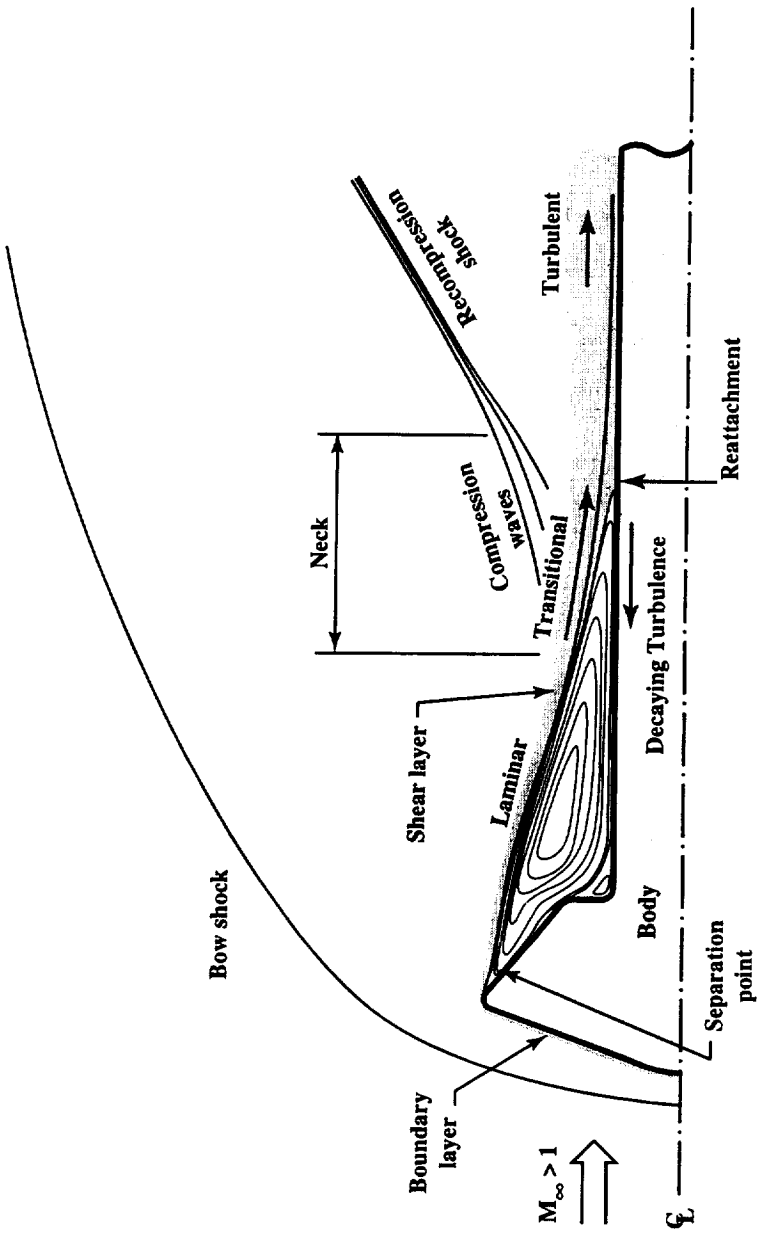

Figure 8.1.75 Transition to Turbulence in Wake

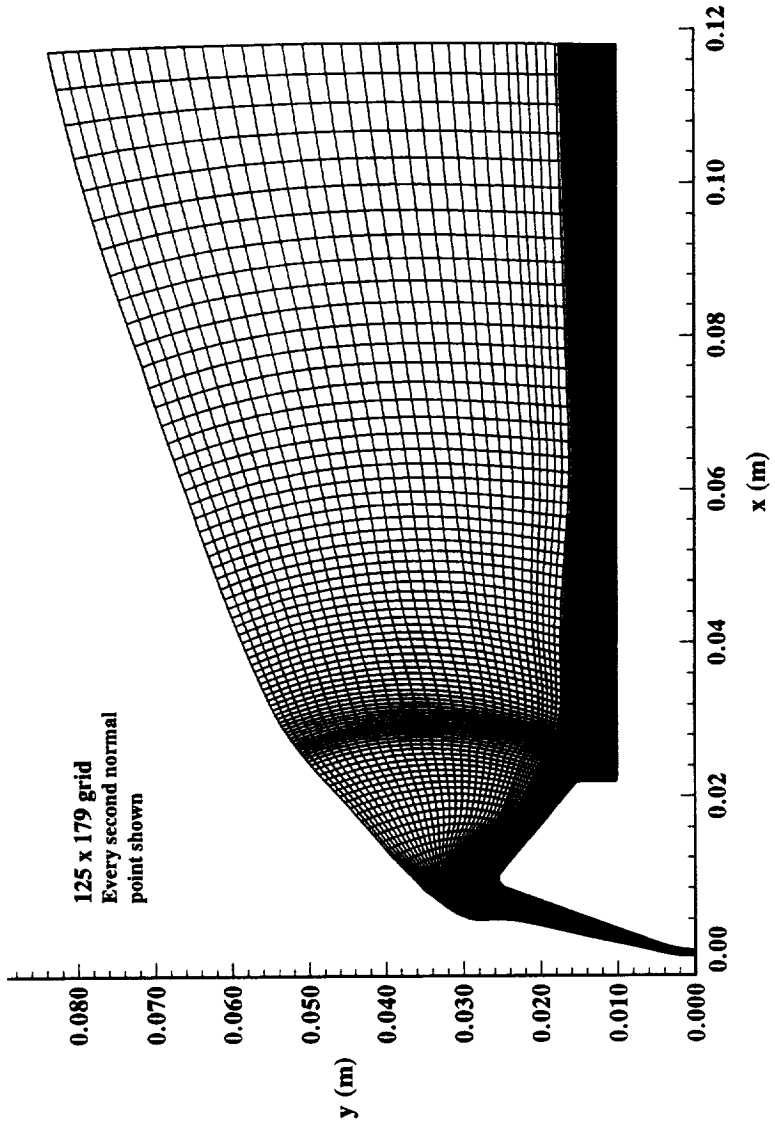

Figure 8.2.1 Computational Grid, MP-1 Configuration
HYPULSE, CO_2

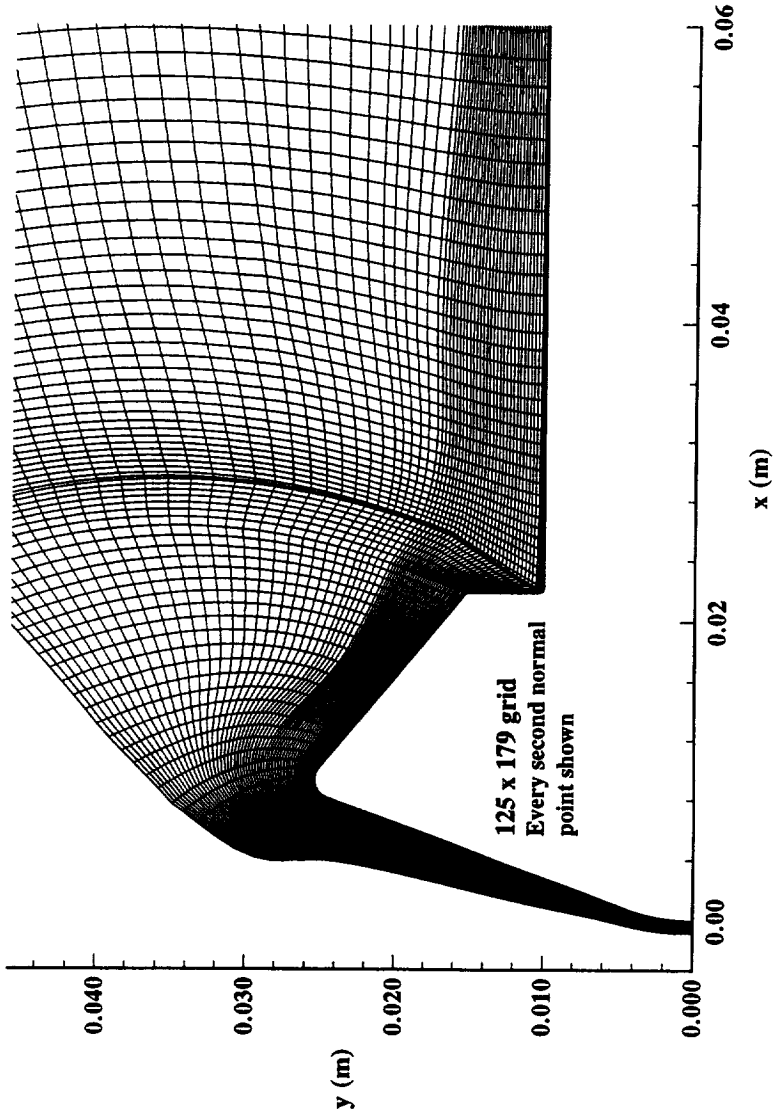

Figure 8.2.2 Computational Grid, MP-1 Configuration, Forebody and Near Wake Details, HYPULSE, CO_2

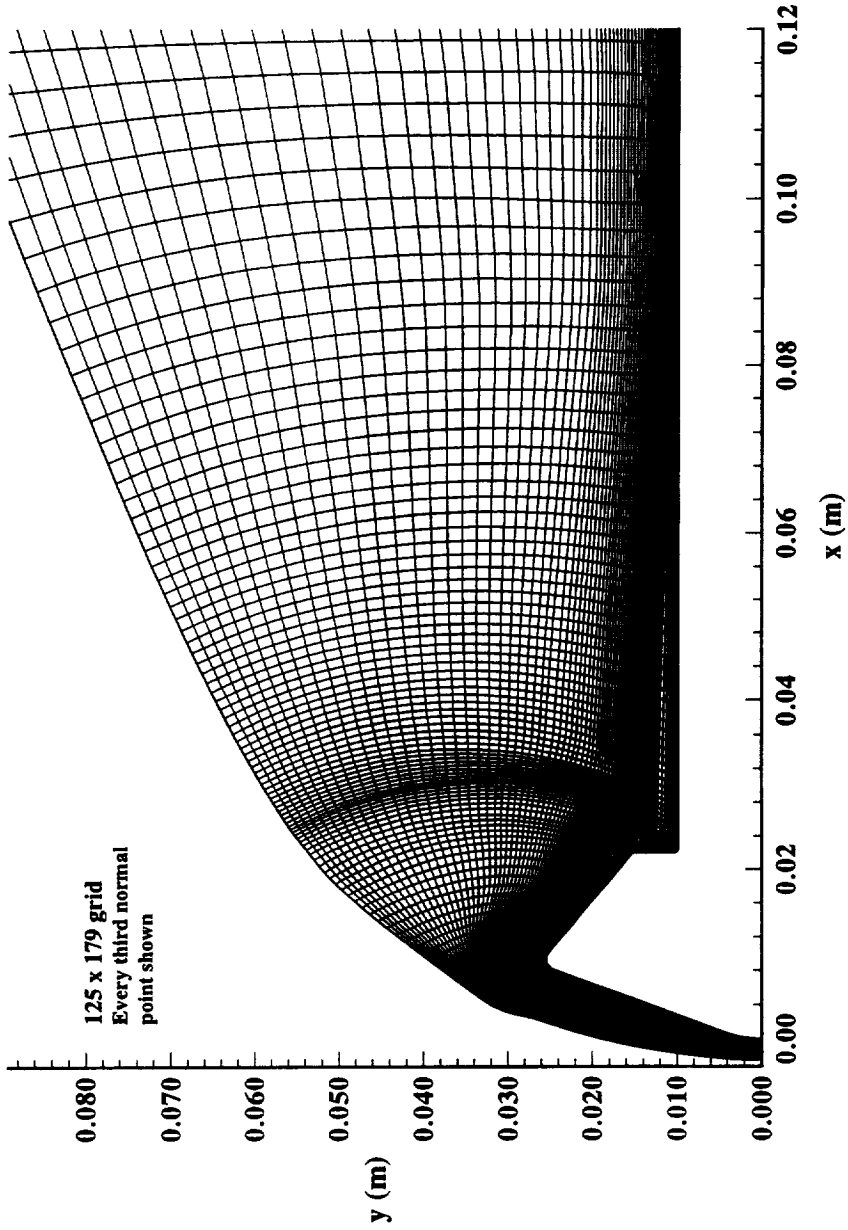

Figure 8.2.3 Computational Grid, MP-1 Configuration
HYPULSE, Air

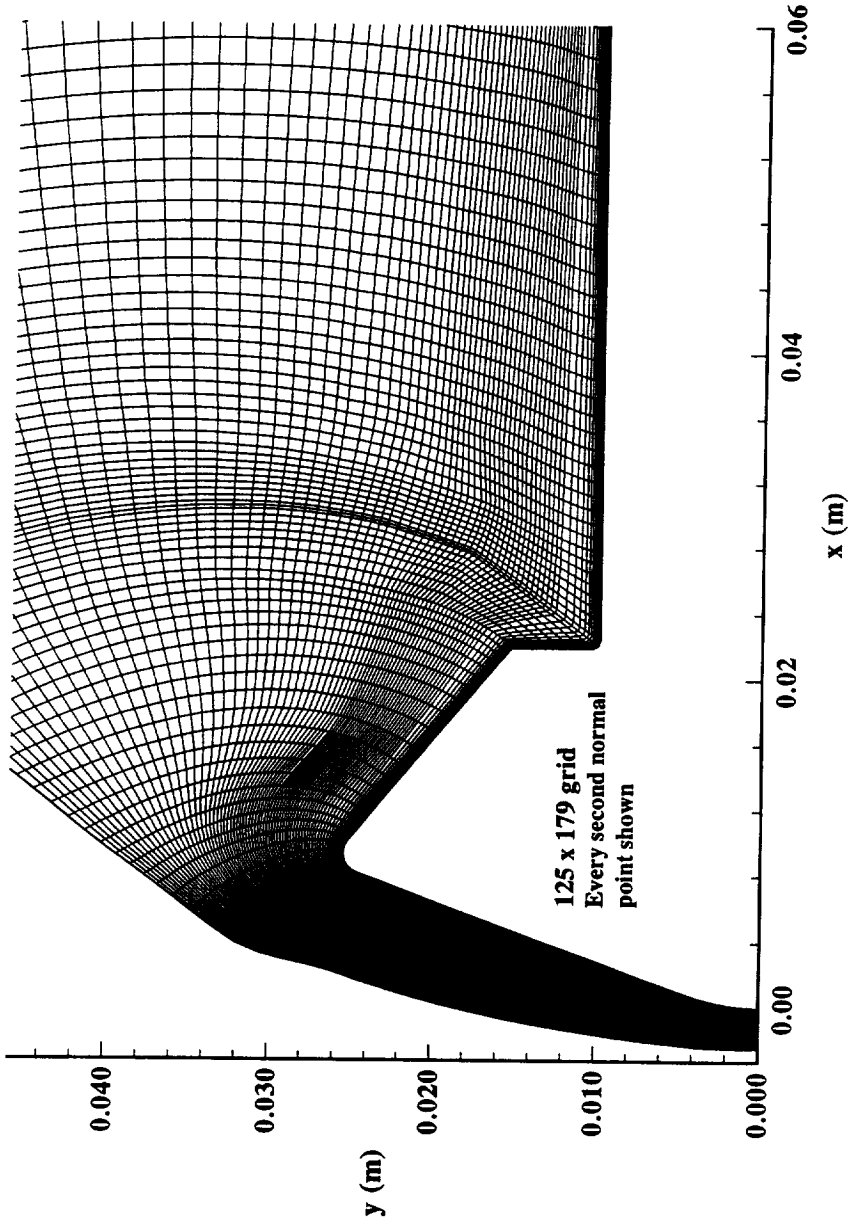

Figure 8.2.4 Computational Grid, MP-1 Configuration, Forebody and Near Wake Details, HYPULSE, Air

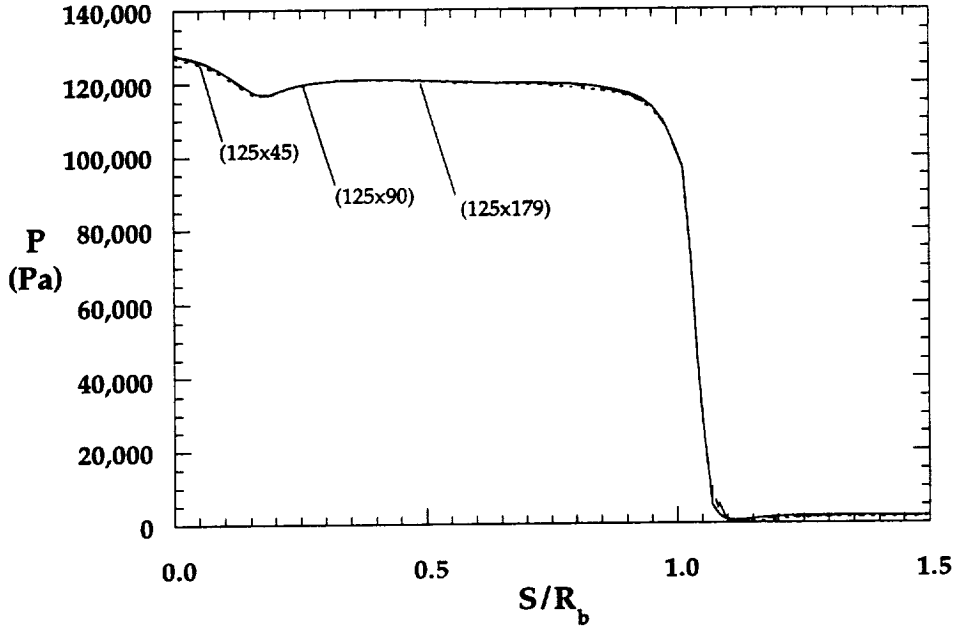

Figure 8.2.5a Grid Resolution Effects on Forebody Pressure, MP-1 Configuration, HYPULSE, CO_2

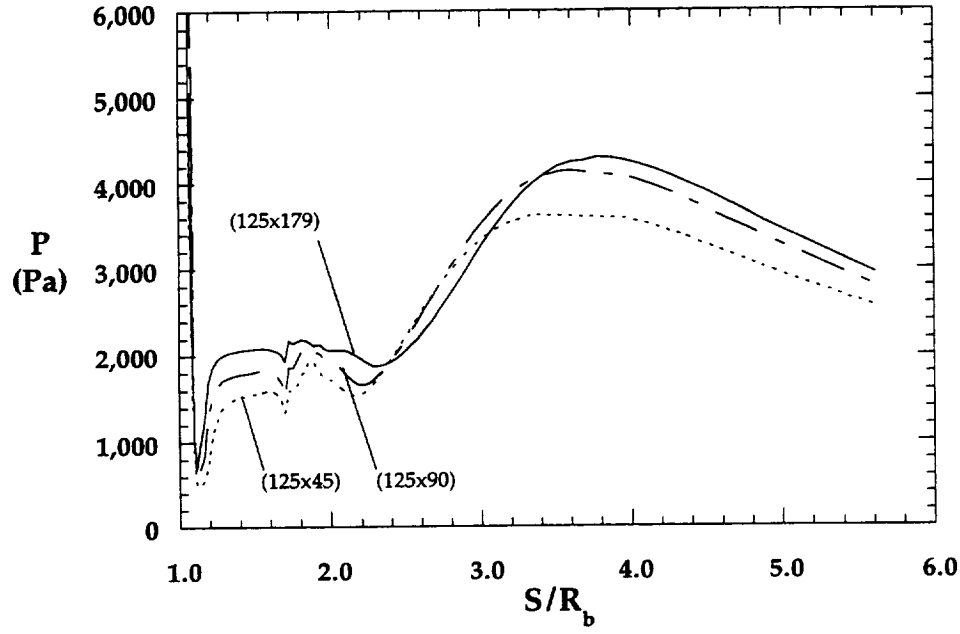

Figure 8.2.5b Grid Resolution Effects on Wake Pressure, MP-1 Configuration, HYPULSE, CO_2

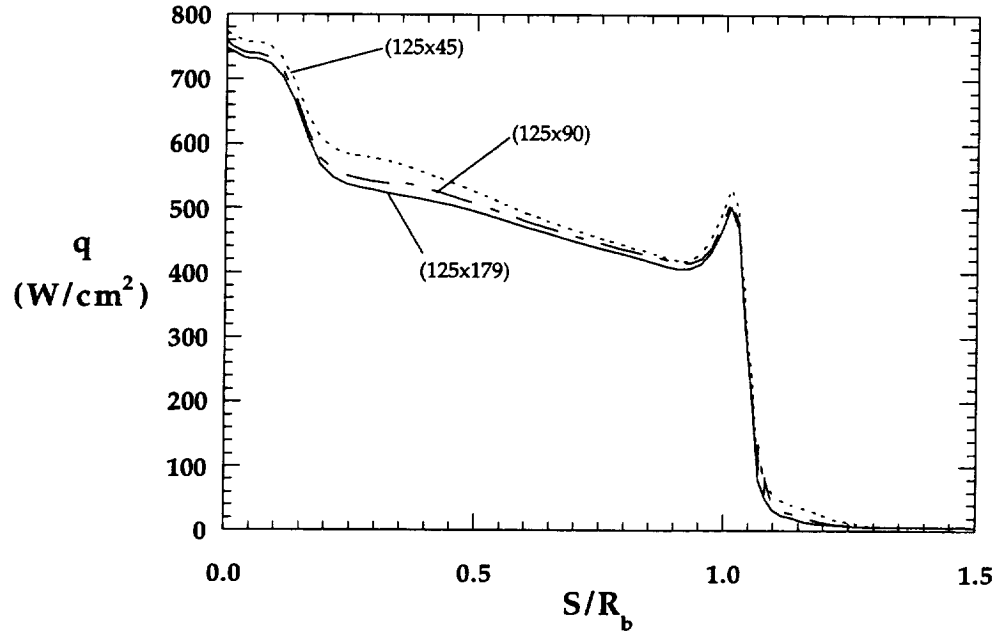

Figure 8.2.6a Grid Resolution Effects on Forebody Heating, MP-1 Configuration, HYPULSE, CO_2

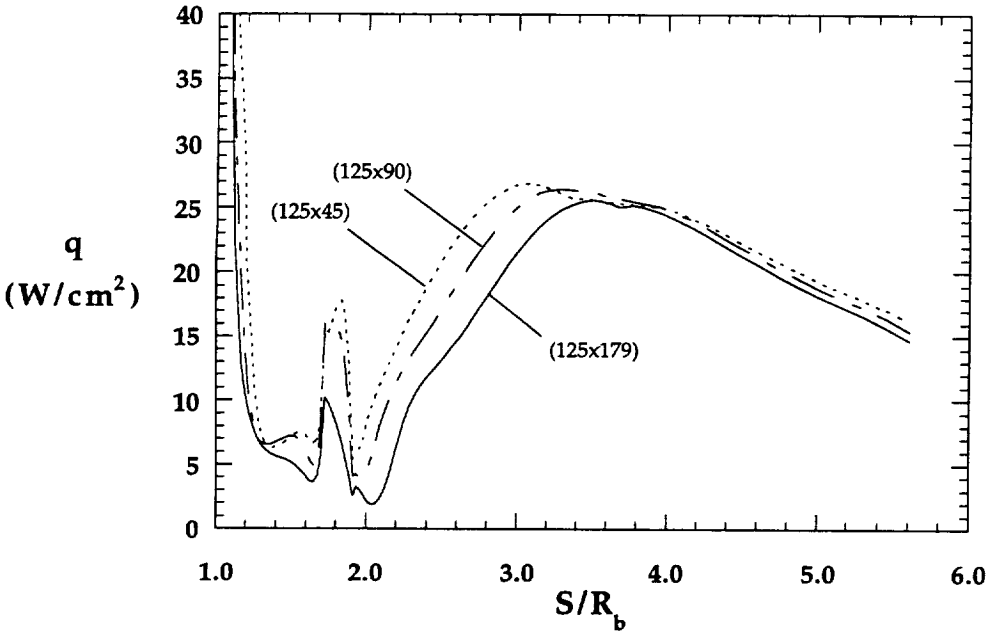

Figure 8.2.6b Grid Resolution Effects on Wake Heating, MP-1 Configuration, HYPULSE, CO_2

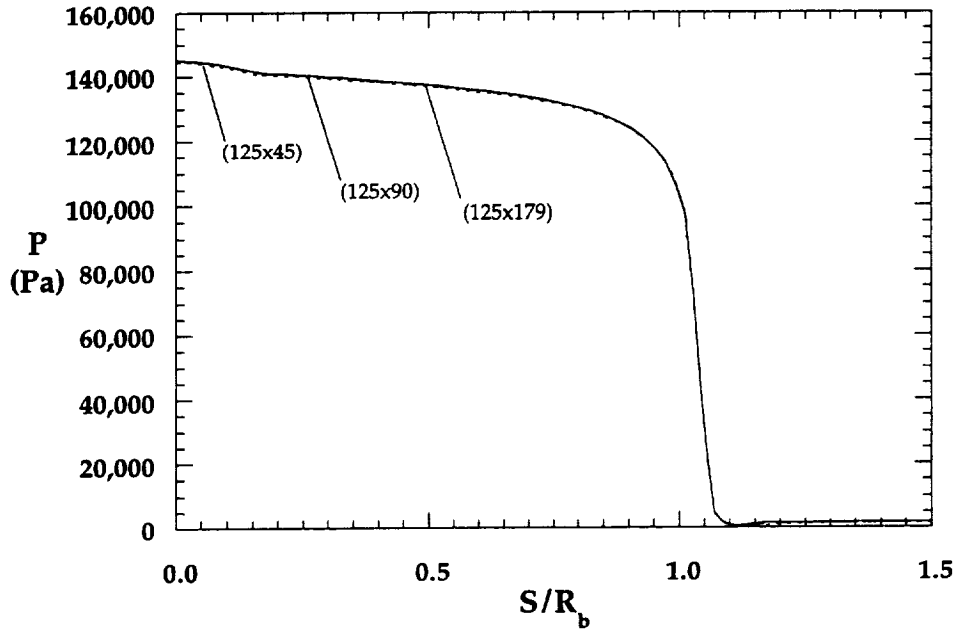

Figure 8.2.7a Grid Resolution Effects on Forebody Pressure, MP-1 Configuration, HYPULSE, Air

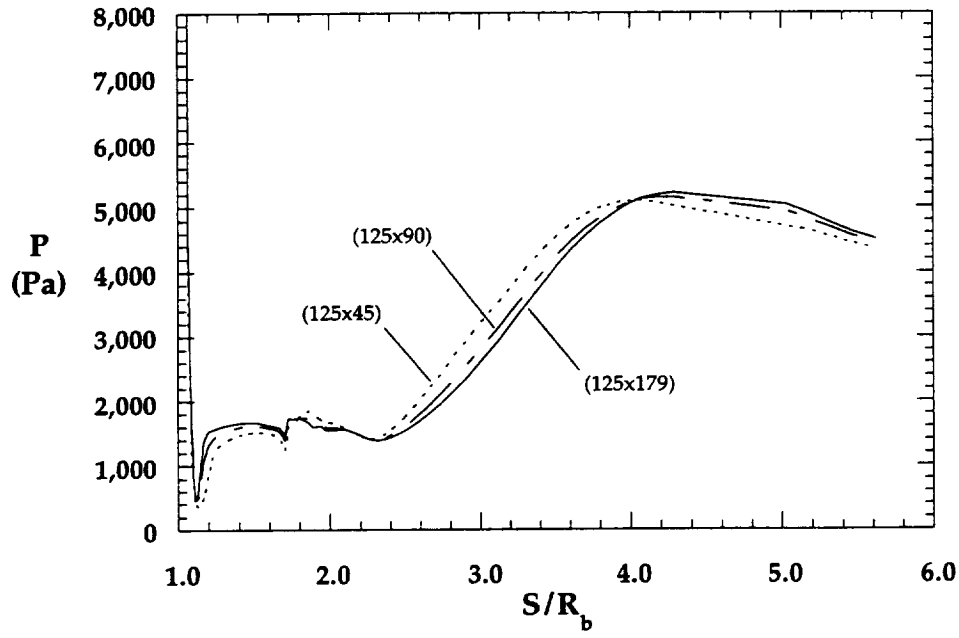

Figure 8.2.7b Grid Resolution Effects on Wake Pressure, MP-1 Configuration, HYPULSE, Air

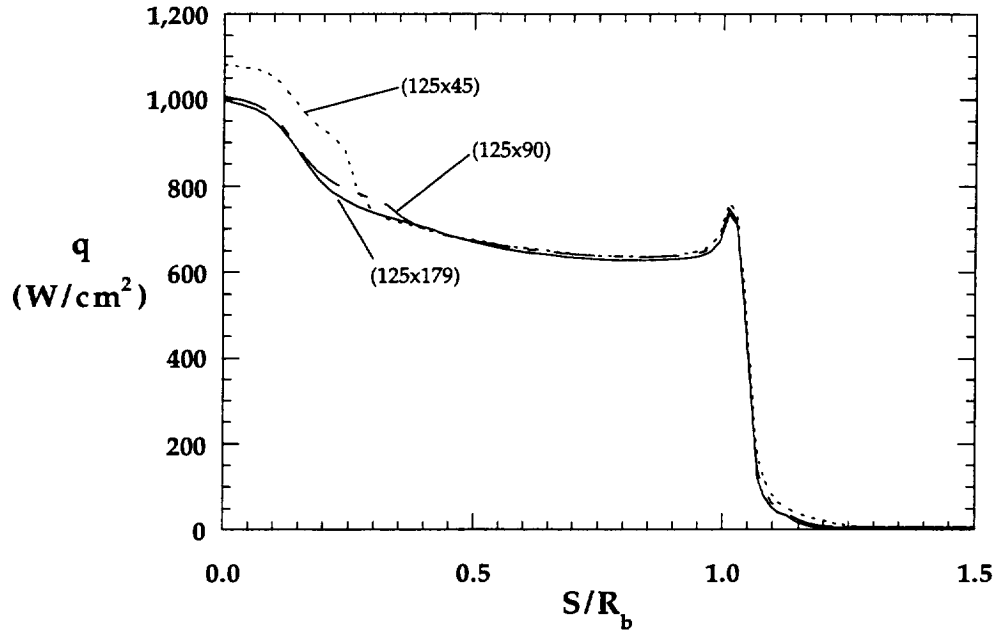

Figure 8.2.8a Grid Resolution Effects on Forebody Heating, MP-1 Configuration, HYPULSE, Air

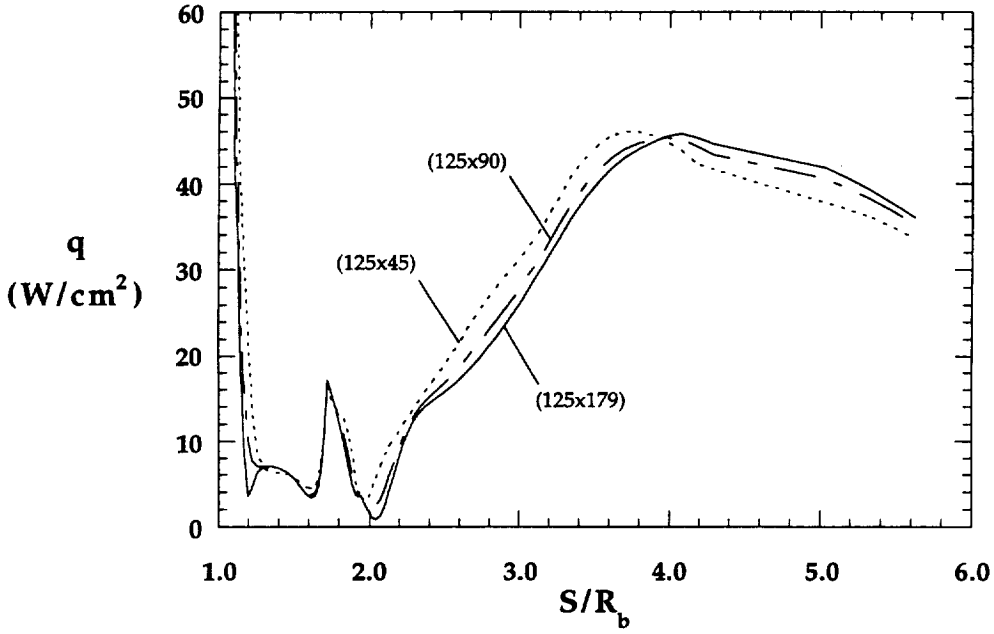

Figure 8.2.8b Grid Resolution Effects on Wake Heating, MP-1 Configuration, HYPULSE, Air

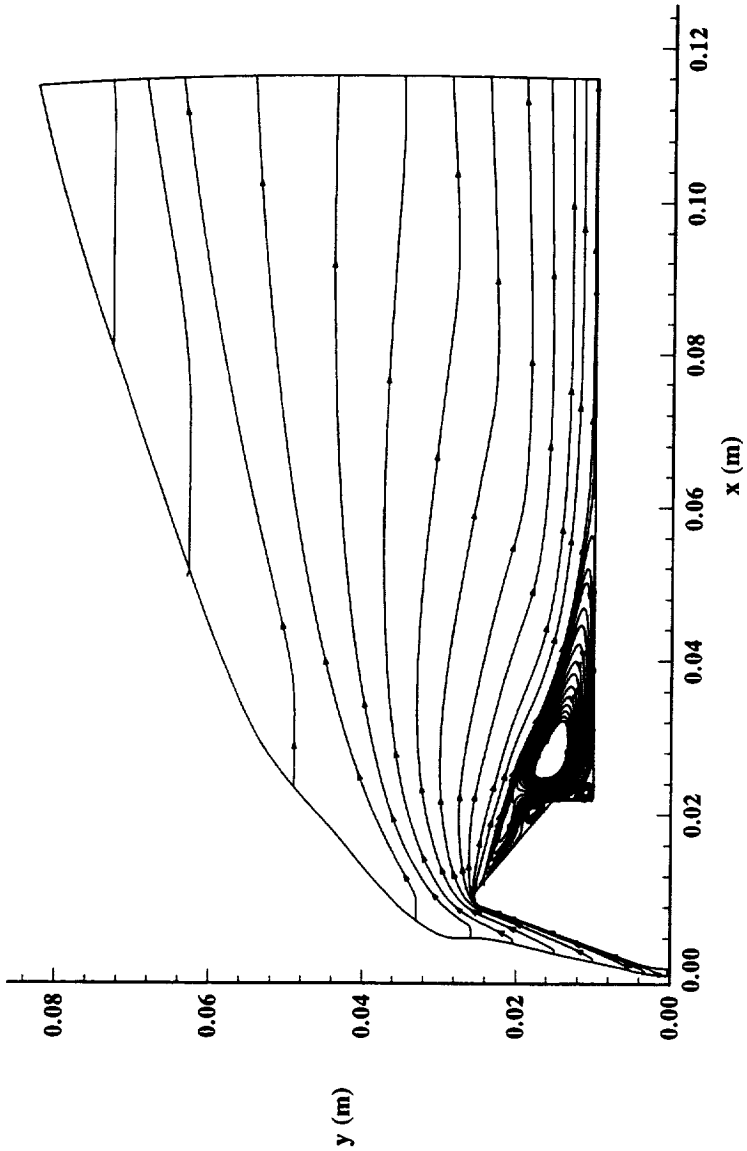

Figure 8.2.9 Computed Streamlines, MP-1 Configuration, HYPULSE, CO_2

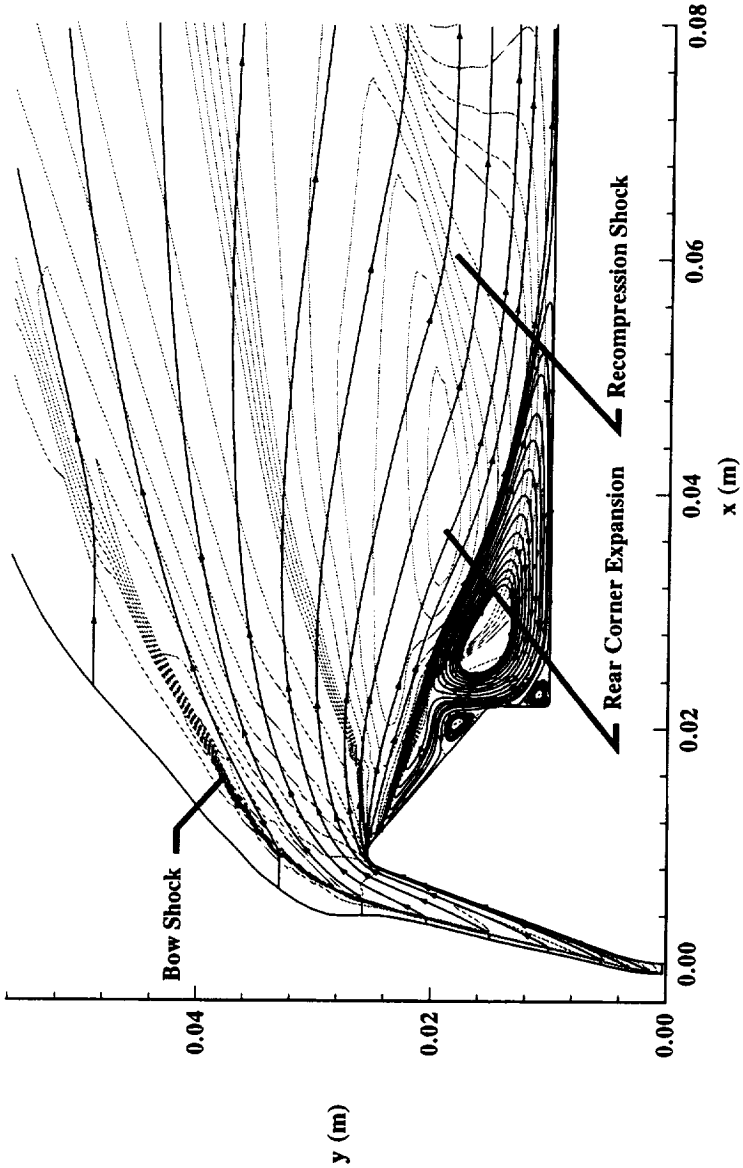

Figure 8.2.10 Computed Streamlines Superimposed on v-Velocity Contours, MP-1 Configuration, HYPULSE, CO_2

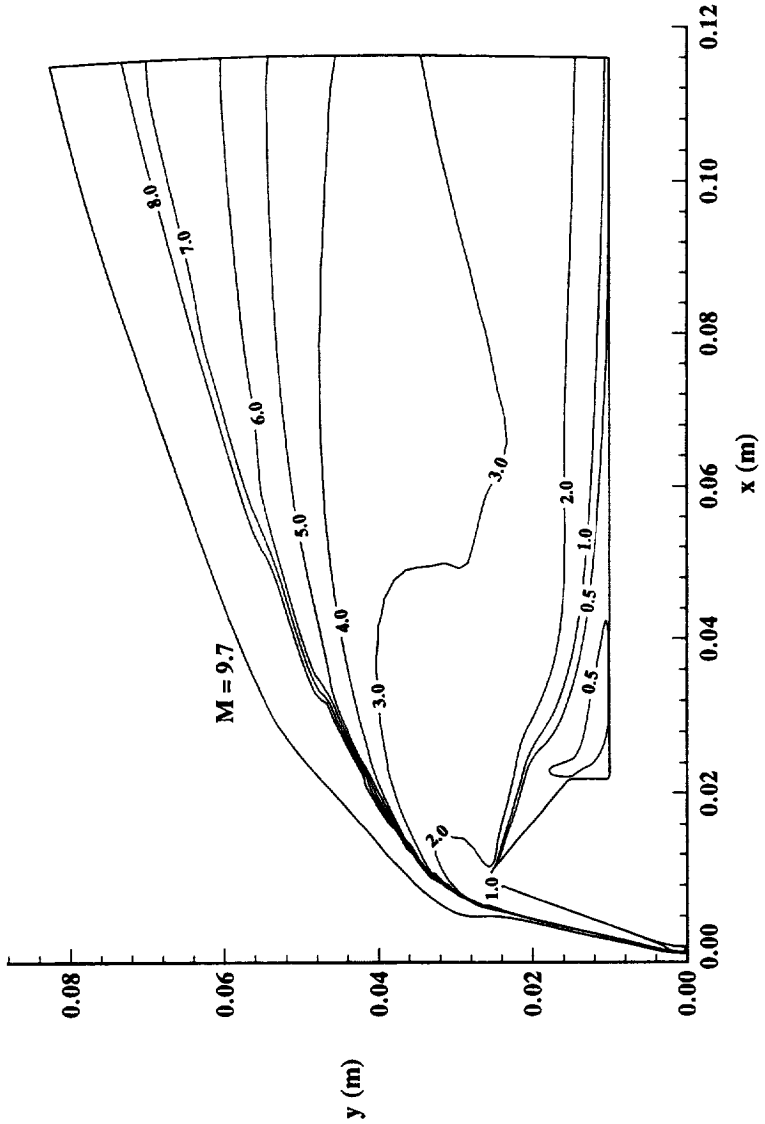

Figure 8.2.11 Computed Mach Contours, MP-1 Configuration, HYPULSE, CO_2

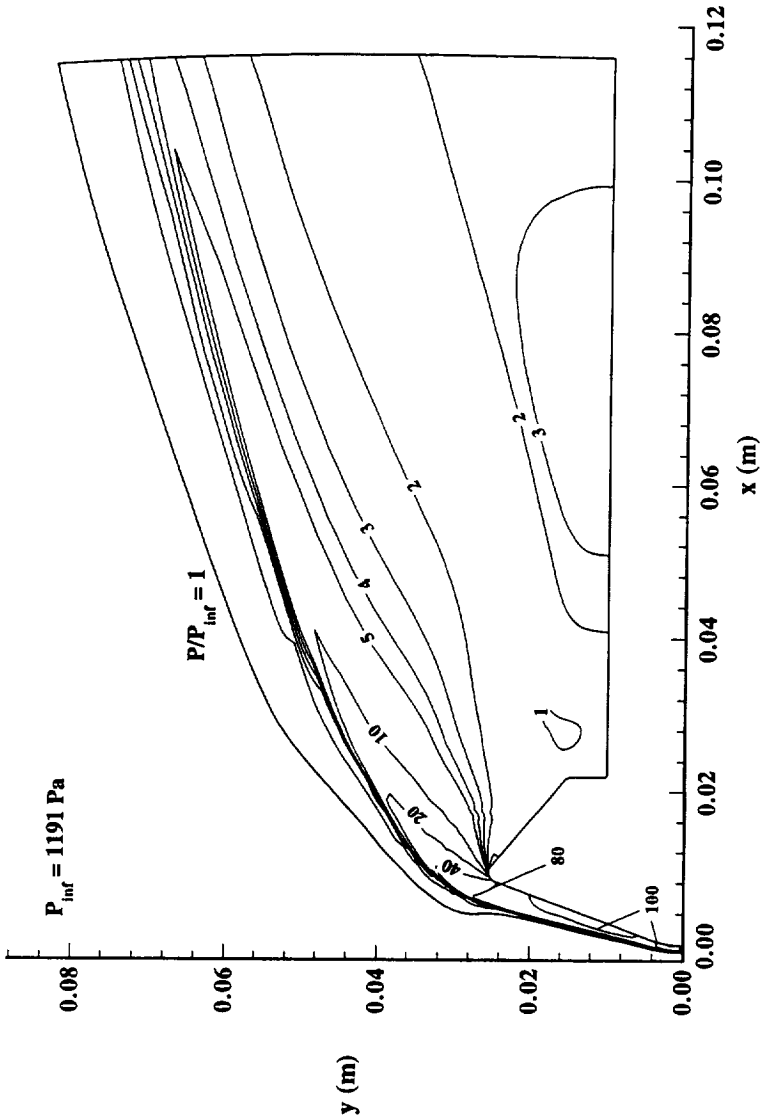

Figure 8.2.12 Computed Pressure Ratio Contours, MP-1 Configuration, HYPULSE, CO_2

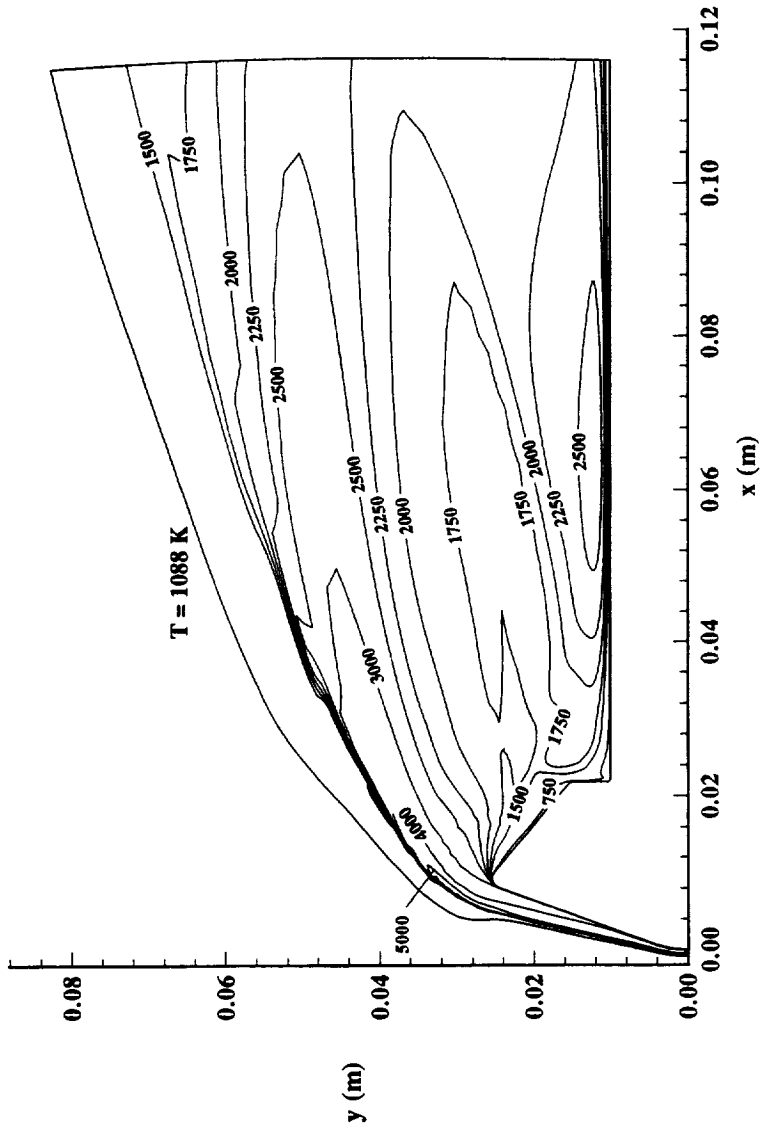

Figure 8.2.13 Computed Temperature Contours, MP-1 Configuration, HYPULSE, CO_2

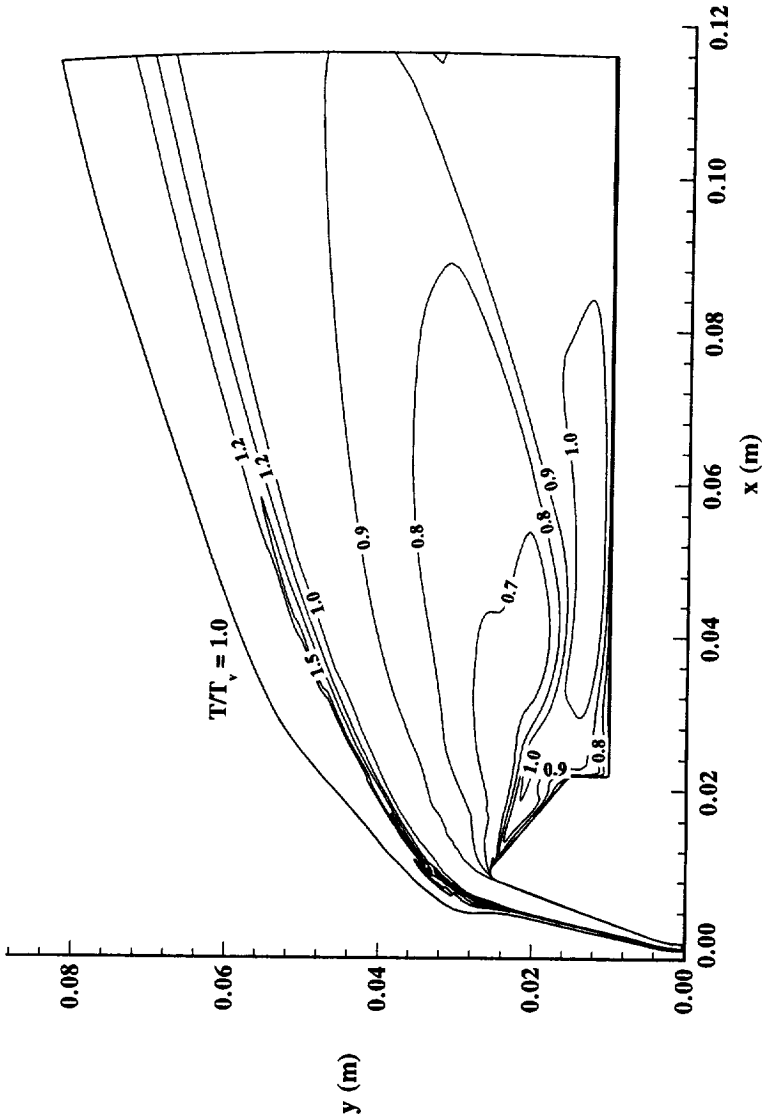

Figure 8.2.14 Computed T/T_v Contours, MP-1 Configuration, HYPULSE, CO_2

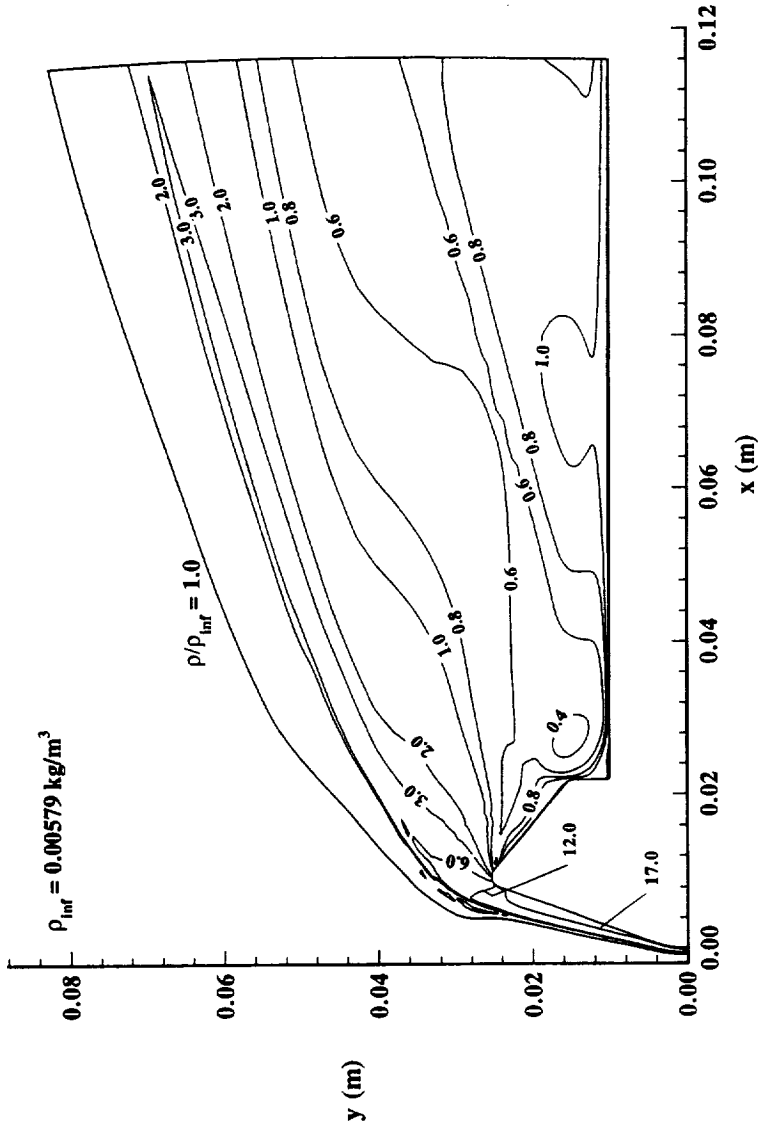

Figure 8.2.15 Computed Density Ratio Contours, MP-1 Configuration, HYPULSE, CO_2

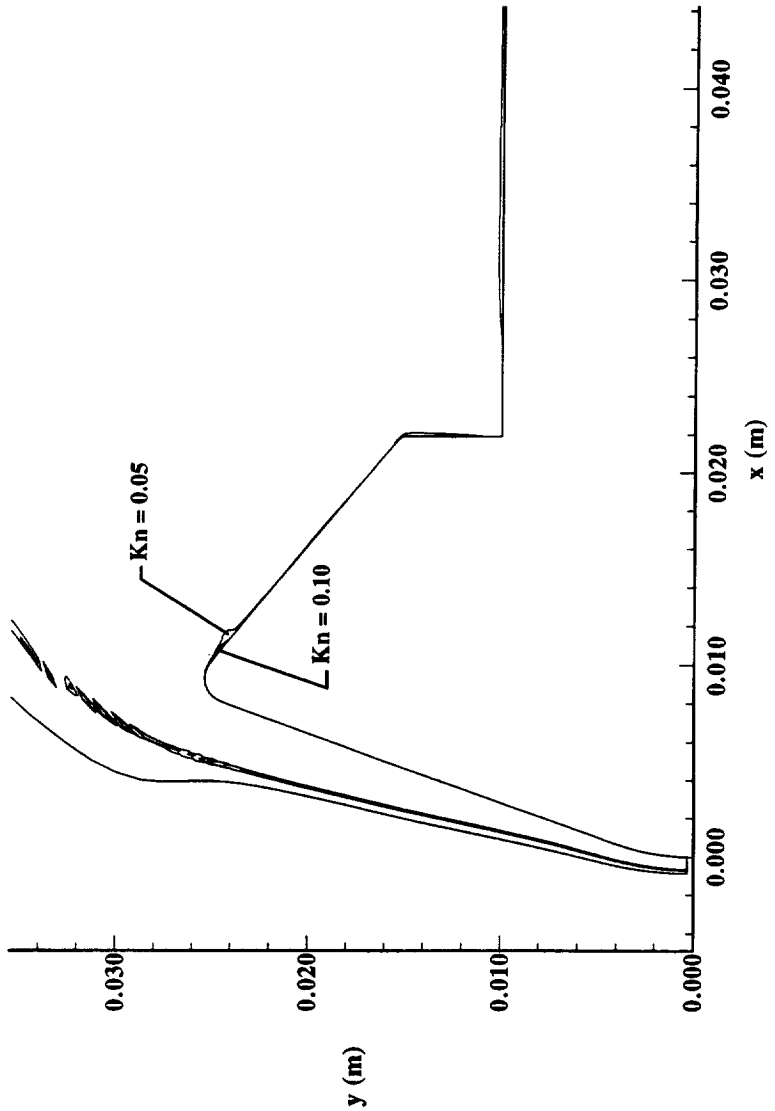

Figure 8.2.16 Computed Local Knudsen Number Contours, MP-1 Configuration, HYPULSE, CO_2

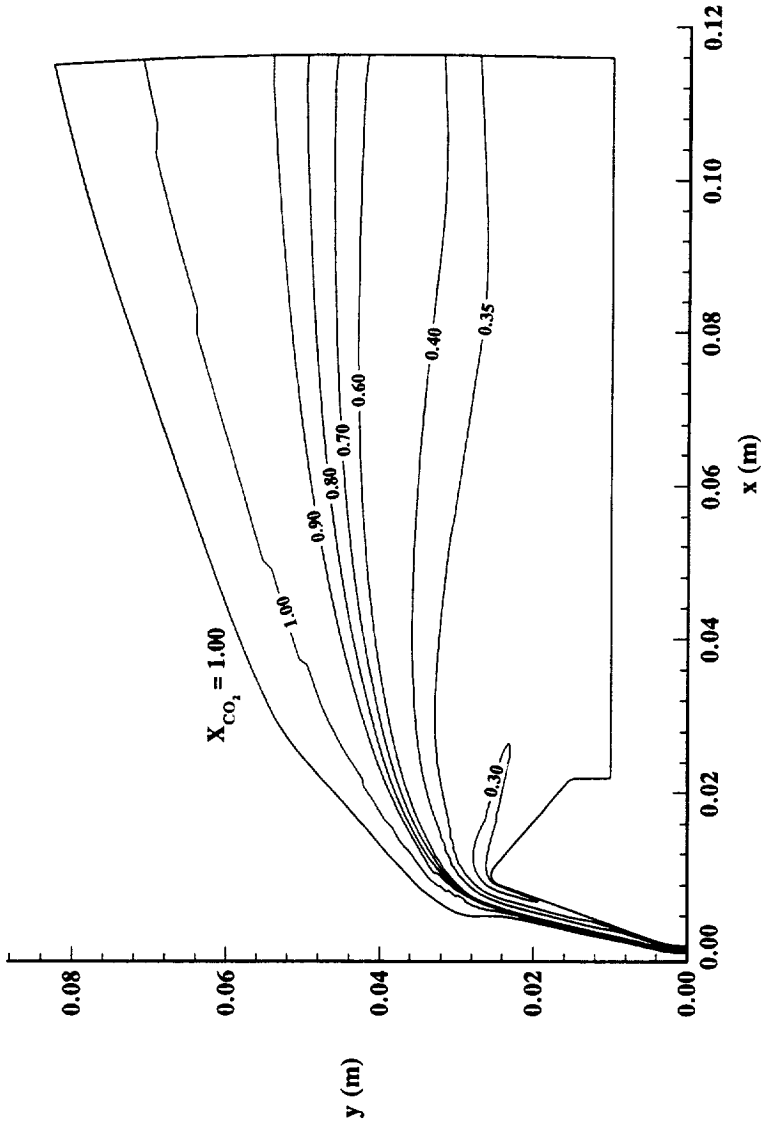

Figure 8.2.17 Computed X(CO_2) Mass Fraction Contours, MP-1 Configuration, HYPULSE, CO_2

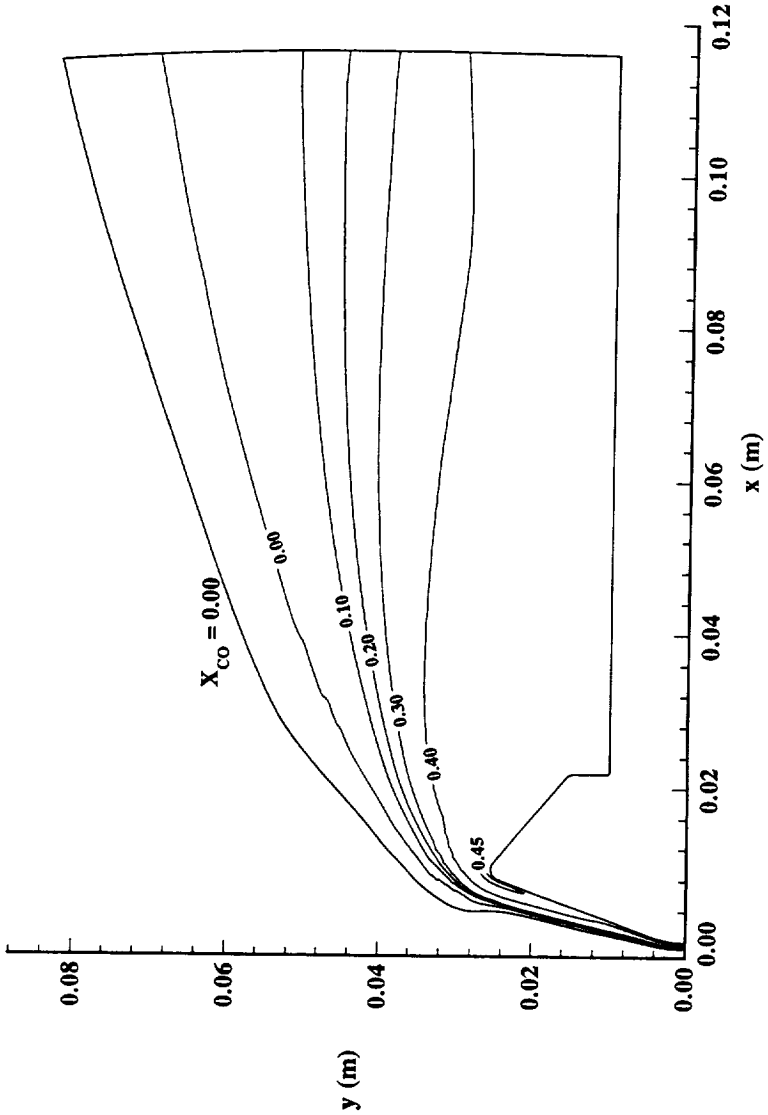

Figure 8.2.18 Computed X(CO) Mass Fraction Contours, MP-1 Configuration, HYPULSE, CO_2

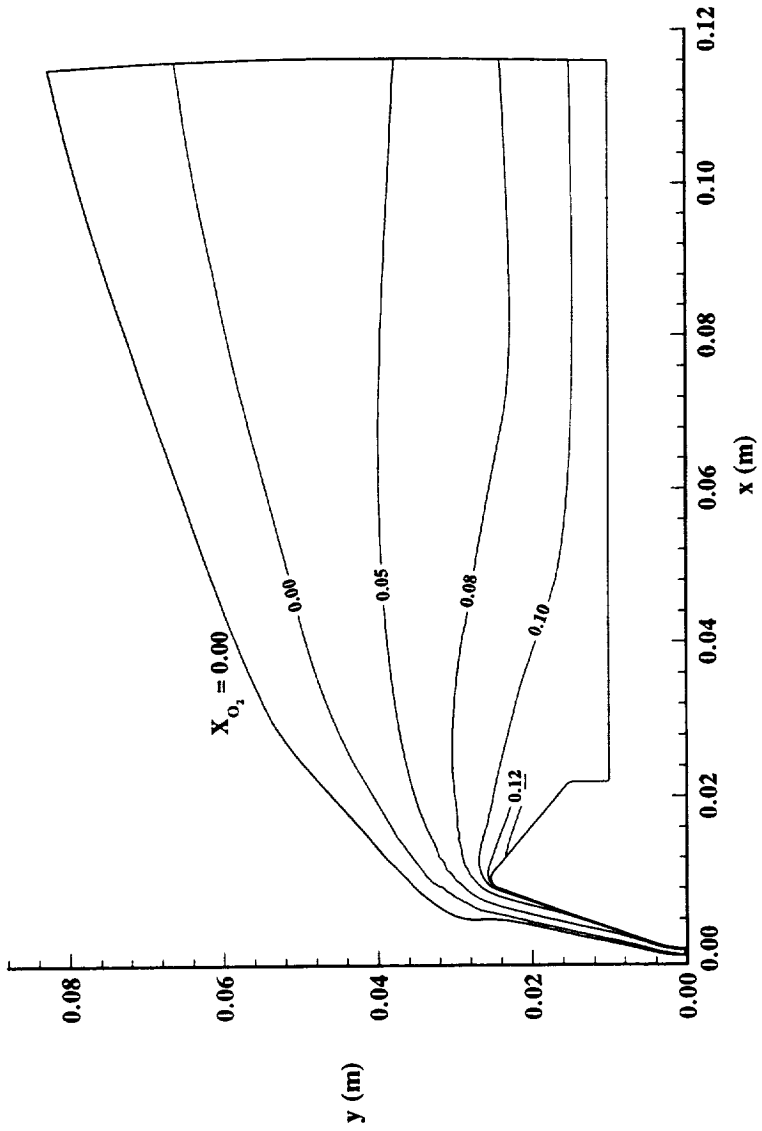

Figure 8.2.19 Computed X(O_2) Mass Fraction Contours, MP-1 Configuration, HYPULSE, CO_2

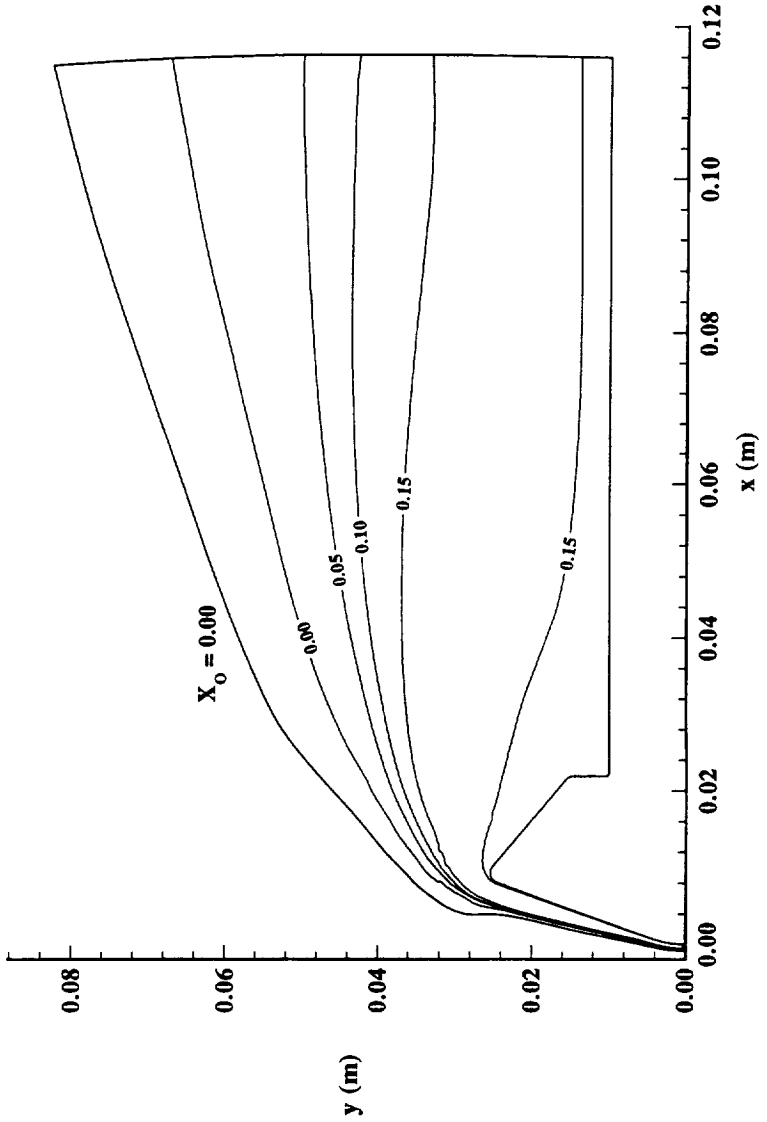

Figure 8.2.20 Computed X(O) Mass Fraction Contours, MP-1 Configuration, HYPULSE, CO_2

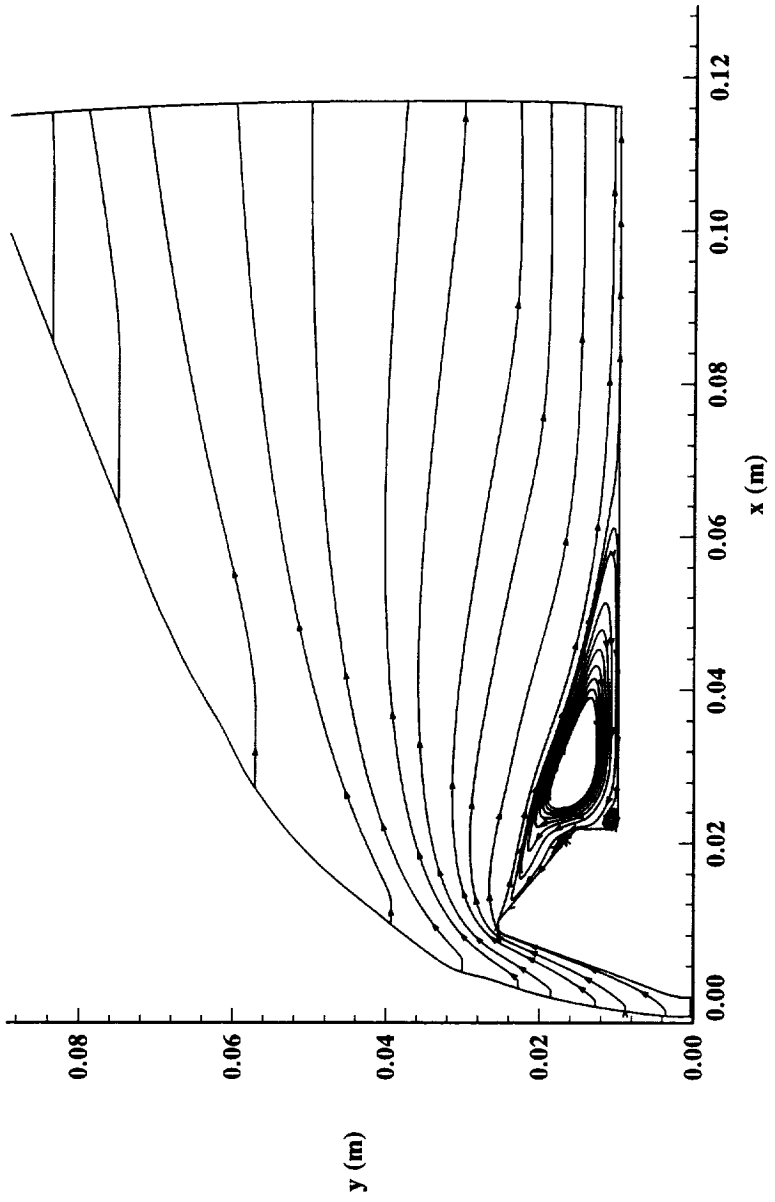

Figure 8.2.21 Computed Streamlines, MP-1 Configuration, HYPULSE, Air

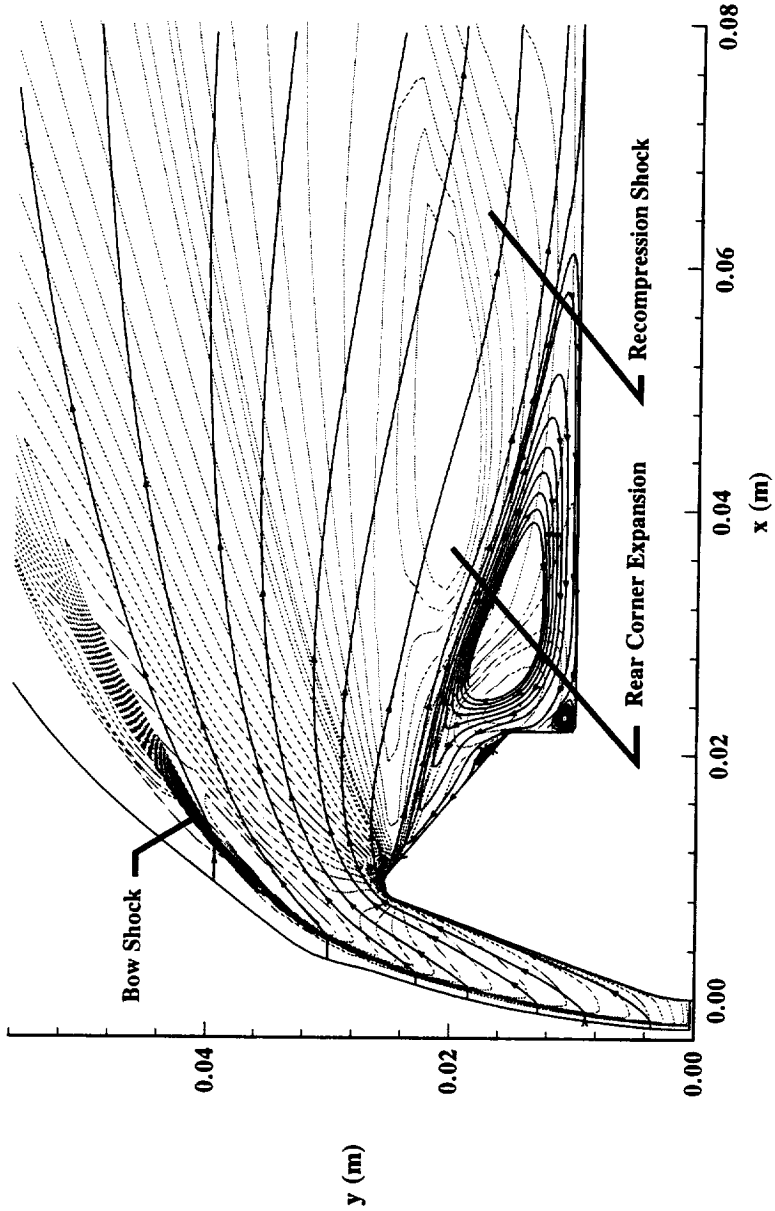

Figure 8.2.22 Computed Streamlines Superimposed on v-Velocity Contours, MP-1 Configuration, HYPULSE, Air

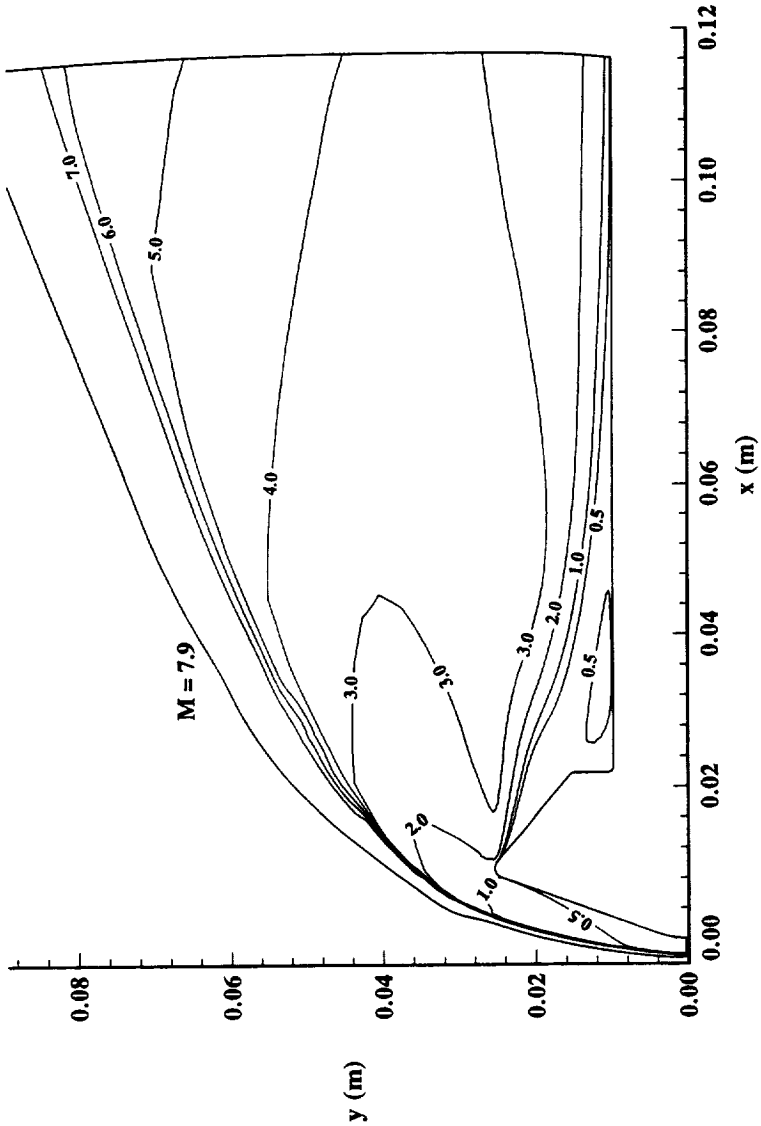

Figure 8.2.23 Computed Mach Contours, MP-1 Configuration, HYPULSE, Air

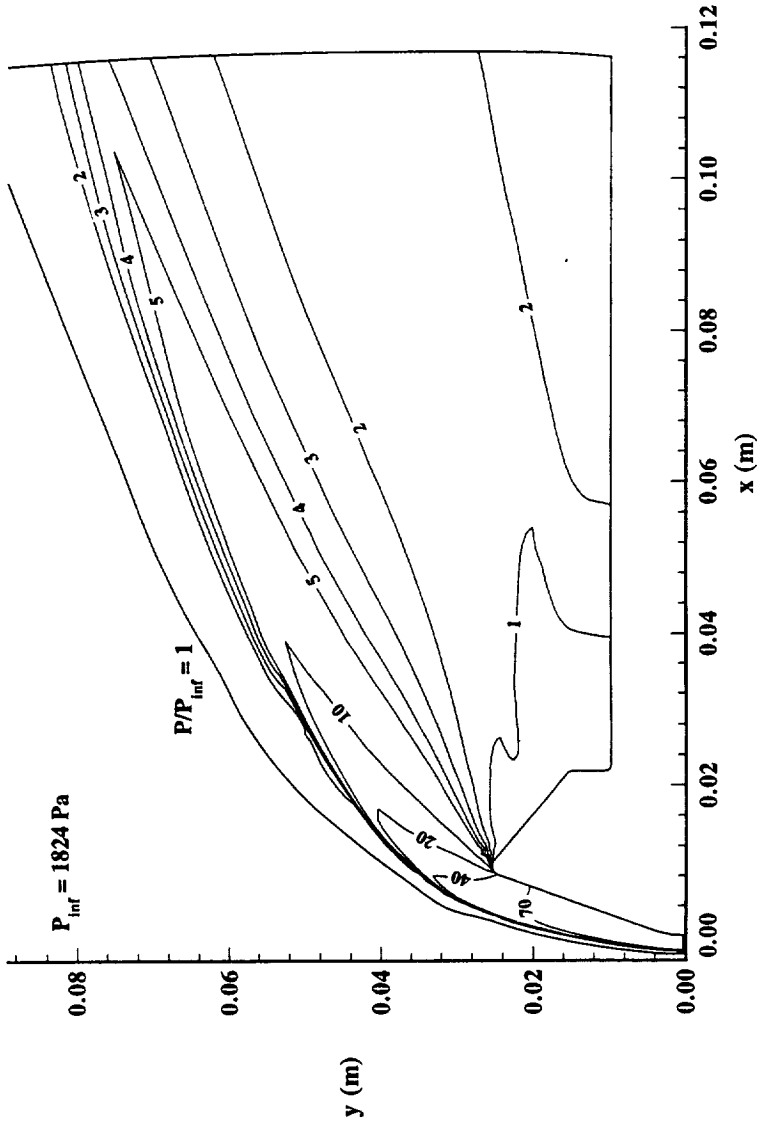

Figure 8.2.24 Computed Pressure Ratio Contours, MP-1 Configuration, HYPULSE, Air

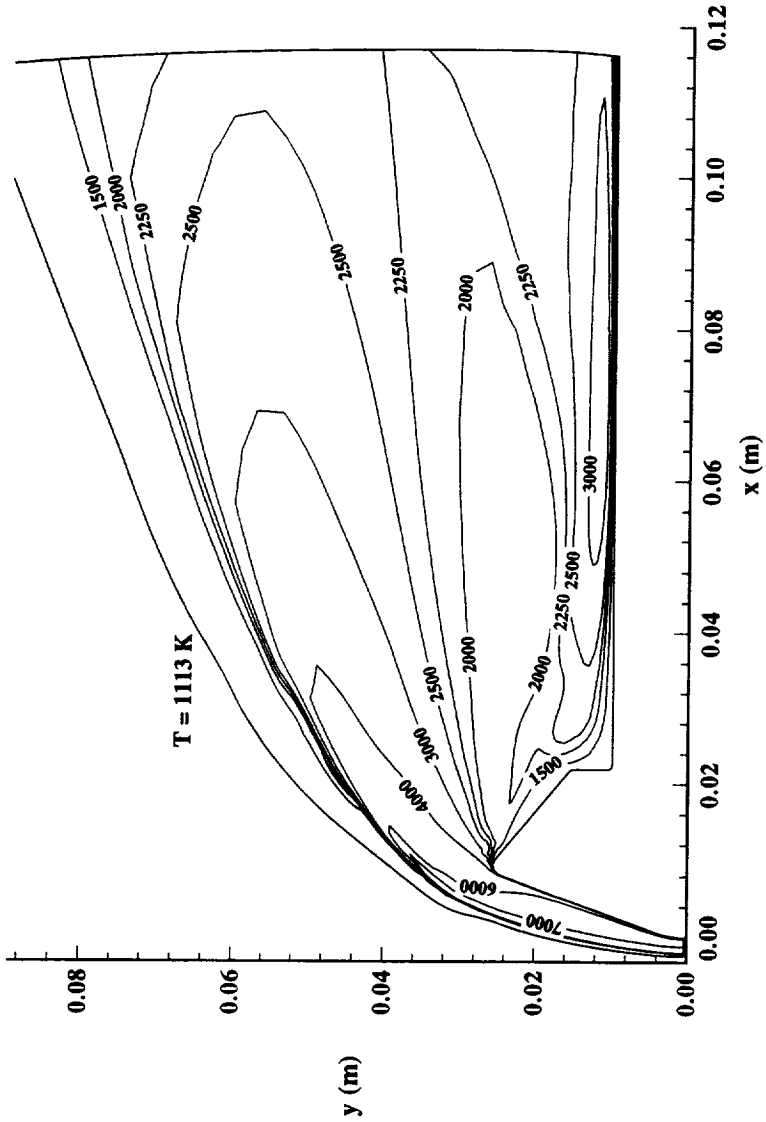

Figure 8.2.25 Computed Temperature Contours, MP-1 Configuration, HYPULSE, Air

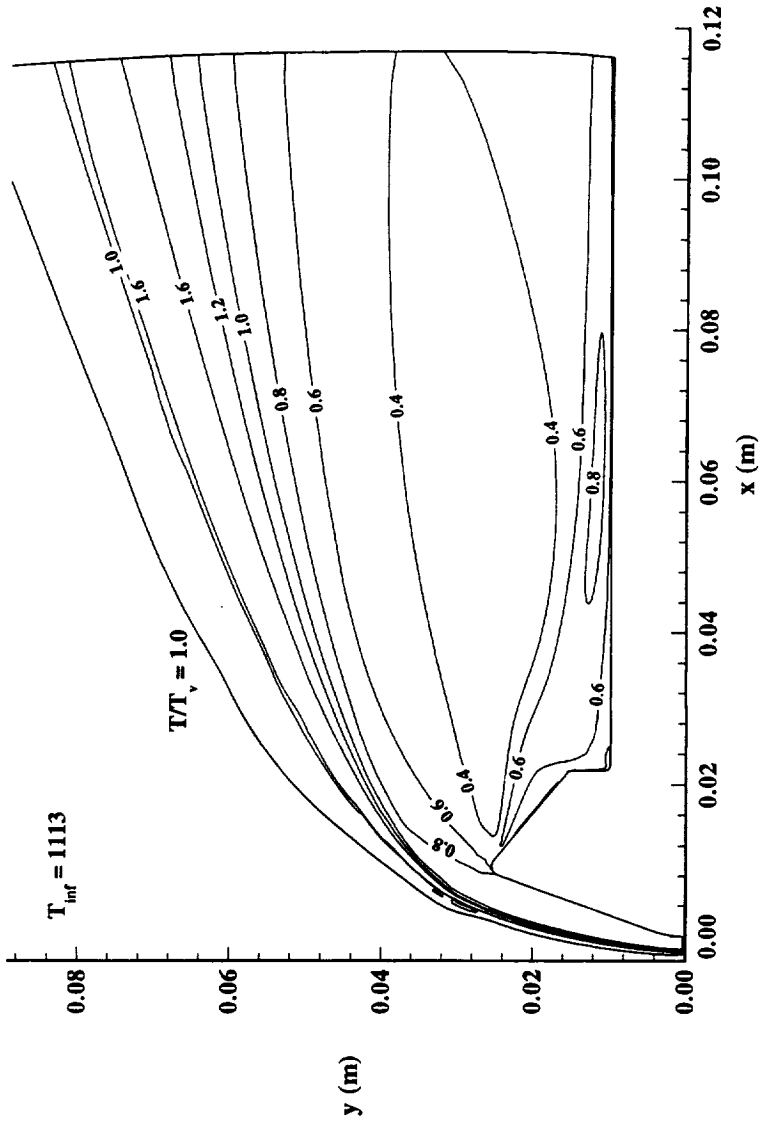

Figure 8.2.26 Computed T/Tv Contours, MP-1 Configuration, HYPULSE, Air

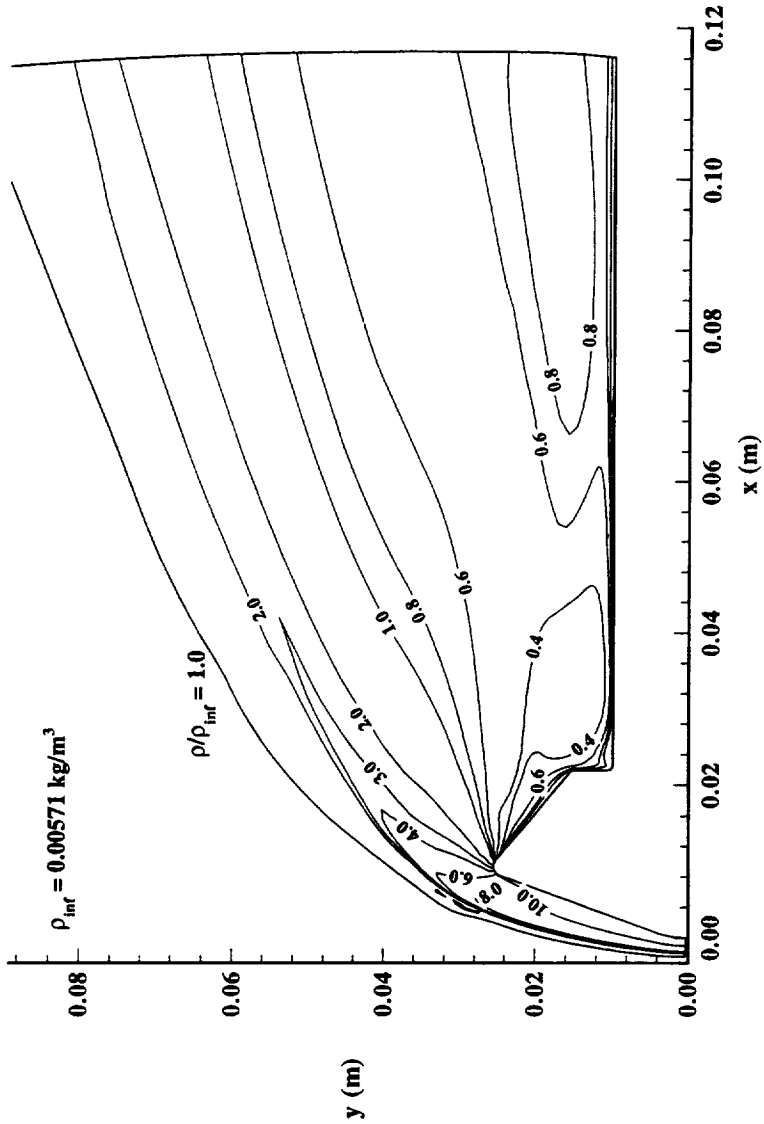

Figure 8.2.27 Computed Density Ratio Contours, MP-1 Configuration, HYPULSE, Air

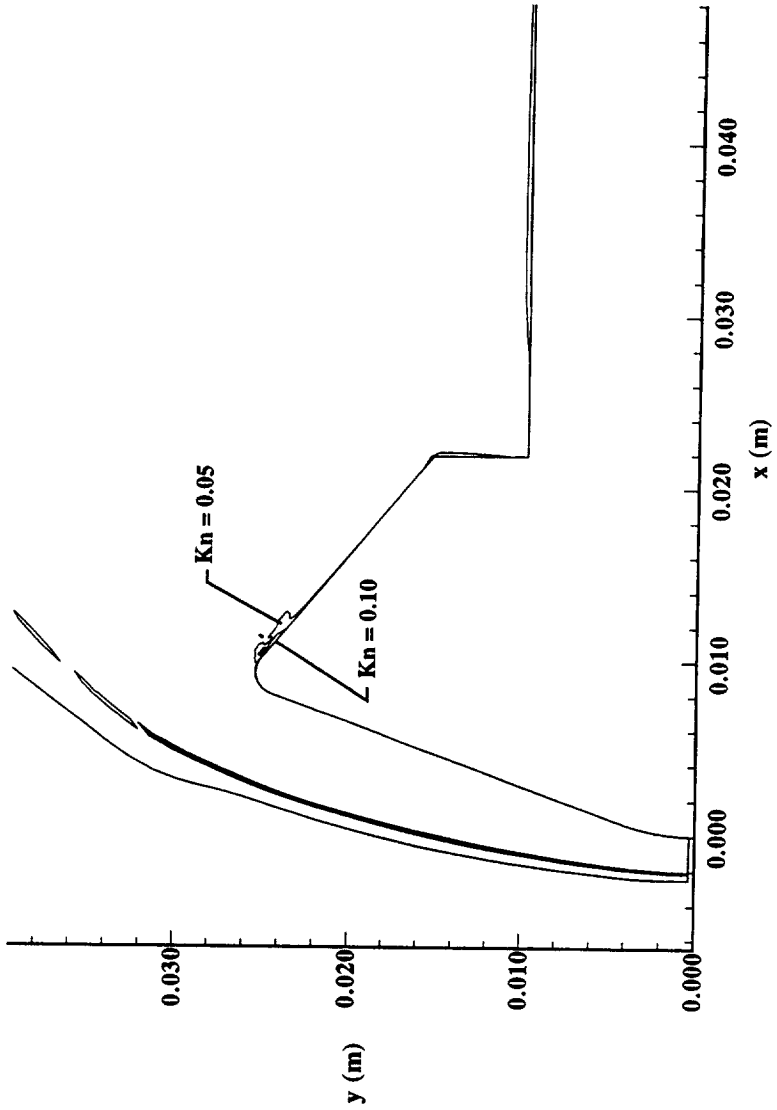

Figure 8.2.28 Computed Local Knudsen Number Contours, MP-1 Configuration, HYPULSE, Air

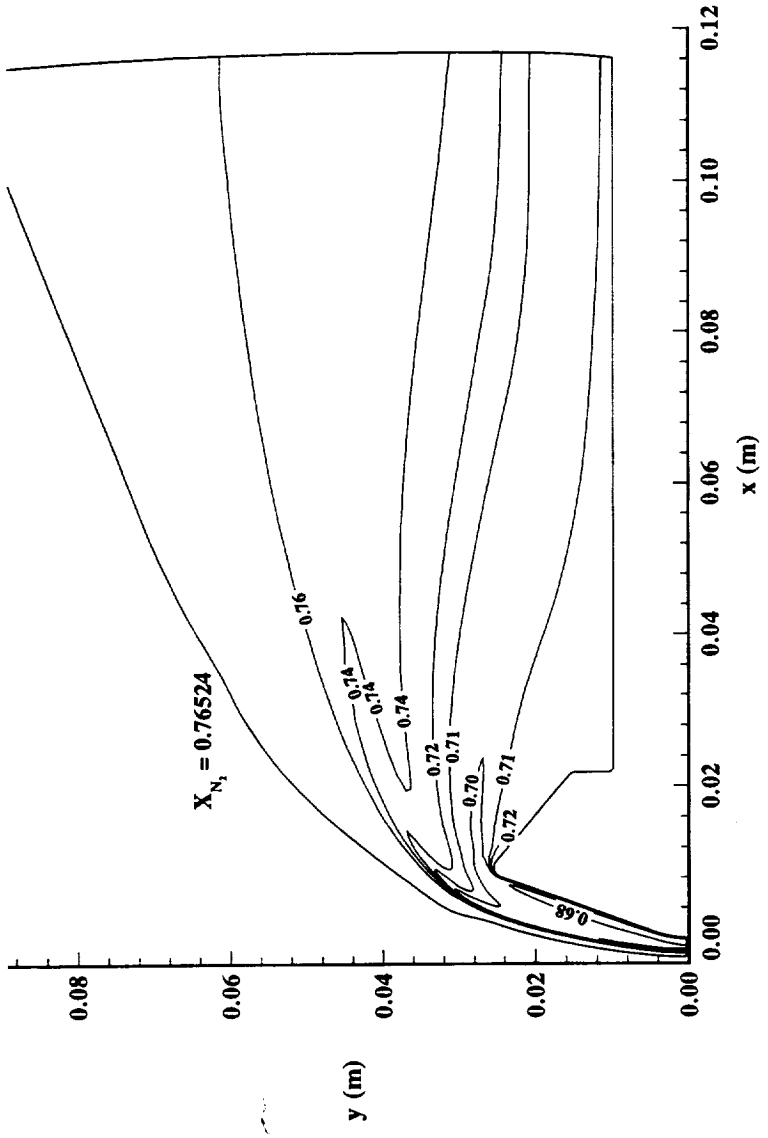

Figure 8.2.29 Computed X(N2) Contours, MP-1 Configuration, HYPULSE, Air

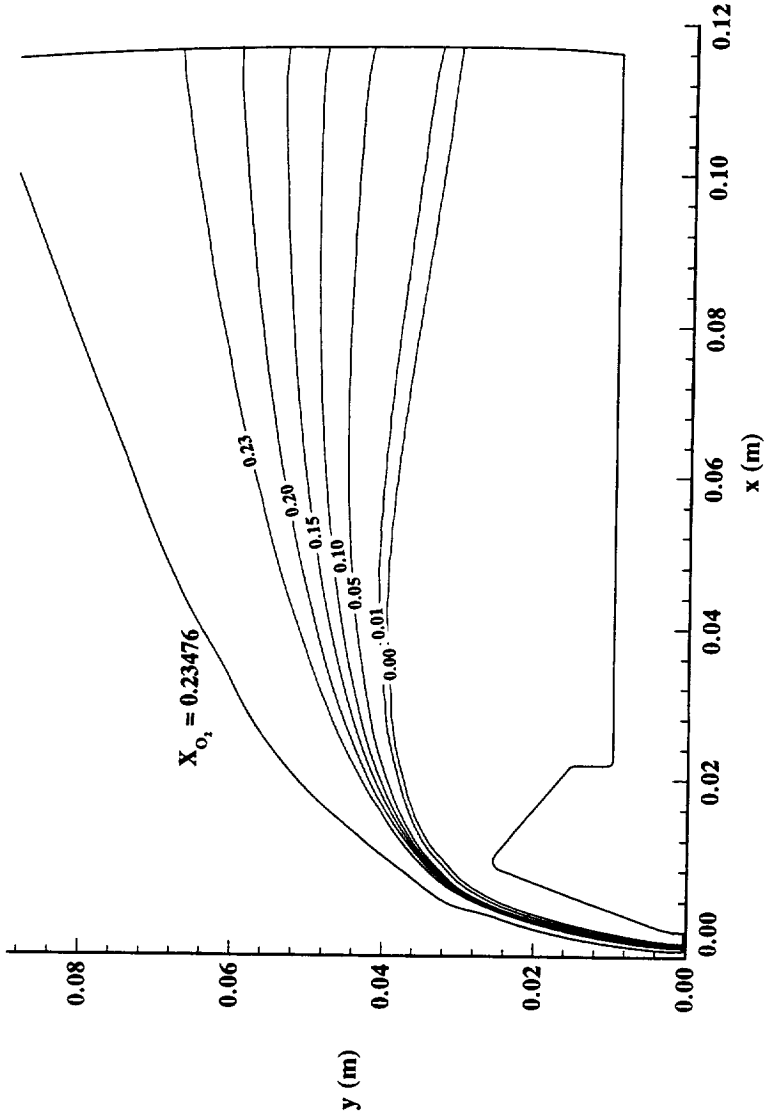

Figure 8.2.30 Computed X(O_2) Contours, MP-1 Configuration, HYPULSE, Air

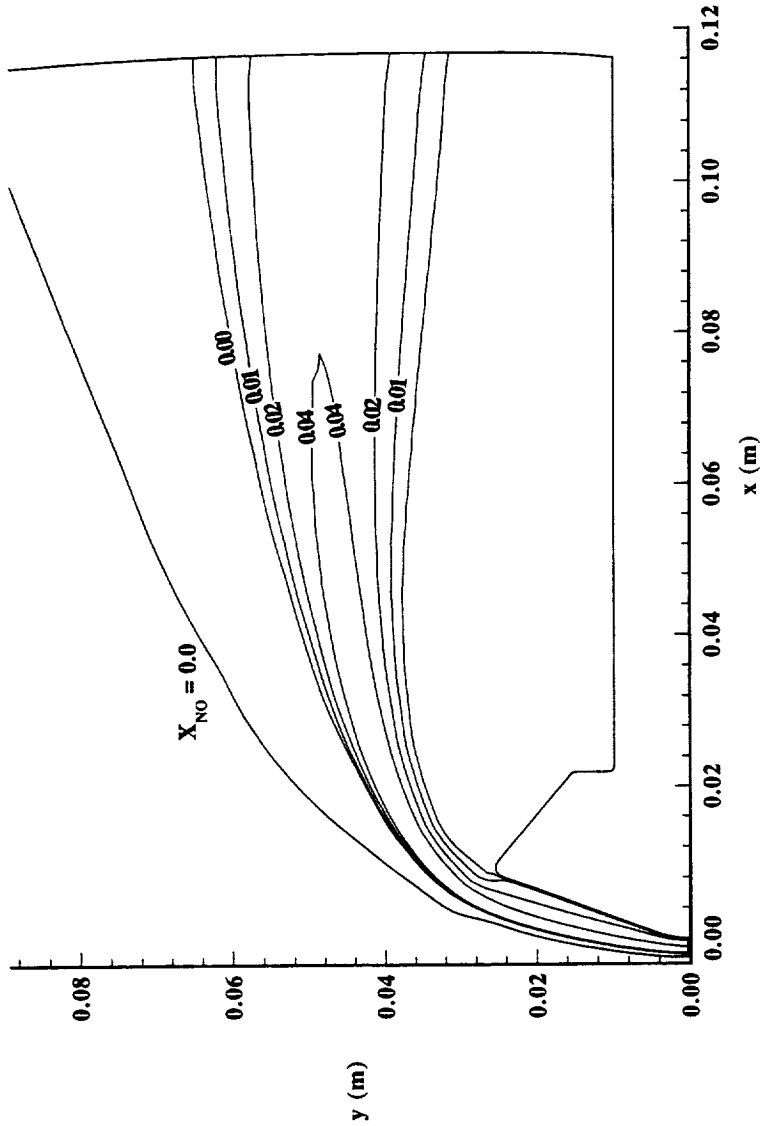

Figure 8.2.31 Computed X(NO) Contours, MP-1 Configuration, HYPULSE, Air

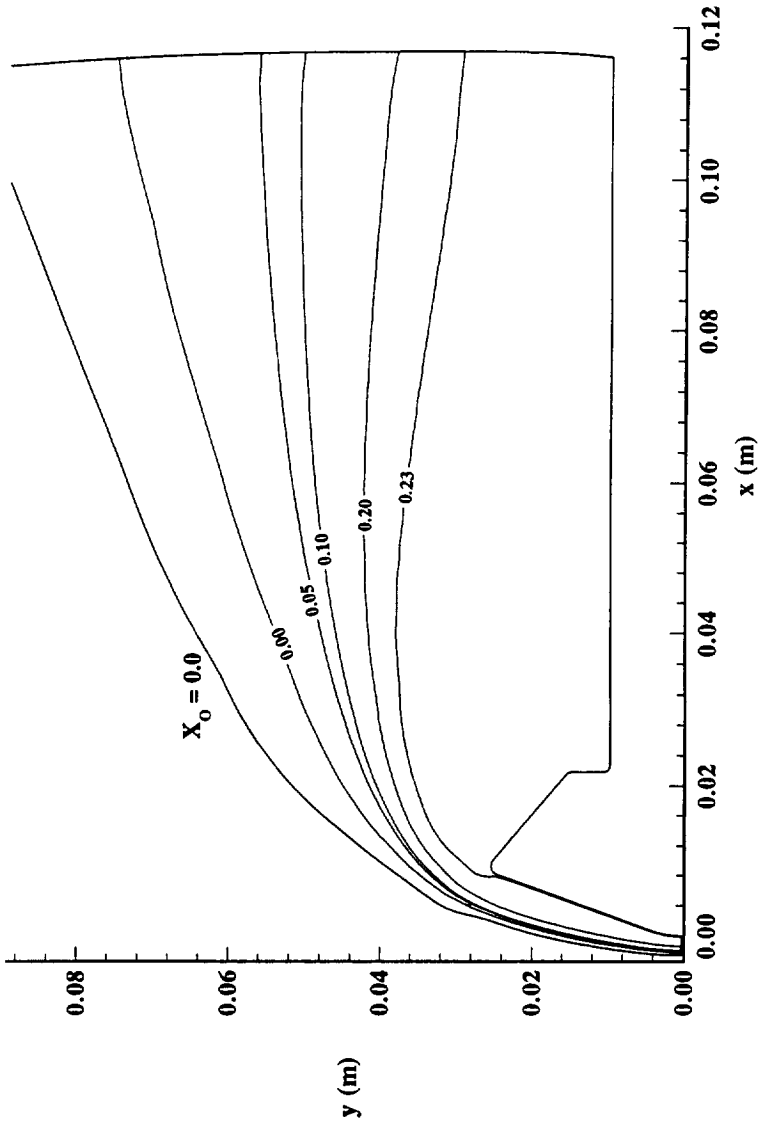

Figure 8.2.32 Computed X(O) Contours, MP-1 Configuration, HYPULSE, Air

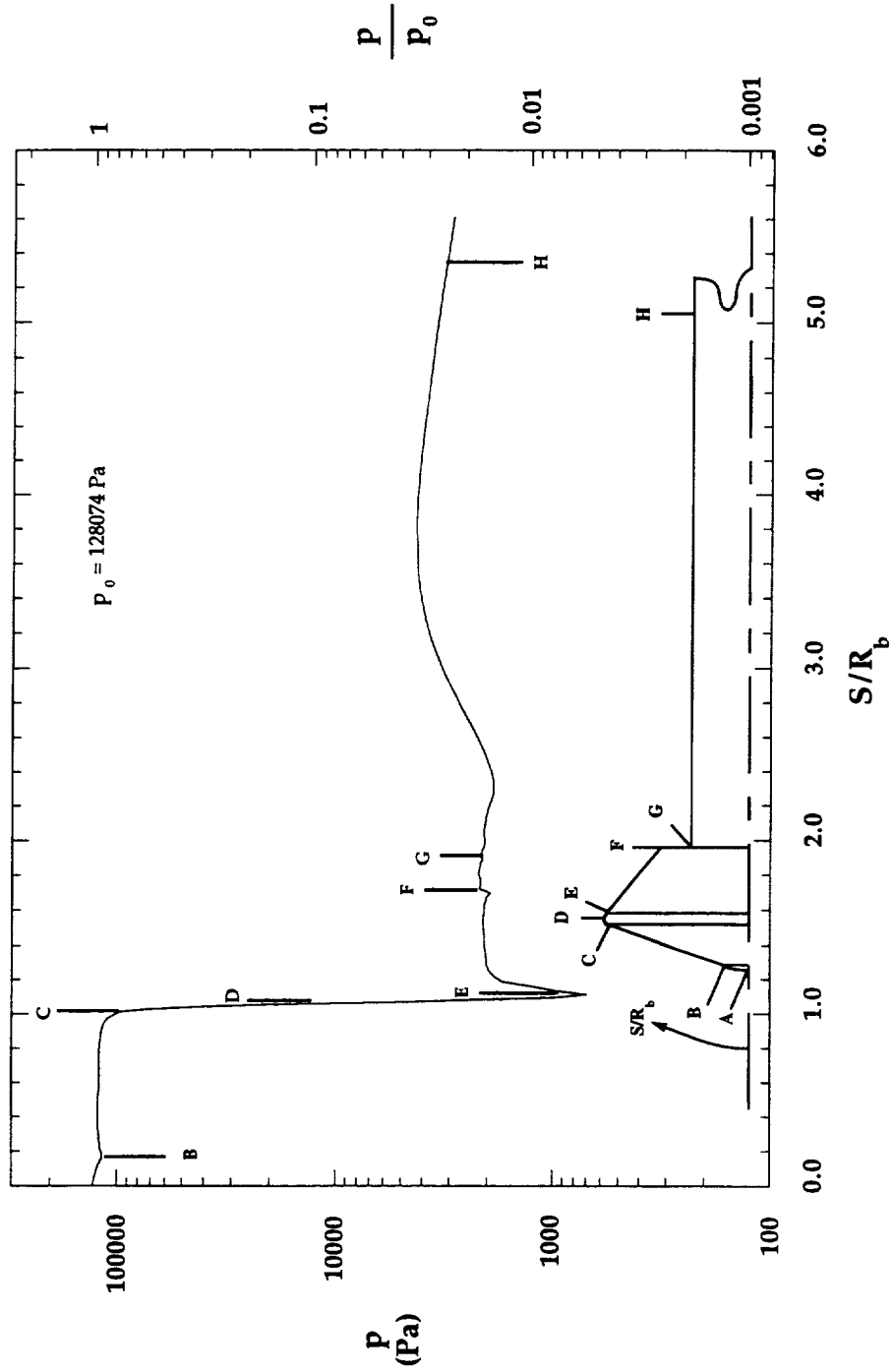

Figure 8.2.33 Computed Surface Pressure Distribution, MP-1 Configuration, HYPULSE, CO_2

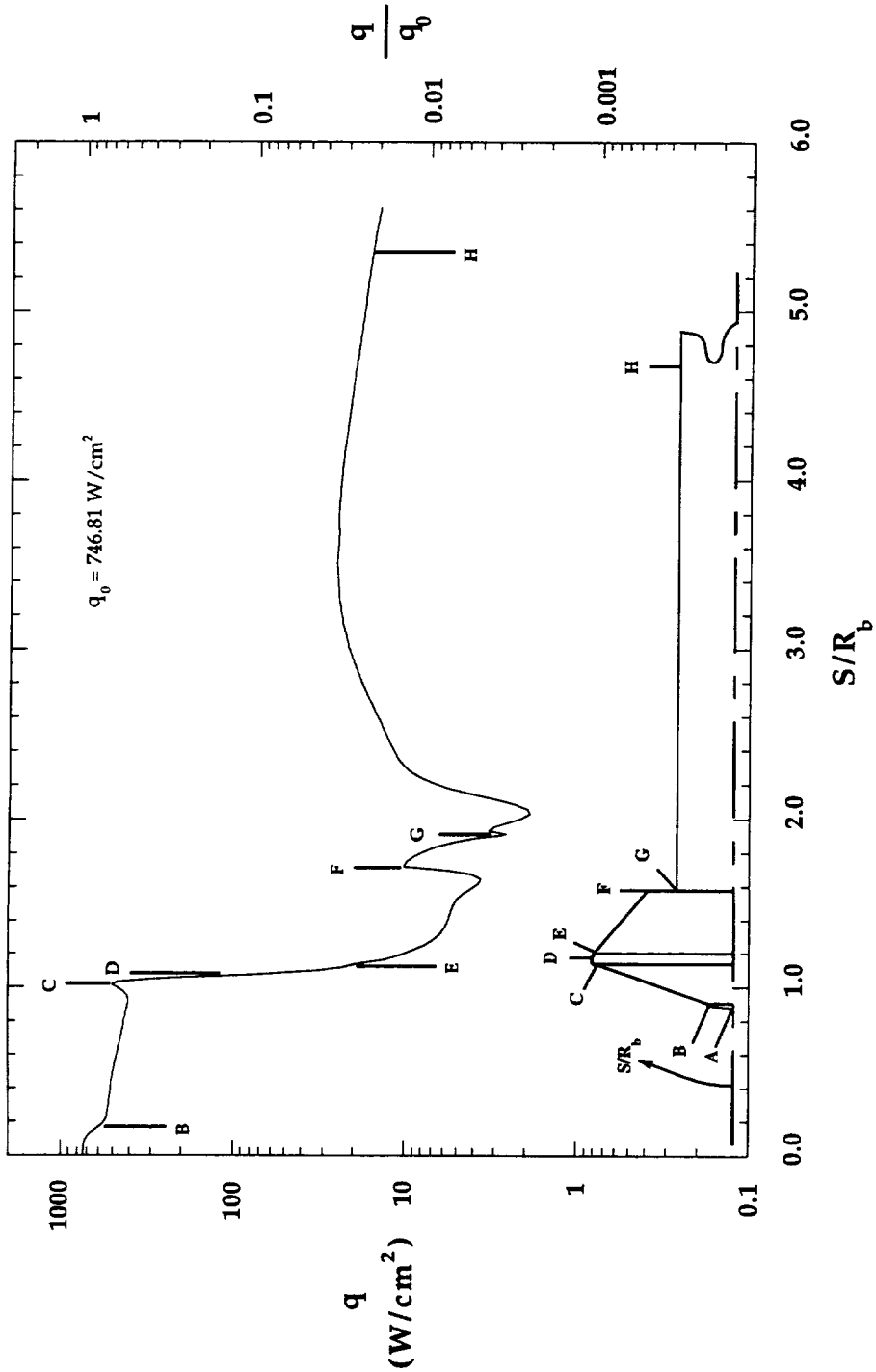

Figure 8.2.34 Computed Surface Heating Distribution, MP-1 Configuration, HYPULSE, CO_2

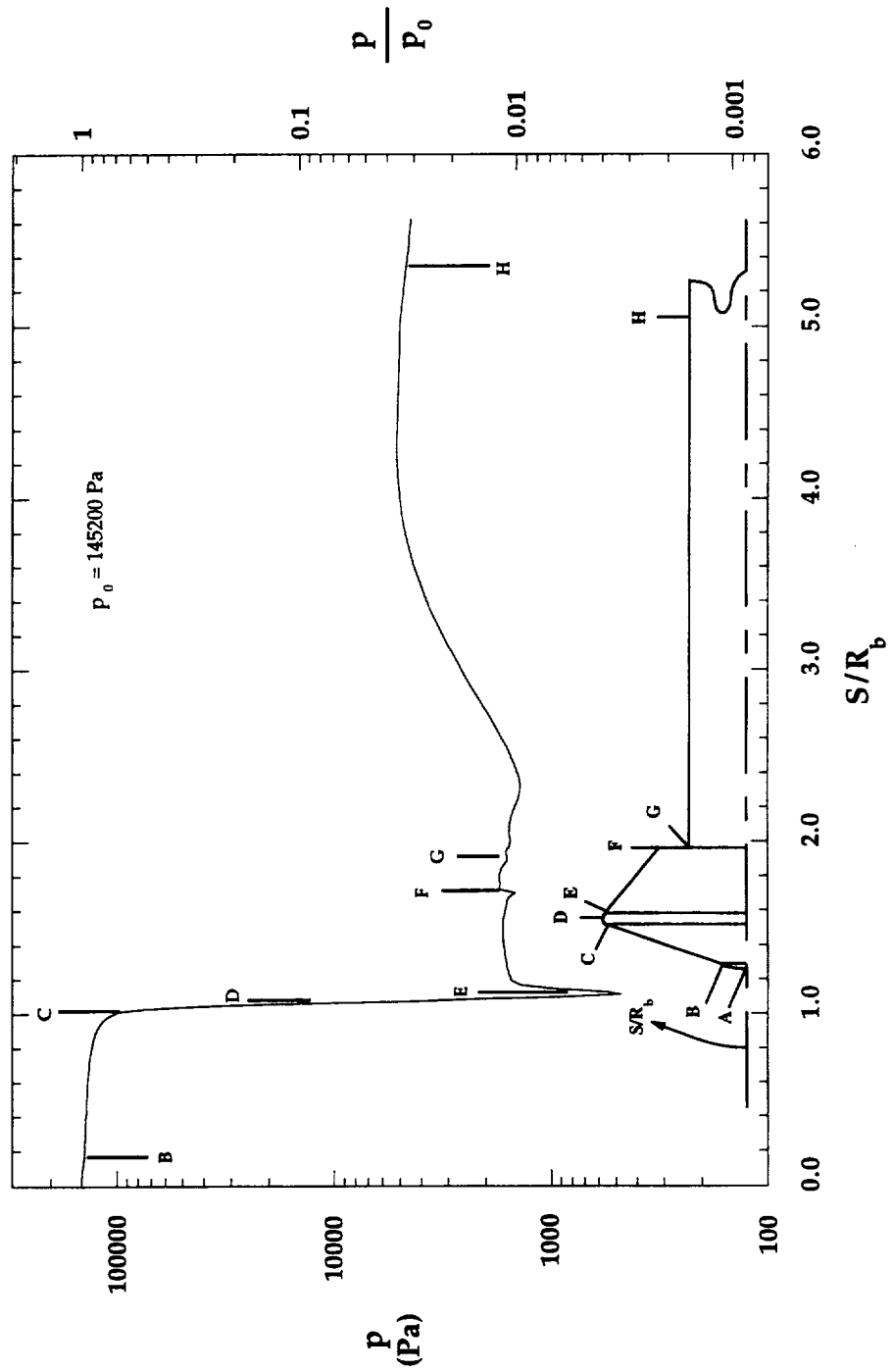

Figure 8.2.35 Computed Surface Pressure Distribution, MP-1 Configuration, HYPULSE, Air

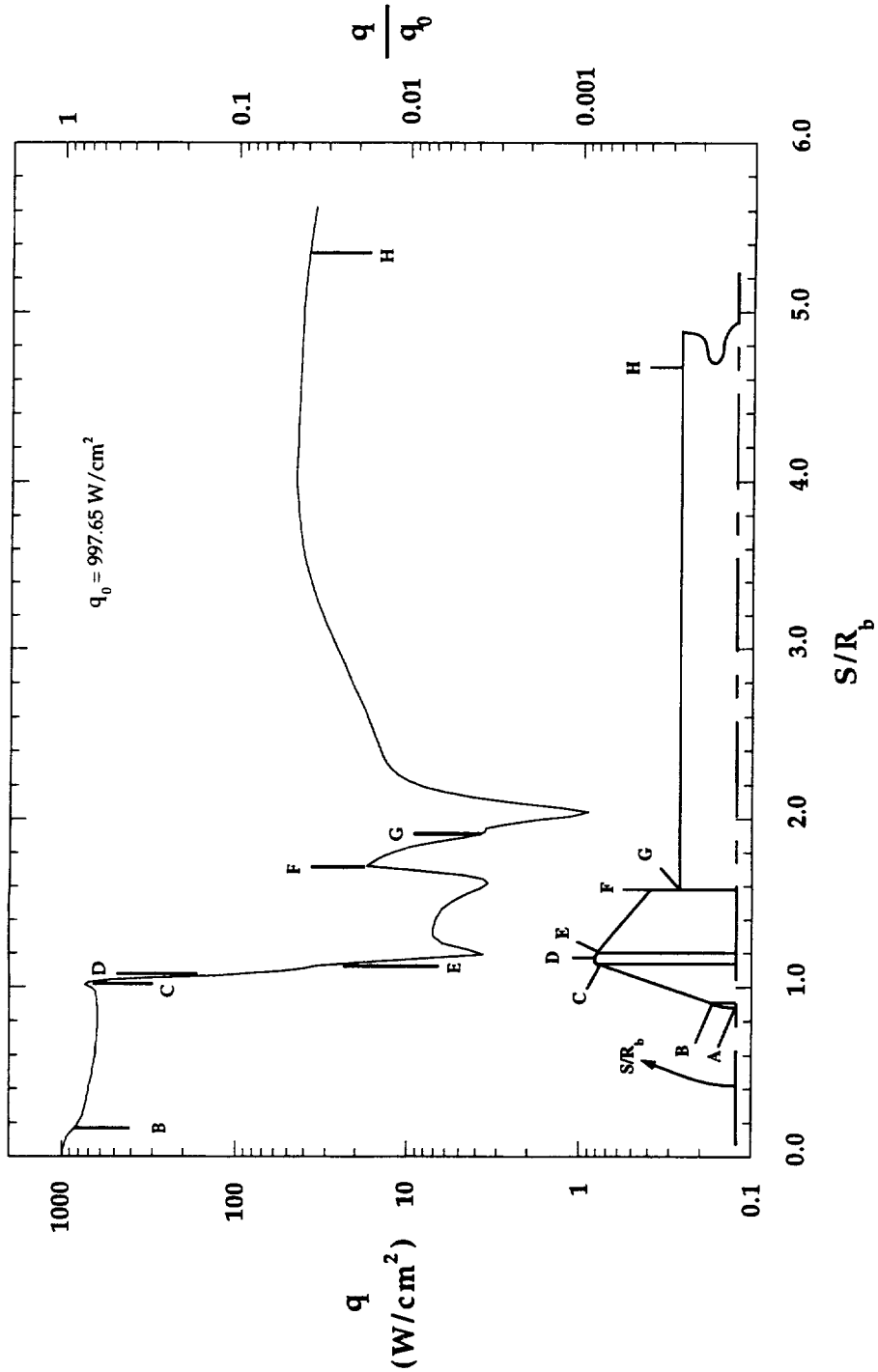

Figure 8.2.36 Computed Surface Heating Distribution, MP-1 Configuration, HYPULSE, Air

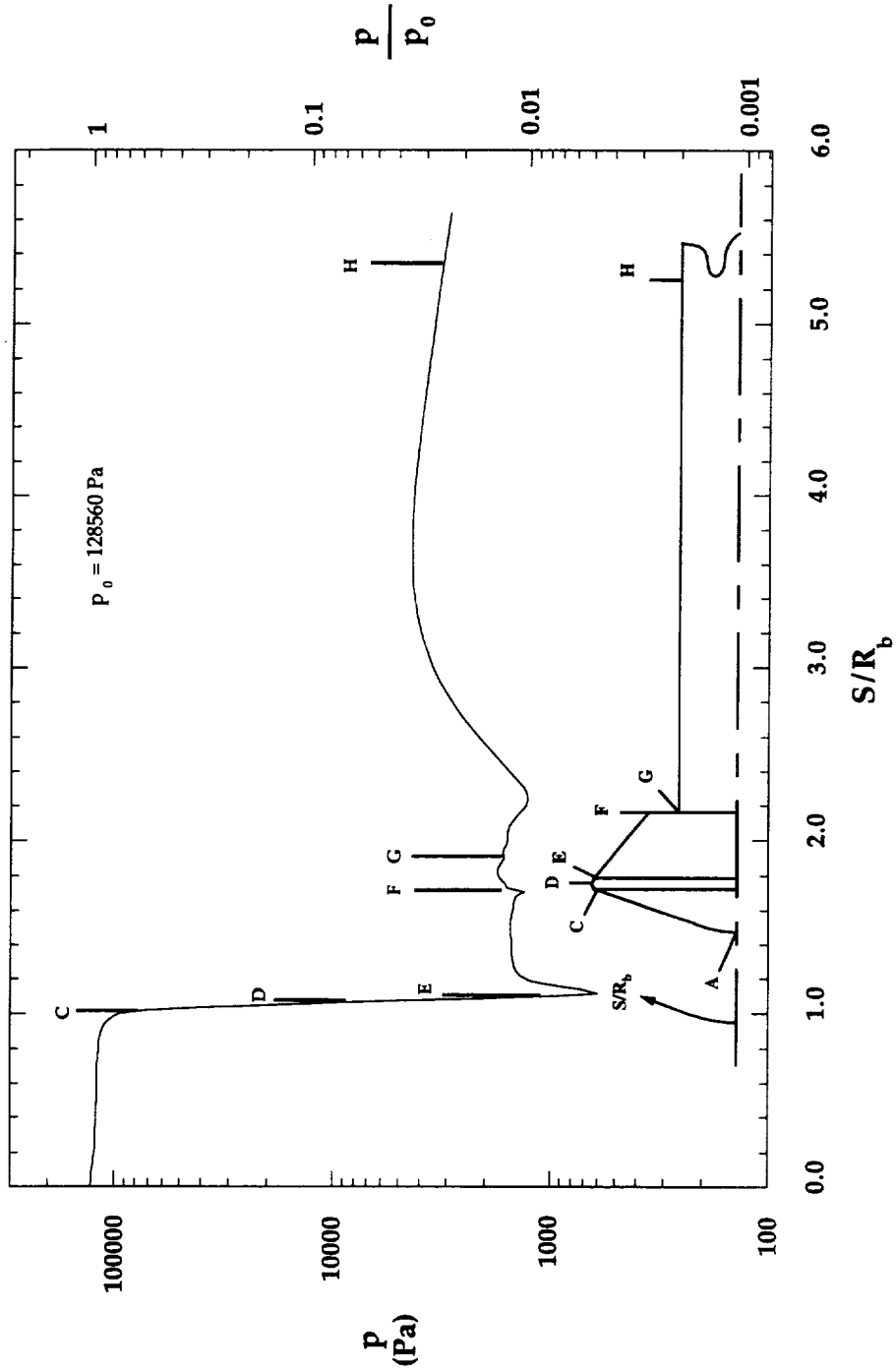

Figure 8.2.37 Computed Surface Pressure Distribution, MP-2 Configuration, HYPULSE, CO_2

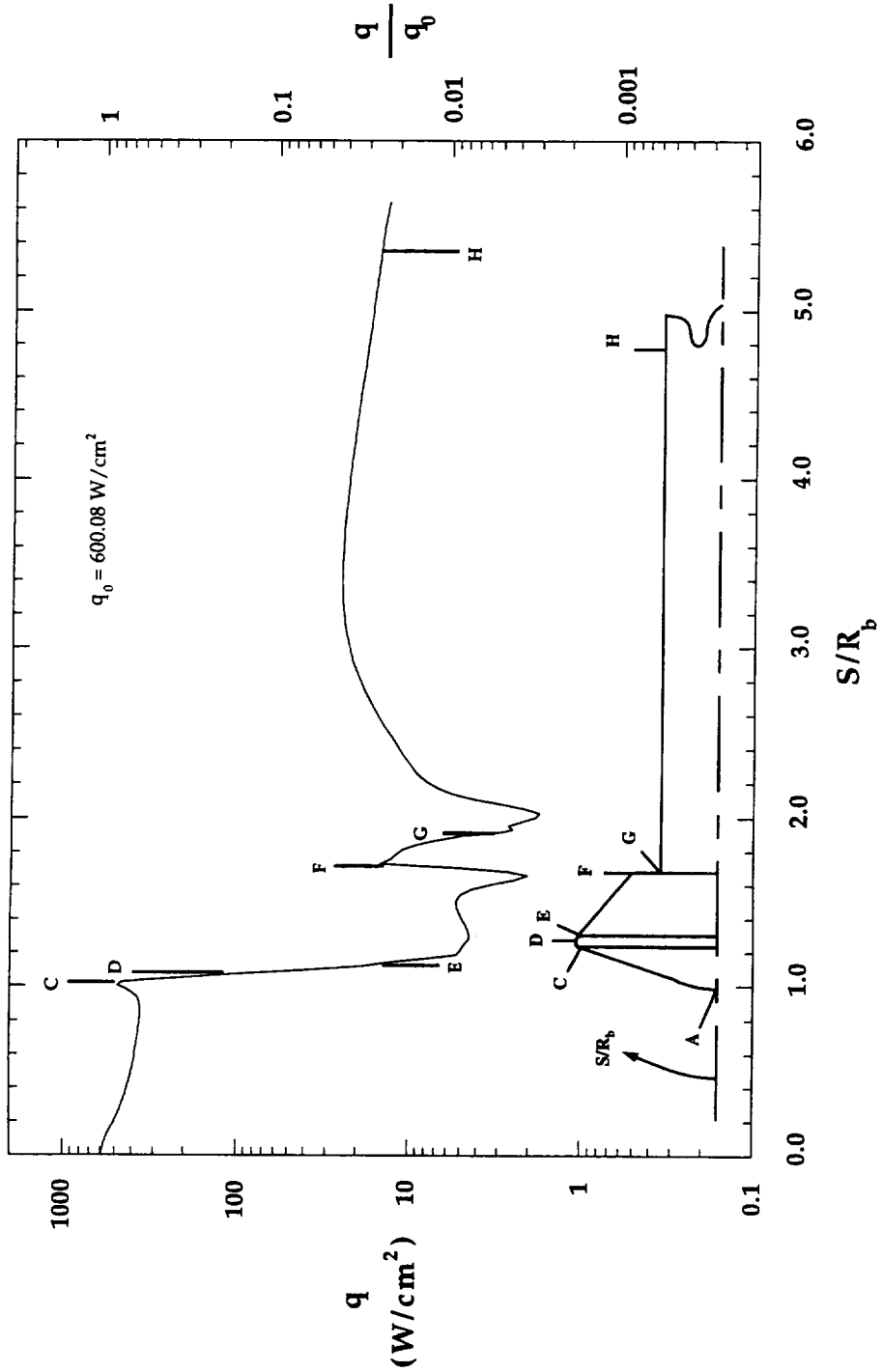

Figure 8.2.38 Computed Surface Heating Distribution, MP-2 Configuration, HYPULSE, CO_2

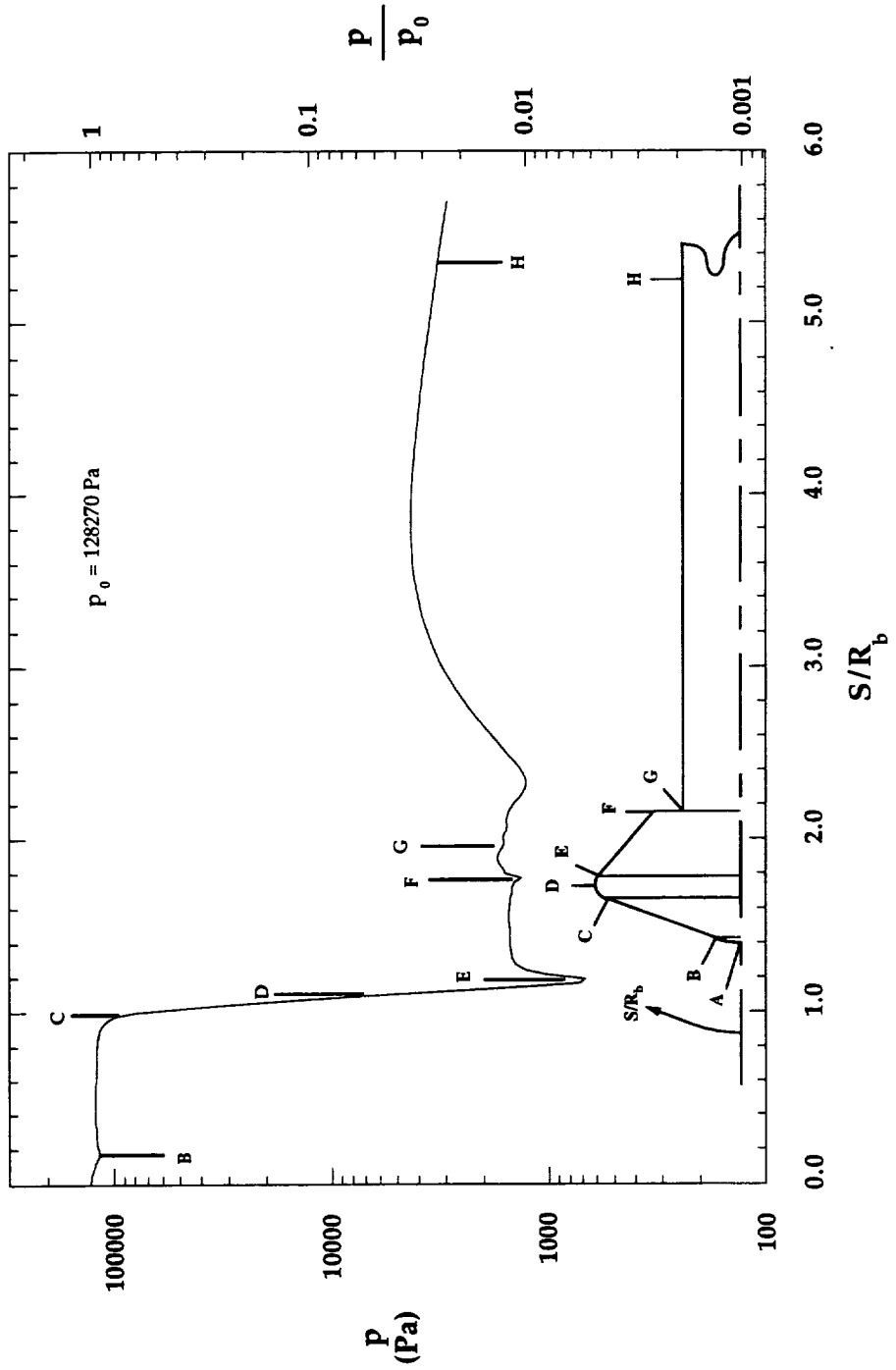

Figure 8.2.39 Computed Surface Pressure Distribution, MP-3 Configuration, HYPULSE, CO_2

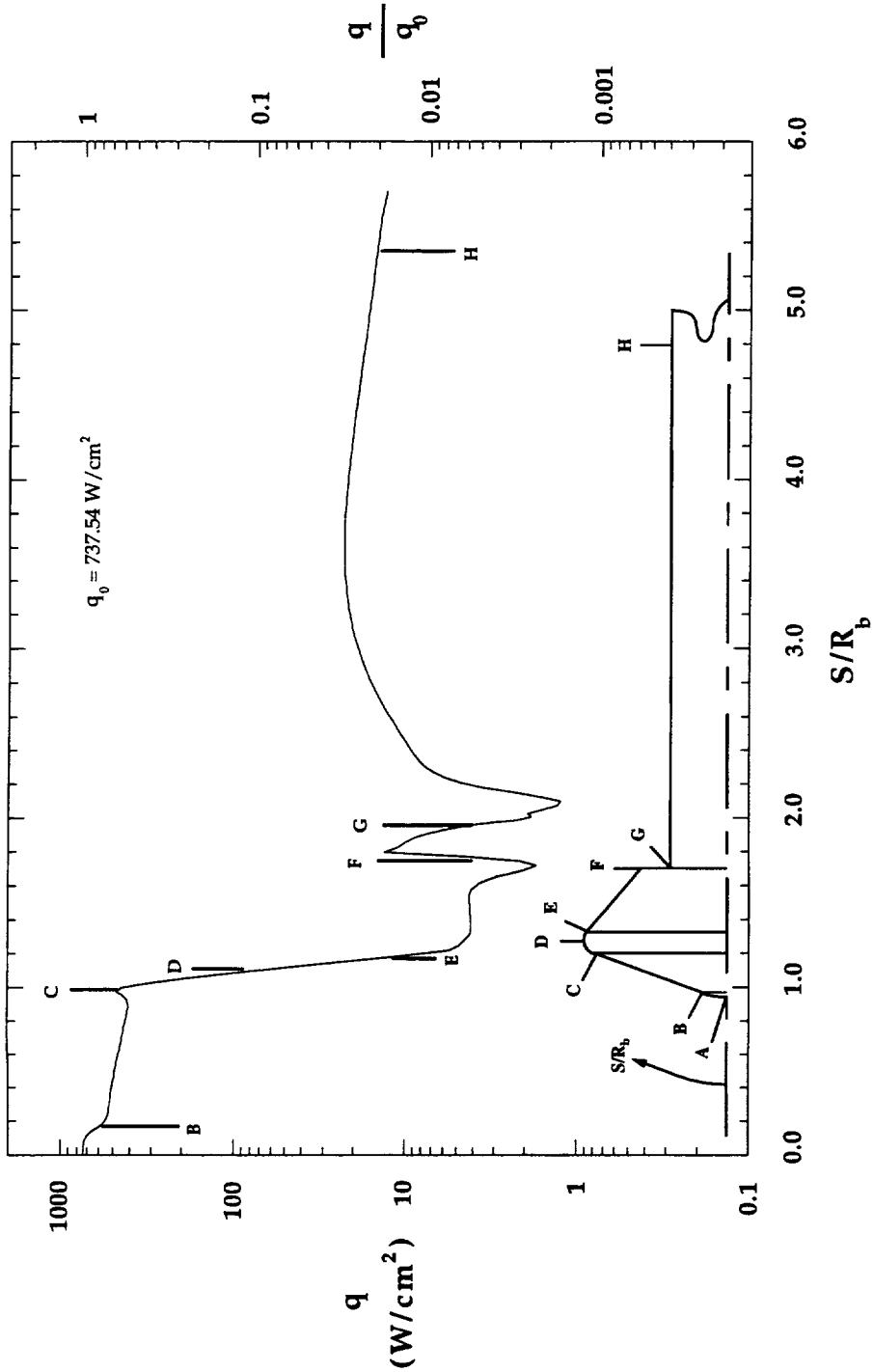

Figure 8.2.40 Computed Surface Heating Distribution, MP-3 Configuration, HYPULSE, CO_2

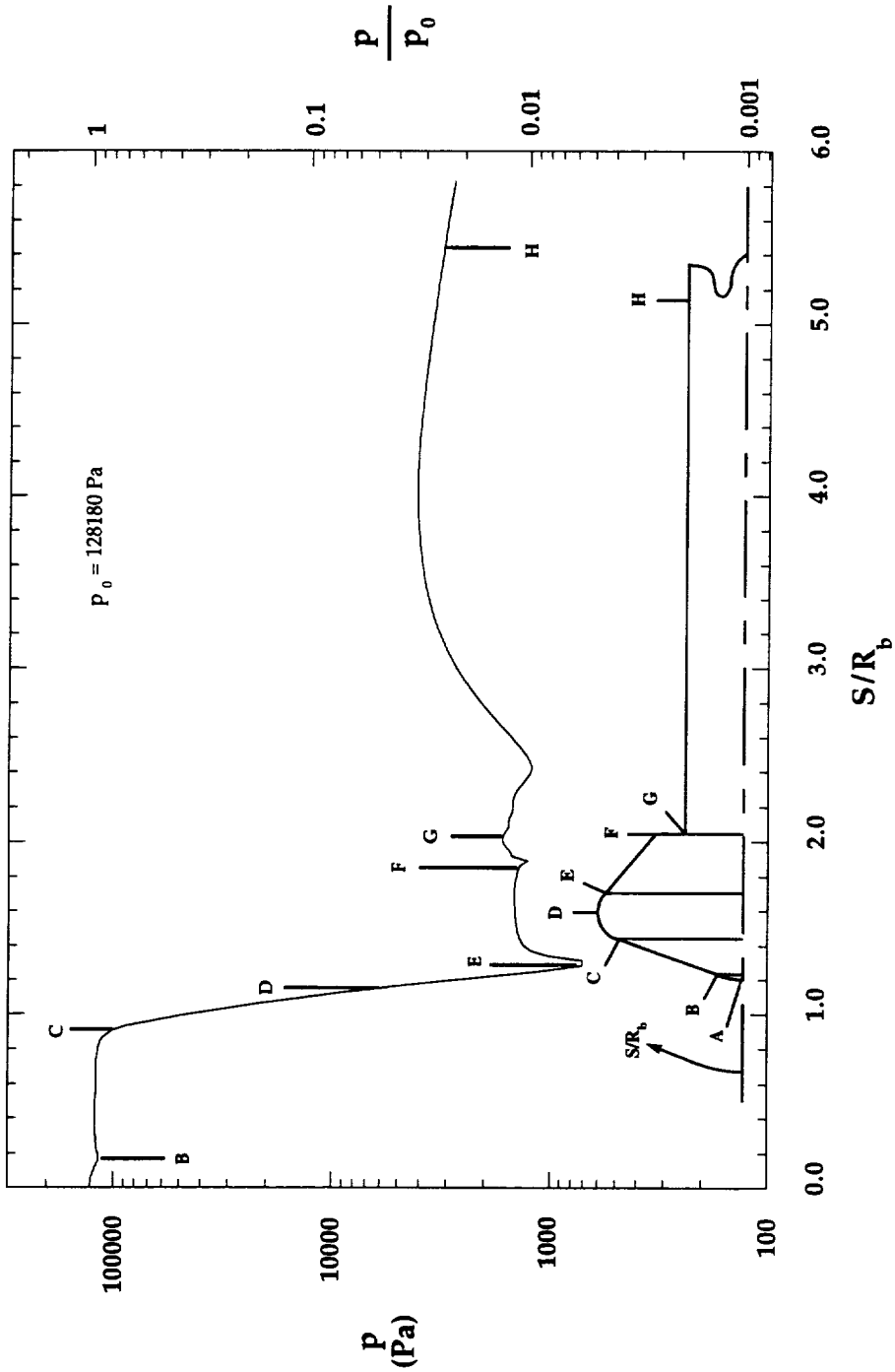

Figure 8.2.41 Computed Surface Pressure Distribution, MP-4 Configuration, HYPULSE, CO_2

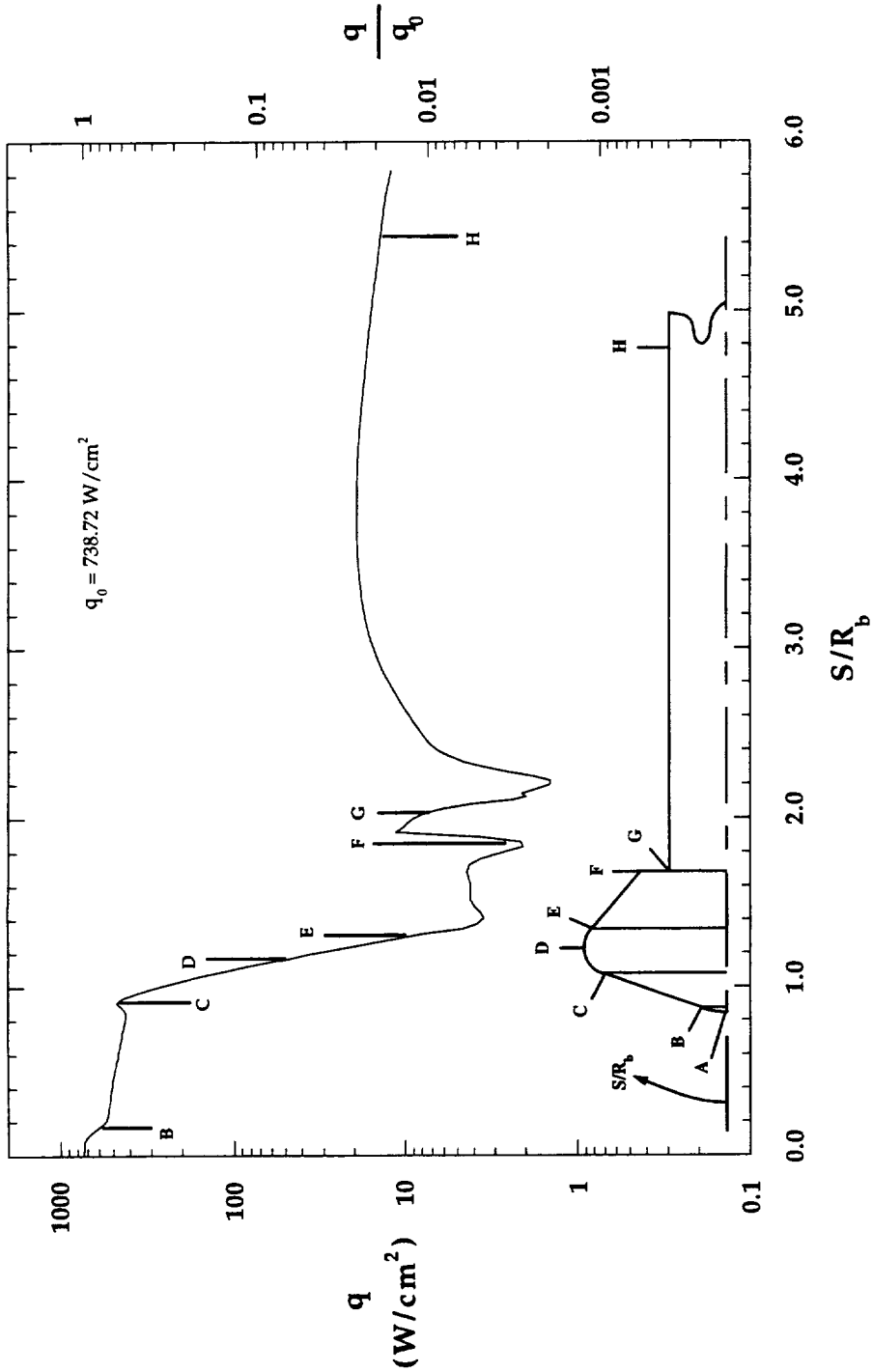

Figure 8.2.42 Computed Surface Heating Distribution, MP-4 Configuration, HYPULSE, CO_2

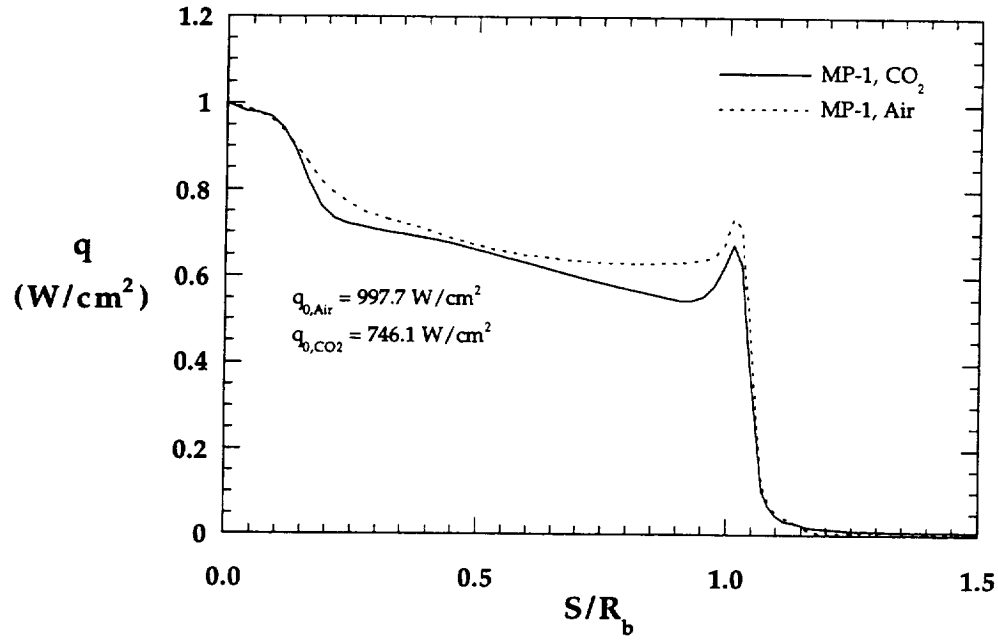

Figure 8.2.43a Test Gas Effects on Forebody Heating Distributions, MP-1 Configuration, HYPULSE

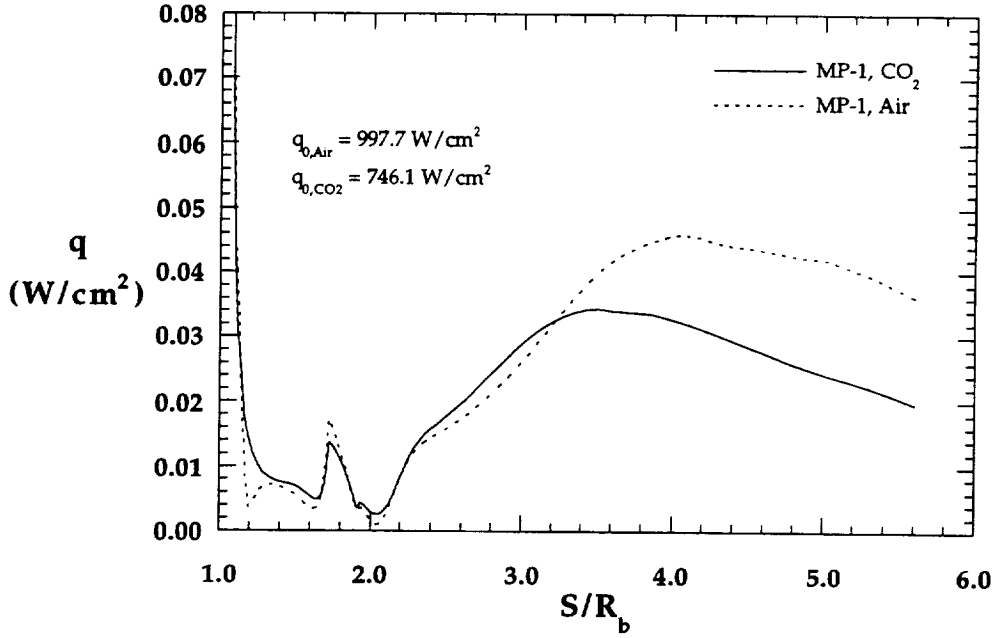

Figure 8.2.43b Test Gas Effects on Wake Heating Distributions, MP-1 Configuration, HYPULSE

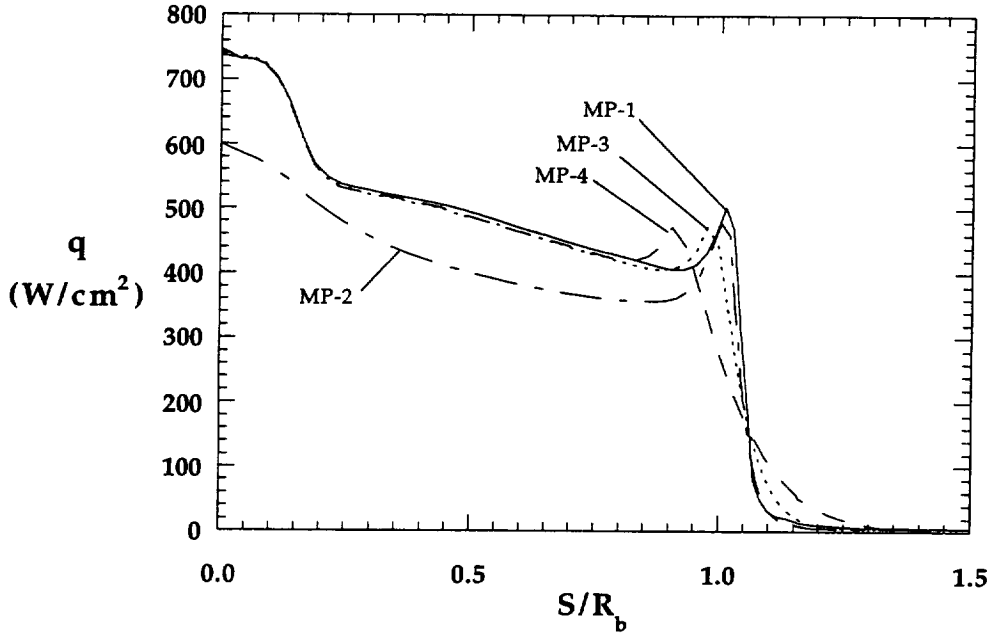

Figure 8.2.44a Configuration Effects on Forebody Heating Distributions, HYPULSE, CO_2

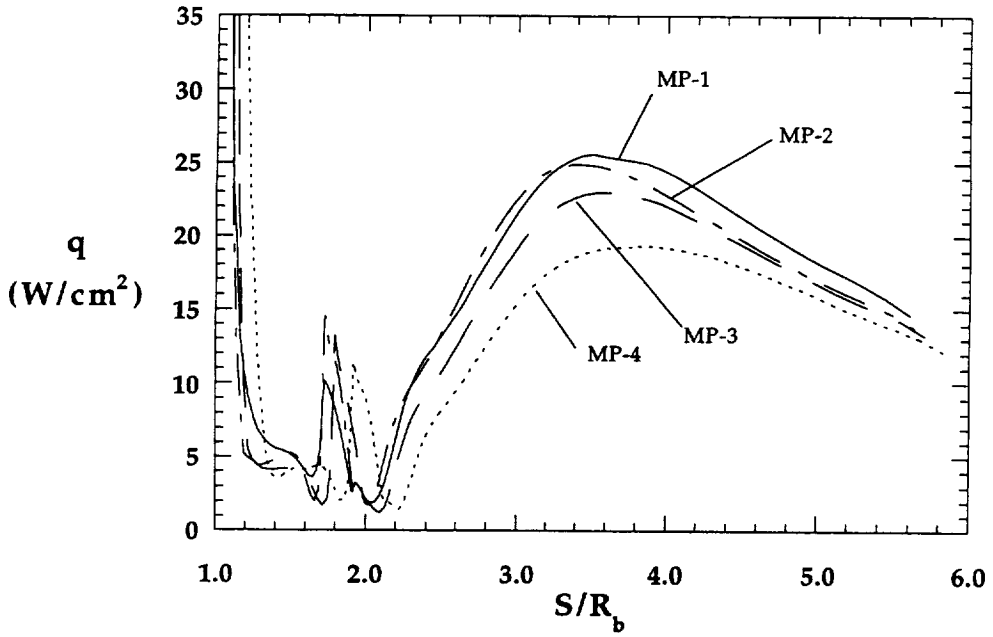

Figure 8.2.44b Configuration Effects on Wake Heating Distributions, HYPULSE, CO_2

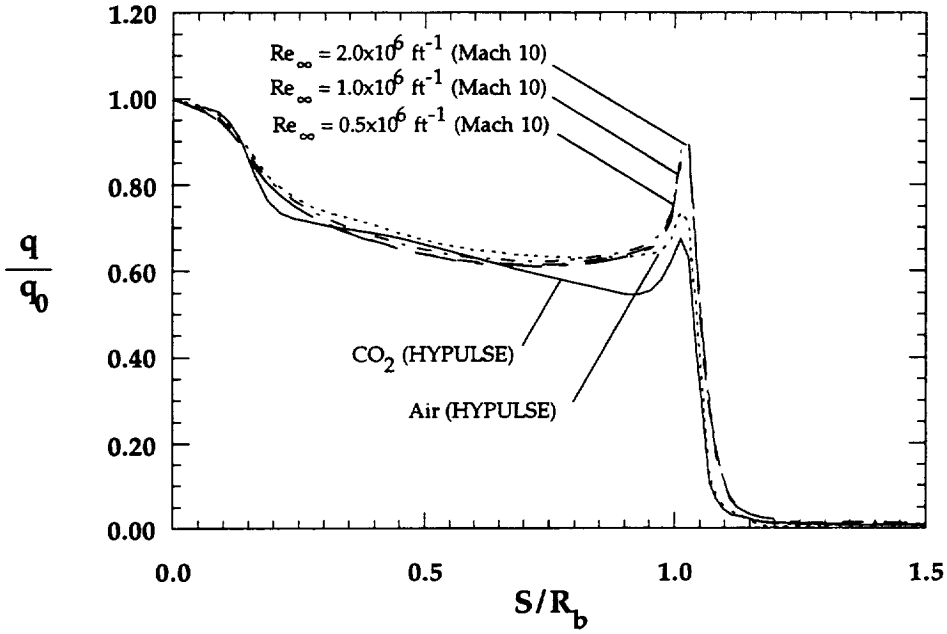

Figure 8.2.45a Comparison of Computed Mach 10 and HYPULSE Heating Distributions, MP-1 Forebody

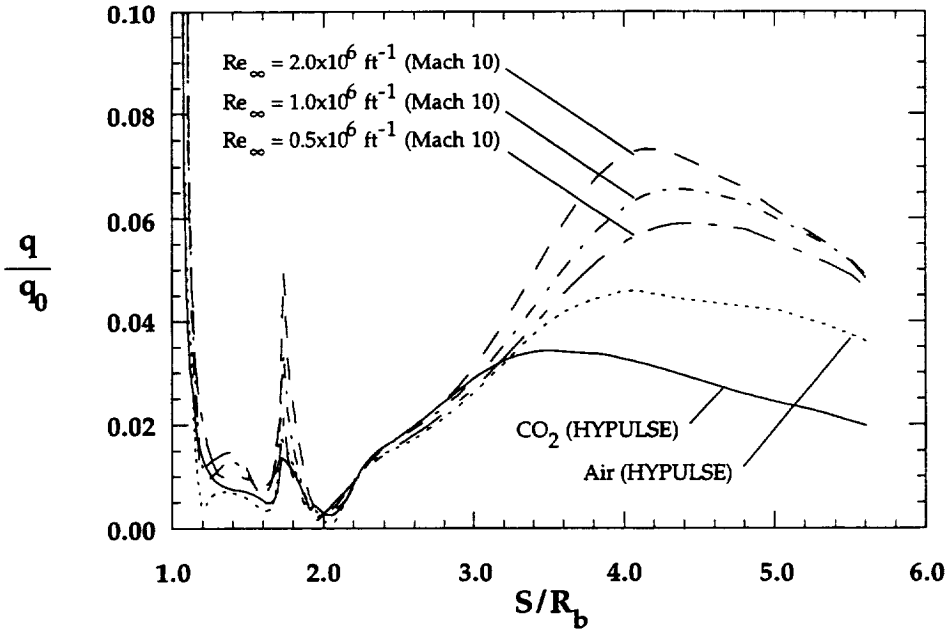

Figure 8.2.45b Comparison of Computed Mach 10 and HYPULSE Heating Distributions, MP-1 Wake

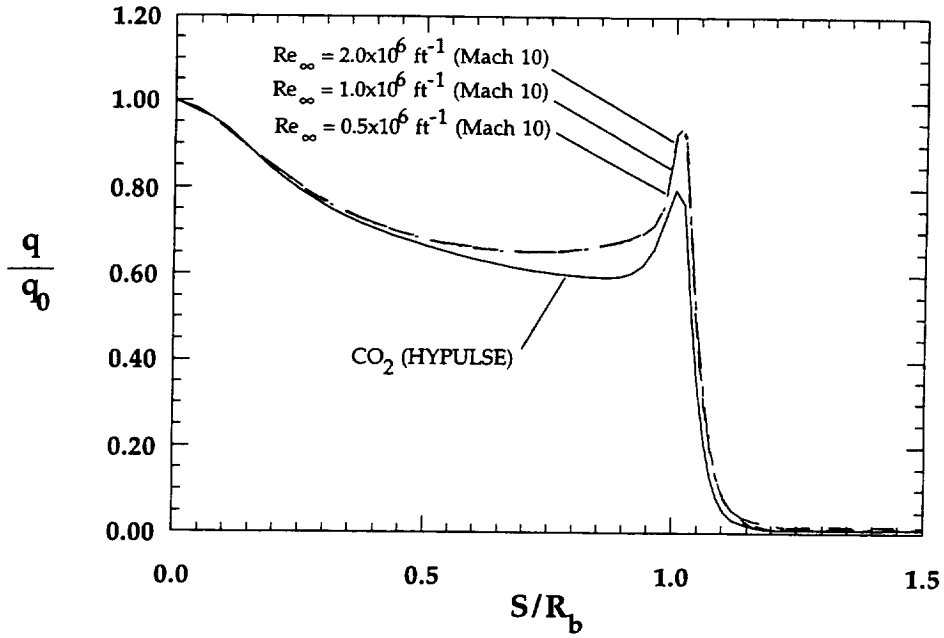

Figure 8.2.46a Comparison of Computed Mach 10 and HYPULSE Heating Distributions, MP-2 Forebody

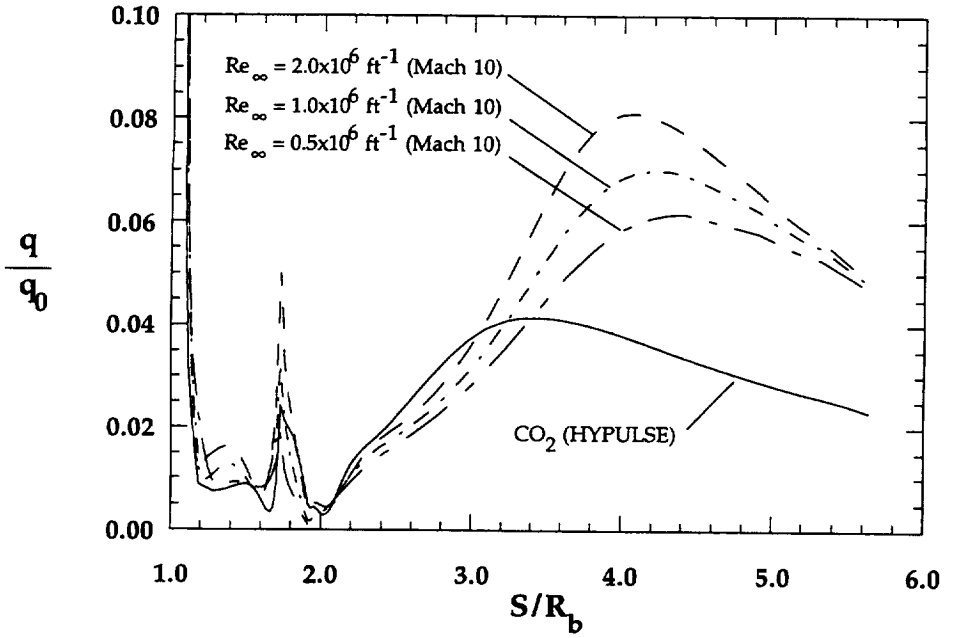

Figure 8.2.46b Comparison of Computed Mach 10 and HYPULSE Heating Distributions, MP-2 Wake

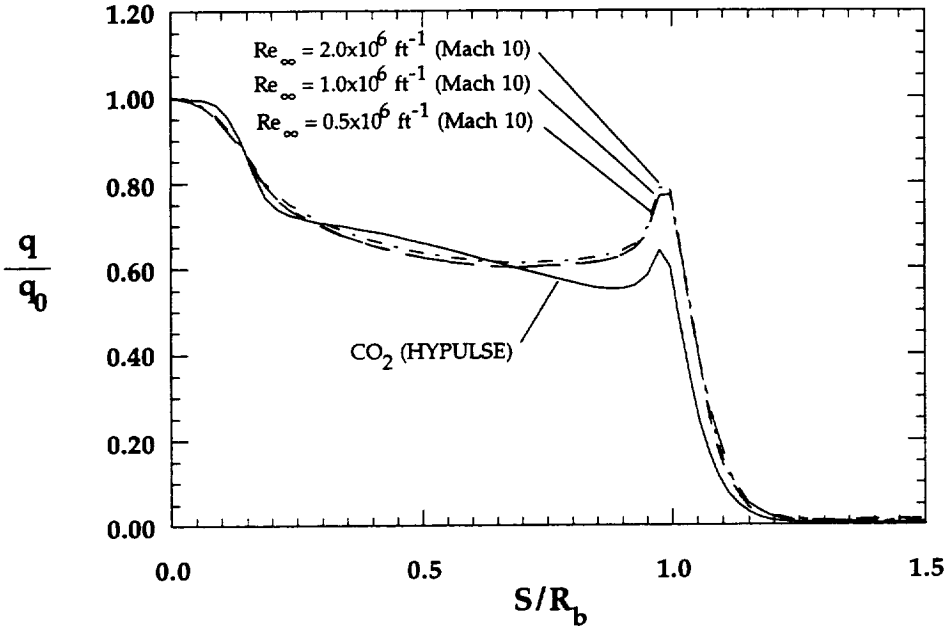

Figure 8.2.47a Comparison of Computed Mach 10 and HYPULSE Heating Distributions, MP-3 Forebody

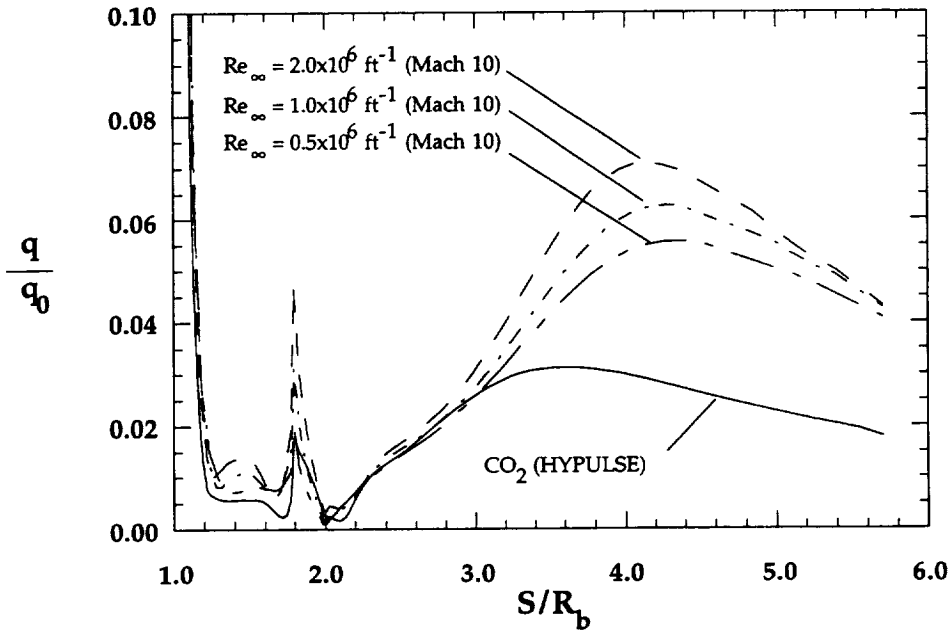

Figure 8.2.47b Comparison of Computed Mach 10 and HYPULSE Heating Distributions, MP-3 Wake

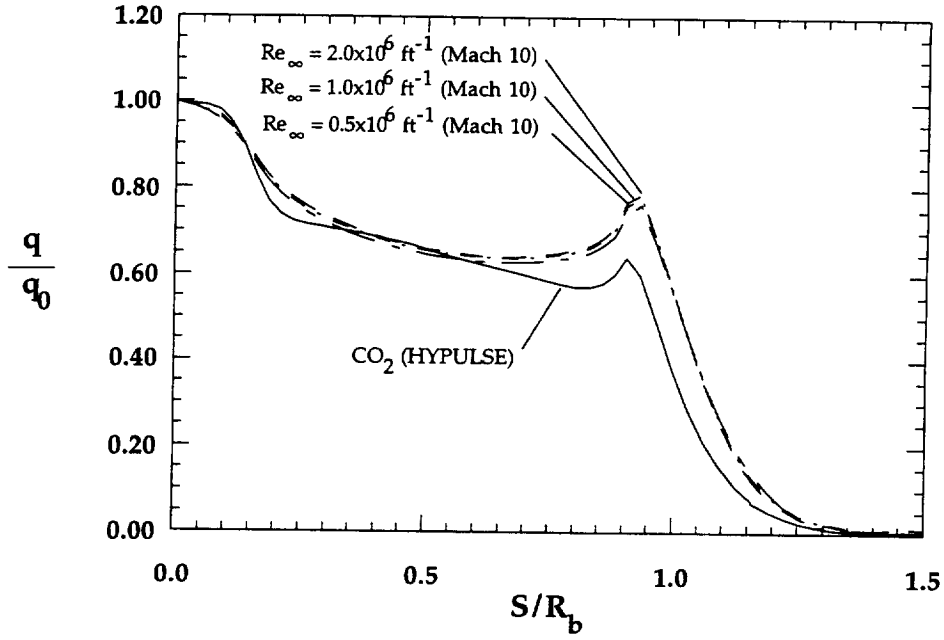

Figure 8.2.48a Comparison of Computed Mach 10 and HYPULSE Heating Distributions, MP-4 Forebody

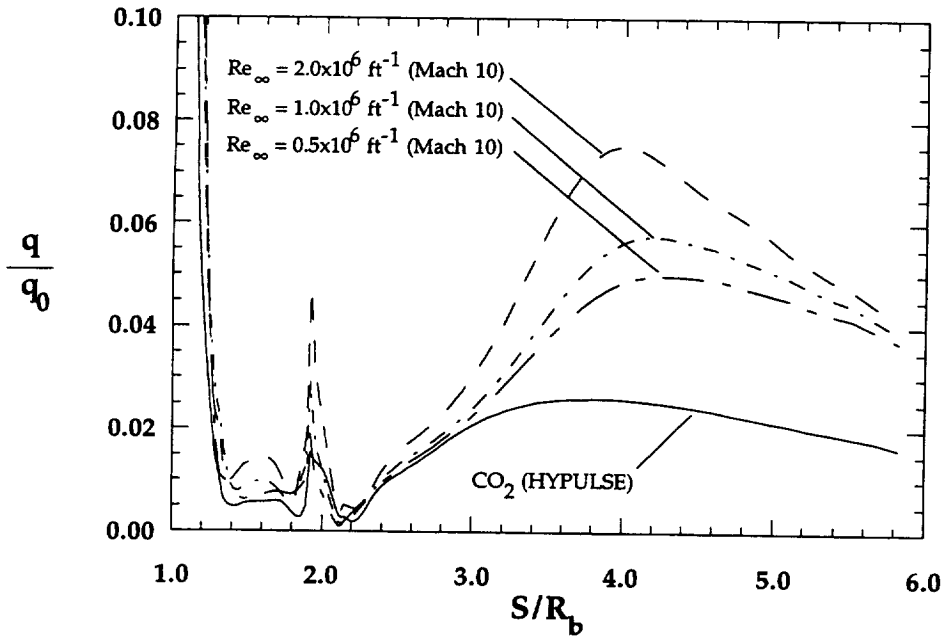

Figure 8.2.48b Comparison of Computed Mach 10 and HYPULSE Heating Distributions, MP-4 Wake

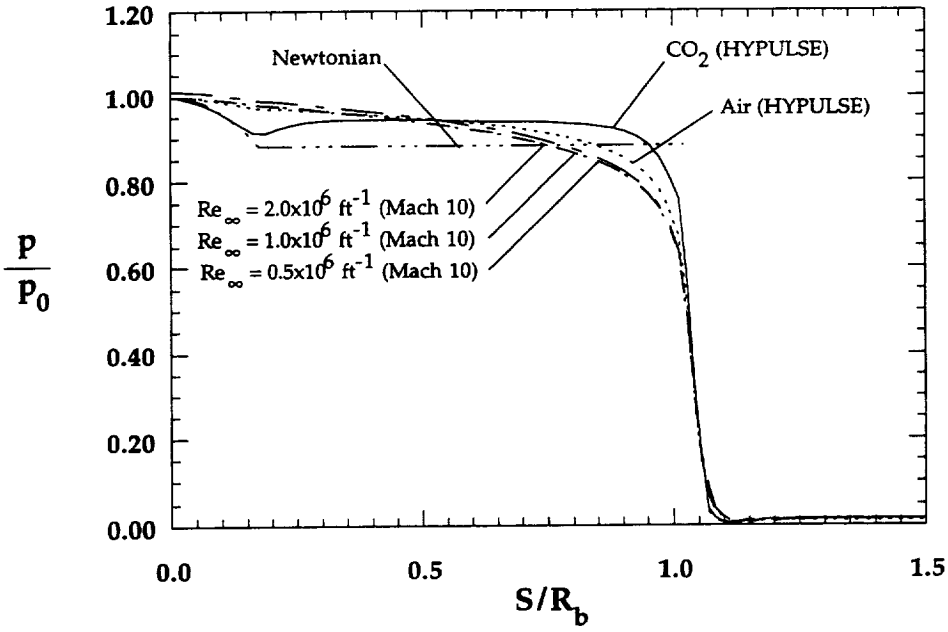

Figure 8.2.49 Comparison of Computed Mach 10 and HYPULSE Pressure Distributions, MP-1 Forebody

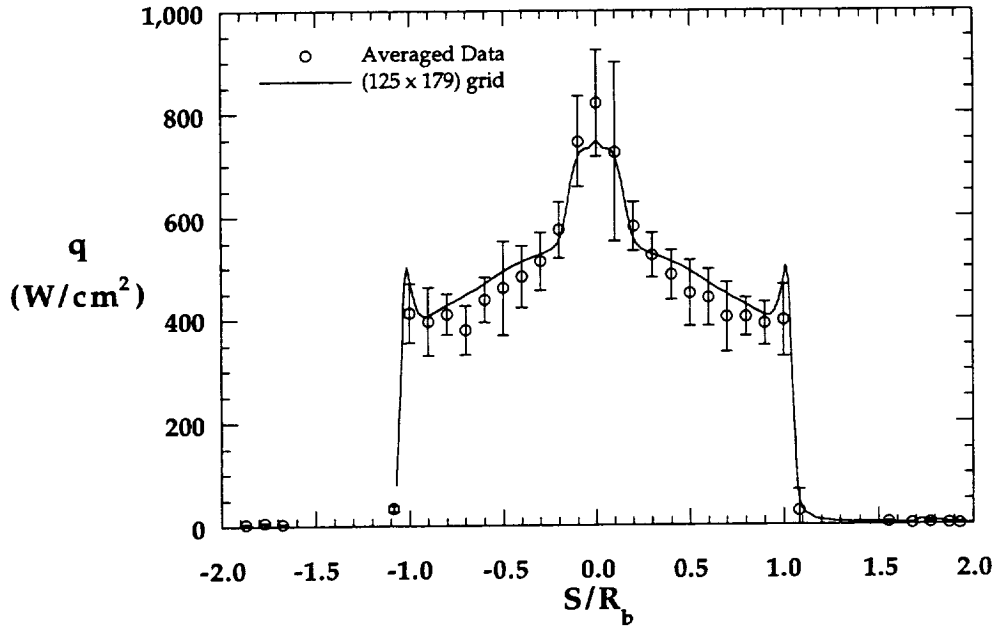

Figure 8.2.50a Comparison with Experimental Forebody Heating Distribution, MP-1 Configuration, HYPULSE, CO_2

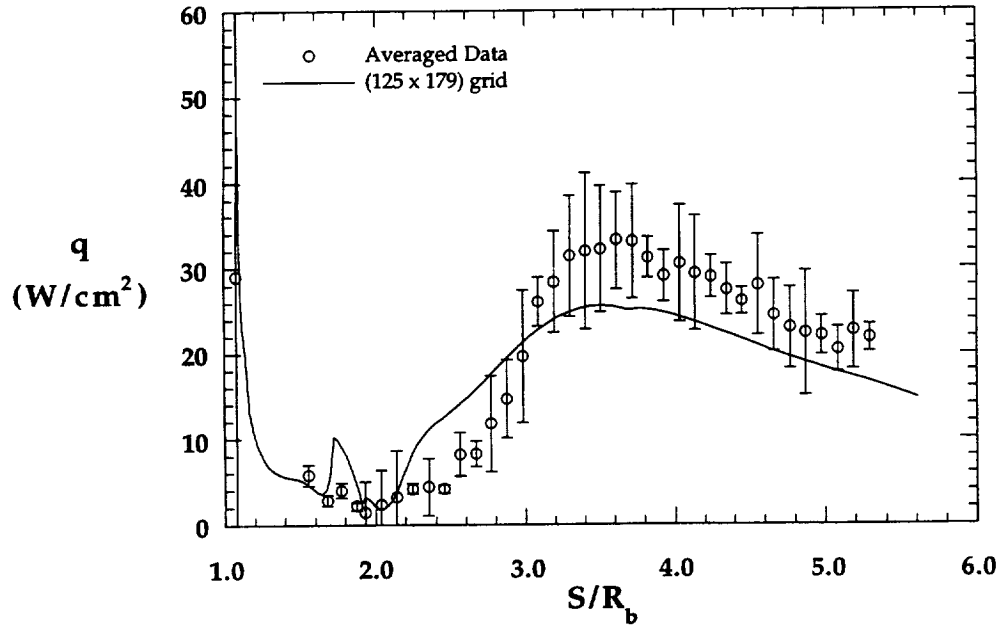

Figure 8.2.50b Comparison with Experimental Wake Heating Distribution, MP-1 Configuration, HYPULSE, CO_2

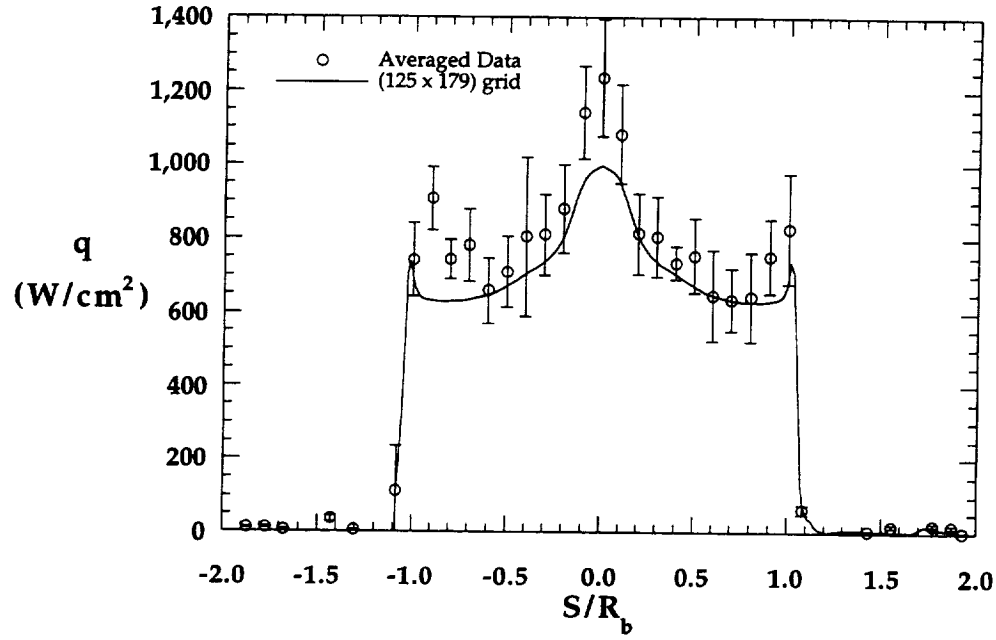

Figure 8.2.51a Comparison with Experimental Forebody Heating Distribution, MP-1 Configuration, HYPULSE, Air

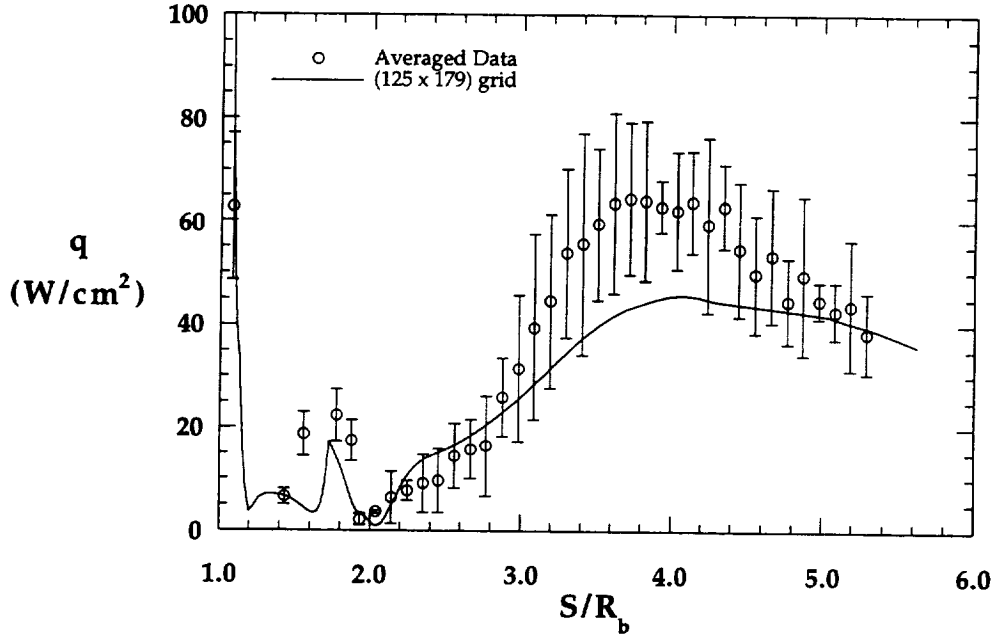

Figure 8.2.51b Comparison with Experimental Wake Heating Distribution, MP-1 Configuration, HYPULSE, Air

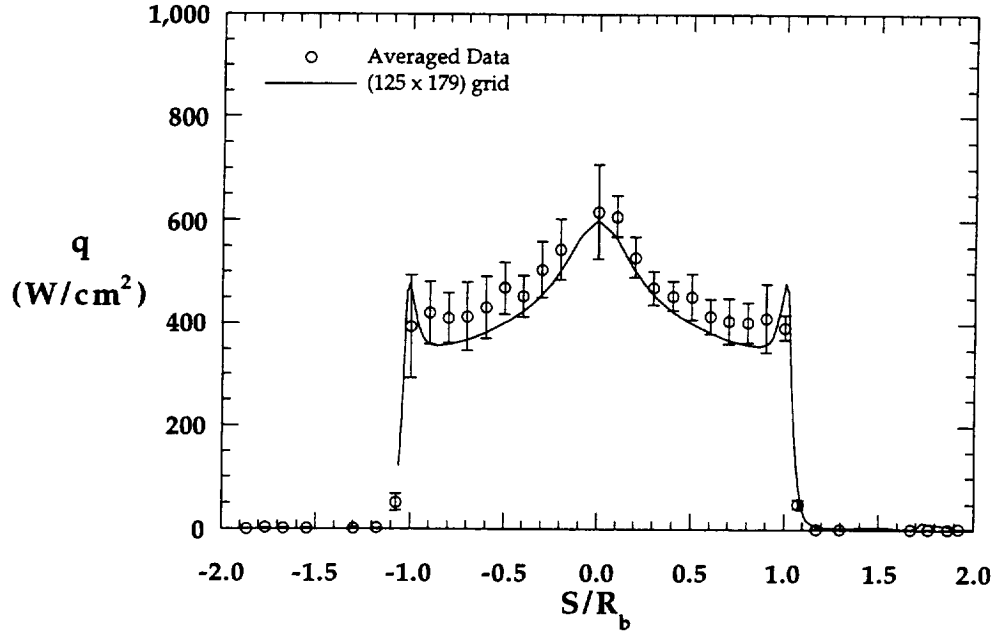

Figure 8.2.52a Comparison with Experimental Forebody Heating Distribution, MP-2 Configuration, HYPULSE, CO_2

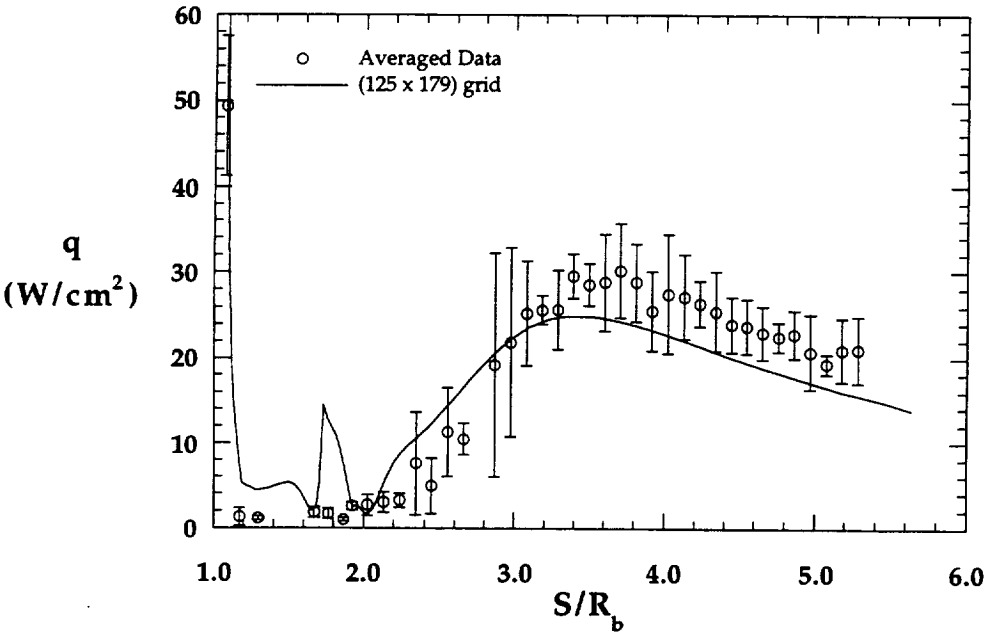

Figure 8.2.52b Comparison with Experimental Wake Heating Distribution, MP-2 Configuration, HYPULSE, CO_2

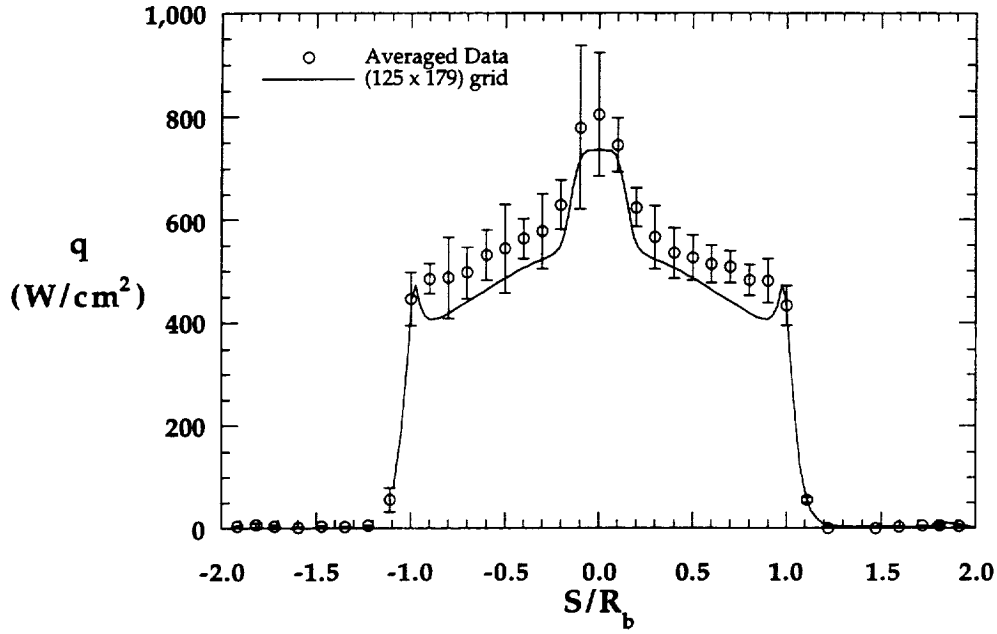

Figure 8.2.53a Comparison with Experimental Forebody Heating Distribution, MP-3 Configuration, HYPULSE, CO_2

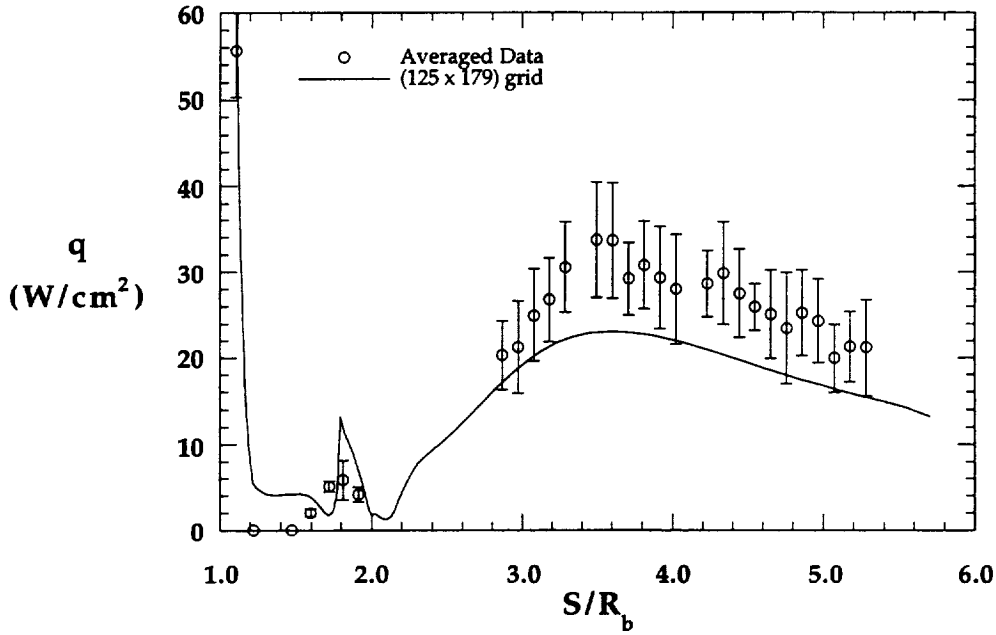

Figure 8.2.53b Comparison with Experimental Wake Heating Distribution, MP-3 Configuration, HYPULSE, CO_2

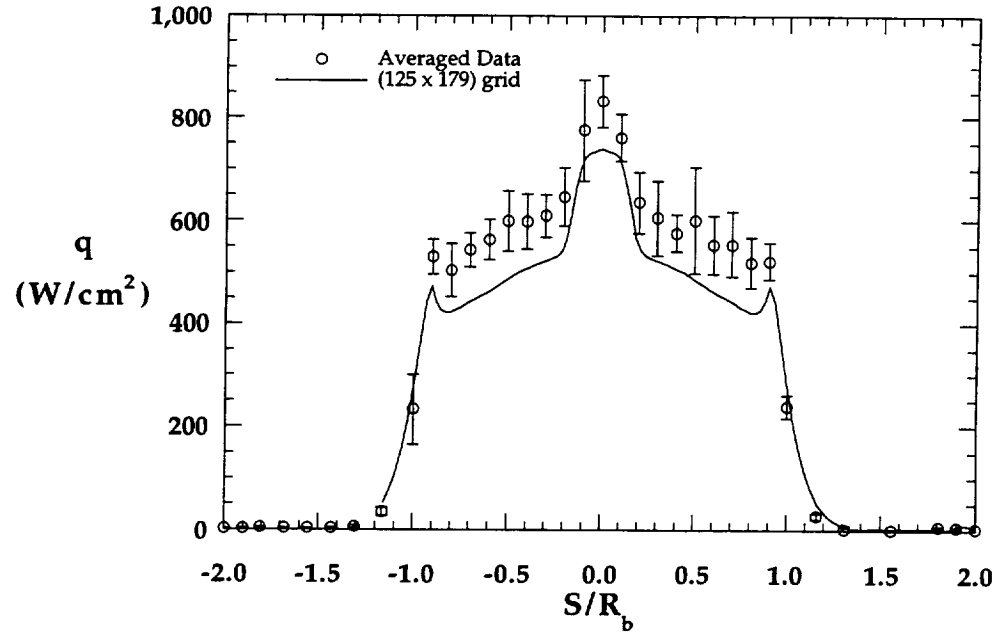

Figure 8.2.54a Comparison with Experimental Forebody Heating Distribution, MP-4 Configuration, HYPULSE, CO_2

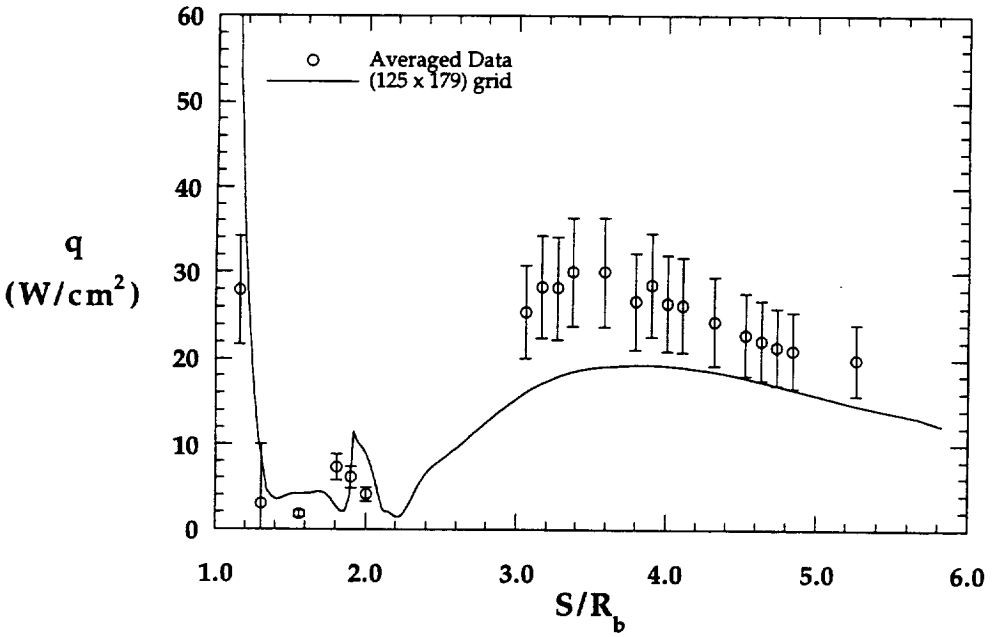

Figure 8.2.54b Comparison with Experimental Wake Heating Distribution, MP-4 Configuration, HYPULSE, CO_2

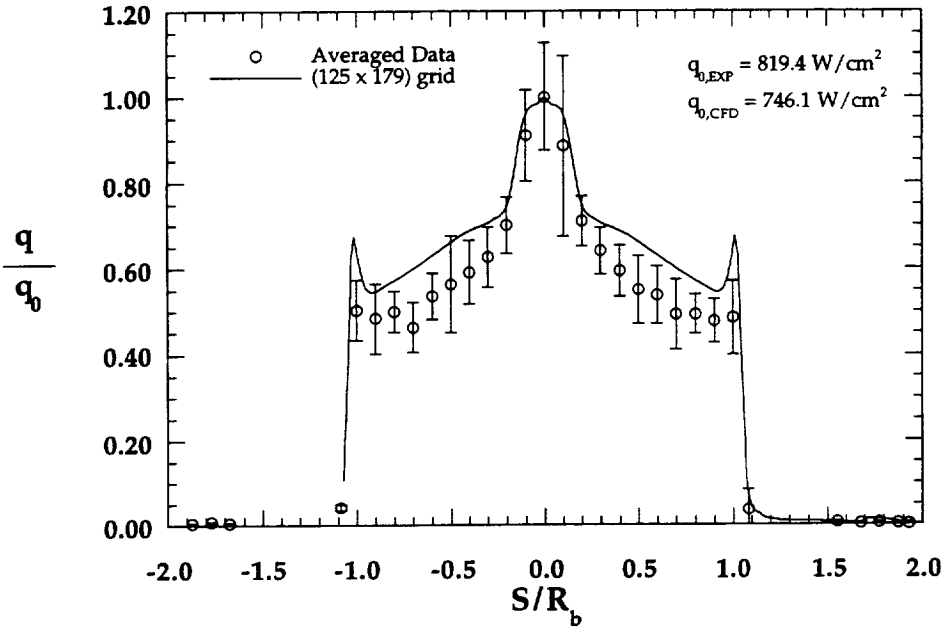

Figure 8.2.55a Normalized Comparison with Experimental Forebody Heating Distribution, MP-1 Configuration, HYPULSE, CO_2

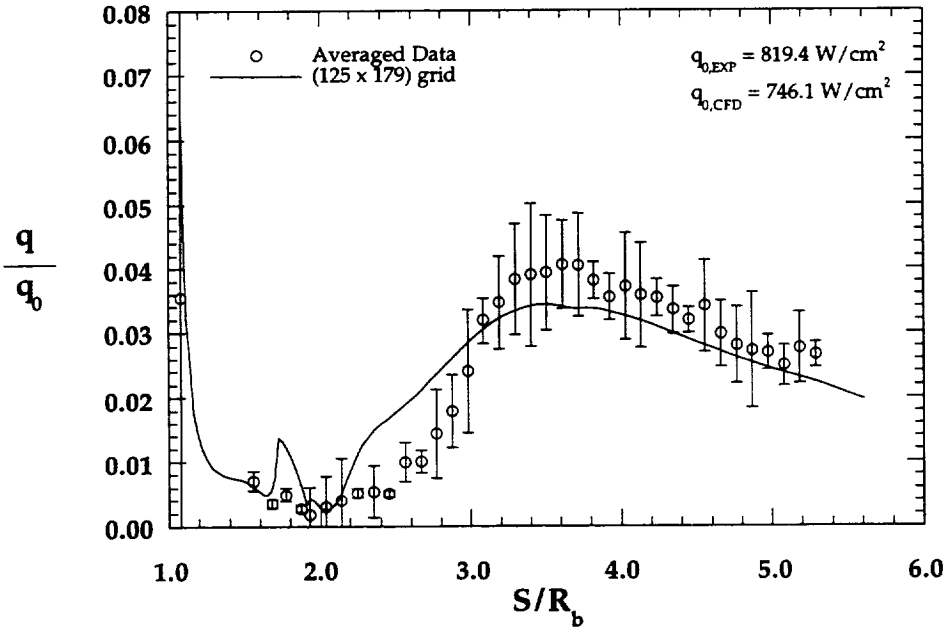

Figure 8.2.55b Normalized Comparison with Experimental Wake Heating Distribution, MP-1 Configuration, HYPULSE, CO_2

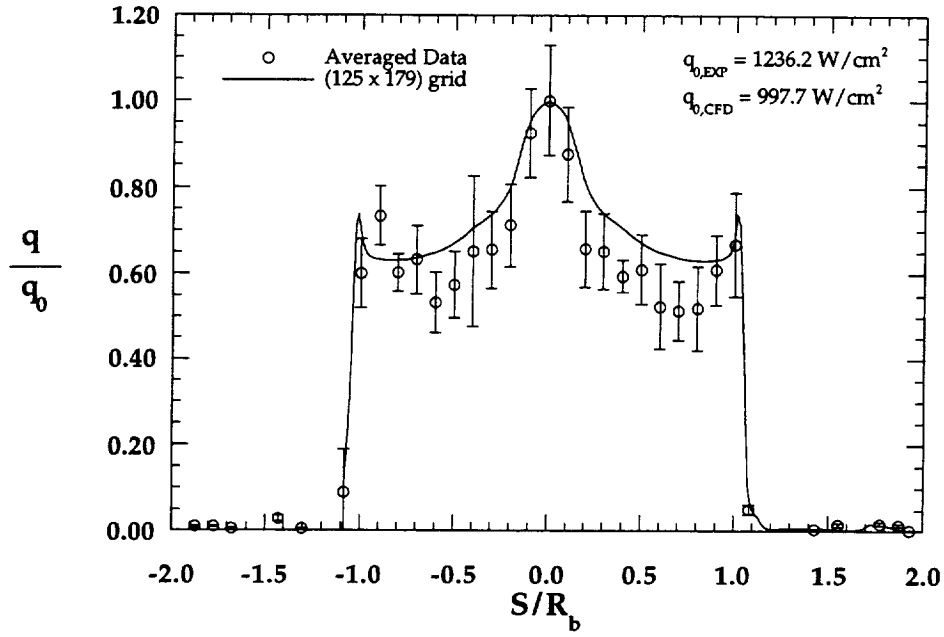

Figure 8.2.56a Normalized Comparison with Experimental Forebody Heating Distribution, MP-1 Configuration, HYPULSE, Air

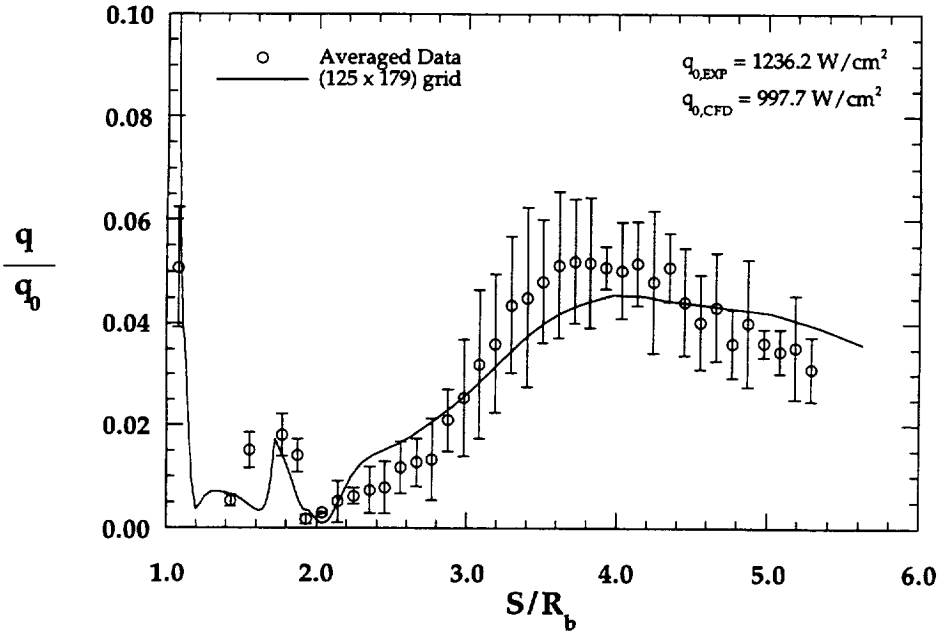

Figure 8.2.56b Normalized Comparison with Experimental Wake Heating Distribution MP-1 Configuration, HYPULSE, Air

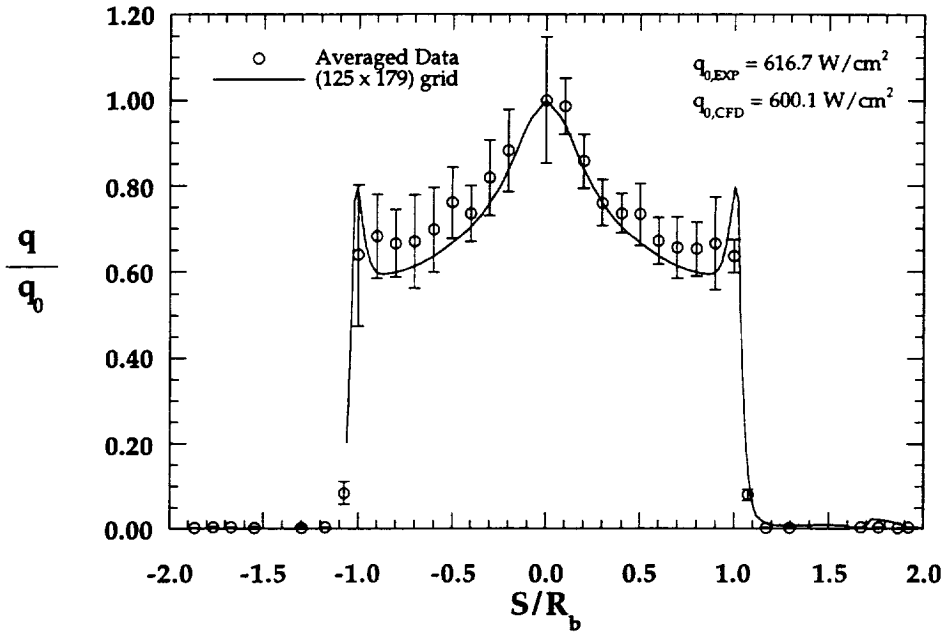

Figure 8.2.57a Normalized Comparison with Experimental Forebody Heating Distribution, MP-2 Configuration, HYPULSE, CO_2

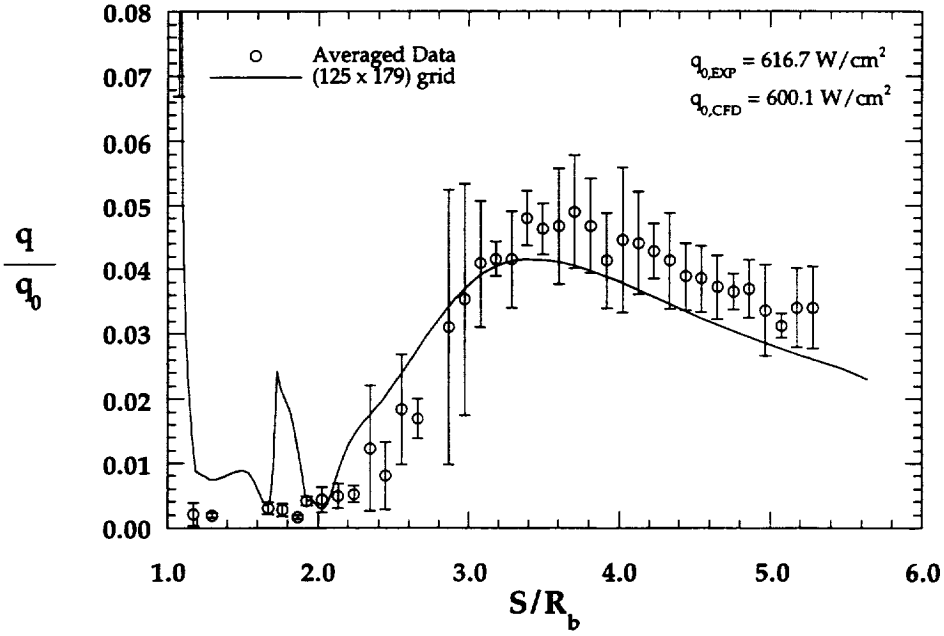

Figure 8.2.57b Normalized Comparison with Experimental Wake Heating Distribution, MP-2 Configuration, HYPULSE, CO_2

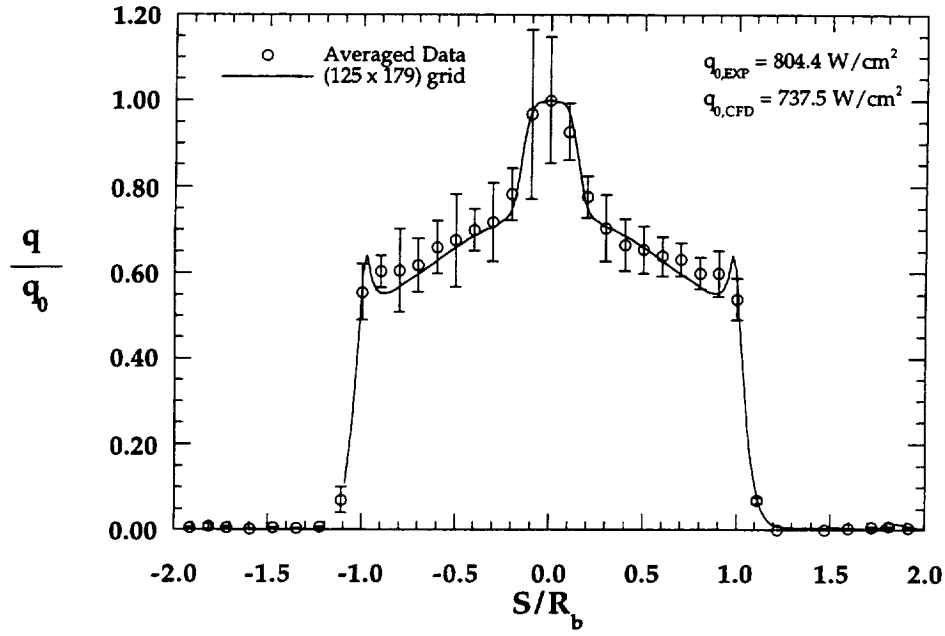

Figure 8.2.58a Normalized Comparison with Experimental Forebody Heating Distribution, MP-3 Configuration, HYPULSE, CO_2

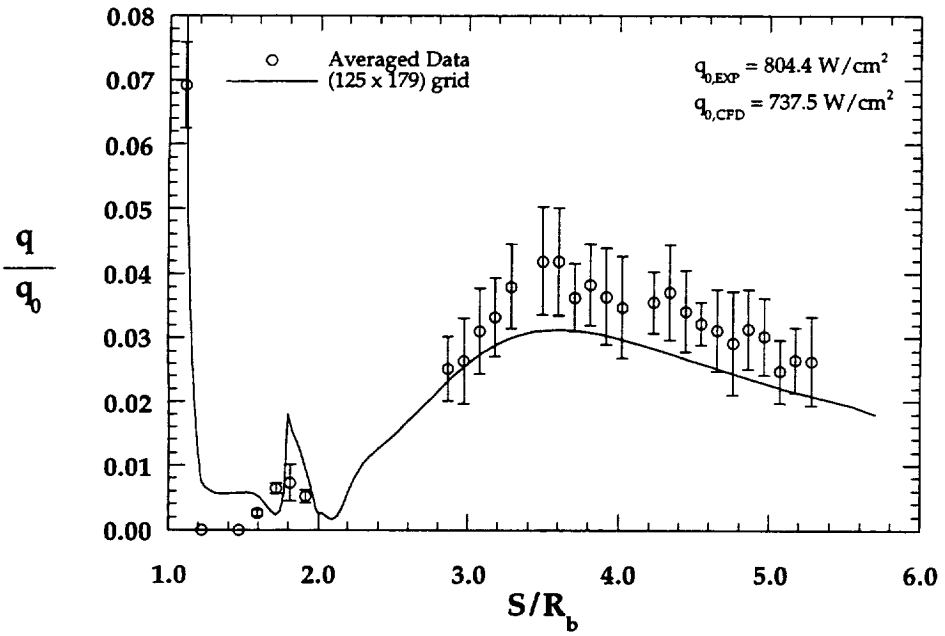

Figure 8.2.58b Normalized Comparison with Experimental Wake Heating Distribution, MP-3 Configuration, HYPULSE, CO_2

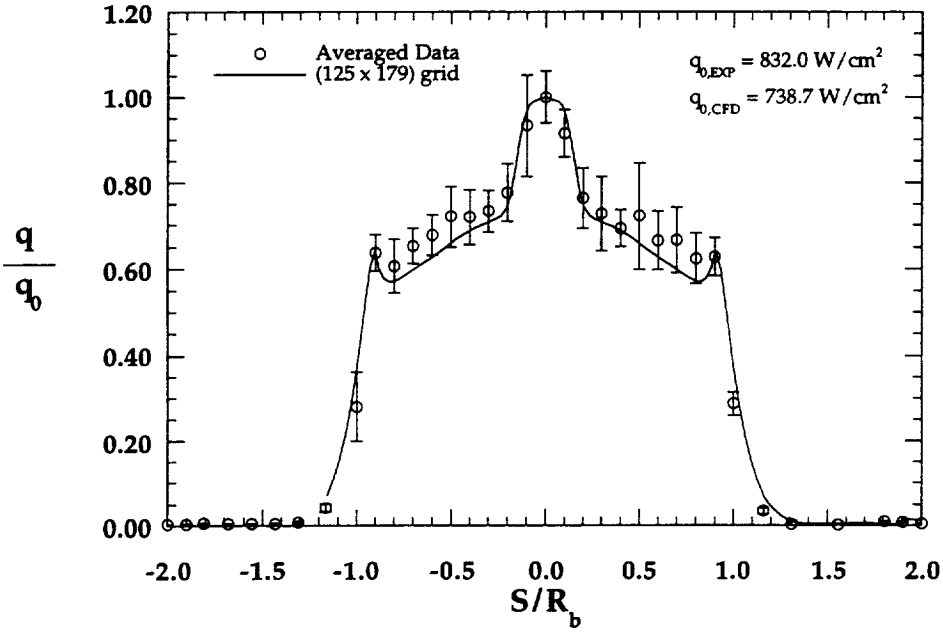

Figure 8.2.59a Normalized Comparison with Experimental Forebody Heating Distribution, MP-4 Configuration, HYPULSE, CO_2

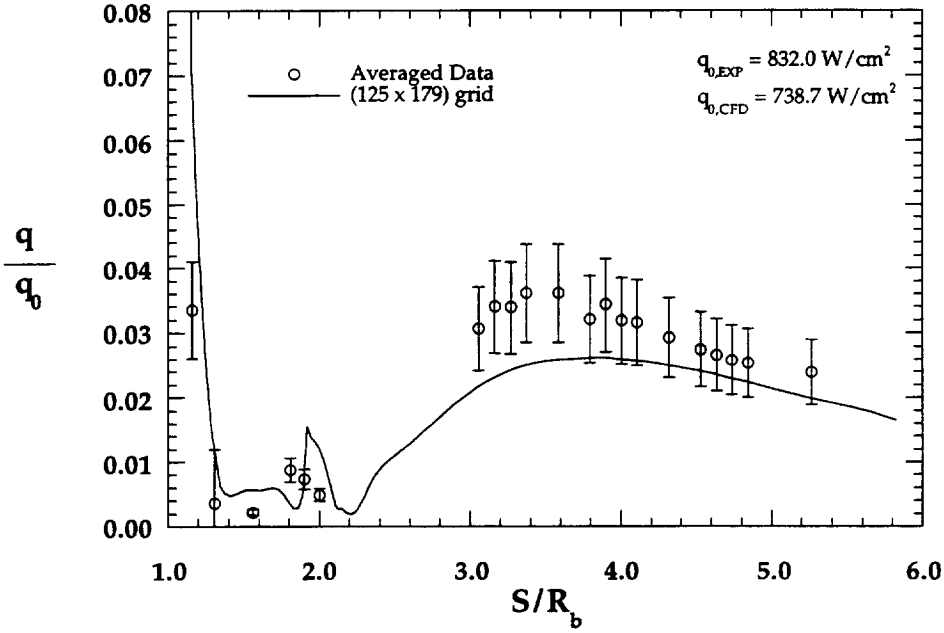

Figure 8.2.59b Normalized Comparison with Experimental Wake Heating Distribution, MP-4 Configuration, HYPULSE, CO_2

CHAPTER 9
SUMMARY, CONCLUSIONS, AND RECOMMENDATIONS

The aerothermodynamic environment of a Mars entry vehicle configuration has been investigated through both experimental and computational methods. Special emphasis was placed on measurements and computations for the flow in the wake of the vehicle because the structure of the wake flow dictates the payload size, payload positioning and afterbody shielding requirements for the vehicle. Thorough understanding of this wake flow environment is becoming more important than ever because of the current trend toward the use of aerobraking during planetary entry, which increases the severity of aerothermodynamic loads on a spacecraft.

While the reliability of current experimental and computational techniques has been demonstrated for attached forebody flows, there is at present much less confidence in their performance with regard to the modeling of separated wake flows. With the aim of increasing the confidence level in wake flow analyses, the present study has had two purposes: first, to demonstrate that a reliable data base on blunt body wake (and forebody) flows can be generated using modern, fast-response instrumentation in both perfect-gas and high-enthalpy facilities, in which the operating characteristics of the facilities are well understood and which have been proven to produce repeatable data. Second, to demonstrate that when combined with state-of-the art grid generation and grid adaptation techniques, computational fluid dynamics simulations can be used to predict both forebody and wake flow characteristics at the test conditions of the experimental facilities to within the accuracy of the experimental data.

The entry vehicle configuration dealt with in this work was derived from that of the NASA Mars-Pathfinder probe, and had a 70 deg sphere-cone forebody with a 40 deg cone-frustrum afterbody. The nose to forebody radius ratio of this geometry was 0.5, and the corner to forebody radius ratio was 0.05. Three

additional parametric configurations, a geometrically matched hyperboloid and two 70 deg sphere-cones with 0.1 and 0.2 corner to forebody radius ratios, were also studied in this research. Heat-transfer test models of these configurations were fabricated from Macor ceramic, and both the forebodies and afterbodies of the models were instrumented with thin-film resistance data. The stainless steel stings on which the models were supported carried Macor inserts with additional thin-film gages.

Experimental heat-transfer testing was first conducted in a perfect-gas air hypersonic wind tunnel. Aerothermodynamic data were obtained for each of the four configurations at Mach 10 across a Reynolds number range of 0.5 to 2.0 $x10^6$ ft^{-1} and angles-of-attack of 0 to -20 deg. Freestream conditions for these tests were demonstrated to be repeatable to within ±2%, while the overall uncertainty in the aerothermodynamic data was estimated to be on the order of 7-8%. This uncertainty was due mainly to uncertainties in the thermal properties of the Macor ceramic from the models were constructed.

For all configurations, normalized forebody heating distributions displayed no influence from the freestream Reynolds number, but a strong dependence was observed for the sting and to a lesser extent for the afterbody. The effect on the wake of increasing Reynolds number was to cause an increase in the normalized heating on the sting and to cause the peak heating point on the sting to move upstream toward the base of the model. That suggested that the wake vortex shrunk as the Reynolds number increased; this was confirmed through surface oil flow pattern photographs, which showed that the free shear-layer reattachment point on the sting did move upstream as the Reynolds number was increased. This behavior is contrary to theoretical predictions for laminar wakes, and suggested transitional/turbulent wake flow. A much smaller movement of the separation point on the afterbody upstream toward the forebody corner was also noted in those photographs.

Data from the three sphere-cone geometries indicated that the influence of the corner radius on the wake flow was not much greater than the experimental uncertainty in the tests. However, a slight decrease in the magnitude of the wake heating peak with increasing corner radius could be observed at all Reynolds number, while its location remained unaffected. Wake heating data for the baseline 70 deg sphere-cone

geometry and the hyperboloid were nearly identical. With respect to the forebody stagnation point heating, peak sting heating varied from 8% of the stagnation point heating at the lowest Reynolds number to 15% at the highest for the baseline configuration.

On the forebody, gage spacing at the corner was too great to completely resolve the narrow corner heating peaks; however, corner heating peaks appeared to broaden and decrease in magnitude as the corner radius was increased. The sphere-cone forebody distributions were otherwise identical. For the hyperboloid geometry, heating as much as 8% lower than for the sphere-cones was observed around the stagnation point, but away from the stagnation point the hyperboloid heating distributions rapidly approached those of the sphere-cones.

Attempts were made to trip the forebody boundary and thus produce a definitively turbulent wake flow. No effect could be seen on the wake flow in the tests in which tripping was attempted, and it was concluded that the freestream Reynolds numbers were too low for forebody transition to occur even with tripping. However, based on the behavior of the wake heating data, it was tentatively concluded that irrespective of attempts to trip the forebody flow, transition in the wake did indeed occur at or around the shear layer reattachment point on the sting, and that the reattached boundary layer on the sting was transitional or turbulent. However, the turbulence ingested into the wake vortex was probably dissipated by the acceleration of the flow in the direction toward the model base from rest at the reattachment stagnation point, and so the behavior of the vortex was not greatly dissimilar to that of a fully laminar flow.

Heat-transfer tests were next conducted in both air at Mach 7.9 and CO_2 at Mach 9.7 in the high-enthalpy expansion tube. The baseline geometry and the hyperboloid were tested at angles-of-attack of 0 and -4 deg in both air and CO_2, and the other two sphere-cone configurations were tested in CO_2 at 0 deg angle-of-attack. The run-to run variations of the individual freestream properties in this facility were found to be between 1 and 10%. The greatest variation was in the freestream static pressure, which varied by 9-10%, while the freestream density and total enthalpy varied by only 1-4%. The uncertainty in the aerothermodynamic data was estimated to be 11-12% for the forebody data and 17-22% for the wake data.

Wake uncertainties were higher because the extremely low wake heating rates resulted in a higher signal-to-noise ration in the data.

Another cause for the higher wake uncertainties was the finite time required for the wake flow to become fully established, which resulted in a smaller time-sample of data being available for the wake than for the forebody, where flow establishment was not a concern. In order to ensure that the reported wake flow data were not biased by the establishment process, a criterion for determining when the wake flow becomes fully established was derived. Application of this criterion showed that the wake flow required approximately 75% of the total available test time to become fully established.

Owing to the higher experimental uncertainties, no definitive conclusions could be reached concerning configuration effects on the wake heating. However, it appeared that the baseline sphere-cone and hyperboloid distributions were closely matched, while those of the larger corner radius sphere-cone geometries showed a small decrease in peak sting heating. Peak sting heating for the baseline geometry was 3-4% of the stagnation point heating in both gases, and the peak occurred considerably further upstream on the sting than in the perfect gas tests at higher Reynolds numbers. This comparison lent further weight to the hypothesis that the perfect-gas wake flow was transitional/turbulent, whereas for the high-enthalpy tests it was concluded that the wake flow remained laminar.

On the forebody, the larger radius sphere-cone models demonstrated noticeably higher heating upstream of the corner than on the baseline geometry, which was in violation of the theoretically expected behavior as the sonic line is located at the corner. However, it was noted there was a definite bias in the flow conditions between these two sets of tests, and the discrepancies were attributed to this bias. Aside from this bias, it was also noted that the corner heating peaks became lower and broader as the corner radius was increased. The hyperboloid distributions in both CO_2 and air were up to 25% lower than the sphere-cones, and the differences extended almost to the forebody corner, which was a much larger configuration influence than observed in the Mach 10 tests.

Computational fluid dynamics solutions were generated using an axisymmetric/2D laminar Navier-

Stokes solver with perfect-gas and thermochemical non-equilibrium Mars and Earth atmosphere models. Computations were performed for freestream conditions equivalent to the operating conditions of the experimental facilities. Wall temperatures were fixed at 300 K, and a non-catalytic surface boundary condition was specified for the high-enthalpy conditions. Computational grids for these cases were constructed using an elliptical grid generation procedure. After computation of initial solutions, grids were adapted to the bow shock and wake free shear layer, and grid points were clustered within the recirculation region using algebraic grid manipulation techniques.

Computations were first carried out for the Mach 10 perfect gas test conditions. A grid resolution and grid adaptation study revealed that while the forebody computations were relatively insensitive to the grid structure, the wake flow computations were strongly dependent on normal point spacing and on alignment of the grid with the free shear layer. These factors are much more important in the wake because the entire wake recirculation zone and free shear layer are dominated by viscous forces. Therefore, grid spacing such as typically seen in attached boundary layers must be employed and the grid lines must be aligned with the shear layer in order to limit the numerical dissipation introduced into the computations. It was shown that computations carried out on a poorly constructed grid severely over-estimated the wake heating and under-predicted the size of the wake vortex. For the Mach 10 perfect-gas cases, it was determined that a shear-layer adapted grid of 125 streamwise by 357 normal points was required in order to obtain a valid computational solution.

Forebody computations for the perfect-gas cases were validated by the experimental data: in the computations, no Reynolds number effects were observed on the forebody, stagnation region heating for the hyperboloid was significantly lower than for the sphere-cones; and the corner heating peaks became broader and decreased in magnitude as the corner radius was increased. Computed forebody heat-transfer rates agreed with the experimental data to within less than the estimated uncertainty for all configurations.

In the wake, the character of the predicted heat-transfer distributions was considerably different than that of those obtained from the wind tunnel tests. Peak heating rates for the baseline configuration varied

with Reynolds number to from 6% to 8% of the stagnation point values, as compared to the 8% to 15% seen in the experimental data. Furthermore, examination of the computed streamlines revealed that while the computed wake vortex sizes agreed reasonably well with the experimental oil flow patterns, there was a small but definite growth in the computed size of the wake vortex with Reynolds number, whereas the oil flow patterns showed that the vortex decreased in size. However, the predicted and experimental flow separation points were close and both demonstrated the same upstream movement with Reynolds number. Also, the computed heating rates within the wake vortex were in much closer agreement with those from the experimental data. These comparisons indicate that the laminar CFD solutions accurately reproduce the actual flow behavior of the shear layer up the reattachment region, at which point transition occurs. The laminar predictions then become increasingly inaccurate with distance downstream from the reattachment point because the growing turbulence in the experimental wake flow is not modeled in the laminar computations. However, the shear layer turbulence ingested into the vortex is dissipated by the acceleration of the vortex flow from rest back toward the base, and so the laminar solutions are fairly accurate within this region.

Grid studies for the high-enthalpy cases revealed the same extreme sensitivity of the wake solutions to grid structure as for the perfect-gas cases, while the forebody solutions were again relatively insensitive to grid structure. Because of the additional computational requirements of the nonequilibrium thermochemical model employed for these cases, the maximum grid resolution was limited to 125 streamwise by 179 normal points. This was expected to be sufficient for the forebody flow and for the wake flow downstream of the reattachment point, but it was estimated that heating rates within the recirculation zone could be over-predicted by up to 10% due to the lesser number of normal grid points used for the high-enthalpy cases.

For the high-enthalpy test conditions, the forebody computations again were in agreement with the experimental data, although the computed heating distributions fell slightly above the experimental uncertainty bounds for the two larger corner radii heating distributions. This was most likely due to the

differences in test conditions discussed previously. Vibrational non-equilibrium was observed in the region just behind the bow shock, and the vibrational and translational temperatures reached equilibrium closer to the wall. For the CO_2 case, CO_2 was about 70% dissociated behind the bow shock, while for the air case, there was minimal N_2 dissociation and near-complete O_2 dissociation behind the bow shock.

The computations showed that expansion of the flow around the forebody corner produces a chemically and vibrationally frozen wake flow. Computed heating distributions for the afterbody and for the sting downstream of reattachment agreed to within or slightly more than the experimental uncertainty, while the heating rates within the recirculation region were over-predicted as expected. For all configurations, the experimental heating data for the reattached flow on the sting was higher than the predicted values. However, unlike the perfect-gas cases, the differences between the two did not increase with distance along the sting. Furthermore, comparison of stagnation-point normalized experimental and computational distributions produced much closer agreement on the sting. It was therefore concluded that at the lower Reynolds numbers of the high-enthalpy test conditions, the wake flow remained laminar.

Satisfactory agreement has been shown in this study between experimental and computational results for laminar, chemically-reacting and perfect gas forebody and wake flows. However, several areas of concern in both the experimental and computational techniques employed have been revealed which merit further consideration.

As a review of current literature will show, laminar wake computations still present a serious challenge, and further work is required in this area before the validation of turbulent wake computations can even be considered. Thus there can be seen to exist a need for low Reynolds number, continuum wake data. However, in the present research, wake flows were non-laminar for all the perfect gas conditions, and so no data were obtained which could be used to validate laminar computations for wake flows. While laminar data were obtained in the high-enthalpy tests, the computational requirements for modeling these flows are much higher. Furthermore, the uncertainties in the thermochemical models must also be considered in any comparisons with experimental data, as must the greater experimental uncertainties encountered in high-

enthalpy testing.

While Macor thermal properties were carefully investigated as part of this study, there still exist some uncertainties in the temperature dependence of these properties. While this uncertainty represents a relatively small percentage of the total uncertainty in high-enthalpy testing, it dominates the uncertainty in perfect-gas tests. Further investigation of the thermal properties of Macor is required to minimize this uncertainty.

The results of grid resolution and grid adaptation studies conducted in this research demonstrated the extreme sensitivity of wake flow solutions to the grid structure. Satisfactory comparisons were achieved for the laminar cases, but only after considerable time spent manually adapting grids to the shear layer. Also, very high numbers of normal grid points were required to accurately model the wake; however, because of the single block structure of the grids, the forebody portion of the grids then had many more normal points than required. Thus, a considerable amount of computational time was expended computing forebody solutions on these over-resolved grids. Efficient, automated means of adapting grids to the wake structure need to be explored, and the use of multi-block grids should be considered in order to provide higher grid resolution in the wake without over-resolving the forebody.

CHAPTER 10
REFERENCES

Allegre, J. and Bisch, D. (1994): "Experimental Study of a Blunted Cone at Rarefied Hypersonic Conditions," CNRS, Meudon, CNRS Report RC 94-7, July 1994.

Allegre, J. and Bisch, D. (1995): "Blunted Cone at Rarefied Hypersonic Conditions. Experimental Density Flowfields, Heating Rates and Aerodynamic Forces," CNRS, Meudon, CNRS Report RC 95-2, September 1995.

Alter, S. J. (1996): "The Volume Grid Manipulator (VGM): A Grid Reusability Tool," NASA CR in preparation for publication in 1996.

Alter, S. J. (1997): "Grid Reusability Through the Use of Volume Grid Manipulations," AIAA Paper in preparation for publication in 1997.

Anderson, J. D. (1989): *Hypersonic and High Temperature Gas Dynamics*, McGraw-Hill, 1989.

Anon. (1995): AIAA Standard S-071-1995, "Assessment of Wind Tunnel Data Uncertainty," American Institute of Aeronautics and Astronautics, Washington, D. C., 1995.

Anon. (1996): AGARD Advisory Report No. 319, "Hypersonic Experimental and Computational Capability, Improvement, and Validation," Ed. Saric, W. S., Muylaert, J., and Dujarric, C., 1996.

Beam, R. M. and Warming, R. F. (1976): "An Implicit Finite-Difference Algorithm for Hyperbolic Systems in Conservation-Law Form," *Journal of Computational Physics*, vol. 22, pp. 87-110, 1976.

Beckwith, I. E., and Miller, C. G. (1990): "Aerothermodynamics and Transition in High-Speed Wind Tunnels at NASA Langley," *Annual Review of Fluid Mechanics*, vol. 22, pp. 419-439, 1990.

Berger, S. A. (1971): *Laminar Wakes*, American Elsevier Publishing, Inc. 1971.

Berry, S. A. and Nowak, R. J. (1996): "Effects of Fin Leading Edge Sweep on Shock-Edge Interaction at Mach 6," AIAA Paper 96-0230, January 1996.

Bird, G. A. (1994): *Molecular Gas Dynamics and the Direct Simulation of Gas Flows*, Clarendon Press, Oxford, 1994.

Bourke, R. D., Golombek, M. P., Spear, A. J., and Sturms, F. M. (1992): "MESUR and its Role in an Evolutionary Mars Exploration Program," IAF Paper 92-0509, September 1992.

Buck, G.M. (1991): "Surface Temperature/Heat Transfer Measurements Using a Quantitative Phosphor Thermography System," AIAA Paper 91-0064, January 1991.

Braun, R. D., Powell, R. W., and Hartung, L. C. (1990): "Effect of Interplanetary Trajectory Options on a Manned Mars Aerobrake Configuration," NASA TP 3109, August 1990.

Campbell, R. C. (1995). "Thermal Diffusivity and Thermal Conductivity of Upilex, Macor, and Quartz," Holometrix Inc. Report NAS-84, January 1995.

Calleja, J., Tamagno, J., and Erdos, J. (1990): "Calibration of the GASL 6-Inch Expansion Tube (HYPULSE) for Air, Helium, and CO_2 Test Gases," GASL TR 325, September 1990.

Candler, G. V. and MacCormack, R. W. (1987): "Hypersonic Flow Past 3-D Configurations," AIAA Paper 87-0480, January 1987.

Candler, G. V. (1988): "The Computation of Weakly Ionized Hypersonic Flow in Thermo-Chemical Nonequilibrium," Ph. D. Thesis, Stanford University, June 1988.

Candler, G. V. (1990): "Computation of Thermo-Chemical Nonequilibrium Martian Atmospheric Entry Flows," AIAA Paper 90-1695, June 1990.

Candler, G. V. and MacCormack, R. W. (1991): "Computation of Weakly Ionized Hypersonic Flows in Thermochemical Nonequilibrium," *Journal of Thermophysics*, vol. 5, no. 3, pp. 266-273, July-Sept 1991.

Chen, Y. K., Henline, W. D., Stewart, D. A. and Candler, G. V. (1993): "Navier-Stokes Solutions with Surface Catalysis for Martian Atmospheric Entry," *Journal of Spacecraft and Rockets*, vol. 30, no. 1, January-February 1993.

Cook, W. J. and Felderman, E. J. (1966): "Reduction of Data from Thin-Film Heat Transfer Gages: A Concise Technique," *AIAA Journal*, vol. 4, no. 3, pp. 561-562, March 1966.

Cook, W. J. (1970a): "Determination of Heat-transfer Rates from Transient Surface Temperature Measurements," *AIAA Journal*, vol. 8, no. 7, pp 1366-1368, July 1970.

Cook, W. J. (1970b): "Unsteady Heat Transfer to a Semi-Infinite Solid With Arbitrary Surface Temperature History and Variable Thermal Properties," Iowa State University Technical Report ISU-ERI-AMES-67500, February 1970.

Creel, T. R. (1976): "A Device for Rapid Determination of Thermophysical Properties of Phase-Change Wind-Tunnel Models," NASA TM X-3421, 1976.

Demetriades, A. (1964): "Hot-Wire Measurement in the Hypersonic Wakes of Slender Bodies," *AIAA Journal*, vol. 2, no. 2, pp. 245-250, February 1964.

DiFulvio, M. (1993), NASA Langley Research Center. Private communication.

Doolan, C. J. and Morgan, R. G. (1994): "Hypervelocity Simulation in a Large Scale Experimental Facility", AIAA Paper 94-2492, June 1994.

Dogra, V. K., Moss, J. N., Wilmoth, R. G., Taylor, J. C., and Hassan, H. A. (1994a): "Rarefaction Effects on Blunt Body Wake Structure for Earth Entry Conditions," AIAA Paper 94-2016, June 1994.

Dogra, V.K., Moss, J. N., Wilmoth, R. G., Taylor, J. C., and Hassan, H. A. (1994b): "Effects of Chemistry on Blunt Body Wake Structure," AIAA Paper 94-0352, January 1994.

Dye, T. P. (1993): "An Experimental and Computational Investigation of the Flowfield About an Aeroassisted Space Transportation Vehicle at Mach 10," Master's Thesis, University of Tennessee, Knoxville, December 1993.

Erdos, J., Calleja, J., and Tamagno, J. (1994): "Increase in the Hypervelocity Test Envelope of the HYPULSE Expansion Tube," AIAA Paper 94-2524, June 1994.

Evans, J.S., Schexnayder, C. J., and Grose, W. L. (1974): "Effects of Nonequilibrium Ablation Chemistry on Viking Radio Blackout," *Journal of Spacecraft and Rockets*, vol. 11, no. 2, pp. 84-88, February 1974.

Fay, J. A. and Riddell, F. R. (1958): "Theory of Stagnation Point Heat Transfer in Dissociated Air," *Journal of the Aeronautical Sciences*, vol. 25, no. 2, pp. 73-85, February 1958.

Gaitonde, D. and Shang, J. S. (1992): "The Performance of Flux-Split Algorithms in High-Speed Viscous Flows," AIAA Paper 92-0186, January 1992.

Gallis, M. A. and Harvey, J. K., (1995): "Analysis of Non-Equilibrium in Mars Atmosphere Entry Flows," AIAA Paper 95-2095, June 1995.

Germain, P., Cummings, E. and Hornung, H. (1993): "Transition on a Sharp Cone at High-Enthalpy; New Measurements in the Shock Tunnel T5 at GALCIT," AIAA Paper 93-0343, 1993.

Gnoffo, P. A. (1989): "A Code Calibration Program in Support of the Aeroassist Flight Experiment," AIAA Paper 89-1673, June 1989.

Gnoffo, P. A., Gupta, R. N., and Shinn, J. L. (1989): "Conservation Equations and Physical Models for Hypersonic Air Flows in Thermal and Chemical Nonequilibrium," NASA TP-2867, February 1989.

Gnoffo, P. A. (1990): "An Upwind-Biased, Point-Implicit Relaxation Algorithm for Viscous, Compressible Perfect-Gas Flows," NASA TP-2953, February 1990.

Gnoffo, P. A., Hartung, L. C., and Greendyke, R. B. (1993): "Heating Analysis for a Lunar Transfer Vehicle at Near-Equilibrium Flow Conditions," AIAA Paper 93-0270, January 1993.

Gochberg, L. A., Allen, G. A., Gallis, M. A., and Deiwert, G. S. (1996): "Comparison of Computations and Experiments for Nonequilibrium Flow Expansions Around a Blunted Cone," AIAA Paper 96–0231, January 1996.

Gupta, R. N., Lee, K. P., and Zoby, E. V. (1993): "Enhancements to Viscous-Shock-Layer Technique," *AIAA Journal of Spacecraft and Rockets*, vol. 30, no. 4, pp. 401-413, 1993.

Gupta, R. N. And Lee, K. P. (1994): "An Aerothermal Study of MESUR Pathfinder Aeroshell," AIAA Paper 94-2025, June 1994.

Haas, B. L. and Venkatapathy, E. (1995): "Mars Pathfinder Computations Including Base-Heating Predictions," AIAA Paper 95-2086, June 1995.

Hamilton, H. H., Weilmuenster, K. J., and DeJarnette, F. R. (1985): "Application of Axisymmetric Analogue for Calculating Heating in Three-Dimensional Flows," AIAA Paper 85-0245, January 1985.

Hamilton, H. H., Millman, D. R., and Greendyke, R. B. (1993): "Finite-Difference Solution for Laminar or Turbulent Boundary Layer Flow Over Axisymmetric Bodies with Ideal Gas, CF_4 or Equilibrium Air Chemistry," NASA TP-3271, 1993.

Hartunian, R. A. And Varwig, R. L. (1962): "On Thin-Film Heat Transfer Measurements in Shock Tubes and Wind Tunnels," *Physics of Fluids*, vol. 15, no. 2, pp. 169-174, February 1962.

Harvey, J.K. And Gallis, M. A. (1995): "Comparison of the Maximum Entropy DSMC Code with Flowfield Measurements," AIAA Paper 95-0413, January 1995.

Hedlund, E. R., Hill, J. A. F., Ragsdale, W. C., and Voisinet, R. L. P. (1980): "Heat Transfer Testing in the NSWC Hypervelocity Wind Tunnel Utilizing Co-axial Surface Thermocouples," NSWC MP 80-151, March 1980.

Hilgenstock, A. (1988): "A Fast Method for the Elliptic Generation of Three-Dimensional Grids with Full Boundary Control," *Numerical Grid Generation in Computational Fluid Mechanics '88*, Pineridge Press Limited, pp. 137-146, 1988.

Hilsenrath, J., Beckett, C. W., Benedict, W. S., Fano, W. S., Hoge, L., Masi, J. F., Nuttall, R. L., Touloukian, Y. S., Wodley, H. W. (1955): "Tables of Thermal Properties of Gases," NBS Circular No. 564, 1955.

Hirschfelder, J. O., Curtiss, C. F. and Bird, R. B. (1954): *The Molecular Theory of Gases and Liquids*, John Wiley and Sons, New York, 1954.

Hoffman, K. A., and Chang, S. T. (1993): *Computational Fluid Dynamics for Engineers - Volume II*, Engineering Education System, Wichita, KS, 1993.

Holden, M. S. (1971): "Establishment Times of Laminar Separated Flow," *AIAA Journal*, vol. 9, no. 11, November 1971.

Holden, M. S., Chadwick, K. M., Gallis, M. A. and Harvey, J. K. (1995): "Comparison Between Shock Tunnel Measurements on a Planetary Probe Configuration and DSMC Predictions," Proceedings of the 20th International Symposium on Shock Waves, Pasadena, CA, July 1995.

Holden, M. S., Kolly, J., and Chadwick, K. (1995): "Calibration, Validation and Evaluation Studies in the LENS Facility," AIAA Paper 95-0291, January 1995.

Hollis, B. R. (1995): "User's Manual for the One-Dimensional Hypersonic Aero-Thermodynamic (1DHEAT) Data Reduction Code," NASA CR 4691, August 1995.

Hollis, B. R. (1996): "Real Gas Flow Properties for NASA Langley Aerothermodynamic Facilities Complex Wind Tunnels," NASA CR 4755, September 1996.

Horvath, T. J., McGinnley, C. B., and Hannemann, K. (1996): "Blunt Body Near Wake Flow Field at Mach 6," AIAA Paper 95-1935, June 1996.

Jansen, M. C. (1987): "The Calculated Effects of Surface Curvature on Blunt AOTV Hypersonic Aerodynamics," AIAA Paper 87-2489, August 1987.

Kastell, D., Horvath, T. J., and Eitelberg, G. (1994): "Nonequilibrium Flow Expansion Experiment Around a Blunt Cone," Second European Symposium on Aerothermodynamics for Space Vehicles and Fourth European High Velocity Database Workshop, ESTEC, Noordwijk, The Netherlands, Nov. 22-25, 1994.

Kastell, D., Hannemann, K., Eitelberg, G., and Horvath, T. J. (1995): "Recompression of Nonequilibrium Flow in the Wake of a Blunted Cone," Proceedings of the 20th International Symposium on Shock Waves, Pasadena, CA, July 1995.

Kendall, D. N., Dixon, W. P., and Schulte, E. H. (1967): "Semiconductor Surface Thermocouples for Determining Heat-Transfer Rates," IEEE Transactions on Aerospace and Electronic Systems, vol. AES-3, no. 4, pp. 596-603, July 1967.

Kuehn, D. M. and Monson, D. J. (1967): "Attached and Separated Boundary Layers on Highly Cooled, Ablating and Nonablating Models at M = 13.8," NASA TN D-4041, June 1967.

Lee, J. H. (1985): "Basic Governing Equations for the Flight Regimes of Aeroassisted Orbital Transfer Vehicles," *Thermal Design of Aeroassisted Vehicles*, H. F. Nelson, Ed., vol. 96 of *Progress in Astronautics and Aeronautics*, American Institute of Aeronautics and Astronautics, Washington D. C., pp. 3-53, 1985.

Lees, L. (1956): "Laminar Heat Transfer over Blunt-Nosed Bodies at Hypersonic Flight Speeds," *Jet Propulsion*, vol. 26, pp. 259-269, 1956.

Lees, L. (1964): "Hypersonic Wakes and Trails," *AIAA Journal*, vol. 2, no. 3, pp. 417-428, March 1964.

Legge, H. (1993): "Heat Transfer and Forces on a Blunted 70° Half-Angle Cone Measured in Hypersonic

Free-Jet Flow," DLR - German Aerospace Research Institute, Göttingen, DLR Report IB 222-93A 33, November 1993.

Legge, H. (1994): "Patterson Probe Measurements in the Wake of a 70° Half-Angle Cone in Hypersonic Rarefied Flow," DLR - German Aerospace Research Institute, Göttingen, DLR Report IB 223-94A 15, 1994.

Li, C. P. (1989): "Calculation of Convective Heat Transfer on Highly Blunt Bodies at Flow Incidence," AIAA Paper 89-0244, January 1989.

MacCormack, R. W. (1985): "Current Status of Numerical Solutions of the Navier-Stokes Equations," AIAA Paper 85-0032, January 1985.

MacCormack, R. W. and Candler, G. V. (1989): "The Solution of the Navier-Stokes Equations Using Gauss-Seidel Line Relaxation," *Computers and Fluids*, vol. 17, no. 1, pp.133-150, 1989.

McGrory, W. D., Slack, D. C., Applebaum, M. P., and Walters, R. W. (1993): *GASP Version 2.2: The General Aerodynamic Simulation Program, GASP v2.2 User's Manual*, Aerosoft Inc., 1993.

Mentre, V. and Consigny, H. (1987): "An Improved Data Reduction Technique for Heat Transfer Measurements Using Surface Thermocouples or Thin-Films," *ICIASF Record 1987*, pp. 369-377.

Merski, N. R., (1991): "A Relative-Intensity Two-Color Phosphor Thermography Technique," NASA TM 104123, September 1991.

Micol, J. R. (1992): "Simulation of Real-Gas Effects on Pressure Distribution for Aeroassist Flight Experiment Vehicle and Comparison with Prediction," NASA TP-3157, 1992.

Micol, J. R. (1995): "Hypersonic Aerodynamic/Aerothermodynamic Testing Capabilities at Langley Research Center: Aerothermodynamic Facilities Complex," AIAA Paper 95-2107, June 1995.

Miller, C. G. (1972): "Computer Program of Data Reduction Procedures for Facilities using CO_2-N_2-O_2-Ar Equilibrium Real-Gas Mixtures," NASA TM X-2512, March 1972.

Miller, C. G. (1977): "Operational Experience in the Langley Expansion Tube with Various Test Gases," NASA TM-78637, December 1997.

Miller, C. G. (1981): "Comparison of Thin-Film Resistance Heat-Transfer Gages with Thin-Skin Transient Calorimeter Gages in Conventional Wind Tunnels," NASA TM 83197, December 1981.

Miller, C. G. and Jones, J. J. (1983) "Development and Performance of the NASA Langley Research Center Expansion Tube/Tunnel, A Hypersonic-Hypervelocity Real-Gas Facility," 14th International Symposium on Shock Tubes and Waves, Sydney, Australia, August 15-18, 1983

Miller, C. G., Micol, J. R., and Gnoffo, P. A. (1985): "Laminar Heat-Transfer Distributions on Biconics at Incidence in Hypersonic Hypervelocity Flows," NASA TP 2213, January 1985.

Miller, C. G. (1990): "Langley Hypersonic Aerodynamic/Aerothermodynamic Testing Capabilities - Present and Future," AIAA Paper 90-1376, 1990.

Millikan, R. C. and White, D. R. (1963): "Systematics of Vibrational Relaxation," *Journal of Chemistry and Physics*, vol. 39, no. 12, pp. 3209-3213, December 1963.

Mitchletree, R. A. (1994): "Aerothermodynamic Methods for a Mars Environmental Survey Mars Entry," *Journal of Spacecraft and Rockets*, vol. 31, no. 3, pp. 516-523, May-June 1994.

Mitchletree, R. A. And Gnoffo, P. A. (1994): "Wake Flow About a MESUR Mars Entry Vehicle," AIAA Paper 94-1958, June 1994.

Mitchletree, R. A. (1995): "Computational Aerothermodynamics for Mars Pathfinder Including Turbulence," AIAA Paper 95-3493, August 1995.

Molvick, G. A. (1989): "A Computational Model for the Prediction of Hypersonic, Reacting Flows," Ph. D. Dissertation, The Pennsylvania State University, December 1989.

Moore, J. A. (1975): "Description and Initial Operating Performance of the Langley 6-Inch Expansion Tube Using Heated Helium Driver Gas," NASA TM-X 3240, September 1975.

Moss, J. N., Dogra, V. K., and Wilmoth, R. G. (1993a): "DSMC Simulations of Mach 20 Nitrogen Flows About a 70° Blunted Cone and Its Wake," NASA TM 107762, August 1993.

Moss, J. N., Mitchletree, R. A, Wilmoth, R. G., and Dogra, V. K. (1993b): "Hypersonic Blunt Body Wake Computations Using DSMC and Navier-Stokes Solvers," AIAA Paper 93-2807, July 1993.

Moss, J. N., Price, J. M., Dogra, V. K., and Hash, D. B. (1995): "Comparison of DSMC and Experimental Results for Hypersonic External Flows," AIAA Paper 95-2028, June 1995.

Neely, A. J. (1991): "Investigation of High Enthalpy, Hypervelocity Flows of Argon in an Expansion Tube," Master of Engineering Science dissertation, Department of Mechanical Engineering, The University of Queensland, 1991.

Neely, A. J., and Morgan, R. G. (1993): "Hypervelocity Aerodynamics in a Superorbital Expansion Tube," Proceedings of the 19th International Symposium on Shock Waves, Marseille, France, July 1993.

Nettlehorst, H. L. and Mitchletree, R. A. (1994): "Grid Resolution and Solution Convergence for Mars Pathfinder Forebody," NASA TM 109173, December 1994.

Papadopoulis, P., Tauber, M. and Chang, I. D. (1990): "Aerobraking in a Dusty Martian Atmosphere," AIAA Paper 90-1700, June 1990.

Park, C. (1985): "On Convergence of Computations of Chemically Reacting Flows," AIAA Paper 86–0230, January 1985.

Park, C. (1987): "Assessment of Two-Temperature Kinetic Model for Ionizing Air," AIAA Paper 87-1574, June 1987.

Pirri, A. N. (1971): "Decay of Boundary Layer Turbulence in the Near Wake Expansion Region of a Slender Body," Avco Everett Research Laboratory Report 367, June 1971.

Porter, L., Mee, D., and Paull, A. (1993): "Drag Measurements on Blunted Cones and a Scramjet Vehicle in Hypersonic Flow," AIAA Paper 93-2979, 1993.

Reddy, N. M. (1980): "Heating Rate Measurements over 30° and 40° (Half-Angle) Blunt Cones in Air and Helium in the Langley Expansion Tube Facility," NASA TM 80207, 1980.

Reddy, N. M. and Miller, C. G. (1986): "Study of Heating Distributions on a Family of Very Large Angle Cones," Unpublished NASA report, 1986.

Rochelle, W.C., Bouslog, S. A., and Ting, P. C. (1990): "Aerothermodynamic Environments for Mars Entry, Mars Return, and Lunar Return Aerobraking Missions," AIAA Paper 90-1701, June 1990.

Ressler, D. E., Shivananda, T. P., Zabrensky, E. F., and Cruz, M. I. (1992): "Drag and Heat Transfer Calculations about a MESUR Aerobrake Vehicle," AIAA Paper 92-2684, June 1992.

Schultz, D. L. and Jones, T. V. (1973): "Heat Transfer Measurements in Short-Duration Hypersonic Facilities," AGARD-AG-165, February 1973.

Shih, P. K. T. And Gay, A. (1984): "Low L/D Aerobrake Heat Transfer Test at Mach 10," AIAA Paper 84-0300, January 1984.

Shimshi, J. P. (1992): "An Investigation of Aerodynamic Heating to Spherically Blunted Cones at Angle of Attack," Master's Thesis, George Washington University, 1992.

Soos, T. (1992): "Thermal Conductivity and Thermal Diffusivity of Ceramic Materials," Holometrix Inc. Report NAS-80, December 1992.

Soos, T. (1993): "Thermal Conductivity and Thermal Diffusivity of Glass and Ceramic Materials," Holometrix Inc. Report NAS-82, June 1993.

Soos, T. (1994): "Thermal Conductivity and Thermal Diffusivity of Macor Ceramics," Holometrix Inc. Report NAS-83, June 1994.

Steger, J. L. and Sorenson, R. L. (1979): "Automatic Mesh-Point Clustering Near a Boundary in Grid Generation with Elliptic Partial Differential Equations," *Journal of Computational Physics*, vol. 33, pp. 405-410, 1979.

Steger, J. L. and Warming, R. F. (1981): "Flux-Vector Splitting of the Inviscid Gasdynamic Equations with Application to Finite-Difference Methods," *Journal of Computational Physics*, vol. 40, pp. 263-293, 1981.

Stewart, D. A. and Marvin, J. G. (1969): "Convective Heat-Transfer Rates on Large-Angle Conical Bodies at Hypersonic Speeds," NASA TN D-5526, November 1969.

Stewart, D. A. and Chen, Y. K. (1993): "Convective Heat Transfer Rate Distributions Over a 140° Blunt Cone at Hypersonic Speeds in Different Gas Environments," AIAA Paper 93-2787, July 1993.

Sychev, V.V., Vasserman, A. A., Kozlov, A. D., Spiridonov, G. A., Tsymarny, V. A. (1987): *National Standard Reference Data Service of the USSR: A Series of Property Tables. Volume 6: Thermodynamic Properties of Air.* Hemisphere Publishing Corp., 1987.

Tamagno, J., Bakos, R., Pulsonetti, M., and Erdos, J. (1990): "Hypervelocity Real Gas Capabilities of GASL's Expansion Tube (HYPULSE) Facility," AIAA Paper 90-1390, June 1990.

Tauber, M., Henline, W., Chargin, M., Papadopoulos, P., Chen, Y., Yang, L., and Hamm, K. (1992): "MESUR Probe Aerobrake Preliminary Design Study," AIAA Paper 92-2952, July 1992.

Thomas, L. H. (1949): "Elliptic Problems in Linear Difference Equations over a Network," Watson Scientific Computing Laboratory Report, Columbia University, New York, 1949.

Thomas, P. D. and Middlecoff, J. F. (1979): "Direct Control of the Grid Point Distribution in Meshes Generated by Elliptic Equations," *AIAA Journal*, vol. 18, no. 6, pp. 652-656, 1979.

Thompson, J. F., Thames, F. C., and Mastin, C. W. (1974): "Automatic Numerical Generation of Body-Fitted Curvilinear Coordinate System for Field Containing any Number of Arbitrary Two-Dimensional Bodies," *Journal of Computational Physics*, vol. 15, pp. 299-319, 1974.

van Leer, B. (1979): "Towards the Ultimate Conservation Difference Scheme Part V, A Second-Order Sequel to Godunov's Method," *Journal of Computational Physics*, vol. 32, pp. 101-136, 1979.

Vidal, R. J. (1956): "Model Instrumentation Techniques for Heat Transfer and Force Measurements in a Hypersonic Shock Tunnel," WADC Technical Note 56-315, AD097238, U.S. Air Force, February 1956.

Vincenti, W. G. and Krueger, C. H. (1965): *Introduction to Physical Gas Dynamics*, Kreiger, 1965.

Walberg, G. D. (1985): "A Survey of Aeroassisted Orbit Transfer," *Journal of Spacecraft and Rockets*, vol. 22, no. 1, pp. 3-17, January-February 1985.

Walberg, G. D. (1988): "A Review of Aerobraking for Mars Missions," IAF Paper 88-196, October 1988.

Walberg, G. D. (1991): "Aerocapture for Manned Mars Missions - Status and Challenges," AIAA Paper 91-2870, August 1991.

Wannenwetsch, G. D., Ticatch, L. A., Kidd, C. T., and Artebury, R. L. (1984): "Results of Wind Tunnel Tests Utilizing the Thin-Film Technique to Measure Leading-Edge Heating Rates," AEDC-TR-83-50, May 1984.

Weilmuenster, K. J. and Hamilton, H. H. (1988): "Calculations of Inviscid Flow Over Shuttle-Like Vehicles at High Angles of Attack and Comparisons with Experimental Data," NASA TP-2103, May 1983.

Wells, W. L. (1988): "Free-Shear-Layer Turning Angle in Wake of Aeroassist Flight Experiment (AFE) Vehicle at Incidence in M = 10 Air and M = 6 CF_4," NASA TM 100479, November 1988.

Wells, W. L. (1990): "Surface Flow and Heating on a Cylinder in Near Wake of Aeroassist Flight Experiment (AFE) Configuration at Incidence in Mach 10 Air," NASA TP 2954, January 1990.

White, F. M. (1988): *Heat and Mass Transfer*, Addison-Wesley Publishing, 1988.

Wilke, C. R. (1950): "A Viscosity Equation for Gas Mixtures," *Journal of Chemical Physics*, vol. 18, no. 4, p. 517, 1950.

Wilmoth, R. G., Mitchletree, R. A., Moss, J. N. and Dogra, V. K. (1993): "Zonally-Decoupled DSMC Solutions of Hypersonic Blunt Body Wake Flows," AIAA Paper 93-2808, July 1993.

Zeiberg, S. L. (1964): "Transition Correlations for Hypersonic Wakes and Trails," *AIAA Journal*, vol. 2, no. 3, pp. 564-565, March 1964.

Zoby, E. V., and Sullivan, E. M. (1964): "Effects of Corner Radius on Stagnation-Point Velocity Gradients on Blunt Axisymmetric Bodies," NASA TM X-1067, 1964.

APPENDIX A
31-INCH MACH 10 AIR TUNNEL DATA

Aerothermodynamic data from Test Series 293 and 307 in the NASA LaRC 31-Inch Mach 10 Air Tunnel are presented in this appendix. Test series run matrices and run flow conditions are given in Tables A.1 and A.2 for Test 293 and in Tables A.3 and A.4 for Test 307. Run data from Test 293 are given in Tables A.5 through A.43 and run data from Test 307 are given in Tables A.44 through A.59. Normalized Stanton numbers distributions are plotted in Figures A.1 through A.39 for Test 293 and in Figures A.40 through A.55 for Test 307.

The test matrices in Tables A.1 and A.3 list the run number, the model configuration tested, the test condition (identified by the nominal freestream unit Reynolds number), the model angle-of-attack, the model roll-angle (based on the rotation angle of the sting gages from vertical) and notes on each run. The flow conditions data in Tables A.2 and A.4 include the freestream Reynolds number, velocity, density, temperature, pressure, Mach number and total enthalpy.

Tables A.5-A.43 and A.44-A.59 list for each thin-film gage the time-averaged Stanton number, C_H, and the normalized standard deviation of the Stanton number over the data-averaging window, s/C_H. The thin-film gages are identified by number, for example, TF19, which is the stagnation-point gage. Gage positions are given by S/R_b, the normalized distance along the surface from the forebody stagnation point, and by L/R_b, the normalized distance along the sting from the base of the model. These positions can be related to specific control-point locations on the models using Figure 6.1.1: gages TF1 through TF7 and TF31 through TF37 are located on the afterbody or base of the model; gages TF8 through TF30 are located on the forebody; and gages TF38 through TF70 are located on the sting.

A normalized Stanton number, either $C_H/C_{H,0}$ or $C_H/C_{H,ref}$, is also given in Table A.5-A.59. For Test 293, $C_H/C_{H,0}$ is listed. This is the Stanton number of each gage normalized by the stagnation-point

gage (TF 19) value from that run. In Test 307 series, $C_H/C_{H,ref}$ is listed because there was no instrumentation on the forebodies of the models in this test series. $C_H/C_{H,ref}$ is the gage Stanton number normalized by the stagnation-point value measured in Test 293 at the corresponding Reynolds number test condition. The normalizing values in each test series, $C_{H,0}$ or $C_{H,ref}$, are listed in the header of each table.

These tables also include for each gage a reference heat-transfer rate, which is the heat-transfer rate at a fictitious uniform 300 K surface temperature. These heat-transfer rates are the values that were used in the CFD comparisons in Chapter 8. The reference heating rates are computed from the definition of the Stanton number by:

$$q_{ref} = C_H\left[\rho_\infty U_\infty \left(h_{tot} - h_{Tref}\right)\right] \tag{A.1}$$

The purpose of this reference heating rate is to simplify CFD comparisons by specifying a constant wall temperature instead of a temperature distribution. Note that in order to compute the heat-transfer rates at this uniform wall temperature, the Stanton numbers distribution must remain constant. This is the case only if the surface temperature increase is small enough so that lateral conduction effects are minimal. This conditions was satisfied in the Mach 10 tests by limiting the data-averaging window to approximately two seconds from model injection. Over this time period, the maximum surface temperature increase was on the order of 150 K. Therefore, Eq. (A.1) should only be used to compute heat-transfer rates at a uniform wall temperature within a temperature range of 300 K - 450 K.

Rows where asterisks, '*', are shown instead of heating data indicate that no data are presented for that gage owing to the gage being destroyed or damaged, or due to a high-signal-to-noise ratio, which is indicative of electrical connection problems.

TABLE A.1 31-Inch Mach 10 Test 293 Run Matrix

RUN	Model	Re_∞ (*10 $^{-6}$/ft) 0.5	1.0	2.0	α (deg) 0	-4	-12	-20	ϕ (deg) 0	90	180	NOTES
005	MP-1	X			X				X			
006	MP-1		X		X				X			
007	MP-1		X		X				X			Repeats Run 006
008	MP-1		X			X			X			
009	MP-1		X					X	X			
010	MP-1			X	X				X			
011	MP-2	X			X				X			
012	MP-2		X		X				X			
013	MP-2		X		X				X			Repeats Run 012
014	MP-2		X			X			X			
015	MP-2			X	X				X			
016	MP-2		X					X	X			
017	MP-3		X		X				X			
018	MP-3	X			X				X			
019	MP-3		X		X				X			Repeats Run 17
020	MP-3			X	X				X			
021	MP-3		X			X			X			
022	MP-3		X					X	X			
023	MP-4	X			X				X			
024	MP-4		X		X				X			
025	MP-4		X		X				X			Repeats Run 024
026	MP-4		X			X			X			
027	MP-4		X					X	X			
028	MP-4			X	X				X			
029	MP-1		X		X					X		
030	MP-1		X		X					X		Repeats Run 029
031	MP-1		X			X					X	D/A system problem (no data)
032	MP-1		X			X					X	
033	MP-1		X				X				X	
034	MP-1		X					X			X	
035	MP-1		X					X		X		
036	MP-1		X				X			X		
037	MP-1		X			X				X		
038	MP-1		X				X		X			
039	MP-2		X			X			X			Repeats Run 014
040	MP-2		X				X		X			
041	MP-2		X			X					X	
042	MP-2		X				X				X	
043	MP-2		X					X			X	

TABLE A.2 31-Inch Mach 10 Test 293 Flow Conditions

Run	Model	Re_∞ (1/ft)	U_∞ (m/sec)	T_∞ (K)	ρ_∞ (kg/m^3)	p_∞ (Pa)	M_∞	h_{tot} - h_{298} (MJ/kg)
005	MP-1	0.506E+06	1413	53.04	4.607E-03	70.11	9.679	0.751
006	MP-1	0.967E+06	1422	52.48	8.644E-03	130.1	9.797	0.764
007	MP-1	0.987E+06	1415	51.63	8.766E-03	130.5	9.799	0.753
008	MP-1	0.984E+06	1417	52.02	8.752E-03	130.6	9.797	0.755
009	MP-1	0.979E+06	1416	51.97	8.703E-03	129.7	9.797	0.754
010	MP-1	1.897E+06	1424	51.97	16.51E-03	242.3	9.930	0.765
011	MP-2	0.490E+06	1417	53.40	4.480E-03	68.65	9.673	0.757
012	MP-2	0.971E+06	1426	52.72	8.697E-03	131.5	9.796	0.769
013	MP-2	0.956E+06	1427	52.83	8.599E-03	130.3	9.795	0.771
014	MP-2	0.962E+05	1426	52.74	8.623E-03	130.5	9.794	0.769
015	MP-2	1.880E+06	1428	51.51	16.43E-03	242.7	9.926	0.771
016	MP-2	0.977E+06	1422	52.41	8.723E-03	131.1	9.799	0.763
017	MP-3	0.967E+06	1423	52.51	8.650E-03	130.3	9.793	0.764
018	MP-3	0.492E+06	1415	53.27	4.488E-03	68.62	9.674	0.755
019	MP-3	0.986E+06	1416	51.95	8.767E-03	130.6	9.799	0.754
020	MP-3	1.870E+06	1427	51.40	16.32E-03	240.5	9.926	0.769
021	MP-3	0.978E+06	1419	52.17	8.712E-03	130.4	9.799	0.759
022	MP-3	0.965E+06	1422	52.69	8.667E-03	131.0	9.771	0.763
023	MP-4	0.488E+06	1419	53.51	4.465E-03	68.55	9.674	0.759
024	MP-4	0.968E+06	1424	52.55	8.661E-03	130.6	9.795	0.766
025	MP-4	0.965E+06	1426	52.71	8.644E-03	130.7	9.797	0.769
026	MP-4	0.984E+06	1416	51.94	8.745E-03	130.3	9.780	0.754
027	MP-4	0.988E+06	1418	52.10	8.791E-03	131.4	9.800	0.758
028	MP-4	1.910E+06	1422	51.02	16.59E-03	242.6	9.931	0.762
029	MP-1	0.971E+06	1423	52.48	8.676E-03	130.6	9.797	0.764
030	MP-1	0.964E+06	1425	52.65	8.632E-03	130.4	9.797	0.768
032*	MP-1	0.970E+06	1422	52.53	8.664E-03	130.3	9.800	0.763
033	MP-1	0.960E+06	1432	53.19	8.643E-03	131.9	9.794	0.778
034	MP-1	0.976E+06	1421	52.35	8.711E-03	130.8	9.800	0.762
035	MP-1	0.955E+06	1430	53.01	8.587E-03	130.6	9.795	0.775
036	MP-1	0.967E+06	1423	52.51	8.650E-03	130.3	9.794	0.764
037	MP-1	0.978E+06	1420	52.27	8.703E-03	130.5	9.796	0.760
038	MP-1	0.973E+06	1429	52.92	8.733E-03	132.6	9.800	0.774
039	MP-2	0.977E+06	1419	52.20	8.707E-03	130.4	9.797	0.759
040	MP-2	0.961E+06	1426	52.74	8.618E-03	130.4	9.794	0.769
041	MP-2	0.946E+06	1432	53.22	8.523E-03	130.1	9.791	0.778
042	MP-2	0.970E+06	1419	52.20	8.649E-03	129.5	9.797	0.759
043	MP-2	0.987E+06	1415	51.90	8.766E-03	130.5	9.799	0.753

* No listing for run 031 (no data)

TABLE A.3 31-Inch Mach 10 Test 307 Run Matrix

RUN	Model	Re_∞ (*10 $^{-6}$/ft) 0.5	1.0	2.0	α (deg) 0	-4	-12	-20	ϕ (deg) 0	90	180	NOTES
008	MP-1	X			X				X			repeats Test 293, Run 005
009	MP-1	X			X				X			D/A system problem, no data
010	MP-1		X		X				X			repeats Test 293, Run 007
011	MP-1			X	X				X			transition grit
012	MP-1			X	X				X			transition grit
013	MP-1		X		X				X			transition grit
014	MP-1		X		X				X			transition grit
015	MP-1	X			X				X			transition grit
016	MP-1	X			X				X			transition grit
017	MP-1			X	X				X			transition grit
018	MP-1		X		X				X			transition grit
019	MP-1		X		X				X			transition grit
020	MP-1			X	X				X			transition grit
021	MP-1	X			X				X			repeats Test 293, Run 005
022	MP-1		X		X				X			repeats Test 293, Run 007
023	MP-1			X	X				X			repeats Test 293, Run 010

TABLE A.4 31-Inch Mach 10 Test 307 Flow Conditions

Run	Model	Re_∞ (1/ft)	U_∞ (m/sec)	T_∞ (K)	ρ_∞ (kg/m^3)	p_∞ (Pa)	M_∞	h_{tot} - h_{298} (MJ/kg)
008*	MP-1	0.566E+06	1415	53.14	4.505E-03	68.71	9.674	0.754E+06
010	MP-1	1.108E+06	1421	52.41	8.634E-03	129.9	9.783	0.762E+06
011	MP-1	2.223E+06	1417	50.56	16.64E-03	241.5	9.935	0.755E+06
012	MP-1	2.245E+06	1416	50.47	16.78E-03	243.0	9.938	0.753E+06
013	MP-1	1.103E+06	1424	52.65	8.622E-03	130.3	9.782	0.766E+06
014	MP-1	1.115E+06	1421	52.42	8.658E-03	130.7	9.783	0.762E+06
015	MP-1	0.547E+06	1419	53.52	4.369E-03	67.11	9.671	0.761E+06
016	MP-1	0.551E+06	1421	53.64	4.412E-03	67.94	9.669	0.763E+06
017	MP-1	2.261E+06	1413	50.20	16.83E-03	242.5	9.942	0.749E+06
018	MP-1	1.108E+06	1424	52.63	8.656E-03	130.8	9.782	0.766E+06
019	MP-1	1.122E+06	1418	52.20	8.714E-03	130.6	9.785	0.758E+06
020	MP-1	2.236E+06	1415	50.41	16.70E-03	241.6	9.937	0.752E+06
021	MP-1	0.566E+06	1417	53.28	4.506E-03	68.91	9.675	0.757E+06
022	MP-1	1.103E+06	1425	52.77	8.634E-03	130.8	9.780	0.768E+06
023	MP-1	2.260E+06	1411	50.05	16.78E-03	241.1	9.944	0.746E+06

* No listing for run 009 (no data)

TABLE A.5 31-Inch Mach 10 Test 293, Run 005 Heating Data
MP-1 Configuration, $Re_\infty = 0.5 \times 10^6$ ft^{-1}, $\alpha = 0$ deg, $\phi = 0$ deg, $C_{H,0} = 0.02821$

GAGE ID	S/R_b	L/R_b	C_H	s/C_H	$C_H/C_{H,0}$	q_{300}(W/cm^2)
TF37	-1.872	-	*	*	*	*
TF36	-1.772	-	*	*	*	*
TF35	-1.678	-	3.026e-04	0.038	0.011	0.148
TF34	-1.554	-	*	*	*	*
TF33	-1.429	-	*	*	*	*
TF32	-1.305	-	2.472e-04	0.091	0.009	0.121
TF31	-1.180	-	1.162e-03	0.324	0.041	0.568
TF30	-1.083	-	1.040e-02	0.064	0.369	5.087
TF29	-1.000	-	1.869e-02	0.009	0.662	9.139
TF28	-0.900	-	1.733e-02	0.002	0.614	8.474
TF27	-0.800	-	1.665e-02	0.003	0.590	8.141
TF26	-0.700	-	*	*	*	*
TF25	-0.600	-	1.668e-02	0.004	0.591	8.155
TF24	-0.500	-	1.734e-02	0.004	0.615	8.479
TF23	-0.400	-	1.818e-02	0.004	0.645	8.892
TF22	-0.300	-	1.955e-02	0.002	0.693	9.558
TF21	-0.200	-	2.214e-02	0.002	0.785	10.827
TF20	-0.100	-	2.686e-02	0.001	0.952	13.136
TF19	0.000	-	2.821e-02	0.001	1.000	13.797
TF18	0.100	-	2.701e-02	0.001	0.957	13.207
TF17	0.200	-	2.346e-02	0.002	0.831	11.471
TF16	0.300	-	1.987e-02	0.002	0.704	9.716
TF15	0.400	-	1.822e-02	0.003	0.646	8.908
TF14	0.500	-	1.742e-02	0.003	0.617	8.516
TF13	0.600	-	1.720e-02	0.007	0.610	8.413
TF12	0.700	-	1.673e-02	0.003	0.593	8.179
TF11	0.800	-	1.672e-02	0.003	0.593	8.178
TF10	0.900	-	1.733e-02	0.002	0.614	8.473
TF9	1.000	-	1.876e-02	0.008	0.665	9.173
TF8	1.083	-	1.149e-02	0.050	0.407	5.619
TF7	1.180	-	1.045e-03	0.331	0.037	0.511
TF6	1.305	-	2.028e-04	0.054	0.007	0.099
TF5	1.429	-	1.740e-04	0.044	0.006	0.085
TF4	1.554	-	1.337e-04	0.165	0.005	0.065
TF3	1.678	-	2.746e-04	0.070	0.010	0.134
TF2	1.772	-	2.450e-04	0.042	0.009	0.120
TF1	1.872	-	1.144e-04	0.158	0.004	0.056
TF38	1.931	0.015	7.517e-05	0.137	0.003	0.037
TF39	2.036	0.120	1.212e-04	0.123	0.004	0.059
TF40	2.141	0.225	2.339e-04	0.052	0.008	0.114
TF41	2.246	0.330	2.825e-04	0.065	0.010	0.138
TF42	2.351	0.435	3.583e-04	0.033	0.013	0.175
TF43	2.456	0.540	4.034e-04	0.036	0.014	0.197
TF44	2.561	0.645	4.686e-04	0.057	0.017	0.229
TF45	2.666	0.750	5.314e-04	0.032	0.019	0.260
TF46	2.771	0.855	5.998e-04	0.039	0.021	0.293
TF47	2.876	0.960	6.672e-04	0.043	0.024	0.326
TF48	2.981	1.065	7.723e-04	0.037	0.027	0.378
TF49	3.086	1.170	9.183e-04	0.034	0.033	0.449
TF50	3.191	1.275	1.034e-03	0.025	0.037	0.506
TF51	3.296	1.380	1.179e-03	0.028	0.042	0.576
TF52	3.401	1.485	1.328e-03	0.030	0.047	0.650
TF53	3.506	1.590	1.467e-03	0.034	0.052	0.717
TF54	3.611	1.695	1.606e-03	0.020	0.057	0.785
TF55	3.716	1.800	1.767e-03	0.026	0.063	0.864
TF56	3.821	1.905	1.890e-03	0.022	0.067	0.924
TF57	3.926	2.010	2.038e-03	0.024	0.072	0.997
TF58	4.031	2.115	2.070e-03	0.023	0.073	1.012
TF59	4.136	2.220	2.175e-03	0.024	0.077	1.063
TF60	4.241	2.325	2.226e-03	0.022	0.079	1.089
TF61	4.346	2.430	2.240e-03	0.023	0.079	1.095
TF62	4.451	2.535	2.304e-03	0.021	0.082	1.127
TF63	4.556	2.640	2.331e-03	0.025	0.083	1.140
TF64	4.661	2.745	2.275e-03	0.025	0.081	1.112
TF65	4.766	2.850	2.261e-03	0.022	0.080	1.105
TF66	4.871	2.955	2.259e-03	0.020	0.080	1.104
TF67	4.976	3.060	2.206e-03	0.019	0.078	1.079
TF68	5.081	3.165	2.167e-03	0.017	0.077	1.060
TF69	5.186	3.270	2.178e-03	0.015	0.077	1.065
TF70	5.291	3.375	2.135e-03	0.019	0.076	1.044

TABLE A.6 31-Inch Mach 10 Test 293, Run 006 Heating Data
MP-1 Configuration, $Re_\infty = 1.0 \times 10^6$ ft^{-1}, $\alpha = 0$ deg, $\phi = 0$ deg, $C_{H,0} = 0.02097$

GAGE ID	S/R_b	L/R_b	C_H	s/C_H	$C_H/C_{H,0}$	q_{300}(W/cm^2)
TF37	-1.872	-	*	*	*	*
TF36	-1.772	-	*	*	*	*
TF35	-1.678	-	2.390e-04	0.066	0.011	0.224
TF34	-1.554	-	*	*	*	*
TF33	-1.429	-	*	*	*	*
TF32	-1.305	-	1.844e-04	0.058	0.009	0.173
TF31	-1.180	-	7.973e-04	0.356	0.038	0.748
TF30	-1.083	-	7.559e-03	0.052	0.360	7.086
TF29	-1.000	-	1.338e-02	0.014	0.638	12.542
TF28	-0.900	-	1.238e-02	0.004	0.590	11.609
TF27	-0.800	-	1.184e-02	0.006	0.565	11.101
TF26	-0.700	-	*	*	*	*
TF25	-0.600	-	1.185e-02	0.005	0.565	11.111
TF24	-0.500	-	1.231e-02	0.003	0.587	11.542
TF23	-0.400	-	1.287e-02	0.003	0.614	12.065
TF22	-0.300	-	1.388e-02	0.003	0.662	13.012
TF21	-0.200	-	1.571e-02	0.002	0.749	14.726
TF20	-0.100	-	1.906e-02	0.002	0.909	17.869
TF19	0.000	-	2.097e-02	0.033	1.000	19.665
TF18	0.100	-	1.911e-02	0.001	0.911	17.913
TF17	0.200	-	1.659e-02	0.003	0.791	15.554
TF16	0.300	-	1.401e-02	0.002	0.668	13.139
TF15	0.400	-	1.284e-02	0.003	0.612	12.042
TF14	0.500	-	1.221e-02	0.004	0.582	11.449
TF13	0.600	-	1.255e-02	0.025	0.598	11.763
TF12	0.700	-	1.173e-02	0.005	0.559	10.999
TF11	0.800	-	1.177e-02	0.006	0.561	11.039
TF10	0.900	-	1.228e-02	0.005	0.586	11.516
TF9	1.000	-	1.340e-02	0.014	0.639	12.563
TF8	1.083	-	8.331e-03	0.039	0.397	7.810
TF7	1.180	-	6.951e-04	0.381	0.033	0.652
TF6	1.305	-	1.415e-04	0.055	0.007	0.133
TF5	1.429	-	1.173e-04	0.061	0.006	0.110
TF4	1.554	-	1.155e-04	0.131	0.006	0.108
TF3	1.678	-	2.135e-04	0.057	0.010	0.200
TF2	1.772	-	1.857e-04	0.064	0.009	0.174
TF1	1.872	-	1.062e-04	0.077	0.005	0.100
TF38	1.931	0.015	7.233e-05	0.085	0.003	0.068
TF39	2.036	0.120	8.598e-05	0.058	0.004	0.081
TF40	2.141	0.225	1.092e-04	0.063	0.005	0.102
TF41	2.246	0.330	1.330e-04	0.058	0.006	0.125
TF42	2.351	0.435	1.904e-04	0.048	0.009	0.178
TF43	2.456	0.540	2.446e-04	0.068	0.012	0.229
TF44	2.561	0.645	2.900e-04	0.035	0.014	0.272
TF45	2.666	0.750	3.661e-04	0.047	0.017	0.343
TF46	2.771	0.855	4.229e-04	0.033	0.020	0.396
TF47	2.876	0.960	4.962e-04	0.030	0.024	0.465
TF48	2.981	1.065	5.858e-04	0.039	0.028	0.549
TF49	3.086	1.170	7.182e-04	0.033	0.034	0.673
TF50	3.191	1.275	8.491e-04	0.036	0.040	0.796
TF51	3.296	1.380	1.009e-03	0.032	0.048	0.946
TF52	3.401	1.485	1.186e-03	0.029	0.057	1.112
TF53	3.506	1.590	1.360e-03	0.026	0.065	1.275
TF54	3.611	1.695	1.527e-03	0.027	0.073	1.432
TF55	3.716	1.800	1.731e-03	0.022	0.083	1.623
TF56	3.821	1.905	1.860e-03	0.020	0.089	1.744
TF57	3.926	2.010	2.011e-03	0.021	0.096	1.886
TF58	4.031	2.115	2.065e-03	0.020	0.098	1.936
TF59	4.136	2.220	2.169e-03	0.017	0.103	2.034
TF60	4.241	2.325	2.216e-03	0.015	0.106	2.078
TF61	4.346	2.430	2.207e-03	0.015	0.105	2.069
TF62	4.451	2.535	2.250e-03	0.015	0.107	2.110
TF63	4.556	2.640	2.261e-03	0.016	0.108	2.120
TF64	4.661	2.745	2.192e-03	0.014	0.105	2.055
TF65	4.766	2.850	2.139e-03	0.014	0.102	2.006
TF66	4.871	2.955	2.114e-03	0.013	0.101	1.982
TF67	4.976	3.060	2.032e-03	0.014	0.097	1.905
TF68	5.081	3.165	1.985e-03	0.010	0.095	1.861
TF69	5.186	3.270	1.954e-03	0.010	0.093	1.832
TF70	5.291	3.375	1.895e-03	0.010	0.090	1.777

TABLE A.7 31-Inch Mach 10 Test 293, Run 007 Heating Data
MP-1 Configuration, $Re_\infty = 1.0 \times 10^6$ ft^{-1}, $\alpha = 0$ deg, $\phi = 0$ deg, $C_{H,0} = 0.01981$

GAGE ID	S/R_b	L/R_b	C_H	s/C_H	$C_H/C_{H,0}$	q_{300}(W/cm^2)
TF37	-1.872	-	*	*	*	*
TF36	-1.772	-	*	*	*	*
TF35	-1.678	-	2.439e-04	0.060	0.012	0.227
TF34	-1.554	-	*	*	*	*
TF33	-1.429	-	*	*	*	*
TF32	-1.305	-	1.880e-04	0.046	0.009	0.175
TF31	-1.180	-	7.894e-04	0.356	0.040	0.735
TF30	-1.083	-	7.482e-03	0.055	0.378	6.969
TF29	-1.000	-	1.331e-02	0.013	0.672	12.396
TF28	-0.900	-	1.231e-02	0.002	0.621	11.462
TF27	-0.800	-	1.182e-02	0.004	0.597	11.011
TF26	-0.700	-	*	*	*	*
TF25	-0.600	-	1.178e-02	0.004	0.595	10.976
TF24	-0.500	-	1.225e-02	0.002	0.619	11.414
TF23	-0.400	-	1.282e-02	0.001	0.647	11.944
TF22	-0.300	-	1.379e-02	0.002	0.696	12.840
TF21	-0.200	-	1.558e-02	0.002	0.786	14.511
TF20	-0.100	-	1.888e-02	0.002	0.953	17.584
TF19	0.000	-	1.981e-02	0.001	1.000	18.449
TF18	0.100	-	1.897e-02	0.002	0.958	17.671
TF17	0.200	-	1.649e-02	0.002	0.833	15.363
TF16	0.300	-	1.393e-02	0.002	0.703	12.973
TF15	0.400	-	1.273e-02	0.003	0.643	11.858
TF14	0.500	-	1.211e-02	0.003	0.612	11.283
TF13	0.600	-	1.187e-02	0.003	0.599	11.056
TF12	0.700	-	1.163e-02	0.004	0.587	10.833
TF11	0.800	-	1.165e-02	0.006	0.588	10.854
TF10	0.900	-	1.216e-02	0.005	0.614	11.330
TF9	1.000	-	1.327e-02	0.014	0.670	12.359
TF8	1.083	-	8.252e-03	0.042	0.417	7.686
TF7	1.180	-	6.934e-04	0.383	0.035	0.646
TF6	1.305	-	1.499e-04	0.067	0.008	0.140
TF5	1.429	-	1.180e-04	0.069	0.006	0.110
TF4	1.554	-	1.160e-04	0.107	0.006	0.108
TF3	1.678	-	2.169e-04	0.055	0.011	0.202
TF2	1.772	-	1.901e-04	0.079	0.010	0.177
TF1	1.872	-	1.095e-04	0.117	0.006	0.102
TF38	1.931	0.015	7.128e-05	0.097	0.004	0.066
TF39	2.036	0.120	8.110e-05	0.082	0.004	0.076
TF40	2.141	0.225	1.169e-04	0.056	0.006	0.109
TF41	2.246	0.330	1.393e-04	0.050	0.007	0.130
TF42	2.351	0.435	1.946e-04	0.053	0.010	0.181
TF43	2.456	0.540	2.522e-04	0.061	0.013	0.235
TF44	2.561	0.645	2.914e-04	0.043	0.015	0.271
TF45	2.666	0.750	3.597e-04	0.032	0.018	0.335
TF46	2.771	0.855	4.198e-04	0.045	0.021	0.391
TF47	2.876	0.960	4.873e-04	0.037	0.025	0.454
TF48	2.981	1.065	5.820e-04	0.031	0.029	0.542
TF49	3.086	1.170	7.109e-04	0.025	0.036	0.662
TF50	3.191	1.275	8.423e-04	0.023	0.043	0.784
TF51	3.296	1.380	9.980e-04	0.024	0.050	0.930
TF52	3.401	1.485	1.189e-03	0.022	0.060	1.108
TF53	3.506	1.590	1.361e-03	0.017	0.069	1.268
TF54	3.611	1.695	1.523e-03	0.017	0.077	1.419
TF55	3.716	1.800	1.737e-03	0.014	0.088	1.618
TF56	3.821	1.905	1.857e-03	0.014	0.094	1.730
TF57	3.926	2.010	2.023e-03	0.013	0.102	1.885
TF58	4.031	2.115	2.074e-03	0.013	0.105	1.932
TF59	4.136	2.220	2.163e-03	0.013	0.109	2.014
TF60	4.241	2.325	2.213e-03	0.012	0.112	2.062
TF61	4.346	2.430	2.215e-03	0.012	0.112	2.063
TF62	4.451	2.535	2.258e-03	0.012	0.114	2.103
TF63	4.556	2.640	2.266e-03	0.014	0.114	2.111
TF64	4.661	2.745	2.200e-03	0.016	0.111	2.049
TF65	4.766	2.850	2.147e-03	0.013	0.108	2.000
TF66	4.871	2.955	2.115e-03	0.012	0.107	1.970
TF67	4.976	3.060	2.043e-03	0.013	0.103	1.903
TF68	5.081	3.165	1.990e-03	0.011	0.100	1.853
TF69	5.186	3.270	1.961e-03	0.009	0.099	1.827
TF70	5.291	3.375	1.903e-03	0.011	0.096	1.773

TABLE A.8 31-Inch Mach 10 Test 293, Run 008 Heating Data
MP-1 Configuration, $Re_\infty = 1.0 \times 10^6$ ft^{-1}, $\alpha = -4$ deg, $\phi = 0$ deg, $C_{H,0} = 0.01979$

GAGE ID	S/R_b	L/R_b	C_H	s/C_H	$C_H/C_{H,0}$	q_{300}(W/cm^2)
TF37	-1.872	-	*	*	*	*
TF36	-1.772	-	*	*	*	*
TF35	-1.678	-	4.440e-04	0.055	0.022	0.415
TF34	-1.554	-	*	*	*	*
TF33	-1.429	-	*	*	*	*
TF32	-1.305	-	2.859e-04	0.024	0.014	0.267
TF31	-1.180	-	7.827e-04	0.332	0.040	0.731
TF30	-1.083	-	6.833e-03	0.058	0.345	6.380
TF29	-1.000	-	1.235e-02	0.014	0.624	11.535
TF28	-0.900	-	1.150e-02	0.004	0.581	10.743
TF27	-0.800	-	1.107e-02	0.005	0.559	10.341
TF26	-0.700	-	*	*	*	*
TF25	-0.600	-	1.108e-02	0.006	0.560	10.345
TF24	-0.500	-	1.153e-02	0.004	0.583	10.769
TF23	-0.400	-	1.209e-02	0.003	0.611	11.292
TF22	-0.300	-	1.302e-02	0.003	0.658	12.159
TF21	-0.200	-	1.486e-02	0.002	0.751	13.877
TF20	-0.100	-	1.846e-02	0.001	0.932	17.234
TF19	0.000	-	1.979e-02	0.002	1.000	18.484
TF18	0.100	-	1.937e-02	0.001	0.979	18.088
TF17	0.200	-	1.723e-02	0.002	0.871	16.093
TF16	0.300	-	1.466e-02	0.001	0.740	13.687
TF15	0.400	-	1.343e-02	0.003	0.678	12.537
TF14	0.500	-	1.277e-02	0.002	0.645	11.926
TF13	0.600	-	1.242e-02	0.006	0.628	11.601
TF12	0.700	-	1.223e-02	0.003	0.618	11.419
TF11	0.800	-	1.225e-02	0.004	0.619	11.442
TF10	0.900	-	1.281e-02	0.003	0.647	11.966
TF9	1.000	-	1.410e-02	0.012	0.712	13.168
TF8	1.083	-	9.001e-03	0.038	0.455	8.405
TF7	1.180	-	7.646e-04	0.369	0.039	0.714
TF6	1.305	-	8.039e-05	0.132	0.004	0.075
TF5	1.429	-	5.940e-05	0.116	0.003	0.055
TF4	1.554	-	5.103e-05	0.111	0.003	0.048
TF3	1.678	-	1.310e-04	0.053	0.007	0.122
TF2	1.772	-	1.452e-04	0.049	0.007	0.136
TF1	1.872	-	8.828e-05	0.147	0.004	0.082
TF38	1.931	0.015	5.110e-05	0.195	0.003	0.048
TF39	2.036	0.120	1.024e-04	0.084	0.005	0.096
TF40	2.141	0.225	2.001e-04	0.052	0.010	0.187
TF41	2.246	0.330	2.380e-04	0.031	0.012	0.222
TF42	2.351	0.435	3.101e-04	0.027	0.016	0.290
TF43	2.456	0.540	3.597e-04	0.030	0.018	0.336
TF44	2.561	0.645	4.162e-04	0.032	0.021	0.389
TF45	2.666	0.750	5.225e-04	0.026	0.026	0.488
TF46	2.771	0.855	6.445e-04	0.029	0.033	0.602
TF47	2.876	0.960	7.958e-04	0.025	0.040	0.743
TF48	2.981	1.065	1.005e-03	0.016	0.051	0.938
TF49	3.086	1.170	1.305e-03	0.015	0.066	1.218
TF50	3.191	1.275	1.586e-03	0.014	0.080	1.481
TF51	3.296	1.380	1.889e-03	0.011	0.095	1.764
TF52	3.401	1.485	2.165e-03	0.012	0.109	2.022
TF53	3.506	1.590	2.344e-03	0.009	0.118	2.189
TF54	3.611	1.695	2.461e-03	0.014	0.124	2.298
TF55	3.716	1.800	2.594e-03	0.015	0.131	2.422
TF56	3.821	1.905	2.563e-03	0.016	0.129	2.393
TF57	3.926	2.010	2.586e-03	0.015	0.131	2.415
TF58	4.031	2.115	2.490e-03	0.013	0.126	2.325
TF59	4.136	2.220	2.453e-03	0.015	0.124	2.291
TF60	4.241	2.325	2.391e-03	0.016	0.121	2.233
TF61	4.346	2.430	2.307e-03	0.016	0.117	2.154
TF62	4.451	2.535	2.282e-03	0.014	0.115	2.131
TF63	4.556	2.640	2.243e-03	0.015	0.113	2.095
TF64	4.661	2.745	2.139e-03	0.017	0.108	1.997
TF65	4.766	2.850	2.063e-03	0.014	0.104	1.927
TF66	4.871	2.955	2.009e-03	0.014	0.102	1.876
TF67	4.976	3.060	1.936e-03	0.014	0.098	1.808
TF68	5.081	3.165	1.886e-03	0.011	0.095	1.761
TF69	5.186	3.270	1.866e-03	0.011	0.094	1.743
TF70	5.291	3.375	1.812e-03	0.012	0.092	1.692

TABLE A.9 31-Inch Mach 10 Test 293, Run 009 Heating Data
MP-1 Configuration, $Re_\infty = 1.0 \times 10^6$ ft^{-1}, $\alpha = -20$ deg, $\phi = 0$ deg, $C_{H,0} = 0.01925$

GAGE ID	S/R_b	L/R_b	C_H	s/C_H	$C_H/C_{H,0}$	q_{300}(W/cm^2)
TF37	-1.872	-	*	*	*	*
TF36	-1.772	-	*	*	*	*
TF35	-1.678	-	5.152e-04	0.042	0.027	0.477
TF34	-1.554	-	*	*	*	*
TF33	-1.429	-	*	*	*	*
TF32	-1.305	-	1.897e-04	0.052	0.010	0.176
TF31	-1.180	-	5.171e-04	0.376	0.027	0.479
TF30	-1.083	-	4.694e-03	0.063	0.244	4.349
TF29	-1.000	-	8.791e-03	0.012	0.457	8.145
TF28	-0.900	-	8.081e-03	0.002	0.420	7.487
TF27	-0.800	-	7.806e-03	0.004	0.405	7.233
TF26	-0.700	-	*	*	*	*
TF25	-0.600	-	8.021e-03	0.003	0.417	7.431
TF24	-0.500	-	8.487e-03	0.002	0.441	7.864
TF23	-0.400	-	9.050e-03	0.003	0.470	8.385
TF22	-0.300	-	9.992e-03	0.005	0.519	9.257
TF21	-0.200	-	1.195e-02	0.009	0.621	11.074
TF20	-0.100	-	1.648e-02	0.004	0.856	15.268
TF19	0.000	-	1.925e-02	0.001	1.000	17.838
TF18	0.100	-	2.038e-02	0.001	1.059	18.885
TF17	0.200	-	1.932e-02	0.002	1.003	17.898
TF16	0.300	-	1.667e-02	0.001	0.866	15.445
TF15	0.400	-	1.538e-02	0.003	0.799	14.250
TF14	0.500	-	1.474e-02	0.003	0.766	13.660
TF13	0.600	-	1.515e-02	0.028	0.787	14.034
TF12	0.700	-	1.444e-02	0.004	0.750	13.379
TF11	0.800	-	1.471e-02	0.005	0.764	13.625
TF10	0.900	-	1.588e-02	0.004	0.825	14.715
TF9	1.000	-	1.901e-02	0.010	0.987	17.614
TF8	1.083	-	1.462e-02	0.023	0.759	13.548
TF7	1.180	-	1.626e-03	0.261	0.084	1.506
TF6	1.305	-	6.827e-04	0.046	0.035	0.633
TF5	1.429	-	6.656e-04	0.025	0.035	0.617
TF4	1.554	-	6.186e-04	0.036	0.032	0.573
TF3	1.678	-	7.373e-04	0.039	0.038	0.683
TF2	1.772	-	4.366e-04	0.084	0.023	0.405
TF1	1.872	-	4.260e-04	0.027	0.022	0.395
TF38	1.931	0.015	2.746e-04	0.065	0.014	0.254
TF39	2.036	0.120	8.388e-04	0.040	0.044	0.777
TF40	2.141	0.225	2.325e-03	0.036	0.121	2.155
TF41	2.246	0.330	4.633e-03	0.009	0.241	4.293
TF42	2.351	0.435	7.269e-03	0.004	0.378	6.735
TF43	2.456	0.540	7.214e-03	0.009	0.375	6.684
TF44	2.561	0.645	6.420e-03	0.010	0.333	5.948
TF45	2.666	0.750	5.829e-03	0.017	0.303	5.401
TF46	2.771	0.855	5.296e-03	0.012	0.275	4.907
TF47	2.876	0.960	4.874e-03	0.011	0.253	4.516
TF48	2.981	1.065	4.661e-03	0.010	0.242	4.319
TF49	3.086	1.170	4.417e-03	0.019	0.229	4.092
TF50	3.191	1.275	4.403e-03	0.010	0.229	4.080
TF51	3.296	1.380	4.304e-03	0.010	0.224	3.988
TF52	3.401	1.485	4.215e-03	0.011	0.219	3.905
TF53	3.506	1.590	4.049e-03	0.010	0.210	3.752
TF54	3.611	1.695	3.978e-03	0.010	0.207	3.685
TF55	3.716	1.800	4.004e-03	0.007	0.208	3.710
TF56	3.821	1.905	3.885e-03	0.010	0.202	3.600
TF57	3.926	2.010	3.897e-03	0.009	0.202	3.611
TF58	4.031	2.115	3.771e-03	0.008	0.196	3.493
TF59	4.136	2.220	3.776e-03	0.011	0.196	3.499
TF60	4.241	2.325	3.740e-03	0.008	0.194	3.465
TF61	4.346	2.430	3.703e-03	0.007	0.192	3.431
TF62	4.451	2.535	3.762e-03	0.009	0.195	3.486
TF63	4.556	2.640	3.807e-03	0.009	0.198	3.527
TF64	4.661	2.745	3.720e-03	0.008	0.193	3.447
TF65	4.766	2.850	3.706e-03	0.007	0.193	3.434
TF66	4.871	2.955	3.748e-03	0.009	0.195	3.472
TF67	4.976	3.060	3.724e-03	0.008	0.193	3.450
TF68	5.081	3.165	3.745e-03	0.006	0.194	3.469
TF69	5.186	3.270	3.838e-03	0.006	0.199	3.556
TF70	5.291	3.375	3.836e-03	0.008	0.199	3.554

TABLE A.10 31-Inch Mach 10 Test 293, Run 010 Heating Data
MP-1 Configuration, $Re_\infty = 2.0 \times 10^6$ ft^{-1}, $\alpha = 0$ deg, $\phi = 0$ deg, $C_{H,0} = 0.01435$

GAGE ID	S/R_b	L/R_b	C_H	s/C_H	$C_H/C_{H,0}$	q_{300}(W/cm^2)
TF37	-1.872	-	*	*	*	*
TF36	-1.772	-	*	*	*	*
TF35	-1.678	-	1.468e-04	0.084	0.010	0.263
TF34	-1.554	-	*	*	*	*
TF33	-1.429	-	*	*	*	*
TF32	-1.305	-	9.097e-05	0.084	0.006	0.163
TF31	-1.180	-	5.104e-04	0.380	0.036	0.916
TF30	-1.083	-	5.367e-03	0.051	0.374	9.632
TF29	-1.000	-	9.605e-03	0.017	0.669	17.238
TF28	-0.900	-	8.862e-03	0.005	0.618	15.905
TF27	-0.800	-	8.524e-03	0.009	0.594	15.298
TF26	-0.700	-	*	*	*	*
TF25	-0.600	-	8.564e-03	0.006	0.597	15.370
TF24	-0.500	-	8.907e-03	0.004	0.621	15.986
TF23	-0.400	-	9.345e-03	0.004	0.651	16.770
TF22	-0.300	-	1.014e-02	0.005	0.706	18.192
TF21	-0.200	-	1.132e-02	0.002	0.789	20.324
TF20	-0.100	-	1.368e-02	0.003	0.953	24.554
TF19	0.000	-	1.435e-02	0.004	1.000	25.755
TF18	0.100	-	1.376e-02	0.003	0.959	24.699
TF17	0.200	-	1.207e-02	0.002	0.841	21.654
TF16	0.300	-	1.020e-02	0.003	0.710	18.297
TF15	0.400	-	9.320e-03	0.005	0.649	16.727
TF14	0.500	-	8.850e-03	0.005	0.617	15.883
TF13	0.600	-	8.826e-03	0.009	0.615	15.839
TF12	0.700	-	8.433e-03	0.007	0.588	15.135
TF11	0.800	-	8.393e-03	0.010	0.585	15.064
TF10	0.900	-	8.700e-03	0.006	0.606	15.614
TF9	1.000	-	9.406e-03	0.015	0.655	16.882
TF8	1.083	-	5.800e-03	0.040	0.404	10.408
TF7	1.180	-	4.429e-04	0.394	0.031	0.795
TF6	1.305	-	8.113e-05	0.065	0.006	0.146
TF5	1.429	-	7.263e-05	0.121	0.005	0.130
TF4	1.554	-	7.881e-05	0.119	0.005	0.141
TF3	1.678	-	1.430e-04	0.080	0.010	0.257
TF2	1.772	-	1.401e-04	0.076	0.010	0.252
TF1	1.872	-	1.015e-04	0.068	0.007	0.182
TF38	1.931	0.015	5.890e-05	0.085	0.004	0.106
TF39	2.036	0.120	7.134e-05	0.064	0.005	0.128
TF40	2.141	0.225	8.426e-05	0.064	0.006	0.151
TF41	2.246	0.330	8.540e-05	0.035	0.006	0.153
TF42	2.351	0.435	1.197e-04	0.058	0.008	0.215
TF43	2.456	0.540	1.627e-04	0.055	0.011	0.292
TF44	2.561	0.645	2.053e-04	0.033	0.014	0.368
TF45	2.666	0.750	2.549e-04	0.038	0.018	0.458
TF46	2.771	0.855	3.096e-04	0.034	0.022	0.556
TF47	2.876	0.960	3.666e-04	0.039	0.026	0.658
TF48	2.981	1.065	4.391e-04	0.026	0.031	0.788
TF49	3.086	1.170	5.449e-04	0.023	0.038	0.978
TF50	3.191	1.275	6.618e-04	0.023	0.046	1.188
TF51	3.296	1.380	8.172e-04	0.017	0.057	1.467
TF52	3.401	1.485	9.977e-04	0.015	0.070	1.791
TF53	3.506	1.590	1.195e-03	0.016	0.083	2.145
TF54	3.611	1.695	1.400e-03	0.015	0.098	2.513
TF55	3.716	1.800	1.647e-03	0.014	0.115	2.956
TF56	3.821	1.905	1.792e-03	0.015	0.125	3.216
TF57	3.926	2.010	1.964e-03	0.015	0.137	3.525
TF58	4.031	2.115	2.026e-03	0.015	0.141	3.637
TF59	4.136	2.220	2.101e-03	0.014	0.146	3.771
TF60	4.241	2.325	2.117e-03	0.015	0.147	3.799
TF61	4.346	2.430	2.095e-03	0.013	0.146	3.761
TF62	4.451	2.535	2.091e-03	0.015	0.146	3.753
TF63	4.556	2.640	2.061e-03	0.014	0.144	3.698
TF64	4.661	2.745	1.945e-03	0.015	0.136	3.491
TF65	4.766	2.850	1.868e-03	0.014	0.130	3.352
TF66	4.871	2.955	1.804e-03	0.014	0.126	3.238
TF67	4.976	3.060	1.709e-03	0.012	0.119	3.067
TF68	5.081	3.165	1.636e-03	0.012	0.114	2.936
TF69	5.186	3.270	1.601e-03	0.012	0.112	2.874
TF70	5.291	3.375	1.525e-03	0.014	0.106	2.737

TABLE A.11 31-Inch Mach 10 Test 293, Run 011 Heating Data
MP-2 Configuration, $Re_\infty = 0.5 \times 10^6$ ft^{-1}, $\alpha = 0$ deg, $\phi = 0$ deg, $C_{H,0} = 0.02630$

GAGE ID	S/R_b	L/R_b	C_H	s/C_H	$C_H/C_{H,0}$	q_{300}(W/cm^2)
TF37	-1.864	-	1.372e-04	0.070	0.005	0.066
TF36	-1.764	-	*	*	*	*
TF35	-1.670	-	3.337e-04	0.042	0.013	0.160
TF34	-1.545	-	2.040e-04	0.080	0.008	0.098
TF33	-1.421	-	1.047e-03	0.347	0.040	0.502
TF32	-1.296	-	2.262e-04	0.038	0.009	0.108
TF31	-1.172	-	2.366e-04	0.065	0.009	0.113
TF30	-1.075	-	1.150e-02	0.053	0.437	5.512
TF29	-1.000	-	1.947e-02	0.011	0.740	9.332
TF28	-0.900	-	1.802e-02	0.002	0.685	8.637
TF27	-0.800	-	1.716e-02	0.003	0.653	8.227
TF26	-0.700	-	1.723e-02	0.004	0.655	8.256
TF25	-0.600	-	1.736e-02	0.004	0.660	8.322
TF24	-0.500	-	1.806e-02	0.004	0.687	8.658
TF23	-0.400	-	1.886e-02	0.005	0.717	9.040
TF22	-0.300	-	2.047e-02	0.003	0.778	9.811
TF21	-0.200	-	2.243e-02	0.003	0.853	10.751
TF20	-0.100	-	2.544e-02	0.003	0.967	12.192
TF19	0.000	-	2.630e-02	0.005	1.000	12.607
TF18	0.100	-	2.534e-02	0.003	0.963	12.146
TF17	0.200	-	2.227e-02	0.005	0.847	10.675
TF16	0.300	-	2.043e-02	0.003	0.777	9.790
TF15	0.400	-	1.866e-02	0.007	0.709	8.944
TF14	0.500	-	*	*	*	*
TF13	0.600	-	1.753e-02	0.020	0.666	8.400
TF12	0.700	-	1.721e-02	0.004	0.654	8.249
TF11	0.800	-	1.729e-02	0.004	0.657	8.286
TF10	0.900	-	1.833e-02	0.016	0.697	8.784
TF9	1.000	-	1.970e-02	0.012	0.749	9.443
TF8	1.075	-	1.129e-02	0.057	0.429	5.414
TF7	1.172	-	1.172e-03	0.344	0.045	0.562
TF6	1.296	-	1.963e-04	0.074	0.007	0.094
TF5	1.421	-	1.680e-04	0.052	0.006	0.081
TF4	1.545	-	1.363e-04	0.062	0.005	0.065
TF3	1.670	-	3.103e-04	0.042	0.012	0.149
TF2	1.764	-	2.542e-04	0.085	0.010	0.122
TF1	1.864	-	1.186e-04	0.098	0.005	0.057
TF38	1.923	0.015	*	*	*	*
TF39	2.027	0.120	1.204e-04	0.113	0.005	0.058
TF40	2.132	0.225	1.967e-04	0.043	0.007	0.094
TF41	2.237	0.330	2.752e-04	0.034	0.010	0.132
TF42	2.342	0.435	3.745e-04	0.047	0.014	0.179
TF43	2.447	0.540	4.064e-04	0.052	0.015	0.195
TF44	2.553	0.645	4.544e-04	0.041	0.017	0.218
TF45	2.658	0.750	5.243e-04	0.030	0.020	0.251
TF46	2.763	0.855	6.089e-04	0.031	0.023	0.292
TF47	2.868	0.960	7.249e-04	0.044	0.028	0.347
TF48	2.973	1.065	8.315e-04	0.028	0.032	0.399
TF49	3.078	1.170	9.412e-04	0.028	0.036	0.451
TF50	3.182	1.275	1.057e-03	0.032	0.040	0.507
TF51	3.287	1.380	1.205e-03	0.027	0.046	0.577
TF52	3.392	1.485	1.379e-03	0.024	0.052	0.661
TF53	3.497	1.590	*	*	*	*
TF54	3.602	1.695	1.675e-03	0.022	0.064	0.803
TF55	3.707	1.800	1.914e-03	0.022	0.073	0.918
TF56	3.813	1.905	2.008e-03	0.020	0.076	0.963
TF57	3.918	2.010	2.069e-03	0.027	0.079	0.992
TF58	4.023	2.115	2.174e-03	0.021	0.083	1.042
TF59	4.128	2.220	2.283e-03	0.019	0.087	1.094
TF60	4.233	2.325	2.291e-03	0.019	0.087	1.098
TF61	4.338	2.430	2.279e-03	0.021	0.087	1.092
TF62	4.443	2.535	2.391e-03	0.016	0.091	1.146
TF63	4.548	2.640	2.294e-03	0.019	0.087	1.100
TF64	4.653	2.745	2.370e-03	0.021	0.090	1.136
TF65	4.758	2.850	2.382e-03	0.017	0.091	1.142
TF66	4.863	2.955	2.332e-03	0.016	0.089	1.118
TF67	4.968	3.060	2.339e-03	0.017	0.089	1.121
TF68	5.073	3.165	2.352e-03	0.019	0.089	1.128
TF69	5.177	3.270	2.257e-03	0.018	0.086	1.082
TF70	5.282	3.375	2.240e-03	0.013	0.085	1.074

TABLE A.12 31-Inch Mach 10 Test 293, Run 012 Heating Data
MP-2 Configuration, $Re_\infty = 1.0 \times 10^6$ ft^{-1}, $\alpha = 0$ deg, $\phi = 0$ deg, $C_{H,0} = 0.01807$

GAGE ID	S/R_b	L/R_b	C_H	s/C_H	$C_H/C_{H,0}$	q_{300}(W/cm^2)
TF37	-1.864	-	1.430e-04	0.030	0.008	0.136
TF36	-1.764	-	5.754e-05	0.524	0.003	0.055
TF35	-1.670	-	2.548e-04	0.048	0.014	0.242
TF34	-1.545	-	1.579e-04	0.059	0.009	0.150
TF33	-1.421	-	6.671e-04	0.373	0.037	0.634
TF32	-1.296	-	1.855e-04	0.050	0.010	0.176
TF31	-1.172	-	1.579e-04	0.061	0.009	0.150
TF30	-1.075	-	8.012e-03	0.046	0.444	7.620
TF29	-1.000	-	1.354e-02	0.013	0.749	12.875
TF28	-0.900	-	1.243e-02	0.004	0.688	11.822
TF27	-0.800	-	1.192e-02	0.004	0.660	11.335
TF26	-0.700	-	1.185e-02	0.002	0.656	11.271
TF25	-0.600	-	1.193e-02	0.003	0.661	11.350
TF24	-0.500	-	1.246e-02	0.003	0.690	11.852
TF23	-0.400	-	1.358e-02	0.024	0.752	12.917
TF22	-0.300	-	1.407e-02	0.001	0.779	13.385
TF21	-0.200	-	1.543e-02	0.002	0.854	14.672
TF20	-0.100	-	1.746e-02	0.002	0.967	16.608
TF19	0.000	-	1.807e-02	0.009	1.000	17.180
TF18	0.100	-	1.733e-02	0.001	0.959	16.483
TF17	0.200	-	1.524e-02	0.003	0.844	14.497
TF16	0.300	-	1.391e-02	0.003	0.770	13.226
TF15	0.400	-	1.277e-02	0.003	0.707	12.142
TF14	0.500	-	*	*	*	*
TF13	0.600	-	1.087e-02	0.005	0.602	10.342
TF12	0.700	-	1.170e-02	0.005	0.648	11.126
TF11	0.800	-	1.180e-02	0.005	0.653	11.221
TF10	0.900	-	1.221e-02	0.007	0.676	11.616
TF9	1.000	-	1.366e-02	0.017	0.756	12.994
TF8	1.075	-	7.885e-03	0.050	0.436	7.499
TF7	1.172	-	7.345e-04	0.382	0.041	0.699
TF6	1.296	-	1.493e-04	0.073	0.008	0.142
TF5	1.421	-	1.203e-04	0.080	0.007	0.114
TF4	1.545	-	1.056e-04	0.101	0.006	0.100
TF3	1.670	-	2.403e-04	0.065	0.013	0.229
TF2	1.764	-	2.046e-04	0.078	0.011	0.195
TF1	1.864	--	1.162e-04	0.090	0.006	0.110
TF38	1.923	0.015	1.768e-04	6.880	0.010	0.168
TF39	2.027	0.120	7.860e-05	0.047	0.004	0.075
TF40	2.132	0.225	9.660e-05	0.105	0.005	0.092
TF41	2.237	0.330	1.323e-04	0.081	0.007	0.126
TF42	2.342	0.435	1.877e-04	0.056	0.010	0.179
TF43	2.447	0.540	2.353e-04	0.053	0.013	0.224
TF44	2.553	0.645	2.917e-04	0.049	0.016	0.277
TF45	2.658	0.750	3.574e-04	0.044	0.020	0.340
TF46	2.763	0.855	4.225e-04	0.044	0.023	0.402
TF47	2.868	0.960	4.922e-04	0.039	0.027	0.468
TF48	2.973	1.065	5.874e-04	0.035	0.033	0.559
TF49	3.078	1.170	7.053e-04	0.026	0.039	0.671
TF50	3.182	1.275	8.417e-04	0.028	0.047	0.800
TF51	3.287	1.380	9.881e-04	0.021	0.055	0.940
TF52	3.392	1.485	1.168e-03	0.024	0.065	1.111
TF53	3.497	1.590	*	*	*	*
TF54	3.602	1.695	1.538e-03	0.019	0.085	1.463
TF55	3.707	1.800	1.735e-03	0.019	0.096	1.650
TF56	3.813	1.905	1.877e-03	0.016	0.104	1.785
TF57	3.918	2.010	1.923e-03	0.017	0.106	1.829
TF58	4.023	2.115	2.102e-03	0.015	0.116	2.000
TF59	4.128	2.220	2.187e-03	0.014	0.121	2.080
TF60	4.233	2.325	2.162e-03	0.011	0.120	2.056
TF61	4.338	2.430	2.135e-03	0.010	0.118	2.030
TF62	4.443	2.535	2.247e-03	0.009	0.124	2.137
TF63	4.548	2.640	2.194e-03	0.011	0.121	2.087
TF64	4.653	2.745	2.127e-03	0.011	0.118	2.023
TF65	4.758	2.850	2.158e-03	0.010	0.119	2.052
TF66	4.863	2.955	2.121e-03	0.007	0.117	2.017
TF67	4.968	3.060	2.090e-03	0.010	0.116	1.987
TF68	5.073	3.165	2.052e-03	0.010	0.114	1.952
TF69	5.177	3.270	1.983e-03	0.008	0.110	1.886
TF70	5.282	3.375	1.940e-03	0.009	0.107	1.845

TABLE A.13 31-Inch Mach 10 Test 293, Run 013 Heating Data
MP-2 Configuration, $Re_\infty = 1.0 \times 10^6$ ft^{-1}, $\alpha = 0$ deg, $\phi = 0$ deg, $C_{H,0} = 0.01817$

GAGE ID	S/R_b	L/R_b	C_H	s/C_H	$C_H/C_{H,0}$	q_{300}(W/cm^2)
TF37	-1.864	-	1.433e-04	0.078	0.008	0.135
TF36	-1.764	-	4.576e-04	0.527	0.025	0.432
TF35	-1.670	-	2.503e-04	0.070	0.014	0.236
TF34	-1.545	-	1.537e-04	0.078	0.008	0.145
TF33	-1.421	-	6.865e-04	0.372	0.038	0.648
TF32	-1.296	-	1.796e-04	0.087	0.010	0.170
TF31	-1.172	-	1.550e-04	0.104	0.009	0.146
TF30	-1.075	-	8.107e-03	0.046	0.446	7.653
TF29	-1.000	-	1.365e-02	0.013	0.751	12.882
TF28	-0.900	-	1.258e-02	0.004	0.692	11.875
TF27	-0.800	-	1.209e-02	0.003	0.665	11.411
TF26	-0.700	-	1.198e-02	0.003	0.659	11.308
TF25	-0.600	-	1.190e-02	0.006	0.655	11.238
TF24	-0.500	-	1.259e-02	0.002	0.693	11.888
TF23	-0.400	-	1.312e-02	0.002	0.722	12.383
TF22	-0.300	-	1.424e-02	0.001	0.784	13.438
TF21	-0.200	-	1.558e-02	0.001	0.857	14.705
TF20	-0.100	-	1.766e-02	0.003	0.972	16.672
TF19	0.000	-	1.817e-02	0.017	1.000	17.149
TF18	0.100	-	1.753e-02	0.001	0.965	16.553
TF17	0.200	-	1.534e-02	0.002	0.844	14.479
TF16	0.300	-	1.406e-02	0.002	0.774	13.276
TF15	0.400	-	1.300e-02	0.002	0.716	12.272
TF14	0.500	-	*	*	*	*
TF13	0.600	-	1.176e-02	0.011	0.648	11.104
TF12	0.700	-	1.183e-02	0.004	0.651	11.168
TF11	0.800	-	1.191e-02	0.004	0.656	11.247
TF10	0.900	-	1.205e-02	0.007	0.663	11.374
TF9	1.000	-	1.380e-02	0.016	0.760	13.025
TF8	1.075	-	7.996e-03	0.049	0.440	7.548
TF7	1.172	-	7.617e-04	0.379	0.042	0.719
TF6	1.296	-	1.564e-04	0.087	0.009	0.148
TF5	1.421	-	1.276e-04	0.111	0.007	0.120
TF4	1.545	-	1.068e-04	0.121	0.006	0.101
TF3	1.670	-	2.416e-04	0.075	0.013	0.228
TF2	1.764	-	2.159e-04	0.085	0.012	0.204
TF1	1.864	-	1.190e-04	0.090	0.007	0.112
TF38	1.923	0.015	1.134e-04	11.307	0.006	0.107
TF39	2.027	0.120	8.488e-05	0.078	0.005	0.080
TF40	2.132	0.225	1.123e-04	0.088	0.006	0.106
TF41	2.237	0.330	1.375e-04	0.079	0.008	0.130
TF42	2.342	0.435	1.918e-04	0.057	0.011	0.181
TF43	2.447	0.540	2.465e-04	0.043	0.014	0.233
TF44	2.553	0.645	2.936e-04	0.053	0.016	0.277
TF45	2.658	0.750	3.607e-04	0.034	0.020	0.340
TF46	2.763	0.855	4.255e-04	0.036	0.023	0.402
TF47	2.868	0.960	4.998e-04	0.029	0.028	0.472
TF48	2.973	1.065	5.943e-04	0.033	0.033	0.561
TF49	3.078	1.170	7.125e-04	0.026	0.039	0.673
TF50	3.182	1.275	8.581e-04	0.023	0.047	0.810
TF51	3.287	1.380	1.001e-03	0.020	0.055	0.945
TF52	3.392	1.485	1.191e-03	0.020	0.066	1.124
TF53	3.497	1.590	*	*	*	*
TF54	3.602	1.695	1.550e-03	0.017	0.085	1.463
TF55	3.707	1.800	1.753e-03	0.016	0.096	1.655
TF56	3.813	1.905	1.902e-03	0.015	0.105	1.795
TF57	3.918	2.010	1.948e-03	0.011	0.107	1.839
TF58	4.023	2.115	2.129e-03	0.013	0.117	2.010
TF59	4.128	2.220	2.213e-03	0.010	0.122	2.089
TF60	4.233	2.325	2.196e-03	0.008	0.121	2.073
TF61	4.338	2.430	2.157e-03	0.009	0.119	2.036
TF62	4.443	2.535	2.279e-03	0.007	0.125	2.151
TF63	4.548	2.640	2.254e-03	0.007	0.124	2.128
TF64	4.653	2.745	2.159e-03	0.010	0.119	2.038
TF65	4.758	2.850	2.183e-03	0.009	0.120	2.060
TF66	4.863	2.955	2.146e-03	0.006	0.118	2.026
TF67	4.968	3.060	2.122e-03	0.008	0.117	2.003
TF68	5.073	3.165	2.082e-03	0.009	0.115	1.965
TF69	5.177	3.270	2.014e-03	0.008	0.111	1.901
TF70	5.282	3.375	1.975e-03	0.008	0.109	1.864

TABLE A.14 31-Inch Mach 10 Test 293, Run 014 Heating Data
MP-2 Configuration, $Re_\infty = 1.0 \times 10^6$ ft^{-1}, $\alpha = -4$ deg, $\phi = 0$ deg, $C_{H,0} = 0.01837$

GAGE ID	S/R_b	L/R_b	C_H	s/C_H	$C_H/C_{H,0}$	q_{300}(W/cm^2)
TF37	-1.864	-	3.426e-04	0.043	0.019	0.323
TF36	-1.764	-	2.278e-03	0.027	0.124	2.148
TF35	-1.670	-	4.323e-04	0.057	0.024	0.408
TF34	-1.545	-	2.708e-04	0.060	0.015	0.255
TF33	-1.421	-	6.877e-04	0.342	0.037	0.648
TF32	-1.296	-	2.812e-04	0.044	0.015	0.265
TF31	-1.172	-	2.798e-04	0.043	0.015	0.264
TF30	-1.075	-	7.338e-03	0.051	0.399	6.918
TF29	-1.000	-	1.257e-02	0.013	0.684	11.855
TF28	-0.900	-	1.173e-02	0.003	0.638	11.059
TF27	-0.800	-	1.129e-02	0.005	0.615	10.648
TF26	-0.700	-	1.119e-02	0.004	0.609	10.553
TF25	-0.600	-	1.122e-02	0.005	0.611	10.580
TF24	-0.500	-	1.187e-02	0.003	0.646	11.190
TF23	-0.400	-	1.241e-02	0.003	0.675	11.698
TF22	-0.300	-	1.352e-02	0.002	0.736	12.749
TF21	-0.200	-	1.498e-02	0.002	0.815	14.123
TF20	-0.100	-	1.719e-02	0.004	0.935	16.204
TF19	0.000	-	1.837e-02	0.027	1.000	17.323
TF18	0.100	-	1.778e-02	0.002	0.968	16.760
TF17	0.200	-	1.573e-02	0.004	0.856	14.832
TF16	0.300	-	1.454e-02	0.002	0.792	13.711
TF15	0.400	-	1.356e-02	0.002	0.738	12.784
TF14	0.500	-	*	*	*	*
TF13	0.600	-	1.234e-02	0.014	0.672	11.638
TF12	0.700	-	1.229e-02	0.004	0.669	11.584
TF11	0.800	-	1.230e-02	0.008	0.670	11.599
TF10	0.900	-	1.259e-02	0.006	0.685	11.869
TF9	1.000	-	1.448e-02	0.018	0.788	13.656
TF8	1.075	-	8.611e-03	0.048	0.469	8.119
TF7	1.172	-	8.180e-04	0.363	0.045	0.771
TF6	1.296	-	9.548e-05	0.081	0.005	0.090
TF5	1.421	-	6.559e-05	0.057	0.004	0.062
TF4	1.545	-	5.508e-05	0.037	0.003	0.052
TF3	1.670	-	1.527e-04	0.043	0.008	0.144
TF2	1.764	-	1.523e-04	0.076	0.008	0.144
TF1	1.864	-	9.106e-05	0.079	0.005	0.086
TF38	1.923	0.015	9.819e-05	7.539	0.005	0.093
TF39	2.027	0.120	9.791e-05	0.069	0.005	0.092
TF40	2.132	0.225	2.094e-04	0.066	0.011	0.197
TF41	2.237	0.330	2.404e-04	0.042	0.013	0.227
TF42	2.342	0.435	2.971e-04	0.036	0.016	0.280
TF43	2.447	0.540	3.557e-04	0.044	0.019	0.335
TF44	2.553	0.645	4.278e-04	0.036	0.023	0.403
TF45	2.658	0.750	5.281e-04	0.030	0.029	0.498
TF46	2.763	0.855	6.450e-04	0.039	0.035	0.608
TF47	2.868	0.960	8.077e-04	0.024	0.044	0.762
TF48	2.973	1.065	1.038e-03	0.026	0.057	0.979
TF49	3.078	1.170	1.323e-03	0.018	0.072	1.248
TF50	3.182	1.275	1.614e-03	0.012	0.088	1.522
TF51	3.287	1.380	1.915e-03	0.015	0.104	1.805
TF52	3.392	1.485	2.197e-03	0.014	0.120	2.071
TF53	3.497	1.590	*	*	*	*
TF54	3.602	1.695	2.520e-03	0.009	0.137	2.376
TF55	3.707	1.800	2.619e-03	0.009	0.143	2.470
TF56	3.813	1.905	2.611e-03	0.009	0.142	2.462
TF57	3.918	2.010	2.484e-03	0.007	0.135	2.342
TF58	4.023	2.115	2.551e-03	0.010	0.139	2.405
TF59	4.128	2.220	2.493e-03	0.007	0.136	2.350
TF60	4.233	2.325	2.358e-03	0.007	0.128	2.224
TF61	4.338	2.430	2.236e-03	0.008	0.122	2.108
TF62	4.443	2.535	2.283e-03	0.004	0.124	2.152
TF63	4.548	2.640	2.207e-03	0.008	0.120	2.080
TF64	4.653	2.745	2.073e-03	0.009	0.113	1.954
TF65	4.758	2.850	2.077e-03	0.008	0.113	1.958
TF66	4.863	2.955	2.017e-03	0.007	0.110	1.901
TF67	4.968	3.060	1.990e-03	0.005	0.108	1.877
TF68	5.073	3.165	1.947e-03	0.007	0.106	1.836
TF69	5.177	3.270	1.888e-03	0.006	0.103	1.780
TF70	5.282	3.375	1.865e-03	0.007	0.102	1.758

TABLE A.15 31-Inch Mach 10 Test 293, Run 015 Heating Data
MP-2 Configuration, $Re_\infty = 2.0 \times 10^6$ ft^{-1}, $\alpha = 0$ deg, $\phi = 0$ deg, $C_{H,0} = 0.01343$

GAGE ID	S/R_b	L/R_b	C_H	s/C_H	$C_H/C_{H,0}$	q_{300}(W/cm^2)
TF37	-1.864	-	1.096e-04	0.038	0.008	0.198
TF36	-1.764	-	*	*	*	*
TF35	-1.670	-	1.450e-04	0.065	0.011	0.262
TF34	-1.545	-	9.598e-05	0.079	0.007	0.173
TF33	-1.421	-	4.442e-04	0.386	0.033	0.801
TF32	-1.296	-	9.495e-05	0.050	0.007	0.171
TF31	-1.172	-	8.230e-05	0.112	0.006	0.148
TF30	-1.075	-	5.685e-03	0.045	0.423	10.253
TF29	-1.000	-	9.604e-03	0.015	0.715	17.320
TF28	-0.900	-	8.857e-03	0.010	0.660	15.974
TF27	-0.800	-	8.573e-03	0.005	0.638	15.462
TF26	-0.700	-	8.464e-03	0.005	0.630	15.265
TF25	-0.600	-	8.320e-03	0.014	0.620	15.006
TF24	-0.500	-	9.002e-03	0.004	0.670	16.236
TF23	-0.400	-	9.434e-03	0.003	0.702	17.014
TF22	-0.300	-	1.020e-02	0.003	0.759	18.395
TF21	-0.200	-	1.117e-02	0.004	0.832	20.138
TF20	-0.100	-	1.256e-02	0.004	0.935	22.653
TF19	0.000	-	1.343e-02	0.021	1.000	24.219
TF18	0.100	-	1.256e-02	0.003	0.936	22.658
TF17	0.200	-	1.069e-02	0.010	0.796	19.277
TF16	0.300	-	1.013e-02	0.002	0.754	18.264
TF15	0.400	-	9.392e-03	0.011	0.699	16.939
TF14	0.500	-	*	*	*	*
TF13	0.600	-	8.559e-03	0.004	0.637	15.436
TF12	0.700	-	8.407e-03	0.006	0.626	15.163
TF11	0.800	-	8.418e-03	0.010	0.627	15.182
TF10	0.900	-	8.555e-03	0.008	0.637	15.428
TF9	1.000	-	9.493e-03	0.020	0.707	17.121
TF8	1.075	-	5.476e-03	0.050	0.408	9.876
TF7	1.172	-	4.826e-04	0.385	0.036	0.870
TF6	1.296	-	8.768e-05	0.082	0.007	0.158
TF5	1.421	-	6.560e-05	0.065	0.005	0.118
TF4	1.545	-	6.902e-05	0.086	0.005	0.124
TF3	1.670	-	1.461e-04	0.040	0.011	0.264
TF2	1.764	-	1.430e-04	0.057	0.011	0.258
TF1	1.864	-	1.008e-04	0.049	0.008	0.182
TF38	1.923	0.015	*	*	*	*
TF39	2.027	0.120	6.908e-05	0.048	0.005	0.125
TF40	2.132	0.225	7.891e-05	0.043	0.006	0.142
TF41	2.237	0.330	8.544e-05	0.055	0.006	0.154
TF42	2.342	0.435	1.144e-04	0.048	0.009	0.206
TF43	2.447	0.540	1.572e-04	0.037	0.012	0.283
TF44	2.553	0.645	2.030e-04	0.034	0.015	0.366
TF45	2.658	0.750	2.521e-04	0.037	0.019	0.455
TF46	2.763	0.855	2.981e-04	0.029	0.022	0.538
TF47	2.868	0.960	3.565e-04	0.031	0.027	0.643
TF48	2.973	1.065	4.365e-04	0.029	0.033	0.787
TF49	3.078	1.170	5.322e-04	0.019	0.040	0.960
TF50	3.182	1.275	6.485e-04	0.021	0.048	1.170
TF51	3.287	1.380	7.925e-04	0.021	0.059	1.429
TF52	3.392	1.485	9.736e-04	0.019	0.073	1.756
TF53	3.497	1.590	*	*	*	*
TF54	3.602	1.695	1.381e-03	0.016	0.103	2.491
TF55	3.707	1.800	1.618e-03	0.015	0.120	2.917
TF56	3.813	1.905	1.778e-03	0.016	0.132	3.207
TF57	3.918	2.010	1.850e-03	0.018	0.138	3.336
TF58	4.023	2.115	2.028e-03	0.017	0.151	3.657
TF59	4.128	2.220	2.102e-03	0.016	0.156	3.790
TF60	4.233	2.325	2.062e-03	0.013	0.154	3.718
TF61	4.338	2.430	1.962e-03	0.006	0.146	3.538
TF62	4.443	2.535	2.064e-03	0.010	0.154	3.722
TF63	4.548	2.640	2.001e-03	0.015	0.149	3.609
TF64	4.653	2.745	1.873e-03	0.017	0.140	3.379
TF65	4.758	2.850	1.876e-03	0.015	0.140	3.383
TF66	4.863	2.955	1.810e-03	0.015	0.135	3.264
TF67	4.968	3.060	1.756e-03	0.015	0.131	3.167
TF68	5.073	3.165	1.692e-03	0.015	0.126	3.052
TF69	5.177	3.270	1.615e-03	0.012	0.120	2.914
TF70	5.282	3.375	1.565e-03	0.012	0.117	2.823

TABLE A.16 31-Inch Mach 10 Test 293, Run 016 Heating Data
MP-2 Configuration, $Re_\infty = 1.0 \times 10^6$ ft^{-1}, $\alpha = -20$ deg, $\phi = 0$ deg, $C_{H,0} = 0.01823$

GAGE ID	S/R_b	L/R_b	C_H	s/C_H	$C_H/C_{H,0}$	q_{300}(W/cm^2)
TF37	-1.864	-	1.185e-04	0.235	0.007	0.112
TF36	-1.764	-	5.763e-02	0.123	3.162	54.410
TF35	-1.670	-	2.492e-04	0.175	0.014	0.235
TF34	-1.545	-	1.910e-04	0.144	0.010	0.180
TF33	-1.421	-	5.168e-04	0.319	0.028	0.488
TF32	-1.296	-	2.804e-04	0.085	0.015	0.265
TF31	-1.172	-	2.314e-04	0.054	0.013	0.218
TF30	-1.075	-	5.013e-03	0.057	0.275	4.733
TF29	-1.000	-	8.903e-03	0.010	0.488	8.405
TF28	-0.900	-	8.413e-03	0.005	0.462	7.943
TF27	-0.800	-	8.005e-03	0.004	0.439	7.558
TF26	-0.700	-	8.215e-03	0.002	0.451	7.756
TF25	-0.600	-	8.522e-03	0.006	0.468	8.046
TF24	-0.500	-	9.147e-03	0.004	0.502	8.636
TF23	-0.400	-	9.857e-03	0.003	0.541	9.306
TF22	-0.300	-	1.114e-02	0.005	0.611	10.515
TF21	-0.200	-	1.289e-02	0.005	0.707	12.167
TF20	-0.100	-	1.573e-02	0.007	0.863	14.850
TF19	0.000	-	1.823e-02	0.039	1.000	17.207
TF18	0.100	-	1.846e-02	0.001	1.013	17.429
TF17	0.200	-	1.710e-02	0.029	0.938	16.147
TF16	0.300	-	1.624e-02	0.002	0.891	15.334
TF15	0.400	-	1.533e-02	0.003	0.841	14.470
TF14	0.500	-	*	*	*	*
TF13	0.600	-	1.389e-02	0.006	0.762	13.114
TF12	0.700	-	1.461e-02	0.003	0.801	13.791
TF11	0.800	-	1.568e-02	0.022	0.860	14.800
TF10	0.900	-	1.553e-02	0.066	0.852	14.664
TF9	1.000	-	2.011e-02	0.014	1.103	18.982
TF8	1.075	-	1.439e-02	0.029	0.790	13.589
TF7	1.172	-	1.769e-03	0.260	0.097	1.670
TF6	1.296	-	7.147e-04	0.050	0.039	0.675
TF5	1.421	-	6.735e-04	0.036	0.037	0.636
TF4	1.545	-	5.959e-04	0.023	0.033	0.563
TF3	1.670	-	8.055e-04	0.045	0.044	0.760
TF2	1.764	-	4.547e-04	0.088	0.025	0.429
TF1	1.864	-	4.515e-04	0.030	0.025	0.426
TF38	1.923	0.015	4.845e-04	0.965	0.027	0.457
TF39	2.027	0.120	7.959e-04	0.038	0.044	0.751
TF40	2.132	0.225	2.139e-03	0.038	0.117	2.020
TF41	2.237	0.330	4.299e-03	0.014	0.236	4.059
TF42	2.342	0.435	6.908e-03	0.009	0.379	6.522
TF43	2.447	0.540	7.124e-03	0.011	0.391	6.726
TF44	2.553	0.645	6.530e-03	0.012	0.358	6.165
TF45	2.658	0.750	6.021e-03	0.012	0.330	5.684
TF46	2.763	0.855	5.346e-03	0.011	0.293	5.048
TF47	2.868	0.960	4.805e-03	0.015	0.264	4.537
TF48	2.973	1.065	4.720e-03	0.012	0.259	4.456
TF49	3.078	1.170	4.583e-03	0.009	0.251	4.327
TF50	3.182	1.275	4.405e-03	0.007	0.242	4.159
TF51	3.287	1.380	4.257e-03	0.007	0.234	4.019
TF52	3.392	1.485	4.175e-03	0.009	0.229	3.941
TF53	3.497	1.590	*	*	*	*
TF54	3.602	1.695	3.981e-03	0.007	0.218	3.758
TF55	3.707	1.800	3.966e-03	0.010	0.218	3.744
TF56	3.813	1.905	3.908e-03	0.007	0.214	3.689
TF57	3.918	2.010	3.735e-03	0.009	0.205	3.526
TF58	4.023	2.115	3.817e-03	0.007	0.209	3.604
TF59	4.128	2.220	3.789e-03	0.006	0.208	3.577
TF60	4.233	2.325	3.668e-03	0.007	0.201	3.463
TF61	4.338	2.430	3.527e-03	0.007	0.194	3.330
TF62	4.443	2.535	3.732e-03	0.006	0.205	3.523
TF63	4.548	2.640	3.661e-03	0.006	0.201	3.457
TF64	4.653	2.745	3.591e-03	0.009	0.197	3.390
TF65	4.758	2.850	3.720e-03	0.008	0.204	3.512
TF66	4.863	2.955	3.740e-03	0.009	0.205	3.531
TF67	4.968	3.060	3.814e-03	0.007	0.209	3.601
TF68	5.073	3.165	3.864e-03	0.008	0.212	3.649
TF69	5.177	3.270	3.861e-03	0.006	0.212	3.645
TF70	5.282	3.375	3.933e-03	0.006	0.216	3.713

TABLE A.17 31-Inch Mach 10 Test 293, Run 017 Heating Data
MP-3 Configuration, $Re_\infty = 1.0 \times 10^6$ ft^{-1}, $\alpha = 0$ deg, $\phi = 0$ deg, $C_{H,0} = 0.02038$

GAGE ID	S/R_b	L/R_b	C_H	s/C_H	$C_H/C_{H,0}$	q_{300}(W/cm^2)
TF1	-1.914	-	1.033e-04	0.081	0.005	0.097
TF2	-1.814	-	1.736e-04	0.109	0.009	0.163
TF3	-1.720	-	1.941e-04	0.097	0.010	0.182
TF4	-1.596	-	8.263e-05	0.124	0.004	0.078
TF5	-1.472	-	1.098e-04	0.081	0.005	0.103
TF6	-1.347	-	1.311e-04	0.095	0.006	0.123
TF7	-1.222	-	4.062e-04	0.214	0.020	0.381
TF8	-1.109	-	6.135e-03	0.054	0.301	5.755
TF9	-1.000	-	1.392e-02	0.018	0.683	13.053
TF10	-0.900	-	1.290e-02	0.006	0.633	12.104
TF11	-0.800	-	1.225e-02	0.008	0.601	11.489
TF12	-0.700	-	1.227e-02	0.006	0.602	11.506
TF13	-0.600	-	1.238e-02	0.006	0.608	11.616
TF14	-0.500	-	1.276e-02	0.004	0.626	11.968
TF15	-0.400	-	1.332e-02	0.004	0.654	12.499
TF16	-0.300	-	1.444e-02	0.001	0.709	13.547
TF17	-0.200	-	1.641e-02	0.001	0.805	15.392
TF18	-0.100	-	1.978e-02	0.001	0.970	18.554
TF19	0.000	-	2.038e-02	0.003	1.000	19.120
TF20	0.100	-	1.959e-02	0.006	0.961	18.378
TF21	0.200	-	1.608e-02	0.003	0.789	15.082
TF22	0.300	-	1.413e-02	0.004	0.693	13.254
TF23	0.400	-	1.299e-02	0.005	0.637	12.186
TF24	0.500	-	1.242e-02	0.003	0.609	11.647
TF25	0.600	-	1.203e-02	0.007	0.590	11.284
TF26	0.700	-	1.195e-02	0.007	0.586	11.208
TF27	0.800	-	1.204e-02	0.006	0.591	11.296
TF28	0.900	-	1.262e-02	0.005	0.619	11.842
TF29	1.000	-	1.372e-02	0.016	0.673	12.870
TF30	1.109	-	5.759e-03	0.057	0.283	5.402
TF31	1.222	-	4.365e-04	0.222	0.021	0.409
TF32	1.347	-	1.293e-04	0.108	0.006	0.121
TF33	1.472	-	1.045e-04	0.125	0.005	0.098
TF34	1.596	-	9.602e-05	0.134	0.005	0.090
TF35	1.720	-	1.940e-04	0.105	0.010	0.182
TF36	1.814	-	1.746e-04	0.085	0.009	0.164
TF37	1.914	-	1.004e-04	0.081	0.005	0.094
TF39	2.028	0.070	8.339e-05	0.098	0.004	0.078
TF40	2.133	0.175	9.656e-05	0.069	0.005	0.091
TF41	2.238	0.280	1.028e-04	0.071	0.005	0.096
TF42	2.343	0.385	1.533e-04	0.046	0.008	0.144
TF43	2.448	0.490	2.151e-04	0.028	0.011	0.202
TF44	2.553	0.595	2.680e-04	0.045	0.013	0.251
TF45	2.658	0.700	3.371e-04	0.033	0.017	0.316
TF46	2.763	0.805	3.798e-04	0.039	0.019	0.356
TF47	2.868	0.910	4.506e-04	0.029	0.022	0.423
TF48	2.973	1.015	5.284e-04	0.034	0.026	0.496
TF49	3.078	1.120	6.502e-04	0.037	0.032	0.610
TF50	3.183	1.225	7.550e-04	0.035	0.037	0.708
TF51	3.288	1.330	8.904e-04	0.029	0.044	0.835
TF52	3.393	1.435	1.053e-03	0.035	0.052	0.988
TF53	3.498	1.540	1.211e-03	0.035	0.059	1.136
TF54	3.603	1.645	1.364e-03	0.034	0.067	1.279
TF55	3.708	1.750	1.561e-03	0.034	0.077	1.464
TF56	3.813	1.855	1.670e-03	0.031	0.082	1.567
TF57	3.918	1.960	1.831e-03	0.030	0.090	1.718
TF58	4.023	2.065	1.884e-03	0.033	0.092	1.767
TF59	4.128	2.170	1.991e-03	0.029	0.098	1.867
TF60	4.233	2.275	2.045e-03	0.029	0.100	1.919
TF61	4.338	2.380	2.061e-03	0.027	0.101	1.934
TF62	4.443	2.485	2.111e-03	0.027	0.104	1.980
TF63	4.548	2.590	2.135e-03	0.029	0.105	2.003
TF64	4.653	2.695	2.072e-03	0.028	0.102	1.943
TF65	4.758	2.800	2.044e-03	0.026	0.100	1.917
TF66	4.863	2.905	2.025e-03	0.026	0.099	1.899
TF67	4.968	3.010	1.961e-03	0.024	0.096	1.839
TF68	5.073	3.115	1.909e-03	0.021	0.094	1.791
TF69	5.178	3.220	1.889e-03	0.021	0.093	1.772
TF70	5.283	3.325	1.837e-03	0.021	0.090	1.723

TABLE A.18 31-Inch Mach 10 Test 293, Run 018 Heating Data
MP-3 Configuration, $Re_\infty = 0.5 \times 10^6$ ft^{-1}, $\alpha = 0$ deg, $\phi = 0$ deg, $C_{H,0} = 0.02876$

GAGE ID	S/R_b	L/R_b	C_H	s/C_H	$C_H/C_{H,0}$	q_{300}(W/cm^2)
TF1	-1.914	-	1.261e-04	0.112	0.004	0.060
TF2	-1.814	-	2.828e-04	0.044	0.010	0.135
TF3	-1.720	-	3.388e-04	0.055	0.012	0.162
TF4	-1.596	-	1.558e-04	0.091	0.005	0.075
TF5	-1.472	-	2.018e-04	0.053	0.007	0.097
TF6	-1.347	-	2.443e-04	0.037	0.008	0.117
TF7	-1.222	-	6.739e-04	0.175	0.023	0.322
TF8	-1.109	-	8.584e-03	0.059	0.298	4.105
TF9	-1.000	-	1.961e-02	0.013	0.682	9.378
TF10	-0.900	-	1.819e-02	0.002	0.633	8.699
TF11	-0.800	-	1.733e-02	0.005	0.603	8.290
TF12	-0.700	-	1.736e-02	0.003	0.604	8.301
TF13	-0.600	-	1.752e-02	0.004	0.609	8.380
TF14	-0.500	-	1.803e-02	0.003	0.627	8.623
TF15	-0.400	-	1.886e-02	0.002	0.656	9.017
TF16	-0.300	-	2.035e-02	0.001	0.708	9.732
TF17	-0.200	-	2.315e-02	0.001	0.805	11.070
TF18	-0.100	-	2.792e-02	0.002	0.971	13.350
TF19	0.000	-	2.876e-02	0.002	1.000	13.753
TF20	0.100	-	2.746e-02	0.001	0.955	13.131
TF21	0.200	-	2.268e-02	0.001	0.789	10.848
TF22	0.300	-	1.999e-02	0.003	0.695	9.559
TF23	0.400	-	1.843e-02	0.006	0.641	8.812
TF24	0.500	-	1.775e-02	0.004	0.617	8.490
TF25	0.600	-	1.720e-02	0.007	0.598	8.225
TF26	0.700	-	1.709e-02	0.006	0.594	8.171
TF27	0.800	-	1.713e-02	0.007	0.596	8.190
TF28	0.900	-	1.800e-02	0.005	0.626	8.609
TF29	1.000	-	1.935e-02	0.015	0.673	9.255
TF30	1.109	-	8.070e-03	0.061	0.281	3.859
TF31	1.222	-	7.114e-04	0.186	0.025	0.340
TF32	1.347	-	2.110e-04	0.066	0.007	0.101
TF33	1.472	-	1.820e-04	0.069	0.006	0.087
TF34	1.596	-	1.532e-04	0.054	0.005	0.073
TF35	1.720	-	3.016e-04	0.037	0.010	0.144
TF36	1.814	-	2.554e-04	0.062	0.009	0.122
TF37	1.914	-	9.768e-05	0.124	0.003	0.047
TF39	2.028	0.070	1.064e-04	0.116	0.004	0.051
TF40	2.133	0.175	1.770e-04	0.073	0.006	0.085
TF41	2.238	0.280	2.243e-04	0.038	0.008	0.107
TF42	2.343	0.385	3.140e-04	0.051	0.011	0.150
TF43	2.448	0.490	3.795e-04	0.039	0.013	0.182
TF44	2.553	0.595	4.276e-04	0.027	0.015	0.205
TF45	2.658	0.700	4.972e-04	0.068	0.017	0.238
TF46	2.763	0.805	5.638e-04	0.035	0.020	0.270
TF47	2.868	0.910	6.320e-04	0.030	0.022	0.302
TF48	2.973	1.015	7.233e-04	0.053	0.025	0.346
TF49	3.078	1.120	8.664e-04	0.030	0.030	0.414
TF50	3.183	1.225	9.542e-04	0.039	0.033	0.456
TF51	3.288	1.330	1.088e-03	0.040	0.038	0.520
TF52	3.393	1.435	1.233e-03	0.037	0.043	0.590
TF53	3.498	1.540	1.372e-03	0.036	0.048	0.656
TF54	3.603	1.645	1.484e-03	0.042	0.052	0.710
TF55	3.708	1.750	1.632e-03	0.038	0.057	0.780
TF56	3.813	1.855	1.738e-03	0.035	0.060	0.831
TF57	3.918	1.960	1.872e-03	0.041	0.065	0.895
TF58	4.023	2.065	1.927e-03	0.036	0.067	0.922
TF59	4.128	2.170	2.012e-03	0.038	0.070	0.962
TF60	4.233	2.275	2.068e-03	0.034	0.072	0.989
TF61	4.338	2.380	2.106e-03	0.033	0.073	1.007
TF62	4.443	2.485	2.181e-03	0.033	0.076	1.043
TF63	4.548	2.590	2.222e-03	0.028	0.077	1.063
TF64	4.653	2.695	2.169e-03	0.033	0.075	1.037
TF65	4.758	2.800	2.159e-03	0.032	0.075	1.033
TF66	4.863	2.905	2.170e-03	0.029	0.075	1.038
TF67	4.968	3.010	2.114e-03	0.026	0.074	1.011
TF68	5.073	3.115	2.091e-03	0.027	0.073	1.000
TF69	5.178	3.220	2.099e-03	0.024	0.073	1.004
TF70	5.283	3.325	2.067e-03	0.028	0.072	0.988

TABLE A.19 31-Inch Mach 10 Test 293, Run 019 Heating Data
MP-3 Configuration, $Re_\infty = 1.0 \times 10^6$ ft^{-1}, $\alpha = 0$ deg, $\phi = 0$ deg, $C_{H,0} = 0.02005$

GAGE ID	S/R_b	L/R_b	C_H	s/C_H	$C_H/C_{H,0}$	q_{300}(W/cm^2)
TF1	-1.914	-	9.950e-05	0.106	0.005	0.093
TF2	-1.814	-	1.678e-04	0.105	0.008	0.157
TF3	-1.720	-	1.906e-04	0.118	0.010	0.178
TF4	-1.596	-	7.303e-05	0.239	0.004	0.068
TF5	-1.472	-	1.040e-04	0.178	0.005	0.097
TF6	-1.347	-	1.296e-04	0.098	0.006	0.121
TF7	-1.222	-	3.916e-04	0.224	0.020	0.366
TF8	-1.109	-	6.051e-03	0.054	0.302	5.648
TF9	-1.000	-	1.372e-02	0.019	0.684	12.810
TF10	-0.900	-	1.268e-02	0.007	0.633	11.840
TF11	-0.800	-	1.208e-02	0.010	0.602	11.273
TF12	-0.700	-	1.210e-02	0.008	0.603	11.294
TF13	-0.600	-	1.224e-02	0.008	0.610	11.422
TF14	-0.500	-	1.257e-02	0.006	0.627	11.730
TF15	-0.400	-	1.318e-02	0.005	0.657	12.305
TF16	-0.300	-	1.420e-02	0.005	0.708	13.252
TF17	-0.200	-	1.615e-02	0.001	0.805	15.075
TF18	-0.100	-	1.945e-02	0.001	0.970	18.157
TF19	0.000	-	2.005e-02	0.003	1.000	18.717
TF20	0.100	-	1.928e-02	0.002	0.962	18.000
TF21	0.200	-	1.582e-02	0.002	0.789	14.770
TF22	0.300	-	1.391e-02	0.001	0.694	12.987
TF23	0.400	-	1.282e-02	0.005	0.640	11.971
TF24	0.500	-	1.228e-02	0.004	0.612	11.462
TF25	0.600	-	1.189e-02	0.007	0.593	11.095
TF26	0.700	-	1.179e-02	0.006	0.588	11.000
TF27	0.800	-	1.187e-02	0.007	0.592	11.079
TF28	0.900	-	1.246e-02	0.006	0.621	11.627
TF29	1.000	-	1.352e-02	0.018	0.674	12.616
TF30	1.109	-	5.673e-03	0.056	0.283	5.295
TF31	1.222	-	4.162e-04	0.235	0.021	0.388
TF32	1.347	-	1.358e-04	0.142	0.007	0.127
TF33	1.472	-	1.026e-04	0.140	0.005	0.096
TF34	1.596	-	8.259e-05	0.193	0.004	0.077
TF35	1.720	-	2.089e-04	0.087	0.010	0.195
TF36	1.814	-	1.814e-04	0.144	0.009	0.169
TF37	1.914	-	1.043e-04	0.126	0.005	0.097
TF39	2.028	0.070	7.340e-05	0.149	0.004	0.069
TF40	2.133	0.175	8.720e-05	0.073	0.004	0.081
TF41	2.238	0.280	1.022e-04	0.055	0.005	0.095
TF42	2.343	0.385	1.573e-04	0.051	0.008	0.147
TF43	2.448	0.490	2.076e-04	0.068	0.010	0.194
TF44	2.553	0.595	2.576e-04	0.076	0.013	0.240
TF45	2.658	0.700	3.200e-04	0.036	0.016	0.299
TF46	2.763	0.805	3.758e-04	0.047	0.019	0.351
TF47	2.868	0.910	4.248e-04	0.046	0.021	0.396
TF48	2.973	1.015	5.182e-04	0.043	0.026	0.484
TF49	3.078	1.120	6.253e-04	0.045	0.031	0.584
TF50	3.183	1.225	7.278e-04	0.042	0.036	0.679
TF51	3.288	1.330	8.673e-04	0.039	0.043	0.810
TF52	3.393	1.435	1.021e-03	0.040	0.051	0.953
TF53	3.498	1.540	1.182e-03	0.035	0.059	1.104
TF54	3.603	1.645	1.323e-03	0.034	0.066	1.235
TF55	3.708	1.750	1.510e-03	0.029	0.075	1.409
TF56	3.813	1.855	1.627e-03	0.026	0.081	1.519
TF57	3.918	1.960	1.782e-03	0.026	0.089	1.663
TF58	4.023	2.065	1.841e-03	0.023	0.092	1.718
TF59	4.128	2.170	1.949e-03	0.020	0.097	1.819
TF60	4.233	2.275	1.999e-03	0.022	0.100	1.866
TF61	4.338	2.380	2.015e-03	0.017	0.100	1.880
TF62	4.443	2.485	2.076e-03	0.017	0.104	1.938
TF63	4.548	2.590	2.092e-03	0.017	0.104	1.953
TF64	4.653	2.695	2.034e-03	0.015	0.101	1.899
TF65	4.758	2.800	2.004e-03	0.014	0.100	1.871
TF66	4.863	2.905	1.985e-03	0.012	0.099	1.853
TF67	4.968	3.010	1.927e-03	0.012	0.096	1.799
TF68	5.073	3.115	1.875e-03	0.013	0.094	1.750
TF69	5.178	3.220	1.854e-03	0.012	0.092	1.731
TF70	5.283	3.325	1.804e-03	0.013	0.090	1.684

TABLE A.20 31-Inch Mach 10 Test 293, Run 020 Heating Data
MP-3 Configuration, $Re_\infty = 2.0 \times 10^6$ ft^{-1}, $\alpha = 0$ deg, $\phi = 0$ deg, $C_{H,0} = 0.01379$

GAGE ID	S/R_b	L/R_b	C_H	s/C_H	$C_H/C_{H,0}$	q_{300}(W/cm^2)
TF1	-1.914	-	1.041e-04	0.080	0.008	0.186
TF2	-1.814	-	1.548e-04	0.095	0.011	0.276
TF3	-1.720	-	1.635e-04	0.060	0.012	0.292
TF4	-1.596	-	7.102e-05	0.108	0.005	0.127
TF5	-1.472	-	7.864e-05	0.100	0.006	0.140
TF6	-1.347	-	9.735e-05	0.085	0.007	0.174
TF7	-1.222	-	2.302e-04	0.266	0.017	0.411
TF8	-1.109	-	4.170e-03	0.049	0.302	7.442
TF9	-1.000	-	9.388e-03	0.014	0.681	16.755
TF10	-0.900	-	8.693e-03	0.003	0.631	15.515
TF11	-0.800	-	8.322e-03	0.003	0.604	14.853
TF12	-0.700	-	8.353e-03	0.001	0.606	14.908
TF13	-0.600	-	8.468e-03	0.001	0.614	15.113
TF14	-0.500	-	8.695e-03	0.002	0.631	15.519
TF15	-0.400	-	9.151e-03	0.001	0.664	16.333
TF16	-0.300	-	9.865e-03	0.012	0.716	17.606
TF17	-0.200	-	1.118e-02	0.004	0.811	19.962
TF18	-0.100	-	1.343e-02	0.002	0.974	23.966
TF19	0.000	-	1.379e-02	0.002	1.000	24.605
TF20	0.100	-	1.325e-02	0.005	0.961	23.641
TF21	0.200	-	1.100e-02	0.011	0.798	19.630
TF22	0.300	-	9.608e-03	0.004	0.697	17.148
TF23	0.400	-	8.879e-03	0.002	0.644	15.847
TF24	0.500	-	8.496e-03	0.002	0.616	15.163
TF25	0.600	-	8.253e-03	0.001	0.599	14.729
TF26	0.700	-	8.225e-03	0.002	0.597	14.680
TF27	0.800	-	8.254e-03	0.006	0.599	14.730
TF28	0.900	-	8.663e-03	0.002	0.628	15.460
TF29	1.000	-	9.395e-03	0.013	0.682	16.768
TF30	1.109	-	3.968e-03	0.054	0.288	7.083
TF31	1.222	-	2.637e-04	0.273	0.019	0.471
TF32	1.347	-	1.067e-04	0.091	0.008	0.190
TF33	1.472	-	8.980e-05	0.110	0.007	0.160
TF34	1.596	-	8.373e-05	0.086	0.006	0.149
TF35	1.720	-	1.877e-04	0.075	0.014	0.335
TF36	1.814	-	1.771e-04	0.082	0.013	0.316
TF37	1.914	-	1.050e-04	0.064	0.008	0.187
TF39	2.028	0.070	8.640e-05	0.088	0.006	0.154
TF40	2.133	0.175	8.589e-05	0.042	0.006	0.153
TF41	2.238	0.280	8.090e-05	0.060	0.006	0.144
TF42	2.343	0.385	1.075e-04	0.031	0.008	0.192
TF43	2.448	0.490	1.348e-04	0.074	0.010	0.241
TF44	2.553	0.595	1.731e-04	0.048	0.013	0.309
TF45	2.658	0.700	2.195e-04	0.035	0.016	0.392
TF46	2.763	0.805	2.633e-04	0.024	0.019	0.470
TF47	2.868	0.910	3.087e-04	0.020	0.022	0.551
TF48	2.973	1.015	3.721e-04	0.024	0.027	0.664
TF49	3.078	1.120	4.523e-04	0.018	0.033	0.807
TF50	3.183	1.225	5.389e-04	0.016	0.039	0.962
TF51	3.288	1.330	6.510e-04	0.013	0.047	1.162
TF52	3.393	1.435	7.811e-04	0.014	0.057	1.394
TF53	3.498	1.540	9.293e-04	0.015	0.067	1.659
TF54	3.603	1.645	1.073e-03	0.012	0.078	1.916
TF55	3.708	1.750	1.265e-03	0.014	0.092	2.258
TF56	3.813	1.855	1.395e-03	0.015	0.101	2.490
TF57	3.918	1.960	1.560e-03	0.014	0.113	2.784
TF58	4.023	2.065	1.634e-03	0.014	0.119	2.916
TF59	4.128	2.170	1.722e-03	0.015	0.125	3.074
TF60	4.233	2.275	1.773e-03	0.014	0.129	3.164
TF61	4.338	2.380	1.787e-03	0.013	0.130	3.189
TF62	4.443	2.485	1.825e-03	0.014	0.132	3.258
TF63	4.548	2.590	1.822e-03	0.014	0.132	3.253
TF64	4.653	2.695	1.749e-03	0.016	0.127	3.122
TF65	4.758	2.800	1.701e-03	0.012	0.123	3.036
TF66	4.863	2.905	1.664e-03	0.013	0.121	2.970
TF67	4.968	3.010	1.593e-03	0.014	0.116	2.844
TF68	5.073	3.115	1.539e-03	0.012	0.112	2.747
TF69	5.178	3.220	1.508e-03	0.012	0.109	2.691
TF70	5.283	3.325	1.445e-03	0.012	0.105	2.579

TABLE A.21 31-Inch Mach 10 Test 293, Run 021 Heating Data
MP-3 Configuration, $Re_\infty = 1.0 \times 10^6$ ft^{-1}, $\alpha = -4$ deg, $\phi = 0$ deg, $C_{H,0} = 0.02019$

GAGE ID	S/R_b	L/R_b	C_H	s/C_H	$C_H/C_{H,0}$	q_{300}(W/cm^2)
TF1	-1.914	-	3.017e-04	0.029	0.015	0.282
TF2	-1.814	-	4.618e-04	0.044	0.023	0.432
TF3	-1.720	-	4.648e-04	0.046	0.023	0.435
TF4	-1.596	-	2.376e-04	0.046	0.012	0.222
TF5	-1.472	-	2.675e-04	0.034	0.013	0.250
TF6	-1.347	-	2.799e-04	0.038	0.014	0.262
TF7	-1.222	-	3.954e-04	0.183	0.020	0.370
TF8	-1.109	-	5.400e-03	0.064	0.267	5.050
TF9	-1.000	-	1.282e-02	0.016	0.635	11.988
TF10	-0.900	-	1.202e-02	0.005	0.595	11.238
TF11	-0.800	-	1.145e-02	0.008	0.567	10.708
TF12	-0.700	-	1.146e-02	0.008	0.568	10.720
TF13	-0.600	-	1.160e-02	0.008	0.574	10.847
TF14	-0.500	-	1.194e-02	0.006	0.591	11.164
TF15	-0.400	-	1.253e-02	0.005	0.621	11.716
TF16	-0.300	-	1.350e-02	0.003	0.669	12.630
TF17	-0.200	-	1.558e-02	0.002	0.772	14.570
TF18	-0.100	-	1.912e-02	0.002	0.947	17.887
TF19	0.000	-	2.019e-02	0.005	1.000	18.882
TF20	0.100	-	1.979e-02	0.002	0.980	18.506
TF21	0.200	-	1.666e-02	0.002	0.825	15.583
TF22	0.300	-	1.475e-02	0.002	0.731	13.798
TF23	0.400	-	1.362e-02	0.004	0.675	12.738
TF24	0.500	-	1.304e-02	0.003	0.646	12.194
TF25	0.600	-	1.263e-02	0.005	0.626	11.811
TF26	0.700	-	1.254e-02	0.003	0.621	11.730
TF27	0.800	-	1.262e-02	0.003	0.625	11.805
TF28	0.900	-	1.326e-02	0.002	0.657	12.400
TF29	1.000	-	1.459e-02	0.013	0.723	13.649
TF30	1.109	-	6.425e-03	0.053	0.318	6.009
TF31	1.222	-	5.246e-04	0.224	0.026	0.491
TF32	1.347	-	7.343e-05	0.110	0.004	0.069
TF33	1.472	-	6.620e-05	0.165	0.003	0.062
TF34	1.596	-	4.088e-05	0.099	0.002	0.038
TF35	1.720	-	1.374e-04	0.100	0.007	0.128
TF36	1.814	-	1.457e-04	0.051	0.007	0.136
TF37	1.914	-	6.762e-05	0.152	0.003	0.063
TF39	2.028	0.070	7.164e-05	0.062	0.004	0.067
TF40	2.133	0.175	1.443e-04	0.068	0.007	0.135
TF41	2.238	0.280	1.932e-04	0.052	0.010	0.181
TF42	2.343	0.385	2.539e-04	0.056	0.013	0.238
TF43	2.448	0.490	3.087e-04	0.049	0.015	0.289
TF44	2.553	0.595	3.780e-04	0.036	0.019	0.354
TF45	2.658	0.700	4.529e-04	0.035	0.022	0.424
TF46	2.763	0.805	5.491e-04	0.037	0.027	0.514
TF47	2.868	0.910	6.898e-04	0.032	0.034	0.645
TF48	2.973	1.015	8.845e-04	0.025	0.044	0.827
TF49	3.078	1.120	1.144e-03	0.022	0.057	1.070
TF50	3.183	1.225	1.407e-03	0.021	0.070	1.316
TF51	3.288	1.330	1.706e-03	0.018	0.085	1.596
TF52	3.393	1.435	1.969e-03	0.016	0.098	1.842
TF53	3.498	1.540	2.188e-03	0.014	0.108	2.047
TF54	3.603	1.645	2.314e-03	0.014	0.115	2.164
TF55	3.708	1.750	2.456e-03	0.013	0.122	2.297
TF56	3.813	1.855	2.434e-03	0.014	0.121	2.276
TF57	3.918	1.960	2.484e-03	0.014	0.123	2.323
TF58	4.023	2.065	2.399e-03	0.012	0.119	2.243
TF59	4.128	2.170	2.380e-03	0.012	0.118	2.226
TF60	4.233	2.275	2.323e-03	0.014	0.115	2.173
TF61	4.338	2.380	2.245e-03	0.013	0.111	2.100
TF62	4.443	2.485	2.221e-03	0.013	0.110	2.078
TF63	4.548	2.590	2.188e-03	0.016	0.108	2.047
TF64	4.653	2.695	2.079e-03	0.018	0.103	1.944
TF65	4.758	2.800	2.014e-03	0.011	0.100	1.883
TF66	4.863	2.905	1.969e-03	0.013	0.098	1.842
TF67	4.968	3.010	1.897e-03	0.013	0.094	1.774
TF68	5.073	3.115	1.844e-03	0.012	0.091	1.724
TF69	5.178	3.220	1.821e-03	0.011	0.090	1.703
TF70	5.283	3.325	1.769e-03	0.010	0.088	1.655

TABLE A.22 31-Inch Mach 10 Test 293, Run 022 Heating Data
MP-3 Configuration, $Re_\infty = 1.0 \times 10^6$ ft^{-1}, $\alpha = -20$ deg, $\phi = 0$ deg, $C_{H,0} = 0.01960$

GAGE ID	S/R_b	L/R_b	C_H	s/C_H	$C_H/C_{H,0}$	q_{300}(W/cm^2)
TF1	-1.914	-	1.061e-04	0.055	0.005	0.099
TF2	-1.814	-	1.808e-04	0.051	0.009	0.170
TF3	-1.720	-	2.013e-04	0.037	0.010	0.189
TF4	-1.596	-	1.137e-04	0.069	0.006	0.107
TF5	-1.472	-	1.633e-04	0.032	0.008	0.153
TF6	-1.347	-	2.270e-04	0.038	0.012	0.213
TF7	-1.222	-	2.600e-04	0.193	0.013	0.244
TF8	-1.109	-	3.347e-03	0.072	0.171	3.139
TF9	-1.000	-	8.810e-03	0.017	0.450	8.263
TF10	-0.900	-	8.270e-03	0.003	0.422	7.757
TF11	-0.800	-	7.924e-03	0.005	0.404	7.432
TF12	-0.700	-	8.086e-03	0.004	0.413	7.584
TF13	-0.600	-	8.322e-03	0.004	0.425	7.805
TF14	-0.500	-	8.757e-03	0.001	0.447	8.213
TF15	-0.400	-	9.352e-03	0.002	0.477	8.771
TF16	-0.300	-	1.030e-02	0.010	0.526	9.661
TF17	-0.200	-	1.238e-02	0.008	0.632	11.614
TF18	-0.100	-	1.705e-02	0.002	0.870	15.991
TF19	0.000	-	1.960e-02	0.003	1.000	18.380
TF20	0.100	-	2.078e-02	0.002	1.061	19.494
TF21	0.200	-	1.879e-02	0.004	0.959	17.622
TF22	0.300	-	1.687e-02	0.003	0.861	15.818
TF23	0.400	-	1.574e-02	0.005	0.803	14.764
TF24	0.500	-	1.526e-02	0.004	0.779	14.315
TF25	0.600	-	1.498e-02	0.006	0.765	14.054
TF26	0.700	-	1.517e-02	0.003	0.774	14.226
TF27	0.800	-	1.563e-02	0.006	0.797	14.657
TF28	0.900	-	1.709e-02	0.002	0.872	16.031
TF29	1.000	-	2.153e-02	0.013	1.099	20.194
TF30	1.109	-	1.295e-02	0.029	0.661	12.143
TF31	1.222	-	1.540e-03	0.158	0.079	1.445
TF32	1.347	-	7.393e-04	0.048	0.038	0.693
TF33	1.472	-	6.564e-04	0.030	0.033	0.616
TF34	1.596	-	5.588e-04	0.026	0.029	0.524
TF35	1.720	-	7.452e-04	0.046	0.038	0.699
TF36	1.814	-	3.982e-04	0.077	0.020	0.373
TF37	1.914	-	3.554e-04	0.020	0.018	0.333
TF39	2.028	0.070	5.605e-04	0.030	0.029	0.526
TF40	2.133	0.175	1.469e-03	0.042	0.075	1.377
TF41	2.238	0.280	2.990e-03	0.017	0.153	2.804
TF42	2.343	0.385	5.840e-03	0.005	0.298	5.477
TF43	2.448	0.490	6.802e-03	0.013	0.347	6.379
TF44	2.553	0.595	6.499e-03	0.011	0.332	6.095
TF45	2.658	0.700	5.971e-03	0.012	0.305	5.600
TF46	2.763	0.805	5.355e-03	0.011	0.273	5.022
TF47	2.868	0.910	4.913e-03	0.011	0.251	4.608
TF48	2.973	1.015	4.690e-03	0.009	0.239	4.399
TF49	3.078	1.120	4.459e-03	0.013	0.228	4.183
TF50	3.183	1.225	4.404e-03	0.008	0.225	4.131
TF51	3.288	1.330	4.300e-03	0.009	0.219	4.033
TF52	3.393	1.435	4.231e-03	0.009	0.216	3.969
TF53	3.498	1.540	4.085e-03	0.010	0.208	3.831
TF54	3.603	1.645	3.997e-03	0.009	0.204	3.749
TF55	3.708	1.750	4.017e-03	0.008	0.205	3.768
TF56	3.813	1.855	3.911e-03	0.009	0.200	3.668
TF57	3.918	1.960	3.924e-03	0.007	0.200	3.681
TF58	4.023	2.065	3.803e-03	0.008	0.194	3.567
TF59	4.128	2.170	3.805e-03	0.008	0.194	3.569
TF60	4.233	2.275	3.783e-03	0.008	0.193	3.548
TF61	4.338	2.380	3.746e-03	0.006	0.191	3.513
TF62	4.443	2.485	3.800e-03	0.008	0.194	3.564
TF63	4.548	2.590	3.844e-03	0.008	0.196	3.606
TF64	4.653	2.695	3.740e-03	0.009	0.191	3.508
TF65	4.758	2.800	3.742e-03	0.008	0.191	3.510
TF66	4.863	2.905	3.768e-03	0.008	0.192	3.535
TF67	4.968	3.010	3.743e-03	0.008	0.191	3.511
TF68	5.073	3.115	3.761e-03	0.006	0.192	3.528
TF69	5.178	3.220	3.844e-03	0.005	0.196	3.606
TF70	5.283	3.325	3.832e-03	0.007	0.196	3.594

TABLE A.23 31-Inch Mach 10 Test 293, Run 023 Heating Data
MP-4 Configuration, $Re_\infty = 0.5 \times 10^6$ ft^{-1}, $\alpha = 0$ deg, $\phi = 0$ deg, $C_{H,0} = 0.02940$

GAGE ID	S/R_b	L/R_b	C_H	s/C_H	$C_H/C_{H,0}$	q_{300}(W/cm^2)
TF1	-2.000	-	*	*	*	*
TF2	-1.900	-	2.979e-04	0.060	0.010	0.143
TF3	-1.806	-	3.075e-04	0.047	0.010	0.147
TF4	-1.682	-	1.801e-04	0.045	0.006	0.086
TF5	-1.557	-	2.023e-04	0.045	0.007	0.097
TF6	-1.433	-	2.527e-04	0.053	0.009	0.121
TF7	-1.308	-	6.123e-04	0.081	0.021	0.294
TF8	-1.161	-	3.840e-03	0.051	0.131	1.842
TF9	-1.000	-	1.581e-02	0.008	0.538	7.585
TF10	-0.900	-	1.981e-02	0.004	0.674	9.501
TF11	-0.800	-	1.774e-02	0.005	0.603	8.508
TF12	-0.700	-	1.747e-02	0.004	0.594	8.380
TF13	-0.600	-	1.738e-02	0.006	0.591	8.338
TF14	-0.500	-	1.804e-02	0.005	0.613	8.651
TF15	-0.400	-	1.887e-02	0.006	0.642	9.053
TF16	-0.300	-	2.043e-02	0.003	0.695	9.797
TF17	-0.200	-	2.340e-02	0.003	0.796	11.223
TF18	-0.100	-	2.815e-02	0.002	0.957	13.502
TF19	0.000	-	2.940e-02	0.003	1.000	14.103
TF20	0.100	-	2.810e-02	0.002	0.956	13.480
TF21	0.200	-	2.308e-02	0.003	0.785	11.067
TF22	0.300	-	2.032e-02	0.003	0.691	9.746
TF23	0.400	-	1.876e-02	0.006	0.638	8.997
TF24	0.500	-	1.829e-02	0.005	0.622	8.773
TF25	0.600	-	1.773e-02	0.005	0.603	8.503
TF26	0.700	-	1.797e-02	0.004	0.611	8.620
TF27	0.800	-	1.828e-02	0.005	0.622	8.770
TF28	0.900	-	2.017e-02	0.004	0.686	9.673
TF29	1.000	-	1.562e-02	0.011	0.531	7.494
TF30	1.161	-	3.652e-03	0.055	0.124	1.752
TF31	1.308	-	5.635e-04	0.083	0.019	0.270
TF32	1.433	-	2.239e-04	0.063	0.008	0.107
TF33	1.557	-	1.518e-04	0.051	0.005	0.073
TF34	1.682	-	1.554e-04	0.056	0.005	0.075
TF35	1.806	-	2.213e-04	0.120	0.008	0.106
TF36	1.900	-	*	*	*	*
TF37	2.000	-	1.076e-04	0.080	0.004	0.052
TF39	2.114	0.070	1.063e-04	0.111	0.004	0.051
TF40	2.219	0.175	1.520e-04	0.050	0.005	0.073
TF41	2.324	0.280	2.057e-04	0.040	0.007	0.099
TF42	2.429	0.385	3.130e-04	0.058	0.011	0.150
TF43	2.534	0.490	3.454e-04	0.029	0.012	0.166
TF44	2.639	0.595	4.102e-04	0.045	0.014	0.197
TF45	2.744	0.700	4.733e-04	0.025	0.016	0.227
TF46	2.849	0.805	5.556e-04	0.037	0.019	0.267
TF47	2.954	0.910	6.490e-04	0.038	0.022	0.311
TF48	3.059	1.015	7.366e-04	0.032	0.025	0.353
TF49	3.164	1.120	8.322e-04	0.030	0.028	0.399
TF50	3.269	1.225	9.406e-04	0.032	0.032	0.451
TF51	3.374	1.330	1.062e-03	0.030	0.036	0.509
TF52	3.479	1.435	1.210e-03	0.032	0.041	0.581
TF53	3.584	1.540	1.334e-03	0.023	0.045	0.640
TF54	3.689	1.645	1.467e-03	0.023	0.050	0.703
TF55	3.794	1.750	1.642e-03	0.024	0.056	0.788
TF56	3.899	1.855	1.637e-03	0.026	0.056	0.785
TF57	4.004	1.960	1.784e-03	0.017	0.061	0.855
TF58	4.109	2.065	1.858e-03	0.020	0.063	0.891
TF59	4.214	2.170	1.953e-03	0.022	0.066	0.937
TF60	4.319	2.275	1.947e-03	0.018	0.066	0.934
TF61	4.424	2.380	1.940e-03	0.021	0.066	0.931
TF62	4.529	2.485	2.058e-03	0.015	0.070	0.987
TF63	4.634	2.590	1.982e-03	0.019	0.067	0.951
TF64	4.739	2.695	2.077e-03	0.020	0.071	0.996
TF65	4.844	2.800	2.067e-03	0.024	0.070	0.991
TF66	4.949	2.905	2.022e-03	0.017	0.069	0.970
TF67	5.054	3.010	2.026e-03	0.018	0.069	0.972
TF68	5.159	3.115	2.044e-03	0.023	0.070	0.980
TF69	5.264	3.220	1.956e-03	0.018	0.067	0.938
TF70	5.369	3.325	1.955e-03	0.018	0.066	0.937

TABLE A.24 31-Inch Mach 10 Test 293, Run 024 Heating Data
MP-4 Configuration, $Re_\infty = 1.0 \times 10^6$ ft^{-1}, $\alpha = 0$ deg, $\phi = 0$ deg, $C_{H,0} = 0.02107$

GAGE ID	S/R_b	L/R_b	C_H	s/C_H	$C_H/C_{H,0}$	q_{300}(W/cm^2)
TF1	-2.000	--	*	*	*	*
TF2	-1.900	-	1.890e-04	0.091	0.009	0.178
TF3	-1.806	-	2.024e-04	0.099	0.010	0.191
TF4	-1.682	-	1.228e-04	0.105	0.006	0.116
TF5	-1.557	-	1.258e-04	0.111	0.006	0.118
TF6	-1.433	-	1.434e-04	0.133	0.007	0.135
TF7	-1.308	-	3.887e-04	0.111	0.018	0.366
TF8	-1.161	-	2.711e-03	0.055	0.129	2.552
TF9	-1.000	-	1.129e-02	0.005	0.536	10.624
TF10	-0.900	-	1.385e-02	0.006	0.657	13.035
TF11	-0.800	-	1.235e-02	0.006	0.586	11.630
TF12	-0.700	-	1.217e-02	0.004	0.577	11.452
TF13	-0.600	-	1.209e-02	0.005	0.574	11.378
TF14	-0.500	-	1.251e-02	0.002	0.594	11.774
TF15	-0.400	-	1.313e-02	0.002	0.623	12.361
TF16	-0.300	-	1.414e-02	0.001	0.671	13.310
TF17	-0.200	-	1.619e-02	0.001	0.768	15.237
TF18	-0.100	-	1.943e-02	0.001	0.922	18.291
TF19	0.000	-	2.107e-02	0.002	1.000	19.837
TF20	0.100	-	1.940e-02	0.002	0.921	18.263
TF21	0.200	-	1.588e-02	0.002	0.754	14.949
TF22	0.300	-	1.397e-02	0.002	0.663	13.148
TF23	0.400	-	1.289e-02	0.006	0.612	12.132
TF24	0.500	-	1.251e-02	0.005	0.594	11.775
TF25	0.600	-	1.214e-02	0.006	0.576	11.432
TF26	0.700	-	1.234e-02	0.005	0.586	11.619
TF27	0.800	-	1.262e-02	0.008	0.599	11.876
TF28	0.900	-	1.406e-02	0.008	0.667	13.232
TF29	1.000	-	1.121e-02	0.006	0.532	10.549
TF30	1.161	-	2.615e-03	0.056	0.124	2.461
TF31	1.308	-	3.425e-04	0.099	0.016	0.322
TF32	1.433	-	1.304e-04	0.058	0.006	0.123
TF33	1.557	-	1.051e-04	0.071	0.005	0.099
TF34	1.682	-	1.067e-04	0.117	0.005	0.100
TF35	1.806	-	1.757e-04	0.089	0.008	0.165
TF36	1.900	-	*	*	*	*
TF37	2.000	-	1.090e-04	0.083	0.005	0.103
TF39	2.114	0.070	7.470e-05	0.123	0.004	0.070
TF40	2.219	0.175	6.723e-05	0.113	0.003	0.063
TF41	2.324	0.280	9.138e-05	0.086	0.004	0.086
TF42	2.429	0.385	1.340e-04	0.052	0.006	0.126
TF43	2.534	0.490	1.860e-04	0.054	0.009	0.175
TF44	2.639	0.595	2.316e-04	0.060	0.011	0.218
TF45	2.744	0.700	2.912e-04	0.042	0.014	0.274
TF46	2.849	0.805	3.556e-04	0.032	0.017	0.335
TF47	2.954	0.910	4.257e-04	0.036	0.020	0.401
TF48	3.059	1.015	5.215e-04	0.031	0.025	0.491
TF49	3.164	1.120	6.116e-04	0.026	0.029	0.576
TF50	3.269	1.225	7.223e-04	0.027	0.034	0.680
TF51	3.374	1.330	8.543e-04	0.022	0.041	0.804
TF52	3.479	1.435	1.012e-03	0.024	0.048	0.953
TF53	3.584	1.540	1.155e-03	0.023	0.055	1.087
TF54	3.689	1.645	1.326e-03	0.023	0.063	1.248
TF55	3.794	1.750	1.526e-03	0.024	0.072	1.437
TF56	3.899	1.855	1.575e-03	0.020	0.075	1.483
TF57	4.004	1.960	1.692e-03	0.020	0.080	1.592
TF58	4.109	2.065	1.786e-03	0.018	0.085	1.681
TF59	4.214	2.170	1.886e-03	0.016	0.089	1.775
TF60	4.319	2.275	1.891e-03	0.016	0.090	1.780
TF61	4.424	2.380	1.870e-03	0.015	0.089	1.760
TF62	4.529	2.485	1.966e-03	0.014	0.093	1.850
TF63	4.634	2.590	1.885e-03	0.013	0.089	1.774
TF64	4.739	2.695	1.933e-03	0.012	0.092	1.820
TF65	4.844	2.800	1.906e-03	0.012	0.090	1.794
TF66	4.949	2.905	1.862e-03	0.010	0.088	1.753
TF67	5.054	3.010	1.846e-03	0.010	0.088	1.737
TF68	5.159	3.115	1.851e-03	0.010	0.088	1.742
TF69	5.264	3.220	1.760e-03	0.008	0.084	1.657
TF70	5.369	3.325	1.736e-03	0.009	0.082	1.635

TABLE A.25 31-Inch Mach 10 Test 293, Run 025 Heating Data
MP-4 Configuration, $Re_\infty = 1.0 \times 10^6$ ft^{-1}, $\alpha = 0$ deg, $\phi = 0$ deg, $C_{H,0} = 0.02048$

GAGE ID	S/R_b	L/R_b	C_H	s/C_H	$C_H/C_{H,0}$	q_{300}(W/cm^2)
TF1	-2.000	-	*	*	*	*
TF2	-1.900	-	2.133e-04	0.072	0.010	0.202
TF3	-1.806	-	2.424e-04	0.059	0.012	0.229
TF4	-1.682	-	1.332e-04	0.067	0.007	0.126
TF5	-1.557	-	1.448e-04	0.044	0.007	0.137
TF6	-1.433	-	1.618e-04	0.101	0.008	0.153
TF7	-1.308	-	3.870e-04	0.110	0.019	0.366
TF8	-1.161	-	2.716e-03	0.055	0.133	2.567
TF9	-1.000	-	1.137e-02	0.005	0.555	10.748
TF10	-0.900	-	1.387e-02	0.007	0.677	13.108
TF11	-0.800	-	1.240e-02	0.006	0.606	11.723
TF12	-0.700	-	1.223e-02	0.004	0.597	11.562
TF13	-0.600	-	1.214e-02	0.005	0.593	11.473
TF14	-0.500	-	1.259e-02	0.003	0.615	11.898
TF15	-0.400	-	1.318e-02	0.003	0.644	12.454
TF16	-0.300	-	1.420e-02	0.002	0.694	13.425
TF17	-0.200	-	1.630e-02	0.001	0.796	15.401
TF18	-0.100	-	1.954e-02	0.001	0.954	18.471
TF19	0.000	-	2.048e-02	0.002	1.000	19.353
TF20	0.100	-	1.951e-02	0.001	0.953	18.441
TF21	0.200	-	1.598e-02	0.001	0.781	15.106
TF22	0.300	-	1.405e-02	0.002	0.686	13.280
TF23	0.400	-	1.297e-02	0.004	0.633	12.255
TF24	0.500	-	1.258e-02	0.005	0.614	11.890
TF25	0.600	-	1.224e-02	0.006	0.598	11.566
TF26	0.700	-	1.242e-02	0.006	0.607	11.737
TF27	0.800	-	1.268e-02	0.007	0.619	11.984
TF28	0.900	-	1.413e-02	0.008	0.690	13.358
TF29	1.000	-	1.127e-02	0.006	0.551	10.654
TF30	1.161	-	2.621e-03	0.057	0.128	2.477
TF31	1.308	-	3.459e-04	0.082	0.017	0.327
TF32	1.433	-	1.451e-04	0.089	0.007	0.137
TF33	1.557	-	1.181e-04	0.066	0.006	0.112
TF34	1.682	-	1.225e-04	0.112	0.006	0.116
TF35	1.806	-	2.035e-04	0.108	0.010	0.192
TF36	1.900	-	*	*	*	*
TF37	2.000	-	1.242e-04	0.075	0.006	0.117
TF39	2.114	0.070	7.864e-05	0.138	0.004	0.074
TF40	2.219	0.175	6.854e-05	0.091	0.003	0.065
TF41	2.324	0.280	8.845e-05	0.081	0.004	0.084
TF42	2.429	0.385	1.378e-04	0.069	0.007	0.130
TF43	2.534	0.490	1.818e-04	0.019	0.009	0.172
TF44	2.639	0.595	2.224e-04	0.051	0.011	0.210
TF45	2.744	0.700	2.916e-04	0.042	0.014	0.276
TF46	2.849	0.805	3.518e-04	0.030	0.017	0.333
TF47	2.954	0.910	4.325e-04	0.025	0.021	0.409
TF48	3.059	1.015	5.195e-04	0.028	0.025	0.491
TF49	3.164	1.120	6.137e-04	0.028	0.030	0.580
TF50	3.269	1.225	7.223e-04	0.024	0.035	0.683
TF51	3.374	1.330	8.562e-04	0.024	0.042	0.809
TF52	3.479	1.435	1.013e-03	0.023	0.049	0.957
TF53	3.584	1.540	1.160e-03	0.021	0.057	1.096
TF54	3.689	1.645	1.322e-03	0.022	0.065	1.249
TF55	3.794	1.750	1.531e-03	0.018	0.075	1.447
TF56	3.899	1.855	1.582e-03	0.019	0.077	1.495
TF57	4.004	1.960	1.692e-03	0.017	0.083	1.600
TF58	4.109	2.065	1.783e-03	0.017	0.087	1.685
TF59	4.214	2.170	1.884e-03	0.016	0.092	1.780
TF60	4.319	2.275	1.885e-03	0.014	0.092	1.782
TF61	4.424	2.380	1.874e-03	0.011	0.092	1.771
TF62	4.529	2.485	1.965e-03	0.013	0.096	1.857
TF63	4.634	2.590	1.885e-03	0.014	0.092	1.781
TF64	4.739	2.695	1.935e-03	0.012	0.094	1.829
TF65	4.844	2.800	1.915e-03	0.011	0.094	1.810
TF66	4.949	2.905	1.858e-03	0.012	0.091	1.756
TF67	5.054	3.010	1.847e-03	0.013	0.090	1.746
TF68	5.159	3.115	1.854e-03	0.014	0.091	1.752
TF69	5.264	3.220	1.763e-03	0.008	0.086	1.666
TF70	5.369	3.325	1.738e-03	0.011	0.085	1.642

TABLE A.26 31-Inch Mach 10 Test 293, Run 026 Heating Data
MP-4 Configuration, $Re_\infty = 1.0 \times 10^6$ ft^{-1}, α = -4 deg, ϕ = 0 deg, $C_{H,0} = 0.02027$

GAGE ID	S/R_b	L/R_b	C_H	s/C_H	$C_H/C_{H,0}$	q_{300}(W/cm^2)
TF1	-2.000	-	*	*	*	*
TF2	-1.900	-	3.859e-04	0.046	0.019	0.359
TF3	-1.806	-	3.695e-04	0.052	0.018	0.344
TF4	-1.682	-	2.253e-04	0.025	0.011	0.210
TF5	-1.557	-	2.326e-04	0.042	0.011	0.217
TF6	-1.433	-	2.415e-04	0.026	0.012	0.225
TF7	-1.308	-	3.045e-04	0.125	0.015	0.284
TF8	-1.161	-	2.171e-03	0.062	0.107	2.021
TF9	-1.000	-	1.003e-02	0.007	0.495	9.336
TF10	-0.900	-	1.275e-02	0.008	0.629	11.870
TF11	-0.800	-	1.157e-02	0.015	0.571	10.770
TF12	-0.700	-	1.134e-02	0.007	0.560	10.560
TF13	-0.600	-	1.129e-02	0.008	0.557	10.516
TF14	-0.500	-	1.172e-02	0.006	0.578	10.915
TF15	-0.400	-	1.230e-02	0.005	0.607	11.449
TF16	-0.300	-	1.328e-02	0.004	0.655	12.369
TF17	-0.200	-	1.537e-02	0.002	0.758	14.310
TF18	-0.100	-	1.892e-02	0.002	0.933	17.617
TF19	0.000	-	2.027e-02	0.003	1.000	18.873
TF20	0.100	-	1.978e-02	0.001	0.976	18.414
TF21	0.200	-	1.658e-02	0.002	0.818	15.441
TF22	0.300	-	1.466e-02	0.003	0.723	13.646
TF23	0.400	-	1.348e-02	0.004	0.665	12.555
TF24	0.500	-	1.309e-02	0.005	0.646	12.184
TF25	0.600	-	1.269e-02	0.005	0.626	11.811
TF26	0.700	-	1.326e-02	0.020	0.654	12.342
TF27	0.800	-	1.309e-02	0.007	0.646	12.184
TF28	0.900	-	1.470e-02	0.006	0.725	13.690
TF29	1.000	-	1.228e-02	0.006	0.606	11.438
TF30	1.161	-	3.173e-03	0.050	0.157	2.954
TF31	1.308	-	4.568e-04	0.089	0.023	0.425
TF32	1.433	-	9.253e-05	0.134	0.005	0.086
TF33	1.557	-	5.511e-05	0.178	0.003	0.051
TF34	1.682	-	6.014e-05	0.081	0.003	0.056
TF35	1.806	-	8.773e-05	0.083	0.004	0.082
TF36	1.900	-	*	*	*	*
TF37	2.000	-	8.561e-05	0.070	0.004	0.080
TF39	2.114	0.070	5.848e-05	0.126	0.003	0.054
TF40	2.219	0.175	1.091e-04	0.068	0.005	0.102
TF41	2.324	0.280	1.736e-04	0.043	0.009	0.162
TF42	2.429	0.385	2.527e-04	0.058	0.012	0.235
TF43	2.534	0.490	2.950e-04	0.023	0.015	0.275
TF44	2.639	0.595	3.593e-04	0.039	0.018	0.335
TF45	2.744	0.700	4.537e-04	0.037	0.022	0.422
TF46	2.849	0.805	5.960e-04	0.031	0.029	0.555
TF47	2.954	0.910	7.696e-04	0.025	0.038	0.717
TF48	3.059	1.015	9.963e-04	0.026	0.049	0.928
TF49	3.164	1.120	1.263e-03	0.028	0.062	1.176
TF50	3.269	1.225	1.529e-03	0.016	0.075	1.423
TF51	3.374	1.330	1.806e-03	0.014	0.089	1.682
TF52	3.479	1.435	2.060e-03	0.015	0.102	1.918
TF53	3.584	1.540	2.195e-03	0.015	0.108	2.044
TF54	3.689	1.645	2.308e-03	0.015	0.114	2.149
TF55	3.794	1.750	2.440e-03	0.015	0.120	2.272
TF56	3.899	1.855	2.365e-03	0.016	0.117	2.202
TF57	4.004	1.960	2.309e-03	0.015	0.114	2.150
TF58	4.109	2.065	2.258e-03	0.016	0.111	2.102
TF59	4.214	2.170	2.252e-03	0.015	0.111	2.097
TF60	4.319	2.275	2.145e-03	0.013	0.106	1.997
TF61	4.424	2.380	2.025e-03	0.013	0.100	1.886
TF62	4.529	2.485	2.052e-03	0.011	0.101	1.911
TF63	4.634	2.590	1.929e-03	0.012	0.095	1.797
TF64	4.739	2.695	1.930e-03	0.011	0.095	1.797
TF65	4.844	2.800	1.880e-03	0.013	0.093	1.750
TF66	4.949	2.905	1.813e-03	0.012	0.089	1.688
TF67	5.054	3.010	1.790e-03	0.010	0.088	1.667
TF68	5.159	3.115	1.788e-03	0.010	0.088	1.665
TF69	5.264	3.220	1.695e-03	0.011	0.084	1.579
TF70	5.369	3.325	1.665e-03	0.011	0.082	1.551

TABLE A.27 31-Inch Mach 10 Test 293, Run 027 Heating Data
MP-4 Configuration, $Re_\infty = 1.0 \times 10^6$ ft^{-1}, $\alpha = -20$ deg, $\phi = 0$ deg, $C_{H,0} = 0.01968$

GAGE ID	S/R_b	L/R_b	C_H	s/C_H	$C_H/C_{H,0}$	q_{300}(W/cm^2)
TF1	-2.000	--	*	*	*	*
TF2	-1.900	-	1.359e-04	0.051	0.007	0.128
TF3	-1.806	-	1.192e-04	0.050	0.006	0.112
TF4	-1.682	-	7.792e-05	0.050	0.004	0.073
TF5	-1.557	-	9.460e-05	0.032	0.005	0.089
TF6	-1.433	-	1.538e-04	0.034	0.008	0.145
TF7	-1.308	-	1.609e-04	0.093	0.008	0.152
TF8	-1.161	-	1.056e-03	0.083	0.054	0.994
TF9	-1.000	-	6.609e-03	0.009	0.336	6.225
TF10	-0.900	-	9.096e-03	0.006	0.462	8.568
TF11	-0.800	-	8.111e-03	0.003	0.412	7.640
TF12	-0.700	-	8.037e-03	0.001	0.408	7.570
TF13	-0.600	-	8.147e-03	0.001	0.414	7.674
TF14	-0.500	-	8.600e-03	0.001	0.437	8.100
TF15	-0.400	-	9.180e-03	0.001	0.467	8.647
TF16	-0.300	-	1.015e-02	0.004	0.516	9.562
TF17	-0.200	-	1.232e-02	0.007	0.626	11.607
TF18	-0.100	-	1.693e-02	0.002	0.860	15.945
TF19	0.000	-	1.968e-02	0.001	1.000	18.534
TF20	0.100	-	2.085e-02	0.003	1.060	19.642
TF21	0.200	-	1.857e-02	0.004	0.944	17.487
TF22	0.300	-	1.657e-02	0.002	0.842	15.608
TF23	0.400	-	1.538e-02	0.004	0.782	14.488
TF24	0.500	-	1.505e-02	0.003	0.765	14.173
TF25	0.600	-	1.477e-02	0.005	0.751	13.916
TF26	0.700	-	1.518e-02	0.005	0.772	14.302
TF27	0.800	-	1.582e-02	0.007	0.804	14.904
TF28	0.900	-	1.886e-02	0.005	0.958	17.763
TF29	1.000	-	1.949e-02	0.002	0.991	18.363
TF30	1.161	-	7.451e-03	0.032	0.379	7.018
TF31	1.308	-	1.333e-03	0.074	0.068	1.255
TF32	1.433	-	7.317e-04	0.029	0.037	0.689
TF33	1.557	-	6.193e-04	0.037	0.031	0.583
TF34	1.682	-	5.584e-04	0.029	0.028	0.526
TF35	1.806	-	5.448e-04	0.032	0.028	0.513
TF36	1.900	-	*	*	*	*
TF37	2.000	-	3.439e-04	0.020	0.017	0.324
TF39	2.114	0.070	4.600e-04	0.038	0.023	0.433
TF40	2.219	0.175	9.986e-04	0.039	0.051	0.941
TF41	2.324	0.280	2.340e-03	0.024	0.119	2.204
TF42	2.429	0.385	4.937e-03	0.004	0.251	4.651
TF43	2.534	0.490	6.013e-03	0.003	0.306	5.664
TF44	2.639	0.595	5.903e-03	0.008	0.300	5.560
TF45	2.744	0.700	5.336e-03	0.008	0.271	5.026
TF46	2.849	0.805	4.991e-03	0.010	0.254	4.701
TF47	2.954	0.910	4.753e-03	0.006	0.242	4.477
TF48	3.059	1.015	4.530e-03	0.002	0.230	4.267
TF49	3.164	1.120	4.340e-03	0.006	0.221	4.088
TF50	3.269	1.225	4.191e-03	0.005	0.213	3.948
TF51	3.374	1.330	4.096e-03	0.006	0.208	3.858
TF52	3.479	1.435	4.057e-03	0.007	0.206	3.821
TF53	3.584	1.540	3.939e-03	0.005	0.200	3.710
TF54	3.689	1.645	3.911e-03	0.005	0.199	3.684
TF55	3.794	1.750	4.023e-03	0.004	0.204	3.789
TF56	3.899	1.855	3.853e-03	0.005	0.196	3.629
TF57	4.004	1.960	3.766e-03	0.007	0.191	3.547
TF58	4.109	2.065	3.758e-03	0.005	0.191	3.540
TF59	4.214	2.170	3.807e-03	0.003	0.193	3.586
TF60	4.319	2.275	3.721e-03	0.004	0.189	3.505
TF61	4.424	2.380	3.597e-03	0.003	0.183	3.388
TF62	4.529	2.485	3.772e-03	0.004	0.192	3.553
TF63	4.634	2.590	3.576e-03	0.003	0.182	3.368
TF64	4.739	2.695	3.763e-03	0.005	0.191	3.545
TF65	4.844	2.800	3.782e-03	0.006	0.192	3.562
TF66	4.949	2.905	3.740e-03	0.004	0.190	3.523
TF67	5.054	3.010	3.816e-03	0.005	0.194	3.595
TF68	5.159	3.115	3.923e-03	0.006	0.199	3.695
TF69	5.264	3.220	3.799e-03	0.004	0.193	3.579
TF70	5.369	3.325	3.902e-03	0.004	0.198	3.676

TABLE A.28 31-Inch Mach 10 Test 293, Run 028 Heating Data
MP-4 Configuration, $Re_\infty = 2.0 \times 10^6$ ft^{-1}, $\alpha = 0$ deg, $\phi = 0$ deg, $C_{H,0} = 0.01464$

GAGE ID	S/R_b	L/R_b	C_H	s/C_H	$C_H/C_{H,0}$	q_{300}(W/cm^2)
TF1	-2.000	-	*	*	*	*
TF2	-1.900	-	1.477e-04	0.071	0.010	0.265
TF3	-1.806	-	1.328e-04	0.067	0.009	0.238
TF4	-1.682	-	8.036e-05	0.067	0.005	0.144
TF5	-1.557	-	7.133e-05	0.080	0.005	0.128
TF6	-1.433	-	7.959e-05	0.090	0.005	0.143
TF7	-1.308	-	1.928e-04	0.143	0.013	0.346
TF8	-1.161	-	1.955e-03	0.062	0.133	3.504
TF9	-1.000	-	8.159e-03	0.004	0.557	14.626
TF10	-0.900	-	9.780e-03	0.009	0.668	17.533
TF11	-0.800	-	8.823e-03	0.008	0.602	15.817
TF12	-0.700	-	8.716e-03	0.006	0.595	15.623
TF13	-0.600	-	8.704e-03	0.007	0.594	15.603
TF14	-0.500	-	9.025e-03	0.004	0.616	16.177
TF15	-0.400	-	9.479e-03	0.004	0.647	16.992
TF16	-0.300	-	1.022e-02	0.003	0.698	18.314
TF17	-0.200	-	1.169e-02	0.002	0.799	20.964
TF18	-0.100	-	1.399e-02	0.002	0.955	25.079
TF19	0.000	-	1.464e-02	0.004	1.000	26.251
TF20	0.100	-	1.397e-02	0.002	0.954	25.050
TF21	0.200	-	1.149e-02	0.002	0.784	20.592
TF22	0.300	-	1.014e-02	0.002	0.692	18.178
TF23	0.400	-	9.599e-03	0.005	0.655	17.207
TF24	0.500	-	9.037e-03	0.004	0.617	16.200
TF25	0.600	-	8.769e-03	0.006	0.599	15.720
TF26	0.700	-	8.800e-03	0.006	0.601	15.774
TF27	0.800	-	8.907e-03	0.008	0.608	15.966
TF28	0.900	-	9.993e-03	0.009	0.682	17.914
TF29	1.000	-	7.922e-03	0.008	0.541	14.201
TF30	1.161	-	1.832e-03	0.060	0.125	3.283
TF31	1.308	-	1.578e-04	0.139	0.011	0.283
TF32	1.433	-	7.370e-05	0.063	0.005	0.132
TF33	1.557	-	5.786e-05	0.078	0.004	0.104
TF34	1.682	-	6.949e-05	0.090	0.005	0.125
TF35	1.806	-	1.265e-04	0.053	0.009	0.227
TF36	1.900	-	*	*	*	*
TF37	2.000	-	1.032e-04	0.059	0.007	0.185
TF39	2.114	0.070	6.458e-05	0.061	0.004	0.116
TF40	2.219	0.175	5.536e-05	0.084	0.004	0.099
TF41	2.324	0.280	6.417e-05	0.069	0.004	0.115
TF42	2.429	0.385	8.477e-05	0.046	0.006	0.152
TF43	2.534	0.490	1.098e-04	0.040	0.007	0.197
TF44	2.639	0.595	1.523e-04	0.043	0.010	0.273
TF45	2.744	0.700	1.905e-04	0.041	0.013	0.342
TF46	2.849	0.805	2.478e-04	0.038	0.017	0.444
TF47	2.954	0.910	3.074e-04	0.035	0.021	0.551
TF48	3.059	1.015	3.783e-04	0.037	0.026	0.678
TF49	3.164	1.120	4.632e-04	0.030	0.032	0.830
TF50	3.269	1.225	5.634e-04	0.030	0.038	1.010
TF51	3.374	1.330	7.009e-04	0.022	0.048	1.256
TF52	3.479	1.435	8.675e-04	0.019	0.059	1.555
TF53	3.584	1.540	1.032e-03	0.018	0.070	1.850
TF54	3.689	1.645	1.222e-03	0.019	0.083	2.190
TF55	3.794	1.750	1.449e-03	0.016	0.099	2.598
TF56	3.899	1.855	1.558e-03	0.014	0.106	2.792
TF57	4.004	1.960	1.658e-03	0.010	0.113	2.972
TF58	4.109	2.065	1.751e-03	0.011	0.120	3.140
TF59	4.214	2.170	1.844e-03	0.010	0.126	3.306
TF60	4.319	2.275	1.839e-03	0.010	0.126	3.296
TF61	4.424	2.380	1.786e-03	0.012	0.122	3.201
TF62	4.529	2.485	1.845e-03	0.010	0.126	3.308
TF63	4.634	2.590	1.720e-03	0.006	0.117	3.083
TF64	4.739	2.695	1.751e-03	0.010	0.120	3.138
TF65	4.844	2.800	1.704e-03	0.012	0.116	3.055
TF66	4.949	2.905	1.628e-03	0.012	0.111	2.918
TF67	5.054	3.010	1.585e-03	0.011	0.108	2.842
TF68	5.159	3.115	1.565e-03	0.012	0.107	2.805
TF69	5.264	3.220	1.444e-03	0.008	0.099	2.589
TF70	5.369	3.325	1.423e-03	0.009	0.097	2.551

TABLE A.29 31-Inch Mach 10 Test 293, Run 029 Heating Data
MP-1 Configuration, $Re_\infty = 1.0 \times 10^6$ ft^{-1}, $\alpha = 0$ deg, $\phi = 90$ deg, $C_{H,0} = 0.01996$

GAGE ID	S/R_b	L/R_b	C_H	s/C_H	$C_H/C_{H,0}$	q_{300}(W/cm^2)
TF1	-1.872	-	1.206e-04	0.093	0.006	0.113
TF2	-1.772	-	1.482e-04	0.078	0.007	0.139
TF3	-1.678	-	1.762e-04	0.078	0.009	0.166
TF4	-1.554	-	1.035e-04	0.110	0.005	0.097
TF5	-1.429	-	1.083e-04	0.131	0.005	0.102
TF6	-1.305	-	1.287e-04	0.062	0.006	0.121
TF7	-1.180	-	6.930e-04	0.376	0.035	0.652
TF8	-1.083	-	8.010e-03	0.048	0.401	7.537
TF9	-1.000	-	1.300e-02	0.006	0.652	12.235
TF10	-0.900	-	1.207e-02	0.004	0.605	11.353
TF11	-0.800	-	1.159e-02	0.002	0.581	10.909
TF12	-0.700	-	1.160e-02	0.002	0.581	10.913
TF13	-0.600	-	1.231e-02	0.009	0.617	11.585
TF14	-0.500	-	1.217e-02	0.002	0.610	11.455
TF15	-0.400	-	1.282e-02	0.002	0.643	12.067
TF16	-0.300	-	1.402e-02	0.003	0.702	13.189
TF17	-0.200	-	1.661e-02	0.003	0.832	15.631
TF18	-0.100	-	1.908e-02	0.002	0.956	17.957
TF19	0.000	-	1.996e-02	0.001	1.000	18.780
TF20	0.100	-	1.904e-02	0.003	0.954	17.920
TF21	0.200	-	1.569e-02	0.002	0.786	14.760
TF22	0.300	-	1.395e-02	0.011	0.699	13.130
TF23	0.400	-	1.289e-02	0.001	0.646	12.130
TF24	0.500	-	1.233e-02	0.001	0.618	11.602
TF25	0.600	-	1.187e-02	0.004	0.595	11.166
TF26	0.700	-	*	*	*	*
TF27	0.800	-	1.185e-02	0.004	0.594	11.149
TF28	0.900	-	1.234e-02	0.002	0.618	11.614
TF29	1.000	-	1.336e-02	0.012	0.669	12.570
TF30	1.083	-	7.444e-03	0.062	0.373	7.004
TF31	1.180	-	7.308e-04	0.384	0.037	0.688
TF32	1.305	-	1.322e-04	0.083	0.007	0.124
TF33	1.429	-	*	*	*	*
TF34	1.554	-	*	*	*	*
TF35	1.678	-	1.674e-04	0.087	0.008	0.158
TF36	1.772	-	*	*	*	*
TF37	1.872	-	*	*	*	*
TF38	1.931	0.015	5.982e-05	0.104	0.003	0.056
TF39	2.036	0.120	8.054e-05	0.155	0.004	0.076
TF40	2.141	0.225	1.396e-04	0.078	0.007	0.131
TF41	2.246	0.330	1.655e-04	0.052	0.008	0.156
TF42	2.351	0.435	2.210e-04	0.050	0.011	0.208
TF43	2.456	0.540	2.800e-04	0.034	0.014	0.263
TF44	2.561	0.645	3.208e-04	0.048	0.016	0.302
TF45	2.666	0.750	3.861e-04	0.040	0.019	0.363
TF46	2.771	0.855	4.438e-04	0.035	0.022	0.418
TF47	2.876	0.960	5.155e-04	0.031	0.026	0.485
TF48	2.981	1.065	6.118e-04	0.032	0.031	0.576
TF49	3.086	1.170	7.400e-04	0.034	0.037	0.696
TF50	3.191	1.275	8.729e-04	0.029	0.044	0.821
TF51	3.296	1.380	1.042e-03	0.028	0.052	0.980
TF52	3.401	1.485	1.228e-03	0.026	0.062	1.156
TF53	3.506	1.590	1.392e-03	0.020	0.070	1.310
TF54	3.611	1.695	1.570e-03	0.018	0.079	1.477
TF55	3.716	1.800	1.774e-03	0.017	0.089	1.670
TF56	3.821	1.905	1.896e-03	0.016	0.095	1.784
TF57	3.926	2.010	2.053e-03	0.017	0.103	1.932
TF58	4.031	2.115	2.110e-03	0.017	0.106	1.985
TF59	4.136	2.220	2.209e-03	0.014	0.111	2.079
TF60	4.241	2.325	2.254e-03	0.015	0.113	2.121
TF61	4.346	2.430	2.253e-03	0.013	0.113	2.120
TF62	4.451	2.535	2.295e-03	0.015	0.115	2.159
TF63	4.556	2.640	2.297e-03	0.016	0.115	2.161
TF64	4.661	2.745	2.213e-03	0.012	0.111	2.082
TF65	4.766	2.850	2.176e-03	0.011	0.109	2.048
TF66	4.871	2.955	2.137e-03	0.011	0.107	2.011
TF67	4.976	3.060	2.066e-03	0.010	0.104	1.944
TF68	5.081	3.165	2.005e-03	0.011	0.100	1.887
TF69	5.186	3.270	1.976e-03	0.009	0.099	1.859
TF70	5.291	3.375	1.915e-03	0.010	0.096	1.802

TABLE A.30 31-Inch Mach 10 Test 293, Run 030 Heating Data
MP-1 Configuration, $Re_\infty = 1.0 \times 10^6$ ft^{-1}, $\alpha = 0$ deg, $\phi = 90$ deg, $C_{H,0} = 0.02010$

GAGE ID	S/R_b	L/R_b	C_H	s/C_H	$C_H/C_{H,0}$	q_{300}(W/cm^2)
TF1	-1.872	-	1.129e-04	0.063	0.006	0.106
TF2	-1.772	-	1.214e-04	0.085	0.006	0.114
TF3	-1.678	-	1.508e-04	0.058	0.008	0.142
TF4	-1.554	-	1.111e-04	0.074	0.006	0.105
TF5	-1.429	-	1.149e-04	0.044	0.006	0.108
TF6	-1.305	-	1.242e-04	0.078	0.006	0.117
TF7	-1.180	-	6.795e-04	0.376	0.034	0.640
TF8	-1.083	-	8.116e-03	0.047	0.404	7.645
TF9	-1.000	-	1.319e-02	0.007	0.656	12.423
TF10	-0.900	-	1.223e-02	0.002	0.609	11.525
TF11	-0.800	-	1.177e-02	0.001	0.586	11.089
TF12	-0.700	-	1.176e-02	0.002	0.585	11.079
TF13	-0.600	-	1.213e-02	0.011	0.603	11.425
TF14	-0.500	-	1.234e-02	0.001	0.614	11.624
TF15	-0.400	-	1.302e-02	0.002	0.648	12.267
TF16	-0.300	-	1.419e-02	0.001	0.706	13.366
TF17	-0.200	-	1.685e-02	0.002	0.839	15.875
TF18	-0.100	-	1.938e-02	0.001	0.964	18.254
TF19	0.000	-	2.010e-02	0.001	1.000	18.933
TF20	0.100	-	1.931e-02	0.001	0.961	18.193
TF21	0.200	-	1.588e-02	0.002	0.790	14.957
TF22	0.300	-	1.399e-02	0.002	0.696	13.178
TF23	0.400	-	1.306e-02	0.003	0.650	12.305
TF24	0.500	-	1.247e-02	0.003	0.620	11.745
TF25	0.600	-	1.201e-02	0.006	0.597	11.310
TF26	0.700	-	*	*	*	*
TF27	0.800	-	1.198e-02	0.006	0.596	11.282
TF28	0.900	-	1.246e-02	0.004	0.620	11.737
TF29	1.000	-	1.351e-02	0.013	0.672	12.725
TF30	1.083	-	7.514e-03	0.062	0.374	7.078
TF31	1.180	-	7.276e-04	0.380	0.036	0.685
TF32	1.305	-	1.583e-04	0.057	0.008	0.149
TF33	1.429	-	*	*	*	*
TF34	1.554	-	*	*	*	*
TF35	1.678	-	1.728e-04	0.023	0.009	0.163
TF36	1.772	-	*	*	*	*
TF37	1.872	-	*	*	*	*
TF38	1.931	0.015	5.532e-05	0.130	0.003	0.052
TF39	2.036	0.120	9.386e-05	0.071	0.005	0.088
TF40	2.141	0.225	1.393e-04	0.049	0.007	0.131
TF41	2.246	0.330	1.603e-04	0.044	0.008	0.151
TF42	2.351	0.435	2.001e-04	0.029	0.010	0.188
TF43	2.456	0.540	2.805e-04	0.038	0.014	0.264
TF44	2.561	0.645	3.292e-04	0.032	0.016	0.310
TF45	2.666	0.750	3.980e-04	0.035	0.020	0.375
TF46	2.771	0.855	4.462e-04	0.043	0.022	0.420
TF47	2.876	0.960	5.127e-04	0.035	0.026	0.483
TF48	2.981	1.065	6.000e-04	0.038	0.030	0.565
TF49	3.086	1.170	7.183e-04	0.034	0.036	0.677
TF50	3.191	1.275	8.457e-04	0.032	0.042	0.797
TF51	3.296	1.380	1.013e-03	0.037	0.050	0.954
TF52	3.401	1.485	1.224e-03	0.035	0.061	1.153
TF53	3.506	1.590	1.408e-03	0.034	0.070	1.326
TF54	3.611	1.695	1.605e-03	0.031	0.080	1.512
TF55	3.716	1.800	1.811e-03	0.030	0.090	1.705
TF56	3.821	1.905	1.956e-03	0.024	0.097	1.843
TF57	3.926	2.010	2.102e-03	0.023	0.105	1.980
TF58	4.031	2.115	2.184e-03	0.021	0.109	2.058
TF59	4.136	2.220	2.253e-03	0.018	0.112	2.122
TF60	4.241	2.325	2.271e-03	0.015	0.113	2.139
TF61	4.346	2.430	2.241e-03	0.013	0.112	2.111
TF62	4.451	2.535	2.263e-03	0.014	0.113	2.131
TF63	4.556	2.640	2.231e-03	0.013	0.111	2.101
TF64	4.661	2.745	2.109e-03	0.014	0.105	1.986
TF65	4.766	2.850	2.043e-03	0.011	0.102	1.924
TF66	4.871	2.955	1.980e-03	0.012	0.099	1.865
TF67	4.976	3.060	1.884e-03	0.007	0.094	1.775
TF68	5.081	3.165	1.817e-03	0.010	0.090	1.711
TF69	5.186	3.270	1.772e-03	0.008	0.088	1.669
TF70	5.291	3.375	1.693e-03	0.010	0.084	1.595

TABLE A.31 31-Inch Mach 10 Test 293, Run 031 Heating Data
MP-1 Configuration, $Re_\infty = 1.0 \times 10^6$ ft^{-1}, $\alpha = -4$ deg, $\phi = 180$ deg

** BAD RUN, NO DATA **

TABLE A.32 31-Inch Mach 10 Test 293, Run 032 Heating Data
MP-1 Configuration, $Re_\infty = 1.0 \times 10^6$ ft^{-1}, $\alpha = -4$ deg, $\phi = 180$ deg, $C_{H,0} = 0.01993$

GAGE ID	S/R_b	L/R_b	C_H	s/C_H	$C_H/C_{H,0}$	q_{300}(W/cm^2)
TF1	-1.872	-	1.092e-04	0.127	0.005	0.102
TF2	-1.772	-	1.773e-04	0.065	0.009	0.166
TF3	-1.678	-	1.418e-04	0.071	0.007	0.133
TF4	-1.554	-	6.214e-05	0.161	0.003	0.058
TF5	-1.429	-	7.754e-05	0.093	0.004	0.073
TF6	-1.305	-	9.113e-05	0.143	0.005	0.085
TF7	-1.180	-	7.803e-04	0.366	0.039	0.732
TF8	-1.083	-	9.055e-03	0.039	0.454	8.492
TF9	-1.000	-	1.414e-02	0.010	0.709	13.258
TF10	-0.900	-	1.288e-02	0.002	0.646	12.076
TF11	-0.800	-	1.229e-02	0.004	0.616	11.524
TF12	-0.700	-	1.223e-02	0.002	0.614	11.473
TF13	-0.600	-	1.248e-02	0.002	0.626	11.706
TF14	-0.500	-	1.286e-02	0.002	0.645	12.060
TF15	-0.400	-	1.354e-02	0.001	0.679	12.697
TF16	-0.300	-	1.480e-02	0.003	0.743	13.882
TF17	-0.200	-	1.738e-02	0.003	0.872	16.296
TF18	-0.100	-	1.951e-02	0.003	0.979	18.300
TF19	0.000	-	1.993e-02	0.001	1.000	18.693
TF20	0.100	-	1.857e-02	0.002	0.932	17.416
TF21	0.200	-	1.495e-02	0.002	0.750	14.017
TF22	0.300	-	1.304e-02	0.002	0.654	12.225
TF23	0.400	-	1.217e-02	0.003	0.610	11.412
TF24	0.500	-	1.161e-02	0.002	0.582	10.883
TF25	0.600	-	1.116e-02	0.004	0.560	10.464
TF26	0.700	-	*	*	*	*
TF27	0.800	-	1.111e-02	0.004	0.557	10.422
TF28	0.900	-	1.155e-02	0.003	0.579	10.831
TF29	1.000	-	1.237e-02	0.013	0.620	11.596
TF30	1.083	-	6.884e-03	0.057	0.345	6.456
TF31	1.180	-	7.921e-04	0.323	0.040	0.743
TF32	1.305	-	2.940e-04	0.039	0.015	0.276
TF33	1.429	-	*	*	*	*
TF34	1.554	-	*	*	*	*
TF35	1.678	-	4.444e-04	0.027	0.022	0.417
TF36	1.772	-	*	*	*	*
TF37	1.872	-	*	*	*	*
TF38	1.931	0.015	2.292e-04	0.043	0.011	0.215
TF39	2.036	0.120	2.224e-04	0.035	0.011	0.209
TF40	2.141	0.225	2.591e-04	0.022	0.013	0.243
TF41	2.246	0.330	2.346e-04	0.028	0.012	0.220
TF42	2.351	0.435	2.414e-04	0.035	0.012	0.226
TF43	2.456	0.540	2.689e-04	0.033	0.013	0.252
TF44	2.561	0.645	2.854e-04	0.032	0.014	0.268
TF45	2.666	0.750	3.123e-04	0.030	0.016	0.293
TF46	2.771	0.855	3.210e-04	0.022	0.016	0.301
TF47	2.876	0.960	3.408e-04	0.035	0.017	0.320
TF48	2.981	1.065	3.605e-04	0.014	0.018	0.338
TF49	3.086	1.170	3.976e-04	0.013	0.020	0.373
TF50	3.191	1.275	4.284e-04	0.029	0.021	0.402
TF51	3.296	1.380	4.703e-04	0.013	0.024	0.441
TF52	3.401	1.485	5.098e-04	0.024	0.026	0.478
TF53	3.506	1.590	5.653e-04	0.029	0.028	0.530
TF54	3.611	1.695	6.036e-04	0.034	0.030	0.566
TF55	3.716	1.800	6.825e-04	0.027	0.034	0.640
TF56	3.821	1.905	7.338e-04	0.035	0.037	0.688
TF57	3.926	2.010	8.135e-04	0.035	0.041	0.763
TF58	4.031	2.115	8.776e-04	0.035	0.044	0.823
TF59	4.136	2.220	9.635e-04	0.042	0.048	0.904
TF60	4.241	2.325	1.043e-03	0.045	0.052	0.979
TF61	4.346	2.430	1.104e-03	0.042	0.055	1.035
TF62	4.451	2.535	1.181e-03	0.036	0.059	1.108
TF63	4.556	2.640	1.275e-03	0.047	0.064	1.196
TF64	4.661	2.745	1.296e-03	0.041	0.065	1.215
TF65	4.766	2.850	1.345e-03	0.041	0.067	1.261
TF66	4.871	2.955	1.390e-03	0.037	0.070	1.303
TF67	4.976	3.060	1.400e-03	0.034	0.070	1.313
TF68	5.081	3.165	1.422e-03	0.033	0.071	1.334
TF69	5.186	3.270	1.458e-03	0.027	0.073	1.367
TF70	5.291	3.375	1.471e-03	0.026	0.074	1.379

TABLE A.33 31-Inch Mach 10 Test 293, Run 033 Heating Data
MP-1 Configuration, $Re_\infty = 1.0 \times 10^6$ ft^{-1}, $\alpha = -12$ deg, $\phi = 180$ deg, $C_{H,0} = 0.02002$

GAGE ID	S/R_b	L/R_b	C_H	s/C_H	$C_H/C_{H,0}$	q_{300}(W/cm^2)
TF1	-1.872	-	2.921e-04	0.053	0.015	0.281
TF2	-1.772	-	3.935e-04	0.024	0.020	0.378
TF3	-1.678	-	2.635e-04	0.070	0.013	0.253
TF4	-1.554	-	1.591e-04	0.058	0.008	0.153
TF5	-1.429	-	1.538e-04	0.110	0.008	0.148
TF6	-1.305	-	2.707e-04	0.091	0.014	0.260
TF7	-1.180	-	1.052e-03	0.329	0.053	1.010
TF8	-1.083	-	1.117e-02	0.033	0.558	10.735
TF9	-1.000	-	1.624e-02	0.010	0.811	15.602
TF10	-0.900	-	1.435e-02	0.002	0.717	13.787
TF11	-0.800	-	1.355e-02	0.005	0.677	13.017
TF12	-0.700	-	1.341e-02	0.004	0.670	12.884
TF13	-0.600	-	1.352e-02	0.061	0.675	12.987
TF14	-0.500	-	1.401e-02	0.004	0.700	13.457
TF15	-0.400	-	1.470e-02	0.007	0.734	14.116
TF16	-0.300	-	1.609e-02	0.004	0.803	15.454
TF17	-0.200	-	1.882e-02	0.003	0.940	18.075
TF18	-0.100	-	2.043e-02	0.002	1.020	19.627
TF19	0.000	-	2.002e-02	0.001	1.000	19.235
TF20	0.100	-	1.782e-02	0.002	0.890	17.121
TF21	0.200	-	1.361e-02	0.004	0.680	13.076
TF22	0.300	-	1.159e-02	0.002	0.579	11.137
TF23	0.400	-	1.073e-02	0.002	0.536	10.309
TF24	0.500	-	1.018e-02	0.001	0.509	9.781
TF25	0.600	-	9.761e-03	0.003	0.487	9.377
TF26	0.700	-	*	*	*	*
TF27	0.800	-	9.638e-03	0.002	0.481	9.258
TF28	0.900	-	9.993e-03	0.002	0.499	9.599
TF29	1.000	-	1.072e-02	0.013	0.535	10.293
TF30	1.083	-	5.779e-03	0.065	0.289	5.552
TF31	1.180	-	6.621e-04	0.337	0.033	0.636
TF32	1.305	-	2.795e-04	0.029	0.014	0.268
TF33	1.429	-	*	*	*	*
TF35	1.554	-	*	*	*	*
TF35	1.678	-	2.608e-04	0.054	0.013	0.251
TF36	1.772	-	*	*	*	*
TF37	1.872	-	*	*	*	*
TF38	1.931	0.015	9.938e-05	0.057	0.005	0.095
TF39	2.036	0.120	1.283e-04	0.032	0.006	0.123
TF40	2.141	0.225	1.762e-04	0.041	0.009	0.169
TF41	2.246	0.330	1.777e-04	0.030	0.009	0.171
TF42	2.351	0.435	1.998e-04	0.036	0.010	0.192
TF43	2.456	0.540	2.363e-04	0.018	0.012	0.227
TF44	2.561	0.645	2.734e-04	0.040	0.014	0.263
TF45	2.666	0.750	3.180e-04	0.020	0.016	0.305
TF46	2.771	0.855	3.547e-04	0.024	0.018	0.341
TF47	2.876	0.960	4.008e-04	0.014	0.020	0.385
TF48	2.981	1.065	4.584e-04	0.018	0.023	0.440
TF49	3.086	1.170	5.360e-04	0.020	0.027	0.515
TF50	3.191	1.275	6.114e-04	0.013	0.031	0.587
TF51	3.296	1.380	7.063e-04	0.014	0.035	0.678
TF52	3.401	1.485	7.973e-04	0.012	0.040	0.766
TF53	3.506	1.590	9.065e-04	0.011	0.045	0.871
TF54	3.611	1.695	9.999e-04	0.010	0.050	0.960
TF55	3.716	1.800	1.139e-03	0.008	0.057	1.094
TF56	3.821	1.905	1.260e-03	0.009	0.063	1.211
TF57	3.926	2.010	1.420e-03	0.009	0.071	1.364
TF58	4.031	2.115	1.532e-03	0.009	0.076	1.471
TF59	4.136	2.220	1.721e-03	0.003	0.086	1.653
TF60	4.241	2.325	1.897e-03	0.003	0.095	1.822
TF61	4.346	2.430	2.061e-03	0.003	0.103	1.980
TF62	4.451	2.535	2.284e-03	0.005	0.114	2.194
TF63	4.556	2.640	2.470e-03	0.003	0.123	2.373
TF64	4.661	2.745	2.564e-03	0.003	0.128	2.463
TF65	4.766	2.850	2.723e-03	0.003	0.136	2.615
TF66	4.871	2.955	2.862e-03	0.003	0.143	2.750
TF67	4.976	3.060	2.941e-03	0.005	0.147	2.825
TF68	5.081	3.165	3.039e-03	0.005	0.152	2.920
TF69	5.186	3.270	3.172e-03	0.004	0.158	3.047
TF70	5.291	3.375	3.195e-03	0.003	0.160	3.069

TABLE A.34 31-Inch Mach 10 Test 293, Run 034 Heating Data
MP-1 Configuration, $Re_\infty = 1.0 \times 10^6$ ft^{-1}, $\alpha = -20$ deg, $\phi = 180$ deg, $C_{H,0} = 0.01931$

GAGE ID	S/R_b	L/R_b	C_H	s/C_H	$C_H/C_{H,0}$	q_{300}(W/cm^2)
TF1	-1.872	-	5.519e-04	0.012	0.029	0.519
TF2	-1.772	-	4.599e-04	0.070	0.024	0.433
TF3	-1.678	-	7.320e-04	0.034	0.038	0.689
TF4	-1.554	-	6.477e-04	0.030	0.034	0.609
TF5	-1.429	-	6.870e-04	0.028	0.036	0.646
TF6	-1.305	-	7.083e-04	0.041	0.037	0.666
TF7	-1.180	-	1.636e-03	0.259	0.085	1.540
TF8	-1.083	-	1.479e-02	0.022	0.766	13.914
TF9	-1.000	-	1.909e-02	0.010	0.989	17.963
TF10	-0.900	-	1.598e-02	0.004	0.828	15.035
TF11	-0.800	-	1.473e-02	0.009	0.763	13.857
TF12	-0.700	-	1.442e-02	0.003	0.747	13.572
TF13	-0.600	-	1.474e-02	0.011	0.763	13.865
TF14	-0.500	-	1.485e-02	0.002	0.769	13.972
TF15	-0.400	-	1.543e-02	0.003	0.799	14.523
TF16	-0.300	-	1.675e-02	0.002	0.868	15.762
TF17	-0.200	-	1.938e-02	0.002	1.004	18.233
TF18	-0.100	-	2.047e-02	0.002	1.060	19.264
TF19	0.000	-	1.931e-02	0.001	1.000	18.169
TF20	0.100	-	1.651e-02	0.003	0.855	15.539
TF21	0.200	-	1.199e-02	0.008	0.621	11.277
TF22	0.300	-	9.970e-03	0.003	0.516	9.381
TF23	0.400	-	9.105e-03	0.001	0.472	8.567
TF24	0.500	-	8.521e-03	0.002	0.441	8.018
TF25	0.600	-	8.044e-03	0.002	0.417	7.569
TF26	0.700	-	*	*	*	*
TF27	0.800	-	7.774e-03	0.003	0.403	7.315
TF28	0.900	-	8.048e-03	0.003	0.417	7.573
TF29	1.000	-	8.772e-03	0.014	0.454	8.254
TF30	1.083	-	4.686e-03	0.062	0.243	4.410
TF31	1.180	-	5.285e-04	0.354	0.027	0.497
TF32	1.305	-	2.193e-04	0.048	0.011	0.206
TF33	1.429	-	*	*	*	*
TF34	1.554	-	*	*	*	*
TF35	1.678	-	1.620e-04	0.075	0.008	0.152
TF36	1.772	-	6.186e-05	0.041	0.003	0.058
TF37	1.872	-	*	*	*	*
TF38	1.931	0.015	*	*	*	*
TF39	2.036	0.120	1.288e-04	0.070	0.007	0.121
TF40	2.141	0.225	2.211e-04	0.048	0.011	0.208
TF41	2.246	0.330	2.377e-04	0.046	0.012	0.224
TF42	2.351	0.435	2.570e-04	0.039	0.013	0.242
TF43	2.456	0.540	2.765e-04	0.046	0.014	0.260
TF44	2.561	0.645	2.635e-04	0.046	0.014	0.248
TF45	2.666	0.750	2.568e-04	0.050	0.013	0.242
TF46	2.771	0.855	2.842e-04	0.080	0.015	0.267
TF47	2.876	0.960	3.736e-04	0.073	0.019	0.352
TF48	2.981	1.065	4.925e-04	0.049	0.026	0.463
TF49	3.086	1.170	6.533e-04	0.037	0.034	0.615
TF50	3.191	1.275	7.787e-04	0.022	0.040	0.733
TF51	3.296	1.380	8.959e-04	0.017	0.046	0.843
TF52	3.401	1.485	1.028e-03	0.021	0.053	0.967
TF53	3.506	1.590	1.133e-03	0.021	0.059	1.066
TF54	3.611	1.695	1.257e-03	0.015	0.065	1.182
TF55	3.716	1.800	1.412e-03	0.012	0.073	1.329
TF56	3.821	1.905	1.553e-03	0.013	0.080	1.461
TF57	3.926	2.010	1.711e-03	0.011	0.089	1.610
TF58	4.031	2.115	1.874e-03	0.005	0.097	1.764
TF59	4.136	2.220	2.029e-03	0.006	0.105	1.909
TF60	4.241	2.325	2.166e-03	0.006	0.112	2.038
TF61	4.346	2.430	2.268e-03	0.005	0.117	2.134
TF62	4.451	2.535	2.360e-03	0.007	0.122	2.220
TF63	4.556	2.640	2.548e-03	0.005	0.132	2.397
TF64	4.661	2.745	2.504e-03	0.005	0.130	2.356
TF65	4.766	2.850	2.604e-03	0.005	0.135	2.450
TF66	4.871	2.955	2.663e-03	0.004	0.138	2.506
TF67	4.976	3.060	2.671e-03	0.004	0.138	2.513
TF68	5.081	3.165	2.702e-03	0.003	0.140	2.543
TF69	5.186	3.270	2.754e-03	0.004	0.143	2.592
TF70	5.291	3.375	2.746e-03	0.005	0.142	2.584

TABLE A.35 31-Inch Mach 10 Test 293, Run 035 Heating Data
MP-1 Configuration, $Re_\infty = 1.0 \times 10^6$ ft^{-1}, $\alpha = -20$ deg, $\phi = 90$ deg, $C_{H,0} = 0.01920$

GAGE ID	S/R_b	L/R_b	C_H	s/C_H	$C_H/C_{H,0}$	q_{300}(W/cm^2)
TF1	-1.872	-	1.617e-04	0.086	0.008	0.153
TF2	-1.772	-	3.224e-04	0.018	0.017	0.306
TF3	-1.678	-	1.446e-04	0.056	0.008	0.137
TF4	-1.554	-	5.267e-05	0.221	0.003	0.050
TF5	-1.429	-	8.291e-05	0.050	0.004	0.079
TF6	-1.305	-	9.859e-05	0.130	0.005	0.094
TF7	-1.180	-	7.181e-04	0.351	0.037	0.681
TF8	-1.083	-	8.066e-03	0.042	0.420	7.651
TF9	-1.000	-	1.297e-02	0.011	0.675	12.299
TF10	-0.900	-	1.197e-02	0.002	0.624	11.359
TF11	-0.800	-	1.145e-02	0.002	0.596	10.858
TF12	-0.700	-	1.144e-02	0.001	0.596	10.855
TF13	-0.600	-	1.169e-02	0.003	0.608	11.084
TF14	-0.500	-	1.195e-02	0.002	0.622	11.333
TF15	-0.400	-	1.272e-02	0.002	0.662	12.063
TF16	-0.300	-	1.378e-02	0.002	0.717	13.067
TF17	-0.200	-	1.653e-02	0.002	0.861	15.680
TF18	-0.100	-	1.897e-02	0.002	0.988	17.992
TF19	0.000	-	1.920e-02	0.001	1.000	18.216
TF20	0.100	-	1.889e-02	0.001	0.984	17.921
TF21	0.200	-	1.542e-02	0.001	0.803	14.626
TF22	0.300	-	1.357e-02	0.003	0.707	12.873
TF23	0.400	-	1.271e-02	0.001	0.662	12.059
TF24	0.500	-	1.214e-02	0.001	0.632	11.514
TF25	0.600	-	1.162e-02	0.001	0.605	11.022
TF26	0.700	-	*	*	*	*
TF27	0.800	-	1.157e-02	0.002	0.602	10.974
TF28	0.900	-	1.196e-02	0.002	0.623	11.346
TF29	1.000	-	1.319e-02	0.007	0.687	12.506
TF30	1.083	-	7.315e-03	0.065	0.381	6.938
TF31	1.180	-	7.630e-04	0.350	0.040	0.724
TF32	1.305	-	1.363e-04	0.053	0.007	0.129
TF33	1.429	-	*	*	*	*
TF34	1.554	-	*	*	*	*
TF35	1.678	-	1.410e-04	0.103	0.007	0.134
TF36	1.772	-	*	*	*	*
TF37	1.872	-	*	*	*	*
TF38	1.931	0.015	9.989e-05	0.102	0.005	0.095
TF39	2.036	0.120	3.021e-04	0.052	0.016	0.287
TF40	2.141	0.225	6.489e-04	0.027	0.034	0.616
TF41	2.246	0.330	8.283e-04	0.041	0.043	0.786
TF42	2.351	0.435	1.218e-03	0.028	0.063	1.155
TF43	2.456	0.540	1.995e-03	0.027	0.104	1.892
TF44	2.561	0.645	2.754e-03	0.013	0.143	2.612
TF45	2.666	0.750	3.189e-03	0.013	0.166	3.024
TF46	2.771	0.855	2.869e-03	0.017	0.149	2.721
TF47	2.876	0.960	2.469e-03	0.018	0.129	2.342
TF48	2.981	1.065	2.171e-03	0.018	0.113	2.059
TF49	3.086	1.170	1.883e-03	0.018	0.098	1.786
TF50	3.191	1.275	1.648e-03	0.020	0.086	1.564
TF51	3.296	1.380	1.542e-03	0.018	0.080	1.462
TF52	3.401	1.485	1.481e-03	0.017	0.077	1.405
TF53	3.506	1.590	1.392e-03	0.018	0.072	1.320
TF54	3.611	1.695	1.364e-03	0.019	0.071	1.294
TF55	3.716	1.800	1.313e-03	0.015	0.068	1.245
TF56	3.821	1.905	1.254e-03	0.019	0.065	1.190
TF57	3.926	2.010	1.226e-03	0.018	0.064	1.163
TF58	4.031	2.115	1.212e-03	0.014	0.063	1.150
TF59	4.136	2.220	1.201e-03	0.020	0.063	1.139
TF60	4.241	2.325	1.177e-03	0.016	0.061	1.116
TF61	4.346	2.430	1.147e-03	0.013	0.060	1.088
TF62	4.451	2.535	1.110e-03	0.019	0.058	1.053
TF63	4.556	2.640	1.155e-03	0.018	0.060	1.095
TF64	4.661	2.745	1.086e-03	0.018	0.057	1.030
TF65	4.766	2.850	1.091e-03	0.015	0.057	1.035
TF66	4.871	2.955	1.078e-03	0.018	0.056	1.022
TF67	4.976	3.060	1.055e-03	0.013	0.055	1.000
TF68	5.081	3.165	1.048e-03	0.015	0.055	0.994
TF69	5.186	3.270	1.041e-03	0.015	0.054	0.988
TF70	5.291	3.375	1.050e-03	0.016	0.055	0.996

TABLE A.36 31-Inch Mach 10 Test 293, Run 036 Heating Data
MP-1 Configuration, $Re_\infty = 1.0 \times 10^6$ ft^{-1}, $\alpha = -12$ deg, $\phi = 90$ deg, $C_{H,0} = 0.01984$

GAGE ID	S/R_b	L/R_b	C_H	s/C_H	$C_H/C_{H,0}$	q_{300}(W/cm^2)
TF1	-1.872	-	1.565e-04	0.051	0.008	0.147
TF2	-1.772	-	2.684e-04	0.057	0.014	0.252
TF3	-1.678	-	2.811e-04	0.061	0.014	0.264
TF4	-1.554	-	1.521e-04	0.054	0.008	0.143
TF5	-1.429	-	1.558e-04	0.049	0.008	0.146
TF6	-1.305	-	1.510e-04	0.063	0.008	0.142
TF7	-1.180	-	7.007e-04	0.366	0.035	0.657
TF8	-1.083	-	8.090e-03	0.049	0.408	7.589
TF9	-1.000	-	1.307e-02	0.005	0.659	12.259
TF10	-0.900	-	1.211e-02	0.003	0.610	11.359
TF11	-0.800	-	1.158e-02	0.002	0.584	10.866
TF12	-0.700	-	1.159e-02	0.002	0.584	10.871
TF13	-0.600	-	1.196e-02	0.009	0.603	11.223
TF14	-0.500	-	1.216e-02	0.002	0.613	11.402
TF15	-0.400	-	1.296e-02	0.004	0.653	12.156
TF16	-0.300	-	1.408e-02	0.002	0.710	13.210
TF17	-0.200	-	*	*	*	*
TF18	-0.100	-	1.940e-02	0.001	0.978	18.199
TF19	0.000	-	1.984e-02	0.002	1.000	18.611
TF20	0.100	-	1.929e-02	0.001	0.972	18.098
TF21	0.200	-	1.580e-02	0.002	0.796	14.822
TF22	0.300	-	1.385e-02	0.003	0.698	12.990
TF23	0.400	-	1.301e-02	0.006	0.656	12.201
TF24	0.500	-	1.238e-02	0.005	0.624	11.617
TF25	0.600	-	1.189e-02	0.006	0.599	11.156
TF26	0.700	-	*	*	*	*
TF27	0.800	-	*	*	*	*
TF28	0.900	-	1.186e-02	0.006	0.598	11.130
TF29	1.000	-	1.225e-02	0.008	0.618	11.494
TF30	1.083	-	1.046e-02	0.014	0.527	9.813
TF31	1.180	-	7.626e-03	0.069	0.384	7.153
TF32	1.305	-	7.342e-04	0.377	0.037	0.689
TF33	1.429	-	*	*	*	*
TF34	1.554	-	*	*	*	*
TF35	1.678	-	1.822e-04	0.058	0.009	0.171
TF36	1.772	-	*	*	*	*
TF37	1.872	-	*	*	*	*
TF38	1.931	0.015	*	*	*	*
TF39	2.036	0.120	*	*	*	*
TF40	2.141	0.225	4.344e-04	0.040	0.022	0.407
TF41	2.246	0.330	*	*	*	*
TF42	2.351	0.435	*	*	*	*
TF43	2.456	0.540	8.771e-05	0.060	0.004	0.082
TF44	2.561	0.645	1.720e-04	0.077	0.009	0.161
TF45	2.666	0.750	2.617e-04	0.046	0.013	0.245
TF46	2.771	0.855	3.526e-04	0.047	0.018	0.331
TF47	2.876	0.960	4.086e-04	0.052	0.021	0.383
TF48	2.981	1.065	5.158e-04	0.044	0.026	0.484
TF49	3.086	1.170	6.475e-04	0.044	0.033	0.607
TF50	3.191	1.275	7.895e-04	0.039	0.040	0.741
TF51	3.296	1.380	9.788e-04	0.034	0.049	0.918
TF52	3.401	1.485	1.278e-03	0.034	0.064	1.199
TF53	3.506	1.590	1.696e-03	0.026	0.085	1.591
TF54	3.611	1.695	2.082e-03	0.022	0.105	1.953
TF55	3.716	1.800	2.483e-03	0.016	0.125	2.329
TF56	3.821	1.905	2.673e-03	0.014	0.135	2.507
TF57	3.926	2.010	2.714e-03	0.013	0.137	2.546
TF58	4.031	2.115	2.582e-03	0.013	0.130	2.422
TF59	4.136	2.220	2.379e-03	0.014	0.120	2.232
TF60	4.241	2.325	2.176e-03	0.014	0.110	2.041
TF61	4.346	2.430	1.969e-03	0.013	0.099	1.847
TF62	4.451	2.535	1.857e-03	0.015	0.094	1.742
TF63	4.556	2.640	1.712e-03	0.014	0.086	1.606
TF64	4.661	2.745	1.612e-03	0.011	0.081	1.513
TF65	4.766	2.850	1.522e-03	0.012	0.077	1.427
TF66	4.871	2.955	1.477e-03	0.012	0.074	1.385
TF67	4.976	3.060	1.409e-03	0.011	0.071	1.322
TF68	5.081	3.165	1.402e-03	0.009	0.071	1.315
TF69	5.186	3.270	1.331e-03	0.014	0.067	1.249
TF70	5.291	3.375	1.326e-03	0.013	0.067	1.244

TABLE A.37 31-Inch Mach 10 Test 293, Run 037 Heating Data
MP-1 Configuration, $Re_\infty = 1.0 \times 10^6$ ft^{-1}, $\alpha = -4$ deg, $\phi = 90$ deg, $C_{H,0} = 0.01985$

GAGE ID	S/R_b	L/R_b	C_H	s/C_H	$C_H/C_{H,0}$	q_{300}(W/cm^2)
TF1	-1.872	-	1.036e-04	0.051	0.005	0.097
TF2	-1.772	-	1.187e-04	0.151	0.006	0.111
TF3	-1.678	-	1.467e-04	0.066	0.007	0.137
TF4	-1.554	-	1.199e-04	0.091	0.006	0.112
TF5	-1.429	-	1.187e-04	0.047	0.006	0.111
TF6	-1.305	-	1.331e-04	0.058	0.007	0.125
TF7	-1.180	-	6.744e-04	0.384	0.034	0.631
TF8	-1.083	-	8.031e-03	0.046	0.405	7.518
TF9	-1.000	-	1.302e-02	0.008	0.656	12.193
TF10	-0.900	-	1.208e-02	0.002	0.609	11.311
TF11	-0.800	-	1.161e-02	0.003	0.585	10.870
TF12	-0.700	-	1.159e-02	0.002	0.584	10.854
TF13	-0.600	-	1.186e-02	0.002	0.598	11.106
TF14	-0.500	-	*	*	*	*
TF15	-0.400	-	1.284e-02	0.002	0.647	12.020
TF16	-0.300	-	1.400e-02	0.001	0.705	13.107
TF17	-0.200	-	1.672e-02	0.001	0.842	15.651
TF18	-0.100	-	1.914e-02	0.001	0.964	17.919
TF19	0.000	-	1.985e-02	0.002	1.000	18.586
TF20	0.100	-	1.905e-02	0.001	0.960	17.837
TF21	0.200	-	1.567e-02	0.002	0.789	14.673
TF22	0.300	-	1.375e-02	0.003	0.692	12.868
TF23	0.400	-	1.288e-02	0.005	0.649	12.054
TF24	0.500	-	1.232e-02	0.004	0.620	11.530
TF25	0.600	-	1.186e-02	0.007	0.597	11.102
TF26	0.700	-	*	*	*	*
TF27	0.800	-	1.184e-02	0.006	0.596	11.085
TF28	0.900	-	1.228e-02	0.005	0.618	11.492
TF29	1.000	-	1.336e-02	0.014	0.673	12.506
TF30	1.083	-	7.433e-03	0.063	0.374	6.959
TF31	1.180	-	7.200e-04	0.389	0.036	0.674
TF32	1.305	-	1.553e-04	0.068	0.008	0.145
TF33	1.429	-	*	*	*	*
TF34	1.554	-	*	*	*	*
TF35	1.678	-	1.692e-04	0.033	0.009	0.158
TF36	1.772	-	*	*	*	*
TF37	1.872	-	*	*	*	*
TF38	1.931	0.015	5.872e-05	0.065	0.003	0.055
TF39	2.036	0.120	9.422e-05	0.034	0.005	0.088
TF40	2.141	0.225	1.370e-04	0.044	0.007	0.128
TF41	2.246	0.330	1.508e-04	0.027	0.008	0.141
TF42	2.351	0.435	2.034e-04	0.023	0.010	0.190
TF43	2.456	0.540	2.789e-04	0.051	0.014	0.261
TF44	2.561	0.645	3.425e-04	0.038	0.017	0.321
TF45	2.666	0.750	3.879e-04	0.041	0.020	0.363
TF46	2.771	0.855	4.375e-04	0.031	0.022	0.410
TF47	2.876	0.960	4.995e-04	0.034	0.025	0.468
TF48	2.981	1.065	5.886e-04	0.032	0.030	0.551
TF49	3.086	1.170	7.068e-04	0.029	0.036	0.662
TF50	3.191	1.275	8.305e-04	0.026	0.042	0.777
TF51	3.296	1.380	9.861e-04	0.031	0.050	0.923
TF52	3.401	1.485	1.188e-03	0.031	0.060	1.112
TF53	3.506	1.590	1.368e-03	0.030	0.069	1.280
TF54	3.611	1.695	1.579e-03	0.028	0.080	1.478
TF55	3.716	1.800	1.782e-03	0.022	0.090	1.668
TF56	3.821	1.905	1.921e-03	0.017	0.097	1.798
TF57	3.926	2.010	2.072e-03	0.019	0.104	1.940
TF58	4.031	2.115	2.154e-03	0.017	0.109	2.017
TF59	4.136	2.220	2.223e-03	0.013	0.112	2.081
TF60	4.241	2.325	2.241e-03	0.011	0.113	2.098
TF61	4.346	2.430	2.217e-03	0.012	0.112	2.075
TF62	4.451	2.535	2.216e-03	0.011	0.112	2.074
TF63	4.556	2.640	2.208e-03	0.012	0.111	2.067
TF64	4.661	2.745	2.090e-03	0.012	0.105	1.957
TF65	4.766	2.850	2.023e-03	0.010	0.102	1.894
TF66	4.871	2.955	1.963e-03	0.013	0.099	1.838
TF67	4.976	3.060	1.875e-03	0.009	0.094	1.755
TF68	5.081	3.165	1.797e-03	0.010	0.091	1.683
TF69	5.186	3.270	1.755e-03	0.011	0.088	1.643
TF70	5.291	3.375	1.677e-03	0.010	0.084	1.570

TABLE A.38 31-Inch Mach 10 Test 293, Run 038 Heating Data
MP-1 Configuration, $Re_\infty = 1.0 \times 10^6$ ft^{-1}, $\alpha = -12$ deg, $\phi = 0$ deg, $C_{H,0} = 0.01978$

GAGE ID	S/R_b	L/R_b	C_H	s/C_H	$C_H/C_{H,0}$	q_{300}(W/cm^2)
TF1	-1.872	-	1.713e-04	0.075	0.009	0.165
TF2	-1.772	-	2.365e-04	0.019	0.012	0.228
TF3	-1.678	-	2.649e-04	0.041	0.013	0.255
TF4	-1.554	-	2.100e-04	0.026	0.011	0.202
TF5	-1.429	-	2.560e-04	0.029	0.013	0.246
TF6	-1.305	-	2.724e-04	0.039	0.014	0.262
TF7	-1.180	-	5.960e-04	0.338	0.030	0.574
TF8	-1.083	-	6.185e-03	0.051	0.313	5.954
TF9	-1.000	-	1.042e-02	0.009	0.527	10.029
TF10	-0.900	-	9.683e-03	0.002	0.490	9.323
TF11	-0.800	-	9.339e-03	0.002	0.472	8.992
TF12	-0.700	-	9.349e-03	0.002	0.473	9.001
TF13	-0.600	-	9.033e-03	0.030	0.457	8.697
TF14	-0.500	-	9.964e-03	0.002	0.504	9.593
TF15	-0.400	-	1.052e-02	0.003	0.532	10.131
TF16	-0.300	-	1.163e-02	0.005	0.588	11.199
TF17	-0.200	-	1.436e-02	0.006	0.726	13.821
TF18	-0.100	-	1.768e-02	0.003	0.894	17.024
TF19	0.000	-	1.978e-02	0.001	1.000	19.042
TF20	0.100	-	2.014e-02	0.002	1.018	19.390
TF21	0.200	-	1.754e-02	0.004	0.887	16.888
TF22	0.300	-	1.556e-02	0.005	0.787	14.981
TF23	0.400	-	1.454e-02	0.004	0.735	14.000
TF24	0.500	-	1.391e-02	0.004	0.703	13.392
TF25	0.600	-	1.342e-02	0.005	0.679	12.923
TF26	0.700	-	*	*	*	*
TF27	0.800	-	1.359e-02	0.005	0.687	13.084
TF28	0.900	-	1.438e-02	0.004	0.727	13.841
TF29	1.000	-	1.639e-02	0.010	0.829	15.783
TF30	1.083	-	1.021e-02	0.046	0.516	9.832
TF31	1.180	-	1.145e-03	0.316	0.058	1.103
TF32	1.305	-	3.005e-04	0.087	0.015	0.289
TF33	1.429	-	*	*	*	*
TF34	1.554	-	*	*	*	*
TF35	1.678	-	2.224e-04	0.076	0.011	0.214
TF36	1.772	-	*	*	*	*
TF37	1.872	-	*	*	*	*
TF38	1.931	0.015	1.359e-04	0.067	0.007	0.131
TF39	2.036	0.120	3.191e-04	0.043	0.016	0.307
TF40	2.141	0.225	5.895e-04	0.039	0.030	0.568
TF41	2.246	0.330	7.575e-04	0.040	0.038	0.729
TF42	2.351	0.435	1.190e-03	0.037	0.060	1.146
TF43	2.456	0.540	1.974e-03	0.025	0.100	1.900
TF44	2.561	0.645	3.018e-03	0.015	0.153	2.906
TF45	2.666	0.750	4.121e-03	0.010	0.208	3.968
TF46	2.771	0.855	4.623e-03	0.007	0.234	4.451
TF47	2.876	0.960	4.611e-03	0.012	0.233	4.439
TF48	2.981	1.065	4.427e-03	0.012	0.224	4.262
TF49	3.086	1.170	4.237e-03	0.013	0.214	4.079
TF50	3.191	1.275	3.922e-03	0.015	0.198	3.776
TF51	3.296	1.380	3.731e-03	0.013	0.189	3.592
TF52	3.401	1.485	3.561e-03	0.015	0.180	3.428
TF53	3.506	1.590	3.377e-03	0.013	0.171	3.252
TF54	3.611	1.695	3.195e-03	0.014	0.162	3.076
TF55	3.716	1.800	3.147e-03	0.013	0.159	3.030
TF56	3.821	1.905	3.003e-03	0.014	0.152	2.891
TF57	3.926	2.010	2.966e-03	0.012	0.150	2.856
TF58	4.031	2.115	2.813e-03	0.013	0.142	2.709
TF59	4.136	2.220	2.772e-03	0.011	0.140	2.669
TF60	4.241	2.325	2.721e-03	0.013	0.138	2.620
TF61	4.346	2.430	2.650e-03	0.012	0.134	2.552
TF62	4.451	2.535	2.656e-03	0.012	0.134	2.557
TF63	4.556	2.640	2.638e-03	0.011	0.133	2.540
TF64	4.661	2.745	2.550e-03	0.013	0.129	2.455
TF65	4.766	2.850	2.516e-03	0.012	0.127	2.422
TF66	4.871	2.955	2.501e-03	0.011	0.126	2.408
TF67	4.976	3.060	2.456e-03	0.010	0.124	2.364
TF68	5.081	3.165	2.435e-03	0.011	0.123	2.344
TF69	5.186	3.270	2.449e-03	0.012	0.124	2.358
TF70	5.291	3.375	2.422e-03	0.012	0.122	2.332

TABLE A.39 31-Inch Mach 10 Test 293, Run 039 Heating Data
MP-2 Configuration, $Re_\infty = 1.0 \times 10^6$ ft^{-1}, $\alpha = -4$ deg, $\phi = 0$ deg, $C_{H,0} = 0.01888$

GAGE ID	S/R_b	L/R_b	C_H	s/C_H	$C_H/C_{H,0}$	q_{300}(W/cm^2)
TF37	-1.864	-	3.048e-04	0.043	0.016	0.285
TF36	-1.764	-	4.535e-04	0.021	0.024	0.424
TF35	-1.670	-	4.355e-04	0.045	0.023	0.407
TF34	-1.545	-	2.671e-04	0.031	0.014	0.250
TF33	-1.421	-	6.802e-04	0.329	0.036	0.636
TF32	-1.296	-	2.869e-04	0.037	0.015	0.268
TF31	-1.172	-	2.719e-04	0.041	0.014	0.254
TF30	-1.075	-	7.226e-03	0.051	0.383	6.755
TF29	-1.000	-	1.244e-02	0.014	0.659	11.630
TF28	-0.900	-	*	*	*	*
TF27	-0.800	-	1.137e-02	0.014	0.602	10.631
TF26	-0.700	-	1.114e-02	0.006	0.590	10.410
TF25	-0.600	-	1.141e-02	0.018	0.604	10.663
TF24	-0.500	-	1.176e-02	0.004	0.623	10.995
TF23	-0.400	-	1.233e-02	0.004	0.653	11.526
TF22	-0.300	-	1.343e-02	0.003	0.711	12.548
TF21	-0.200	-	1.487e-02	0.003	0.788	13.901
TF20	-0.100	-	1.718e-02	0.002	0.910	16.059
TF19	0.000	-	1.888e-02	0.058	1.000	17.649
TF18	0.100	-	1.778e-02	0.001	0.942	16.623
TF17	0.200	-	1.538e-02	0.012	0.815	14.379
TF16	0.300	-	1.459e-02	0.002	0.773	13.636
TF15	0.400	-	1.346e-02	0.003	0.713	12.585
TF14	0.500	-	*	*	*	*
TF13	0.600	-	1.226e-02	0.010	0.650	11.464
TF12	0.700	-	1.241e-02	0.003	0.657	11.600
TF11	0.800	-	*	*	*	*
TF10	0.900	-	1.235e-02	0.004	0.654	11.543
TF9	1.000	-	1.455e-02	0.016	0.771	13.599
TF8	1.075	-	8.614e-03	0.048	0.456	8.052
TF7	1.172	-	8.166e-04	0.368	0.043	0.763
TF6	1.296	-	7.637e-05	0.115	0.004	0.071
TF5	1.421	-	7.100e-05	0.092	0.004	0.066
TF4	1.545	-	5.130e-05	0.107	0.003	0.048
TF3	1.670	-	1.581e-04	0.061	0.008	0.148
TF2	1.764	-	1.561e-04	0.061	0.008	0.146
TF1	1.864	-	9.813e-05	0.093	0.005	0.092
TF38	1.923	0.015	*	*	*	*
TF39	2.027	0.120	9.845e-05	0.057	0.005	0.092
TF40	2.132	0.225	2.022e-04	0.049	0.011	0.189
TF41	2.237	0.330	2.382e-04	0.041	0.013	0.223
TF42	2.342	0.435	2.978e-04	0.036	0.016	0.278
TF43	2.447	0.540	3.584e-04	0.039	0.019	0.335
TF44	2.553	0.645	*	*	*	*
TF45	2.658	0.750	5.248e-04	0.034	0.028	0.491
TF46	2.763	0.855	6.640e-04	0.036	0.035	0.621
TF47	2.868	0.960	7.795e-04	0.039	0.041	0.729
TF48	2.973	1.065	1.056e-03	0.027	0.056	0.987
TF49	3.078	1.170	1.352e-03	0.019	0.072	1.264
TF50	3.182	1.275	1.646e-03	0.020	0.087	1.539
TF51	3.287	1.380	1.951e-03	0.018	0.103	1.824
TF52	3.392	1.485	2.232e-03	0.016	0.118	2.086
TF53	3.497	1.590	2.426e-03	0.014	0.128	2.267
TF54	3.602	1.695	2.548e-03	0.015	0.135	2.382
TF55	3.707	1.800	2.622e-03	0.012	0.139	2.451
TF56	3.813	1.905	2.636e-03	0.014	0.140	2.464
TF57	3.918	2.010	2.531e-03	0.011	0.134	2.365
TF58	4.023	2.115	2.556e-03	0.014	0.135	2.389
TF59	4.128	2.220	2.502e-03	0.014	0.133	2.339
TF60	4.233	2.325	2.364e-03	0.011	0.125	2.210
TF61	4.338	2.430	2.234e-03	0.012	0.118	2.089
TF62	4.443	2.535	2.288e-03	0.010	0.121	2.139
TF63	4.548	2.640	2.200e-03	0.010	0.117	2.056
TF64	4.653	2.745	2.093e-03	0.010	0.111	1.956
TF65	4.758	2.850	2.075e-03	0.010	0.110	1.940
TF66	4.863	2.955	2.007e-03	0.010	0.106	1.876
TF67	4.968	3.060	1.982e-03	0.007	0.105	1.853
TF68	5.073	3.165	1.947e-03	0.010	0.103	1.820
TF69	5.177	3.270	1.848e-03	0.008	0.098	1.727
TF70	5.282	3.375	1.850e-03	0.007	0.098	1.729

TABLE A.40 31-Inch Mach 10 Test 293, Run 040 Heating Data
MP-2 Configuration, $Re_\infty = 1.0 \times 10^6$ ft^{-1}, $\alpha = -12$ deg, $\phi = 0$ deg, $C_{H,0} = 0.01944$

GAGE ID	S/R_b	L/R_b	C_H	s/C_H	$C_H/C_{H,0}$	q_{300}(W/cm^2)
TF37	-1.864	-	1.349e-04	0.063	0.007	0.127
TF36	-1.764	-	2.208e-04	0.061	0.011	0.208
TF35	-1.670	-	2.589e-04	0.052	0.013	0.244
TF34	-1.545	-	2.078e-04	0.024	0.011	0.196
TF33	-1.421	-	5.261e-04	0.350	0.027	0.496
TF32	-1.296	-	2.870e-04	0.018	0.015	0.270
TF31	-1.172	-	2.497e-04	0.037	0.013	0.235
TF30	-1.075	-	6.020e-03	0.066	0.310	5.672
TF29	-1.000	-	1.088e-02	0.012	0.560	10.252
TF28	-0.900	-	*	*	*	*
TF27	-0.800	-	1.027e-02	0.024	0.528	9.677
TF26	-0.700	-	9.900e-03	0.003	0.509	9.329
TF25	-0.600	-	1.014e-02	0.005	0.521	9.551
TF24	-0.500	-	1.065e-02	0.002	0.548	10.036
TF23	-0.400	-	1.128e-02	0.003	0.580	10.629
TF22	-0.300	-	1.249e-02	0.002	0.642	11.767
TF21	-0.200	-	1.415e-02	0.002	0.728	13.332
TF20	-0.100	-	1.685e-02	0.002	0.867	15.875
TF19	0.000	-	1.944e-02	0.049	1.000	18.316
TF18	0.100	-	1.864e-02	0.005	0.959	17.563
TF17	0.200	-	1.639e-02	0.014	0.843	15.444
TF16	0.300	-	1.582e-02	0.008	0.814	14.911
TF15	0.400	-	1.481e-02	0.018	0.762	13.958
TF14	0.500	-	*	*	*	*
TF13	0.600	-	1.342e-02	0.021	0.690	12.645
TF12	0.700	-	1.382e-02	0.016	0.711	13.017
TF11	0.800	-	*	*	*	*
TF10	0.900	-	1.394e-02	0.007	0.717	13.131
TF9	1.000	-	1.714e-02	0.020	0.882	16.152
TF8	1.075	-	1.070e-02	0.045	0.550	10.078
TF7	1.172	-	1.008e-03	0.356	0.052	0.950
TF6	1.296	-	2.991e-04	0.053	0.015	0.282
TF5	1.421	-	1.463e-04	0.058	0.008	0.138
TF4	1.545	-	1.193e-04	0.054	0.006	0.112
TF3	1.670	-	2.522e-04	0.092	0.013	0.238
TF2	1.764	-	3.389e-04	0.038	0.017	0.319
TF1	1.864	-	2.133e-04	0.073	0.011	0.201
TF38	1.923	0.015	*	*	*	*
TF39	2.027	0.120	2.914e-04	0.043	0.015	0.275
TF40	2.132	0.225	5.663e-04	0.045	0.029	0.534
TF41	2.237	0.330	7.220e-04	0.037	0.037	0.680
TF42	2.342	0.435	1.108e-03	0.030	0.057	1.044
TF43	2.447	0.540	1.827e-03	0.025	0.094	1.721
TF44	2.553	0.645	*	*	*	*
TF45	2.658	0.750	4.041e-03	0.010	0.208	3.808
TF46	2.763	0.855	4.640e-03	0.008	0.239	4.372
TF47	2.868	0.960	4.658e-03	0.010	0.240	4.389
TF48	2.973	1.065	4.570e-03	0.008	0.235	4.306
TF49	3.078	1.170	4.330e-03	0.008	0.223	4.080
TF50	3.182	1.275	4.036e-03	0.008	0.208	3.803
TF51	3.287	1.380	3.772e-03	0.007	0.194	3.555
TF52	3.392	1.485	3.589e-03	0.007	0.185	3.382
TF53	3.497	1.590	3.413e-03	0.005	0.176	3.216
TF54	3.602	1.695	3.264e-03	0.006	0.168	3.076
TF55	3.707	1.800	3.176e-03	0.006	0.163	2.992
TF56	3.813	1.905	3.067e-03	0.005	0.158	2.890
TF57	3.918	2.010	2.882e-03	0.005	0.148	2.716
TF58	4.023	2.115	2.898e-03	0.004	0.149	2.731
TF59	4.128	2.220	2.840e-03	0.004	0.146	2.676
TF60	4.233	2.325	2.692e-03	0.004	0.138	2.537
TF61	4.338	2.430	2.575e-03	0.003	0.132	2.427
TF62	4.443	2.535	2.674e-03	0.003	0.138	2.520
TF63	4.548	2.640	2.583e-03	0.004	0.133	2.433
TF64	4.653	2.745	2.530e-03	0.006	0.130	2.384
TF65	4.758	2.850	2.552e-03	0.004	0.131	2.405
TF66	4.863	2.955	2.521e-03	0.004	0.130	2.376
TF67	4.968	3.060	2.531e-03	0.005	0.130	2.385
TF68	5.073	3.165	2.526e-03	0.006	0.130	2.380
TF69	5.177	3.270	2.451e-03	0.006	0.126	2.310
TF70	5.282	3.375	2.505e-03	0.005	0.129	2.360

TABLE A.41 31-Inch Mach 10 Test 293, Run 041 Heating Data
MP-2 Configuration, $Re_\infty = 1.0 \times 10^6$ ft^{-1}, $\alpha = -4$ deg, $\phi = 180$ deg, $C_{H,0} = 0.01966$

GAGE ID	S/R_b	L/R_b	C_H	s/C_H	$C_H/C_{H,0}$	q_{300}(W/cm^2)
TF37	-1.864	-	9.865e-05	0.106	0.005	0.093
TF36	-1.764	-	1.561e-04	0.040	0.008	0.148
TF35	-1.670	-	1.168e-04	0.067	0.006	0.111
TF34	-1.545	-	7.295e-05	0.060	0.004	0.069
TF33	-1.421	-	7.223e-04	0.386	0.037	0.684
TF32	-1.296	-	1.022e-04	0.087	0.005	0.097
TF31	-1.172	-	7.503e-05	0.094	0.004	0.071
TF30	-1.075	-	9.145e-03	0.046	0.465	8.661
TF29	-1.000	-	1.512e-02	0.014	0.769	14.321
TF28	-0.900	-	*	*	*	*
TF27	-0.800	-	1.351e-02	0.006	0.687	12.792
TF26	-0.700	-	1.292e-02	0.003	0.657	12.237
TF25	-0.600	-	1.302e-02	0.014	0.662	12.334
TF24	-0.500	-	1.353e-02	0.002	0.688	12.814
TF23	-0.400	-	1.411e-02	0.003	0.718	13.362
TF22	-0.300	-	1.521e-02	0.002	0.774	14.408
TF21	-0.200	-	1.660e-02	0.002	0.844	15.718
TF20	-0.100	-	1.859e-02	0.005	0.945	17.603
TF19	0.000	-	1.966e-02	0.047	1.000	18.618
TF18	0.100	-	1.779e-02	0.001	0.905	16.848
TF17	0.200	-	1.498e-02	0.023	0.762	14.190
TF16	0.300	-	1.395e-02	0.003	0.710	13.214
TF15	0.400	-	1.271e-02	0.009	0.647	12.041
TF14	0.500	-	*	*	*	*
TF13	0.600	-	1.181e-02	0.030	0.601	11.187
TF12	0.700	-	1.165e-02	0.005	0.592	11.030
TF11	0.800	-	*	*	*	*
TF10	0.900	-	1.174e-02	0.008	0.597	11.116
TF9	1.000	-	1.304e-02	0.017	0.663	12.346
TF8	1.075	-	7.347e-03	0.057	0.374	6.959
TF7	1.172	-	7.606e-04	0.340	0.039	0.720
TF6	1.296	-	2.970e-04	0.050	0.015	0.281
TF5	1.421	-	2.770e-04	0.023	0.014	0.262
TF4	1.545	-	2.464e-04	0.026	0.013	0.233
TF3	1.670	-	5.045e-04	0.070	0.026	0.478
TF2	1.764	-	5.117e-04	0.049	0.026	0.485
TF1	1.864	-	3.290e-04	0.058	0.017	0.312
TF38	1.923	0.015	*	*	*	*
TF39	2.027	0.120	2.411e-04	0.030	0.012	0.228
TF40	2.132	0.225	2.700e-04	0.050	0.014	0.256
TF41	2.237	0.330	2.421e-04	0.045	0.012	0.229
TF42	2.342	0.435	2.630e-04	0.034	0.013	0.249
TF43	2.447	0.540	2.872e-04	0.042	0.015	0.272
TF44	2.553	0.645	*	*	*	*
TF45	2.658	0.750	3.283e-04	0.032	0.017	0.311
TF46	2.763	0.855	3.512e-04	0.022	0.018	0.333
TF47	2.868	0.960	3.592e-04	0.033	0.018	0.340
TF48	2.973	1.065	3.818e-04	0.024	0.019	0.362
TF49	3.078	1.170	4.082e-04	0.019	0.021	0.387
TF50	3.182	1.275	4.378e-04	0.027	0.022	0.415
TF51	3.287	1.380	4.749e-04	0.034	0.024	0.450
TF52	3.392	1.485	5.153e-04	0.023	0.026	0.488
TF53	3.497	1.590	5.665e-04	0.031	0.029	0.537
TF54	3.602	1.695	6.153e-04	0.028	0.031	0.583
TF55	3.707	1.800	6.785e-04	0.025	0.035	0.643
TF56	3.813	1.905	7.436e-04	0.026	0.038	0.704
TF57	3.918	2.010	7.921e-04	0.024	0.040	0.750
TF58	4.023	2.115	8.800e-04	0.021	0.045	0.833
TF59	4.128	2.220	9.566e-04	0.027	0.049	0.906
TF60	4.233	2.325	1.012e-03	0.024	0.051	0.958
TF61	4.338	2.430	1.049e-03	0.021	0.053	0.994
TF62	4.443	2.535	1.170e-03	0.022	0.060	1.108
TF63	4.548	2.640	1.231e-03	0.032	0.063	1.166
TF64	4.653	2.745	1.266e-03	0.024	0.064	1.199
TF65	4.758	2.850	1.350e-03	0.026	0.069	1.279
TF66	4.863	2.955	1.402e-03	0.023	0.071	1.328
TF67	4.968	3.060	1.449e-03	0.019	0.074	1.373
TF68	5.073	3.165	1.494e-03	0.019	0.076	1.415
TF69	5.177	3.270	1.467e-03	0.015	0.075	1.389
TF70	5.282	3.375	1.526e-03	0.017	0.078	1.445

TABLE A.42 31-Inch Mach 10 Test 293, Run 042 Heating Data
MP-2 Configuration, $Re_\infty = 1.0 \times 10^6$ ft^{-1}, $\alpha = -12$ deg, $\phi = 180$ deg, $C_{H,0} = 0.01891$

GAGE ID	S/R_b	L/R_b	C_H	s/C_H	$C_H/C_{H,0}$	q_{300}(W/cm^2)
TF37	-1.864	-	2.188e-04	0.064	0.012	0.203
TF36	-1.764	-	3.522e-04	0.035	0.019	0.327
TF35	-1.670	-	2.344e-04	0.086	0.012	0.218
TF34	-1.545	-	1.622e-04	0.098	0.009	0.151
TF33	-1.421	-	1.015e-03	0.327	0.054	0.942
TF32	-1.296	-	2.551e-04	0.073	0.013	0.237
TF31	-1.172	-	1.506e-04	0.105	0.008	0.140
TF30	-1.075	-	1.105e-02	0.039	0.585	10.264
TF29	-1.000	-	1.707e-02	0.012	0.902	15.846
TF28	-0.900	-	*	*	*	*
TF27	-0.800	-	1.438e-02	0.016	0.761	13.355
TF26	-0.700	-	1.378e-02	0.007	0.728	12.790
TF25	-0.600	-	1.299e-02	0.036	0.687	12.064
TF24	-0.500	-	1.432e-02	0.005	0.757	13.293
TF23	-0.400	-	1.489e-02	0.005	0.787	13.824
TF22	-0.300	-	1.590e-02	0.003	0.841	14.762
TF21	-0.200	-	1.714e-02	0.005	0.906	15.911
TF20	-0.100	-	1.884e-02	0.004	0.996	17.490
TF19	0.000	-	1.891e-02	0.012	1.000	17.556
TF18	0.100	-	1.683e-02	0.002	0.890	15.621
TF17	0.200	-	1.361e-02	0.010	0.720	12.638
TF16	0.300	-	1.250e-02	0.002	0.661	11.609
TF15	0.400	-	1.131e-02	0.009	0.598	10.505
TF14	0.500	-	*	*	*	*
TF13	0.600	-	1.027e-02	0.030	0.543	9.535
TF12	0.700	-	9.935e-03	0.003	0.525	9.224
TF11	0.800	-	*	*	*	*
TF10	0.900	-	9.780e-03	0.002	0.517	9.080
TF9	1.000	-	1.097e-02	0.011	0.580	10.190
TF8	1.075	-	6.042e-03	0.062	0.320	5.610
TF7	1.172	-	6.589e-04	0.326	0.035	0.612
TF6	1.296	-	2.768e-04	0.034	0.015	0.257
TF5	1.421	-	2.514e-04	0.018	0.013	0.233
TF4	1.545	-	1.847e-04	0.035	0.010	0.172
TF3	1.670	-	3.006e-04	0.050	0.016	0.279
TF2	1.764	-	2.515e-04	0.047	0.013	0.234
TF1	1.864	-	1.488e-04	0.042	0.008	0.138
TF38	1.923	0.015	*	*	*	*
TF39	2.027	0.120	1.391e-04	0.055	0.007	0.129
TF40	2.132	0.225	1.746e-04	0.049	0.009	0.162
TF41	2.237	0.330	1.824e-04	0.034	0.010	0.169
TF42	2.342	0.435	2.054e-04	0.031	0.011	0.191
TF43	2.447	0.540	2.342e-04	0.032	0.012	0.217
TF44	2.553	0.645	*	*	*	*
TF45	2.658	0.750	3.202e-04	0.016	0.017	0.297
TF46	2.763	0.855	3.583e-04	0.013	0.019	0.333
TF47	2.868	0.960	3.992e-04	0.021	0.021	0.371
TF48	2.973	1.065	4.604e-04	0.015	0.024	0.427
TF49	3.078	1.170	5.302e-04	0.014	0.028	0.492
TF50	3.182	1.275	6.044e-04	0.011	0.032	0.561
TF51	3.287	1.380	6.862e-04	0.010	0.036	0.637
TF52	3.392	1.485	7.890e-04	0.007	0.042	0.733
TF53	3.497	1.590	8.912e-04	0.007	0.047	0.827
TF54	3.602	1.695	1.000e-03	0.005	0.053	0.929
TF55	3.707	1.800	1.140e-03	0.006	0.060	1.058
TF56	3.813	1.905	1.279e-03	0.005	0.068	1.187
TF57	3.918	2.010	1.335e-03	0.007	0.071	1.240
TF58	4.023	2.115	1.564e-03	0.003	0.083	1.452
TF59	4.128	2.220	1.734e-03	0.004	0.092	1.610
TF60	4.233	2.325	1.832e-03	0.005	0.097	1.701
TF61	4.338	2.430	1.954e-03	0.004	0.103	1.814
TF62	4.443	2.535	2.279e-03	0.006	0.121	2.116
TF63	4.548	2.640	2.415e-03	0.007	0.128	2.242
TF64	4.653	2.745	2.552e-03	0.005	0.135	2.369
TF65	4.758	2.850	2.757e-03	0.003	0.146	2.560
TF66	4.863	2.955	2.862e-03	0.006	0.151	2.658
TF67	4.968	3.060	3.063e-03	0.005	0.162	2.844
TF68	5.073	3.165	3.163e-03	0.004	0.167	2.936
TF69	5.177	3.270	3.130e-03	0.005	0.166	2.906
TF70	5.282	3.375	3.304e-03	0.005	0.175	3.068

TABLE A.43 31-Inch Mach 10 Test 293, Run 043 Heating Data
MP-2 Configuration, $Re_\infty = 1.0 \times 10^6$ ft^{-1}, $\alpha = -20$ deg, $\phi = 180$ deg, $C_{H,0} = 0.01817$

GAGE ID	S/R_b	L/R_b	C_H	s/C_H	$C_H/C_{H,0}$	q_{300}(W/cm^2)
TF37	-1.864	-	3.191e-04	0.034	0.018	0.297
TF36	-1.764	-	4.120e-04	0.082	0.023	0.384
TF35	-1.670	-	7.347e-04	0.042	0.040	0.684
TF34	-1.545	-	6.476e-04	0.029	0.036	0.603
TF33	-1.421	-	1.613e-03	0.261	0.089	1.503
TF32	-1.296	-	7.107e-04	0.052	0.039	0.662
TF31	-1.172	-	6.727e-04	0.028	0.037	0.627
TF30	-1.075	-	1.466e-02	0.026	0.807	13.654
TF29	-1.000	-	2.016e-02	0.013	1.109	18.774
TF28	-0.900	-	*	*	*	*
TF27	-0.800	-	1.551e-02	0.015	0.853	14.444
TF26	-0.700	-	1.470e-02	0.009	0.809	13.695
TF25	-0.600	-	1.405e-02	0.065	0.773	13.089
TF24	-0.500	-	1.500e-02	0.003	0.826	13.973
TF23	-0.400	-	1.547e-02	0.005	0.852	14.413
TF22	-0.300	-	1.633e-02	0.003	0.899	15.211
TF21	-0.200	-	1.736e-02	0.004	0.955	16.168
TF20	-0.100	-	1.864e-02	0.005	1.026	17.360
TF19	0.000	-	1.817e-02	0.011	1.000	16.924
TF18	0.100	-	1.564e-02	0.002	0.861	14.572
TF17	0.200	-	1.243e-02	0.022	0.684	11.574
TF16	0.300	-	1.108e-02	0.002	0.610	10.320
TF15	0.400	-	9.754e-03	0.008	0.537	9.085
TF14	0.500	-	*	*	*	*
TF13	0.600	-	8.769e-03	0.031	0.483	8.168
TF12	0.700	-	8.236e-03	0.009	0.453	7.671
TF11	0.800	-	*	*	*	*
TF10	0.900	-	7.740e-03	0.001	0.426	7.209
TF9	1.000	-	8.936e-03	0.013	0.492	8.323
TF8	1.075	-	4.889e-03	0.060	0.269	4.553
TF7	1.172	-	5.364e-04	0.342	0.030	0.500
TF6	1.296	-	2.218e-04	0.040	0.012	0.207
TF5	1.421	-	1.790e-04	0.056	0.010	0.167
TF4	1.545	-	1.164e-04	0.074	0.006	0.108
TF3	1.670	-	2.124e-04	0.055	0.012	0.198
TF2	1.764	-	1.846e-04	0.080	0.010	0.172
TF1	1.864	-	1.076e-04	0.060	0.006	0.100
TF38	1.923	0.015	*	*	*	*
TF39	2.027	0.120	1.284e-04	0.043	0.007	0.120
TF40	2.132	0.225	2.203e-04	0.069	0.012	0.205
TF41	2.237	0.330	2.474e-04	0.056	0.014	0.230
TF42	2.342	0.435	2.784e-04	0.039	0.015	0.259
TF43	2.447	0.540	2.804e-04	0.056	0.015	0.261
TF44	2.553	0.645	*	*	*	*
TF45	2.658	0.750	2.925e-04	0.072	0.016	0.272
TF46	2.763	0.855	3.137e-04	0.081	0.017	0.292
TF47	2.868	0.960	3.809e-04	0.069	0.021	0.355
TF48	2.973	1.065	5.046e-04	0.051	0.028	0.470
TF49	3.078	1.170	6.207e-04	0.027	0.034	0.578
TF50	3.182	1.275	7.558e-04	0.020	0.042	0.704
TF51	3.287	1.380	8.699e-04	0.015	0.048	0.810
TF52	3.392	1.485	1.006e-03	0.014	0.055	0.937
TF53	3.497	1.590	1.124e-03	0.014	0.062	1.047
TF54	3.602	1.695	1.251e-03	0.015	0.069	1.165
TF55	3.707	1.800	1.414e-03	0.015	0.078	1.317
TF56	3.813	1.905	1.611e-03	0.007	0.089	1.500
TF57	3.918	2.010	1.649e-03	0.011	0.091	1.536
TF58	4.023	2.115	1.901e-03	0.006	0.105	1.771
TF59	4.128	2.220	2.074e-03	0.008	0.114	1.932
TF60	4.233	2.325	2.104e-03	0.003	0.116	1.960
TF61	4.338	2.430	2.135e-03	0.004	0.117	1.988
TF62	4.443	2.535	2.414e-03	0.004	0.133	2.248
TF63	4.548	2.640	2.490e-03	0.003	0.137	2.319
TF64	4.653	2.745	2.520e-03	0.004	0.139	2.347
TF65	4.758	2.850	2.666e-03	0.004	0.147	2.483
TF66	4.863	2.955	2.681e-03	0.004	0.148	2.497
TF67	4.968	3.060	2.810e-03	0.005	0.155	2.617
TF68	5.073	3.165	2.846e-03	0.004	0.157	2.651
TF69	5.177	3.270	2.786e-03	0.005	0.153	2.595
TF70	5.282	3.375	2.867e-03	0.004	0.158	2.671

TABLE A.44 31-Inch Mach 10 Test 307, Run 008 Heating Data
MP-1 Configuration, $Re_\infty = 0.5 \times 10^6$ ft^{-1}, $\alpha = 0$ deg, $\phi = 0$ deg, $C_{H,ref} = 0.02821$

GAGE ID	S/R_b	L/R_b	C_H	s/C_H	$C_H/C_{H,ref}$	q_{300}(W/cm^2)
TF37	-1.870	-	*	*	*	*
TF36	-1.770	-	*	*	*	*
TF35	-1.680	-	3.200e-04	0.030	0.011	0.149
TF34	-1.550	-	2.230e-04	0.041	0.008	0.104
TF33	-1.430	-	2.210e-04	0.056	0.008	0.103
TF32	-1.300	-	2.290e-04	0.078	0.008	0.106
TF31	-1.180	-	1.150e-03	0.312	0.041	0.535
TF30	-1.080	-	1.040e-02	0.063	0.369	4.840
TF29	-1.000	-	1.850e-02	0.013	0.657	8.630
TF28	-0.900	-	1.730e-02	0.002	0.613	8.050
TF27	-0.800	-	1.650e-02	0.004	0.585	7.680
TF26	-0.700	-	*	*	*	*
TF25	-0.600	-	1.650e-02	0.004	0.583	7.660
TF24	-0.500	-	1.710e-02	0.002	0.607	7.970
TF23	-0.400	-	1.800e-02	0.004	0.639	8.390
TF22	-0.300	-	1.750e-02	0.002	0.622	8.160
TF21	-0.200	-	2.190e-02	0.002	0.775	10.200
TF20	-0.100	-	2.640e-02	0.002	0.937	12.300
TF19	0.000	-	2.760e-02	0.002	0.978	12.800
TF18	0.100	-	2.660e-02	0.002	0.942	12.400
TF17	0.200	-	2.240e-02	0.001	0.793	10.400
TF16	0.300	-	1.940e-02	0.001	0.689	9.050
TF15	0.400	-	1.790e-02	0.003	0.633	8.310
TF14	0.500	-	1.700e-02	0.003	0.602	7.910
TF13	0.600	-	*	*	*	*
TF12	0.700	-	1.640e-02	0.003	0.581	7.630
TF11	0.800	-	1.650e-02	0.005	0.584	7.670
TF10	0.900	-	1.700e-02	0.003	0.603	7.910
TF9	1.000	-	1.840e-02	0.011	0.651	8.550
TF8	1.080	-	1.140e-02	0.047	0.402	5.280
TF7	1.180	-	1.010e-03	0.353	0.036	0.469
TF6	1.300	-	2.080e-04	0.092	0.007	0.097
TF5	1.430	-	1.880e-04	0.029	0.007	0.088
TF4	1.550	-	1.630e-04	0.048	0.006	0.076
TF3	1.680	-	2.790e-04	0.037	0.010	0.130
TF2	1.770	-	2.300e-04	0.032	0.008	0.107
TF1	1.870	-	1.020e-04	0.075	0.004	0.047
TF38	1.930	0.000	*	*	*	*
TF39	2.040	0.120	1.220e-04	0.042	0.004	0.057
TF40	2.140	0.225	1.900e-04	0.064	0.007	0.088
TF41	2.250	0.330	2.690e-04	0.042	0.010	0.125
TF42	2.350	0.435	3.430e-04	0.018	0.012	0.160
TF43	2.460	0.540	4.080e-04	0.052	0.014	0.190
TF44	2.560	0.645	4.760e-04	0.043	0.017	0.221
TF45	2.670	0.750	5.400e-04	0.043	0.019	0.251
TF46	2.770	0.855	6.180e-04	0.037	0.022	0.287
TF47	2.880	0.960	7.050e-04	0.037	0.025	0.328
TF48	2.980	1.070	8.020e-04	0.039	0.028	0.373
TF49	3.090	1.170	9.200e-04	0.032	0.033	0.428
TF50	3.190	1.280	1.070e-03	0.033	0.038	0.496
TF51	3.300	1.380	1.210e-03	0.035	0.043	0.561
TF52	3.400	1.490	1.350e-03	0.034	0.048	0.629
TF53	3.510	1.590	1.580e-03	0.034	0.056	0.735
TF54	3.610	1.700	1.690e-03	0.029	0.060	0.784
TF55	3.720	1.800	1.840e-03	0.033	0.065	0.856
TF56	3.820	1.910	1.970e-03	0.032	0.070	0.916
TF57	3.930	2.010	2.090e-03	0.032	0.074	0.970
TF58	4.030	2.120	*	*	*	*
TF59	4.140	2.220	2.280e-03	0.026	0.081	1.060
TF60	4.240	2.330	2.310e-03	0.028	0.082	1.070
TF61	4.350	2.430	2.350e-03	0.026	0.083	1.100
TF62	4.450	2.540	2.410e-03	0.025	0.085	1.120
TF63	4.560	2.640	2.380e-03	0.023	0.084	1.110
TF64	4.660	2.750	2.390e-03	0.026	0.085	1.110
TF65	4.770	2.850	2.380e-03	0.025	0.084	1.110
TF66	4.870	2.960	2.360e-03	0.024	0.083	1.100
TF67	4.980	3.060	2.320e-03	0.024	0.082	1.080
TF68	5.080	3.170	2.290e-03	0.023	0.081	1.060
TF69	5.190	3.270	2.250e-03	0.023	0.080	1.050
TF70	5.290	3.380	2.200e-03	0.024	0.078	1.030

TABLE A.45 31-Inch Mach 10 Test 307, Run 009 Heating Data
MP-1 Configuration, $Re_\infty = 1.0 \times 10^6$ ft^{-1}, $\alpha = 0$ deg, $\phi = 0$ deg

*** BAD RUN, NO DATA ***

TABLE A.46 31-Inch Mach 10 Test 307, Run 010 Heating Data
MP-1 Configuration, $Re_\infty = 1.0 \times 10^6$ ft^{-1}, $\alpha = 0$ deg, $\phi = 0$ deg, $C_{H,ref} = 0.01981$

GAGE ID	S/R_b	L/R_b	C_H	s/C_H	$C_H/C_{H,ref}$	q_{300}(W/cm^2)
TF37	-1.870	-	*	*	*	*
TF36	-1.770	-	*	*	*	*
TF35	-1.680	-	2.030e-04	0.137	0.010	0.184
TF34	-1.550	-	1.380e-04	0.154	0.007	0.125
TF33	-1.430	-	1.340e-04	0.133	0.007	0.121
TF32	-1.300	-	1.630e-04	0.103	0.008	0.147
TF31	-1.180	-	7.000e-04	0.388	0.035	0.634
TF30	-1.080	-	7.180e-03	0.057	0.362	6.500
TF29	-1.000	-	1.330e-02	0.017	0.672	12.000
TF28	-0.900	-	1.180e-02	0.004	0.597	10.700
TF27	-0.800	-	1.130e-02	0.004	0.573	10.300
TF26	-0.700	-	*	*	*	*
TF25	-0.600	-	1.130e-02	0.002	0.572	10.300
TF24	-0.500	-	1.180e-02	0.001	0.598	10.700
TF23	-0.400	-	1.250e-02	0.001	0.631	11.300
TF22	-0.300	-	1.210e-02	0.002	0.609	10.900
TF21	-0.200	-	1.510e-02	0.002	0.763	13.700
TF20	-0.100	-	1.820e-02	0.002	0.921	16.500
TF19	0.000	-	1.900e-02	0.001	0.962	17.200
TF18	0.100	-	1.840e-02	0.003	0.929	16.700
TF17	0.200	-	1.550e-02	0.002	0.781	14.000
TF16	0.300	-	1.350e-02	0.002	0.682	12.200
TF15	0.400	-	1.230e-02	0.002	0.622	11.200
TF14	0.500	-	1.170e-02	0.001	0.591	10.600
TF13	0.600	-	1.160e-02	0.089	0.584	10.500
TF12	0.700	-	1.130e-02	0.003	0.568	10.200
TF11	0.800	-	1.130e-02	0.004	0.572	10.300
TF10	0.900	-	1.170e-02	0.003	0.591	10.600
TF9	1.000	-	1.270e-02	0.011	0.642	11.500
TF8	1.080	-	7.890e-03	0.044	0.398	7.140
TF7	1.180	-	6.250e-04	0.400	0.032	0.566
TF6	1.300	-	1.240e-04	0.178	0.006	0.112
TF5	1.430	-	1.010e-04	0.168	0.005	0.092
TF4	1.550	-	9.280e-05	0.123	0.005	0.084
TF3	1.680	-	1.590e-04	0.113	0.008	0.144
TF2	1.770	-	1.640e-04	0.148	0.008	0.149
TF1	1.870	-	9.850e-05	0.138	0.005	0.089
TF38	1.930	0.015	*	*	*	*
TF39	2.040	0.120	6.390e-05	0.086	0.003	0.058
TF40	2.140	0.225	7.330e-05	0.073	0.004	0.066
TF41	2.250	0.330	1.100e-04	0.047	0.006	0.100
TF42	2.350	0.435	1.720e-04	0.051	0.009	0.156
TF43	2.460	0.540	2.330e-04	0.039	0.012	0.211
TF44	2.560	0.645	2.870e-04	0.026	0.014	0.259
TF45	2.670	0.750	3.470e-04	0.040	0.018	0.314
TF46	2.770	0.855	4.190e-04	0.039	0.021	0.380
TF47	2.880	0.960	4.920e-04	0.035	0.025	0.446
TF48	2.980	1.070	5.820e-04	0.035	0.029	0.527
TF49	3.090	1.170	6.940e-04	0.035	0.035	0.628
TF50	3.190	1.280	8.350e-04	0.032	0.042	0.756
TF51	3.300	1.380	9.900e-04	0.027	0.050	0.896
TF52	3.400	1.490	1.180e-03	0.031	0.059	1.060
TF53	3.510	1.590	1.420e-03	0.029	0.072	1.290
TF54	3.610	1.700	1.560e-03	0.026	0.079	1.420
TF55	3.720	1.800	1.770e-03	0.027	0.089	1.600
TF56	3.820	1.910	1.930e-03	0.029	0.097	1.740
TF57	3.930	2.010	2.080e-03	0.026	0.105	1.880
TF58	4.030	2.120	*	*	*	*
TF59	4.140	2.220	2.250e-03	0.025	0.113	2.030
TF60	4.240	2.330	2.290e-03	0.024	0.116	2.070
TF61	4.350	2.430	2.340e-03	0.027	0.118	2.120
TF62	4.450	2.540	2.350e-03	0.026	0.119	2.130
TF63	4.560	2.640	2.310e-03	0.025	0.117	2.090
TF64	4.660	2.750	2.280e-03	0.026	0.115	2.070
TF65	4.770	2.850	2.240e-03	0.023	0.113	2.020
TF66	4.870	2.960	2.180e-03	0.025	0.110	1.980
TF67	4.980	3.060	2.130e-03	0.028	0.107	1.930
TF68	5.080	3.170	2.080e-03	0.025	0.105	1.880
TF69	5.190	3.270	2.020e-03	0.022	0.102	1.830
TF70	5.290	3.380	1.960e-03	0.022	0.099	1.770

TABLE A.47 31-Inch Mach 10 Test 307, Run 011 Heating Data
MP-1 Configuration, $Re_\infty = 2.0 \times 10^6$ ft^{-1}, $\alpha = 0$ deg, $\phi = 0$ deg, $C_{H,ref} = 0.01435$

GAGE ID	S/R_b	L/R_b	C_H	s/C_H	$C_H/C_{H,ref}$	q_{300}(W/cm^2)
TF38	1.930	0.015	4.660e-05	0.094	0.003	0.080
TF39	2.040	0.120	5.620e-05	0.076	0.004	0.097
TF40	2.140	0.225	5.980e-05	0.066	0.004	0.103
TF41	2.250	0.330	8.140e-05	0.028	0.006	0.140
TF42	2.350	0.435	1.160e-04	0.029	0.008	0.200
TF43	2.460	0.540	1.630e-04	0.030	0.011	0.281
TF44	2.560	0.645	2.100e-04	0.033	0.015	0.362
TF45	2.670	0.750	2.600e-04	0.028	0.018	0.449
TF46	2.770	0.855	3.120e-04	0.036	0.022	0.538
TF47	2.880	0.960	3.760e-04	0.033	0.026	0.648
TF48	2.980	1.070	4.490e-04	0.040	0.031	0.775
TF49	3.090	1.170	5.480e-04	0.035	0.038	0.944
TF50	3.190	1.280	6.760e-04	0.032	0.047	1.160
TF51	3.300	1.380	8.250e-04	0.028	0.058	1.420
TF52	3.400	1.490	1.010e-03	0.029	0.070	1.740
TF53	3.510	1.590	1.250e-03	0.027	0.087	2.150
TF54	3.610	1.700	1.420e-03	0.027	0.099	2.440
TF55	3.720	1.800	1.630e-03	0.027	0.114	2.810
TF56	3.820	1.910	1.790e-03	0.028	0.125	3.080
TF57	3.930	2.010	*	*	*	*
TF58	4.030	2.120	*	*	*	*
TF59	4.140	2.220	2.040e-03	0.027	0.142	3.510
TF60	4.240	2.330	2.030e-03	0.027	0.141	3.500
TF61	4.350	2.430	2.020e-03	0.030	0.141	3.480
TF62	4.450	2.540	1.980e-03	0.029	0.138	3.420
TF63	4.560	2.640	1.910e-03	0.028	0.133	3.290
TF64	4.660	2.750	1.840e-03	0.029	0.128	3.160
TF65	4.770	2.850	1.770e-03	0.029	0.123	3.050
TF66	4.870	2.960	1.690e-03	0.030	0.118	2.920
TF67	4.980	3.060	1.620e-03	0.030	0.113	2.800
TF68	5.080	3.170	1.560e-03	0.028	0.108	2.680
TF69	5.190	3.270	1.500e-03	0.029	0.105	2.590
TF70	5.290	3.380	1.440e-03	0.027	0.100	2.480

TABLE A.48 31-Inch Mach 10 Test 307, Run 012 Heating Data
MP-1 Configuration, $Re_\infty = 2.0 \times 10^6$ ft^{-1}, $\alpha = 0$ deg, $\phi = 0$ deg, $C_{H,ref} = 0.01435$

GAGE ID	S/R_b	L/R_b	C_H	s/C_H	$C_H/C_{H,ref}$	q_{300}(W/cm^2)
TF38	1.930	0.015	5.010e-05	0.086	0.003	0.087
TF39	2.040	0.120	5.410e-05	0.060	0.004	0.094
TF40	2.140	0.225	5.840e-05	0.056	0.004	0.101
TF41	2.250	0.330	7.830e-05	0.041	0.005	0.136
TF42	2.350	0.435	1.100e-04	0.040	0.008	0.191
TF43	2.460	0.540	1.550e-04	0.050	0.011	0.269
TF44	2.560	0.645	2.020e-04	0.037	0.014	0.349
TF45	2.670	0.750	2.490e-04	0.036	0.017	0.431
TF46	2.770	0.855	3.020e-04	0.035	0.021	0.523
TF47	2.880	0.960	3.650e-04	0.031	0.025	0.633
TF48	2.980	1.070	4.390e-04	0.027	0.031	0.761
TF49	3.090	1.170	5.360e-04	0.026	0.037	0.929
TF50	3.190	1.280	6.650e-04	0.025	0.046	1.150
TF51	3.300	1.380	8.170e-04	0.023	0.057	1.420
TF52	3.400	1.490	1.010e-03	0.024	0.071	1.750
TF53	3.510	1.590	1.260e-03	0.022	0.088	2.190
TF54	3.610	1.700	1.440e-03	0.020	0.100	2.500
TF55	3.720	1.800	1.670e-03	0.021	0.117	2.900
TF56	3.820	1.910	1.840e-03	0.020	0.128	3.190
TF57	3.930	2.010	*	*	*	*
TF58	4.030	2.120	*	*	*	*
TF59	4.140	2.220	2.120e-03	0.020	0.148	3.670
TF60	4.240	2.330	2.100e-03	0.021	0.146	3.630
TF61	4.350	2.430	2.110e-03	0.022	0.147	3.650
TF62	4.450	2.540	2.070e-03	0.020	0.144	3.590
TF63	4.560	2.640	2.000e-03	0.019	0.139	3.460
TF64	4.660	2.750	1.920e-03	0.021	0.134	3.330
TF65	4.770	2.850	1.850e-03	0.021	0.129	3.200
TF66	4.870	2.960	1.770e-03	0.020	0.123	3.070
TF67	4.980	3.060	1.700e-03	0.020	0.118	2.940
TF68	5.080	3.170	1.630e-03	0.019	0.113	2.820
TF69	5.190	3.270	1.570e-03	0.019	0.109	2.710
TF70	5.290	3.380	1.500e-03	0.018	0.104	2.590

TABLE A.49 31-Inch Mach 10 Test 307, Run 013 Heating Data
MP-1 Configuration, $Re_\infty = 1.0 \times 10^6$ ft^{-1}, $\alpha = 0$ deg, $\phi = 0$ deg, $C_{H,ref} = 0.01981$

GAGE ID	S/R_b	L/R_b	C_H	s/C_H	$C_H/C_{H,ref}$	q_{300}(W/cm^2)
TF38	1.930	0.015	4.970e-05	0.124	0.003	0.045
TF39	2.040	0.120	5.670e-05	0.123	0.003	0.052
TF40	2.140	0.225	7.380e-05	0.069	0.004	0.067
TF41	2.250	0.330	1.150e-04	0.047	0.006	0.105
TF42	2.350	0.435	1.700e-04	0.037	0.009	0.155
TF43	2.460	0.540	2.240e-04	0.021	0.011	0.204
TF44	2.560	0.645	2.770e-04	0.018	0.014	0.252
TF45	2.670	0.750	3.280e-04	0.019	0.017	0.299
TF46	2.770	0.855	3.830e-04	0.025	0.019	0.349
TF47	2.880	0.960	4.520e-04	0.020	0.023	0.412
TF48	2.980	1.070	5.360e-04	0.022	0.027	0.488
TF49	3.090	1.170	6.340e-04	0.021	0.032	0.577
TF50	3.190	1.280	7.620e-04	0.027	0.038	0.694
TF51	3.300	1.380	9.040e-04	0.026	0.046	0.823
TF52	3.400	1.490	1.060e-03	0.028	0.054	0.967
TF53	3.510	1.590	1.270e-03	0.030	0.064	1.160
TF54	3.610	1.700	1.400e-03	0.027	0.071	1.270
TF55	3.720	1.800	1.550e-03	0.027	0.078	1.410
TF56	3.820	1.910	1.680e-03	0.032	0.085	1.530
TF57	3.930	2.010	*	*	*	*
TF58	4.030	2.120	*	*	*	*
TF59	4.140	2.220	1.970e-03	0.036	0.100	1.790
TF60	4.240	2.330	2.000e-03	0.038	0.101	1.820
TF61	4.350	2.430	2.040e-03	0.043	0.103	1.860
TF62	4.450	2.540	2.060e-03	0.045	0.104	1.870
TF63	4.560	2.640	2.030e-03	0.046	0.102	1.850
TF64	4.660	2.750	2.020e-03	0.046	0.102	1.840
TF65	4.770	2.850	1.990e-03	0.041	0.100	1.810
TF66	4.870	2.960	1.940e-03	0.043	0.098	1.770
TF67	4.980	3.060	1.910e-03	0.046	0.096	1.740
TF68	5.080	3.170	1.860e-03	0.042	0.094	1.700
TF69	5.190	3.270	1.810e-03	0.043	0.091	1.650
TF70	5.290	3.380	1.770e-03	0.040	0.089	1.610

TABLE A.50: 31-Inch Mach 10 Test 307, Run 014 Heating Data
MP-1 Configuration, $Re_\infty = 1.0 \times 10^6$ ft^{-1}, $\alpha = 0$ deg, $\phi = 0$ deg, $C_{H,ref} = 0.01981$

GAGE ID	S/R_b	L/R_b	C_H	s/C_H	$C_H/C_{H,ref}$	q_{300}(W/cm^2)
TF38	1.930	0.015	3.970e-05	0.090	0.002	0.036
TF39	2.040	0.120	4.450e-05	0.075	0.002	0.040
TF40	2.140	0.225	7.140e-05	0.045	0.004	0.065
TF41	2.250	0.330	1.150e-04	0.044	0.006	0.104
TF42	2.350	0.435	1.730e-04	0.049	0.009	0.157
TF43	2.460	0.540	2.260e-04	0.035	0.011	0.206
TF44	2.560	0.645	2.690e-04	0.034	0.014	0.244
TF45	2.670	0.750	3.170e-04	0.052	0.016	0.288
TF46	2.770	0.855	3.730e-04	0.044	0.019	0.338
TF47	2.880	0.960	4.380e-04	0.037	0.022	0.398
TF48	2.980	1.070	5.240e-04	0.040	0.026	0.476
TF49	3.090	1.170	6.190e-04	0.034	0.031	0.562
TF50	3.190	1.280	7.420e-04	0.031	0.038	0.674
TF51	3.300	1.380	8.810e-04	0.027	0.045	0.799
TF52	3.400	1.490	1.040e-03	0.028	0.052	0.944
TF53	3.510	1.590	1.240e-03	0.024	0.063	1.130
TF54	3.610	1.700	1.390e-03	0.021	0.070	1.260
TF55	3.720	1.800	1.570e-03	0.021	0.079	1.420
TF56	3.820	1.910	1.710e-03	0.022	0.086	1.550
TF57	3.930	2.010	*	*	*	*
TF58	4.030	2.120	*	*	*	*
TF59	4.140	2.220	2.010e-03	0.017	0.101	1.820
TF60	4.240	2.330	2.060e-03	0.018	0.104	1.870
TF61	4.350	2.430	2.110e-03	0.020	0.106	1.910
TF62	4.450	2.540	2.130e-03	0.020	0.108	1.930
TF63	4.560	2.640	2.100e-03	0.018	0.106	1.910
TF64	4.660	2.750	2.080e-03	0.020	0.105	1.890
TF65	4.770	2.850	2.050e-03	0.016	0.103	1.860
TF66	4.870	2.960	2.000e-03	0.018	0.101	1.820
TF67	4.980	3.060	1.970e-03	0.020	0.099	1.780
TF68	5.080	3.170	1.910e-03	0.018	0.097	1.740
TF69	5.190	3.270	1.870e-03	0.019	0.094	1.690
TF70	5.290	3.380	1.810e-03	0.018	0.091	1.640

TABLE A.51: 31-Inch Mach 10 Test 307, Run 015 Heating Data
MP-1 Configuration, $Re_\infty = 0.5 \times 10^6$ ft^{-1}, $\alpha = 0$ deg, $\phi = 0$ deg, $C_{H,ref} = 0.02821$

GAGE ID	S/R_b	L/R_b	C_H	s/C_H	$C_H/C_{H,ref}$	q_{300}(W/cm^2)
TF38	1.930	0.015	5.030e-05	0.158	0.002	0.023
TF39	2.040	0.120	1.170e-04	0.040	0.004	0.053
TF40	2.140	0.225	1.970e-04	0.055	0.007	0.090
TF41	2.250	0.330	2.700e-04	0.036	0.010	0.123
TF42	2.350	0.435	3.310e-04	0.046	0.012	0.151
TF43	2.460	0.540	4.030e-04	0.015	0.014	0.184
TF44	2.560	0.645	4.630e-04	0.036	0.016	0.211
TF45	2.670	0.750	5.170e-04	0.032	0.018	0.236
TF46	2.770	0.855	6.080e-04	0.029	0.022	0.278
TF47	2.880	0.960	6.880e-04	0.037	0.024	0.314
TF48	2.980	1.070	7.830e-04	0.017	0.028	0.358
TF49	3.090	1.170	8.870e-04	0.026	0.031	0.405
TF50	3.190	1.280	1.020e-03	0.021	0.036	0.466
TF51	3.300	1.380	1.140e-03	0.022	0.041	0.523
TF52	3.400	1.490	1.300e-03	0.023	0.046	0.593
TF53	3.510	1.590	1.500e-03	0.015	0.053	0.687
TF54	3.610	1.700	1.600e-03	0.017	0.057	0.730
TF55	3.720	1.800	1.740e-03	0.022	0.062	0.796
TF56	3.820	1.910	1.850e-03	0.018	0.066	0.847
TF57	3.930	2.010	*	*	*	*
TF58	4.030	2.120	*	*	*	*
TF59	4.140	2.220	2.150e-03	0.020	0.076	0.981
TF60	4.240	2.330	2.180e-03	0.020	0.077	0.996
TF61	4.350	2.430	2.250e-03	0.019	0.080	1.030
TF62	4.450	2.540	2.270e-03	0.019	0.081	1.040
TF63	4.560	2.640	2.290e-03	0.021	0.081	1.040
TF64	4.660	2.750	2.270e-03	0.023	0.080	1.040
TF65	4.770	2.850	2.280e-03	0.020	0.081	1.040
TF66	4.870	2.960	2.250e-03	0.020	0.080	1.030
TF67	4.980	3.060	2.230e-03	0.026	0.079	1.020
TF68	5.080	3.170	2.200e-03	0.020	0.078	1.000
TF69	5.190	3.270	2.170e-03	0.022	0.077	0.990
TF70	5.290	3.380	2.130e-03	0.021	0.075	0.972

TABLE A.52 31-Inch Mach 10 Test 307, Run 016 Heating Data
MP-1 Configuration, $Re_\infty = 0.5 \times 10^6$ ft^{-1}, $\alpha = 0$ deg, $\phi = 0$ deg, $C_{H,ref} = 0.02821$

GAGE ID	S/R_b	L/R_b	C_H	s/C_H	$C_H/C_{H,ref}$	q_{300}(W/cm^2)
TF38	1.930	0.015	5.390e-05	0.225	0.002	0.025
TF39	2.040	0.120	1.130e-04	0.109	0.004	0.052
TF40	2.140	0.225	1.890e-04	0.048	0.007	0.087
TF41	2.250	0.330	2.630e-04	0.029	0.009	0.122
TF42	2.350	0.435	3.240e-04	0.048	0.012	0.150
TF43	2.460	0.540	3.970e-04	0.036	0.014	0.184
TF44	2.560	0.645	4.590e-04	0.035	0.016	0.213
TF45	2.670	0.750	5.230e-04	0.026	0.019	0.242
TF46	2.770	0.855	5.990e-04	0.030	0.021	0.277
TF47	2.880	0.960	6.740e-04	0.030	0.024	0.312
TF48	2.980	1.070	7.840e-04	0.030	0.028	0.363
TF49	3.090	1.170	8.830e-04	0.029	0.031	0.409
TF50	3.190	1.280	1.020e-03	0.029	0.036	0.473
TF51	3.300	1.380	1.140e-03	0.024	0.040	0.528
TF52	3.400	1.490	1.290e-03	0.024	0.046	0.596
TF53	3.510	1.590	1.490e-03	0.028	0.053	0.689
TF54	3.610	1.700	1.590e-03	0.021	0.056	0.735
TF55	3.720	1.800	1.750e-03	0.025	0.062	0.809
TF56	3.820	1.910	1.860e-03	0.024	0.066	0.860
TF57	3.930	2.010	*	*	*	*
TF58	4.030	2.120	*	*	*	*
TF59	4.140	2.220	2.150e-03	0.018	0.076	0.997
TF60	4.240	2.330	2.180e-03	0.019	0.077	1.010
TF61	4.350	2.430	2.230e-03	0.019	0.079	1.030
TF62	4.450	2.540	2.270e-03	0.017	0.081	1.050
TF63	4.560	2.640	2.270e-03	0.017	0.080	1.050
TF64	4.660	2.750	2.270e-03	0.020	0.081	1.050
TF65	4.770	2.850	2.270e-03	0.019	0.080	1.050
TF66	4.870	2.960	2.260e-03	0.020	0.080	1.050
TF67	4.980	3.060	2.220e-03	0.018	0.079	1.030
TF68	5.080	3.170	2.200e-03	0.021	0.078	1.020
TF69	5.190	3.270	2.180e-03	0.017	0.077	1.010
TF70	5.290	3.380	2.130e-03	0.021	0.075	0.987

TABLE A.53 31-Inch Mach 10 Test 307, Run 017 Heating Data
MP-1 Configuration, $Re_\infty = 2.0 \times 10^6$ ft^{-1}, $\alpha = 0$ deg, $\phi = 0$ deg, $C_{H,ref} = 0.01435$

GAGE ID	S/R_b	L/R_b	C_H	s/C_H	$C_H/C_{H,ref}$	q_{300}(W/cm^2)
TF38	1.930	0.015	9.280e-05	0.052	0.006	0.160
TF39	2.040	0.120	9.800e-05	0.063	0.007	0.169
TF40	2.140	0.225	8.580e-05	0.030	0.006	0.148
TF41	2.250	0.330	1.050e-04	0.065	0.007	0.181
TF42	2.350	0.435	1.300e-04	0.073	0.009	0.225
TF43	2.460	0.540	1.680e-04	0.091	0.012	0.290
TF44	2.560	0.645	2.040e-04	0.069	0.014	0.352
TF45	2.670	0.750	2.470e-04	0.065	0.017	0.427
TF46	2.770	0.855	3.020e-04	0.050	0.021	0.521
TF47	2.880	0.960	3.650e-04	0.041	0.025	0.630
TF48	2.980	1.070	4.340e-04	0.033	0.030	0.748
TF49	3.090	1.170	5.250e-04	0.027	0.037	0.906
TF50	3.190	1.280	6.460e-04	0.031	0.045	1.110
TF51	3.300	1.380	7.830e-04	0.035	0.055	1.350
TF52	3.400	1.490	9.570e-04	0.039	0.067	1.650
TF53	3.510	1.590	1.190e-03	0.049	0.083	2.050
TF54	3.610	1.700	1.360e-03	0.051	0.095	2.340
TF55	3.720	1.800	1.580e-03	0.056	0.110	2.730
TF56	3.820	1.910	1.850e-03	0.046	0.129	3.190
TF57	3.930	2.010	*	*	*	*
TF58	4.030	2.120	*	*	*	*
TF59	4.140	2.220	2.100e-03	0.051	0.147	3.630
TF60	4.240	2.330	2.110e-03	0.046	0.147	3.640
TF61	4.350	2.430	2.130e-03	0.047	0.149	3.680
TF62	4.450	2.540	2.110e-03	0.042	0.147	3.650
TF63	4.560	2.640	2.050e-03	0.038	0.143	3.540
TF64	4.660	2.750	1.990e-03	0.035	0.139	3.430
TF65	4.770	2.850	1.930e-03	0.032	0.134	3.320
TF66	4.870	2.960	1.860e-03	0.031	0.129	3.200
TF67	4.980	3.060	1.790e-03	0.029	0.124	3.080
TF68	5.080	3.170	1.710e-03	0.028	0.119	2.950
TF69	5.190	3.270	1.650e-03	0.025	0.115	2.850
TF70	5.290	3.380	1.580e-03	0.022	0.110	2.720

TABLE A.54 31-Inch Mach 10 Test 307, Run 018 Heating Data
MP-1 Configuration, $Re_\infty = 1.0 \times 10^6$ ft^{-1}, $\alpha = 0$ deg, $\phi = 0$ deg, $C_{H,ref} = 0.01981$

GAGE ID	S/R_b	L/R_b	C_H	s/C_H	$C_H/C_{H,ref}$	q_{300}(W/cm^2)
TF38	1.930	0.015	8.390e-05	0.182	0.004	0.077
TF39	2.040	0.120	8.950e-05	0.125	0.005	0.082
TF40	2.140	0.225	8.700e-05	0.037	0.004	0.079
TF41	2.250	0.330	1.220e-04	0.047	0.006	0.112
TF42	2.350	0.435	1.670e-04	0.059	0.008	0.152
TF43	2.460	0.540	2.160e-04	0.078	0.011	0.197
TF44	2.560	0.645	2.620e-04	0.086	0.013	0.239
TF45	2.670	0.750	3.170e-04	0.086	0.016	0.290
TF46	2.770	0.855	3.830e-04	0.068	0.019	0.350
TF47	2.880	0.960	4.530e-04	0.069	0.023	0.414
TF48	2.980	1.070	5.510e-04	0.068	0.028	0.504
TF49	3.090	1.170	6.470e-04	0.063	0.033	0.591
TF50	3.190	1.280	7.870e-04	0.052	0.040	0.719
TF51	3.300	1.380	9.250e-04	0.051	0.047	0.845
TF52	3.400	1.490	1.090e-03	0.044	0.055	0.996
TF53	3.510	1.590	1.310e-03	0.042	0.066	1.200
TF54	3.610	1.700	1.460e-03	0.032	0.074	1.340
TF55	3.720	1.800	1.680e-03	0.022	0.085	1.540
TF56	3.820	1.910	1.860e-03	0.017	0.094	1.700
TF57	3.930	2.010	*	*	*	*
TF58	4.030	2.120	*	*	*	*
TF59	4.140	2.220	2.230e-03	0.007	0.112	2.040
TF60	4.240	2.330	2.280e-03	0.009	0.115	2.090
TF61	4.350	2.430	2.370e-03	0.012	0.120	2.170
TF62	4.450	2.540	2.400e-03	0.014	0.121	2.190
TF63	4.560	2.640	2.370e-03	0.017	0.120	2.170
TF64	4.660	2.750	2.350e-03	0.014	0.119	2.150
TF65	4.770	2.850	2.300e-03	0.014	0.116	2.100
TF66	4.870	2.960	2.250e-03	0.013	0.114	2.060
TF67	4.980	3.060	2.230e-03	0.014	0.113	2.040
TF68	5.080	3.170	2.160e-03	0.012	0.109	1.980
TF69	5.190	3.270	2.120e-03	0.012	0.107	1.930
TF70	5.290	3.380	2.030e-03	0.012	0.103	1.860

TABLE A.55 31-Inch Mach 10 Test 307, Run 019 Heating Data
MP-1 Configuration, $Re_\infty = 1.0 \times 10^6$ ft^{-1}, $\alpha = 0$ deg, $\phi = 0$ deg, $C_{H,ref} = 0.01981$

GAGE ID	S/R_b	L/R_b	C_H	s/C_H	$C_H/C_{H,ref}$	q_{300}(W/cm^2)
TF38	1.930	0.015	7.640e-05	0.084	0.004	0.069
TF39	2.040	0.120	7.840e-05	0.069	0.004	0.071
TF40	2.140	0.225	8.350e-05	0.046	0.004	0.076
TF41	2.250	0.330	1.110e-04	0.063	0.006	0.100
TF42	2.350	0.435	1.480e-04	0.069	0.007	0.134
TF43	2.460	0.540	1.910e-04	0.043	0.010	0.173
TF44	2.560	0.645	2.340e-04	0.031	0.012	0.212
TF45	2.670	0.750	2.860e-04	0.040	0.014	0.259
TF46	2.770	0.855	3.400e-04	0.047	0.017	0.308
TF47	2.880	0.960	4.000e-04	0.053	0.020	0.363
TF48	2.980	1.070	4.780e-04	0.054	0.024	0.433
TF49	3.090	1.170	5.720e-04	0.055	0.029	0.519
TF50	3.190	1.280	6.880e-04	0.056	0.035	0.624
TF51	3.300	1.380	8.220e-04	0.054	0.041	0.746
TF52	3.400	1.490	9.680e-04	0.050	0.049	0.878
TF53	3.510	1.590	1.510e-03	0.102	0.076	1.370
TF54	3.610	1.700	1.290e-03	0.049	0.065	1.170
TF55	3.720	1.800	1.450e-03	0.042	0.073	1.320
TF56	3.820	1.910	1.590e-03	0.042	0.080	1.450
TF57	3.930	2.010	*	*	*	*
TF58	4.030	2.120	*	*	*	*
TF59	4.140	2.220	1.940e-03	0.033	0.098	1.760
TF60	4.240	2.330	1.980e-03	0.033	0.100	1.790
TF61	4.350	2.430	2.020e-03	0.032	0.102	1.830
TF62	4.450	2.540	2.060e-03	0.033	0.104	1.860
TF63	4.560	2.640	2.030e-03	0.029	0.102	1.840
TF64	4.660	2.750	2.020e-03	0.030	0.102	1.830
TF65	4.770	2.850	2.020e-03	0.025	0.102	1.830
TF66	4.870	2.960	1.980e-03	0.028	0.100	1.800
TF67	4.980	3.060	1.920e-03	0.030	0.097	1.740
TF68	5.080	3.170	1.880e-03	0.025	0.095	1.700
TF69	5.190	3.270	1.840e-03	0.025	0.093	1.670
TF70	5.290	3.380	1.810e-03	0.025	0.092	1.650

TABLE A.56 31-Inch Mach 10 Test 307, Run 020 Heating Data
MP-1 Configuration, $Re_\infty = 2.0 \times 10^6$ ft^{-1}, $\alpha = 0$ deg, $\phi = 0$ deg, $C_{H,ref} = 0.01435$

GAGE ID	S/R_b	L/R_b	C_H	s/C_H	$C_H/C_{H,ref}$	q_{300}(W/cm^2)
TF38	1.930	0.015	4.260e-05	0.132	0.003	0.073
TF39	2.040	0.120	5.360e-05	0.140	0.004	0.092
TF40	2.140	0.225	6.470e-05	0.097	0.005	0.111
TF41	2.250	0.330	1.030e-04	0.079	0.007	0.176
TF42	2.350	0.435	1.490e-04	0.089	0.010	0.257
TF43	2.460	0.540	2.030e-04	0.085	0.014	0.349
TF44	2.560	0.645	2.620e-04	0.108	0.018	0.451
TF45	2.670	0.750	3.120e-04	0.101	0.022	0.537
TF46	2.770	0.855	3.660e-04	0.098	0.025	0.630
TF47	2.880	0.960	4.230e-04	0.082	0.030	0.727
TF48	2.980	1.070	4.840e-04	0.066	0.034	0.833
TF49	3.090	1.170	5.730e-04	0.050	0.040	0.985
TF50	3.190	1.280	6.750e-04	0.026	0.047	1.160
TF51	3.300	1.380	8.090e-04	0.017	0.056	1.390
TF52	3.400	1.490	9.860e-04	0.012	0.069	1.700
TF53	3.510	1.590	1.230e-03	0.017	0.085	2.110
TF54	3.610	1.700	1.420e-03	0.024	0.099	2.440
TF55	3.720	1.800	1.680e-03	0.033	0.117	2.890
TF56	3.820	1.910	1.890e-03	0.037	0.132	3.250
TF57	3.930	2.010	*	*	*	*
TF58	4.030	2.120	*	*	*	*
TF59	4.140	2.220	2.280e-03	0.041	0.159	3.930
TF60	4.240	2.330	*	*	*	*
TF61	4.350	2.430	2.330e-03	0.036	0.162	4.010
TF62	4.450	2.540	2.310e-03	0.031	0.161	3.970
TF63	4.560	2.640	2.230e-03	0.028	0.155	3.840
TF64	4.660	2.750	2.180e-03	0.027	0.152	3.750
TF65	4.770	2.850	2.100e-03	0.026	0.146	3.610
TF66	4.870	2.960	2.010e-03	0.024	0.140	3.460
TF67	4.980	3.060	1.930e-03	0.021	0.135	3.330
TF68	5.080	3.170	1.850e-03	0.019	0.129	3.190
TF69	5.190	3.270	1.780e-03	0.017	0.124	3.060
TF70	5.290	3.380	1.700e-03	0.013	0.119	2.930

TABLE A.57 31-Inch Mach 10 Test 307, Run 021 Heating Data
MP-1 Configuration, $Re_\infty = 0.5 \times 10^6$ ft^{-1}, $\alpha = 0$ deg, $\phi = 0$ deg, $C_{H,ref} = 0.02821$

GAGE ID	S/R_b	L/R_b	C_H	s/C_H	$C_H/C_{H,ref}$	q_{300}(W/cm^2)
TF38	1.930	0.015	5.730e-05	0.170	0.002	0.027
TF39	2.040	0.120	1.190e-04	0.051	0.004	0.056
TF40	2.140	0.225	1.840e-04	0.068	0.007	0.086
TF41	2.250	0.330	2.550e-04	0.044	0.009	0.120
TF42	2.350	0.435	3.160e-04	0.029	0.011	0.148
TF43	2.460	0.540	3.860e-04	0.025	0.014	0.181
TF44	2.560	0.645	4.410e-04	0.039	0.016	0.206
TF45	2.670	0.750	5.070e-04	0.040	0.018	0.237
TF46	2.770	0.855	5.840e-04	0.029	0.021	0.273
TF47	2.880	0.960	6.700e-04	0.030	0.024	0.314
TF48	2.980	1.070	7.710e-04	0.023	0.027	0.361
TF49	3.090	1.170	8.770e-04	0.027	0.031	0.411
TF50	3.190	1.280	1.010e-03	0.025	0.036	0.473
TF51	3.300	1.380	1.140e-03	0.028	0.041	0.535
TF52	3.400	1.490	1.300e-03	0.024	0.046	0.609
TF53	3.510	1.590	1.510e-03	0.031	0.053	0.706
TF54	3.610	1.700	1.620e-03	0.020	0.057	0.758
TF55	3.720	1.800	1.770e-03	0.022	0.063	0.828
TF56	3.820	1.910	1.890e-03	0.024	0.067	0.883
TF57	3.930	2.010	*	*	*	*
TF58	4.030	2.120	*	*	*	*
TF59	4.140	2.220	2.200e-03	0.023	0.078	1.030
TF60	4.240	2.330	2.230e-03	0.023	0.079	1.050
TF61	4.350	2.430	2.320e-03	0.025	0.082	1.090
TF62	4.450	2.540	2.340e-03	0.024	0.083	1.100
TF63	4.560	2.640	2.330e-03	0.026	0.083	1.090
TF64	4.660	2.750	2.330e-03	0.023	0.083	1.090
TF65	4.770	2.850	2.340e-03	0.026	0.083	1.090
TF66	4.870	2.960	2.310e-03	0.027	0.082	1.080
TF67	4.980	3.060	2.280e-03	0.024	0.081	1.070
TF68	5.080	3.170	2.250e-03	0.024	0.080	1.050
TF69	5.190	3.270	2.230e-03	0.026	0.079	1.040
TF70	5.290	3.380	2.170e-03	0.023	0.077	1.020

TABLE A.58 31-Inch Mach 10 Test 307, Run 022 Heating Data
MP-1 Configuration, $Re_\infty = 1.0 \times 10^6$ ft^{-1}, $\alpha = 0$ deg, $\phi = 0$ deg, $C_{H,ref} = 0.01981$

GAGE ID	S/R_b	L/R_b	C_H	s/C_H	$C_H/C_{H,ref}$	q_{300}(W/cm^2)
TF38	1.930	0.015	4.230e-05	0.105	0.002	0.039
TF39	2.040	0.120	5.340e-05	0.100	0.003	0.049
TF40	2.140	0.225	7.160e-05	0.059	0.004	0.065
TF41	2.250	0.330	1.080e-04	0.077	0.005	0.099
TF42	2.350	0.435	1.630e-04	0.056	0.008	0.149
TF43	2.460	0.540	2.170e-04	0.049	0.011	0.199
TF44	2.560	0.645	2.680e-04	0.054	0.014	0.245
TF45	2.670	0.750	3.240e-04	0.038	0.016	0.297
TF46	2.770	0.855	3.880e-04	0.034	0.020	0.355
TF47	2.880	0.960	4.570e-04	0.037	0.023	0.418
TF48	2.980	1.070	5.440e-04	0.032	0.027	0.497
TF49	3.090	1.170	6.450e-04	0.033	0.033	0.591
TF50	3.190	1.280	7.880e-04	0.024	0.040	0.721
TF51	3.300	1.380	9.350e-04	0.030	0.047	0.855
TF52	3.400	1.490	1.110e-03	0.025	0.056	1.020
TF53	3.510	1.590	1.340e-03	0.022	0.068	1.230
TF54	3.610	1.700	1.500e-03	0.020	0.075	1.370
TF55	3.720	1.800	1.700e-03	0.025	0.086	1.560
TF56	3.820	1.910	1.860e-03	0.023	0.094	1.700
TF57	3.930	2.010	*	*	*	*
TF58	4.030	2.120	*	*	*	*
TF59	4.140	2.220	2.180e-03	0.020	0.110	1.990
TF60	4.240	2.330	2.230e-03	0.020	0.112	2.040
TF61	4.350	2.430	2.270e-03	0.022	0.115	2.080
TF62	4.450	2.540	2.290e-03	0.021	0.116	2.100
TF63	4.560	2.640	2.260e-03	0.021	0.114	2.070
TF64	4.660	2.750	2.230e-03	0.021	0.112	2.040
TF65	4.770	2.850	2.180e-03	0.019	0.110	2.000
TF66	4.870	2.960	2.130e-03	0.022	0.108	1.950
TF67	4.980	3.060	2.080e-03	0.020	0.105	1.910
TF68	5.080	3.170	2.030e-03	0.020	0.102	1.850
TF69	5.190	3.270	1.980e-03	0.019	0.100	1.810
TF70	5.290	3.380	1.910e-03	0.021	0.096	1.750

TABLE A.59 31-Inch Mach 10 Test 307, Run 023 Heating Data
MP-1 Configuration, $Re_\infty = 2.0 \times 10^6$ ft^{-1}, $\alpha = 0$ deg, $\phi = 0$ deg, $C_{H,ref} = 0.01435$

GAGE ID	S/R_b	L/R_b	C_H	s/C_H	$C_H/C_{H,ref}$	q_{300}(W/cm^2)
TF38	1.930	0.015	4.820e-05	0.066	0.003	0.082
TF39	2.040	0.120	5.910e-05	0.049	0.004	0.101
TF40	2.140	0.225	6.120e-05	0.020	0.004	0.105
TF41	2.250	0.330	8.340e-05	0.036	0.006	0.143
TF42	2.350	0.435	1.070e-04	0.032	0.007	0.182
TF43	2.460	0.540	1.490e-04	0.038	0.010	0.255
TF44	2.560	0.645	1.920e-04	0.029	0.013	0.329
TF45	2.670	0.750	2.390e-04	0.027	0.017	0.409
TF46	2.770	0.855	2.900e-04	0.028	0.020	0.496
TF47	2.880	0.960	3.510e-04	0.023	0.024	0.601
TF48	2.980	1.070	4.200e-04	0.027	0.029	0.718
TF49	3.090	1.170	5.230e-04	0.022	0.036	0.894
TF50	3.190	1.280	6.460e-04	0.022	0.045	1.100
TF51	3.300	1.380	7.970e-04	0.021	0.056	1.360
TF52	3.400	1.490	9.940e-04	0.020	0.069	1.700
TF53	3.510	1.590	1.240e-03	0.020	0.087	2.130
TF54	3.610	1.700	1.420e-03	0.020	0.099	2.440
TF55	3.720	1.800	1.650e-03	0.019	0.115	2.830
TF56	3.820	1.910	1.830e-03	0.019	0.128	3.130
TF57	3.930	2.010	*	*	*	*
TF58	4.030	2.120	*	*	*	*
TF59	4.140	2.220	2.110e-03	0.015	0.147	3.610
TF60	4.240	2.330	2.110e-03	0.014	0.147	3.610
TF61	4.350	2.430	2.100e-03	0.016	0.146	3.590
TF62	4.450	2.540	2.060e-03	0.016	0.144	3.530
TF63	4.560	2.640	1.980e-03	0.013	0.138	3.380
TF64	4.660	2.750	1.910e-03	0.015	0.133	3.260
TF65	4.770	2.850	1.830e-03	0.015	0.128	3.130
TF66	4.870	2.960	1.750e-03	0.015	0.122	3.000
TF67	4.980	3.060	1.680e-03	0.017	0.117	2.870
TF68	5.080	3.170	1.610e-03	0.017	0.112	2.750
TF69	5.190	3.270	1.550e-03	0.017	0.108	2.650
TF70	5.290	3.380	1.480e-03	0.017	0.103	2.530

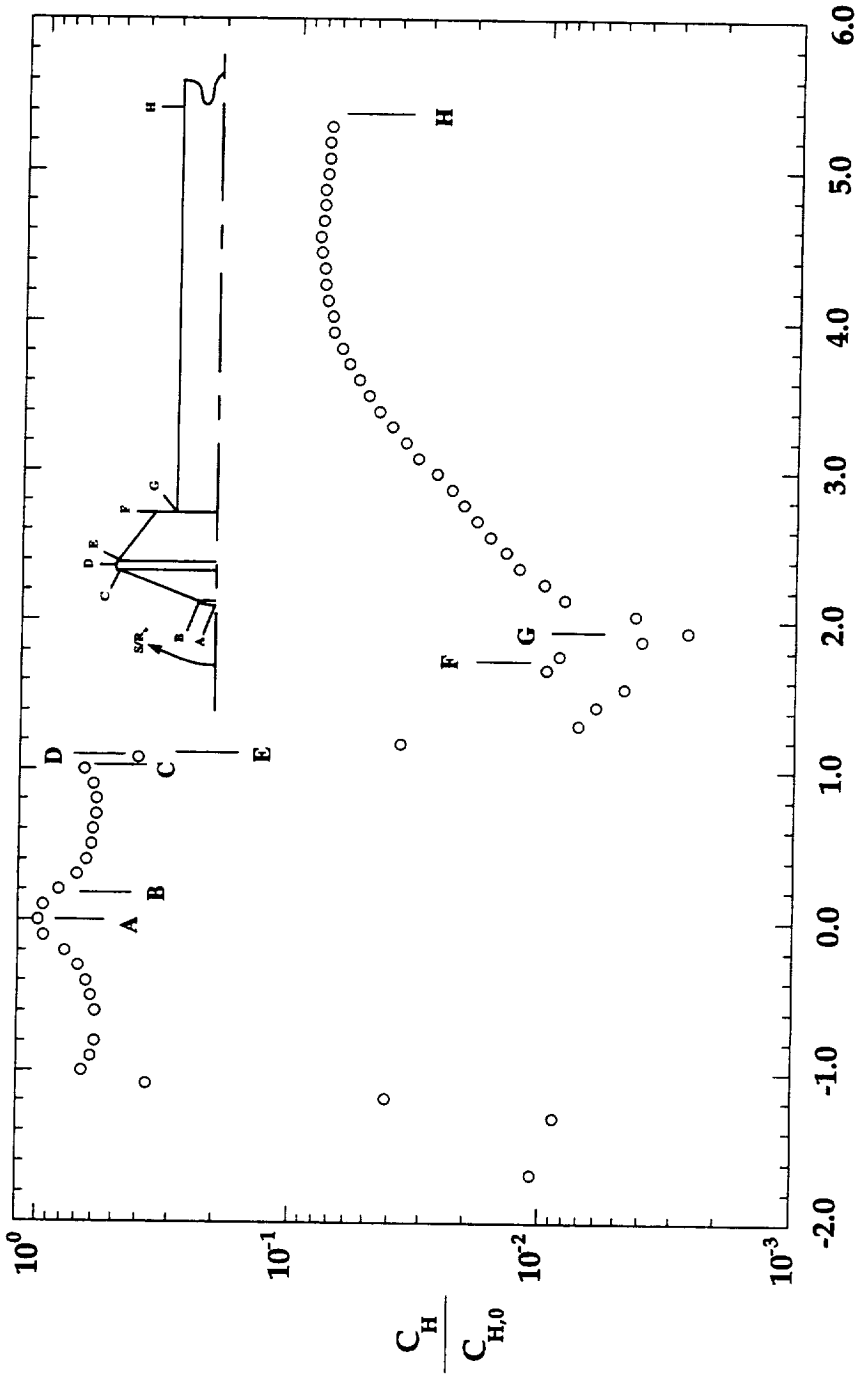

Figure A-1: 31-Inch Mach 10 Test 293, Run 005, MP-1 Configuration, $Re_\infty = 0.5 \times 10^6$ ft^{-1}, $\alpha = 0°$, $\phi = 0°$

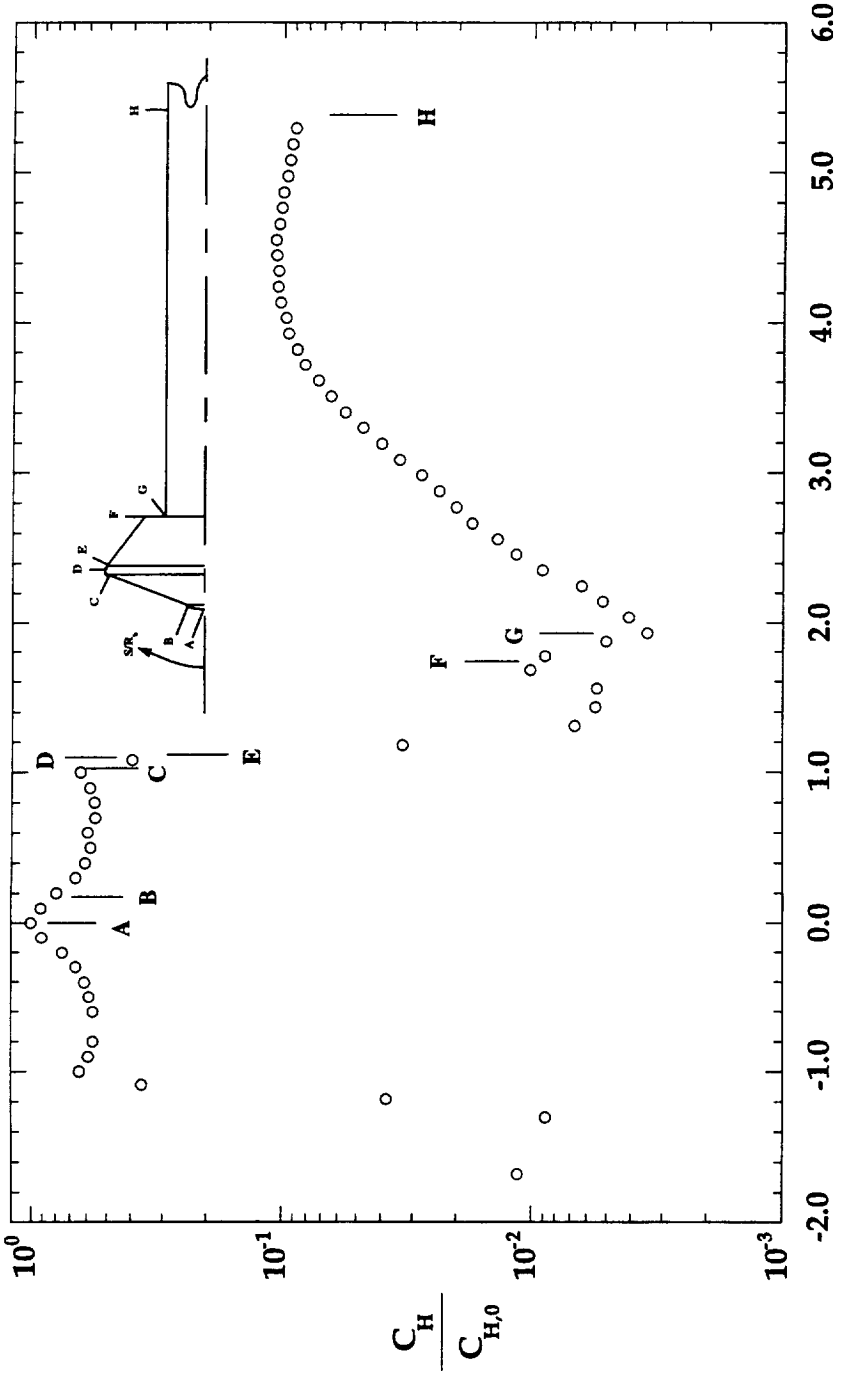

Figure A-2: 31-Inch Mach 10 Test 293, Run 006, MP-1 Configuration, $Re_\infty = 1.0 \times 10^6$ ft^{-1}, $\alpha = 0°$, $\phi = 0°$

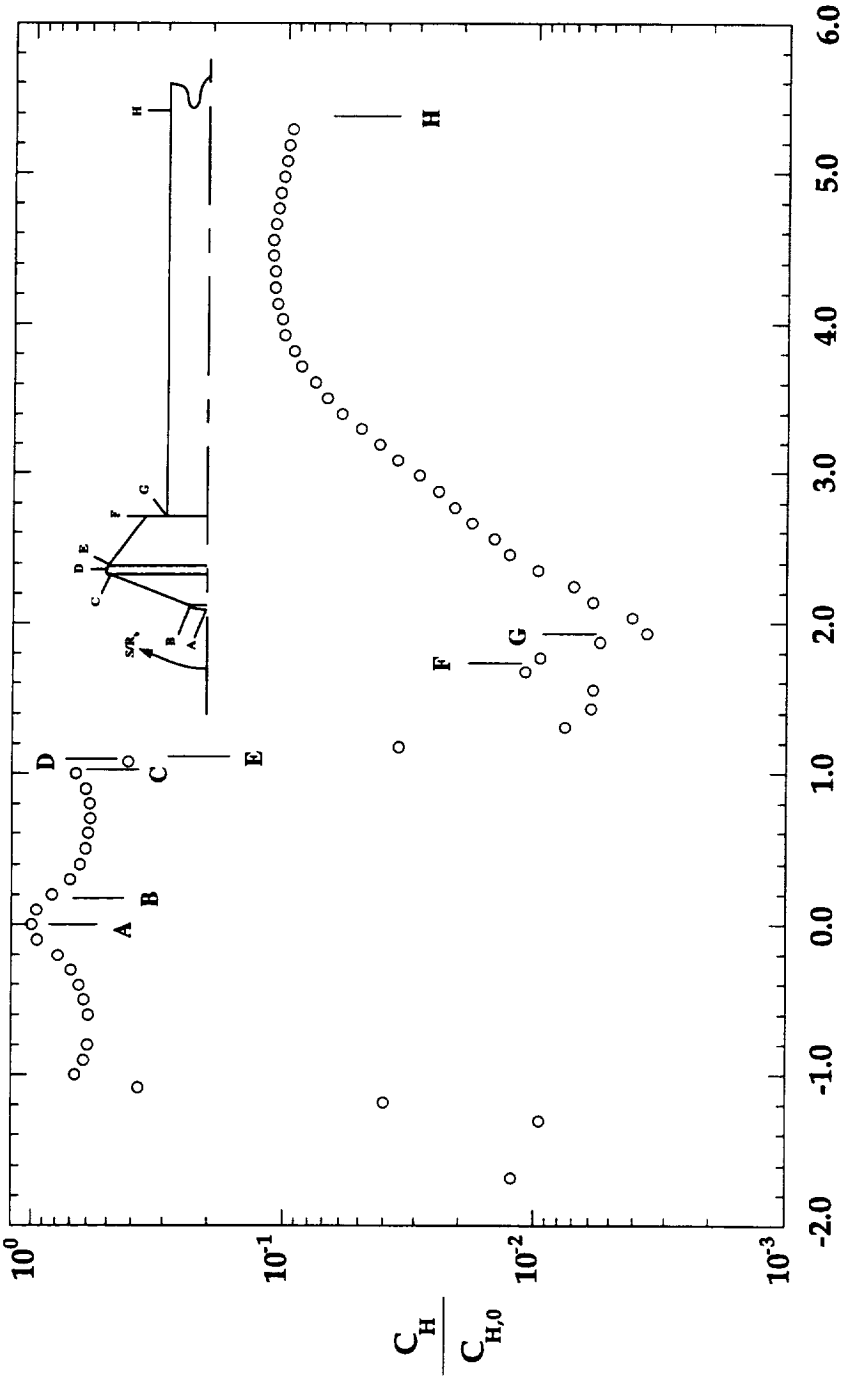

Figure A-3: 31-Inch Mach 10 Test 293, Run 007, MP-1 Configuration, $Re_\infty = 1.0 \times 10^6$ ft^{-1}, $\alpha = 0°$, $\phi = 0°$

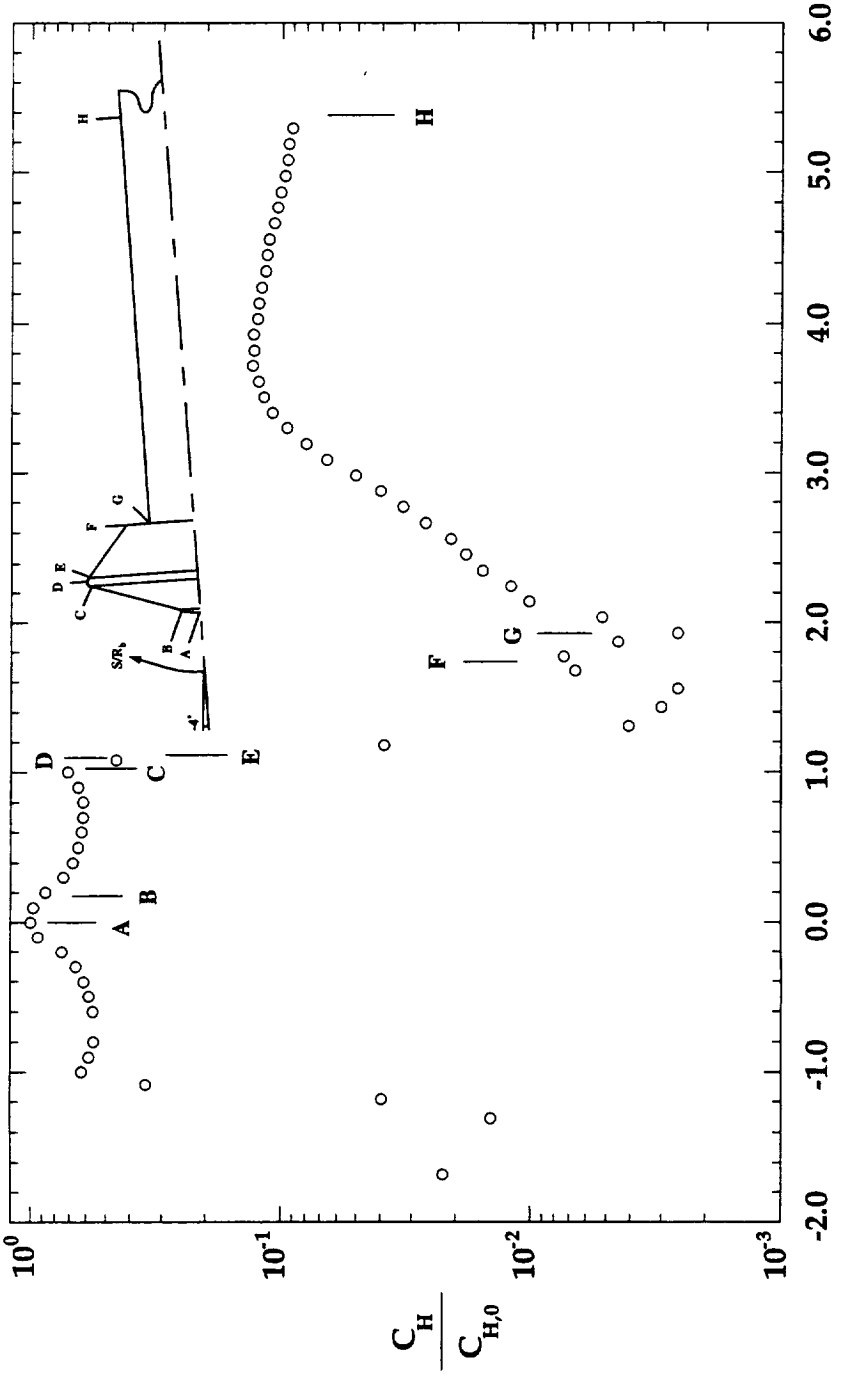

Figure A-4: 31-Inch Mach 10 Test 293, Run 008, MP-1 Configuration, $Re_\infty = 1.0 \times 10^6$ ft^{-1}, $\alpha = -4°$, $\phi = 0°$

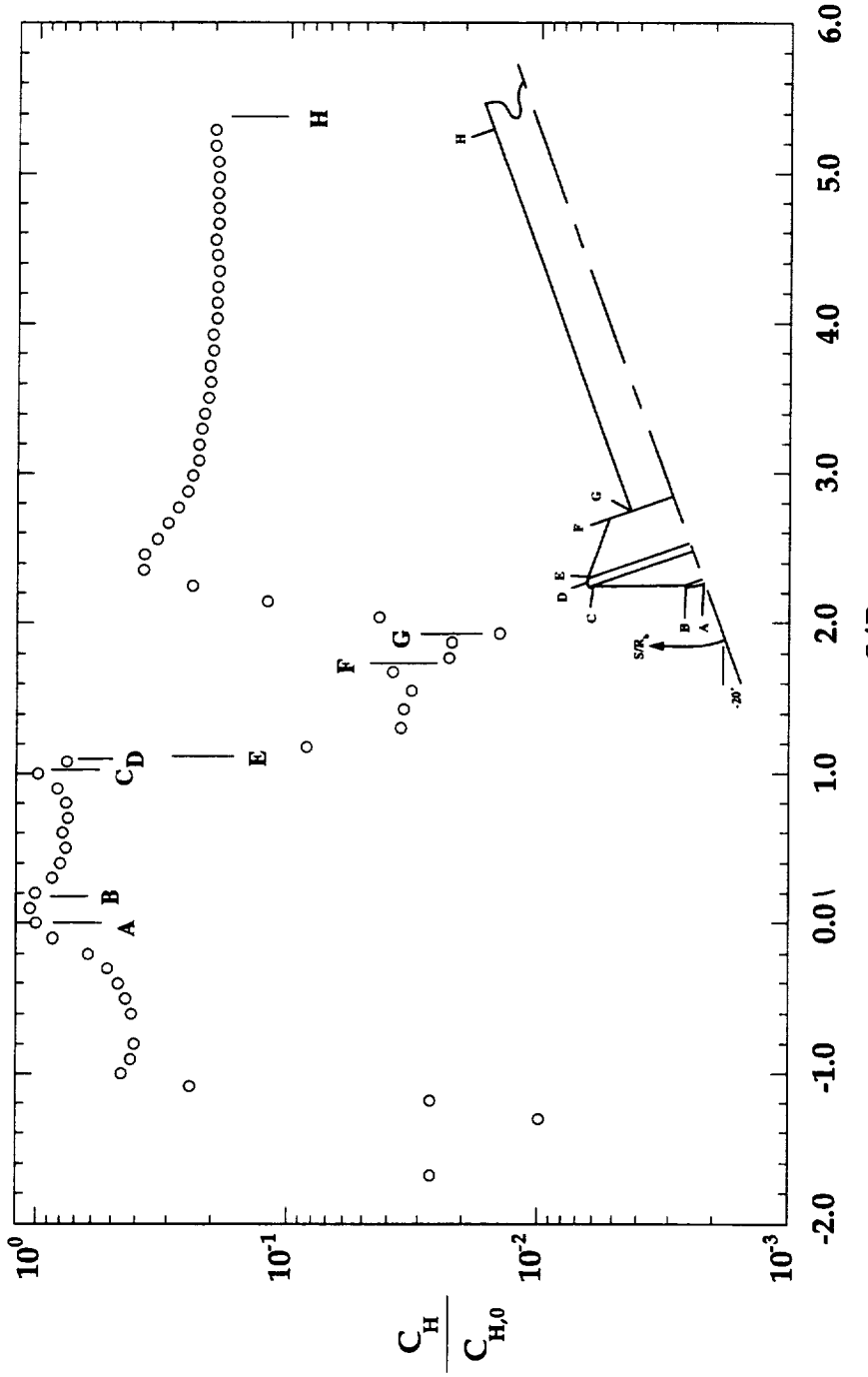

Figure A-5: 31-Inch Mach 10 Test 293, Run 009, MP-1 Configuration, $Re_\infty = 1.0 \times 10^6$ ft^{-1}, $\alpha = -20°$, $\phi = 0°$

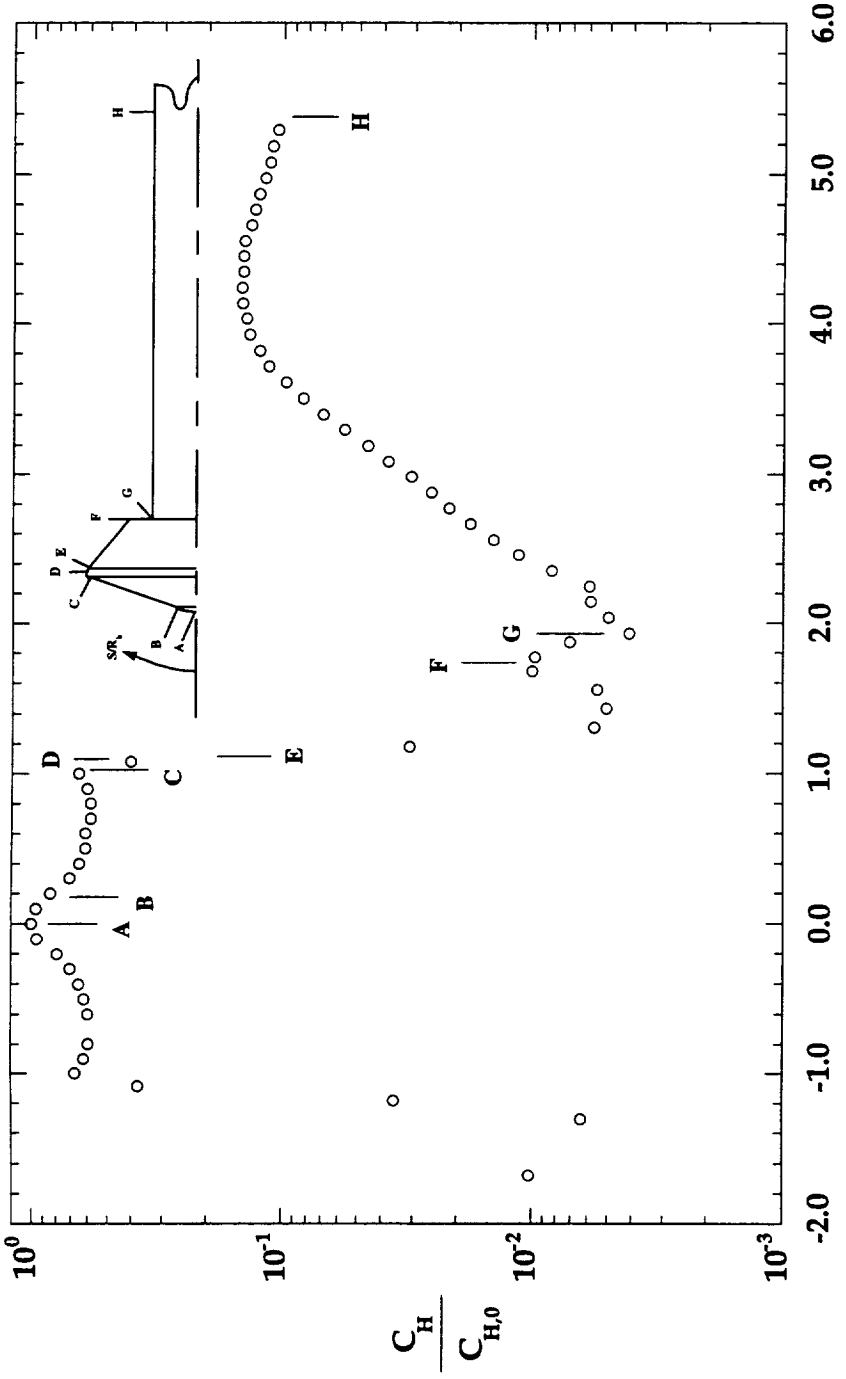

Figure A-6: 31-Inch Mach 10 Test 293, Run 010, MP-1 Configuration, $Re_\infty = 2.0 \times 10^6$ ft^{-1}, $\alpha = 0°$, $\phi = 0°$

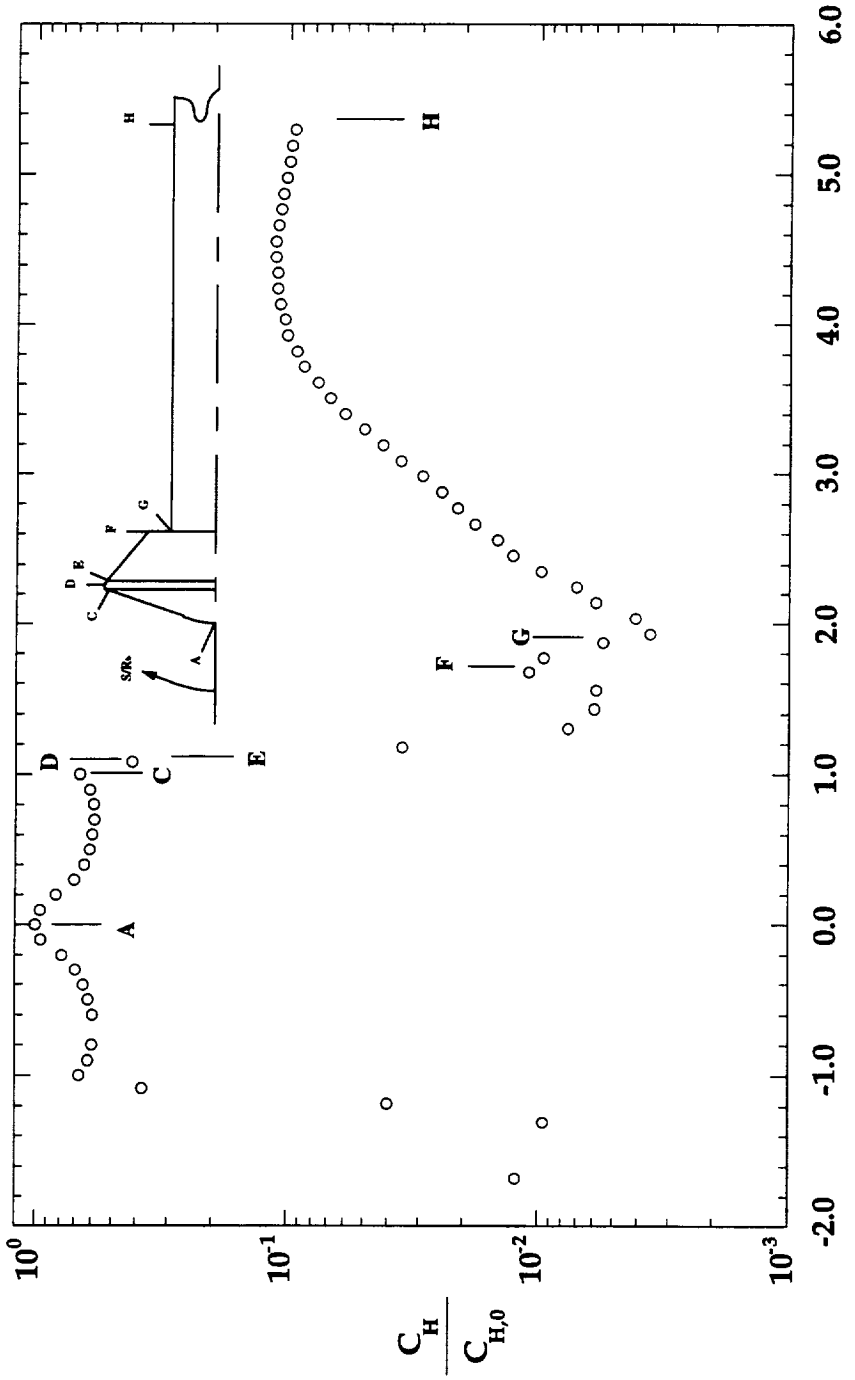

Figure A-7: 31-Inch Mach 10 Test 293, Run 011, MP-2 Configuration, $Re_\infty = 0.5 \times 10^6$ ft^{-1}, $\alpha = 0°$, $\phi = 0°$

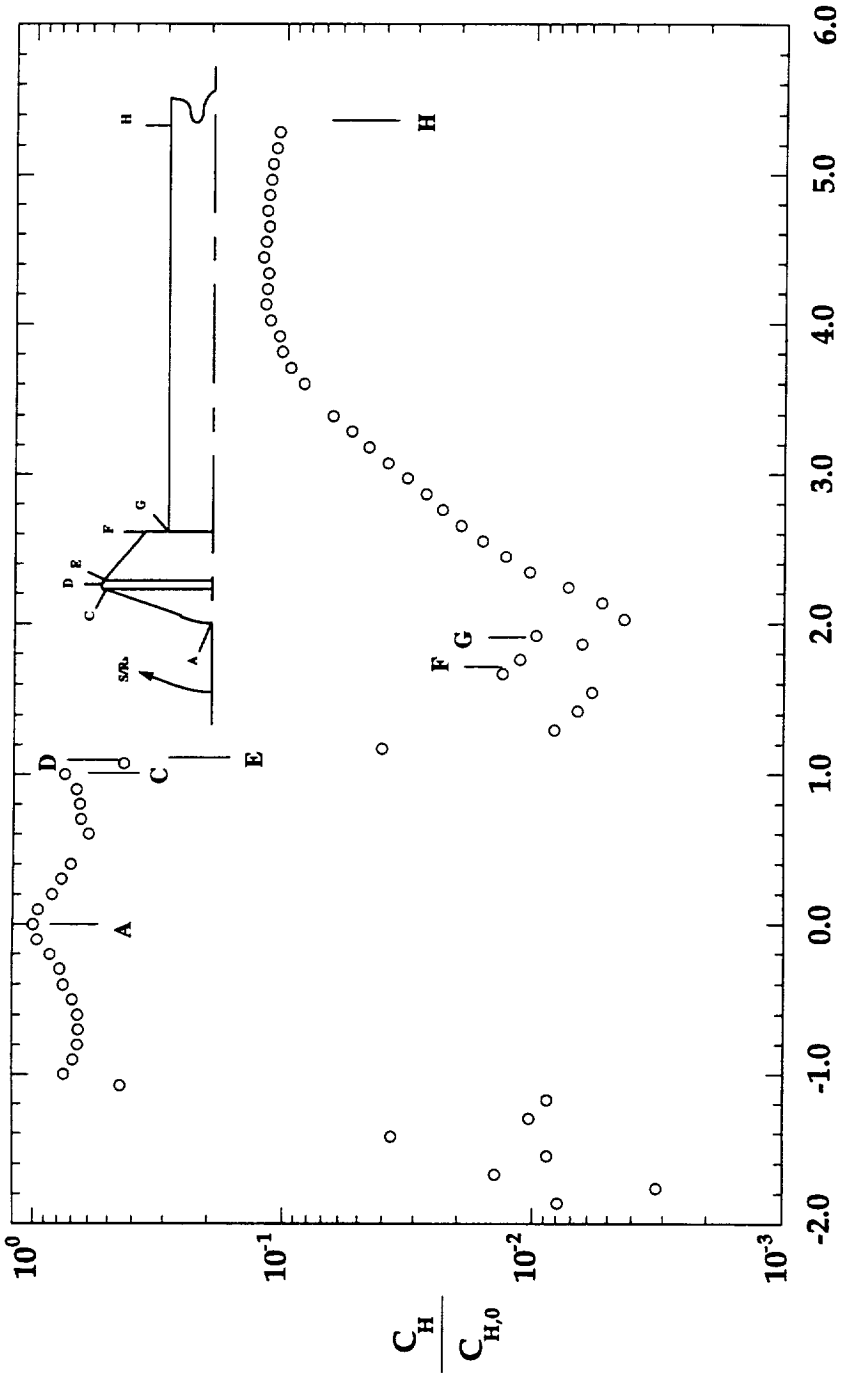

Figure A-8: 31-Inch Mach 10 Test 293, Run 012, MP-2 Configuration, $Re_\infty = 1.0 \times 10^6$ ft^{-1}, $\alpha = 0°$, $\phi = 0°$

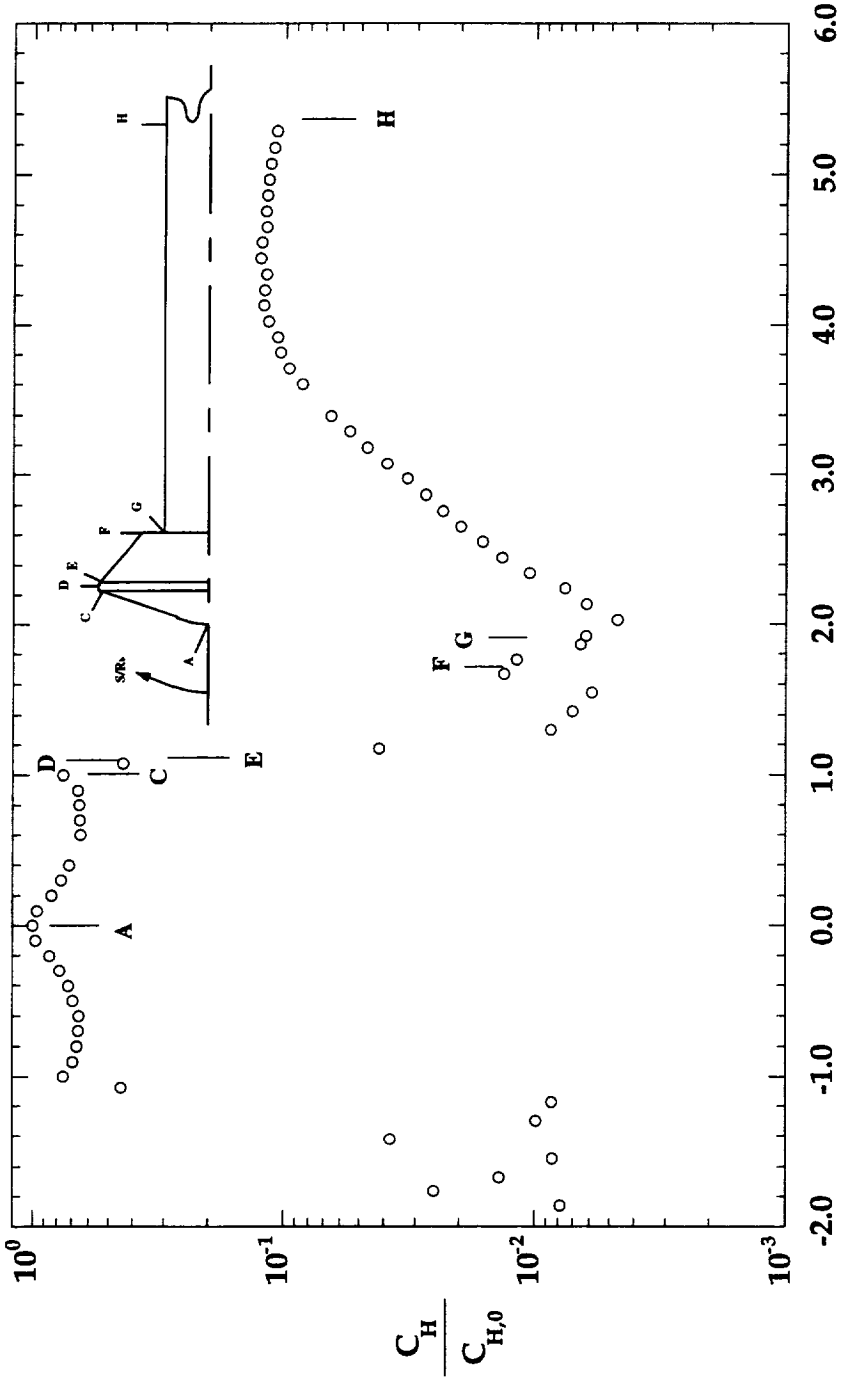

Figure A-9: 31-Inch Mach 10 Test 293, Run 013, MP-2 Configuration, $Re_\infty = 1.0 \times 10^6$ ft^{-1}, $\alpha = 0°$, $\phi = 0°$

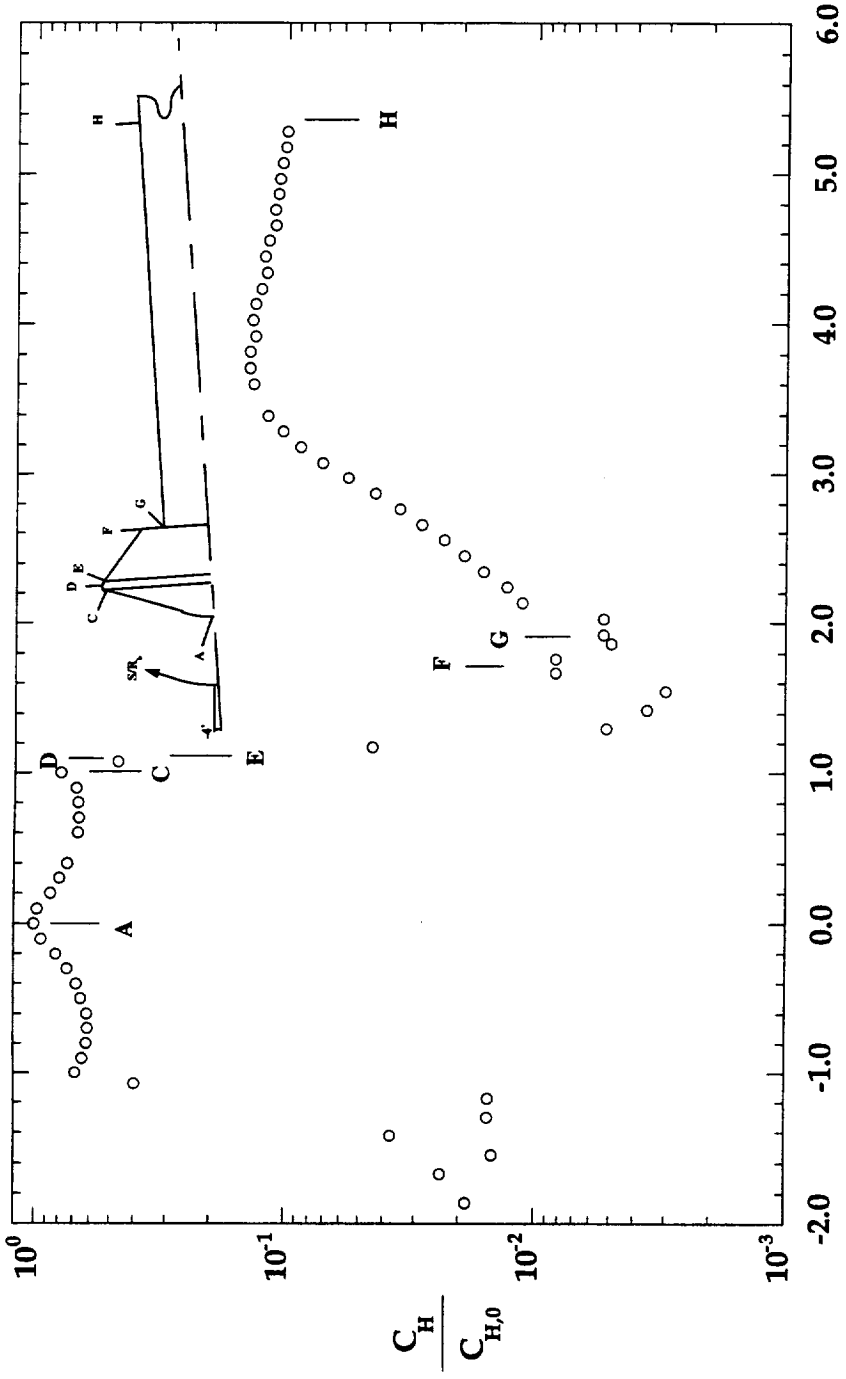

Figure A-10: 31-Inch Mach 10 Test 293, Run 014, MP-2 Configuration, $Re_\infty = 1.0 \times 10^6$ ft^{-1}, $\alpha = -4°$, $\phi = 0°$

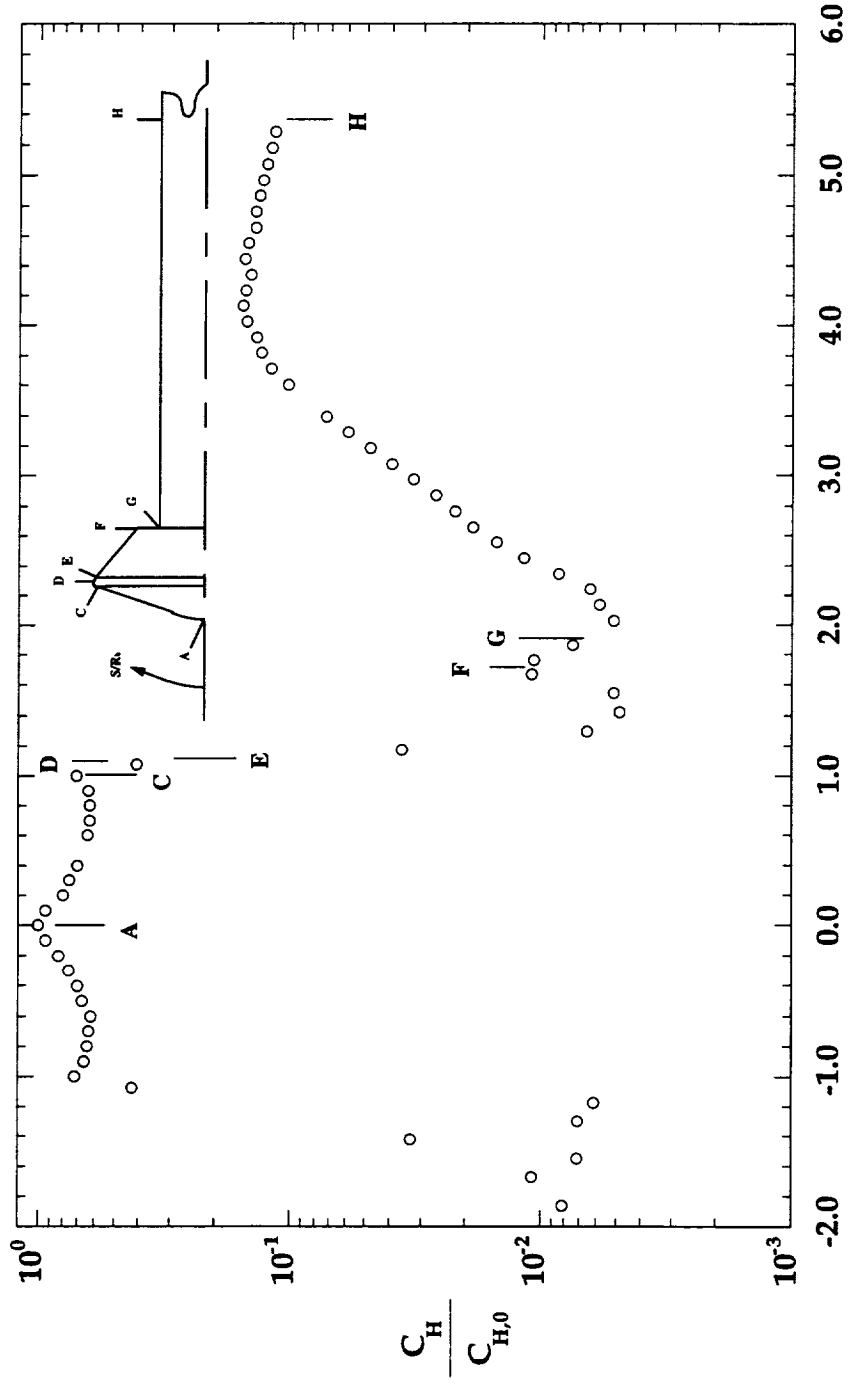

Figure A-11: 31-Inch Mach 10 Test 293, Run 015, MP-2 Configuration, $Re_\infty = 2.0 \times 10^6$ ft^{-1}, $\alpha = 0°$, $\phi = 0°$

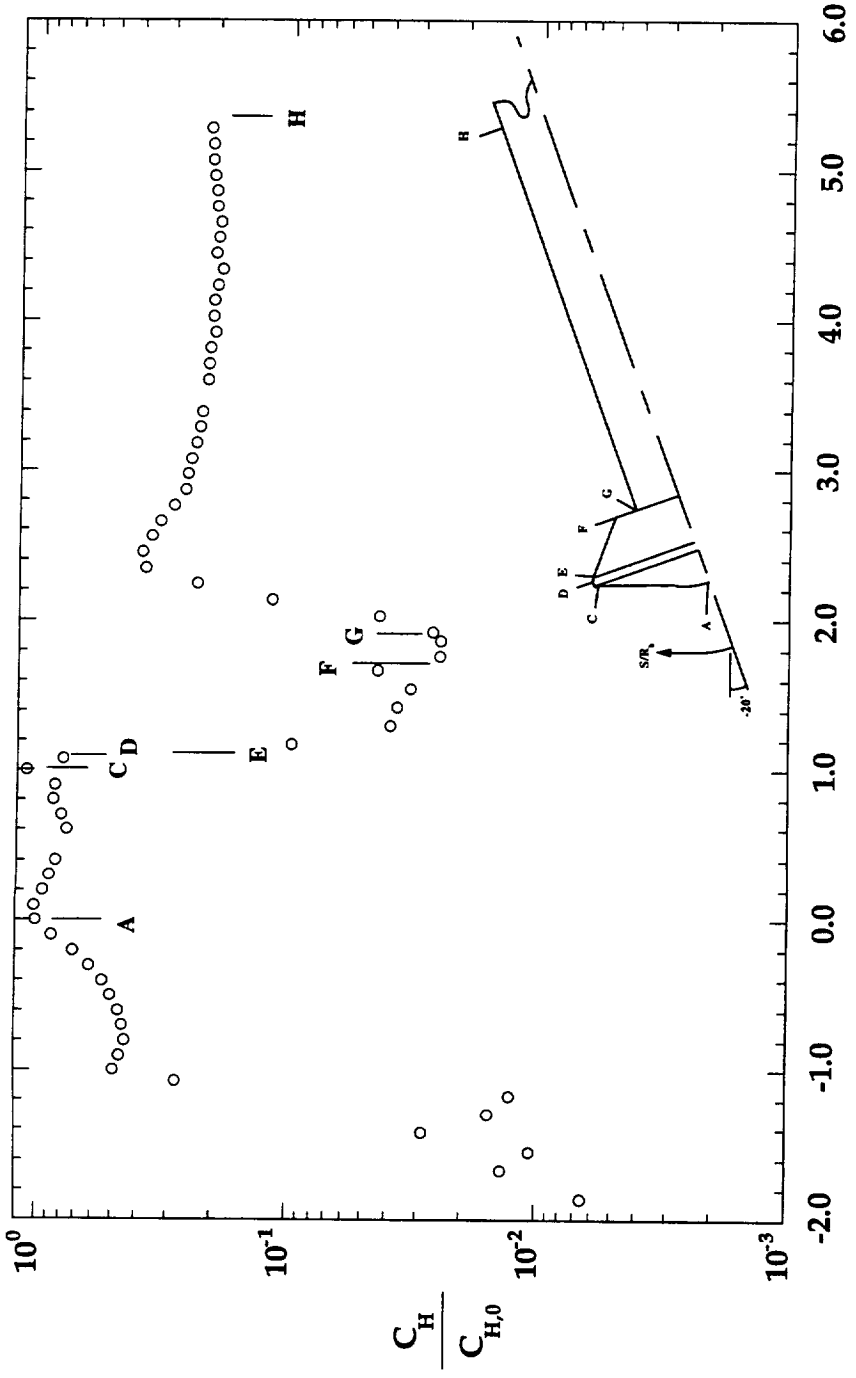

Figure A-12: 31-Inch Mach 10 Test 293, Run 016, MP-2 Configuration, $Re_\infty = 1.0 \times 10^6$ ft^{-1}, α = -20°, ϕ=0°

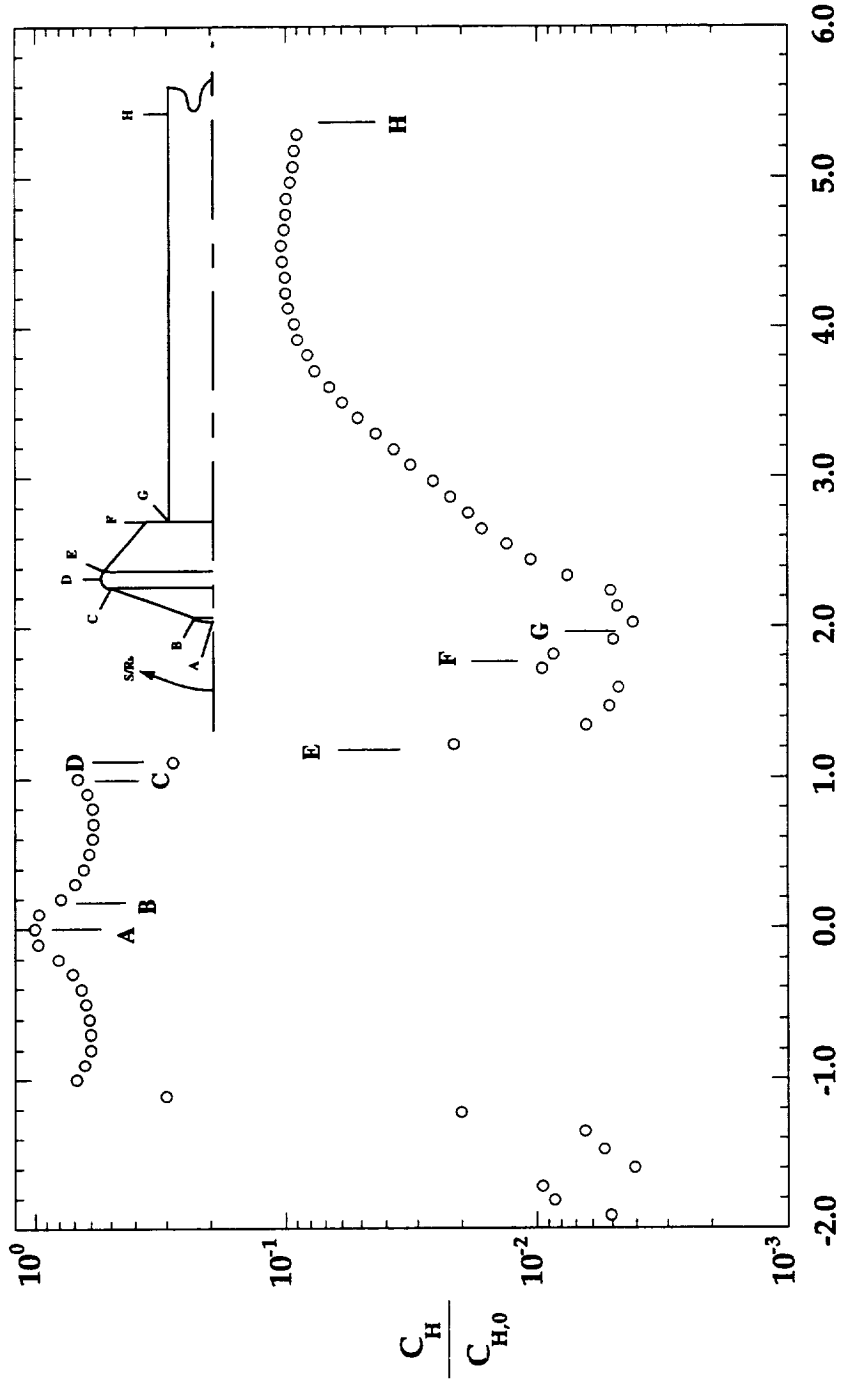

Figure A-13: 31-Inch Mach 10 Test 293, Run 017, MP-3 Configuration, $Re_\infty = 1.0 \times 10^6$ ft^{-1}, $\alpha = 0°$, $\phi = 0°$

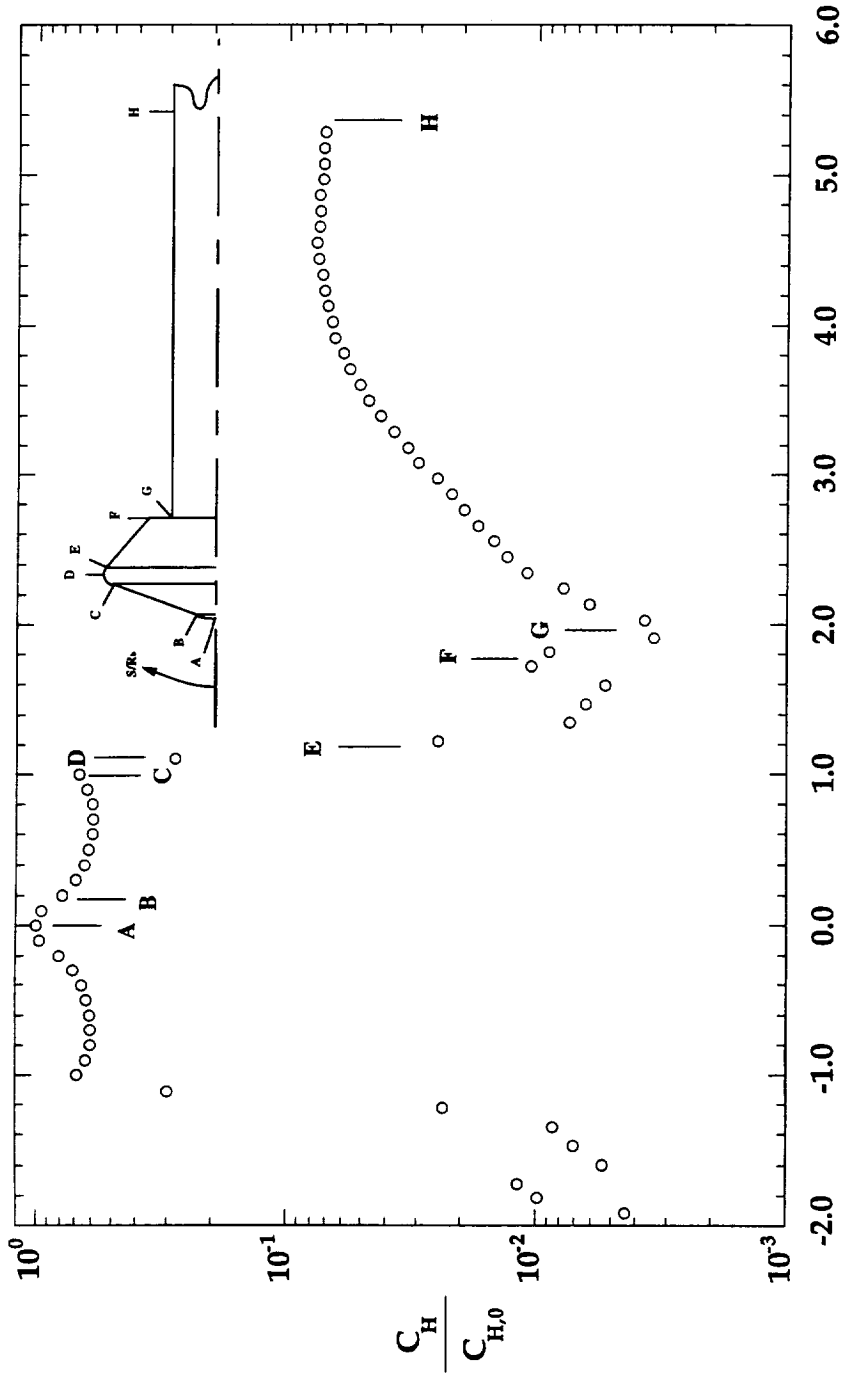

Figure A-14: 31-Inch Mach 10 Test 293, Run 018, MP-3 Configuration, $Re_\infty = 0.5 \times 10^6$ ft^{-1}, $\alpha = 0°$, $\phi = 0°$

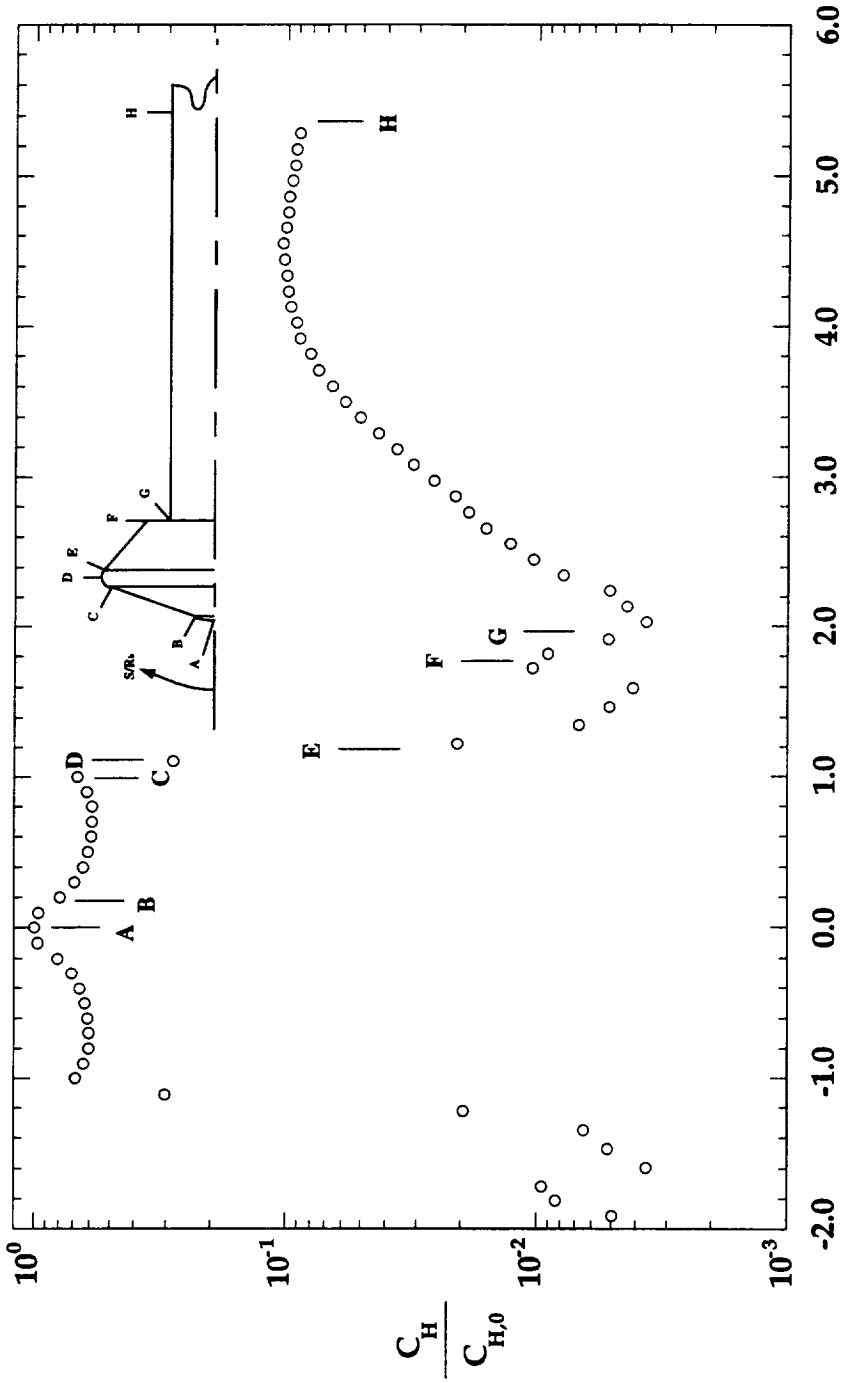

Figure A-15: 31-Inch Mach 10 Test 293, Run 019, MP-3 Configuration, $Re_\infty = 1.0 \times 10^6$ ft^{-1}, $\alpha = 0°$, $\phi = 0°$

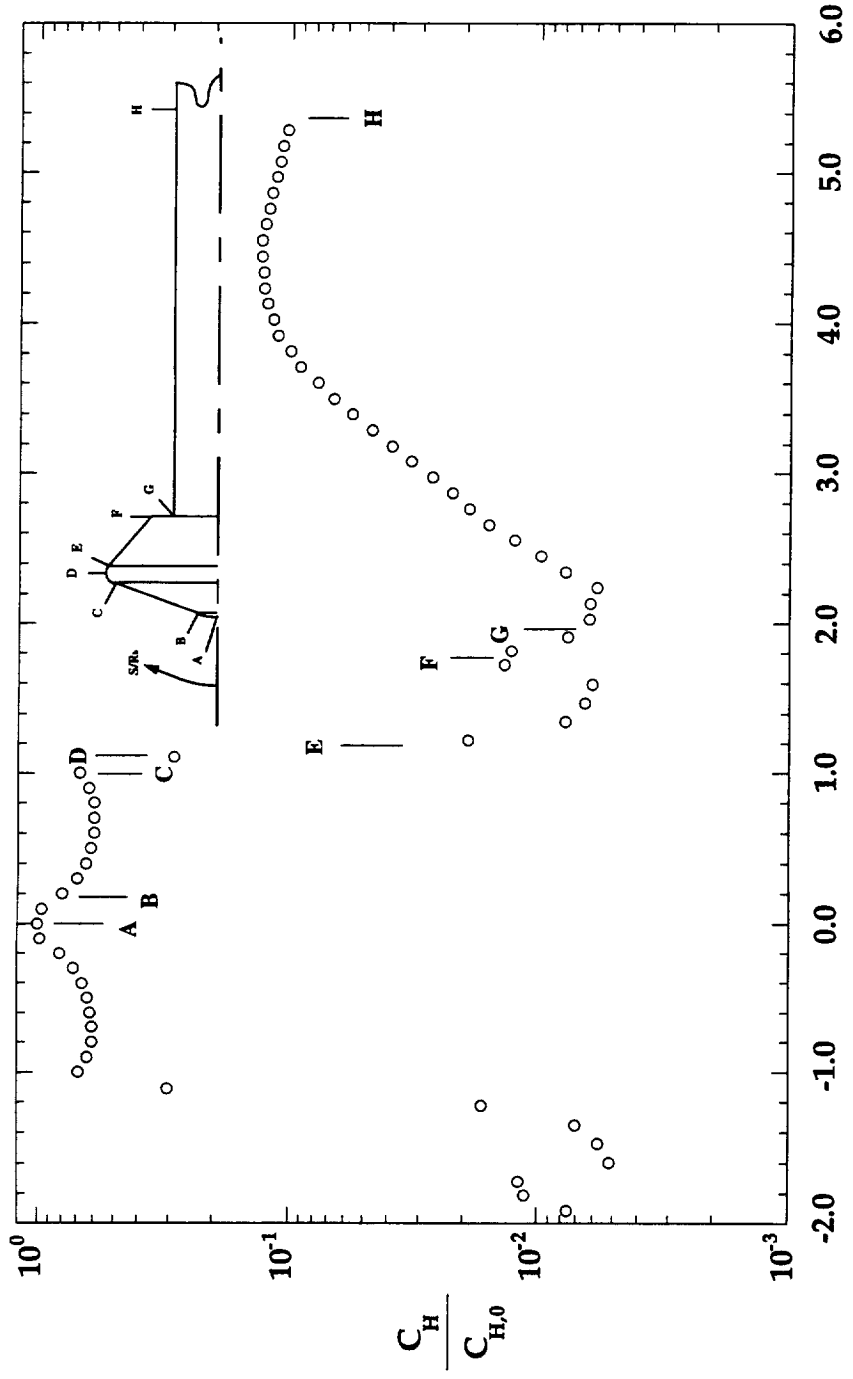

Figure A-16: 31-Inch Mach 10 Test 293, Run 020, MP-3 Configuration, $Re_\infty = 2.0 \times 10^6$ ft^{-1}, $\alpha = 0°$, $\phi = 0°$

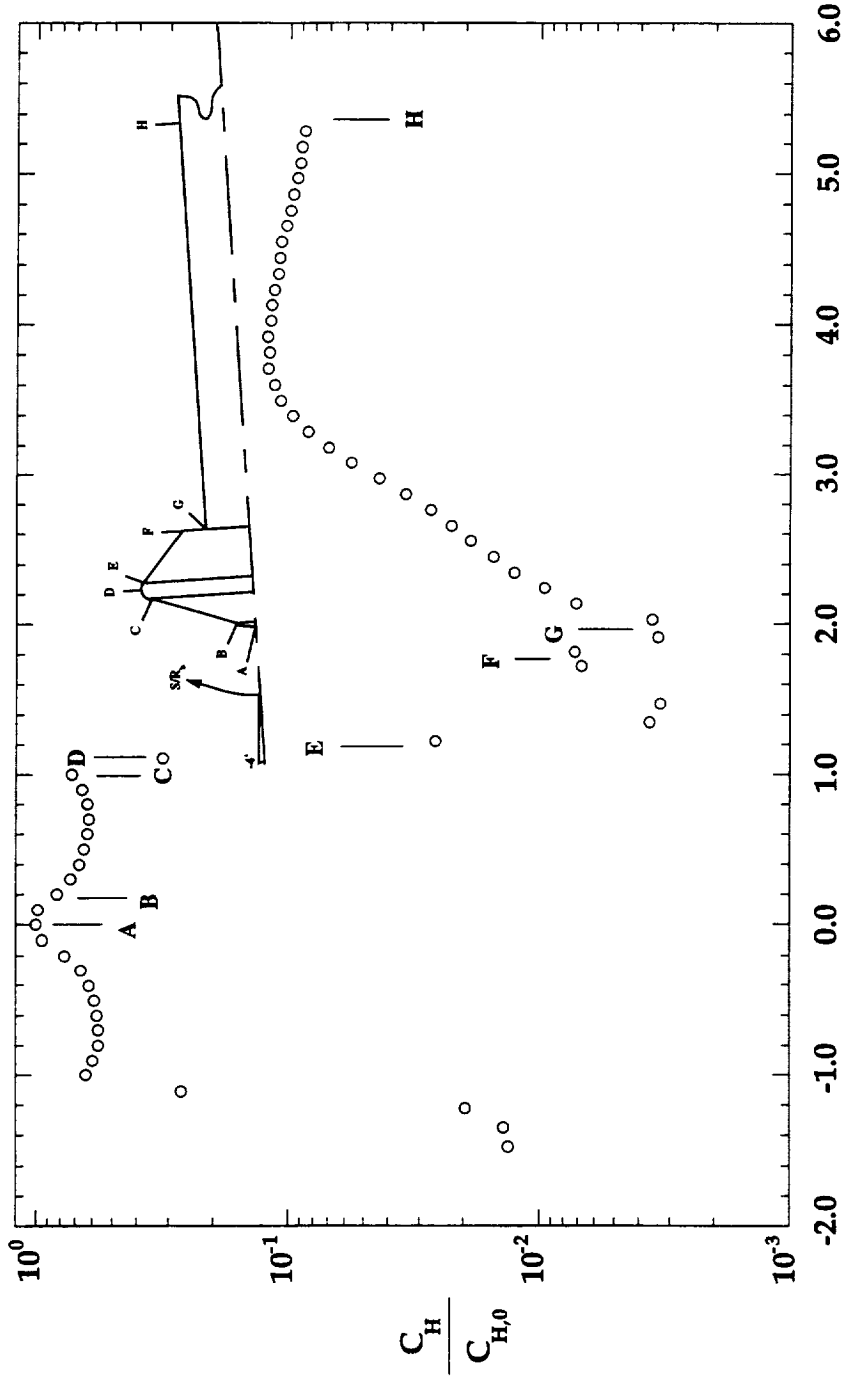

Figure A-17: 31-Inch Mach 10 Test 293, Run 021, MP-3 Configuration, $Re_\infty = 1.0 \times 10^6$ ft^{-1}, $\alpha = -4°$, $\phi = 0°$

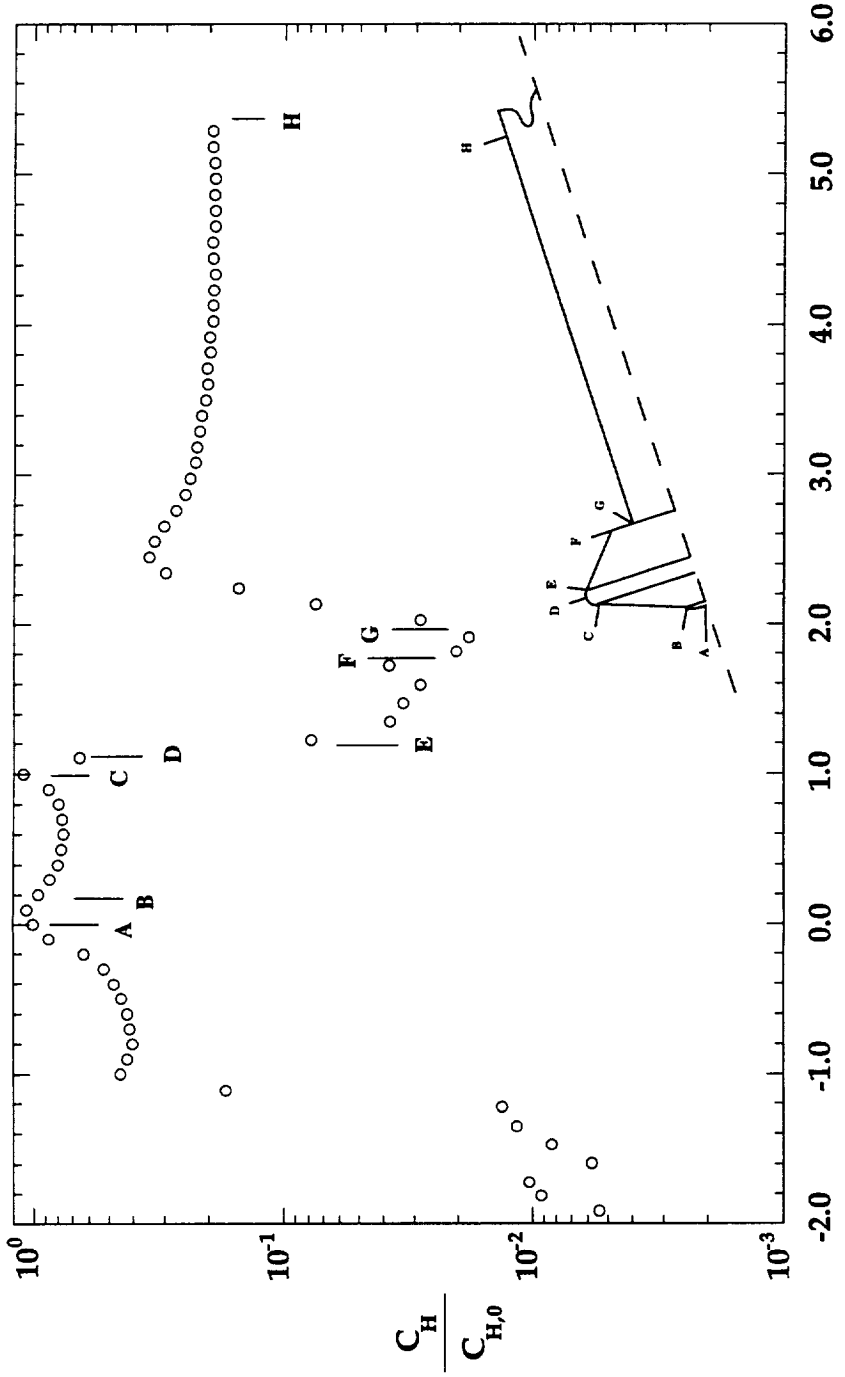

Figure A-18: 31-Inch Mach 10 Test 293, Run 022, MP-3 Configuration, $Re_\infty = 1.0 \times 10^6$ ft^{-1}, α = -20°, ϕ=0°

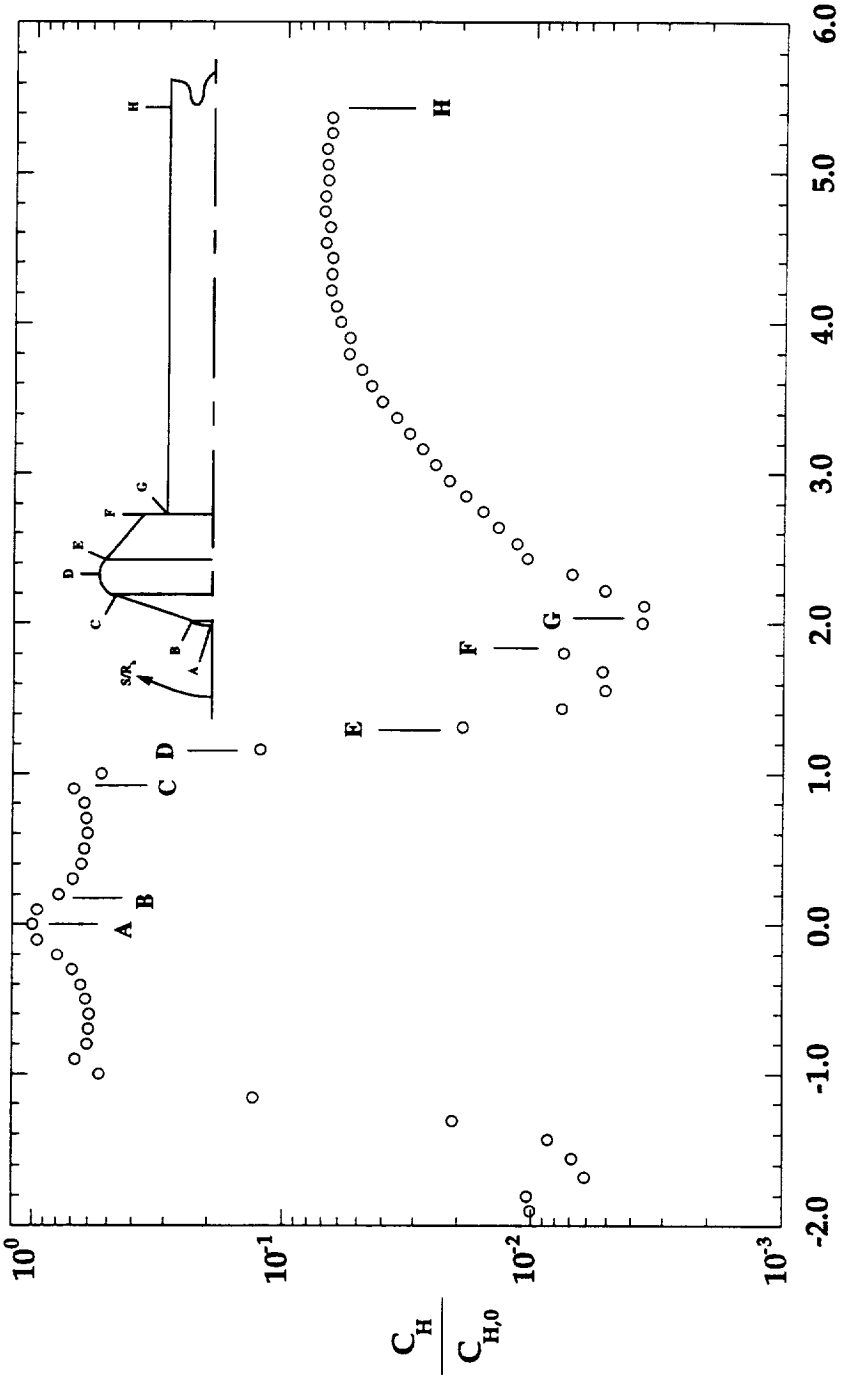

Figure A-19: 31-Inch Mach 10 Test 293, Run 023, MP-4 Configuration,

$Re_\infty = 0.5 \times 10^6$ ft^{-1}, $\alpha = 0°$, $\phi = 0°$

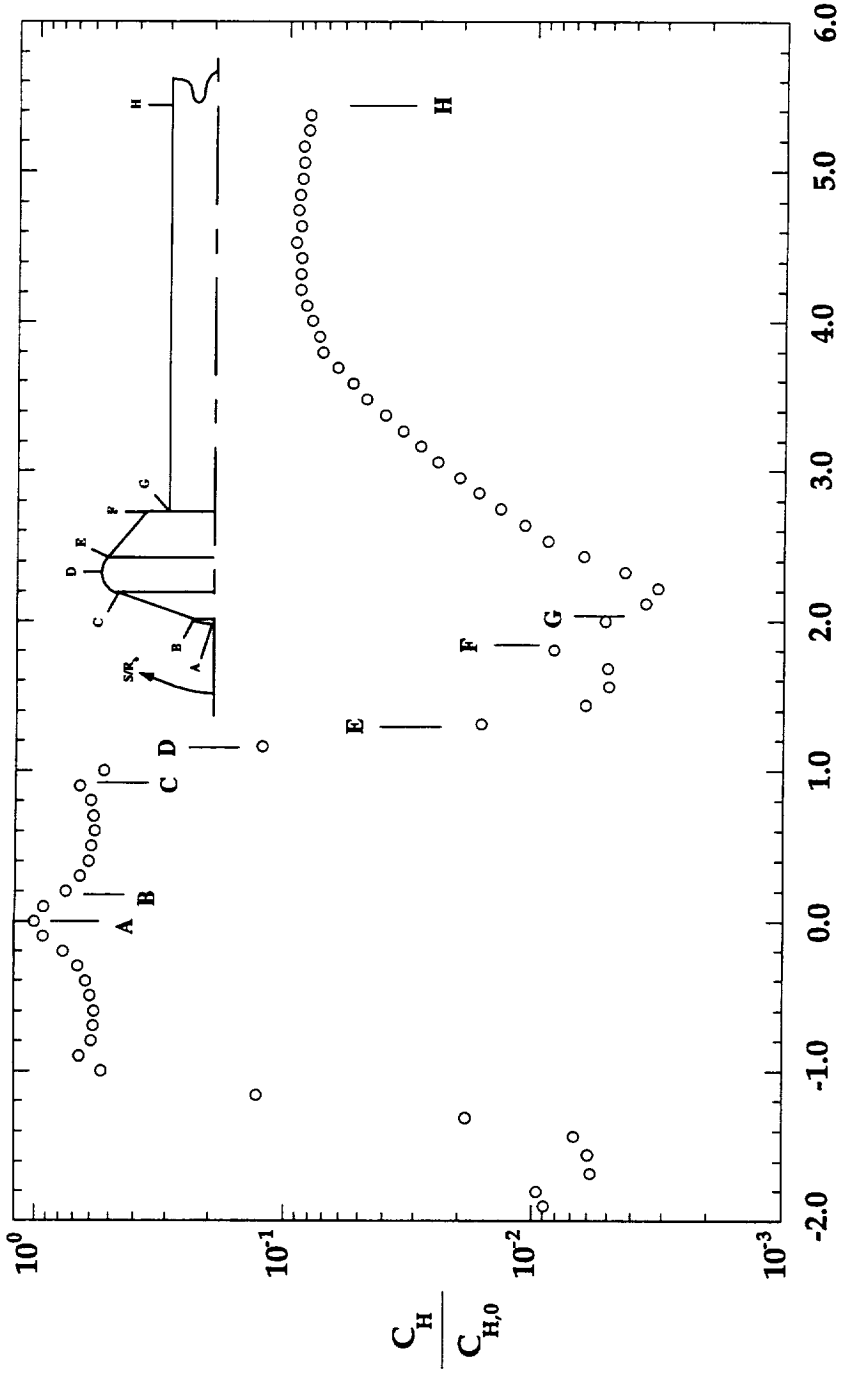

Figure A-20: 31-Inch Mach 10 Test 293, Run 024, MP-4 Configuration, $Re_\infty = 1.0 \times 10^6$ ft^{-1}, $\alpha = 0°$, $\phi = 0°$

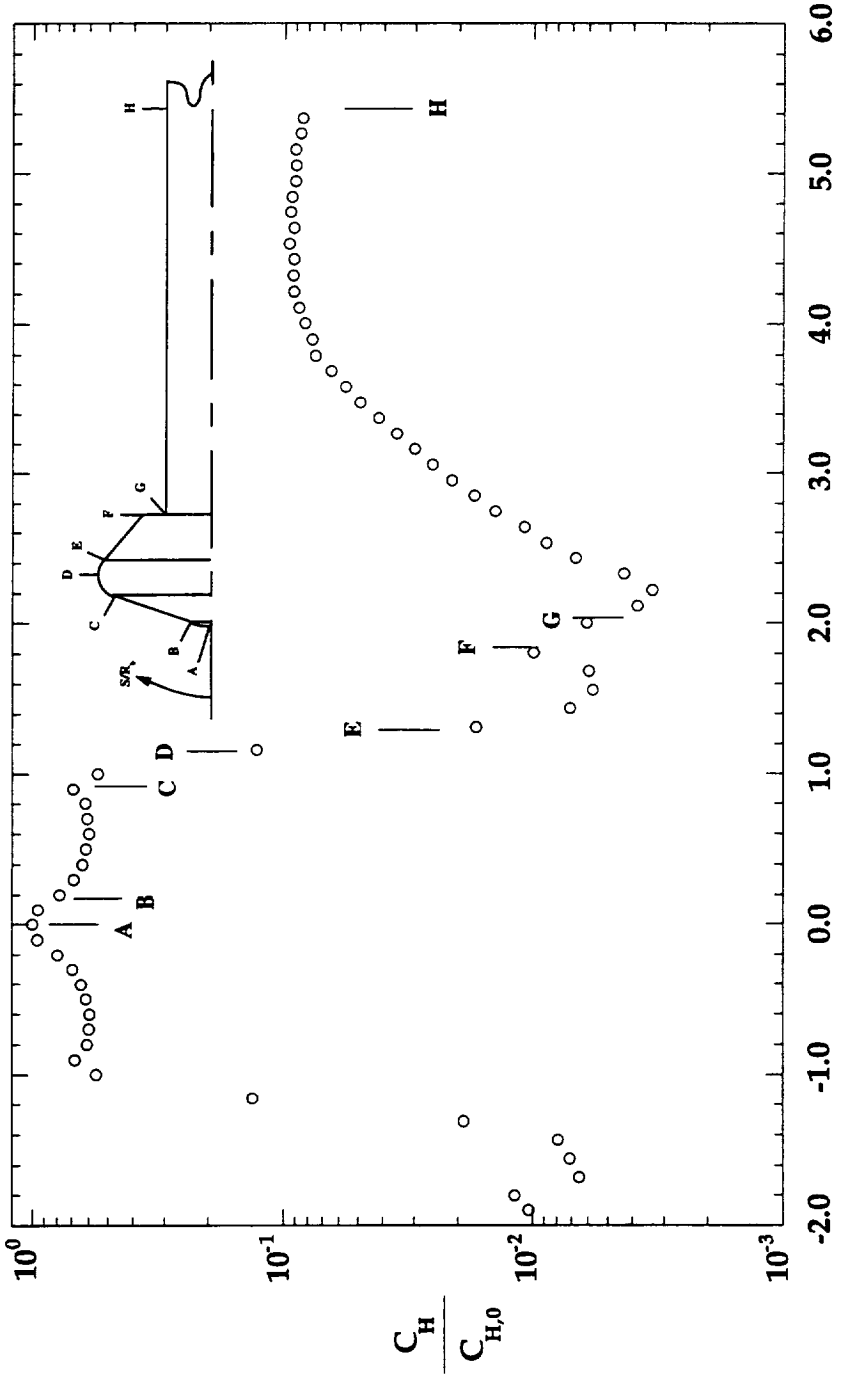

Figure A-21: 31-Inch Mach 10 Test 293, Run 025, MP-4 Configuration, $Re_\infty = 1.0 \times 10^6$ ft^{-1}, $\alpha = 0°$, $\phi = 0°$

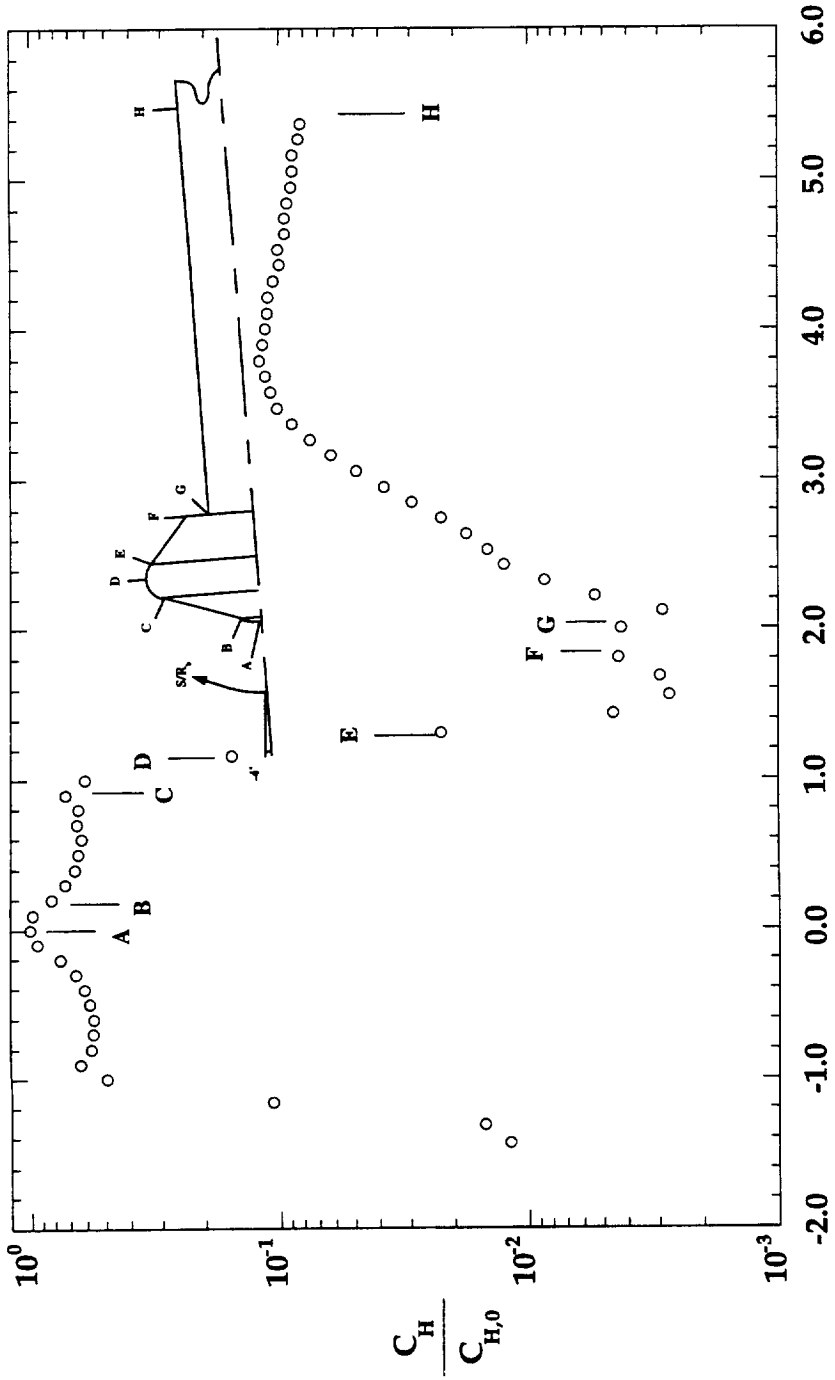

Figure A-22: 31-Inch Mach 10 Test 293, Run 026, MP-4 Configuration,

$Re_\infty = 1.0 \times 10^6$ ft^{-1}, $\alpha = -4°$, $\phi = 0°$

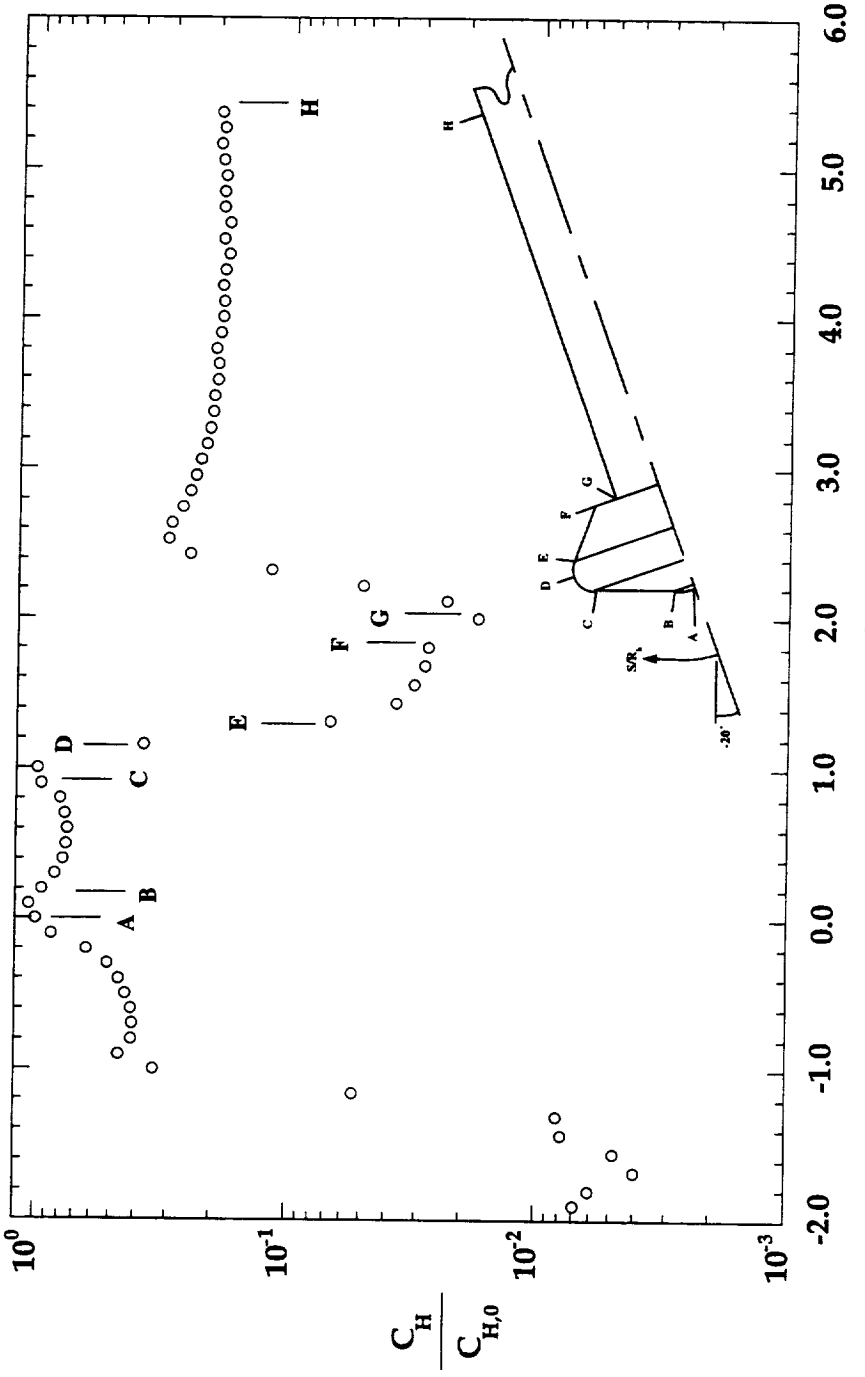

Figure A-23: 31-Inch Mach 10 Test 293, Run 027, MP-4 Configuration,

$Re_\infty = 1.0 \times 10^6$ ft^{-1}, α = -20°, ϕ=0°

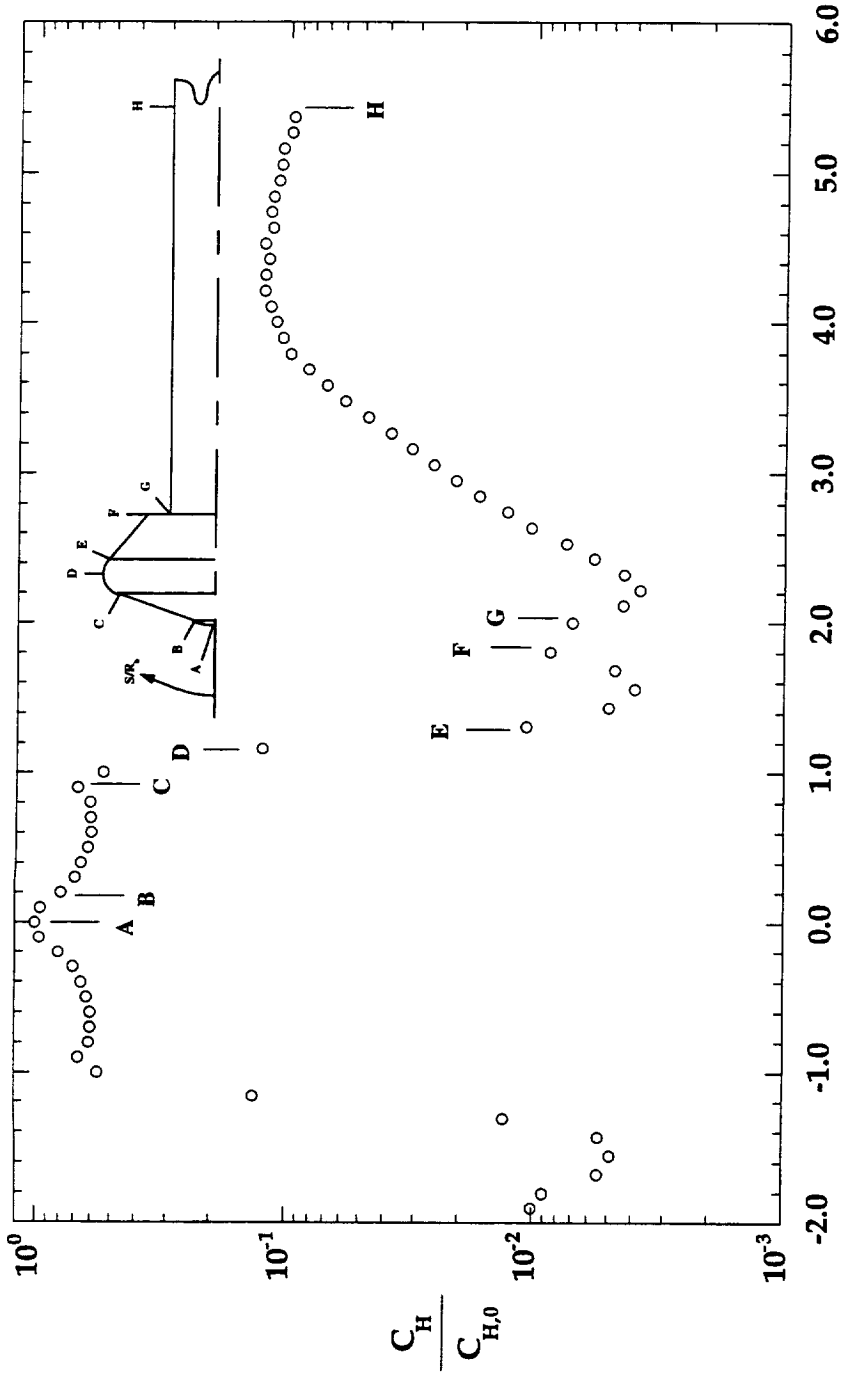

Figure A-24: 31-Inch Mach 10 Test 293, Run 028, MP-4 Configuration, $Re_\infty = 2.0 \times 10^6$ ft^{-1}, $\alpha = 0°$, $\phi = 0°$

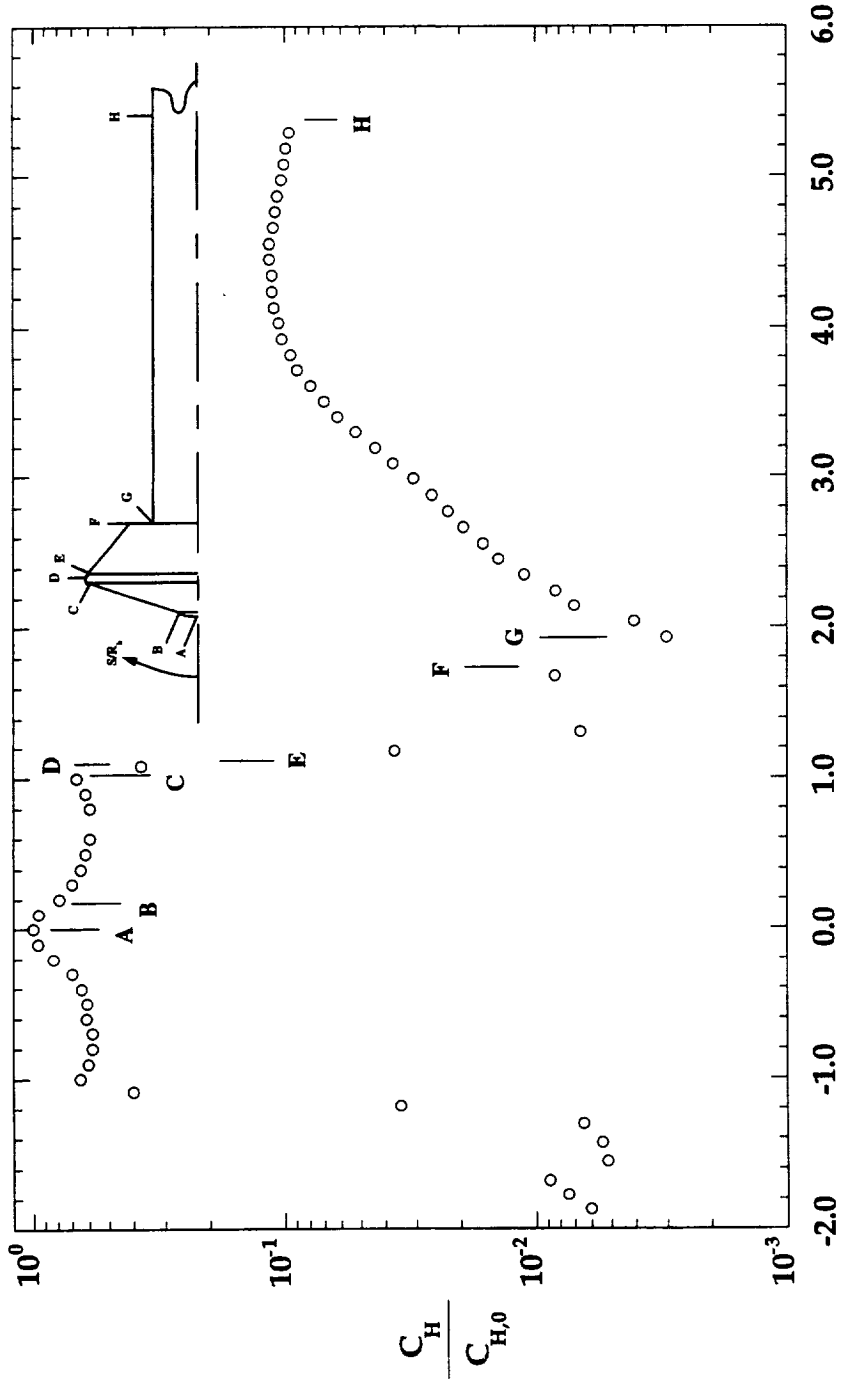

Figure A-25: 31-Inch Mach 10 Test 293, Run 029, MP-1 Configuration, $Re_\infty = 1.0 \times 10^6$ ft^{-1}, $\alpha = 0°$, $\phi = 90°$

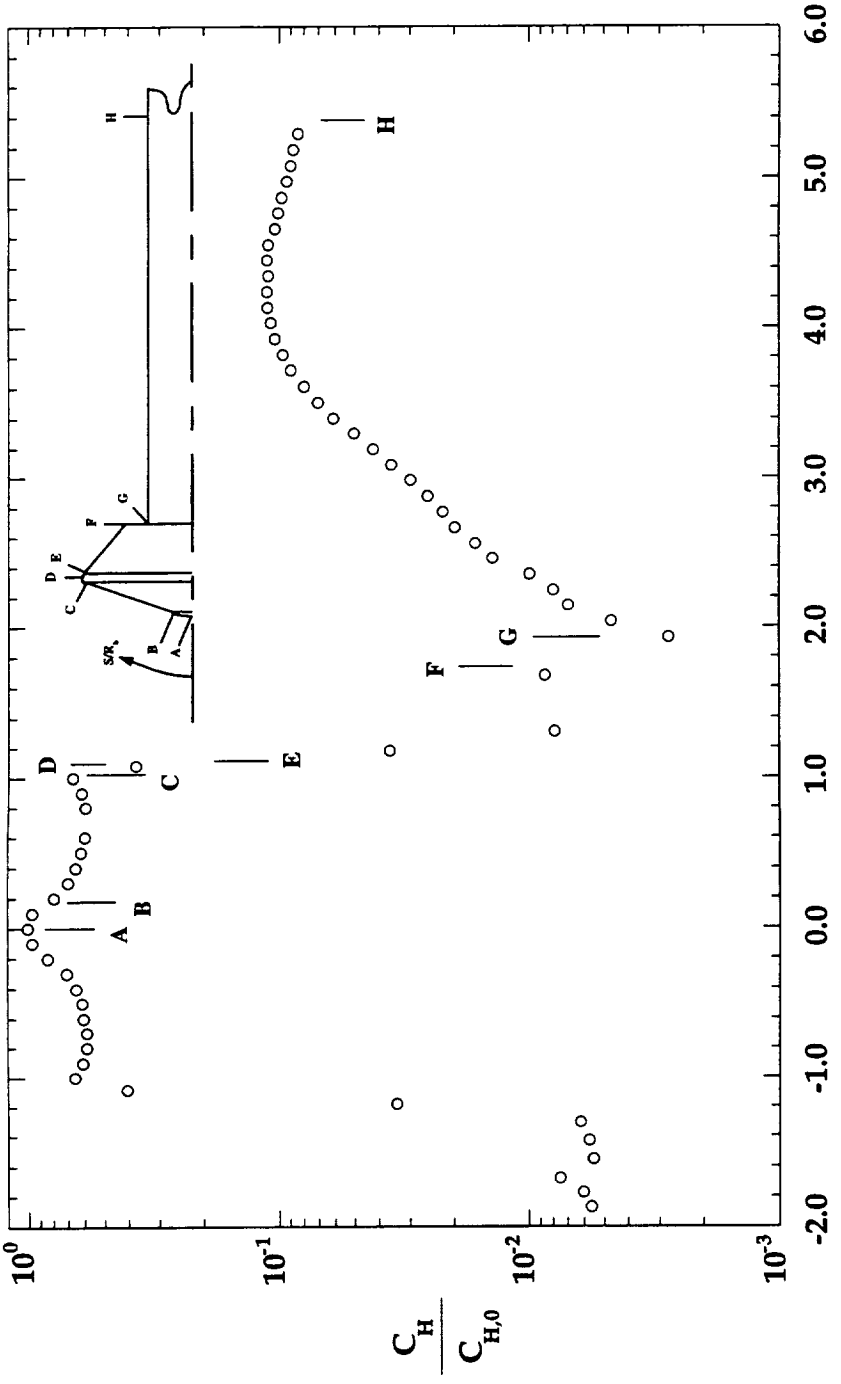

Figure A-26: 31-Inch Mach 10 Test 293, Run 030, MP-1 Configuration, $Re_\infty = 1.0 \times 10^6$ ft^{-1}, $\alpha = 0°$, $\phi = 90°$

*** BAD RUN, NO DATA ***

Figure A-27: 31-Inch Mach 10 Test 293, Run 027, MP-1 Configuration, Re_∞ = 1.0x106 ft-1, $\alpha = -4^\circ$, $\phi = 0^\circ$

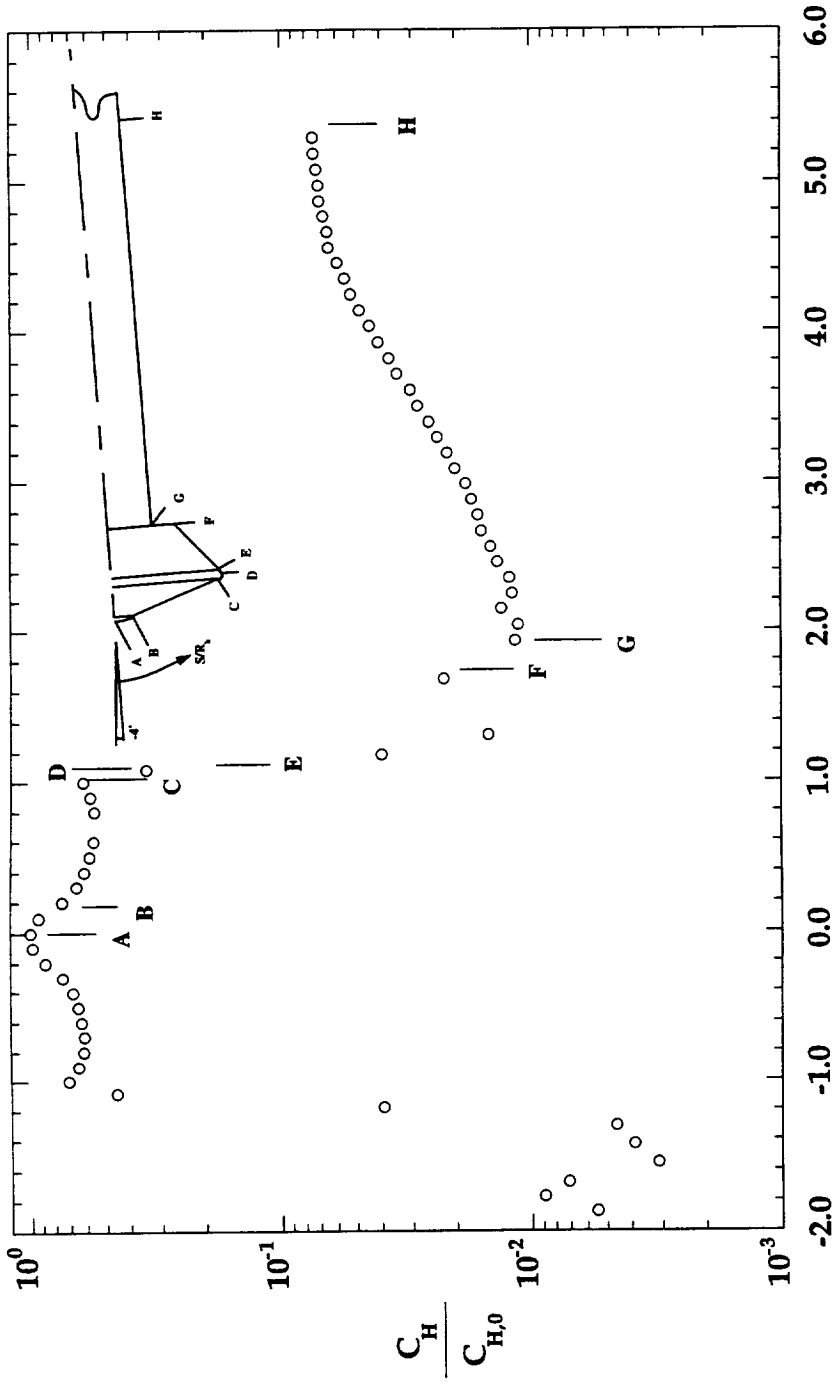

Figure A-28: 31-Inch Mach 10 Test 293, Run 032, MP-1 Configuration, $Re_\infty = 1.0 \times 10^6$ ft^{-1}, $\alpha = -4°$, $\phi = 180°$

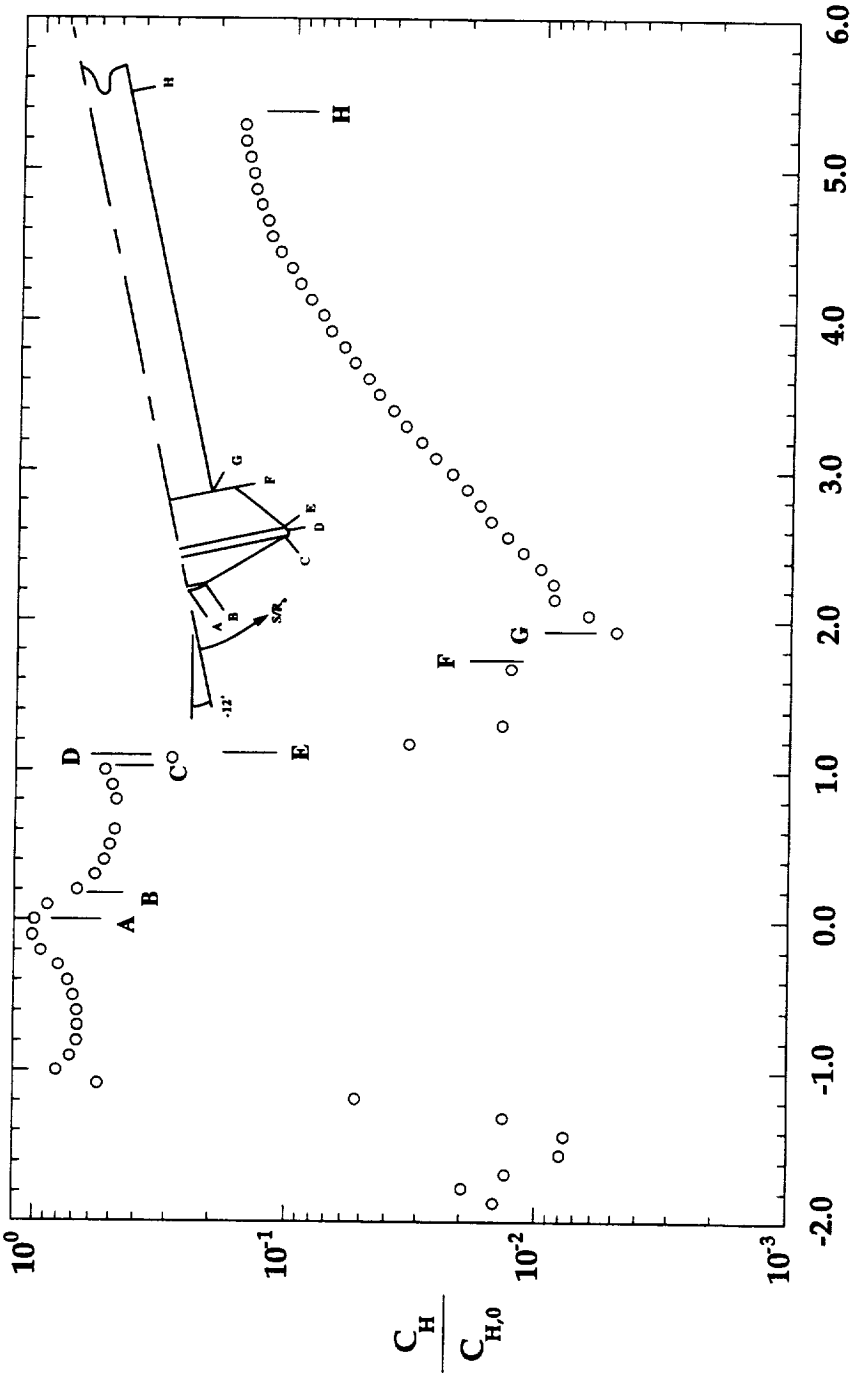

Figure A-29: 31-Inch Mach 10 Test 293, Run 033, MP-1 Configuration, $Re_\infty = 1.0 \times 10^6$ ft^{-1}, α = -12°, ϕ=180°

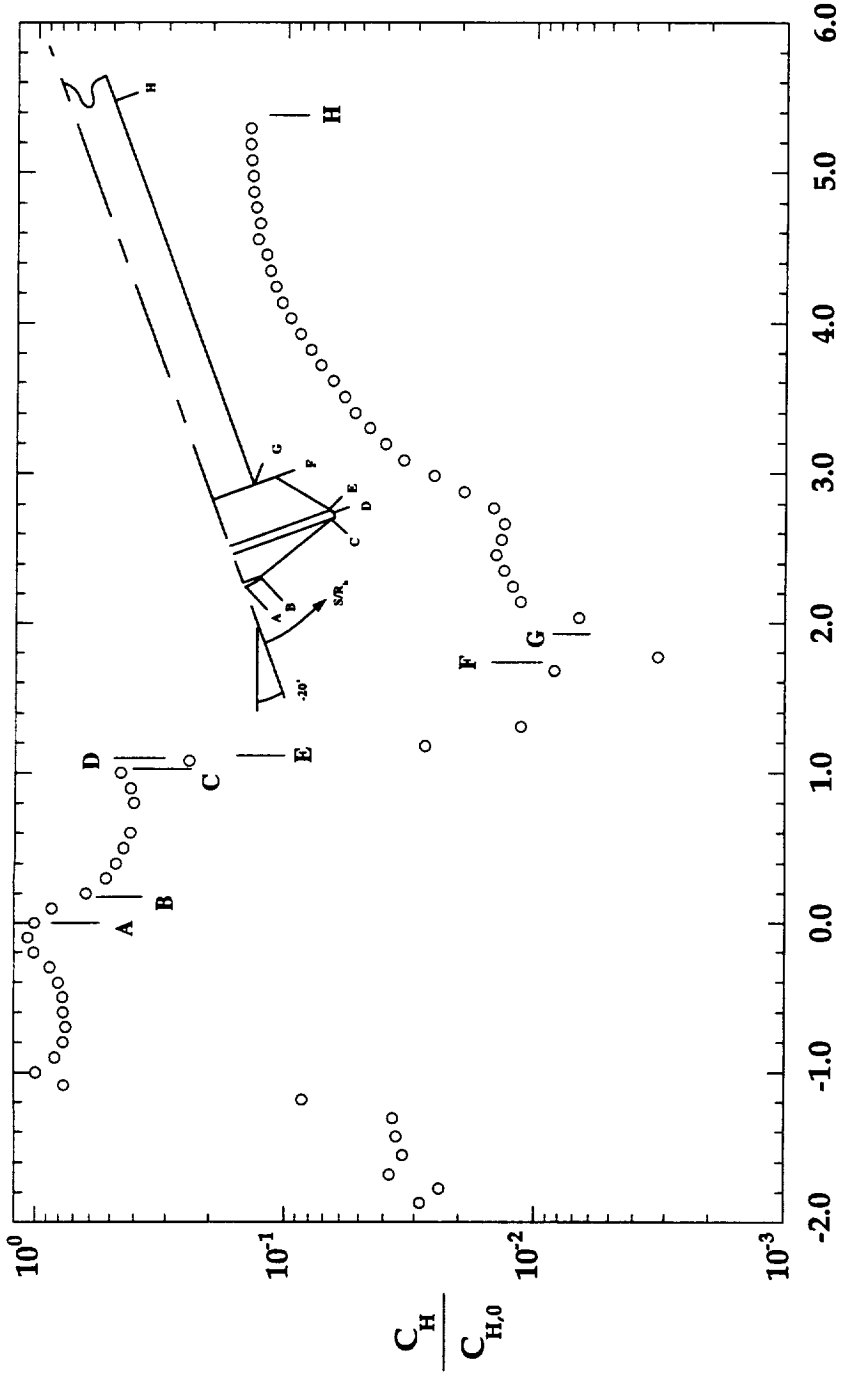

Figure A-30: 31-Inch Mach 10 Test 293, Run 034, MP-1 Configuration, $Re_\infty = 1.0 \times 10^6$ ft^{-1}, α = -20°, ϕ=180°

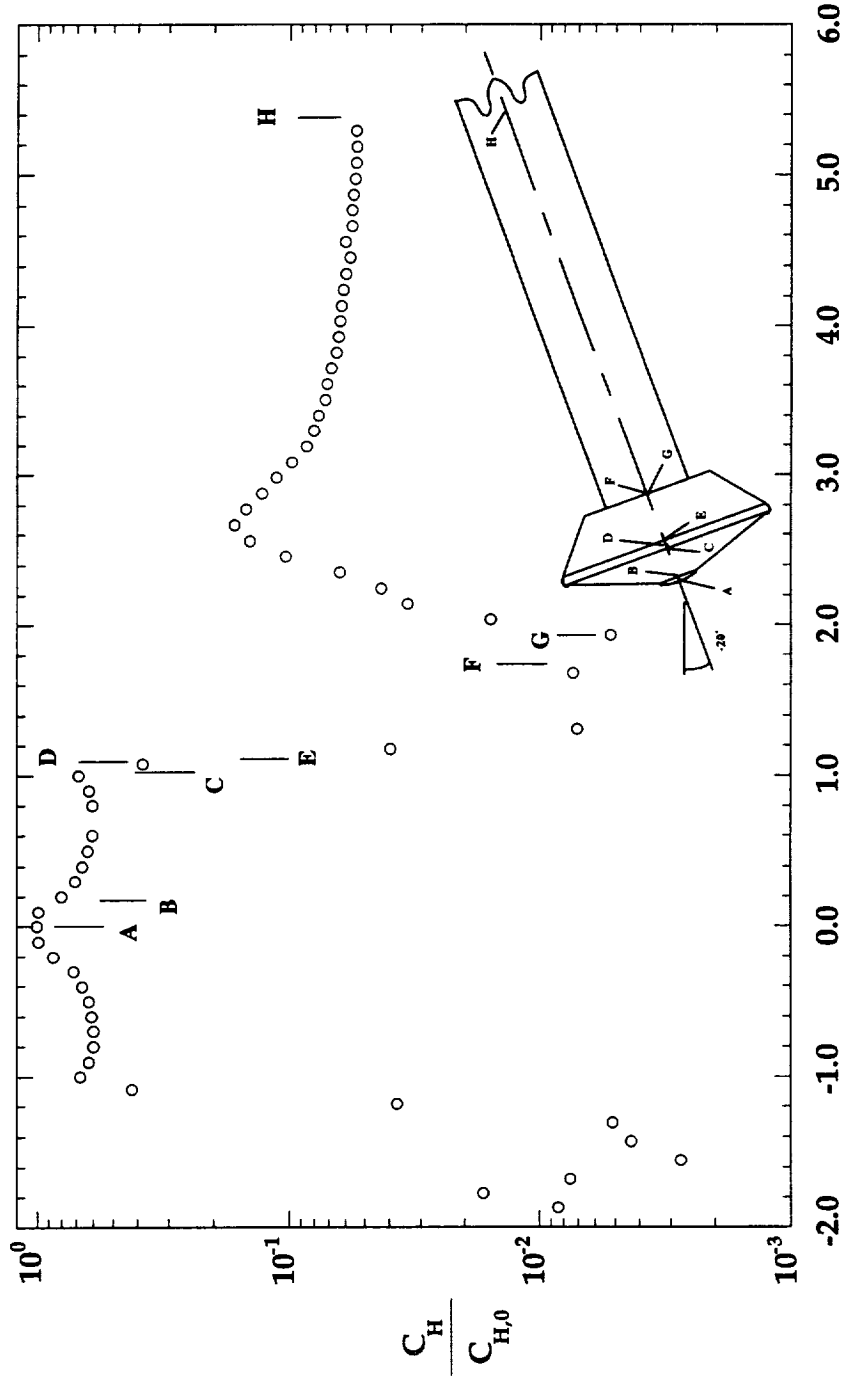

Figure A-31: 31-Inch Mach 10 Test 293, Run 035, MP-1 Configuration, $Re_\infty = 1.0 \times 10^6$ ft^{-1}, $\alpha = -20°$, $\phi = 90°$

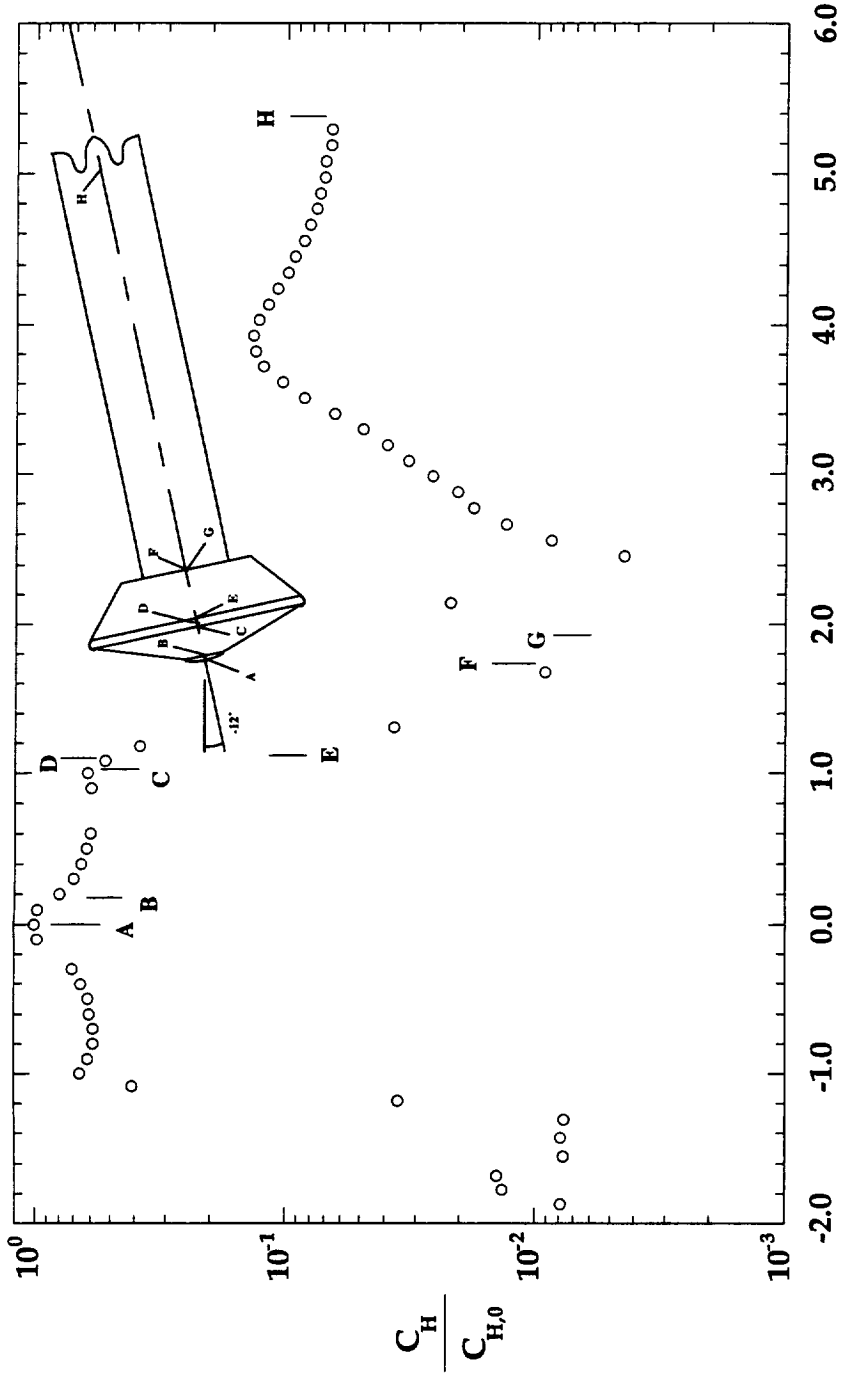

Figure A-32: 31-Inch Mach 10 Test 293, Run 036, MP-1 Configuration, $Re_\infty = 1.0 \times 10^6$ ft^{-1}, $\alpha = -12°$, $\phi = 90°$

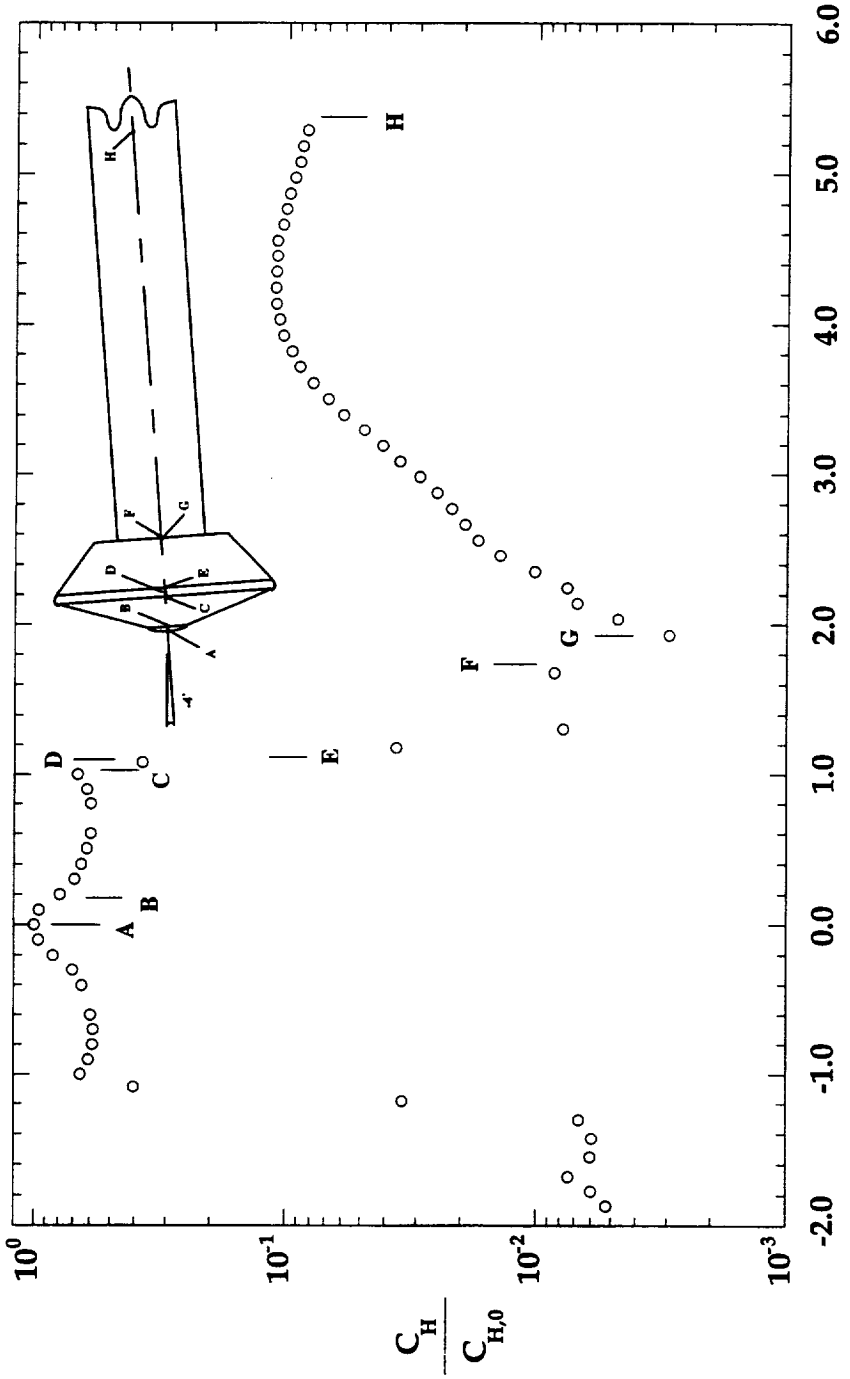

Figure A-33: 31-Inch Mach 10 Test 293, Run 037, MP-1 Configuration, $Re_\infty = 1.0 \times 10^6$ ft^{-1}, α = -4°, ϕ=90°

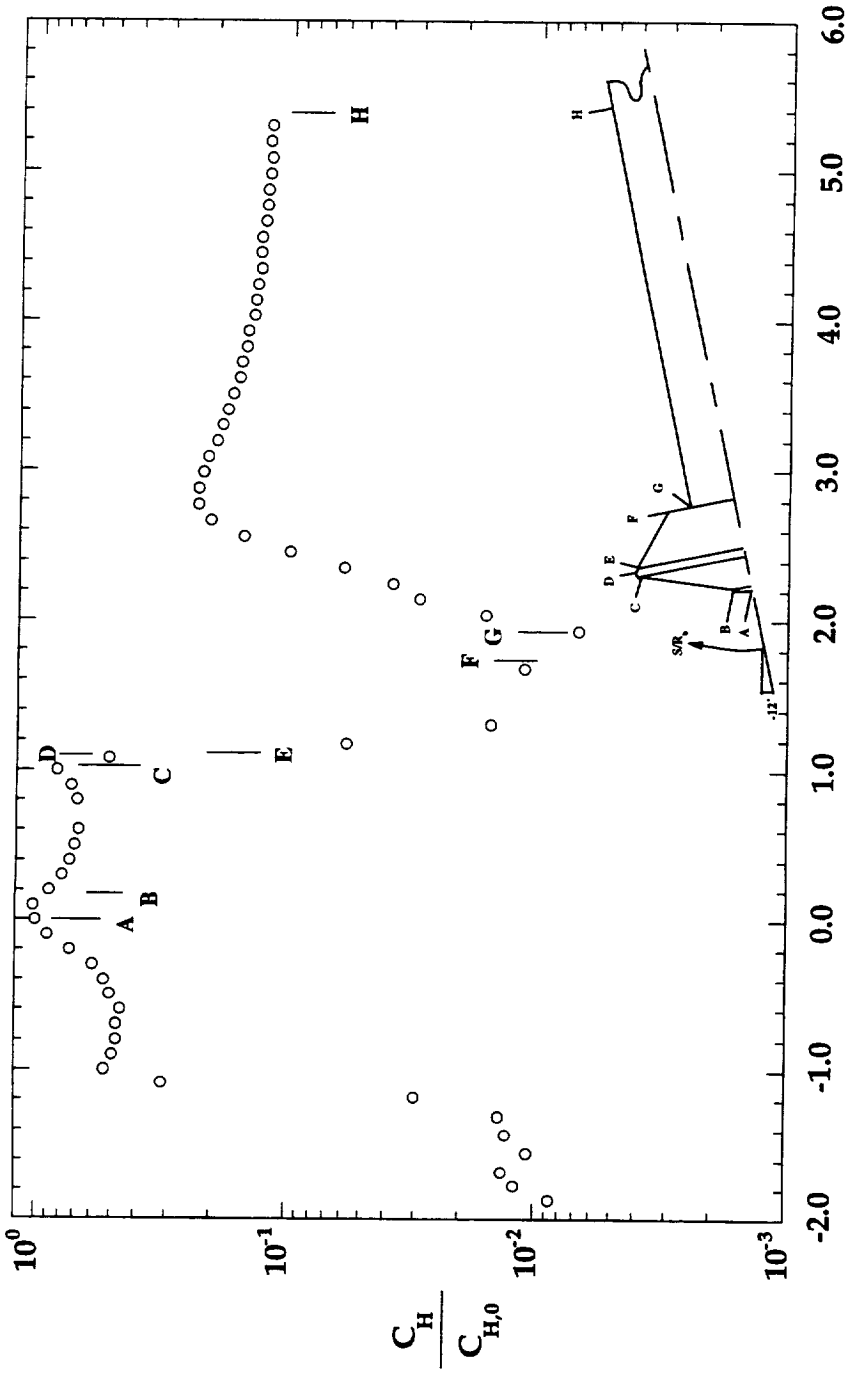

Figure A-34: 31-Inch Mach 10 Test 293, Run 038, MP-1 Configuration, $Re_\infty = 1.0 \times 10^6$ ft^{-1}, $\alpha = -12°$, $\phi = 0°$

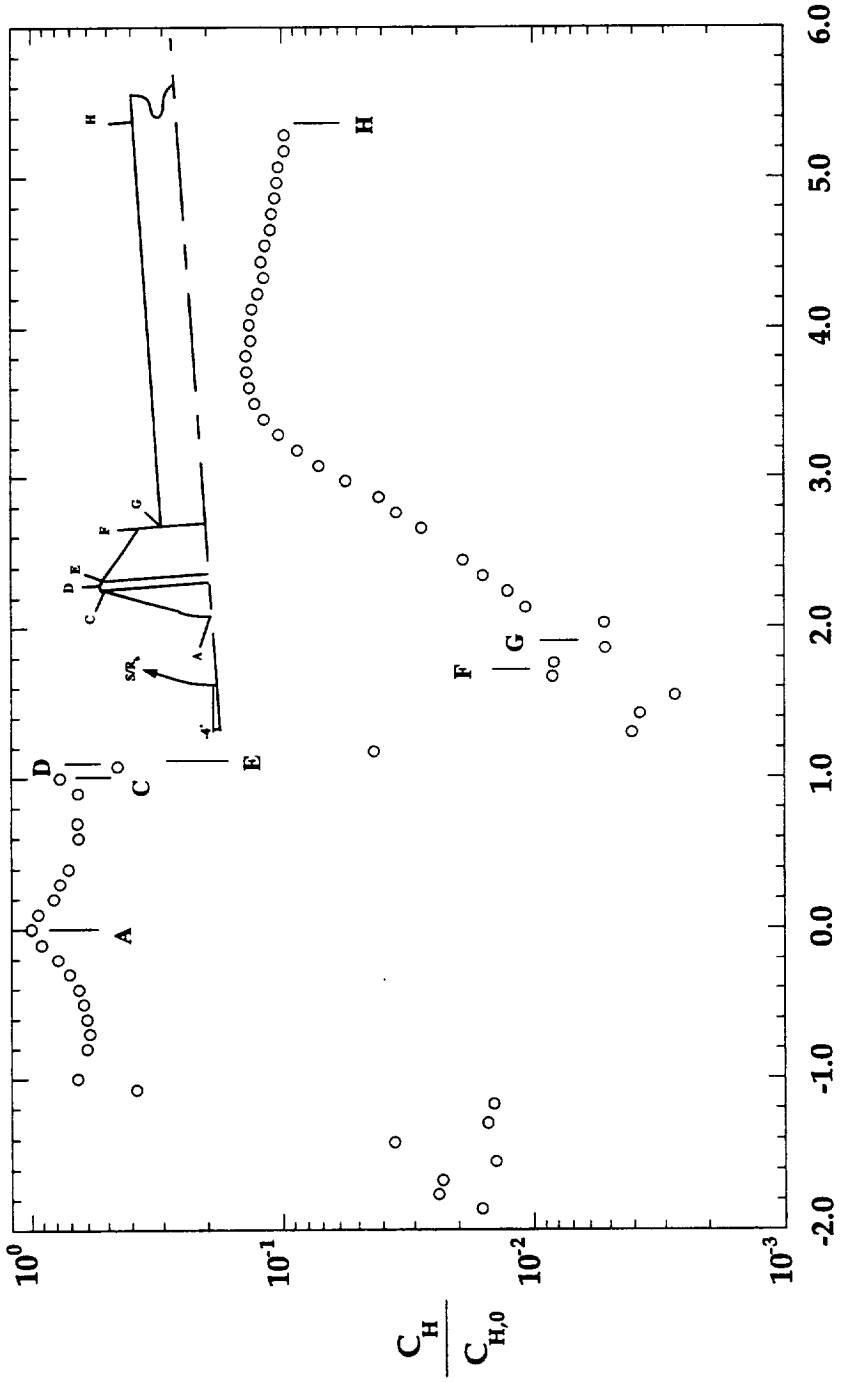

Figure A-35: 31-Inch Mach 10 Test 293, Run 039, MP-2 Configuration, $Re_\infty = 1.0 \times 10^6$ ft^{-1}, $\alpha = -4°$, $\phi = 0°$

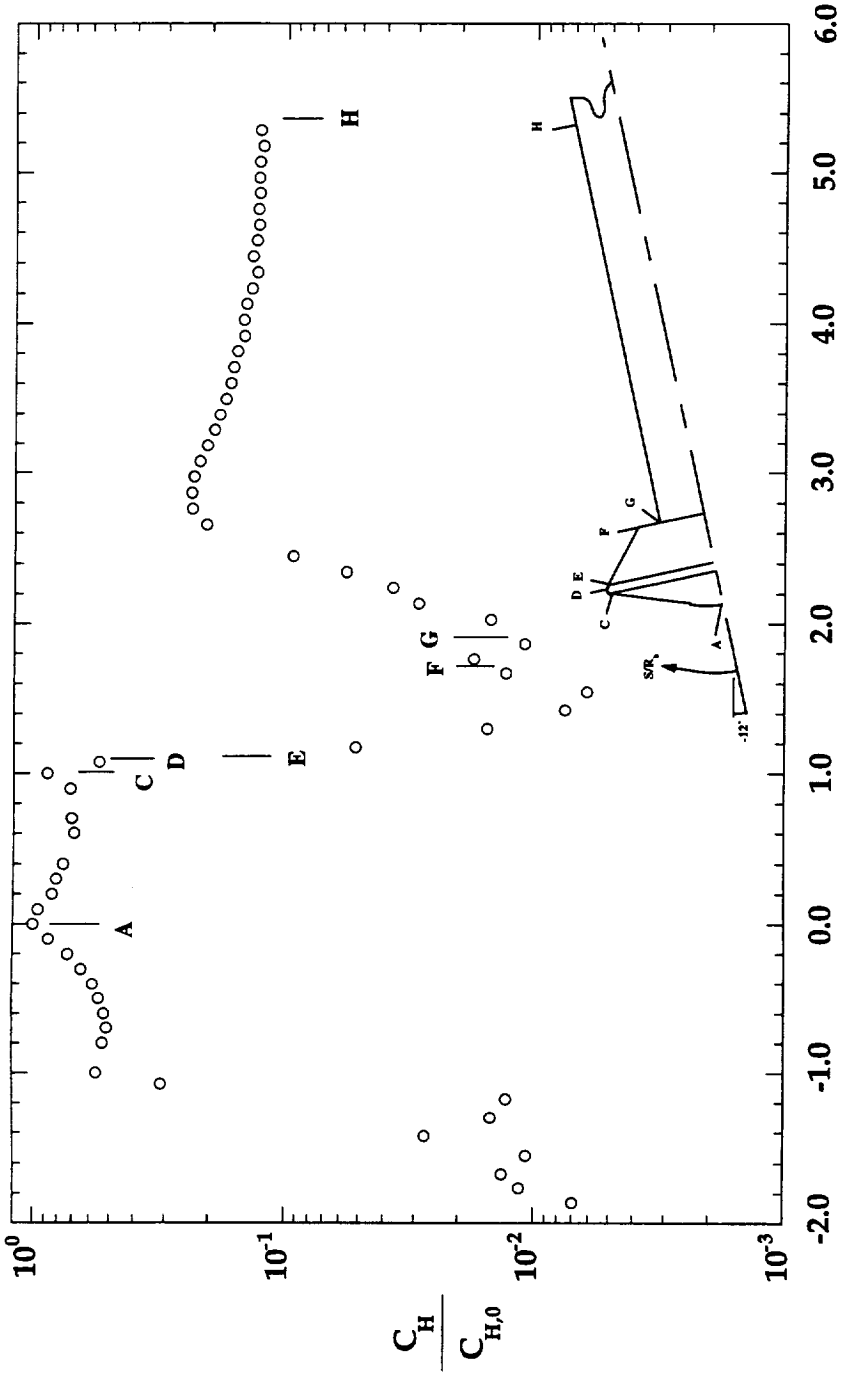

Figure A-36: 31-Inch Mach 10 Test 293, Run 040, MP-2 Configuration, $Re_\infty = 1.0 \times 10^6$ ft^{-1}, $\alpha = -12°$, $\phi = 0°$

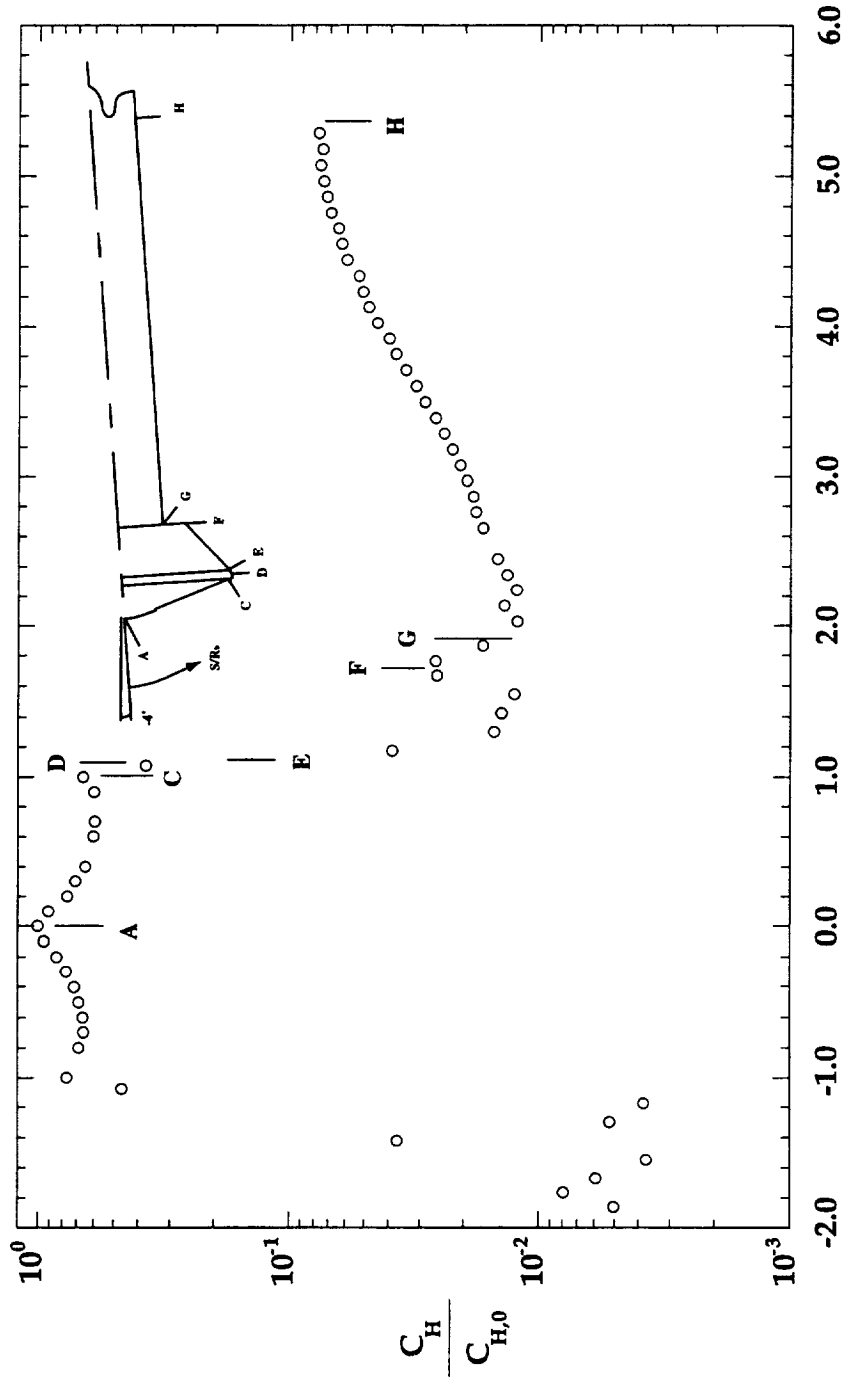

Figure A-37: 31-Inch Mach 10 Test 293, Run 041, MP-2 Configuration, $Re_\infty = 1.0 \times 10^6$ ft^{-1}, $\alpha = -4°$, $\phi = 180°$

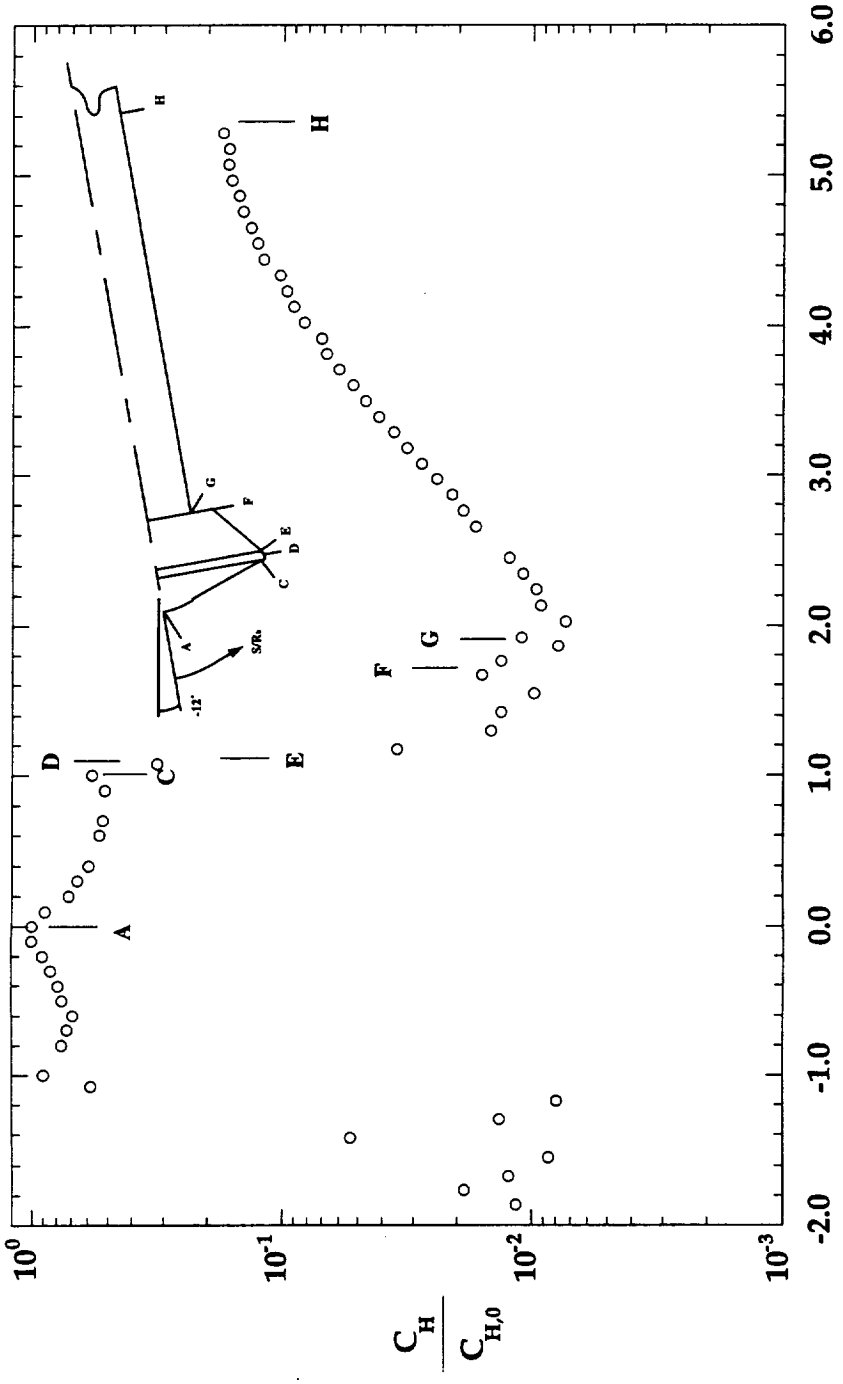

Figure A-38: 31-Inch Mach 10 Test 293, Run 042, MP-2 Configuration, $Re_\infty = 1.0 \times 10^6$ ft^{-1}, $\alpha = -12°$, $\phi = 180°$

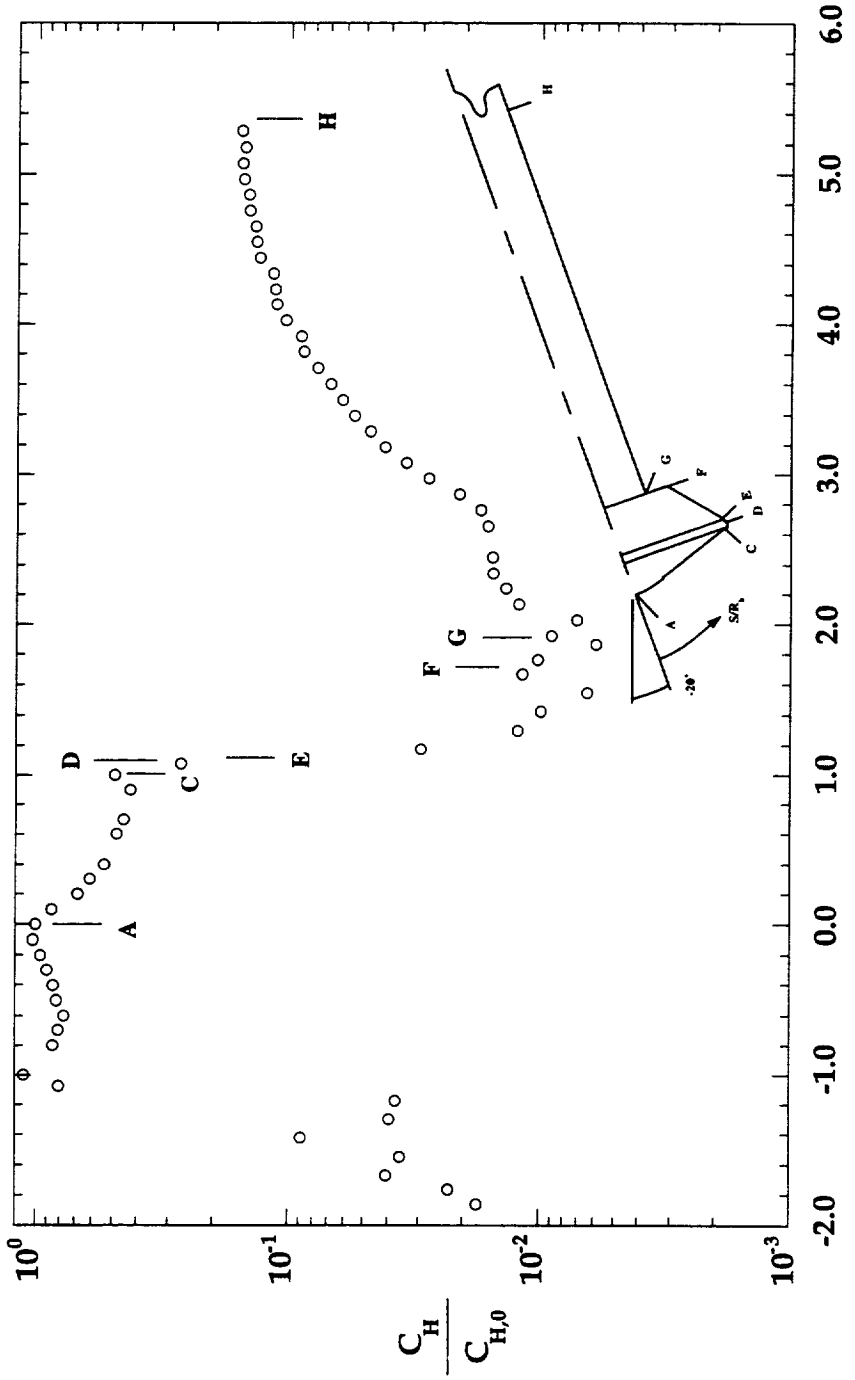

Figure A-39: 31-Inch Mach 10 Test 293, Run 043, MP-2 Configuration, $Re_\infty = 1.0 \times 10^6$ ft^{-1}, α = -20°, ϕ=180°

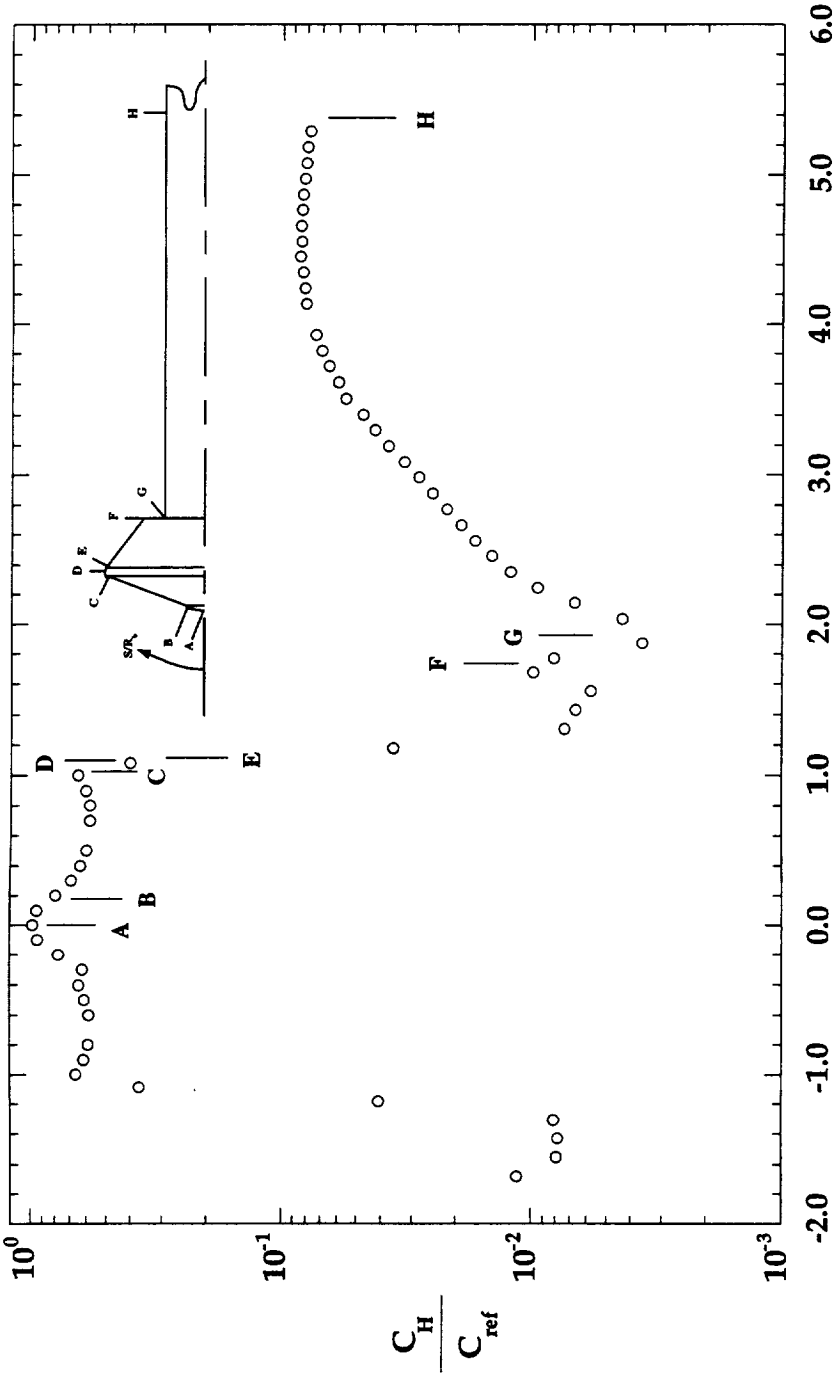

Figure A-40: 31-Inch Mach 10 Test 307, Run 008, MP-1 Configuration,

$Re_\infty = 0.5 \times 10^6$ ft^{-1}, $\alpha = 0°$, $\phi = 0°$

*** BAD RUN, NO DATA ***

Figure A-41: 31-Inch Mach 10 Test 307, Run 009, MP-1 Configuration, $Re_\infty = 0.5x106$ ft-1, $\alpha = 0°$, $\phi = 0°$

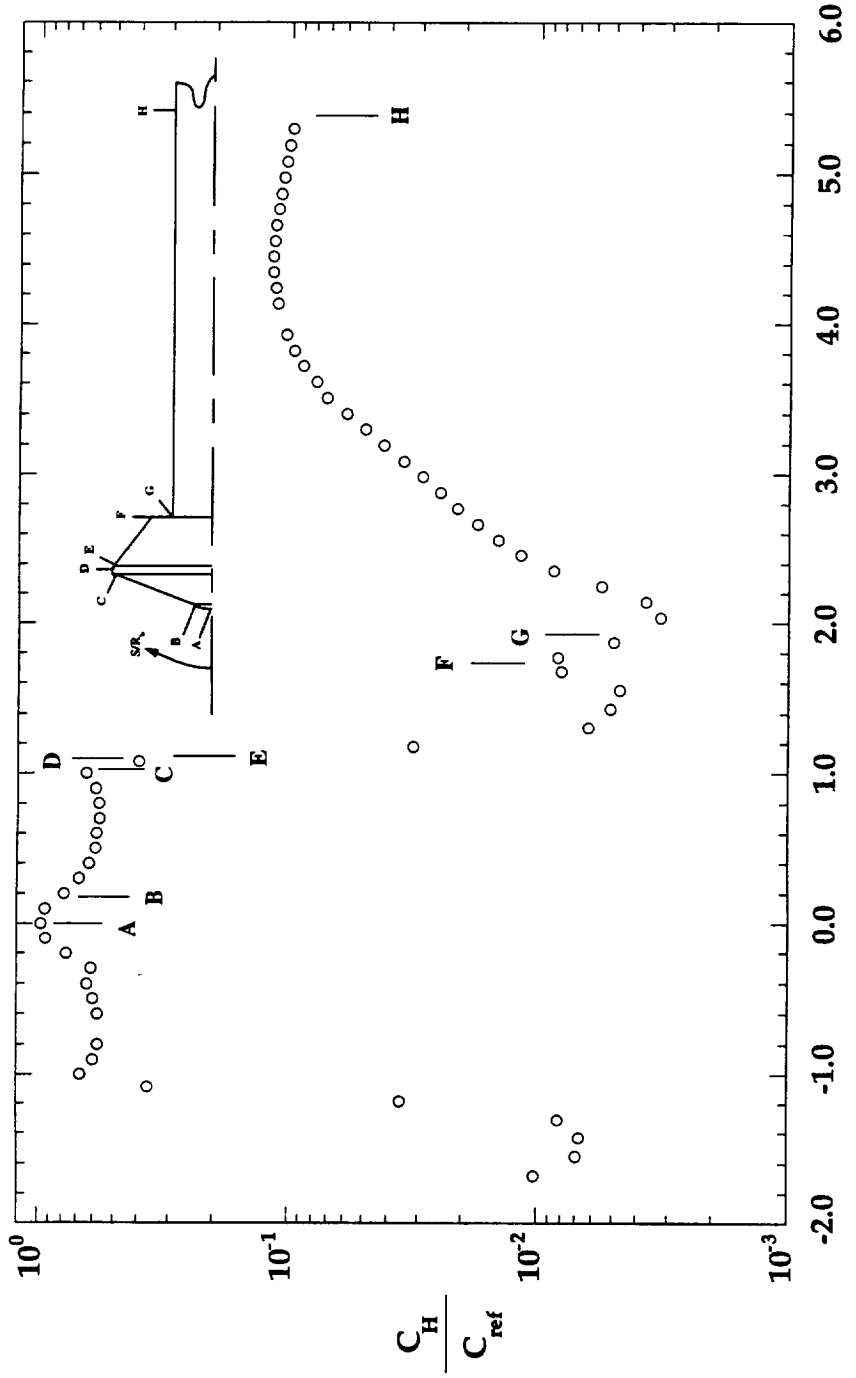

Figure A-42: 31-Inch Mach 10 Test 307, Run 010, MP-1 Configuration, $Re_\infty = 1.0 \times 10^6$ ft^{-1}, $\alpha = 0°$, $\phi = 0°$

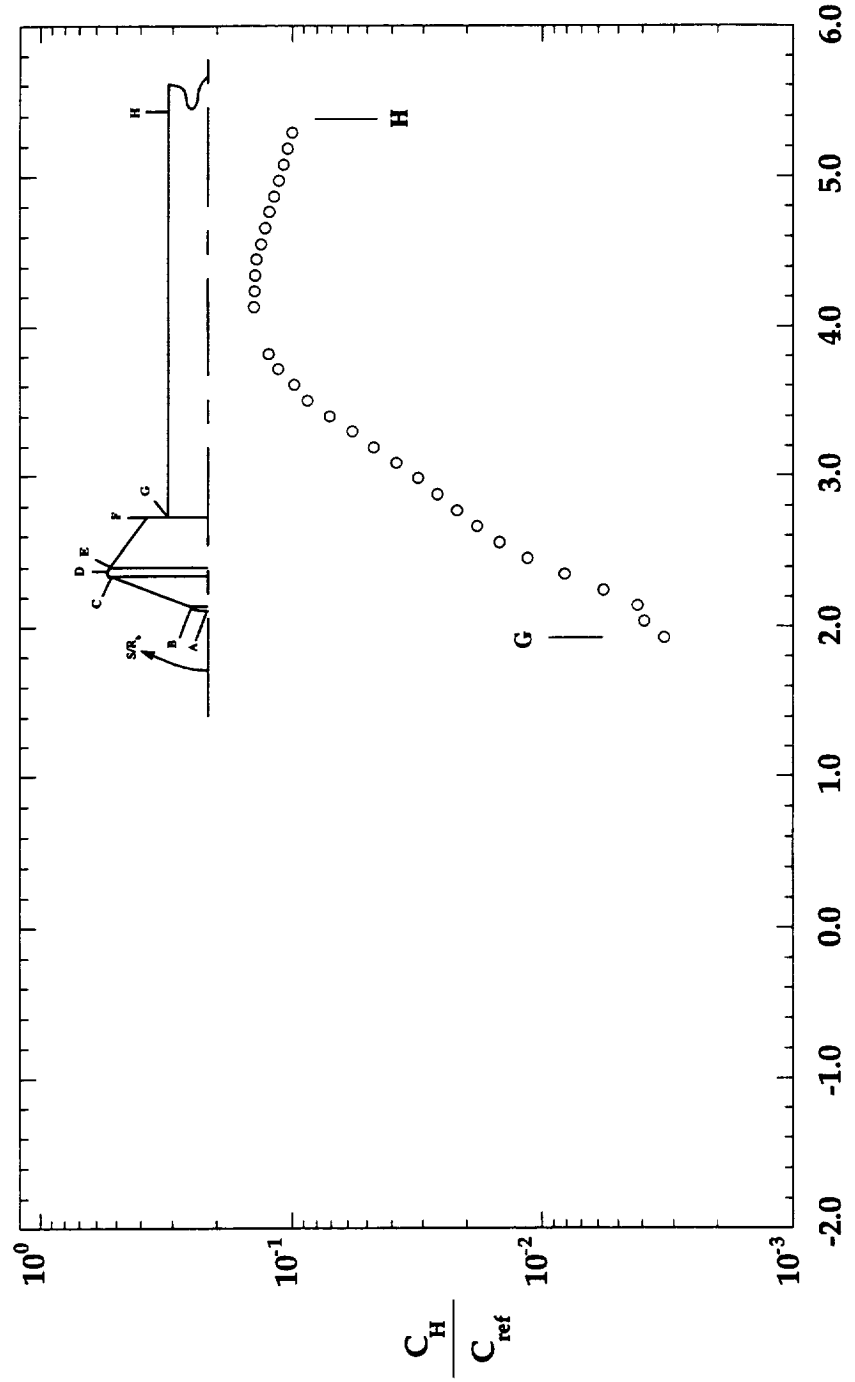

Figure A-43: 31-Inch Mach 10 Test 307, Run 011, MP-1 Configuration, $Re_\infty = 2.0 \times 10^6$ ft^{-1}, $\alpha = 0°$, $\phi = 0°$, Surface Grit on Model

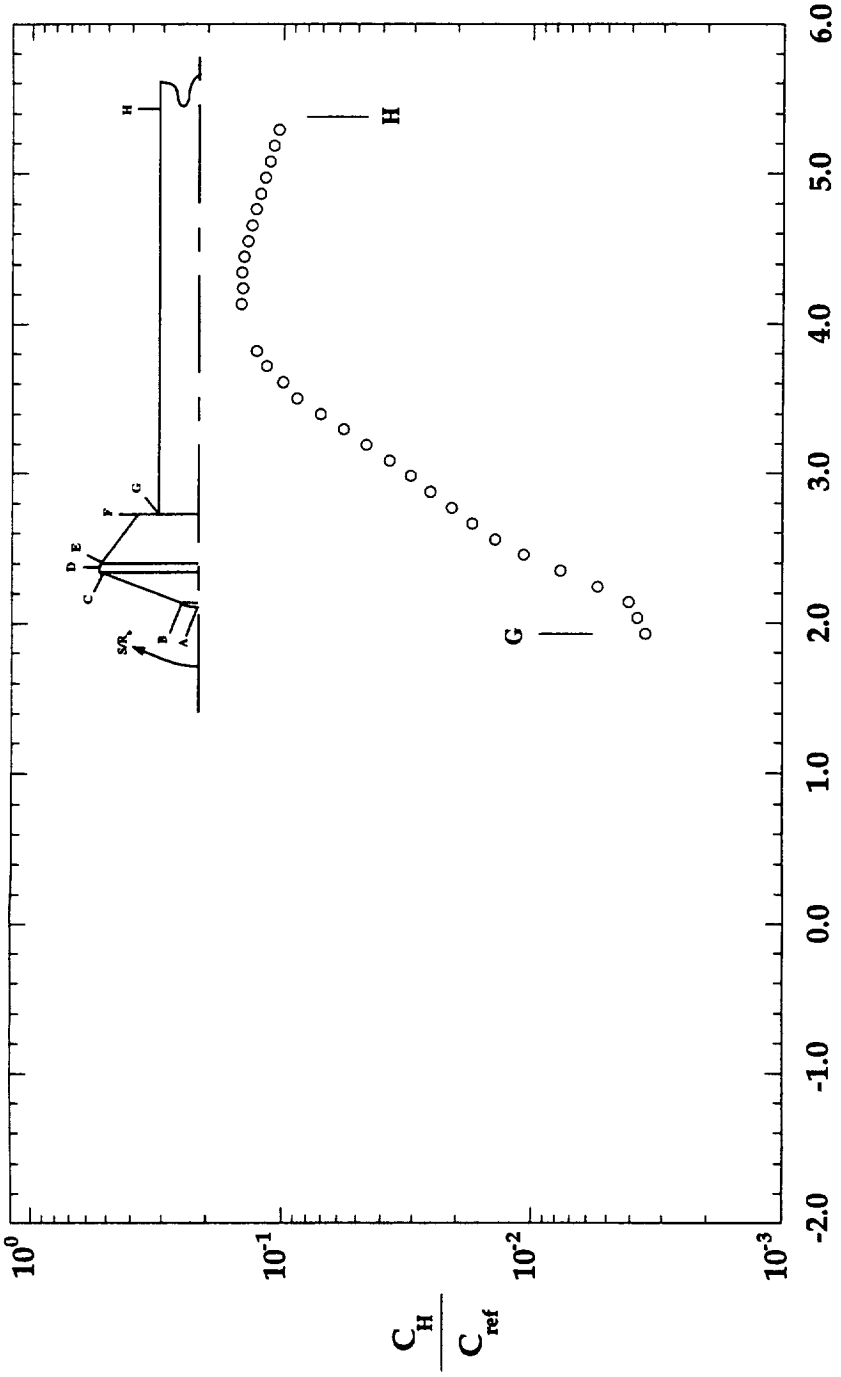

Figure A-44: 31-Inch Mach 10 Test 307, Run 012, MP-1 Configuration, $Re_\infty = 2.0 \times 10^6$ ft^{-1}, $\alpha = 0°$, $\phi = 0°$, Surface Grit on Model

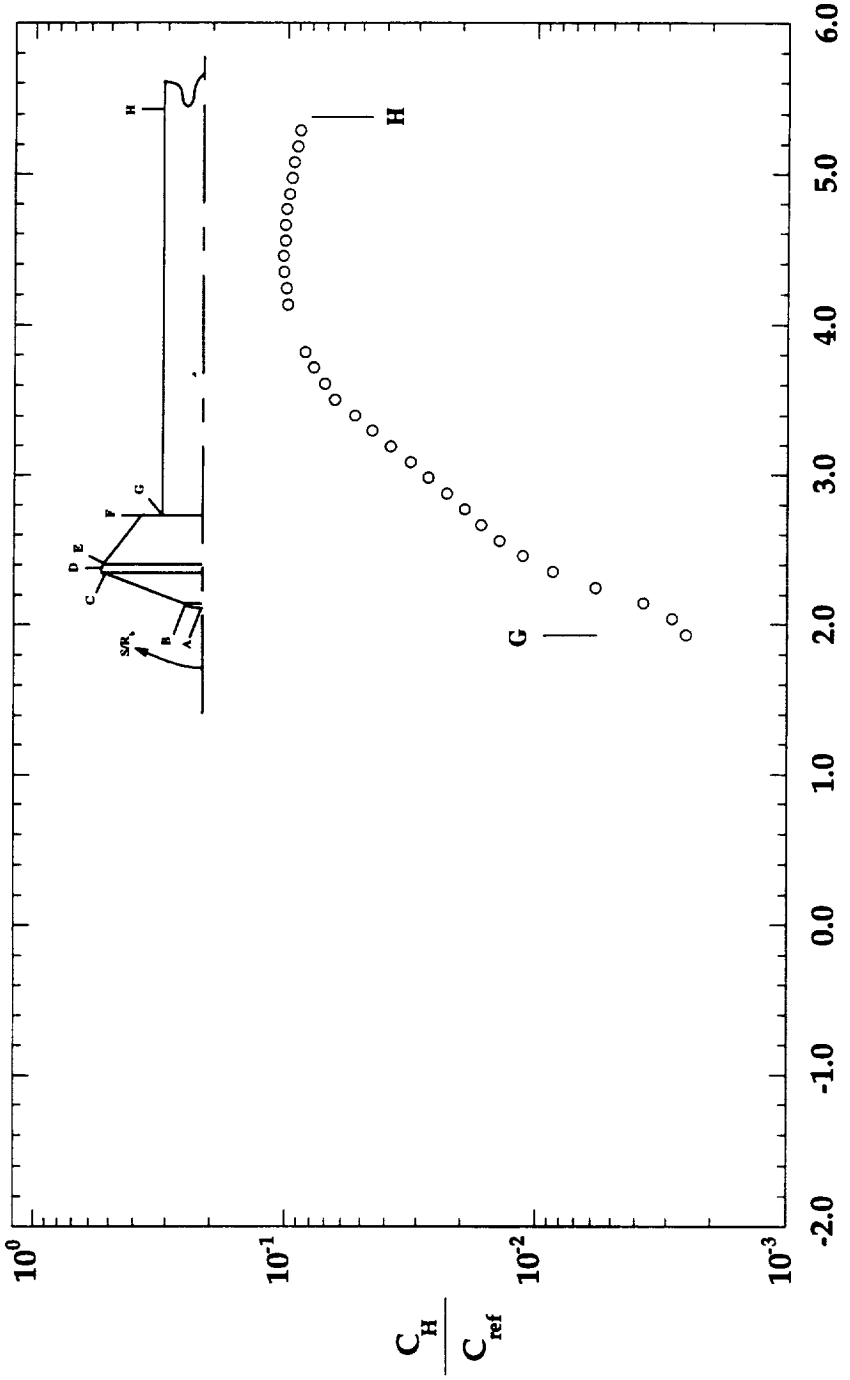

Figure A-45: 31-Inch Mach 10 Test 307, Run 013, MP-1 Configuration, $Re_\infty = 1.0 \times 10^6$ ft^{-1}, $\alpha = 0°$, $\phi = 0°$, Surface Grit on Model

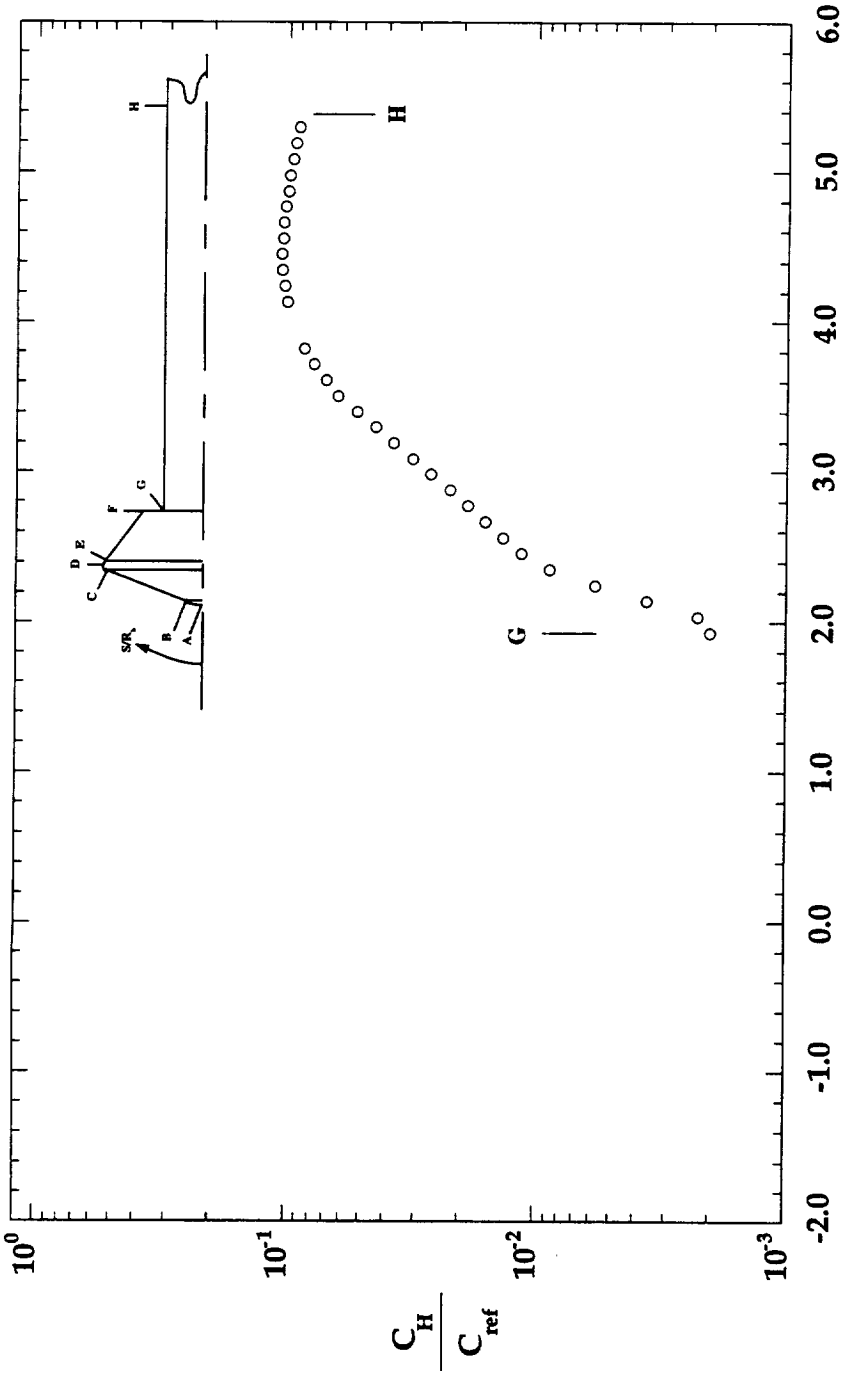

Figure A-46: 31-Inch Mach 10 Test 307, Run 014, MP-1 Configuration, $Re_\infty = 1.0 \times 10^6$ ft^{-1}, $\alpha = 0°$, $\phi = 0°$, Surface Grit on Model

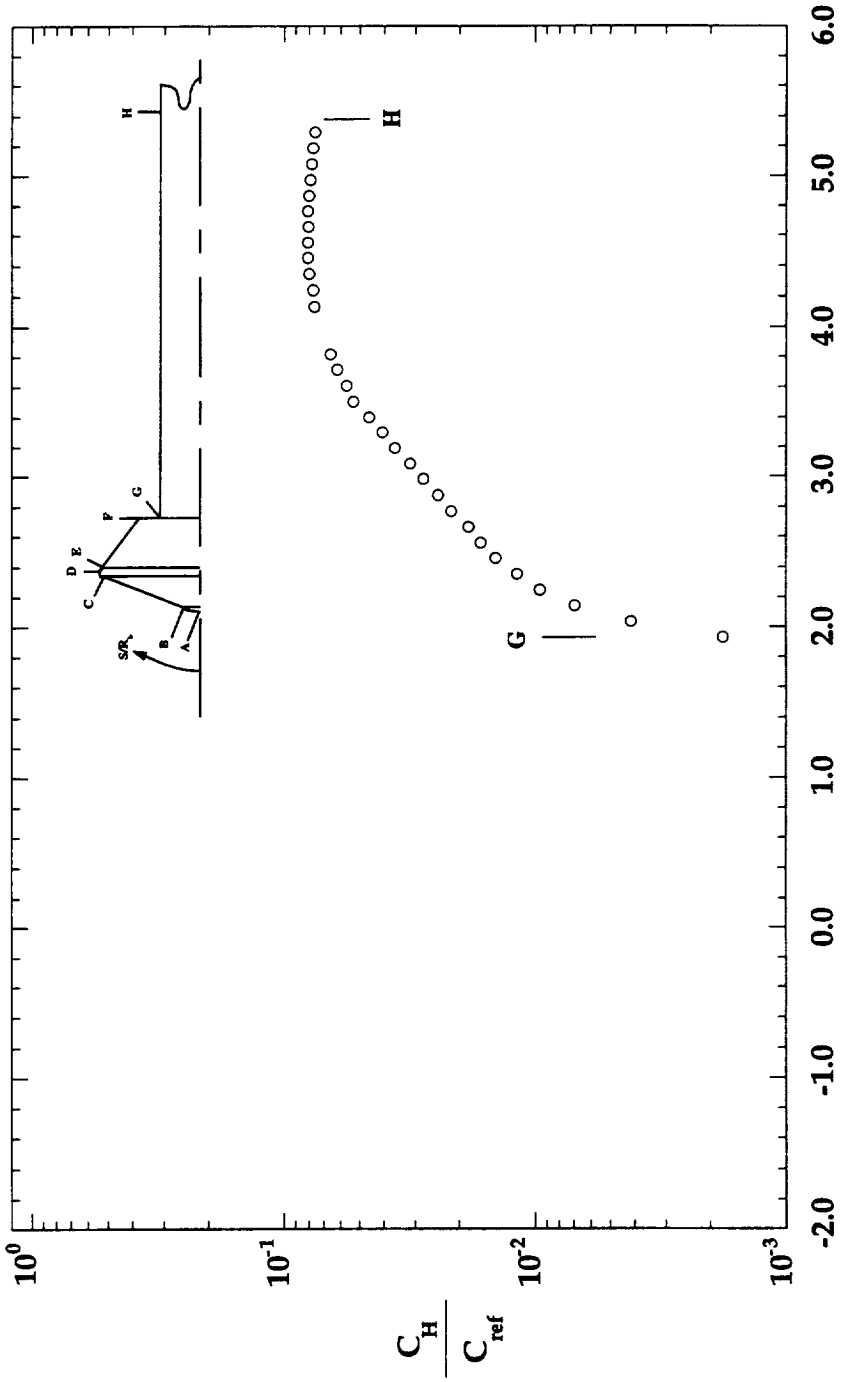

Figure A-47: 31-Inch Mach 10 Test 307, Run 015, MP-1 Configuration, $Re_\infty = 0.5 \times 10^6$ ft^{-1}, $\alpha = 0°$, $\phi = 0°$, Surface Grit on Model

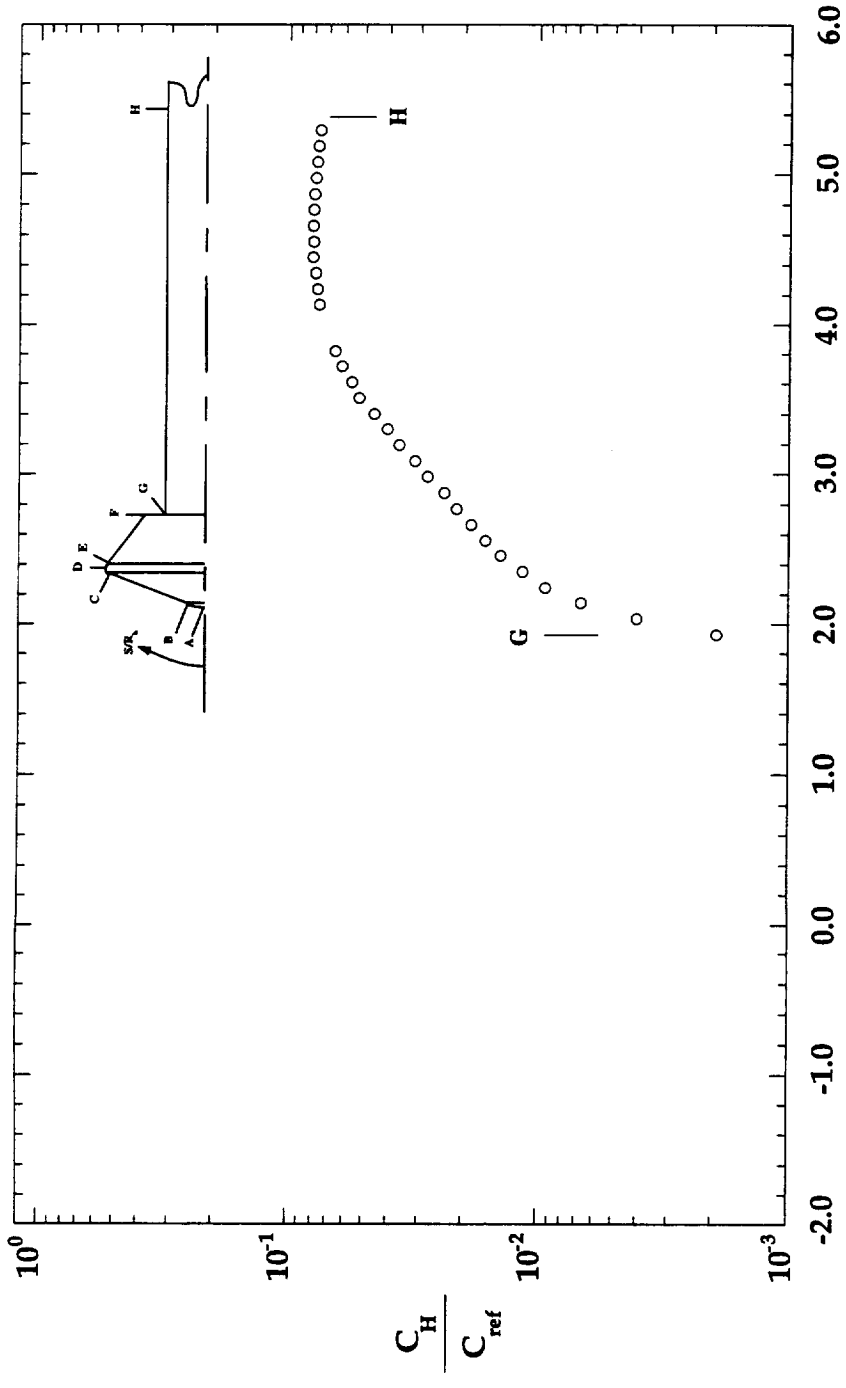

Figure A-48: 31-Inch Mach 10 Test 307, Run 016, MP-1 Configuration, $Re_\infty = 0.5 \times 10^6$ ft^{-1}, $\alpha = 0°$, $\phi = 0°$, Surface Grit on Model

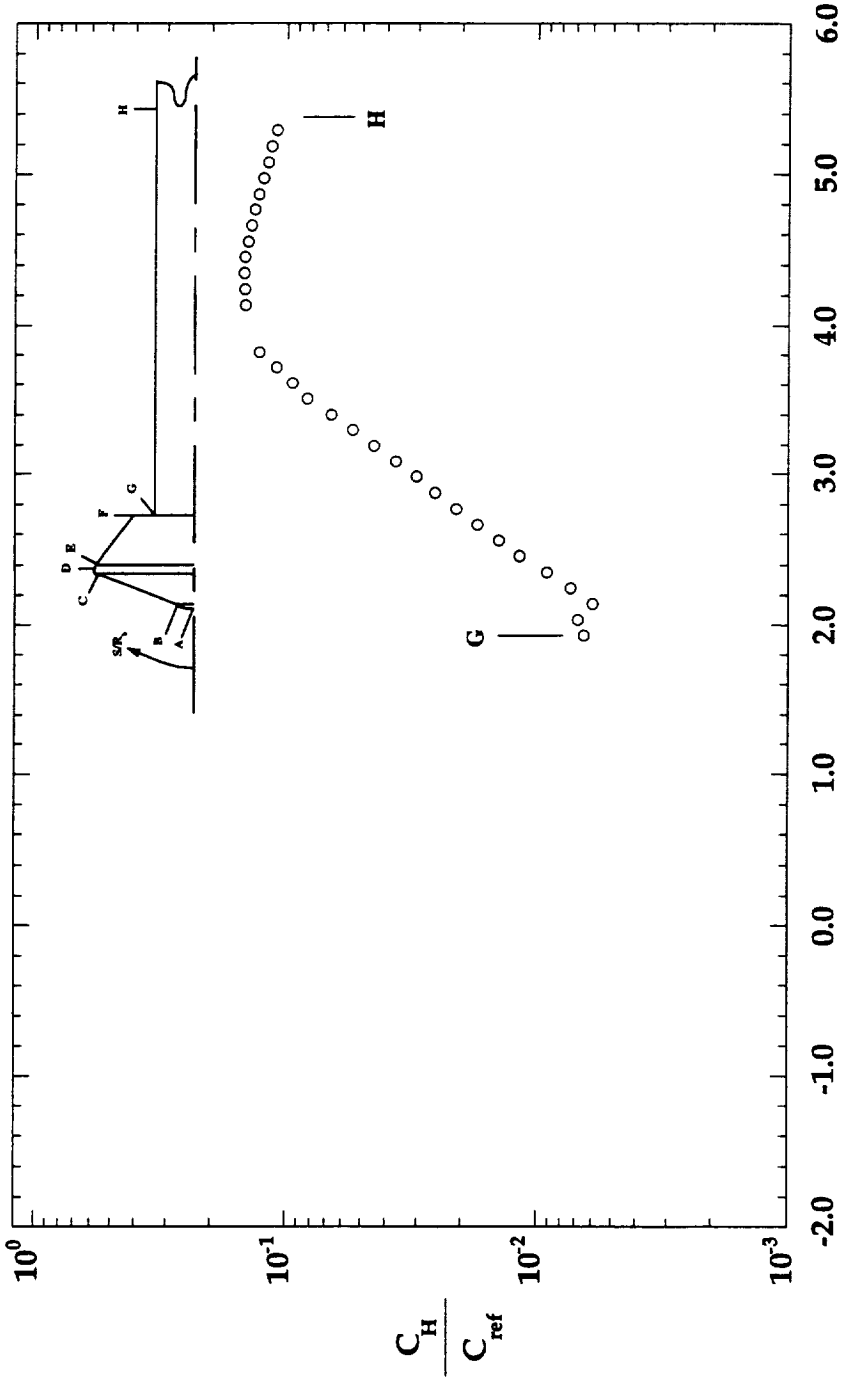

Figure A-49: 31-Inch Mach 10 Test 307, Run 017, MP-1 Configuration, $Re_\infty = 2.0 \times 10^6$ ft^{-1}, $\alpha = 0°$, $\phi = 0°$, Surface Grit on Model

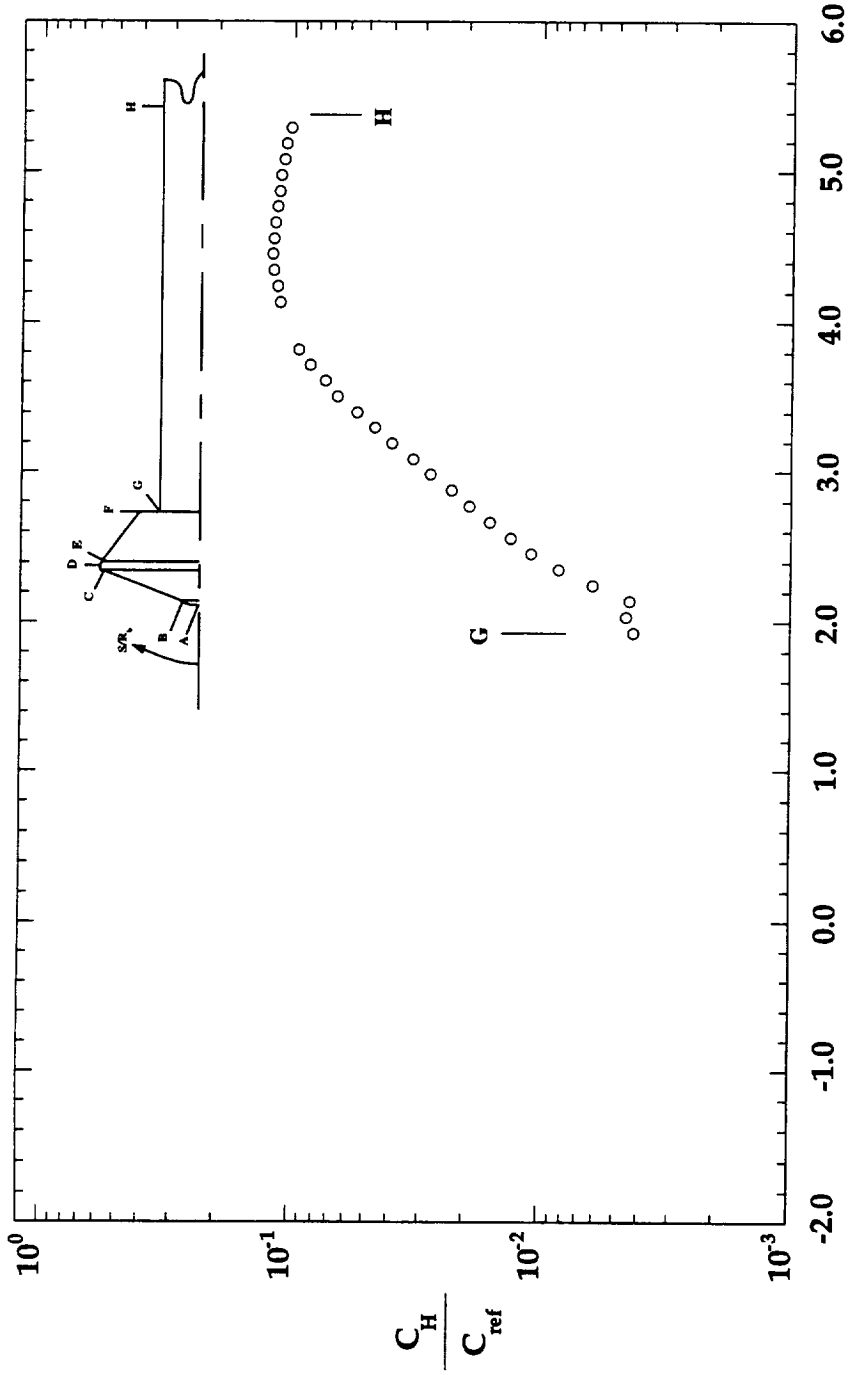

Figure A-50: 31-Inch Mach 10 Test 307, Run 018, MP-1 Configuration, $Re_\infty = 1.0 \times 10^6$ ft^{-1}, $\alpha = 0°$, $\phi = 0°$, Surface Grit on Model

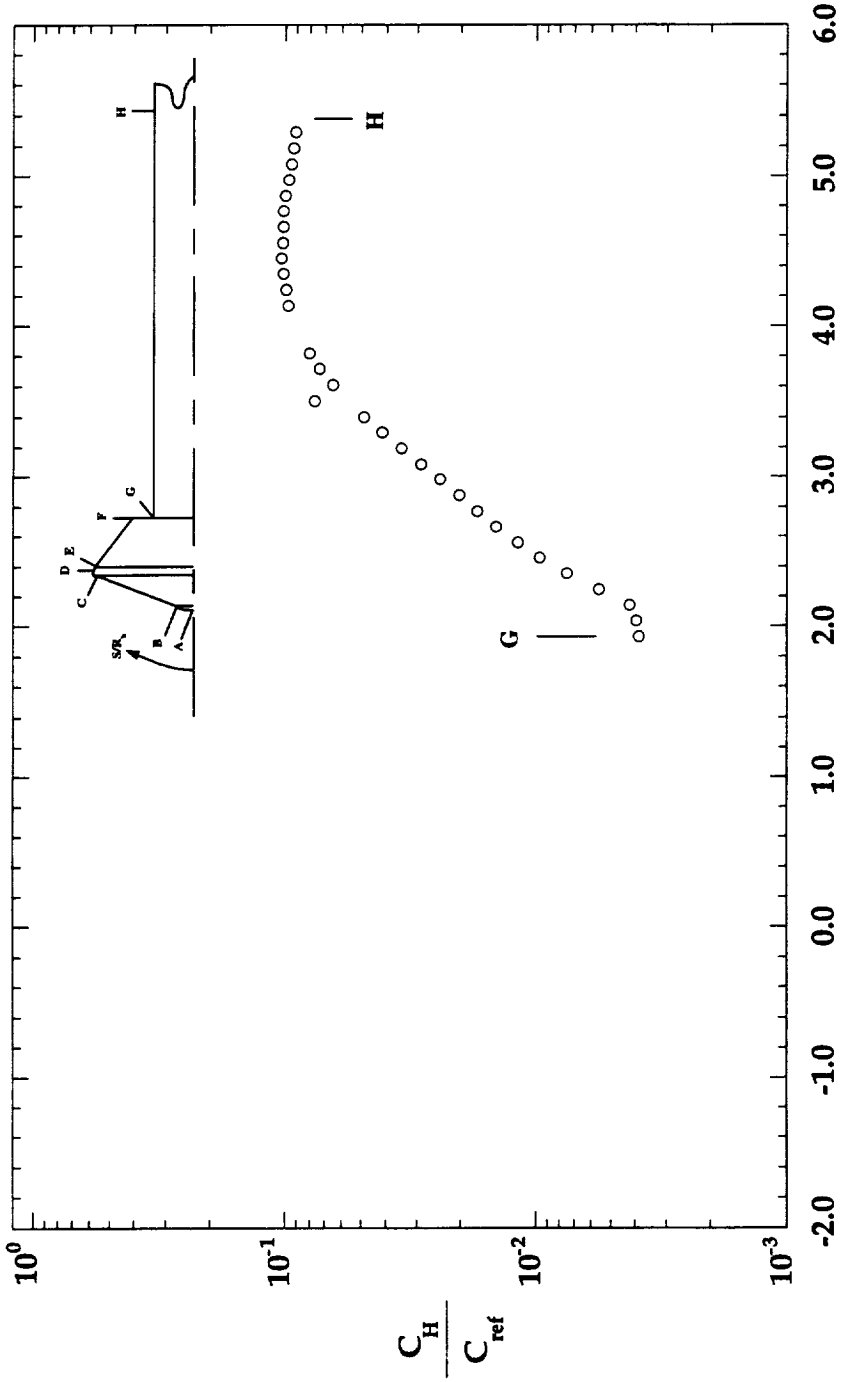

Figure A-51: 31-Inch Mach 10 Test 307, Run 019, MP-1 Configuration, $Re_\infty = 1.0 \times 10^6$ ft^{-1}, $\alpha = 0°$, $\phi = 0°$, Surface Grit on Model

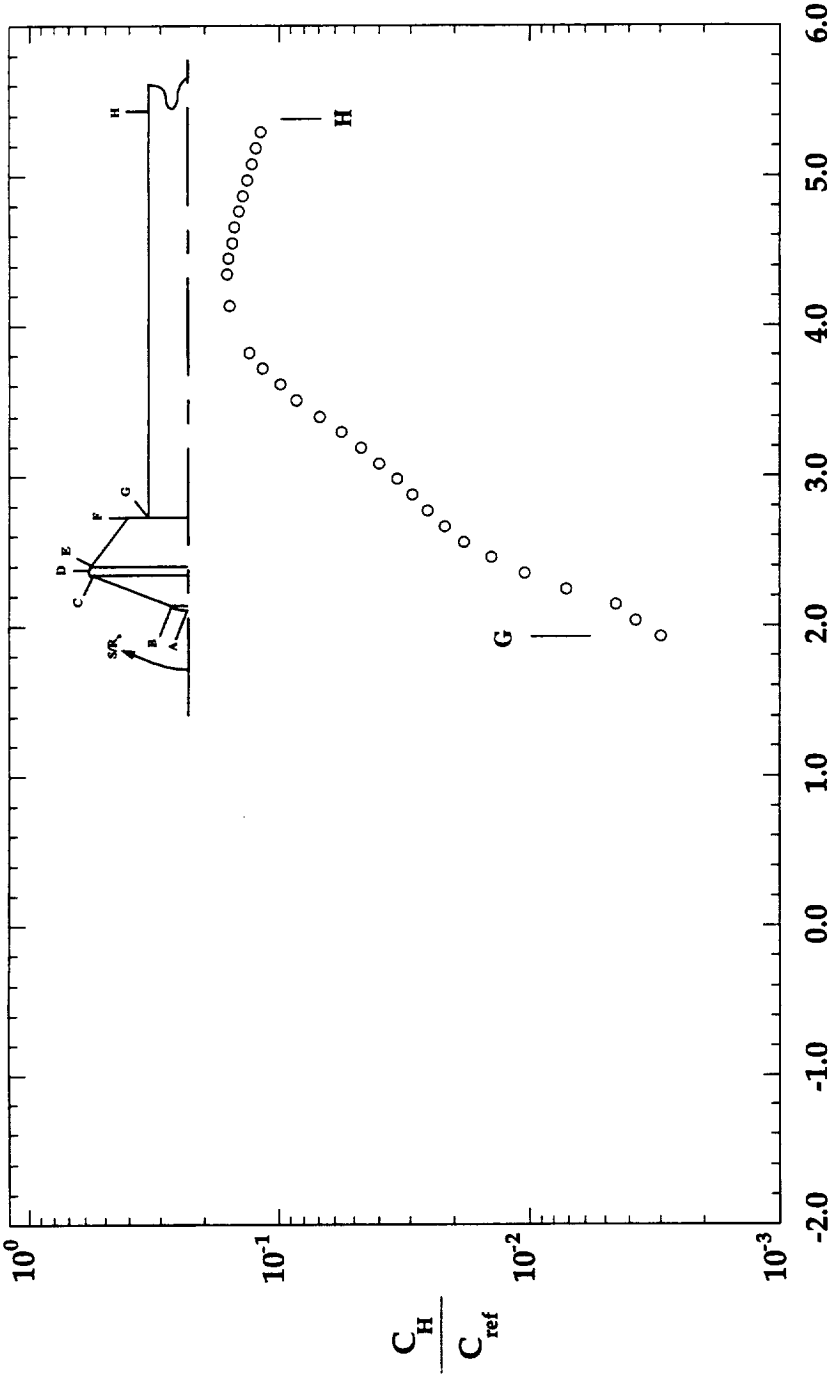

Figure A-52: 31-Inch Mach 10 Test 307, Run 020, MP-1 Configuration, $Re_\infty = 2.0 \times 10^6$ ft^{-1}, $\alpha = 0°$, $\phi = 0°$, Surface Grit on Model

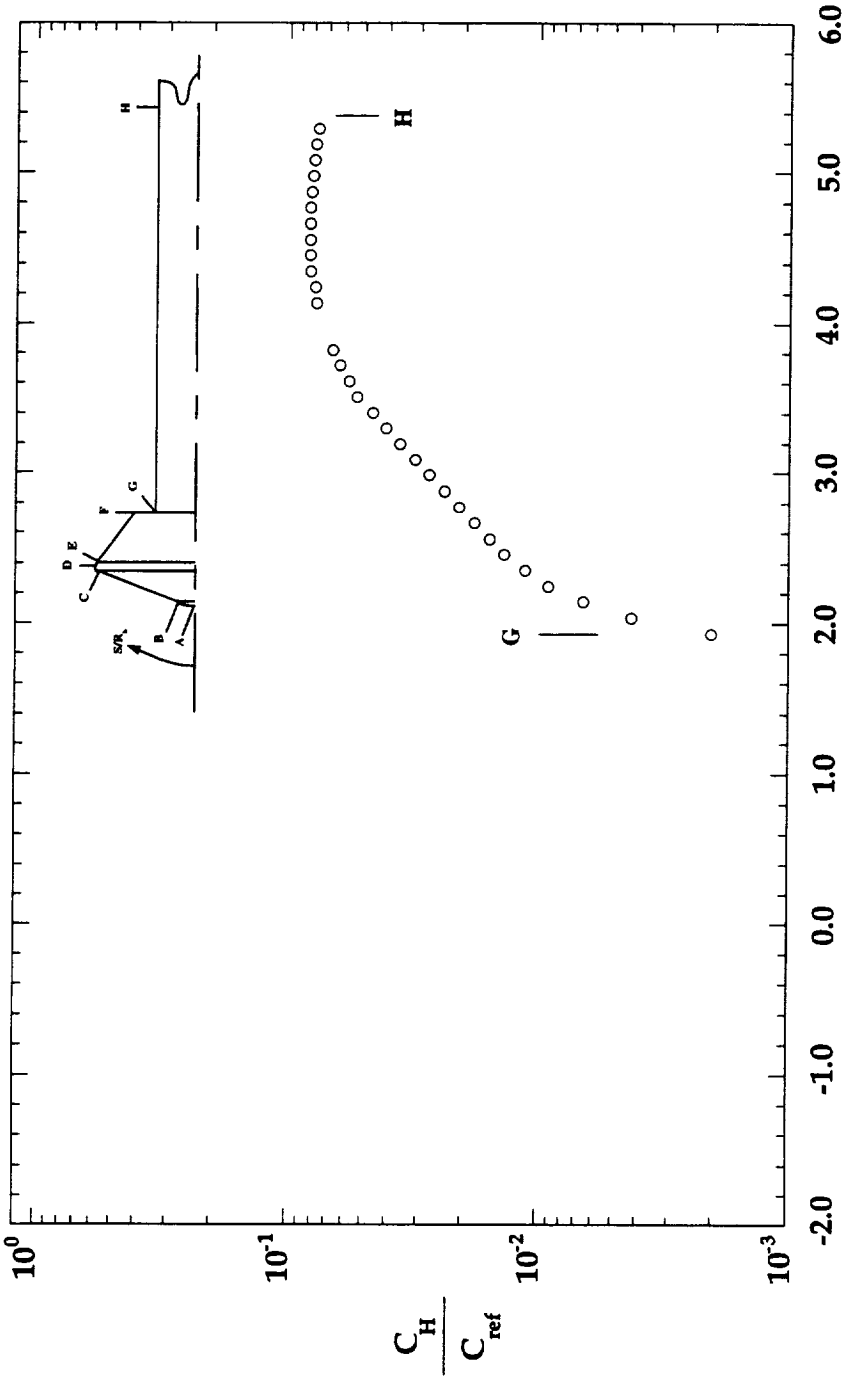

Figure A-53: 31-Inch Mach 10 Test 307, Run 021, MP-1 Configuration,
$Re_\infty = 0.5 \times 10^6$ ft^{-1}, $\alpha = 0°$, $\phi = 0°$

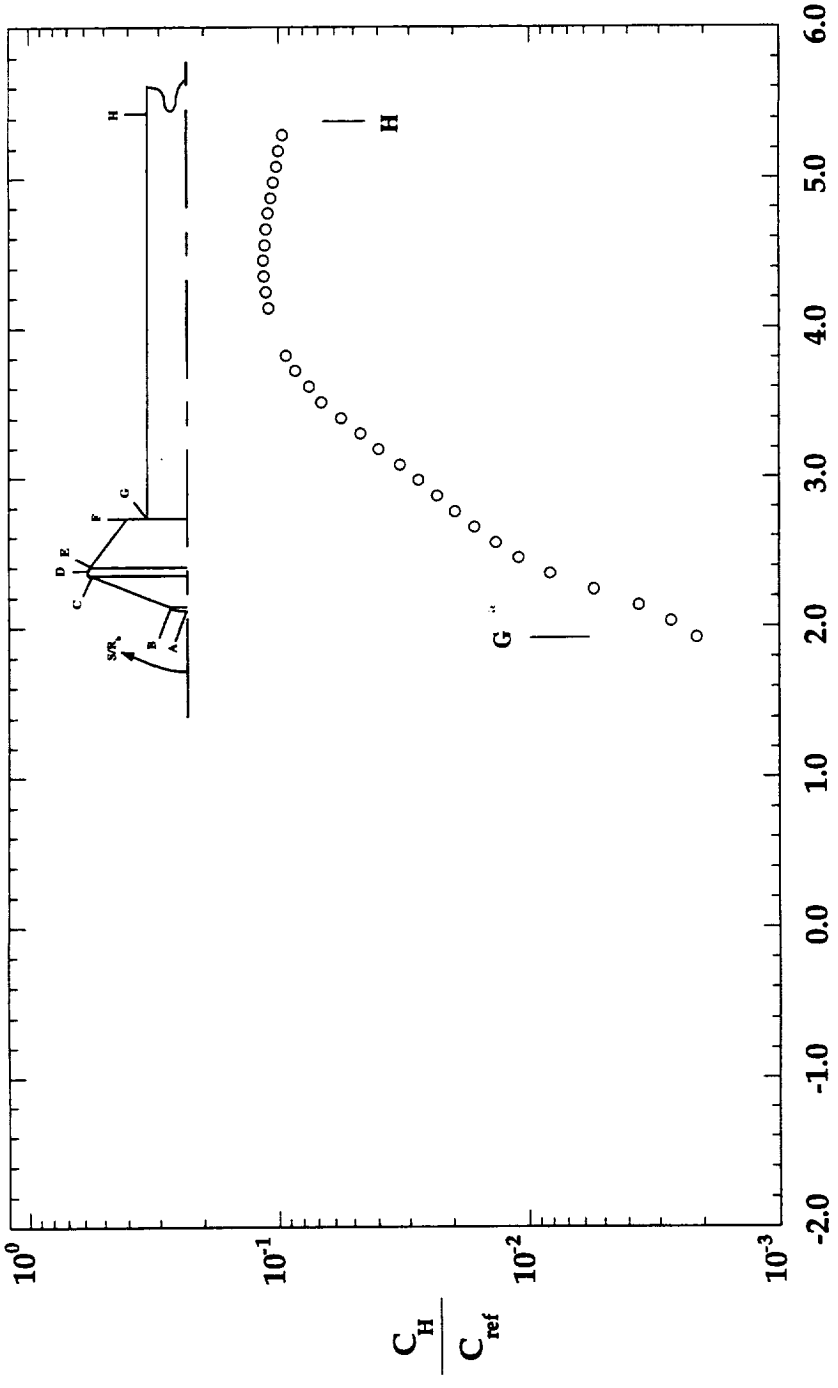

Figure A-54: 31-Inch Mach 10 Test 307, Run 022, MP-1 Configuration, $Re_\infty = 1.0 \times 10^6$ ft^{-1}, $\alpha = 0°$, $\phi = 0°$

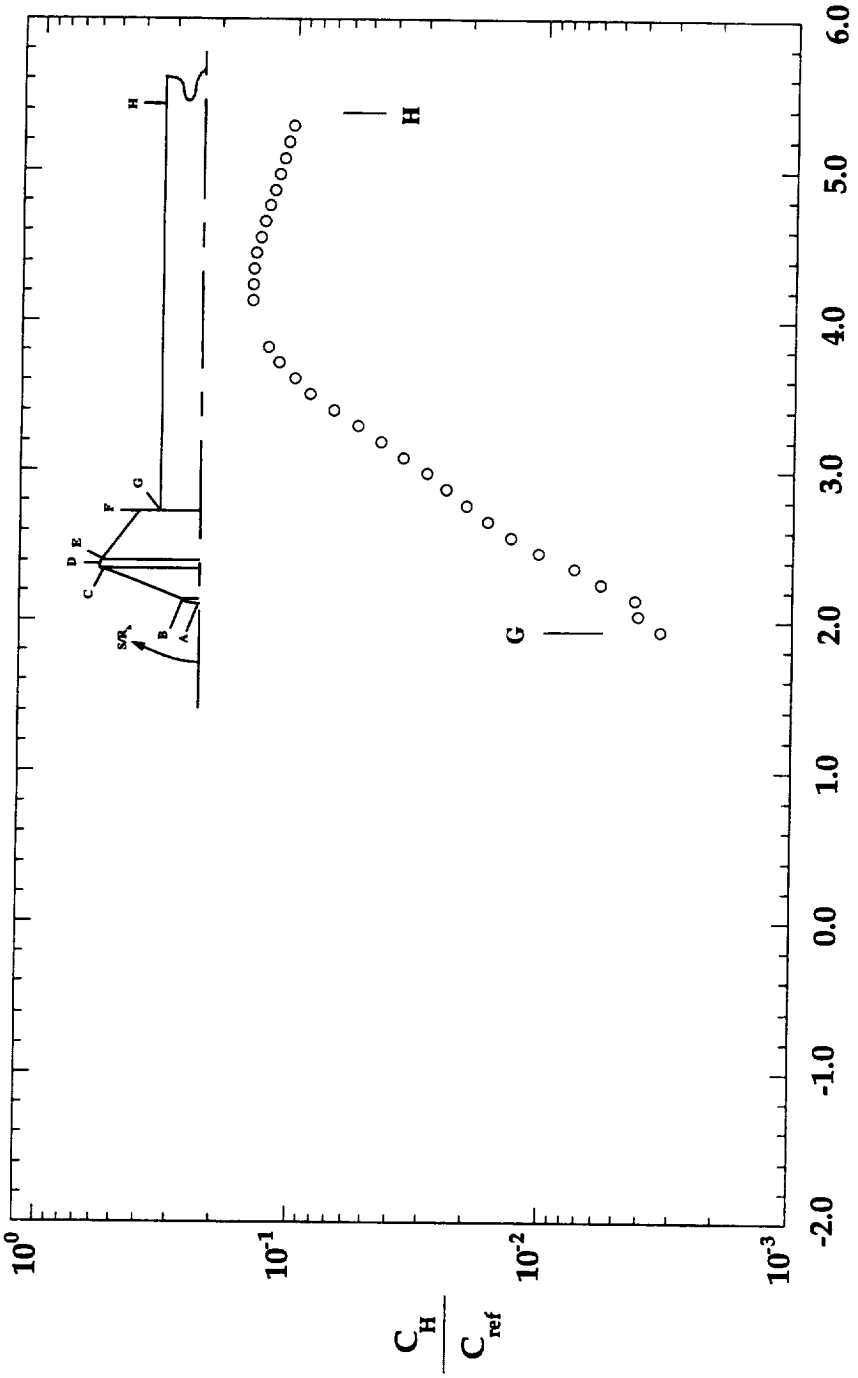

Figure A-55: 31-Inch Mach 10 Test 307, Run 023, MP-1 Configuration, $Re_\infty = 2.0 \times 10^6$ ft^{-1}, $\alpha = 0°$, $\phi = 0°$

APPENDIX B
HYPULSE EXPANSION TUBE DATA

Aerothermodynamic data from tests in the NASA HYPULSE Expansion Tube are presented in this appendix. The test run matrix and the run flow conditions are given in Tables B.1 and B.2. Run data from the HYPULSE test series are given in Tables B.3 through B.40. Normalized Stanton numbers distributions are plotted in Figs. B.1 through B.38.

The test matrix in Table B.1 lists the run number, the model configuration tested, the test gas, the model angle-of-attack, whether or not acceptable data were obtained on the forebody and in the wake ("Y" for good data or "N" for bad data, and "-" indicates no instrumentation in that region) and notes on each run. The flow conditions data in Table B.2 include the test gas, freestream velocity, density, temperature, pressure, and Mach number and the total enthalpy.

Tables B.3-B.40 list for each thin-film gage the time-averaged Stanton number, C_H, and the normalized standard deviation of the Stanton number over the data-averaging window, s/C_H. The thin-film gages are identified by number, for example, TF19, which is the stagnation-point gage. Gage positions are given by S/R_b, the normalized distance along the surface from the forebody stagnation point, and by L/R_b, the normalized distance along the sting from the base of the model. These positions can be related to specific control-point locations on the models using Figure 6.1.1: gages TF1 through TF7 and TF31 through TF37 are located on the afterbody or base of the model; gages TF8 through TF30 are located on the forebody; and gages TF38 through TF70 are located on the sting.

A normalized Stanton number, $C_H/C_{H,ref}$, is also given in Tables B.3-B.40. Because there was no instrumentation on the forebodies of several of the models tested in HYPULSE, all data are normalized by a fixed reference value. For air tests, $C_{H,ref}$ is either the measured stagnation point value from Run 754 for the MP-1 models or the value from Run 755 for the MP-2 models. For CO_2 tests, $C_{H,ref}$ is the

measured stagnation point value from Run 749 for the sphere-cone models (MP-1, MP-3 and MP-4) or the measured value from Run 792 for the MP-2 models. The normalizing value used for each run is listed in the header of each table.

These tables also include for each gage a reference heat-transfer rate, which is the heat-transfer rate at a fictitious uniform 300 K surface temperature. These heat-transfer rates are the values that were used in the CFD comparisons in Chapter 8. The reference heating rates are computed from the definition of the Stanton number by:

$$q_{ref} = C_H\left[\rho_\infty U_\infty \left(h_{tot} - h_{Tref}\right)\right] \tag{B.1}$$

The purpose of this reference heating rate is to simplify CFD comparisons by specifying a constant wall temperature instead of a temperature distribution. Note that in order to compute the heat-transfer rates at this uniform wall temperature, the Stanton numbers distribution must remain constant. This is the case only if the surface temperature increase is small enough so that lateral conduction effects are minimal. These conditions were met in the HYPULSE tests because the maximum surface temperature rise over the ~100-200 μsec run-time was only on the order of 150 K, which is negligible in comparison to the HYPULSE freestream stagnation temperatures of 6030 K in air or 3700 K in CO_2. However, Eq. (B.1) should only be used to compute heat-transfer rates at a uniform wall temperature within the range of surface temperatures (300 K - 450 K) which were produced in these tests.

Rows where asterisks, '*', are shown instead of heating data indicate that no data are presented for that gage owing to the gage being destroyed or damaged, or due to a high-signal-to-noise ratio, which is indicative of electrical connection problems.

TABLE B.1 HYPULSE Expansion Tube Run Matrix

Run	Model	Gas	α	Fore	Wake	Notes
747	MP-1	CO_2	0°	Y	N	No wake establishment
748	MP-1	CO_2	-4°	Y	Y	
749	MP-1	CO_2	0°	Y	Y	Repeats Run 747
750	MP-2	CO_2	0°	Y	Y	
751	MP-2	CO_2	0°	N	Y	Repeats Run 750, forebody gages damaged
752	MP-1	Air	0°	N	N	Bad run, no data
753	MP-2	Air	0°	Y	Y	
754	MP-1	Air	0°	Y	Y	
755	MP-2	Air	0°	Y	Y	Repeats Run 753
756	MP-2	CO_2	-4°	Y	Y	
757	MP-1	CO_2	-4°	Y	Y	Repeats Run 748
783	MP-1 (SS)	Air	0°	-	Y	Repeats Run 754
784	MP-1 (SS)	Air	-4°	-	Y	
785	MP-1 (SS)	CO_2	-4°	-	Y	Repeats Run 748
786	MP-1 (SS)	CO_2	-8°	-	Y	
787	MP-2 (SS)	Air	0°	-	N	No wake establishment
788	MP-2 (SS)	Air	-4°	-	Y	
789	MP-2 (SS)	CO_2	-4°	-	Y	Repeats Run 756
790	MP-1	Air	0°	Y	N	Repeats Run 754, no wake establishment
791	MP-2	CO_2	-4°	Y	Y	Repeats Run 756
792	MP-2	CO_2	0°	Y	Y	Repeats Run 750
793	MP-3	CO_2	0°	Y	Y	
794	MP-4	CO_2	0°	Y	N	No wake establishment
795	MP-1	Air	-4°	Y	Y	Repeats Run 784
796	MP-3	CO_2	0°	Y	Y	Repeats Run 793
797	MP-4	CO_2	0°	Y	Y	Repeats Run 794
903	MP-1 (SS)	CO_2	0°	-	Y	
904	MP-1 (SS)	CO_2	0°	-	Y	Repeats Run 903
905	MP-1 (SS)	Air	0°	-	Y	
906	MP-1 (SS)	Air	0°	-	Y	Repeats Run 905
907	MP-1 (75%)	CO_2	0°	-	Y	
908	MP-1 (75%)	CO_2	0°	-	Y	Repeats Run 907
909	MP-1 (88%)	CO_2	0°	-	Y	
910	MP-1 (88%)	CO_2	0°	-	Y	Repeats Run 909
911	MP-1 (75%)	Air	0°	-	Y	
912	MP-1 (75%)	Air	0°	-	Y	Repeats Run 912
913	MP-1 (88%)	Air	0°	-	Y	
914	MP-1 (88%)	Air	0°	-	N	Repeats Run 913, no wake establishment

TABLE B.2 HYPULSE Expansion Tube Flow Conditions

Run	Model	Test Gas	U_∞ (m/s)	T_∞ (K)	ρ_∞ (kg/m^3)	p_∞ (Pa)	M_∞	h_{tot}-h_{298} (MJ/kg)
747	MP-1	CO_2	4733	1083	5.899E-03	1207	9.64	12.06
748	MP-1	CO_2	4733	1083	5.899E-03	1208	9.64	12.06
749	MP-1	CO_2	4769	1045	5.750E-03	1133	9.89	12.18
750	MP-2	CO_2	4806	1095	5.700E-03	1180	9.79	12.41
751	MP-2	CO_2	4769	1152	5.867E-03	1278	9.42	12.32
753*	MP-2	Air	5124	1066	5.772E-03	1766	8.03	13.90
754	MP-1	Air	5167	1133	5.713E-03	1859	7.87	14.20
755	MP-2	Air	5167	1182	5.749E-03	1950	7.71	14.26
756	MP-2	CO_2	4788	1147	5.803E-03	1258	9.49	12.40
757	MP-1	CO_2	4769	1028	5.737E-03	1115	9.95	12.16
783	MP-1 SS	Air	5167	1132	5.713E-03	1856	7.87	14.20
784	MP-1 SS	Air	5167	1178	5.746E-03	1943	7.72	14.14
785	MP-1 SS	CO_2	4769	1107	5.819E-03	1218	9.61	12.26
786	MP-1 SS	CO_2	4769	1220	5.936E-03	1369	9.17	12.40
788**	MP-2 SS	Air	5167	1120	5.716E-03	1835	7.91	14.18
789	MP-2 SS	CO_2	4769	1082	5.793E-03	1185	9.72	12.23
790	MP-1	Air	5188	1098	5.634E-03	1776	8.02	14.27
791	MP-2	CO_2	4806	1089	5.691E-03	1171	9.76	12.42
792	MP-2	CO_2	4806	1012	5.585E-03	1035	10.27	12.69
793	MP-3	CO_2	4769	1083	5.793E-03	1186	9.71	12.23
794	MP-4	Air	4787	1097	5.754E-03	1193	9.67	12.33
795	MP-1	CO_2	5167	1111	5.699E-03	1817	7.97	14.17
796	MP-3	CO_2	4882	1213	5.602E-03	1284	9.41	12.94
797	MP-4	CO_2	4806	999	5.606E-03	1059	10.17	12.30
903	MP-1 SS	CO_2	4788	896	5.580E-03	942	10.67	12.09
904	MP-1 SS	CO_2	4806	1071	5.674E-03	1149	9.84	12.36
905	MP-1 SS	Air	4980	956	6.076E-03	1668	8.21	13.10
906	MP-1 SS	Air	5105	1033	5.800E-03	1719	8.12	14.08
907	MP-1 75%	CO_2	4806	1061	5.661E-03	1135	9.88	12.38
908	MP-1 75%	CO_2	4769	1013	5.719E-03	1095	10.03	12.14
909	MP-1 88%	CO_2	4806	946	5.510E-03	992	10.45	12.24
910	MP-1 88%	CO_2	4751	1028	5.789E-03	1125	9.92	12.08
911	MP-1 75%	Air	5167	1055	5.644E-03	1712	8.14	14.16
912	MP-1 75%	Air	5188	1096	5.634E-03	1772	8.03	14.31
913***	MP-1 88%	Air	5188	1065	5.609E-03	1714	8.13	14.28

* No listing for Run 752 (bad data)
** No listing for Run 787 (bad data)
*** No listing for Run 914 (bad data)

TABLE B-3: HYPULSE Run 747 Heating Data

MP-1 Configuration, CO_2 Test Gas, $\alpha = 0$ deg, $C_{H,ref} = 0.024208$

GAGE ID	S/R_b	L/R_b	C_H	s/C_H	$C_H/C_{H,ref}$	q_{300} (W/cm^2)
TF1	-1.872	-	*	0.413	0.004	3.398
TF2	-1.772	-	*	0.250	0.007	5.381
TF3	-1.678	-	*	*	*	*
TF4	-1.554	-	*	*	*	*
TF5	-1.429	-	*	2.516	0.003	2.651
TF6	-1.305	-	*	*	*	*
TF7	-1.180	-	*	*	*	*
TF8	-1.083	-	1.083e-03	0.398	0.045	36.455
TF9	-1.000	-	1.273e-02	0.472	0.526	428.630
TF10	-0.900	-	1.106e-02	0.111	0.457	372.350
TF11	-0.800	-	1.179e-02	0.061	0.487	397.040
TF12	-0.700	-	1.120e-02	0.130	0.463	377.060
TF13	-0.600	-	1.259e-02	0.055	0.520	423.680
TF14	-0.500	-	1.270e-02	0.115	0.525	427.560
TF15	-0.400	-	1.429e-02	0.066	0.590	481.120
TF16	-0.300	-	1.465e-02	0.206	0.605	493.190
TF17	-0.200	-	1.652e-02	0.112	0.682	556.150
TF18	-0.100	-	2.125e-02	0.167	0.878	715.370
TF19	0.000	-	*	*	*	*
TF20	0.100	-	1.968e-02	0.160	0.813	662.420
TF21	0.200	-	1.685e-02	0.150	0.696	567.320
TF22	0.300	-	1.582e-02	0.162	0.654	532.600
TF23	0.400	-	1.395e-02	0.140	0.576	469.770
TF24	0.500	-	1.268e-02	0.145	0.524	427.020
TF25	0.600	-	1.251e-02	0.101	0.517	421.170
TF26	0.700	-	1.125e-02	0.200	0.465	378.740
TF27	0.800	-	1.162e-02	0.141	0.480	391.220
TF28	0.900	-	1.118e-02	0.232	0.462	376.220
TF29	1.000	-	1.104e-02	0.135	0.456	371.580
TF30	1.083	-	1.272e-03	0.337	0.053	42.808
TF31	1.180	-	*	*	*	*
TF32	1.305	-	*	*	*	*
TF33	1.429	-	*	*	*	*
TF34	1.554	-	*	*	*	*
TF35	1.678	-	*	*	*	*
TF36	1.772	-	*	*	*	*
TF37	1.872	-	*	*	*	*
TF38	1.931	0.015	*	*	*	*
TF39	2.036	0.120	*	*	*	*
TF40	2.141	0.225	*	*	*	*
TF41	2.246	0.330	*	*	*	*
TF42	2.351	0.435	*	*	*	*
TF43	2.456	0.540	*	*	*	*
TF44	2.561	0.645	*	*	*	*
TF45	2.666	0.750	*	*	*	*
TF46	2.771	0.855	*	*	*	*
TF47	2.876	0.960	*	*	*	*
TF48	2.981	1.065	*	*	*	*
TF49	3.086	1.170	*	*	*	*
TF50	3.191	1.275	*	*	*	*
TF51	3.296	1.380	*	*	*	*
TF52	3.401	1.485	*	*	*	*
TF53	3.506	1.590	*	*	*	*
TF54	3.611	1.695	*	*	*	*
TF55	3.716	1.800	*	*	*	*
TF56	3.821	1.905	*	*	*	*
TF57	3.926	2.010	*	*	*	*
TF58	4.031	2.115	*	*	*	*
TF59	4.136	2.220	*	*	*	*
TF60	4.241	2.325	*	*	*	*
TF61	4.346	2.430	*	*	*	*
TF62	4.451	2.535	*	*	*	*
TF63	4.556	2.640	*	*	*	*
TF64	4.661	2.745	*	*	*	*
TF65	4.766	2.850	*	*	*	*
TF66	4.871	2.955	*	*	*	*
TF67	4.976	3.060	*	*	*	*
TF68	5.081	3.165	*	*	*	*
TF69	5.186	3.270	*	*	*	*
TF70	5.291	3.375	*	*	*	*

TABLE B-4: HYPULSE Run 748 Heating Data
MP-1 Configuration, CO_2 Test Gas, α = -4 deg, $C_{H,ref}$ = 0.024208

GAGE ID	S/R_b	L/R_b	C_H	s/C_H	$C_H/C_{H,ref}$	q_{300} (W/cm^2)
TF37	-1.872	-	2.224e-04	0.263	0.009	7.488
TF36	-1.772	-	4.600e-04	0.137	0.019	15.487
TF35	-1.678	-	3.525e-04	0.256	0.015	11.866
TF34	-1.554	-	*	*	*	*
TF33	-1.429	-	*	*	*	*
TF32	-1.305	-	*	*	*	*
TF31	-1.180	-	*	*	*	*
TF30	-1.083	-	2.090e-03	0.350	0.086	70.361
TF29	-1.000	-	1.283e-02	0.129	0.530	431.920
TF28	-0.900	-	*	*	*	*
TF27	-0.800	-	1.329e-02	0.118	0.549	447.430
TF26	-0.700	-	*	*	*	*
TF25	-0.600	-	1.233e-02	0.055	0.509	415.110
TF24	-0.500	-	*	*	*	*
TF23	-0.400	-	1.725e-02	0.085	0.713	580.780
TF22	-0.300	-	*	*	*	*
TF21	-0.200	-	2.252e-02	0.108	0.930	758.290
TF20	-0.100	-	*	*	*	*
TF19	0.000	-	*	*	*	*
TF18	0.100	-	2.593e-02	0.129	1.071	873.080
TF17	0.200	-	2.260e-02	0.103	0.933	760.740
TF16	0.300	-	*	*	*	*
TF15	0.400	-	1.925e-02	0.085	0.795	648.080
TF14	0.500	-	*	*	*	*
TF13	0.600	-	1.722e-02	0.073	0.711	579.700
TF12	0.700	-	*	*	*	*
TF11	0.800	-	1.657e-02	0.077	0.685	558.030
TF10	0.900	-	*	*	*	*
TF9	1.000	-	1.466e-02	0.091	0.606	493.650
TF8	1.083	-	1.489e-03	0.574	0.062	50.122
TF7	1.180	-	2.803e-04	0.542	0.012	9.436
TF6	1.305	-	4.009e-04	0.260	0.017	13.498
TF5	1.429	-	3.129e-04	0.088	0.013	10.533
TF4	1.554	-	2.853e-04	0.320	0.012	9.605
TF3	1.678	-	1.185e-04	0.242	0.005	3.990
TF2	1.772	-	1.538e-04	0.233	0.006	5.177
TF1	1.872	-	1.045e-04	0.540	0.004	3.519
TF38	1.931	0.015	6.225e-05	0.879	0.003	2.096
TF39	2.036	0.120	9.564e-05	0.696	0.004	3.220
TF40	2.141	0.225	1.573e-04	0.480	0.006	5.294
TF41	2.246	0.330	2.602e-04	0.413	0.011	8.761
TF42	2.351	0.435	*	*	*	*
TF43	2.456	0.540	4.658e-04	0.192	0.019	15.681
TF44	2.561	0.645	1.028e-03	0.108	0.042	34.600
TF45	2.666	0.750	1.216e-03	0.137	0.050	40.932
TF46	2.771	0.855	*	*	*	*
TF47	2.876	0.960	1.347e-03	0.119	0.056	45.349
TF48	2.981	1.065	1.321e-03	0.114	0.055	44.481
TF49	3.086	1.170	1.270e-03	0.132	0.052	42.749
TF50	3.191	1.275	1.239e-03	0.141	0.051	41.705
TF51	3.296	1.380	1.198e-03	0.081	0.050	40.345
TF52	3.401	1.485	*	*	*	*
TF53	3.506	1.590	1.115e-03	0.070	0.046	37.553
TF54	3.611	1.695	1.105e-03	0.083	0.046	37.190
TF55	3.716	1.800	1.105e-03	0.045	0.046	37.193
TF56	3.821	1.905	1.085e-03	0.079	0.045	36.518
TF57	3.926	2.010	1.142e-03	0.061	0.047	38.453
TF58	4.031	2.115	1.102e-03	0.067	0.046	37.089
TF59	4.136	2.220	1.049e-03	0.036	0.043	35.307
TF60	4.241	2.325	*	*	*	*
TF61	4.346	2.430	9.674e-04	0.080	0.040	32.568
TF62	4.451	2.535	1.002e-03	0.086	0.041	33.737
TF63	4.556	2.640	9.769e-04	0.100	0.040	32.888
TF64	4.661	2.745	9.585e-04	0.093	0.040	32.268
TF65	4.766	2.850	9.261e-04	0.075	0.038	31.180
TF66	4.871	2.955	1.001e-03	0.078	0.041	33.711
TF67	4.976	3.060	9.171e-04	0.091	0.038	30.877
TF68	5.081	3.165	9.641e-04	0.092	0.040	32.458
TF69	5.186	3.270	9.784e-04	0.070	0.040	32.941
TF70	5.291	3.375	9.714e-04	0.084	0.040	32.702

TABLE B-5 : HYPULSE Run 749 Heating Data

MP-1 Configuration, CO_2 Test Gas, $\alpha = 0$ deg, $C_{H,ref} = 0.024208$

GAGE ID	S/R_b	L/R_b	C_H	s/C_H	$C_H/C_{H,ref}$	q_{300} (W/cm^2)
TF1	-1.872	-	1.204e-04	0.373	0.005	4.020
TF2	-1.772	-	1.873e-04	0.466	0.008	6.255
TF3	-1.678	-	1.303e-04	0.771	0.005	4.350
TF4	-1.554	-	*	*	*	*
TF5	-1.429	-	*	*	*	*
TF6	-1.305	-	*	*	*	*
TF7	-1.180	-	*	*	*	*
TF8	-1.083	-	9.603e-04	1.203	0.040	32.070
TF9	-1.000	-	1.164e-02	0.137	0.481	388.830
TF10	-0.900	-	1.235e-02	0.215	0.510	412.420
TF11	-0.800	-	1.243e-02	0.113	0.513	415.000
TF12	-0.700	-	*	*	*	*
TF13	-0.600	-	1.333e-02	0.080	0.550	445.010
TF14	-0.500	-	1.454e-02	0.228	0.601	485.510
TF15	-0.400	-	*	*	*	*
TF16	-0.300	-	1.565e-02	0.219	0.646	522.630
TF17	-0.200	-	1.741e-02	0.060	0.719	581.430
TF18	-0.100	-	2.281e-02	0.173	0.942	761.790
TF19	0.000	-	2.421e-02	0.132	1.000	808.420
TF20	0.100	-	2.317e-02	0.188	0.957	773.740
TF21	0.200	-	1.752e-02	0.081	0.724	584.940
TF22	0.300	-	1.519e-02	0.162	0.627	507.140
TF23	0.400	-	1.478e-02	0.066	0.611	493.650
TF24	0.500	-	1.391e-02	0.187	0.575	464.510
TF25	0.600	-	1.352e-02	0.060	0.559	451.680
TF26	0.700	-	1.257e-02	0.174	0.519	419.910
TF27	0.800	-	1.222e-02	0.054	0.505	408.230
TF28	0.900	-	1.190e-02	0.209	0.491	397.330
TF29	1.000	-	1.242e-02	0.067	0.513	414.820
TF30	1.083	-	4.448e-04	1.966	0.018	14.853
TF31	1.180	-	*	*	*	*
TF32	1.305	-	*	*	*	*
TF33	1.429	-	*	*	*	*
TF34	1.554	-	1.709e-04	1.229	0.007	5.708
TF35	1.678	-	8.483e-05	0.505	0.004	2.833
TF36	1.772	-	1.190e-04	0.415	0.005	3.973
TF37	1.872	-	6.565e-05	0.506	0.003	2.192
TF38	1.931	0.015	*	*	*	*
TF39	2.036	0.120	9.568e-05	0.455	0.004	3.195
TF40	2.141	0.225	1.351e-04	0.409	0.006	4.512
TF41	2.246	0.330	1.337e-04	0.322	0.006	4.464
TF42	2.351	0.435	1.855e-04	0.169	0.008	6.194
TF43	2.456	0.540	1.269e-04	0.312	0.005	4.238
TF44	2.561	0.645	2.099e-04	0.191	0.009	7.011
TF45	2.666	0.750	2.563e-04	0.191	0.011	8.559
TF46	2.771	0.855	*	*	*	*
TF47	2.876	0.960	5.021e-04	0.164	0.021	16.769
TF48	2.981	1.065	6.427e-04	0.131	0.027	21.463
TF49	3.086	1.170	7.330e-04	0.129	0.030	24.477
TF50	3.191	1.275	8.393e-04	0.112	0.035	28.028
TF51	3.296	1.380	8.839e-04	0.169	0.037	29.519
TF52	3.401	1.485	9.563e-04	0.089	0.040	31.934
TF53	3.506	1.590	9.603e-04	0.133	0.040	32.070
TF54	3.611	1.695	9.590e-04	0.142	0.040	32.026
TF55	3.716	1.800	1.010e-03	0.137	0.042	33.715
TF56	3.821	1.905	9.370e-04	0.150	0.039	31.292
TF57	3.926	2.010	8.835e-04	0.118	0.036	29.505
TF58	4.031	2.115	8.817e-04	0.144	0.036	29.444
TF59	4.136	2.220	8.763e-04	0.112	0.036	29.264
TF60	4.241	2.325	*	*	*	*
TF61	4.346	2.430	7.887e-04	0.133	0.033	26.340
TF62	4.451	2.535	7.701e-04	0.164	0.032	25.718
TF63	4.556	2.640	8.267e-04	0.128	0.034	27.608
TF64	4.661	2.745	7.264e-04	0.139	0.030	24.258
TF65	4.766	2.850	6.785e-04	0.127	0.028	22.658
TF66	4.871	2.955	7.351e-04	0.131	0.030	24.547
TF67	4.976	3.060	6.648e-04	0.140	0.027	22.200
TF68	5.081	3.165	*	*	*	*
TF69	5.186	3.270	7.162e-04	0.148	0.030	23.919
TF70	5.291	3.375	6.515e-04	0.156	0.027	21.757

TABLE B-6: HYPULSE Run 750 Heating Data

MP-2 Configuration, CO_2 Test Gas, $\alpha = 0$ deg, $C_{H,ref} = 0.019086$

GAGE ID	S/R_b	L/R_b	C_H	s/C_H	$C_H/C_{H,ref}$	q_{300} (W/cm^2)
TF1	-1.864	-	*	*	*	*
TF2	-1.764	-	7.084e-05	2.781	0.004	2.408
TF3	-1.670	-	5.014e-05	1.539	0.003	1.704
TF4	-1.545	-	5.195e-05	2.569	0.003	1.766
TF5	-1.421	-	*	*	*	*
TF6	-1.296	-	1.306e-05	14.847	0.001	0.444
TF7	-1.172	-	*	*	*	*
TF8	-1.075	-	1.373e-03	0.296	0.072	46.666
TF9	-1.000	-	1.061e-02	0.104	0.556	360.580
TF10	-0.900	-	1.185e-02	0.129	0.621	402.730
TF11	-0.800	-	1.170e-02	0.122	0.613	397.740
TF12	-0.700	-	1.156e-02	0.102	0.606	392.820
TF13	-0.600	-	1.214e-02	0.113	0.636	412.680
TF14	-0.500	-	*	*	*	*
TF15	-0.400	-	1.308e-02	0.116	0.685	444.530
TF16	-0.300	-	*	*	*	*
TF17	-0.200	-	*	*	*	*
TF18	-0.100	-	1.894e-02	0.068	0.992	643.880
TF19	0.000	-	1.735e-02	0.061	0.909	589.880
TF20	0.100	-	1.811e-02	0.074	0.949	615.530
TF21	0.200	-	1.586e-02	0.051	0.831	539.060
TF22	0.300	-	1.368e-02	0.117	0.717	465.030
TF23	0.400	-	1.332e-02	0.119	0.698	452.800
TF24	0.500	-	1.299e-02	0.143	0.681	441.550
TF25	0.600	-	1.201e-02	0.158	0.629	408.370
TF26	0.700	-	*	*	*	*
TF27	0.800	-	1.219e-02	0.139	0.639	414.400
TF28	0.900	-	1.277e-02	0.125	0.669	434.140
TF29	1.000	-	1.158e-02	0.144	0.607	393.700
TF30	1.075	-	1.380e-03	0.288	0.072	46.897
TF31	1.172	-	4.969e-05	3.930	0.003	1.689
TF32	1.296	-	3.514e-05	5.413	0.002	1.194
TF33	1.421	-	*	*	*	*
TF34	1.545	-	*	*	*	*
TF35	1.670	-	4.869e-05	0.753	0.003	1.655
TF36	1.764	-	4.413e-05	2.947	0.002	1.500
TF37	1.864	-	*	*	*	*
TF38	1.923	0.015	7.565e-05	0.647	0.004	2.572
TF39	2.027	0.120	9.209e-05	0.665	0.005	3.131
TF40	2.132	0.225	1.088e-04	0.607	0.006	3.700
TF41	2.237	0.330	8.243e-05	0.802	0.004	2.802
TF42	2.343	0.435	*	*	*	*
TF43	2.447	0.540	1.456e-04	0.273	0.008	4.949
TF44	2.553	0.645	*	*	*	*
TF45	2.658	0.750	*	*	*	*
TF46	2.763	0.855	*	*	*	*
TF47	2.868	0.960	3.971e-04	0.099	0.021	13.500
TF48	2.973	1.065	4.818e-04	0.106	0.025	16.378
TF49	3.078	1.170	6.662e-04	0.179	0.035	22.646
TF50	3.182	1.275	7.510e-04	0.247	0.039	25.527
TF51	3.288	1.380	*	*	*	*
TF52	3.392	1.485	8.862e-04	0.203	0.046	30.124
TF53	3.497	1.590	8.730e-04	0.120	0.046	29.675
TF54	3.602	1.695	9.071e-04	0.190	0.048	30.833
TF55	3.707	1.800	8.926e-04	0.140	0.047	30.340
TF56	3.813	1.905	8.951e-04	0.189	0.047	30.426
TF57	3.918	2.010	*	*	*	*
TF58	4.023	2.115	8.829e-04	0.157	0.046	30.011
TF59	4.128	2.220	8.030e-04	0.110	0.042	27.296
TF60	4.233	2.325	8.149e-04	0.141	0.043	27.701
TF61	4.338	2.430	*	*	*	*
TF62	4.443	2.535	7.459e-04	0.194	0.039	25.354
TF63	4.548	2.640	6.729e-04	0.139	0.035	22.872
TF64	4.653	2.745	6.345e-04	0.132	0.033	21.568
TF65	4.758	2.850	6.478e-04	0.124	0.034	22.021
TF66	4.863	2.955	6.414e-04	0.143	0.034	21.803
TF67	4.968	3.060	5.555e-04	0.163	0.029	18.881
TF68	5.073	3.165	5.687e-04	0.133	0.030	19.330
TF69	5.177	3.270	5.712e-04	0.097	0.030	19.415
TF70	5.282	3.375	5.771e-04	0.119	0.030	19.616

TABLE B-7: HYPULSE Run 751 Heating Data

MP-2 Configuration, CO_2 Test Gas, $\alpha = 0$ deg, $C_{H,ref} = 0.019086$

GAGE ID	S/R_b	L/R_b	C_H	s/C_H	$C_H/C_{H,ref}$	q_{300} (W/cm^2)
TF1	-1.864	-	*	*	*	*
TF2	-1.764	-	*	*	*	*
TF3	-1.670	-	*	*	*	*
TF4	-1.545	-	*	*	*	*
TF5	-1.421	-	*	*	*	*
TF6	-1.296	-	*	*	*	*
TF7	-1.172	-	*	*	*	*
TF8	-1.075	-	*	*	*	*
TF9	-1.000	-	*	*	*	*
TF10	-0.900	-	*	*	*	*
TF11	-0.800	-	*	*	*	*
TF12	-0.700	-	*	*	*	*
TF13	-0.600	-	*	*	*	*
TF14	-0.500	-	*	*	*	*
TF15	-0.400	-	*	*	*	*
TF16	-0.300	-	*	*	*	*
TF17	-0.200	-	*	*	*	*
TF18	-0.100	-	*	*	*	*
TF19	0.000	-	*	*	*	*
TF20	0.100	-	*	*	*	*
TF21	0.200	-	*	*	*	*
TF22	0.300	-	*	*	*	*
TF23	0.400	-	*	*	*	*
TF24	0.500	-	*	*	*	*
TF25	0.600	-	*	*	*	*
TF26	0.700	-	*	*	*	*
TF27	0.800	-	*	*	*	*
TF28	0.900	-	*	*	*	*
TF29	1.000	-	*	*	*	*
TF30	1.075	-	*	*	*	*
TF31	1.172	-	*	*	*	*
TF32	1.296	-	*	*	*	*
TF33	1.421	-	*	*	*	*
TF34	1.545	-	*	*	*	*
TF35	1.670	-	*	*	*	*
TF36	1.764	-	*	*	*	*
TF37	1.864	-	*	*	*	*
TF38	1.923	0.015	*	*	*	*
TF39	2.027	0.120	6.707e-05	0.318	0.004	2.312
TF40	2.132	0.225	7.764e-05	1.031	0.004	2.676
TF41	2.237	0.330	1.042e-04	0.379	0.005	3.591
TF42	2.342	0.435	1.618e-04	0.224	0.008	5.577
TF43	2.447	0.540	9.926e-05	0.183	0.005	3.421
TF44	2.553	0.645	2.795e-04	0.176	0.015	9.635
TF45	2.658	0.750	3.088e-04	0.276	0.016	10.644
TF46	2.763	0.855	*	*	*	*
TF47	2.868	0.960	5.251e-04	0.152	0.028	18.098
TF48	2.973	1.065	6.468e-04	0.137	0.034	22.292
TF49	3.078	1.170	7.306e-04	0.123	0.038	25.182
TF50	3.182	1.275	7.644e-04	0.133	0.040	26.346
TF51	3.287	1.380	7.579e-04	0.333	0.040	26.121
TF52	3.392	1.485	8.420e-04	0.155	0.044	29.022
TF53	3.497	1.590	8.243e-04	0.275	0.043	28.412
TF54	3.603	1.695	*	*	*	*
TF55	3.707	1.800	*	*	*	*
TF56	3.813	2.905	*	*	*	*
TF57	3.918	2.010	*	*	*	*
TF58	4.023	2.115	*	*	*	*
TF59	4.128	2.220	*	*	*	*
TF60	4.233	2.325	7.679e-04	0.196	0.040	26.468
TF61	4.338	2.430	*	*	*	*
TF62	4.443	2.535	6.624e-04	0.203	0.035	22.830
TF63	4.548	2.640	*	*	*	*
TF64	4.653	2.745	7.146e-04	0.124	0.037	24.628
TF65	4.758	2.850	6.726e-04	0.061	0.035	23.182
TF66	4.863	2.955	7.119e-04	0.094	0.037	24.535
TF67	4.968	3.060	6.073e-04	0.058	0.032	20.932
TF68	5.073	3.165	*	*	*	*
TF69	5.177	3.270	6.138e-04	0.107	0.032	21.157
TF70	5.282	3.375	6.035e-04	0.045	0.032	20.802

TABLE B-8: HYPULSE Run 752 Heating Data
MP-1 Configuration, Air Test Gas, $\alpha = 0$ deg, $C_{H,ref} = 0.031279$

** BAD RUN, NO DATA **

TABLE B-9: HYPULSE Run 753 Heating Data

MP-2 Configuration, Air Test Gas, $\alpha = 0$ deg, $C_{H,ref} = 0.025565$

GAGE ID	S/R_b	L/R_b	C_H	s/C_H	$C_H/C_{H,ref}$	q_{300} (W/cm^2)
TF1	-1.864	-	2.330e-04	0.191	0.009	9.576
TF2	-1.764	-	*	*	*	*
TF3	-1.670	-	2.418e-04	0.357	0.009	9.938
TF4	-1.545	-	8.623e-04	0.220	0.034	35.445
TF5	-1.421	-	7.542e-04	0.198	0.030	31.002
TF6	-1.296	-	1.238e-03	0.125	0.048	50.903
TF7	-1.172	-	7.657e-04	0.315	0.030	31.472
TF8	-1.075	-	3.410e-03	0.301	0.133	140.170
TF9	-1.000	-	*	*	*	*
TF10	-0.900	-	*	*	*	*
TF11	-0.800	-	1.961e-02	0.152	0.767	806.140
TF12	-0.700	-	*	*	*	*
TF13	-0.600	-	1.808e-02	0.242	0.707	743.300
TF14	-0.500	-	1.969e-02	0.261	0.770	809.530
TF15	-0.400	-	1.956e-02	0.289	0.765	804.000
TF16	-0.300	-	2.261e-02	0.309	0.885	929.520
TF17	-0.200	-	2.169e-02	0.549	0.849	891.690
TF18	-0.100	-	2.552e-02	0.178	0.998	1048.900
TF19	0.000	-	*	*	*	*
TF20	0.100	-	2.600e-02	0.085	1.017	1068.900
TF21	0.200	-	2.311e-02	0.103	0.904	949.850
TF22	0.300	-	1.913e-02	0.184	0.748	786.430
TF23	0.400	-	1.667e-02	0.102	0.652	685.010
TF24	0.500	-	1.596e-02	0.122	0.624	656.000
TF25	0.600	-	1.515e-02	0.053	0.592	622.610
TF26	0.700	-	1.681e-02	0.179	0.658	690.950
TF27	0.800	-	1.628e-02	0.118	0.637	669.120
TF28	0.900	-	1.747e-02	0.180	0.683	718.170
TF29	1.000	-	1.759e-02	0.099	0.688	723.190
TF30	1.075	-	2.638e-03	0.195	0.103	108.430
TF31	1.172	-	3.010e-04	0.536	0.012	12.374
TF32	1.296	-	5.329e-04	0.231	0.021	21.906
TF33	1.421	-	5.731e-04	0.348	0.022	23.556
TF34	1.545	-	5.602e-04	0.346	0.022	23.028
TF35	1.670	-	4.243e-04	0.239	0.017	17.440
TF36	1.764	-	*	*	*	*
TF37	1.864	-	4.362e-04	0.168	0.017	17.928
TF38	1.923	0.015	*	*	*	*
TF39	2.028	0.120	*	*	*	*
TF40	2.133	0.225	*	*	*	*
TF41	2.238	0.330	*	*	*	*
TF42	2.343	0.435	*	*	*	*
TF43	2.448	0.540	*	*	*	*
TF44	2.553	0.645	*	*	*	*
TF45	2.658	0.750	*	*	*	*
TF46	2.763	0.855	*	*	*	*
TF47	2.868	0.960	7.792e-04	0.194	0.030	32.027
TF48	2.973	1.065	9.191e-04	0.200	0.036	37.778
TF49	3.078	1.170	8.942e-04	0.354	0.035	36.756
TF50	3.288	1.275	*	*	*	*
TF51	3.393	1.380	*	*	*	*
TF52	3.392	1.485	1.302e-03	0.296	0.051	53.498
TF53	3.497	1.485	1.404e-03	0.132	0.055	57.704
TF54	3.602	1.590	1.382e-03	0.271	0.054	56.811
TF55	3.707	1.695	1.441e-03	0.158	0.056	59.248
TF56	3.813	1.800	*	*	*	*
TF57	3.918	2.010	1.477e-03	0.247	0.058	60.718
TF58	4.023	2.115	*	*	*	*
TF59	4.128	2.220	1.430e-03	0.272	0.056	58.790
TF60	4.233	2.325	*	*	*	*
TF61	4.338	2.430	1.417e-03	0.249	0.055	58.264
TF62	4.443	2.535	1.457e-03	0.183	0.057	59.900
TF63	4.548	2.640	1.323e-03	0.232	0.052	54.371
TF64	4.653	2.745	*	*	*	*
TF65	4.758	2.850	*	*	*	*
TF66	4.863	2.955	*	*	*	*
TF67	4.968	3.060	*	*	*	*
TF68	5.073	3.165	*	*	*	*
TF69	5.178	3.270	*	*	*	*
TF70	5.283	3.375	*	*	*	*

TABLE B-10: HYPULSE Run 754 Heating Data

MP-1 Configuration, Air Test Gas, $\alpha = 0$ deg, $C_{H,ref} = 0.031279$

GAGE ID	S/R_b	L/R_b	C_H	s/C_H	$C_H/C_{H,ref}$	q_{300} (W/cm^2)
TF1	-1.872	-	2.698e-04	2.023	0.009	11.307
TF2	-1.772	-	2.746e-04	2.105	0.009	11.508
TF3	-1.678	-	1.500e-04	0.780	0.005	6.285
TF4	-1.554	-	*	*	*	*
TF5	-1.429	-	8.517e-04	2.175	0.027	35.694
TF6	-1.305	-	1.286e-04	17.853	0.004	5.389
TF7	-1.180	-	*	*	*	*
TF8	-1.083	-	3.708e-03	2.334	0.119	155.410
TF9	-1.000	-	*	*	*	*
TF10	-0.900	-	2.227e-02	0.778	0.712	933.200
TF11	-0.800	-	1.753e-02	0.331	0.561	734.800
TF12	-0.700	-	1.796e-02	0.621	0.574	752.660
TF13	-0.600	-	1.574e-02	0.136	0.503	659.770
TF14	-0.500	-	1.697e-02	0.330	0.543	711.270
TF15	-0.400	-	1.748e-02	0.159	0.559	732.520
TF16	-0.300	-	1.938e-02	0.322	0.619	812.080
TF17	-0.200	-	2.107e-02	0.051	0.674	883.000
TF18	-0.100	-	2.829e-02	0.035	0.905	1185.900
TF19	0.000	-	3.128e-02	0.186	1.000	1310.900
TF20	0.100	-	2.397e-02	0.161	0.766	1004.500
TF21	0.200	-	*	*	*	*
TF22	0.300	-	*	*	*	*
TF23	0.400	-	1.764e-02	0.170	0.564	739.440
TF24	0.500	-	*	*	*	*
TF25	0.600	-	1.646e-02	0.186	0.526	689.650
TF26	0.700	-	*	*	*	*
TF27	0.800	-	1.633e-02	0.816	0.522	684.320
TF28	0.900	-	*	*	*	*
TF29	1.000	-	1.858e-02	0.575	0.594	778.560
TF30	1.083	-	*	*	*	*
TF31	1.180	-	*	*	*	*
TF32	1.305	-	*	*	*	*
TF33	1.429	-	1.579e-04	12.478	0.005	6.619
TF34	1.554	-	4.467e-04	4.109	0.014	18.724
TF35	1.678	-	*	*	*	*
TF36	1.772	-	5.347e-04	1.208	0.017	22.411
TF37	1.872	-	4.165e-04	1.547	0.013	17.454
TF38	1.931	0.015	*	*	*	*
TF39	2.036	0.120	*	*	*	*
TF40	2.141	0.225	*	*	*	*
TF41	2.246	0.330	*	*	*	*
TF42	2.351	0.435	*	*	*	*
TF43	2.456	0.540	*	*	*	*
TF44	2.561	0.645	*	*	*	*
TF45	2.666	0.750	*	*	*	*
TF46	2.771	0.855	*	*	*	*
TF47	2.876	0.960	6.507e-04	0.085	0.021	27.272
TF48	2.981	1.065	8.359e-04	0.082	0.027	35.031
TF49	3.086	1.170	1.046e-03	0.110	0.033	43.852
TF50	3.191	1.275	1.279e-03	0.137	0.041	53.589
TF51	3.296	1.380	1.347e-03	0.099	0.043	56.453
TF52	3.401	1.485	*	*	*	*
TF53	3.506	1.590	1.593e-03	0.045	0.051	66.748
TF54	3.611	1.695	1.760e-03	0.055	0.056	73.754
TF55	3.716	1.800	1.634e-03	0.063	0.052	68.476
TF56	3.821	1.905	*	*	*	*
TF57	3.926	2.010	*	*	*	*
TF58	4.031	2.115	*	*	*	*
TF59	4.136	2.220	*	*	*	*
TF60	4.241	2.325	*	*	*	*
TF61	4.346	2.430	1.582e-03	0.138	0.051	66.309
TF62	4.451	2.535	*	*	*	*
TF63	4.556	2.640	*	*	*	*
TF64	4.661	2.745	1.449e-03	0.107	0.046	60.726
TF65	4.766	2.850	*	*	*	*
TF66	4.871	2.955	1.448e-03	0.125	0.046	60.699
TF67	4.976	3.060	*	*	*	*
TF68	5.081	3.165	*	*	*	*
TF69	5.186	3.270	1.260e-03	0.120	0.040	52.789
TF70	5.291	3.375	1.043e-03	0.085	0.033	43.722

TABLE B-11: HYPULSE Run 755 Heating Data

MP-2 Configuration, Air Test Gas, $\alpha = 0$ deg, $C_{H,ref} = 0.025565$

GAGE ID	S/R_b	L/R_b	C_H	s/C_H	$C_H/C_{H,ref}$	q_{300} (W/cm^2)
TF1	-1.864	-	1.110e-04	0.325	0.004	4.699
TF2	-1.764	-	*	*	*	*
TF3	-1.670	-	2.490e-04	0.068	0.010	10.547
TF4	-1.545	-	*	*	*	*
TF5	-1.421	-	6.770e-04	0.112	0.026	28.675
TF6	-1.296	-	9.134e-04	0.047	0.036	38.684
TF7	-1.172	-	9.064e-04	0.095	0.035	38.389
TF8	-1.075	-	3.738e-03	0.071	0.146	158.310
TF9	-1.000	-	2.342e-02	0.137	0.916	992.000
TF10	-0.900	-	2.045e-02	0.121	0.800	866.090
TF11	-0.800	-	1.874e-02	0.065	0.733	793.740
TF12	-0.700	-	1.795e-02	0.256	0.702	760.020
TF13	-0.600	-	1.798e-02	0.044	0.703	761.430
TF14	-0.500	-	1.759e-02	0.273	0.688	745.150
TF15	-0.400	-	1.808e-02	0.023	0.707	765.700
TF16	-0.300	-	1.738e-02	0.078	0.680	736.220
TF17	-0.200	-	2.165e-02	0.040	0.847	917.050
TF18	-0.100	-	*	*	*	*
TF19	0.000	-	2.557e-02	0.067	1.000	1082.800
TF20	0.100	-	*	*	*	*
TF21	0.200	-	2.208e-02	0.075	0.864	935.280
TF22	0.300	-	2.027e-02	0.125	0.793	858.590
TF23	0.400	-	1.703e-02	0.076	0.666	721.330
TF24	0.500	-	1.695e-02	0.076	0.663	718.060
TF25	0.600	-	1.540e-02	0.057	0.602	652.200
TF26	0.700	-	1.551e-02	0.039	0.607	657.050
TF27	0.800	-	1.592e-02	0.054	0.623	674.360
TF28	0.900	-	1.736e-02	0.075	0.679	735.120
TF29	1.000	-	1.809e-02	0.038	0.708	766.230
TF30	1.075	-	3.041e-03	0.048	0.119	128.800
TF31	1.172	-	4.785e-04	0.155	0.019	20.267
TF32	1.296	-	2.821e-04	0.166	0.011	11.947
TF33	1.421	-	1.338e-04	0.256	0.005	5.667
TF34	1.545	-	3.694e-04	0.146	0.014	15.646
TF35	1.670	-	2.415e-04	0.314	0.009	10.227
TF36	1.764	-	5.585e-04	0.214	0.022	23.654
TF37	1.864	-	*	*	*	*
TF38	1.923	0.015	*	*	*	*
TF39	2.028	0.120	*	*	*	*
TF40	2.133	0.225	*	*	*	*
TF41	2.238	0.330	*	*	*	*
TF41	2.343	0.435	*	*	*	*
TF43	2.448	0.540	*	*	*	*
TF44	2.553	0.645	*	*	*	*
TF45	2.658	0.750	*	*	*	*
TF46	2.763	0.855	*	*	*	*
TF47	2.868	0.960	3.934e-04	0.096	0.015	16.661
TF48	2.973	1.065	4.951e-04	0.067	0.019	20.968
TF49	3.078	1.170	7.800e-04	0.143	0.031	33.036
TF50	3.182	1.275	9.414e-04	0.198	0.037	39.871
TF51	3.287	1.380	*	*	*	*
TF52	3.392	1.485	*	*	*	*
TF53	3.497	1.590	1.300e-03	0.194	0.051	55.068
TF54	3.602	1.695	1.311e-03	0.192	0.051	55.513
TF55	3.707	1.800	1.398e-03	0.157	0.055	59.205
TF56	3.813	1.905	*	*	*	*
TF57	3.918	2.010	*	*	*	*
TF58	4.023	2.115	*	*	*	*
TF59	4.128	2.220	*	*	*	*
TF60	4.233	2.325	1.229e-03	0.085	0.048	52.068
TF61	4.338	2.430	1.373e-03	0.101	0.054	58.139
TF62	4.443	2.535	*	*	*	*
TF63	4.548	2.535	*	*	*	*
TF64	4.653	2.745	1.292e-03	0.118	0.051	54.740
TF65	4.758	2.850	*	*	*	*
TF66	4.863	2.955	*	*	*	*
TF67	4.968	3.060	*	*	*	*
TF68	5.073	3.165	*	*	*	*
TF69	5.177	3.270	7.555e-04	0.266	0.030	31.998
TF70	5.282	3.375	6.367e-04	0.168	0.025	26.964

TABLE B-12: HYPULSE Run 756 Heating Data
MP-2 Configuration, CO_2 Test Gas, α = -4 deg, $C_{H,ref}$ = 0.019086

GAGE ID	S/R_b	L/R_b	C_H	s/C_H	$C_H/C_{H,ref}$	q_{300} (W/cm^2)
TF37	-1.864	-	2.357e-04	0.365	0.012	8.119
TF36	-1.764	-	2.159e-04	0.318	0.011	7.437
TF35	-1.670	-	1.685e-04	0.546	0.009	5.805
TF34	-1.545	-	1.419e-04	1.014	0.007	4.889
TF33	-1.421	-	1.585e-04	1.164	0.008	5.461
TF32	-1.296	-	5.454e-05	1.978	0.003	1.879
TF31	-1.172	-	1.534e-04	0.327	0.008	5.285
TF30	-1.075	-	2.774e-03	0.039	0.145	95.567
TF29	-1.000	-	1.079e-02	0.047	0.565	371.820
TF28	-0.900	-	1.049e-02	0.047	0.550	361.280
TF27	-0.800	-	1.045e-02	0.029	0.548	360.090
TF26	-0.700	-	9.893e-03	0.116	0.518	340.800
TF25	-0.600	-	1.028e-02	0.083	0.539	354.090
TF24	-0.500	-	1.128e-02	0.082	0.591	388.750
TF23	-0.400	-	1.132e-02	0.115	0.593	389.800
TF22	-0.300	-	1.248e-02	0.106	0.654	429.960
TF21	-0.200	-	1.316e-02	0.091	0.690	453.390
TF20	-0.100	-	1.639e-02	0.095	0.859	564.500
TF19	0.000	-	1.655e-02	0.147	0.867	570.180
TF18	0.100	-	1.790e-02	0.048	0.938	616.720
TF17	0.200	-	1.451e-02	0.112	0.760	500.000
TF16	0.300	-	1.312e-02	0.079	0.687	451.810
TF15	0.400	-	1.295e-02	0.072	0.678	445.950
TF14	0.500	-	1.246e-02	0.196	0.653	429.300
TF13	0.600	-	1.272e-02	0.116	0.667	438.210
TF12	0.700	-	*	*	*	*
TF11	0.800	-	*	*	*	*
TF10	0.900	-	1.376e-02	0.143	0.721	473.980
TF9	1.000	-	1.330e-02	0.117	0.697	458.030
TF8	1.075	-	2.034e-03	0.180	0.107	70.063
TF7	1.172	-	2.131e-04	0.211	0.011	7.341
TF6	1.296	-	3.450e-04	0.134	0.018	11.885
TF5	1.421	-	2.571e-04	0.187	0.013	8.858
TF4	1.545	-	*	*	*	*
TF3	1.670	-	8.072e-05	0.508	0.004	2.781
TF2	1.764	-	1.865e-04	0.232	0.010	6.425
TF1	1.864	-	6.571e-05	2.037	0.003	2.263
TF38	1.923	0.015	*	*	*	*
TF39	2.028	0.120	*	*	*	*
TF40	2.133	0.225	*	*	*	*
TF41	2.238	0.330	*	*	*	*
TF42	2.343	0.435	*	*	*	*
TF43	2.448	0.540	*	*	*	*
TF44	2.553	0.645	*	*	*	*
TF45	2.658	0.750	*	*	*	*
TF46	2.763	0.855	*	*	*	*
TF47	2.868	0.960	1.370e-03	0.052	0.072	47.187
TF48	2.973	1.065	1.325e-03	0.075	0.069	45.656
TF49	3.078	1.170	1.204e-03	0.112	0.063	41.489
TF50	3.183	1.275	*	*	*	*
TF51	3.288	1.380	*	*	*	*
TF52	3.393	1.485	*	*	*	*
TF53	3.498	1.590	*	*	*	*
TF54	3.603	1.695	*	*	*	*
TF55	3.707	1.800	1.087e-03	0.194	0.057	37.444
TF56	3.813	1.905	*	*	*	*
TF57	3.918	1.905	1.152e-03	0.103	0.060	39.699
TF58	4.023	2.010	1.025e-03	0.166	0.054	35.319
TF59	4.128	2.115	1.087e-03	0.185	0.057	37.443
TF60	4.233	2.220	9.871e-04	0.181	0.052	34.005
TF61	4.338	2.325	1.031e-03	0.159	0.054	35.499
TF62	4.443	2.430	1.027e-03	0.141	0.054	35.370
TF63	4.548	2.640	1.032e-03	0.177	0.054	35.538
TF64	4.653	2.745	*	*	*	*
TF65	4.758	2.850	*	*	*	*
TF66	4.863	2.955	*	*	*	*
TF67	4.968	3.060	*	*	*	*
TF68	5.073	3.165	*	*	*	*
TF69	5.178	3.270	*	*	*	*
TF70	5.283	3.375	*	*	*	*

TABLE B-13: HYPULSE Run 757 Heating Data

MP-1 Configuration, CO_2 Test Gas, α = -4 deg, $C_{H,ref}$ = 0.024208

GAGE ID	S/R_b	L/R_b	C_H	s/C_H	$C_H/C_{H,ref}$	q_{300} (W/cm^2)
TF37	-1.872		3.272e-04	0.652	0.014	10.884
TF36	-1.772	-	1.456e-04	0.695	0.006	4.843
TF35	-1.678	-	*	*	*	*
TF34	-1.554	-	*	*	*	*
TF33	-1.429	-	*	*	*	*
TF32	-1.305	-	*	*	*	*
TF31	-1.180	-	*	*	*	*
TF30	-1.083	-	9.086e-03	0.261	0.375	302.260
TF29	-1.000	-	*	*	*	*
TF28	-0.900	-	1.002e-02	0.199	0.414	333.170
TF27	-0.800	-	*	*	*	*
TF26	-0.700	-	1.231e-02	0.211	0.508	409.350
TF25	-0.600	-	*	*	*	*
TF24	-0.500	-	1.293e-02	0.278	0.534	429.970
TF23	-0.400	-	1.421e-02	0.686	0.587	472.520
TF22	-0.300	-	1.789e-02	0.312	0.739	595.200
TF21	-0.200	-	*	*	*	*
TF20	-0.100	-	*	*	*	*
TF19	0.000	-	2.469e-02	0.347	1.020	821.480
TF18	0.100	-	2.080e-02	0.432	0.859	692.030
TF17	0.200	-	1.729e-02	0.977	0.714	575.130
TF16	0.300	-	1.493e-02	0.350	0.617	496.790
TF15	0.400	-	*	*	*	*
TF14	0.500	-	1.491e-02	0.251	0.616	496.040
TF13	0.600	-	1.444e-02	0.452	0.596	480.210
TF12	0.700	-	*	*	*	*
TF11	0.600	-	*	*	*	*
TF10	0.900	-	1.408e-02	0.288	0.582	468.450
TF9	1.000	-	1.226e-02	0.070	0.506	407.730
TF8	1.083	-	*	*	*	*
TF7	1.180	-	*	*	*	*
TF6	1.305	-	*	*	*	*
TF5	1.429	-	*	*	*	*
TF4	1.554	-	*	*	*	*
TF3	1.678	-	1.451e-04	1.068	0.006	4.826
TF2	1.772	-	5.387e-05	4.762	0.002	1.792
TF1	1.872	-	*	*	*	*
TF38	1.931	0.015	*	*	*	*
TF39	2.036	0.120	*	*	*	*
TF40	2.141	0.225	*	*	*	*
TF41	2.246	0.330	*	*	*	*
TF42	2.351	0.435	*	*	*	*
TF43	2.456	0.540	*	*	*	*
TF44	2.561	0.645	*	*	*	*
TF45	2.666	0.750	*	*	*	*
TF46	2.771	0.855	*	*	*	*
TF47	2.876	0.960	*	*	*	*
TF48	2.981	1.065	1.262e-03	0.064	0.052	41.977
TF49	3.086	1.170	1.208e-03	0.093	0.050	40.177
TF50	3.191	1.275	*	*	*	*
TF51	3.296	1.380	*	*	*	*
TF52	3.401	1.485	*	*	*	*
TF53	3.506	1.590	*	*	*	*
TF54	3.611	1.695	*	*	*	*
TF55	3.716	1.800	1.104e-03	0.142	0.046	36.730
TF56	3.821	1.905	*	*	*	*
TF57	3.926	2.010	1.034e-03	0.176	0.043	34.413
TF58	4.031	2.115	*	*	*	*
TF59	4.136	2.220	1.057e-03	0.135	0.044	35.160
TF60	4.241	2.325	9.979e-04	0.135	0.041	33.195
TF61	4.346	2.430	9.858e-04	0.101	0.041	32.794
TF62	4.451	2.535	*	*	*	*
TF63	4.556	2.640	*	*	*	*
TF64	4.661	2.745	*	*	*	*
TF65	4.766	2.850	*	*	*	*
TF66	4.871	2.955	*	*	*	*
TF67	4.976	3.060	*	*	*	*
TF68	5.081	3.165	*	*	*	*
TF69	5.186	3.270	*	*	*	*
TF70	5.291	3.375	*	*	*	*

TABLE B-14: HYPULSE Run 783 Heating Data
MP-1 (SS) Configuration, Air Test Gas, $\alpha = 0$ deg, $C_{H,ref} = 0.031279$

GAGE ID	S/R_b	L/R_b	C_H	s/C_H	$C_H/C_{H,ref}$	q_{300} (W/cm^2)
TF38	1.931	0.015	*	*	*	*
TF39	2.036	0.120	*	*	*	*
TF40	2.141	0.225	2.008e-04	0.143	0.006	8.416
TF41	2.246	0.330	2.095e-04	0.175	0.007	8.779
TF42	2.351	0.435	2.552e-04	0.103	0.008	10.698
TF43	2.456	0.540	3.076e-04	0.128	0.010	12.892
TF44	2.561	0.645	3.613e-04	0.111	0.012	15.145
TF45	2.666	0.750	4.326e-04	0.095	0.014	18.130
TF46	2.771	0.855	5.223e-04	0.124	0.017	21.888
TF47	2.876	0.960	6.168e-04	0.148	0.020	25.852
TF48	2.981	1.065	7.237e-04	0.204	0.023	30.331
TF49	3.086	1.170	8.868e-04	0.196	0.028	37.167
TF50	3.191	1.275	1.032e-03	0.200	0.033	43.273
TF51	3.296	1.380	1.141e-03	0.176	0.036	47.838
TF52	3.401	1.485	1.168e-03	0.171	0.037	48.956
TF53	3.506	1.590	1.304e-03	0.152	0.042	54.666
TF54	3.611	1.695	1.363e-03	0.129	0.044	57.119
TF55	3.716	1.800	1.353e-03	0.120	0.043	56.723
TF56	3.821	1.905	1.334e-03	0.115	0.043	55.914
TF57	3.926	2.010	*	*	*	*
TF58	4.031	2.115	1.336e-03	0.110	0.043	55.975
TF59	4.136	2.220	1.402e-03	0.111	0.045	58.765
TF60	4.241	2.325	1.281e-03	0.119	0.041	53.700
TF61	4.346	2.430	1.384e-03	0.148	0.044	58.021
TF62	4.451	2.535	1.201e-03	0.111	0.038	50.335
TF63	4.556	2.640	1.191e-03	0.118	0.038	49.927
TF64	4.661	2.745	1.088e-03	0.112	0.035	45.605
TF65	4.766	2.850	1.001e-03	0.104	0.032	41.960
TF66	4.871	2.955	1.048e-03	0.114	0.034	43.933
TF67	4.976	3.060	1.043e-03	0.110	0.033	43.714
TF68	5.081	3.165	*	*	*	*
TF69	5.186	3.270	9.331e-04	0.128	0.030	39.108
TF70	5.291	3.375	8.685e-04	0.112	0.028	36.399

TABLE B-15: HYPULSE Run 784 Heating Data
MP-1 (SS) Configuration, Air Test Gas, α = -4 deg, $C_{H,ref}$ = 0.031279

GAGE ID	S/R_b	L/R_b	C_H	s/C_H	$C_H/C_{H,ref}$	q_{300} (W/cm^2)
TF38	1.931	0.015	*	*	*	*
TF39	2.036	0.120	*	*	*	*
TF40	2.141	0.225	3.115e-04	0.464	0.010	13.075
TF41	2.246	0.330	3.875e-04	0.367	0.012	16.264
TF42	2.351	0.435	4.649e-04	0.159	0.015	19.515
TF43	2.456	0.540	6.218e-04	0.280	0.020	26.102
TF44	2.561	0.645	8.313e-04	0.280	0.027	34.894
TF45	2.666	0.750	1.087e-03	0.217	0.035	45.627
TF46	2.771	0.855	1.438e-03	0.197	0.046	60.345
TF47	2.876	0.960	1.755e-03	0.233	0.056	73.659
TF48	2.981	1.065	1.907e-03	0.186	0.061	80.063
TF49	3.086	1.170	2.031e-03	0.196	0.065	85.268
TF50	3.191	1.275	2.010e-03	0.178	0.064	84.363
TF51	3.296	1.380	2.083e-03	0.191	0.067	87.431
TF52	3.401	1.485	1.974e-03	0.161	0.063	82.858
TF53	3.506	1.590	2.042e-03	0.131	0.065	85.716
TF54	3.611	1.695	2.027e-03	0.119	0.065	85.070
TF55	3.716	1.800	2.006e-03	0.090	0.064	84.189
TF56	3.821	1.905	1.902e-03	0.071	0.061	79.828
TF57	3.926	2.010	*	*	*	*
TF58	4.031	2.115	1.931e-03	0.045	0.062	81.032
TF59	4.136	2.220	1.865e-03	0.041	0.060	78.291
TF60	4.241	2.325	1.772e-03	0.064	0.057	74.382
TF61	4.346	2.430	1.809e-03	0.064	0.058	75.915
TF62	4.451	2.535	1.731e-03	0.055	0.055	72.642
TF63	4.556	2.640	*	*	*	*
TF64	4.661	2.745	1.677e-03	0.055	0.054	70.407
TF65	4.766	2.850	1.601e-03	0.055	0.051	67.190
TF66	4.871	2.955	1.686e-03	0.058	0.054	70.777
TF67	4.976	3.060	1.631e-03	0.065	0.052	68.458
TF68	5.081	3.165	*	*	*	*
TF69	5.186	3.270	1.593e-03	0.049	0.051	66.877
TF70	5.291	3.375	1.570e-03	0.059	0.050	65.901

TABLE B-16: HYPULSE Run 785 Heating Data

MP-1 (SS) Configuration, CO_2 Test Gas, α = -4 deg, $C_{H,ref}$ = 0.024208

GAGE ID	S/R_b	L/R_b	C_H	s/C_H	$C_H/C_{H,ref}$	q_{300} (W/cm^2)
TF38	1.931	0.015	*	*	*	*
TF39	2.036	0.120	*	*	*	*
TF40	2.141	0.225	1.249e-04	0.264	0.005	4.250
TF41	2.246	0.330	1.995e-04	0.330	0.008	6.788
TF42	2.351	0.435	3.885e-04	0.066	0.016	13.215
TF43	2.456	0.540	7.990e-04	0.199	0.033	27.179
TF44	2.561	0.645	1.098e-03	0.138	0.045	37.350
TF45	2.666	0.750	1.244e-03	0.081	0.051	42.301
TF46	2.771	0.855	1.237e-03	0.082	0.051	42.069
TF47	2.876	0.960	1.175e-03	0.087	0.049	39.967
TF48	2.981	1.065	1.171e-03	0.120	0.048	39.850
TF49	3.086	1.170	1.076e-03	0.142	0.044	36.590
TF50	3.191	1.275	1.074e-03	0.165	0.044	36.538
TF51	3.296	1.380	1.071e-03	0.223	0.044	36.427
TF52	3.401	1.485	*	*	*	*
TF53	3.506	1.590	1.052e-03	0.220	0.043	35.794
TF54	3.611	1.695	1.029e-03	0.228	0.042	34.990
TF55	3.716	1.800	1.011e-03	0.240	0.042	34.390
TF56	3.821	1.905	1.019e-03	0.245	0.042	34.679
TF57	3.926	2.010	*	*	*	*
TF58	4.031	2.115	9.562e-04	0.243	0.039	32.528
TF59	4.136	2.220	*	*	*	*
TF60	4.241	2.325	*	*	*	*
TF61	4.346	2.430	*	*	*	*
TF62	4.451	2.535	9.458e-04	0.268	0.039	32.173
TF63	4.556	2.640	*	*	*	*
TF64	4.661	2.745	9.621e-04	0.260	0.040	32.729
TF65	4.766	2.850	9.503e-04	0.262	0.039	32.327
TF66	4.871	2.955	9.760e-04	0.253	0.040	33.201
TF67	4.976	3.060	9.481e-04	0.253	0.039	32.253
TF68	5.081	3.165	*	*	*	*
TF69	5.186	3.270	9.253e-04	0.276	0.038	31.478
TF70	5.291	3.375	9.597e-04	0.258	0.040	32.648

TABLE B-17: HYPULSE Run 786 Heating Data
MP-1 (SS) Configuration, CO_2 Test Gas, α = -8 deg, $C_{H,ref}$ = 0.024208

GAGE ID	S/R_b	L/R_b	C_H	s/C_H	$C_H/C_{H,ref}$	q_{300} (W/cm^2)
TF38	1.931	0.015	*	*	*	*
TF39	2.036	0.120	*	*	*	*
TF40	2.141	0.225	2.536e-04	0.443	0.010	8.902
TF41	2.246	0.330	5.502e-04	0.348	0.023	19.312
TF42	2.351	0.435	1.114e-03	0.257	0.046	39.100
TF43	2.456	0.540	1.528e-03	0.184	0.063	53.638
TF44	2.561	0.645	1.629e-03	0.192	0.067	57.178
TF45	2.666	0.750	1.581e-03	0.223	0.065	55.472
TF46	2.771	0.855	1.508e-03	0.225	0.062	52.943
TF47	2.876	0.960	1.450e-03	0.261	0.060	50.884
TF48	2.981	1.065	1.396e-03	0.265	0.058	48.989
TF49	3.086	1.170	1.363e-03	0.270	0.056	47.838
TF50	3.191	1.275	1.338e-03	0.266	0.055	46.957
TF51	3.296	1.380	1.334e-03	0.259	0.055	46.821
TF52	3.401	1.485	*	*	*	*
TF53	3.506	1.590	1.239e-03	0.241	0.051	43.490
TF54	3.611	1.695	1.227e-03	0.241	0.051	43.079
TF55	3.716	1.800	1.187e-03	0.242	0.049	41.667
TF56	3.821	1.905	1.145e-03	0.212	0.047	40.186
TF57	3.926	2.010	1.118e-03	0.139	0.046	39.222
TF58	4.031	2.115	1.157e-03	0.213	0.048	40.608
TF59	4.136	2.220	*	*	*	*
TF60	4.241	2.325	1.102e-03	0.239	0.046	38.667
TF61	4.346	2.430	*	*	*	*
TF62	4.451	2.535	1.085e-03	0.220	0.045	38.073
TF63	4.556	2.640	*	*	*	*
TF64	4.661	2.745	1.082e-03	0.214	0.045	37.994
TF65	4.766	2.850	1.046e-03	0.231	0.043	36.702
TF66	4.871	2.955	1.067e-03	0.217	0.044	37.465
TF67	4.976	3.060	1.059e-03	0.213	0.044	37.178
TF68	5.081	3.165	*	*	*	*
TF69	5.186	3.270	1.026e-03	0.213	0.042	36.017
TF70	5.291	3.375	1.064e-03	0.237	0.044	37.356

TABLE B-18: HYPULSE Run 787 Heating Data
MP-2 (SS) Configuration, Air Test Gas, $\alpha = 0$ deg, $C_{H,ref} = 0.025565$

** BAD RUN, NO DATA **

TABLE B-19: HYPULSE Run 788 Heating Data
MP-2 (SS) Configuration, Air Test Gas, α = -4 deg, $C_{H,ref}$ = 0.025565

GAGE ID	S/R_b	L/R_b	C_H	s/C_H	$C_H/C_{H,ref}$	q_{300} (W/cm^2)
TF38	1.923	0.015	*	*	*	*
TF39	2.028	0.120	*	*	*	*
TF40	2.132	0.225	2.305e-04	0.480	0.009	9.634
TF41	2.237	0.330	2.851e-04	0.314	0.011	11.916
TF42	2.342	0.435	3.582e-04	0.211	0.014	14.972
TF43	2.447	0.540	4.205e-04	0.191	0.016	17.577
TF44	2.553	0.645	5.399e-04	0.121	0.021	22.568
TF45	2.658	0.750	6.712e-04	0.120	0.026	28.059
TF46	2.763	0.855	9.217e-04	0.152	0.036	38.529
TF47	2.868	0.960	1.137e-03	0.157	0.044	47.514
TF48	2.973	1.065	1.426e-03	0.156	0.056	59.612
TF49	3.078	1.170	1.719e-03	0.113	0.067	71.868
TF50	3.182	1.275	1.974e-03	0.099	0.077	82.492
TF51	3.287	1.380	2.169e-03	0.078	0.085	90.657
TF52	3.392	1.485	*	*	*	*
TF53	3.497	1.590	2.278e-03	0.081	0.089	95.225
TF54	3.602	1.695	2.262e-03	0.089	0.088	94.558
TF55	3.707	1.800	2.189e-03	0.088	0.086	91.501
TF56	3.813	1.905	2.051e-03	0.109	0.080	85.725
TF57	3.918	2.010	1.994e-03	0.242	0.078	83.372
TF58	4.023	2.115	1.960e-03	0.097	0.077	81.946
TF59	4.128	2.220	*	*	*	*
TF60	4.233	2.325	2.000e-03	0.096	0.078	83.593
TF61	4.338	2.430	1.731e-03	0.088	0.068	72.372
TF62	4.443	2.535	1.711e-03	0.098	0.067	71.531
TF63	4.548	2.640	*	*	*	*
TF64	4.653	2.745	1.563e-03	0.114	0.061	65.343
TF65	4.758	2.850	1.450e-03	0.098	0.057	60.599
TF66	4.863	2.955	1.470e-03	0.093	0.057	61.440
TF67	4.968	3.060	1.444e-03	0.088	0.056	60.378
TF68	5.073	3.165	*	*	*	*
TF69	5.177	3.270	1.362e-03	0.094	0.053	56.939
TF70	5.282	3.375	1.281e-03	0.112	0.050	53.551

TABLE B-20: HYPULSE Run 789 Heating Data
MP-2 (SS) Configuration, CO_2 Test Gas, α = -4 deg, $C_{H,ref}$ = 0.019086

GAGE ID	S/R_b	L/R_b	C_H	s/C_H	$C_H/C_{H,ref}$	q_{300} (W/cm^2)
TF38	1.923	0.015	*	*	*	*
TF39	2.028	0.120	*	*	*	*
TF40	2.132	0.225	1.093e-04	0.606	0.006	3.692
TF41	2.237	0.330	1.720e-04	0.266	0.009	5.810
TF42	2.342	0.435	3.678e-04	0.170	0.019	12.425
TF43	2.447	0.540	6.872e-04	0.153	0.036	23.216
TF44	2.553	0.645	1.017e-03	0.112	0.053	34.344
TF45	2.658	0.750	1.220e-03	0.079	0.064	41.231
TF46	2.763	0.855	1.271e-03	0.093	0.067	42.947
TF47	2.868	0.960	1.203e-03	0.117	0.063	40.632
TF48	2.973	1.065	1.152e-03	0.094	0.060	38.920
TF49	3.078	1.170	1.117e-03	0.138	0.059	37.734
TF50	3.182	1.275	1.097e-03	0.129	0.057	37.071
TF51	3.287	1.380	1.055e-03	0.160	0.055	35.633
TF52	3.392	1.485	*	*	*	*
TF53	3.497	1.590	1.051e-03	0.099	0.055	35.504
TF54	3.602	1.695	9.879e-04	0.183	0.052	33.376
TF55	3.707	1.800	9.979e-04	0.145	0.052	33.711
TF56	3.813	1.905	9.599e-04	0.160	0.050	32.428
TF57	3.918	2.010	*	*	*	*
TF58	4.023	2.115	8.983e-04	0.141	0.047	30.347
TF59	4.128	2.220	*	*	*	*
TF60	4.233	2.325	9.884e-04	0.169	0.052	33.390
TF61	4.338	2.430	9.084e-04	0.142	0.048	30.687
TF62	4.443	2.535	9.099e-04	0.172	0.048	30.738
TF63	4.548	2.640	*	*	*	*
TF64	4.653	2.745	8.774e-04	0.197	0.046	29.641
TF65	4.758	2.850	9.067e-04	0.172	0.048	30.630
TF66	4.863	2.955	9.132e-04	0.181	0.048	30.851
TF67	4.968	3.060	9.226e-04	0.187	0.048	31.170
TF68	5.073	3.165	*	*	*	*
TF69	5.177	3.270	9.085e-04	0.158	0.048	30.691
TF70	5.282	3.375	9.155e-04	0.210	0.048	30.930

TABLE B-21: HYPULSE Run 790 Heating Data

MP-1 Configuration, Air Test Gas, $\alpha = 0$ deg, $C_{H,ref} = 0.031279$

GAGE ID	S/R_b	L/R_b	C_H	s/C_H	$C_H/C_{H,ref}$	q_{300} (W/cm^2)
TF1	-1.872	-	3.259e-04	0.258	0.010	13.592
TF2	-1.772	-	7.432e-04	0.188	0.024	30.994
TF3	-1.678	-	4.850e-04	0.315	0.016	20.227
TF4	-1.554	-	1.454e-03	0.324	0.046	60.623
TF5	-1.429	-	1.937e-03	0.371	0.062	80.774
TF6	-1.305	-	8.265e-04	0.514	0.026	34.468
TF7	-1.180	-	5.200e-04	1.079	0.017	21.684
TF8	-1.083	-	1.637e-03	0.423	0.052	68.252
TF9	-1.000	-	1.774e-02	0.042	0.567	739.790
TF10	-0.900	-	2.116e-02	0.252	0.676	882.370
TF11	-0.800	-	1.802e-02	0.128	0.576	751.510
TF12	-0.700	-	1.942e-02	0.223	0.621	810.090
TF13	-0.600	-	*	*	*	*
TF14	-0.500	-	*	*	*	*
TF15	-0.400	-	2.103e-02	0.105	0.672	876.850
TF16	-0.300	-	*	*	*	*
TF17	-0.200	-	*	*	*	*
TF18	-0.100	-	2.640e-02	0.080	0.844	1014.500
TF19	0.000	-	2.788e-02	0.069	0.891	1100.900
TF20	0.100	-	*	*	*	*
TF21	0.200	-	1.946e-02	0.066	0.622	811.650
TF22	0.300	-	1.928e-02	0.278	0.616	804.170
TF23	0.400	-	1.750e-02	0.247	0.560	729.870
TF24	0.500	-	1.805e-02	0.294	0.577	752.980
TF25	0.600	-	1.448e-02	0.045	0.463	603.910
TF26	0.700	-	1.520e-02	0.268	0.486	634.100
TF27	0.800	-	1.439e-02	0.207	0.460	599.950
TF28	0.900	-	1.800e-02	0.266	0.575	750.660
TF29	1.000	-	2.096e-02	0.151	0.670	874.010
TF30	1.083	-	1.503e-03	0.357	0.048	62.697
TF31	1.180	-	5.618e-04	0.122	0.018	23.429
TF32	1.305	-	1.154e-03	0.152	0.037	48.147
TF33	1.429	-	8.549e-04	0.082	0.027	35.651
TF34	1.554	-	4.453e-04	0.130	0.014	18.572
TF35	1.678	-	3.289e-04	0.160	0.011	13.718
TF36	1.772	-	4.846e-04	0.276	0.015	20.208
TF37	1.872	-	3.330e-04	0.095	0.011	13.885
TF38	1.931	0.015	*	*	*	*
TF39	2.036	0.120	2.197e-04	0.158	0.007	9.163
TF40	2.141	0.225	2.589e-04	0.191	0.008	10.799
TF41	2.246	0.330	3.460e-04	0.107	0.011	14.431
TF42	2.351	0.435	4.236e-04	0.074	0.014	17.667
TF43	2.456	0.540	3.669e-04	0.077	0.012	15.300
TF44	2.561	0.645	5.147e-04	0.157	0.016	21.466
TF45	2.666	0.750	3.970e-04	0.139	0.013	16.556
TF46	2.771	0.855	*	*	*	*
TF47	2.876	0.960	9.658e-04	0.212	0.031	40.276
TF48	2.981	1.065	1.165e-03	0.253	0.037	48.569
TF49	3.086	1.170	1.343e-03	0.254	0.043	55.994
TF50	3.191	1.275	1.320e-03	0.250	0.042	55.050
TF51	3.296	1.380	1.460e-03	0.240	0.047	60.896
TF52	3.401	1.485	*	*	*	*
TF53	3.506	1.590	1.720e-03	0.199	0.055	71.732
TF54	3.611	1.695	*	*	*	*
TF55	3.716	1.800	1.753e-03	0.149	0.056	73.091
TF56	3.821	1.905	*	*	*	*
TF57	3.926	2.010	1.799e-03	0.159	0.058	75.011
TF58	4.031	2.115	1.803e-03	0.138	0.058	75.183
TF59	4.136	2.220	1.787e-03	0.135	0.057	74.525
TF60	4.241	2.325	1.799e-03	0.111	0.058	75.027
TF61	4.346	2.430	1.710e-03	0.139	0.055	71.313
TF62	4.451	2.535	1.708e-03	0.138	0.055	71.245
TF63	4.556	2.640	1.675e-03	0.151	0.054	69.858
TF64	4.661	2.745	1.531e-03	0.117	0.049	63.863
TF65	4.766	2.850	1.482e-03	0.164	0.047	61.828
TF66	4.871	2.955	1.424e-03	0.179	0.046	59.391
TF67	4.976	3.060	1.419e-03	0.170	0.045	59.179
TF68	5.081	3.165	1.448e-03	0.186	0.046	60.382
TF69	5.186	3.270	1.382e-03	0.172	0.044	57.634
TF70	5.291	3.375	1.304e-03	0.166	0.042	54.377

TABLE B-22: HYPULSE Run 791 Heating Data

MP-2 Configuration, CO_2 Test Gas, $\alpha = -4$ deg, $C_{H,ref} = 0.019086$

GAGE ID	S/R_b	L/R_b	C_H	s/C_H	$C_H/C_{H,ref}$	q_{300} (W/cm^2)
TF37	-1.864	-	7.186e-05	0.392	0.004	2.441
TF36	-1.764	-	1.968e-04	0.322	0.010	6.686
TF35	-1.670	-	9.373e-05	0.354	0.005	3.184
TF34	-1.545	-	*	*	*	*
TF33	-1.421	-	*	*	*	*
TF32	-1.296	-	*	*	*	*
TF31	-1.172	-	7.086e-05	1.015	0.004	2.407
TF30	-1.075	-	2.701e-03	0.072	0.141	91.727
TF29	-1.000	-	1.146e-02	0.060	0.601	389.310
TF28	-0.900	-	1.101e-02	0.053	0.577	374.090
TF27	-0.800	-	1.150e-02	0.061	0.603	390.640
TF26	-0.700	-	1.188e-02	0.077	0.622	403.430
TF25	-0.600	-	1.216e-02	0.072	0.637	412.960
TF24	-0.500	-	*	*	*	*
TF23	-0.400	-	1.261e-02	0.035	0.661	428.370
TF22	-0.300	-	1.407e-02	0.062	0.737	478.030
TF21	-0.200	-	1.497e-02	0.042	0.784	508.540
TF20	-0.100	-	1.696e-02	0.044	0.889	576.040
TF19	0.000	-	1.716e-02	0.049	0.899	582.840
TF18	0.100	-	*	*	*	*
TF17	0.200	-	1.551e-02	0.054	0.813	526.790
TF16	0.300	-	*	*	*	*
TF15	0.400	-	1.450e-02	0.051	0.760	492.520
TF14	0.500	-	1.400e-02	0.042	0.734	475.650
TF13	0.600	-	1.367e-02	0.052	0.716	464.410
TF12	0.700	-	1.344e-02	0.054	0.704	456.440
TF11	0.800	-	1.272e-02	0.063	0.667	432.090
TF10	0.900	-	1.250e-02	0.075	0.655	424.640
TF9	1.000	-	1.269e-02	0.059	0.665	431.050
TF8	1.075	-	1.369e-03	0.120	0.072	46.506
TF7	1.172	-	1.326e-04	0.398	0.007	4.504
TF6	1.296	-	1.916e-04	0.287	0.010	6.508
TF5	1.421	-	1.852e-04	0.355	0.010	6.290
TF4	1.545	-	1.165e-04	0.245	0.006	3.957
TF3	1.670	-	5.854e-05	0.753	0.003	1.988
TF2	1.764	-	6.144e-05	0.833	0.003	2.087
TF1	1.864	-	7.470e-05	0.382	0.004	2.537
TF38	1.923	0.015	*	*	*	*
TF39	2.028	0.120	*	*	*	*
TF40	2.132	0.225	*	*	*	*
TF41	2.237	0.330	*	*	*	*
TF42	2.342	0.435	*	*	*	*
TF43	2.447	0.540	*	*	*	*
TF44	2.553	0.645	*	*	*	*
TF45	2.658	0.750	*	*	*	*
TF46	2.763	0.855	*	*	*	*
TF47	2.868	0.960	*	*	*	*
TF48	2.973	1.065	*	*	*	*
TF49	3.078	1.170	*	*	*	*
TF50	3.183	1.275	*	*	*	*
TF51	3.288	1.380	*	*	*	*
TF52	3.393	1.485	*	*	*	*
TF53	3.497	1.590	*	*	*	*
TF54	3.603	1.695	*	*	*	*
TF55	3.708	1.800	*	*	*	*
TF56	3.813	1.905	*	*	*	*
TF57	3.918	2.010	*	*	*	*
TF58	4.023	2.115	*	*	*	*
TF59	4.128	2.220	*	*	*	*
TF60	4.233	2.325	*	*	*	*
TF61	4.338	2.430	*	*	*	*
TF62	4.443	2.535	*	*	*	*
TF63	4.548	2.640	*	*	*	*
TF64	4.653	2.745	*	*	*	*
TF65	4.758	2.850	*	*	*	*
TF66	4.863	2.955	*	*	*	*
TF67	4.968	3.060	*	*	*	*
TF68	5.073	3.165	*	*	*	*
TF69	5.177	3.270	*	*	*	*
TF70	5.282	3.375	*	*	*	*

TABLE B-23: HYPULSE Run 792 Heating Data

MP-2 Configuration, CO_2 Test Gas, $\alpha = 0$ deg, $C_{H,ref} = 0.019086$

GAGE ID	S/R_b	L/R_b	C_H	s/C_H	$C_H/C_{H,ref}$	q_{300} (W/cm^2)
TF1	-1.864	0.000	2.041e-05	3.710	0.001	0.695
TF2	-1.764	0.000	*	*		*
TF3	-1.670	0.000	3.819e-05	1.847	0.002	1.301
TF4	-1.545	0.000	1.360e-05	6.815	0.001	0.463
TF5	-1.421	0.000	*	*	*	*
TF6	-1.296	0.000	6.737e-05	1.077	0.004	2.295
TF7	-1.172	0.000	5.926e-05	1.010	0.003	2.018
TF8	-1.075	0.000	1.710e-03	0.172	0.090	58.232
TF9	-1.000	0.000	1.265e-02	0.045	0.663	430.860
TF10	-0.900	0.000	1.299e-02	0.118	0.681	442.460
TF11	-0.800	0.000	1.256e-02	0.030	0.658	427.840
TF12	-0.700	0.000	1.285e-02	0.048	0.673	437.540
TF13	-0.600	0.000	1.328e-02	0.037	0.696	452.380
TF14	-0.500	0.000	1.386e-02	0.064	0.726	472.060
TF15	-0.400	0.000	1.369e-02	0.043	0.717	466.210
TF16	-0.300	0.000	1.491e-02	0.035	0.781	507.720
TF17	-0.200	0.000	1.607e-02	0.033	0.842	547.430
TF18	-0.100	0.000	1.861e-02	0.027	0.975	633.720
TF19	0.000	0.000	1.909e-02	0.025	1.000	650.010
TF20	0.100	0.000	1.780e-02	0.032	0.933	606.320
TF21	0.200	0.000	1.539e-02	0.033	0.807	524.250
TF22	0.300	0.000	1.402e-02	0.041	0.735	477.580
TF23	0.400	0.000	1.346e-02	0.054	0.705	458.270
TF24	0.500	0.000	1.372e-02	0.057	0.719	467.200
TF25	0.600	0.000	1.247e-02	0.063	0.653	424.700
TF26	0.700	0.000	1.195e-02	0.068	0.626	406.870
TF27	0.800	0.000	1.157e-02	0.088	0.606	394.140
TF28	0.900	0.000	1.149e-02	0.130	0.602	391.350
TF29	1.000	0.000	1.161e-02	0.098	0.608	395.400
TF30	1.075	0.000	1.538e-03	0.194	0.081	52.393
TF31	1.172	0.000	2.735e-05	3.036	0.001	0.932
TF32	1.296	0.000	*	*	*	*
TF33	1.421	0.000	*	*	*	*
TF34	1.545	0.000	*	*	*	*
TF35	1.670	0.000	6.113e-05	0.519	0.003	2.082
TF36	1.764	0.000	5.646e-05	0.925	0.003	1.923
TF37	1.864	0.000	3.090e-05	2.313	0.002	1.052
TF38	1.923	0.015	*	*	*	*
TF39	2.028	0.120	*	*	*	*
TF40	2.132	0.225	8.192e-05	0.500	0.004	2.790
TF41	2.237	0.330	9.825e-05	0.600	0.005	3.346
TF42	2.342	0.435	2.874e-04	0.497	0.015	9.787
TF43	2.447	0.540	1.950e-04	0.454	0.010	6.642
TF44	2.553	0.645	3.885e-04	0.570	0.020	13.230
TF45	2.658	0.750	*	*	*	*
TF46	2.763	0.855	*	*	*	*
TF47	2.868	0.960	7.764e-04	0.276	0.041	26.444
TF48	2.973	1.065	8.065e-04	0.255	0.042	27.466
TF49	3.078	1.170	8.385e-04	0.245	0.044	28.557
TF50	3.182	1.275	*	*	*	*
TF51	3.288	1.380	*	*	*	*
TF52	3.392	1.485	8.938e-04	0.225	0.047	30.439
TF53	3.497	1.590	8.339e-04	0.237	0.044	28.401
TF54	3.602	1.695	7.960e-04	0.263	0.042	27.109
TF55	3.707	1.800	*	*	*	*
TF56	3.813	1.905	8.075e-04	0.270	0.042	27.502
TF57	3.918	2.010	7.533e-04	0.358	0.039	25.656
TF58	4.023	2.115	7.421e-04	0.372	0.039	25.275
TF59	4.128	2.220	*	*	*	*
TF60	4.233	2.325	7.556e-04	0.386	0.040	25.734
TF61	4.338	2.430	7.528e-04	0.403	0.039	25.640
TF62	4.443	2.535	7.163e-04	0.436	0.038	24.394
TF63	4.548	2.640	7.315e-04	0.444	0.038	24.912
TF64	4.653	2.745	6.853e-04	0.481	0.036	23.338
TF65	4.758	2.850	6.747e-04	0.479	0.035	22.979
TF66	4.863	2.955	6.680e-04	0.497	0.035	22.752
TF67	4.968	3.060	6.778e-04	0.497	0.036	23.084
TF68	5.073	3.165	5.716e-04	0.507	0.030	19.468
TF69	5.177	3.270	6.745e-04	0.502	0.035	22.972
TF70	5.282	3.375	6.824e-04	0.530	0.036	23.240

TABLE B-24: HYPULSE Run 793 Heating Data
MP-3 Configuration, CO_2 Test Gas, $\alpha = 0$ deg, $C_{H,ref} = 0.024208$

GAGE ID	S/R_b	L/R_b	C_H	s/C_H	$C_H/C_{H,ref}$	q_{300} (W/cm^2)
TF1	-1.914	-	*	*	*	*
TF2	-1.814	-	1.363e-04	1.190	0.006	4.606
TF3	-1.720	-	1.558e-04	0.674	0.006	5.265
TF4	-1.596	-	*	*	*	*
TF5	-1.472	-	*	*	*	*
TF6	-1.347	-	*	*	*	*
TF7	-1.222	-	*	*	*	*
TF8	-1.109	-	1.419e-03	0.296	0.059	47.937
TF9	-1.000	-	1.365e-02	0.080	0.564	461.120
TF10	-0.900	-	1.437e-02	0.091	0.594	485.510
TF11	-0.800	-	1.515e-02	0.076	0.626	511.700
TF12	-0.700	-	1.510e-02	0.101	0.624	510.080
TF13	-0.600	-	1.606e-02	0.093	0.664	542.700
TF14	-0.500	-	1.690e-02	0.115	0.698	570.930
TF15	-0.400	-	1.683e-02	0.088	0.695	568.510
TF16	-0.300	-	1.774e-02	0.127	0.733	599.140
TF17	-0.200	-	1.890e-02	0.118	0.781	638.550
TF18	-0.100	-	2.459e-02	0.093	1.016	830.760
TF19	0.000	-	2.489e-02	0.064	1.028	840.770
TF20	0.100	-	2.231e-02	0.078	0.922	753.650
TF21	0.200	-	1.851e-02	0.090	0.764	625.210
TF22	0.300	-	1.726e-02	0.229	0.713	583.270
TF23	0.400	-	1.619e-02	0.059	0.669	546.860
TF24	0.500	-	1.586e-02	0.078	0.655	535.920
TF25	0.600	-	1.537e-02	0.081	0.635	519.280
TF26	0.700	-	1.499e-02	0.128	0.619	506.340
TF27	0.800	-	1.426e-02	0.126	0.589	481.820
TF28	0.900	-	1.389e-02	0.132	0.574	469.100
TF29	1.000	-	1.251e-02	0.130	0.517	422.700
TF30	1.109	-	1.688e-03	0.250	0.070	57.024
TF31	1.222	-	*	*	*	*
TF32	1.347	-	*	*	*	*
TF33	1.472	-	*	*	*	*
TF34	1.596	-	6.048e-05	1.820	0.002	2.043
TF35	1.720	-	1.467e-04	0.596	0.006	4.958
TF36	1.814	-	1.496e-04	1.213	0.006	5.054
TF37	1.914	-	1.231e-04	1.269	0.005	4.157
TF38	0.000	-	*	*	*	*
TF39	2.028	0.070	*	*	*	*
TF40	2.133	0.175	*	*	*	*
TF41	2.238	0.280	*	*	*	*
TF42	2.343	0.385	*	*	*	*
TF43	2.448	0.490	*	*	*	*
TF44	2.553	0.595	*	*	*	*
TF45	2.658	0.700	*	*	*	*
TF46	2.763	0.805	*	*	*	*
TF47	2.868	0.910	5.982e-04	0.194	0.025	20.209
TF48	2.973	1.015	6.819e-04	0.203	0.028	23.036
TF49	3.078	1.120	7.915e-04	0.167	0.033	26.741
TF50	3.183	1.225	8.389e-04	0.143	0.035	28.341
TF51	3.288	1.330	9.542e-04	0.151	0.039	32.235
TF52	3.393	1.435	*	*	*	*
TF53	3.498	1.540	9.963e-04	0.127	0.041	33.659
TF54	3.603	1.645	9.940e-04	0.118	0.041	33.581
TF55	3.708	1.750	9.026e-04	0.106	0.037	30.493
TF56	3.813	1.855	9.585e-04	0.109	0.040	32.380
TF57	3.918	1.960	9.255e-04	0.119	0.038	31.267
TF58	4.023	2.065	8.907e-04	0.121	0.037	30.090
TF59	4.128	2.170	*	*	*	*
TF60	4.233	2.275	8.812e-04	0.144	0.036	29.769
TF61	4.338	2.380	8.816e-04	0.139	0.036	29.784
TF62	4.443	2.485	8.628e-04	0.140	0.036	29.149
TF63	4.548	2.590	7.885e-04	0.146	0.033	26.638
TF64	4.653	2.695	7.922e-04	0.141	0.033	26.763
TF65	4.758	2.800	7.597e-04	0.154	0.031	25.663
TF66	4.863	2.905	7.448e-04	0.148	0.031	25.160
TF67	4.968	3.010	7.174e-04	0.130	0.030	24.237
TF68	5.073	3.115	5.890e-04	0.207	0.024	19.899
TF69	5.178	3.220	6.691e-04	0.167	0.028	22.605
TF70	5.283	3.325	6.825e-04	0.171	0.028	23.057

TABLE B-25: HYPULSE Run 794 Heating Data
MP-4 Configuration, CO_2 Test Gas, $\alpha = 0$ deg, $C_{H,ref} = 0.024208$

GAGE ID	S/R_b	L/R_b	C_H	s/C_H	$C_H/C_{H,ref}$	q_{300} (W/cm^2)
TF1	-2.000	-	*	*	*	*
TF2	-1.900	-	*	*	*	*
TF3	-1.806	-	*	*	*	*
TF4	-1.682	-	*	*	*	*
TF5	-1.557	-	*	*	*	*
TF6	-1.433	-	*	*	*	*
TF7	-1.308	-	2.286e-04	0.821	0.009	7.700
TF8	-1.161	-	1.106e-03	0.252	0.046	37.261
TF9	-1.000	-	7.575e-03	0.059	0.313	255.130
TF10	-0.900	-	1.581e-02	0.042	0.653	532.610
TF11	-0.800	-	1.533e-02	0.042	0.633	516.300
TF12	-0.700	-	1.609e-02	0.051	0.665	542.050
TF13	-0.600	-	1.646e-02	0.053	0.680	554.220
TF14	-0.500	-	1.819e-02	0.071	0.752	612.780
TF15	-0.400	-	1.728e-02	0.036	0.714	582.100
TF16	-0.300	-	1.818e-02	0.032	0.751	612.330
TF17	-0.200	-	1.952e-02	0.037	0.806	657.320
TF18	-0.100	-	2.383e-02	0.033	0.984	802.630
TF19	0.000	-	2.449e-02	0.039	1.012	824.900
TF20	0.100	-	2.251e-02	0.041	0.930	758.040
TF21	0.200	-	1.877e-02	0.038	0.775	632.120
TF22	0.300	-	1.725e-02	0.056	0.713	581.040
TF23	0.400	-	1.698e-02	0.044	0.701	571.900
TF24	0.500	-	1.676e-02	0.053	0.692	564.520
TF25	0.600	-	1.589e-02	0.030	0.656	535.270
TF26	0.700	-	1.583e-02	0.024	0.654	533.090
TF27	0.800	-	1.495e-02	0.034	0.618	503.620
TF28	0.900	-	1.527e-02	0.053	0.631	514.270
TF29	1.000	-	*	*	*	*
TF30	1.161	-	7.622e-04	0.350	0.031	25.673
TF31	1.308	-	1.691e-05	7.779	0.001	0.570
TF32	1.433	-	*	*	*	*
TF33	1.557	-	*	*	*	*
TF34	1.682	-	*	*	*	*
TF35	1.806	-	*	*	*	*
TF36	1.900	-	*	*	*	*
TF37	2.000	-	*	*	*	*
TF38	-	-	-	-	-	-
TF39	2.114	0.070	*	*	*	*
TF40	2.219	0.175	*	*	*	*
TF41	2.324	0.280	*	*	*	*
TF42	2.429	0.385	*	*	*	*
TF43	2.534	0.490	*	*	*	*
TF44	2.639	0.595	*	*	*	*
TF45	2.744	0.700	*	*	*	*
TF46	2.849	0.805	*	*	*	*
TF47	2.954	0.910	*	*	*	*
TF48	3.059	1.015	*	*	*	*
TF49	3.164	1.120	*	*	*	*
TF50	3.269	1.225	*	*	*	*
TF51	3.374	1.330	*	*	*	*
TF52	3.479	1.435	*	*	*	*
TF53	3.584	1.540	*	*	*	*
TF54	3.689	1.645	*	*	*	*
TF55	3.794	1.750	*	*	*	*
TF56	3.899	1.855	*	*	*	*
TF57	4.004	1.960	*	*	*	*
TF58	4.109	2.065	*	*	*	*
TF59	4.214	2.170	*	*	*	*
TF60	4.319	2.275	*	*	*	*
TF61	4.424	2.380	*	*	*	*
TF62	4.529	2.485	*	*	*	*
TF63	4.634	2.590	*	*	*	*
TF64	4.739	2.695	*	*	*	*
TF65	4.844	2.800	*	*	*	*
TF66	4.949	2.905	*	*	*	*
TF67	5.054	3.010	*	*	*	*
TF68	5.159	3.115	*	*	*	*
TF69	5.264	3.220	*	*	*	*
TF70	5.369	3.325	*	*	*	*

TABLE B-26: HYPULSE Run 795 Heating Data

MP-1 Configuration, Air Test Gas, α = -4 deg, $C_{H,ref}$ = 0.031279

GAGE ID	S/R_b	L/R_b	C_H	s/C_H	$C_H/C_{H,ref}$	q_{300} (W/cm^2)
TF1	-1.872	-	3.593e-04	0.084	0.011	14.989
TF2	-1.772	-	3.965e-04	0.224	0.013	16.542
TF3	-1.678	-	2.638e-04	0.307	0.008	11.006
TF4	-1.554	-	5.380e-04	0.266	0.017	22.444
TF5	-1.429	-	7.069e-04	0.272	0.023	29.492
TF6	-1.305	-	9.835e-04	0.419	0.031	41.032
TF7	-1.180	-	8.808e-04	0.485	0.028	36.746
TF8	-1.083	-	2.811e-03	0.214	0.090	117.290
TF9	-1.000	-	1.554e-02	0.049	0.497	648.220
TF10	-0.900	-	1.631e-02	0.106	0.522	680.580
TF11	-0.800	-	1.659e-02	0.094	0.530	692.100
TF12	-0.700	-	1.681e-02	0.263	0.537	701.120
TF13	-0.600	-	2.004e-02	0.073	0.641	836.040
TF14	-0.500	-	1.751e-02	0.210	0.560	730.380
TF15	-0.400	-	1.843e-02	0.046	0.589	768.700
TF16	-0.300	-	1.950e-02	0.049	0.623	813.470
TF17	-0.200	-	2.077e-02	0.045	0.664	866.490
TF18	-0.100	-	2.562e-02	0.041	0.819	1068.700
TF19	0.000	-	*	*	*	*
TF20	0.100	-	3.787e-02	0.112	1.211	1580.000
TF21	0.200	-	2.340e-02	0.040	0.748	976.210
TF22	0.300	-	2.036e-02	0.053	0.651	849.360
TF23	0.400	-	1.928e-02	0.036	0.616	804.180
TF24	0.500	-	2.070e-02	0.064	0.662	863.700
TF25	0.600	-	1.909e-02	0.063	0.610	796.670
TF26	0.700	-	2.091e-02	0.094	0.668	872.250
TF27	0.800	-	1.760e-02	0.113	0.563	734.190
TF28	0.900	-	1.945e-02	0.182	0.622	811.410
TF29	1.000	-	2.167e-02	0.071	0.693	904.210
TF30	1.083	-	3.192e-03	0.641	0.102	133.190
TF31	1.180	-	2.953e-04	1.957	0.009	12.318
TF32	1.305	-	4.792e-04	2.119	0.015	19.993
TF33	1.429	-	1.157e-03	0.791	0.037	48.270
TF34	1.554	-	1.199e-03	0.351	0.038	50.011
TF35	1.678	-	2.757e-04	0.229	0.009	11.501
TF36	1.772	-	4.557e-04	0.446	0.015	19.011
TF37	1.872	-	3.756e-04	0.179	0.012	15.670
TF38	1.931	0.015	*	*	*	*
TF39	2.036	0.120	*	*	*	*
TF40	2.141	0.225	*	*	*	*
TF41	2.246	0.330	*	*	*	*
TF42	2.351	0.435	*	*	*	*
TF43	2.456	0.540	*	*	*	*
TF44	2.561	0.645	*	*	*	*
TF45	2.666	0.750	*	*	*	*
TF46	2.771	0.855	*	*	*	*
TF47	2.876	0.960	*	*	*	*
TF48	2.981	1.065	1.625e-03	0.267	0.052	67.777
TF49	3.086	1.170	1.833e-03	0.239	0.059	76.484
TF50	3.191	1.275	1.905e-03	0.245	0.061	79.476
TF51	3.296	1.380	1.979e-03	0.220	0.063	82.551
TF52	3.401	1.485	*	*	*	*
TF53	3.506	1.590	1.997e-03	0.232	0.064	83.335
TF54	3.611	1.695	*	*	*	*
TF55	3.716	1.800	1.845e-03	0.218	0.059	76.988
TF56	3.821	1.905	1.982e-03	0.240	0.063	82.673
TF57	3.926	2.010	1.802e-03	0.232	0.058	75.199
TF58	4.031	2.115	1.718e-03	0.177	0.055	71.653
TF59	4.136	2.220	*	*	*	*
TF60	4.241	2.325	1.715e-03	0.182	0.055	71.558
TF61	4.346	2.430	*	*	*	*
TF62	4.451	2.535	1.627e-03	0.188	0.052	67.883
TF63	4.556	2.640	1.629e-03	0.195	0.052	67.951
TF64	4.661	2.745	1.547e-03	0.172	0.049	64.547
TF65	4.766	2.850	1.494e-03	0.184	0.048	62.330
TF66	4.871	2.955	*	*	*	*
TF67	4.976	3.060	*	*	*	*
TF68	5.081	3.165	1.245e-03	0.183	0.040	51.955
TF69	5.186	3.270	1.338e-03	0.273	0.043	55.826
TF70	5.291	3.375	1.235e-03	0.336	0.039	51.514

TABLE B-27: HYPULSE Run 796 Heating Data

MP-3 Configuration, CO_2 Test Gas, $\alpha = 0$ deg, $C_{H,ref} = 0.024208$

GAGE ID	S/R_b	L/R_b	C_H	s/C_H	$C_H/C_{H,ref}$	q_{300} (W/cm^2)
TF1	-1.914	-	1.298e-04	0.337	0.005	4.591
TF2	-1.814	-	2.339e-04	0.214	0.010	8.276
TF3	-1.720	-	1.073e-04	0.561	0.004	3.795
TF4	-1.596	-	5.063e-05	0.597	0.002	1.792
TF5	-1.472	-	1.284e-04	0.697	0.005	4.542
TF6	-1.347	-	8.826e-05	0.248	0.004	3.123
TF7	-1.222	-	1.422e-04	0.292	0.006	5.033
TF8	-1.109	-	1.918e-03	0.292	0.079	67.853
TF9	-1.000	-	1.272e-02	0.099	0.525	450.020
TF10	-0.900	-	1.430e-02	0.124	0.591	506.100
TF11	-0.800	-	1.363e-02	0.079	0.563	482.420
TF12	-0.700	-	1.426e-02	0.086	0.589	504.670
TF13	-0.600	-	1.529e-02	0.068	0.632	541.230
TF14	-0.500	-	1.523e-02	0.050	0.629	538.950
TF15	-0.400	-	1.643e-02	0.044	0.679	581.560
TF16	-0.300	-	1.639e-02	0.054	0.677	579.970
TF17	-0.200	-	1.828e-02	0.028	0.755	646.880
TF18	-0.100	-	2.143e-02	0.035	0.885	758.400
TF19	0.000	-	2.264e-02	0.031	0.935	801.200
TF20	0.100	-	2.175e-02	0.017	0.898	769.600
TF21	0.200	-	1.838e-02	0.024	0.759	650.520
TF22	0.300	-	1.619e-02	0.047	0.669	572.720
TF23	0.400	-	1.543e-02	0.019	0.637	545.940
TF24	0.500	-	1.522e-02	0.050	0.629	538.620
TF25	0.600	-	1.497e-02	0.035	0.618	529.740
TF26	0.700	-	1.502e-02	0.059	0.621	531.600
TF27	0.800	-	1.421e-02	0.042	0.587	502.960
TF28	0.900	-	1.454e-02	0.072	0.601	514.600
TF29	1.000	-	1.311e-02	0.060	0.542	463.920
TF30	1.109	-	1.600e-03	0.117	0.066	56.611
TF31	1.222	-	*	*	*	*
TF32	1.347	-	*	*	*	*
TF33	1.472	-	*	*	*	*
TF34	1.596	-	*	*	*	*
TF35	1.720	-	1.578e-04	0.082	0.007	5.583
TF36	1.814	-	1.966e-04	0.086	0.008	6.957
TF37	1.914	-	*	*	*	*
TF38	0.000	-	*	*	*	*
TF39	2.028	0.070	*	*	*	*
TF40	2.133	0.175	*	*	*	*
TF41	2.238	0.280	*	*	*	*
TF42	2.343	0.385	*	*	*	*
TF43	2.448	0.490	*	*	*	*
TF44	2.553	0.595	*	*	*	*
TF45	2.658	0.700	*	*	*	*
TF46	2.763	0.805	*	*	*	*
TF47	2.763	0.805	*	*	*	*
TF48	2.973	1.015	5.730e-04	0.130	0.024	20.276
TF49	3.078	1.120	6.832e-04	0.089	0.028	24.174
TF50	3.183	1.225	7.421e-04	0.067	0.031	26.260
TF51	3.288	1.330	8.514e-04	0.044	0.035	30.126
TF53	3.498	1.540	*	*	*	*
TF54	3.603	1.645	*	*	*	*
TF55	3.708	1.750	8.230e-04	0.072	0.034	29.122
TF56	3.813	1.855	8.595e-04	0.073	0.036	30.412
TF57	3.918	1.960	8.061e-04	0.067	0.033	28.524
TF58	4.023	2.065	7.614e-04	0.101	0.031	26.941
TF59	4.128	2.170	*	*	*	*
TF60	4.233	2.275	8.094e-04	0.120	0.033	28.642
TF61	4.338	2.380	*	*	*	*
TF62	4.443	2.485	7.616e-04	0.117	0.031	26.951
TF63	4.548	2.590	7.424e-04	0.095	0.031	26.268
TF64	4.653	2.695	6.890e-04	0.115	0.028	24.379
TF65	4.758	2.800	6.271e-04	0.139	0.026	22.189
TF66	4.863	2.905	*	*	*	*
TF67	4.968	3.010	*	*	*	*
TF68	5.073	3.115	*	*	*	*
TF69	5.178	3.220	5.884e-04	0.116	0.024	20.820
TF70	5.283	3.325	5.686e-04	0.111	0.023	20.121

TABLE B-28: HYPULSE Run 797 Heating Data

MP-4 Configuration, CO_2 Test Gas, $\alpha = 0$ deg, $C_{H,ref} = 0.024208$

GAGE ID	S/R_b	L/R_b	C_H	s/C_H	$C_H/C_{H,ref}$	q_{300} (W/cm^2)
TF1	-2.000	-	8.676e-05	0.379	0.004	2.875
TF2	-1.900	-	1.018e-04	0.207	0.004	3.372
TF3	-1.806	-	1.448e-04	0.640	0.006	4.799
TF4	-1.682	-	1.126e-04	0.351	0.005	3.730
TF5	-1.557	-	1.130e-04	0.466	0.005	3.745
TF6	-1.433	-	1.206e-04	0.558	0.005	3.995
TF7	-1.308	-	1.705e-04	0.444	0.007	5.650
TF8	-1.161	-	9.503e-04	0.245	0.039	31.487
TF9	-1.000	-	6.198e-03	0.087	0.256	205.360
TF10	-0.900	-	1.554e-02	0.076	0.642	514.820
TF11	-0.800	-	1.446e-02	0.075	0.598	479.290
TF12	-0.700	-	1.601e-02	0.072	0.661	530.340
TF13	-0.600	-	1.683e-02	0.078	0.695	557.790
TF14	-0.500	-	1.723e-02	0.084	0.712	571.050
TF15	-0.400	-	1.807e-02	0.078	0.747	598.800
TF16	-0.300	-	1.782e-02	0.095	0.736	590.500
TF17	-0.200	-	1.867e-02	0.070	0.771	618.520
TF18	-0.100	-	2.201e-02	0.086	0.909	729.440
TF19	0.000	-	2.467e-02	0.062	1.019	817.290
TF20	0.100	-	2.247e-02	0.077	0.928	744.520
TF21	0.200	-	*	*	*	*
TF22	0.300	-	1.852e-02	0.133	0.765	613.680
TF23	0.400	-	1.710e-02	0.093	0.706	566.610
TF24	0.500	-	*	*	*	*
TF25	0.600	-	1.683e-02	0.079	0.695	557.510
TF26	0.700	-	1.694e-02	0.112	0.700	561.230
TF27	0.800	-	1.573e-02	0.064	0.650	521.230
TF28	0.900	-	1.561e-02	0.092	0.645	517.100
TF29	1.000	-	7.059e-03	0.064	0.292	233.890
TF30	1.161	-	8.876e-04	0.166	0.037	29.409
TF31	1.308	-	1.623e-04	0.761	0.007	5.377
TF32	1.433	-	*	*	*	*
TF33	1.557	-	5.382e-05	0.661	0.002	1.783
TF34	1.682	-	*	*	*	*
TF35	1.806	-	2.158e-04	0.232	0.009	7.152
TF36	1.900	-	1.801e-04	0.217	0.007	5.969
TF37	2.000	-	1.203e-04	0.903	0.005	3.988
TF38	-	-	-	-	-	-
TF39	2.114	0.070	*	*	*	*
TF40	2.219	0.175	*	*	*	*
TF41	2.324	0.280	*	*	*	*
TF42	2.429	0.385	*	*	*	*
TF43	2.534	0.490	*	*	*	*
TF44	2.639	0.595	*	*	*	*
TF45	2.744	0.700	*	*	*	*
TF46	2.849	0.805	*	*	*	*
TF47	2.954	0.910	*	*	*	*
TF48	3.059	1.015	7.520e-04	0.167	0.031	24.916
TF49	3.164	1.120	8.372e-04	0.116	0.035	27.740
TF50	3.269	1.225	8.332e-04	0.099	0.034	27.609
TF51	3.374	1.330	8.887e-04	0.090	0.037	29.447
TF52	3.479	1.435	*	*	*	*
TF53	3.584	1.540	8.885e-04	0.089	0.037	29.440
TF54	3.689	1.645	*	*	*	*
TF55	3.794	1.750	7.875e-04	0.068	0.033	26.092
TF56	3.899	1.855	8.432e-04	0.065	0.035	27.940
TF57	4.004	1.960	7.826e-04	0.057	0.032	25.932
TF58	4.109	2.065	7.759e-04	0.049	0.032	25.709
TF59	4.214	2.170	*	*	*	*
TF60	4.319	2.275	7.195e-04	0.095	0.030	23.840
TF61	4.424	2.380	*	*	*	*
TF62	4.529	2.485	6.742e-04	0.105	0.028	22.341
TF63	4.634	2.590	6.547e-04	0.105	0.027	21.693
TF64	4.739	2.695	6.337e-04	0.123	0.026	20.999
TF65	4.844	2.800	6.224e-04	0.126	0.026	20.624
TF66	4.949	2.905	*	*	*	*
TF67	5.054	3.010	*	*	*	*
TF68	5.159	3.115	*	*	*	*
TF69	5.264	3.220	5.884e-04	0.183	0.024	19.498
TF70	5.283	3.325	*	*	*	*

TABLE B-29: HYPULSE Run 903 Heating Data
MP-1 (SS) Configuration, CO_2 Test Gas, $\alpha = 0$ deg, $C_{H,ref} = 0.024208$

GAGE ID	S/R_b	L/R_b	C_H	s/C_H	$C_H/C_{H,ref}$	q_{300} (W/cm^2)
TF38	1.931	0.015	8.056e-05	0.703	0.003	2.592
TF39	2.036	0.120	1.140e-04	0.339	0.005	3.668
TF40	2.141	0.225	1.500e-04	0.404	0.006	4.827
TF41	2.246	0.330	1.174e-04	0.959	0.005	3.776
TF42	2.351	0.435	1.072e-04	0.937	0.004	3.449
TF43	2.456	0.540	1.175e-04	0.950	0.005	3.780
TF44	2.561	0.645	2.318e-04	0.701	0.010	7.456
TF45	2.666	0.750	2.200e-04	0.411	0.009	7.077
TF46	2.771	0.855	4.053e-04	0.201	0.017	13.038
TF47	2.876	0.960	3.681e-04	0.284	0.015	11.842
TF48	2.981	1.065	4.495e-04	0.515	0.019	14.459
TF49	3.086	1.170	8.018e-04	0.090	0.033	25.793
TF50	3.191	1.275	*	*	*	*
TF51	3.296	1.380	8.557e-04	0.103	0.035	27.528
TF52	3.401	1.485	8.054e-04	0.089	0.033	25.909
TF53	3.506	1.590	8.412e-04	0.103	0.035	27.061
TF54	3.611	1.695	9.169e-04	0.108	0.038	29.496
TF55	3.716	1.800	8.738e-04	0.125	0.036	28.109
TF56	3.821	1.905	9.070e-04	0.112	0.037	29.178
TF57	3.926	2.010	8.335e-04	0.131	0.034	26.812
TF58	4.031	2.115	8.133e-04	0.141	0.034	26.162
TF59	4.136	2.220	7.680e-04	0.101	0.032	24.705
TF60	4.241	2.325	8.386e-04	0.139	0.035	26.978
TF61	4.346	2.430	7.899e-04	0.167	0.033	25.410
TF62	4.451	2.535	7.771e-04	0.207	0.032	24.999
TF63	4.556	2.640	*	*	*	*
TF64	4.661	2.745	6.632e-04	0.200	0.027	21.336
TF65	4.766	2.850	*	*	*	*
TF66	4.871	2.955	5.848e-04	0.262	0.024	18.812
TF67	4.976	3.060	6.216e-04	0.249	0.026	19.997
TF68	5.081	3.165	5.791e-04	0.191	0.024	18.629
TF69	5.186	3.270	6.926e-04	0.171	0.029	22.279
TF70	5.291	3.375	6.526e-04	0.234	0.027	20.994

TABLE B-30: HYPULSE Run 904 Heating Data

MP-1 (SS) Configuration, CO_2 Test Gas, $\alpha = 0$ deg, $C_{H,ref} = 0.024208$

GAGE ID	S/R_b	L/R_b	C_H	s/C_H	$C_H/C_{H,ref}$	q_{300} (W/cm^2)
TF38	1.931	0.015	6.247e-06	8.306	0.000	0.211
TF39	2.036	0.120	5.140e-06	4.580	0.000	0.173
TF40	2.141	0.225	7.122e-06	7.038	0.000	0.240
TF41	2.246	0.330	1.240e-04	0.341	0.005	4.179
TF42	2.351	0.435	9.735e-05	0.561	0.004	3.280
TF43	2.456	0.540	1.265e-04	0.133	0.005	4.264
TF44	2.561	0.645	2.808e-04	0.187	0.012	9.463
TF45	2.666	0.750	2.532e-04	0.087	0.010	8.532
TF46	2.771	0.855	2.888e-04	0.241	0.012	9.733
TF47	2.876	0.960	4.287e-04	0.156	0.018	14.448
TF48	2.981	1.065	6.501e-04	0.264	0.027	21.910
TF49	3.086	1.170	7.763e-04	0.109	0.032	26.162
TF50	3.191	1.275	*	*	*	*
TF51	3.296	1.380	1.042e-03	0.112	0.043	35.099
TF52	3.401	1.485	1.068e-03	0.085	0.044	35.981
TF53	3.506	1.590	1.051e-03	0.086	0.043	35.436
TF54	3.611	1.695	1.068e-03	0.072	0.044	36.004
TF55	3.716	1.800	1.053e-03	0.063	0.044	35.488
TF56	3.821	1.905	*	*	*	*
TF57	3.926	2.010	*	*	*	*
TF58	4.031	2.115	1.004e-03	0.091	0.041	33.829
TF59	4.136	2.220	9.569e-04	0.055	0.040	32.247
TF60	4.241	2.325	8.730e-04	0.120	0.036	29.421
TF61	4.346	2.430	8.530e-04	0.136	0.035	28.746
TF62	4.451	2.535	7.681e-04	0.256	0.032	25.885
TF63	4.556	2.640	*	*	*	*
TF64	4.661	2.745	7.770e-04	0.090	0.032	26.185
TF65	4.766	2.850	*	*	*	*
TF66	4.871	2.955	*	*	*	*
TF67	4.976	3.060	6.695e-04	0.100	0.028	22.564
TF68	5.081	3.165	6.270e-04	0.226	0.026	21.128
TF69	5.186	3.270	5.971e-04	0.165	0.025	20.121
TF70	5.291	3.375	6.290e-04	0.295	0.026	21.199

TABLE B-31: HYPULSE Run 905 Heating Data

MP-1 (SS) Configuration, Air Test Gas, $\alpha = 0$ deg, $C_{H,ref} = 0.031279$

GAGE ID	S/R_b	L/R_b	C_H	s/C_H	$C_H/C_{H,ref}$	q_{300} (W/cm^2)
TF38	1.931	0.015	5.968e-05	0.857	0.002	2.365
TF39	2.036	0.120	8.865e-05	0.408	0.003	3.513
TF40	2.141	0.225	1.701e-04	0.396	0.005	6.742
TF41	2.246	0.330	1.811e-04	0.250	0.006	7.176
TF42	2.351	0.435	2.586e-04	0.119	0.008	10.250
TF43	2.456	0.540	2.313e-04	0.179	0.007	9.168
TF44	2.561	0.645	4.122e-04	0.110	0.013	16.338
TF45	2.666	0.750	3.996e-04	0.107	0.013	15.838
TF46	2.771	0.855	2.955e-04	0.307	0.009	11.710
TF47	2.876	0.960	7.141e-04	0.124	0.023	28.302
TF48	2.981	1.065	9.194e-04	0.210	0.029	36.437
TF49	3.086	1.170	1.171e-03	0.129	0.037	46.421
TF50	3.191	1.275	*	*	*	*
TF51	3.296	1.380	1.537e-03	0.126	0.049	60.911
TF52	3.401	1.485	1.624e-03	0.124	0.052	64.348
TF53	3.506	1.590	1.545e-03	0.108	0.049	61.222
TF54	3.611	1.695	1.618e-03	0.112	0.052	64.138
TF55	3.716	1.800	1.729e-03	0.086	0.055	68.536
TF56	3.821	1.905	1.687e-03	0.091	0.054	66.866
TF57	3.926	2.010	1.533e-03	0.082	0.049	60.764
TF58	4.031	2.115	1.564e-03	0.094	0.050	61.975
TF59	4.136	2.220	1.580e-03	0.074	0.051	62.624
TF60	4.241	2.325	*	*	*	*
TF61	4.346	2.430	1.510e-03	0.094	0.048	59.865
TF62	4.451	2.535	*	*	*	*
TF63	4.556	2.640	*	*	*	*
TF64	4.661	2.745	1.253e-03	0.119	0.040	49.650
TF65	4.871	2.850	*	*	*	*
TF66	4.871	2.955	1.100e-03	0.151	0.035	43.616
TF67	4.976	3.060	1.093e-03	0.163	0.035	43.302
TF68	5.081	3.165	9.822e-04	0.132	0.031	38.929
TF69	5.186	3.270	9.696e-04	0.085	0.031	38.427
TF70	5.291	3.375	9.209e-04	0.103	0.029	36.497

TABLE B-32: HYPULSE Run 906 Heating Data
MP-1 (SS) Configuration, Air Test Gas, $\alpha = 0$ deg, $C_{H,ref} = 0.031279$

GAGE ID	S/R_b	L/R_b	C_H	s/C_H	$C_H/C_{H,ref}$	q_{300} (W/cm^2)
TF38	1.931	0.015	4.184e-05	0.457	0.001	1.744
TF39	2.036	0.120	8.668e-05	0.273	0.003	3.613
TF40	2.141	0.225	8.420e-05	0.410	0.003	3.510
TF41	2.246	0.330	1.646e-04	0.642	0.005	6.859
TF42	2.351	0.435	1.418e-04	0.676	0.005	5.909
TF43	2.456	0.540	1.601e-04	0.407	0.005	6.673
TF44	2.561	0.645	2.667e-04	0.318	0.009	11.119
TF45	2.666	0.750	3.029e-04	0.162	0.010	12.626
TF46	2.771	0.855	3.666e-04	0.191	0.012	15.283
TF47	2.876	0.960	5.028e-04	0.191	0.016	20.958
TF48	2.981	1.065	5.311e-04	0.250	0.017	22.137
TF49	3.086	1.170	6.789e-04	0.134	0.022	28.298
TF50	3.191	1.275	8.859e-04	0.069	0.028	36.927
TF51	3.296	1.380	1.135e-03	0.051	0.036	47.314
TF52	3.401	1.485	1.202e-03	0.101	0.038	50.125
TF53	3.506	1.590	1.251e-03	0.122	0.040	52.156
TF54	3.611	1.695	1.338e-03	0.127	0.043	55.793
TF55	3.716	1.800	1.451e-03	0.122	0.046	60.480
TF56	3.821	1.905	1.573e-03	0.101	0.050	65.578
TF57	3.926	2.010	1.477e-03	0.060	0.047	61.576
TF58	4.031	2.115	1.559e-03	0.096	0.050	65.000
TF59	4.136	2.220	1.601e-03	0.085	0.051	66.753
TF60	4.241	2.325	1.561e-03	0.088	0.050	65.051
TF61	4.346	2.430	1.550e-03	0.084	0.050	64.596
TF62	4.451	2.535	1.413e-03	0.089	0.045	58.884
TF63	4.556	2.640	*	*	*	*
TF64	4.661	2.745	1.321e-03	0.102	0.042	55.075
TF65	4.766	2.850	1.133e-03	0.083	0.036	47.214
TF66	4.871	2.955	1.142e-03	0.115	0.037	47.616
TF67	4.976	3.060	1.077e-03	0.142	0.034	44.887
TF68	5.081	3.165	1.063e-03	0.072	0.034	44.290
TF69	5.186	3.270	1.023e-03	0.088	0.033	42.632
TF70	5.291	3.375	8.416e-04	0.097	0.027	35.082

TABLE B-33: HYPULSE Run 907 Heating Data

MP-1 (75%) Configuration, CO_2 Test Gas, $\alpha = 0$ deg, $C_{H,ref} = 0.024208$

GAGE ID	S/R_b	L/R_b	C_H	s/C_H	$C_H/C_{H,ref}$	q_{300} (W/cm^2)
TF38	1.500	0.165	1.396e-04	0.250	0.006	4.700
TF39	1.605	0.270	2.122e-04	0.121	0.009	7.147
TF40	1.710	0.375	3.140e-04	0.207	0.013	10.575
TF41	1.815	0.480	3.906e-04	0.131	0.016	13.153
TF42	1.920	0.585	4.756e-04	0.157	0.020	16.015
TF43	2.025	0.690	4.581e-04	0.164	0.019	15.427
TF44	2.130	0.795	7.034e-04	0.133	0.029	23.689
TF45	2.235	0.900	7.282e-04	0.174	0.030	24.524
TF46	2.340	1.005	7.051e-04	0.148	0.029	23.745
TF47	2.445	1.110	8.251e-04	0.133	0.034	27.788
TF48	2.550	1.215	*	*	*	*
TF49	2.655	1.320	8.649e-04	0.130	0.036	29.129
TF50	2.760	1.425	7.477e-04	0.059	0.031	25.179
TF51	2.865	1.530	7.919e-04	0.063	0.033	26.669
TF52	2.970	1.635	6.907e-04	0.065	0.029	23.262
TF53	3.075	1.740	6.893e-04	0.058	0.028	23.212
TF54	3.180	1.845	6.527e-04	0.077	0.027	21.979
TF55	3.285	1.950	6.883e-04	0.068	0.028	23.180
TF56	3.390	2.055	6.773e-04	0.074	0.028	22.808
TF57	3.495	2.160	5.753e-04	0.078	0.024	19.374
TF58	3.600	2.265	6.828e-04	0.167	0.028	22.993
TF59	3.705	2.370	6.955e-04	0.148	0.029	23.421
TF60	3.810	2.475	6.124e-04	0.112	0.025	20.623
TF61	3.915	2.580	*	*	*	*
TF62	4.020	2.685	5.816e-04	0.179	0.024	19.586
TF63	4.075	2.740	*	*	*	*
TF64	4.230	2.895	6.226e-04	0.240	0.026	20.967
TF65	4.335	3.000	5.575e-04	0.146	0.023	18.777
TF66	4.440	3.105	*	*	*	*
TF67	4.545	3.210	*	*	*	*
TF68	4.650	3.315	*	*	*	*
TF69	4.755	3.420	*	*	*	*
TF70	4.860	3.525	*	*	*	*

TABLE B-34: HYPULSE Run 908 Heating Data

MP-1 (75%) Configuration, CO_2 Test Gas, $\alpha = 0$ deg, $C_{H,ref} = 0.024208$

GAGE ID	S/R_b	L/R_b	C_H	s/C_H	$C_H/C_{H,ref}$	q_{300} (W/cm^2)
TF38	1.500	0.165	1.162e-04	0.465	0.005	3.846
TF39	1.605	0.270	1.430e-04	0.293	0.006	4.734
TF40	1.710	0.375	2.489e-04	0.271	0.010	8.238
TF41	1.815	0.480	2.989e-04	0.190	0.012	9.896
TF42	1.920	0.585	4.503e-04	0.234	0.019	14.908
TF43	2.025	0.690	5.755e-04	0.243	0.024	19.052
TF44	2.130	0.795	*	*	*	*
TF45	2.235	0.900	9.255e-04	0.185	0.038	30.639
TF46	2.340	1.005	9.482e-04	0.168	0.039	31.391
TF47	2.445	1.110	*	*	*	*
TF48	2.550	1.215	*	*	*	*
TF49	2.655	1.320	*	*	*	*
TF50	2.760	1.425	1.166e-03	0.139	0.048	38.600
TF51	2.865	1.530	1.204e-03	0.124	0.050	39.846
TF52	2.970	1.635	1.100e-03	0.119	0.045	36.420
TF53	3.075	1.740	1.009e-03	0.115	0.042	33.410
TF54	3.180	1.845	1.077e-03	0.091	0.044	35.655
TF55	3.285	1.950	1.036e-03	0.099	0.043	34.301
TF56	3.390	2.055	1.023e-03	0.085	0.042	33.868
TF57	3.495	2.160	9.300e-04	0.094	0.038	30.790
TF58	3.600	2.265	9.258e-04	0.145	0.038	30.651
TF59	3.705	2.370	8.516e-04	0.134	0.035	28.193
TF60	3.810	2.475	9.336e-04	0.129	0.039	30.908
TF61	3.915	2.580	8.088e-04	0.151	0.033	26.777
TF62	4.020	2.685	7.909e-04	0.190	0.033	26.182
TF63	4.075	2.740	*	*	*	*
TF64	4.230	2.895	*	*	*	*
TF65	4.335	3.000	7.288e-04	0.124	0.030	24.129
TF66	4.440	3.105	5.454e-04	0.211	0.023	18.056
TF67	4.545	3.210	*	*	*	*
TF68	4.650	3.315	6.266e-04	0.176	0.026	20.744
TF69	4.755	3.420	5.982e-04	0.109	0.025	19.804
TF70	4.860	3.525	6.137e-04	0.099	0.025	20.318

TABLE B-35: HYPULSE Run 909 Heating Data

MP-1 (88%) Configuration, CO_2 Test Gas, $\alpha = 0$ deg, $C_{H,ref} = 0.024208$

GAGE ID	S/R_b	L/R_b	C_H	s/C_H	$C_H/C_{H,ref}$	q_{300} (W/cm^2)
TF38	1.738	0.115	8.100e-05	0.483	0.003	2.645
TF39	1.843	0.220	1.401e-04	0.366	0.006	4.575
TF40	1.948	0.325	1.413e-04	0.543	0.006	4.615
TF41	2.053	0.430	2.042e-04	0.409	0.008	6.667
TF42	2.158	0.535	3.885e-04	0.286	0.016	12.684
TF43	2.263	0.640	4.988e-04	0.252	0.021	16.286
TF44	2.368	0.745	*	*	*	*
TF45	2.473	0.850	8.578e-04	0.210	0.035	28.006
TF46	2.578	0.955	8.704e-04	0.184	0.036	28.417
TF47	2.683	1.060	*	*	*	*
TF48	2.788	1.165	*	*	*	*
TF49	2.893	1.270	*	*	*	*
TF50	2.998	1.375	1.012e-03	0.125	0.042	33.037
TF51	3.103	1.480	*	*	*	*
TF52	3.208	1.585	1.025e-03	0.112	0.042	33.461
TF53	3.313	1.690	9.413e-04	0.145	0.039	30.732
TF54	3.418	1.795	1.025e-03	0.126	0.042	33.459
TF55	3.523	1.900	9.793e-04	0.092	0.040	31.973
TF56	3.628	2.005	9.979e-04	0.098	0.041	32.582
TF57	3.733	2.110	9.984e-04	0.141	0.041	32.596
TF58	3.838	2.215	8.831e-04	0.159	0.036	28.834
TF59	3.943	2.320	7.846e-04	0.189	0.032	25.618
TF60	4.048	2.425	7.484e-04	0.239	0.031	24.435
TF61	4.153	2.530	7.864e-04	0.164	0.032	25.676
TF62	4.258	2.635	6.978e-04	0.268	0.029	22.783
TF63	4.363	2.740	*	*	*	*
TF64	4.468	2.845	*	*	*	*
TF65	4.573	2.950	*	*	*	*
TF66	4.678	3.055	*	*	*	*
TF67	4.783	3.160	*	*	*	*
TF68	4.888	3.265	*	*	*	*
TF69	4.993	3.370	*	*	*	*
TF70	5.098	3.475	*	*	*	*

TABLE B-36: HYPULSE Run 910 Heating Data
MP-1 (88%) Configuration, CO_2 Test Gas, $\alpha = 0$ deg, $C_{H,ref} = 0.024208$

GAGE ID	S/R_b	L/R_b	C_H	s/C_H	$C_H/C_{H,ref}$	q_{300} (W/cm^2)
TF38	1.738	0.115	8.942e-05	0.414	0.004	2.970
TF39	1.843	0.220	1.506e-04	0.345	0.006	5.003
TF40	1.948	0.325	9.839e-05	0.534	0.004	3.268
TF41	2.053	0.430	1.545e-04	0.146	0.006	5.134
TF42	2.158	0.535	1.966e-04	0.120	0.008	6.530
TF43	2.263	0.640	3.049e-04	0.114	0.013	10.128
TF44	2.368	0.745	3.866e-04	0.088	0.016	12.842
TF45	2.473	0.850	5.221e-04	0.053	0.022	17.345
TF46	2.578	0.955	6.169e-04	0.112	0.025	20.495
TF47	2.683	1.060	7.787e-04	0.154	0.032	25.867
TF48	2.788	1.165	9.627e-04	0.114	0.040	31.980
TF49	2.893	1.270	*	*	*	*
TF50	2.998	1.375	1.037e-03	0.062	0.043	34.447
TF51	3.103	1.480	*	*	*	*
TF52	3.208	1.585	1.019e-03	0.079	0.042	33.839
TF53	3.313	1.690	9.009e-04	0.048	0.037	29.927
TF54	3.418	1.795	9.131e-04	0.056	0.038	30.332
TF55	3.523	1.900	8.712e-04	0.113	0.036	28.940
TF56	3.628	2.005	8.175e-04	0.123	0.034	27.158
TF57	3.733	2.110	7.566e-04	0.096	0.031	25.135
TF58	3.838	2.215	6.755e-04	0.077	0.028	22.440
TF59	3.943	2.320	7.234e-04	0.128	0.030	24.030
TF60	4.048	2.425	6.457e-04	0.176	0.027	21.451
TF61	4.153	2.530	6.255e-04	0.127	0.026	20.781
TF62	4.258	2.635	*	*	*	*
TF63	4.363	2.740	*	*	*	*
TF64	4.468	2.845	*	*	*	*
TF65	4.573	2.950	*	*	*	*
TF66	4.678	3.055	5.412e-04	0.095	0.022	17.979
TF67	4.783	3.160	5.582e-04	0.108	0.023	18.543
TF68	4.888	3.265	6.001e-04	0.120	0.025	19.935
TF69	4.993	3.370	*	*	*	*
TF70	5.098	3.475	*	*	*	*

TABLE B-37: HYPULSE Run 911 Heating Data
MP-1 (75%) Configuration, Air Test Gas, $\alpha = 0$ deg, $C_{H,ref} = 0.031279$

GAGE ID	S/R_b	L/R_b	C_H	s/C_H	$C_H/C_{H,ref}$	q_{300} (W/cm^2)
TF38	1.500	0.165	2.605e-04	0.178	0.008	10.777
TF39	1.605	0.270	3.107e-04	0.103	0.010	12.854
TF40	1.710	0.375	4.485e-04	0.074	0.014	18.554
TF41	1.815	0.480	4.591e-04	0.090	0.015	18.992
TF42	1.920	0.585	6.923e-04	0.115	0.022	28.640
TF43	2.025	0.690	8.072e-04	0.098	0.026	33.392
TF44	2.130	0.795	1.081e-03	0.101	0.035	44.711
TF45	2.235	0.900	*	*	*	*
TF46	2.340	1.005	1.160e-03	0.067	0.037	47.990
TF47	2.445	1.110	*	*	*	*
TF48	2.550	1.215	*	*	*	*
TF49	2.655	1.320	1.460e-03	0.121	0.047	60.408
TF50	2.760	1.425	1.391e-03	0.058	0.044	57.553
TF51	2.865	1.530	*	*	*	*
TF52	2.970	1.635	1.384e-03	0.068	0.044	57.242
TF53	3.075	1.740	1.332e-03	0.047	0.043	55.103
TF54	3.180	1.845	1.293e-03	0.072	0.041	53.482
TF55	3.285	1.950	1.242e-03	0.089	0.040	51.358
TF56	3.390	2.055	1.204e-03	0.059	0.038	49.805
TF57	3.495	2.160	1.116e-03	0.080	0.036	46.179
TF58	3.600	2.265	1.146e-03	0.100	0.037	47.411
TF59	3.705	2.370	1.076e-03	0.084	0.034	44.492
TF60	3.810	2.475	1.170e-03	0.126	0.037	48.386
TF61	3.915	2.580	1.017e-03	0.128	0.033	42.090
TF62	4.020	2.685	1.012e-03	0.141	0.032	41.879
TF63	4.125	2.790	*	*	*	*
TF64	4.230	2.895	9.449e-04	0.092	0.030	39.090
TF65	4.335	3.000	*	*	*	*
TF66	4.440	3.105	8.568e-04	0.107	0.027	35.445
TF67	4.545	3.210	9.210e-04	0.144	0.029	38.101
TF68	4.650	3.315	8.757e-04	0.115	0.028	36.228
TF69	4.755	3.420	7.466e-04	0.129	0.024	30.885
TF70	4.860	3.525	6.903e-04	0.250	0.022	28.556

TABLE B-38: HYPULSE Run 912 Heating Data
MP-1 (75%) Configuration, Air Test Gas, $\alpha = 0$ deg, $C_{H,ref} = 0.031279$

GAGE ID	S/R_b	L/R_b	C_H	s/C_H	$C_H/C_{H,ref}$	q_{300}(W/cm^2)
TF38	1.500	0.165	2.032e-04	0.256	0.006	8.499
TF39	1.605	0.270	2.962e-04	0.159	0.009	12.388
TF40	1.710	0.375	3.992e-04	0.184	0.013	16.696
TF41	1.815	0.480	5.502e-04	0.283	0.018	23.012
TF42	1.920	0.585	7.297e-04	0.204	0.023	30.515
TF43	2.025	0.690	8.793e-04	0.176	0.028	36.773
TF44	2.130	0.795	1.031e-03	0.191	0.033	43.115
TF45	2.235	0.900	*	*	*	*
TF46	2.340	1.005	1.280e-03	0.253	0.041	53.553
TF47	2.445	1.110	*	*	*	*
TF48	2.550	1.215	*	*	*	*
TF49	2.655	1.320	1.524e-03	0.179	0.049	63.732
TF50	2.760	1.425	1.474e-03	0.119	0.047	61.653
TF51	2.865	1.530	*	*	*	*
TF52	2.970	1.635	1.369e-03	0.199	0.044	57.271
TF53	3.075	1.740	*	*	*	*
TF54	3.180	1.845	*	*	*	*
TF55	3.285	1.950	1.300e-03	0.128	0.042	54.357
TF56	3.390	2.055	1.364e-03	0.136	0.044	57.043
TF57	3.495	2.160	*	*	*	*
TF58	3.600	2.265	1.177e-03	0.175	0.038	49.213
TF59	3.705	2.370	1.148e-03	0.181	0.037	48.012
TF60	3.810	2.475	*	*	*	*
TF61	3.915	2.580	1.075e-03	0.231	0.034	44.973
TF62	4.020	2.685	1.133e-03	0.212	0.036	47.375
TF63	4.125	2.790	*	*	*	*
TF64	4.230	2.895	1.071e-03	0.176	0.034	44.770
TF65	4.335	3.000	*	*	*	*
TF66	4.440	3.105	1.049e-03	0.170	0.034	43.858
TF67	4.545	3.210	1.009e-03	0.175	0.032	42.214
TF68	4.650	3.315	9.852e-04	0.115	0.031	41.201
TF69	4.755	3.420	9.250e-04	0.184	0.030	38.684
TF70	4.860	3.525	8.948e-04	0.271	0.029	37.420

TABLE B-39: HYPULSE Run 913 Heating Data

MP-1 (88%) Configuration, Air Test Gas, $\alpha = 0$ deg, $C_{H,ref} = 0.031279$

GAGE ID	S/R_b	L/R_b	C_H	s/C_H	$C_H/C_{H,ref}$	q_{300} (W/cm^2)
TF38	1.738	0.115	1.656e-04	0.325	0.005	6.882
TF39	1.843	0.220	2.308e-04	0.194	0.007	9.592
TF40	1.948	0.325	2.746e-04	0.305	0.009	11.408
TF41	2.053	0.430	3.431e-04	0.159	0.011	14.257
TF42	2.158	0.535	4.164e-04	0.179	0.013	17.302
TF43	2.263	0.640	4.434e-04	0.162	0.014	18.424
TF44	2.368	0.745	6.172e-04	0.222	0.020	25.642
TF45	2.473	0.850	8.216e-04	0.238	0.026	34.136
TF46	2.578	0.955	8.813e-04	0.214	0.028	36.618
TF47	2.683	1.060	1.120e-03	0.135	0.036	46.514
TF48	2.788	1.165	1.389e-03	0.223	0.044	57.699
TF49	2.893	1.270	1.413e-03	0.131	0.045	58.717
TF50	2.998	1.425	*	*	*	*
TF51	3.103	1.530	*	*	*	*
TF52	3.208	1.635	*	*	*	*
TF53	3.313	1.690	*	*	*	*
TF54	3.418	1.795	1.733e-03	0.156	0.055	72.004
TF55	3.523	1.900	1.585e-03	0.086	0.051	65.842
TF56	3.628	2.005	1.611e-03	0.101	0.052	66.947
TF57	3.733	2.110	1.362e-03	0.131	0.044	56.598
TF58	3.838	2.215	1.421e-03	0.152	0.045	59.047
TF59	3.705	2.370	*	*	*	*
TF60	4.048	2.425	1.194e-03	0.129	0.038	49.622
TF61	3.915	2.580	*	*	*	*
TF62	4.258	2.635	1.285e-03	0.196	0.041	53.397
TF63	4.125	2.790	*	*	*	*
TF64	4.468	2.845	1.198e-03	0.118	0.038	49.756
TF65	4.335	3.000	*	*	*	*
TF66	4.678	3.055	1.010e-03	0.205	0.032	41.957
TF67	4.783	3.160	1.020e-03	0.145	0.033	42.389
TF68	4.888	3.265	9.115e-04	0.157	0.029	37.871
TF69	4.993	3.370	9.485e-04	0.131	0.030	39.410
TF70	5.098	3.475	9.332e-04	0.163	0.030	38.772

TABLE B-40: HYPULSE Run 914 Heating Data
MP-1 (88%) Configuration, Air Test Gas, $\alpha = 0$ deg, $C_{H,ref} = 0.031279$

** BAD RUN, NO DATA **

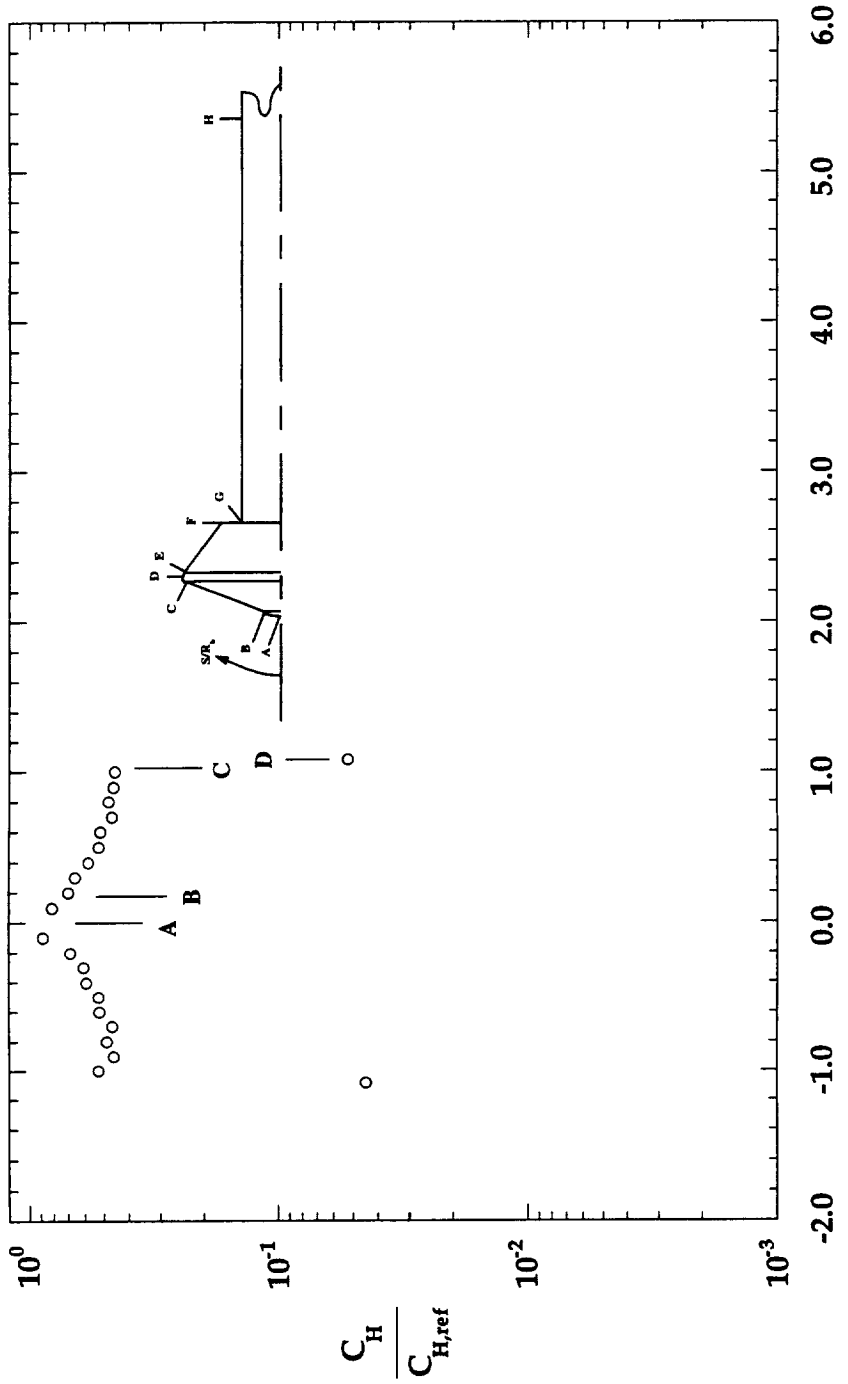

Figure B-1: HYPULSE Run 747, MP-1 Configuration, CO_2 Test Gas, $\alpha = 0°$

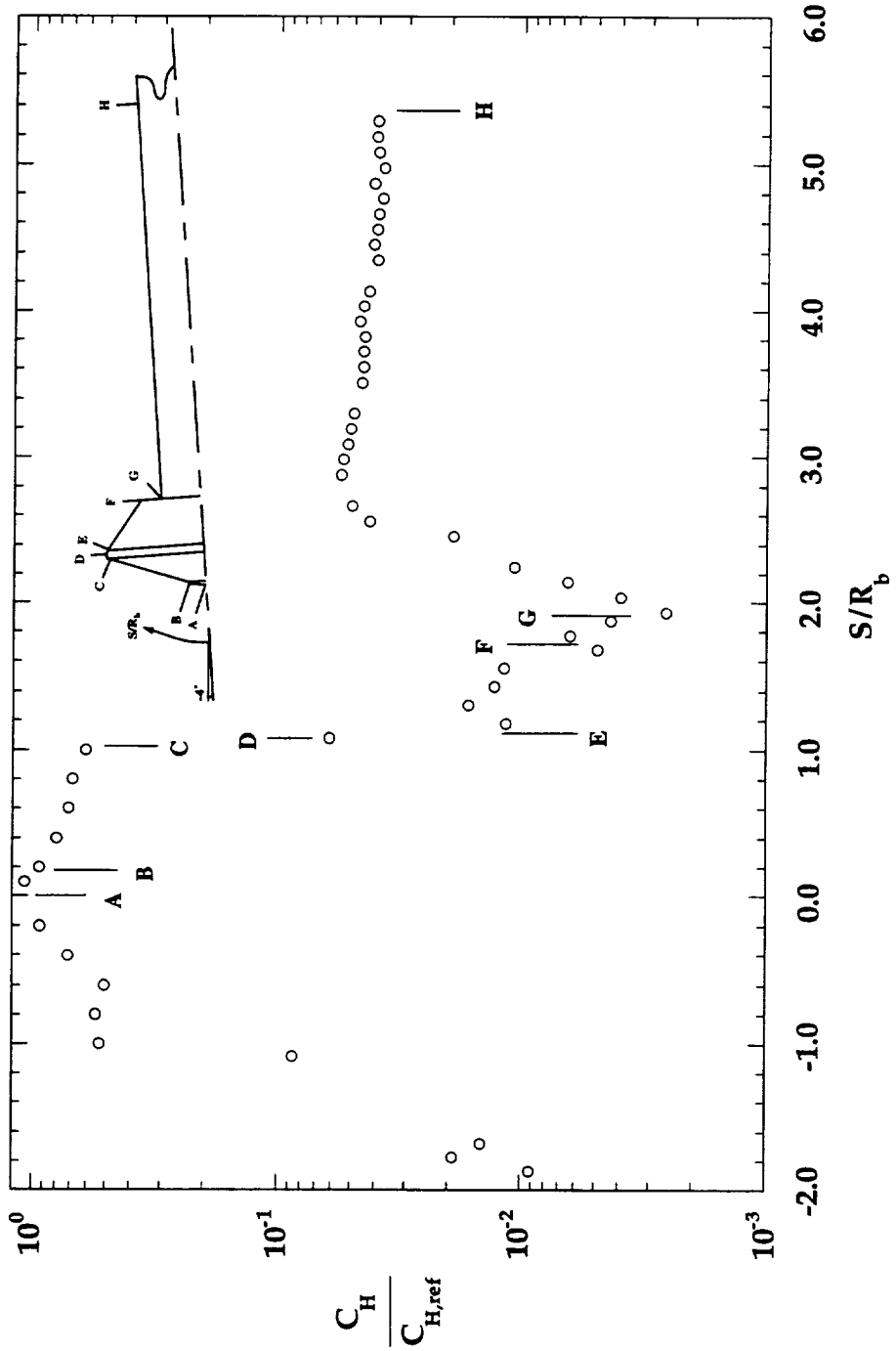

Figure B-2: HYPULSE Run 748, MP-1 Configuration, CO_2 Test Gas, α = -4°

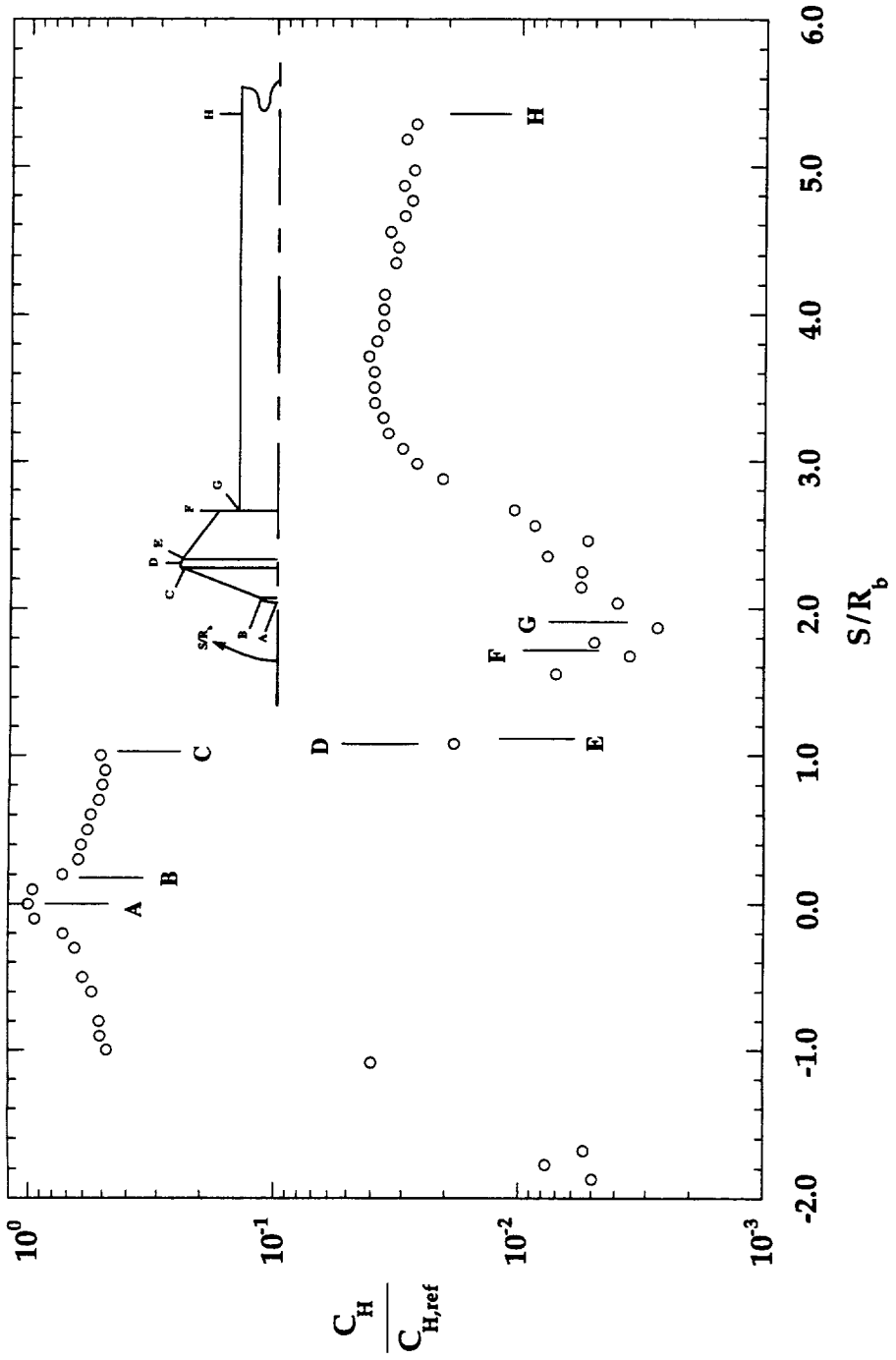

Figure B-3: HYPULSE Run 749, MP-1 Configuration, CO_2 Test Gas, $\alpha = 0°$

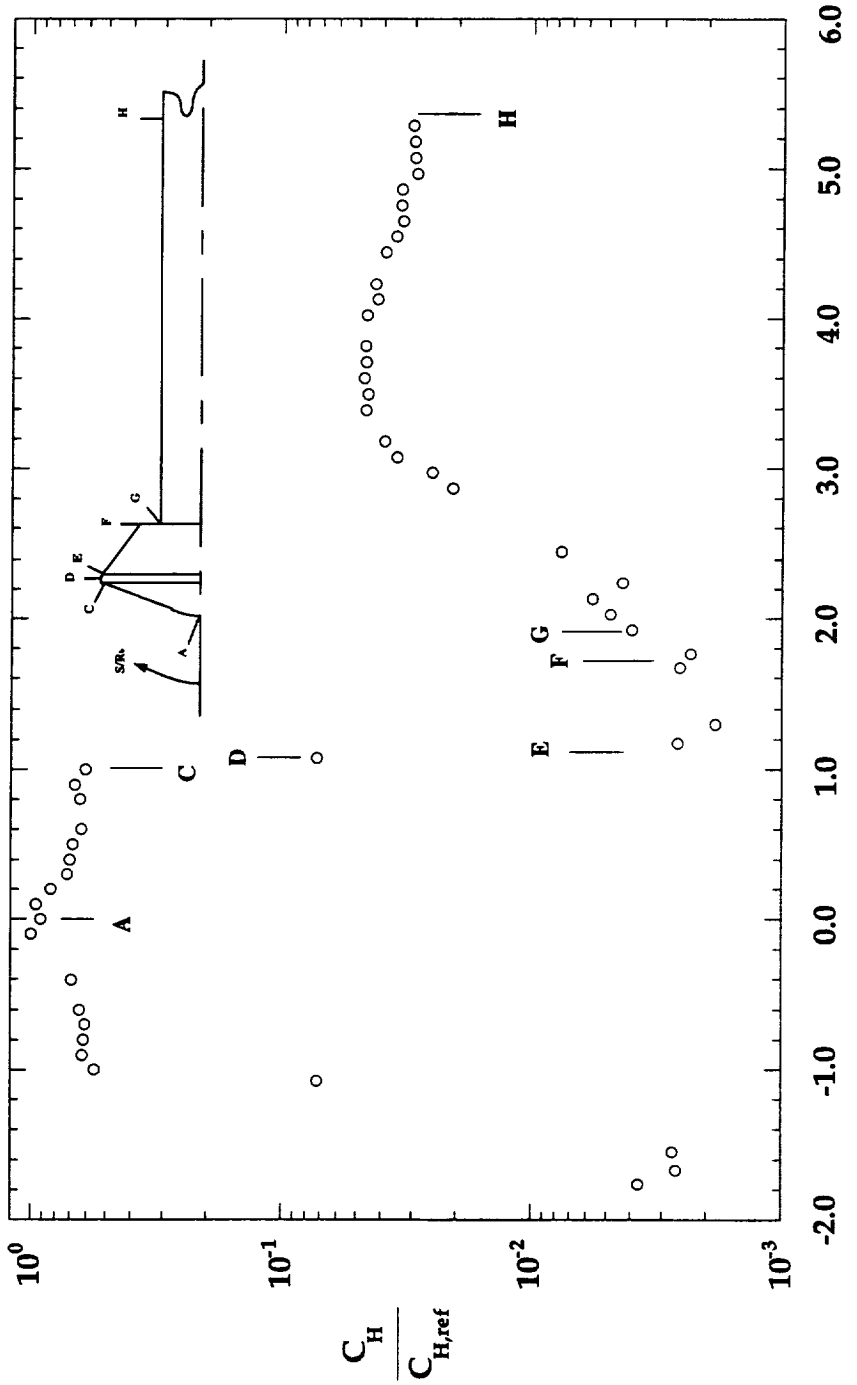

Figure B-4: HYPULSE Run 750, MP-2 Configuration, CO_2 Test Gas, $\alpha = 0°$

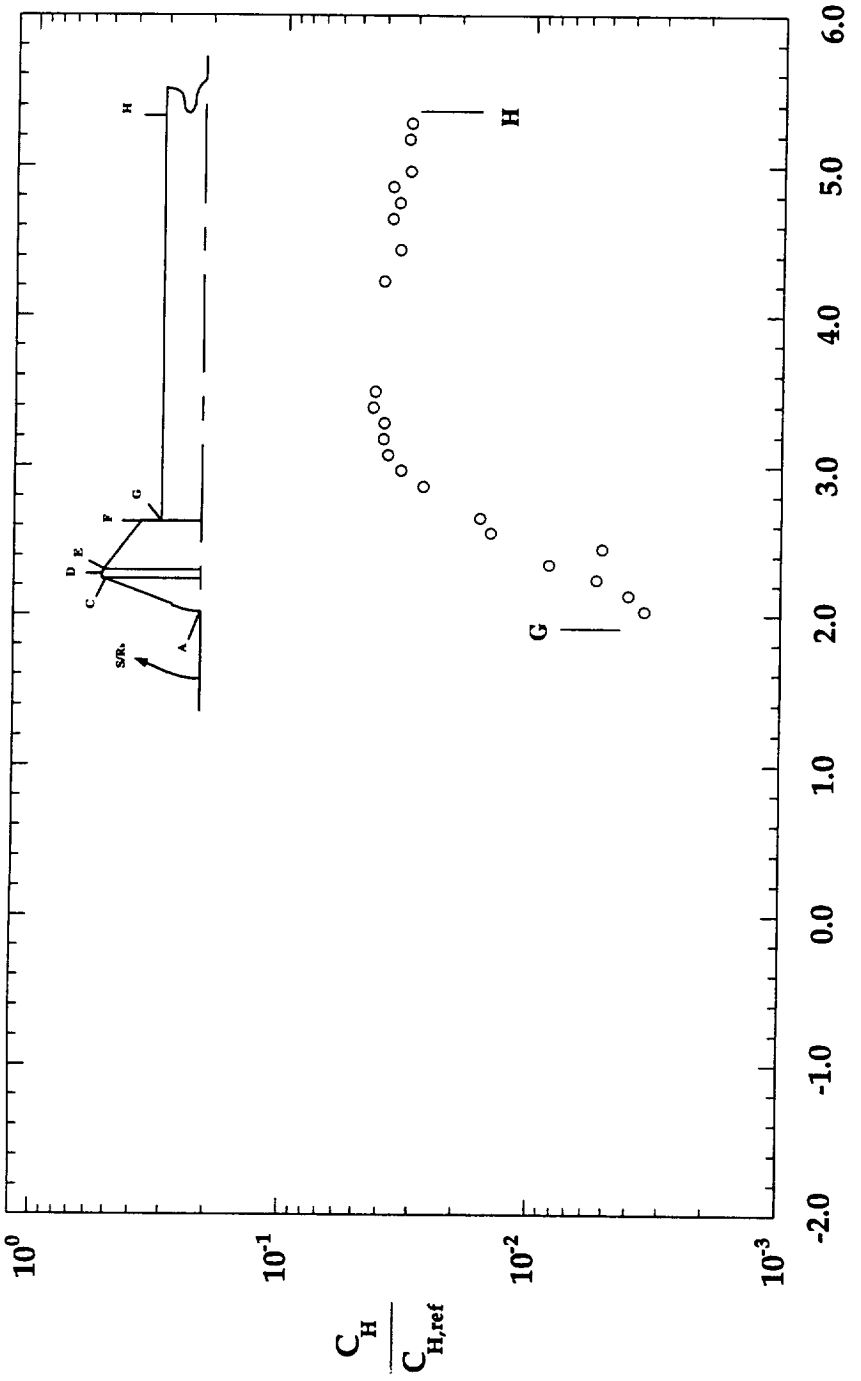

Figure B-5: HYPULSE Run 751, MP-2 Configuration, CO_2 Test Gas, $\alpha = 0°$

*** BAD RUN, NO DATA ***

Figure B-6: HYPULSE Run 752, MP-1 Configuration, Air Test Gas, $\alpha = 0$

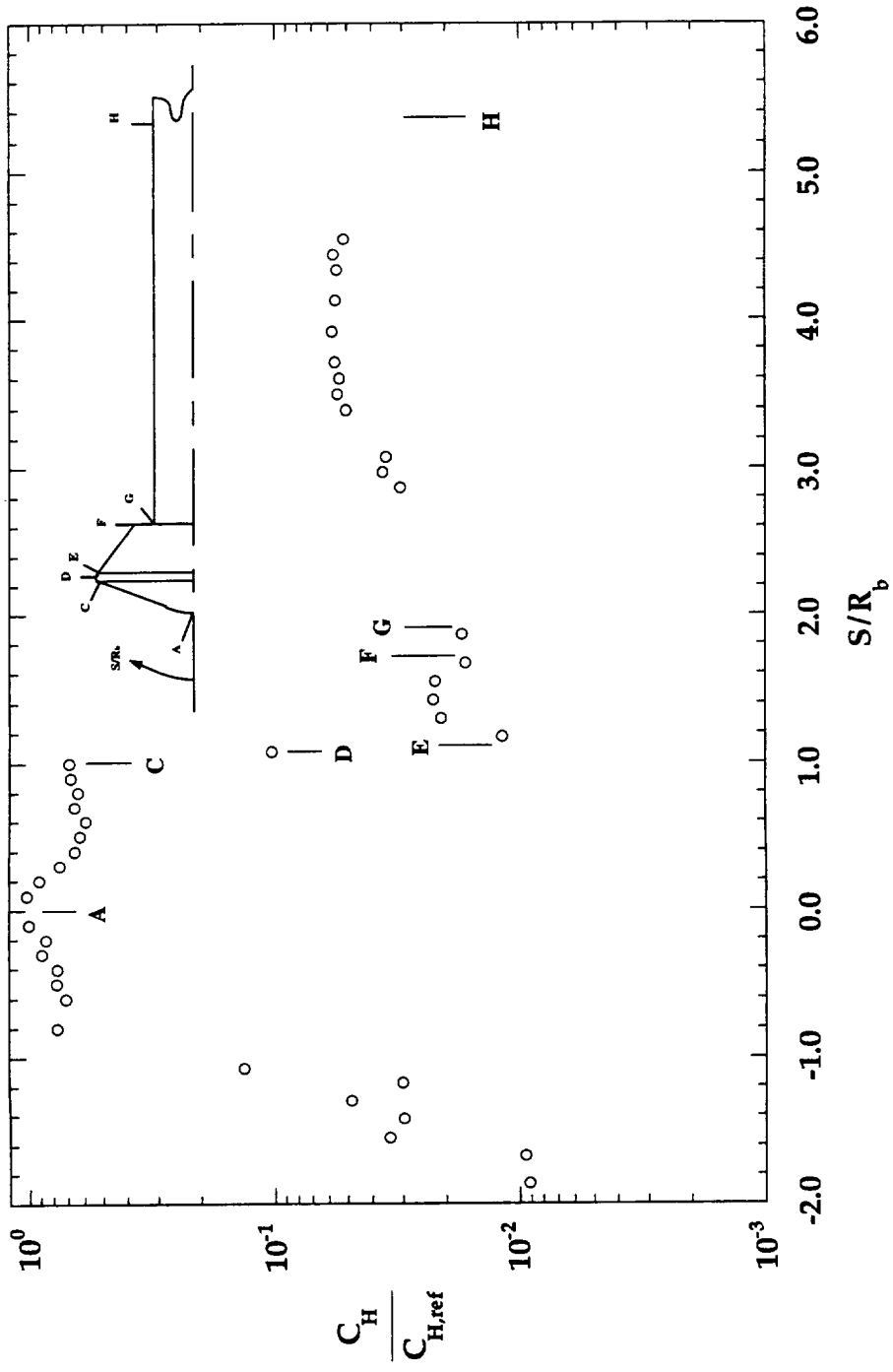

Figure B-7: HYPULSE Run 753, MP-2 Configuration, Air Test Gas, $\alpha = 0°$

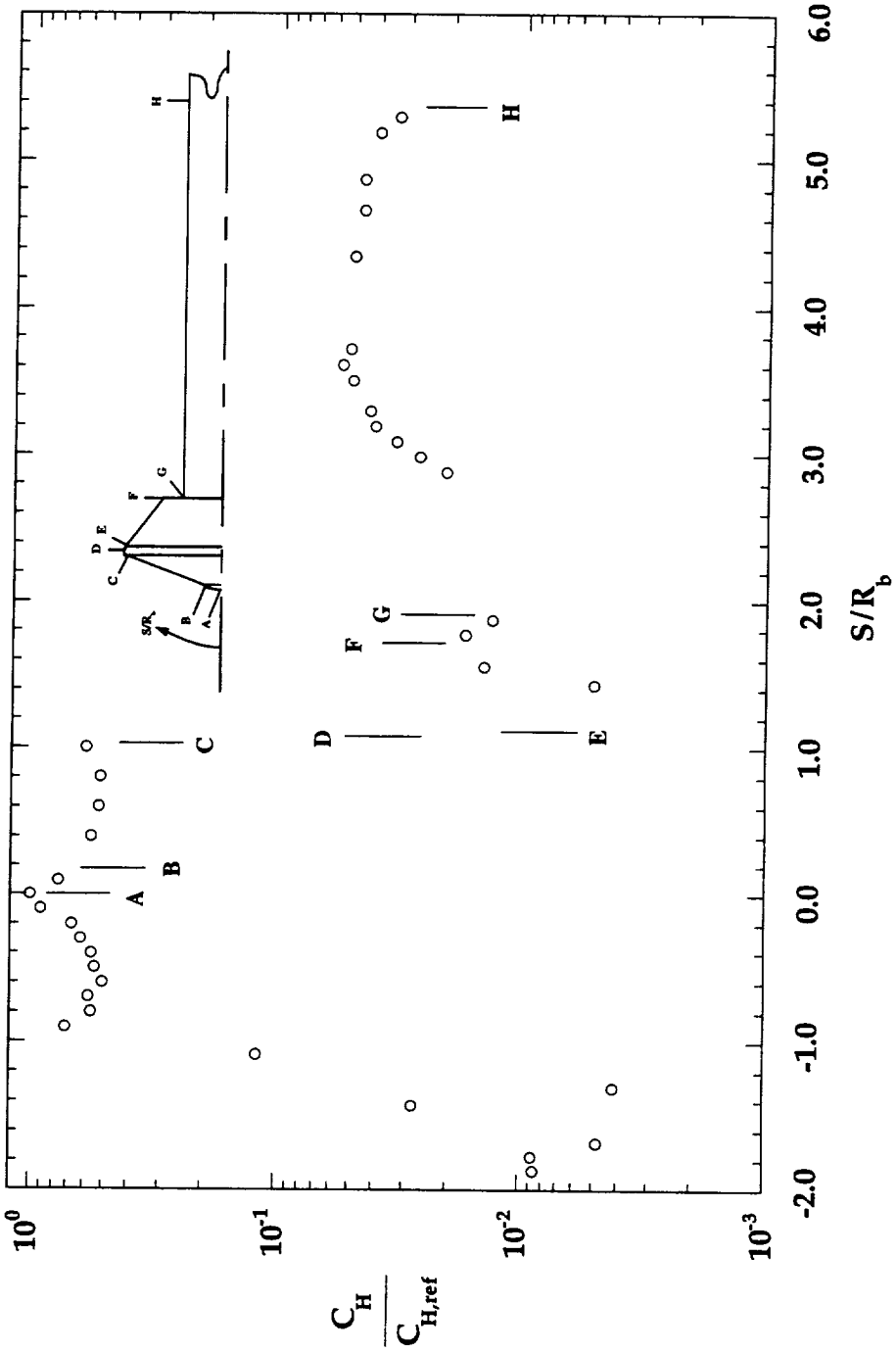

Figure B-8: HYPULSE Run 754, MP-1 Configuration, Air Test Gas, $\alpha = 0°$

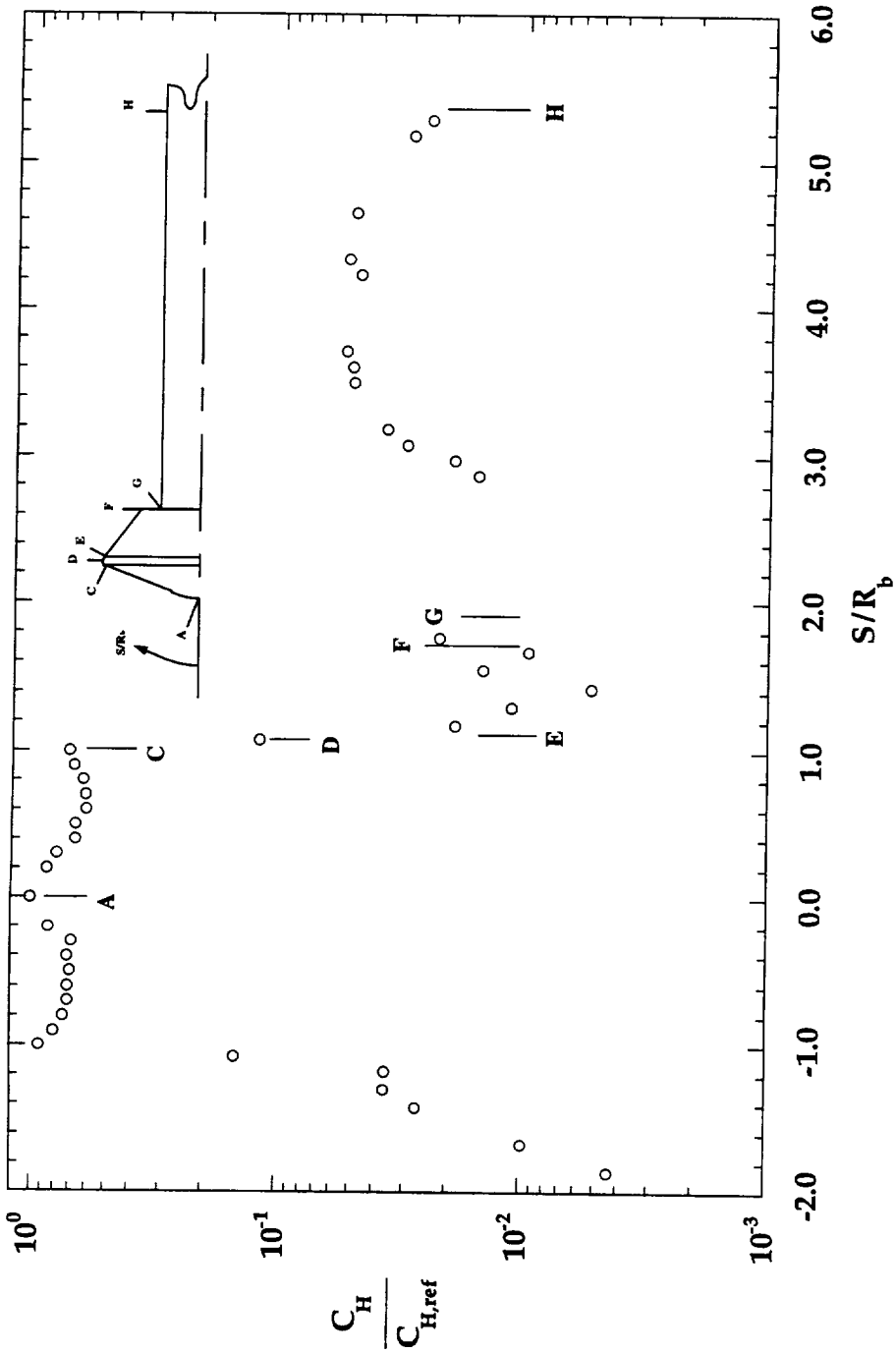

Figure B-9: HYPULSE Run 755, MP-2 Configuration, Air Test Gas, $\alpha = 0°$

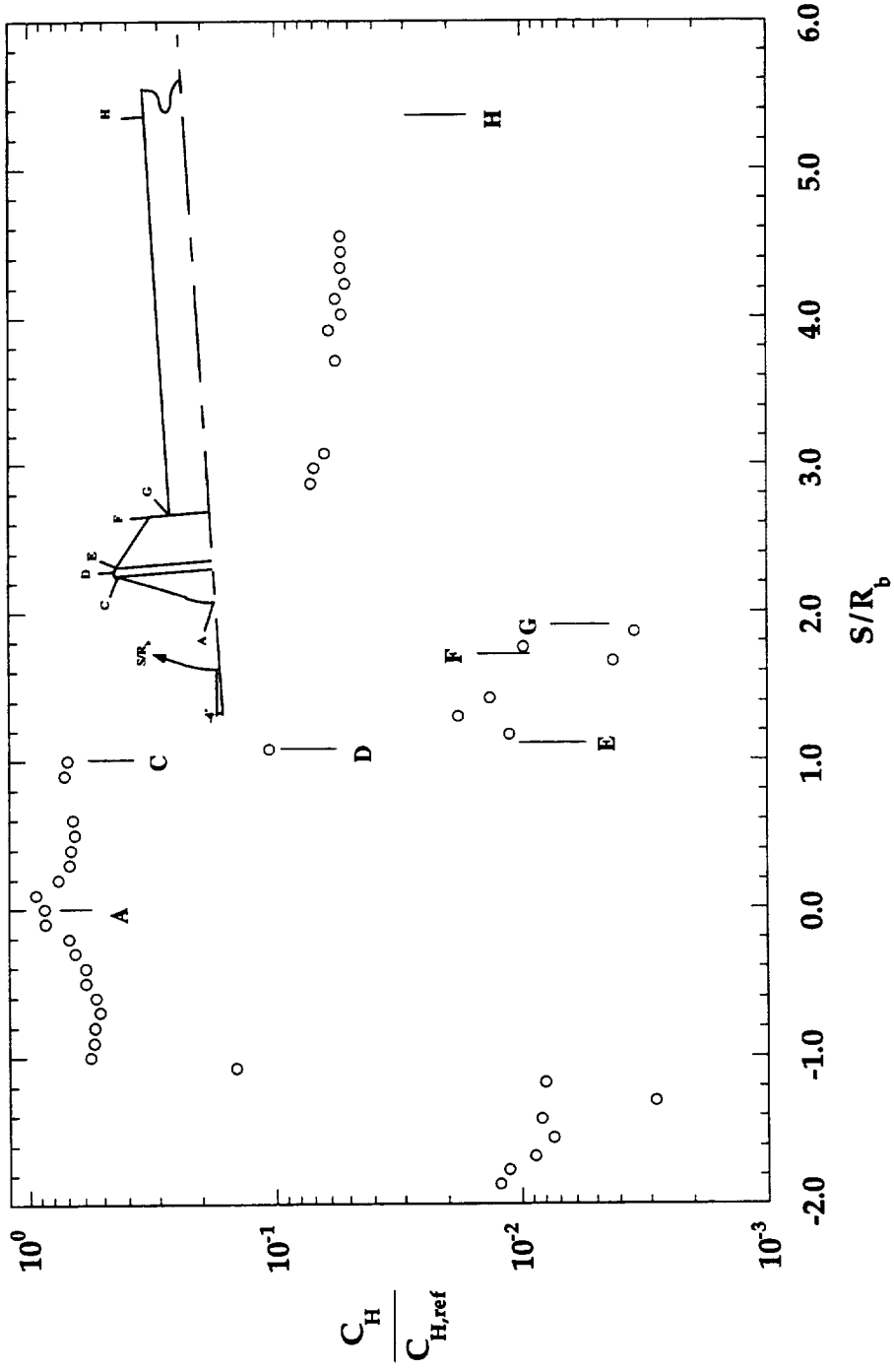

Figure B-10: HYPULSE Run 756, MP-2 Configuration, CO_2 Test Gas, α = -4°

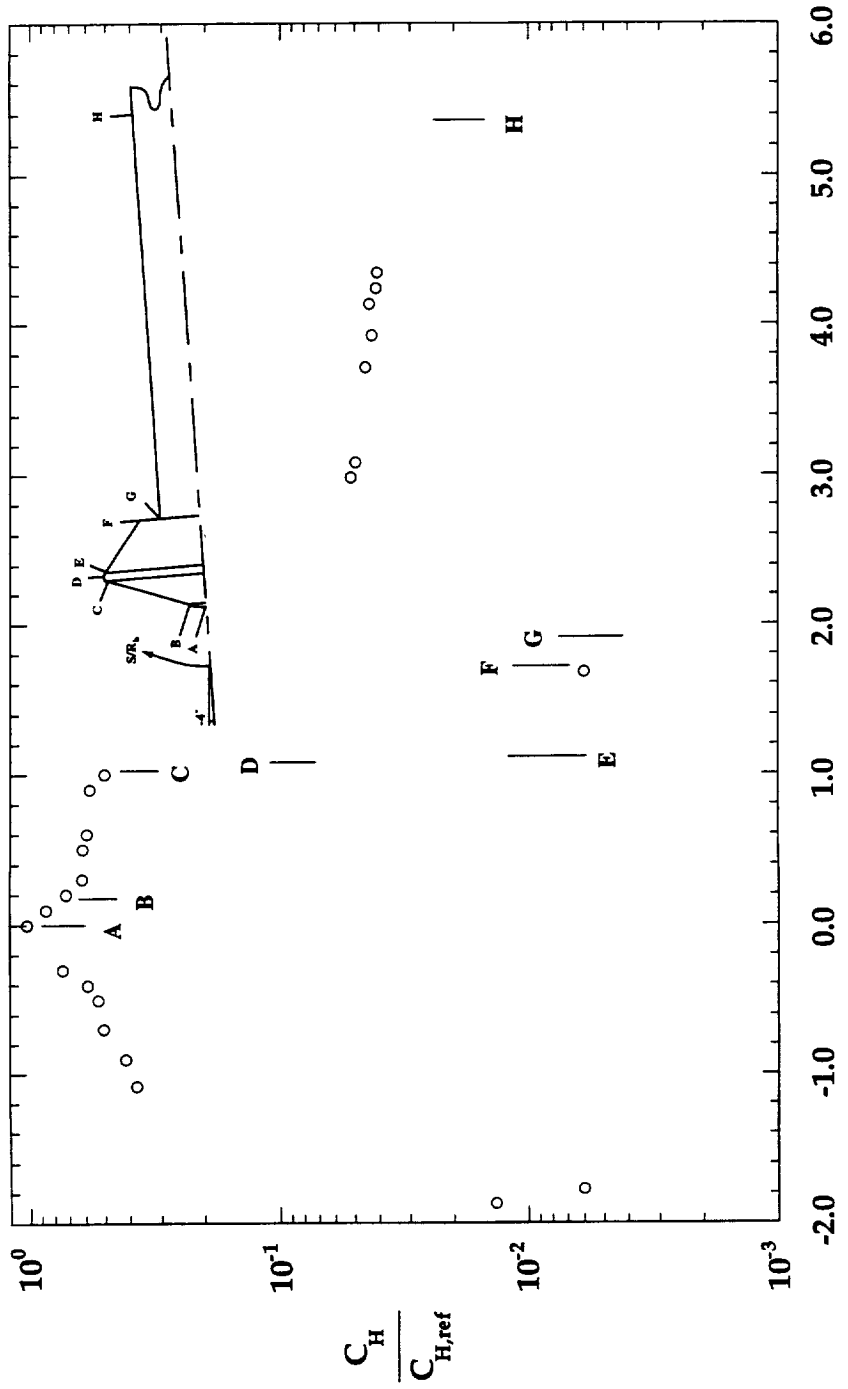

Figure B-11: HYPULSE Run 757, MP-1 Configuration, CO_2 Test Gas, α = -4°

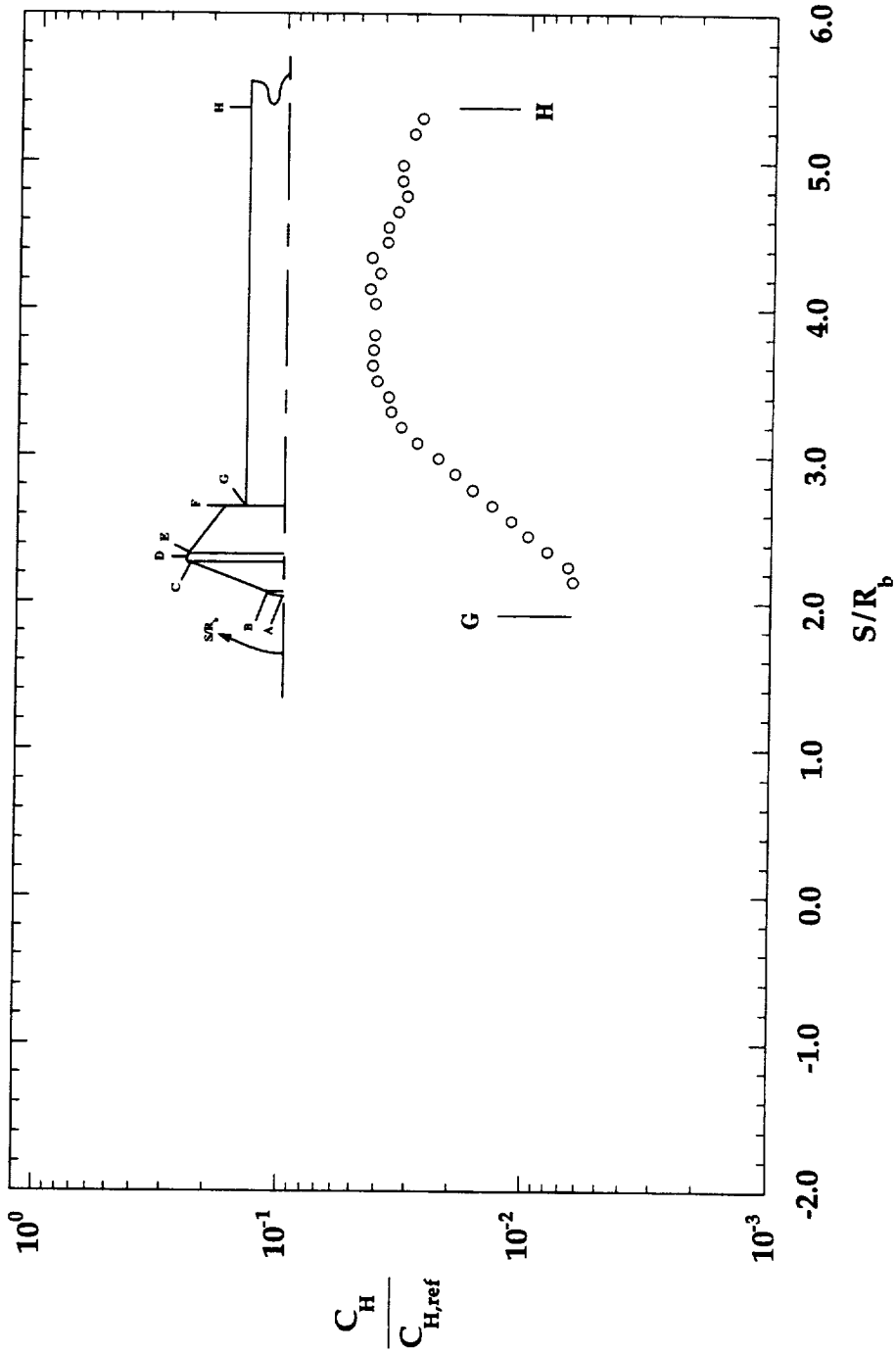

Figure B-12: HYPULSE Run 783, MP-1 Configuration, Air Test Gas, $\alpha = 0°$

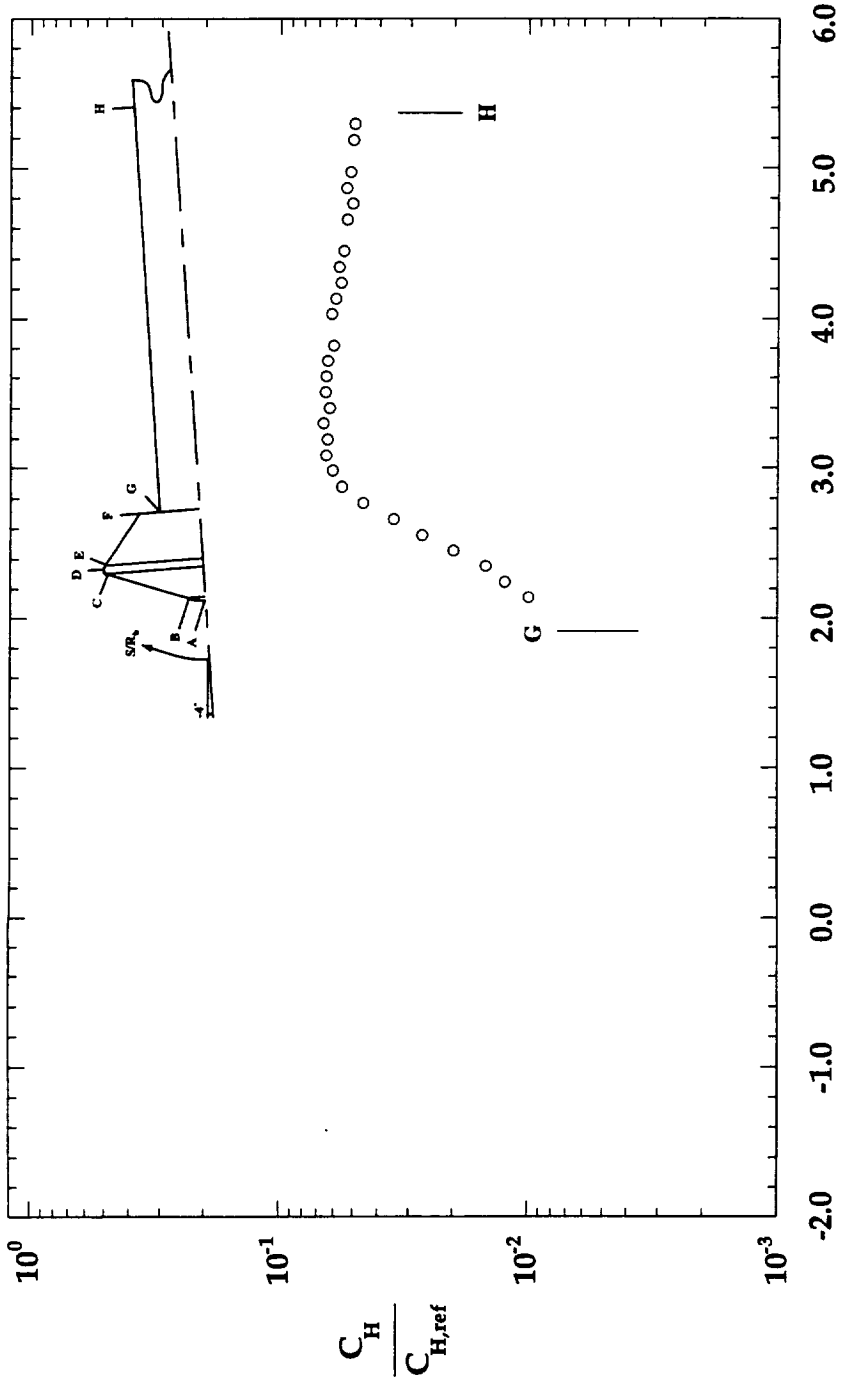

Figure B-13: HYPULSE Run 784, MP-1 Configuration, Air Test Gas, α = -4°

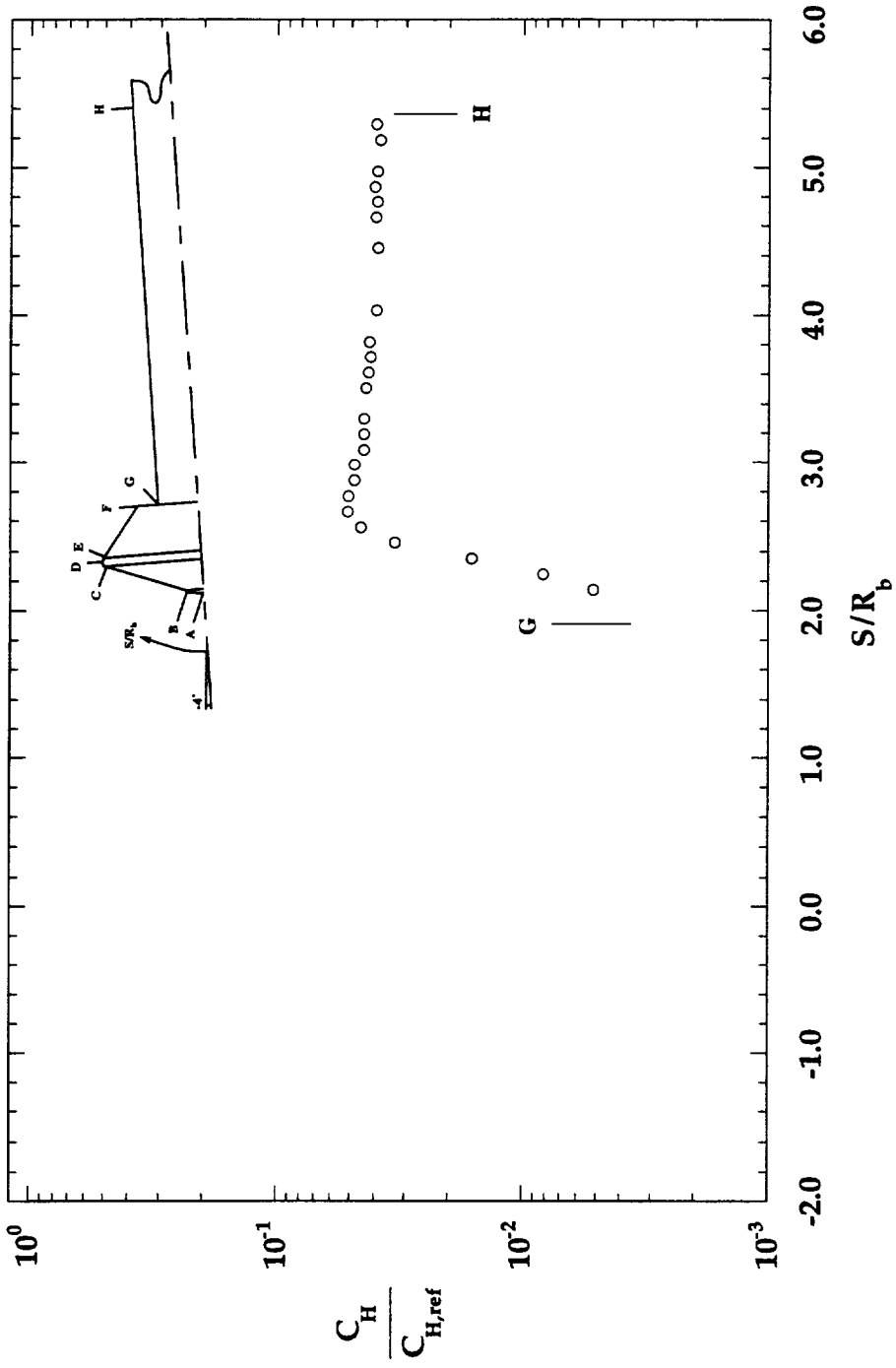

Figure B-14: HYPULSE Run 785, MP-1 Configuration, CO_2 Test Gas, α = -4°

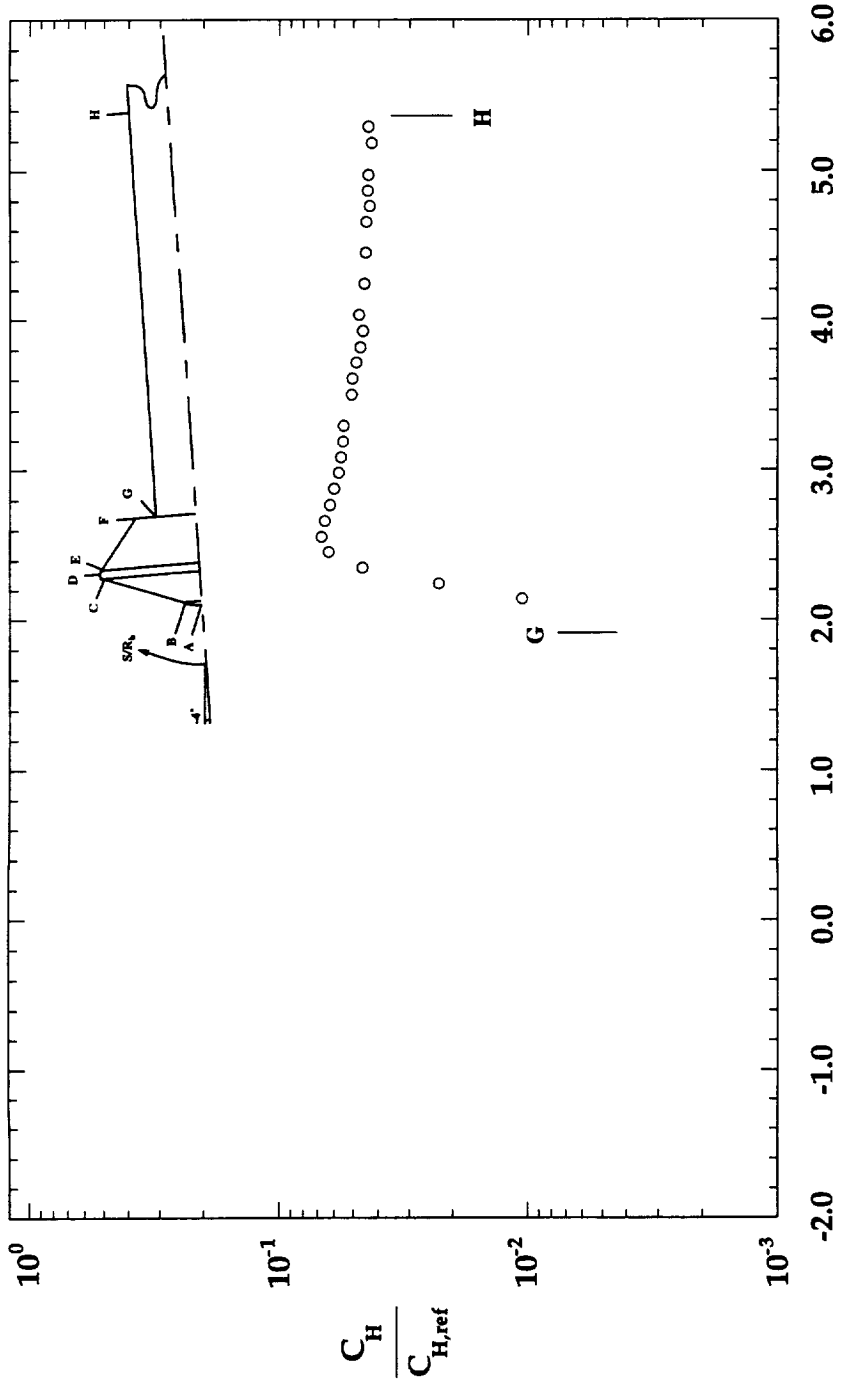

Figure B-15: HYPULSE Run 786, MP-1 Configuration, CO_2 Test Gas, α = -8°

*** BAD RUN, NO DATA ***

Figure B-16: HYPULSE Run 787, MP-2 Configuration, Air Test Gas, $\alpha = 0$

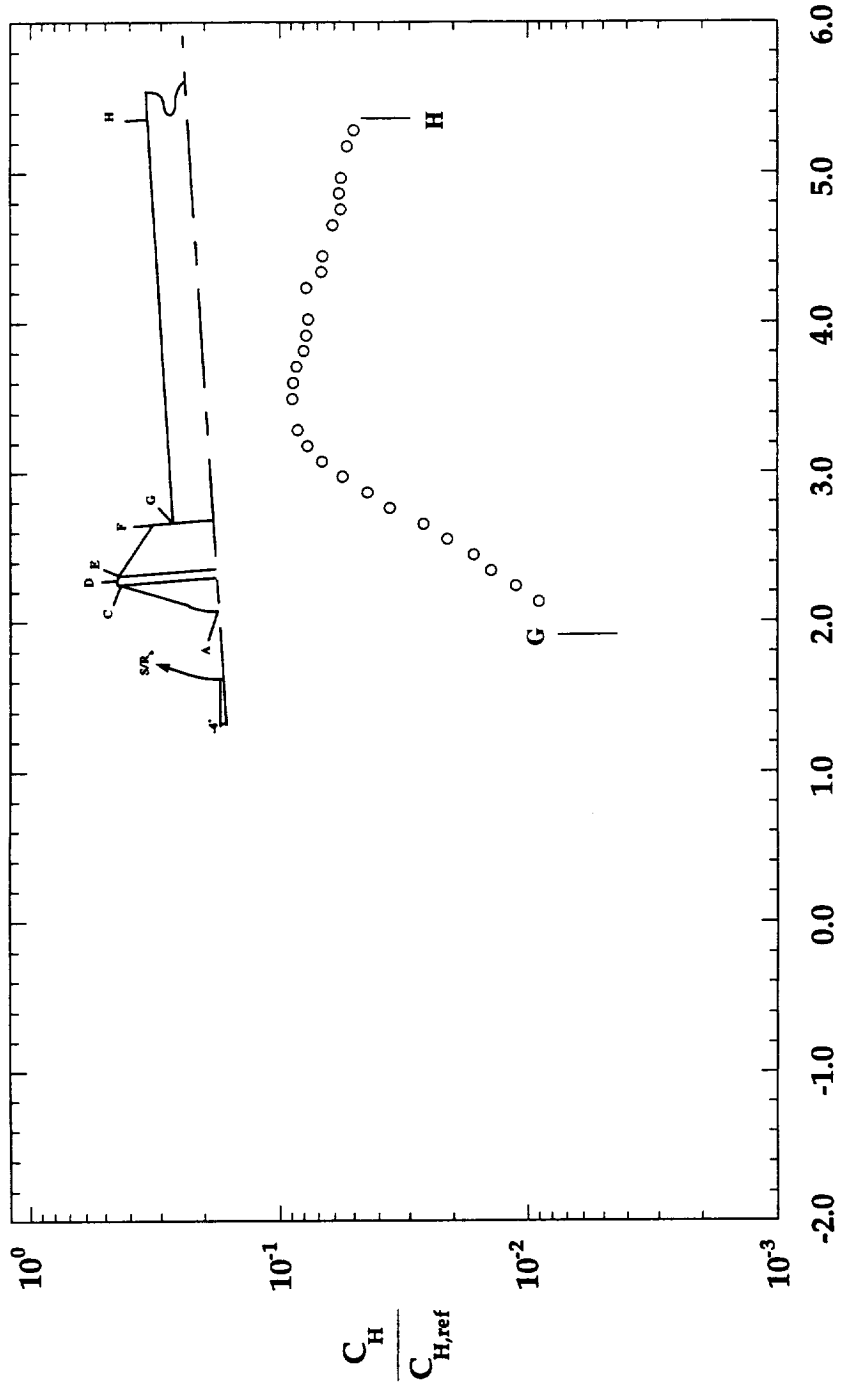

Figure B-17: HYPULSE Run 788, MP-2 Configuration, Air Test Gas, α = -4°

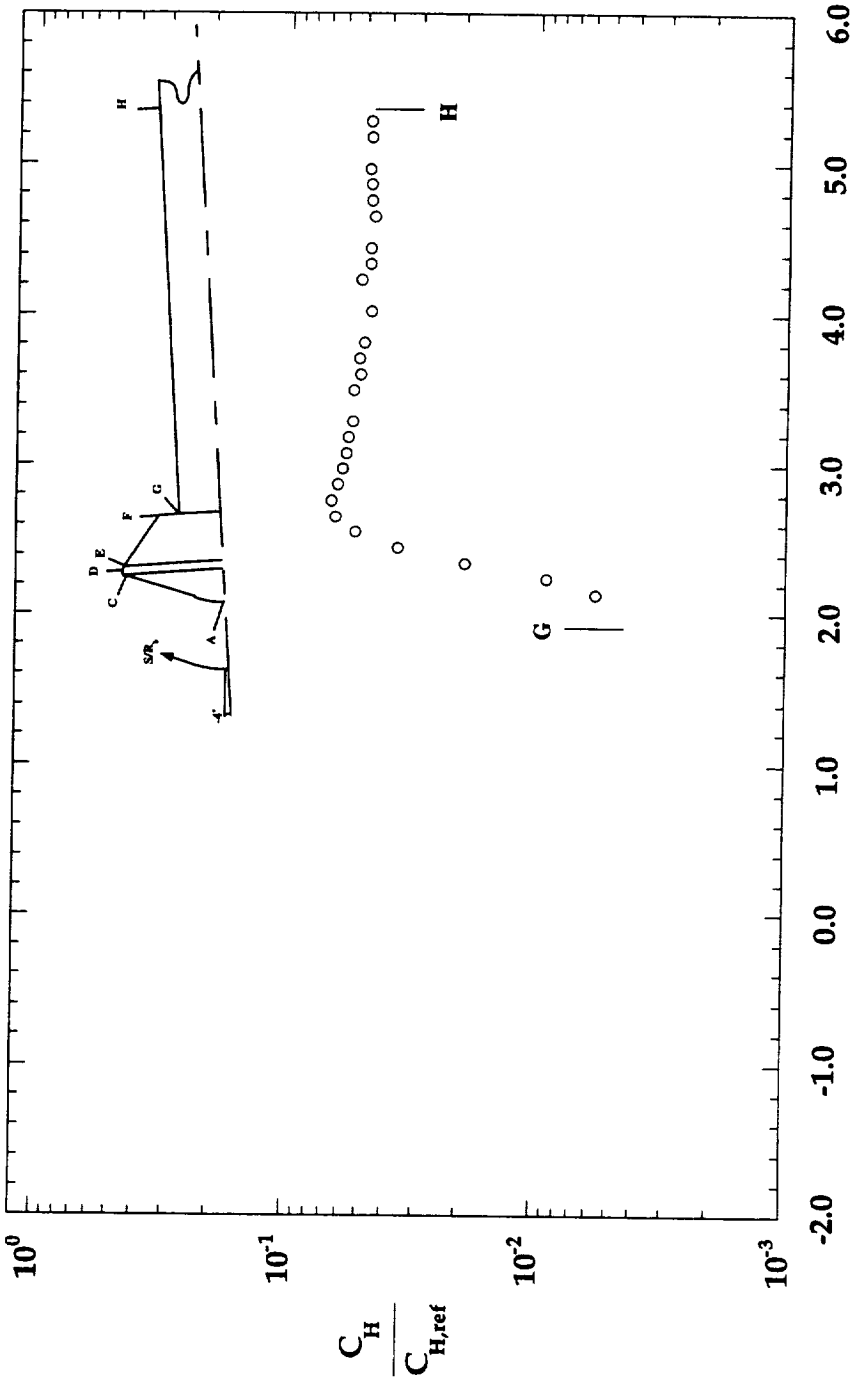

Figure B-18: HYPULSE Run 789, MP-2 Configuration, CO_2 Test Gas, α = -4°

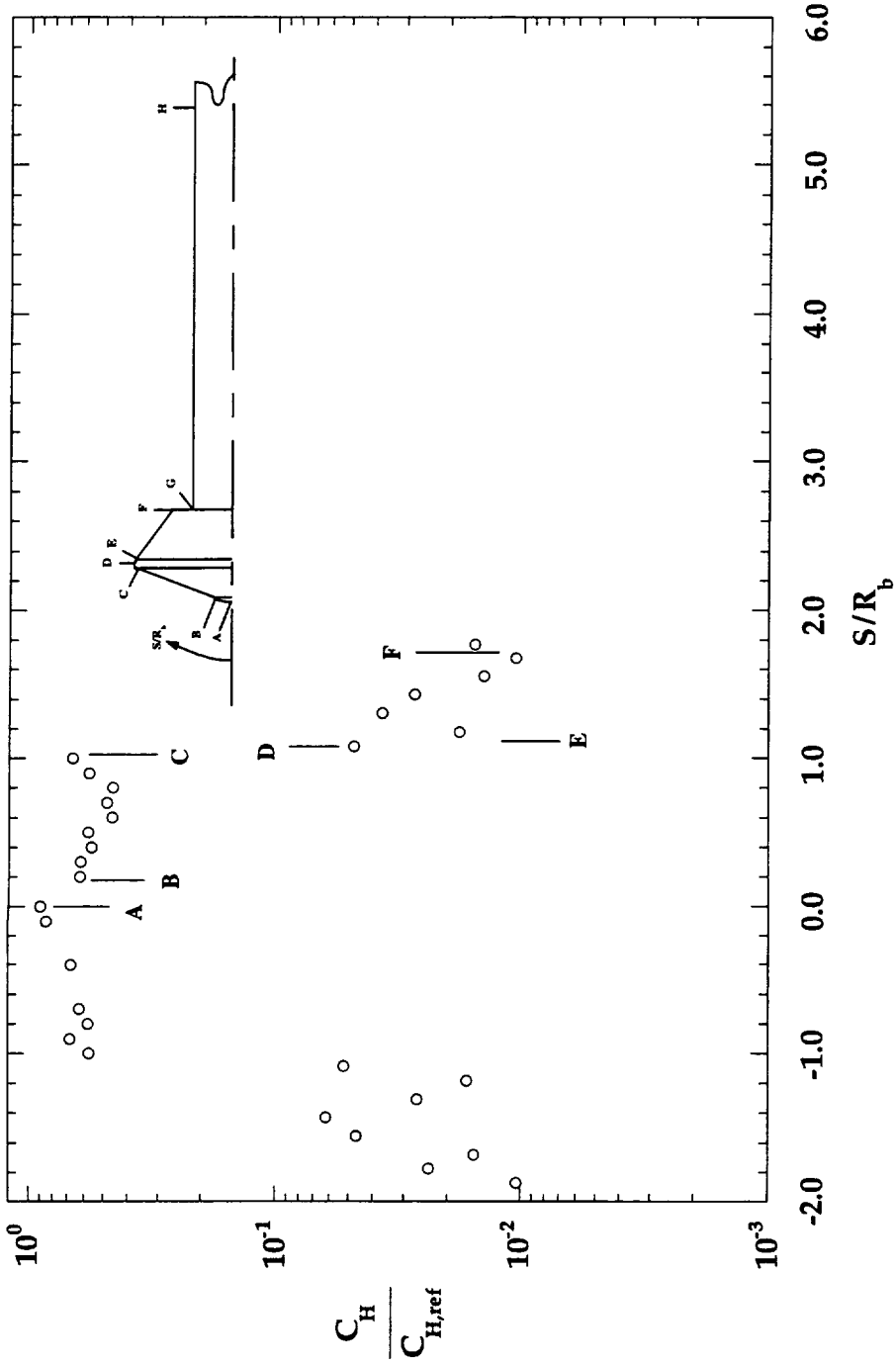

Figure B-19: HYPULSE Run 790, MP-1 Configuration, Air Test Gas, $\alpha = 0°$

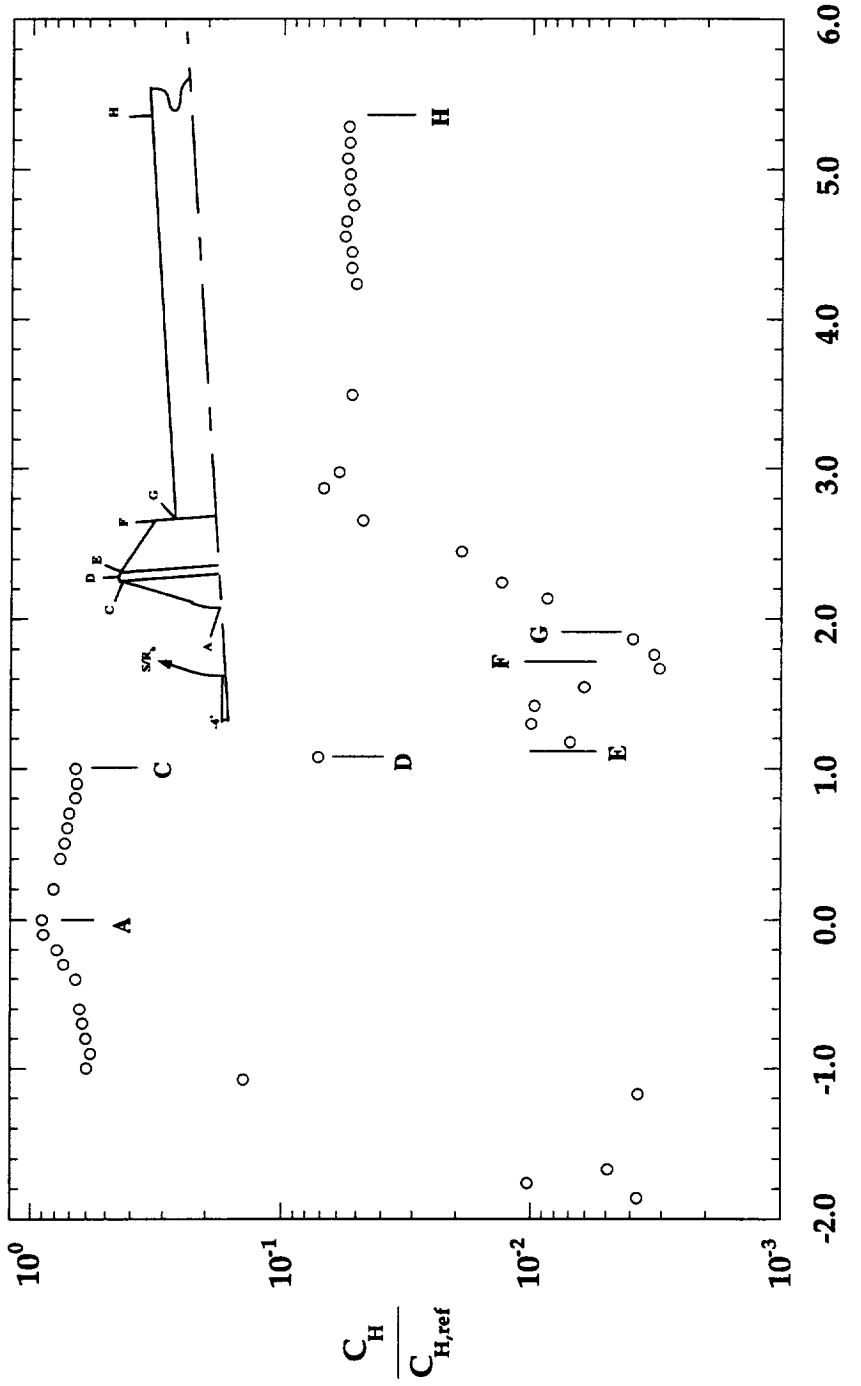

Figure B-20: HYPULSE Run 791, MP-2 Configuration, CO_2 Test Gas, α = -4°

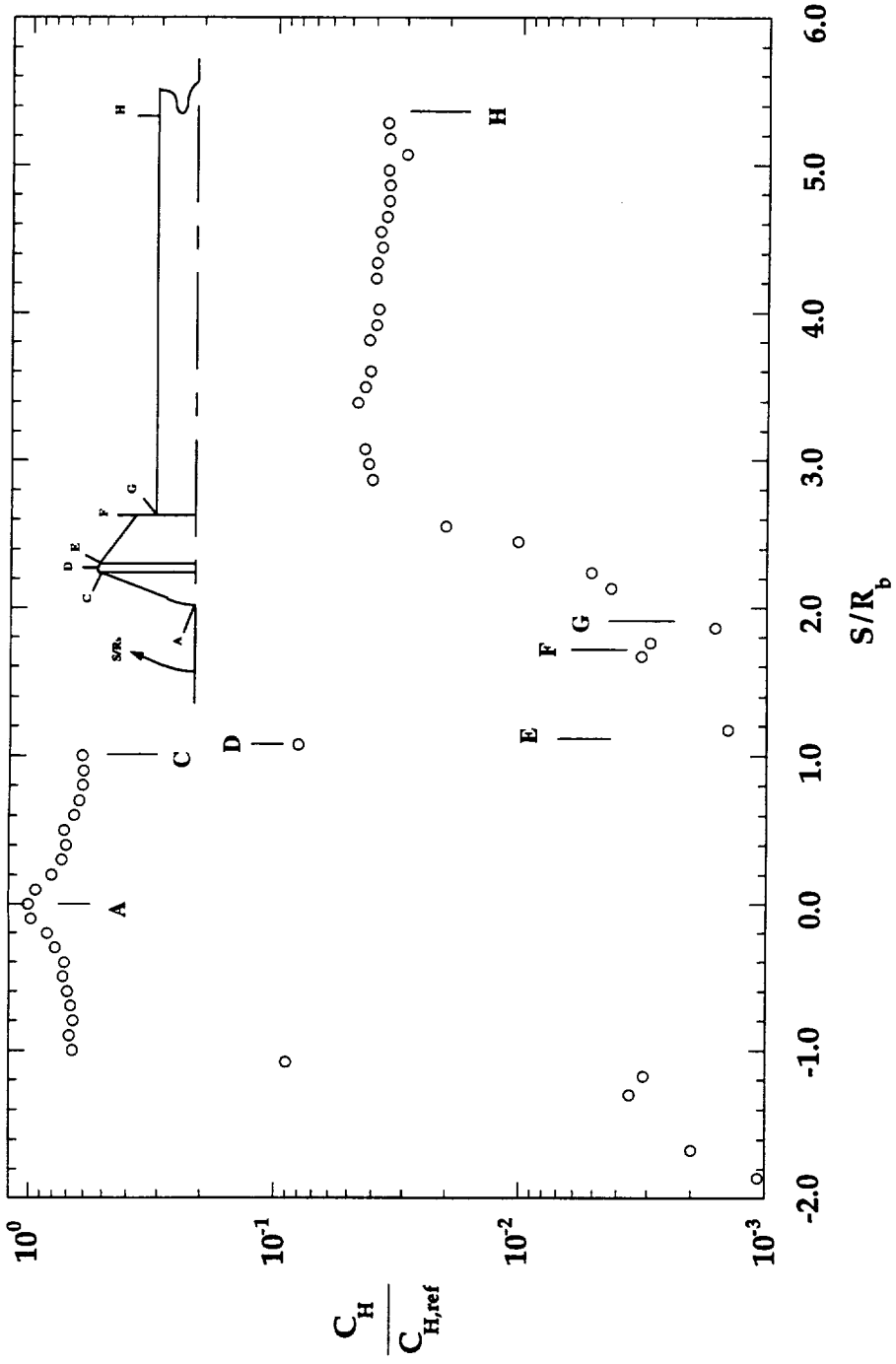

Figure B-21: HYPULSE Run 792, MP-2 Configuration, CO_2 Test Gas, $\alpha = 0°$

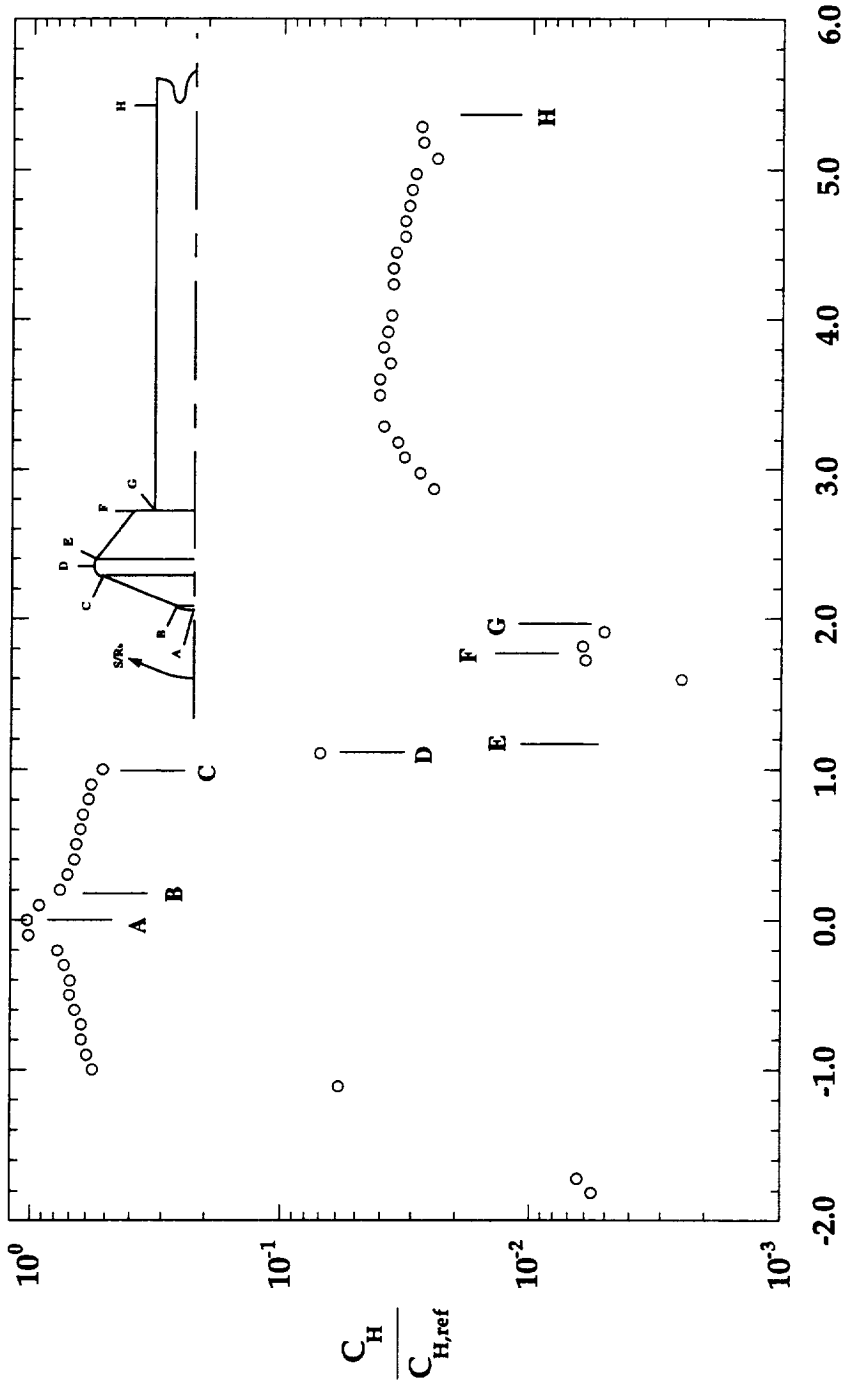

Figure B-22: HYPULSE Run 793, MP-3 Configuration, CO_2 Test Gas, $\alpha = 0°$

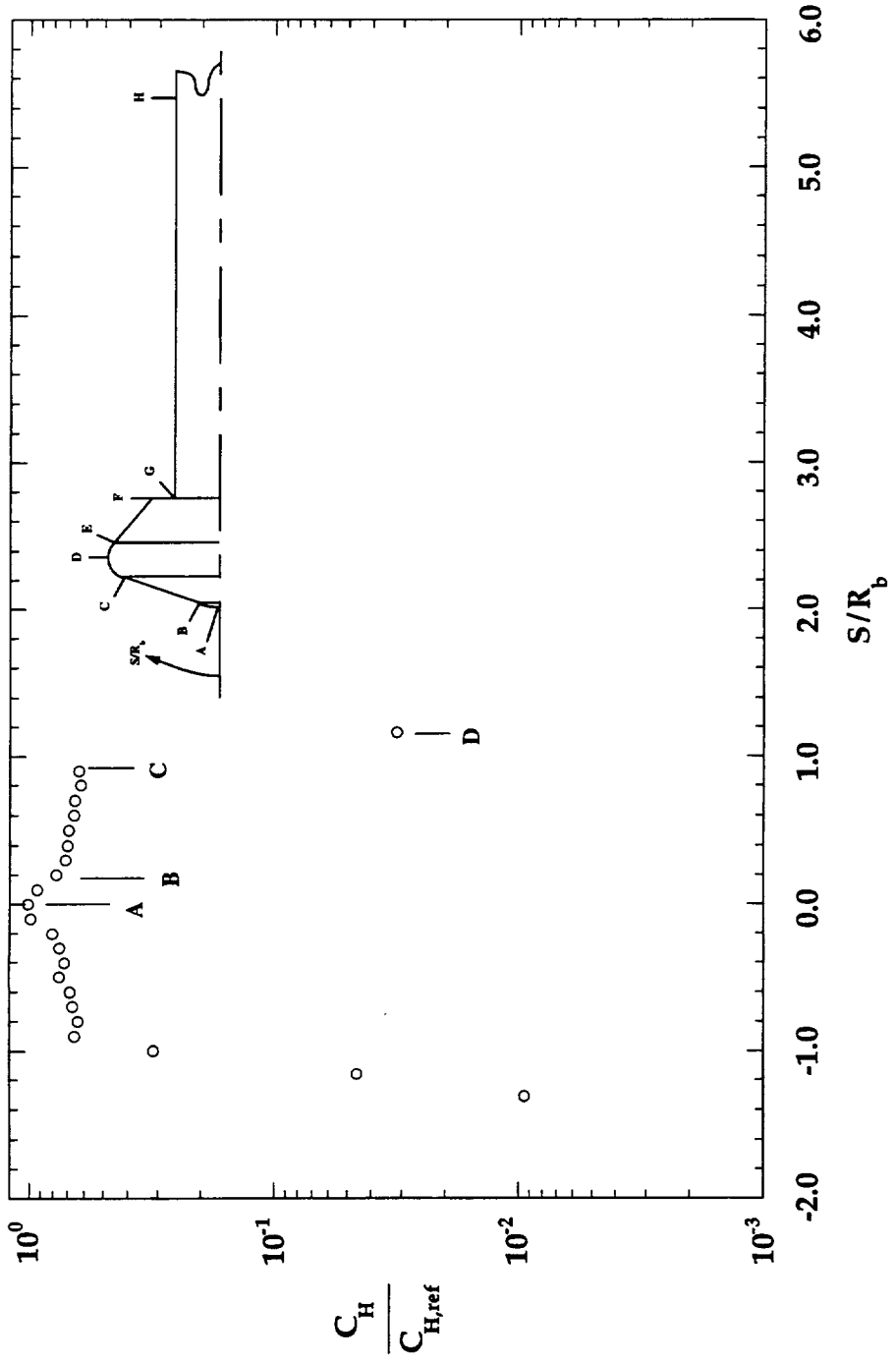

Figure B-23: HYPULSE Run 794, MP-4 Configuration, CO_2 Test Gas, $\alpha = 0°$

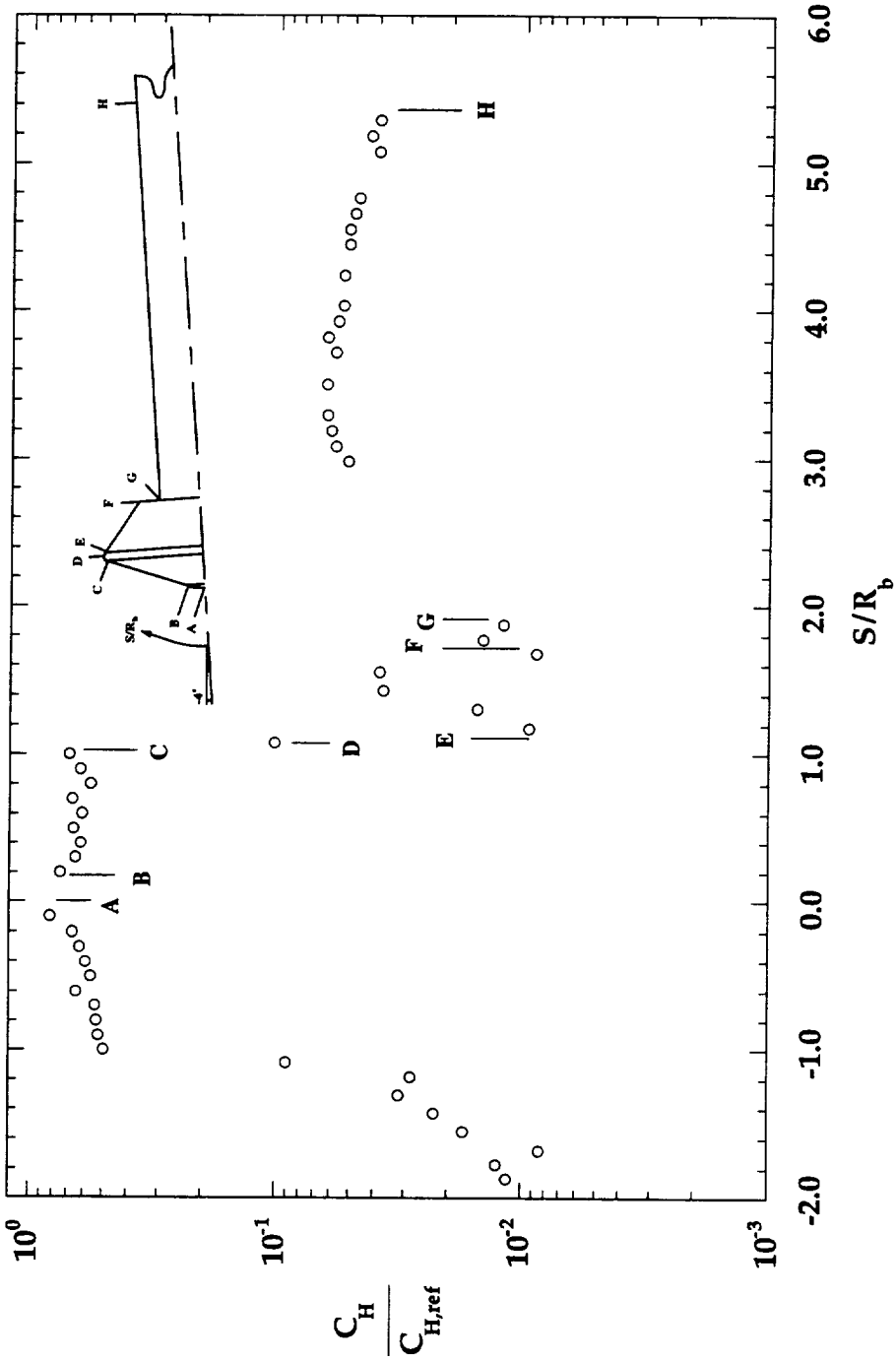

Figure B-24: HYPULSE Run 795, MP-1 Configuration, Air Test Gas, α = -4°

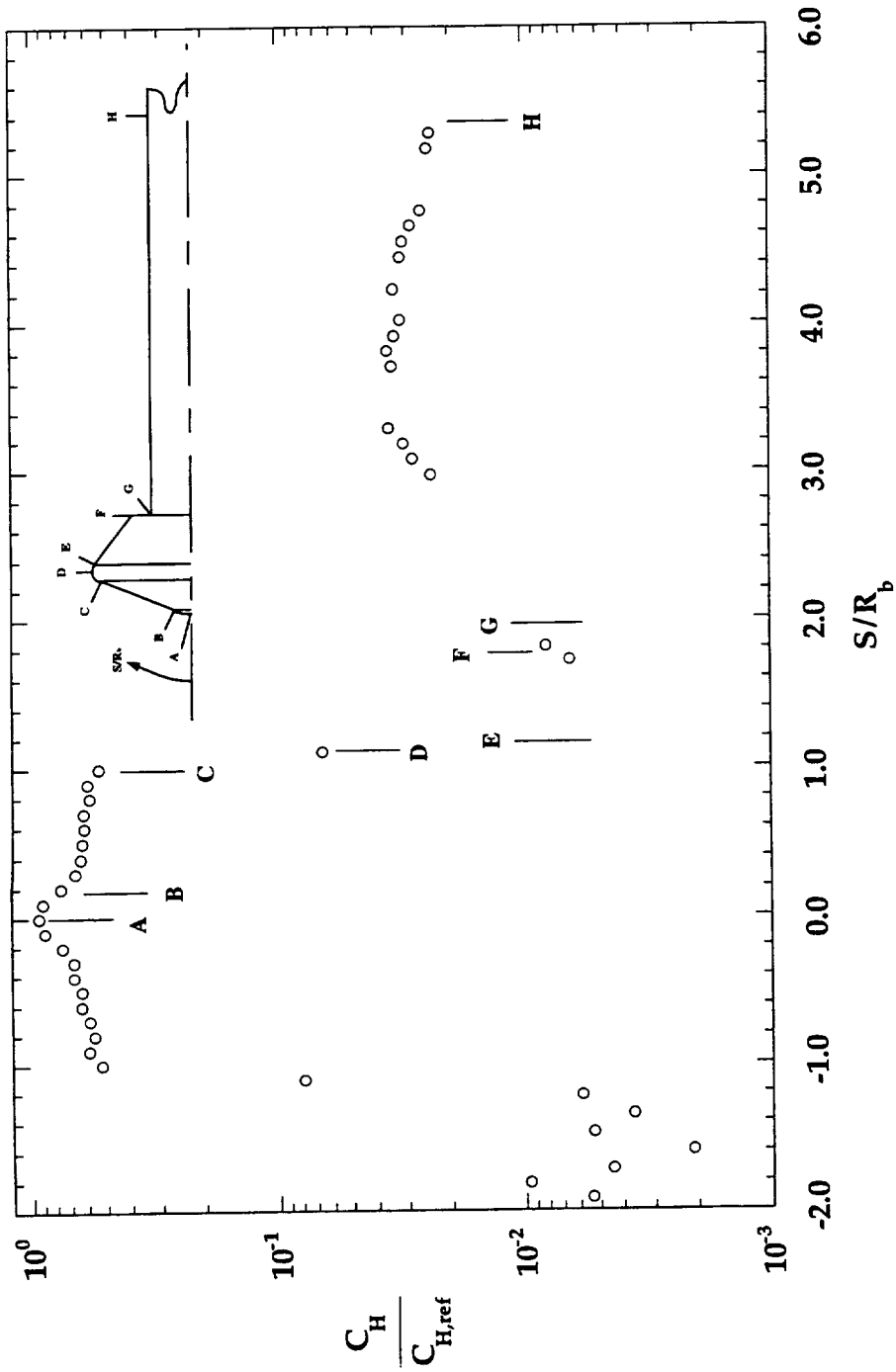

Figure B-25: HYPULSE Run 796, MP-3 Configuration, CO_2 Test Gas, $\alpha = 0°$

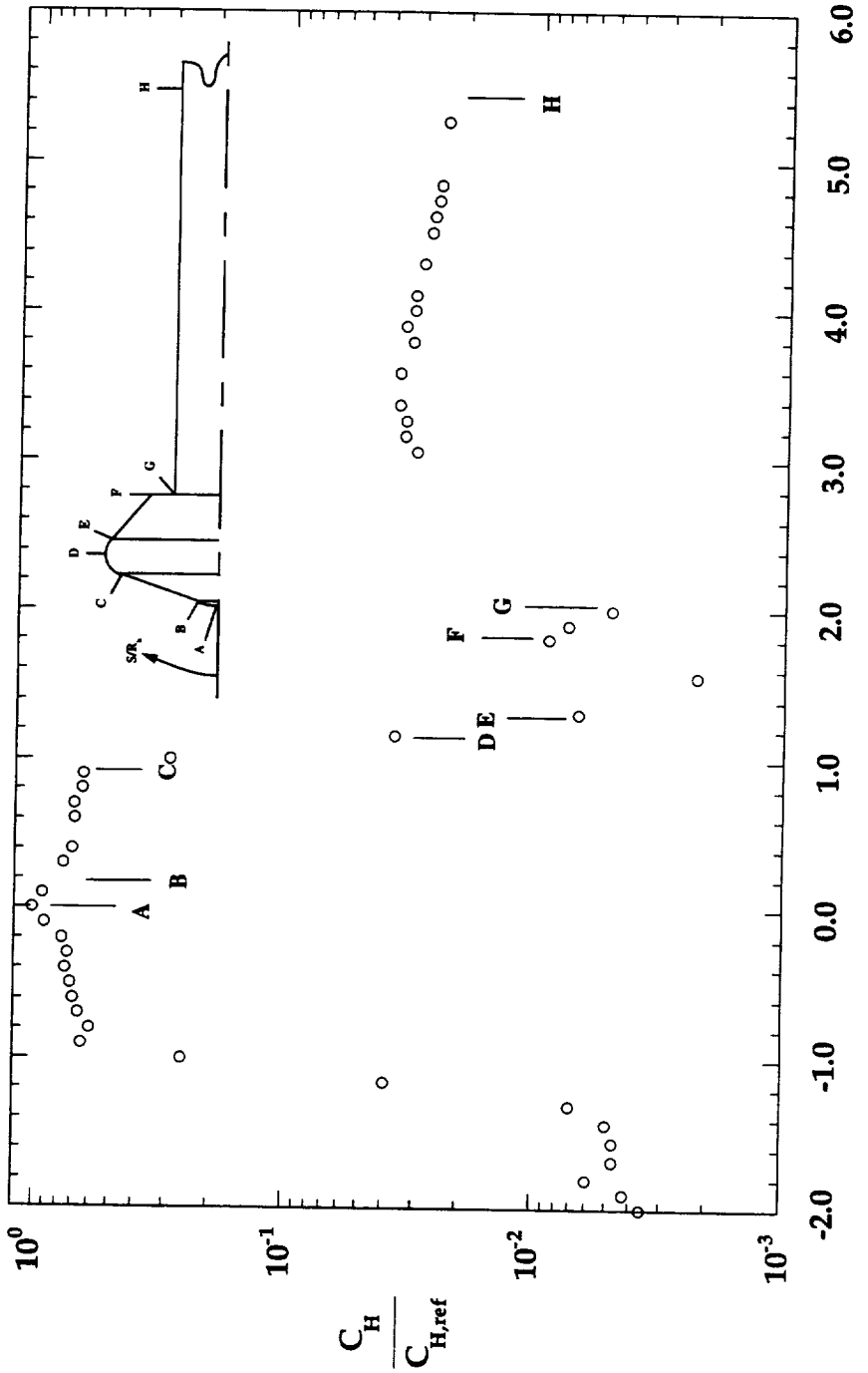

Figure B-26: HYPULSE Run 797, MP-4 Configuration, CO_2 Test Gas, $\alpha = 0°$

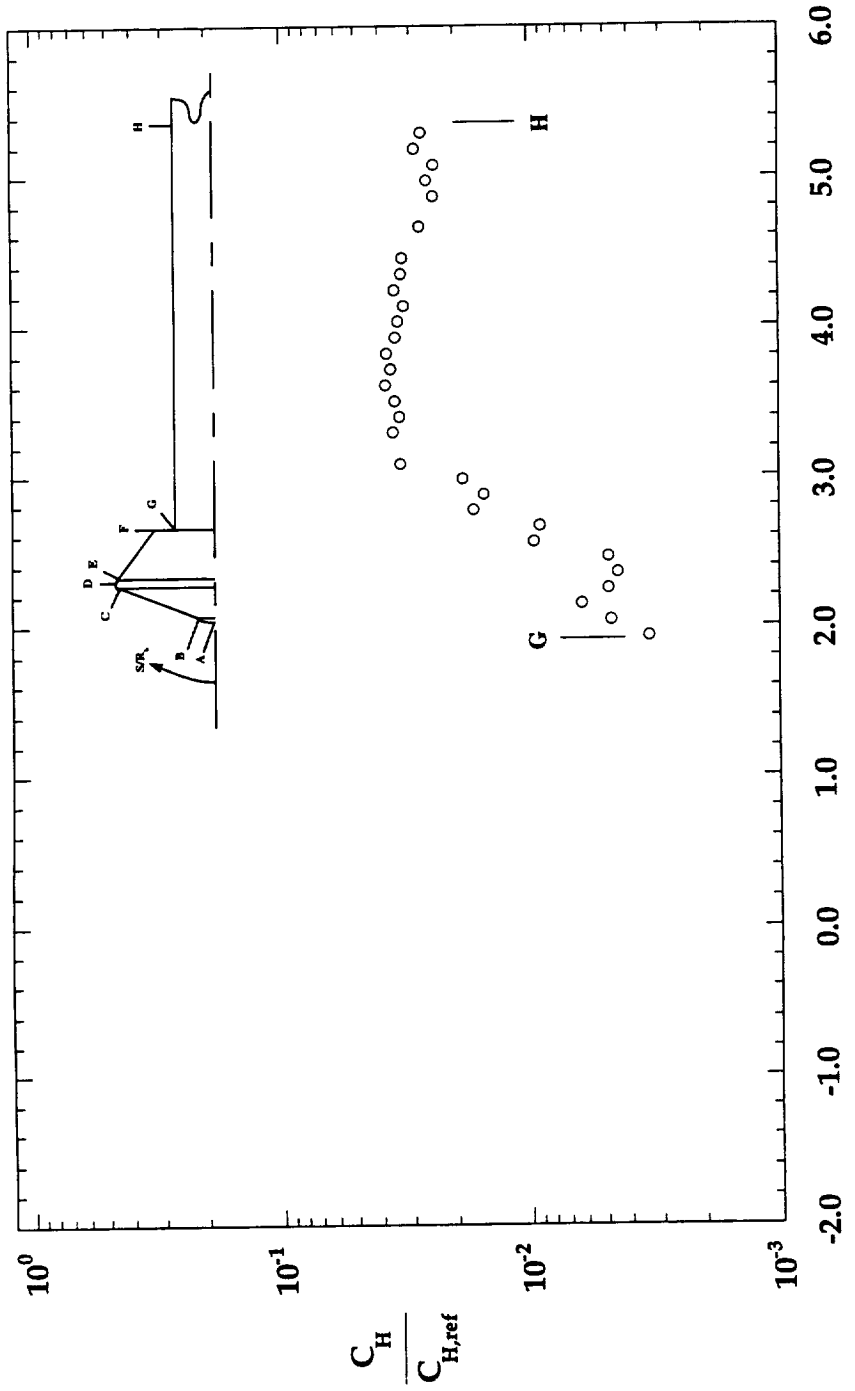

Figure B-27: HYPULSE Run 903, MP-1 Configuration, CO_2 Test Gas, $\alpha = 0°$

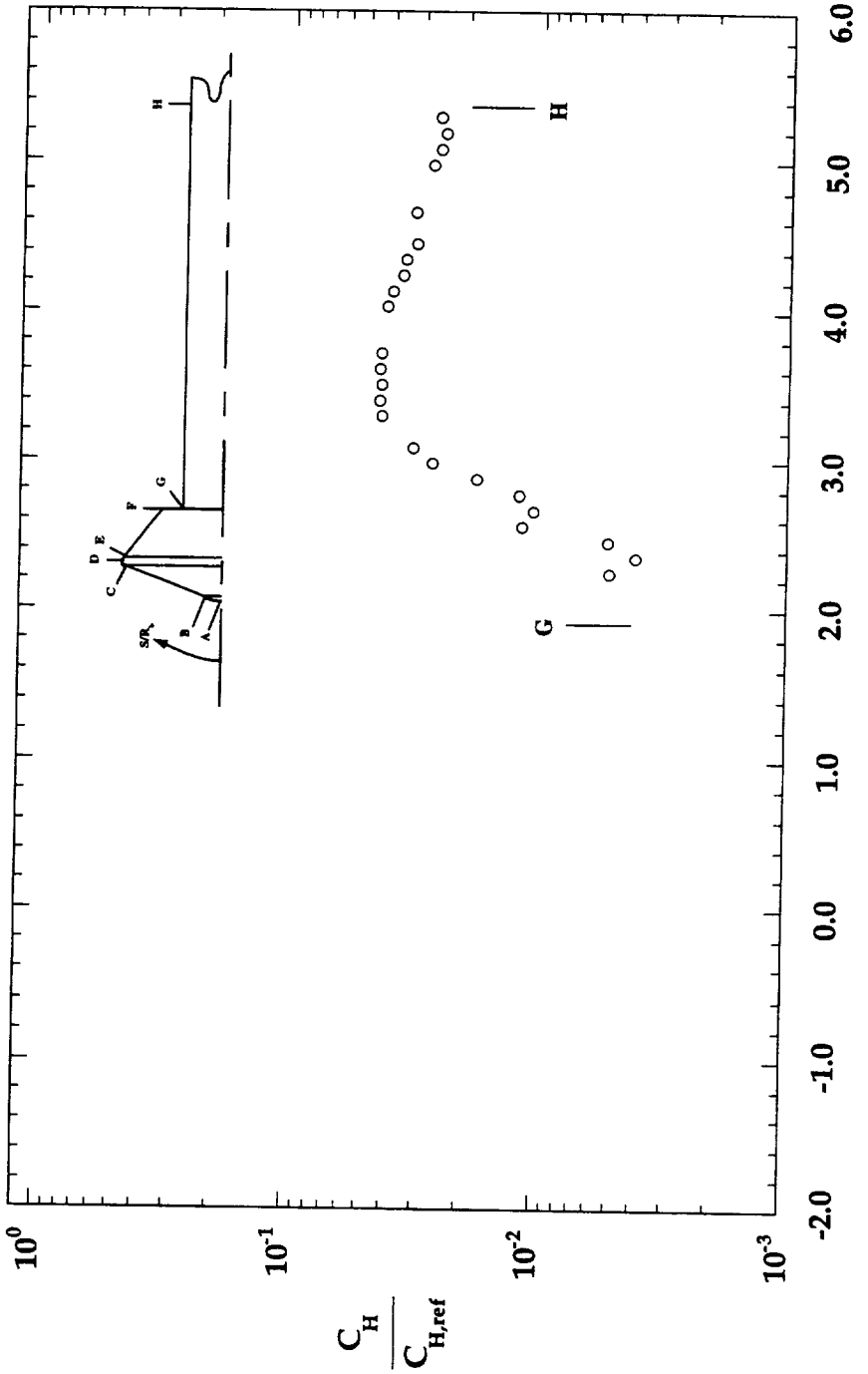

Figure B-28: HYPULSE Run 904, MP-1 Configuration, CO_2 Test Gas, $\alpha = 0°$

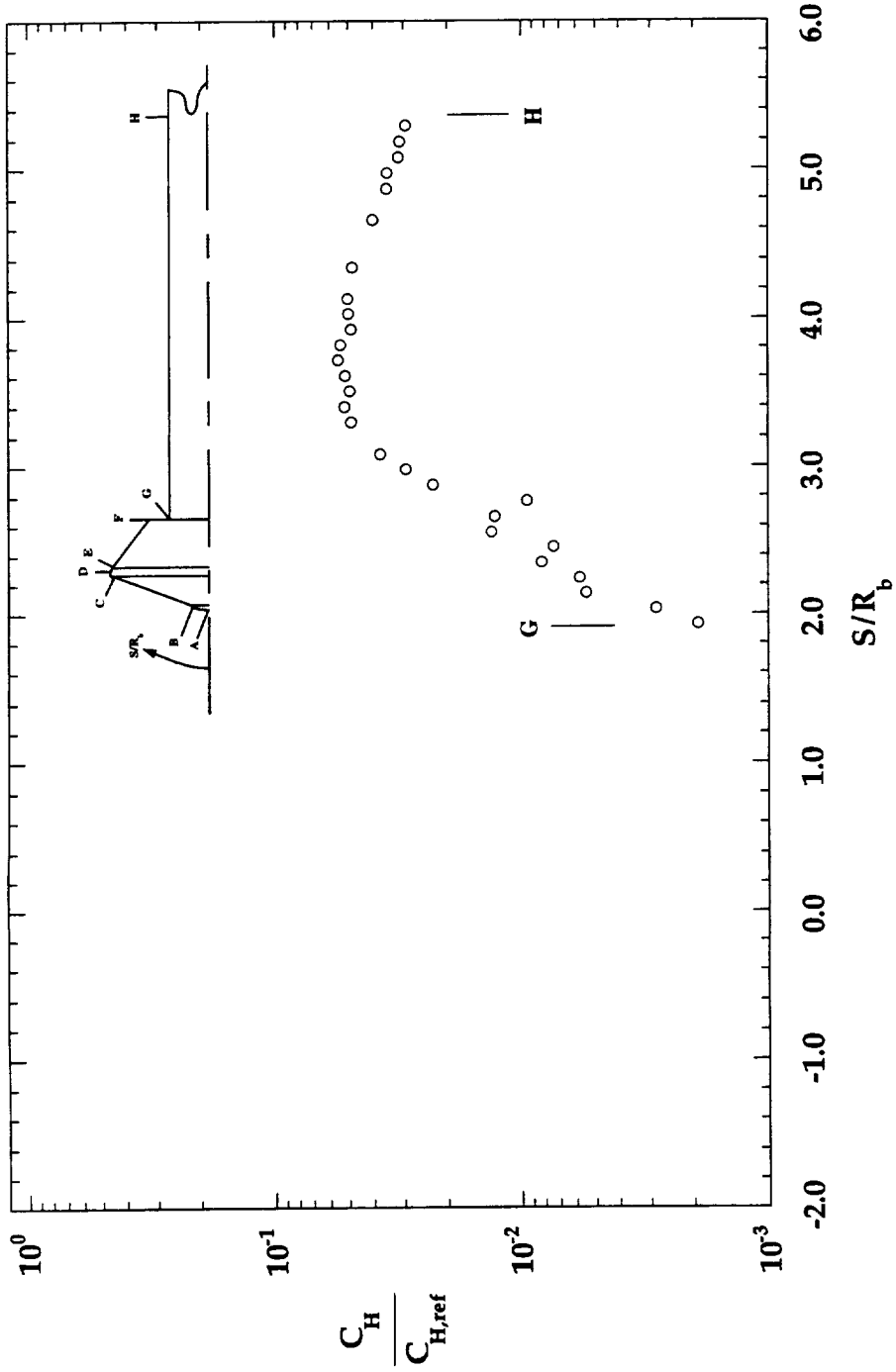

Figure B-29: HYPULSE Run 905, MP-1 Configuration, Air Test Gas, $\alpha = 0°$

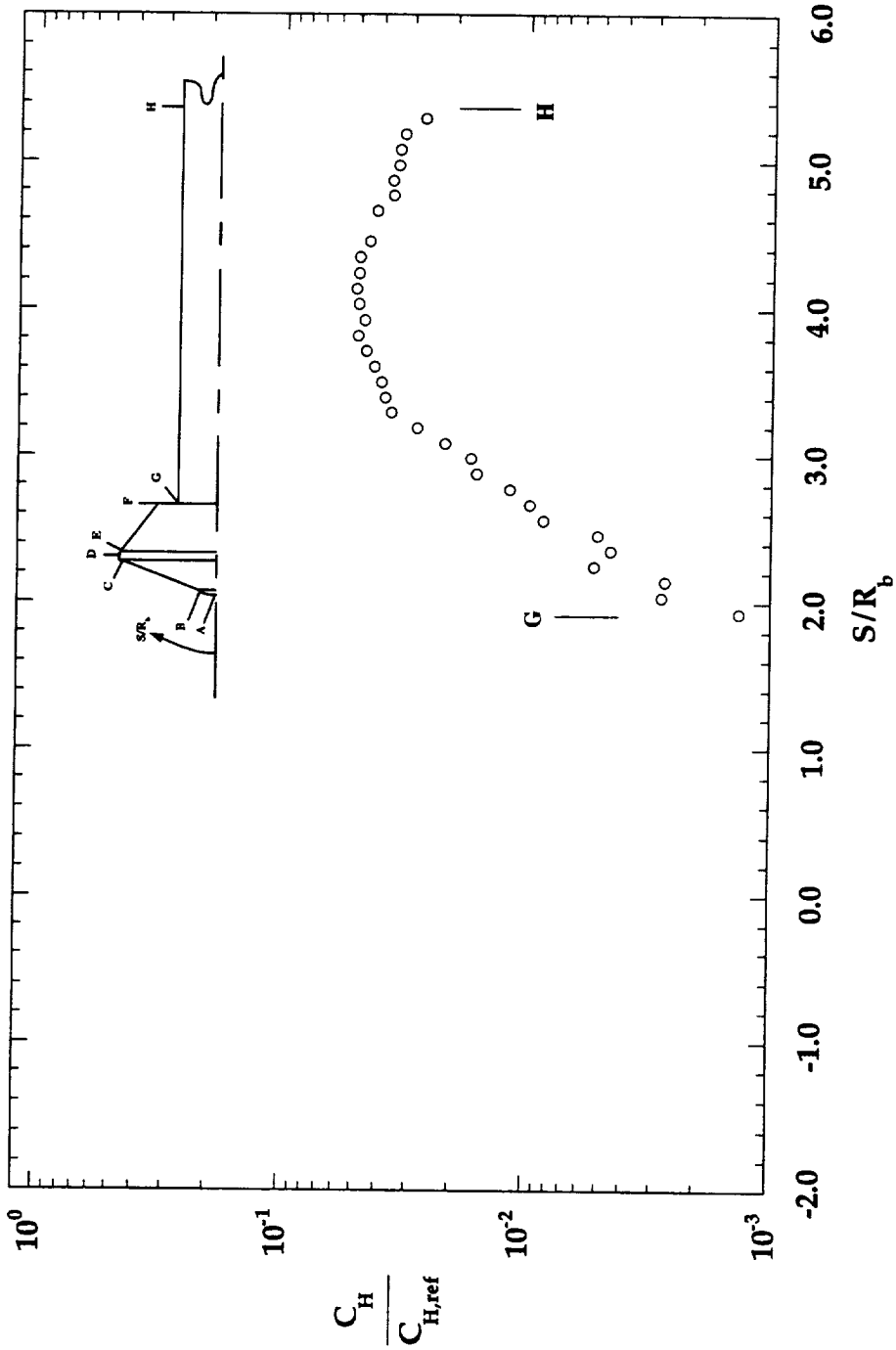

Figure B-30: HYPULSE Run 906, MP-1 Configuration, Air Test Gas, $\alpha = 0°$

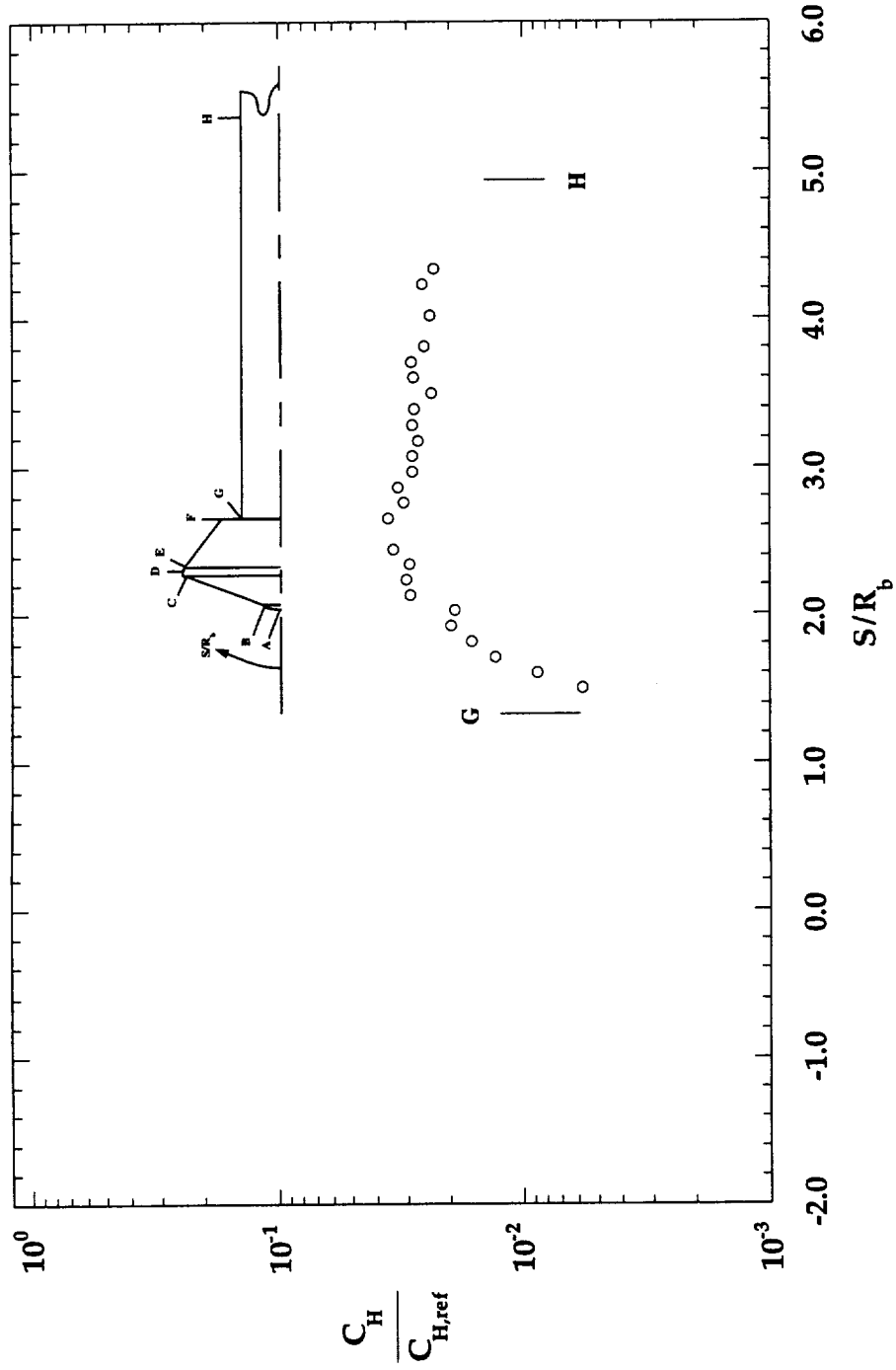

Figure B-31: HYPULSE Run 907, MP-1 (75%) Configuration, CO_2 Test Gas, $\alpha = 0°$

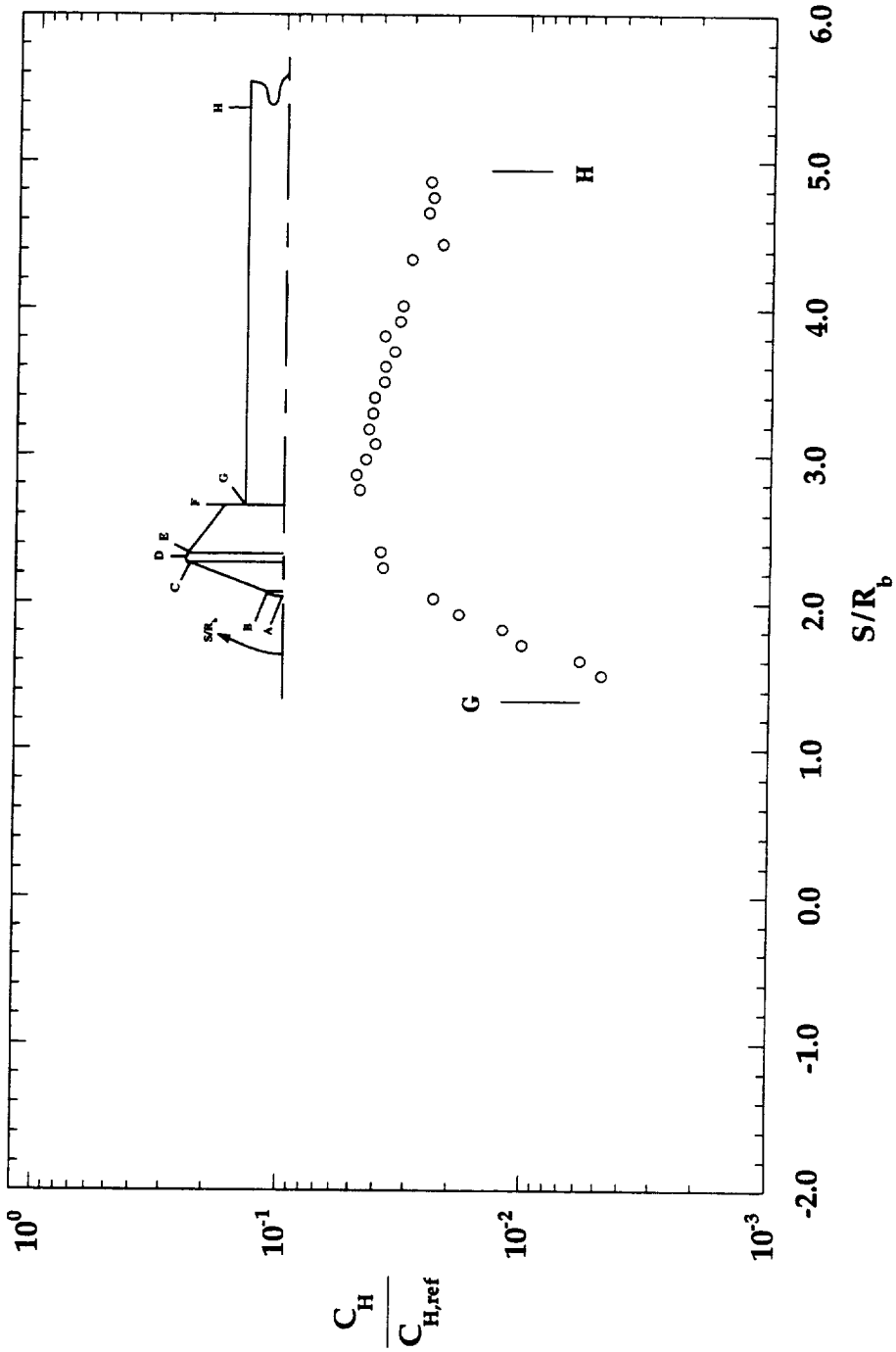

Figure B-32: HYPULSE Run 908, MP-1 (75%) Configuration, CO_2 Test Gas, $\alpha = 0°$

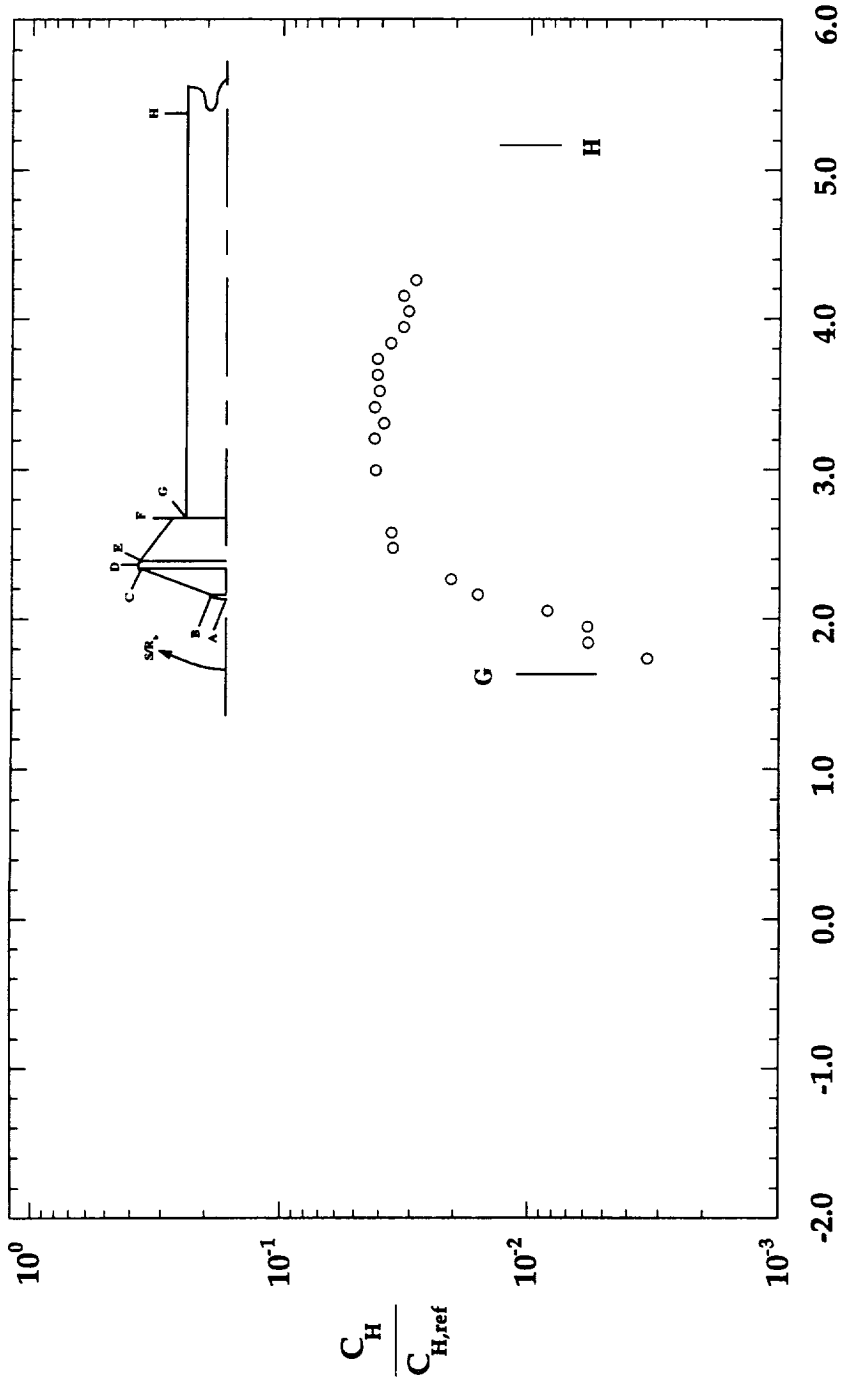

Figure B-33: HYPULSE Run 909, MP-1 (88%) Configuration, CO_2 Test Gas, $\alpha = 0°$

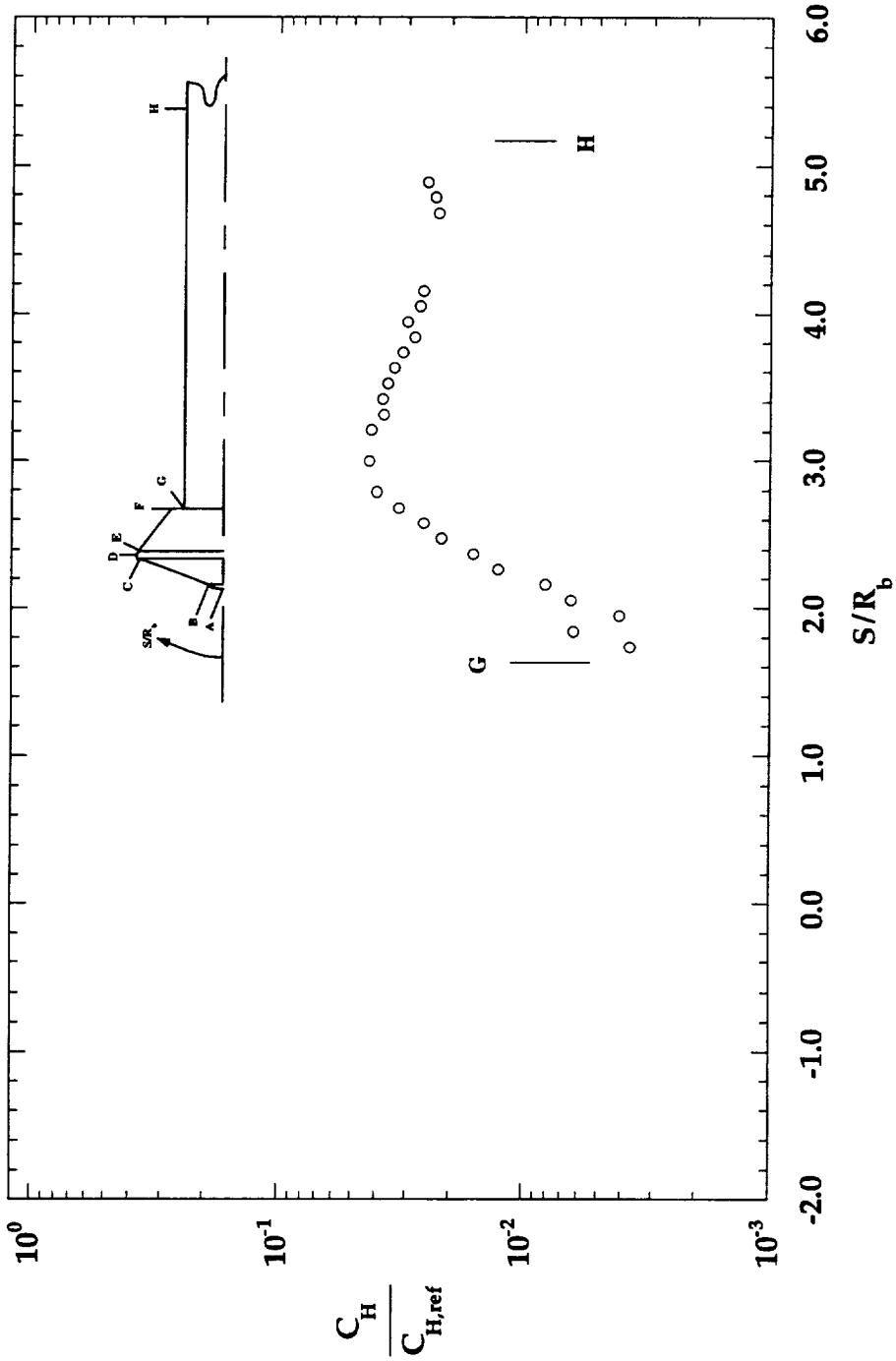

Figure B-34: HYPULSE Run 910, MP-1 (88%) Configuration, CO_2 Test Gas, $\alpha = 0°$

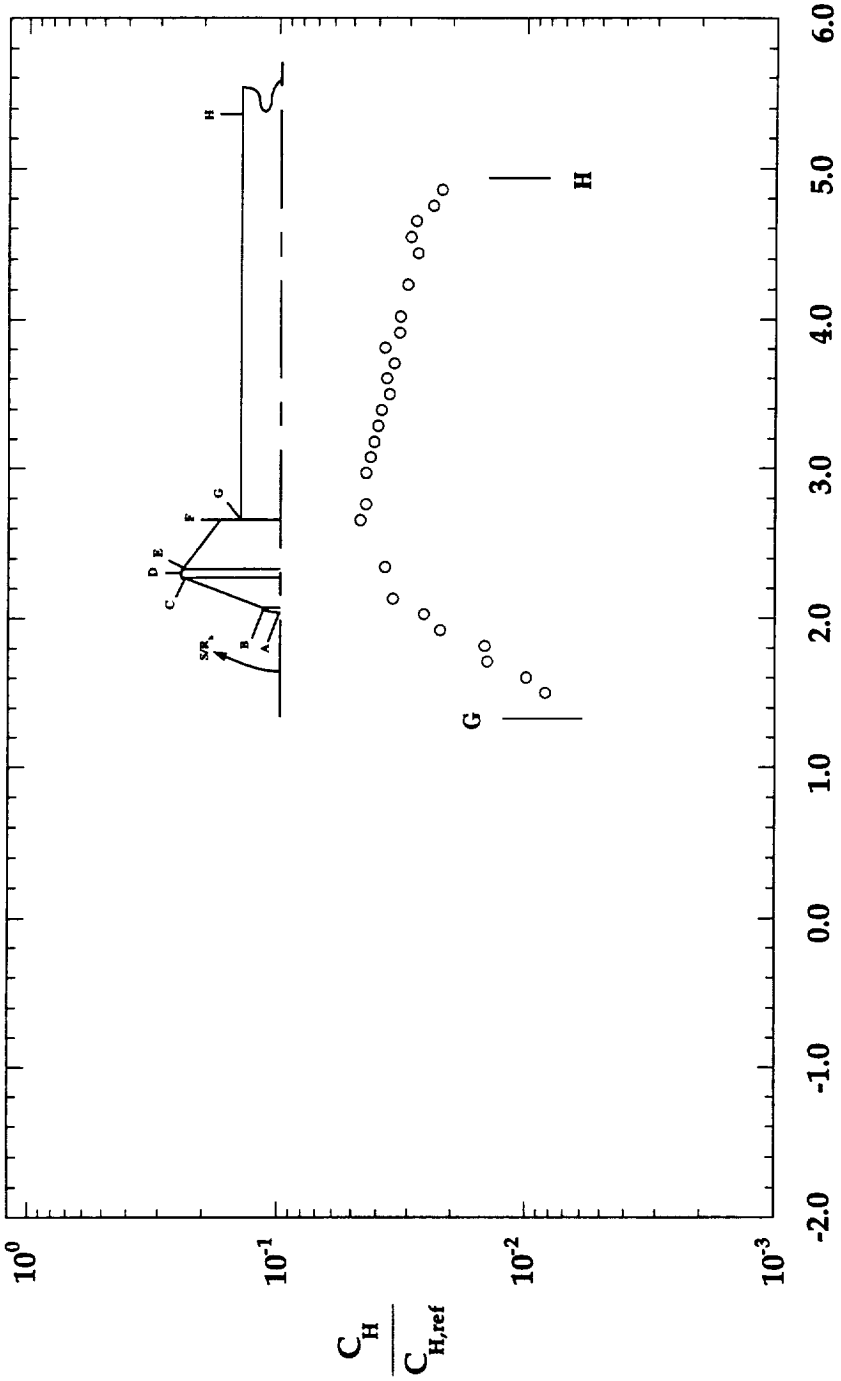

Figure B-35: HYPULSE Run 911, MP-1 (75%) Configuration, Air Test Gas, $\alpha = 0°$

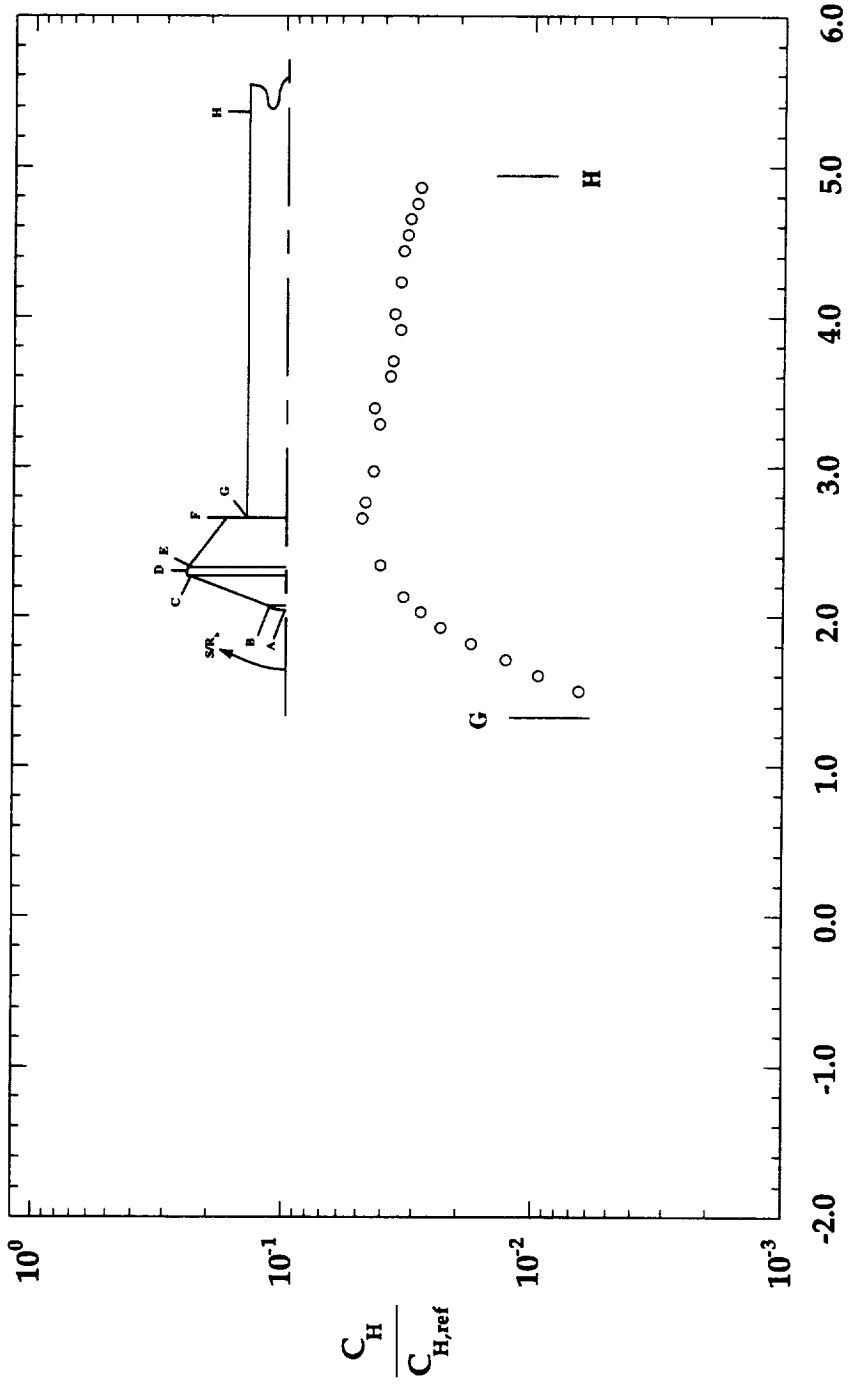

Figure B-36: HYPULSE Run 912, MP-1 (75%) Configuration, Air Test Gas, $\alpha = 0°$

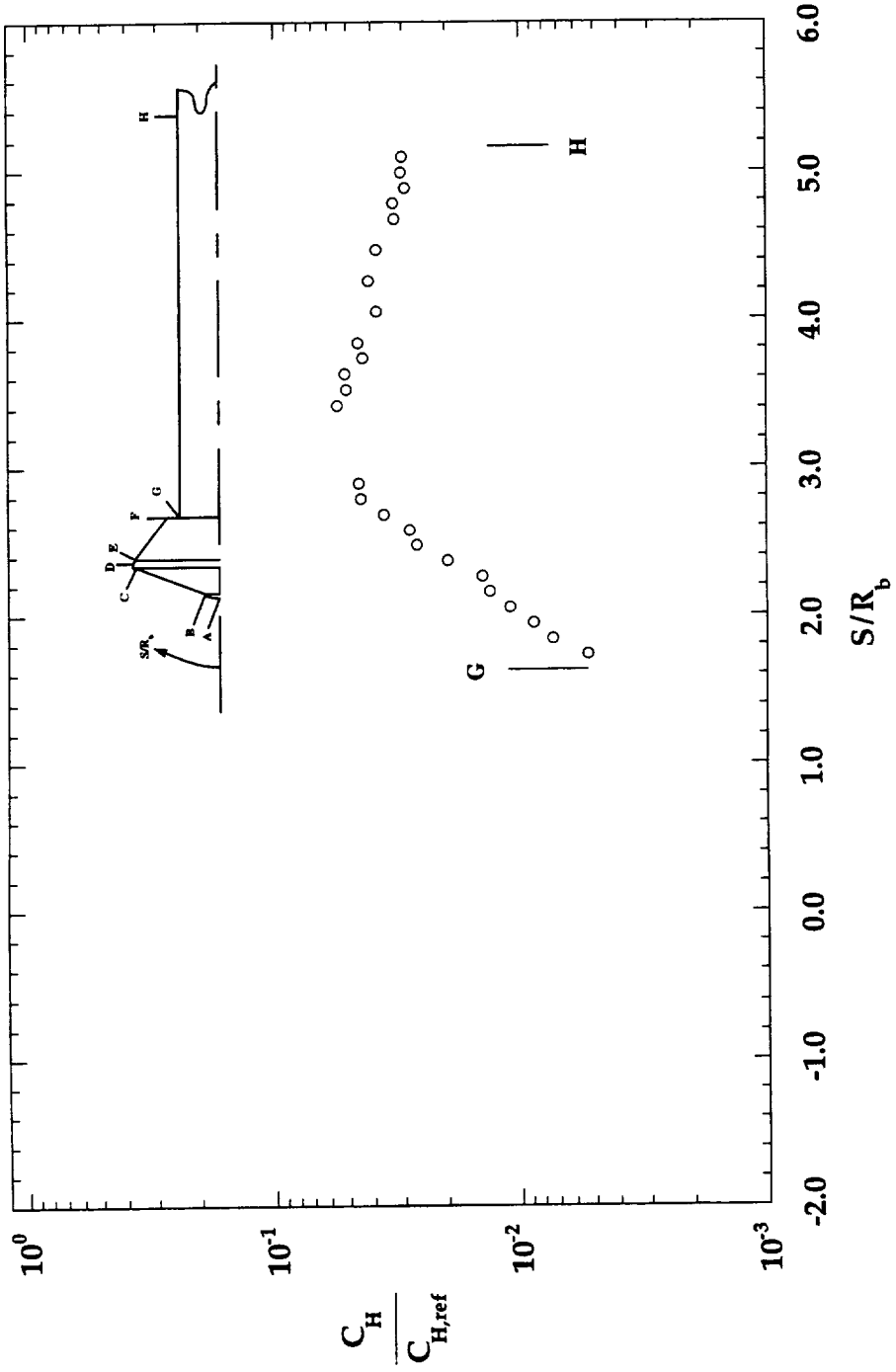

Figure B-37: HYPULSE Run 913, MP-1 (88%) Configuration, Air Test Gas, $\alpha = 0°$

*** BAD RUN, NO DATA ***

Figure B-38: HYPULSE Run 914, MP-1 (88%) Configuration, Air Test Gas, $\alpha = 0$

APPENDIX C
HEMISPHERE CALIBRATION TESTS

In addition to the entry vehicle tests in both the HYPULSE Expansion Tube and the 31-Inch Mach 10 Air Tunnel, tests also were conducted with hemisphere models of various radii in both facilities. In the Mach 10 Tunnel, tests were conducted with 2-in. diameter hemispheres of both quartz and Macor. In HYPULSE, tests were conducted with Macor hemispheres of 1/2-in., 3/4-in. and 1-in. diameters. The tests in these two facilities were conducted for calibration and evaluation purposes. The Macor and quartz hemisphere tests in the Mach 10 Tunnel were carried out in order to evaluate the accuracy of the thermal property data available for these materials and the magnitude of the resulting error in aerothermodynamic measurements due to material properties uncertainties. The hemisphere tests in HYPULSE were conducted in order to evaluate the quality of the aerothermodynamic data from this facility, as well as to evaluate the performance of the NEQ2D code for non-equilibrium flows. The hemisphere geometry was chosen for the tests because simple engineering theory can be used to evaluate the stagnation point heating rate (e. g. Fay and Riddell, 1958) and because this is a relatively simple geometry for which to generate computational grids and perform numerical solutions

Section C.1 31-Inch Mach 10 Air Tunnel Tests

A survey of existing data on the thermal properties of Macor, the substance from which the entry vehicle test models were fabricated, revealed that despite its widespread use in the aerospace community, there exists a great deal of uncertainty concerning Macor thermal properties. This uncertainty is not only in the variation of the thermal properties with temperature, but even in the room-temperature properties of

Macor. The existing database on Macor encompasses the works of several researchers, and includes a variety of measurements of different thermal properties using a number of different techniques. Unfortunately, there is very little consistency in these data. This can be seen in Figure C.1.1, in which the temperature dependance of the thermal product, β, as determined by different researchers is presented. The values used in this research (identified as Holometrix data) are also shown in this figure for comparison. The data in Figure C.1.1 represent either direct measurements of the thermal product or values computed from measured thermal conductivity, specific heat and thermal diffusivity data. For clarity, symbols are plotted for all data sets, although the values shown may represent either individual measurements or curve fits to data. The reliability of these data are plainly unacceptable. Even at room temperature, the highest β value shown is almost 33% greater than the lowest value. Furthermore, the rate of change of β with temperature is different in almost every data set.

Because of the large scatter in the available data, it was decided that the best course to follow in the present work would be to ignore the existing data and compile an entirely new database on Macor thermal properties. This work was done by a qualified laboratory, Holometrix Incorporated, which specializes in material properties testing. Over a four year period, four different sets of Macor samples were sent to Holometrix for testing. For each Macor sample, Holometrix provided measurements of the thermal conductivity and thermal diffusivity over a 300 K temperature range from 300 K to 600K (Soos, 1992, 1993, 1994, Campbell, 1995).

The thermal conductivity data obtained from all the samples tested by Holometrix are plotted in Figure C.1.2, and the thermal diffusivity data are plotted in Figure C.1.3. Curve fits to these data are also shown in these figures. The curve fits are given by:

$$k = 0.33889 + 7.4682 \cdot 10^{-3} \cdot T - 1.6118 \cdot 10^{-5} \cdot T^2 + 1.2376 \cdot 10^{-8} \cdot T^3 \ \text{(W/m-K)} \qquad \text{(C.1.1)}$$

$$\alpha = 1.3003 \cdot 10^{-6} - 2.2523 \cdot 10^{-9} \cdot T + 1.8571 \cdot 10^{-12} \cdot T^2 \ \text{(m}^2\text{/sec)} \qquad \text{(C.1.2)}$$

and the density of Macor is:

$$\rho = 2543.84 \quad (\mathrm{kg/m^3}) \tag{C.1.3}$$

In addition to the Macor thermal properties samples, several quartz samples (Dynasil 1100 Grade) were also sent to Holometrix. This was done so that quartz models also could be tested in the 31-Inch Mach 10 Air Tunnel and the quartz model heating data could then be used as a reference standard to which Macor model heating data could be compared. The quartz thermal conductivity data and thermal diffusivity data are presented in Figures C.1.4 and C.1.5. Curve fits to these data are given by:

$$k = 0.96157 + 9.5491 \cdot 10^{-4} \cdot T + 5.5465 \cdot 10^{-7} \cdot T^2 \quad (\mathrm{W/m-K}) \tag{C.1.4}$$

$$\alpha = 1.5191 \cdot 10^{-6} - 4.136 \cdot 10^{-9} \cdot T + 7.2707 \cdot 10^{-12} \cdot T^2 - 4.4242 \cdot 10^{-15} \cdot T^3 \ (\mathrm{m^2/sec}) \tag{C.1.5}$$

and the density of quartz is:

$$\rho = 2192.5 \ (\mathrm{kg/m^3}) \tag{C.1.6}$$

In order to evaluate the reliability of the Macor data, a series of aerothermodynamic tests was carried out in the 31-Inch Mach 10 Air Tunnel as part of Test Series 307. In these tests, 2-in. diameter Macor and quartz hemispheres were tested side-by-side in the Mach 10 Tunnel at each of its three Reynolds number operating points. Flow conditions for these tests are given in Table C.1.1. Test data are given in Tables C.1.2 through C.1.13, and the C_H distributions from these tests are plotted in Figures C.1.6

through C.1.8. Distributions obtained from viscous-shock-layer (e.g. Gupta, Lee and Zoby, 1993) computations (courtesy of Roop Gupta, NASA, LaRC) are also shown in these figures. Both sets of distributions are normalized by the computed Fay-Riddell stagnation point values for these test conditions.

The normalized quartz and Macor values differed consistently by approximately 8%, with the nondimensional heating rates on the quartz model being higher than on the Macor model. The VSL (viscous-shock-layer) solutions were consistently higher than the Macor data and were just slightly lower than those on the quartz model. At the lowest Reynolds number test condition, VSL stagnation point heating was approximately 3% higher than that of the Macor hemisphere; at the highest Reynolds number condition, the VSL solution was approximately 6% higher than the Macor data. In comparison to the quartz data, the VSL solutions varied from about 3% lower than the quartz data to about 1% lower. The Fay-Riddell results nearly split the difference between the quartz and Macor model data at all test conditions.

In light of the discrepancies in previous thermal properties data, the comparisons in Figures C.1.6 through C.1.8 are highly encouraging. These comparisons prove that experimental data reduced with the new Macor thermal properties data produce heating results that agree well not only with theoretical results, but with data obtained from side-by-side tests of identical models fabricated from different materials. Furthermore, good agreement was observed in the comparisons presented in Chapter 8 between experimental and computational data for the entry vehicle tests in both the 31-Inch Mach 10 Air Tunnel and the HYPULSE Expansion Tube. However, while the current data is felt to be much more reliable than the previously existing database, these comparisons should by no means be taken as a justification for doing no further research on the properties of Macor (or other materials). One issue which should be further investigated is that experimental perfect-gas heating results obtained with Macor models were generally lower than those obtained from analytical or computational solutions. While the source of this bias could certainly be within the computational methods, the unreliability of the previously existing Macor database and the present comparison between Macor and quartz results suggests the possibility that the bias could be due to the Macor thermal properties data.

One final issue which must be addressed in regard to Macor thermal properties is the derivation of empirical correction factors for the temperature dependence of Macor for use in the constant properties analytical data reduction techniques presented in Chapter 5. The correction factor is applied to a constant properties solution via:

$$q_{\beta T)} = q_{\beta_0}\left(1 + \lambda\, \Delta T_s\right) \tag{C.1.7}$$

where $q_{\beta 0}$ is the constant properties solution, and λ is the correction factor. The correction factor was derived through comparison of heating rate time-histories produced from a parabolic temperature time-history, $T = T(t^{1/2})$, (Figure C.1.9) for a case in which the substrate thermal properties were assumed to remain fixed and for a case in which the thermal properties varied with temperature. The variable-property heating time-history was determined using the finite-volume method presented in Chapter 5 with the curve fits presented in this section, while the constant-properties heating time-history was computed using one of the analytical methods. These time histories are shown in Figure C.1.10 along with the correction factor values, which are derived from:

$$\lambda(\Delta T_s) = \frac{\left(\frac{q_{\beta T)}}{q_{\beta_0}} - 1\right)}{\Delta T_s} \tag{C.1.8}$$

where ΔT_s is the surface temperature rise with respect to an initial ambient temperature of 298 K. A linear fit to the resulting values for λ gives:

$$\lambda = 7.380 \cdot 10^{-4} - 4.604 \cdot 10^{-7} \cdot \Delta T_s \tag{C.1.9}$$

which is considered to be valid for temperatures up to 600 K. Quartz correction factors were derived in the same manner as those for Macor. The correction factor equation for quartz is:

$$\lambda = 9.414 \cdot 10^{-4} - 8.018 \cdot 10^{-7} \cdot \Delta T_s \qquad \text{(C.1.10)}$$

and is also considered to be valid for temperatures up to 600 K.

While the linear fits are less accurate at low temperatures (the correction factor should go to zero a room temperature), the actual correction to the heating rate is the correction factor times the temperature rise, and so the error is negligible at low temperatures. The use of the correction factor given by Equation (C.1.9) is illustrated in Figure C.1.11, in which corrected and uncorrected heating time-histories are compared to the variable thermal properties finite-volume solution for the parabolic temperature time-history. Agreement between the corrected analytical solution and the numerical finite-volume solution is excellent.

Although this correction factor equation was derived on the basis of a parabolic temperature time-history, experience has shown that it appears to be valid for any temperature-time relationship within the stipulated temperature range. A sample comparison between a corrected constant-properties heating time-history and one from a finite-volume computation is presented in Figure C.1.12. This results are based on actual temperature time-history from a run in the 31-Inch Mach 10 Air Tunnel. As can be seen, the agreement is again very good. Nevertheless, it should be emphasized that this method of correcting the analytical solutions is strictly empirical, and that for a rigorous analysis of heating data, heating rates should be computed with a numerical technique such as that discussed in Section 5.2.2.

Section C.2 HYPULSE Expansion Tube Tests

A set of hemisphere models was tested in HYPULSE in order to evaluate the quality of data from the facility and to provide simple test cases for the NEQ2D code before computing solutions for the entry vehicle test cases. Hemispheres of 1/2-in., 3/4-in. and 1-in. diameters were tested side-by-side in HYPULSE in He, air, and CO_2 test gases. Flow conditions for these tests are given in Table C.2.1. The test data are given in Tables C.2.2 through C.2.7, and the distributions are plotted in Figures C.2.1 through C.2.3. For each test gas, the run-to-run variation in heating rates was no greater than about ±7%, which lent confidence to the repeatability of facility operating conditions. Furthermore, as shown in Figure C.2.4, the stagnation point heating rates of the various size hemispheres correlated nearly linearly with $R^{-1/2}$. A linear variation with $R^{-1/2}$ is predicted for equilibrium or frozen flows (Fay and Riddell, 1958), and across the small range of nose radii of these models, the variation can be expected to remain fairly close to linear. That a nearly linear variation was observed in these tests, in which three models of different radii were tested simultaneously, demonstrated that there was relatively little non-uniformity across the HYPULSE tests core.

The NEQ2D code was used to compute solutions for the flow around the 1-in. diam. hemisphere for the air and CO_2 test cases. Heating distributions obtained from these computations are shown in Figures C.2.5 and C.2.6 along with the experimental data. For these computations, grids of 30x50 and 30x100 streamwise and normal points were employed. Computed heating rates changed by less than 2% between the two grids. For the air test case, computed heating rates were approximately 7% higher than the experimental data, while for the CO_2 case, the computed heating rates were about 3% higher than the experimental data. This over-prediction is consistent with the comparisons for the Mach 10 hemisphere tests, which lends more weight to the hypothesis that the Macor thermal properties data curve fits may cause a slight under-prediction of heating when used to reduce experimental data.

TABLE C.1.1 31-Inch Mach 10 Test 307 Flow Conditions

Run	Model	Re_∞ (1/ft)	U_∞ (m/sec)	T_∞ (K)	ρ_∞ (kg/m^3)	p_∞ (Pa)	M_∞	$h_{tot} - h_{298}$ (MJ/kg)
002	2-in. Hemis.	0.490E+06	1411	52.90	4.451E-03	67.63	9.675	0.747
003	2-in. Hemis.	0.497E+06	1410	52.92	4.514E-03	68.52	9.676	0.748
004	2-in. Hemis.	0.969E+06	1423	52.49	8.666E-03	130.5	9.796	0.764
005	2-in. Hemis.	0.982E+06	1416	51.95	8.729E-03	130.1	9.800	0.754
006	2-in. Hemis.	1.915+E06	1420	50.86	16.61E-03	242.1	9.930	0.758
007	2-in. Hemis.	1.947E+06	1420	50.17	16.76E-03	240.9	9.936	0.745

TABLE C.1.2a 31-Inch Mach 10 Test 307, Run 002 Heating Data
2-in. diam. Macor Hemisphere, $Re_\infty = 0.5 \times 10^6$ ft^{-1}

GAGE ID	S/R	θ	C_H	s/C_H	q_{300}(W/cm^2)
TF6	-1.527	-87.5	2.632e-03	0.005	1.272
TF7	-1.396	-80.0	3.922e-03	0.009	1.895
TF8	-0.960	-55.0	1.152e-02	0.002	5.566
TF9	-0.698	-40.0	1.761e-02	0.001	8.509
TF10	-0.524	-30.0	2.162e-02	0.002	10.447
TF11	-0.349	-20.0	2.495e-02	0.002	12.056
TF12	-0.262	-15.0	2.606e-02	0.002	12.594
TF13	-0.175	-10.0	2.668e-02	0.003	12.890
TF14	-0.131	-7.5	2.697e-02	0.002	13.035
TF15	-0.087	-5.0	2.734e-02	0.003	13.211
TF16	-0.044	-2.5	2.771e-02	0.002	13.390
TF17	0.000	0.0	2.797e-02	0.002	13.518
TF18	0.044	2.5	*	*	*
TF19	0.087	5.0	2.729e-02	0.001	13.188
TF20	0.131	7.5	2.689e-02	0.001	12.994
TF21	0.175	10.0	2.668e-02	0.002	12.896
TF22	0.262	15.0	2.622e-02	0.003	12.673
TF23	0.349	20.0	2.495e-02	0.001	12.057
TF24	0.524	30.0	2.162e-02	0.001	10.449
TF25	0.698	40.0	1.761e-02	0.002	8.509
TF26	0.960	50.0	1.126e-02	0.002	5.442
TF27	1.396	80.0	3.779e-03	0.003	1.826
TF28	1.527	87.5	2.476e-03	0.006	1.196

TABLE C.1.2b 31-Inch Mach 10 Test 307, Run 002 Heating Data
2-in. diam. Quartz Hemisphere, $Re_\infty = 0.5 \times 10^6$ ft^{-1}

GAGE ID	S/R	θ	C_H	s/C_H	q_{300}(W/cm^2)
TF1	-1.527	-87.5	4.120e-03	0.004	1.923
TF2	-1.396	-80.0	6.043e-03	0.004	2.821
TF3	-0.960	-55.0	1.521e-02	0.003	7.098
TF4	-0.698	-40.0	2.173e-02	0.003	10.144
TF5	-0.524	-30.0	2.583e-02	0.004	12.055
TF6	-0.349	-20.0	2.925e-02	0.004	13.651
TF7	-0.262	-15.0	3.044e-02	0.003	14.208
TF8	-0.175	-10.0	3.081e-02	0.005	14.379
TF9	-0.131	-7.5	3.095e-02	0.006	14.447
TF10	-0.087	-5.0	3.136e-02	0.005	14.639
TF11	-0.044	-2.5	3.164e-02	0.005	14.770
TF12	0.000	0.0	3.156e-02	0.005	14.732
TF13	0.044	2.5	3.162e-02	0.005	14.761
TF14	0.087	5.0	3.190e-02	0.005	14.887
TF15	0.131	7.5	3.131e-02	0.005	14.614
TF16	0.175	10.0	3.067e-02	0.004	14.313
TF17	0.262	15.0	3.038e-02	0.001	14.178
TF18	0.349	20.0	2.892e-02	0.002	13.499
TF19	0.524	30.0	2.569e-02	0.003	11.990
TF20	0.698	40.0	2.164e-02	0.002	10.100
TF21	0.960	50.0	1.516e-02	0.001	7.074
TF22	1.396	80.0	6.015e-03	0.003	2.807
TF23	1.527	87.5	4.165e-03	0.002	1.944

TABLE C.1.3a 31-Inch Mach 10 Test 307, Run 003 Heating Data
2-in. diam. Macor Hemisphere, $Re_\infty = 0.5 \times 10^6$ ft^{-1}

GAGE ID	S/R	θ	C_H	s/C_H	q_{300}(W/cm^2)
TF6	-1.527	-87.5	2.608e-03	0.005	1.276
TF7	-1.396	-80.0	3.886e-03	0.009	1.901
TF8	-0.960	-55.0	1.141e-02	0.002	5.584
TF9	-0.698	-40.0	1.745e-02	0.001	8.537
TF10	-0.524	-30.0	2.142e-02	0.002	10.481
TF11	-0.349	-20.0	2.472e-02	0.002	12.096
TF12	-0.262	-15.0	2.583e-02	0.002	12.636
TF13	-0.175	-10.0	2.643e-02	0.003	12.934
TF14	-0.131	-7.5	2.673e-02	0.002	13.078
TF15	-0.087	-5.0	2.709e-02	0.003	13.254
TF16	-0.044	-2.5	2.746e-02	0.002	13.434
TF17	0.000	0.0	2.772e-02	0.002	13.562
TF18	0.044	2.5	*	*	*
TF19	0.087	5.0	2.705e-02	0.001	13.232
TF20	0.131	7.5	2.665e-02	0.001	13.038
TF21	0.175	10.0	2.644e-02	0.002	12.938
TF22	0.262	15.0	2.599e-02	0.003	12.715
TF23	0.349	20.0	2.472e-02	0.001	12.097
TF24	0.524	30.0	2.143e-02	0.001	10.484
TF25	0.698	40.0	1.745e-02	0.002	8.536
TF26	0.960	50.0	1.116e-02	0.002	5.459
TF27	1.396	80.0	3.743e-03	0.003	1.832
TF28	1.527	87.5	2.452e-03	0.006	1.200

TABLE C.1.3b 31-Inch Mach 10 Test 307, Run 003 Heating Data
2-in. diam. Quartz Hemisphere, $Re_\infty = 0.5 \times 10^6$ ft^{-1}

GAGE ID	S/R	θ	C_H	s/C_H	q_{300}(W/cm^2)
TF1	-1.527	-87.5	4.031e-03	0.006	1.915
TF2	-1.396	-80.0	5.929e-03	0.007	2.817
TF3	-0.960	-55.0	1.491e-02	0.002	7.085
TF4	-0.698	-40.0	2.132e-02	0.003	10.126
TF5	-0.524	-30.0	2.528e-02	0.006	12.007
TF6	-0.349	-20.0	2.870e-02	0.003	13.631
TF7	-0.262	-15.0	2.990e-02	0.004	14.204
TF8	-0.175	-10.0	3.026e-02	0.006	14.376
TF9	-0.131	-7.5	3.037e-02	0.006	14.427
TF10	-0.087	-5.0	3.073e-02	0.006	14.595
TF11	-0.044	-2.5	3.102e-02	0.005	14.736
TF12	0.000	0.0	*	*	*
TF13	0.044	2.5	3.105e-02	0.006	14.749
TF14	0.087	5.0	3.132e-02	0.005	14.877
TF15	0.131	7.5	3.073e-02	0.006	14.596
TF16	0.175	10.0	3.007e-02	0.005	14.284
TF17	0.262	15.0	2.975e-02	0.002	14.132
TF18	0.349	20.0	2.834e-02	0.003	13.460
TF19	0.524	30.0	2.517e-02	0.003	11.958
TF20	0.698	40.0	2.120e-02	0.002	10.068
TF21	0.960	50.0	1.483e-02	0.001	7.047
TF22	1.396	80.0	5.879e-03	0.004	2.792
TF23	1.527	87.5	4.064e-03	0.004	1.931

TABLE C.1.4a 31-Inch Mach 10 Test 307, Run 004 Heating Data
2-in. diam. Macor Hemisphere, $Re_\infty = 1.0 \times 10^6$ ft^{-1}

GAGE ID	S/R	θ	C_H	s/C_H	q_{300}(W/cm^2)
TF6	-1.527	-87.5	1.827e-03	0.009	1.769
TF7	-1.396	-80.0	2.750e-03	0.012	2.662
TF8	-0.960	-55.0	8.179e-03	0.008	7.918
TF9	-0.698	-40.0	1.249e-02	0.003	12.089
TF10	-0.524	-30.0	1.533e-02	0.003	14.844
TF11	-0.349	-20.0	1.763e-02	0.002	17.069
TF12	-0.262	-15.0	1.843e-02	0.002	17.842
TF13	-0.175	-10.0	1.884e-02	0.002	18.242
TF14	-0.131	-7.5	1.904e-02	0.002	18.429
TF15	-0.087	-5.0	1.928e-02	0.002	18.664
TF16	-0.044	-2.5	1.953e-02	0.003	18.911
TF17	0.000	0.0	1.972e-02	0.003	19.091
TF18	0.044	2.5	*	*	*
TF19	0.087	5.0	1.923e-02	0.003	18.617
TF20	0.131	7.5	1.891e-02	0.004	18.302
TF21	0.175	10.0	1.881e-02	0.004	18.213
TF22	0.262	15.0	1.850e-02	0.003	17.903
TF23	0.349	20.0	1.755e-02	0.003	16.989
TF24	0.524	30.0	1.525e-02	0.001	14.759
TF25	0.698	40.0	1.246e-02	0.001	12.058
TF26	0.960	50.0	7.984e-03	0.002	7.729
TF27	1.396	80.0	2.652e-03	0.006	2.567
TF28	1.527	87.5	1.690e-03	0.002	1.636

TABLE C.1.4b 31-Inch Mach 10 Test 307, Run 004 Heating Data
2-in. diam. Quartz Hemisphere, $Re_\infty = 1.0 \times 10^6$ ft^{-1}

GAGE ID	S/R	θ	C_H	s/C_H	q_{300}(W/cm^2)
TF1	-1.527	-87.5	2.845e-03	0.012	2.674
TF2	-1.396	-80.0	4.211e-03	0.009	3.958
TF3	-0.960	-55.0	1.065e-02	0.004	10.012
TF4	-0.698	-40.0	1.519e-02	0.002	14.275
TF5	-0.524	-30.0	1.797e-02	0.003	16.891
TF6	-0.349	-20.0	2.031e-02	0.004	19.087
TF7	-0.262	-15.0	2.116e-02	0.004	19.884
TF8	-0.175	-10.0	2.138e-02	0.007	20.098
TF9	-0.131	-7.5	2.137e-02	0.008	20.085
TF10	-0.087	-5.0	2.170e-02	0.008	20.397
TF11	-0.044	-2.5	2.193e-02	0.007	20.610
TF12	0.000	0.0	*	*	*
TF13	0.044	2.5	2.191e-02	0.007	20.594
TF14	0.087	5.0	2.211e-02	0.007	20.785
TF15	0.131	7.5	2.167e-02	0.008	20.368
TF16	0.175	10.0	2.121e-02	0.007	19.935
TF17	0.262	15.0	2.099e-02	0.005	19.724
TF18	0.349	20.0	2.002e-02	0.006	18.816
TF19	0.524	30.0	1.779e-02	0.005	16.722
TF20	0.698	40.0	1.498e-02	0.004	14.084
TF21	0.960	50.0	1.054e-02	0.003	9.903
TF22	1.396	80.0	4.129e-03	0.006	3.881
TF23	1.527	87.5	2.821e-03	0.008	2.652

TABLE C.1.5a 31-Inch Mach 10 Test 307, Run 005 Heating Data
2-in. diam. Macor Hemisphere, $Re_\infty = 1.0 \times 10^6$ ft^{-1}

GAGE ID	S/R	θ	C_H	s/C_H	q_{300}(W/cm^2)
TF6	-1.527	-87.5	1.808e-03	0.008	1.732
TF7	-1.396	-80.0	2.714e-03	0.011	2.599
TF8	-0.960	-55.0	8.089e-03	0.008	7.746
TF9	-0.698	-40.0	1.236e-02	0.004	11.834
TF10	-0.524	-30.0	1.521e-02	0.003	14.564
TF11	-0.349	-20.0	1.771e-02	0.002	16.961
TF12	-0.262	-15.0	1.826e-02	0.002	17.485
TF13	-0.175	-10.0	1.867e-02	0.002	17.875
TF14	-0.131	-7.5	1.886e-02	0.002	18.057
TF15	-0.087	-5.0	1.909e-02	0.003	18.284
TF16	-0.044	-2.5	1.932e-02	0.002	18.505
TF17	0.000	0.0	1.953e-02	0.003	18.699
TF18	0.044	2.5	*	*	*
TF19	0.087	5.0	1.904e-02	0.003	18.235
TF20	0.131	7.5	1.872e-02	0.004	17.930
TF21	0.175	10.0	1.863e-02	0.003	17.840
TF22	0.262	15.0	1.831e-02	0.003	17.532
TF23	0.349	20.0	1.738e-02	0.003	16.641
TF24	0.524	30.0	1.509e-02	0.002	14.454
TF25	0.698	40.0	1.231e-02	0.002	11.787
TF26	0.960	50.0	7.894e-03	0.002	7.559
TF27	1.396	80.0	2.623e-03	0.007	2.512
TF28	1.527	87.5	1.667e-03	0.003	1.597

TABLE C.1.5b 31-Inch Mach 10 Test 307, Run 005 Heating Data
2-in. diam. Quartz Hemisphere, $Re_\infty = 1.0 \times 10^6$ ft^{-1}

GAGE ID	S/R	θ	C_H	s/C_H	q_{300}(W/cm^2)
TF1	-1.527	-87.5	2.799e-03	0.011	2.602
TF2	-1.396	-80.0	4.158e-03	0.010	3.866
TF3	-0.960	-55.0	1.052e-02	0.004	9.783
TF4	-0.698	-40.0	1.502e-02	0.002	13.964
TF5	-0.524	-30.0	1.773e-02	0.004	16.480
TF6	-0.349	-20.0	2.014e-02	0.003	18.721
TF7	-0.262	-15.0	2.092e-02	0.003	19.446
TF8	-0.175	-10.0	2.121e-02	0.006	19.717
TF9	-0.131	-7.5	2.116e-02	0.007	19.672
TF10	-0.087	-5.0	2.153e-02	0.006	20.014
TF11	-0.044	-2.5	2.176e-02	0.007	20.230
TF12	0.000	0.0	*	*	*
TF13	0.044	2.5	2.172e-02	0.007	20.190
TF14	0.087	5.0	2.180e-02	0.007	20.270
TF15	0.131	7.5	2.151e-02	0.008	19.993
TF16	0.175	10.0	2.104e-02	0.007	19.559
TF17	0.262	15.0	2.079e-02	0.004	19.323
TF18	0.349	20.0	1.982e-02	0.005	18.428
TF19	0.524	30.0	1.760e-02	0.005	16.358
TF20	0.698	40.0	1.482e-02	0.004	13.781
TF21	0.960	50.0	1.040e-02	0.002	9.667
TF22	1.396	80.0	4.080e-03	0.006	3.793
TF23	1.527	87.5	2.787e-03	0.008	2.591

TABLE C.1.6a 31-Inch Mach 10 Test 307, Run 006 Heating Data
2-in. diam. Macor Hemisphere, $Re_\infty = 2.0 \times 10^6$ ft^{-1}

GAGE ID	S/R	θ	C_H	s/C_H	q_{300}(W/cm^2)
TF6	-1.527	-87.5	1.313e-03	0.013	2.411
TF7	-1.396	-80.0	1.997e-03	0.017	3.668
TF8	-0.960	-55.0	5.984e-03	0.011	10.990
TF9	-0.698	-40.0	9.077e-03	0.006	16.673
TF10	-0.524	-30.0	1.113e-02	0.004	20.453
TF11	-0.349	-20.0	1.275e-02	0.003	23.414
TF12	-0.262	-15.0	1.328e-02	0.003	24.396
TF13	-0.175	-10.0	1.354e-02	0.006	24.860
TF14	-0.131	-7.5	1.371e-02	0.005	25.173
TF15	-0.087	-5.0	1.385e-02	0.006	25.430
TF16	-0.044	-2.5	1.404e-02	0.006	25.782
TF17	0.000	0.0	1.416e-02	0.007	26.014
TF18	0.044	2.5	*	*	*
TF19	0.087	5.0	1.379e-02	0.007	25.333
TF20	0.131	7.5	1.355e-02	0.007	24.883
TF21	0.175	10.0	1.349e-02	0.007	24.785
TF22	0.262	15.0	1.325e-02	0.005	24.335
TF23	0.349	20.0	1.260e-02	0.005	23.146
TF24	0.524	30.0	1.096e-02	0.004	20.140
TF25	0.698	40.0	8.964e-03	0.003	16.464
TF26	0.960	50.0	5.759e-03	0.003	10.577
TF27	1.396	80.0	1.902e-03	0.009	3.493
TF28	1.527	87.5	1.187e-03	0.011	2.181

TABLE C.1.6b 31-Inch Mach 10 Test 307, Run 006 Heating Data
2-in. diam. Quartz Hemisphere, $Re_\infty = 2.0 \times 10^6$ ft^{-1}

GAGE ID	S/R	θ	C_H	s/C_H	q_{300}(W/cm^2)
TF1	-1.527	-87.5	2.068e-03	0.016	3.688
TF2	-1.396	-80.0	3.076e-03	0.013	5.486
TF3	-0.960	-55.0	7.761e-03	0.006	13.840
TF4	-0.698	-40.0	1.102e-02	0.004	19.649
TF5	-0.524	-30.0	1.294e-02	0.005	23.081
TF6	-0.349	-20.0	1.462e-02	0.006	26.080
TF7	-0.262	-15.0	1.522e-02	0.008	27.131
TF8	-0.175	-10.0	1.532e-02	0.011	27.320
TF9	-0.131	-7.5	1.518e-02	0.013	27.069
TF10	-0.087	-5.0	1.554e-02	0.011	27.714
TF11	-0.044	-2.5	1.579e-02	0.010	28.151
TF12	0.000	0.0	*	*	*
TF13	0.044	2.5	1.565e-02	0.013	27.913
TF14	0.087	5.0	1.578e-02	0.011	28.142
TF15	0.131	7.5	1.563e-02	0.013	27.868
TF16	0.175	10.0	1.527e-02	0.013	27.223
TF17	0.262	15.0	1.511e-02	0.009	26.951
TF18	0.349	20.0	1.441e-02	0.009	25.691
TF19	0.524	30.0	1.280e-02	0.008	22.821
TF20	0.698	40.0	1.080e-02	0.005	19.264
TF21	0.960	50.0	7.597e-03	0.003	13.547
TF22	1.396	80.0	2.977e-03	0.009	5.309
TF23	1.527	87.5	2.016e-03	0.013	3.594

TABLE C.1.7a 31-Inch Mach 10 Test 307, Run 007 Heating Data
2-in. diam. Macor Hemisphere, $Re_\infty = 2.0 \times 10^6$ ft^{-1}

GAGE ID	S/R	θ	C_H	s/C_H	q_{300}(W/cm^2)
TF6	-1.527	-87.5	1.299e-03	0.012	2.350
TF7	-1.396	-80.0	1.977e-03	0.019	3.577
TF8	-0.960	-55.0	5.928e-03	0.011	10.727
TF9	-0.698	-40.0	9.001e-03	0.006	16.288
TF10	-0.524	-30.0	1.100e-02	0.003	19.901
TF11	-0.349	-20.0	1.261e-02	0.003	22.822
TF12	-0.262	-15.0	1.315e-02	0.004	23.792
TF13	-0.175	-10.0	1.341e-02	0.006	24.274
TF14	-0.131	-7.5	1.356e-02	0.004	24.534
TF15	-0.087	-5.0	1.368e-02	0.006	24.755
TF16	-0.044	-2.5	1.386e-02	0.006	25.075
TF17	0.000	0.0	1.401e-02	0.006	25.349
TF18	0.044	2.5	*	*	*
TF19	0.087	5.0	1.363e-02	0.007	24.658
TF20	0.131	7.5	1.341e-02	0.007	24.270
TF21	0.175	10.0	1.335e-02	0.007	24.157
TF22	0.262	15.0	1.312e-02	0.005	23.736
TF23	0.349	20.0	1.248e-02	0.005	22.586
TF24	0.524	30.0	1.086e-02	0.003	19.647
TF25	0.698	40.0	8.871e-03	0.003	16.053
TF26	0.960	50.0	5.698e-03	0.004	10.311
TF27	1.396	80.0	1.876e-03	0.012	3.395
TF28	1.527	87.5	1.170e-03	0.007	2.117

TABLE C.1.7b 31-Inch Mach 10 Test 307, Run 007 Heating Data
2-in. diam. Quartz Hemisphere, $Re_\infty = 2.0 \times 10^6$ ft^{-1}

GAGE ID	S/R	θ	C_H	s/C_H	q_{300}(W/cm^2)
TF1	-1.527	-87.5	2.043e-03	0.016	3.589
TF2	-1.396	-80.0	3.044e-03	0.013	5.347
TF3	-0.960	-55.0	7.677e-03	0.005	13.487
TF4	-0.698	-40.0	1.092e-02	0.002	19.190
TF5	-0.524	-30.0	1.287e-02	0.008	22.604
TF6	-0.349	-20.0	1.454e-02	0.005	25.540
TF7	-0.262	-15.0	1.494e-02	0.007	26.248
TF8	0.175	10.0	*	*	*
TF9	-0.131	-7.5	1.522e-02	0.010	26.741
TF10	-0.087	-5.0	1.541e-02	0.009	27.075
TF11	-0.044	-2.5	1.564e-02	0.009	27.470
TF12	0.000	0.0	*	*	*
TF13	0.044	2.5	1.545e-02	0.011	27.150
TF14	0.087	5.0	1.579e-02	0.010	27.737
TF15	0.131	7.5	1.550e-02	0.011	27.236
TF16	0.175	10.0	1.510e-02	0.011	26.533
TF17	0.262	15.0	1.494e-02	0.006	26.245
TF18	0.349	20.0	1.428e-02	0.007	25.088
TF19	0.524	30.0	1.270e-02	0.005	22.305
TF20	0.698	40.0	1.071e-02	0.003	18.813
TF21	0.960	50.0	7.515e-03	0.004	13.202
TF22	1.396	80.0	2.939e-03	0.010	5.164
TF23	1.527	87.5	1.996e-03	0.012	3.507

TABLE C.2.1 HYPULSE Expansion Tube Flow Conditions

Run	Model	Test Gas	u_∞ (m/s)	T_∞ (K)	ρ_∞ (kg/m^3)	p_∞ (Pa)	M_∞	h_{tot}-h_{298} (MJ/kg)
758	Hemis.	He	6139	291.7	2.412E-03	1456	6.11	18.80
759	Hemis.	He	6200	313.3	2.419E-03	1566	5.96	19.29
760	Hemis.	Air	5167	1061	5.659E-03	1724	8.11	14.17
761	Hemis.	Air	5145	1072	5.723E-03	1760	8.04	14.06
751	Hemis.	CO_2	4806	1042	5.644E-03	1111	9.97	12.36
763	Hemis.	CO_2	4844	1041	5.539E-03	1090	10.05	12.54

TABLE C.2.2 HYPULSE Run 758 Heating Data, He Test Gas, 1/2-in. diam., 3/4-in. diam., 1.0-in. diam. Hemispheres

GAGE ID	S/R	θ	C_H	s/C_H	$q_{300}(W/cm^2)$
1/2-in.diam					
TF1	0.000	0.0	5.736e-02	0.027	1600.900
3/4-in.diam					
TF2	-1.571	-90.0	3.353e-03	0.035	93.580
TF3	-1.047	-60.0	1.539e-02	0.035	429.480
TF4	-0.524	-30.0	3.762e-02	0.043	1050.100
TF5	0.000	0.0	4.930e-02	0.037	1376.000
TF6	0.524	30.0	3.487e-02	0.036	973.370
TF7	1.047	60.0	1.344e-02	0.032	375.100
TF8	1.571	90.0	3.275e-03	0.035	91.403
1.0-in.diam					
TF9	-1.571	-90.0	2.495e-03	0.052	69.644
TF10	-1.309	-75.0	6.021e-03	0.072	168.050
TF11	-1.047	-60.0	1.332e-02	0.102	371.650
TF12	-0.785	-45.0	2.315e-02	0.028	646.150
TF13	-0.524	-30.0	3.262e-02	0.055	910.360
TF14	-0.393	-22.5	3.646e-02	0.029	1017.500
TF15	-0.262	-15.0	3.943e-02	0.034	1100.700
TF16	-0.131	-7.5	4.001e-02	0.051	1116.700
TF17	0.000	0.0	4.032e-02	0.049	1125.300
TF18	0.131	7.5	3.842e-02	0.034	1072.500
TF19	0.262	15.0	3.564e-02	0.053	994.650
TF20	0.393	22.5	*	*	*
TF21	0.524	30.0	3.033e-02	0.053	846.480
TF22	0.785	45.0	2.183e-02	0.055	609.170
TF23	1.047	60.0	1.167e-02	0.066	325.810
TF24	1.309	75.0	6.228e-03	0.066	173.840
TF25	1.571	90.0	2.691e-03	0.080	75.119

TABLE C.2.3 HYPULSE Run 759 Heating Data, He Test Gas, 1/2-in. diam., 3/4-in. diam., 1.0-in. diam. Hemispheres

GAGE ID	S/R	θ	C_H	s/C_H	q_{300}(W/cm^2)
1/2-in.diam					
TF1	0.000	0.0	5.382e-02	0.029	1556.200
3/4-in.diam					
TF2	-1.571	-90.0	3.710e-03	0.026	107.290
TF3	-1.047	-60.0	1.459e-02	0.022	421.870
TF4	-0.524	-30.0	3.463e-02	0.041	1001.300
TF5	0.000	0.0	4.414e-02	0.019	1276.400
TF6	0.524	30.0	3.375e-02	0.026	975.860
TF7	1.047	60.0	1.456e-02	0.028	420.880
TF8	1.571	90.0	3.718e-03	0.030	107.500
1.0-in.diam					
TF9	-1.571	-90.0	2.819e-03	0.032	81.517
TF10	-1.309	-75.0	5.800e-03	0.031	167.720
TF11	-1.047	-60.0	1.253e-02	0.029	362.310
TF12	-0.785	-45.0	2.085e-02	0.034	602.760
TF13	-0.524	-30.0	3.010e-02	0.032	870.470
TF14	-0.393	-22.5	3.661e-02	0.158	1058.500
TF15	-0.262	-15.0	3.919e-02	0.043	1133.100
TF16	-0.131	-7.5	4.044e-02	0.030	1169.400
TF17	0.000	0.0	4.133e-02	0.037	1195.000
TF18	0.131	7.5	3.968e-02	0.022	1147.300
TF19	0.262	15.0	3.713e-02	0.033	1073.700
TF20	0.393	22.5	3.507e-02	0.013	1014.000
TF21	0.524	30.0	3.087e-02	0.021	892.470
TF22	0.785	45.0	2.193e-02	0.037	634.200
TF23	1.047	60.0	1.233e-02	0.028	356.550
TF24	1.309	75.0	6.465e-03	0.033	186.940
TF25	1.571	90.0	2.616e-03	0.039	75.629

TABLE C.2.4 HYPULSE Run 760 Heating Data, Air Test Gas, 1/2-in. diam., 3/4-in. diam., 1.0-in. diam. Hemispheres

GAGE ID	S/R	θ	C_H	s/C_H	q_{300}(W/cm²)
1/2-in.diam					
TF1	0.000	0.0	4.062e-02	0.120	1688.700
3/4-in.diam					
TF2	-1.571	-90.0	2.977e-03	0.106	123.350
TF3	-1.047	-60.0	1.106e-02	0.047	458.130
TF4	-0.524	-30.0	2.553e-02	0.017	1057.700
TF5	0.000	0.0	3.524e-02	0.011	1459.800
TF6	0.524	30.0	2.612e-02	0.019	1081.900
TF7	1.047	60.0	1.191e-02	0.023	493.510
1.0-in.diam					
TF9	-1.571	-90.0	3.657e-03	0.584	151.490
TF10	-1.309	-75.0	*	*	*
TF11	-1.047	-60.0	1.379e-02	0.215	571.320
TF12	-0.785	-45.0	2.277e-02	0.107	943.270
TF13	-0.524	-30.0	3.875e-02	0.277	1605.500
TF14	-0.393	-22.5	3.773e-02	0.219	1563.100
TF15	-0.262	-15.0	3.404e-02	0.133	1410.100
TF16	-0.131	-7.5	3.755e-02	0.105	1555.400
TF17	0.000	0.0	3.470e-02	0.109	1437.600
TF18	0.131	7.5	2.442e-02	0.251	1011.500
TF19	0.262	15.0	3.326e-02	0.113	1378.100
TF20	0.393	22.5	3.304e-02	0.085	1368.800
TF21	0.524	30.0	2.557e-02	0.096	1059.300
TF22	0.785	45.0	1.873e-02	0.087	775.820
TF24	1.309	75.0	5.889e-03	0.082	243.980
TF25	1.571	90.0	2.965e-03	0.143	122.830

TABLE C.2.5 HYPULSE Run 761 Heating Data, Air Test Gas, 1/2-in. diam., 3/4-in. diam., 1.0-in. diam. Hemispheres

GAGE ID	S/R	θ	C_H	s/C_H	q_{300}(W/cm^2)
1/2-in.diam					
TF1	0.000	0.0	0.042	0.115	1770.100
3/4-in.diam					
TF2	-1.571	-90.0	0.003	0.021	144.170
TF3	-1.047	-60.0	0.011	0.011	478.680
TF4	-0.524	-30.0	0.026	0.012	1078.100
TF5	0.000	0.0	0.037	0.025	1538.300
TF6	0.524	30.0	0.027	0.021	1130.400
TF7	1.047	60.0	0.011	0.020	454.100
TF8	1.571	90.0	0.003	0.035	130.300
1.0-in.diam					
TF10	-1.309	-75.0	0.005	0.022	212.100
TF11	-1.047	-60.0	0.009	0.030	367.780
TF12	-0.785	-45.0	0.016	0.015	675.710
TF13	-0.524	-30.0	0.023	0.020	956.740
TF14	-0.393	-22.5	0.026	0.019	1070.100
TF15	-0.262	-15.0	0.027	0.021	1148.700
TF16	-0.131	-7.5	*	*	*
TF17	0.000	0.0	0.029	0.024	1226.200
TF18	0.131	7.5	0.028	0.026	1172.200
TF19	0.262	15.0	0.028	0.016	1173.200
TF20	0.393	22.5	0.026	0.019	1096.600
TF21	0.524	30.0	0.024	0.022	1004.300
TF22	0.785	45.0	0.018	0.043	763.030
TF23	1.047	60.0	0.009	0.085	379.940
TF24	1.309	75.0	0.005	0.023	213.310
TF25	1.571	90.0	0.003	0.026	113.190

TABLE C.2.6 HYPULSE Run 762 Heating Data, CO_2 Test Gas, 1/2-in. diam., 3/4-in. diam., 1.0-in. diam. Hemispheres

GAGE ID	S/R	θ	C_H	s/C_H	$q_{300}(W/cm^2)$
1/2-in.diam					
TF1	0.000	0.0	3.108e-02	0.045	1041.700
3/4-in.diam					
TF2	-1.571	-90.0	2.023e-03	0.225	67.813
TF3	-1.047	-60.0	8.646e-03	0.043	289.820
TF4	-0.524	-30.0	1.897e-02	0.022	636.060
TF5	0.000	0.0	2.673e-02	0.018	896.090
TF6	0.524	30.0	2.130e-02	0.021	714.010
TF7	1.047	60.0	8.611e-03	0.042	288.640
TF8	1.571	90.0	2.111e-03	0.199	70.767
1.0-in.diam					
TF9	-1.571	-90.0	1.835e-03	0.844	56.178
TF11	-1.047	-60.0	6.641e-03	0.081	200.840
TF12	-0.785	-45.0	1.361e-02	0.085	410.850
TF13	-0.524	-30.0	*	*	*
TF14	-0.393	-22.5	2.128e-02	0.089	642.130
TF15	-0.262	-15.0	2.246e-02	0.098	677.370
TF16	-0.131	-7.5	2.380e-02	0.091	718.160
TF17	0.000	0.0	2.449e-02	0.086	739.100
TF18	0.131	7.5	2.378e-02	0.090	717.420
TF19	0.262	15.0	2.371e-02	0.088	715.290
TF20	0.393	22.5	2.227e-02	0.089	671.630
TF21	0.524	30.0	2.006e-02	0.096	605.190
TF22	0.785	45.0	1.364e-02	0.090	411.550
TF24	1.309	75.0	3.679e-03	0.112	111.240
TF25	1.571	90.0	1.704e-03	0.499	51.528

TABLE C.2.7 HYPULSE Run 763 Heating Data, CO_2 Test Gas, 1/2-in. diam., 3/4-in. diam., 1.0-in. diam. Hemispheres

GAGE ID	S/R	θ	C_H	s/C_H	$q_{300}(W/cm^2)$
1/2-in.diam					
TF1	0.000	0.0	3.066e-02	0.036	1031.500
3/4-in.diam					
TF2	-1.571	-90.0	2.292e-03	0.116	77.096
TF3	-1.047	-60.0	9.279e-03	0.082	312.140
TF4	-0.524	-30.0	1.870e-02	0.045	628.950
TF5	0.000	0.0	2.682e-02	0.030	902.100
TF6	0.524	30.0	1.962e-02	0.043	660.130
TF7	1.047	60.0	9.160e-03	0.034	308.150
TF8	1.571	90.0	2.283e-03	0.091	76.796
1.0-in.diam					
TF9	-1.571	-90.0	1.813e-03	0.186	60.983
TF10	-1.309	-75.0	3.258e-03	0.201	109.600
TF11	-1.047	-60.0	6.830e-03	0.065	229.780
TF12	-0.785	-45.0	1.161e-02	0.049	390.400
TF13	-0.524	-30.0	1.706e-02	0.057	574.080
TF14	-0.393	-22.5	1.893e-02	0.049	636.850
TF15	-0.262	-15.0	2.018e-02	0.047	678.860
TF16	-0.131	-7.5	2.010e-02	0.046	676.180
TF17	0.000	0.0	2.145e-02	0.044	721.690
TF18	0.131	7.5	2.080e-02	0.061	699.860
TF19	0.262	15.0	2.012e-02	0.074	677.030
TF20	0.393	22.5	1.963e-02	0.048	660.250
TF21	0.524	30.0	*	*	*
TF22	0.785	45.0	1.202e-02	0.073	404.250
TF24	1.309	75.0	3.105e-03	0.230	104.450
TF25	1.571	90.0	1.798e-03	0.416	60.494

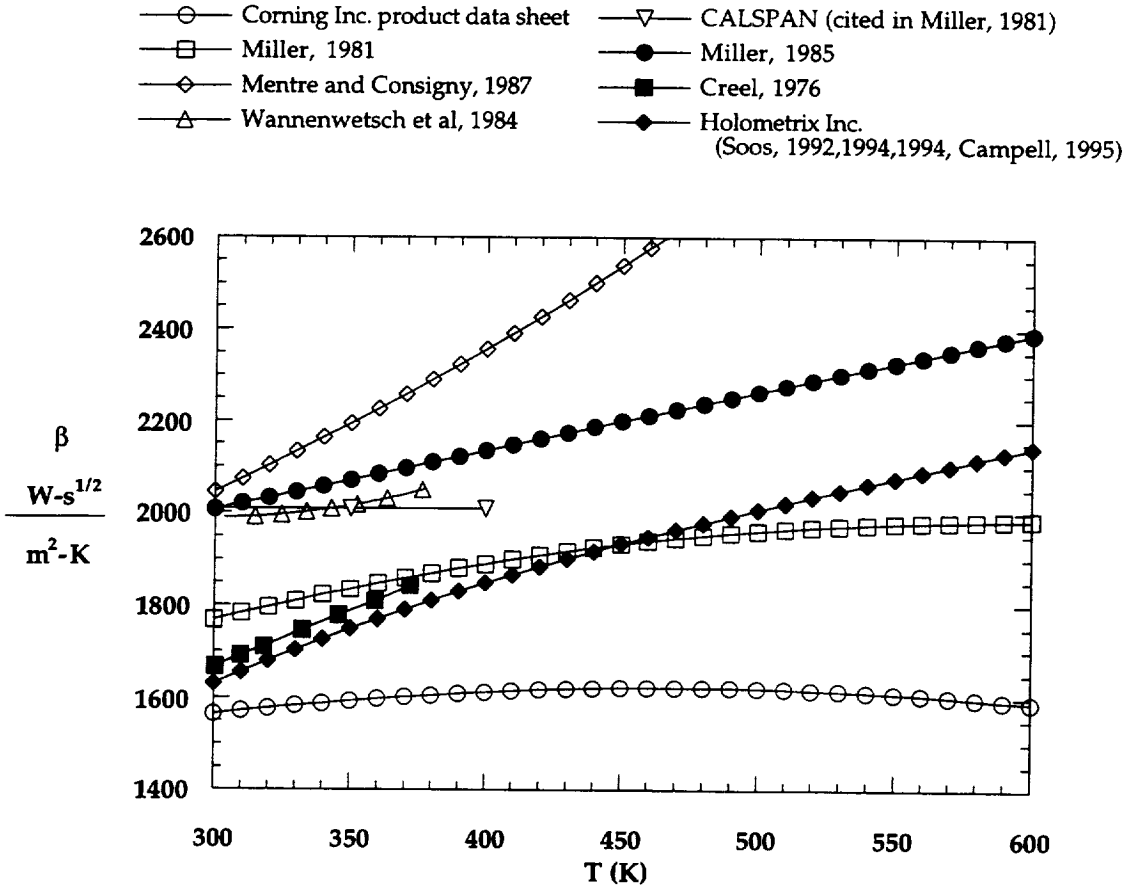

Figure C.1.1 Comparison of Available Data for Macor Thermal Product

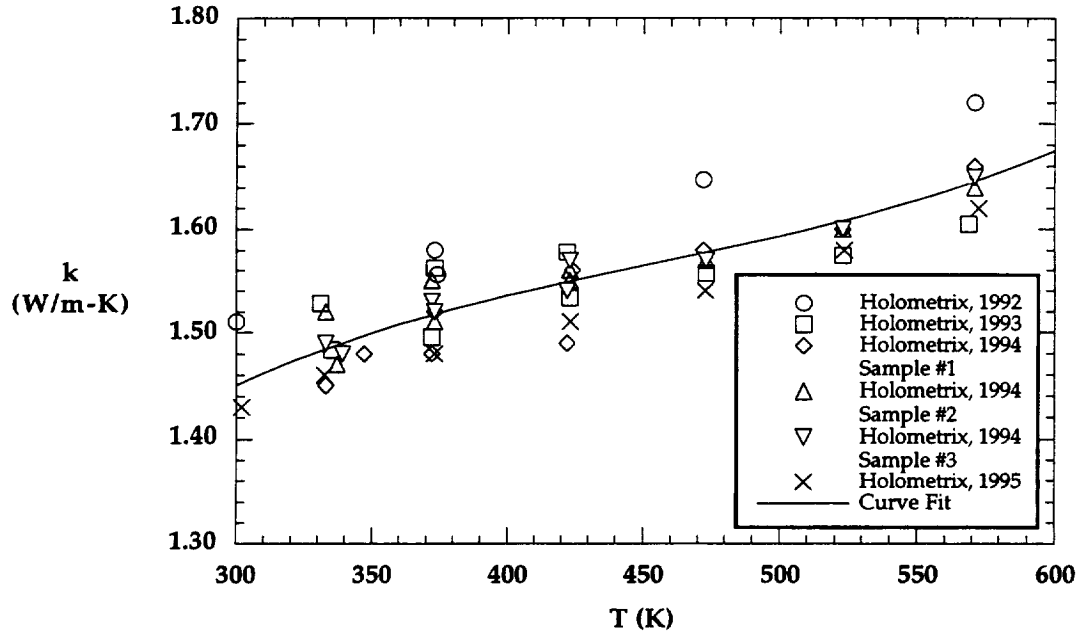

Figure C.1.2 Macor Thermal Conductivity Data from Holometrix

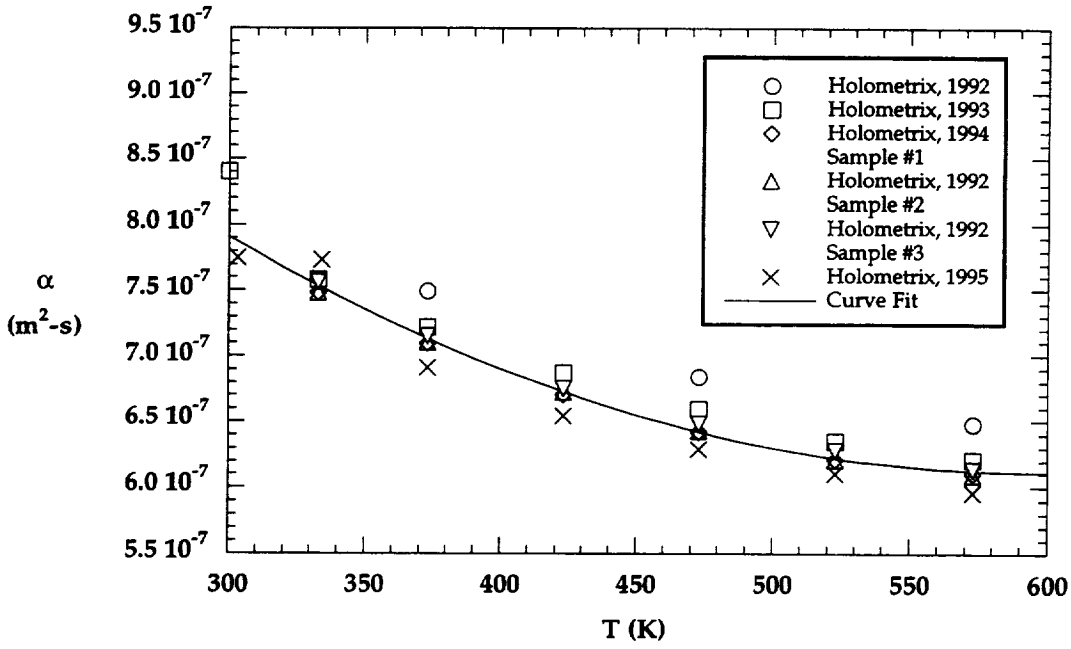

Figure C.1.3 Macor Thermal Diffusivity Data from Holometrix

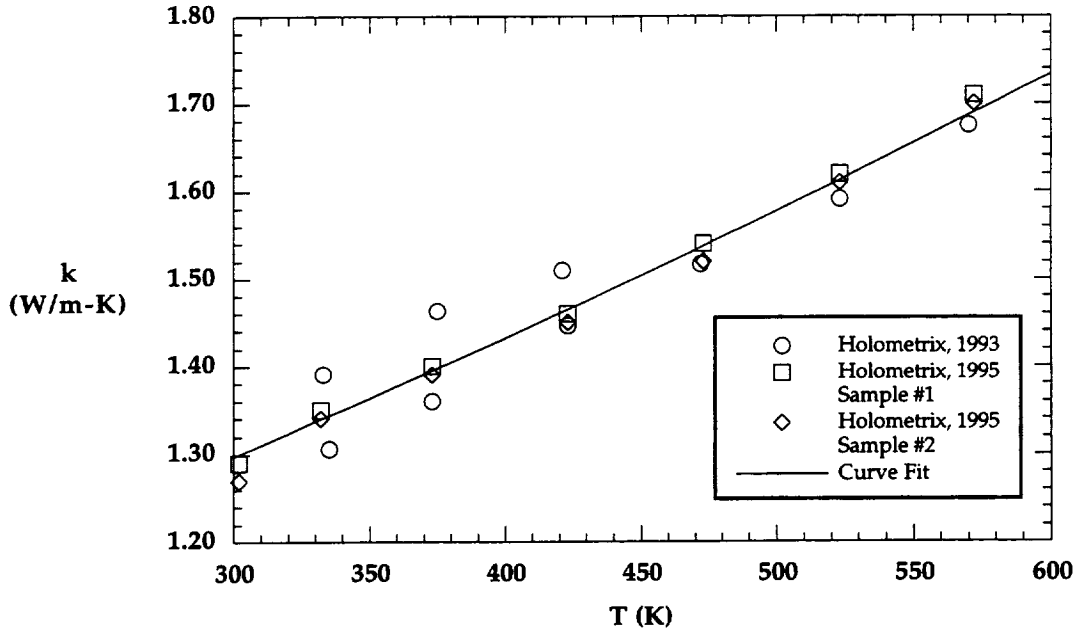

Figure C.1.4 Quartz Thermal Conductivity Data from Holometrix

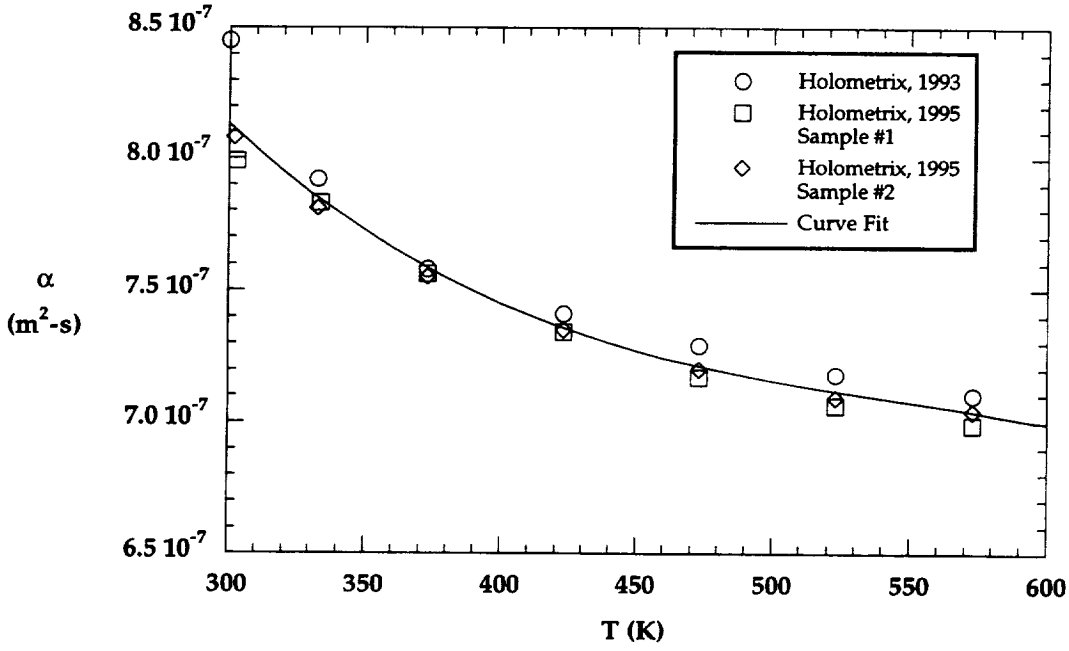

Figure C.1.5 Quartz Thermal Diffusivity Data from Holometrix

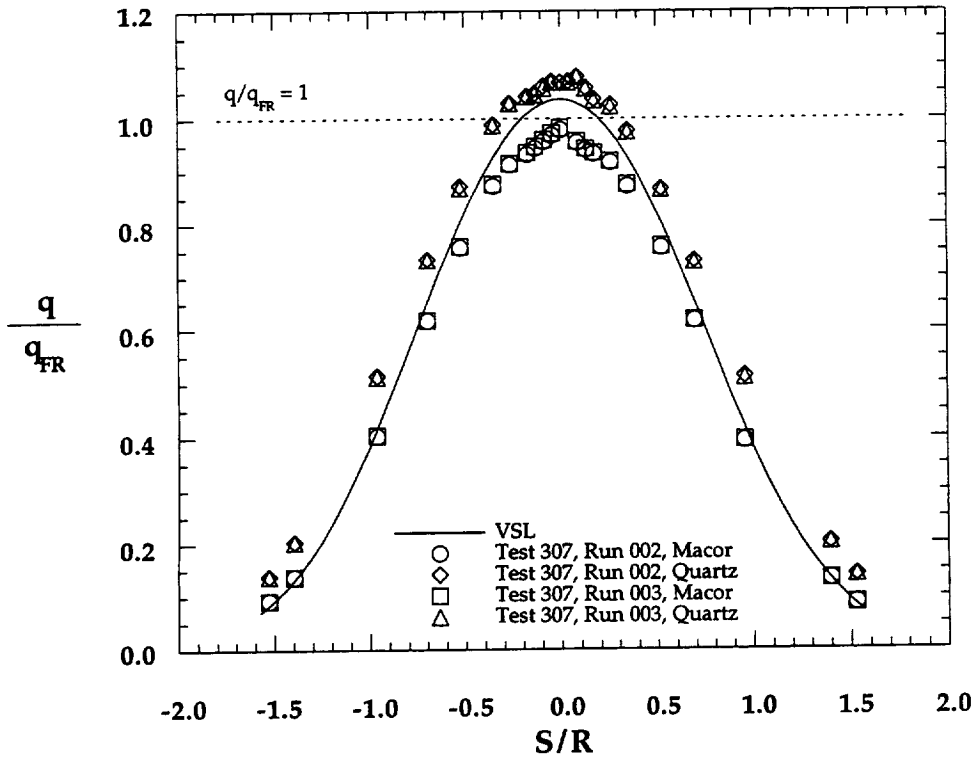

Figure C.1.6 Hemisphere Calibration Test Data, $Re_\infty = 0.5x10^6$ ft^{-1}

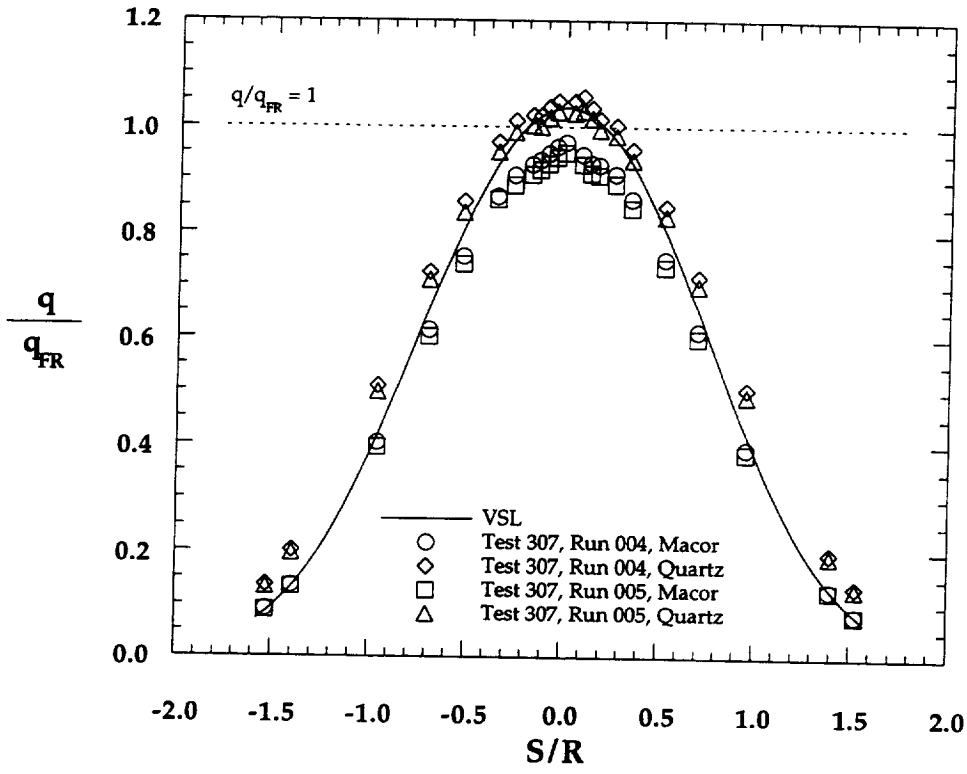

Figure C.1.7 Hemisphere Calibration Test Data, $Re_\infty = 1.0x10^6$ ft^{-1}

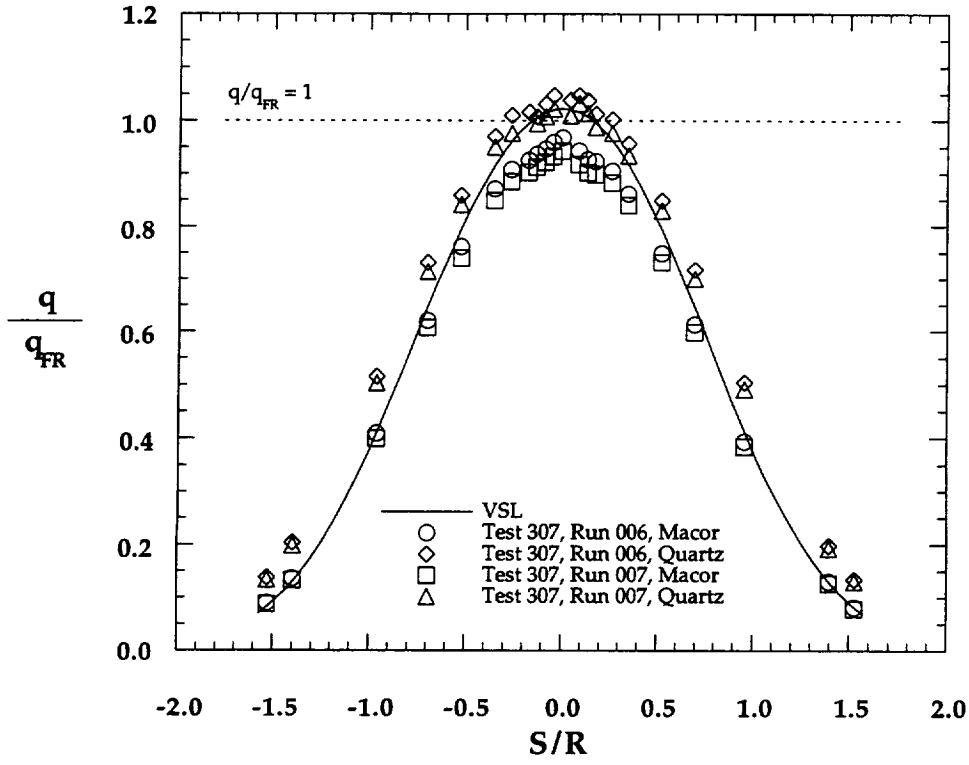

Figure C.1.8 Hemisphere Calibration Test Data, $Re_\infty = 2.0x10^6$ ft^{-1}

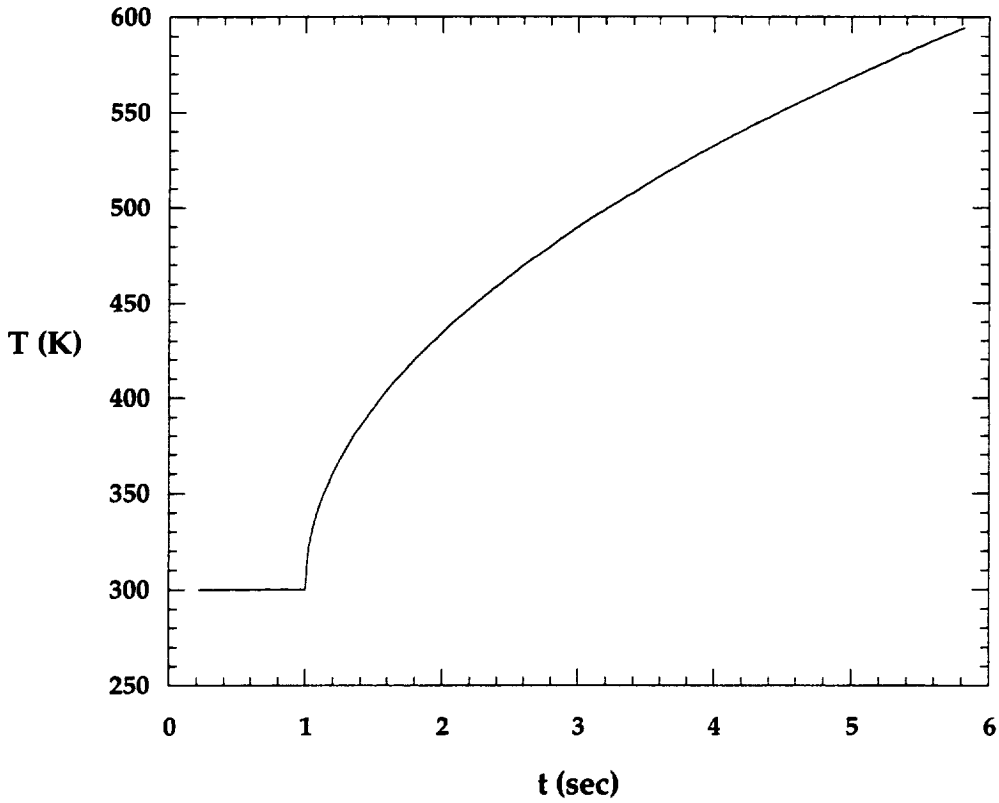

Figure C.1.9 Parabolic Temperature Time-History

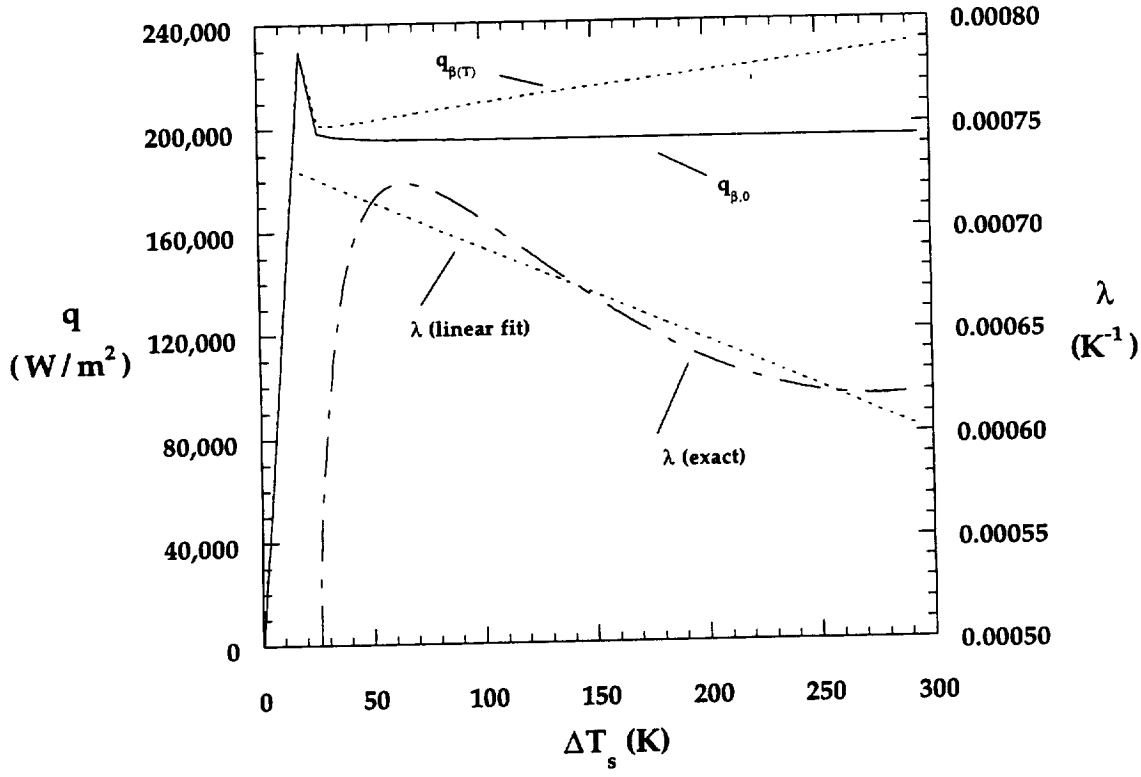

Figure C.1.10 Correction Factor Derivation

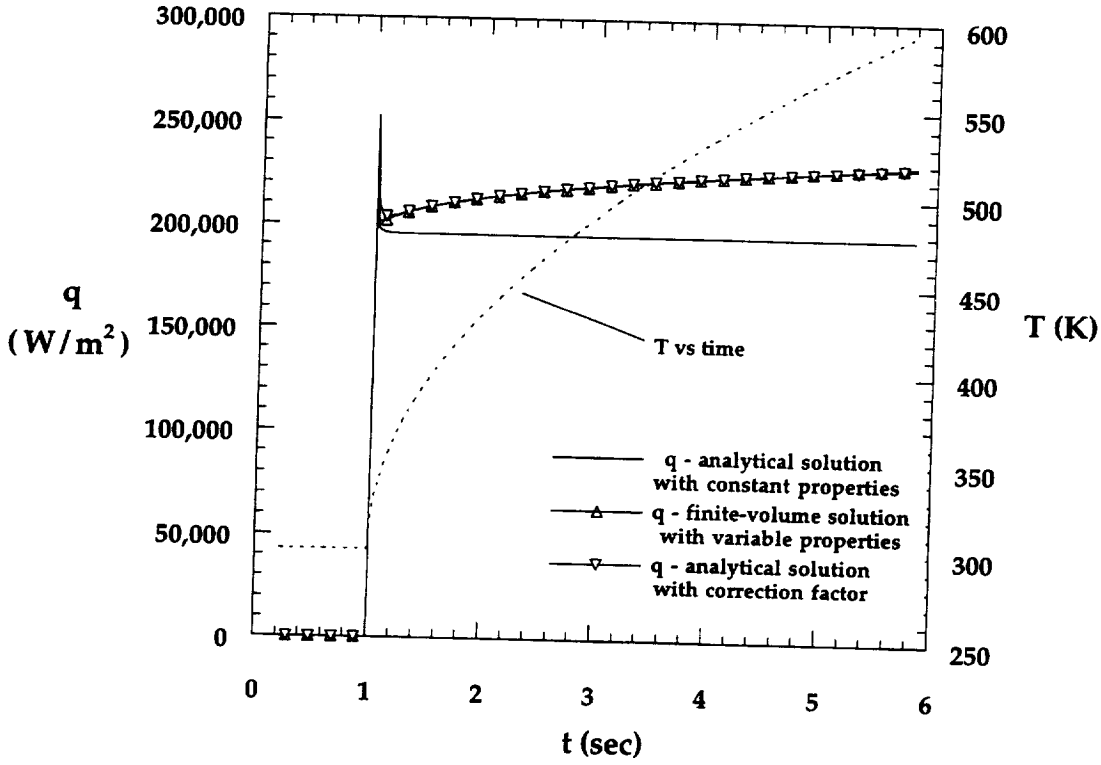

Figure C.1.11 Correction Factor Applied to Parabolic Temperature Time-History Data

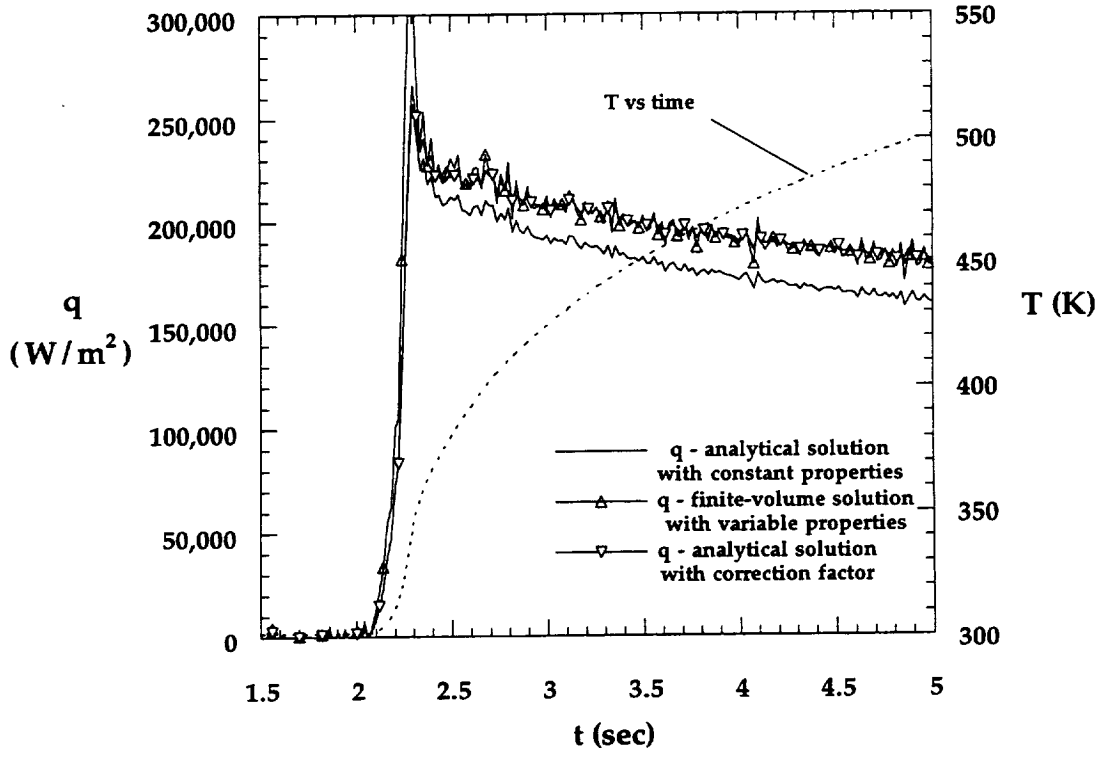

Figure C.1.12 Correction Factor Applied to Real Temperature Time-History Data

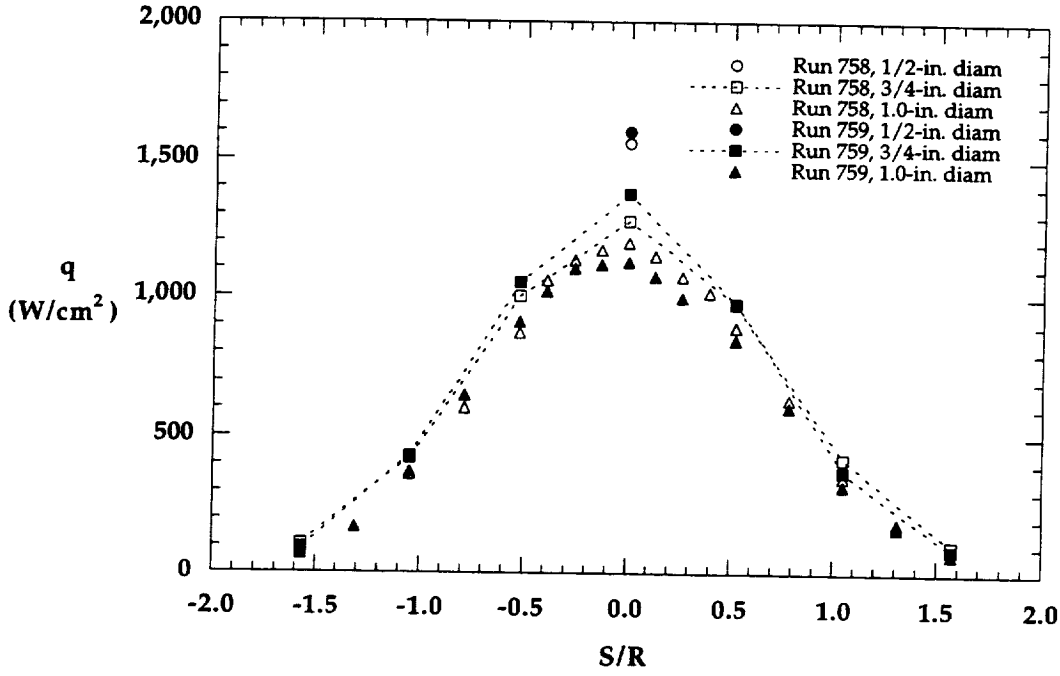

Figure C.2.1 HYPULSE Hemisphere Heating Data, He Tests

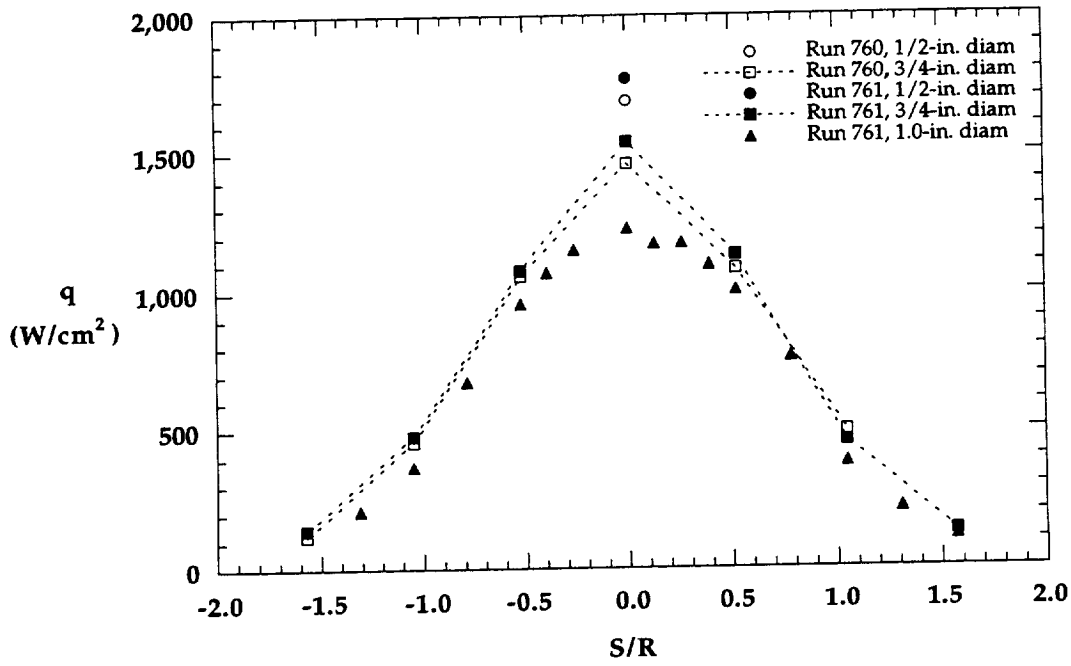

Figure C.2.2 HYPULSE Hemisphere Heating Data, Air Tests

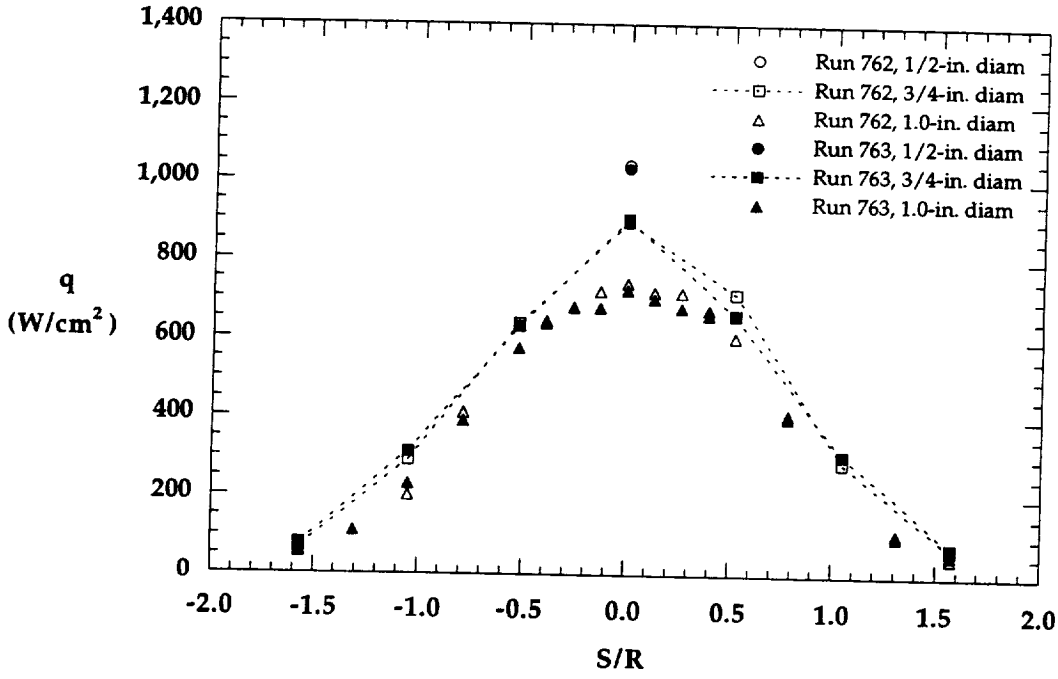

Figure C.2.3 HYPULSE Hemisphere Heating Data, CO_2 Tests

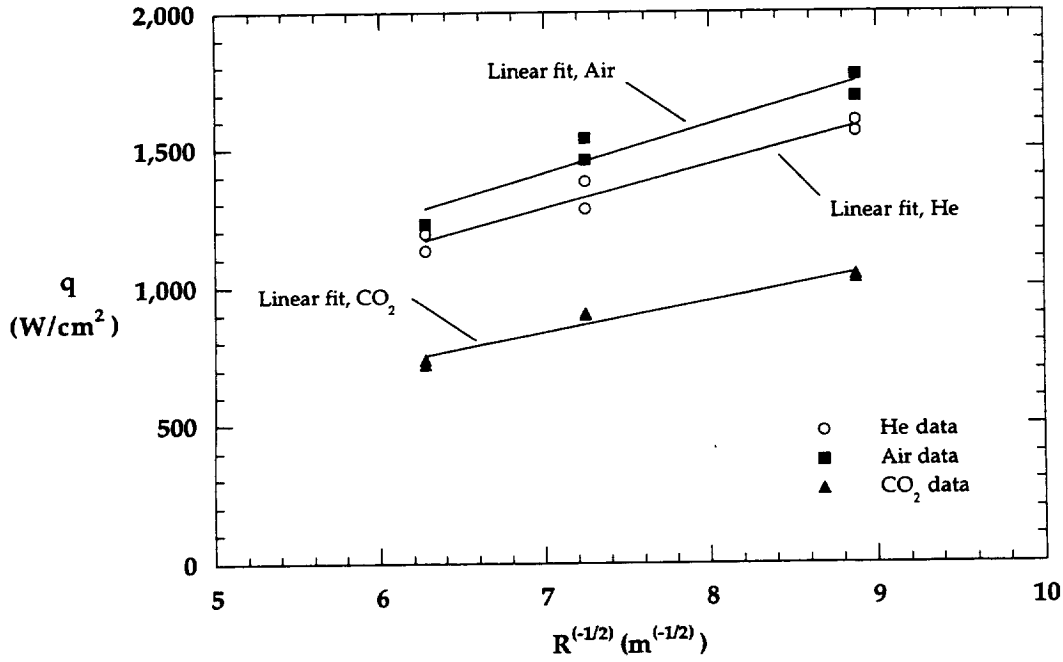

Figure C.2.4 Hemisphere Stagnation Point Heating vs $R^{-1/2}$

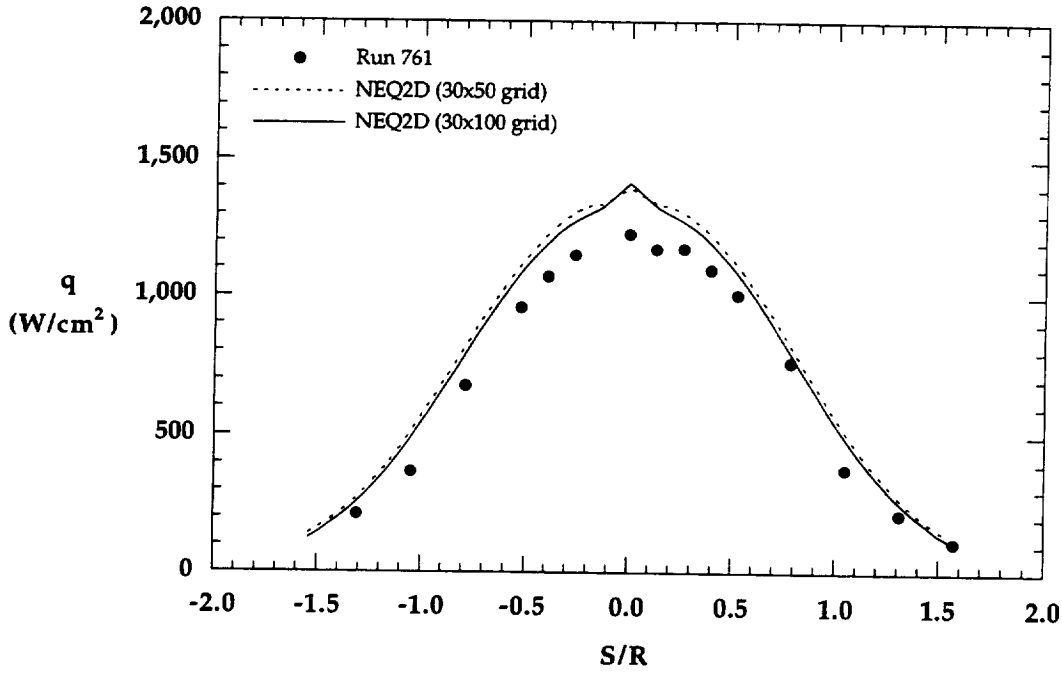

Figure C.2.5 Computed Heating Rates vs Experimental Data, Air Tests, 1-in. diam Hemisphere

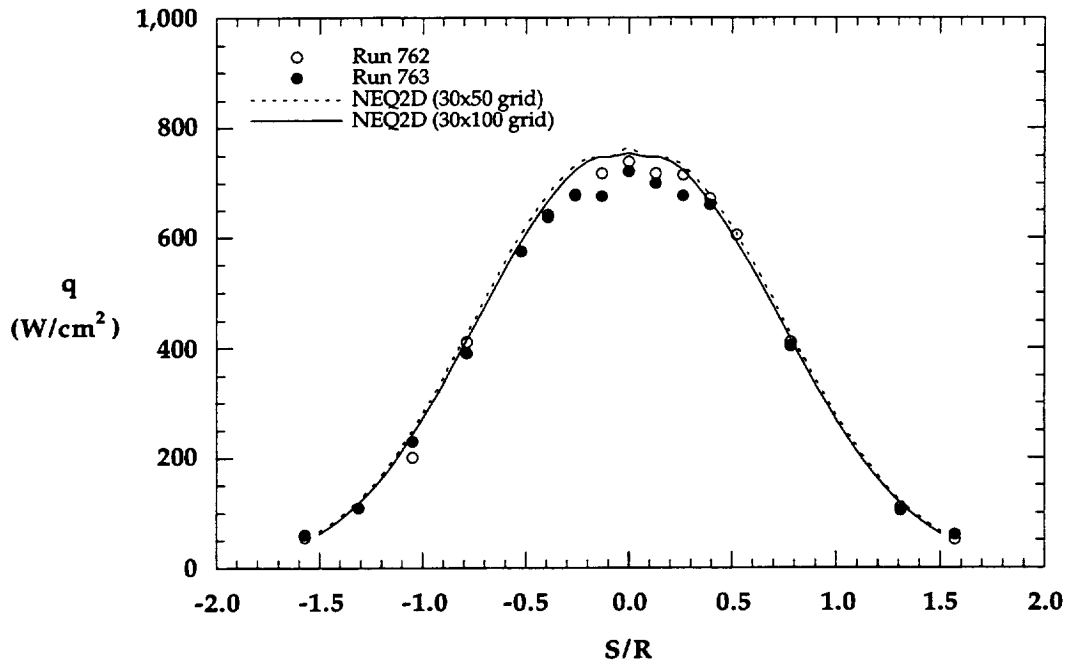

Figure C.2.6 Computed Heating Rates vs Experimental Data, CO_2 Tests, 1-in. diam Hemisphere

REPORT DOCUMENTATION PAGE

Form Approved
OMB No. 0704-0188

1. AGENCY USE ONLY (*Leave blank*)	2. REPORT DATE	3. REPORT TYPE AND DATES COVERED
	December 1996	Contractor Report

4. TITLE AND SUBTITLE
Experimental and Computational Aerothermodynamics of a Mars Entry Vehicle

5. FUNDING NUMBERS
G NAG1-1663
G NAGW-1331
WU 242-80-01-01

6. AUTHOR(S)
Brian R. Hollis

7. PERFORMING ORGANIZATION NAME(S) AND ADDRESS(ES)
North Carolina State University
Raleigh, North Carolina 27607

8. PERFORMING ORGANIZATION REPORT NUMBER

9. SPONSORING / MONITORING AGENCY NAME(S) AND ADDRESS(ES)
National Aeronautics and Space Administration
Langley Research Center
Hampton, VA 23681-0001

10. SPONSORING / MONITORING AGENCY REPORT NUMBER
NASA CR-201633

11. SUPPLEMENTARY NOTES
Langley Technical Monitor: Harris H. Hamilton

12a. DISTRIBUTION / AVAILABILITY STATEMENT
Unclassified-Unlimited
Subject Category 34

12b. DISTRIBUTION CODE

13. ABSTRACT (*Maximum 200 words*)

An aerothermodynamic database has been generated through both experimental testing and computational fluid dynamics simulations for a 70 deg sphere-cone configuration based on the NASA Mars Pathfinder entry vehicle. The aerothermodynamics of several related parametric configurations were also investigated. Experimental heat-transfer data were obtained at hypersonic test conditions in both a perfect gas air wind tunnel and in a hypervelocity, high-enthalpy expansion tube in which both air and carbon dioxide were employed as test gases. In these facilities, measurements were made with thin-film temperature-resistance gages on both the entry vehicle models and on the support stings of the models. Computational results for freestream conditions equivalent to those of the test facilities were generated using an axisymmetric/2D laminar Navier-Stokes solver with both perfect-gas and nonequilibrium thermochemical models. Forebody computational and experimental heating distributions agreed to within the experimental uncertainty for both the perfect-gas and high-enthalpy test conditions. In the wake, quantitative differences between experimental and computational heating distributions for the perfect-gas conditions indicated transition of the free shear layer near the reattachment point on the sting. For the high enthalpy cases, agreement to within, or slightly greater than, the experimental uncertainty was achieved in the wake except within the recirculation region, where further grid resolution appeared to be required. Comparisons between the perfect-gas and high-enthalpy results indicated that the wake remained laminar at the high-enthalpy test conditions, for which the Reynolds number was significantly lower than that of the perfect-gas conditions.

14. SUBJECT TERMS
entry vehicle, wake flow, computational fluid dynamics, wind tunnel, expansion tube, grid adaptation, aerothermodynamics, Mars

15. NUMBER OF PAGES
636

16. PRICE CODE
A99

17. SECURITY CLASSIFICATION OF REPORT	18. SECURITY CLASSIFICATION OF THIS PAGE	19. SECURITY CLASSIFICATION OF ABSTRACT	20. LIMITATION OF ABSTRACT
unclassified	unclassified	unclassified	unlimited